

Intelligent Mechatronic Systems

Rochdi Merzouki · Arun Kumar Samantaray
Pushparaj Mani Pathak
Belkacem Ould Bouamama

Intelligent Mechatronic Systems

Modeling, Control and Diagnosis

Rochdi Merzouki
Ecole Polytechnique de Lille
Université des Sciences et Technologies
de Lille (USTL)
Villeneuve D'Ascq CX
France

Pushparaj Mani Pathak
Department of Mechanical and Industrial
Engineering
Indian Institute of Technology
Roorkee
India

Arun Kumar Samantaray
Department of Mechanical Engineering
Indian Institute of Technology
Kharagpur
India

Belkacem Ould Bouamama
Ecole Polytechnique de Lille
Université des Sciences et Technologies
de Lille (USTL)
Villeneuve D'Ascq CX
France

ISBN 978-1-4471-4627-8 ISBN 978-1-4471-4628-5 (eBook)
DOI 10.1007/978-1-4471-4628-5
Springer London Heidelberg New York Dordrecht

Library of Congress Control Number: 2012950394

© Springer-Verlag London 2013

Phantom Omni © Copyright 2012 Sensable. All rights reserved. RobuCAR & Robosoft © ROBOSOFT 1985-2006 Khepera II robot © 2002–2012 K-Team Corporation. All Rights Reserved. © Numexia S.A.

This work is subject to copyright. All rights are reserved by the Publisher, whether the whole or part of the material is concerned, specifically the rights of translation, reprinting, reuse of illustrations, recitation, broadcasting, reproduction on microfilms or in any other physical way, and transmission or information storage and retrieval, electronic adaptation, computer software, or by similar or dissimilar methodology now known or hereafter developed. Exempted from this legal reservation are brief excerpts in connection with reviews or scholarly analysis or material supplied specifically for the purpose of being entered and executed on a computer system, for exclusive use by the purchaser of the work. Duplication of this publication or parts thereof is permitted only under the provisions of the Copyright Law of the Publisher's location, in its current version, and permission for use must always be obtained from Springer. Permissions for use may be obtained through RightsLink at the Copyright Clearance Center. Violations are liable to prosecution under the respective Copyright Law.

The use of general descriptive names, registered names, trademarks, service marks, etc. in this publication does not imply, even in the absence of a specific statement, that such names are exempt from the relevant protective laws and regulations and therefore free for general use.

While the advice and information in this book are believed to be true and accurate at the date of publication, neither the authors nor the editors nor the publisher can accept any legal responsibility for any errors or omissions that may be made. The publisher makes no warranty, express or implied, with respect to the material contained herein.

Printed on acid-free paper

Springer is part of Springer Science+Business Media (www.springer.com)

*To
Our families who have sacrificed a lot for
this book*

- A.K.S., P.M.P., R.M. and B.O.B.

Preface

Mechatronics systems are, inherently, multidisciplinary. These systems are composed of interacting subsystems or parts from different engineering disciplines requiring an integration of mechanical engineering, electrical engineering, electronics engineering, and control engineering. The interactions between different subsystems of a process are often very complex. Therefore, a concurrent design approach is needed for analysis of such systems. Moreover, design of proper control laws almost always requires a well-developed system model.

Various books have been written so far to address the above-mentioned issues in mechatronic system design. Most of these books use abstract mathematical models instead of a structured representation suitable for multidisciplinary systems. However, in our opinion, the choice of a proper modeling method, which is suitable for the analysis of the multidisciplinary system's behavior, control synthesis and at the same time, clearly exposes the interplay between various subsystems, is very important because it can greatly reduce the mechatronic system development time. This is the reason for using bond graph models in this book.

Bond graphs were introduced as early as 1959 by Professor Henry Paynter of the Massachusetts Institute of Technology, Cambridge, USA. Since then, application of bond graphs to various domains has seen rapid growth. Bond graph (BG) modeling has also been successfully applied to model various engineering systems. Furthermore, BG-based techniques have been developed for the analysis of structural control properties, sensor placements, fault diagnosis, system inversion, input–output decoupling, system identification, parameter estimation, model order reduction, robustness studies, and actuator sizing; to name a few. These recent developments in the field of systems and control engineering have been integrated in this book to embed machine intelligence into mechatronic systems.

One aim of this book is to present the in-depth state of the art of applications of bond graph modeling to mechatronics systems. This book arose from our individual experiences in research and in teaching spanning more than two decades.

During our professional lives we have had the opportunities to interact personally with many leading personalities who have made significant contributions to the fields covered in this book. Consequently, those interactions have shaped our research directions and motivated us to write this book.

From our teaching experiences as well as those of our colleagues, we understand that bond graph-based teachings of physical system modeling and model-based control are well appreciated by student communities because the methodologies are graphical, follow step-by-step approach to model building and more importantly, retain close relationship to the physical system so that mathematical complexities do not obscure the ability to analyze and reason intuitively. This book is written for the student and research communities who are concerned with the mechatronic systems and control field.

This book is a result of collaboration between a few Indian and French researchers. Individual chapters are either written by single researcher or two researchers. The first eight chapters of this book deal with general topics whereas the last six chapters deal with specialized applications. [Chapter 1](#) written by Pathak introduces general concepts in mechatronics. [Chapter 2](#) written by Ould Bouamama and Samantaray builds the foundation of this book. It introduces bond graph modeling tool for multi-energy domain system modeling. [Chapter 3](#) written by Pathak and Samantaray, deals with modeling of sensors, actuators, and electronic circuits. [Chapter 4](#) written by Samantaray discusses physical model-based control. [Chapter 5](#) authored by Samantaray deals with modeling of various mechanical (rigid and flexible body) systems and micro-electro-mechanical systems (MEMS). [Chapter 6](#), again written by Samantaray, exclusively discusses modeling of vehicle mechatronic systems. Ould Bouamama and Samantaray introduce model-based fault diagnosis approach in the [Chap. 7](#). [Chapter 8](#), written by Pathak, gives introduction to robotic manipulators. Pathak then discusses robust overwhelming control and impedance control in [Chap. 9](#) and applies those to space robots in [Chap. 10](#). Merzouki introduces the concept of intelligent transportation systems in [Chap. 11](#) where model-based control and diagnosis has been integrated in real-life applications. In [Chap. 12](#), Merzouki discusses telediagnosis applications. Finally, in [Chap. 13](#), Samantaray discusses a vehicle simulator system as a virtual reality application.

Compilation of this book has been coordinated by Samantaray. He thanks his coauthors and research students for extending all the support he needed. Samantaray especially thanks his ex-students Dr. Tarun Kumar Bera and Dr. P. Vijay for helping with the content and figures. Pathak thanks his masters students Balkrishna V. Jagdale, Pushpendra Kumar, Jatin Mania, Rishikesh Rathee, Ganesh Kumar K., Rohit Khandekar, Sonam and Ph.D. students Amit Kumar, V. L. Krishnan,

Haresh Patolia, Mihir Sutar, and Mehul Gor for their help in drawing the figures and proofreading of the manuscript. We also thankfully acknowledge the critical inputs from Professors R. Bhattacharyya, A. Mukherjee, and R. Karmakar of IIT Kharagpur.

Kharagpur, July 2012
Roorkee
Lille

Arun Kumar Samantaray
Pushparaj Mani Pathak
Rochdi Merzouki
Belkacem Ould Bouamama

Contents

Part I Theory

1	Elements of Mechatronic Systems	3
1.1	Introduction	3
1.2	Actuators	4
1.3	Sensors	4
1.4	Input Signal Conditioning and Interfacing	5
1.5	Digital Control Architecture	5
1.6	Output Signal Conditioning and Interfacing	6
1.7	Displays	6
1.8	Intelligent System	6
1.9	Reconfigurable Systems	6
1.10	Autonomous Supervisory Control	7
1.11	Artificial Intelligence	7
1.12	Knowledgebase	8
1.13	Decision Support System	10
1.14	Diagnosis	10
1.15	Fault, Failure, and Safety	10
1.16	Fault Tolerance	11
1.17	Examples of Mechatronic Systems	11
	1.17.1 A Copy Machine	11
	1.17.2 Walking Robot	12
1.18	Why Mechatronics System Simulation?	13
1.19	Future of Mechatronics	14
	References	14
2	Bond Graph Modeling of Mechatronic Systems	15
2.1	Why Bond Graph for Mechatronics?	15
2.2	Bond Graph for Modeling, Control, and Diagnosis	16
2.3	Bond Graph Modeling Theory	17
	2.3.1 Concepts and Definitions	17

2.3.2	Power as a Unified Coordinate System	18
2.3.3	Power Variables	19
2.3.4	Energy Variables	20
2.3.5	Pseudo Bond Graph	21
2.3.6	Analogy of Energy Variables	23
2.4	Bond Graph Elements	23
2.4.1	One-Port Passive Elements	25
2.4.2	Active Elements	31
2.4.3	Junctions	32
2.4.4	Two-Port Elements: Transformer and Gyrator	34
2.4.5	Information Bond	37
2.5	Causality	42
2.5.1	Sequential Causality Assignment Procedure (SCAP)	44
2.5.2	Derivative Causality and Its Implications	46
2.5.3	Bicausal Bond Graphs	49
2.6	Causal Path	50
2.6.1	Different Types of Causal Paths	50
2.6.2	Closed Causal Paths	52
2.6.3	Causal Path Gain	52
2.7	State-Space Equations	55
2.7.1	State Equations	56
2.7.2	Properties of State Variables	56
2.7.3	Steps for Equation Derivation	57
2.7.4	Example: State-Space Equation of an Electrical System	57
2.7.5	Deriving Block Diagram Model from Bond Graph Model	59
2.7.6	Model Structure	60
2.8	The Art of Constructing Bond Graph Models	62
2.8.1	A Note on Power Directions	62
2.8.2	Simplification Rules	63
2.8.3	Bond Graphs for Electrical Systems	65
2.8.4	Bond Graphs for Equivalent Networks	68
2.8.5	Bond Graphs for Mechanical Systems	69
2.8.6	Bond Graphs for Multi-Energy Domain Systems	77
2.8.7	Nonlinear Models	79
2.9	Multiport Field Elements	82
2.9.1	RS Element	82
2.9.2	Multiport Elements in Process Engineering	83
2.9.3	C-Field	86
2.9.4	I-Field	88
2.9.5	IC-Field	91
2.9.6	R-Field	92

2.9.7	Vector Junction	93
2.9.8	Multiport Transformers and Gytrators	93
2.9.9	Vector Bond Graph for Rigid-Body Dynamics.	95
2.10	Bond Graph Modeling of Uncertain Systems	97
2.10.1	Linear Fractional Transformation (LFT)	97
2.10.2	LFT Modeling of Bond Graph Elements	98
2.11	Automated Modeling: An Application Example	100
2.11.1	Bond Graph Software	100
2.11.2	Description of the System	102
2.11.3	Word Bond Graph	102
2.11.4	Bond Graph Model	103
2.11.5	Simulation Block Diagram	104
2.11.6	State Equations and Simulation	105
	References	107
3	Modeling of Actuators, Sensors, and Electronic Circuits	111
3.1	Models of Actuators	111
3.1.1	Models of Mechanical Actuators	112
3.1.2	Models of Electrical Actuators.	130
3.1.3	Models of Hydraulic Servo-Actuator.	151
3.1.4	Model of Pneumatic Actuators.	153
3.2	Modeling of Sensors	162
3.2.1	Performance Terminology	163
3.2.2	Static and Dynamic Characteristics.	164
3.2.3	Classification of Sensors	164
3.2.4	Selection Criteria	165
3.2.5	Activation of Bonds	165
3.2.6	Power Associated with Activated Bonds	166
3.2.7	Modeling Mechatronic Systems with Activated Bonds	166
3.2.8	Position Sensors	168
3.2.9	Velocity Sensors	174
3.2.10	Acceleration Sensors.	175
3.2.11	Force and Pressure Sensors	177
3.3	Models of Electronic Circuit Components	180
3.3.1	Signal Conditioning	180
3.3.2	Operational Amplifiers	181
3.3.3	Op-Amp Circuits	187
3.3.4	Semiconductor Diode	196
3.3.5	Transistor	205
3.4	Conclusions	227
	References	229

4	Physical Model-Based Control	231
4.1	Introduction	231
4.2	Model Conversions	232
4.2.1	Construction of Signal Flow Graph	232
4.2.2	Transfer Function from State-Space Models	238
4.2.3	Block Diagram Models	240
4.3	Causal Paths	244
4.3.1	Transfer Function from Causal Paths	245
4.3.2	Closed-Loop Transfer Function	246
4.4	Controller and Observer Design	251
4.4.1	Pole Placement	252
4.4.2	Controllability and Observability	253
4.5	Structural Analysis of Control Properties	256
4.5.1	Structural Rank	259
4.5.2	Structural Controllability	262
4.5.3	Structural Observability	264
4.5.4	Infinite Zeroes and Relative Degree	266
4.5.5	Zero Dynamics	272
4.6	Discrete-Time Models	274
4.7	Actuator Sizing	276
	References	279
5	Rigid Body, Flexible Body, and Micro Electromechanical Systems	281
5.1	Introduction	281
5.2	Planar Multibody Systems	282
5.2.1	Bond Graph Modeling of Flexible Two-Force Members	282
5.2.2	Model of Rigid Planar Links	284
5.2.3	Modeling Revolute Joints	285
5.2.4	Detailed Model of Revolute Joint	287
5.2.5	Model of the Slider Component	291
5.2.6	Case Study-I: Rapson Slide	294
5.2.7	Case Study-II: A Seven-Body Mechanism	297
5.2.8	Modeling Hydraulic Actuators	300
5.3	Spatial Multibody Systems	306
5.3.1	Noninertial Reference Frame	306
5.3.2	Euler Angles	307
5.3.3	Coordinate Transformation	310
5.3.4	Transformation of Angular Velocities	312
5.3.5	Model of a Spinning Top	315
5.3.6	Model of Three-Dimensional Prismatic Joint	318
5.4	Flexible Body Systems	321
5.4.1	Beams	322
5.4.2	Euler–Bernoulli Beam Model	322

- 5.4.3 Beam Columns. 328
- 5.4.4 Rayleigh Beam Model 331
- 5.4.5 Centrifugal Stiffening 337
- 5.4.6 Beams Made of Two Layers 340
- 5.4.7 Bimetallic Strip 341
- 5.4.8 Piezoelectric Effect. 345
- 5.4.9 MEMS Devices 360
- 5.4.10 Micromirrors 360
- 5.4.11 Micromotors 364
- 5.4.12 Energy Harvesting System. 370
- 5.4.13 Micropumps. 372
- 5.4.14 Shape-Memory Alloys 376
- 5.4.15 A Note on Memristor and Memcapacitance. 387
- 5.5 Bearings and Rotors 393
 - 5.5.1 Rolling Element Bearings 393
 - 5.5.2 Journal Bearing 397
 - 5.5.3 Magnetic Bearing 402
 - 5.5.4 Source Interaction in Rotor Dynamics. 414
 - 5.5.5 Shape-Memory Alloy Based Control
of Passage Through Resonance 424
- References 427

Part II Advanced Topics and Applications

- 6 Vehicle Mechatronic Systems 437**
 - 6.1 Model of a Four Wheel Vehicle. 438
 - 6.1.1 Word Bond Graph Representation 439
 - 6.1.2 Tire Slip Forces and Moments 439
 - 6.1.3 Vehicle Body. 442
 - 6.1.4 Suspension System 444
 - 6.1.5 Wheels 444
 - 6.1.6 Steering System 446
 - 6.1.7 Slider-Crank System. 447
 - 6.1.8 Engine 449
 - 6.1.9 Gearbox 458
 - 6.1.10 Differential 459
 - 6.1.11 Transmission Line 462
 - 6.1.12 Engine Dynamics Simulation. 463
 - 6.1.13 Clutch. 466
 - 6.1.14 Integrated Four Wheel Vehicle Model 473
 - 6.1.15 Simulation Results for Four Wheel Model. 473
 - 6.2 Suspension Systems 475
 - 6.2.1 Passive Liquid-Spring Shock Absorber 477
 - 6.2.2 Active Suspensions. 483
 - 6.2.3 Semi-active Suspensions 492

- 6.3 Anti-Roll Bar and Ride Height Management 497
 - 6.3.1 Passive Anti-Roll Bar 498
 - 6.3.2 Active Anti-Roll and Ride Height Management System 499
- 6.4 Power Steering 501
 - 6.4.1 Drive-by-Wire System 501
 - 6.4.2 Integral Power Steering 501
 - 6.4.3 Differential-Type Power Steering 502
 - 6.4.4 Electric Power-Assisted Steering Model 504
- 6.5 Antilock Braking System 505
 - 6.5.1 Antilock Braking Algorithm 507
 - 6.5.2 Bicycle Vehicle Model 509
 - 6.5.3 ABS Performance Simulation 512
 - 6.5.4 ABS Performance While Braking and Maneuvering 513
 - 6.5.5 Sliding Mode ABS Control 514
- 6.6 Regenerative Braking System 517
 - 6.6.1 Regenerative Braking Algorithm 519
 - 6.6.2 Validation of Regenerative Braking 521
 - 6.6.3 Modified Full Vehicle Model 522
 - 6.6.4 Performance of SMC-Based ABS with Regeneration 523
- 6.7 Hybrid Vehicles 525
 - 6.7.1 Classification of Hybrid Vehicles 525
 - 6.7.2 Power-Split Device 526
- 6.8 Automatic Transmission 529
 - 6.8.1 Components of Automatic Transmission System 530
 - 6.8.2 Bond Graph Model of Automatic Transmission 532
 - 6.8.3 Torque Converter Model 533
 - 6.8.4 Gear Shift Logic and Transmission System Model 535
- 6.9 Fuel Cells 537
 - 6.9.1 Classification of Fuel Cells 538
 - 6.9.2 Solid Oxide Fuel Cell 539
 - 6.9.3 Chemical Equilibrium 540
 - 6.9.4 Bond Graph Model of Chemical Reaction Kinetics 541
 - 6.9.5 SOFC Modeling 544
 - 6.9.6 SOFC Control 562
 - 6.9.7 Proton Exchange Membrane Fuel Cell 564
 - 6.9.8 PEMFC Control 565
 - 6.9.9 PEMFC Bond Graph Model 567
- References 571

7	Model-Based Fault Diagnosis and Fault Tolerant Control	577
7.1	Introduction	577
7.2	Quantitative Fault Detection	580
7.2.1	Analytical Redundancy Relations	581
7.2.2	Fault Signature Matrix	583
7.2.3	Coherence Vector	583
7.3	Bond Graph Model-Based Diagnosis	584
7.4	Example Application: An Autonomous Vehicle	585
7.4.1	System Description	585
7.4.2	Bond Graph Model	587
7.4.3	Generation of Fault Indicators	589
7.4.4	Fault Isolation	591
7.4.5	Fault Accommodation Through Reconfiguration	592
7.4.6	Fault Tolerant Control	592
7.4.7	Simulation Results	593
7.5	Diagnosis of Uncertain Systems	595
7.5.1	LFT Bond Graphs for Robust FDI	596
7.5.2	Generation of Robust Residuals	597
7.5.3	Sensitivity Analysis	599
7.5.4	Application to a Mechatronic System	603
7.5.5	Robust FDI Procedure	605
7.5.6	Simulation Results	608
7.5.7	Experimental Results	611
7.6	Conclusion	612
	References	613
8	Introduction to Robotic Manipulators	619
8.1	Introduction	619
8.2	Types of Robots	620
8.3	Basic Terminology	620
8.4	Manipulator Transformations	622
8.4.1	Notations	623
8.4.2	Rotation	623
8.4.3	Translating Coordinate Frames	626
8.4.4	Homogeneous Transformation Matrices	627
8.5	D-H Parameters	629
8.5.1	Assigning Coordinate Frames	629
8.5.2	Special Cases	630
8.5.3	D-H Parameters	630
8.6	Manipulator Kinematics	632
8.6.1	Forward Kinematics	632
8.6.2	Inverse Kinematics	634

8.7	Linear and Rotational Frames in Rigid Bodies	636
8.7.1	Translational Motion of Rigid Bodies	636
8.7.2	Rotational Motion of Rigid Bodies	637
8.7.3	Velocity Propagation from Link to Link	639
8.7.4	Jacobian	640
8.8	Manipulator Dynamics	640
8.8.1	Lagrange Formulation	642
8.8.2	Newton–Euler Formulation	645
8.8.3	Bond Graph Modeling	645
8.9	Modeling of Flexible-Arm Manipulators	661
8.9.1	Beam Models	662
8.9.2	Euler–Bernoulli Formulation	662
8.10	Mechatronic Design and Control of a Planar Cooperative Robot	667
8.10.1	Trajectory Plots	667
8.10.2	Manipulator Dynamic Equation	668
8.10.3	Controller Design	669
8.10.4	Design of Cooperative Robot System	671
8.10.5	Controller Description	672
8.10.6	Trajectory Tracking	675
8.11	Haptic Robots	676
8.11.1	Working Principle of Haptic Device	677
8.11.2	Applications of Haptic Devices	679
8.11.3	Experiments with PHANTOM Omni Haptic Device	680
	References	682
9	Robust Overwhelming Control and Impedance Control	683
9.1	Introduction	683
9.2	Concept of Robust Overwhelming Control	683
9.3	Robust Controller for Terrestrial Manipulators	686
9.3.1	Case 1: Effort as a Reference Input	686
9.3.2	Case 2: Flow as a Reference Input	689
9.4	Robust Overwhelming Controller for Terrestrial Manipulator on a Flexible Foundation	691
9.5	Impedance Controller for Terrestrial Robots	694
9.5.1	Considerations for a Position-Force Controller for Ground Robots	694
9.5.2	A Robust Impedance Controller for Terrestrial Robot	695
9.6	Concept of Virtual Foundation	698
	References	701

10	Modeling and Control of Space Robots	703
10.1	Introduction	703
10.2	Space Robot as a Nonholonomic System.	707
10.3	Stationary Versus Space Robot’s Formulation	708
10.4	Mechanics of Space Robots	709
10.4.1	Notation	709
10.4.2	Assumptions	710
10.4.3	Space Vehicle Dynamics	710
10.4.4	Arm Dynamics	712
10.4.5	Free-Flying Robot Dynamics	714
10.5	Bond Graph Modeling of Space Robots	716
10.5.1	Modeling of a Two DOF Planar Space Robot	716
10.5.2	Object-Oriented Modeling of Space Robots	718
10.6	Trajectory Control of Space Robot	729
10.6.1	Robust Overwhelming Controller	730
10.6.2	A Free-Floating Space Manipulator	734
10.6.3	Simulation and Validation	735
10.7	Impedance Control of Space Robots	737
10.7.1	Introduction	737
10.7.2	Force Control by Impedance Control	739
10.7.3	Modeling of One Translational DOF Impedance Controller	740
10.7.4	Force Control of a Two DOF Planar Space Robot	750
10.7.5	Torque Control of a Two DOF Planar Space Robot	761
10.8	Conclusions	767
	References	767
11	Intelligent Transportation Systems	769
11.1	Introduction	769
11.2	Modeling of a Class of Intelligent Autonomous Vehicles	774
11.2.1	RobuCar’s Electric Vehicle Description	774
11.2.2	Word Bond Graph of RobuCar’s System.	779
11.2.3	Kinematic and Geometric Models.	780
11.3	Quarter Vehicle Model	782
11.3.1	Tire Modeling	784
11.3.2	Electromechanical Traction System	800
11.4	Dynamic Modeling of the Chassis	815
11.4.1	Longitudinal Dynamic Modeling	815
11.4.2	Lateral Dynamic Modeling	816
11.4.3	Yaw Dynamic Modeling	817
11.4.4	Suspension Dynamics Modeling.	818
11.4.5	Pitch Dynamics Modeling	824
11.4.6	Roll Dynamics Modeling.	826

11.5	Fault Detection and Isolation	828
11.5.1	ARRs Generation	828
11.5.2	Results of Co-Simulation.	831
11.6	Robust Diagnosis	834
11.6.1	Principle and Definitions.	834
11.6.2	LFT Bond Graph Model	836
11.6.3	Robust ARR's Generation	838
11.6.4	Results of Co-Simulation.	839
11.7	Fault Tolerant Control.	843
11.7.1	Objectives and Principle	843
11.7.2	Active Reconfiguration and Co-Simulation Results	846
11.8	Homogeneous Cooperation of Intelligent Autonomous Vehicles	852
11.8.1	Modeling of Homogeneous Train of Intelligent Autonomous Vehicles	852
11.8.2	Modeling of Operation Modes of Intelligent Transportation System.	854
11.8.3	Case Studies	858
11.8.4	Results of Co-Simulation.	863
11.9	Conclusion.	864
	References	865
12	Telediagnosis of Mechatronic Systems	869
12.1	Introduction	869
12.2	Examples.	870
12.2.1	Online Robot Supervision Using a Mobile Phone.	870
12.2.2	Cooperation Between Omnidirectional Robots	873
12.2.3	Intelligent Human–Robot Interaction	874
12.3	Fault Diagnosis in Networked Control System.	874
12.4	Hybrid Model-Based Fault Diagnosis in NCS: Application to Telerobotics	876
12.4.1	Network Part Modeling and Fault Diagnosis Observer.	876
12.4.2	Control System Modeling and Fault Diagnosis.	879
12.5	Application to Telerobotic System	882
12.5.1	Robot System Description	882
12.5.2	Word Bond Graph	883
12.5.3	Modeling and Fault Diagnosis of Serial Cable	885
12.5.4	Modeling and Fault Diagnosis of the Robot Part	888
12.6	Conclusion.	906
	References	907

- 13 Road Vehicle Driving Simulator** 909
 - 13.1 Human–Machine Interface 909
 - 13.2 Overwhelming Controller as a System Inversion Tool. 910
 - 13.3 Modeling of 3D Stewart Platform. 915
 - 13.3.1 3D Stewart Platform Model Without Leg Inertia 916
 - 13.3.2 3D Actuator Model. 918
 - 13.3.3 3D Stewart Platform Model with Leg Inertia. 921
 - 13.3.4 Inverse Model of 3D Stewart Platform 921
 - 13.4 Graphics Interface 921
 - 13.5 Stewart Platform for Vehicle Simulator. 926
 - 13.6 Results of Test Drive of Driving Simulator 928
 - 13.7 Conclusions 931
 - References 933

- Index** 935

Abbreviations

3-D	Three Dimensional
ABS	Antilock Braking System
AC	Alternating Current
A/D	Analog to Digital
AFC	Alkaline Fuel Cell
AFM	Atomic Force Microscope
AFTC	Active Fault Tolerant Control
AGV	Automated Guided Vehicle
AI	Artificial Intelligence
AMB	Active Magnetic Bearing
ANN	Artificial Neural Network
API	Application Program Interface
APV	Automated Passenger Vehicle
ARR	Analytical Redundancy Relation
AU	Air Utilization
AUV	Autonomous Underwater Vehicle
AVP	Angular Velocity Propagation
BD	Block Diagram
BDC	Bottom Dead Center
BG	Bond Graph
BJT	Bipolar Junction Transistor
CAD	Computer Aided Design
CAM	Computer Aided Manufacturing
CETF	Coupling Element for Thermo-Fluids
CFD	Computational Fluid Dynamics
CG	Center of Gravity
CM	Center of Mass
CMOS	Complementary Metal–Oxide-Semiconductor
COM	Serial Communication Physical Interface
CPU	Central Processing Unit
CR	Control Reconfigurability

CTE	Coefficient of Thermal Expansion
CTF	Coordinate Transformation
CV	Control Volume
CVT	Continuously Variable Transmission
D/A	Digital to Analog
DB	DataBase
DBG	Diagnostic Bond Graph
DC	Direct Current
DCE	Data Circuit-terminating Equipment
DH	Denavit-Hartenberg
DI	Detectability Index
DI	De-ionize
DLP	Digital Light Processing
DMD	Digital Micromirror Device
DOF	Degrees of Freedom
DSS	Decision Support System
DTE	Data Terminal Equipment
EAP	Electro-active Polymer
EATF	Euler Angle Transformation
ECASS	Electronically Controlled Active Suspension System
ECM	Electrochemical
ECU	Electronic Control Unit
EIS	Electrochemical Impedance Spectroscopy
EJS	Euler Junction Structure
EJST	Euler Junction Structure for Translation
EMF	Electromotive Force
ENV	Environment
EOM	Equations of Motion
EPAS	Electric Power Assisted Steering
FC	Flow Controller
FDD	Fault Detection and Diagnosis
FDI	Fault Detection and Isolation
FE	Finite Element
FEM	Finite Element Modeling
FET	Field Effect Transistor
FFT	Fast Fourier Transform
FSM	Fault Signature Matrix
FTC	Fault Tolerant Control
FU	Fuel Utilization
GDI	Graphics Device Interface
GLUT	Graphic Library Utility Toolkit
GPS	Global Positioning System
GSM	Global System for Mobile Communications
GUI	Graphical User Interface
HCCI	Homogeneous Charge Compression Ignition

HDAPI	Haptic Device Application Programming Interface
HEV	Hybrid Electric Vehicle
HILS	Hardware-in-the-Loop Simulation
HLAPI	Haptic Library Application Programming Interface
HSD	Hybrid Synergy Drive
HX	Heat eXchanger
IAV	Intelligent Autonomous Vehicle
IC	Integrated Circuit
IC	Internal Combustion
IM	Induction Motor
I/O	Input–Output
IR	Infrared
ISC	Inverted-Series Connected
ISM	Inertial Sliding Motion
ITS	Intelligent Transportation System
JFET	Junction Field Effect Transistor
KB	KnowledgeBase
KE	Kinetic Energy
KERS	Kinetic Energy Recovery System
LDR	Light Dependent Diode
LED	Light Emitting Diode
LFT	Linear Fractional Transformation
L.H.S.	Left Hand Side
LHV	Lower Heating Value
LMI	Linear Matrix Inequality
LQ	Linear Quadratic
LQR	Linear Quadratic Regulator
LSM	Lanthanum Strontium Manganite
LTI	Linear Time Invariant
LVP	Linear Velocity Propagation
MCFC	Molten Carbonate Fuel Cell
MEA	Membrane Electrode Assembly
MEMS	Micro-Electromechanical System
MHD	Magnetohydrodynamic
MI	Moment of Inertia
MIMO	Multi-Input Multi-Output
MMF	Magnetomotive Force
MMN	Memory Neural Network
MMV	Matrix Manifold and Valve System
MOSFET	Metal–Oxide–Semiconductor Field-Effect Transistor
MR	Magneto-Rheological
MRI	Magnetic Resonance Imaging
MVD	Matrix Vasoconstriction Device
NASA	National Aeronautics and Space Administration
NBG	Neural Bond Graph

NCS	Networked Control System
NDT	Non-Destructive Testing
Nitinol	Nickel Titanium Naval Ordnance Laboratories
NLS	Non-linear Least Squares
NTU	Number of Transfer Units
ODE	Ordinary Differential Equation
OM	Operating Mode
OOM	Object Oriented Modeling
Op-Amp	Operational Amplifier
OU	Oxygen Utilization
PAFC	Phosphoric Acid Fuel Cell
PAS	Power Assisted Steering
PBI	Polybenzimidazole
PDE	Partial Differential Equation
PE	Potential Energy
PEMFC	Proton Exchange Membrane Fuel Cell
PFTC	Passive Fault Tolerant Control
PI	Proportional and Integral
PIC	Peripheral Interface Controller
PID	Proportional, Integral and Derivative
P&ID	Process and Instrumentation Diagram
PLC	Programmable Logic Controller
PSD	Power Split Device
P-V	Pressure–Volume
PWM	Pulse Width Modulation
PZT	Lead Zirconate Titanate
RAMS	Reliability, Availability, Maintainability and Safety
RCS	Reaction Control System
R.H.S.	Right Hand Side
RIA	Robot Institute of America
RL	Resistance and Inductance
RLC	Resistance, Inductance and Capacitance
ROC	Robust Overwhelming Controller
RPY	Roll, Pitch and Yaw
RS	Resistance Source/Sink
RTD	Resistance Thermal Device
SCAP	Sequential Causality Assignment Procedure
SFG	Signal Flow Graph
SILS	Software-In-the-Loop Simulation
SISO	Single-Input Single-Output
SLAM	Simultaneous Localization And Mapping
SMA	Shape Memory Alloy
SMC	Sliding Mode Control
SNR	Signal to Noise Ratio
SOC	State of Charge

SOFC	Solid Oxide Fuel Cell
SPICE	Simulation Program with Integrated Circuit Emphasis
SPST	Single Pole Single Through
SS	Source Sensor
STM	Scanning Tunneling Microscope
SWT	Stationary Wavelet Transform
TCG	Temporal Causal Graph
TCP/IP	Transmission Control Protocol and Internet Protocol
TDC	Top Dead Center
TPB	Triple Phase Boundary
TTL	Time to live, limit on data lifespan in a network
TTT	Time-Temperature-Transformation
USB	Universal Serial Bus
USOM	User Selected Operating Mode
UV-LIGA	Lithography, Electroplating, and Molding with Ultraviolet Light
V8	Eight cylinders mounted on crankcase in two banks of four cylinders
V2I	Vehicle-to-Infrastructure
V-I	Voltage-Current
V2V	Vehicle-to-Vehicle
VSC	Vehicle Stability Control
Wifi	Wireless local area network (WLAN) device with IEEE 802.11 standard
Wii	Home video game console by Nintendo
Wiimote	Primary remote controller of Wii console
YSZ	Yttria Stabilized Zirconia
ZCP	Zero-Order Causal Path
ZOH	Zero-Order Hold

Part I

Theory

“The important thing in science is not so much to obtain new facts as to discover new ways of thinking about them.”

–William Lawrence Bragg

This part gives an introduction to mechatronic systems and their modeling through bond graph tool. The first chapter introduces general concepts related to mechatronic systems. In the second chapter, we introduce bond graph modeling method as the multi-energy domain modeling tool. Bond graph modeling is used throughout this book as a common tool for system modeling, simulation, and control system design. Several examples of modeling mechanical, electrical, and electromechanical systems are considered and their behavioral equations are derived from causal bond graph models for formal model simulation.

Various types of actuators, sensors, electronic devices and analog electronic circuits are modeled in the third chapter. The fourth chapter discusses conversion of bond graph models into other forms of modeling like signal flow graph, transfer function, block diagram and state space equation models. Furthermore, the graph theoretic properties from causal bond graph models are exploited to derive structural control properties like controllability, observability, zero dynamics, etc.

The fifth chapter deals with modeling and design of complex mechatronics system components. Basic concepts in rigid body and flexible body mechanics, thermodynamics, hydraulics, metallurgy, and electromagnetism are recalled to lay the foundations of this chapter. This chapter considers modeling of several micro electro-mechanical systems (MEMS) like micro motors, micro pumps, wet shape memory alloy (SMA) actuator, and piezoelectric sensors and actuators.

Chapter 1

Elements of Mechatronic Systems

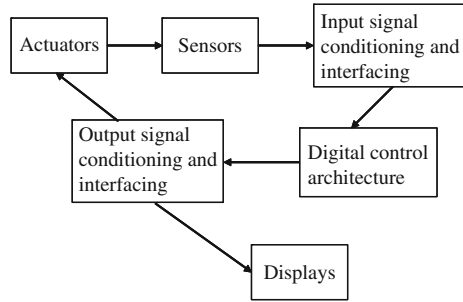
1.1 Introduction

The word mechatronics is composed of “mecha” from mechanism and the “tronics” from electronics. It is the synergistic integration of mechanical engineering, with electronics and intelligent computer control in the design and manufacturing of industrial products and processes. Mechatronics involves:

- Implementing electronics control in a mechanical system.
- Enhancing existing mechanical design with intelligent control.
- Replacing mechanical component with an electronic solution.

The growth of mechatronic systems has been fuelled by the growth in the constituent areas. Advancements in traditional disciplines has also fuelled the growth of mechatronics systems by providing technologies. For example, the invention of the microprocessor had effected a lot on the redesign of mechanical systems and design of new mechatronics systems. We can recall the spring-driven table clocks. These have been replaced by microprocessor-based table clocks. There are many examples of intelligent systems in all walks of life, including smart home appliances such as dishwashers, vacuum cleaners, microwaves, and wireless network-enabled devices. However it is the automobile market which has been the motivation for the development of mechatronic systems. Before we move further let us see the principal mechatronic components. The mechatronic components essentially consist of actuators, sensors, input signal conditioning and interfacing unit, digital control architecture, output signal conditioning and interfacing, and displays. The signal flows among these elements is shown in Fig. 1.1. In the following sections, we discuss about some of these mechatronic components and the issues involved in mechatronic system design and implementation.

Fig. 1.1 Various elements of a mechatronic system



1.2 Actuators

Actuators are mechanical devices for moving or controlling something. These are responsible for transformation of output of a microprocessor into a controlling action on machine or device. For example electrical outputs of controller transforms into linear motion of a load or say electrical output of controller transforms into an action which controls the amount of liquid passing along a pipe. The actuators can be classified as

- Electric Motors and Drives: These actuators transform electrical energy into mechanical energy. There are various types of electric actuators, such as
 - DC Motors
 - AC Motors
 - Linear Motors
 - Stepper Motors
- Hydraulic Drives
- Pneumatic Drives
- Internal Combustion hybrids
- Actuators of the future.

1.3 Sensors

Sensors are elements of a mechatronic system which produce signals relating to the quantities being measured. Let us take an example of electrical resistance thermometer. The quantity being measured here is temperature. The sensor transforms it into change of resistance of the sensor material. Examples of sensors include switches, potentiometers, thermocouples, strain gauges, digital encoders, and accelerometers and micro-electromechanical systems.

A transducer is an element that when subjected to some physical change experiences a related change. Thus we can say that sensors are transducers.

1.4 Input Signal Conditioning and Interfacing

An important question is why do we require signal conditioning? The simple answer is because we want to feed the sensor data to a microprocessor. The signal conditioning process provides protection; it ensures that we get the signal to be of right type and of right level. The signal conditioning process also eliminates or reduces the noise. Sometimes we require signal manipulation for making it linear function of some variable.

Interfacing is needed because we want to connect peripheral devices such as sensors, keyboards, actuators, etc., to microprocessor. Due to different signal forms and levels they cannot be directly connected.

We can list some basic interface requirements as

1. Electrical buffering/isolation—when peripherals operate at a different current or voltage than the microprocessor bus system or ground references are different.
2. Timing control—when the data transfer rates of the peripheral and the microprocessor are different, i.e., interfacing a microprocessor to a slower peripheral. This can be achieved by using special lines between the microprocessor and the peripheral to control the transfer of data. Such lines are called handshake lines and the process is called handshaking.
3. Code conversion—when codes used by peripherals are different to that used by microprocessor.
4. Changing the number of lines—when microprocessor uses different bits such as 4, 8, or 16 bits. This determines the number of lines in microprocessor data bus. Note that peripherals may have different number of lines.
5. Serial to parallel and vice versa data transfer—a 8 bit microprocessor manipulates 8 bits of data at same time. This can be done by parallel data transfer where all data are send simultaneously whereas in serial data transfer signals are sent one by one.
6. Conversion from analog to digital and vice versa—when both are used together.

The examples of input signal conditioning and interfacing are discrete circuits, analog to digital converters, digital to analog converters, filters, and amplifiers.

1.5 Digital Control Architecture

Microprocessor system has three parts (i) Central Processing Unit (CPU), (ii) Input and Output interfaces, and (iii) Memory.

Microprocessor having memory, input and output arrangements all on same chip are microcontrollers. Digital control architecture may include components such as different logic circuits, microcontrollers, control algorithms, program logic controllers, etc.

1.6 Output Signal Conditioning and Interfacing

The components of this system may include digital to analog, analog to digital converter, amplifiers, power transistors, power op amps, pulse width modulation, etc.

1.7 Displays

A display provides visual feedbacks to user based on which he/she can take some decisions. The examples of displays include LED's, digital display, cathode ray tubes, liquid crystal displays, etc.

1.8 Intelligent System

We can define an intelligent system as a system that learns during its existence. Or we can say that the system senses its environment with the help of sensors; it learns, what action for each situation it should take so that it achieves its objectives. Thus, an intelligent system can be defined only if the system exists along with surrounding, with which it interacts. The system must be able to receive communications from the surrounding. This communication is for transmitting information. An intelligent system must have an objective and should have ability to check whether the last action which it performed has been able to move it closer to its objective or not.

1.9 Reconfigurable Systems

A process may continue to operate as long as all of its critical faults can be detected and it remains observable and controllable. A reconfigurable system is one which can accommodate the faults using the redundancies present in the system. The redundancies are usually in the form of additional actuators and sensors present in the system than the minimum required.

The fault indicators, fault signature analysis and the fault isolation (root cause analysis) schemes must be modified every time a system is reconfigured. The functional services offered by the components are organized into coherent subsets called Operating Modes (OM), where each OM is associated to a functional model. Automation specifies the conditions to change from one OM to another. Theoretically, a process can operate normally, as long as at least one device is available for each basic function. When a device fails, the branch associated with it is removed and the system is reconfigured using the next device, according to a defined hierarchy.

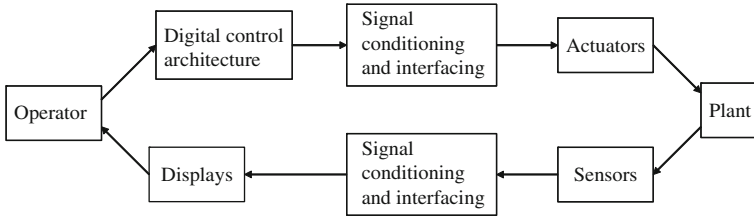


Fig. 1.2 Schematic representation of supervisory control

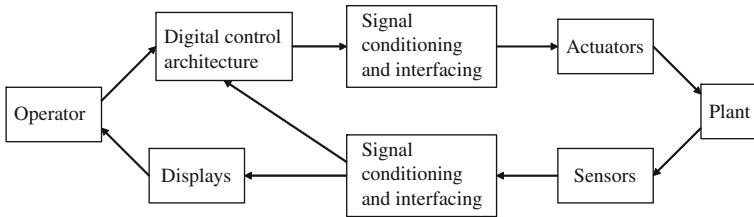


Fig. 1.3 Schematic representation of autonomous supervisory control

1.10 Autonomous Supervisory Control

The supervisory control is derived from the supervisor’s control of the subordinate staff in a manufacturing plant. The supervisory control in mechatronic system means that provision for human operator intervention in a control process exists. The intervention may be in the form of person programming intermittently and receiving data from a computer which is connected through various sensors in a controlled process.

The controlled process can be the trajectory following action to be carried by tip of a manipulator. In case of autonomous supervisory control, human intervention is not present. The schematic representation of supervisory control and autonomous supervisory control are shown in Figs. 1.2 and 1.3, respectively.

1.11 Artificial Intelligence

Humans demonstrate intelligence by communicating effectively and by learning. Artificial intelligence (AI) is the field of study for simulation of human behavior and cognitive process on a computer. It is the study of the nature of the whole space of intelligent minds. AI takes help of computational techniques for performing job that requires intelligence when performed by humans. The issue of AI involves knowledge representation, search, perception, and inference. An intelligent machine has built-in capability to reason. They perform functions that require intelligence when performed by people. Intelligent system can be constructed from explicit, declarative knowledgebases, operated by general, formal reasoning mechanism. They have the

ability to synthesize discrete pieces of information in creating a new understanding of any problem and its possible solution. Some important AI terminologies are

- Perception: It is the collection of information using sensors by the intelligent system and organization of gathered information so that decisions can be taken.
- Reasoning: It is the process of going from what is known to what is unknown. The reasoning can be either deterministic or nondeterministic. Deterministic reasoning uses if-then rules whereas nondeterministic reasoning makes predictions based on probability.
- Learning: It is the adoption of the environment based on experience by the intelligent system.

Important AI systems are

- (i) Expert system
- (ii) Fuzzy system
- (iii) Artificial neural network
- (iv) Genetic algorithm
- (v) Evolutionary programming
- (vi) Ant colony intelligent system
- (vii) Particle swarm intelligent system.

1.12 Knowledgebase

A knowledgebase is a special kind of database for knowledge management [1], providing the means for the computerized collection, organization, and retrieval of knowledge. It aims to provide right information at right moment. Knowledgebases are categorized into two major types:

Machine-readable knowledgebases store knowledge in a computer-readable form, usually for the purpose of having automated deductive reasoning applied to them. They contain a set of data, often in the form of rules that describe the knowledge in a logically consistent manner. An ontology can define the structure of stored data—what types of entities are recorded and what their relationships are. Logical operators, such as And (conjunction), Or (disjunction), material implication, and negation may be used to build it up from simpler pieces of information. Consequently, classical deduction can be used to reason about the knowledge in the knowledgebase. Some machine-readable knowledgebases are used with artificial intelligence, for example as part of an expert system that focuses on a domain-like prescription drugs or customs law.

Human-readable knowledgebases are designed to allow people to retrieve and use the knowledge they contain. They are commonly used to complement a help desk or for sharing information among employees within an organization. They might store troubleshooting information, articles, white papers, user manuals, or answers

to frequently asked questions. Typically, a search engine is used to locate information in the system, or users may browse through a classification scheme.

Any smart control system includes a knowledgebase [3]. Information on the mechatronic systems that include the equipment being controlled, as well as the controllable process, may contain errors and inconsistencies and may be incomplete. In other words, knowledge regarding mechatronic systems is characterized by indeterminacy. In constructing a knowledgebase, the main criterion is minimization of the following components of the indeterminacy: incompleteness, inadequacy (errors), and inconsistency. Another goal is to minimize the redundancy of the data in the knowledgebase. Accordingly, a method of formalized representation of knowledge regarding the mechatronic system must not only include representation of the relevant knowledge but also determination and modeling of the indeterminacies in the knowledge. Thus, mechatronic system modeling may help in enriching the existing knowledgebase of the mechatronic system. Information from the knowledgebase may be used in the synthesis, control, prediction, and diagnostic systems for mechatronic systems. It also helps in creating systems to support design and technological decision making, and in the operation of mechatronic systems.

The integration of mechatronic systems can be performed by the components [2] (hardware-integration) and by information processing (software-integration). The information processing consists of low-level and high-level feedback control, supervision and diagnosis, and general process management. Special signal processing, model-based, and adaptive methods are applied. With the aid of a knowledgebase and inference mechanisms mechatronic systems with increasing intelligence will be developed.

The integration by information processing (software integration) is mostly based on advanced control functions. Besides a basic feedforward and feedback control an additional influence may take place through the process knowledge and corresponding online information processing. This means a processing of available signals in higher levels. This includes the solution of tasks such as supervision with fault diagnosis, optimization and general process management. The respective problem solutions result in real-time algorithms which must be adapted to the mechanical process properties, for example expressed by mathematical models in the form of static characteristics, differential equations, etc. Therefore, a knowledgebase is required for organizing the methods for design and information gaining, process models, and performance criteria. By this way the mechanical parts are governed in various ways through higher level information processing with intelligent properties, possibly including learning, thus forming an integration by process adapted software.

The knowledgebase contains quantitative and qualitative knowledge. The quantitative part operates with analytic (mathematical) process models, parameter and state estimation methods, analytic design methods (e.g., for control and fault detection), and quantitative optimization methods. Similar modules hold for the qualitative knowledge, e.g., in form of rules (fuzzy and soft computing). Further knowledge is the past history in the memory and the possibility to predict the behavior. Finally, tasks or schedules may be included.

The knowledgebase consists of mathematical process models, parameter estimation, and controller design methods and control performance criteria. The feedback control is organized in lower level and higher level controllers, a reference value generation module and controller parameter adaptation. With this structure the main control functions of mechatronic systems can be organized.

1.13 Decision Support System

A decision support system (DSS) for a mechatronic system is a computer-based information system that supports organizational decision-making activities. DSSs may serve the operations, and planning levels of a microprocessor and help to make decisions, which may be rapidly changing and not easily specified in advance. DSSs include knowledgebased systems. A properly designed DSS for a mechatronic system may be software-based system intended to help compile useful information from a combination of raw data, or system models to identify and solve problems and make decisions. Let us take an example. Say a walking robot is moving in a straight line but if some obstruction comes in path of the walking robot then decision support system must be able to gather the data from sensor such as infrared and accordingly actuate the motors so that the path of the robot is changed and obstruction is not encountered.

1.14 Diagnosis

Diagnosis in a mechatronic system refers to identification of nature and cause for failures of mechatronic components, say actuators, sensors, and microcontrollers.

1.15 Fault, Failure, and Safety

Modern technological systems rely on sophisticated control systems to meet increased performance and safety requirements. Over the last three decades, the growing demand for identification of fault, resulting failure and safety concerns from such failure has attracted lot of research in the area. Apart from safety, reliability, maintainability, and survivability in technical systems has drawn significant research in Fault Detection and Diagnosis (FDD). Such efforts have led to the development of many FDD techniques. On the other hand, research on reconfigurable fault-tolerant control systems has increased progressively since the initial research on restructurable control and self-repairing flight control systems began in the early 1980s.

1.16 Fault Tolerance

Fault-tolerant control has proved to be a powerful tool for improving the safety in mechatronic system. Modern technological systems rely on sophisticated control systems to meet increased performance and safety requirements. A conventional feedback control design for a complex system may result in an unsatisfactory performance, or even instability, in the event of malfunctions in actuators, sensors or other system components. To overcome such weaknesses, new approaches to control system design have been developed in order to tolerate component malfunctions while maintaining desirable stability and performance properties. This is particularly important for safety-critical systems, such as aircraft, spacecraft, nuclear power plants, and specially automobile and mechatronics systems. In such systems, the consequences of a minor fault in a system component can be catastrophic. Therefore, the demand on reliability, safety and fault tolerance is generally high. It is necessary to design control systems which are capable of tolerating potential faults in these systems in order to improve the reliability and availability while providing a desirable performance. These types of control systems are often known as fault-tolerant control systems (FTCS). More precisely, FTCS are control systems which possess the ability to accommodate component failures automatically. They are capable of maintaining overall system stability and acceptable performance in the event of such failures.

Fault-Tolerant Control (FTC) relates to recovery from fault such that the system is controlled under actual constraints without replacing part(s) of the faulty system. FTC approaches can be classified into two categories: passive approach (e.g., robust control) and active approach (e.g., adaptive control). In active FTC, plant faults are diagnosed and estimated and subsequently the controller is redesigned for fault accommodation. Historically, from the point of view of practical application, a significant amount of research on fault-tolerant control systems was motivated by aircraft flight control system designs. The goal was to provide “self-repairing” capability in order to ensure a safe landing in the event of severe faults in the aircraft. Increased air traffic has necessitated the need for fault-tolerant flight control systems. Fault tolerance is no longer limited to high-end systems, and consumer products, such as automobiles. It is increasingly dependent on microelectronic/mechatronic systems, on-board communication networks, and software, thus requiring new techniques for achieving fault tolerance.

1.17 Examples of Mechatronic Systems

1.17.1 A Copy Machine

It is an excellent example of mechatronic system. It has analog and digital circuits, sensors, actuators, and microprocessors. The working of copy machine can be stated as follows:

1. User places an original in a loading bin and pushes a button to start the process.
2. The original is transported to the platen glass.
3. A high-intensity light source scans the original and transfers the corresponding image as a charge distribution to a drum.
4. Blank piece of paper is retrieved from loading cartridge, and image is transferred onto the paper with an electrostatic deposition of ink toner powder that is heated to bond to the paper.
5. A sorting mechanism then delivers the copy to an appropriate bin.

Now, let us see the mechatronic components in copy machine.

1. Actuators: In a copy machine servomotor or stepper motor is used as actuator. The principal job of actuator here is to load and transport the paper, turn the drum, and index the drum.
2. Sensors: Optical sensors and microswitches detect the presence or absence of paper, its proper positioning, and check whether or not door and latches are in proper position. Encoders are used to track motor rotation.
3. Control: Analog circuits control the lamp, heater, and other power circuit. Digital circuit controls digital display, indicator lights, buttons, and switches, forming the user interface. Other digital circuits used include logic circuit and microprocessor that coordinates all the functions of the machine.

1.17.2 Walking Robot

A walking robot is another good example of mechatronic system. It has following mechatronic components:

1. Actuators: Servo motors or direct current (DC) motor or stepper motor can be used as an actuator to propel the legs and body.
2. Sensors: A walking robot may have many sensors depending upon the level of intelligence required in it. Some of the sensors can be
 - Infrared (IR) sensor for obstruction detection.
 - Bumper sensor for obstruction detection.
 - Compass for orientation detection.
 - Accelerometer for tilt detection.
 - Ultrasonic sensor for range detection.
3. Micro Controller: One can use any microcontroller such as PIC, ATmega for coordinating the activity of actuators and sensors.

1.18 Why Mechatronics System Simulation?

Mechatronic system designs are complex by nature, and are becoming more complex day by day. As the number of system's peripheral components grow to accommodate ever increasing demands for functionality and performance from consumers, the system design must integrate analog and digital hardware, as well as the software that controls them. As mechatronic system integrates different components its behavior is determined by interdependencies between different components. Therefore, an integrated and interdisciplinary engineering approach is necessary. So, engineers must be assisted by tools which allow a systems analysis with respect to capabilities, capacities, and behavior without really constructing the system. This necessitates an appropriate modeling and simulation tool for mechatronic systems.

A mechatronic system design requires an integrated modeling and simulation approach where the whole system needs to be designed together to meet the desired performance specifications. The first level of modeling is called a conceptual model. The concept of a new product needs to be validated before additional resources are allocated to design and fabricate that product. Simulation is great tool for concept validation. Once the conceptual model has been validated, the system level design goes a step further where one determines the constraints on integration of components of the system. These constraints relate to the specifications for various components such as the power requirements in the actuators (called actuator sizing) and sensor limits.

The next step in the design of an autonomous mechatronic system involves integration of the control system model with the system model. Besides the selection of control laws, the control system parameters have to be tuned in this stage so that the performance specifications are met with desired accuracy. The controller design also involves selection and placement of sensors and actuators in the system. Note that the actuator specifications cannot be determined if the system is not modelled with its control laws; the actuator must be able to deliver the desired output dictated by the controller. Moreover, if the sensor response time and feedback delay etc. are not accounted for in the model then one might get a wrong design. Thus, the system model needs integration of all components of the mechatronic system so that the actuator, sensor and system dynamics are all accounted for during the design stage.

The detailed design of components is done after the system-level design and control integration has been validated through simulation. Note that initial system level design uses gross or approximate parameter values. The detailed design accounts for further constraints such as the mechanical strength of components (load limit, fatigue life, etc.), geometric or assembly compatibilities, logistical issues (electrical or hydraulic power delivery lines) and packaging of electronic components (cooling system, heat exchangers, etc.). The detailed design gives more accurate estimation of system parameter values which have to be again used in the system level model. An iterative process then converges to the final system design which will be used to fabricate the mechatronic system. The computerized modeling and simulation to evolve a product design called virtual prototyping. Like manufacturing of a

physical product can be optimized through rapid prototyping tools, the virtual prototyping through modeling and simulation offers a solution to quick, maintainable, optimized, and evolving product design. With availability of a virtual prototype of a product, it becomes easier to perform product redesign or enhancement.

1.19 Future of Mechatronics

We can expect continued advancements in cost-effective actuators, sensors, micro-processors and microcontrollers development enabled by advancements in applications of microelectromechanical systems (MEMS), adaptive control methodologies, real-time programming methods, networking and wireless technologies, and software tools for advanced system modeling, virtual prototyping, and testing. The Internet when utilized in combination with wireless technology, may also lead to new mechatronic products. While developments in automobile technology provide vivid examples of mechatronics development, there are numerous examples of intelligent systems in all walks of life. In area of medical science we can expect advances in robot-assisted surgery, in vivo robots and implantable sensors and actuators. Other areas that will benefit from mechatronic advances may include robotics, manufacturing, space technology, underwater exploration, and transportation.

References

1. <http://en.wikipedia.org/wiki/knowledgebase>. Accessed 03 July 2012
2. R. Isermann, Mechatronic systems—a challenge for control engineering. in *Proceedings of the American Control Conference*, pp. 2617–2632, Albuquerque, New Mexico, June 1997
3. V.Ts. Zoriktuev, S.G. Goncharova, I.F. Mesyagutov, Representation and derivation of knowledge in the control systems of mechatronic machine-tool systems. *Russ. Eng. Res.* **28**, 177–181 (2008)

Chapter 2

Bond Graph Modeling of Mechatronic Systems

2.1 Why Bond Graph for Mechatronics?

One of the main and most challenging steps in the design and analysis of a mechatronics system is to generate a computer model for control analysis, diagnosis design, sensor selection/positioning, and actuator sizing. Modeling is a difficult task especially for mechatronic systems. Indeed, mechatronic systems are governed by many effects of different engineering disciplines (mechanical, electrical, pneumatic, thermal, etc.) and various technological components (sensors, controllers, actuators, transducers, etc.). This is why the bond graph modeling as a unified approach is well suited for modeling them. For modeling task, this methodology allows, (independent of the physical nature of the studied system), precisely by its graphical nature, to display the exchange of power in a system, including storage, dissipation, and transformation. The bond graph model can be refined by adding graphically more elements like friction, stiffness effects, without having to start all over again. Because of their complexity, mechatronics systems need a structured approach to represent the step-by-step modeling process in a hierarchical way by using one unified language. In this way, four levels of modeling can be represented by a bond graph model.

1. *The technological level.* This level represents the architecture of the system by assembling the different subsystem models in iconic form, which correspond to different plant items (heat exchanger, boiler, pipe, etc.). The technological level can be represented by the so-called *word bond graph*. This means that the system is represented as interconnected subsystems. Unlike block diagrams (where the inputs and outputs are information variables), the interconnection in word bond graph is realized by the power variables (pair of efforts and flows).
2. *The physical level.* At this level, the modeling uses an energetic description of the physical phenomena. One uses the basic concepts of physics such as dissipation of energy, transformation, accumulation, sources, and so on by considering the relevant physical phenomena (inertia, friction, and compressibility), in a discretized form, to introduce the system dynamics through a graphical

description. Here, the bond graph is used as a universal language for lumped parameter modeling of all the domains of physics.

3. *Mathematical level.* The mathematical model is represented by the mathematical equations (algebraic and differential equations) which describe the system behavior. The mathematical level is obtained from a bond graph by writing the constitutive equations of the components and constraints.
4. *Algorithmic level.* The algorithmic level is connected directly to information processing. This level indicates how the mathematical models are calculated. The algorithmic problem is solved in the bond graph methodology by systematic assignment of causalities, which are shown by the perpendicular lines at the ends of the bonds.

The advantages offered by bond graph modeling are as follows:

- it is a unique language for all physical domains,
- it clearly shows the cause and effect relations in the model,
- it allows further possible development and evolution of the model,
- and it is also a tool for analyzing the system's structural properties.

2.2 Bond Graph for Modeling, Control, and Diagnosis

The bond graph approach for modeling mechatronic systems is well developed in the literature. The first book was presented in 1959 by Paynter, the inventor of bond graphs [41]. The approach was later extended by Karnopp et al. in [24], where the presentation starts with the basic elements and leads to sophisticated mathematical models suitable for automated computer simulation. The reader can consult more such applications in [33, 56, 57]. One commonly used software for automatic generation of dynamic models is Symbols [35, 40]. In [6], simulation results for several engineering examples are given using another software named 20sim [58]. Another software CAMP-G uses bond graphs in order to generate computer models (integrated with MATLAB–SIMULINK) automatically [17]. This ability to generate formal dynamic models is due to the graphical aspect of bond graphs.

The bond graph is not only a powerful modeling and simulation tool of mechatronics systems as developed in the cited references, but also allows control and diagnosis analysis. This is why the bond graph is used in this book as an integrated and computer-aided design (CAD) tool for mechatronics system design and synthesis. As shown in Fig. 2.1, the dynamic bond graph model deduced directly from the physical mechatronic system is used not only for simulation (using any number of software tools) but also for diagnosability [38, 39, 45, 48, 54, 55], controllability and observability analysis [42, 51–53] and sensor placement [25, 47].

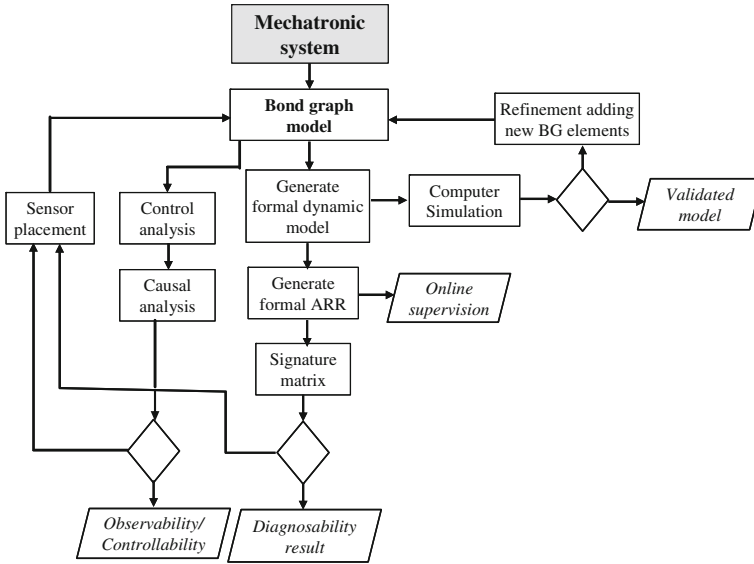


Fig. 2.1 Bond graph modeling for control and diagnosis design

2.3 Bond Graph Modeling Theory

2.3.1 Concepts and Definitions

Consider two systems S_1 and S_2 , respectively, represented by a DC motor and a load, which exchange power as shown in Fig. 2.2a. This exchanged power is represented by a bond labeled by two variables named effort (e) and flow (f), which are called power variables. Effort is the intensive variable (e.g. pressure, electrical potential, temperature, chemical potential, force, torque, etc.) and flow is the derivative of extensive variable (e.g. volume flow, current, entropy flow, velocity, molar flow, etc.). For representation purposes, the effort variable may be placed on one side of the bond and the flow variable on the other side, although such placements are not necessary in many cases except for the purpose of explanation. The assumed direction of the power exchange (flow) is represented by the half arrow on the bond as shown in Fig. 2.2b and it is formally called power direction. It may be noted here that the power direction is only a reference (like a coordinate system) and it does not mean that the power will actually flow in the assumed direction. In the bond graph theory, bonds (named *power bonds*) represent power exchange conduit between connected multiports. This power is the product of the two power variables. In the considered mechanical example the effort is the torque τ and the flow is the angular velocity ω (Fig. 2.2c). The exchanged power is $P = \tau\omega$ because $e = \tau$ and $f = \omega$.

Fig. 2.2 Energetic connection represented by bonds and ports in bond graph representation

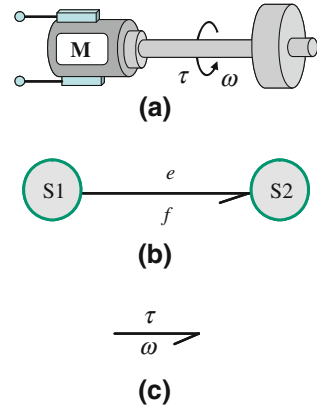
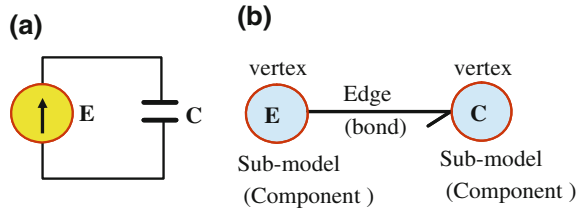


Fig. 2.3 A basic bond graph



Definition 2.1 A bond graph is a collection of multiport elements connected together. In the general sense, it is a linear graph whose nodes are multiport elements and whose branches are bonds. The key feature of bond graph modeling is the representation (by a bond) of exchanged power as the product of generalized efforts (e) and generalized flows (f) with elements acting between these variables and junction structures (algebraic constraints) to reproduce the global model as interconnected subsystems. The power variables are the generalized flow and the generalized effort variables as developed below.

Bond graphs are labeled as directed graphs, in which the vertices represent sub-models (or elements) and the edges represent an ideal energy connection between power ports as illustrated by the electrical circuit example shown in Fig. 2.3a, b. The vertices are idealized descriptions of physical phenomena: they are concepts, denoting the relevant aspects of the dynamic behavior of the system. The edges are called bonds. They denote point-to-point connections between submodel ports. The bond transfers power as product of two generic power variables.

2.3.2 Power as a Unified Coordinate System

In bond graph theory, bonds (or *power bonds*) represent power (consequently energy) exchange between connected multiports. This power is the product of two power

variables: a potential variable (e.g. pressure, electrical potential, temperature, chemical potential, force, etc.) called generalized effort (e) and a current variable (e.g. volume flow, current, entropy flow, velocity, molar flow, etc.) referred to as generalized flow (f). The positive sense of power flow is represented by the half arrow on the bond. The energy is exchanged according to the sense represented by a power direction (half arrow head) only when the two power variables have the same sign, i.e., either both are positive or both are negative; otherwise, the energy transfer is in the opposite direction to the assigned power direction. The choice of the coordinate system is usually decided by the concerned engineering domain (e.g. Cartesian, cylindrical, or spherical coordinate systems in mechanics, assumed direction of current flow in electrical networks, etc.). In some engineering domains, it is very difficult to choose the appropriate coordinate system (e.g. chemical engineering, thermodynamics). Further difficulty arises when subsystems belonging to different energy domains are to be coupled together. This is why, for multi-disciplinary model synthesis, power direction is a generalized approach of the coordinate system assignment in bond graph theory.

The invention of bond graphs is attached to the need for a common language to model systems involving different energetic domains. Bond graph is a topological modeling language, where the energy exchange between the components of a dynamic system are captured in a graphical form. The methodology was invented by Paynter in 1959 [41] and was developed later for different modeling applications: electromechanical [59], thermofluidic and thermal [57], chemical and thermochemical [21]. This analogy approach has been even extended to non-energetic systems such as economic and sociological systems [4, 5, 13]. The model can be introduced in a graphical form and simulated using specialized software [35, 58]. This tool is widely used in the industry for mechatronics and integrated system designs.

2.3.3 Power Variables

Power interactions are always present when two multiports are passively connected. In bond graph language, the various power variables are classified into a universal scheme so as to describe all types of multiports in a common language. Power variables are generally referred to as *effort* and *flow*; additional qualifications pertaining to the domain under consideration may also be included in the model. Table 2.1 gives effort and flow variables for some of the physical domains. The power P_u exchanged at the port is the product effort and flow:

$$P_u(t) = e(t)f(t) \tag{2.1}$$

This type of a bond graph is then called a true bond graph.

Table 2.1 Power variables in a true bond graph

Domain	Effort $e(t)$	Flow $f(t)$
<i>Electrical</i>	Voltage u (V)	Current i (A)
<i>Mechanical rotation</i>	Torque Γ (N m)	Angular velocity ω (Rad/s)
<i>Mechanical translation</i>	Force F (N)	Velocity v (m/s)
<i>Hydraulics</i>	Pressure (Pa)	Volume flow rate \dot{V} (m ³ /s)
<i>Thermodynamics</i>	Temperature (K)	Entropy flow (J/(Ks))
<i>Chemical transformation</i>	Chemical potential μ (J/mole)	Molar flow rate \dot{n} (mole/s)
<i>Chemical kinetics</i>	Chemical affinity A (J/mole)	Rate of reaction $\dot{\xi}$ (mole/s)
<i>Economics</i>	Unit price P_u (\$/unit)	Order flow rate f_c (units/period)

Table 2.2 Power and energy variables in a true bond graph

Domain	Impulse $p(t)$	Displacement $q(t)$
<i>Electrical</i>	Flux linkage λ (Vs)	Charge q (C) or (As)
<i>Mechanical rotation</i>	Angular momentum p_ω (N m s)	Angle ω (Rad)
<i>Mechanical translation</i>	Momentum p (N s)	Displacement x (m)
<i>Hydraulics</i>	Pressure momentum p_p (Pa s)	Volume V (m ³)
<i>Thermodynamics</i>	–	Entropy S (J/K)
<i>Chemistry</i>	–	Molar mass N (mole)
<i>Economics</i>	Economic momentum p_e	Accumulation of orders q_e

2.3.4 Energy Variables

Two additional physical quantities are used in bond graph modeling. They are called energy variables and are important for dynamic system representation and are associated with state variables. Two kinds of energy variables are used: *generalized momentum*, $p(t)$, and *generalized displacement*, $q(t)$. They are obtained by integration of the power variables with respect to time.

$$\begin{aligned}
 p(t) &\equiv \int_{-\infty}^t e(\tau) d\tau = p_0 + \int_{t_0}^t e(\tau) d\tau, \\
 q(t) &\equiv \int_{-\infty}^t f(\tau) d\tau = q_0 + \int_{t_0}^t f(\tau) d\tau.
 \end{aligned}
 \tag{2.2}$$

Energy variables for some modeling domains are given in Table 2.2.

In chemical and thermal domains, the time integral of efforts (temperature or chemical potential) do not have any direct physical meaning. This is why, the generalized momentum $p(t)$ is not defined in Table 2.2 for these domains.

Let us explain why those variables are termed “energy variables”. Equation 2.2 can be rewritten in differential form as follows:

$$\begin{aligned}
 \frac{dp(t)}{dt} &= e(t) \Rightarrow e(t)dt = dp(t), \\
 \frac{dq(t)}{dt} &= f(t) \Rightarrow f(t)dt = dq(t).
 \end{aligned}
 \tag{2.3}$$

Energy $E(t)$ is computed by integration of the power:

$$E(t) = \int_{-\infty}^t P_u(\tau) d\tau = \int_0^t e(\tau) f(\tau) d\tau + E_0. \quad (2.4)$$

Based on Eq. 2.3 ($e(t)dt = dp(t)$ and $f(t)dt = dq(t)$), it is easy to express E as a function of energy variables q or p :

$$E(t) = \int_0^t e(\tau) \frac{dq(\tau)}{d\tau} d\tau + E_0 \quad \text{or} \quad E(t) = \int_0^t f(\tau) \frac{dp(\tau)}{d\tau} d\tau + E_0. \quad (2.5)$$

As will be shown later, the variables $e(t)$ and $f(t)$ can be expressed as functions of q and p : $e(t) = e(q)$ and $f(t) = f(p)$. Finally, energy E (Eq. 2.5) can be rewritten as function of energy variables q or p :

$$E(q) = \int_{q_0}^q e(q) dt + E_{(q=q_0)}. \quad (2.6)$$

$$E(p) = \int_{p_0}^p f(p) dt + E_{(p=p_0)}. \quad (2.7)$$

For example, let us consider potential energy E_p stored by a spring. The power flow into the spring (port) leads to storage of energy E . If during the process, no energy is lost, then energy E is

$$E_p(t) = \int_0^{t_0} e(\tau) f(\tau) d\tau + E_{(t=0)} \quad (2.8)$$

where, effort e and flow f are, respectively, the force and the velocity. If the force is proportional to the displacement x ($F = kx$), where $x = q = \int f(\tau) d\tau$ is the energy variable, then the stored energy is

$$E_p(t) = \int_{q_0}^{q_1} e(q) dq = \int_{x_0}^{x_1} kx dx = \frac{1}{2}k (x_1^2 - x_0^2). \quad (2.9)$$

2.3.5 Pseudo Bond Graph

2.3.5.1 Why Pseudo Bond Graph?

In complex processes, several phenomena (chemical, thermal, hydraulic) are coupled [15, 18, 20–22]. For example, thermofluid systems involve additional complexity in the modeling task, since the mass that flows through the process transports the internal energy which is stored in it from one location to another. If one has to include chemical

Table 2.3 Power variables in process engineering

Domain	Pseudo bond graph power variables	
	Effort (e)	Flow (f)
Chemical		
Transformation	C (mole/m ³)	\dot{n} (mole/s)
Kinetics	C (mole/m ³)	\dot{n} (mole/s)
Hydraulics	P (Pa)	\dot{m} (kg/s)
Thermal		
Conduction	T (K)	\dot{Q} (J/s)
Convection	T or h (J/kg)	\dot{H} (J/s)

reactions in addition to thermal phenomena, then three energy domains are involved in a general process engineering system. Power variables of process engineering models are thus presented in vectorial form as

$$\mathbf{e} = [e_h \ e_t \ e_c]^T, \quad \text{and} \quad \mathbf{f} = [f_h \ f_t \ f_c]^T, \quad (2.10)$$

where e_t , e_h and e_c represent, respectively, the thermal effort (the specific enthalpy or the temperature), the hydraulic effort (the pressure), and the chemical effort (the chemical potential, chemical affinity, or the concentration); and f_t , f_h and f_c represent, respectively, the thermal (or entropy) flow (by conduction \dot{Q} or by convection \dot{H} , i.e. enthalpy flow), hydraulic flow (mass flow \dot{m} or volume flow \dot{V}) and chemical flow (mole flow \dot{n}).

Table 2.3 shows the pseudo power variables used in modeling of process engineering systems. More details and motivations for the specific selection of power variables is given in [57].

In the hydraulic domain, the pair (\dot{m}, P) is preferred because \dot{m} acts as a common variable for both incompressible and compressible fluid flow modeling and if thermofluidics is considered, then the energies being coupled, the enthalpy flow \dot{H} is calculated from mass flow \dot{m} . In the convection of thermal energy (from a Lagrangian point of view), the pair enthalpy flow-temperature (or specific enthalpy) $(\dot{H}, h$ (or T)) is used as power variables. In the case of thermal conduction (from Eulerian point of view [1]), the pair (T, \dot{Q}) is used.

In chemical systems, the concentration C is used as the effort variable instead of the chemical potential and the molar flow \dot{n} is used as the flow variable. Other research works use the concentration of the substance as effort variable instead of the chemical potential and the derivative of the concentration as the flow variable. This approach is extensively used in [27] because it allows to manipulate variables more intuitively (therefore easy to simulate) and the power variables (e.g. concentration) are measurable quantities.

Table 2.4 Energy variables in process engineering

Domain	Pseudo bond graph energy variables	
	Impulse (p)	Displacement (q)
Chemical	–	Number of moles N (mole)
Hydraulic	Pressure momentum p_p	Mass m (kg)
Thermal	–	
Conduction	–	Thermal energy Q (J)
Convection	–	Internal energy U (J)

2.3.5.2 Pseudo Energy Variable

The energy variables (or state variables) in pseudo bond graph of process engineering systems are time integral of mass flow ($m = \int \dot{m} dt$), time integral of enthalpy flow ($H = \int \dot{H} dt$), time integral of mole flow ($N = \int \dot{n} dt$) and time integral of thermal flow ($Q = \int \dot{Q} dt$). Consequently, the energy variables (as summarized in Table 2.4) are:

- mass m stored by any accumulator,
- total enthalpy H (or internal energy) stored in any heated accumulator,
- number of moles N accumulated in a reactor,
- and thermal energy Q stored by any metallic body.

The time integral of temperature or chemical potential have no physical meaning. This is why, impulse variables do not exist for thermal or chemical processes. To be more precise, impulse variables are associated with inertial motion. However, thermal processes are irreversible and the kind of chemical kinetics considered in this book is also irreversible, i.e., in such processes, there will be no inertial effects. Note that thermal equivalent of inertia is undefined, as it would violate the laws of thermodynamics.

2.3.6 Analogy of Energy Variables

The analogy of displacement and impulse variables for different systems are given in Figs. 2.4 and 2.5.

2.4 Bond Graph Elements

In bond graph language, two active elements (namely sources) (**Se** and **Sf**), three generalized passive elements (**I**, **C**, and **R**), two junctions (**0** and **1**) and two trans-

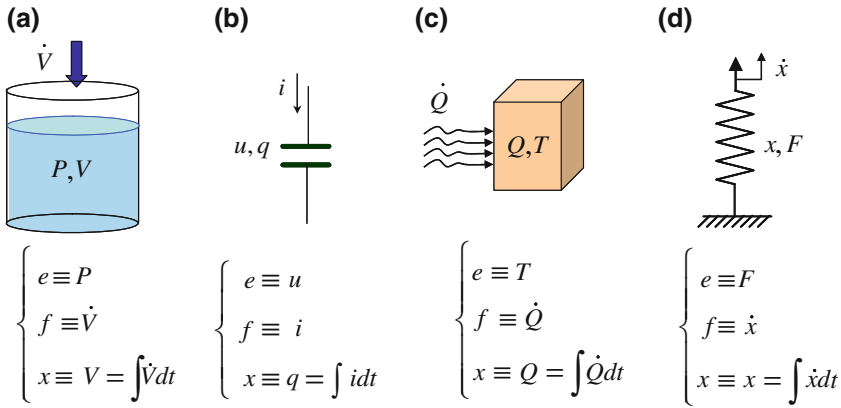
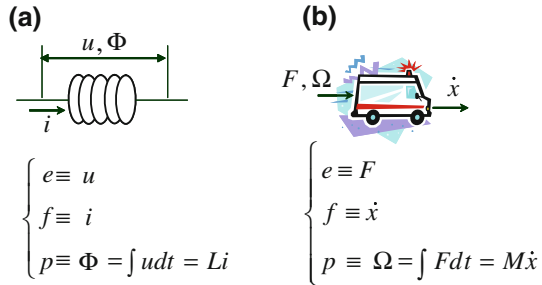


Fig. 2.4 Displacement variables for hydraulic (a), electrical (b), thermal (c), and mechanical (d) systems

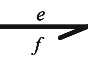
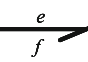
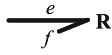
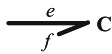
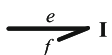

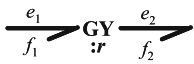
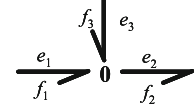
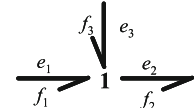
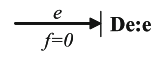
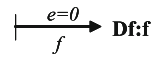
Fig. 2.5 Impulse variables for electrical (a) and mechanical (b) systems



ducers (**TF** and **GY**) are used to model any energetic process. When the exchanged power is negligible, or power is drawn from some unmodeled external source (e.g. the tank circuit in an amplifier), then it is represented by an information bond having full arrows to show the direction of information imposition. The full arrow in the information bond (also called activated bond) can represent the signal transmitted by a sensor, integrator, sum member, etc.

There are nine basic multiport elements, grouped into four categories according to their energy characteristics. These elements and their definitions are summarized in Table 2.5. The junctions and two-port (1, 0, TF, and GY) elements define the constraints in the model. These constraints are usually conservation relations such as force and moment balance equations, kinematic constraints, Kirchoff's voltage and current laws, etc. The constraint relations depend upon the domain being modeled. The sources excite the system. The passive elements (I, C, and R) model the kinetic and potential energy storage and dissipation. The energy is exchanged between various segments of the system through the junctions.

Table 2.5 Definitions of the basic bond graph elements

	Symbol	Constitutive equation	Name
Sources	Se:e 	$\begin{cases} e(t) \text{ given by the source} \\ f(t) \text{ arbitrary} \end{cases}$	Source of effort
	Sf:f 	$\begin{cases} f(t) \text{ given by the source} \\ e(t) \text{ arbitrary} \end{cases}$	Source of flow
Passive elements	Dissipator 	$\Phi_R(e, f) = 0$	Resistance
	Energy stores 	$\Phi_C(e, q) = 0$	Capacitance
		$\Phi_I(f, p) = 0$	Inertance
Junctions	Transducers 	$\begin{cases} e_1 = me_2 \\ f_2 = mf_1 \end{cases}$	Transformer
		$\begin{cases} e_1 = rf_2 \\ e_2 = rf_1 \end{cases}$	Gyrator
	Junctions 	$\begin{cases} e_1 = e_2 = e_3 \\ f_1 - f_2 + f_3 = 0 \end{cases}$	Zero junction : common effort junction
		$\begin{cases} f_1 = f_2 = f_3 \\ e_1 - e_2 + e_3 = 0 \end{cases}$	One junction : common flow junction
Sensors	Sensors 	$\begin{cases} e = e(t) \\ f = 0 \end{cases}$	Sensors (Detectors)
		$\begin{cases} f = f(t) \\ e = 0 \end{cases}$	

2.4.1 One-Port Passive Elements

The bond graph elements are called passive because they transform received power into dissipated power (R-element), store power in the form of potential energy (C-element) or kinetic energy (I-element). These elements are called one-port elements because they are connected to another system by one port. By convention, the half arrow is oriented towards the port as shown in Fig. 2.6 where J indicates a junction (1 or 0).

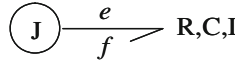


Fig. 2.6 Representation of 1-port passive elements

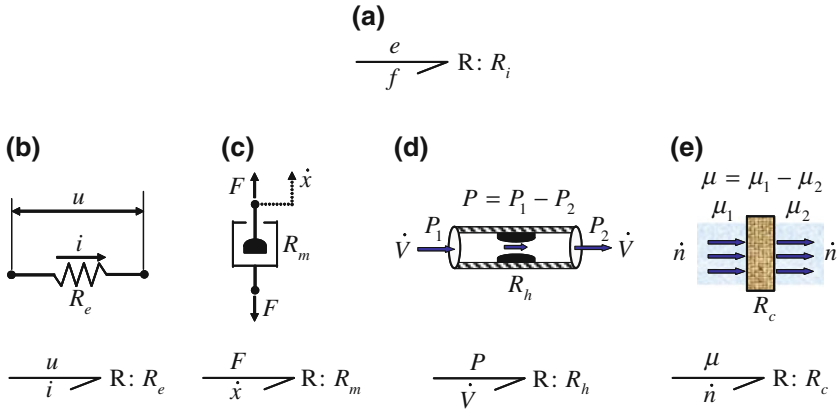


Fig. 2.7 R-element: **a** bond graph, **b** electrical resistance, **c** mechanical damper, **d** hydraulic resistor, and **e** chemical membrane

Depending on how the power is transformed by the port, the passive elements are classified into resistive (R), storage (C) and inertial (I) elements.

2.4.1.1 Resistive R-Element

Definition 2.2 A bond graph element is of type R-element (resistor or dissipater) if it defines an algebraic constitutive equation between effort and flow. This element models all energy dissipation-type phenomena.

Figure 2.7 shows the bond graph model and sketches of resistors in several energy domains. As technological systems representing R -element, one can cite electrical resistors, mechanical frictions, hydraulic resistors, and chemical resistances (membrane in a fuel cell, for example). The type of the phenomenon, represented by an R -element, is usually identified by the associated power variables or subscripts (some nomenclature) given to the associated parameter used in the element’s constitutive equation: R_e, R_m, R_h or R_c .

The constitutive equation of R -element is a static function:

$$\Phi_R(e, f) = 0. \tag{2.11}$$

This relation can be linear or nonlinear. Examples are:

- Ohm's law in the electrical domain: $u - R_e i = 0$,
- mechanical friction: $F - R_m \dot{x} = 0$,
- Bernoulli's law in hydraulics: $\Delta P - R_h \dot{V}^2 = 0$,
- or chemical diffusion law between two substances of different potential through a membrane: $\Delta\mu - R_C \dot{n} = 0$.

It should be noted that the R -element usually withdraws power from the system and transforms it mostly into useless heat, illustrating the fact that the dissipation phenomenon is irreversible. In certain cases, the resistance can be negative if it supplies power. For example, the dry friction phenomena, flow-induced excitation phenomena, torque-speed characteristic of motors or pressure difference-volume flow characteristic for pump can be modeled as R -elements [37] with negative values for parameter R so that energy is imported into the system.

2.4.1.2 Storage C-Element

Definition 2.3 A bond graph element is called C-element (storage) if it is defined by a dynamic constitutive equation relating displacement (time integral of flow) and effort. This element represents any system that transforms the received power into potential energy without loss.

In Fig. 2.8, the bond graph symbol and some physical examples of related storage phenomena are given. Typical examples are electrical capacitor, mechanical spring, storage reservoir and torsion bars, etc. The constitutive law for C-element always relates the effort e to the time integral of flow (displacement q):

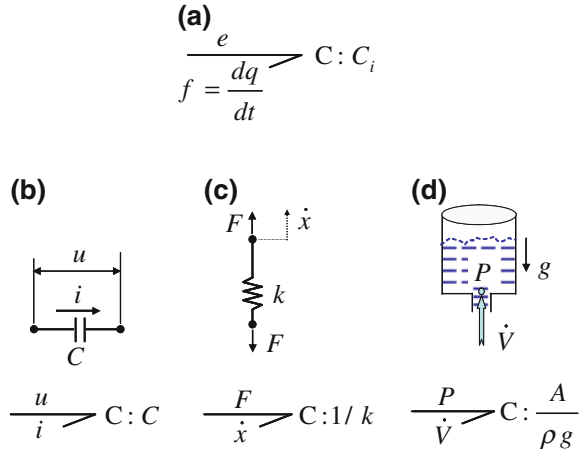
$$\Phi_C(e, q) = 0, \quad \text{or} \quad \Phi_C\left(e, \int f(\tau) d\tau\right) = 0. \quad (2.12)$$

Remark 2.1 The constitutive equation associated with bond graph elements are called *behavioral equations*. The physical laws expressing how the energy is transformed are mathematically described by the behavior model. In a bond graph model, they describe the physical phenomena which are represented by lumped-parameter bond graph elements (R, C, and I). These equations are called “constitutive laws”.

$$F_B = \{F_C\} \cup \{F_I\} \cup \{F_R\}. \quad (2.13)$$

From a functional point of view (see [40]), C-element is a processor which receives power as input and produces potential energy as output by storage. From the plant item point of view, those processes are receivers, boilers, tanks, condensers, etc., which are classified as storage processes.

Fig. 2.8 Storage C-element: **a** bond graph model, **b** electrical capacitor, **c** spring, and **d** storage tank



Thus, if the flow f is the input to a C -element, it is first integrated to find q and then e is an output computed from q . The linear form of such constitutive law is:

$$e = \frac{1}{C} \int f dt = \frac{q}{C}. \tag{2.14}$$

In the linear case, the constitutive law is $u = \frac{1}{C} \int i dt = \frac{q}{C}$ in electrical systems, $F = \frac{1}{C} \int \dot{x} dt = Kx$ in mechanical systems, and $P = \frac{1}{C} \int \dot{V} dt = \frac{V}{C} = \frac{\rho g}{A} V$ in hydraulic storage tanks having uniform cross-section.

For mechanical systems, it is common to use the *spring constant* K , rather the *compliance* $C \equiv 1/K$, which is analogous to the electrical capacitance. For a spring, the potential energy of a linear compliant element (Eq. 2.9) is given by

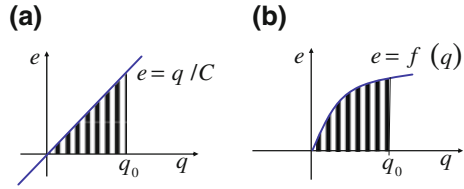
$$\Delta E = \int_{x_0}^{x_1} Kx \cdot dx = \frac{K}{2} (x_1^2 - x_0^2), \tag{2.15}$$

or

$$\Delta E = \int_{t_0}^{t_1} e \cdot f \cdot dt = \int_{t_0}^{t_1} e \cdot \frac{1}{K} \frac{de}{dt} \cdot dt = \int_{e(t_0)}^{e(t_1)} \frac{e}{K} de = \frac{1}{2K} (e^2(t_1) - e^2(t_0)). \tag{2.16}$$

In a hydraulic system (gravity tank), the capacitance C is equal to $A/(\rho g)$. Indeed the pressure of the fluid of the density ρ (kg/m^3) at the bottom of the cylindrical tank of cross-section A can be expressed as a function of the volume V , as $P(V) = \frac{\rho g}{A} V$.

Fig. 2.9 Energy storage in a C-element: **a** linear case and **b** nonlinear case



Based on Eq. 2.6, the potential energy stored by a hydraulic capacitor (tank or accumulator) can be evaluated as follows:

$$E_p = \int_{V_0}^{V_1} P(V)dV = \frac{\rho g}{2A} (V_1^2 - V_0^2). \tag{2.17}$$

C-element does not dissipate energy but stores it and discharges it on demand by the rest of the system.

The stored energy $E(q)$ may be interpreted graphically as shown in Fig. 2.9. The area under the curve represents the energy E . If q (volume, entropy, charge) goes from 0 to q_0 then energy is being stored, if q starts returning to 0, stored energy is being released (e.g. discharge of a capacitor). During this process, no energy is lost.

2.4.1.3 Inertia I-Element

Definition 2.4 A bond graph element is called I-element (storage) if it is defined by a dynamic constitutive equation relating momentum (time integral of effort) and flow. This element models any system that transforms the received power into kinetic energy without loss.

I-element (Inertia) transforms the received power into kinetic energy for mechanical systems and magnetic field energy for electrical systems. The bond graph symbol and some physical examples are shown in Fig. 2.10. The **I**-element is used to model inductance phenomenon in electrical systems, mass or inertia effects in mechanical or hydraulic processes. The constitutive law is a dynamic relation relating integral of effort (momentum) and flow. *An inertia element does not dissipate energy but stores it.* A well-known example from mechanics is the flywheel with its large moment of inertia. When it is brought back to its original state, e.g., when the flywheel is slowed down, it returns the entire energy to the system. The usual relation given for *I*-element is between the time derivative of the flow and the effort, or in other words, between flow and the integral of effort.

$$\Phi_I(f, p) = 0 \quad \text{or} \quad \Phi_I \left(f, \int e(\tau)d\tau \right) = 0. \tag{2.18}$$

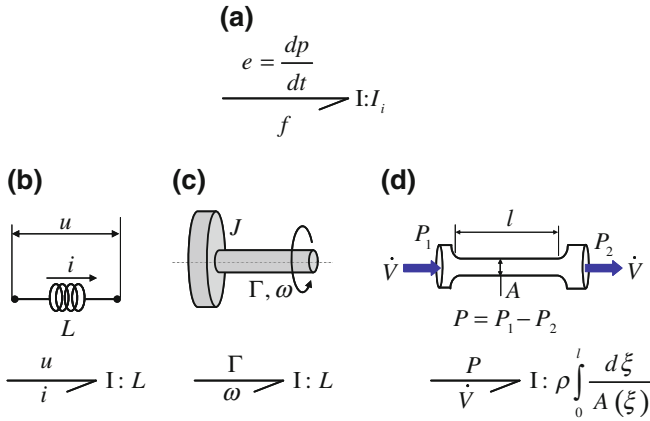


Fig. 2.10 Inertia or I-element: **a** bond graph model and **b** electrical, **c** mechanical, and **d** hydraulic examples

Examples: $\int u dt = Li$ or $\Phi = Li$ in electricity, $\int \Gamma dt = J\omega$ or $p_\omega = J\omega$ in mechanical rotation and $\int F dt = m \frac{dx}{dt}$ or $p = m \frac{dx}{dt}$ in linear motion. The inductance, mass, or moment of inertia is the inertia parameter.

In hydraulics, the inertia due to the mass of the fluid of density ρ flowing in a pipe of length l and cross-sectional area A can be derived (Fig. 2.10d) by assuming that the driving force is due to the difference of pressure ΔP . Newton’s law for the mass of the fluid ($m = \rho A l$) circulating in the pipe yields

$$\rho A l \frac{d(\dot{V}/A)}{dt} = A(P_1 - P_2) \Rightarrow \dot{V} = \frac{A}{\rho l} \int \Delta P dt = \frac{1}{I} p_h, \tag{2.19}$$

where p_h is the pressure momentum.

The parameter of inertia of the fluid is then $I = \frac{\rho l}{A}$ for a volume of constant area A . If A is not constant, $I = \rho \int_0^l \frac{d\ell}{A(\ell)}$.

If we consider \dot{x} as the linear velocity of a fluid control volume of mass m then Eq. 2.21 can be written as:

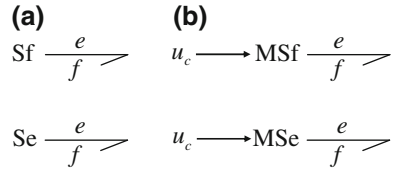
$$p_h = \frac{\rho l}{A} \dot{V} = \frac{m}{A^2} \dot{V} = \frac{m}{A^2} A \dot{x} = \frac{1}{A} m \dot{x}. \tag{2.20}$$

From Eq. 2.20, the pressure momentum can be considered as momentum per unit surface area:

$$p_h = \frac{P}{A}. \tag{2.21}$$

Based on the equation ($p = m\dot{x}$), the kinetic energy stored in a mechanical inertial element of mass m can be obtained

Fig. 2.11 Active elements:
a flow and effort sources and
b modulated flow and effort sources



$$E_c = \int_{p_0}^{p_1} f(p)dp = \int_{p_0}^{p_1} \frac{p}{m} dp = \frac{1}{2m} (p_1^2 - p_0^2). \tag{2.22}$$

Note that both *C* and *I* elements are associated with energy storage.

2.4.2 Active Elements

Definition 2.5 Sources are called active elements in bond graph notation. They supply power to the process. Their type is indicated either by a subscript “e” or “f” depending on whether source imposes an effort or a flow on the system.

Depending on the type of power variable the source provides, bond graph modeling has two source elements: effort source (*Se*) and flow source (*Sf*). Figure 2.11a shows the bond graph representation of such elements. Since sources provide power, the bond is conventionally oriented towards the system to which the power is imposed.

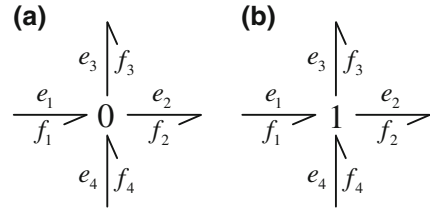
2.4.2.1 Effort Source

It imposes an effort, which can be a function of time, but independent of the required flow. Examples are the electric voltage generator, pressure pump, temperature source, gravity, etc.

2.4.2.2 Flow Source

It provides a flow independent of the required effort. Examples are electric current generator, imposed velocity in mechanics, and hydrostatic pump driven with constant rotation frequency, where the volume flow is practically independent of the opposed pressure. If such a pump is equipped with an ideal pressure regulator then it becomes an effort source with the effort (pressure) independent of the flow.

Fig. 2.12 “1” and “0” junctions in bond graphs



2.4.2.3 Modulated Sources

Many effort and flow sources are controlled (by a signal). They are named modulated sources (*MSe* or *MSf*) and are highlighted by a letter *M* “modulated” preceding the source symbols as given in Fig. 2.15b. For example, a pump can be controlled by an external control signal to regulate its speed.

2.4.3 Junctions

To express other constraints of the global system being modeled, bond graph elements (R,C,I) are interconnected by “0” junctions when interconnected ports have a common effort and by “1” junction if their flow is the same. Formerly, these junctions have been called *P* (parallel)- and *S* (series)-junctions by author Jean Thoma. This is better for generating computer code but has been abandoned for international standardization because in fact, the series and parallel aspects of the junctions are more obvious in the electrical than in the mechanical systems. Sometimes called three ports, the junctions allow to connect the elements (in parallel and series connections). Bond graph representation of “0” and “1” junctions are shown in Fig. 2.12.

Remark 2.2 The equation deduced from junction are called *structural equations*: they represent a set of conservation laws (of mass, energy, etc.) and/or equilibrium equations.

In all junctions we have power conservation, which can be expressed as:

$$\sum_{i=1}^n e_i f_i = 0, \quad (2.23)$$

where n is the number of ports and \sum is the algebraic sum. The sign is taken (+) when the power direction is towards the junction and (−) when it is outwards from the junction. For the bond graph model of Fig. 2.12, two power directions are into the junction (the bonds 1 and 4) and two power direction are out of the junction (the bonds 2 and 3); thereby giving the conservation law:

$$e_1 f_1 + e_4 f_4 - e_2 f_2 - e_3 f_3 = 0. \quad (2.24)$$

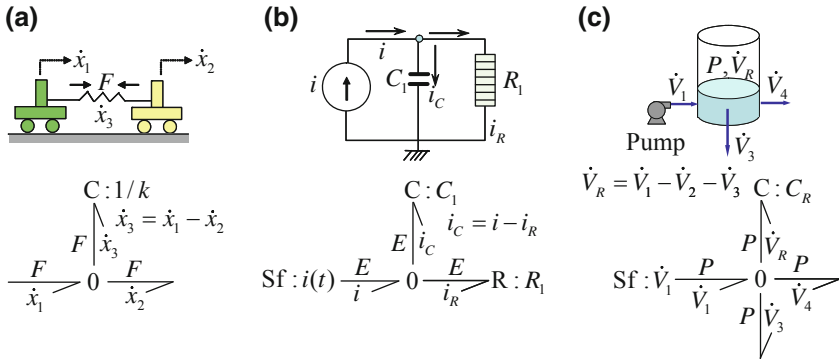


Fig. 2.13 0 junction in a Mechanical, b electrical, and c hydraulic systems

- *0-junction (common effort junction)*: It associates elements with the same effort, which means parallel circuit in electricity and oil hydraulics, and series circuit in mechanics. This corresponds to the Kirchoff’s current law in electricity. The constitutive equation and representation of such junction are described by Fig. 2.12a. The efforts on all bonds are identical, and algebraic sum of flows is equal to zero. The constitutive equations (from Fig. 2.12) may be written as

$$\begin{cases} f_1 + f_4 - f_2 - f_3 = 0, \\ e_1 = e_2 = e_3 = e_4 = 0. \end{cases} \quad (2.25)$$

In mechanical engineering, “0” junction represents a geometric compatibility for a situation involving a single force and many velocities which algebraically sums to zero. It represents for electrical system a Kirchoff’s law for a node where conductors join. In hydraulic systems, it represents a conservation of volume/mass flow rate at a point where several pipes join. Those physical interpretations are illustrated in Fig. 2.13.

- *1-junction (common flow junction)*: It associates elements with the same flow, which means series circuit in electricity and oil hydraulics but parallel circuit in mechanics. The flows in all bonds are identical, and algebraic sum of efforts is equal to zero. The constitutive equations (from Fig. 2.12) are written as

$$\begin{cases} e_1 + e_4 - e_2 - e_3 = 0, \\ f_1 = f_2 = f_3 = f_4 = 0. \end{cases} \quad (2.26)$$

Examples of 1-junctions are given in Fig. 2.14. “1” junction represents in mechanical engineering a dynamic equilibrium of forces associated with a common velocity (Fig. 2.14a). If an inertia is involved, Newton’s law for the mass element can be deduced. In electrical circuit (Fig. 2.14b), 1-junction represents circuits in series connection: Kirchoff’s law for voltage can be written. When hydraulic components

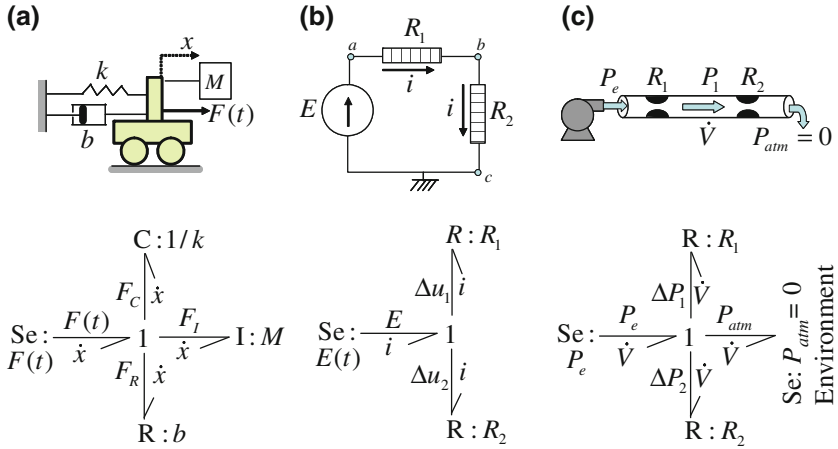


Fig. 2.14 1 junction in a Mechanical, b electrical, and c hydraulic systems

are in serial connection, the flow is the same and the pressure drops around the circuit are summed up. Corresponding to Fig. 2.14c, the constitutive equation is:

$$P_e - \Delta P_1 - \Delta P_2 - P_{atm} = 0, \tag{2.27}$$

where $\Delta P_1 = P_e - P_1$, $\Delta P_2 = P_1 - P_{atm}$ and atmospheric pressure $P_{atm} = 0$.

2.4.4 Two-Port Elements: Transformer and Gyration

• Transformer element—TF

Definition 2.6 A transformer element, denoted by TF, is a conservative two-port bond graph element which scales like power variables, sometimes transforming energy from one domain into another. It's constitutive relations (Eq. (2.28)) algebraically link inlet and outlet efforts and inlet and outlet flows. The effort in the first port is proportional to the effort in the second port and the flow in the second port is proportional to the flow in the first port with the same proportionality constant.

This energy conservative element models electric transformers, gear reducers in rotary mechanics, or simply levers in rectilinear mechanics. Since TF element does not store energy, we have power direction of one bond pointing towards the element and the other is oriented away from the element.

The constitutive relations of a transformer element are between input and output efforts, and between input and output flows:

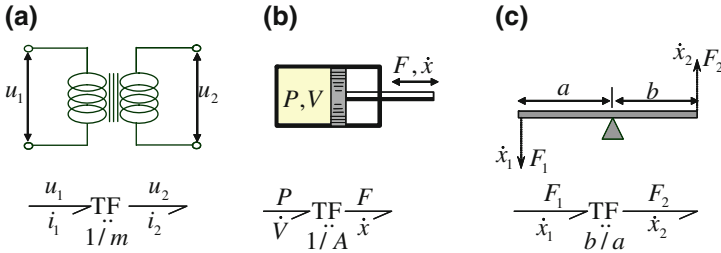


Fig. 2.15 Examples of TF-element: **a** Electrical transformer, **b** hydraulic piston, and **c** mechanical lever

$$\begin{cases} e_1 = m e_2, \\ f_2 = m f_1, \end{cases} \quad (2.28)$$

where m is called the *modulus of the transformer* or *transformer modulus* and subscripts 1 and 2, respectively, represent the sides with power direction into the TF-element and out of the TF-element. Obviously, $e_1 f_1 = m e_2 \times f_2 / m = e_2 f_2$. If the modulus m of the transformer is not constant, but depends on time or any other parameter, then it is called an *MTF (modulated transformer)* element. The *MTF* element still models a power conserving transformation.

Examples for transformers are pumps and cylinders in fluid power engineering, and levers and gear boxes in mechanical engineering (Fig. 2.15). The constitutive equations for the piston-cylinder (Fig. 2.15b) mechanism of cross-section A is:

$$\begin{cases} P = F/A, \\ \dot{x} = \frac{\dot{V}}{A}. \end{cases} \quad (2.29)$$

Transformers are of two different kinds:

1. Impedance transformers, where the input and output variables are of the same energy domain or class.
2. Class transformers, where the input and output variables belong to different energy domains or classes, e.g., hydraulic cylinders and pumps connecting hydraulic variables with mechanical variables. Hydraulic power is transduced into mechanical power in the piston.

Depending upon the physical system being modeled, the transformer modulus is defined by taking the power direction into consideration. For example, if the power directions are reversed in Fig. 2.15c then the transformer modulus becomes a/b .

Remark 2.3 The transformer modulus is defined in such a way that the flows in the bonds are scaled according to the power direction. The effort variables are scaled in the reverse direction. To decouple the dependence of transformer modulus from the power direction, another convention is sometimes used. In this convention, a directed arc called transformer orientation is placed near the transformer modulus

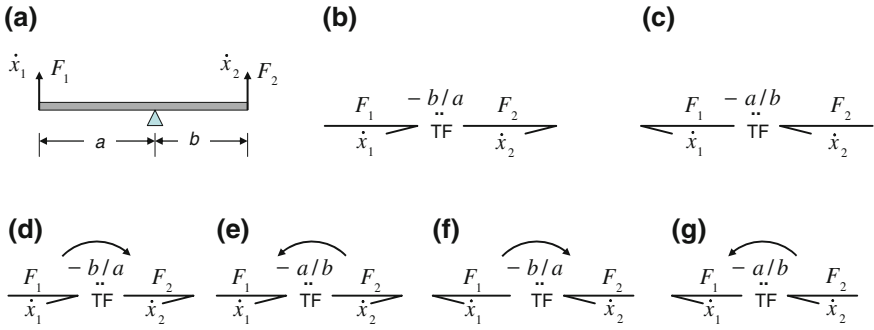


Fig. 2.16 Various ways of defining transformer modulus: **a** a simple lever with assumed positive coordinates, **b** and **c** model without transformer orientation *arrow*, and **d–g** model with transformer orientation *arrow*

to indicate the direction of flow scaling. The efforts are scaled in the opposite way. This convention allows independent assignment of power and scaling directions. In this book, the transformer orientation convention is used in some of the chapters.

Figure 2.16a shows a mechanical lever with the positive sense of velocities and forces indicated at its two ends. Respecting this coordinate system, we can see that $\dot{x}_2 = (-b/a)\dot{x}_1$ and $F_1 = (-b/a)F_2$ so that the power conservation relation $F_1\dot{x}_1 = F_2\dot{x}_2$ is satisfied. The lever can be modeled as a TF-element as shown in Fig. 2.16b, c with the scaling factor decided by the power direction. If the scaling factor is decided separately by transformer orientation then it becomes independent of power direction as shown in Fig. 2.16d–g. The constitutive relation is the same in all these models. Note that if the transformer orientation is the same way as the power direction as in Fig. 2.16d, g then the transformer modulus matches with that for the normal convention, i.e., as given in Fig. 2.16b, c, respectively.

• Gyrator GY

Definition 2.7 A Gyrator element, denoted by GY, is a conservative two-port bond graph element which scales dissimilar power variables, generally transforming energy from one domain into another. The effort in any side of the GY two-port is proportional to the flow on the opposite side of that two-port (Eq. 2.30).

Gyrators are also called transducers, and they allow to transform energy from one domain into another (gyroscope, electric motor). An example is the electric motor, that transforms electric power into mechanical rotary power (Fig. 2.17a). The constant of proportionality r is called *gyrator ratio* or *modulus*. Unlike TF-element, the constitutive equation for GY is “crossed”, i.e., between dissimilar power variables:

$$\begin{cases} e_1 = rf_2, \\ e_2 = rf_1. \end{cases} \quad (2.30)$$

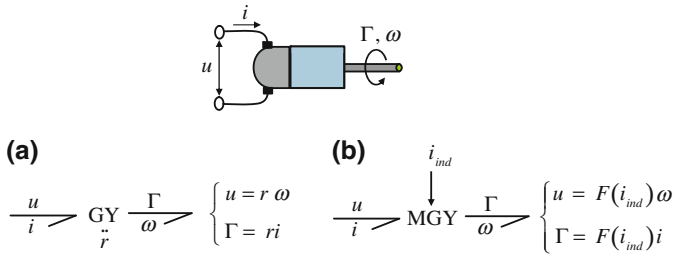


Fig. 2.17 a Gyrator element and b modulated Gyrator element

The gyrator may be adjustable, and its conversion ratio can be modulated by a signal applied through an activated bond. This is represented by the symbol *MGY* (*modulated gyrator*). An example is the electric motor with variable field strength (Fig. 2.17b). Note that the modulated signal (activated bond) means that no power is associated with the change in *m* and *r* (in both TF- and GY-elements), thus the power $e_1 f_1$ is equal to $e_2 f_2$. This is contrary to other passive elements, e.g., *C*-element where the stored energy changes when the information signal changes. One example of the later case is a capacitor with movable plates.

2.4.5 Information Bond

In measurement, instrumentation, and control system, the energy transferred by the signal is negligible when compared to that exchanged between the physical components. Such control system components are said to be active components. Most often, external power is supplied to the active components in the instrumentation circuit, e.g., power amplifier, capacitive sensor, etc. This external power supplied to the active components does not interfere with the passive parts of the system. Thus, for modeling purposes, we need to distinguish between passive and active components and their connections.

The signal is represented by an information or signal bond, which corresponds to block diagram’s arrows. It is shown as a full arrow on the bond and can represent the signal transmitted by a sensor, integrator, sum member, controller, etc. The information bond does not need a power direction because no power is transmitted from the physical system. Out of the two factors of power, only one is present in an information bond. The other power variable is assumed to be zero from the physical system’s perspective. Note that the complementary power variable may not be actually zero, but no power or negligible power is drawn from the passive parts of the system. For example, the voltage drop across a moving coil galvanometer used to measure current is never zero, but negligible. A laser-based speed sensor does not apply any force on the object whose speed is measured, but the sensor requires

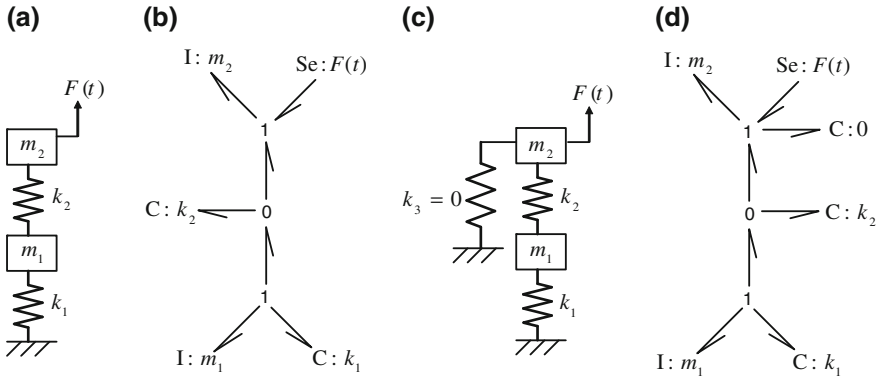


Fig. 2.18 Conceptual representation of displacement and flow sensors

power from an external supply to operate the laser. Thus, modeling of sensors and information flow considers the power to be zero in information bonds from the point of view of the considered physical system only; the external power supply to the active components are exogenous to the physical system and the power transfer in those parts are not modeled.

Let us now have a look at the concept of a sensor from a bond graph perspective. There are two power variables: flow and effort, and there are two kinds of sensors to measure them. They are called detector of flow (flow sensor) and detector of effort (effort sensor). Figure 2.18a shows a two-degrees-of-freedom system and its bond graph model is shown in Fig. 2.18b. In Fig. 2.18b, the lower 1-junction for common flow indicates that the velocity of mass m_1 and the rate of deformation of the spring k_1 are the same. The upper 1-junction indicates that the point of application of force $F(t)$ moves at the same velocity as that of mass m_2 . The 0-junction in between the two 1-junctions represents the fact that the force generated in the spring k_2 is the same as that applied on the upper mass and the lower mass; the direction of applied force is adjusted by the power directions. An alternative explanation is that the 0-junction is a common effort and flow sum junction and the latter property establishes that the flow or rate of deformation of spring k_2 is the difference between velocities of mass m_1 and mass m_2 .

Note that a simulation performed on a bond graph model gives the values of state variables and rate of change of state variables with respect to time as its outputs. The bond graph model in Fig. 2.18b has four state variables which are the momenta of the two masses and the deformations of the two springs. In addition to those state or energy variables, their time derivatives, i.e., the resultant forces acting on those masses and the rate of deformation of the springs are also the outputs. However, if one needs to measure the position of mass m_2 , there is no directly available output for it. It can be obtained as the sum of the deformations of the two springs or as integration of the momentum of mass m_2 divided by the value of the mass m_2 . In

Fig. 2.19 Representation of sensor elements in bond graphs

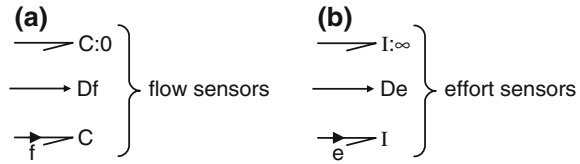
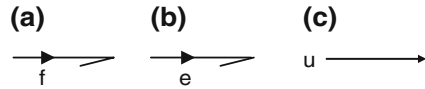


Fig. 2.20 Signal and activated bonds for information flow modeling in bond graphs



order to directly generate a pseudo-state for the displacement of mass m_2 , one can think of a spring attached to mass m_2 at one end and fixed to the ground in its other end as shown in Fig. 2.18c. Let the stiffness of the new spring k_3 be zero. The bond graph model of the new system is shown in Fig. 2.18d where the model for spring $k_3 = 0$ is attached to the upper 1-junction. This new spring does not generate any force on the mass point because its stiffness is zero. However, it introduces a new state variable which gives the position and its time derivative gives velocity of mass point m_2 as outputs. Indeed, the new spring acts as a flow sensor (position sensor on integration).

Instead of using a passive spring element and setting its stiffness to zero, we can represent the same in a concise manner by using a detector of flow element (Df element) or a flow activated C -element as shown in Fig. 2.19a. A bond is called activated, if one of its power conjugated variable is set to zero. The Df element or flow activation (indicated by symbol f placed near the full arrow) means that only flow information is transmitted and the effort variable is zero. Thus, there is no need to define the value of the C -element (shown or hidden) to be zero.

The effort detector can be defined likewise. If we apply a force on an infinitely heavy mass then the mass will have negligible motion. However, because it has infinite mass, it will have a finite momentum whose time derivative would give us the value of the applied force. Thus, addition of a fictitious infinite mass generates a new state and its time derivative as outputs. This fictitious infinite mass can be simplistically modeled as a detector of effort element (De element) or effort activated (symbol e placed near the full arrow) I -element as shown in Fig. 2.19b where the information or activated bond carries only effort information and the flow in the bond is zero. By definition, a sensor carries information of one signal (as defined by activation type) and there is no reaction from the sensor to the system (Fig. 2.20).

One obvious observation can be made from the above discussions: a flow sensor is usually attached to a 1-junction and an effort sensor is usually attached to a 0-junction. However, exceptions are possible. The type of sensor is actually determined by the causality at the port. The concept of causality is discussed in the next section.

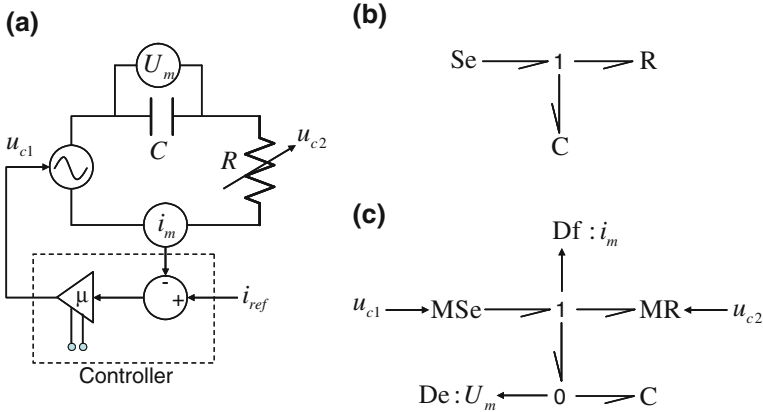


Fig. 2.21 a A closed-loop control system, b its basic bond graph and c bond graph with modulated sources and elements

Let us now demonstrate how an instrumented system can be modeled in bond graph form. Figure 2.21a shows a series RC electrical circuit with a variable resistor and a modulated voltage source. The circuit is instrumented to measure the current through the wire (i_m) and the potential across the capacitor (U_m). The control objective is to maintain a constant current through the circuit even when the resistance is changed by an external signal u_{c2} . For that, a proportional control scheme is adopted where the measured current (i_m) is compared to a reference current (i_{ref}) and the error is amplified through a power amplifier to modulate the voltage source. The details of voltage source modulation device (e.g., a variable transformer) are not shown here and we will not model it.

The bond graph model of the core system (series RC circuit with the voltage source) is shown in Fig. 2.21b. If we include the modulations of the source and the resistor and also model the sensors, then the bond graph model assumes the form shown in Fig. 2.21c. Note that the current in the circuit is measured by the Df element at the 1-junction through which MSe and MR elements are connected. If voltage across the capacitor is not measured then the C-element should be directly connected to that 1-junction. However, to measure potential across the capacitor, we need to add a detector of effort. As has been discussed earlier, the effort information can be tapped from a common effort junction. Therefore, a 0-junction is introduced in Fig. 2.21c to which the C and De elements are connected. Note that the current (flow) in the De element is zero. Thus, the flow through the C-element is still equal to the flow at the 1-junction.

The control circuit model may now be introduced in block diagram form as shown in Fig. 2.22a where a comparator block is introduced to compute the error between the reference command and the measured current and an amplifier or gain block is introduced to proportionally scale the error for input voltage regulation. The type of

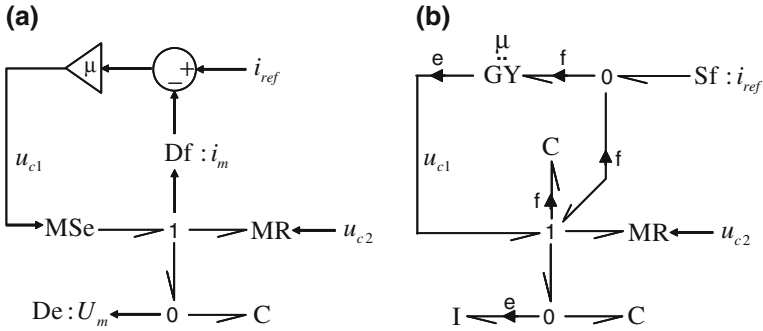


Fig. 2.22 Bond graph model of the controlled system using **a** signal bonds and **b** using activated bonds

the signal (effort or flow) is not distinguished in this model. In this type of model with all active connections represented through signal or information bonds, the control signal is tapped from a sensor and the output from controller is applied to a modulated source.

The bond graph model of the control system can be developed in another form by using activated bonds. In this form, the type of the signals (effort or flow) has to be distinguished. Because the measured current (i_m) and the reference command (i_{ref}) are flow variables, the comparison of both requires a flow algebra node. Therefore, in the bond graph model shown in Fig. 2.22b, the reference command is modeled as a flow source and the flow comparison is done at a 0-junction. If efforts have to be compared then a 1-junction should be used. Three bonds are connected to this 0-junction: the flow source giving reference command (i_{ref}), a bond connected to 1-junction giving measured current (i_m), and a bond which outputs the error $i_{ref} - i_m$. Note that the measurements in this model are done through flow activated C-element and effort activated I-element. The signal tapped from the circuit for comparison is not taken from the sensor, but from the junction itself. The effort variables in all the bonds connected to the 0-junction modeling the comparator are zero, thus all those bonds are flow activated. The power directions of the bonds at the 0-junction establish the negative sign in the flow sum to determine error as $i_{ref} - i_m$. In this form of modeling through activated bonds, we identify that the error signal is a flow variable. This flow variable needs to be scaled by an amplifier and the result is an effort variable (the source voltage). Thus, the transformation between flow and effort is represented by a GY element whose modulus is equal to the amplification or proportional gain. If like variables have to be scaled (flow to flow or effort to effort) then one should use a TF-element to represent the gain. Here, the output of the amplifier is a voltage which is directly applied at the 1-junction without the need for a modulated source. One port of the GY element is flow activated (zero effort), whereas the other port is effort activated (zero flow). Note that in this type of modeling with activated bonds, the inputs to the active circuit model are taken

from junctions (not from sensors) and the outputs are connected to junctions (not to modulated sources).

Some advantages and disadvantages exist for both the approaches. The signal or information bond-based approach explicitly shows the sensors and actuators in the model. It can be used to model complex control laws in which the control law can be represented as a block. It is possible to apply structural analysis methods and fault diagnosis filter design methods, which are discussed in Chap. 4, on such a bond graph. This simpler form is also easier to understand. On the other hand, the activated bond-based approach does not show the sensors and actuators. However, it shows the quality of the signal and does not require additional bond graph elements (De, Df, MSe, MSf, etc.). It is not possible to model implementation of complex control laws in activated bond graph form and one has to use block diagrams. Note that most bond graph modeling software accept one of the presented forms and thus the model should be built keeping in the view the software to be used for simulation. In international communications, the information or signal bond representation is usually adopted.

2.5 Causality

If we need to efficiently simulate the physical behavior described by the model, we have to decide the order in which the variables (effort and flow) are to be computed. Consequently, we need to make a series of cause and effect decisions, which is described by the notion of *causality*. When two physical components are interconnected, they exchange a power. This exchanged power is represented by a bond as developed before. Each component is described by its behavior (called a constitutive equation) and constraints (junctions and two-ports) link the components. If we need to simulate the physical phenomena (the model), we have to decide in which order the variables (effort and flow) will be computed. Thus, we will introduce the block diagram simulation which is causal. Consequently, we need to make a series of cause and effect decisions: this is the concept of *causality*. To make the bond graph model causal, the founders of this theory introduced a perpendicular stroke. This single mark or stroke on a bond, called “*causal stroke*” indicates how the information flow path for variables e and f are simultaneously determined on a causal bond. The stroked end receives effort information and the unstroked end receives flow information. It is never the case that one end receives both the effort and flow informations. Thus the information flow paths for effort and flow are always counter-orientated. This form of causality is also called uncausality.

For example, $ax + by = 0$ with a and b being two constants and x and y being two variables is an acausal equation or model which appears as constitutive relation for two-ports and R-elements. Causality orders these equations. The causal relation can be written in such a way that only one variable is the output, e.g., $x = -(b/a)y$ is a causal relation in which y is the cause (antecedent) and x is the effect (consequence) or, $y = -(a/b)x$ is another causal relation in which x is the cause (antecedent) and

y is the effect (consequence). Note that more than one variable can appear on the RHS of the equation, but only one variable should appear on the LHS. For example, if the relation $f_1 + f_2 - f_3 = 0$ holds good at a 0-junction (flow sum junction) with three bonds, then the possible causal relations are $f_1 = -f_2 + f_3$, $f_2 = -f_1 + f_3$, and $f_3 = f_1 + f_2$. However, a relation like $f_1 + f_2 = f_3$ is not causal because from known value of f_3 only, we cannot compute two unknown variables. As a consequence, flow in only one bond (called a strong bond) can be determined at a 0-junction when flows in other bonds are known. Likewise, the effort in only one bond can be determined at a 1-junction. More details on these rules are discussed below.

Causal analysis determines the direction of the effort and flow information exchange in a bond graph model. This information exchange is a mathematical or computational aspect of the problem and it is not related to the physics of the problem. The result is a causal bond graph which can be considered as a compact block diagram. From causal bond graph we can directly derive an equivalent block diagram. It is the algorithmic level of modeling.

Causal propagation is useful to analyze bond graph model. Indeed the causal strokes give information about causal conflict (incompatibility of equations), derivative causalities (loss of states), algebraic and causal loops (solvability and complication level of the numerical model), and control and monitoring properties.

Let us consider an electrical system which consists of a source of voltage E connected with a resistance R (Fig. 2.23a). The voltage E and the current i are complementary power variables. For the voltage source E is an output variable and i is an input variable. Thus, we have a fixed causality at the source. Consequently, for the resistance, E given by the source is an input variable and $i = E/R$ is an output variable. This computation form of the model is represented by the causal bond graph (Fig. 2.23 (a₁)). Its corresponding block diagram is given in Fig. 2.23 (a₂): e is known for R . In Fig. 2.23b we have a source of current. The provided current I (representing the flow variable f) is an input for R and the voltage $e_R = Ri$ (as effort variable) is an output from R . The causal bond graph and the associated block diagrams are given in Fig. 2.23 (b₁) and (b₂), respectively.

Based on the causality concept, the determination of causes and effects in the system is directly deduced from the graphical representation and shows at the same time the transition to the block diagram. The simulation algorithm is then indicated by the position of the causal stroke in the bond graph which becomes *causal bond graph*. Causality is a symmetric relationship. When one side “causes” effort, the other side “causes” flow. The rule is as follows:

Remark 2.4 The causal stroke is placed near (respectively, far from) the bond graph element for which the effort (respectively, flow) is known.

For remembering this convention or rule, a graphical representation is shown in Fig. 2.24: *effort pushes and the response is a flow*. The stroked end receives effort information and the unstroked end receives flow information.

Fig. 2.23 Causalities in bond graphs. **a** Effort is known for R. **b** Flow is known for R

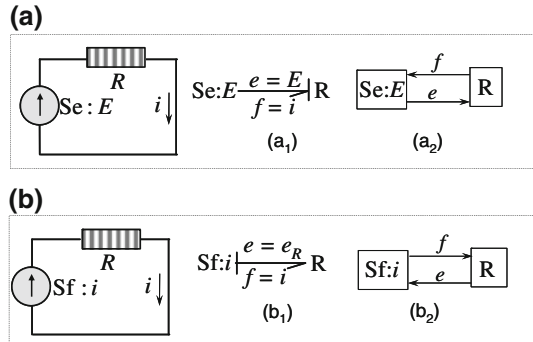
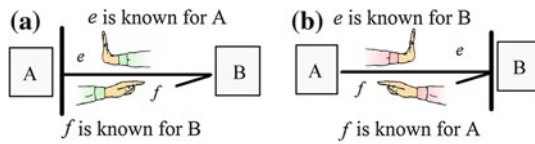


Fig. 2.24 Implication of the causal stroke



2.5.1 Sequential Causality Assignment Procedure (SCAP)

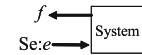
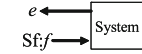
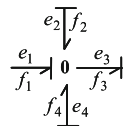
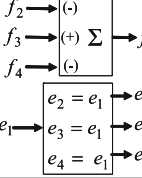
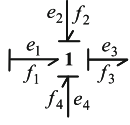
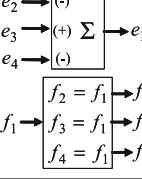
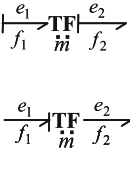
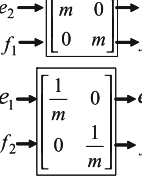
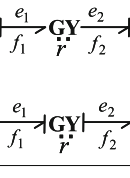
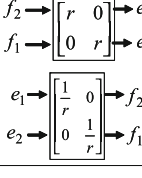
Causality results in compatibility constraints. Clearly, only one end of a power bond can define the effort and so only one end of a bond can have a causal stroke. Based on this, the causality propagation or extension rules can be derived as given below:

1. Note that efforts are equal in a 0-junction and flows are equal in a 1-junction. Thus, only one bond can cause the effort in a 0-junction and only one bond can cause the flow in a 1-junction. Thus, if the causality of one bond of a junction is known, the causality of the others is also known. That one bond is called the strong bond.
2. Likewise, if the causality in one port of a two-port element is known, the causality of the other port is automatically established. For a TF element, if flow (or effort) on one side is known then the flow (or effort) of the other side is computed from it.
3. Likewise, in a gyrator, if the flow is known in one bond then the effort of the other bond is computed from it and if the effort is known in one bond then the flow of the other bond is computed from it.

The causal forms of different bond graph elements, their corresponding causal equations and block diagrams, and the causality assignment rules are given in Table 2.6.

When causalling a complete bond graph model, in order to predict how the final equations will turn out and to avoid inconsistency, the procedure given below (called sequential causality assignment) must be followed in strict order.

Table 2.6 Causality assignment for bond graph elements

Element	Bond graph	Causal equation	Block diagrams	Rule
Effort source	Se: $e \rightarrow $	e is known	$f \leftarrow$ 	Output of Se (of Sf) is an effort (flow) and is an input for the system.
Flow source	Sf: $f \rightarrow$	f is known	$e \leftarrow$ 	<i>Rule : The causality is compulsory</i>
0 Junction		$\begin{cases} e_2 = e_1 \\ e_3 = e_1 \\ e_4 = e_1 \\ f_1 = -f_2 + f_3 - f_4 \end{cases}$		Only one effort (here e_1) is input. <i>Rule : Only one bond can have causal stroke near the 0 junction.</i>
1 Junction		$\begin{cases} f_2 = f_1 \\ f_3 = f_1 \\ f_4 = f_1 \\ e_1 = -e_2 + e_3 - e_4 \end{cases}$		Only one flow (here f_1) is an input. <i>Rule : Only one bond can have causal stroke away from the 1 junction.</i>
TF		$\begin{cases} e_1 = me_2 \\ f_2 = mf_1 \\ e_2 = \frac{1}{m} e_1 \\ f_1 = \frac{1}{m} f_2 \end{cases}$		Only one effort and one flow are inputs <i>Rule : One causal stroke near TF</i>
GY		$\begin{cases} e_1 = rf_2 \\ e_2 = rf_1 \\ f_2 = \frac{1}{r} e_1 \\ f_1 = \frac{1}{r} e_2 \end{cases}$		Two efforts or two flows are inputs <i>Rule : Two or no causal strokes near GY</i>
C	$\int \frac{e}{f} C:C_1$ $\frac{e}{f} C:C_1$	$e = \Phi_C(\int f dt) = \Phi_C(q)$ $f = \frac{d}{dt}(\Phi_C^{-1}(e))$	$f \rightarrow \Phi_C(\int f dt) \rightarrow e$ $e \rightarrow \frac{d}{dt}(\Phi_C^{-1}(e)) \rightarrow f$	Integral causality: effort is an output Derivative causality: flow is an output
I	$\frac{e}{f} I:I_1$ $\int \frac{e}{f} I:I_1$	$f = \Phi_I(\int e dt) = \Phi_I(p)$ $e = \frac{d}{dt}(\Phi_I^{-1}(f))$	$e \rightarrow \Phi_I(\int e dt) \rightarrow f$ $f \rightarrow \frac{d}{dt}(\Phi_I^{-1}(f)) \rightarrow e$	Integral causality: flow is an output Derivative causality: effort is an output
R	$\int \frac{e}{f} R:R_1$ $\frac{e}{f} R:R_1$	$e = \Phi_R(f)$ $f = \Phi_R^{-1}(e)$	$f \rightarrow \Phi_R(f) \rightarrow e$ $e \rightarrow \Phi_R^{-1}(e) \rightarrow f$	Resistance causality: output is an effort Conductance causality: flow is an output

1. The sources always impose one causality: effort is imposed by effort sources and flow is imposed by flow sources. Then choose any Se or Sf and assign its required causality. Immediately extend the causal implications, using all 0, 1, TF , and GY restrictions that apply, as shown in Table 2.6.
2. Choose any C or I and assign integral causality (well adapted to numerical calculations) as shown in Table 2.6. Again extend the causal implications of this action, using 0, 1, TF , and GY restrictions.
3. Choose any R that for which causality is yet unassigned and give it an arbitrary causality. In linear R -elements, the causality is in principle indifferent, but indicates whether resistance or conductance need to be entered as parameter. In nonlinear R -elements, equations are more comfortable in one direction according to the equation form. After arbitrary causality assignment to R -element, extend the causal implications, using 0, 1, TF and GY restrictions.

The causality is an important aspect of bond graph. By propagating the causality graphically throughout the model, analysis of large-scale models becomes easier. Causality assignment shows the information coupling between various elements in the system. It also allows the detection of a modeling situation where a causal loop exists; that is the situation when a variable is defined recursively as a function of itself or a derivative causality. The causal property of bond graph is used not only for simulation purpose but also for control analysis (controllability and observability analysis) [8, 51–53] and diagnosability (ability to detect an isolate faults) [26, 29, 31, 32, 44, 46, 54].

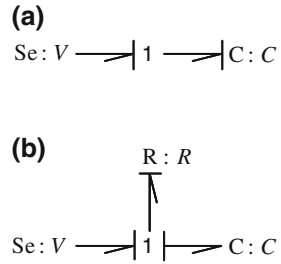
2.5.2 Derivative Causality and Its Implications

Let us recall the concept of energy or state variables (See Sect. 2.3.4). The deformation of a spring defines its state, i.e., the potential energy. Likewise, the impulse of a mass is its state which defines the kinetic energy. These states admit initial conditions. For example, the coupled first order differential equations for a certain single degree-of-freedom mechanical system (mass m , stiffness k , damping r and a forcing $F(t)$) given as

$$\begin{aligned}\dot{p} &= -kx - \frac{r}{m}p + F(t) \\ \dot{x} &= p/m \text{ with } p = m\dot{x} \text{ and } \dot{p} = m\ddot{x}\end{aligned}$$

can be solved for state variables $x(t)$ and $p(t)$ (consequently, $\dot{x}(t) = p(t)/m$) and their time derivatives if parameter values (value of mass m , stiffness k , and damping r), excitation $F(t)$ and initial values at a certain time, say $t = 0$ (i.e., $x(0)$ and $p(0)$) are known. Note that in a bond graph model, the boundary conditions are already implemented in the model structure (e.g., one end of the spring fixed to ground). The initial values are used during integration of the differential equa-

Fig. 2.25 Example of differential causality



tions. Thus, if the constitutive relation for the storage element (I- or C-element) is in non-integral form then it does not lead to a state variable and one cannot assign an initial condition to it. The state variables are results of integration. For deterministic systems, a fundamental concept is that the present (initial value) decides what will happen next and once that value in the next step is known, it and the excitation at that time together decide what will happen further next. Sometimes, the past history may be useful. However, the future cannot decide the past. Thus, the response of a deterministic dynamic system is always given by a history function, integration being the tool to model this time history. If the energy, including the initial energy, in a storage element has to be considered in the model then the storage element must be integrally causalled (See Table 2.6), i.e., the causal stroke must be placed near the I-element and away from the C-element.

The ability to automatically identify impossible configurations or modeling errors, such as differential causality or causal loops, is a major advantage of bond graphs. For example, let us connect a capacitor directly to a battery. The bond graph model is then a source of effort connected to a C-element through a 1- or 0-junction (any one is fine). When we assign causality, we see that the C-element receives derivative or differential causality as shown in Fig. 2.25a. Let us see what the problem is with this model. If Q is the final charge stored in the capacitor at steady-state then $V = Q/C$ or $Q = VC$. The energy stored in the capacitor is then $E_C = \frac{1}{2}Q^2/C$. However, the energy drawn from the voltage source is $E_S = \int_0^\infty Vidt = \int_0^Q Vdq = VQ = Q^2/C$. Thus, the energy stored in the capacitor is not the same as the energy drawn from the source; half of the energy from the source is missing somewhere. In fact, this energy should be dissipated by some resistance. We do not have a charging time constant in our model because if we connect the voltage source to the capacitor then the capacitor would be instantly charged. Thus, differential causality almost always indicates the loss of a time constant or a state. To remedy this problem, let us introduce the series circuit resistance (or charging resistance) to the circuit. The bond graph model then assumes the form given in Fig. 2.25a which can be causalled without derivative causality. Note that introduction of a parallel circuit resistance does not solve the problem but a series resistance does. Here, the bond graph had indicated that a resistor needs to be put in series with the capacitor to develop the correct energetically consistent model.

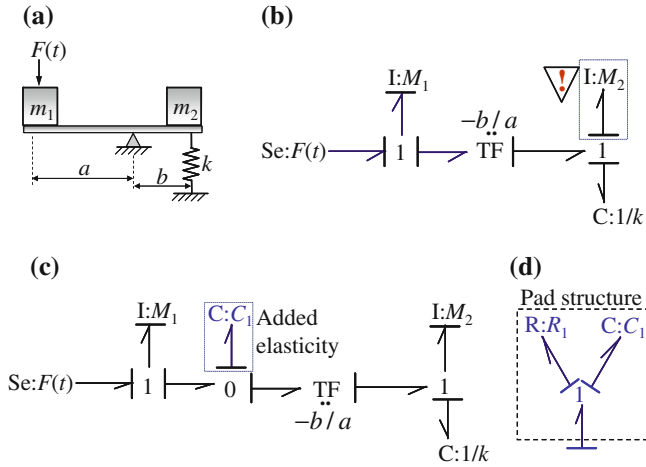


Fig. 2.26 a A mechanical system, b its bond graph model in derivative causality, c bond graph model in integral causality by adding a coupling capacitor, and d pad structure

As another example, a mechanical body submitted to an external force $F(t)$ through a leverage system is shown in Fig. 2.26a. The bond graph model as given in Fig. 2.26b shows a derivative causality. We can easily identify that a time constant is missing between the velocities of two masses; these velocities are algebraically coupled. Thus, while we have introduced two I-elements in our model, they are actually not leading to additional degrees-of-freedom. In order to present the global system in integral causality, an equivalent elasticity of the lever can be introduced and it can be assumed that the stiffness of the lever is very large (this has to be ensured during numerical simulation by properly giving the parameter values). The resulting model shown in Fig. 2.26c is completely in integral causality. The new C-element has introduced a time constant into the system. While the rigid lever system had one degree-of-freedom, the revised system has two-degrees-of-freedom but approaches the single-degree-of-freedom system as parameter $C_1 \rightarrow 0$ or stiffness $k_1 \rightarrow \infty$. Another approach is to refer the mass on one side of the lever to the other side and then model the single-degree-of-freedom system with only one I-element. For example, we can model this whole system with a single mass of $m_1 + (b/a)^2 m_2$, force $F(t)$ and stiffness $(b/a)^2 k$. This approach requires knowledge of transformer and gyrator equivalence which will be discussed in the subsequent chapters.

The approach of introducing a C-element in a mechanical system model to remove differential causality is also followed in hydraulic and thermo-fluid systems. Such a C-element is called a *coupling capacitor*. However, introducing a very stiff spring or coupling capacitor increases the numerical solution stiffness, i.e., it introduces a new time constant which is vastly different from time constants in the other parts of the system. This spread of time constants leads to slower simulation because the high frequency components introduced by the stiff spring requires smaller solution

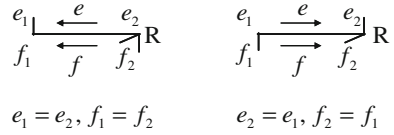
time steps. Therefore, a resistance is often included with the stiff spring as shown in Fig. 2.26d. The combination of a stiff spring and damper, called a pad structure, is very useful in modeling of various mechanical systems such as mechanisms and robots.

Note that we are using integration as a history function to build our model for simulation. Such a simulation is often referred to as forward or behavioral simulation and it gives us predictions about the behavior or time evolution of the states of the system. Forward simulation is a design tool. On the other hand, sometimes one needs backward simulation. An example of backward simulation is to reconstruct the sequence of events that has led to some catastrophic road accident. Likewise, we often diagnose faults in a system from the recorded data of the system's past behavior. In all such situations, we are not interested in a history function, rather we would prefer to determine the cause from the effects (this is contrary to the philosophy of forward modeling where we try to derive the effect from the cause). Thus, for diagnosis and backward simulation, one usually uses derivative causality in the model. Such applications of derivative causality will be shown in the subsequent chapters. A bond graph model can be thus causalled depending upon the user's preference, i.e., what is the objective of the user. Thus, the preferred causality in the model can be either preferred integral causality (for simulation, design, etc.) or preferred derivative/differential causality (for diagnosis, system inversion, etc.). In preferred integral causality, one tries to maximize the number of integral causalities and minimize the number of differential causalities (ideally, we should have no differential causalities) in storage elements. The converse is required in preferred derivative causality assignment. While pads and coupling capacitors are useful to assign preferred integral causality, removal of some large stiffnesses can be useful to assign preferred derivative causality.

2.5.3 *Bicausal Bond Graphs*

As we have seen, causality imposes a certain propagation throughout the bond graph. It implies that if effort acts in one sense, flow acts in the reverse sense, which is true for all physical systems. For some special applications like system inversion, actuator sizing, fault diagnosis, etc., we will need the effort and flow informations to travel in the same way. Thus, in system inversion and fault diagnosis, other causality rules are necessary [19]. This special need can be explained for a very simple case of parameter estimation. Real parameter estimation process is a recursive optimization to match the actual response of a dynamic system to the response of a simulated model. However, we will consider a simple case involving no optimization and would thus term it as a parameter measurement process. Let us consider how we measure resistance of a resistor in a multimeter. The multimeter has a battery for voltage source and when its two terminals are connected to two sides of a resistor, a current flows which is measured by the multimeter. The ratio of the supplied voltage to current gives the value of the resistance. If we model this as a block diagram then we have a block to

Fig. 2.27 Bicausal bond graph



which both effort (voltage) and current are inputs and the value of the resistance is the output from the block. We cannot represent this scenario in a bond graph model where the two conjugate power variable information are imposed on an R-element whose parameter value becomes a signal output (contrary to simulation models where parameter values are known).

One generalization of the causality selection proposed in [14, 16, 36] is the bicausal bond graph. There, one divides the causality stroke into two. One half, on the same side as the half arrow indicating power direction, indicates the direction of flow information imposition, and the other half indicates the direction of effort information imposition. If flow and effort information are co-oriented then the causal forms appear as shown in Fig. 2.27.

In the second case shown in Fig. 2.27, the causality of R indicates that both effort and flow are available to a block representing the constitutive relation of the R -element. This allows to calculate the resistance R , i.e., it helps in parameter estimation.

When the flow and effort information are counter-oriented then the half-causal strokes on both sides of the bond merge to create a full causal stroke. This situation is the normal causality (or unicausality) which we have discussed earlier. More details on bicausality notation and its use are given in Chap. 4.

2.6 Causal Path

Definition 2.8 (causal path) A causal path between two ports is an alternation of bonds and basic bond graph elements (named nodes) such that (i) all nodes have a correct and complete causality, and (ii) two bonds of the path have opposite causal stroke direction in the same node as seen from the node.

A causal path is equivalent to a signal loop in a block diagram or signal flow graph. In Fig. 2.28a, an RLC circuit is shown where the current is measured by the effort detector $Df : i$. From its bond graph model, different causal paths are deduced. The causal paths from the bond graph effort source (Se: E) to the C-element (represented by dashed line) and effort detector are given, respectively, in Fig. 2.28c, d.

2.6.1 Different Types of Causal Paths

Different types of causal paths are represented in Fig. 2.29. The simple direct causal path is covered following only one variable (effort or flow). However, there are two

Fig. 2.28 a RLC circuit, b its bond graph model, and c, d two causal paths

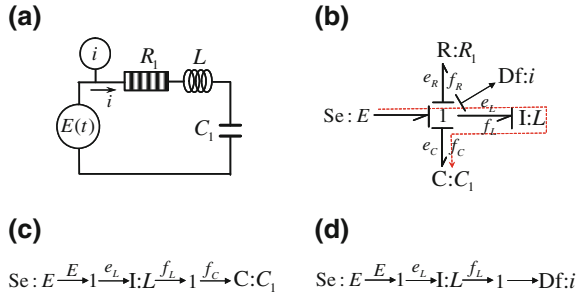
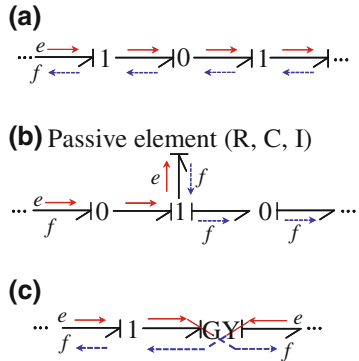


Fig. 2.29 Simple (a), indirect (b), and mixed (c) causal paths



sequences of bonds and nodes following effort or flow (see Fig. 2.29a). The causal path is said to be indirect if one passive element (R, C, I) should be crossed along the path Fig. 2.29b. Finally, the causal path is mixed if it comprises a gyrator (GY) imposing the change of followed variable (Fig. 2.29c).

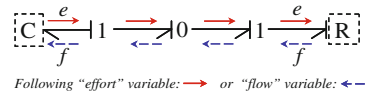
A causal path does not return through a source or a sensor. The followed variable changes (e to f , or vice versa) when the path passes through a passive element (I, C, or R) or a gyrator (GY).

Definition 2.9 The length or order of a causal path is the difference between the number of integrally causal and differentially causal storage elements encountered in the path. The count is incremented by 1 for each integrally causal I- and C-element while it is decremented by 1 for each differentially causal storage element.

Definition 2.10 When they contain at least one dynamical element, two causal paths are said to be different if they do not have any common dynamical element.

Definition 2.11 A forward path is a causal path between a source (actuator) and an output (represented by a detector). This path is used to determine forward path gain during transfer function evaluation.

Fig. 2.30 Closed causal paths while following “effort” variable → or “flow” variable ← --



2.6.2 Closed Causal Paths

Definition 2.12 A closed causal path starts and ends at the same node. It can exist between two elements of R, C, or I type (Fig. 2.30). It can also start and end at the same junction. A causal loop cannot involve a source or a sensor.

Definition 2.13 Two closed causal paths are disjoint if they have neither junctions nor bonds in common while following the same type of variable.

- A closed-causal loop with its length or order equaling zero is called a zero-order causal path (ZCP).
- A ZCP involving only junction structure elements (1, 0, TF, GY) and R-elements is an *algebraic loop*.
- A ZCP involving only junction structure elements (1, 0, TF, GY) is a causal loop which leads to the failure in the equation derivation process. Usually, a causal loop can expose some identities and hidden differential causalities in the model.

2.6.3 Causal Path Gain

Definition 2.14 The causal path gain is determined by the product of the gains of all the elements contained in the path.

The causal path gains (in a linear case) are calculated as follows:

- Directed causal path gain

$$K = (-1)^{n_0+n_1} \prod_i (m_i)^{k_i} \prod_j (r_j)^{l_j} \tag{2.31}$$

- Indirect causal path gain

$$K = (-1)^{n_0+n_1} \prod_i (m_i)^{k_i} \prod_j (r_j)^{l_j} \prod_e g_e \tag{2.32}$$

- Closed causal path gain or loop gain

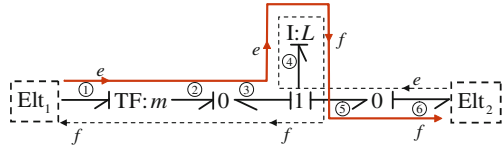
$$K = (-1)^{n_0+n_1} \prod_i (m_i^2)^{k_i} \prod_j (r_j^2)^{l_j} \prod_e g_e \tag{2.33}$$

where

Table 2.7 Passive element gains

Element	Causality	Gain
R	Resistance causality	R
	Conductance causality	$1/R$
C	Integral causality	$1/(Cs)$ or k/s
	Derivative causality	Cs or s/k
I	Integral causality	$1/(Is)$
	Derivative causality	Is

Fig. 2.31 Indirect causal path between two elements



- n_0 : Number of inversions in the direction of the half arrows at the 0-junctions when following the flow variable along the path
- n_1 : Number of inversions in the direction of the half arrows at the 1-junctions when following the effort variable along the path
- m_i : modulus of TF_i , $k_i = +1$ or -1 depending on TF_i causality
- r_j : modulus of GY_j , $k_j = +1$ or -1 depending on GY_j causality
- g_e : gain of the e th passive element (impedance or admittance).

These gains are given in Table 2.7 where s is the Laplace variable. The gains are essentially elementary transfer functions when a signal enters and returns from a linear passive element.

Example 2.1 Consider the bond graph shown in Fig. 2.31 where elements Elt1 and Elt2 are linked by an indirect causal path.

- The causal path gain $Elt1 \rightarrow Elt2$ represented in dashed line is:

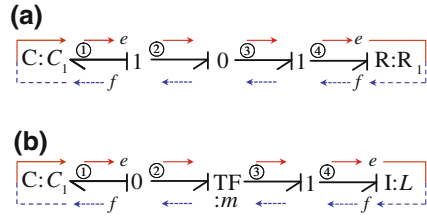
$$K_{Elt1 \rightarrow Elt2} = (-1)^{n_0+n_1} \frac{1}{m} \frac{1}{Ls} = -\frac{1}{m} \frac{1}{Ls} \quad \text{with } n_0 = 0 \quad \text{and } n_1 = 1 \quad (2.34)$$

There is only one inversion in the direction of the half arrow while crossing 1-junction following effort (from bond 3 to bond 4), thus $n_1 = 1$. But there is no inversion while crossing 0-junction following flow ($n_0 = 0$): from bond 5 to bond 6. The power direction inversion at 0-junction between bonds 2 and 3 is not considered because effort is being followed in that part and effort does not change at a 0-junction.

- The causal path gain $Elt2 \rightarrow Elt1$ shown in continuous line is:

$$K_{Elt2 \rightarrow Elt1} = (-1)^{n_0+n_1} \frac{1}{m} \frac{1}{Ls} = \frac{1}{m} \frac{1}{Ls} \quad \text{with } n_0 = 1 \quad \text{and } n_1 = 1 \quad (2.35)$$

Fig. 2.32 Examples of causal loops



Along the path ($El2 \rightarrow El1$), there is one inversion in the direction of the half arrow while crossing 1-junction following effort from bond 5 to bond 4 ($n_1 = 1$), and one more inversion while crossing 0-junction following flow from bond 3 to bond 2 ($n_0 = 1$). Note that while crossing 0-junction from bond 5 to bond 6 following flow, there is no inversion in the direction of the half arrow.

We can likewise determine causal path gains from $El1 \rightarrow El1$ and $El2 \rightarrow El2$.

Example 2.2 Consider the causal loop gains of bond graph models in Fig. 2.32.

- According to the formula 2.33, the loop gain $C : C_1 \rightarrow R : R_1$ of the bond graph model given in Fig. 2.32a is:

$$K_{C \rightarrow R} = (-1)^{n_0+n_1} \frac{1}{R_1} \frac{1}{C_1 s}, \quad \text{with } n_0 = 0 \text{ and } n_1 = 1 \quad (2.36)$$

There is only one inversion in the direction of the half arrow while crossing 1-junction following effort (from bond 1 to bond 2, $n_1 = 1$), and no inversion in the direction of the half arrow while crossing 0-junction following flow, ($n_0 = 0$).

The causal loop gain $C : C_1 \rightarrow I : L_1$ for the bond graph model in Fig. 2.32b is

$$K_{C \rightarrow I} = (-1)^{n_0+n_1} \frac{1}{m^2} \frac{1}{C_1 s} \frac{1}{L s}, \quad \text{with } n_0 = 1 \text{ and } n_1 = 0 \quad (2.37)$$

There is no inversion in the direction of the half arrow while crossing 1-junction following effort ($n_1 = 0$), and one inversion in the direction of the half arrow while crossing 0-junction following flow (from bond 2 to bond 1, $n_0 = 1$).

The causal path gains and loop gains are used to compute the transfer function or transfer function matrix between the inputs and outputs of a bond graph model by using Mason's gain rule. For one specific pair of input and output variables, it is given as follows:

$$G(s) = \frac{\sum_i P_i \Delta_i}{\Delta}, \quad (2.38)$$

where P_i = gain of the i -th forward path from the input (controlled source) to the output (sensor), the graph determinant

$$\begin{aligned} \Delta &= 1 - \Sigma \text{all individual loop gains} \\ &+ \Sigma \text{all possible gain products of two non-touching loops} \\ &- \Sigma \text{all possible gain products of three non-touching loops} \\ &+ \dots \end{aligned}$$

and Δ_i = the Δ for the part of the model which does not touch the i th forward path. The non-touching loops are disjoint closed causal paths.

Thus, a bond graph model allows direct derivation of transfer functions in symbolic form which can be converted into numeric form by putting in the parameter values. The symbolic transfer function is useful for many control theoretic analyses. Note that the bond graph model of a linear system can be converted into a signal flow graph (SFG) in frequency domain by applying the same rules that are used to construct time-domain block diagram models and by replacing the integrations by $1/s$ and differentiations by s (Laplace operator for frequency domain analysis). The rules for conversion of bond graph models to block diagram models are discussed in the next section. The transfer function can then be derived by applying Mason's gain rule on the SFG. However, direct application of loop rules on the bond graph model avoids the intermediate steps involved in the model conversion.

For example, consider the bond graph model of the system shown in Fig. 2.28b. The transfer function between the voltage input (Se:E) to the flow sensor (Df) can be obtained as follows: There is only one forward causal path from the source to the sensor as shown in Fig. 2.28d and its forward path gain is $P_1 = 1/(Ls)$. If we remove all junctions along with bonds connected to them then there is no remaining part in the model. Thus, $\Delta_1 = 1$. There are two loops in the model. They are between C- and I-elements through the 1-junction, and R- and I-elements through the 1-junction. The associated loop gains are $L_1 = -(\frac{1}{Cs})(\frac{1}{Ls})$ and $L_2 = -R(\frac{1}{Ls})$. These two loops touch each other (i.e., are not disjoint) because they pass through a common junction (here, 1-junction). Then the input to output transfer function is given as

$$\begin{aligned} G(s) &= \frac{i(s)}{E(s)} = \frac{P_1 \Delta_1}{1 - (L_1 + L_2)} = \frac{1/(Ls)}{1 + 1/(LCs^2) + R/(Ls)} \\ &= \frac{Cs}{LCs^2 + RCs + 1}. \end{aligned} \quad (2.39)$$

2.7 State-Space Equations

To simulate a model, we have to find the differential equations of the system under consideration. The differential equations for a system can be derived in a variety of ways: Newtonian approach, Lagrange's equations, Hamilton's principle, principle of virtual work, etc. Generally, depending upon the domain of the problem, a specific approach is chosen. Bond graph models yield state-space equations as a general form for all problem domains.

2.7.1 State Equations

In system theory, the state equation form is well suited for simulation, and control analysis and synthesis. State equations can be systematically deduced from a bond graph in a linear or nonlinear form:

$$\begin{aligned} \text{Linear form: } & \begin{cases} \dot{x} = Ax + Bu \\ y = Cx + Du \end{cases} \\ \text{Non linear form: } & \begin{cases} \dot{x} = F(x, u) \\ y = G(x, u) \end{cases} \end{aligned} \quad (2.40)$$

where x is called the state vector, u is the input vector, y is the output (measurement) vector, and A , B , C , and D are matrices with appropriate dimensions. This modeling procedure can be automated as it will be shown below. Note that the input vector u represents the sources in the bond graph (Se and Sf), and y represents the effort and flow variables measured by the detectors (De and Df). In the nonlinear form of the model, F and G are two functions. Note that derivatives of inputs can appear on the RHS if there are derivative causalities in the model. The more general form of the nonlinear model in presence of derivative causalities in the model is given as

$$\text{Non linear form: } \begin{cases} F(x, \dot{x}, u, \dot{u}) = 0 \\ G(y, x, u, \dot{u}) = 0 \end{cases} \quad (2.41)$$

which is solved using special numerical techniques like backward difference method.

The state vector, denoted by x , is composed of variables p and q , which are the energy variables of I - and C -elements, respectively.

$$x = \begin{bmatrix} p_I \\ q_C \end{bmatrix} \quad (2.42)$$

2.7.2 Properties of State Variables

- The state vector does not appear on the bond graph, but its derivative or power variables appear:

$$\dot{x} = \begin{bmatrix} \dot{e}_I \\ \dot{f}_C \end{bmatrix} = \begin{bmatrix} \dot{p}_I \\ \dot{q}_C \end{bmatrix} \quad (2.43)$$

- The dimension of the state vector is equal to the number of C - and I -elements in integral causality.
- If among the n C and I -elements, n_I are in derivative causality, then the order of the model is $n_o = n - n_I$.

2.7.3 Steps for Equation Derivation

In general, for a bond graph model with no derivative causalities, the state-space equations can be deduced through the following steps:

1. Write structural or constraint laws associated with junction structure (0,1, TF, GY),
2. write constitutive equations of each element (R, C, I),
3. and finally combine these different laws to obtain state equation through sequential ordering and substitutions.

Some bond graph models have typical causal structures called zero-order-causal-paths (ZCPs) which are discussed later in this chapter. The ZCPs appear due to algebraic or differential algebraic loops, causal loops, etc. The above discussed procedure will not work for such models and additional steps that has been discussed in [33] would be required.

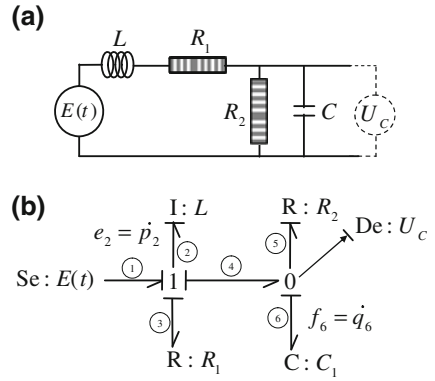
2.7.4 Example: State-Space Equation of an Electrical System

Consider a simple electrical system example given by its schema and causal bond graph model in Fig. 2.33a, b, respectively. The same current flows through the voltage source $E(t)$, inductor L , resistance R_1 , and a combined impedance X (where X is the parallel connection between the voltage sensor V , resistance R_2 , and capacitor C). Thus, to develop the bond graph model, $SE:E(t)$, $I:L$, $R:R_1$, and X can be attached to a 1-junction or same flow junction. The combined impedance X can now be explored further. In this impedance, the potential difference across the terminals of all the elements is the same. Thus, the impedance X can be replaced by a 0-junction (common effort junction) connected to De (effort sensor), $R:R_2$, and C -elements. This approach of modeling an electrical circuit in a step-by-step manner where complex impedances are initially denoted by some representative symbol and then their models are gradually expanded further is called the *method of gradual uncover*. This method can be used for simple electrical circuits. For complex circuits, we need to use the *point potential method* which will be discussed later.

The state-space equation from the bond graph model given in Fig. 2.33b will be derived in the form: $\dot{x}(t) = \mathbf{A}x(t) + \mathbf{B}u$ and $y = \mathbf{C}x + \mathbf{D}u$, where the state variable x , the control input u , and the measurement y are, respectively, the energy variables in dynamic bond graph element (C and I), the source (Se), and the effort detector (De):

$$\begin{aligned} x &= \begin{bmatrix} p_2 \\ q_6 \end{bmatrix} = \begin{bmatrix} \int e_2 dt \\ \int f_6 dt \end{bmatrix}, \\ u &= Se = E(t), \\ y &= De = e_6. \end{aligned} \tag{2.44}$$

Fig. 2.33 **a** An example electrical system and **b** its bond graph model



The structural equations are the constitutive equations of “0” and “1” junction (energy or power balance equation):

$$\begin{cases}
 \text{1 junction:} & \begin{cases} f_1 = f_2, & f_3 = f_2, & f_4 = f_2, \\ & e_2 = e_1 - e_3 - e_4. \end{cases} \\
 \text{0 junction:} & \begin{cases} e_4 = e_6, & e_5 = e_6, \\ & f_6 = f_4 - f_5. \end{cases}
 \end{cases} \tag{2.45}$$

The following equations are the constitutive behavioral equations of bond graph R , C and I elements:

$$\begin{cases}
 f_2 = \frac{1}{L} \int e_2 dt = \frac{p_2}{L}, \\
 e_6 = \frac{1}{C} \int f_6 dt = \frac{q_6}{C}, \\
 e_3 = R_1 f_3, \\
 f_5 = \frac{1}{R_2} e_5.
 \end{cases} \tag{2.46}$$

Combining Eqs. 2.45 and 2.46, and noting that $\dot{p}_2 = e_2$ and $\dot{q}_6 = f_6$, we obtain the state-space equations:

$$\begin{bmatrix} \dot{p}_2 \\ \dot{q}_6 \end{bmatrix} = \begin{bmatrix} -\frac{R_1}{L} & -\frac{1}{C} \\ \frac{1}{L} & -\frac{1}{R_2 C} \end{bmatrix} \begin{bmatrix} p_2 \\ q_6 \end{bmatrix} + \begin{bmatrix} 1 \\ 0 \end{bmatrix} E(t), \tag{2.47}$$

$$y = e_6 = \begin{bmatrix} 0 & \frac{1}{C} \end{bmatrix} \begin{bmatrix} p_2 \\ q_6 \end{bmatrix}. \tag{2.48}$$

More details of sequential ordering to obtain state equations are given in [33]. Note that for some specific forms, state equations cannot be obtained as simply through

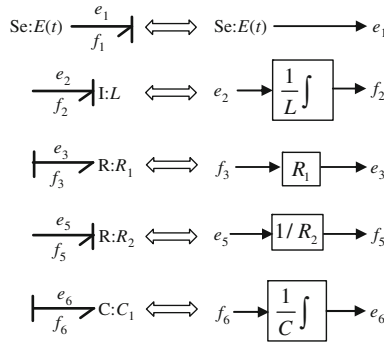


Fig. 2.34 Conversion of causal bond graph element constitutive relations into block diagram form

sequential ordering and substitutions. These situations arise due to algebraic loops and differential causality. A causal loop [33] is another situation, where it becomes impossible to eliminate unknown variables.

2.7.5 Deriving Block Diagram Model from Bond Graph Model

Block diagram models can be easily constructed from a causal bond graph model. For this task, each power bond has to be replaced by two equivalent bilateral signals. As an example consider the bond graph model given in Fig. 2.33. To create a block diagram, the following steps have to be performed.

- Replace elements by corresponding block diagram symbols. Use the correct effort and flow description given in Table 2.6. For example, block diagram descriptions for Se, I, R, and C-elements are given in Fig. 2.34.
- Each junction has a strong and a weak law. The strong law pertains to equality of variables, i.e., flows at 1-junction and efforts at 0-junctions. The weak law is derived from power conservation and the strong law and it leads to a signed sum relation. Replace the junctions by signal summation (algebraic sum of efforts (for 1-junction) and flows (for 0-junction)) to represent the weak law. Also, use signal splitters (efforts or flow equality) to represent the strong law. Such conversions for a 1-junction and a 0-junction are shown in Fig. 2.35a, b, respectively.
- Finally, connect the constraints (junction models) to element constitutive relations to obtain the global block diagram model as shown in Fig. 2.36. Note that two-port elements have two constitutive relations. A further methodical approach to obtain block diagrams of linear as well as nonlinear systems is detailed in Chap. 4.

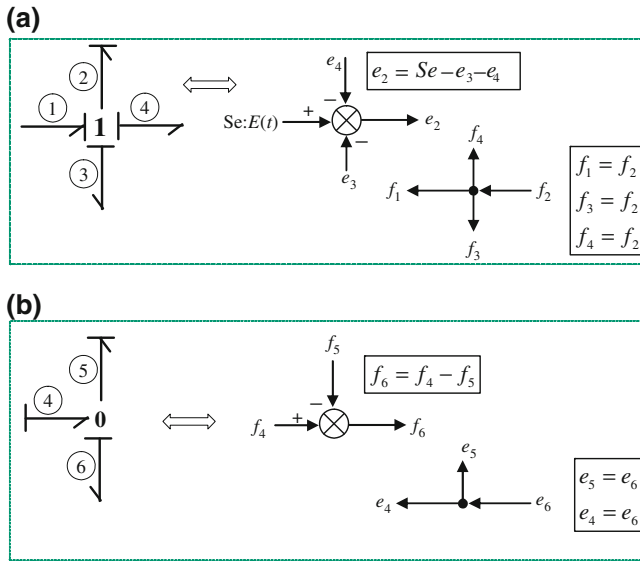


Fig. 2.35 Conversion of causal bond graph junction structures into block diagram form

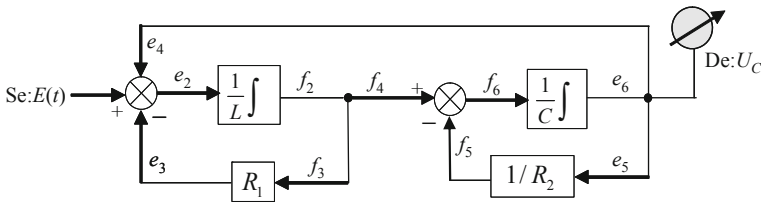


Fig. 2.36 Block diagram model of the system shown in Fig. 2.33a

2.7.6 Model Structure

The bond graph is an advantageous modeling tool because it exposes both the structure and the behavior of the studied system. In order to illustrate this property let us consider a simple electrical example given by its schema and causal bond graph models (Fig. 2.37). The integral causality (Fig. 2.37b) is recommended for engineering simulation. Here, the dynamics evolves from given initial conditions. The derivative causality (Fig. 2.37c) is used more in diagnosis because the initial conditions are unknown, rather we have the final values. In both the models shown in Fig. 2.37b, c, the current and the voltage are measured, respectively, by the flow sensor (Df) and effort sensor (De). The sensors, assumed to be ideal, are connected to the junction structure by means of signal bonds indicating that there is no power transfer between the system and sensors.

Fig. 2.37 a An electrical system and its bond graph model in **b** preferred integral and **c** preferred derivative causality

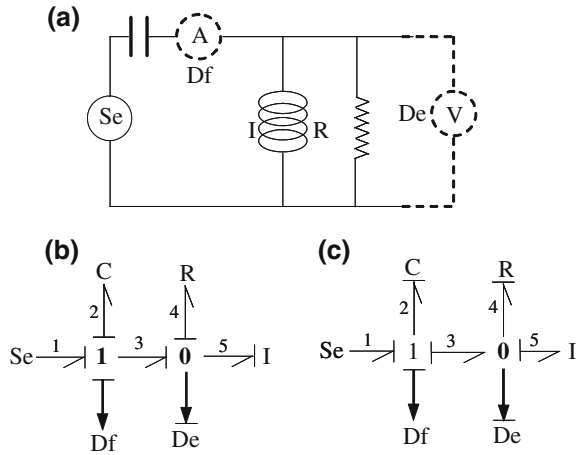
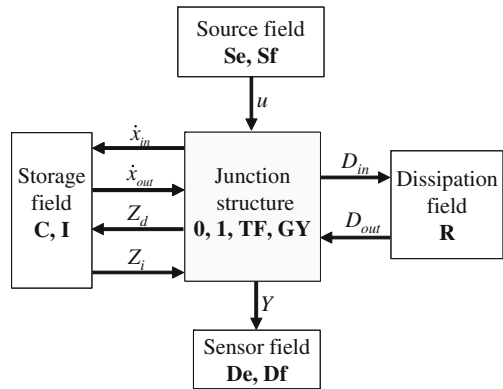


Fig. 2.38 Partitioned representation of model structure



The bond graph model can be represented in a vectorial way (Fig. 2.38) showing the junction structure and the different fields it is composed of.

The key vectors associated with the representation are: X : the state vector (generalized momentum “ p ” on “ I -element” and generalized displacement “ q ” on “ C -element”) divided into x_i and x_d ; the subvectors, respectively, associated with the components in integral and derivative causality, \dot{X} : the time derivative of the state vector divided into \dot{x}_i and \dot{x}_d , Z : The complementary state vector (“ f ” on “ I ” and “ e ” on “ C ”) divided into Z_i and Z_d , U : Source input vector, Y : Sensor output vector, D_{in} : input vector to R elements, and D_{out} : output vector from R -elements. This representation leads to the junction structure matrix S such that:

$$\begin{bmatrix} \dot{x}_i \\ Z_d \\ D_{in} \\ Y \end{bmatrix} = \begin{bmatrix} S_{11} & S_{12} & S_{13} & S_{14} \\ S_{21} & S_{22} & S_{23} & S_{24} \\ S_{31} & S_{32} & S_{33} & S_{34} \\ S_{41} & S_{42} & S_{43} & S_{44} \end{bmatrix} \begin{bmatrix} Z_i \\ \dot{x}_d \\ D_{out} \\ U \end{bmatrix} \quad (2.49)$$

The matrix \mathbf{S} has $(n_C + n_S)$ rows, where n_C and n_S are, respectively, the number of components (I , R , or C) and sensors in the systems (De and Df). This matrix is composed of 0 , -1 , $+1$, m , r or $1/m$, and $1/r$, where m and r are the moduli of different transformer TF and gyrator GY elements. More details on the model structure and its implications can be found in [23].

2.8 The Art of Constructing Bond Graph Models

There are some well-established and methodical approaches to build bond graph models of complex systems. These methods can be used together and model making becomes easier by following these guidelines. Before proceeding further, let us first clarify the concept of power directions and also demonstrate certain bond graph simplification rules.

2.8.1 A Note on Power Directions

Assigning power directions to bonds serves as a unified approach for coordinate system selection during bond graph modeling. Power direction shows the assumed direction of power flow on a bond when the effort and flow variables in that bond have the same sign, i.e., both are positive or both are negative. This does not mean that the power cannot be exchanged in the opposite direction to the indicated power direction, in fact power flows in the opposite direction when the effort and flow variables have opposite signs, i.e., one is positive and the other is negative. For example, a source is usually assigned a power direction that indicates that it supplies power. If positive current is drawn from a battery with constant positive potential difference across its terminals then it supplies power. However, if the current is reversed while the battery maintains the same potential difference across its terminals then the battery is getting charged, i.e., it is drawing power instead of supplying power. Thus, the power can flow into a source under certain situations.

To further explain this concept, let us consider a spring-mass system shown in Fig. 2.39a and its bond graph model given in Fig. 2.39b. It seems that power flows to both I- and C-elements at the same time. This is not true. Let us give an initial condition to the system so that it starts free vibration. Let the mass be initially displaced by x_0 in positive direction (upward force and displacement are positive) and released from there. Then the mass will move down because the spring will try to pull it down. At this condition, the force on the mass is negative ($e_m < 0$) and its

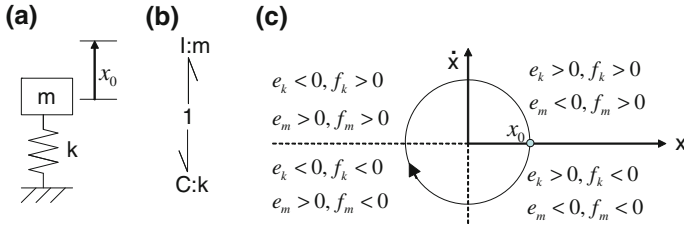


Fig. 2.39 Explanation of power direction

velocity is negative ($f_m < 0$). At the same time, the spring is in an extended state, so the force in the spring is positive ($e_k > 0$), and its length is decreasing or its rate of deformation is negative ($f_k < 0$). In any case, $f_m = f_k$ and they should have the same sign. So, we see that $e_m f_m > 0$ and $e_k f_k < 0$, i.e., the mass is gaining kinetic energy and the spring is losing potential energy or the power flows into the I-element and flows out of the C-element. In fact, $e_m f_m + e_k f_k = 0$ at the 1-junction indicates that $e_m = -e_k$. Thus, whatever may be the motion, this relation has to be satisfied (See Fig. 2.39c). After releasing the mass from $x = x_0$ with $\dot{x} = 0$, the displacement-velocity relation is described by the fourth quadrant in Fig. 2.39c and as the displacement becomes zero, it enters into the third quadrant and so on. In all quadrants, we find that power is flowing into one element and out of the other element, thus, conserving the power in this non-dissipative system.

2.8.2 Simplification Rules

When one constructs the bond graph models for electrical, mechanical, or any other system for the first time, one often lands up with a large model with many spurious junction structure elements which can be simplified to obtain a compact final model. Note that the bond graph model of the same system can be drawn in different ways and shapes by different people. Thus, understanding of the equivalence of junction structures and reduction rules is necessary. Some of these simplification rules are shown in Fig. 2.40 where J_1, J_2 etc., indicate junction structure elements (1, 0, TF, and GY) or other elements (Se, Sf, I, C, R).

Figure 2.40a shows that any 1-junction with only two bonds which are power directed in such a way that one bond is power directed towards the junction and the other away from the junction is redundant and it can be removed from the model. This is fairly easy to prove: the flows in two bonds are the same ($f_1 = f_2$) and application of the weak junction law shows ($e_1 - e_2 = 0$). Thus, $e_1 = e_2$ and $f_1 = f_2$ which means the 1-junction is useless. Similarly, a 0-junction with only two bonds can be simplified as shown in Fig. 2.40b.

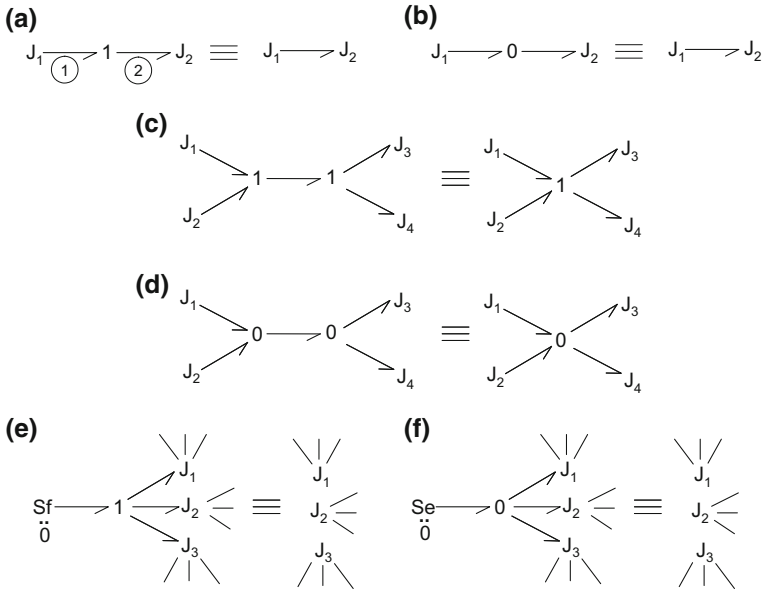


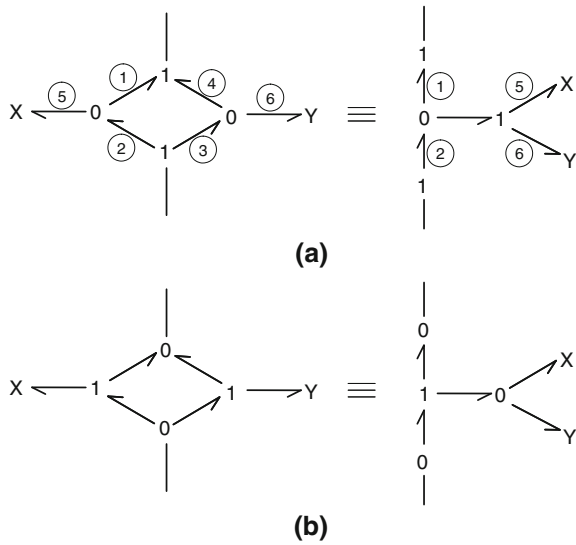
Fig. 2.40 Bond graph reduction steps

Two adjacent connected 1-junctions can be merged to a single 1-junction because the flows in bonds connected to the first 1-junction are also the same as those connected to the second 1-junction. The power direction between the two 1-junctions is irrelevant in this reduction. Likewise, two adjacent connected 0-junctions can be merged to a single 0-junction. These reductions are shown in Fig. 2.40c, d.

If a zero flow source is connected to a 1-junction then the flows in all bonds connected to that 1-junction become zero. Thus, the power in all bonds of that 1-junction are zero and the 1-junction with all connected bonds can be removed. This reduction is shown in Fig. 2.40d. Likewise, Fig. 2.40e shows that a 0-junction with all its connected bonds can be removed if it is connected to a zero source of effort. It can also be shown that any zero source of effort connected to a 1-junction and any zero source of flow connected to a 0-junction can be removed while retaining the junction and all its other bonds.

Two further typical reductions are shown in Fig. 2.41. In the bond graph substructure shown in Fig. 2.41a, X and Y are some junctions or elements. It can be seen from the strong laws of the two 1-junctions in the bond graph that $f_1 = f_4$ and $f_2 = f_3$. From the weak laws of two 0-junctions, we get $f_5 = f_2 - f_1$ and $f_6 = f_3 - f_4$ which establishes $f_5 = f_6$. Thus, the items X and Y can be modeled at a 1-junction in which the flow in all bonds is $f_2 - f_1$ as shown in the equivalent structure. The effort between the 0-junction and the new 1-junction is $e_5 + e_6$. Similarly, the equivalence shown in Fig. 2.41b can be proved.

Fig. 2.41 Further bond graph reduction steps



There are many more advanced reduction and equivalent forms for various bond graph structures. The most important among them are the transformer and gyrator equivalences. These equivalences allow us to construct the so-called dual bond graphs and thus obtain equivalent systems for a given system. An example is finding the different electrical or electronic equivalent circuits for a given mechanical system for analog simulation. It can be shown that with dual formulation, a bond graph of any system can be constructed with only one storage element (I or C), resistance (R), one junction (0 or 1), one two-port gyrator (GY), one source (Se or Sf), and one sensor (De or Df). These important equivalences will be discussed in Chap. 4.

2.8.3 Bond Graphs for Electrical Systems

We have earlier discussed how the method of gradual uncover can be used to construct bond graph models of simple electrical circuits. However, this approach fails in cases where it becomes difficult to identify the same flow and the same potential difference conditions, i.e., the series and parallel nature of the connections between circuit elements in an electrical circuit. One example of such a configuration is shown in Fig. 2.42 where it is not possible to decide on the series or parallel nature of the connection for the cross impedance in the bridge circuit. Therefore, we will use the *point potential method* to model this circuit. Point potential method is a general approach to model all kinds of electrical circuits. We will later show that mechanical systems too can be modeled through an equivalent method.

Fig. 2.42 An example electrical circuit

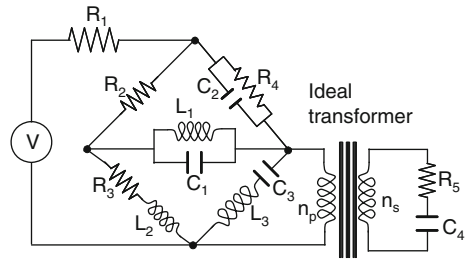
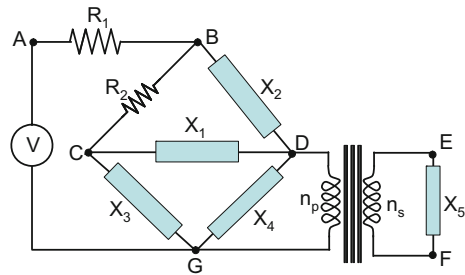


Fig. 2.43 Different potential points marked on the example electrical circuit



At this stage, we will assume that the electrical transformer in the circuit is ideal. The real electrical transformer with its magnetic circuit, losses, etc., will be modeled in the subsequent chapters. For applying the point potential method, we have to first enumerate all the distinct potential points in the circuit. To avoid too many different potential points, we can initially encapsulate some complex impedances. For example, the block containing the inductance L_1 and capacitor C_1 can be together represented by an impedance X_1 . Similarly, other complex blocks can be encapsulated. The new intermediate circuit with different potential points marked as A, B, C, and so on is shown in Fig. 2.43.

Now, for each distinct potential point, we will introduce a 0-junction so that bonds attached to it will have the same effort or voltage. These 0-junctions for tag point voltages are shown in Fig. 2.44. Then we will insert a 1-junction with three bonds between two 0-junctions and connect this 1-junction to the two 0-junctions with opposite power directions, i.e., power in one bond is directed into the 1-junction and the other is directed away. From the weak junction law at 1-junction, the effort in the unconnected bond of the 1-junction is then the difference of the potentials in the connected 0-junctions. This is the potential difference across the impedance appearing between the tag points or earlier marked common potential points. Thus, the model of the impedance can be attached to the remaining bond of the 1-junction appearing between the two 0-junctions.

So, we introduce a 1-junction between 0_A and 0_G and then connect the source of effort (Se:V) to the 1-junction. Likewise, the resistance R_1 is connected to the

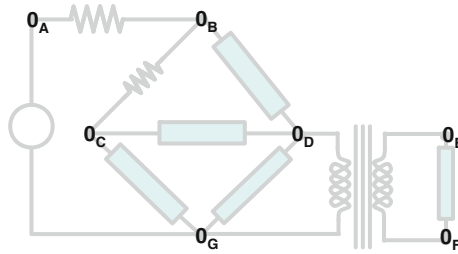


Fig. 2.44 Representation of point potentials by 0-junctions in bond graph model

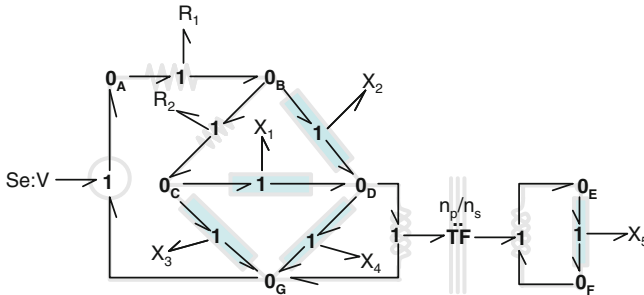


Fig. 2.45 Representation of potential differences across impedances by 1-junctions between two 0-junctions in the bond graph model

1-junction between 0_A and 0_B . The completed model then appears as shown in Fig. 2.45.

The bond graph model given in Fig. 2.45 is that of a floating circuit in which there is no reference potential. It is like the model of a free-floating body without an inertial reference frame. To complete the model, we have to specify the reference potential. Usually, the reference potential is zero, i.e., the ground potential. Note that for this circuit, the two sides of the electrical transformer have to be separately grounded. Thus, depending upon the situation, we will select the ground nodes. Usually, the negative end of the voltage source is assumed to be the ground node. Here, we will assume that the nodes G and F are grounded, i.e., the potential at these nodes is zero. This will be imposed on the model by adding two zero effort sources (Se:0 elements) to the model as shown in Fig. 2.46.

After implementing the ground nodes, we can substitute models for all encapsulated items like X_1 , X_2 , etc. Then we can perform the model simplifications. We can remove those 0-junctions connected to Se:0 along with the bonds connected to those 0-junctions. Moreover, we can remove all junctions with only two bonds (e.g., 0_A junction) and also merge adjacent junctions of equal type. The model of the electrical circuit after these simplifications is shown in Fig. 2.47. Note that a benzene-ring-like structure results for almost all bridge circuits.

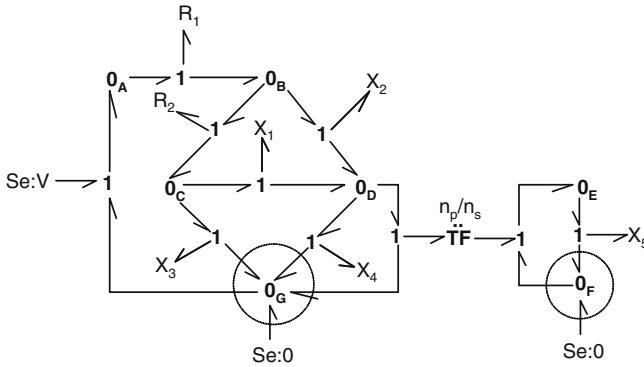
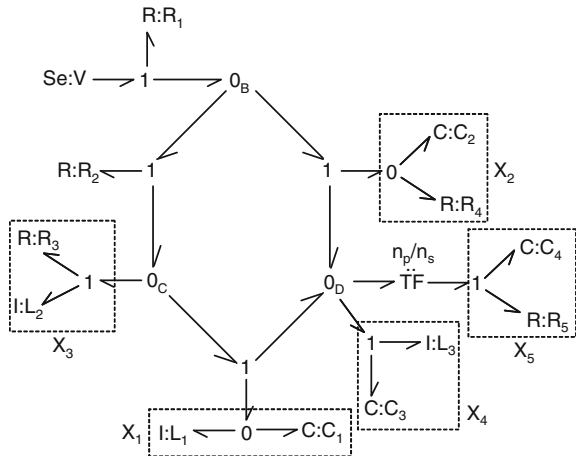


Fig. 2.46 Implementation of ground nodes in bond graph model of the example electrical circuit

Fig. 2.47 Final reduced bond graph model of the example electrical circuit



Note that the part of the bond graph model to the right of the TF element could have been directly drawn by using method of gradual uncover but the part of the model to the left of TF element has to be developed from the method of point potential.

2.8.4 Bond Graphs for Equivalent Networks

Analogous approaches to the point potential method can be used to model hydraulic and heat transfer problems. Hydraulic and heat transfer problems can be represented in equivalent electrical circuit form and thus the same approach is justified.

In hydraulic systems, we can introduce 0-junctions for each distinct pressure point and take the pressure difference at 1-junctions placed between those 0-junctions. The hydraulic inertia, resistance etc. can be modeled at the 1-junctions. The hydraulic capacities are modeled at the 0-junctions. The sump or plenum pressure is the ground node in hydraulic circuits.

For heat transfer problems, the distinct common temperature nodes can be represented by 0-junctions and the heat transfer resistances (conduction, convection, radiation, etc.) can be modeled at a 1-junction between two 0-junctions. In this way, a pseudo-bond graph model for any heat transfer problem can be easily constructed. The heat capacities of different bodies are modeled at 0-junctions. The ground node in heat transfer problems is usually the environment/ambient temperature and because it is nonzero, models cannot be usually reduced to very simple forms.

2.8.5 Bond Graphs for Mechanical Systems

It is easy to construct bond graph models for electrical and hydraulic systems. Electrical and hydraulic systems can be represented as networks and then it becomes possible to apply the method of gradual uncover, method of point potential, or a mix of the two methods (see [33]) to arrive at compact bond graph representations. For mechanical systems, *method of flow map* and *method of effort map* are developed in [33]. The method of flow map is generally used because kinematic relations can be used to construct the bond graph model. You will see that with practice, it becomes possible to produce the bond graph model directly by looking at the system morphology, skipping all intermediate steps. The method of flow map is equivalent to the point potential method. It is in fact the dual formulation: electrical series is a 1-junction, whereas mechanical parallel is a 1-junction. Thus, bond graph modeling of mechanical systems is the dual formulation of bond graph modeling of electrical systems.

In the method of flow map for mechanical systems, we introduce 1-junctions for each distinct velocity points (this is dual to introduction of 0-junctions for each distinct potential points in electrical circuit models). Then we introduce a 0-junction between two 1-junctions so that we can compute relative velocities (this is dual to introduction of 1-junctions between two 0-junctions in electrical system modeling). The impedance is then connected to the 0-junction representing the relative velocity. Finally, ground, if present, is specified by a zero flow source ($Sf:0$) and the model is reduced to a compact form. These steps shown in Fig. 2.48 are as follows:

1. Fix reference axes for velocities as shown in step 1 of Fig. 2.48a. Mask complicated impedances under encapsulated items (e.g., Y in Fig. 2.48).
2. Consider all different velocities (absolute velocities for mass and inertia) and relative velocities for others as shown in step 2 of Fig. 2.48.
3. For each distinct velocity, establish a 1-junction. Express the relationships between velocities. Add 0-junction (used to represent those relationships) for

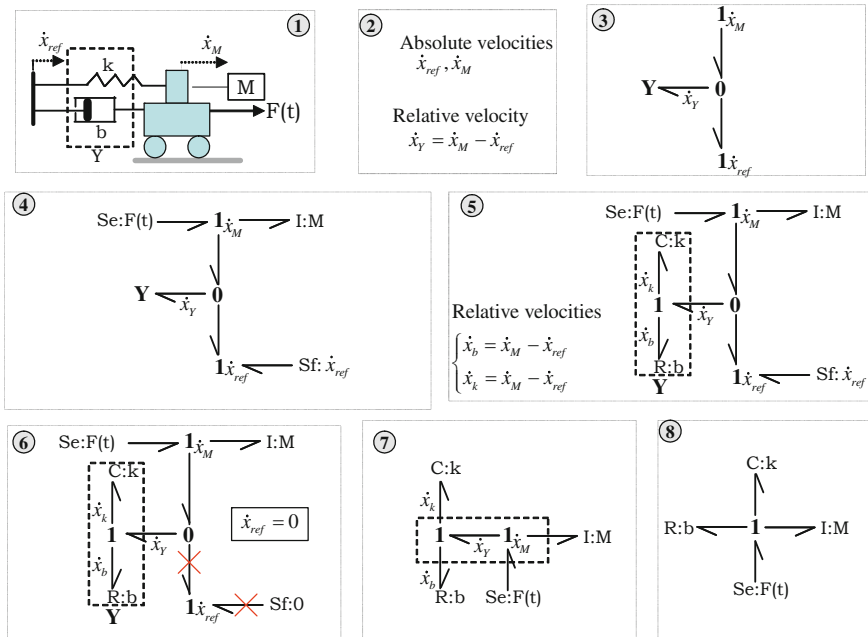


Fig. 2.48 Steps for construction of bond graph models of mechanical translation

each relationship between 1-junctions and attach impedances to them such as Y as shown in step 3 of Fig. 2.48.

4. Attach to the 1-junction corresponding bond graph elements such as I elements for mass. Place effort sources such as gravity and force excitations, and flow sources such as ground.
5. Expand the encapsulated item models.
6. Simplify the bond graph structure by taking into account the power directions. Eliminate any zero velocity 1-junctions and their bonds. Remove junctions with only two bonds.
7. Further simplify the bond graph model by merging adjacent junctions of the same type.

The final bond graph obtained in the last step (\dot{x}_{ref} has been assumed to be zero in step 6) could as well be derived in a much simplified manner. If we assume $\dot{x}_{ref} = 0$ from the very beginning then we may note that the velocity of the mass point and the applied load must be the same; moreover, the velocity of the mass point is equal to the rate of extension of the spring and the damper. Although these rates (velocities or deformation rates) are qualitatively different, they have equal magnitude and hence they should be connected to the same 1-junction.

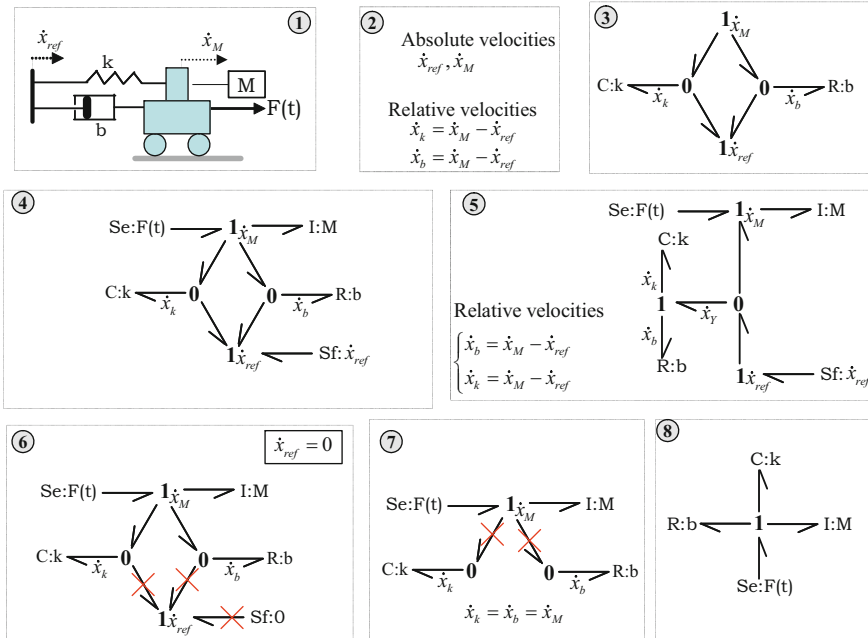


Fig. 2.49 Alternative steps for construction of bond graph models of mechanical translation

If complex impedances are not simplified then the same system can be modeled as shown in Fig. 2.49. The same steps as detailed above would be followed and the same final bond graph is obtained.

A simple mechanical double oscillator system and its corresponding bond graph models are given in Fig. 2.50. The bond graph model can be simplified while the reference velocity $Sf:\dot{x}_{ref}$ is considered null ($\dot{x}_{ref} = 0$).

The equation from Newton's law can be easily deduced for mass m_1 from bond graph model given in Fig. 2.50c.

From $I:m_1$ element and 1-junction:

$$\dot{x}_1 = \frac{1}{m_1} \int F_{m_1} dt = \frac{1}{m_1} \int (m_1 g - F_{K1} - F_{K2}) dt \quad (2.50)$$

From $C:K_1$, $C:K_2$ elements and 0-Junction:

$$F_{K2} = K_2 \int \dot{x}_2 dt = K_2 \int (\dot{x}_1 - \dot{x}_2) dt, \quad F_{K1} = K_1 \int \dot{x}_1 dt = K_1 \int \dot{x}_1 dt \quad (2.51)$$

Finally, we obtain from Eq. 2.50:

$$m_1 \ddot{x}_1 = m_1 g - K_2 (x_1 - x_2) - K_1 x_1 \quad (2.52)$$

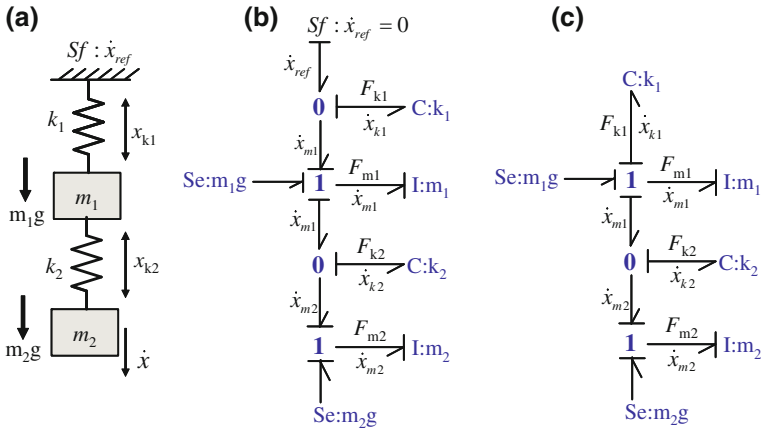


Fig. 2.50 A mechanical double oscillator (a) and its corresponding detailed (b) and simplified (c) bond graph models

Likewise, the equation for mass m_2 can be obtained:

$$m_2 \ddot{x}_2 = m_2 g + K_2 (x_1 - x_2) \quad (2.53)$$

There are four state variables: two of them are associated with momentums of inertias (p_{m1} and p_{m2}) and two are displacements representing the spring deformations (x_{k1} and x_{k2}). Weight of the two mass represented by sources of effort can be considered as inputs.

$$\mathbf{x} = [p_{m1} \ p_{m2} \ x_{k1} \ x_{k2}] \quad \text{and} \quad \mathbf{u} = [m_1 g \ m_2 g] \quad (2.54)$$

The state equations may be developed from the constitutive equations of dynamic bond graph elements and constraint (0, 1, TF, and GY) relations:

$$\begin{aligned} \dot{x}_{m2} &= \frac{1}{m_2} \int F_{m2} dt = \frac{p_{m2}}{m_2} = \frac{1}{m_2} \int (m_2 g + K_2 x_{K2}) dt \\ \dot{x}_{m1} &= \frac{1}{m_1} \int F_{m1} dt = \frac{p_{m1}}{m_1} = \frac{1}{m_1} \int (m_1 g - K_1 x_{K1} - K_2 x_{K2}) dt \\ F_{K1} &= K_1 \int \dot{x}_{K1} dt = K_1 x_{k1} = K_1 \int \dot{x}_{m1} dt \\ F_{K2} &= K_2 \int \dot{x}_{K2} dt = K_2 x_{k2} = K_2 \int (\dot{x}_{m1} - \dot{x}_{m2}) dt \end{aligned} \quad (2.55)$$

From Eq. 2.55, state equations are given:

$$\begin{aligned} \dot{p}_{m2} &= m_2 g + K_2 x_{K2} \\ \dot{p}_{m1} &= m_1 g - K_2 x_{K2} - K_1 x_{K1} \\ \dot{x}_{k2} &= \frac{p_{m1}}{m_1} - \frac{p_{m2}}{m_2} \\ \dot{x}_{k1} &= \frac{p_{m1}}{m_1} \end{aligned} \quad (2.56)$$

Equation 2.56 is more suited for automatic control analysis. If a Lagrangian approach is used, with (x_{K1}, x_{K2}) , as generalized coordinates, the following second order differential equations can be obtained from Eq. 2.56:

$$\begin{aligned}\ddot{x}_{k1} &= g - \frac{K_2 x_{K2} + K_1 x_{K1}}{m_1} \\ \ddot{x}_{k2} &= -K_2 x_{K2} \left(\frac{1}{m_1} + \frac{1}{m_2} \right) - \frac{K_1 x_{K1}}{m_1}\end{aligned}\quad (2.57)$$

Let us explore how the simulation results will be interpreted. The positive momentum of masses mean downward velocities (as shown in Fig. 2.50a) and this is in agreement with the positive value of sources modeling the self-weight. Let us now have a look at the states associated with deformation of springs. Positive value of x_{k1} means tension in spring K_1 because $\dot{x}_{k1} = \frac{p_{m1}}{m_1} = \dot{x}_{m1}$. Likewise, positive value of x_{k2} means $\int \left(\frac{p_{m1}}{m_1} - \frac{p_{m2}}{m_2} \right) dt > 0$ or $\int \frac{p_{m1}}{m_1} dt - \int \frac{p_{m2}}{m_2} dt > 0$ or $x_{m1} > x_{m2}$. Thus, positive x_{k2} corresponds to compression of spring K_2 .

Let us now consider a typical system shown in Fig. 2.51a which includes a so-called half-a-degree of freedom. If the resistance r_2 is removed from this system then one obtains a fourth order equations of motion for the system. However, when resistance r_2 is present, one obtains a fifth order equations of motion. However, in state-space form, both configurations have four states. The half-degree of freedom is associated with the resistance r_2 whose one end is connected to a mass point but the other end is not connected to a mass point. Thus, to derive the equations of motion for this system using any classical approach such as Newton's equations, one needs to introduce a temporary variable (\dot{x}_2 shown in Fig. 2.51b) which is to be finally eliminated from the equations through algebraic manipulations.

To construct bond graph model of this system, the base junction structure is first constructed by including the temporary nodal velocity \dot{x}_2 . Subsequent simplifications yield the final model shown in Fig. 2.51d. The half-degree of freedom introduces a so-called algebraic loop in the model and needs special techniques to derive the equations of motion of this system. The same variable may appear both on the LHS and RHS of the equation and it has to be algebraically solved.

Elementary mechanical rotations can be modeled in a similar manner to mechanical translation. Complex rotations about three axes will be discussed in Chap. 4. Here, we will consider a special system where both mechanical translation and rotation are present.

The schematic diagram of a vehicle traveling over a rough or undulating road is shown in Fig. 2.52 where a and b are, respectively, the distances of the rear and the front axles from the vehicle's center of mass. The vertical position of the center of mass is not important in this model. We will develop a pitch plane model of the vehicle where horizontal displacements, tyre deformations, steering etc., will not be considered. Only vertical heave and pitch motions will be modeled. Such a pitch-plane model of a vehicle is often used to design and optimize vehicle suspension

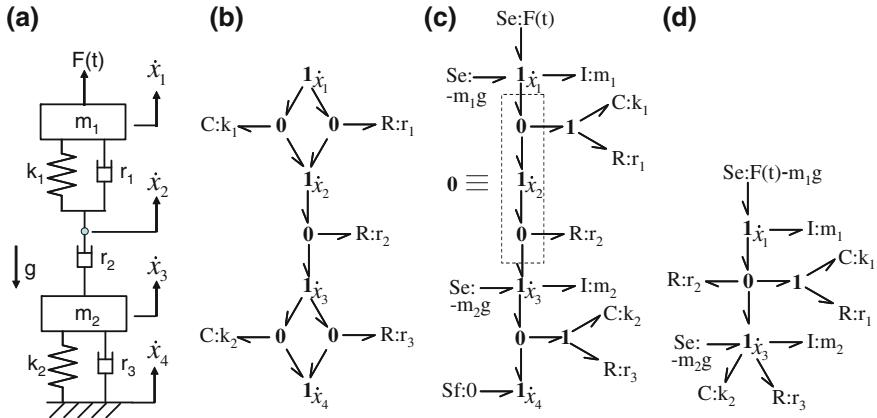


Fig. 2.51 a A typical mechanical system, b its base junction structure, c initial bond graph, and d final reduced bond graph

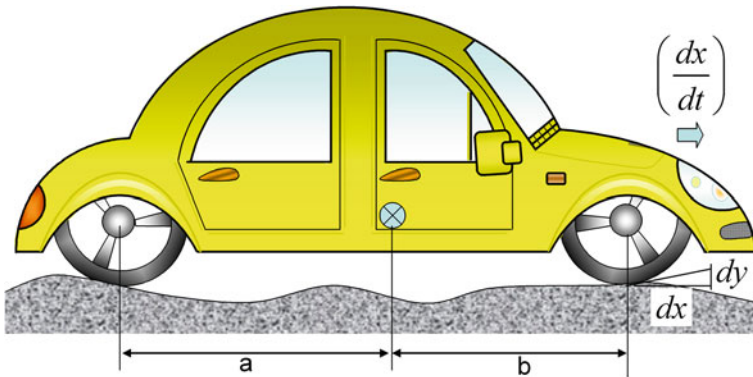


Fig. 2.52 Schematic of a vehicle moving on an undulating surface

systems for ride comfort. However, this model is not useful for other studies like vehicle handling behavior and stability evaluation. The full vehicle model is developed in Chap. 6 by taking into account all of its dynamics like tyre properties and auxiliary systems (suspensions, brakes, steering, engine, etc.).

The pitch-plane behavior of the vehicle can be modeled using an equivalent mechanical system shown in Fig. 2.53. In the equivalent system, the vehicle body mass is M , the rotary inertia of the vehicle body about z-axis at the center of mass is J , and the axle mass including the tyre mass is m_a . The stiffness and damping of the rear suspension are k_r and r_r , respectively, and those for the front suspension are k_f and r_f , respectively. The damping in the inflated tyres is usually neglected. Depending upon the tyre pressure and construction, the tyre stiffness in the front and

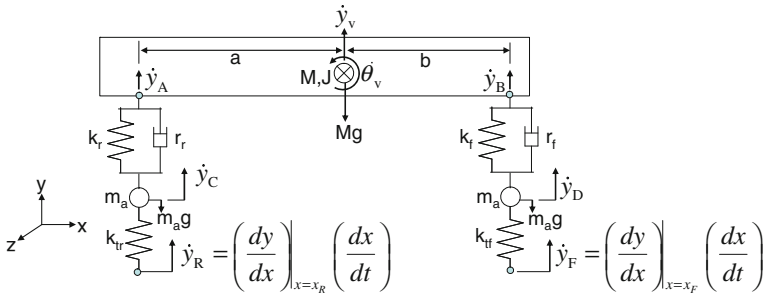


Fig. 2.53 Equivalent system considered to develop pitch-plane model of a vehicle

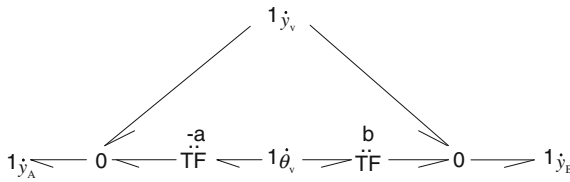


Fig. 2.54 Basic kinematic junction structure of the pitch-plane model of a vehicle

rear wheels are k_{tr} and k_{tr} , respectively. We will assume that the tyres are always in contact with the ground. As the vehicle moves forward, the vertical excitation from the ground is given as

$$\frac{dy}{dt} = \frac{dy}{dx} \frac{dx}{dt} \tag{2.58}$$

If the vehicle speed is assumed to be constant and a road profile $y = \phi(x)$ is provided then one can always write $y = \psi(t)$, where ϕ and ψ are given functions.

To model this vehicle with method of flow map, we first recognize the various flow points in the model. The vehicles vertical velocity of the vehicle center of mass is denoted as \dot{y}_v and the angular velocity about z-axis (pitch velocity) is $\dot{\theta}_v$. The linear velocities of suspension fixation points on the carbody at points A and B are, respectively, found from kinematic relations as

$$\dot{y}_A = \dot{y}_v - a\dot{\theta}_v \tag{2.59}$$

$$\dot{y}_B = \dot{y}_v + b\dot{\theta}_v \tag{2.60}$$

By taking these kinematic relations as the starting point, we can use TF elements with appropriate moduli to construct a bond graph junction structure shown in Fig. 2.54.

Now, one can incorporate the inertias (linear inertia or mass $I:M$ is connected to 1-junction for \dot{y}_v and rotary inertia $I:J$ to 1-junction for $\dot{\theta}_v$), self-weights, suspension

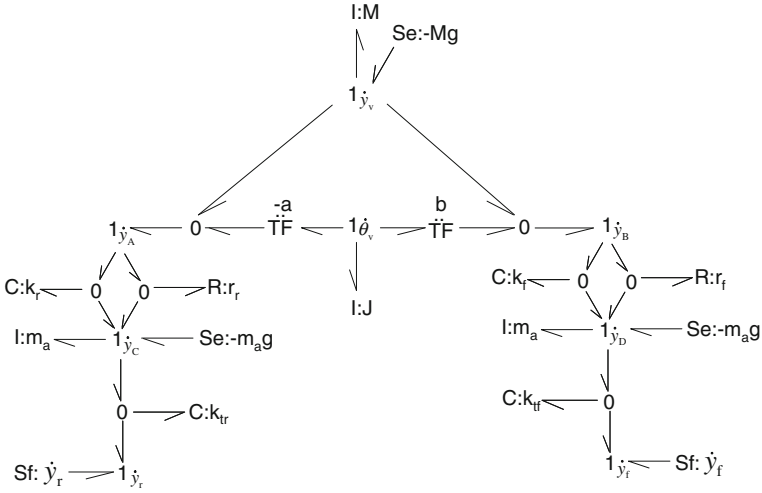


Fig. 2.55 Bond graph model of the pitch-plane dynamics of a vehicle

and tyre models, and ground excitations into the model by using the usual method of flow map. The resulting model is shown in Fig. 2.55. Let us now have a look at this model and understand how to interpret the states of this system. The momenta associated with model are positive for upward motions and anticlockwise rotation. The difficulty arises in interpreting the deformation states (q 's). From the power directions at rear suspension C-element $C:k_r$ connected to 0-junction, we find that the flow to it is positive if $\dot{y}_A > \dot{y}_C$. Thus, positive deformation of the rear suspension ($q_r > 0$) implies that the suspension is in tension and negative deformation implies it is in compression. Similar arguments can be used to determine the nature of states associated with the other C-elements. These interpretations are necessary to understand the simulation results.

The model shown in Fig. 2.55 can then be simplified to a form shown in Fig. 2.56. We have assigned causality to the final reduced model. Such a power directed and causalled model is often called an *augmented model*. Note that the two 0-junctions labeled as 0_{FR} and 0_{FR} indicate the rear and front suspension forces. The same suspension force acts on the vehicle body at the suspension fixation point and also on the axle with opposite directions.

We can easily see from this model that the net force acting on the linear inertia (I:M) is as evaluated from weak law at 1-junction for \dot{y}_v is

$$e_v = m\ddot{y}_v = -F_r - F_f - Mg \tag{2.61}$$

and the net moment acting on the rotary inertia (I:J) as evaluated from 1-junction for $\dot{\theta}_v$ is

$$e_\theta = J\ddot{\theta}_v = aF_f - bF_f. \tag{2.62}$$

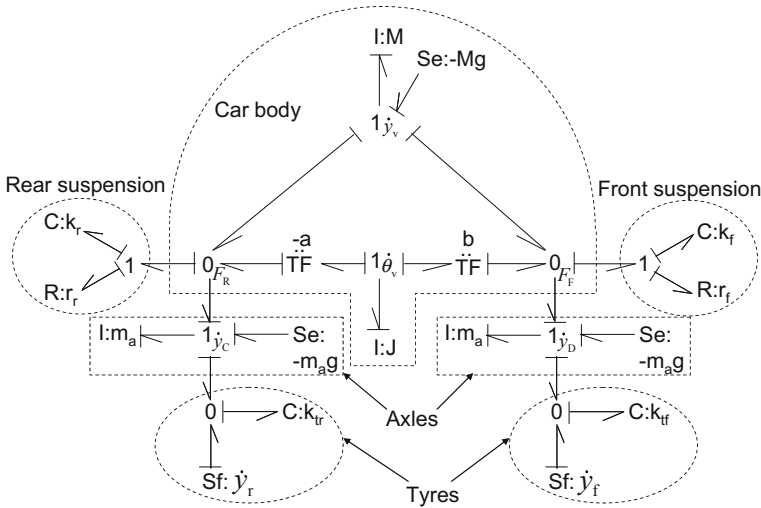


Fig. 2.56 Reduced bond graph model of the pitch-plane dynamics of a vehicle

The above two equations are indeed the force and moment balance equations for the car body. *Although we have developed our model from kinematic analysis or method of flow map, it turns out that the efforts are automatically balanced. This is because of the power conserving property of the junction structure.* Thus, one can model a mechanical system on the basis of flow balance or force balance or a mixture of the two.

2.8.6 Bond Graphs for Multi-Energy Domain Systems

Most mechatronic systems involve multiple energy domains. A vehicle is an excellent example of a multi-energy domain system. Let us consider the pitch plane dynamics of a vehicle shown in Fig. 2.57a. The rear wheels of the vehicle are driven by geared DC motors (Fig. 2.57b) and the front wheels roll freely. The suspensions are oleo-pneumatic (Fig. 2.57c) where the stiffness of the suspension is due to the entrapped gas, whereas the damping comes from the incompressible fluid or oil flowing through the orifices.

The vehicle system integrates electrical domain (geared DC motors), mechanical domain (vehicle dynamics), pneumatic domain (compressed gas in suspension struts), and hydraulic domain (hydraulic damping in orifices). For pitch-plane dynamics, we will model only half of the vehicle with one rear and one front wheel.

The bond graph model of the vehicle system is shown in Fig. 2.58. The vehicle body dynamics model is straightforward (similar to the one developed before in Fig. 2.56) and it includes the tire stiffness, axle load, suspension, and body inertias. The suspension model uses a transformer (TF) with modulus A_p which is the area of the piston rod. Note that the net change in volume of fluid and gas inside the

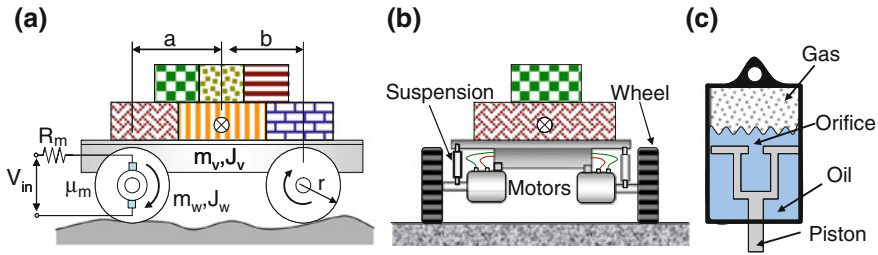


Fig. 2.57 A vehicle as a multi-energy domain system with electric motors and hydro-pneumatic suspension

suspension strut is due to the different amounts of intrusion of the piston rod into the fluid chamber. Furthermore, the fluid is incompressible and the volume change is actually that of the gas. The TF element converts the suspension deformation rate into the rate of volume change. The C-element modeling the tire stiffness thus models the gas compressibility. If one assumes adiabatic conditions because the thermal dynamics is much slower then the gas pressure can be given by the nonlinear relation

$$P = P_0 (V_0/V)^\gamma$$

$$\text{or } e = P_0 \left(V_0 / \int f dt \right)^\gamma \tag{2.63}$$

where P_0 is the initial gas pressure (depends on vehicle weight), V_0 is the initial volume, and γ is a gas constant given by the ratio of specific heats. The gas pressure generates the suspension force through the transformer. The rate of incompressible oil flow through the orifice is the same as the rate of volume change. Thus, the additional pressure generated by the damper is given as a nonlinear relation

$$e = C_d \dot{V}^2 = C_d f^2$$

where C_d is the effective orifice discharge coefficient. Note that C_d depends on various factors like orifice area, length, fluid viscosity, etc., and it is generally obtained through experiments.

The electrical part comprising the DC motor is modeled through a gyrator. Note that the rotation of the wheel in the inertial frame is the sum of the rotation of the vehicle and the rotation of the motor. This is modeled at a 0-junction (0_T junction in Fig. 2.58). This 0-junction performs an important function. It also models the opposite reaction moment acting on the vehicle body (through the bond between 0_T and 1_δ junctions) due to the motor trying to rotate the wheel. This is how a bond graph model ensures proper physics in the system model.

The linear motion of the vehicle is modeled at $1_{\dot{x}}$ junction. The tire driving forces are generated due to friction at the wheel-ground contact. The positive tire slip for

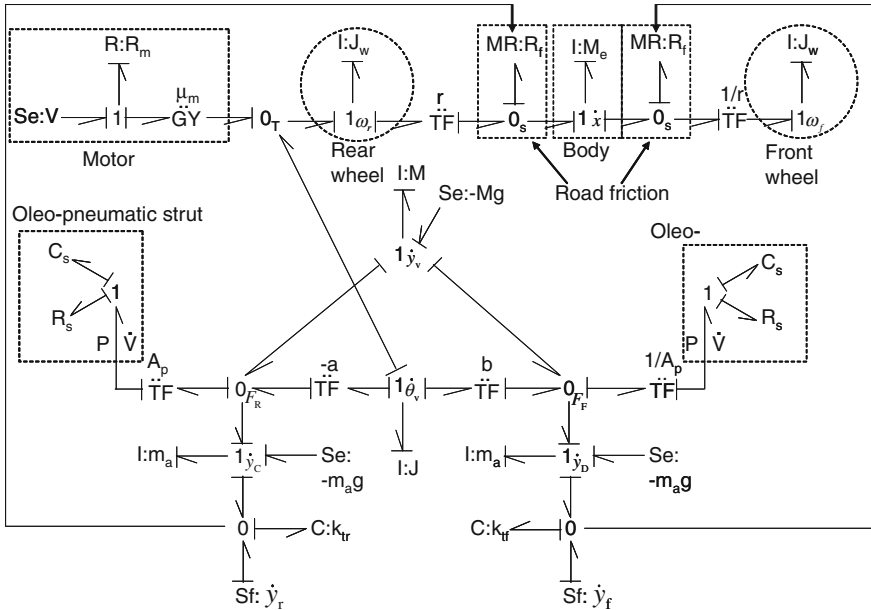


Fig. 2.58 Bond graph model of multi-energy domain vehicle system

the driven wheel is $\omega_r r - \dot{x}$ and it generates the traction force. The small negative slip ($\omega_r r - \dot{x}$) at the front wheel is negative and it generates a small retarding force (rolling resistance). These slips are modeled at 0_S junctions. The tire–road friction is a complicated phenomena and it is usually described by some empirical relations. Here, a modulated R-element (MR:R_f) models this force. Note that the friction force needs the information of normal force which is supplied through effort signal bonds from the respective junctions modeling tire stiffness in vehicle’s vertical motion model.

2.8.7 Nonlinear Models

The systems modeled so far are mostly linear systems whose equation models can be written in state-space matrix form. Let us consider a nonlinear system shown in Fig. 2.59 where the lever is assumed to be massless and there is no friction anywhere. The lever ratio is controlled based upon the position of mass *M*. Moreover, it is assumed that mass *m* is connected to a hardening spring which generates a force $F = k_1 y^2$ where k_1 is the hardening coefficient and *y* is the spring deformation.

To develop the bond graph model of this system, we need to introduce a modulated transformer element (MTF). The modulus of this MTF element can be described as a

Fig. 2.59 Schematic diagram of a nonlinear system

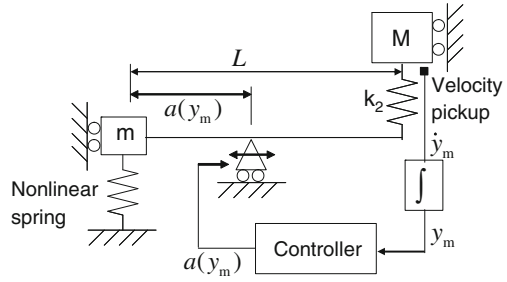
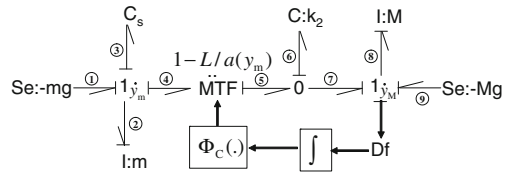


Fig. 2.60 Bond graph model of the considered nonlinear system



function of the position y_M of mass M . If $a(y_M)$ is the position of the lever measured from mass m then the lever ratio turns out to be $-(L-a(y_M))/a(y_M) = 1-L/a(y_M)$. The augmented (numbered, power directed, and causalled) bond graph model of the system is then developed as shown in Fig. 2.60. Note that while the C-element for the linear spring is shown as $C:k_2$, that for the nonlinear spring is simply denoted as C_s . Note that the integrator block in the model introduces an additional state y_M into the model. This is equivalent to use of a flow activated C-element in place of the Df element.

The states of this system (i.e., energy variables in integrally causalled storage elements I and C), the inputs and the outputs, respectively, are

$$x = [p_2 \ p_8 \ q_3 \ q_6 \ y_M]^T, \quad u = [Se_1 \ Se_9], \quad \text{and} \quad y = [f_8]$$

where superscript T indicates matrix transpose.

We can write the state equations as follows:

The junction equations for 1 junction for \dot{y}_m are

$$f_1 = f_3 = f_4 = f_2, \tag{2.64}$$

$$e_2 = e_1 - e_3 - e_4. \tag{2.65}$$

The junction equations for 1 junction for \dot{y}_M are

$$f_7 = f_9 = f_8, \tag{2.66}$$

$$e_8 = e_7 + e_9. \tag{2.67}$$

The equations for the 0 junction are

$$e_5 = e_7 = e_6, \quad (2.68)$$

$$f_6 = f_5 - f_7. \quad (2.69)$$

The transformer equations are

$$f_5 = (1 - L/a(y_M))f_4, \quad (2.70)$$

$$e_4 = (1 - L/a(y_M))e_5. \quad (2.71)$$

The element constitutive relations are written as follows:

$$e_1 = -mg, \quad (2.72)$$

$$f_2 = p_2/m, \quad (2.73)$$

$$e_3 = k_1q_3 |q_3|, \quad (2.74)$$

$$e_6 = k_2q_6, \quad (2.75)$$

$$f_8 = p_8/M, \quad (2.76)$$

$$e_9 = -Mg. \quad (2.77)$$

In addition, the output equation is written as

$$\dot{y}_M = f_8 = p_8/M. \quad (2.78)$$

Note that Eq. 2.74 is written as $e_3 = k_1q_3 |q_3|$ in place of $e_3 = k_1q_3^2$ so that both positive and negative forces are generated for positive and negative values of deformation.

The state-space equations will be given in nonlinear form as

$$\begin{aligned} \dot{x} &= F(x, u) \\ y &= G(x, u) \end{aligned} \quad (2.79)$$

Let us derive the state equation for \dot{p}_2 by using the above-mentioned constraint equations and element constitutive relations. It can be derived as follows:

$$\begin{aligned} \dot{p}_2 &= e_2 = e_1 - e_3 - e_4 \\ &= -mg - k_1q_3 |q_3| - (1 - L/a(y_M))e_5 \\ &= -mg - k_1q_3 |q_3| - (1 - L/a(y_M))k_2q_6. \end{aligned} \quad (2.80)$$

Likewise, we can derive other state equations which are finally written as

$$\begin{aligned} \dot{p}_2 &= -mg - k_1q_3 |q_3| - (1 - L/a(y_M))k_2q_6 \\ \dot{p}_8 &= -Mg + k_2q_6 \end{aligned}$$

$$\begin{aligned}
 \dot{q}_3 &= p_2/m \\
 \dot{q}_6 &= (1 - L/a(y_M)) (p_2/m) - p_8/M \\
 \dot{y}_M &= p_8/M
 \end{aligned}
 \tag{2.81}$$

2.9 Multiport Field Elements

Although I, C, and R elements have been termed one-port elements, they can actually be connected to more than one bonds. Then they are called I, C, and R field elements. A field element has at least two bonds connected to it. Field elements are very useful when more than one energy domains are coupled. For example, in a piezoelectric material, mechanical and electrical domains are coupled.

2.9.1 RS Element

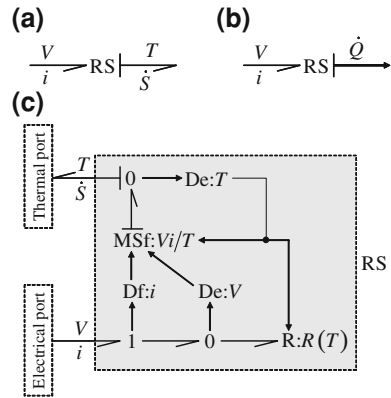
In mechatronic system modeling, we will often be dealing with resistances which act like a source. For example, a diode is a resistance and if we have a light emitting diode (LED) then it is also a source of light. Likewise, a heating coil is an electrical resistance, but also acts as a thermal source. Such resistances couple one energy domain to another. The source and resistance properties are modeled together by the RS element. The RS element, in its simplest form is a two-port resistance. Two bond are attached to the RS element. One of the bonds belongs to the domain from where energy is dissipated (e.g., mechanical domain for power loss due to friction, electrical domain for power loss due to resistance, etc.). The other bond belongs to the domain which receives full or part of the power dissipated by the other domain, e.g., heat, light, sound, etc.

The RS element for modeling an electrical resistance is shown in Fig. 2.61a. Here, the power variables in the electrical port are voltage (V) and current (i). The power variables in the thermal port are temperature (T) and entropy flow or generation rate (\dot{S}). The entropy generated is given as

$$\begin{aligned}
 \dot{S} &= \frac{\dot{Q}}{T} = \frac{Vi}{T} \\
 &= \frac{i^2 R}{T} = \frac{V^2}{RT}
 \end{aligned}
 \tag{2.82}$$

Sometimes, pseudo-bond graphs are used to model thermal systems. In that case, the heat flow is the output variable of RS element. Because heat flow calculation ($\dot{Q} = Vi$) does not require the temperature information, the thermal port of the RS element can be modeled as a signal bond as shown in Fig. 2.61b.

Fig. 2.61 RS element



Most often, the electrical resistance would be a function of the operating temperature. Thus, one would require the temperature information. The resulting expansion of the RS element can then be given as shown in Fig. 2.61c where the R-element is internally modulated by the temperature signal. The RS element is called a defined element. A defined element is a simplified abstraction of a specific part of the model and it is possible to replace that defined element by an expanded bond graph structure. As we proceed further, we will see another important defined element called EJS (Euler junction structure) which is used in multibody system modeling.

2.9.2 Multiport Elements in Process Engineering

In complex process engineering systems, several phenomena (chemical, thermal, hydraulic) are coupled. For such systems, power variables are in defined in a vectorial form:

$$E = [e_h \ e_t \ e_c]^t, \quad F = [f_h \ f_t \ f_c]^t \tag{2.83}$$

where the effort variables e_t , e_h and e_c , respectively, represent the thermal effort (the specific enthalpy or the temperature), the hydraulic effort (the pressure), and the chemical effort (the chemical potential, chemical affinity, or the concentration). The flow variables f_t , f_h and f_c represent, respectively, the thermal (or entropy) flow (heat conduction, \dot{Q} , or enthalpy flow by convection, \dot{H}), hydraulic flow (mass flow \dot{m} or volume flow \dot{V}) and chemical flow (molar flow \dot{n}).

Their coupling can be represented by a small ring around the bond (Fig. 2.62a) as proposed by Thoma in [57] or by multibonds (Fig. 2.62c) as proposed by Breedveld in [3]. Multiple bonds connect the nodes of a bond graph. The dimension of a multi-bond represents the number of elements in the effort or flow vector. This number can be optionally written between two lines. Some authors [23] distinguish the type

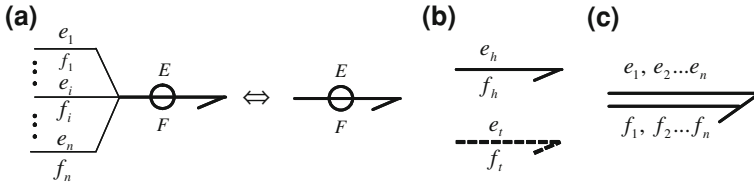


Fig. 2.62 Representation of multibond graph

of energy using full lines for hydraulic bonds and dotted lines for thermal bonds (Fig. 2.62b). Multibonds are also called vector bonds. A bond graph that uses vector bonds is called a vector bond graph.

2.9.2.1 Pipe with Restriction as a Multiport R

In thermodynamic processes, the dissipation phenomenon is modeled by a two-port **R** field element. The main phenomena modeled by the multiport **R** are evaporation, vapor condensation [30], convection [39] through a pipe (as given in Fig. 2.63a). The **R**-field can be represented by a ring around the bond (Fig. 2.63b) or **R:Rc** field (Fig. 2.63d). According to affected causality, outputs of the two-port **R**-field in Fig. 2.63 are the thermal flow \dot{H} and the hydraulic flow \dot{m} . The suffixes *in* and *out* identify the physical input and output sides of the pipe, respectively.

For an incompressible fluid, respecting the continuity equation ($F_{in} = F_{out}$) and assuming no thermal loss in the pipe, the flows leaving the **R**-field are calculated as follows:

$$F = \begin{bmatrix} \dot{m} \\ \dot{H} \end{bmatrix} = \begin{bmatrix} \Phi_{RH}(T_{in}, T_{out}, P_{in}, P_{out}) \\ \Phi_{RT}(T_{in}, T_{out}, P_{in}, P_{out}) \end{bmatrix} \quad (2.84)$$

The constitutive functions Φ_{RH} and Φ_{RT} are nonlinear and depend mainly on the thermodynamic state of the fluid and on the modeling hypothesis. The constitutive relation here involves effort variables and flow variables only; the integrals or derivatives of power variables are not required in the constitutive relation. Thus, the constitutive relation indicates a dissipation phenomena (**R**-element). Because more than one effort and one flow variables are used in the constitutive relation, we have an **R**-field.

Consider that the flow through a pipe under isothermal conditions is given as $\dot{m} = \Phi_{RH}(P_{in} - P_{out})$. Then we can simply use a 1-junction to compute the effort difference $P_{in} - P_{out}$ and connect it to a one-port **R**. However, suppose that the mass flow relation is given as $\dot{m} = \Phi_{RH}(P_{in}/P_{out})$. This relation cannot be modeled by a one-port **R**, we need both P_{in} and P_{out} signals to be input to the **R**-element as opposed to one signal $P_{in} - P_{out}$ in the earlier case.

In the following, we consider two types of technological components modeled by **R**-multiport: a nozzle and a pipe with a restriction.

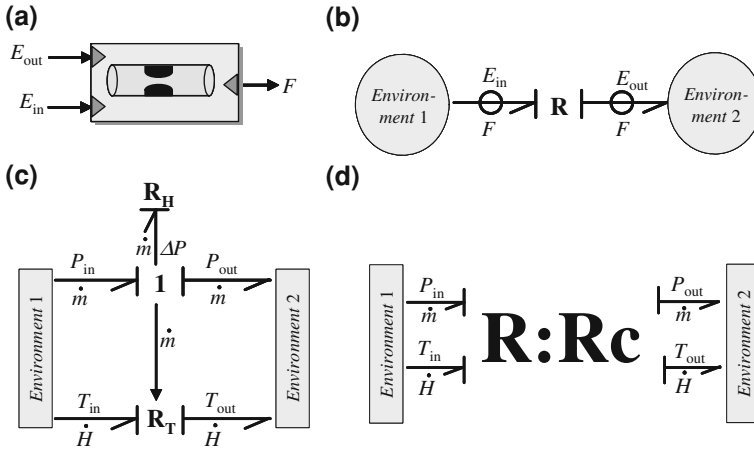


Fig. 2.63 **a** A pipe in process engineering **a** and **b**, **c**, and **d** different representations of the R-field bond graph model

2.9.2.2 Nozzle

The general form of constitutive relation given in Eq. 2.84 is useful when a restrictor can choke due to supersonic flow at its throat. Then the mass flow rate depends not only on the pressure difference, but also on the pressure ratio P_r :

$$P_r = \frac{P_{out}}{P_{in}}. \tag{2.85}$$

It is then possible to predict, with acceptable accuracy, the mass flow rate by using the upstream and downstream pressures [23]:

$$\dot{m} = A \frac{P_{in}}{\sqrt{T_{in}}} (P_r)^{\frac{1}{\gamma}} \sqrt{\frac{2\gamma}{R_G (\gamma - 1)} \left[1 - (P_r)^{\frac{\gamma-1}{\gamma}} \right]}, \quad \text{if } P_r \geq b; \tag{2.86}$$

$$\dot{m} = A \frac{P_{in}}{\sqrt{T_{in}}} \sqrt{\frac{\gamma}{R_G} \left(\frac{2}{\gamma + 1} \right)^{\frac{\gamma-1}{\gamma}}}, \quad \text{if } P_r \leq b;$$

where

$$b = \left(\frac{2}{\gamma + 1} \right)^{\frac{\gamma-1}{\gamma}}, \tag{2.87}$$

R_G is the gas constant, A is the exit area, $\gamma = c_p/c_v$, c_p is the specific heat at constant pressure and c_v is the specific heat at constant volume. The enthalpy flow rate is given as

$$\dot{H} = \dot{m}c_v T_{in} \quad (2.88)$$

2.9.2.3 Thermofluid Transport Phenomena in a Pipe

The drawback of the aforementioned modeling approach is that in the opposite causality, the effort cannot be calculated from such a nonlinear equation (Eq. 2.86). In industrial process engineering, we generally assume low velocity or subsonic flow. Thus, it is sufficient to assume that the mass flow rate \dot{m} is a function of the pressure difference. We assume first that the flow-field properties are constant in the pipe and the accumulation of mass, momentum, and energy in such component are of negligible order. The flow is regular and the fluid is Newtonian. The bond graph model, with these simplifying assumptions, is given in Fig. 2.63c, where the **I**-element for fluid inertia (developed earlier) may be included to take fluid momentum into account. Readers may look into [34] for detailed models of hydraulic transport phenomena with flow saturation characteristics, which are derived from the first principles.

The energy coupling is modeled by the fictive thermal resistor R_T modulated (using information bond) by the hydraulic flow variable \dot{m} . According to the conductive causality assigned to **R**-element, the commonly used form of the constitutive relation is given by Bernoulli's law, i.e.,

$$\begin{bmatrix} \dot{m} \\ \dot{H} \end{bmatrix} = \begin{bmatrix} C_d \cdot \text{sign}(P_{in} - P_{out}) \sqrt{|P_{in} - P_{out}|} \\ C_d \cdot \text{sign}(P_{in} - P_{out}) c_v \sqrt{|P_{in} - P_{out}|} \cdot T_{in} \end{bmatrix}, \quad (2.89)$$

where C_d is the valve discharge coefficient which can be determined for turbulent and laminar flow conditions. If the fluid state is saturated, the temperature T_{in} is calculated as a function of the pressure P_{in} by using thermodynamic tables.

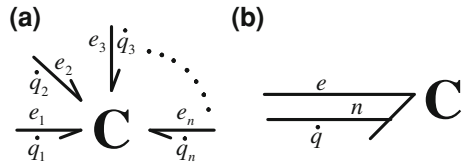
2.9.3 C-Field

A C-field shown in Fig. 2.64 stores potential energy. Its constitutive relation associates a set of displacements to a set of efforts. In the figure, there are n -ports in the C-field and the flow at the i th port has been labeled $\dot{q}_i = f_i$ (derivative of displacement $q_i = \int f_i dt$). If all ports of the C-field are integrally causalled then the C-field leads to n state variables.

The constitutive relation for the C-field is given as

$$\Phi_C(E, Q) = \Phi_C \left(E, \int F dt \right) = 0 \quad (2.90)$$

Fig. 2.64 n-port C-field and its bond graph representation



where

$$Q = [q_1 \dots q_n]^T$$

$$E = [e_1 \dots e_n]^T$$

Note that the efforts e_i depend on all displacements $q_i = \int f_i dt$. The relation can be linear, given by a matrix, or nonlinear, given by a set of functions. For a linear C-field with all its bonds integrally causalled, the constitutive relation is given as

$$\begin{bmatrix} e_1 \\ e_2 \\ \vdots \\ e_n \end{bmatrix} = \begin{bmatrix} k_{11} & k_{12} & \dots & k_{1n} \\ k_{21} & k_{22} & \dots & k_{2n} \\ \vdots & \vdots & \vdots & \vdots \\ k_{n1} & k_{n2} & \dots & k_{nn} \end{bmatrix} \begin{bmatrix} q_1 \\ q_2 \\ \vdots \\ q_n \end{bmatrix} \tag{2.91}$$

If all off-diagonal terms of the above stiffness matrix are zero then the C-field degenerates to n number of one-port C-elements. The compliance matrix is the inverse of the stiffness matrix. For a conservative system, the stiffness matrix is always symmetric.

The energy stored in the C-field is

$$E = \int_{t_0}^t \sum_{i=1}^n (e_i f_i) dt = \int_{t_0}^t \sum_{i=1}^n (e_i \dot{q}_i) dt$$

$$= \int_{q_0}^q \sum_{i=1}^n e_i(q) dq_i = \int_{q_0}^q \sum_{i=1}^n e(q) dq = E(q) \tag{2.92}$$

Example 2.3 Consider the example given in [24] which consists of a thin beam (assumed to be mass-less) with masses attached at two locations indicated by the pair of power variables (F_1, \dot{x}_1) and (F_2, \dot{x}_2) as shown in Fig. 2.65a. If the beam can be considered as a pure elastic structure then its corresponding bond graph model can be given as shown in Fig. 2.65b.

One can use the influence coefficients (deflections caused at a certain location due to unit force applied at a specified location) and method of superposition to determine the compliance matrix of the elastic structure. For the given loading configuration, the displacements can be expressed as a function of forces in compliance form as

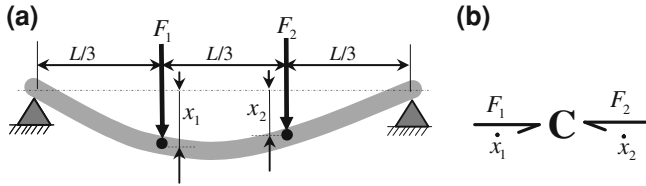


Fig. 2.65 Example of uniform beam deformed by action of two forces represented by two-port C-field

follows:

$$\begin{bmatrix} x_1 \\ x_2 \end{bmatrix} = \frac{L^3}{243EI} \begin{bmatrix} 4 & \frac{7}{2} \\ \frac{7}{2} & 4 \end{bmatrix} \begin{bmatrix} F_1 \\ F_2 \end{bmatrix} \quad (2.93)$$

where E is the modulus of elasticity, and I is the second moment of area of the beam cross-section about the neutral axis. One can then write

$$\begin{bmatrix} F_1 \\ F_2 \end{bmatrix} = \frac{243EI}{L^3} \begin{bmatrix} 4 & \frac{7}{2} \\ \frac{7}{2} & 4 \end{bmatrix}^{-1} \begin{bmatrix} \int \dot{x}_1 dt \\ \int \dot{x}_2 dt \end{bmatrix} \quad (2.94)$$

The bond graph model of the system is then given by connecting the C-field to two 1-junctions at its two ends to which the inertia elements can be connected. In addition, the structural (material) and external damping can be included in the model. The structural damping is modeled as a two-port R-field between the two 1-junctions (exactly like the two-port C-field) and the damping matrix is assumed to be proportional to the stiffness matrix. The coefficient of proportionality is a material parameter. For more details on modeling of static or spinning beams, see [50].

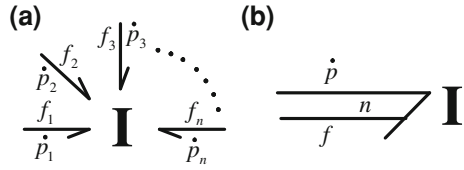
As in the case of 1-port C-elements, a C-field can have derivative or integral causality in all its ports. But, a multiport C-field also admits mixed integral-derivative causalities. In mechanical systems (using force F and linear velocity \dot{x}) the compliance form corresponds to derivative causality and the stiffness form to integral causality.

2.9.4 I-Field

An inertia field (called I-multiport or I-field) is analogous to the C-field. Its constitutive relation is expressed between flow f and momenta p . The generic form of I-field is shown in Fig. 2.66.

The constitutive relation of a I-field with all its bonds in integral causality is given as

Fig. 2.66 I-field representation



$$\begin{bmatrix} f_1 \\ f_2 \\ \vdots \\ f_n \end{bmatrix} = \begin{bmatrix} m_{11} & m_{12} & \dots & m_{1n} \\ m_{21} & m_{22} & \dots & m_{2n} \\ \vdots & \vdots & \vdots & \vdots \\ m_{n1} & m_{n2} & \dots & m_{nn} \end{bmatrix}^{-1} \begin{bmatrix} p_1 \\ p_2 \\ \vdots \\ p_n \end{bmatrix} \tag{2.95}$$

Note that the multiport I is analogous to the multiport C , only the effort and displacement are turned into flow f_i and momentum p_i . The mass matrix is symmetric and positive definite. The energy stored in the I-field is given as

$$\begin{aligned} E &= \int_{t_0}^t \sum_{i=1}^n (e_i f_i) dt = \int_{t_0}^t \sum_{i=1}^n (f_i \dot{p}_i) dt = \int_{p_0}^p \sum_{i=1}^n f_i(p) dp_i \\ &= \int_{p_0}^p \sum_{i=1}^n f_i(p) dp = E(p) \end{aligned} \tag{2.96}$$

where

$$\begin{aligned} p &= [p_1 \dots p_n]^T \\ f &= [f_1 \dots f_n]^T \end{aligned}$$

Example 2.4 Any rigid body motion can be modeled as an I -field. Consider a simple example of a long thin rigid bar as shown in Fig. 2.67a.

Consider only vertical motion of the center of mass G and small angular rotation θ relative to a horizontal axis. Such approximations are made in pitch-plane model of a vehicle going over a rough surface. The mechanical system is described by two pairs of power variables: (F, \dot{x}) for linear translation and (T, ω) for angular translation. In Figure $F, \dot{x}, \theta, \omega, p_G, p_\theta$ represent force, linear velocity, angular displacement, angular velocity, linear momentum, and angular momentum, respectively.

Recall that the momentum (used as state variable) is related to the flow variable:

$$\dot{x} = \frac{p_G}{m}, \quad \omega = \frac{p_\theta}{J} \tag{2.97}$$

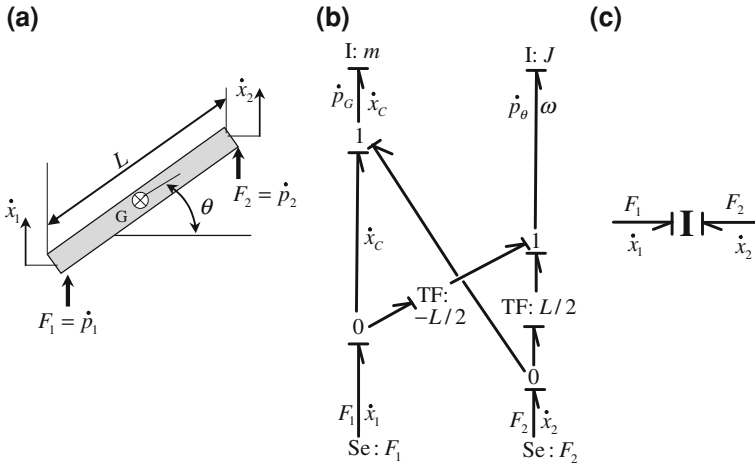


Fig. 2.67 A rigid bar in plane motion as an I-field: **a** Schematic principle, **b** decoupled implicit bond graph model, and **c** I-field explicit representation

where the mass m and rotary inertia J are:

$$m = \rho AL, \quad J = \frac{mL^2}{12}. \tag{2.98}$$

where A , ρ and L are cross-section area, mass density, and length of the bar, respectively. The rate of linear and angular momentum variables are

$$\dot{p}_G = F_1 + F_2, \quad \dot{p}_\theta = -\frac{L}{2}F_1 + \frac{L}{2}F_2 \tag{2.99}$$

Then the bond graph model of the system can be constructed as shown in Fig. 2.67b. It can also be constructed from the following kinematic relations:

$$\begin{aligned} \dot{x}_2 &= \dot{x} + L\dot{\theta}/2 \\ \dot{x}_1 &= \dot{x} - L\dot{\theta}/2 \end{aligned} \tag{2.100}$$

If we consider only vertical displacements and small rotations around G, the rigid body can be described by a linear two-port I-field as shown in Fig. 2.67c. Under these assumptions, the explicit I-field constitutive equation (linking flow and momentum, i.e., integral of effort) can be easily deduced:

$$\begin{bmatrix} \dot{x}_1 \\ \dot{x}_2 \end{bmatrix} = \mathbf{M}^{-1} \begin{bmatrix} p_1 \\ p_2 \end{bmatrix} \tag{2.101}$$

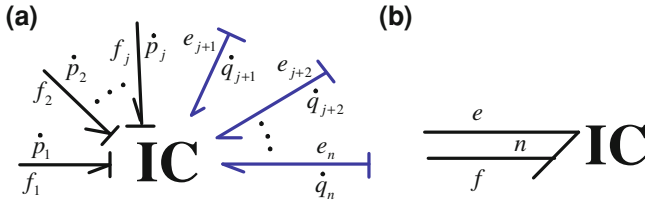


Fig. 2.68 IC-field representation

where the inverse of the mass matrix (\mathbf{M}) is given as

$$\mathbf{M}^{-1} = \begin{bmatrix} (1/m) + (L^2/4J) & (1/m) - (L^2/4J) \\ (1/m) - (L^2/4J) & (1/m) + (L^2/4J) \end{bmatrix} \quad (2.102)$$

A direct method to derive the mass matrix or consistent mass matrix is to write the kinetic energy as

$$\begin{aligned} E_k &= \frac{1}{2}m\dot{x}^2 + \frac{1}{2}J\dot{\theta}^2 \\ &= \frac{1}{2}m \left(\frac{\dot{x}_1 + \dot{x}_2}{2} \right)^2 + \frac{1}{2} \left(\frac{mL^2}{12} \right) \left(\frac{\dot{x}_2 - \dot{x}_1}{L} \right)^2 \end{aligned} \quad (2.103)$$

The mass matrix is given as

$$\mathbf{M} = \begin{bmatrix} \frac{\partial^2 E_k}{\partial \dot{x}_1^2} & \frac{\partial^2 E_k}{\partial \dot{x}_1 \partial \dot{x}_2} \\ \frac{\partial^2 E_k}{\partial \dot{x}_1 \partial \dot{x}_2} & \frac{\partial^2 E_k}{\partial \dot{x}_2^2} \end{bmatrix} \quad (2.104)$$

If large motions are considered in planar motion for an arbitrary shaped body, then the y velocities of end points have to be included in the model. It can be represented by a four-port I field as developed in [2].

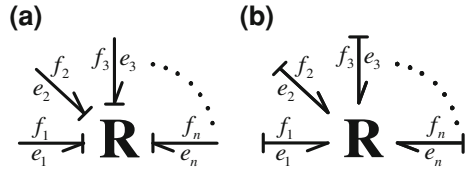
2.9.5 IC-Field

We have also a combination between I and C multiport, having j ports as multiport I and $(n - j)$ ports as multiport C , as shown in Fig. 2.68.

The stored energy is:

$$E = \int_{t_0}^t \sum_{i=1}^n e_i f_i dt = \int_{p_0}^p \sum_{i=1}^j f_i dp_i + \int_{q_0}^q \sum_{k=j+1}^n e_k dq_k \quad (2.105)$$

Fig. 2.69 R-field in con-
ductance (a) and resistance
causality (b)



Here, p is the momentum vector and q the displacement vector. The first j ports represent a multiport I and ports from $j + 1$ to n represent the multiport C . The multiport IC is used mostly for electromagnetic effects with mechanical parts where the electric part is modeled as a multiport I and the mechanical part as a multiport C . A typical example of an IC -field is an electrical solenoid transducer.

2.9.6 R-Field

An R -field with n -ports essentially represents a coupled resistor network, the constitutive laws of which is an algebraic relation between n flows and n efforts without energy storage. The constitutive law can be linear, like Ohm’s law or nonlinear, like the hydraulic resistors. The constitutive laws for the resistance and conductance causality shown in Fig. 2.69 may be written as follows:

$$\begin{aligned} e_i &= \Phi_{Ri}(f_1, f_2, \dots, f_n), \quad i = 1, \dots, n \\ f_i &= \Phi_{Ri}^{-1}(e_1, e_2, \dots, e_n), \quad i = 1, \dots, n \end{aligned} \tag{2.106}$$

One example of a multiport R -element is the true bond graph for heat transfer across a metallic plate. If the two surfaces of the plate are at temperatures T_1 and T_2 with $T_1 > T_2$ then we can write

$$\dot{Q}_1 = \dot{Q}_2 = \lambda (T_1 - T_2) \tag{2.107}$$

and this can be modeled as a simple resistance at a 1-junction with the pair (T, Q) as the pseudo-bond graph power variables. However, if we have to model a true bond graph then the flow variable should be entropy flow, and the power variables is the pair (T, \dot{S}) . The entropy flows are

$$\dot{S}_1 = \frac{\dot{Q}_1}{T_1} = \lambda \frac{(T_1 - T_2)}{T_1} \tag{2.108}$$

$$\dot{S}_2 = -\frac{\dot{Q}_2}{T_2} = -\lambda \frac{(T_1 - T_2)}{T_2} \tag{2.109}$$

where \dot{S}_1 and \dot{S}_2 are, respectively, the entropy flow rates into and out of the thermal interface.

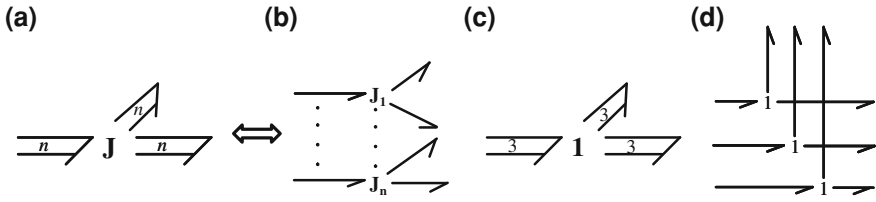


Fig. 2.70 **a** Vector junction representation, **b** dissociation to scalar bonds, and **c** and **d** vector and scalar bond graph equivalence of a three-dimension vector 1-junction

Obviously, the entropy flow rates have a nonlinear relation with the interface temperatures and it cannot be modeled as a 1-port R-element. The constitutive relation not only requires the relative temperatures but also absolute values. Thus, we represent this coupling by a two-port R-field.

2.9.7 Vector Junction

Vector junctions are used for compact representation of a set of similar junction structures. The n dimensional junction is represented in Fig. 2.70 where J indicates either 0 or 1.

The constitutive equations for a vector 1-junction, where n is the bond dimension and m is the number of bonds, are

$$\begin{aligned} & i = 1, \dots, n \\ \sum_j e_j^i &= 0, \quad j = 1, \dots, m \\ f_j^i &= f_1^i, \quad j = 2, \dots, m \end{aligned} \tag{2.110}$$

and those for vector 0-junction, where n is the bond dimension and m is the number of bonds, are

$$\begin{aligned} & i = 1, \dots, n \\ \sum_j f_j^i &= 0, \quad j = 1, \dots, m \\ e_j^i &= e_1^i, \quad j = 2, \dots, m \end{aligned} \tag{2.111}$$

A bond graph represented using vector bonds and junctions is called a vector bond graph. A vector bond graph can be expanded to a normal bond graph (called a scalar bond graph) form.

2.9.8 Multiport Transformers and Gytrators

If TF and GY elements as (described before) are extended to the multibond graph, they become multiport elements and can be represented as shown in Fig. 2.71. The

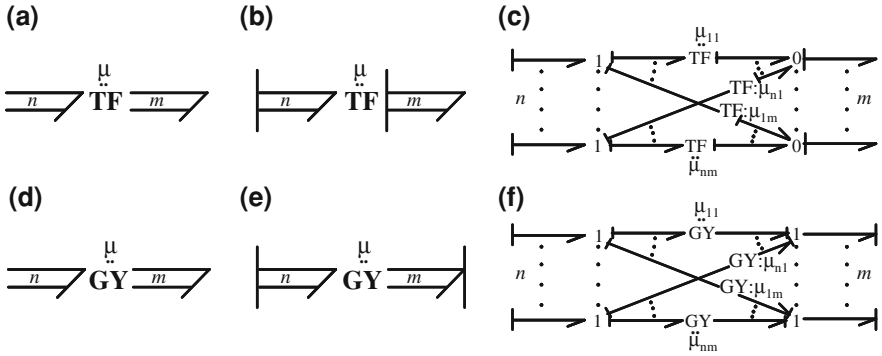


Fig. 2.71 Vector bond graphs for two-port elements and their scalar equivalences

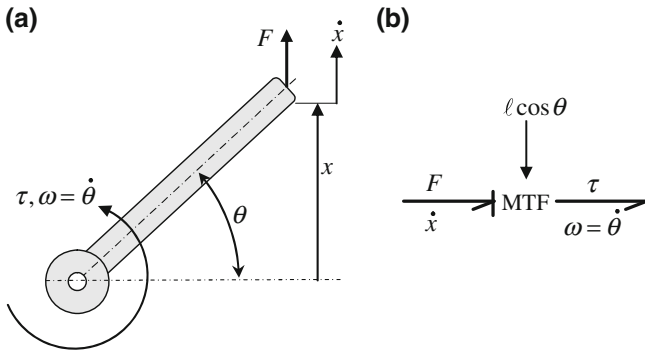


Fig. 2.72 Example of two-port modulated transformer

modulus of such a two-port vector element is a matrix which relates the input variables to the output variables.

Note that the dimension of bonds in the two ports of a vector two-port element can be different. The scalar equivalent structure of a vector two-port depends on the causality. Figure 2.71b, c show dissociation of a vector TF to scalar equivalent form. If the same TF element in Fig. 2.71b is causalled differently then 0-junctions will appear on LHS and 1-junctions will appear on the RHS side of the scalar equivalent bond graph given in Fig. 2.71c. Likewise, the dissociation of the vector GY element in Fig. 2.71e to the scalar form in Fig. 2.71f is appropriate if the causal strokes are away from the GY element. If the causal strokes are placed near the GY element then the 1-junctions in Fig. 2.71f should be replaced by 0-junctions.

Signal or activated bonds are used to modulate other passive bond graph elements (MI, MC, and MR), two-ports (MTF and MGY) and sources (MSe and MSf). As example of a modulated transformer, consider a rigid pivoted bar shown in Fig. 2.72a.

The constitutive equation for the MTF element in bond graph model shown in Fig. 2.72b can be written as

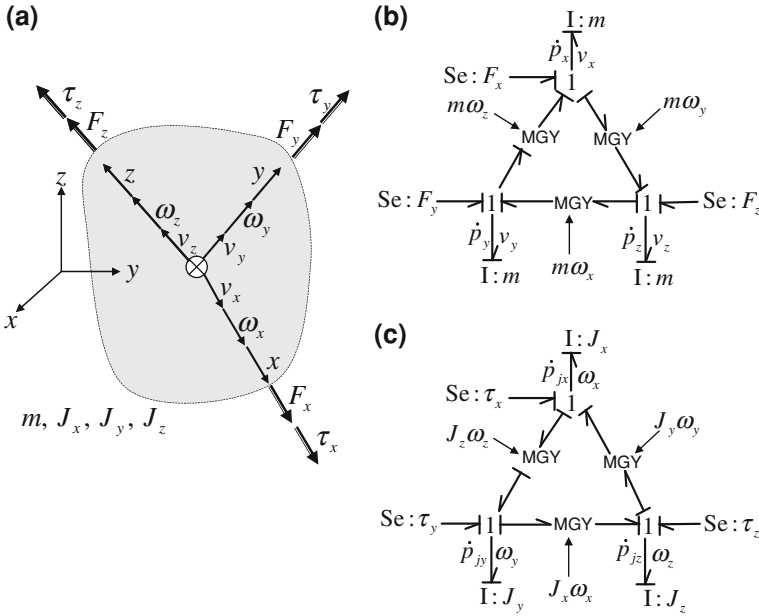


Fig. 2.73 **a** Body-fixed frame and velocities in a rigid body in general motion, **b** bond graph model of Newton's equations in non-inertial frame, and **c** bond graph model of Euler's equations

$$\begin{bmatrix} \tau \\ \dot{x} \end{bmatrix} = \begin{bmatrix} \ell \cos \theta & 0 \\ 0 & \ell \cos \theta \end{bmatrix} \begin{bmatrix} F \\ \omega \end{bmatrix} \tag{2.112}$$

Multiport transformers and gyrators can be similarly modulated by vector signals.

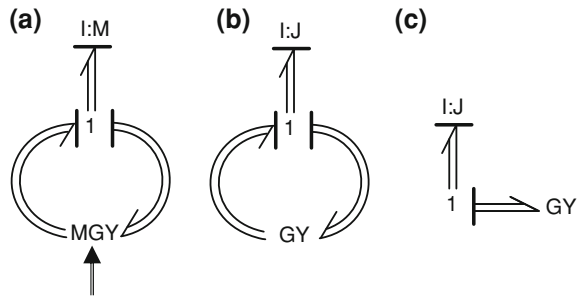
2.9.9 Vector Bond Graph for Rigid-Body Dynamics

Multibonds are frequently used to model rigid body mechanics. Typical examples are vehicle dynamic, mechanisms, and robotic systems.

A general rigid body translating and rotating in space is shown in Fig. 2.73a. The rigid body has absolute linear velocities v_x, v_y, v_z and angular velocities $\omega_x, \omega_y, \omega_z$ taken along a body-fixed frame which is momentarily aligned with the principal axes of the body. The mass of the body is m and the principal moments of inertia are J_x, J_y and J_z , respectively, about the body-fixed x, y , and z axes. This is the standard form for modeling the motion of an arbitrary rigid body in a non-inertial reference frame.

The bond graph model for translation motion is derived from the Newton's equations written in the body-aligned moving frame and it is shown in Fig. 2.73b. The

Fig. 2.74 **a** Multibond graph representation of Newton's equations for a rigid body motion, **b** multibond graph of Euler's equations, and **c** compact representation of Euler's equations



pseudo-forces appear because of the transformation of accelerations in non-inertial frame to the inertial frame. These pseudo-forces are modeled by a set of modulated gyrators called a gyrator ring. The rotary motions are described by Euler's equations and they are represented in bond graph form as shown in Fig. 2.73c. F_x, F_y and F_z are the external force components taken along body-fixed axes and they are modeled by effort sources. Likewise, external torque components (τ_x, τ_y and τ_z) are modeled. The state variables are angular momenta p_{J_x}, p_{J_y} and p_{J_z} and linear momenta p_x, p_y and p_z .

From bond graph models, the state equations are:

$$\begin{bmatrix} \dot{p}_x \\ \dot{p}_y \\ \dot{p}_z \\ \dot{p}_{J_x} \\ \dot{p}_{J_y} \\ \dot{p}_{J_z} \end{bmatrix} = \begin{bmatrix} 0 & \frac{m\omega_z}{m} & -\frac{m\omega_y}{m} & 0 & 0 & 0 \\ -\frac{m\omega_z}{m} & 0 & \frac{m\omega_x}{m} & 0 & 0 & 0 \\ \frac{m\omega_y}{m} & -\frac{m\omega_x}{m} & 0 & 0 & 0 & 0 \\ 0 & 0 & 0 & 0 & -\frac{J_z\omega_z}{J_y} & \frac{J_y\omega_y}{J_z} \\ 0 & 0 & 0 & \frac{J_z\omega_z}{J_x} & 0 & -\frac{J_x\omega_x}{J_z} \\ 0 & 0 & 0 & -\frac{J_y\omega_y}{J_x} & \frac{J_x\omega_x}{J_y} & 0 \end{bmatrix} \begin{bmatrix} p_x \\ p_y \\ p_z \\ p_{J_x} \\ p_{J_y} \\ p_{J_z} \end{bmatrix} + \begin{bmatrix} F_x \\ F_y \\ F_z \\ \tau_x \\ \tau_y \\ \tau_z \end{bmatrix} \tag{2.113}$$

where

$$\omega_x = \frac{p_{J_x}}{J_x}, \quad \omega_y = \frac{p_{J_y}}{J_y}, \quad \omega_z = \frac{p_{J_z}}{J_z} \tag{2.114}$$

The above equations can be represented in a compact form as a multi-bond graph shown in Fig. 2.74 where M is a 6×6 diagonal matrix with its diagonals being the linear and rotary inertias and the modulus of MGY element is a 6×6 matrix whose diagonal elements are zero. Note that the modulating signal connected to MGY element is a vector of dimension 3 containing the angular velocities.

The above model can be broken into two parts: linear motion model and rotational motion model. These two models are identical to the model shown in Fig. 2.74a, b, but the dimension of each vector bond is three and each mass matrix is 3×3 diagonal matrix. These two models are in fact compact representations of the part models given in Fig. 2.73b, c, separately. The part model Fig. 2.73c is often simply shown by a symbol EJS (Euler junction structure) or a triangle (Δ) which is a three-port element

allowing connections to external moments. Note that the model in Fig. 2.74a requires angular velocities as modulation inputs, whereas the model in Fig. 2.74b does not need external modulation. When both linear and rotational models are put together, it is symbolized by a star (\star) which is a 6-port element allowing connection to external forces and moments. A further compact representation of the EJS can be given as shown in Fig. 2.74c where the 1-port multibond GY means the bonds start and end at the same junction structure. The dimension of a bond in one-port GY is twice that of the corresponding two-port GY.

2.10 Bond Graph Modeling of Uncertain Systems

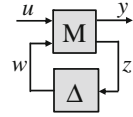
During control and diagnosis of uncertain systems, it is necessary to account for the uncertainty in the modeling stage. This improves the robustness of the control or diagnostic system. The main advantage of using bond graph modeling for uncertain systems is that parametric uncertainties can be directly associated with bond graph elements [9–11] while disturbances can be modeled as random input sources and measurement uncertainties (sensor noise, bias, etc.) can be modeled in block diagram form in the active part of the system. Thus, the uncertainties can be introduced graphically in the bond graph model rather than waiting for equation derivation and later introduction of uncertainties in equation form as followed in other modeling approaches. The final objective is to use the uncertain model to improve the robustness of the controller or decision procedure in Fault Detection and Isolation (FDI) algorithms [9]. The methodology for diagnosis of uncertain systems by using the Bond Graph (BG) tool is developed in a later chapter of this book. The bond graph modeling of uncertain systems, as developed here, is based on Linear Fractional Transformation (LFT) theory.

2.10.1 Linear Fractional Transformation (LFT)

Linear Fractional Transformation was introduced by Redheffer in 1960 [43] and it was adapted to bond graph models by Dauphin-Tanguy in 1999 [7].

Linear fractional transformation (LFT) form represented in Fig. 2.75, is widely used for uncertain system modeling. The nominal values are grouped in an augmented matrix denoted M , supposed to be proper, and all the uncertainties (structured and unstructured uncertainties, measurement noise, etc.) are gathered together in a matrix Δ with a diagonal structure. It is used for stability analysis and for control law synthesis using μ -analysis and synthesis principles, by separating the nominal part of the model from its uncertain part as shown in Fig. 2.75. Generality of the LFT representation is due to the fact that any rational expression can be written under this form.

Fig. 2.75 LFT representation



In the linear case, this standard form leads to a state-space representation of the form

$$\begin{cases} \dot{x} = Ax + B_1w + B_2u \\ z = C_1x + D_{11}w + D_{12}u \\ y = C_2x + D_{21}w + D_{22}u \end{cases} \quad (2.115)$$

where $x \in R^n$ is the state vector of the system, $u \in R^m$ and $y \in R^p$ are the vectors gathering, respectively, the control inputs and the measured outputs of the system, $w \in R^l$ and $z \in R^l$ include, respectively, the auxiliary inputs and outputs, and n , m , l , and p are positive integers. A , B_1 , B_2 , C_1 , C_2 , D_{11} , D_{12} , D_{21} , and D_{22} are matrices of appropriate dimensions. Equation (2.115) are not easy to obtain in case of complex systems, particularly because of the requirement that the matrix Δ has to be diagonal.

2.10.2 LFT Modeling of Bond Graph Elements

An uncertainty on a parameter value θ can be introduced under either an additive form or a multiplicative form:

$$\theta = \theta_n + \Delta\theta \quad (2.116)$$

$$\theta = \theta_n \cdot (1 + \delta_\theta) \quad (2.117)$$

where $\Delta\theta$ and $\delta_\theta = \frac{\Delta\theta}{\theta_n}$ are, respectively, the absolute and relative deviations around the nominal value θ_n . When the element characteristic law is written in terms of $\frac{1}{\theta}$, Eq. (2.117) appears as

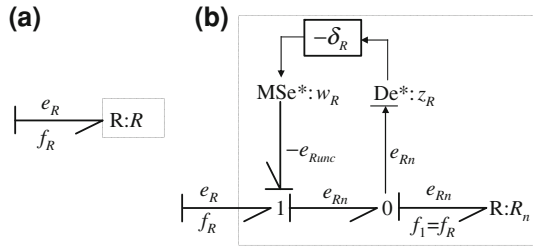
$$\frac{1}{\theta} = \frac{1}{\theta_n} \cdot \left(1 + \delta_{\frac{1}{\theta}}\right) \quad (2.118)$$

with $\delta_{\frac{1}{\theta}} = -\frac{\Delta\theta}{\theta_n + \Delta\theta}$.

Modeling of bond graph elements (R, I, C, TF, GY) in the LFT form consists of decoupling the nominal element ($R_n, I_n, C_n, TF_n, GY_n$) part from its uncertain part δ ($\delta_R \cdot R_n, \delta_I \cdot I_n, \delta_C \cdot C_n, \delta_{TF} \cdot TF_n, \delta_{GY} \cdot GY_n$) with δ being a multiplicative uncertainty on the associated parameter.

Consider a linear R-element in resistance (imposed flow) causality. The characteristic law corresponding to R-element in the linear case (Fig. 2.76a) is given as

Fig. 2.76 Deterministic (a) and uncertain or LFT form (b) bond graph R-element in resistance causality



follows:

$$e_R = R \cdot f_R \tag{2.119}$$

In case of uncertainty on the parameter R , Eq.(2.119) is written as

$$e_R = R_n (1 + \delta_R) f_R = R_n \cdot f_R + \delta_R R_n f_R = e_{R_n} + e_{R_{unc}} = e_{R_n} + w_R \tag{2.120}$$

Constitutive Eq. (2.120) can be represented as LFT BG of an uncertain R-element shown in Fig. 2.76b by introducing a modulated source MSe associated with auxiliary input w_R and a virtual effort sensor associated with the auxiliary output z_R . In Fig. 2.76b, $z_R = R_n f_R$, R_n , $\delta_R = \frac{\Delta R}{R_n}$, ΔR , e_R and f_R represent, respectively, the nominal effort value, the nominal parameter value, the multiplicative uncertainty, the additive uncertainty, the effort, and the flow variables of the uncertain R element. Note that w_R is a fictitious input that represents the effort added by the parameter uncertainty. Fictive inputs are represented as MSe^* and MSf^* in uncertain BG. In The symbols De^* and Df^* correspond to virtual sensors in uncertain BG. The suffix or superscript $*$ is used to distinguish the real sources and measurements from the fictitious ones.

For an R-element in conductance (imposed effort) causality, the procedure is the same:

$$f_R = \frac{1}{R} \cdot e_R \tag{2.121}$$

$$f_R = \frac{1}{R_n} \cdot \left(1 + \delta_{\frac{1}{R}}\right) \cdot e_R = \frac{1}{R_n} \cdot e_R + \frac{\delta_{\frac{1}{R}}}{R_n} \cdot e_R = f_{R_n} + f_{R_{unc}} \tag{2.122}$$

which can be written as Eq. (2.122) and leads to LFT BG shown in Fig. 2.77b.

In [9–11], the LFT Bond graph models of passive and junction elements are described in detail. The sources are supposed to be known without uncertainty, except in the case of closed-loop models. The uncertain bond graph models of storage (C and I) and two-port (GY and TF) elements are given in Figs. 2.78 and 2.79, respectively.

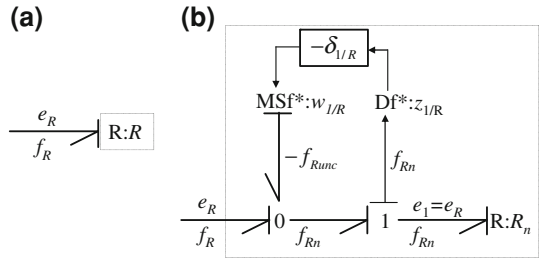


Fig. 2.77 Deterministic (a) and uncertain or LFT form (b) bond graph R-element in conductance causality

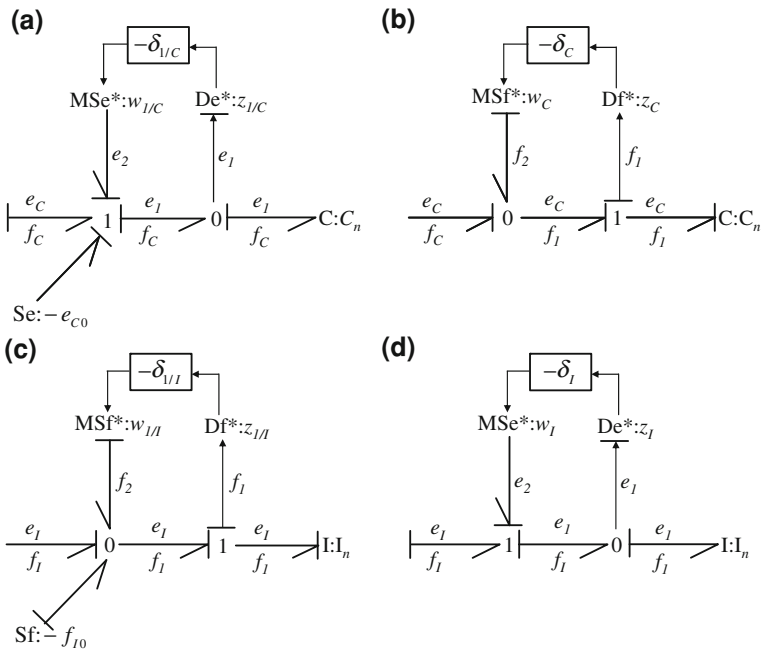


Fig. 2.78 Uncertain LFT bond graph of C-element in a integral and b derivative causality, and uncertain LFT bond graph of I element in c integral, and d derivative causality

2.11 Automated Modeling: An Application Example

2.11.1 Bond Graph Software

Bond graph modeling is supported by many dedicated software. The model can be graphically introduced in these software and the dynamic model can be automati-

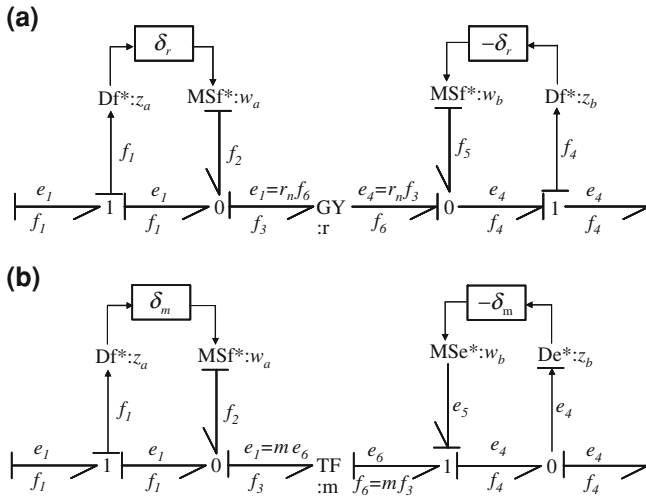


Fig. 2.79 Uncertain LFT bond graph of **a** GY and **b** TF elements

cally generated. It can be completely and automatically transformed into a simulation program for the problem to be analyzed. Most of these software also support control theoretic analysis. One of the first software using bond graph was Camp-G [17] which has capabilities to graphically enter the model and interface outputs with Matlab-Simulink [28] (well-known software for automatic control community). Bond graph models can be described in Modelica language as connection of submodels [12] for which the constitutive equations are introduced by the user. The 20-sim software [58] developed at the University of Twente (Netherlands) is based on the well-known block-oriented TUTSIM simulation program. The model can be entered in graphical or textual format. Symbols (SYstem Modeling by Bondgraph Language and Simulation) is another software developed at the Indian Institute of Technology in Kharagpur (India), which allows use of the full potential of bond graph modeling as an integrated computer-aided tool [35]. Symbols is an object-oriented hierarchical hybrid modeling, simulation, and control analysis software. It allows users to create models using bond graph, block-diagram, and equation models. Authors Ould Bouamama and Samantary have created a new module in order to use this software not only for modeling but for diagnosis and monitoring of process engineering systems as well [40, 49]. A generic plant item database, which consists of a set of predefined process components, controllers, actuators, and sensor classes, has been incorporated as a set of submodels (called capsules in the software Symbols). The designer can easily build the dynamic and functional models of most thermofluid processes from the Process and Instrumentation Diagram (P&I D) of the plant, and automatically generate dynamic models under state equations or nonlinear form. The model can be used for fault diagnosis and process supervision system design.

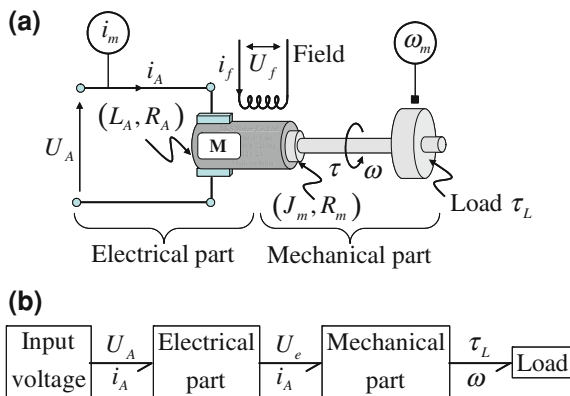


Fig. 2.80 Schematic (a) and word bond graph (b) of a separately excited DC motor

Table 2.8 Variables of the simplified DC motor system

Symbol	Designation	Symbol	Designation
τ_e	Electromagnetic torque	i_A	Stator current
τ_L	Mechanical torque (Load)	i_R, i_L	Current in the resistance and coil
τ_R	Friction torque	U_A	Input voltage
τ_I	Inertial torque	U_L	Induced voltage
ω	Angular velocity	U_R	Resistive voltage
ω_m	Measured angular velocity	R_A	Resistance of the stator
J_M	Inertia of rotor and load	L_A	Inductance of the stator
R_M	Viscous friction	δ_x	Uncertainty in parameter x

2.11.2 Description of the System

In order to illustrate the bond graph modeling methodology we use a simple example of a separately excited DC motor described by an equivalent circuit shown in Fig. 2.80a.

The notation presented in Table 2.8 will be used to describe the DC motor dynamics.

2.11.3 Word Bond Graph

Any mechatronic system can be seen as a set of interconnected subsystems. Engineers are more familiar with block diagram representation, where the input and output of each subsystem is a signal. The block is represented by a functional relation

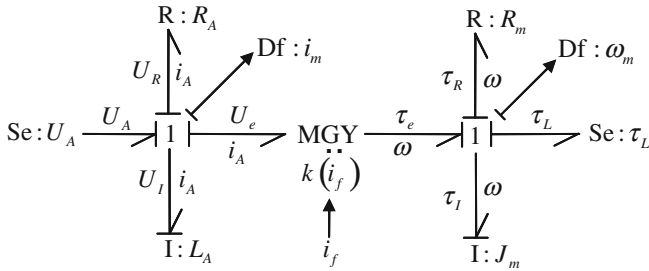


Fig. 2.81 Bond graph model of separately excited DC motor

(linear, nonlinear) between the input and output signal(s). Block diagram is then a computational structure and it does not reflect the physical structure of a system. The number of subsystems to be considered in a block diagram model depends on the complexity of the global system. Concerning our example, four parts can be considered as shown in Fig. 2.80b: input voltage source, electrical part, mechanical part, and the load. While the modeled system is electromechanical, two pairs of power variables are used: voltage-current (U, i) and torque-angular velocity (τ, ω) .

Contrary to the block diagram, the word bond graph represents the physical structure of the system. Inputs and outputs are the power variables. There is no need to decide whether an interface power variable is an input or output signal in the real system. The direction of half arrow indicates the orientation of the power. However, the computational structure can be superimposed on a bond graph by adding a perpendicular stroke (causal stroke) to each bond. Then the calculation (simulation) structure can be deduced. This modular representation is important for understanding complex systems for their diagnosis and control.

Definition 2.15 A word bond graph is an initial or a template bond graph where the vertices represent subsystems or technological components denoted in words and the connections are through bonds.

2.11.4 Bond Graph Model

The Bond graph model of the presented DC motor (Fig. 2.80) is shown in Fig. 2.81 with preferred integral causality assigned to storage elements (two I-elements).

The input variables are represented by energy sources: source of voltage $\mathbf{Se}:U_A$, and mechanical load torque $\mathbf{Se}:\tau_L$. The input power is transformed into dissipated power by the \mathbf{R} -elements ($R:R_A$ in the electrical domain, and $R:R_M$ in the mechanical domain). Energy storage occurs in the two \mathbf{I} -elements (electrical inductance $I:L_A$ and mechanical inertia $I:J_M$). The transformation of power from the

electrical domain to the mechanical rotation domain is modeled by a modulated (by a current value of the inductor current i_f) gyrator (**MGY**). Finally, to reproduce the global architecture of the system to be modeled, bond graph elements are interconnected by common flow junctions (**1**-junctions). When one includes the measurement and control processes in the model, the energy transferred by the measurement and control signals is negligible compared to the energy exchanged between physical components. Therefore, signals are represented by information bonds, which correspond to block diagram arrows. They are shown as full arrows in the model and represent the signal transmitted by sensors, integrators, and other members. The instrumentation architecture is represented by a detector of effort, **De**, and a detector of flow, **Df**. In the given example, the two sensors are the current sensor, **Df**: i_m , and angular velocity sensor, **Df**: ω_m .

2.11.5 Simulation Block Diagram

Two kind of equations can be deduced from the bond graph model: structural and behavioral. The set of equations are given in Eq. 2.123. Structural equations represent a set of conservation laws: they are deduced from the junctions (C_{J1A} and C_{J1M} in Eq. 2.123) and two-ports (C_{GY} in Eq. 2.123). The physical laws, i.e., the constitutive laws of the components (bond graph elements), are described by the behavior model. They are given as C_{RA} , C_{LA} , C_{RM} and C_{JM} in Eq. 2.123. The measurement model expresses the way in which the sensors transform some state variables into output signals. They are given as C_{m1} and C_{m2} in Eq. 2.123.

$$\begin{aligned}
 C_{J1A} : U_I &= U_A - U_R - U_e, \quad i_A = i_R = i_l \\
 C_{J1M} : \tau_I &= \tau_e - \tau_L - \tau_R, \quad \omega = \omega_R = \omega_I \\
 C_{GY} : \begin{cases} U_e = K(i_f)\omega \\ \tau_e = K(i_f)i_A \end{cases} \\
 C_{RA} : U_R &= R_A i_A, \quad C_{LA} : i_A = \frac{1}{L_A} \int U_I dt + i_{A0} \\
 C_{RM} : \tau_R &= R_M \omega, \quad C_{JM} : \tau_I = \frac{1}{J_M} \int \omega dt + \omega_0 \\
 C_{m1} : i_m &= i_A, \quad C_{m2} : \omega_m = \omega
 \end{aligned} \tag{2.123}$$

The simulation block diagram obtained from the bond graph model of the DC motor is given in Fig. 2.82.

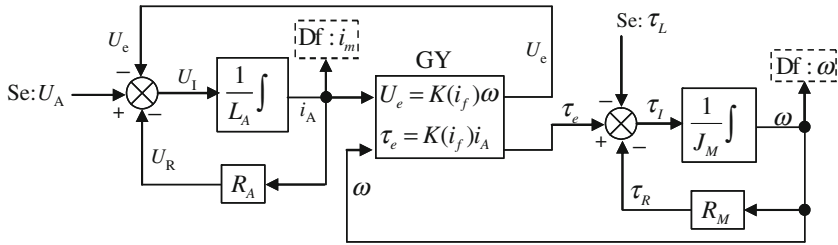


Fig. 2.82 Block diagram of the DC motor

2.11.6 State Equations and Simulation

In more detail, linear and nonlinear forms of state equations, i.e., $\dot{x} = f(x, u)$, $y = C(x)$, can be systematically derived from a bond graph model. As developed before, the state variables, input variables, and measurements are deduced from the bond graph model. For the DC motor, the input variables are

$$u = [U_A \quad -\tau_L].$$

State variables are energy variables, i.e., the linkage flux in the electrical part and angular momentum in mechanical part:

$$x = [P_A \quad P_M] = [\int U_I dt \quad \int \tau_I dt]$$

The state equations for the DC motor system can be derived as

$$\begin{aligned} \begin{bmatrix} \dot{p}_A \\ \dot{p}_M \end{bmatrix} &= \begin{bmatrix} -\frac{R_A}{L_A} & -\frac{K(i_f)}{J_M} \\ \frac{K(i_f)}{L_A} & -\frac{R_M}{J_M} \end{bmatrix} \begin{bmatrix} p_A \\ p_M \end{bmatrix} + \begin{bmatrix} 1 & 0 \\ 0 & 1 \end{bmatrix} \begin{bmatrix} Se_A \\ Se_M \end{bmatrix} \\ y = Cx &\Rightarrow \begin{bmatrix} i_m \\ \omega_m \end{bmatrix} = \begin{bmatrix} \frac{1}{L_A} & 0 \\ 0 & \frac{1}{J_M} \end{bmatrix} \begin{bmatrix} p_A \\ p_M \end{bmatrix} \end{aligned} \quad (2.124)$$

The conversion of the graphical bond graph model into state-space equations has been automated in software such as Symbols [35], Twentesim (20-sim) [58], and CAMP-G [17]. For instance, using Symbols software, the bond graph model can be graphically drawn as shown in Fig. 2.83.

After checking the causality, the state equations are automatically generated. Dedicated sensor elements (De and Df) can also be used. The generated behavioral equations are given with bond numbers subscripts and they can be compared with Eq. 2.124 with the following mapping: $p_A = P_4$, $p_M = P_8$, $Se_A = SE1$, $Se_M = SE9$, $L_A = M4$, $J_M = M8$, $R_A = R3$, $R_M = R7$, and $K(i_f) = \mu$. One can define nonlinear constitutive relations. Symbols can then simulate these equations by receiving input data for parameter values, initial conditions, and simulation settings. The model can

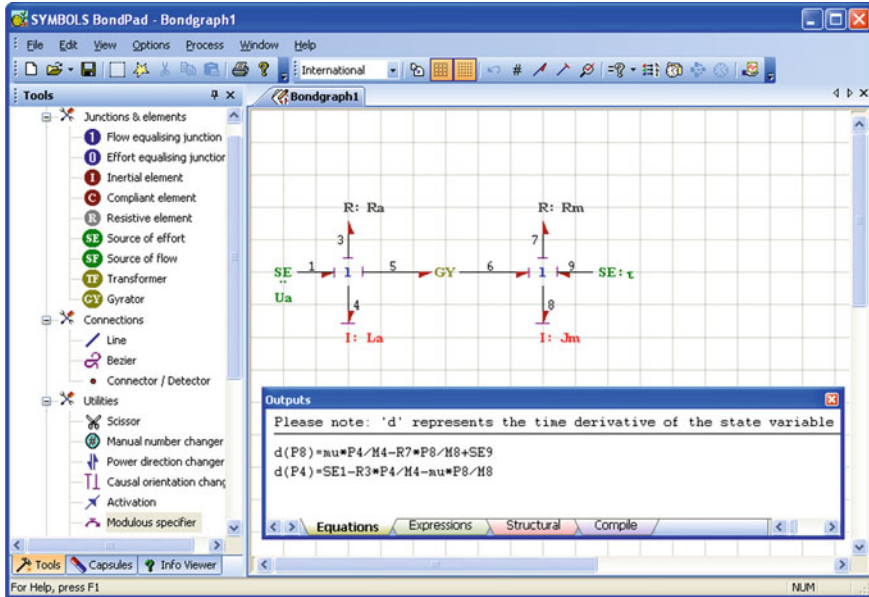


Fig. 2.83 Automatic generation of the dynamic model under state equations format by Symbols software

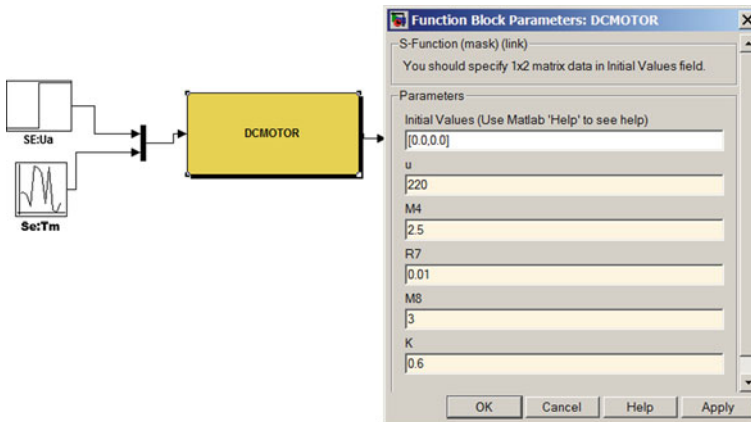


Fig. 2.84 Generation of a Simulink block diagram from bond graph model using Symbols software

be transformed into transfer function or numerical state-space matrix form for control theoretical analysis.

Furthermore, an S-function block diagram for Matlab-Simulink can be automatically generated. The block diagram of the DC motor generated from a bond graph model by using Symbols software is shown in Fig. 2.84. The numerical values for parameters and initial conditions can be introduced for simulation.

Bond graph software can also be used to model uncertain bond graphs. The software can then generate the dynamic model (equations) of the uncertain model. This uncertain bond graph model is well suited for robust diagnosis in order to improve decision procedures in fault detection and isolation systems [9].

References

1. J.J. Beaman, P.C. Breedveld, Physical modeling with Eulerian frames and bond graphs. *J. Dyn. Syst. Meas. Control* **110**, 182–188 (1988)
2. T.K. Bera, A.K. Samantaray, Consistent bond graph modeling of planar multibody systems. *World J. Model. Simul.* **7**(3), 173–178 (2011)
3. P.C. Breedveld, Multibond graph elements in physical systems theory. *J. Frankl. Inst.* **319**(1/2), 1–36 (1985)
4. J.W. Brewer, Progress in the bond graph representations of economics and population dynamics. *J. Frankl. Inst.* **328**(5/6), 675–696 (1991)
5. J.W. Brewer, P.P. Craig, Bilinear dynamic single-ports and bond graphs of economic systems. *J. Frankl. Inst.* **313**(4), 185–196 (1982)
6. S. Das, *Mechatronic Modeling and Simulation Using Bond Graphs* (CRC Press, Boca Raton, USA, 2009)
7. G. Dauphin-Tanguy, C. Siè Kam, How to model parameter uncertainties in a bond graph framework, in *ESS 99 1999*, pp. 121–125
8. G. Dauphin-Tanguy, A. Rahmani, C. Sueur, Bond graph aided design of controlled systems. *Simul. Pract. Theory* **7**(5–6), 493–513 (1999)
9. M.A. Djeziri, R. Merzouki, B. Ould Bouamama, Robust monitoring of an electric vehicle with structured and unstructured uncertainties. *IEEE Trans. Veh. Technol.* **58**, 4710–4719 (2009)
10. M.A. Djeziri, B. Ould-Bouamama, R. Merzouki, Modelling and robust FDI of steam generator using uncertain bond graph model. *J. Process Control* **19**(1), 149–162 (2009)
11. M.A. Djeziri, R. Merzouki, B. Ould-Bouamama, G. Dauphin-Tanguy, Robust fault diagnosis using bond graph approach. *IEEE/ASME Trans. Mechatron.* **12**(6), 599–611 (2007)
12. H. Elmqvist, D. Brück, M. Otter, *Dymola-User's manual*. Dynasim AB (Lund, Sweden, 1996), see also <http://www.Dynasim.se>
13. O.I. Franksen, Basic concepts in engineering and economics, in *Physical Structure in Systems Theory: Network Approaches to Engineering and Economics*, eds. by J.J. van Dixhoorn, F.J. Evans (Academic Press, San Francisco, 1974)
14. P.J. Gawthrop, Bicausal bond graphs, in *International Conference on Bond Graph Modeling and Simulation (IBGM'95)*, Las Vegas, USA, 1995
15. P.J. Gawthrop, Thermal modeling using mixed energy and pseudo bond graphs. *Proc. IMechE J. Syst. Control Eng.* **213**, 201–216 (1999)
16. P.J. Gawthrop, Physical interpretation of inverse dynamics using bicausal bond graphs. *J. Frankl. Inst.* **337**(6), 743–769 (2000)
17. J.J. Granda, The role of bond graph modeling and simulation in mechatronics systems: an integrated software tool: CAMP-G, MATLAB-SIMULINK. *Mechatronics* **12**, 1271–1295 (2002)
18. C. Heny, D. Simanca, M. Delgado, Pseudo-bond graph model and simulation of a continuous stirred tank reactor. *J. Frankl. Inst.* **337**(1), 21–42 (2000)
19. B.J. Joseph, H.R. Martens, The method of relaxed causality in the bond graph analysis of nonlinear systems. *J. Dyn. Syst. Meas. Control* **1**, 95–99 (1974)
20. D.C. Karnopp, State variables and pseudo-bond graphs for compressible thermo-fluid systems. *J. Dyn. Syst. Meas. Control* **101**(3), 201–204 (1979)
21. D.C. Karnopp, Bond graph models for electrochemical energy storage: electrical, chemical and thermal effects. *J. Frankl. Inst.* **327**, 983–992 (1990)

22. D.C. Karnopp, S. Azerbaijani, Pseudo bond graphs for generalised compartmental models in engineering and physiology. *J. Frankl. Inst.* **312**(2), 95–108 (1981)
23. D.C. Karnopp, D. Margolis, R. Rosenberg, *Systems Dynamics: A Unified Approach*, 2nd edn. (Wiley, New York, 1990)
24. D.C. Karnopp, D.L. Margolis, R.C. Rosenberg, *System Dynamics: Modeling and Simulation of Mechatronic Systems* (Wiley, New York, 2000)
25. M. Khemliche, B. Ould Bouamama, H. Haffaf, Sensor placement for component diagnosability using bond-graph. *Sens. Actuators A Phys.* **132**(2), 547–556 (2006)
26. T. Kohda, H. Katsubi, H. Fujihara, K. Inoue, Identification of system failure causes using bond graph models. *IEEE Trans. Syst. Man Cybern.* **5**, 269–274 (1993)
27. J. Lefèvre, J. Barreto, A mixed block diagram bond graph approach for biochemical models with mass action rate law kinetics. *J. Frankl. Inst.* **319**(1/2), 201–215 (1985)
28. The Mathworks Inc., MATLAB, <http://www.mathworks.com>
29. K. Medjaher, A.K. Samantaray, B. Ould Bouamama, M. Staroswiecki, Supervision of an industrial steam generator. Part II: Online implementation. *Control Eng. Pract.* **14**(1), 85–96 (2005)
30. K. Medjaher, A.K. Samantaray, B. Ould Bouamama, Bond graph model of a vertical U-tube steam condenser coupled with a heat exchanger. *Simul. Model. Pract. Theory* **17**(1), 228–239 (2009)
31. R. Merzouki, K. Medjaher, M.A. Djeziri, B. Ould Bouamama, Backlash fault detection in mechatronic system. *Mechatronics* **17**(6), 299–310 (2007)
32. P.J. Mosterman, G. Biswas, Diagnosis of continuous valued systems in transient operating regions. *IEEE Trans. Syst. Man Cybern.* **29**(6), 554–565 (1999)
33. A. Mukherjee, R. Karmakar, *Modelling and Simulation of Engineering Systems Through Bond Graphs* (Alpha Sciences International, Pangbourne, 2000)
34. A. Mukherjee, R. Karmakar, A.K. Samantaray, *Bond Graph in Modeling, Simulation and Fault Identification* (CRC Press, Boca Raton, 2006) ISBN: 978-8188237968, 1420058657
35. A. Mukherjee, A.K. Samantaray, System modelling through bond graph objects on SYMBOLS 2000, in *International Conference on Bond Graph Modeling and Simulation (ICBGM'01)*, Simulation Series, vol. 33, no. 1, 2001, pp. 164–170, ISBN 1-56555-103-6
36. R.F. Ngwompo, S. Scavarda, Dimensioning problems in system design using bicausal bond graphs. *Simul. Pract. Theory* **7**, 577–587 (1999)
37. B. Ould Bouamama, Bond graph approach as analysis tool in thermofluid model library conception. *J. Frankl. Inst.* **340**(1), 1–23 (2003)
38. B. Ould Bouamama, K. Medjaher, M. Bayart, A.K. Samantaray, B. Conrard, Fault detection and isolation of smart actuators using bond graphs and external models. *Control Eng. Pract.* **13**(2), 159–175 (2005)
39. B. Ould Bouamama, K. Medjaher, A.K. Samantaray, M. Staroswiecki, Supervision of an industrial steam generator. Part I: Bond graph modelling. *Control Eng. Pract.* **14**(1), 71–83 (2005)
40. B. Ould Bouamama, A.K. Samantaray, K. Medjaher, M. Staroswiecki, G. Dauphin-Tanguy, Model builder using functional and bond graph tools for FDI design. *Control Eng. Pract.* **13**(7), 875–891 (2005)
41. H.M. Paynter, *Analysis and Design of Engineering Systems* (M.I.T. Press, Cambridge, 1961)
42. A. Rahmani, C. Sueur, G. Dauphin-Tanguy, Approche des bond graphs pour l'analyse structurelle des systèmes linéaires. *Linear Algebra Appl.* **259**, 101–131 (1997)
43. R. Redheffer, On a certain linear fractional transformation. *EMJ Maths Phys.* **39**, 269–286 (1960)
44. A.K. Samantaray, S.K. Ghoshal, Sensitivity bond graph approach to multiple fault isolation through parameter estimation. *Proc. MechE Part-I J. Syst. Control Eng.* **221**(4), 577–587 (2007)
45. A.K. Samantaray, S.K. Ghoshal, Bicausal bond graphs for supervision: from fault detection and isolation to fault accommodation. *J. Frankl. Inst.* **345**(1), 1–28 (2008)
46. A.K. Samantaray, S.K. Ghoshal, S. Chakraborty, A. Mukherjee, Improvements to single-fault isolation using estimated parameters. *Simulation* **81**(12), 827–845 (2005)
47. A.K. Samantaray, K. Medjaher, B. Ould Bouamama, M. Staroswiecki, G. Dauphin-Tanguy, Component based modelling of thermo-fluid systems for sensor placement and fault detection. *Simul. Trans. Soc. Model. Simul. Int.* **80**(7–8), 381–398 (2004)

48. A.K. Samantaray, K. Medjaher, B. Ould Bouamama, M. Staroswiecki, G. Dauphin-Tanguy, Diagnostic bond graphs for online fault detection and isolation. *Simul. Model. Pract. Theory* **14**(3), 237–262 (2005)
49. A.K. Samantaray, B. Ould Bouamama, *Model-Based Process Supervision—A Bond Graph Approach* (Springer, London, 2008)
50. A.K. Samantaray, S.S. Dasgupta, R. Bhattacharyya, Bond graph modeling of an internally damped nonideal flexible spinning shaft. *J. Dyn. Syst. Meas. Control Trans. ASME* **132**(6), art. no. 061502 (2010)
51. C. Sueur, G. Dauphin-Tanguy, Structural controllability/observability of linear systems represented by bond graphs. *J. Frankl. Inst.* **326**(6), 869–883 (1989)
52. C. Sueur, G. Dauphin-Tanguy, Bond graph approach for structural analysis of MIMO linear systems. *J. Frankl. Inst.* **328**(1), 55–70 (1991)
53. C. Sueur, G. Dauphin-Tanguy, Controllability indices for structured systems. *Linear Algebra Appl.* **250**, 275–287 (1997)
54. M. Tagina, J.P. Cassar, G. Dauphin-Tanguy, M. Staroswiecki, Bond graph models for direct generation of formal fault detection systems. *Syst. Anal. Model. Simul.* **23**, 1–17 (1996)
55. M. Tagina, JPh Cassar, G. Dauphin-Tanguy, M. Staroswiecki, Localisation de défaillances par l'approche bond-graph. *J. Européen des Systèmes Automatisés (JESA)* **31**, 1489–1508 (1998)
56. J.U. Thoma, *Introduction to Bond Graphs and Their Applications* (Pergamon Press, Oxford, 1975)
57. J.U. Thoma, B. Ould Bouamama, *Modelling and Simulation in Thermal and Chemical Engineering. Bond Graph Approach* (Springer, Telos, 2000)
58. Twentesim, *Users Manual of Twentesim (20sim)* (Controllab Products Inc., Enschede, 1996)
59. J. Van-Dijk, *On the Role of Bond Graph Causality in Modelling Mechatronic Systems* Ph.D. Thesis, University of Twente, The Netherlands, 1994

Chapter 3

Modeling of Actuators, Sensors, and Electronic Circuits

Actuation system is an element of control system responsible for transformation of output of a microprocessor into a controlling action on a machine or device. Various types of actuation systems are

- Mechanical actuation system
- Electrical actuation system
- Hydraulic actuation system
- Pneumatic actuation system

Mechanical actuation system may consist of linkages, gears, cams, chains, or belts. Input power is supplied at one element of these systems and output power is received at the other element of the system. Essentially these are elements which convert motion from one form to other. Electrical actuation system consists of devices such as solenoids, DC motors, AC motors, brushless DC motors, stepper motors. The input to these devices is electrical energy and the output is mechanical energy. Hydraulic and pneumatic actuation system uses fluid power to drive linear or rotary actuators. In the first, the working fluid is usually oil (sometimes water–oil emulsions), and in the second, it is compressed air. The hydraulic system is preferred where one requires high power but leakage of liquid is often a problem with these systems. On the other hand, leakage problem is not there with pneumatic system but compressibility of air affects the control action.

3.1 Models of Actuators

Modeling of actuators is helpful in knowing the behavior of the actuators. With the help of actuator model in the integrated mechatronic system we can size the actuator and determine its various parameters such as torque/force requirement or voltage and current requirement. First of all we will take up the mechanical actuators and we will try to understand how can we draw the bond graph models of mechanical actuators. In this chapter, we develop models of simple actuators.

3.1.1 Models of Mechanical Actuators

Mechanical actuators consists of mechanisms. Mechanisms are devices to convert one form of motion to another, say linear to rotary. They use linkages, cams, gears, rack and pinion, chain, and belt drives. Cams and linkages are used to get a particular form of motion. The motors used in mechatronic systems have very high speed and low torque, whereas our usual requirement is low speed and high torque. This requirement is achieved by the use of gears. Parallel shaft gears are used to reduce shaft speed. Bevel gears are used to transmit rotary motion through 90° . Rack and pinion arrangement is used to convert rotational motion to linear motion. Toothed belts and chains are used to transmit positive rotary motion.

Many jobs previously done by mechanisms are now replaced by microprocessors. However, we need mechanical actuators for tasks, such as force/torque amplification, change of speed by gears, transfer of motion from one axis to other by timing belt. We may also require a particular type of motion such as quick return motion where we may require mechanical actuation.

3.1.1.1 Mechanisms and Linkages

Design of many mechanisms is based on two basic forms of kinematic chains (i) Slider crank mechanism (ii) Four bar mechanism. Let us begin our study with slider crank mechanism.

Slider Crank Mechanism

The schematic diagram of the typical slider crank mechanism is shown in Fig. 3.1. Note that this system has a single degree of freedom. Thus, all velocities are related to the crank rotation.

The bond graph of the system is shown in Fig. 3.2. The input crank is driven by an effort source τ . The slider is moving against a spring of stiffness K and frictional damper R_s . The angular motion of the crank is represented by the $1_{\dot{\theta}}$ junction with the I element attached to junction. This I element represents the rotary inertia (J_1) of crank about its axis. The I element here models the complete dynamics of the crank. R_j represents the joint resistance. The connecting rod motion is resolved into motion of its center of mass in two principal directions x and y and its rotation about the center of mass. The linear velocities in x and y directions are represented by the junctions $1_{\dot{x}_2}$ and $1_{\dot{y}_2}$ with I elements for the mass (m_2) of connecting rod. The rotational motion is modeled by $1_{\dot{\alpha}_2}$ junction with rotary inertia of connecting rod (J_2) about its axis. The $1_{\dot{s}}$ junction represents the slider motion. To this junction a I element is attached which represents the slider mass (m_3). The C element represents the spring. The motion of the connecting rod and slider are found by the modulated

Fig. 3.1 Schematic diagram of slider crank mechanism

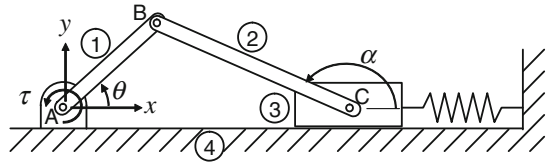
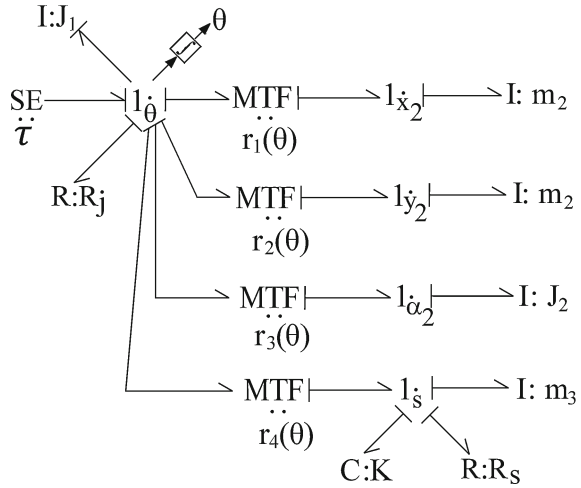


Fig. 3.2 Bond graph model of slider crank mechanism



transformers from the crank rotation. The moduli of transformers may be obtained from the kinematic analysis of the mechanism as follows:

Let the length of the crank be L_1 and that of the connecting rod (link 2 between points B and C) be L_2 . Then we can write

$$L_1 \sin \theta = L_2 \sin \alpha \tag{3.1}$$

where α is the angular position of link 2. Thus, we obtain

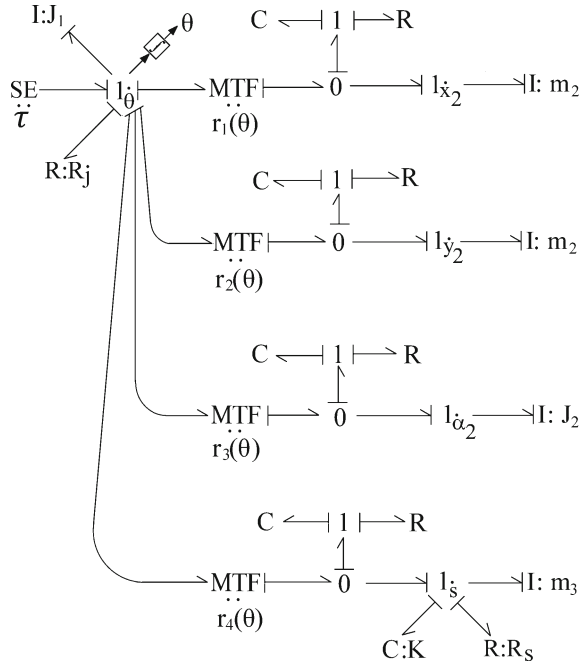
$$\alpha = \sin^{-1} \left(\frac{L_1}{L_2} \sin \theta \right) \tag{3.2}$$

The above is a fundamental relation which indicates that the crank cannot rotate fully if $L_1 > L_2$, α is a function of θ and $\pi/2 < \alpha < 3\pi/2$. Taking time derivatives of both sides of Eq. 3.1, we obtain

$$L_1 \dot{\theta} \cos \theta = L_2 \dot{\alpha} \cos \alpha \tag{3.3}$$

$$\dot{\alpha} = \frac{L_1 \cos \theta}{L_2 \cos \alpha} \dot{\theta} = r_3(\theta) \dot{\theta} \tag{3.4}$$

Fig. 3.3 Modified bond graph model of slider crank mechanism



If \dot{s} is the x-velocity of the slider then the x-components of velocities of point B on link 1 and link 2 can be equated as follows:

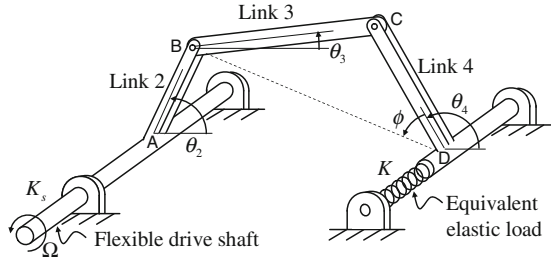
$$\begin{aligned} \dot{x}_B &= L_1 \dot{\theta} \sin \theta = \dot{s} + L_2 \dot{\alpha} \sin \alpha = \dot{s} + L_1 \dot{\alpha} \sin \theta \\ \Rightarrow \dot{s} &= L_1 (\dot{\theta} - \dot{\alpha}) \sin \theta = L_1 (1 - r_3(\theta)) \sin \theta \dot{\theta} = r_4(\theta) \dot{\theta} \end{aligned} \quad (3.5)$$

Other transformer moduli ($r_1(\theta)$ and $r_2(\theta)$) can be determined in similar fashion. These kinematic relations may be taken from the well-known LINKPAC library given in [29]. An integrator in the crank rotation junction records the crank rotation. This crank position is required for specifying the transformer moduli.

We can see from Fig. 3.2 that four I elements in the bond graph have differential causalities. This is natural because except one inertia (rotational degree of freedom), other inertias follow dependent or constrained motion and do not have separate degrees of freedom. These differential causalities can be removed by introducing pads [16] which are the lumped flexibility at appropriate points in the graph. The pads decouple the kinematic constraints and introduce independent degrees of freedom. These pads can be thought of as implicit representation of link and joint flexibility referred to relevant locations. The resulting bond graph model is shown in Fig. 3.3.

Note that a detailed model of the system can be developed from multibody approach with the model of the revolute joints as given in [2] (see the Rapson slide and Andrew’s or seven-body mechanism models given therein) and then the

Fig. 3.4 Schematic diagram of four-bar mechanism



differential causality problem can be avoided. However, such a model turns out to be very complex and the number of states in the model increase. On the other hand, one need not perform complex kinematic analysis to create those models.

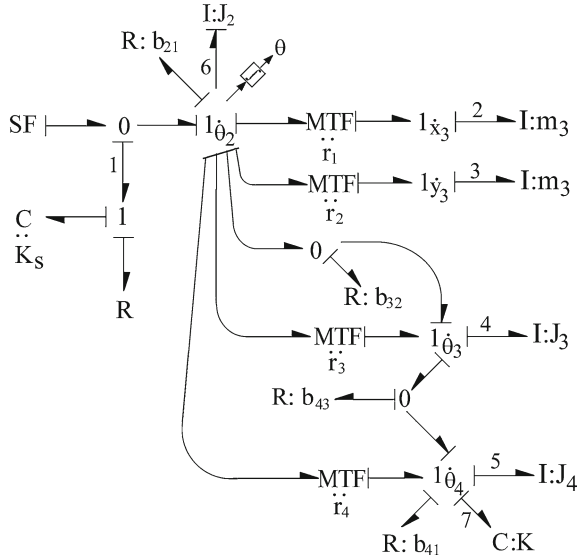
Four-Bar Mechanism

Figure 3.4 represents a typical four-bar mechanism driven by a flexible shaft at constant speed. It consists of four links, the first link (ground link) being fixed. An elastic load is attached to output link 4.

Figure 3.5 represents the bond graph model of four-bar mechanism. This can be drawn similar to slider crank mechanism. In the bond graph input crank rotation is represented by $1_{\dot{\theta}_2}$ junction and output link rotation is represented by $1_{\dot{\theta}_4}$ junction. The velocity source SF drives the elastic crank or link 2. The links 3 and 4 form a dyad. Crank elasticity is represented by 1-C-R structure. In the bond graph of Fig. 3.5 various joint resistances are modeled by the R elements with coefficients b_{21} , b_{32} , b_{43} , b_{41} for joint between second and first link, third and second link, fourth and third link, and fourth and first link, respectively. The linear motion of the coupler (link 3) center of mass is resolved into principal directions x_3 and y_3 . These motions can be determined from the crank rotation using transformers. Junction $1_{\dot{\theta}_3}$ with the I element models the rotational motion of the coupler. Output link 4, receives rotational motion from crank rotation through coupler link 3. This is represented by modulated transformer connecting $1_{\dot{\theta}_2}$ junction with $1_{\dot{\theta}_3}$ junction. The masses and rotary inertias of links are denoted as m_i and J_i , where subscript i enumerates the links. The moduli of all modulated transformers can be obtained from kinematic analysis.

Let us assume that the connection point between link 2 and link 1 (ground link) is A, between links 2 and 3 is B, between links 3 and 4 is C, and between links 4 and 1 is D. Here, A and D are fixed points. The link lengths may be denoted as L_1 , L_2 , L_3 , and L_4 where subscripts refer to the link number. Let distance between points B and D be L_5 which is not a constant. If line BD makes angle α with the ground link then from geometry, we can write

Fig. 3.5 Bond graph model of four-bar mechanism



$$L_2 \sin \theta_2 = L_5 \sin \alpha \tag{3.6}$$

$$L_2 \cos \theta_2 - L_5 \cos \alpha = L_1 \tag{3.7}$$

The above two equations can be used to solve for L_5 and α as purely functions of θ_2 . If we know L_5 then lengths of all sides of triangle BDC is known. The angle $\angle BDC = \phi$ can be determined and then $\theta_4 = \alpha - \phi$ is a function of θ_2 . Taking time derivatives of both sides, we obtain the transformer modulus $r_4(\theta_2)$. Other moduli can be similarly obtained.

From Fig. 3.5 it is seen that except for the I element connected at $1_{\dot{\theta}_2}$ junction all the I elements are differentially causalled, which indicates that they have dependent motions. These differential causalities can be removed with the help of pads [21] as shown in Fig. 3.6.

Note that the four-bar mechanism can be modeled differently using multibody dynamics approach given in [2, 3]. A much complex seven-bar mechanism’s bond graph model is detailed in [2].

3.1.1.2 Cam Drive

A cam is a reciprocating, oscillating, or a rotating body which is in contact with another body and imparts reciprocating or oscillating motion to it. As the cam rotates, the follower is made to rise, dwell, and fall. The length of time spent at each of these positions depends on the shape of the cam. The rise section drives the follower upwards, the fall section lowers the follower, whereas the dwell section keeps the follower at same level.

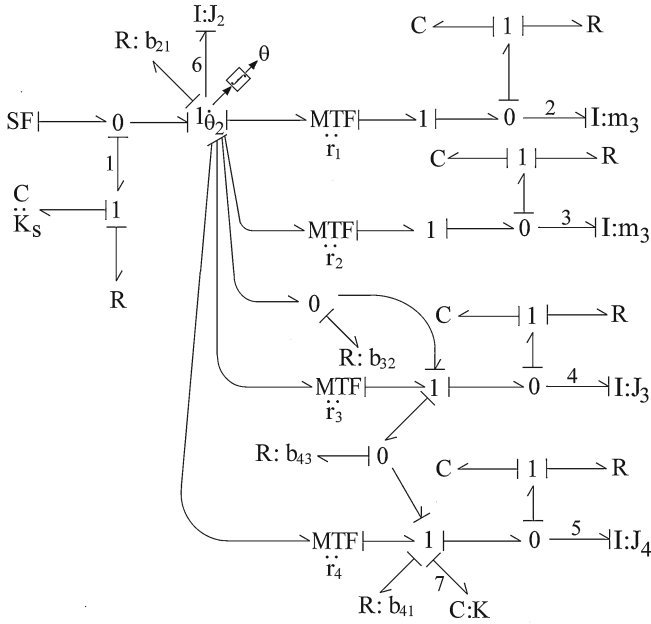
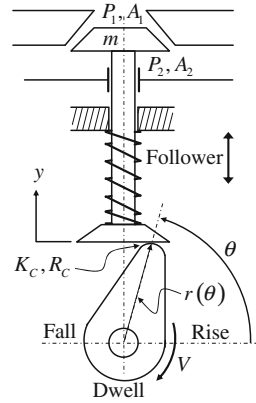


Fig. 3.6 Modified bond graph model of four-bar mechanism

Fig. 3.7 Schematic diagram of cam drive

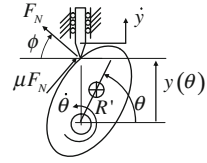


• Model with flow input:

Let us consider a general cam and follower arrangement shown in Fig. 3.7. This cam follower arrangement is used to operate a valve. Let the cam is driven by a velocity V . Let at a position θ cam radius be $r(\theta)$.

The contact between cam and follower has contact stiffness K_c and damping R_c . Let the follower has mass m . A spring of stiffness K_s is attached to a follower as shown in figure. Let the force acting at the other end of the follower be represented

Fig. 3.8 Cam with knife-edge follower



by F_{ext} which in this case will be $P_2A_2 - P_1A_1$ where P_1 , P_2 , A_1 , and A_2 are the pressures and areas on valve faces.

The follower shown in the figure is flat faced. In other follower designs, one can have a rotating (roller) follower or knife-edge followers. Moreover, the follower axis can be offset from the cam center of rotation. Usually, the cam designer represents the follower motion or travel in terms of the angle of rotation of the cam. This is achieved through the inversion method which generates the different cam profile curves such as the pitch and working curves and the pressure angles.

The flat-faced follower arrangement is slightly complicated because the contact with the follower does not take place at a fixed offset. We will rather consider a simple knife-edge follower as shown in Fig. 3.8. The velocity of the cam at contact point in the vertical direction will be given by $y(\theta)$ which is assumed to be known function determined from cam profile. For example, in a cam giving simple harmonic motion,

$$y(\theta) = \begin{cases} \frac{h}{2} \left(1 - \cos \frac{\pi\theta}{\beta} \right) & \text{for } 0 \leq \theta \leq \beta \\ 0, & \text{otherwise} \end{cases} \quad (3.8)$$

where h is the maximum follower travel, β is the angle associated with motion event, $0 < \theta < \beta/2$ is the rise duration, $\beta/2 < \theta < \beta$ is the fall duration, and the rest is the dwell duration.

The velocity and acceleration profiles are derived from the displacement profile through successive derivatives and by assuming unit angular speed. If the follower is constrained to move vertically and the follower offset is zero as shown in the figure, then the follower velocity is given by

$$\frac{dy}{dt} = \frac{dy}{d\theta} \cdot \frac{d\theta}{dt} = \Psi(\theta) \dot{\theta} \quad (3.9)$$

where $\Psi(\theta)$ is purely a function of the cam's angular rotation from a reference position.

Figure 3.9 shows the bond graph model of the cam follower (knife-edge follower) system. Here the valve jump is modeled by contact stiffness K_c and contact damping R_c . If there is no contact then the stiffness and damping forces are made zero.

- Model with effort input:

Figure 3.10 shows the general schematic diagram of a cam follower system with a flat-faced follower. Here, the cam is driven through a torque input and its angular

Fig. 3.9 Bond graph model of cam drive with flow input and no follower offset

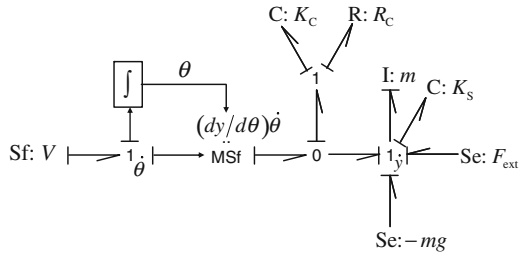
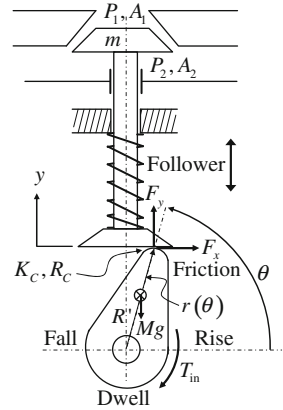


Fig. 3.10 Schematic diagram of cam drive with torque input



speed is variable. In this case, the cam rotation speed depends on the load dynamics. The normal and friction forces from the follower oppose the cam rotation. Moreover, the self weight of the cam and its rotary inertia are also significant factors that decide cam speed.

For knife-edge follower, we can refer to Fig. 3.8 where the normal and frictional forces are shown as F_N and μF_N with μ as the coefficient of kinematic friction. The direction of the surface normal at contact point is defined by an angle ϕ which is related to the pressure angle and can be written in terms of the cam angular position. Thus, ϕ is a dependent variable. We can use other kinds of friction forces. The component of the forces along the follower motion direction is

$$F_y = F_N \sin \phi + \mu F_N \cos \phi \tag{3.10}$$

If the follower reaction force is known, then $F_N = F_y / (\sin \phi + \mu \cos \phi)$. Thus, the force component along the perpendicular direction to the follower motion is given as

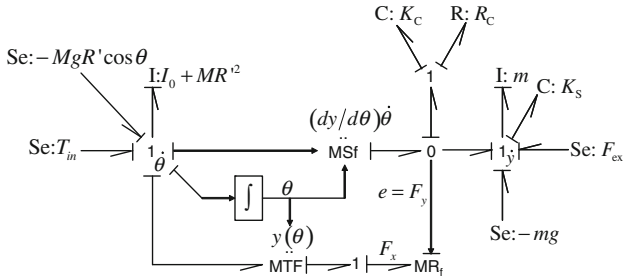


Fig. 3.11 Bond graph model of cam drive with torque input and no follower offset

$$F_x = \mu F_N \sin \phi - F_N \cos \phi = \frac{\mu \sin \phi - \cos \phi}{\sin \phi + \mu \cos \phi} F_y \tag{3.11}$$

$$= \Phi(\theta) F_y \tag{3.12}$$

where $\Phi(\theta)$ (because ϕ can be represented in terms of θ) is purely a function of the cam angular position. The reaction torque applied on the cam is thus $F_x y(\theta)$. Note that even without friction, there is a horizontal force component $F_x = -F_y / \tan \phi$.

The corresponding bond graph is shown in Fig. 3.11. The rotary inertia of the cam about the axis of revolution is calculated from parallel axis theorem with I_0 as the rotary inertia about the center of gravity and R' as the distance of center of gravity from cam axis.

The Se element at the 1-junction modeling rotation is the moment of the cam self-weight about the cam axis. The friction and normal force components creating reactive moment on the cam are modeled by MR_f element which is modulated by the follower force (F_y). It is to be noted that friction force F_x acts only when there is contact, i.e., $F_y > 0$. Various friction formulations can be used as constitutive relation for MR_f element. Those will be discussed later in this chapter. Note that if there is a follower offset e then an additional reactive moment $F_y e$ will act on the cam rotational motion.

3.1.1.3 Gear Drive

Gears are used for transmission of motion or power. Ideally gears are positive drive. There are different types of gears, depending on the way we are interested in transmitting motion. Spur gearing is used when shafts connected by gears are parallel. In bevel gearing the axes of shafts intersect. Other forms are skew or spiral gearings. Another popular form of gearing is helical gearing, in which the connecting shafts are parallel, the teeth are cut on helices rather than straight across the wheels parallel to the axes. Helical gears have the advantage that engagement of tooth is gradual which results in smooth drive and prolonged life of gears. However, the inclined teeth results in an axial force component on the shaft bearing. This can be overcome

Fig. 3.12 Schematic diagram of gear drive with resistive load

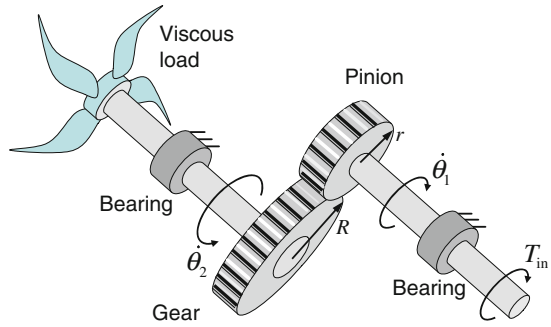


Fig. 3.13 Bond graph model of gear drive

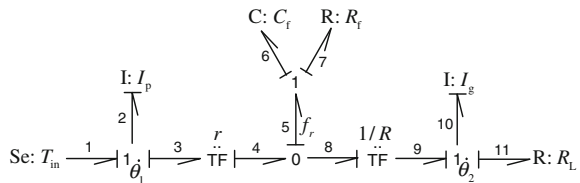
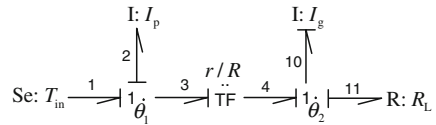


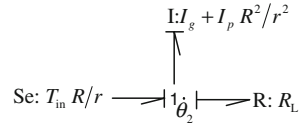
Fig. 3.14 Reduced bond graph of gear drive



by using double helical teeth. Another form of popular gearing used in mechatronic system is rack and pinion. This arrangement is basically two inter-meshed gears with one having a base circle of infinite radius. This type of gearing is used to transform either linear motion to rotary motion or rotary motion to linear motion. When two gears are in mesh, the larger wheel is called gear, while smaller wheel is called pinion. Any combination of gear wheels by means of which motion is transmitted from one shaft to another shaft is called gear train. A single gear train may include any or all forms of gear wheels, such as spur, bevel, helical, spiral, etc. Let us consider a gear drive driving a resistive load as shown in Fig. 3.12.

Figure 3.13 shows the bond graph of the system where I_p , I_g , and R_L represent the pinion rotary inertia, gear rotary inertia, and load resistance, respectively. Here it is to be noted that backlash and teeth flexibility has been modeled by C_f and R_f elements. If meshing stiffness, friction, and backlash are neglected then the bond graph can be reduced as shown in Fig. 3.14. In this Fig. 3.14 we observe that the I element corresponding to pinion is differentially causalled, showing its speed dependence on gear speed. This differential causality can be avoided by combing the pinion and gear inertia. To do this let us do some simple mathematical manipulation. From bond graph of Fig. 3.14 we see that

Fig. 3.15 Reduced bond graph of gear drive



$$\begin{aligned}
 I_g \frac{d\dot{\theta}_2}{dt} &= e_4 - R_L \dot{\theta}_2 \\
 &= \frac{R}{r} e_3 - R_L \dot{\theta}_2 \\
 &= \frac{R}{r} \left[T_{in} - I_p \frac{d\dot{\theta}_1}{dt} \right] - R_L \dot{\theta}_2 \\
 &= \frac{R}{r} \left[T_{in} - I_p \frac{R}{r} \frac{d\dot{\theta}_2}{dt} \right] - R_L \dot{\theta}_2 \\
 &= \frac{R}{r} T_{in} - I_p \left(\frac{R}{r} \right)^2 \frac{d\dot{\theta}_2}{dt} - R_L \dot{\theta}_2 \\
 T_{in} \frac{R}{r} &= \left(I_g + I_p \frac{R^2}{r^2} \right) \frac{d\dot{\theta}_2}{dt} + R_L \dot{\theta}_2 \tag{3.13}
 \end{aligned}$$

Thus reduced bond graph can be shown in Fig. 3.15. Here combined gear and pinion inertia is represented by $(I_g + I_p R^2/r^2)$. From Eq. 3.13 we can derive the expression for acceleration of combined inertia as

$$\frac{d\dot{\theta}_2}{dt} = \frac{T_{in} \cdot \frac{R}{r} - R_L \dot{\theta}_2}{\left(I_g + I_p \cdot \frac{R^2}{r^2} \right)} \tag{3.14}$$

If we consider that the input shaft is flexible, then bond graph shown in Fig. 3.13 can be modified to incorporate the shaft flexibility. The modified bond graph is shown in Fig. 3.16. In this figure, J is polar moment of inertia of shaft and R_s is the damping present in the shaft. Shaft flexibility is represented by C-1-R element with stiffness of shaft given by $K_\theta = GJ/L$, where G is modulus of rigidity of shaft and L is shaft length. The shaft damping is proportional to stiffness with the proportionality factor λ being a material property. Note that half of the shaft rotary inertia ($\rho JL/2$) has been lumped here at the two ends of the flexible shaft.

Rack and Pinion

Rack and pinion are used to transform linear motion to rotational motion or vice versa. Let us consider a rack and pinion arrangement as shown in Fig. 3.17. The pinion is supplied with input torque T_{in} and it rotates at a velocity $\dot{\theta}$. Let the pinion

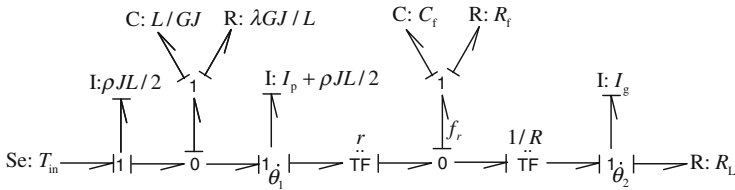


Fig. 3.16 Bond graph model of gear drive with flexible input shaft

Fig. 3.17 Schematic diagram of rack and pinion arrangement

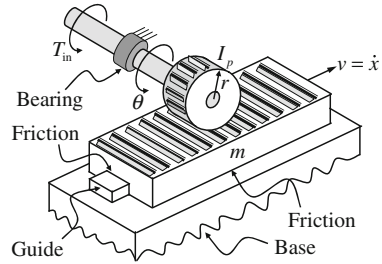
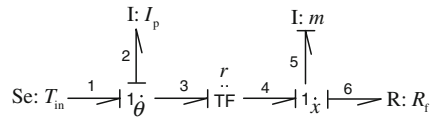


Fig. 3.18 Bond graph model of rack and pinion transmission system



polar moment of inertia be I_p and its radius be r . The rack has mass m and it translates with velocity v . Let R be the frictional resistance between the rack and the guideways. Then the bond graph model for the system can be drawn as shown in Fig. 3.18.

From the bond graph model, we see that

$$e_4 = e_5 + e_6$$

$$\frac{T_3}{r} = m \frac{dv}{dt} + Rv$$

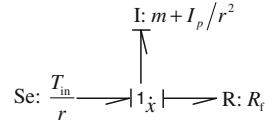
$$\frac{T_{in} - I_p \frac{1}{r} \frac{dv}{dt}}{r} = m \frac{dv}{dt} + Rv$$

$$T_{in} - \frac{I_p}{r} \frac{dv}{dt} = mr \frac{dv}{dt} + Rvr$$

$$T_{in} - Rvr = \frac{dv}{dt} \left(mr + \frac{I_p}{r} \right)$$

$$\frac{T_{in}}{r} - Rv = \frac{dv}{dt} \left(m + \frac{I_p}{r^2} \right)$$

Fig. 3.19 Reduced bond graph model of rack and pinion power transmission system



$$\frac{T_{in}}{r} = \frac{dv}{dt} \left(m + \frac{I_p}{r^2} \right) + Rv \quad (3.15)$$

The reduced bond graph can be drawn as shown in Fig. 3.19.

The expression for acceleration of rack can be given as

$$\frac{dv}{dt} = \left(\frac{r}{I_p + mr^2} \right) (T_{in} - Rrv) \quad (3.16)$$

3.1.1.4 Modeling Backlash

In general backlash refers to free-play between adjacent moveable components within a mechanical system. To explain it in simple form let us consider two gears in mesh as shown in Fig. 3.20. The bond graph for the system is shown in Fig. 3.21. The contact between the teeth is modeled by a contact stiffness (C_C) and damping (R_C) which are switched on when there is contact and switched off when there is no contact. The constitutive relation for C_C is given as [23]

$$e = \begin{cases} K_C \left(\int f_C dt - b \right) & \text{for } \int f_C dt > b \\ K_C \left(\int f_C dt + a \right) & \text{for } \int f_C dt < -a \\ 0, & \text{otherwise} \end{cases} \quad (3.17)$$

Similarly constitutive relation for R_C is given as

$$e = \begin{cases} R_C f_C & \text{for } \int f_C dt > b \text{ or } \int f_C dt < -a \\ 0, & \text{otherwise} \end{cases} \quad (3.18)$$

Further discussion on modeling of backlash will be presented in subsequent chapters.

Fig. 3.20 Schematic representation of backlash

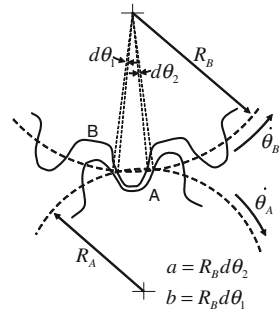
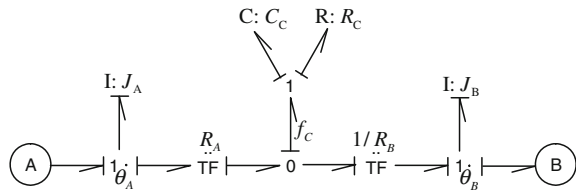


Fig. 3.21 Bond graph model of backlash



3.1.1.5 Modeling Friction

Friction is almost always present in actuators and mechanisms used in mechatronic systems. It is often responsible for the poor performance of mechatronic components. In general, friction term refers to a resistive force that appears when a relative motion exists between two bodies in contact. The term dry friction refers to friction between solid to solid contact.

Coulomb’s law states that the friction force is given by the product of normal component of the contact force and coefficient of friction. This coefficient of friction depends on materials. Friction models can be divided into static and dynamic models. The static model assumes a static relationship between friction force and relative velocity whereas dynamic model takes care of various phenomenon, such as pre-sliding displacement, frictional lag, varying breakaway force, and stick-slip motion.

In the simplest form friction force is always represented by a linear relationship with velocity. However, this is not the accurate representation of mechanical friction. Figure 3.22 shows the various mechanical friction force laws. They are (i) Linear law, (ii) Real friction law, and (iii) General law.

- (i) Linear law: This law is used to study simple systems such as damper, where friction force is given by

$$F_f = cV \tag{3.19}$$

where V is the relative velocity between contact surface and c is the damping coefficient.

- (ii) Real friction law: This law is used to study simple systems such as damper where friction force is given by [23]

Fig. 3.22 Several mechanical friction laws

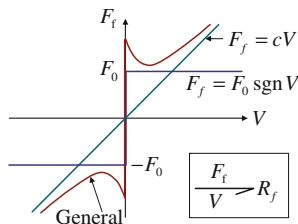
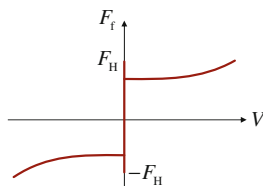


Fig. 3.23 Stick-Slip friction laws



$$F_f = F_0 \operatorname{sgn}(V) \tag{3.20}$$

where the signum function $\operatorname{sgn}(V)$ is defined as

$$\operatorname{sgn}(V) = \begin{cases} 1, & \text{if } V > 0 \\ 0, & \text{if } V = 0 \\ -1, & \text{if } V < 0 \end{cases}$$

If $F_0 = \mu_k N$ where μ_k is the coefficient of kinematic friction and N is the normal reaction then we get the Coulomb friction law. This law does not work well near region $V = 0$ because the transition from kinematic to static friction coefficient is not modeled.

- (iii) General law: The general law is more realistic in the sense that it models the system behavior that if a block is placed on a table then usually it requires more force to start the block than force required to keep the block moving at slow speed.

Stick-slip Friction

The simulation of Stick-slip friction is difficult because of strong nonlinear behavior in the vicinity of zero velocity [14]. Stick-Slip friction can be represented by the general behavior of the system represented in Fig. 3.22. The Stick-Slip friction implies a dry friction law as shown in Fig. 3.23.

Here friction force value at $V = 0$ is more than the friction force value at moderate value of V . The representation of friction law for Fig. 3.23 is difficult because F is not a unique function of V . Karnopp [14] modeled the Stick-slip behavior with fixed causality and hence with a single set of state equations.

Fig. 3.24 Sketch of friction law

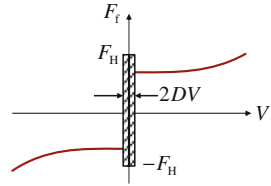
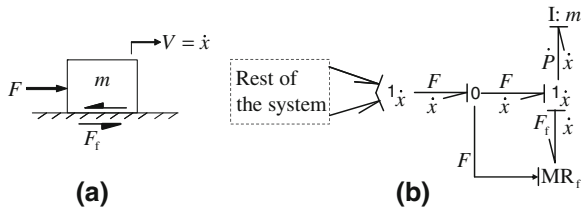


Fig. 3.25 a Mass acted upon by a net force and friction.
b Bond graph model of mass acted upon by a net force and friction



The Basic Model of Stick-slip Friction

The friction law is shown in Fig. 3.24. From this figure it is seen that friction force F is always a function of V . A small region in the vicinity of $V = 0$ is defined. This region ranges for velocity say $-DV < V < DV$. Inside this region we approximate $V = 0$ and F is determined by other forces in the system such that V remains in the region until the breakaway value of force is reached. Outside the region F is an arbitrary function of V .

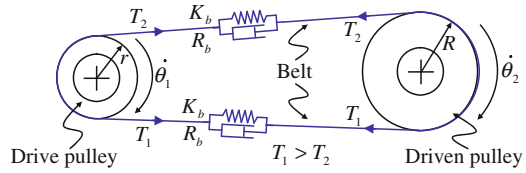
To explain the concept further, let us consider a mass m placed on the surface as shown in Fig. 3.25a. A force F is applied on the mass so that it gains a velocity V , and thus momentum P . A friction force F_f acts on the mass at the contact surface. Figure 3.25b shows the bond graph of the system. Although the constant causality $F_f = F_f(V)$ is assumed, the signal bond shows that the force F affects the evaluation of F_f .

The friction force given by the MR_f element is defined through the following constitutive relation

$$F_f = \begin{cases} -F & \text{if } |\dot{x}| \leq DV \text{ and } |F| \leq F_H \\ -F_H \text{sgn}(F) & \text{if } |\dot{x}| \leq DV \text{ and } |F| > F_H \\ -F_{\text{slip}} \text{ (e.g., } \mu_k N \text{sgn}(\dot{x})) & \text{if } |\dot{x}| > DV \end{cases} \quad (3.21)$$

Note that the slip force F_{slip} can be defined in various ways. The above model has discontinuities at $\dot{x} = \pm DV$. Therefore, some models use $\tanh()$ function to define the sticking force. Another model called honey-drop model uses a heavy relaxation resistance (leakage resistance) that allows slow build-up of velocity even when a force less than the limiting force is applied and as the velocity exceeds the threshold critical value $\pm DV$, the heavy resistance is turned off and a normal resistance is applied. The leakage resistance is modeled at a 0-junction which is connected to the $1_{\dot{x}}$ junction, MR_f element, and the leakage resistance R_L .

Fig. 3.26 Schematic diagram of a belt drive



3.1.1.6 Belt Drive

When power is to be transmitted between two shafts which are at considerable distance apart, a belt drive is used. In belt drive the power transmitted depends upon the friction between the belt and pulley rim. If the pulley is mounted on a shaft and the shaft is supported in bearings, then effective tangential force exerted by the belt on the pulley may be used to transmit power from belt to pulley and finally to shaft. Figure 3.26 shows a belt drive. In Fig. 3.26 let r and R be the radii of driver and driven pulleys, respectively, and $\dot{\theta}_1$ and $\dot{\theta}_2$ be angular velocities of driver and driven pulleys, respectively. Also let J_{dr} and J_{dn} represent the polar moments of inertia of driver and driven pulleys, respectively.

If the tension at one end of the belt is T_2 and tension T_1 at other end is gradually increased, the belt will finally begin to slip bodily round the pulley rim. The value of T_1 at which belt slips will depend upon the values of T_2 , β (angle of lap or wrap), and coefficient of friction μ between the belt and the rim. From mechanics, assuming centrifugal force on the belt is negligible, we know that the limiting ratio of tension T_1 and T_2 for a flat belt is given by

$$\frac{T_1}{T_2} = e^{\mu\beta} \tag{3.22}$$

The above relation can be modified for other belt types such as V-belts. At this limiting ratio belt is just about to slip bodily round the pulley rim. The actual ratio of the tensions is usually a much lower value. The bond graph model as shown in Fig. 3.27 can be drawn by neglecting centrifugal and inertial forces on the belt, the gravity effects, transverse and lateral belt vibrations, wave propagation, etc. In this figure, slip between driver pulley and belt is modeled by R_{s1} element while between belt and driven pulley is modeled by R_{s2} element. The angle of wrap for each pulley and the ratio T_1/T_2 governs the values of the slip resistances R_{s1} and R_{s2} . Under no slip operation, the resistances are large and when slip starts, the resistances are made low. The constitutive law for slip resistance is given as

$$R_s = \begin{cases} R_{high}, & \text{if } \frac{T_1}{T_2} < e^{\mu\beta} \\ R_{low}, & \text{if otherwise} \end{cases}$$

One may also include a stick-slip formulation here. Once slip has started, the limiting ratio is changed to $T_1/T_2 = e^{\mu_k\beta}$ where μ_k is the coefficient of

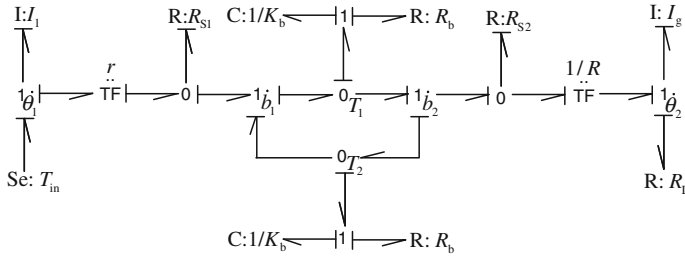
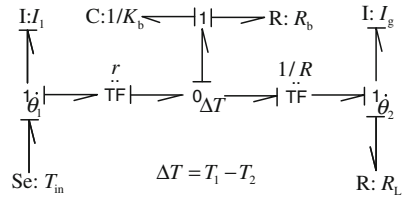


Fig. 3.27 Bond graph model of belt drive

Fig. 3.28 Reduced bond graph model of belt drive



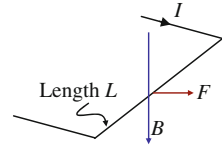
kinematic friction. In Fig. 3.27, K_b , and R_b are the stiffness and damping present in belt.

The state variables associated with $C:K_b$ elements in Fig. 3.27 are to be initialized for initial belt tensions T_1 and T_2 . Initially $T_1 = T_2 = F/2$ where F is the tightening force. The state variables associated with C -elements are used to modulate the slip resistances. Simulation studies show that the belts start slipping initially (because $T_1/T_2 = 1 < e^{\mu\beta}$) and as the pulleys start rotating, the taut side tension grows and the slack side tension falls while the sum of the two tensions remains constant. After reaching the critical tension value (no-slip condition), steady belt tensions are obtained.

If it is known a-priori that there will be no belt slip then the bond graph model of the belt drive can be reduced to the form shown in Fig. 3.28. This model does not show the build up of belt tensions, but gives the approximate behavior in steady-state operation.

In Fig. 3.28, the state variable associated with $C:K_b$ element is initialized to zero because it generates the difference between the tensions ($T_1 - T_2$) in the taut and slack sides and initially, this difference is zero. Although this model does not directly output the values of individual tensions, knowing the difference between the tensions and noting that the sum of the tensions is always constant, one can solve for the individual tensions. It is also possible to include the slip resistances in the reduced model by inserting the necessary 0-junctions and R-elements for slip resistances. In this model, $F = T_1 + T_2$ becomes an input parameter. However, this reduced model of belt drive represents the system like a pair of gears and does not account for the true physics of the system.

Fig. 3.29 Force on a current carrying conductor



3.1.2 Models of Electrical Actuators

In mechatronic systems electric motors are often used as actuators. They are mostly used in position and/or speed control systems. Electric motors are of two types:

- DC Motors (mostly used in modern control systems)
- AC Motors

3.1.2.1 DC Motors

Basic Principle

The basic principle of operation of a motor can be explained with the help of Fig. 3.29.

1. A force is exerted on a current carrying conductor placed in a magnetic field (Lorentz's law). This force, called Lorentz force is given as

$$F = BIL \quad (3.23)$$

where B is the magnetic field strength, I is current through conductor, and L is length of conductor.

2. When a conductor moves in a magnetic field then an electromotive force (e.m.f.) is induced across it. The induced emf is equal to the rate at which the magnetic flux ϕ swept through by the conductor changes (Faraday's law)

$$e = -\frac{d\phi}{dt} \quad (3.24)$$

The negative sign is because the emf is in such a direction as to oppose the change producing it (Lenz's Law), i.e. direction of induced emf is such that it produces the current. The current sets up magnetic fields which tend to neutralize the change in magnetic flux linked by the coil and which was responsible for the emf. That is why, the induced potential is called as back emf. Figure 3.30 shows the schematic arrangement of permanent magnet and one loop of rotor coil. Here for rotation to continue, when the coil passes through the vertical position, the current direction through the coil has to be reversed. If the current direction is not reversed then the moment generated by the Lorentz forces after passing the vertical position would

Fig. 3.30 Basics of DC motor

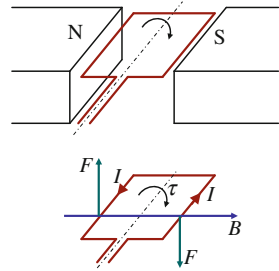
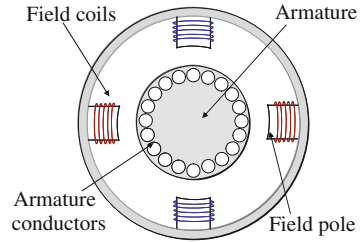


Fig. 3.31 Field magnet DC motor



oppose the motion and the rotor will stall. For changing the current direction, the ends of each armature coil are connected to adjacent segments of a segmental ring called the commutator with electrical contacts made to the segments through carbon contacts called brushes. The direction of rotation can be reversed either by reversing the armature current or the field current (in case of field magnet, Fig. 3.31).

3.1.2.2 Permanent Magnet DC Motor

The torque generated by a DC motor can be explained with help of Fig. 3.30. Force at right angle to conductor is given as $F = BIL$. With N such conductors, the net force becomes $F = NBIL$. Because the conductor bars are arranged in such a way that counter current flows at the exact opposite side, these forces result in a torque T about the coil axis given by $T = Fb$ where b is the width or mean diameter of the coil. The torque generated can be written as

$$T = NBILb \tag{3.25}$$

If we take $K_t = NBLb$, then

$$T = K_t I \tag{3.26}$$

Here K_t is the torque constant. Since armature is rotating in a magnetic field, electromagnetic induction occurs and back emf is induced. The back emf V_b is directly proportional to the rate in which flux linked by the coil changes. For a constant magnetic field (say, due to a permanent magnet), the back emf is directly

Fig. 3.32 Equivalent circuit of DC motor

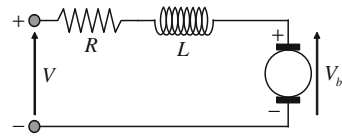


Fig. 3.33 Bond graph model of DC motor

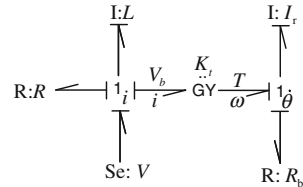
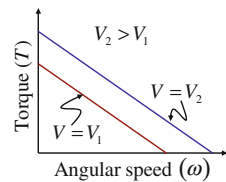


Fig. 3.34 Torque speed characteristic of DC motor



proportional to angular velocity (ω) of rotation. Thus back emf is given as

$$V_b = K_v \omega \tag{3.27}$$

where K_v is back emf constant. Figure 3.32 shows the equivalent circuit of motor in which armature coil is represented by resistor R and inductor L in series.

If we assume no losses in the magnetic field then for conservative transformation $K_t = K_v$ which satisfies $T \omega = V_b I$. Therefore, we can draw the bond graph model of the DC motor as shown in Fig. 3.33 where I_r and R_b , respectively represent the rotor polar moment of inertia and bearing damping.

If inductance is neglected or the steady-state operation is considered then

$$I = \frac{(V - V_b)}{R} \tag{3.28}$$

$$I = \frac{(V - K_t \omega)}{R} \tag{3.29}$$

Since Torque $T = K_t I$, the expression for steady-state torque can be given as

$$T = K_t \frac{(V - K_t \omega)}{R} \tag{3.30}$$

With the help of Eq. 3.30, we can draw the torque speed characteristic of DC motor as shown in Fig. 3.34.

Fig. 3.35 Series wound DC motor

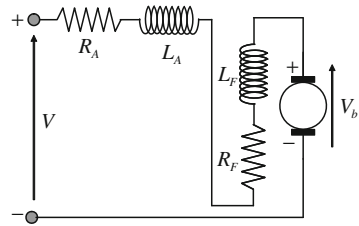
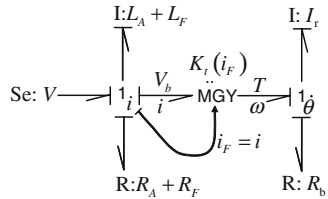


Fig. 3.36 Bond graph model of series wound DC motor



During starting, $\omega = 0$, thus $T = K_t V / R$ is the stall or brake torque; while when there is no load, i.e., $T = 0$, $\omega = V / K_t$ which is the no load speed.

3.1.2.3 DC Motor with Field Coils

Series Wound

If field coil is in series with armature coil, it is called a series wound DC motor. Figure 3.35 shows the series wound DC motor. Following are the characteristics of series wound DC motor.

1. Motor has higher starting torque and higher no load speed.
2. Reversing the polarity of supply has no effect on the direction of rotation of motor. It will rotate in the same direction since both field and armature currents are reversed.

Figure 3.36 shows the bond graph model of series wound DC motor. The armature inductance is L_A and the effective field inductance is $L_F = L_m + L_S$, where L_m and L_S are the mutual and stator inductances, respectively. The electromechanical transformation is modeled as a modulated gyrator (MGY) with its modulus defined as

$$K_t(i_F) = L_m i_F N_A / N_S \tag{3.31}$$

where i_F is the field current (here, $i_F = i_A$), and N_A and N_S are the number of turns in the armature and the stator, respectively. If the field is externally energized or constant (as in permanent magnet motor) then K_t becomes a constant.

Fig. 3.37 Shunt wound DC motor

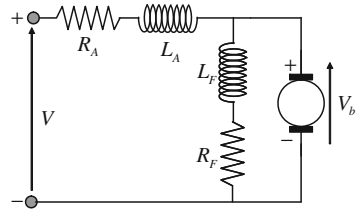
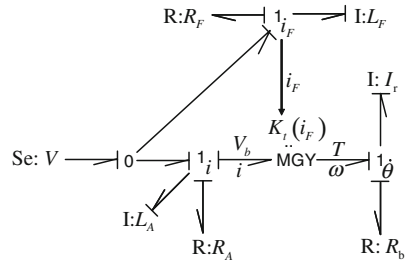


Fig. 3.38 Bond graph model of shunt wound DC motor



Shunt Wound

If field coil is parallel with armature coil then it is called a shunt wound DC motor. Figure 3.37 shows schematic representation of the shunt wound DC motor. Following are the characteristics of shunt wound DC motor.

1. It provides lowest starting torque, lower no load speed, and good speed regulation.
2. Constant speed regulation of load is possible around near no load speed.
3. To reverse the direction of rotation either the armature or field supply is to be reversed.

Figure 3.38 shows the bond graph model of shunt wound DC motor. The electro-mechanical transformation is modeled as a modulated gyrator (MGY) whose modulus is a function of the field current which has been discussed before.

Compound Wound

Compound wound DC motor is a combination of series and shunt wound. Schematic representation of compound wound DC motor is shown in Fig. 3.39. Figure 3.40 shows the torque speed characteristic of series, shunt, and compound wound DC motors.

3.1.2.4 Permanent Magnet DC Motor Characteristic

Figure 3.41 shows the torque speed characteristic of a permanent magnet DC motor.

Fig. 3.39 Compound wound DC motor

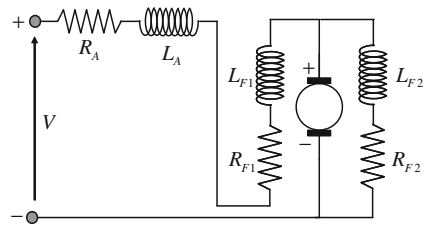


Fig. 3.40 Torque speed characteristics of DC motor

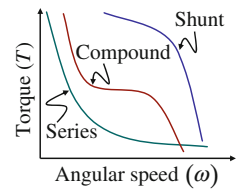
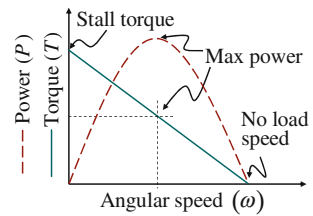


Fig. 3.41 Torque, speed, and power characteristics of permanent magnet DC motor



If the starting torque is T_s (i.e., $\omega = 0$ at $T(\omega) = T_s$) and no load speed of motor is ω_{max} (i.e., $T(\omega) = 0$ at $\omega = \omega_{max}$) then torque speed relationship can be expressed as

$$T(\omega) = T_s \left(1 - \frac{\omega}{\omega_{max}} \right) \tag{3.32}$$

Also we know that

$$\begin{aligned} T &= \frac{K_t(V - K_v\omega)}{R} \\ T &= \frac{K_t V}{R} - \frac{K_v K_t \omega}{R} \end{aligned} \tag{3.33}$$

i.e., at $\omega = 0$, $T_s = \frac{K_t V}{R}$. Also, the maximum speed of motor can be obtained as (by substituting $T = 0$ in Eq.3.33) $\omega_{max} = \frac{T_s R}{K_v K_t}$

Thus, the power delivered by the motor will be

$$P(\omega) = T\omega$$

Fig. 3.42 Representation of PWM scheme

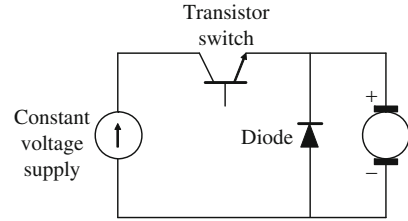
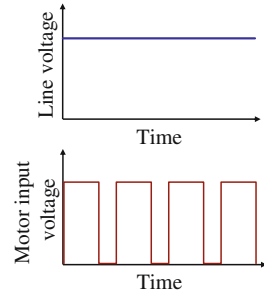


Fig. 3.43 Principle of PWM (Varying the average armature voltage by chopping the DC voltage)



$$P(\omega) = \omega T_s \left(1 - \frac{\omega}{\omega_{\max}} \right) \quad (3.34)$$

The variation of power with speed can be explained with the help of Fig. 3.41. For maximum power

$$\frac{dP}{d\omega} = T_s \left(1 - \frac{2\omega}{\omega_{\max}} \right) = 0$$

i.e.,

$$\omega = \frac{\omega_{\max}}{2}$$

Control of DC Motors

In a DC motor, speed is controlled by varying the voltage applied to the armature. Since fixed voltage supplies are often used, a variable voltage is obtained by an electronic application. Generally DC motors are controlled by control signals emerging from a microprocessor. In such cases, pulse width modulation (PWM) is generally used. The scheme of PWM is shown in Figs. 3.42 and 3.43. The pulse width is modulated through a transistor which is switched on and off by means of signal applied to its base. In Fig. 3.42, the diode provides a path for current when the transistor is off and the motor is acting as a generator. This circuit can be used to drive the motor in one direction only.

For driving the motor in both directions, an arrangement shown in Fig. 3.44 is used. This arrangement is called H-bridge circuit. This allows current to flow through the

Fig. 3.44 Schematic representation of H bridge

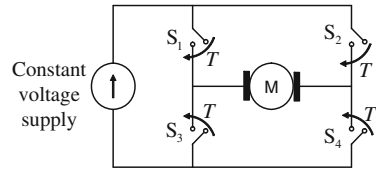


Fig. 3.45 H bridge circuit

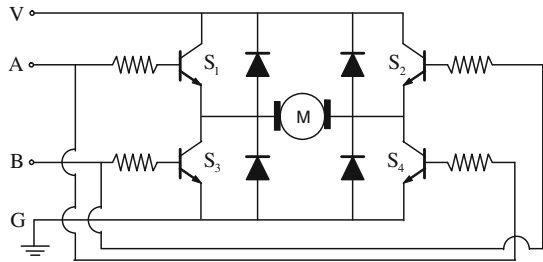
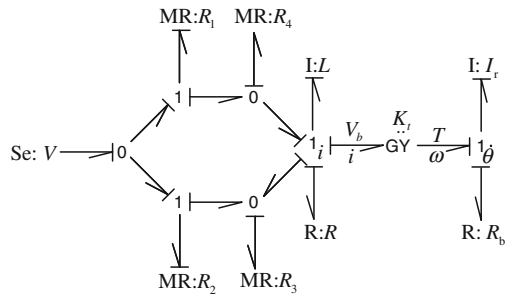


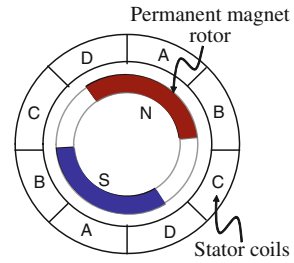
Fig. 3.46 Bond graph model of H bridge circuit



electrical motor in two directions. The motor rotates in one direction when switches S_1 and S_4 are closed and rotates in opposite direction when switches S_2 and S_3 are closed. In practice, these switches are realized by transistors and diodes as shown in Fig. 3.45. For forward direction rotation, potential A will be high and potential B will be low and for reverse direction rotation, potential A will be low and potential B will be high. Here PWM signal applied to transistor base controls the switching.

The detailed model of transistor operation as a switch will be discussed later in this chapter. At present, we will model the transistor as a switch and represent it as a modulated resistance (MR) element. Figure 3.46 shows the bond graph model of H bridge controlled DC motor. The right side of the bond graph models the DC motor and the mechanical load, and the left side models the PWM. Here switching action has been achieved by modulation of switched resistances. For forward direction rotation R_1 and R_4 values are low while R_2 and R_3 values are high. For reverse direction rotation, R_2 and R_3 values are low while R_1 and R_4 values are high. Note that switching through resistances introduces losses. If ideal switching has to be modeled then the junction structure connected to R_1 and R_4 can be replaced by a modulated transformer and that connected to R_2 and R_3 can be replaced by another

Fig. 3.47 Brushless permanent magnet DC motor



modulated transformer. The moduli of these MTF elements are toggled between 0 and 1 by the PWM signal which decides the duration for which a switch is on or off.

3.1.2.5 Brushless Permanent Magnet DC Motors

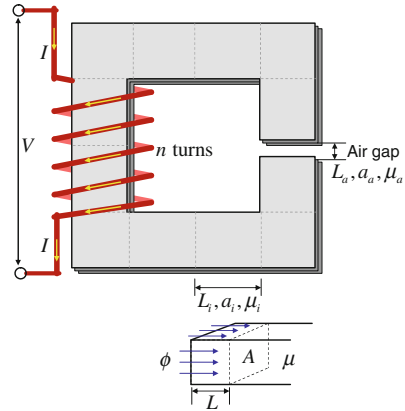
A simple DC motor uses a commutator to change the direction of current through the armature. However, the commutator wears out over a period of time due to continuous sparks. Therefore, the motor needs regular maintenance in which the brush has to be periodically changed. The brushless DC motor design removes this problem. A brushless DC motor has a sequence of stator coils and permanent magnet rotor. We already know that a current carrying conductor in a magnetic field experiences a force. Then, according to Newton's law, the magnet will also experience an equal and opposite force. Therefore, we can put the current carrying conductors (coils) in the stator and the permanent magnet in the rotor. The brushless permanent magnet DC motor works on this simple principle. It is schematically shown in Fig. 3.47.

As the permanent magnet rotor rotates, Hall sensors are generally used to sense the position of the rotor and depending upon the rotor position, the current through the stator coil is switched by transistors. The Hall sensors are positioned around the stator.

3.1.2.6 AC Motors

AC motors can be broadly classified into two categories as single phase motors and polyphase motors. Single phase motors are used for low power applications while polyphase motors are used for high power applications. Each of these motors can be further subclassified into induction motors and synchronous motors. AC motors are cheaper compared to DC motors, but it is difficult to control their speed. Speed control of AC motor is based on the provision of variable frequency supply, since the motor speed is determined by the frequency of the supply voltage. Before we discuss AC motors, let us discuss the modeling of electromagnetic induction which is the basic principle on which the AC motor operates. We will take the help of an example (an electrical transformer) to explain it.

Fig. 3.48 Magnetic core with coil



3.1.2.7 Model of Magnetic Circuit

In an electrical transformer, two domains of energy interact. These are electrical and magnetic domains. Let us consider a magnetic core with a coil wound around one of the limbs as shown in Fig. 3.48. In this figure, the core can be discretized into many finite sections with length L_i , cross-sectional area a_i , and magnetic permeability μ_i . Let an air gap be present whose length is given by L_a , cross-sectional area a_a , and magnetic permeability μ_a . We assume that flux is continuous across the cross sections and losses, such as fringe flux, leakage flux, and core loss, etc. can be approximated by a single resistance.

The governing relations required to model magnetic induction are

$$\text{Magnetic flux, } \phi = Ba \tag{3.35}$$

$$\text{Flux Density, } B = \frac{\mu(MMF)}{L} \tag{3.36}$$

$$\text{Induced Voltage, } V = -n\dot{\phi} \tag{3.37}$$

$$\text{Magneto Motive Force, } MMF = nI \tag{3.38}$$

From Eqs. 3.35 and 3.36, magneto motive force (MMF) is given as

$$MMF = \frac{BL}{\mu} = \frac{\phi L}{a\mu} = \frac{L}{a\mu}\phi \tag{3.39}$$

Equation 3.39 is constitutive equation for a storage element (C element). MMF corresponds to generalized effort, flux rate $\dot{\phi}$ corresponds to generalized flow, ϕ corresponds to generalized displacement, and $L/a\mu$ corresponds to equivalent stiffness or reluctance. Thus Eq. 3.39 can be written as,

Fig. 3.49 Bond graph representation of magnetic circuit

$$\frac{e = MMF}{f = \dot{\phi}} \rightarrow 1; \phi \rightarrow C: \frac{L}{\mu a}$$

Fig. 3.50 Bond graph model of complete magnetic circuit

$$\frac{e = MMF = nI}{f = \dot{\phi}} \rightarrow 1; \phi \rightarrow C: \sum \frac{L_i}{\mu_i a_i}$$

Fig. 3.51 Bond graph model of complete magnetic circuit with air gap reluctance shown separately

$$\frac{e = MMF = nI}{f = \dot{\phi}} \rightarrow 1; \phi \begin{cases} \rightarrow C: \sum \frac{L_i}{\mu_i a_i} \\ \rightarrow C: \frac{L_a}{\mu_a a_a} \end{cases}$$

Fig. 3.52 Bond graph model of electromagnetic induction with both electrical and magnetic domain shown

$$\frac{e = V}{I} \rightarrow \overset{n}{\underset{\cdot}{G}} \overset{\cdot}{Y} \frac{e = nI}{f = \dot{\phi}} \rightarrow 1; \phi \begin{cases} \rightarrow C: \sum \frac{L_i}{\mu_i a_i} \\ \rightarrow C: \frac{L_a}{\mu_a a_a} \\ \downarrow R: R_{core} \end{cases}$$

$$e = K\phi = K \int \dot{\phi} dt \tag{3.40}$$

Equations 3.38 and 3.40 can be expressed in bond graph form as shown in Fig. 3.49.

Since same flux (ϕ) is going through each element, stiffness (reluctance) of all elements in the magnetic circuit is given by $\sum_{i=1}^n \frac{L_i}{\mu_i a_i}$. Furthermore, from Eq. 3.38, we know that the total MMF is nI . Thus,

$$nI = \sum_{i=1}^n \frac{L_i}{\mu_i a_i} \phi \tag{3.41}$$

Equation 3.41 can be expressed in the form of bond graph as shown in Fig. 3.50. In this figure, reluctance of air gap is also included. However, if one wishes to represent the reluctance of air gap separately, it can be shown by one more C element as shown in Fig. 3.51.

To complete the picture, let us consider the modeling of electrical domain also. We can see from Eq. 3.37 that effort (V , voltage) in the electrical domain is equal to product of a constant (n , number of turns) and flow ($\dot{\phi}$) in magnetic domain. This can be modeled by a gyrator element. Thus the complete picture can be shown by the model given in Fig. 3.52 where R_{core} models all the core losses.

Fig. 3.53 Schematic representation of an ideal transformer

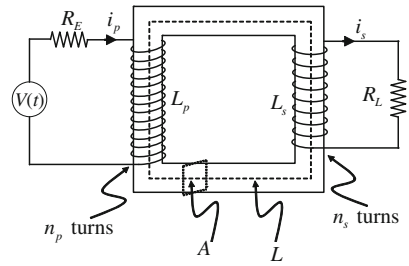
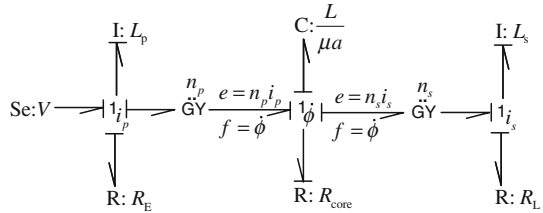


Fig. 3.54 Bond graph model of an ideal transformer



For an ideal transformer shown in Fig. 3.53 with a uniform core cross-section, mean core length L , and external load R_L , the bond graph can be represented by Fig. 3.54.

3.1.2.8 Bond Graph Model of a Basic Induction Motor

In a brushed DC motor electric power is conducted to the armature (rotor) through brushes and commutators. Hence DC motors are also known as conduction motors. In AC motors, rotor receives power by induction in contrast to DC motors which receives power by conduction. The induction in AC motor is similar to the secondary side of a two winding transformer which receives its power from primary. In fact an induction motor can be treated as a transformer whose primary winding is stationary but the secondary is free to rotate. The major difference is the air gap between the rotor and the stator through which the flux passes. We will discuss the model of basic induction motor as given in [20]. It is a two-phase four-pole motor as shown in Fig. 3.55.

First of all, let us consider the bond graph model of the magnetic circuit comprising the stator, rotor, and air gap as shown in Fig. 3.56. The suffixes of various 0-junctions indicate the potentials at various points in the magnetic circuit. One of the 0-junction can be taken as ground (connected to a zero source of effort, $Se:0$). The C-elements in Fig. 3.56 model various reluctances: K_{ag} models the air gap reluctance, and K_{cx} and K_{cy} model the reluctances in x and y poles, respectively.

The reluctance of metallic portions are much smaller than the air gaps. So, those reluctances can be removed from the model. The reduced bond graph model after

Fig. 3.55 Schematic representation of a two-phase four-pole induction motor

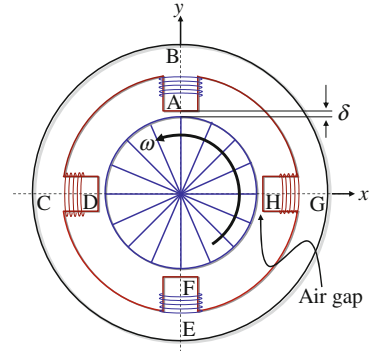


Fig. 3.56 Bond graph model of magnetic circuit comprising of stator, rotor, and air gap of a two-phase four-pole induction motor

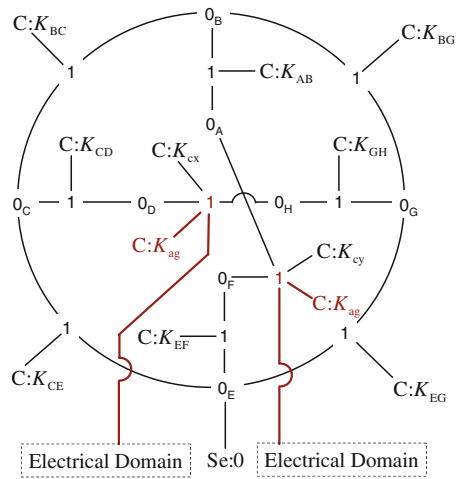
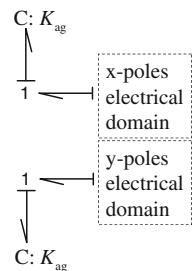


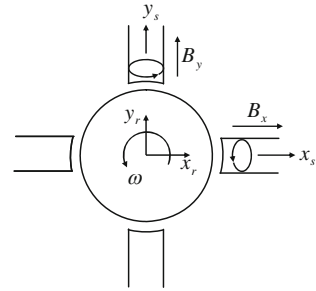
Fig. 3.57 Reduced bond graph model of magnetic circuit comprising of stator, rotor, and air gap of a two-phase-four pole induction motor after removal of ground



removal of ground, neglected reluctances, and bonds with zero power (due to zero effort) is shown in Fig. 3.57.

Now let us analyze the generation of electric field and potential differences as viewed from the stator and the rotor. Figure 3.58 shows the poles, rotor, and frame of a two-phase four-pole induction motor description.

Fig. 3.58 Poles, rotor, and frame description of a two-phase four-pole induction motor



For the stator we can write,

$$\nabla \times \bar{E}_s = - \left(\frac{\partial \bar{B}}{\partial t} \right)_{\text{as seen from stator}} \quad (3.42)$$

Taking area integral of Eq. 3.42 over one X and one Y coil of the stator, and multiplying it with total number of coils one can get the potential difference applied to the coils of these poles. We obtain

$$V_{x_s} = -n_s \frac{\partial \phi_{x_s}}{\partial t} = -n_s \dot{\phi}_{x_s} \quad (3.43)$$

and

$$V_{y_s} = -n_s \frac{\partial \phi_{y_s}}{\partial t} = -n_s \dot{\phi}_{y_s} \quad (3.44)$$

The above two relations are constitutive relations for two gyrator (GY) elements. For the rotor we can write

$$\nabla \times \bar{E}_r = - \left(\frac{\partial \bar{B}}{\partial t} \right)_{\text{as seen from rotor}} \quad (3.45)$$

or

$$\nabla \times \bar{E}_r = - \left(\frac{\partial \bar{B}}{\partial t} \right)_{\text{as seen from stator}} - \omega \hat{k} \times (\bar{B})_{\text{as seen from stator}} \quad (3.46)$$

Taking area integral of Eq. 3.46 over one X and one Y coil of the rotor and then multiplying it by equivalent number of rotor coils per stator pole pair (i.e., total number of rotor coils divided by number of stator pole pairs) one gets

$$V_{x_r} = -n_r \{ \dot{\phi}_{x_s} + \omega \phi_{y_s} \} \quad (3.47)$$

and

$$V_{y_r} = -n_r \{ \dot{\phi}_{y_s} - \omega \phi_{x_s} \} \quad (3.48)$$

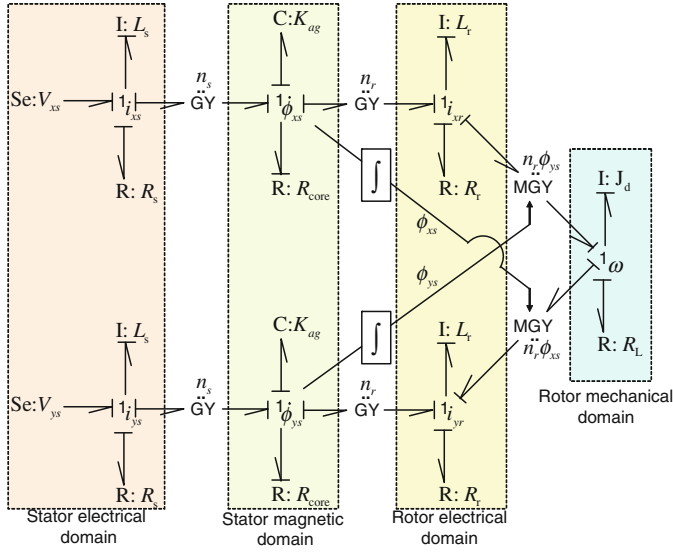


Fig. 3.59 Bond graph model of a two-phase four-pole induction motor

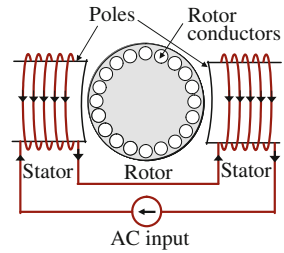
We recognize that each of the above two equations relates flows ($\dot{\phi}_{x_s}$ and ω , and $\dot{\phi}_{y_s}$ and ω) to efforts (V_{x_r} and V_{y_r}). Thus, these relations can be expressed as conservative transformations through gyrator (GY) and modulated gyrator (MGY) elements. Now the bond graph model of the two-phase four-pole induction motor can be created as shown in Fig. 3.59. This model can be extended for more stator poles.

Note that the supply voltages should be expressed with proper phase for the motor to start functioning. If $V_{x_r} = V_{y_r}$ then $\phi_{x_s} = \phi_{y_s}$ and the net motor torque applied on the rotor at 1_ω junction through the two MGY elements becomes zero resulting in no rotation of the rotor. The three-phase induction motor model can be likewise developed and it can be reduced to an equivalent two-phase model (see [20] for details).

Single Phase Squirrel-Cage Induction Motor

In common forms of AC induction motors, the rotor resembles a squirrel cage. A squirrel cage, which is an exercise tool for pet or captive hamsters and squirrels allowing them to run fast in a limited space, is made of free to rotate drum fixed on an axle with two end plates and short bars connecting the two drums. An electric motor with a rotor resembling a squirrel cage (squirrel-cage rotor) is termed a squirrel-cage motor. The actual rotor is a cylinder mounted on a shaft where longitudinal conductive bars (usually, copper or aluminium bars) are set into grooves inside the

Fig. 3.60 End view of single phase squirrel-cage induction motor



rotor drum and these bars are connected at both ends by shorting rings. Figure 3.60 shows the end view of the single phase squirrel-cage induction motor.

These conductor bars fit into slots in end rings and form the circuit in which current is induced. There is no external connection to the rotor. The stator consists of set of windings. When an alternating current passes through the stator windings an alternating magnetic field is produced. Because of the alternating magnetic field, electromagnetic induction takes place in rotor and emf are induced. Thus, current flows through the rotor conductor bars. This condition is similar to that of a current carrying conductor placed in the magnetic field and as a result, Lorentz force (and torque because of opposite force at the exact opposite side rotor bar) is produced. Here the rotor rotates at the speed determined by the frequency of the alternating current applied to the stator. The bond graph model for this motor has been described in detail in [9, 13].

3.1.2.9 Stepper Motors

Stepper motors are special type of DC motors. They are classified as permanent magnet or variable reluctance stepper motors. In the case of a permanent magnet stepper motor, the stator consists of wound poles, and the rotor poles are permanent magnets. When we excite different stator winding combinations, the rotor moves and holds in different positions. The variable reluctance stepper motor has ferromagnetic rotor rather than the permanent magnet rotor. Motion and holding results from the attraction of stator and rotor poles to position with minimum magnetic reluctance that allow for maximum magnetic flux.

The following terminologies are associated with stepper motors:

- Phase—It is defined as number of independent windings in the stator.
- Step angle—It is defined as rotor rotation for one switching change for stator coils.
- Holding torque—It is defined as maximum torque that can be applied to a powered motor without moving it from its rest position and reversing spindle rotation.

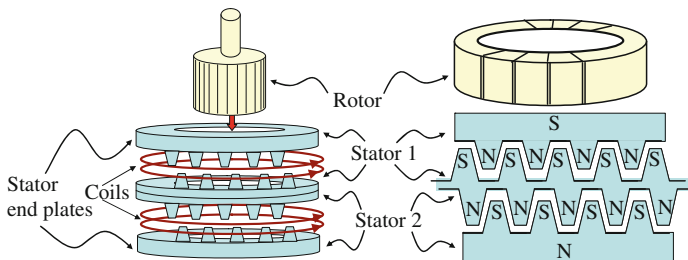


Fig. 3.61 Schematic representation of two coil claw pole stepper motor with permanent magnet rotor

Two Coil Claw Pole Stepper Motor with Permanent Magnet Rotor

Figure 3.61 shows the claw pole stepper motor with permanent magnet. In Fig. 3.61 there are two stators. Each stator has a north and a south lamination, with a coil enclosed between the laminations. There is one permanent magnet rotor which has p poles along its periphery. Each lamination has $p/2$ teeth which when assembled, mesh with each other as shown in Fig. 3.61. When the coil is energized with a current as shown in Fig. 3.61, all the teeth of the top(north) lamination will become north poles while all the teeth of bottom(south) lamination will become the south poles. Thus, in this condition, a torque will be exerted on the permanent magnet rotor to align its north poles with the teeth of south lamination and south poles with the teeth of north lamination. Now reversing the direction of current in stator coils reverses the polarity of the stator teeth and the resultant torque moves the rotor one step. With only one stator, however, the rotor is likely to turn in either forward or backward direction. To avoid this and turn the rotor in a definite direction, the second stator which is physically displaced by 90 electrical degrees (one fourth of the pole pitch) is introduced. The number of teeth on the rotor and stator determine the step angle that will occur each time the step pulse is applied and the polarity of the winding is reversed. The more the number of teeth, the smaller is the step angle.

The working of the motor can be explained with the help of sectional view of permanent magnet stepper motor as shown in Fig. 3.62. A permanent magnet stepper motor consists of a stator with individually controllable windings (W_1 and W_2) and a rotor with a permanent magnet. The rotor may be configured as a cylindrical ferrite rod with multipole magnetization along its circumference. The permanent-magnetic rotor aligns itself with the right polarity relative to the stator winding.

The electromagnetic torque developed in the two coil claw pole stepper motor with a permanent magnet can be given as [22]

$$T(\theta) = I_{s1}N_1p^2\phi_1 \sin(p\theta) + I_{s2}N_2p^2\phi_2 \cos(p\theta) \tag{3.49}$$

where I_{s1} and I_{s2} are the currents in the stator 1 and 2, respectively; N_1 and N_2 are the number of turns in coil 1 and 2 of stator, respectively; p is the number of

Fig. 3.62 Principle of working of permanent magnet stepper motor

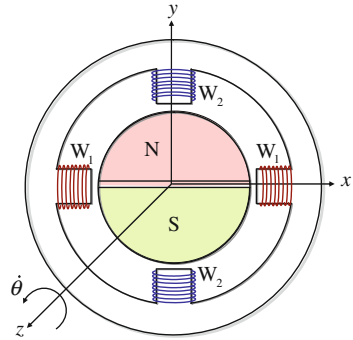
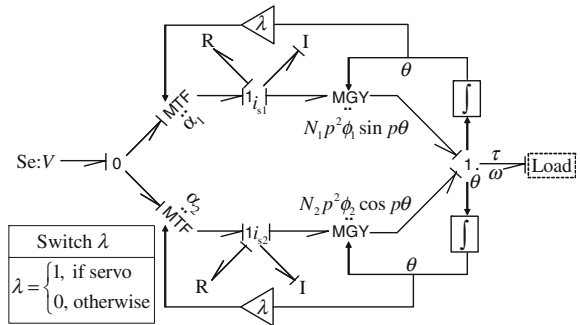


Fig. 3.63 Bond graph model of two coil claw pole stepper motor with permanent magnet



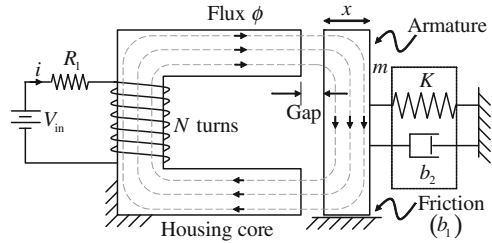
pair of poles; ϕ_1 and ϕ_2 are maximum values of magnetic flux in air gaps 1 and 2, respectively; and θ is the rotor position. Here the mechanical angle between the two stator is 90° . For two poles, $p = 2$. Generally $N_1 = N_2$ and $\phi_1 = \phi_2$. Figure 3.63 shows the bond graph model of stepper motor. In this figure, transformer moduli α_1 and α_2 model the switches which can be made on or off at fixed time intervals to simulate the energization pulses. If the motor has to be position or speed controlled (i.e., a servo motor) then the transformer moduli α_1 and α_2 are switched according to the angular position or velocity feedback taken from the rotor.

3.1.2.10 Magnetic Actuators

Solenoids

A solenoid transforms an electrical signal into mechanical movement. A typical solenoid consists of a coil of wire wrapped around a fixed iron core. There is a movable iron core named as armature and a spring and damper as shown in Fig. 3.64. An increase in voltage (V_{in}), causes the current to rise in the coil, thus increasing the core flux (ϕ). The increasing flux generates a magnetic force in the air gap which pulls the armature closer to the static housing core.

Fig. 3.64 Schematic diagram of solenoid



The bond graph model of solenoid is shown in Fig. 3.65. The bond graph model can be divided into electrical, electromagnetic, and magneto-mechanical parts.

The electrical model accounts for the change of current in the coil. The effective voltage across the coil (effort in bond 3 in bond graph shown in Fig. 3.65) is given by

$$e = V_{in} - R_1 i \quad (3.50)$$

Here, V_{in} is the voltage input from the driver, R_1 is the resistance in the coil, and i is the current. The electromagnetic model describes the change of magnetic flux in the moving and stationary iron core, and air gaps. We can apply Faraday's law to the coil, in order to model this part. We know from Faraday's law that

$$e = \dot{\lambda} = N \dot{\phi} \quad (3.51)$$

$$M = Ni \quad (3.52)$$

where λ is the flux linkage, N is the number of turns in coil, ϕ is the flux, and M is magnetomotive force. Equations 3.51 and 3.52 are modeled using a gyrator element with gyrator modulus N as shown in Fig. 3.65. The effort which establishes the flux in the core is the magnetomotive force which can be further written as

$$M = M_g + M_c \quad (3.53)$$

where M_g and M_c are the magnetomotive forces in the gap and core, respectively. The 1 junction in the model indicates that the flow (flux) in gap and core are same. In the iron core the magnetomotive force (M_c) and flux are related by a nonlinear relation which is a function of material properties and geometry. To characterize a core material, usually the B-H curve is used where B is the magnetic flux density (weber/m²), H is the field strength (Ampere-Turn/m), and

$$M_c = f(\phi) \quad (3.54)$$

In the gap, the relation between the magnetomotive force and flux is defined by

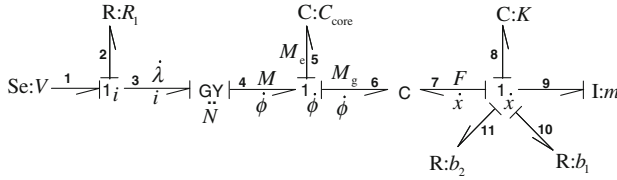
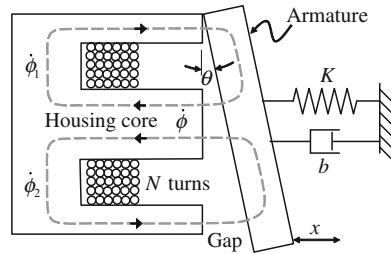


Fig. 3.65 Bond graph model of solenoid

Fig. 3.66 Schematic diagram of clapper solenoid



$$M_g = \left(\frac{x_g}{\mu_0 A_g} \right) \phi \tag{3.55}$$

where x_g is the instantaneous gap length, μ_0 is the permeability of free space ($4\pi \times 10^{-7} \text{Tm/A}$) assuming that the free space is filled with air, and A_g is the gap area. The mechanical force due to the magnetic flux is given by

$$F_g = \frac{\phi^2}{2\mu_0 A_g} \tag{3.56}$$

Equations 3.55 and 3.56 show that a C field can be used to model magneto-mechanical portion in the bond graph model. The magnetomotive force causes motion of the armature, described by $1_{\dot{x}}$ junction in bond graph model. The flow in this junction is determined by mass (m) of armature. Two R elements are attached at this junction to model the damping due to friction (b_1) and damping due to stop (b_2). A C element is also attached to the junction to model the stiffness of the stop. The stop parameters are zero unless the armature comes into contact with it.

3.1.2.11 Clapper Solenoid

Figure 3.66 shows a schematic diagram of a clapper solenoid. In this solenoid the armature swings about hinge, which results in a non-uniform air gap.

Figure 3.67 shows the bond graph model of clapper solenoid. The model for the electrical portion is same as discussed for regular solenoid. The flux generated by the coil (ϕ) gets divided into two unequal parts ϕ_1 and ϕ_2 . This has been shown by a

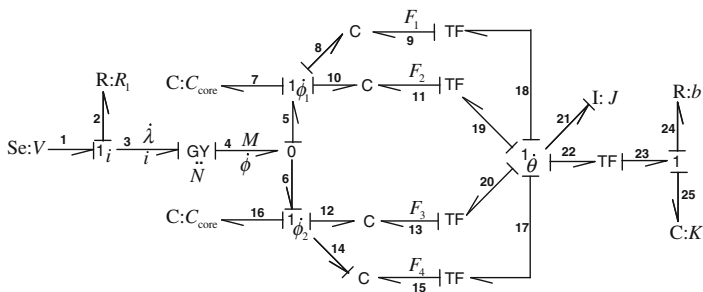


Fig. 3.67 Bond graph model of clapper solenoid

0-junction connecting bonds 4–5–6. Each flux travels through its own housing core shown by dashed lines in Fig. 3.66 and their path has compliances (reluctances) shown by C_{core} in bonds 7 and 16 as shown in Fig. 3.67. The computation of reluctances has been discussed before during electrical transformer modeling. At the top portion of the solenoid flux ϕ_1 also passes through two unequal, time varying air gap. These air gaps can be modeled in bond graph by two C fields connected to bonds 8–9 and 10–11 in Fig. 3.67. Similarly for the bottom portion of the solenoid, passage of flux ϕ_2 through the air gap can be modeled by two more C fields connected to bonds 12–13 and 14–15. Here it is to be noted that in bond 14, the C-field element is differentially causalled indicating that this C field element is not dynamically independent. The force generated in the gaps are represented by efforts in bonds 9, 11, 13, and 15. These forces are multiplied by the moment arms (TF elements) in order to get the moments which cause rotational motion of the armature about the hinge point. These moments are summed up at a 1 junction where rotary inertia of the armature is appended. A TF element is used to convert the rotary motion to translational motion where R and C elements representing the stiffness and damper of the return mechanism are appended.

3.1.2.12 Electrostatic Actuator

Figure 3.68 shows the schematic diagram of an electrostatic actuator [15]. It consists of a parallel plate capacitor with one plate fixed while the other is movable. In [15], the plates of the capacitor are connected to a current source and a parallel resistor. We consider a voltage source and series resistance which includes the resistance to current flow through the capacitor. Mass, stiffness, and damper may represent the mechanical structure of a flexible plate, or membrane supporting a central iron disc, on which the actuation is to be applied.

Figure 3.69 shows the bond graph model of the electrostatic actuator. For a parallel plate capacitor, the capacitance can be given as $\epsilon_0 A/x$, where ϵ_0 is permittivity of air, A is plate area, and x is separation between plates. The voltage across the plates is given by

Fig. 3.68 Schematic diagram of an electrostatic actuator

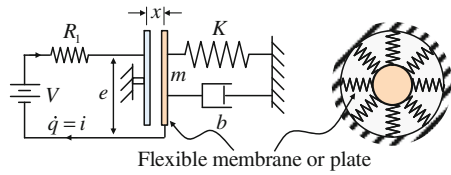
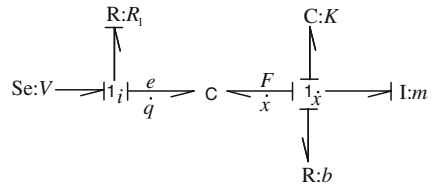


Fig. 3.69 Bond graph model of electrostatic actuator



$$e = \left(\frac{x}{\epsilon_0 A} \right) q \tag{3.57}$$

where q is the charge stored in capacitor plates. The stored energy, at any given state (separation x and charge q) can be evaluated as

$$W(x, q) = \int_0^q e dq = \frac{1}{2} \left(\frac{x}{\epsilon_0 A} \right) q^2 \tag{3.58}$$

Then the potential across the capacitor plates and attracting force can be given as

$$e = \frac{\partial W}{\partial q} = \left(\frac{x}{\epsilon_0 A} \right) q \tag{3.59}$$

$$F = \frac{\partial W}{\partial x} = \left(\frac{1}{2\epsilon_0 A} \right) q^2 \tag{3.60}$$

Equations 3.59 and 3.60 suggest that the relationship can be modeled by a bond graph C field as shown in Fig. 3.69.

3.1.3 Models of Hydraulic Servo-Actuator

Figure 3.70 shows the schematic representation of a hydraulic servosystem. In this figure, a positive displacement pump is driven by a speed controlled motor. A coupling connects the motor with the pump shaft. The positive displacement pump takes the liquid from sump and supplies it to an accumulator. The accumulator supplies liquid to servo valve from where it goes to cylinder which is given a reference

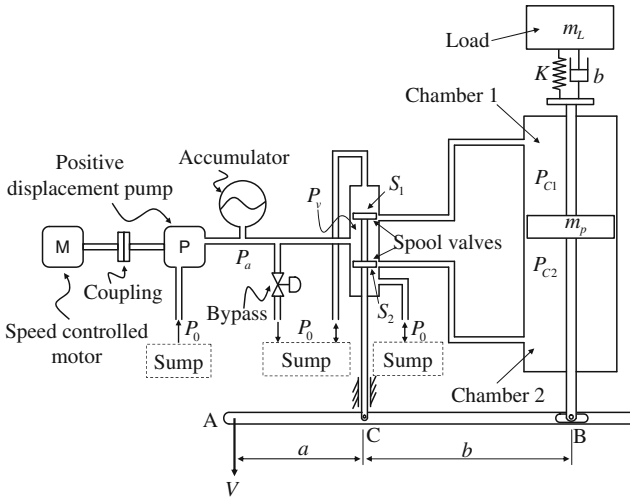


Fig. 3.70 Schematic diagram of a hydraulic servomotor

command through a lever arrangement. The piston in the cylinder receives the reference command and lifts a load.

Figure 3.71 shows the bond graph model of hydraulic servomotor. In the bond graph model, Sf: ω_P is the driving speed of the pump shaft, TF with modulus μ_P relates the driving speed to ideal volume flow rate, R: R_{lm} represents the leakage in the pump, C: K_a represents the compliance of the accumulator (i.e., the trapped air), R: R_b represents the resistivity of bypass valve, and R: R_o represents the Bernoulli resistance of the inlet port to the spool valve.

In the spool valve model, resistance R: R_{S1} represents the Bernoulli resistance for valve port S_1 when it is supplying to chamber 1 while resistance and R: R_{S2} represents the Bernoulli resistance for valve port S_2 when it is supplying to chamber 2. In the bond graph model, inertia I: m_{S1} represents the inertia of the oil flowing through port S_1 to inlet of chamber 1 while I: m_{S2} represents the inertia of the oil flowing through S_2 to inlet of chamber 2. The fluid inertia and Bernoulli resistance in the return path to sump from chamber 1 are modeled as I: m_{S1}^* and R: R_{S1}^* , respectively, and those from chamber 2 are modeled as I: m_{S2}^* R: R_{S2}^* , respectively.

The bulk compliance of the fluids in chambers 1 and 2 are modeled by C: K_{c1} and C: K_{c2} , respectively. Pressure at $0_{P_{c1}}$ and $0_{P_{c2}}$ ports when multiplied with piston area (A) through two TF elements give the force applied on the respective sides of the piston. Note that pressure in chamber 1 produces downward force and thus the corresponding TF modulus is negative. Those transformers also model the volume flow rate for given piston velocity. In the mechanical part model, I: m_p represents the mass of the piston, I: m_L represents the inertia of the load, C: K and R: b represent the compliance and damping between load and piston, respectively, and R: R_f represents the viscous friction in the piston rings. The hydraulic servomotor is driven by

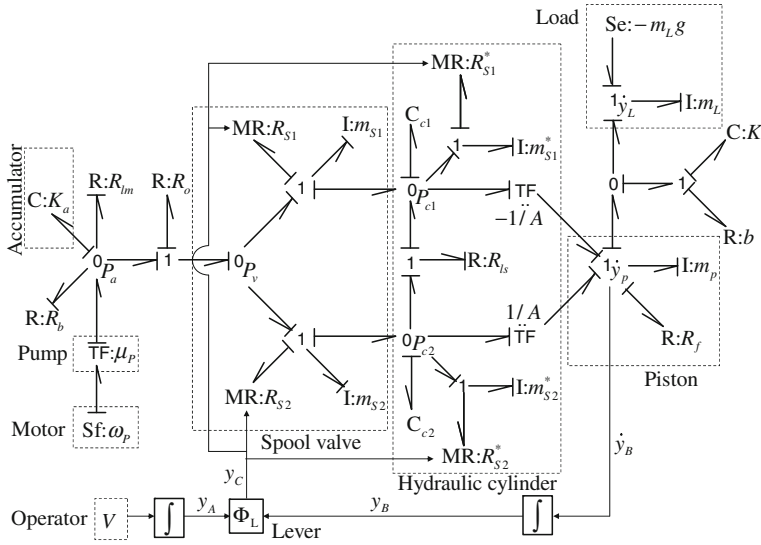


Fig. 3.71 Bond graph model of a hydraulic servomotor

a velocity command (point A in Fig. 3.70). The position of puppet or spool is determined by displacement (y_C) of point C. As point C moves up, R_{s1} becomes low, R_{s1}^* becomes high, R_{s2} becomes high, and R_{s2}^* becomes low. In this position, pumped fluid enters chamber 1 and exits to sump from chamber 2. The reverse happens when point C moves down.

The position of point C is required to modulate the port resistances. Note that the fluid inertias should also be modulated. However, these inertias are negligible and can be removed from the model. Thus, only the hydraulic resistances and compliances are important. The position of point C is obtained from position of point B (piston position, $y_B = y_p$) and position of the actuating end (y_A) as $y_C = y_A + (y_B - y_A) a / (a + b)$. This is modeled in a block diagram form by function Φ_L in Fig. 3.71.

3.1.4 Model of Pneumatic Actuators

Figure 3.72 shows the schematic diagram of a pneumatic actuator. It consists of a double acting pneumatic cylinder connected to a two position four way valve. In Fig. 3.72, \dot{m}_1 , and \dot{m}_2 represent mass flow rates. Pseudo-bond graph models of this system are given in [28]. However, it is very difficult to guarantee energy conservation in a pseudo-bond graph model. Here, we will develop a true bond graph model of the system from the first principles.

Fig. 3.72 Schematic diagram of double acting pneumatic actuator

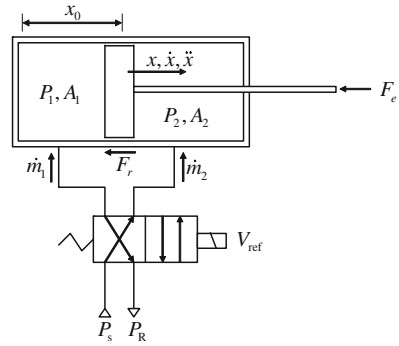
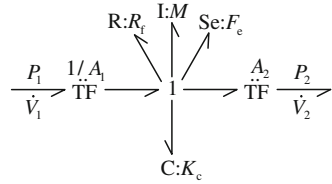


Fig. 3.73 Bond graph model of the mechanical part of double acting pneumatic actuator



• **Mechanical Part**

Let us first start from the Newton’s law applied to the free-body of the piston:

$$M\ddot{x} = P_1 A_1 - P_2 A_2 - F_e - F_r \tag{3.61}$$

where $A_2 = A_1 - A_r$ with A_r being the cross-section area of the piston rod, F_e is the external force, and F_r is the friction force. We will not model the friction force (stick-slip, viscous, etc.) in details here and would simply represent it as a resistance in bond graph form so that any constitutive relation can be plugged in at a later stage. The bond graph model of the mechanical part can thus be given as shown in Fig. 3.73.

The C element in the model is used to account for the reactions on the piston from the supports at dead ends when it contacts them on exceeding some stroke length. This contact can take place on either side and hence the constitutive relation for the C-element is given in terms of the piston displacement (a state associated with the C-element) as follows:

$$e = \begin{cases} 0 & \text{for } x_{\min} \leq x \leq x_{\max} \\ k(x - x_{\max}) & \text{for } x > x_{\max} \\ k(x - x_{\min}) & \text{for } x < x_{\min} \end{cases} \tag{3.62}$$

Moreover, the mechanical friction generated heat is stored in the metallic body (cylinder and piston). We can use an RS element in place of the R_f element to model this energetic coupling of mechanical and thermal domains as shown in Fig. 3.74

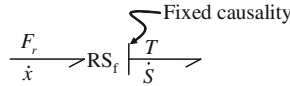
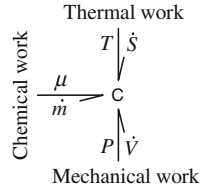


Fig. 3.74 Bond graph model of the energetic coupling of mechanical and thermal domains of double acting pneumatic actuator

Fig. 3.75 The internal energy storage represented as a three-port C-field



where T is the temperature of the metallic body and $\dot{S} = \dot{Q}/T = F_r \dot{x}/T$ is the entropy flow rate generated due to friction.

• **Energy Storage**

Let us now consider a control volume as an open thermodynamic system with dynamic gas volume, gas mass, and entropy. The rate of change of internal energy U can be written as

$$\dot{U} = \frac{\partial U}{\partial V} \dot{V} + \frac{\partial U}{\partial S} \dot{S} + \frac{\partial U}{\partial m} \dot{m} \tag{3.63}$$

where V , S , and m are dynamic gas volume, entropy, and mass, respectively. Noting that pressure $p = -\frac{\partial U}{\partial V}$, temperature $T = \frac{\partial U}{\partial S}$, and chemical potential $\mu = \frac{\partial U}{\partial m}$, we can write Eq. 3.63 as

$$\dot{U} = -p\dot{V} + T\dot{S} + \mu\dot{m} \tag{3.64}$$

For constructing a true bond graph, we can make use of Eq. 3.64 and define the flow variables as \dot{V} , \dot{S} , and \dot{m} with the corresponding effort variables as p , T , and μ , respectively. The internal energy storage is a kind of potential energy which can be given as a three-port C-field as shown in Fig. 3.75. In integral causality, the state variables arising out of this C-field are V , S , and m .

The constitutive relations for the C-field can be written in terms of these state variables. For unit mass of gas ($\dot{m} = 0$), freezing the time, we can write Eq. 3.64 in terms of the specific quantities as

$$du = c_v dT = -pdv + Tds \tag{3.65}$$

where $u = c_v T$ is the specific internal energy (i.e., internal energy per unit mass), $v = V/m$ is the specific volume, and $s = S/m$ is the specific entropy. Using ideal gas law as $pv = RT$ with R being the specific gas constant, Eq. 3.65 can be written as

$$ds = R \frac{dv}{v} + c_v \frac{dT}{T}. \quad (3.66)$$

By integrating Eq. 3.66 from some initial reference state (v_0, s_0) to a final state (v, s) , we obtain

$$s - s_0 = R \ln \left(\frac{v}{v_0} \right) + c_v \ln \left(\frac{T}{T_0} \right) \quad (3.67)$$

from which temperature can be written as

$$T = T_0 e^{(s-s_0)/c_v} \left(\frac{v}{v_0} \right)^{-R/c_v} \quad (3.68)$$

In terms of total quantities instead of the specific quantities, we can write

$$T = T_0 \exp \left(\frac{S}{mc_v} - \frac{S_0}{m_0 c_v} \right) \left(\frac{V}{V_0} \right)^{-R/c_v} \left(\frac{m}{m_0} \right)^{R/c_v} \quad (3.69)$$

From $p v = RT$, the pressure can be written as

$$\begin{aligned} p \left(\frac{V}{m} \right) &= RT_0 \exp \left(\frac{S}{mc_v} - \frac{S_0}{m_0 c_v} \right) \left(\frac{V}{V_0} \right)^{-R/c_v} \left(\frac{m}{m_0} \right)^{R/c_v} \\ p &= \frac{m_0 RT_0}{V_0} \exp \left(\frac{S}{mc_v} - \frac{S_0}{m_0 c_v} \right) \left(\frac{V}{V_0} \right)^{-R/c_v - 1} \left(\frac{m}{m_0} \right)^{1+R/c_v} \end{aligned}$$

or

$$p = p_0 \exp \left(\frac{S}{mc_v} - \frac{S_0}{m_0 c_v} \right) \left(\frac{V}{V_0} \right)^{-\gamma} \left(\frac{m}{m_0} \right)^{\gamma} \quad (3.70)$$

where $R = c_p - c_v$ and $\gamma = c_p/c_v$. Finally, for chemical potential, we can write

$$\mu = u + p v - T s = c_v T + RT - T s = h - T s \quad (3.71)$$

Furthermore, $h = h_0 + \int C_p dT$. By using the detailed derivations given in [30–33], we can write

$$\mu = \mu_0(T) + RT \ln \left(\frac{p}{p_0} \right) \quad (3.72)$$

where μ_0 is a reference chemical potential given purely as a function of temperature T . Note that p and T are already derived in Eqs. 3.69 and 3.70. Thus, the effort variables are now completely defined in terms of the state variables which are time integrals of the flow variables.

The energy storage in a metallic body need not consider pressure and chemical potential terms. Then, considering the mass and volume to be constant, Eq. 3.69 can be written as

$$T = T_0 \exp\left(\frac{S - S_0}{mc_v}\right) \quad (3.73)$$

which can be modeled in bond graph form as a one-port nonlinear C-element with temperature and entropy flow rate as the effort and flow variables, respectively, in the connected bond.

• Mass Transfer

Let us now consider the flow through the ports. We will denote upstream and downstream sides through subscripts u and d , respectively, and the standard air condition will be denoted by subscript 0. For sonic or choked-flow condition ($p_d/p_u < b$ where b is the critical pressure ratio), the flow saturates and the mass flow rate through valves is given as

$$\dot{m} = \rho_0 p_u C_d(x_v) \sqrt{\frac{T_0}{T_u}} \quad (3.74)$$

where ρ_0 is the density at standard air condition, $C_d(x)$ is the valve discharge coefficient, and x_v is the valve or spool position or port opening parameter. The dependence of discharge coefficient on the amount of port opening can be consulted in [4] where the four way control valve is also modeled. The parameter x_v is modulated or regulated by a controller (usually, a current controlled solenoid).

For subsonic condition ($p_d/p_u \geq b$), mass flow rate is given as

$$\dot{m} = \rho_0 p_u C_d(x_v) \sqrt{\frac{T_0}{T_u}} \sqrt{1 - \left(\frac{p_d/p_u - b}{1 - b}\right)^2} \quad (3.75)$$

Note that Eq. 3.75 yields $\dot{m} = 0$ for $p_u = p_d$ and it yields the same result as Eq. 3.74 for $p_d/p_u = b$, i.e., the function is continuous and it can be shown that the first derivative of this function is also continuous.

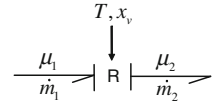
Note that pressure-driven flow model does not yield a true bond graph because when pressure is the effort variable and mass flow rate is the flow variable, their product does not become a true power variable. Thus, for a true bond graph model with mass flow rate as the flow variable, chemical potential (defined per unit mass) should be the effort variable. Accordingly, we can write Eqs. 3.74 and 3.75 as

$$\dot{m} = \begin{cases} \rho_0 \phi(\mu_u, T_u) C_d(x_v) \sqrt{\frac{T_0}{T_u}} & \text{for } \phi(\mu_u, T_u) / \phi(\mu_d, T_d) > b, \\ \rho_0 \phi(\mu_u, T_u) C_d(x_v) \sqrt{\frac{T_0}{T_u}} \sqrt{1 - \left(\frac{\phi(\mu_d, T_d) / \phi(\mu_u, T_u) - b}{1 - b}\right)^2} & \text{for } \phi(\mu_u, T_u) / \phi(\mu_d, T_d) \leq b \end{cases} \quad (3.76)$$

where

$$\phi(\mu, T) = p = p_o \exp\left(\frac{\mu - \mu_0(T)}{RT}\right) \quad (3.77)$$

Fig. 3.76 Mass flow through the ports can be modeled as a nonlinear two-port R-element



Thus the mass flow through the ports can be modeled as a nonlinear two-port R-element (see Fig. 3.76) which is modulated by the temperature of the upstream side. However, because we have to model flow in both directions where upstream and downstream sides can be interchanged, and we have to determine the flow condition, we should modulate the R-field with temperatures of gas on both sides of the port.

• Heat Transfer

The heat transfer can in general comprise three mechanisms: conduction, radiation, and convection. Let us write the entropy of a gas as $S = ms$ where m is its mass and s is its specific entropy. Taking time derivative,

$$\dot{S} = m\dot{s} + \dot{m}s \quad (3.78)$$

where the term $m\dot{s}$ is the heat transfer from the gas to the surrounding taking place at a constant mass and $\dot{m}s$ is the heat convected into or out of the control volume due to mass transfer.

The heat transfer from a constant mass of gas at temperature T_1 to the surrounding at temperature T_2 can be written as

$$Q = \alpha (T_1 - T_2) + \beta (T_1 - T_2) + \gamma (T_1^4 - T_2^4) \quad (3.79)$$

where α , β , and γ are the parameters related to the overall heat transfer coefficients associated with conduction, convection, and radiation heat transfer. Other forms of heat transfer such as Nusselt's formulae can be used in place of Eq. 3.79. In true bond graph, the flow variables are entropy flow rate which are then given as

$$\dot{S}_1 = -Q/T_1 \text{ and } \dot{S}_2 = Q/T_2. \quad (3.80)$$

Note that if $T_1 > T_2$ then $Q > 0$ and the change in entropy of the whole system or universe is $\dot{S}_1 + \dot{S}_2 = Q(1/T_2 - 1/T_1) > 0$. The same can be shown for $T_1 < T_2$. The heat transfer at constant gas mass is then modeled as an R-field with two-ports as shown in Fig. 3.77. Here, the R-field has a fixed conductive causality because the entropy flow rates can be computed from given interface temperatures, but not the vice versa.

When a mass of gas is leaving out of the control volume, the specific entropy is the specific entropy of the gas contained in the control volume. However, when a mass of gas is entering a control volume, it enters with the specific entropy of the upstream side gas. Thus, the value of specific entropy in the term $\dot{m}s$ changes according to



Fig. 3.77 Heat transfer at constant gas mass modeled as an R-field with two-ports

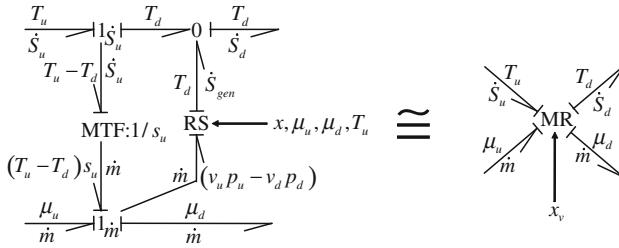


Fig. 3.78 Bond graph model of heat transfer due to mass transfer

the direction of flow. In addition, when a gas with a different specific entropy enters a control volume, it has to mix with the existing gas and equilibrate with it. In this process, we have to account for a different term called *entropy of mixing* or *entropy generated due to mixing*. Thus, while the heat transfer at constant mass ($m\dot{s}$ term) is quite simple to model, the convection part needs careful consideration. The right way to model is to use the Gibbs–Duhem [31] equation.

Assuming the mass transfer through the ports to be isenthalpic, the specific enthalpy of the gas entering one side of the port must be same as that exiting from the port. From Gibbs–Duhem equation

$$-p_u v_u + T_u s_u + \mu_u = -p_d v_d + T_d s_d + \mu_d \tag{3.81}$$

Thus, the enthalpy difference is given as

$$p_u v_u - p_d v_d = (T_u - T_d) s_u + \mu_u - \mu_d \tag{3.82}$$

and the entropy generated due to mixing in the downstream side is found as

$$\dot{S}_{gen} = \frac{\dot{m} (p_u v_u - p_d v_d)}{T_d} = \frac{\dot{m} (T_u - T_d) s_u + \dot{m} (\mu_u - \mu_d)}{T_d} \tag{3.83}$$

Thus, heat convected due to mass transfer can be modeled as shown in Fig. 3.78 where $1_{\dot{m}}$ junction models Gibbs–Duhem equation, the RS element models entropy generation due to mixing and the MTF element models the second term in Eq. 3.78.

The complete model of mass transfer integrated with entropy transfer and generation can be encapsulated as sub-model MR as shown in Fig. 3.78. The four-port MR element receives information of upstream and downstream side effort variables (temperatures and chemical potentials). It then internally computes the pressure using Eq. 3.77 and the mass flow rate using Eq. 3.76. Once the mass flow rate is known, the

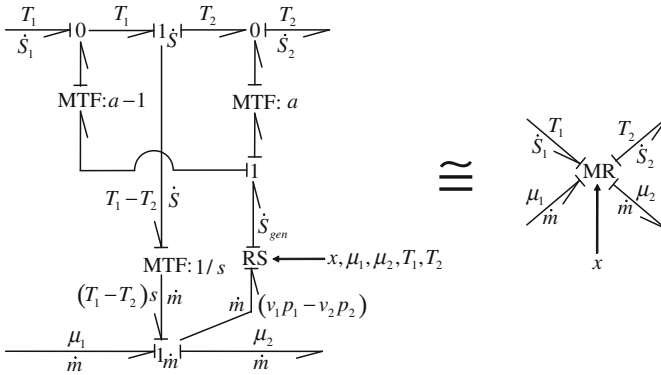


Fig. 3.79 Modified bond graph model of four-port MR element

downstream and upstream entropy flow rates are computed using the second term of Eqs. 3.78 and 3.83. Note that the MR element now substitutes the mass transfer through the port model given earlier in Fig. 3.76. Further note that the spool position modulates the port discharge coefficient $C_d(x)$ and the spool overlap or underlap can be modeled there (see [4] for details).

In our case, there is no fixed upstream or downstream side. Flow can in fact take place in either direction depending on which side of the piston is connected to the supply or return side. The controller actuates the spool valve and can reverse the flow direction. Thus, the detailed internal model of the four-port MR element needs modifications to account for flow in any direction. Because there is no fixed upstream or downstream side, we will denote the two sides of the flow port by subscripts 1 and 2. The modified bond graph model of four-port MR element is now given in Fig. 3.79.

In Fig. 3.79, the moduli of three MTF elements are modulated by the mass flow rate or the pressure difference from which the flow direction is obtained. In the MTF element with modulus $1/s$, $s = s_1$ if $\dot{m} \geq 0$ and $s = s_2$ if $\dot{m} < 0$. Likewise, the binary variable $a = 1$ if $\dot{m} \geq 0$ and $a = 0$ if $\dot{m} < 0$. In this modified form, the temperature variable in the thermal port of the RS element is not fixed and thus both the temperature variables are included in its modulating signal.

• **Complete Model of the Pneumatic Actuator**

Here, we will not consider the detailed model of the control valve such as the solenoid actuation, the forward and reverse path flow resistances, and leakage through the ports, etc. Those can be added at a later stage according to the developments presented in [4]. Thus, the simplified bond graph model of the system can be constructed as shown in Fig. 3.80.

In Fig. 3.80, the two three-port C-fields C_1 and C_2 model the thermodynamic storage and the two four-port R-fields MR_1 and MR_2 model the mass and entropy flow into or out of the control volumes on the two sides of the piston. Two port R-fields R_1 and R_2 model heat transfer from the gas to the metallic piston-cylinder

Fig. 3.80 Bond graph model of pneumatic actuator

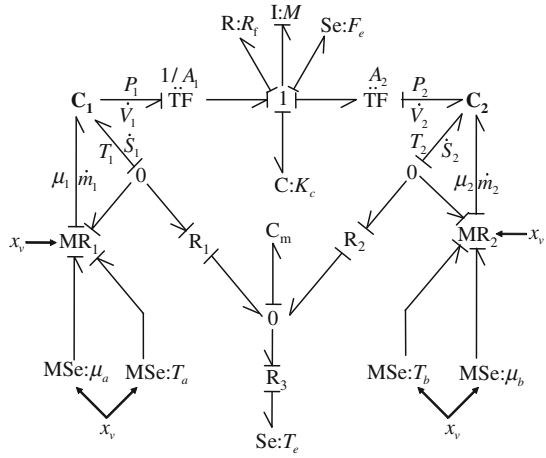
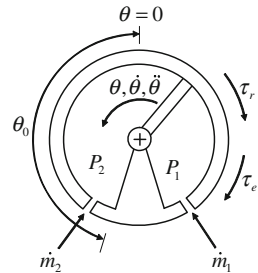


Fig. 3.81 Schematic diagram of vane rotary actuator



assembly and two-port R-field R_3 model heat transfer between the metallic body and the environment at constant temperature T_e . The thermal energy storage in the metallic body is modeled by C_m element whose constitutive relation is given in Eq. 3.73.

The spool valve position x_v is decided by the controller and it decides the port opening areas (discharge coefficients), and the chemical potentials and temperatures at the flow ports. The four MSe elements in the model impose external effort variables on the system. For some range of the spool valve position, $\mu_a = \mu_s$, $T_a = T_s$, $\mu_b = \mu_r$, and $T_b = T_r$ where subscripts s and r refer to supply and return sides. For other values of spool valve position, $\mu_a = \mu_r$, $T_a = T_r$, $\mu_b = \mu_s$, and $T_b = T_s$. The cross-port leakage can be modeled between the two MR elements.

Similarly, we can model the vane rotary actuator. Figure 3.81 shows the schematic diagram of vane rotary actuator.

The equation of motion (mechanical part) for vane actuator can be written as

$$\frac{V_\theta}{2\theta_0} (P_1 - P_2) - \tau_e - \tau_r - I\ddot{\theta} = 0 \tag{3.84}$$

In Eq. 3.84, V_θ represents vane motor displacement, θ_0 represents half stroke, P_1 and P_2 are the absolute pressures at two sides, τ_e and τ_r are external torque and friction torque, respectively, I represents the rotary inertia of vane actuator and θ is the vane actuator displacement. The bond graph model of the vane actuator maintains the same structure as that for the linear actuator with some minor modifications: the rotary inertia must be substituted in place of the mass as parameter of the I element and both the transformer moduli A_1 and A_2 should be replaced by $\frac{V_\theta}{2\theta_0}$. In addition, the external force should be replaced by an external torque and the friction and buffer stiffness models (R_f and K_c) have to be modified to account for angular motions.

For hydraulic actuation in place of pneumatic actuation, one need not consider the temperature variation. In that case, the bulk modulus of the fluid decides the pressure as follows:

$$\Delta P = -\beta \left(\frac{\Delta V}{V_0} \right) = -\beta \frac{\left(\frac{m}{\rho_0} - V \right)}{\left(\frac{m}{\rho_0} \right)} = -\beta \left(1 - \frac{\rho_0 V}{m} \right) = -\beta \left(1 - \frac{\rho_0}{\rho} \right), \quad (3.85)$$

where ΔV is the reduction in volume of fluid with respect to free space volume V_0 at $P = P_0$, ρ is the instantaneous fluid density, ρ_0 is the free space fluid density, m is the instantaneous mass contained within the control volume, and β is the fluid's Bulk modulus. Taking free space pressure as reference (i.e., $P_0 = 0$), the gauge isotropic pressure (compression is taken as positive pressure) $P = -\Delta P$.

Note that the compressibility of the fluid should only be considered when the volume contained in the control volume is large. Equation 3.85 can be modeled in pseudo-bond graph form as a two-port C-field with pressure as effort variable in both its ports and volume flow rate as flow variable in one port and mass flow rate as flow variable in the other port (see [25] for details).

3.2 Modeling of Sensors

Sensors are important elements of any mechatronic system as they determine the current state or outputs of the system. Sensors and amplifiers are designed to operate at low-power efficiency. An ideal sensor extracts information from a system without absorbing any power and it provides the information to other system at finite power. If we talk about an amplifier as a signal conditioning element in a mechatronic system, it accepts an input signal at almost zero power level and influences another system at a much higher power level. The difference between sensors and transducers is often confusing. A transducer is defined as element that when subjected to some physical change affects another change which is related to the physical change. We use the term sensor for an element which produces a signal relating to the quantity that we intend to measure. For example, the quantity being measured in an electrical resistance thermometer is temperature and the sensor transforms it to change of resistance. Thus we can conclude that sensors are transducers.

Transducers can be active or passive. High efficiency transducers are usually passive as they do not use power sources. Active transducers require power sources. Passive transducers can further be classified as power transducers and energy storing transducers. Power transducers usually transmit less power than they receive whereas energy storing transducers have capability to store energy by virtue of which they can temporarily deliver excess power. Before we go further on sensors let us see some basic terminologies related with performance of sensors.

3.2.1 Performance Terminology

The following terms are used to define the performance of transducers.

- **Accuracy:** It is an extent to which the value indicated by sensor might be wrong. For a temperature measuring device, an accuracy of $\pm 1^\circ\text{C}$ means reading of sensor may lie $+$ or -1°C of the true value. It is also expressed as percentage of full range output. Thus for a resistance thermal device (RTD) with range of $0\text{--}300^\circ\text{C}$, accuracy $\pm 5\%$, means result is expected to lie within $+$ or -15°C of the sensor reading.
- **Precision:** It has ability to reproduce repeatedly with a given accuracy.
- **Sensitivity:** It is the relationship indicating how much output one gets per unit input. A resistance thermometer may have a sensitivity of $0.5\ \Omega/^\circ\text{C}$. Many times sensitivity is expressed for input which is not being measured.
- **Resolution:** It is defined as smallest change in input value that will produce an observable change in output value.
- **Range:** It is the limits between which the input can vary. For example, a RTD might have a range of -200 to 500°C .
- **Span:** It is the difference between the maximum and minimum allowable values of the input. For example, a RTD having a range of -200 to 500°C has span of 700°C .
- **Error:** It is the difference between measured value and true value of the quantity being measured. For example, a sensor might give a resistance change of $5.5\ \Omega$ when the true change is $5.8\ \Omega$. The error is thus $(5.8 - 5.5\ \Omega)$ i.e., $0.3\ \Omega$.
- **Hysteresis error:** It is defined as different output for the same value of the input, depending upon whether it has been obtained for increasing value or for decreasing value of the input.
- **Linearity:** It is the percentage of deviation from the best-fit linear calibration curve.
- **Nonlinearity Error:** The common assumption in sensors is its linear behavior over the working range. However, this relationship rarely exists. The nonlinearity error is defined as maximum difference from the straight line depicting the linear behavior with the actual input–output curve.
- **Repeatability:** It is the ability to give same output for repeated application of same input.

- **Stability:** It is defined as the ability of transducer to give same output when used to measure a constant input over a period of time.
- **Drift:** It is used to define the change of output over time. Zero drift is used for changes that occur in output when there is zero input.
- **Dead band:** It is defined as range of input values for which no output is produced.
- **Dead time:** It is defined as length of time from the application of an input until the output begins to respond to the change.
- **Bandwidth:** It is defined as the frequency at which the output magnitude drops by 3 dB.
- **Resonance:** It is defined as the frequency at which the output magnitude peak occurs.
- **Signal-to-noise ratio (SNR):** It is defined as the ratio between the magnitudes of the signal and the noise at the output.

3.2.2 *Static and Dynamic Characteristics*

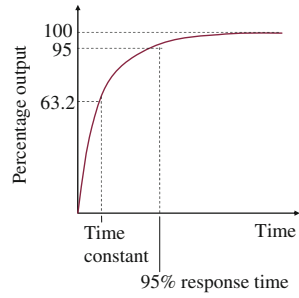
- **Static characteristic:** It is the value given when steady-state condition occurs i.e. the sensor response (value) settles down after receiving the input.
- **Dynamic Characteristic:** It refers to the characteristics of the transient response of transducer. The following terminologies are associated with the dynamic characteristic of a sensor.
 1. **Response time:** It is the time which elapses after a constant (step) input is applied, up to the point at which transducer gives values corresponding to some specific percentage of the value of the output.
 2. **Time constant:** It is defined as time elapsed after which 63.2% of the final output value is reached. It measures inertia of the sensor and shows how fast it reacts to the changes in the input.
 3. **Rise time:** It is defined as time taken for the output to rise to some specific percentage of steady-state output (say 10–90% of the steady-state value).
 4. **Settling time:** It is defined as the time taken for the output to settle within some percentage (say 4% of the steady-state value).

Figure 3.82 shows the exaggerated schematic response of a transducer to step input.

3.2.3 *Classification of Sensors*

- **Binary or digital sensors:** These sensors produce on–off signals. For example, a limit switch contact might close whenever the switch is mechanically actuated. Here the contact is either open or closed, there is no intermediate position.

Fig. 3.82 Response of a transducer to a step input



- Analog sensors: These sensors produce proportional or analog signals. For example, a linear potentiometer might be used to indicate position, with the voltage measured at the potentiometer slide wire proportional to the position.

3.2.4 Selection Criteria

A number of static and dynamic factors must be considered in selecting a suitable sensor to measure the desired physical parameter. These parameters can be (i) range, (ii) resolution, (iii) accuracy, (iv) precision, (v) sensitivity, (vi) linearity, (vii) response time, (viii) bandwidth, (ix) resonance, (x) operating temperature, (xi) deadband, and (xii) signal-to-noise ratio.

3.2.5 Activation of Bonds

In a mechatronic system we often require information from different sensors. These information are used in control laws for actuators. Bond graph bonds are power bonds. But we know that information bonds carry only information at zero power. This pure exchange of information is represented by activation of a bond. A bond may either be flow activated or effort activated. A flow activated bond imparts only flow information to the system at the port which is flow causalled, i.e., the end without the causal stroke. The effort in flow activated bond is zero. Similarly an effort activated bond imparts only effort information to the system at the port which is effort causalled, i.e. the end with the causal stroke. An effort activated bond carries no flow information.

For activation, a full arrow is added within the bond signifying that the bond is an information bond and a letter e or f is written near the full arrow to indicate that it carries effort or flow information, respectively. These activated bonds may be used with two-port elements to indicate the variation of moduli of two port elements.

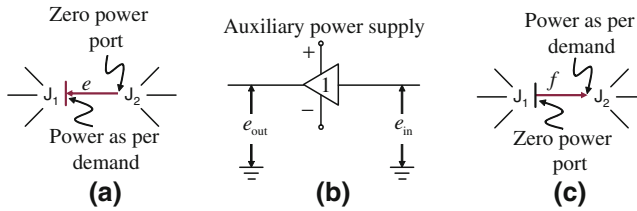


Fig. 3.83 **a** Description of an effort-caused bond, **b** equivalence of an effort-activated bond, and **c** description of a flow-activated bond

Activated bonds are also called signal bonds and they can be represented in different forms (see Chap. 2).

3.2.6 Power Associated with Activated Bonds

Consider a situation shown in Fig. 3.83a. Here the bond is effort-activated. The effort-caused end of this bond gives effort information to J_1 junction and it acts like a source of effort. It may impart any amount of power as demanded by the system to accommodate this information. The power imparted by this bond at J_2 junction is zero. Such an activated bond does not conserve power. It may create or absorb power. A natural question then comes to our mind: from where does this power come? To answer this question, we can assume an effort-activated bond as an effort-to-effort amplifier with unit gain as shown in Fig. 3.83b. All such amplifiers are active systems having a power supply (auxiliary power source connected to the amplifier). The output power is derived from this. The input impedance being very high (ideally infinite), the input power is small (ideally zero). Similarly in a flow-activated bond as shown in Fig. 3.83c, the effort-caused end is powerless and the flow-caused end provides any amount of power demanded by the system at that port.

3.2.7 Modeling Mechatronic Systems with Activated Bonds

Figure 3.84 shows a spring-mass-damper system. The block has mass M , spring has stiffness K , and damper has damping coefficient R . A velocity pickup senses the velocity of the block. This velocity is amplified by a power amplifier having gain μ and it drives a linear actuator which applies a force proportional to the velocity of the block. Let us draw the bond graph model of the mechatronic system and derive its system equations.

We will model this system using the concept of activated bonds as discussed in this and the previous chapter. The spring-mass-damper system can be modeled using C , I , and R elements attached to a 1 junction as shown in Fig. 3.85. The velocity

Fig. 3.84 Spring mass damper system with velocity pickup and actuation

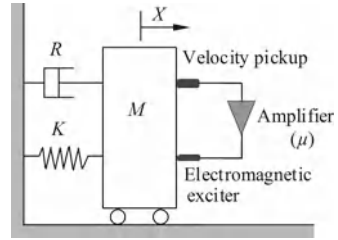
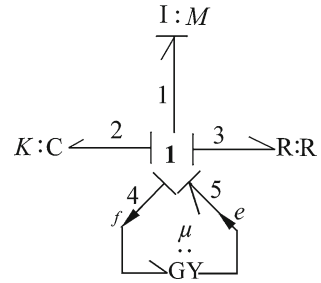


Fig. 3.85 Bond graph model of spring mass damper system with velocity pickup and actuation



amplification and the application of force by linear actuator can be modeled in two ways. We can use a flow detector (D_f element) at the 1 junction and the signal from the flow detector can be used to modulate an effort source (MSe element) at the same 1 junction. Another approach is to use a gyrator element with activation as shown in Fig. 3.85 where bond 4 acts as the sensor and bond 5 acts as the modulated effort source.

The state variables here are momentum (P) of mass block and displacement (Q) of the spring. The system equations can be derived now using the following logic.

1. Element constitutive relations:

$$f_1 = \frac{P_1}{M}; \quad e_2 = K Q_2; \quad e_3 = R f_3; \quad e_5 = \mu f_4. \quad (3.86)$$

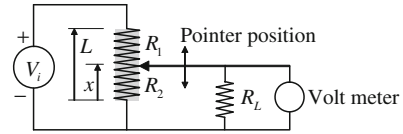
Note that we only write one constitutive relation for GY element because activations mean $e_4 = \mu f_5 = 0$ is a trivial relation.

2. Junction structure constraints:

$$f_2 = f_3 = f_4 = f_1 = \frac{P_1}{M} \quad (3.87)$$

$$\begin{aligned} e_1 &= -e_3 - e_2 + e_5 \\ &= -R \frac{P_1}{M} - K Q_2 + \mu \frac{P_1}{M} \end{aligned} \quad (3.88)$$

Fig. 3.86 Schematic diagram of potentiometer



3. The state equations are for $\dot{P}_1 = e_1$ and $\dot{Q}_2 = f_2$:

$$\dot{P}_1 = -R \frac{P_1}{M} - K Q_2 + \mu \frac{P_1}{M} \quad (3.89)$$

$$\dot{Q}_2 = \frac{P_1}{M} \quad (3.90)$$

4. Above equations can be written in state space form as

$$\begin{Bmatrix} \dot{P}_1 \\ \dot{Q}_2 \end{Bmatrix} = \begin{bmatrix} \frac{-R}{M} + \frac{\mu}{M} & -K \\ \frac{1}{M} & 0 \end{bmatrix} \begin{Bmatrix} P_1 \\ Q_2 \end{Bmatrix} \quad (3.91)$$

Note that force feedback proportional to velocity appears together with the resistance in the state equations. Thus, variable μ tunes the damping of the system.

3.2.8 Position Sensors

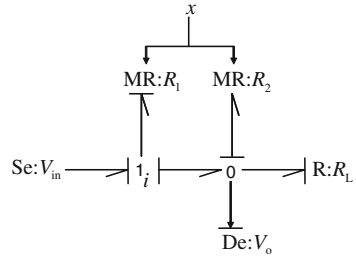
Position sensors can be of three types. These are displacement, position, and proximity sensors. Displacement sensor measures the amount by which the object has moved. Position sensor measures the position of an object with respect to some reference position. The proximity sensor tells whether the object has moved within some particular distance from the sensor or not. Position sensors can be of following types: (i) potentiometer type, (ii) strain gauge element, (iii) capacitive element, (iv) differential transformer, (v) eddy current proximity sensors, (vi) inductive proximity switches, (vii) optical encoders, (viii) pneumatic sensors, (ix) proximity switches, and (x) Hall effect sensors. Let us discuss a few of the above-mentioned sensors.

3.2.8.1 Potentiometers

Potentiometer is a displacement measuring device. It is a variable resistance device whose output resistance changes as the wiper connected to a moving object moves across a resistive surface. Figure 3.86 shows the schematic diagram of a potentiometer. In Fig. 3.86, V_i is the input voltage, V_o is the output voltage, R_1 and R_2 are variable resistances, and R_L is the internal resistance of the voltmeter.

Potentiometer can be calibrated as follows: when $x = 0$, $R_1 = R_{max}$; $R_2 = 0$ and when $x = x_{max}$, $R_2 = R_{max}$, $R_1 = 0$. Thus, the expressions for R_1 and R_2 can be written as

Fig. 3.87 Bond graph model of potentiometer



$$R_1 = \left(1 - \frac{x}{x_{\max}}\right) R_{\max} \tag{3.92}$$

$$R_2 = \frac{x}{x_{\max}} R_{\max} \tag{3.93}$$

Bond graph for the potentiometer can be drawn as shown in Fig. 3.87. From the bond graph model, we can see that $V_i - V_o = i R_1$ or $i = (V_i - V_o)/R_1$. We also see that if R_L is very large then $V_o = i R_2$ or $V_o = \left(\frac{V_i - V_o}{R_1}\right) R_2$. Thus,

$$V_o \frac{R_1}{R_2} = V_i - V_o$$

$$V_o = \left(\frac{R_2}{R_1 + R_2}\right) V_i = \left(\frac{R_2}{R_{\max}}\right) V_i \tag{3.94}$$

where $R_{\max} = R_1 + R_2$. From Eqs. 3.92, 3.93, and 3.94, we get

$$V_o = \left(\frac{V_i}{x_{\max}}\right) x \tag{3.95}$$

An effort detector can be used in the bond graph to measure the output voltage.

3.2.8.2 Encoders

An encoder is a device that converts a linear or angular displacement into a sequence of pulses. By counting these pulses we can obtain the linear or angular displacement. Encoders come in two basic forms, i.e., incremental encoders and absolute encoders. Incremental encoders give the rotation with respect to some reference position whereas absolute encoders give the actual position.

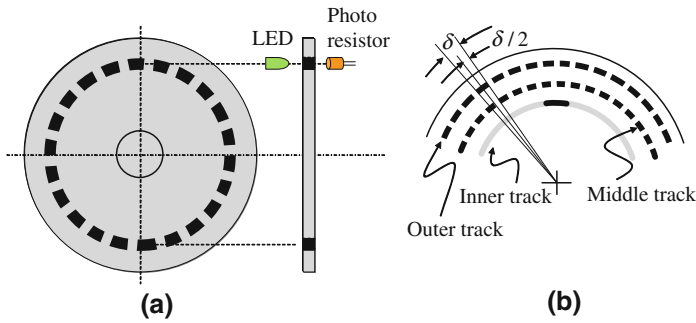


Fig. 3.88 Schematic diagram of incremental encoder

Incremental Encoder

Figure 3.88a shows the schema of an incremental encoder. A beam of light (from a LED) passes through slots in a disc. This beam of light is detected by a light sensor (photoresistor) placed at the other side of the disc. When the disc rotates, a pulsed output is produced by the photoresistor. The number of pulses received by photoresistor is proportional to the angle through which the disc has rotated.

Actually, three concentric tracks with three sensors are used in incremental encoders as shown in Fig. 3.88b where δ is the angle subtended by each hole. The inner track has one hole and it locates the home position of the disc. The middle and outer track have equally spaced holes around the periphery of the disc. Holes in the middle track are at an offset equal to half the width of a hole in comparison to outer track holes. If the shaft rotates in clockwise direction then the pulses in the outer track lead those in the middle track, whereas if the shaft rotates in anticlockwise direction the pulses in the outer track lag those in the middle track. This allows identification of the direction of rotation.

Figure 3.89 shows the bond graph model of incremental encoder. Here, the model has been shown for two tracks. The location of holes between two tracks differ by angle ϕ . The current i_{out} shows the presence or absence of pulses. The current signal (number of pulses) and the time record are then processed in a microprocessor or computer to determine the angular position and average angular velocity.

In Fig. 3.89, LEDs are modeled as RS elements. The RS element models an electrical resistance and the power lost by the resistor (sometimes multiplied with some factor such as efficiency of conversion of heat to visible or infrared light) is a signal output. The light intensity signal Q passes through a switch which is modulated by the angular position of the disc (θ or $\theta + \phi$, depending on the track). The output intensity from the switch modulates the MR element which models the photo resistor. The resistance of the photo resistor changes when light fall on it. The current passing through the photoresistor generates the pulse which is fed to the post-processing device such as a microprocessor. The voltage supplied to both LEDs

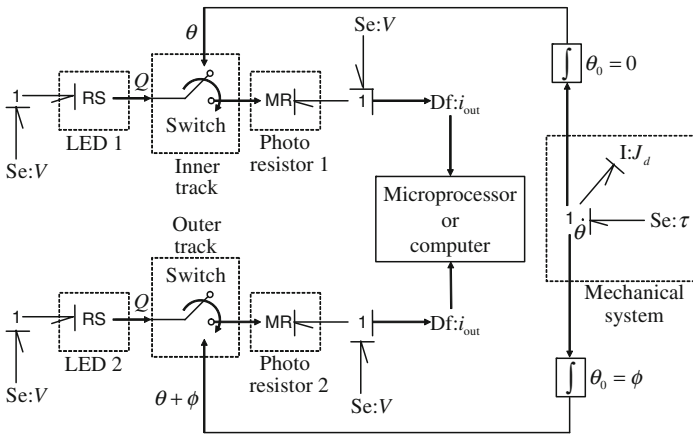


Fig. 3.89 Bond graph model of incremental encoder

and photoresistors is V and the rotary inertia and torque applied on the mechanical rotating system are J_d and τ , respectively.

Absolute Encoder

Figure 3.90 shows the schematic diagram of an absolute encoder for the measurement of angular displacement. Here we get the output in the form of a binary number of several digits. Here each number represents a particular angular position. Figure 3.90 shows a four-bit absolute encoder where the rotating disc has four concentric circles of slots. There are four light emitting diodes (LEDs) to emit the light and four photo resistors to detect the light. These slots are arranged in such a way (as shown in Fig. 3.90) that the sequential output from the sensors is a number in binary code. The number of tracks decides the number of bits in the binary number. For four tracks, there will be four bits and the number of positions that can be detected will be 2^4 . Thus the resolution of encoder will be $360/2^4$ i.e., 22.5° . More number of circles improves the resolution.

The most common types of numerical encoding used in the absolute encoders are gray codes. The gray code is designed so that only one track (one bit) will change state for each count transition, unlike the binary code where multiple tracks (bits) change at certain count transitions. For the gray code, the uncertainty during a transition is only one count, unlike with the binary code, where the uncertainty could be multiple counts. Table 3.1 shows the decimal code, rotation range in degrees, normal binary code, and the gray code for a four-bit absolute encoder.

Although the gray code provides data with the least uncertainty, the natural binary code is the preferred choice for direct interface to computers and other digital devices. Thus, a circuit to convert from gray to binary code is desirable. This circuit can utilize

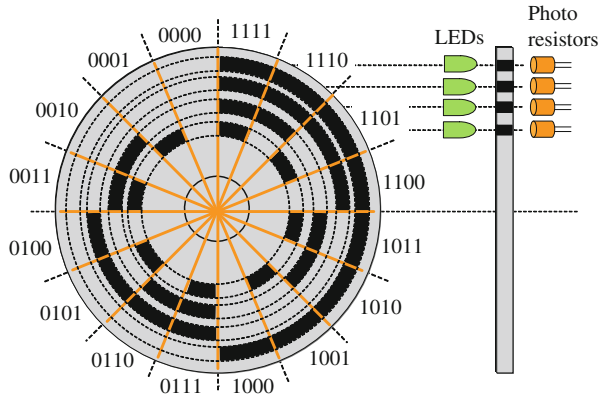


Fig. 3.90 Schematic diagram of absolute encoder

Table 3.1 Binary and gray codes for a four-bit absolute encoder

Decimal code	Rotation range (°)	Binary code	Gray code
0	0–22.5	0000	0000
1	22.5–45	0001	0001
2	45–67.5	0010	0011
3	67.5–90	0011	0010
4	90–112.5	0100	0110
5	112.5–135	0101	0111
6	135–157.5	0110	0101
7	157.5–180	0111	0100
8	180–202.5	1000	1100
9	202.5–225	1001	1101
10	225–247.5	1010	1111
11	247.5–270	1011	1110
12	270–292.5	1100	1010
13	292.5–315	1101	1011
14	315–337.5	1110	1001
15	337.5–360	1111	1000

exclusive OR gates (XOR) to perform this function. For a gray code to binary code conversion of any number of bits N , the most significant bits (MSB) of the binary and gray code are always identical, and for each other bit, the binary bit is the exclusive OR (XOR) combination of adjacent gray code bits.

Figure 3.91 shows the bond graph model of absolute encoder. Here a RS element models the LED and MR element models the photoresistor.

The constitutive relation for RS element can be given as

$$i = \frac{V}{R}, Q = \eta i^2 R \tag{3.96}$$

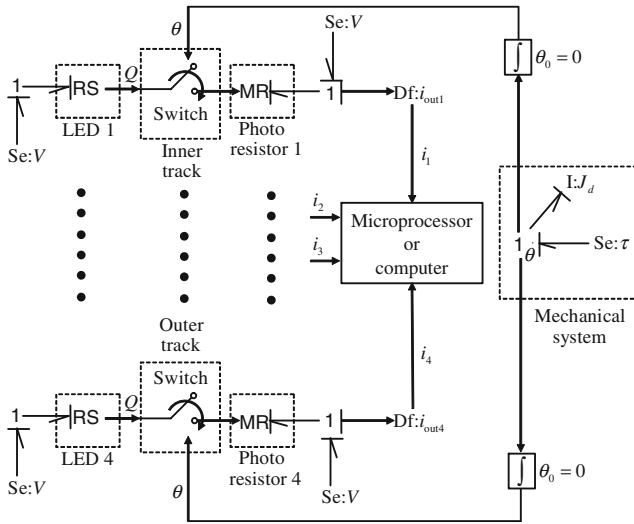


Fig. 3.91 Bond graph model for one LED, one track, and one light sensor (photo resistor) of absolute encoder

where η is an efficiency factor. The constitutive relation for MR element can be given (assuming $Q < 0$ is not a possibility) as

$$R = \phi(Q) = \begin{cases} R_{\text{high}}; & \text{if } Q = 0 \\ R_{\text{low}}; & \text{if } Q > 0 \end{cases}$$

3.2.8.3 Mechanical Switch

Limit switches are common types of mechanical switches used in mechatronic applications. These switches can be pushed by a button or lever operated mechanism. Figure 3.92 shows the schematic diagram of single pole single through (SPST) device that opens or closes a single connection. In addition, a switch locking mechanism may be used. A pole is a moving element in the switch that makes or breaks the connection. The through is a contact point for the pole. Figure 3.93 shows the bond graph for the SPST switch. Here Df element is current detector which detects the current once the circuit is closed. The constitutive relation for the R element in the bond graph is given as

$$R = \begin{cases} R_{\text{high}}, & \text{if } x < x_{\text{lim}} \\ R_{\text{low}}, & \text{if } x \geq x_{\text{lim}} \end{cases} \quad (3.97)$$

where R_{high} represents the resistance of the air gap.

Fig. 3.92 Schematic representation of SPST switch

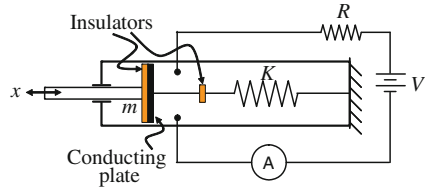
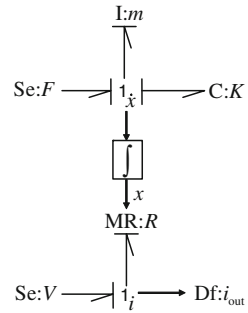


Fig. 3.93 Bond graph model of SPST switch



3.2.8.4 Proximity Sensors

A proximity sensor consists of an element that changes the state of its own or of an analogue signal when it is in proximity of an object. A photo emitter (LED), photo detector (photo resistor) pair can be used as a proximity sensor. Here the interruption or reflection of the beam of light from LED is used to detect the presence of an object without touching the object.

Limit switches discussed in previous section can also be used as proximity sensors. If an extension can be provided in the rod then when an object comes in proximity and touches the end of the rod, the circuit gets completed and current is obtained. This type of sensors are used as bumper sensor in walking robots to detect the presence of an obstacle, so that the robot can change its path.

3.2.9 Velocity Sensors

3.2.9.1 Incremental Encoders

Incremental encoders can be used to measure the angular velocity of the shaft. Here we have to find the number of pulses produced per second in order to determine the angular velocity of the shaft.

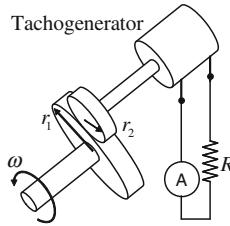


Fig. 3.94 Schematic diagram of use of tachogenerator

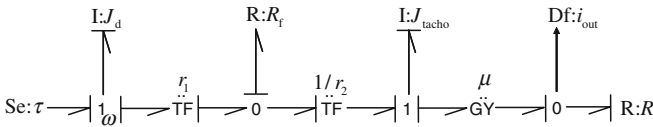


Fig. 3.95 Bond graph model of tachogenerator

3.2.9.2 Tachogenerators

Tachogenerator is a sensor to measure the angular or linear velocity (through a pinion). In principle it is similar to AC generator. It consists of a rotor which is mounted on a rotating shaft as shown in Fig. 3.94. The rotor rotates in a magnetic field produced by either a permanent magnet or an electromagnet. When rotor rotates in the magnetic field an alternating emf is produced in the rotor. The amplitude or the frequency of the alternating emf produced can be a measure of angular velocity of the shaft. The alternating emf may be rectified to give DC output voltage.

Figure 3.95 shows the bond graph model of the tachogenerator where the R element between the two transformers models the friction between the two wheels. The tachogenerator is modeled here as a DC generator with μ as the gyrator modulus.

3.2.10 Acceleration Sensors

3.2.10.1 Seismic Accelerometer

Accelerometer is a sensor to measure acceleration of an object. It is mechanically attached or bonded to object whose acceleration is to be measured. The accelerometer measures acceleration along one axis and is insensitive to motion in other orthogonal directions. Strain gauges or piezoelectric elements form the sensing element of an accelerometer. They convert the vibration signal into voltage signal. Design of an accelerometer is based on the inertial effect associated with a mass connected to the moving object/structure/machine element through spring, damper, and a displacement sensor. Figure 3.96 shows the schematic diagram of the seismic accelerometer.

In the seismic accelerometer, a permanent magnet core moves inside solenoid coils in response to base excitation. The rate of change of flux induces emf in the solenoid

Fig. 3.96 Schematic representation of seismic accelerometer

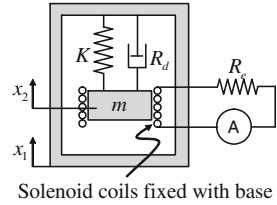


Fig. 3.97 Bond graph model of seismic accelerometer

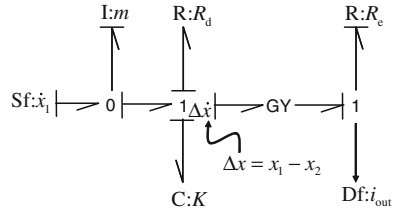
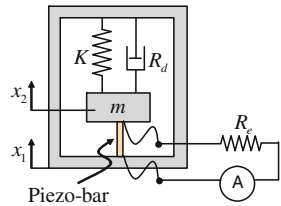


Fig. 3.98 Schematic representation of piezo-type seismic accelerometer



which is measured. If magnetic circuit is idealized and losses are neglected then the induced emf is directly related to the velocity of the permanent magnet. Figure 3.97 shows the bond graph model of the seismic accelerometer where the gyrator element directly models ideal mechanical to electrical domain transformation much like a permanent magnet DC motor model.

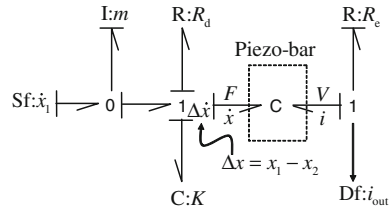
Figure 3.98 shows the schematic representation of piezo-type seismic accelerometer. In this accelerometer piezoelectric element is the sensing element. Piezoelectric materials are ionic crystals. When these materials are subjected to tension or compression electric charge distribution takes place in the crystal with one face of material becoming positively charged and the opposite face becoming negatively charged.

Bond graph models of a piezoelectric layer polarized in a single axis under isothermal conditions are developed in [24]. In open circuit configuration, the net charge (Q) on a surface is proportional to amount (x) by which the charges are displaced. The displacement of charges is proportional to force (F), i.e.,

$$Q = Kx = sF \tag{3.98}$$

where K is a constant and s is also a constant which is called charge sensitivity. This is called direct piezoelectric effect.

Fig. 3.99 Bond graph model of piezo-type seismic accelerometer



For closed circuit configuration, taking into account the direct and converse piezo-electric effects, the constitutive relations can be written as

$$T = c^D S - h D \tag{3.99}$$

$$E = -h S + \beta^S D \tag{3.100}$$

where D , T , E , and S are the electric displacement, stress, electric field, and strain, respectively, c^D is stiffness under constant electric displacement, h is the piezoelectric constant, and β^S is the impermeability at constant strain. One may now assume that the induced electric field is perfectly perpendicular at the surface of the layer in the direction of polarization and the material is isotropic. Under these assumptions, $E \simeq V/l$ and $Q \simeq DA$ where V is the induced potential (in sensor mode), Q is the electric charge, l is the layer thickness, and A is the actuator area. If x is the actuator displacement and F is the actuator force then $S = x/l$ and $F = TA$. Equations 3.99 and 3.100 can now be written as

$$\begin{pmatrix} F \\ V \end{pmatrix} = \begin{bmatrix} c^D A/l & -h \\ -h & \beta^S l/A \end{bmatrix} \begin{pmatrix} x \\ Q \end{pmatrix} = \begin{bmatrix} c^D A/l & -h \\ -h & \beta^S l/A \end{bmatrix} \begin{pmatrix} \int \dot{x} dt \\ \int i dt \end{pmatrix} \tag{3.101}$$

The bond graph model of the piezo-type accelerometer is shown in Fig. 3.99 where R_e is the circuit resistance. Equation 3.101 is the constitutive relation of the two-port bond graph C-field used to model the piezobar element in the sensor.

3.2.11 Force and Pressure Sensors

Forces are commonly measured using displacement. An excellent example of this is the spring balance where we measure the weight using the displacement of a spring.

3.2.11.1 Strain Gauge

Strain gauge works on the principle that when a force is applied on an element it causes strain in the element and the electrical resistance of the element changes due

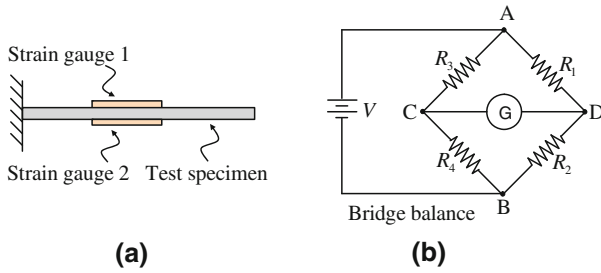


Fig. 3.100 Schematic representation of use of strain gauge in a cantilever beam without force at end

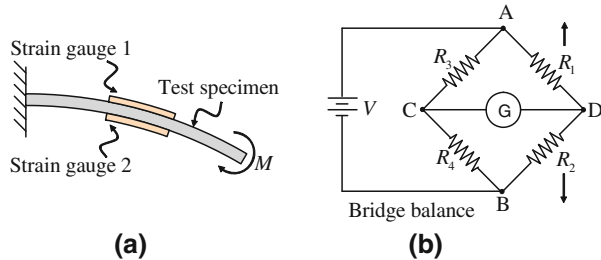


Fig. 3.101 Schematic representation of use of strain gauge in a cantilever beam with force at end

to this strain. This change of electrical resistance can be calibrated in terms of the applied forces. The strain gauges can be placed in such ways that they can sense the strain due to bending, compression, or stretching. The arrangement of strain gauges for measurement of force is called load cell. Measurement of triaxial state of stress requires complex combination of strain gauges. For plain strain condition (two orthogonal linear strains and one angular strain), one can use measurements from three strain gauges arranged in specific configurations called strain rosettes.

We will take up an example of uniaxial strain measurement. Figure 3.100a shows an example where strain gauges are put at the top and bottom portions of a cantilever beam. In the undeflected beam position, these strain gauges when connected as the arms of the Wheatstone bridge circuit cause the bridge to be balanced with no reading in the ammeter or Galvanometer (G in Fig. 3.100b).

Figure 3.101a shows the case when an end load (pure moment or pure bending load) has been applied on the cantilever causing the bending of the cantilever with strain gauge 1 subjected to stretching whereas strain gauge 2 is subjected to compression. In this case, the beam bends with constant curvature along its length and as a result, the resistances R_1 and R_2 in the bridge circuit shown in Fig. 3.101b change. The Galvanometer reading then becomes non-zero and the bridge can be balanced by varying the resistances R_3 and R_4 so that the Galvanometer gives zero reading. This balancing can be automated by using junction field effect transistors (JFETs).

For the balanced circuit, we can show that

Fig. 3.102 Bond graph model of strain gauge arrangement in a cantilever beam

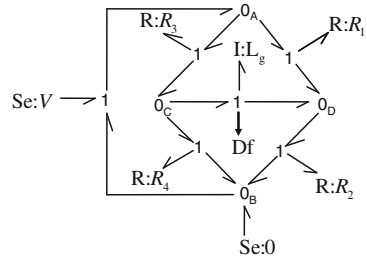
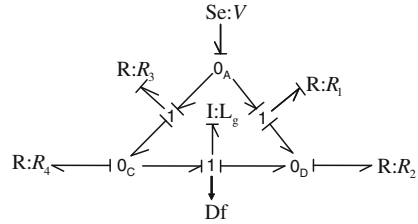


Fig. 3.103 Reduced bond graph model of strain gauge arrangement in a cantilever beam



$$\frac{R_1}{R_2} = \frac{R_3}{R_4} \tag{3.102}$$

Usually, in a bridge circuit, only one resistance is unknown and it can be determined from the three known resistances if the bridge is balanced. In the special case considered here, initially $R_3 = R_4 = R$ and the bridge is balanced when $R_1 = R_2$. For the considered example of an isotropic beam under pure bending, the magnitudes of tensile and compressive strains on the top and bottom fibers are same. Thus, accounting for the change in resistance $\pm \Delta R$, we can write

$$\begin{aligned} \frac{R_1}{R_2} &= \frac{R + \Delta R}{R - \Delta R} \\ \Rightarrow \varepsilon &= \pm \frac{\Delta R}{R} = \pm \frac{R_1 - R_2}{R_1 + R_2} \end{aligned} \tag{3.103}$$

Note that in the above, we have assumed that the strain is directly proportional to the change in resistance and neglected the variation in cross-sectional area of the strain gauge element. Otherwise, we can reformulate the strain relation by accounting for the Poisson’s ratio of the strain gauge material.

Figure 3.102 shows the bond graph model of the bridge circuit arrangement. Here the model has been developed by using the point potential method [19]. In this model, $I:L_g$ models the internal inductance of the Galvanometer and the flow detector measures the current through it.

Figure 3.103 shows the reduced bond graph model obtained from Fig. 3.102 by removing all bonds with zero effort (grounded terminals) and simplifying the bond graph junction structure.

3.3 Models of Electronic Circuit Components

The sensors discussed in previous section may give too small outputs, which may require amplification. Moreover, interference in signals also have to be removed. The signal may be nonlinear requiring linearization. It may be an analog one to be made digital or may be a digital one to be made analog. It is also possible that the transducer works on principle of resistance change and this change is to be converted into current change. Another situation can be a transducer giving voltage change which is to be converted into current change. All the above-cited changes in existing signal may be called as signal conditioning.

3.3.1 Signal Conditioning

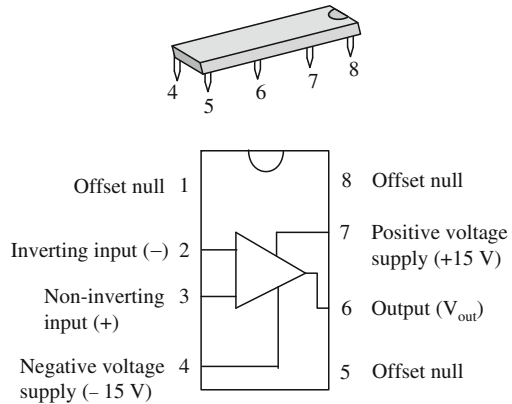
In general, signal conditioning is done in a unit called interface. The interface protects microprocessor against excessive voltage or signals of wrong polarity. Microprocessor requires input to be digital. Thus, if sensor output is analogue then one requires analogue to digital conversion (A/D conversion) before feeding the signal to microprocessor. We may also require analogue signal to be amplified before conversion to digital signal. Actuators require analogue signal and thus, the digital output from microprocessor needs to be converted into analogue signal (D/A conversion) and amplified through a power amplifier before being input to the actuator.

So, in general, we can say that the following processes are involved in signal conditioning:

1. Safeguarding to prevent damage to a microprocessor, as a result of high voltage and current, and wrong polarity.
2. Converting the signal into the right type, e.g., conversion to DC voltage or current, and A/D or D/A conversion as the case may be.
3. Getting the right level of signal, e.g., the thermocouple signal in millivolts needs to be amplified (may use operational amplifiers).
4. Eliminating or reducing noise, e.g., use of filters.
5. Signal manipulation to making it a linear function of some variable, e.g., flow-meter signal is nonlinear and so a signal conditioner is used to linearize the output.

In this section, we will discuss some of the electronic devices which are used in signal conditioning process. In signal conditioning devices, electrical power source resides in the background to make it possible for the device to impart signal to the rest of the circuit. Thus, activated bonds are used in bond graph models of such systems. For studying the dynamics of an electronic system, a black box approach turns out to be handy and practical. A complex electronic device is not analyzed in detail. We will follow an approach where the electronic device will be identified by a suitable bond graph element based on its characteristics.

Fig. 3.104 Packaging and pin number of 741 op-amp and the pin descriptions



3.3.2 Operational Amplifiers

Operational amplifier which is often called op-amp, is a high gain DC voltage amplifier with a differential input and, usually a single ended output. The gain is of the order of 100,000 or more. Ideally, it increases the amplitude of a signal without affecting the phase relationship of different components of the signal. It is supplied as an integrated circuit (IC) on a silicon chip. It is packaged in eight-pin dual in-line package integrated circuit chip. Figure 3.104 shows the available packaging with pin connection of one of the widely used 741 operational amplifier.

Figure 3.105 illustrates the internal design of a commercially available 741 IC. This circuit consists of transistors, resistors, and capacitors.

Op-amp can be combined with external discrete components to create a wide variety of signal processing circuits. It is the building block for more complex electronic circuits like inverting amplifier, noninverting amplifier, summing amplifier, integrating amplifier, differential amplifier, logarithmic amplifier, comparator, analogue to digital (A/D) and digital to analogue (D/A) converters, active filters, and sample and hold devices.

Ideal Model for Operational Amplifiers

Figure 3.106 shows the symbolic representation and terminal nomenclature for an ideal op-amp. It is a differential input, single output amplifier assumed to have infinite gain. Voltages are referenced to common ground. Since it is an active device, it requires connection to an external power supply (usually +15 and -15 V). Since op-amp is an active device, output voltages and currents can be larger than the values applied to the inverting and noninverting terminals. An op-amp circuit usually has feedback from the output to the inverting input as shown in Fig. 3.107. This feedback results in stabilization of the amplifier and helps in control of the gain.

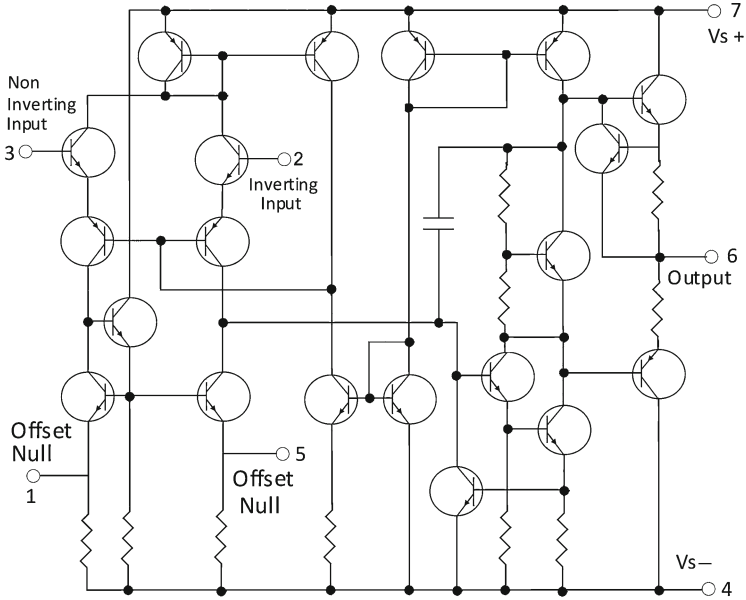


Fig. 3.105 Internal design of 741 op-amp

Fig. 3.106 Symbol of Op-amp

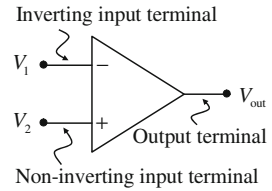
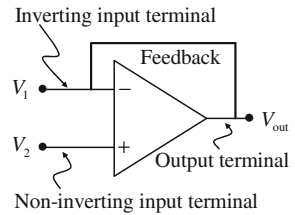


Fig. 3.107 Op-amp with feedback



A model of op-amp can be created by considering its equivalent circuit [6, 12, 18] as shown in Fig. 3.108 where μ is the op-amp gain.

Based on Fig. 3.108, we can create the bond graph model of op-amp as shown in Fig. 3.109.

We can use an activated transformer to model the op-amp as shown in Fig. 3.110. This is with the assumption that activated bond incorporates a suitable tank circuit

Fig. 3.108 Op-amp equivalent circuit

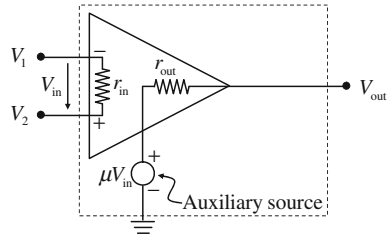


Fig. 3.109 Bond graph model of op-amp with signal bonds

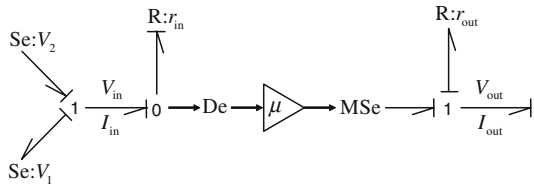
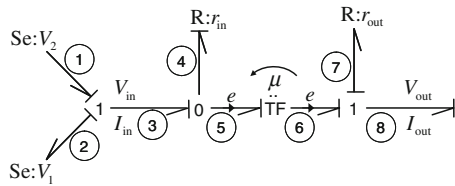


Fig. 3.110 Bond graph model of op-amp with activated bonds



(external power supply) so that any desired power can be delivered on the output port.

It is important to note that bond 5 is powerless where as power in bond 6 depends on what power is drawn by the load. The following equation can be written from the bond graph model.

$$V_{in} - r_{in}I_{in} = 0 \tag{3.104}$$

$$\mu V_{in} = r_{out}I_{out} + V_{out} \tag{3.105}$$

where $V_{in} = V_2 - V_1$.

Now we can further simplify the bond graph shown in Fig. 3.109 with the assumption that theoretically the input impedance is very high, i.e., $r_{in} \rightarrow \infty$ and the output impedance is very low, i.e., $r_{out} \rightarrow 0$. With the first assumption ($r_{in} \rightarrow \infty$), current through the resistor will be zero, while with second assumption ($r_{out} \rightarrow 0$), the voltage drop across the resistor will be zero. Thus power loss in both these resistors (effort times flow) is zero and both the resistors r_{in} and r_{out} can be dropped from the bond graph model. The reduced bond graph model is then shown in Fig. 3.111.

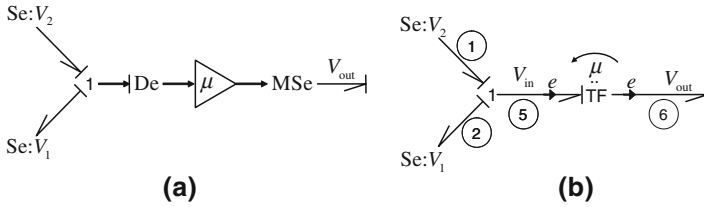


Fig. 3.111 Reduced bond graph model of op-amp using **a** signal bonds and **b** activated bonds

Fig. 3.112 Inverting amplifier

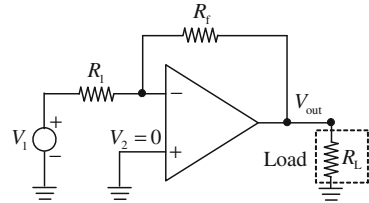
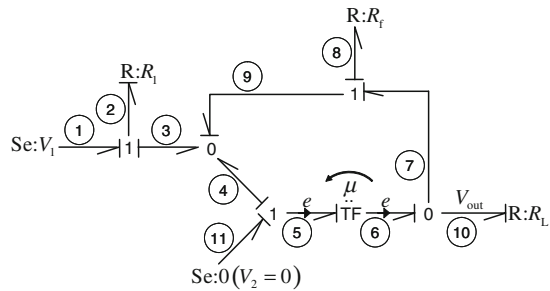


Fig. 3.113 Bond graph model of inverting amplifier



3.3.2.1 Inverting Configuration

As the name implies an inverting amplifier inverts and amplifies the input voltage. To achieve this, two external resistors are connected to op-amp as shown in Fig. 3.112. Figure 3.113 shows the bond graph model of the inverting amplifier.

From the bond graph model, we can analyze for the gain of amplifier as follows:

$$e_6 = \mu e_5 = -\mu e_4 = -\mu e_9 = -\mu (e_7 - e_8) = -\mu (e_6 - R_F f_8) \tag{3.106}$$

or

$$e_6 = \frac{\mu R_F f_8}{1 + \mu} \tag{3.107}$$

Again assuming $f_4 = f_5 = 0$,

$$f_8 = f_9 = -f_3 = -f_2$$

or

$$f_8 = -\frac{(V_1 - e_3)}{R_1} = -\frac{(V_1 - e_9)}{R_1} \tag{3.108}$$

Thus

$$e_6 = -\frac{\mu R_F}{R_1 (1 + \mu)} (V_1 - e_9) \quad (3.109)$$

or

$$-\mu e_9 = -\frac{\mu R_F (V_1 - e_9)}{R_1 (1 + \mu)}$$

or

$$e_9 = \frac{R_F V_1}{R_1 \left(1 + \mu + \frac{R_F}{R_1}\right)} \quad (3.110)$$

From the above equations,

$$e_6 = -\mu e_9 = -\frac{\mu R_F V_1}{R_1 \left(1 + \mu + \frac{R_F}{R_1}\right)}$$

Thus gain of the inverting amplifier can be defined as

$$\begin{aligned} k = \frac{e_6}{V_1} &= -\frac{\mu R_F}{R_1 \left(1 + \mu + \frac{R_F}{R_1}\right)} \\ &= -\frac{R_F}{R_1 \left(\frac{1}{\mu} + 1 + \frac{R_F}{\mu R_1}\right)} \end{aligned} \quad (3.111)$$

The gain of the op-amp μ is in the order of 10^5 to 10^6 . Thus, if we take $\mu \rightarrow \infty$, we get

$$k = \frac{e_6}{V_1} = -\frac{R_F}{R_1}$$

Thus the voltage gain of the amplifier is determined by external resistors R_F and R_1 and it is always negative. We can also say that it reverses the polarity of the signal.

3.3.2.2 Non-Inverting Configuration

A non-inverting amplifier amplifies the signal without inverting it. Here the input signal is applied to the non-inverting input. A portion of the output is fed back to the inverting input. The schematic representation of the non-inverting amplifier is shown in Fig. 3.114. Figure 3.115 shows the bond graph model of non-inverting amplifier.

From the bond graph we can analyze for the gain of amplifier as follows:

$$\begin{aligned} e_7 &= \mu e_6 = \mu(e_5 - e_4) = \mu(e_5 - e_{11}) = \mu(e_5 - e_9 + e_{10}) \\ e_7 &= \mu(e_5 - e_7 + R_F f_{10}) \end{aligned} \quad (3.112)$$

Fig. 3.114 Non-inverting amplifier

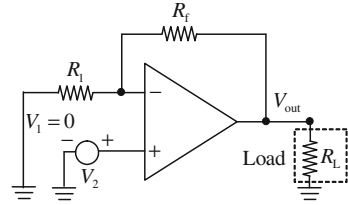
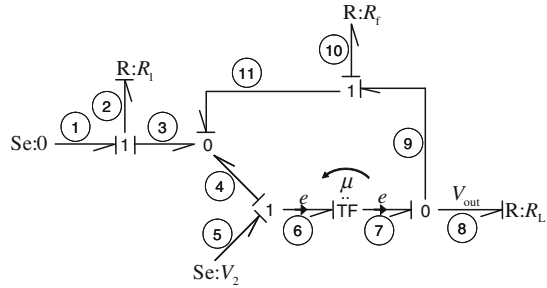


Fig. 3.115 Bond graph model of non-inverting amplifier



$$\begin{aligned}
 f_{10} &= f_{11} = -f_3 = -f_2 = -\frac{(0 - e_3)}{R_1} = \frac{e_3}{R_1} = \frac{e_{11}}{R_1} \\
 f_{10} &= \frac{(e_9 - f_{10}R_F)}{R_1} \\
 f_{10} &= \frac{e_7}{R_1} - \frac{f_{10}R_F}{R_1} \\
 f_{10} &= \frac{e_7}{R_1 + R_F}
 \end{aligned} \tag{3.113}$$

Substituting from Eqs. 3.113 to 3.112, we get

$$e_7 = \mu \left(e_5 - e_7 + \frac{R_F e_7}{R_1 + R_F} \right) \tag{3.114}$$

Simplifying Eq. 3.114 we can get the gain of the non-inverting amplifier as

$$k = \frac{e_7}{e_5} = \frac{1}{\left(\frac{1}{\mu} + 1 - \frac{R_F}{R_1 + R_F} \right)} \tag{3.115}$$

As $\mu \rightarrow \infty$, the gain of the non-inverting amplifier can be derived as

$$k = \frac{e_7}{e_5} = 1 + \frac{R_F}{R_1} \tag{3.116}$$

Fig. 3.116 Schematic representation of buffer

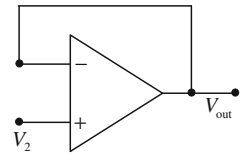


Fig. 3.117 Adder circuit

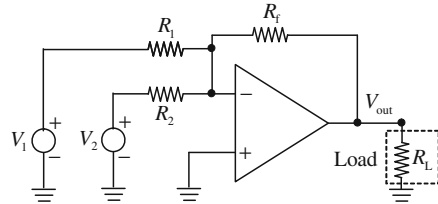
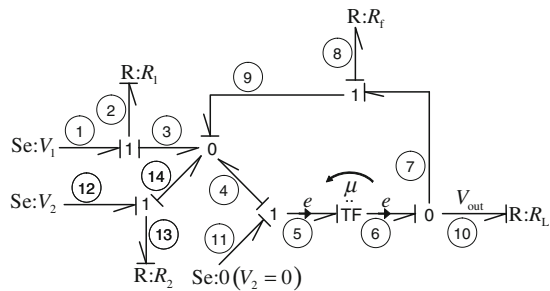


Fig. 3.118 Bond graph model of adder circuit



From Eq. 3.116, we can see that the non-inverting amplifier has a positive gain more than or equal to one. If we take $R_F = 0$ and $R_1 = \infty$ in Eq. 3.116, then we get $k = 1$, or the output voltage is equal to the input voltage. Thus, we have high input impedance and low output impedance. Here, the high input impedance isolates the source from the rest of the circuit. Thus, this circuit is called a buffer. We can draw the reduced buffer circuit as shown in Fig. 3.116.

3.3.3 Op-Amp Circuits

3.3.3.1 Adder Circuit

An adder circuit is used to add two analogue signals. Here the input signals to be added are supplied to the inverting input of op-amp. A portion of the output is fed back to inverting input. The schematic representation of the adder circuit is shown in Fig. 3.117.

Figure 3.118 shows the bond graph model of the adder circuit. From the bond graph we can analyze for the gain of amplifier as follows:

$$e_6 = \mu e_5 = -\mu e_4 = -\mu e_9 = -\mu (e_7 - e_8) = -\mu (e_6 - R_F f_8) \quad (3.117)$$

or

$$e_6 = \frac{\mu R_F f_8}{1 + \mu} \quad (3.118)$$

Again assuming $f_4 = 0$,

$$f_8 = f_9 = -f_3 - f_{14} = -f_2 - f_{13}$$

or

$$f_8 = -\frac{(V_1 - e_3)}{R_1} - \frac{(V_2 - e_{14})}{R_2} = -\frac{(V_1 - e_9)}{R_1} - \frac{(V_2 - e_9)}{R_2} \quad (3.119)$$

Thus,

$$e_6 = -\frac{\mu R_F}{(1 + \mu)} \left[\frac{(V_1 - e_9)}{R_1} + \frac{(V_2 - e_9)}{R_2} \right] \quad (3.120)$$

$$= -\frac{\mu R_F}{(1 + \mu)} \left[\frac{(V_1 + e_6/\mu)}{R_1} + \frac{(V_2 + e_6/\mu)}{R_2} \right] \quad (3.121)$$

$$= -\frac{\mu R_F}{(1 + \mu)} \left[\left(\frac{V_1}{R_1} + \frac{V_2}{R_2} \right) + \frac{e_6}{\mu} \left(\frac{1}{R_1} + \frac{1}{R_2} \right) \right] \quad (3.122)$$

or

$$e_6 \left[1 + \frac{R_F}{(1 + \mu)} \left(\frac{1}{R_1} + \frac{1}{R_2} \right) \right] = -\frac{\mu R_F}{(1 + \mu)} \left(\frac{V_1}{R_1} + \frac{V_2}{R_2} \right) \quad (3.123)$$

or

$$e_6 \left[1 + \mu + R_F \left(\frac{1}{R_1} + \frac{1}{R_2} \right) \right] = -\mu R_F \left(\frac{V_1}{R_1} + \frac{V_2}{R_2} \right) \quad (3.124)$$

or

$$e_6 = -\frac{\mu R_F \left(\frac{V_1}{R_1} + \frac{V_2}{R_2} \right)}{\left[1 + \mu + R_F \left(\frac{1}{R_1} + \frac{1}{R_2} \right) \right]} \quad (3.125)$$

or

$$e_6 = -\frac{\mu R_F \left(\frac{V_1}{R_1} + \frac{V_2}{R_2} \right)}{\left[1 + \mu + R_F \left(\frac{1}{R_1} + \frac{1}{R_2} \right) \right]} \quad (3.126)$$

$$= -\frac{R_F \left(\frac{V_1}{R_1} + \frac{V_2}{R_2} \right)}{\left[\frac{1}{\mu} + 1 + \frac{R_F}{\mu} \left(\frac{1}{R_1} + \frac{1}{R_2} \right) \right]} \quad (3.127)$$

Fig. 3.119 Subtraction amplifier circuit

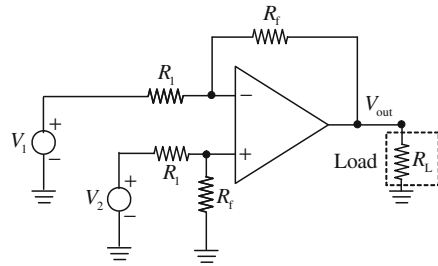
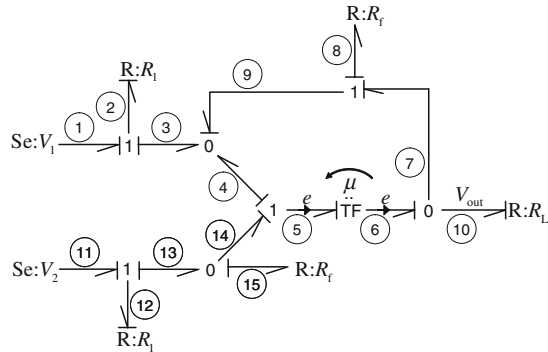


Fig. 3.120 Bond graph model of subtraction amplifier circuit



As $\mu \rightarrow \infty$, Eq. 3.127 reduces to

$$e_6 = -R_F \left(\frac{V_1}{R_1} + \frac{V_2}{R_2} \right) \tag{3.128}$$

If we take $R_1 = R_2 = R_F$, then

$$e_6 = -(V_1 + V_2) \tag{3.129}$$

i.e., the output signal is the sum of the two input signals.

3.3.3.2 Subtraction Circuit

The subtraction circuit is used to subtract two analog signals. The schematic representation of the subtraction circuit is shown in Fig. 3.119.

Figure 3.120 shows the bond graph model of the subtraction amplifier circuit. From the bond graph we can analyze for the gain of amplifier as follows:

Assuming $f_4 = f_{14} = f_5 = 0$ due to effort activation in bond 5,

$$e_{15} = R_F f_{15} = R_F f_{13} = R_F \left(\frac{V_2 - e_{13}}{R_1} \right) = R_F \left(\frac{V_2 - e_{15}}{R_1} \right)$$

$$e_{15} = \frac{R_F V_2}{R_1 + R_F}$$

$$e_6 = \mu e_5 = \mu(e_{14} - e_4) = \mu(e_{15} - e_9) = \mu \left(\frac{R_F V_2}{R_1 + R_F} - e_9 \right) \quad (3.130)$$

$$e_6 = \mu \left[\frac{R_F V_2}{R_1 + R_F} - (e_6 - f_8 R_F) \right] \quad (3.131)$$

or

$$e_6 = \frac{\mu}{1 + \mu} \left[\frac{R_F V_2}{R_1 + R_F} + f_8 R_F \right] \quad (3.132)$$

Again assuming $f_4 = 0$,

$$f_8 = f_9 = -f_3 = -f_2$$

or

$$f_8 = -\frac{(V_1 - e_3)}{R_1} = -\frac{(V_1 - e_9)}{R_1} = -\left[\frac{V_1 - (e_6 - R_F f_8)}{R_1} \right] \quad (3.133)$$

$$f_8 R_1 = -V_1 + e_6 - R_F f_8 \quad (3.134)$$

$$f_8 = \frac{(-V_1 + e_6)}{R_1 + R_F} \quad (3.135)$$

Substituting the value of f_8 in Eq. 3.132 we get

$$e_6 = \frac{\mu}{1 + \mu} \left[\frac{R_F V_2}{R_1 + R_F} + \frac{(-V_1 + e_6)}{R_1 + R_F} R_F \right] \quad (3.136)$$

$$e_6(1 + \mu) = \frac{\mu}{R_1 + R_F} [R_F V_2 - R_F V_1 + e_6 R_F] \quad (3.137)$$

$$e_6 \left[1 + \mu - \frac{\mu R_F}{R_1 + R_F} \right] = \frac{\mu R_F}{R_1 + R_F} [V_2 - V_1] \quad (3.138)$$

$$e_6 [R_1 + R_F + \mu R_1] = \mu R_F [V_2 - V_1] \quad (3.139)$$

$$e_6 = \frac{R_F [V_2 - V_1]}{\left[\frac{R_1 + R_F}{\mu} + R_1 \right]} \quad (3.140)$$

As $\mu \rightarrow \infty$, Eq. 3.140 reduces to

$$e_6 = \frac{R_F}{R_1} [V_2 - V_1] \quad (3.141)$$

i.e., the output signal is the subtraction of two input signals when $R_F = R_1$.

3.3.3.3 Integrator Circuit

We can get the integrating amplifier if we replace the feedback resistor of the inverting op-amp circuit (Fig. 3.112) by a capacitor. Figure 3.121 shows the schematic diagram of an ideal integrator.

Figure 3.122 shows the bond graph model of an ideal integrator. From the bond graph we can analyze for the gain of integrator amplifier as follows:

$$e_6 = \mu e_5 = -\mu e_9 = -\mu (e_7 - e_8) = -\mu \left(e_6 - \frac{1}{C_F} \int f_8 dt \right) \quad (3.142)$$

or

$$e_6(1 + \mu) = \frac{\mu}{C_F} \int f_8 dt \quad (3.143)$$

Again

$$f_8 = f_9 = -f_3 = -f_2$$

or

$$f_8 = -\frac{(V_1 - e_3)}{R_1} = -\frac{(V_1 - e_9)}{R_1} \quad (3.144)$$

Thus,

$$e_6(1 + \mu) = -\frac{\mu}{C_F} \int \frac{(V_1 - e_9)}{R_1} dt \quad (3.145)$$

or

$$-\mu e_9 (1 + \mu) = -\frac{\mu}{C_F R_1} \int V_1 dt + \frac{\mu}{C_F R_1} \int e_9 dt$$

Noting that if $F(s) = \mathcal{L}(f(t))$ then $\mathcal{L}(\int f(t) dt) = F(s)/s$, Laplace transform of both sides gives

$$E_9 (1 + \mu) = \frac{1}{C_F R_1} \frac{V_1(s)}{s} - \frac{1}{C_F R_1} \frac{E_9}{s} \quad (3.146)$$

or

$$E_9 \left[(1 + \mu) + \frac{1}{s C_F R_1} \right] = \frac{1}{C_F R_1} \frac{V_1(s)}{s}$$

Thus the gain of the integrator amplifier can be defined as

$$k = \frac{E_6}{E_1} = \frac{-\mu E_9}{V_1(s)} = -\frac{\frac{\mu}{s C_F R_1}}{\left[(1 + \mu) + \frac{1}{s C_F R_1} \right]}$$

Fig. 3.121 Ideal integrator

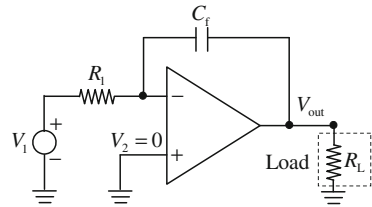
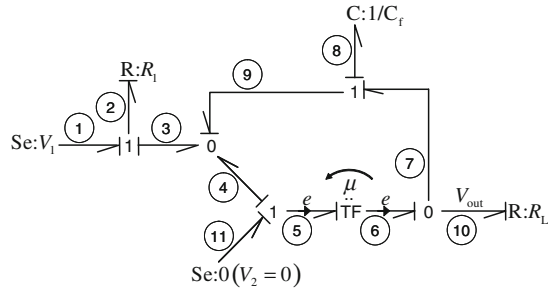


Fig. 3.122 Bond graph model of ideal integrator



$$k = -\frac{\frac{1}{sC_F R_1}}{\left[(1/\mu + 1) + \frac{1}{\mu s C_F R_1} \right]} \tag{3.147}$$

If we take $\mu \rightarrow \infty$, we get

$$k = \frac{E_6}{E_1} = -\frac{1}{sC_F R_1}$$

Thus the output of the amplifier is inverted and scaled integral of the input signal. In time domain, we get

$$e_6 = \beta \int e_1 dt \tag{3.148}$$

where $\beta = -1/(C_F R_1)$ is the integrator gain.

3.3.3.4 Differentiator Circuit

We can get the differentiator circuit if we replace the input resistor of the inverting op-amp circuit (Fig. 3.112) by a capacitor. Figure 3.123 shows the schematic diagram of an ideal differentiator.

Figure 3.124 shows the bond graph model of an ideal differentiator. From the bond graph we can analyze for the gain of differentiator amplifier. The treatment is similar to that of the integrator amplifier.

Starting from $f_4 = f_5 = 0$, we can write

Fig. 3.123 Differentiator op-amp circuit

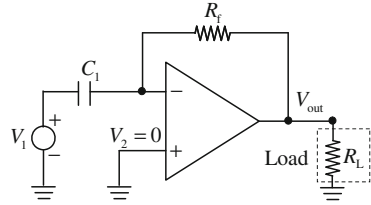
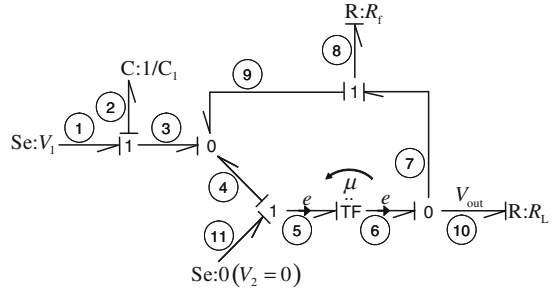


Fig. 3.124 Bond graph model of differentiator



$$f_2 = f_3 = -f_9 = -f_8 = -(e_7 - e_9) / R_F \tag{3.149}$$

$$= -(-\mu e_3 - e_3) / R_F \tag{3.150}$$

$$= (1 + \mu) e_3 / R_F = (1 + \mu) (e_1 - e_2) / R_F \tag{3.151}$$

From constitutive relation of C-element, $e_2 = C_1^{-1} \int f_2 dt$ which by taking Laplace transform of both sides with initial conditions taken as zero gives $E_2 = F_2 / (C_1 s)$, where $E_2 = e_2(s) = \mathcal{L}(e_2(t))$ and likewise Laplace transform of other variables are indicated by upper case letters. Then, we can write

$$F_2 = (1 + \mu) (E_1 - E_2) / R_F = \frac{(1 + \mu)}{R_F} \left(E_1 - \frac{F_2}{C_1 s} \right) \tag{3.152}$$

Equation 3.152 can be simplified to obtain

$$F_2 = \frac{(1 + \mu) C_1 s}{1 + \mu + R_F C_1 s} E_1$$

which gives

$$E_2 = \frac{F_2}{C_1 s} = \frac{(1 + \mu)}{1 + \mu + R_F C_1 s} E_1 \tag{3.153}$$

and

$$E_3 = E_1 - E_2 = \frac{R_F C_1 s}{1 + \mu + R_F C_1 s} E_1 \tag{3.154}$$

Fig. 3.125 Sample and hold circuit

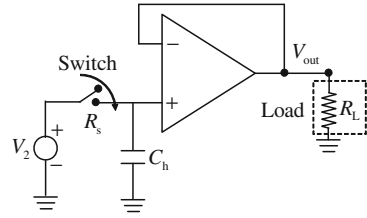
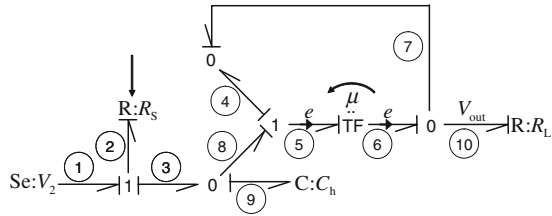


Fig. 3.126 Bond graph model of sample and hold circuit



From $e_6 = -\mu e_3$, we get

$$E_6 = \frac{-\mu R_F C_1 s}{1 + \mu + R_F C_1 s} E_1 \tag{3.155}$$

If we take $\mu \rightarrow \infty$, we get

$$k = \frac{E_6}{E_1} = -R_F C_1 s$$

Thus the output of the amplifier is inverted and scaled differentiation of the input signal, i.e.,

$$e_6 = \beta \frac{de_1}{dt} \tag{3.156}$$

where $\beta = -C_1 R_F$ is the differentiator gain. If we choose $R_F = 1/C_1$ and use an additional inverting amplifier with unit gain then we obtain ideal differentiation of an input signal.

3.3.3.5 Sample and Hold Devices

This device is used in analogue to digital conversion. Here a signal value must be established while it is converted to digital representation. Figure 3.125 shows the schematic diagram of a sample and hold circuit.

Figure 3.126 shows the bond graph model of a sample and hold circuit. From the bond graph we can analyze the behavior of sample and hold circuit.

Fig. 3.127 Comparator

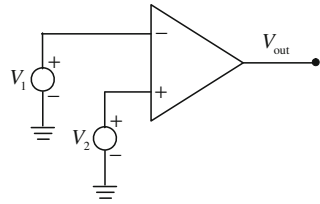
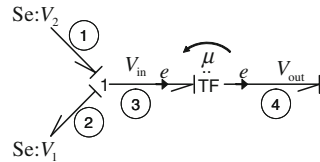


Fig. 3.128 Bond graph model of comparator



From the bond graph model, we see that

$$f_2 = \frac{V_2 - e_3}{R_s} \tag{3.157}$$

If R_s is very high, $f_2 \approx 0$, and the circuit is broken. If $R_s = R_{normal}$, Eq. 3.157 provides the value of the current which will charge the capacitor till $e_3 = e_9 = V_2$. Since the current taken by the op-amp will be zero the output voltage e_6 will be equal to V_2 . When switch breaks the contact $R_s = R_{high}$, the capacitor will hold the input voltage corresponding to last sampled value, and e_9 will be given as

$$e_9 = \frac{Q_9}{C_h} = \frac{\int f_2 dt}{C_h} \tag{3.158}$$

These sample and hold amplifiers are used to hold an instantaneous value of analog voltage until an analog to digital (A/D) converter is ready to convert it into digital output.

3.3.3.6 Comparator

A comparator compares two voltage signals, i.e., it shows which of the two voltage signal is larger. An op-amp with no feedback can be used as a comparator, i.e., in open loop configuration. One of the voltage is applied to inverting input and other is applied to non-inverting input. Figure 3.127 shows the schematic diagram of a comparator.

Figure 3.128 shows the bond graph model of comparator. From the bond graph we can analyze the behavior of comparator.

$$e_4 = \mu e_3 = \mu(V_2 - V_1)$$

If $V_2 = V_1$ then $e_4 = 0$, i.e., there is no output. If $V_1 > V_2$, i.e. inverting input is more than the non-inverting input then e_4 is negative. If $V_2 > V_1$, i.e. non-inverting input is more than the inverting input then e_4 is positive.

3.3.4 Semiconductor Diode

The aim of this section is to provide a general modeling of semiconductor diode. A diode, as a rectifier, allows electric current flow in one direction and blocks it in the opposite direction. A diode in an electronic circuit is equivalent to a check valve in a hydraulic circuit. The unidirectional current flow behavior is called rectification. Rectification is used to convert alternating current to direct current (AC/DC conversion).

As we all are aware that if a p-type region of silicon is created adjacent to a n-type region by appropriate doping, a pn junction is created as shown in Fig. 3.129a. At the pn junction, electrons from the n-type silicon diffuse to occupy the holes in the p-type silicon, creating a depletion region. The p-type side of diode is called anode while n-type side of diode is called cathode. A small electric field develops across the depletion region due to diffusion of electrons. It results in a small voltage difference across the depletion region which is called contact potential. For silicon, this contact potential is of the order 0.6–0.7 V. The positive side of contact potential is in the n-type region whereas negative side is in the p-type region since diffusion of electrons has taken place. If the positive side of a voltage source is connected to anode of diode and negative side of voltage source is connected to cathode of the diode, a complete circuit is formed. The diode in this condition is said to be forward biased as shown in Fig. 3.129b.

The applied voltage has to overcome the contact potential for current to flow through the circuit. As the applied voltage approaches the contact potential value i.e. 0.6–0.7 V the current through diode increases exponentially. This is described by the diode characteristic equation or Shockley diode equation as

$$I_d = I_0 \left(e^{qV_d/(\eta kT)} - 1 \right) \quad (3.159)$$

where I_d is the current through junction, I_0 is reverse saturation current, q is the charge of one electron, k is Boltzmann's constant, V_d is forward bias voltage across the junction, η is diode ideality factor (for silicon, it is between 1 and 2), and T is the absolute temperature of the junction in Kelvins. The voltage drop across a forward-biased diode does not practically change with the current. However, as seen from Eq. 3.159, it is dependent on temperature. Thus, specially designed diodes can be used as temperature sensors. The variation of the forward voltage with temperature is the basic principle on which the temperature measurement device called thermal diode is developed.

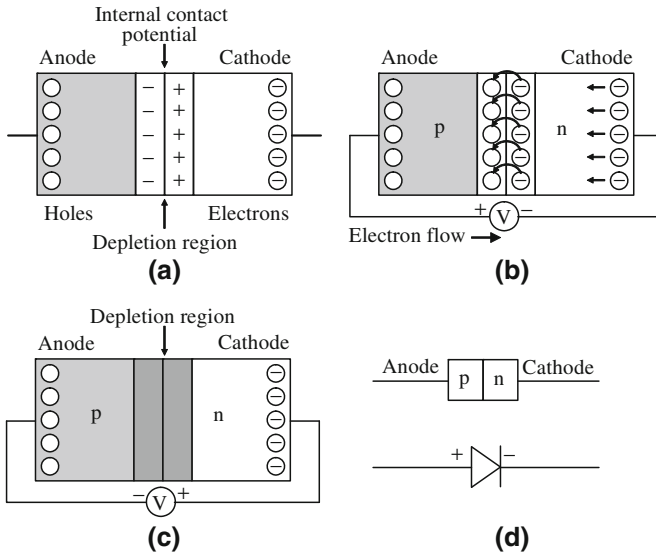
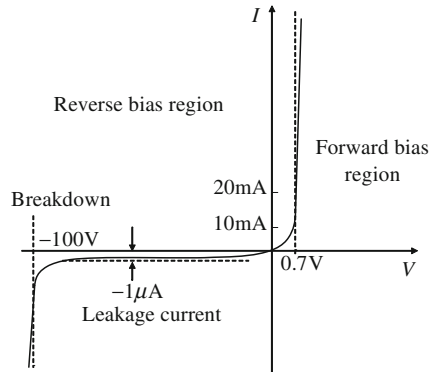


Fig. 3.129 a pn junction b pn junction in forward bias c pn junction in reverse bias d symbol of semiconductor diode

Fig. 3.130 Current voltage characteristic of diode



If the positive side of a voltage source is connected to cathode of diode and negative side of voltage source is connected to anode of a diode, the diode is said to be reversed biased as shown in Fig. 3.129c. In this condition, the depletion region gets enlarged prohibiting the diffusion of electrons. Thus, we see that a semiconductor diode passes current in only one direction, i.e., when it is forward biased. Note that a special diode called Zener diode allows backward current when potential across it exceeds the breakdown voltage. The schematic symbol for semiconductor diode is shown in Fig. 3.129d.

Figure 3.130 shows the current voltage characteristic of semiconductor diode. From this figure it is seen that current–voltage characteristic of semiconductor diode

Fig. 3.131 Approximation of current voltage characteristic of diode

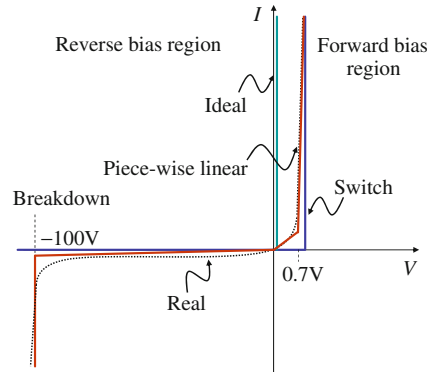
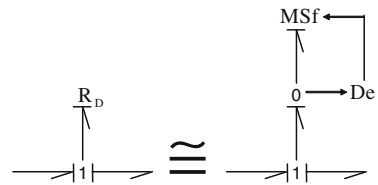


Fig. 3.132 Modeling of diode in conductive causality



is exponential when forward biased. There is a very high increase in current as voltage reaches 0.7 V. When the diode is reverse biased it can withstand a reverse voltage up to a certain limit called breakdown voltage. In this position diode fails because of large increase in reverse current.

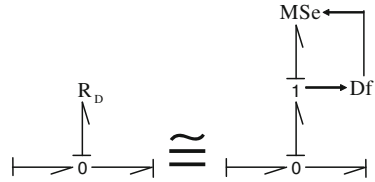
In Fig. 3.131, dotted line shows the real behavior of the diode and other lines show its various approximations. In ideal diode approximation, the diode is fully on if forward bias voltage is more than or equal to zero and when it is reverse biased, the reverse saturation current is assumed to be zero. In Fig. 3.131, switch approximation shows that unlimited current can flow (off course, the limit on the current will be set by other elements in the circuit) when the applied voltage exceeds the 0.7 V and the current is zero if the applied voltage is less than 0.7 V. The piece-wise linear approximation fits one or more straight line segments near the knee-voltage and works well for numerical simulations.

The bond graph model of diode can be created using a nonlinear R element [1, 6]. If the R element appears in conductive causality then we can also model it with a virtual effort sensor and modulated source of flow as shown in Fig. 3.132.

If the diode comes in resistive causality then we can also model it with virtual flow sensor and modulated source of effort as shown in Fig. 3.133.

Special kind of diodes need special modeling. A photodiode can convert incident light into either voltage or current. The solar cell is in fact a large area photodiode. The symbol of photodiode contains two additional inclined rays pointing to the triangle in the diode symbol. Photodiodes use PIN junctions instead of pn junctions to improve the response time. A PIN diode contains a wide, lightly doped intrinsic semiconductor

Fig. 3.133 Modeling of diode in resistive causality



region in between the p and n-type semiconductor regions. Contrary to ordinary diodes, a photodiode is designed to operate in reverse bias. When light falls on the diode (usually, the diode has a window or optical fiber connection for the incident light), the current flows in reverse direction. When photodiode is used in photovoltaic mode or zero bias mode, the photocurrent cannot flow out of the device and as a result, the voltage builds up. This principle called photovoltaic effect is the basis on which solar cells are designed. When the photodiode is used in photoconductive mode, it is reverse biased. The reverse bias induces the saturation or back current for which a given spectral distribution of incident light is proportional to the illuminance or irradiance. The constitutive relation for the photodiode is similar to the normal diode with the reverse saturation current expressed as a function of the illuminance. Thus, it is modeled as a modulated nonlinear R element with the illuminance as the modulating signal.

A light-emitting diode (LED) works on the principle of electroluminescence. LED is formed from a direct band-gap semiconductor. In a forward biased LED, electrons recombine with holes within the device and release the amount of energy depending on the energy gap (band gap) of the semiconductor. The released energy is in the form of photons. The energy of the photon, i.e., the energy gap of the semiconductor, determines the wavelength or color of the emitted light. For example, Gallium arsenide (GaAs) LED emits infrared range light whereas Indium gallium nitride (InGaN) LED can emit yellow, blue, or violet light. A laser can be formed by embedding an LED in a resonant cavity formed by polishing the parallel end faces. Such diodes are called laser diodes. They are commonly used in optical storage devices and laser pointers.

The symbol of LED contains two additional inclined rays pointing out from the triangle in the diode symbol. An LED begins to emit light when its on-voltage, which is around two to three volts, is exceeded. In contrast of usual diodes, the materials used for LEDs must have very high refractive indices. Construction of typical LEDs is complicated because angled facets similar to a jewel must be provided for the emitted light to escape out and not get trapped in internal reflections. The characteristic of an LED is similar to a normal diode. Thus, the LED can be modeled as a nonlinear RS (resistance-source) element as shown in Fig. 3.134.

For small signal AC analysis, usually one includes the diode or junction capacitance in the model [17]. This capacitance appears due to the dynamic depletion or accumulation of charges across the anode and cathode junction sides of the pn junction. This generalized model is shown in Fig. 3.135.

Fig. 3.134 LED modeled by RS-element

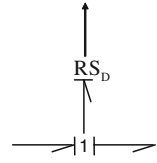
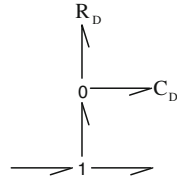


Fig. 3.135 Diode model with junction capacitance



We can revise Eq. 3.159 to the form

$$I_d = I_0 \left(e^{V_d/(\eta V_T)} - 1 \right) \tag{3.160}$$

where η is a material factor (1 for silicon and 2 for Germanium, etc.) and $V_T = kT/q = T/11600$ is the thermal voltage (approximately 26 mV at normal temperature of 300 K). The voltage across the diode V_d is determined from the state Q_d associated with total diode capacitance C: C_d in the model given in Fig. 3.135 as $V_d = Q_d/C_d$. Note that the total capacitance is due to the junction capacitance and the diffusion capacitance. The total capacitance is modulated between two values: $C_d = C_F$ for forward bias or positive flow and $C_d = C_R$ for reverse bias or negative flow. Typically, value of C_F is in the order of tens of μF and C_R is in the order of tens of pF.

For small signal analysis, the total capacitance can be written as

$$C_d = I_Q \tau_F / V_T + C_J \tag{3.161}$$

where $I_Q > 0$ is the DC component (bias) of the current about operating point, τ_F is the forward transit time of charge carriers, C_J is the junction capacitance, and $I_Q \tau_F / V_T$ is the diffusion capacitance. Again, for small signal model, the approximate linear resistance about an operating point (called Q-point) can be taken to be

$$R_d = \eta V_T / I_Q$$

where I_Q is the DC component (bias) of the current (the small variation due to AC component does not change resistance).

Let us consider a circuit with diodes as shown in Fig. 3.136. This circuit is one form of the Wien bridge oscillator which can generate a sine wave with a large range of frequencies. Wien bridge oscillator is used in various applications like measurement of capacitance and radio frequencies. The basic circuit contains four resistances, two

Fig. 3.136 Wien bridge oscillator with diodes for amplitude stabilization

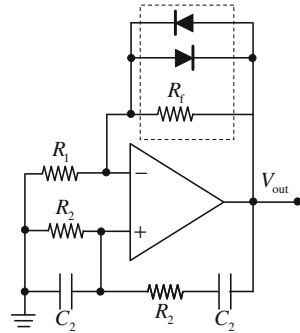
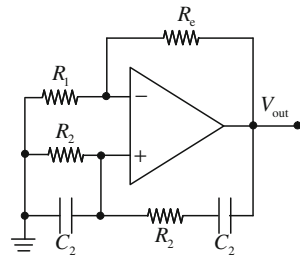


Fig. 3.137 Wien bridge oscillator with equivalent resistance



capacitors, and an op-amp. The feedback resistance R_f in parallel with two diodes can be considered to be one equivalent resistance. As we will see later, the two diodes are used to stabilize the oscillator.

When the two diodes and the feedback resistance are replaced by the equivalent resistance R_e , the resulting circuit can be drawn as shown in Fig. 3.137. In reality, all the resistances and capacitances can have different values. For simplicity of analysis, we have assumed same values for some of the resistances and capacitances.

The bond graph model of the Wien bridge oscillator can be drawn as shown in Fig. 3.138. This model is developed with point potential approach [19]. The ground node is represented by a zero effort source. We can remove all bonds with zero effort from the model. In addition, junctions with only two bonds can also be removed and its two bonds can be merged to a single bond. Likewise, two adjacent junctions of same type can be merged together. These are some of the bond graph reduction steps as detailed in [19] and other bond graph text books.

The reduced bond graph model of the system is shown in Fig. 3.139. This bond graph modeled is properly causalled with integral causality assigned to the two storage elements. Moreover, bonds have also been numbered in the model so that we can analyze the model. One can very easily see that this causalled model contains many causal and algebraic loops (zero-order causal paths) and thus it is difficult to analyze such a system manually. Thus, we will try to remove some of these zero-order causal paths (ZCPs) as a preprocessing step.

Fig. 3.138 Bond graph model of Wien bridge oscillator with equivalent resistance

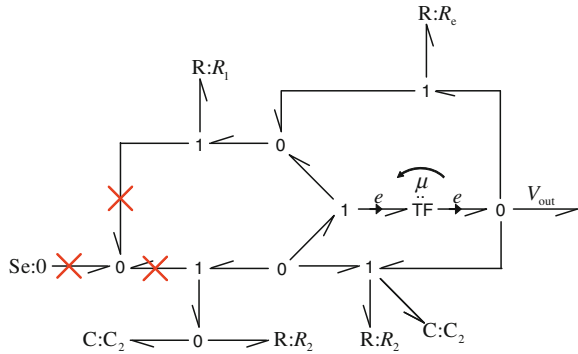
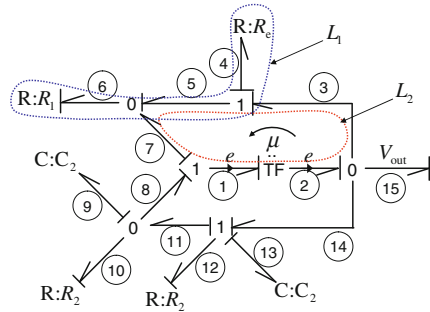


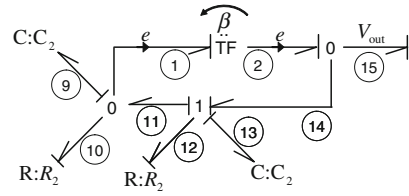
Fig. 3.139 Reduced bond graph model of Wien bridge oscillator with equivalent resistance



Initially, we will consider only the top part of the model which does not contain any states. We try to replace the junction structure between bond number 8 and bond number 14 by an equivalent transformer. This is possible because all causal paths in this zone have zero order (no states). Thus this part is simply a resistive structure which can be modeled as a two-port R field. Moreover, the flow in bonds 1, 7, and 8 are zero which implies there is only one non-zero output from the equivalent two-port R field connected to bonds 8 and 14. In the given causality, the inputs of the R-field are e_8 and f_{14} , and the outputs are $f_8 = 0$ and e_{14} . Thus, the R-field can now be replaced by a simple one way connection (activated transformer) between e_8 and e_{14} and we can find that gain. Recall the concept of causal paths and gains from Chap. 2. The causal path through the transformer element with effort activated bonds do not exist when following the flow variable. The collocated gain $f_8/e_8 = 0$ and $f_8/f_{14} = 0$ because $f_8 = 0$. We can see that the contribution to gain e_{14}/f_{14} from the top part of the model is zero because all causal paths from f_{14} to e_{14} pass through the lower part. Thus, there exists only one gain between bonds 8 and 14 which means it has to be an active connection.

The forward path gain between e_8 and e_{15} is found from causal path $e_8 \rightarrow e_1 \rightarrow TF \rightarrow e_2 \rightarrow e_{14}$ and it is $p_1 = \mu$ where μ is the op-amp gain. The loop gains are found from the loops shown by dotted paths in the bond graph model. They are $e_7 \rightarrow e_1 \rightarrow TF \rightarrow e_2 \rightarrow e_3 \rightarrow e_5 \rightarrow e_7$ and $f_4 \rightarrow R_e \rightarrow e_4 \rightarrow e_5 \rightarrow$

Fig. 3.140 Reduced bond graph model of Wien bridge oscillator with equivalent resistance after removal of the zero-order causal paths (ZCPs)



$e_6 \rightarrow R_1 \rightarrow f_6 \rightarrow f_5 \rightarrow f_4$, with the associated loop gains $L_1 = -\mu$ (one power direction reversal in bond 7) and $L_2 = -R_e/R_1$ (one power direction reversal in bond 4).

The loop with gain L_2 does not touch the forward path. There are no mutuality non-touching loops. Thus, application of Mason’s gain rule gives

$$\begin{aligned} \frac{e_{14}}{e_8} &= \frac{p_1 \Delta_1}{\Delta} = \frac{p_1 (1 - L_2)}{1 - (L_1 + L_2)} \\ &= \frac{\mu (1 + R_e/R_1)}{1 + \mu + R_e/R_1} \end{aligned} \tag{3.162}$$

If we assume the op-amp gain to be very high, i.e., $\mu \rightarrow \infty$, then

$$\beta = \frac{e_{14}}{e_8} = 1 + \frac{R_e}{R_1} \tag{3.163}$$

where β is a gain parameter.

The bond graph model shown in Fig. 3.139 can now be revised to a form as shown in Fig. 3.140.

There are two states (Q_9 and Q_{13}) in the bond graph model associated with two integrally causal storage elements. The state equations can be written as follows:

$$\begin{aligned} \dot{Q}_{13} &= f_{13} = f_{12} = e_{12}/R_2 \\ &= (e_{14} - e_{11} - e_{13})/R_2 = (\beta e_{11} - e_{11} - e_{13})/R_2 \\ &= ((\beta - 1)e_9 - e_{13})/R_2 \\ &= \frac{(\beta - 1) Q_9 - Q_{13}}{R_2 C_2} \end{aligned} \tag{3.164}$$

and

$$\begin{aligned} \dot{Q}_9 &= f_9 = f_{11} - f_{10} = f_{13} - e_{10}/R_2 = f_{13} - e_9/R_2 \\ &= ((\beta - 1)e_9 - e_{13})/R_2 - e_9/R_2 \\ &= \frac{(\beta - 2) Q_9 - Q_{13}}{R_2 C_2} \end{aligned} \tag{3.165}$$

We can write the above state equations in state space matrix form as follows:

$$\frac{d}{dt} \begin{Bmatrix} Q_9 \\ Q_{13} \end{Bmatrix} = \underbrace{\begin{bmatrix} \kappa(\beta - 2) & -\kappa \\ \kappa(\beta - 1) & -\kappa \end{bmatrix}}_A \begin{Bmatrix} Q_9 \\ Q_{13} \end{Bmatrix} \quad (3.166)$$

where $\kappa = (R_2 C_2)^{-1}$ and β has been defined earlier as $\beta = 1 + R_e/R_1$.

The oscillator is stable when real part of eigenvalues of matrix A are negative. To find the stability condition, we can write the characteristic equation as $|\lambda I - A| = 0$ where λ is a eigenvalue and I is a 2×2 identity matrix. This gives

$$\begin{vmatrix} \lambda - \kappa(\beta - 2) & \kappa \\ -\kappa(\beta - 1) & \lambda + \kappa \end{vmatrix} = 0$$

or

$$\lambda^2 + \kappa(3 - \beta)\lambda + \kappa^2 = 0 \quad (3.167)$$

From Eq. 3.167, we find that real parts of roots are negative only when $3 - \beta > 0$, i.e., the stability condition is given by

$$R_e/R_1 < 2 \text{ for } \kappa > 0 \quad (3.168)$$

Thus, the oscillator gives stable decaying output for $R_e/R_1 < 2$ and unstable output for $R_e/R_1 > 2$. To make the oscillator oscillate perpetually, we have to set $R_e/R_1 = 2$, i.e., make it marginally stable. Note that this is not a passive system where oscillating solution means a conservative system, rather here energy is continuously dissipated by four resistances and pumped by the active op-amp.

In early Wien bridge oscillators, it was not possible to correctly tune the resistances to operate the oscillator in metastable mode. In 1938, Meacham proposed the use of a lamp as a variable resistance in the circuit. William Hewlett, when working for the master thesis at Stanford University in 1939 came up with a solution where he used an incandescent bulb in place of resistance R_1 and chose the bulb of proper wattage such that R_e is slightly larger than $2R_1$. Initially, the bulb resistance is such that the oscillator is unstable and as the bulb heats up, resistance R_1 reduces and the oscillator becomes stable. The thermal time constant of the system is so large that the bulb ultimately operates at an equilibrium temperature and sustains the oscillator.

Modern Wien bridge oscillators use diodes, thermistors, field effect transistors, etc. in place of incandescent bulbs. The circuit shown in Fig. 3.136 uses two counter-oriented diodes which allow free flow of current if the voltage V_f across resistance R_f exceeds the knee voltage, i.e., $|V_f| > 0.7\text{V}$. In this condition, the effective resistance R_e is almost zero and thus $R_e/R_1 < 2$ and the oscillator is stable. When the voltage across the diodes is lower than the knee voltage, i.e., $-0.7\text{V} < V_f < 0.7\text{V}$, then the effective resistance R_e is almost same as R_f (the diodes in this case offer theoretically infinite resistance). Thus, by choosing a value of R_f marginally higher

than $2R_1$ (nominally unstable oscillator), the oscillator becomes initially unstable and as its generated voltage tries to exceed knee voltage it becomes stable. This way, a confinement of the output voltage amplitudes around the knee voltage is achieved.

The frequency of the oscillator can be tuned by changing the time constant. From Eq. 3.167, in marginally stable state ($\beta = 3$), the eigenvalues are $\lambda = \pm i\kappa$ with oscillation frequency $\omega = \kappa = 1/(R_2C_2)$.

3.3.5 Transistor

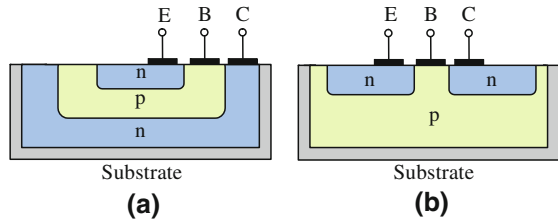
The basic building block of modern electronic devices is a semiconductor device called transistor which means transfer resistor. Complex integrated circuits (ICs) contain millions or billions of transistors. A transistor has three or more terminals. It is primarily used as an amplifier or switch. One pair of terminals of a transistor can be used as the controlling terminal to which a voltage can be applied in order to change the current flowing through another pair of terminals. Like the op-amp, the output power can be higher than the power at the control input. In fact, an op-amp contains several transistors (see the internal design of an op-amp given in Fig. 3.105). Thus, a transistor can be used to amplify a signal. It can be used as an electronic switch.

Transistors are categorized by the type of semiconductor material used, the structure (bipolar junction transistor or BJT, field effect (unipolar) transistor or JFET, etc.) and electrical polarity (NPN, PNP, etc.). The categories can be mixed such as in the metal–oxide–semiconductor field-effect transistor (MOSFET) which exposes the material and the structure in its name.

In this book, we will deal with bipolar junction transistors or BJTs. BJT is widely used because it offers high output resistance and transconductance compared to other transistors. BJT also performs better in very high-frequency applications in the range of radio frequency and above, such as those used in wireless communications. A BJT is made by stacking three differently doped semiconductor regions. These are emitter, base, and collector regions. Each of these semiconductor region is connected to a terminal. The terminals are named according to the region to which they are connected, i.e., emitter (E), base (B), and collector (C) terminals, as shown in Fig. 3.141a. Physically, the base lies between the emitter and the collector. The doping of the three semiconductor regions decides the electrical polarity of the transistor. In a PNP BJT, one uses p-type emitter, n-type base, and p-type collector. In a NPN BJT, one uses n-type emitter, p-type base, and n-type collector.

A transistor physical structure may give a false feeling of two oppositely biased diodes in series with a shared base (e.g., PN+NP=PNP). However, there are some basic differences which cause the transistor to behave differently. The BJT is asymmetrically doped, i.e., the doping level in the collector and the emitter are different. The base, which physically lies between the emitter and the collector, is made from high resistivity material with light doping. The collector is lightly doped whereas the emitter is heavily doped. Note that the collector–base junction is reverse biased for normal operation of the transistor. The lightly doped collector allows breakdown

Fig. 3.141 Schema of cross-section of **a** parallel and **b** lateral NPN transistors with terminals



of the collector–base junction under application of a large reverse bias voltage. The heavily doped emitter increases the emitter injection efficiency, i.e., more carriers are injected by the emitter in comparison to the base. During amplification, the emitter injects most of the carriers injected into the emitter–base junction. The collector is the output terminal and it surrounds the emitter region completely (see Fig. 3.141a). Usually a large collector base junction area in comparison to emitter–base junction area ensures that all carriers are trapped by the collector. Thus, the emitter is the source from which the output power at the collector is drawn. The controlling terminal is the base. When a small controlling potential difference is applied across the base-emitter terminal, a large current flows between the emitter and the collector.

The transistor with schematic cross-section as shown in Fig. 3.141a is said to be a parallel BJT. The schematic cross-section of a lateral BJT is shown in Fig. 3.141b. A lateral BJT is symmetrical with equal base–collector and base-emitter areas. Thus, lateral BJTs give inefficient performance, low amplification, and breakdown voltage. However, they are suitable for special applications like in CMOS (complementary metal–oxide–semiconductor) used in ICs and microprocessors, etc.

To explain the working principle of BJT further, let us look at the schematic of NPN BJT shown in Fig. 3.142. The transistor can be operated in various modes depending upon the voltages applied across the terminals. Here, we will consider the forward active mode operation. The n-type emitter is heavily doped as compared to n-type collector and the p-type base is lightly doped. Moreover, the collector–base junction is reverse-biased whereas the emitter–base junction is forward biased. The shared base is so thin that carriers can diffuse across the base in a short time (this time duration has to be smaller than the semiconductor’s so-called minority carrier lifetime). The control potential V_{BE} is applied across the base-emitter junction. Application of V_{BE} disturbs the equilibrium between thermally generated carriers (the travelling vacancies in the valence-band electron population or holes) and the repelling electric field of the depletion region. This disturbance causes injection of thermally excited electrons into the base region which then diffuse through the base to the collector side. The base thickness must be much less than the diffusion length of the electrons to allow the electrons reach the base–collector interface. Because the base is p-type, the electrons in the base are minority carriers whereas the holes in the base are majority carriers. The concentration of electrons varies from a higher value at base-emitter junction to a lower value at base–collector junction. The electrons that diffuse through the base toward the collector are sucked into the collector (by

Fig. 3.142 Schema of NPN BJT showing charge transfer when emitter–base junction is forward biased and base–collector junction is reverse biased

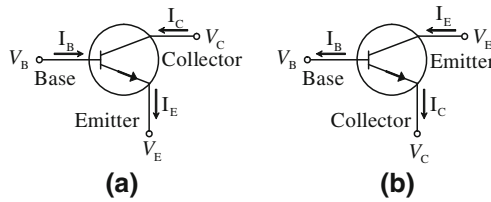
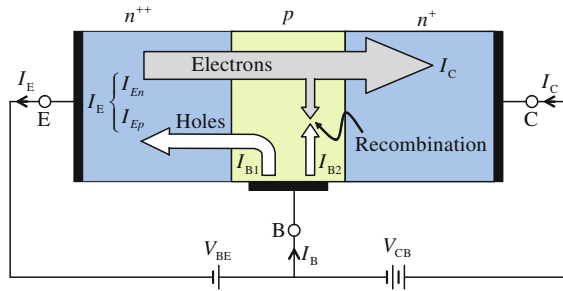


Fig. 3.143 **a** Schematic representation of NPN transistor. **b** Schematic representation of PNP transistor

breaking down the base–collector junction) by the electric field in the depletion region of the collector–base junction.

Thus, in forward active mode operation of a NPN BJT, the base–emitter voltage and collector–base voltage are positive which cause forward biased emitter–base junction and reverse biased base–collector junction. In this mode, electrons are injected from the emitter region into the base from where they diffuse toward the collector and are swept away or sucked in by the electric field in the reverse biased base–collector junction. As can be seen from Fig. 3.142, the current through emitter $I_E = I_{En} + I_{Ep}$, where I_{En} is due to diffusion of electrons from the emitter to the collector and $I_{Ep} = I_{B1}$ is due to holes or base majority carriers wandering into the emitter. Note that a hole entering is equivalent to an electron leaving. The diffusion current I_{En} combines with some holes (I_{B2}) within the base and depletes the current. This is called recombination and it can be reduced when the base is sufficiently thin (much less than diffusion length of electrons). From Fig. 3.142, we can write $I_E = I_C + I_B$ where $I_C \gg I_B$. The ratio of the currents is defined by factors $\alpha_F = I_C/I_E$ and $\beta_F = I_C/I_B$. These factors are influenced by the operating temperature. At room temperature, the emitter current increases by about a factor of 10 for a small increase in V_{BE} by approximately 50 to 60 mV.

Figure 3.143 shows the schematic representation of the NPN and PNP transistors. In case of the NPN transistors, the principal current flows in at the collector and it comes out at emitter (also see Fig. 3.142). In case of PNP transistor the principal current flows in at the emitter and comes out at the collector. In both cases (i.e., NPN and PNP types) the control signal is applied to the base.

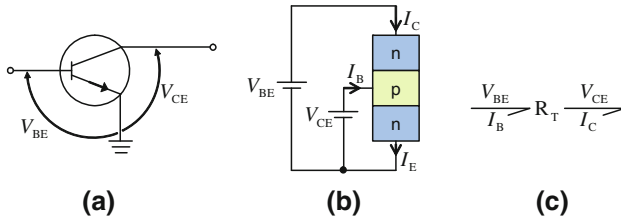
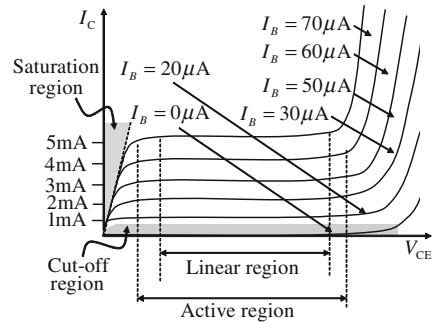


Fig. 3.144 a and b Grounded emitter representations of the NPN transistor and c bond graph model of grounded emitter model of the NPN transistor

Fig. 3.145 BJT characteristic curve



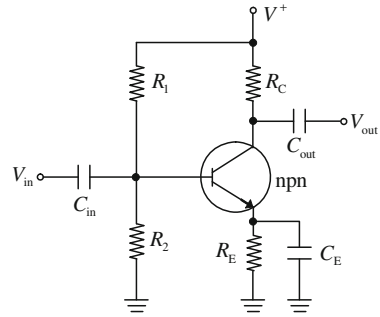
Now let us take the case of the NPN transistor shown in Fig. 3.143a. Let us apply an arbitrary voltage $-V_E$ at the three terminals of the transistor. This makes the emitter grounded, symbolically as shown in Fig. 3.144a or schematically as in Fig. 3.144b. This kind of setting a reference potential (or ground potential) leads to the common emitter model of a transistor. A bond graph model for this grounded emitter configuration can be created as two-port R field [22] as shown in Fig. 3.144c. We will detail the constitutive relation of the R-field at a later stage. Note that with known emitter point potential, the two-port R field relates the emitter referenced voltages to base and collector currents (I_B and I_C). The emitter current is not an independent output because $I_E = I_C + I_B$.

3.3.5.1 Transistor as an Amplifier

Transistors are nonlinear devices. However, for some steady value of control input, it can have an approximately linear characteristic. One characteristic curve of a typical BJT operating in forward active mode is shown in Fig. 3.145. As can be seen from the figure, the transistor behaves linearly away from the two knee points (marked as linear region in Fig. 3.145). Moreover, it can be seen that if there is a small change in base current I_B , one can get a large change in collector current I_C .

A transistor can operate in three operating regions. In the active region, the collector current is proportional to the base current with a large amplification gain. The

Fig. 3.146 An amplifier circuit using transistor



operating conditions of the transistor in cut-off region are zero input base current I_B , zero output collector current I_C , and maximum collector voltage V_{CE} which results in a large depletion layer and no current flowing through the device. In this condition, the transistor is said to be fully switched off. In the saturation region, the transistor is biased in a manner to result in maximum amount of base current which causes maximum collector current, minimum collector emitter voltage drop, and small depletion layer. In this condition, maximum current flows through the transistor and it is said to be fully switched on. The power loss from the transistor is least when it is fully off or fully on.

This characteristic of the transistor is exploited in various ways to design different electronic circuits. For use as an amplifier, the transistor is operated in the active region. For use as switch, the transistor is operated outside the active region, i.e., its operation is shifted back and forth between the saturation and cut-off regions.

To illustrate how to create the bond graph model of a circuit using transistors, let us take an example as shown in Fig. 3.146 where transistor has been used as an amplifier. For this system, the bond graph can be drawn as shown in Fig. 3.147. Here transistor has been modeled as a R field. The R-field parameters change depending upon the causalities at the ports, i.e., the base, emitter, and collector terminal connections [19, 22]. These parameters (usually linearized about some operating point because the V-I characteristic is linear in the active region) are termed z, y, h, and g-parameters in electronics literature. For the causality assigned to the R-field in Fig. 3.147, y parameter will be used.

The R-field used in the bond graph model does not clearly show the energy flow path. In fact, the flow injection (as shown earlier in Fig. 3.142) can be better revealed if we expand the R-field. In the given causality, the R field receives two effort signals (V_{BE} and V_{CE}) and computes two flow signals (I_B and I_C). The two direct or diagonal resistances in the R-field can be retained as two one-port resistances. The cross resistances modeling dependence of I_B on V_{BE} and I_C on V_{BE} can be modeled by active feedbacks through effort detectors and modulated flow sources (called flow injections). In this type of model, internal current components are clearly revealed as shown in the bond graph model given in Fig. 3.148. These current components are the transistor's linking current, i.e., the current that flows from the collector through

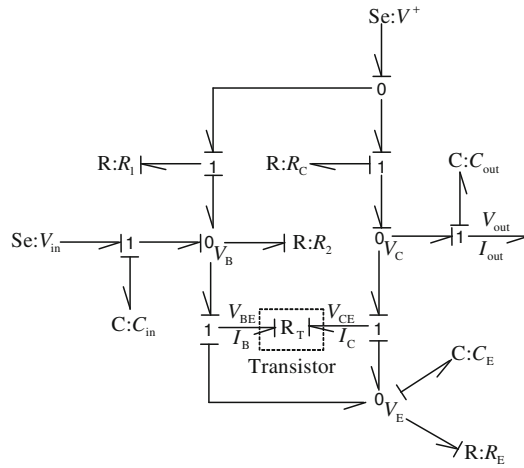


Fig. 3.147 Bond graph of an amplifier circuit using transistor

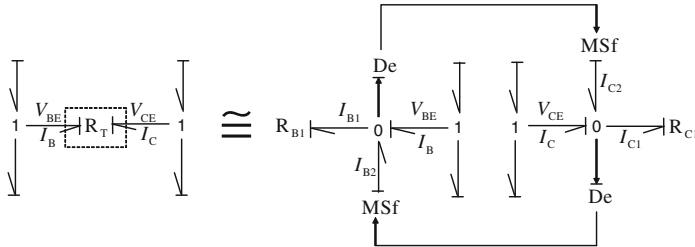


Fig. 3.148 Flow injections in the BJT two-port model

the base and finally into the emitter. The two source of flows in the model illustrate the active nature of the transistor.

3.3.5.2 Transistor as a Switch

In mechatronic systems transistor is often used as a switch. When using the transistor as a switch, a small base or input current controls a much larger collector or output load current. To understand how transistor can be used as a switch, let us consider the common emitter configuration of the transistor as shown in Fig. 3.149.

Applying Kirchoff's voltage rule to input and output sides of the circuit, we get

$$V_{BB} = I_B R_B + V_{BE} \tag{3.169}$$

and

$$V_{CE} = V_{CC} - I_C R_C \tag{3.170}$$

Fig. 3.149 Common emitter configuration of NPN BJT used as a switch

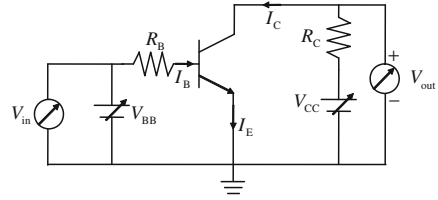
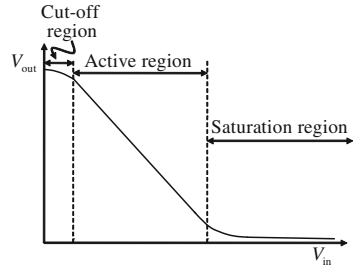


Fig. 3.150 Saturation, cut-off, and active operating regimes of a transistor



Let us take V_{BB} as DC input voltage V_{in} and V_{CE} as DC output voltage V_{out} . Then we can write Eqs. 3.169 and 3.170 as

$$V_{in} = I_B R_B + V_{BE} \tag{3.171}$$

and

$$V_{out} = V_{CC} - I_C R_C \tag{3.172}$$

Let us try to understand how V_{out} changes as we increase V_{in} from zero value onwards for silicon NPN BJT.

The transistor behavior can be described for three conditions by keeping V_{CC} fixed and varying the control signal or the base input voltage $V_{in} = V_{BB}$ (see Fig. 3.150):

1. When both $V_{BE} < 0$ and $V_{BC} < 0$ (this is always so for reverse biasing collector–base junction), both collector–base and emitter–base junctions are reverse biased and the transistor is in the cut-off region. For silicon NPN BJT, this actually happens when $V_{in} < 0.6\text{ V}$ (approximately, 0.7 V is the knee voltage of junction diode). In this condition, there will be no output current (i.e., $I_C = 0$) and the transistor is said to be in fully off-state (Fig. 3.150). Thus, from Eq. 3.172, we find $V_{out} = V_{CC}$.
2. When $V_{in} > 0.6\text{ V}$, the collector–based junction is reverse biased and the emitter–base junction is forward biased. In this condition, there is some output current I_C and the transistor is said to be in forward active state as shown in Fig. 3.150. From Eq. 3.172, V_{out} decreases as I_C increases. With increase of V_{in} , I_C increases almost linearly and thus V_{out} decreases linearly till its value becomes less than almost 1.0 V .

3. If V_{in} is increased further then relation between V_{in} and V_{out} becomes nonlinear. Due to increase of I_C , V_{out} value becomes very small though it may never become zero and transistor is said to have gone into a state of saturation. Note that $V_{out} = V_{CE}$. The nonlinear portion of the transistor characteristic will be discussed later when we discuss the large signal model of a transistor (Fig. 3.159). The transistor is now said to be fully on.

If we observe the schematic plot between V_{out} and V_{in} given in Fig. 3.150, it can be seen that the transitions from cut-off state to active state and from active state to saturation state are not sharply defined.

Use of a transistor as a switch has been discussed many times in this chapter. For example, we can consider the switches in the H-bridge arrangement for pulse-width modulation and in sample and hold device. Let us see how transistor can be used as a switch with base voltage ($V_{in} = V_{BB}$) as the controlling signal.

- If V_{in} is lower than cut-off threshold such that it is unable to forward bias the emitter–base junction then I_C is low and V_{out} is high. The transistor is said to be fully switched off (or the equivalent mechanical switch is open and breaks the circuit).
- If V_{in} is high enough to drive the transistor into saturation then I_C is high and V_{out} is low. The transistor is said to be fully switched on (or the equivalent mechanical switch is closed).

Thus, if we determine the lower and higher input voltage thresholds corresponding to cut-off and saturation of the transistor then we can regulate the output of the transistor between two discrete states.

Note that for inductive or capacitive loads (e.g., a relay) the actual circuit needed to operate the NPN BJT as a switch needs an additional diode (called a flywheel diode or protective diode) in parallel to the load resistor so that large instantaneous inductive reverse collector current is isolated. For heavy load applications needing large output current, the amplification (or DC current gain) of the BJT may become too low. In this case, a small gain input transistor is used to switch on or off a larger gain second or output transistor as shown in Fig. 3.151. The two transistors are connected in series, which is referred to as a complementary gain compounding configuration or more commonly as a Darlington transistor or Darlington pair configuration. Darlington transistors contain two BJTs in series so that the net current gain is the product of the current gains of individual transistors and the whole device behaves like a single transistor switch with a large effective current gain for a much smaller base current.

Transistor as a switch is also used in a buck converter. A buck converter is a step-down DC to DC converter. A buck converter can operate at efficiency above 95%. Note that a potentiometer like arrangement (see Fig. 3.86) can also be used to step-down DC voltage. However, such step-down of DC voltage can be useful only for DC voltage measurement. If one needs to draw power on the output side, such as to drive a motor, then current must flow through the resistor which will lead to heavy power loss. Thus, a buck converter is used as DC step-down transformer when the output load draws enough current.

Fig. 3.151 Darlington transistor configuration using NPN BJT

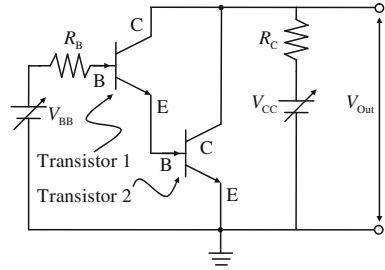
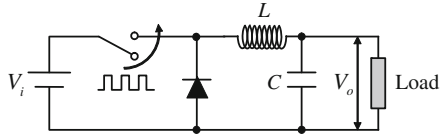


Fig. 3.152 Buck converter configuration using NPN BJT



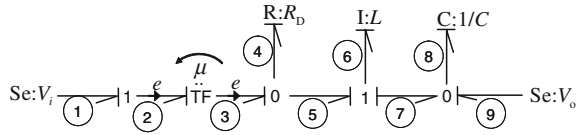
The buck converter is typically used in laptop computers, mobile phone battery chargers, etc. It is generally used to convert 12V battery output in a laptop to few volts needed by the processors. Its high efficiency means that a fully charged battery can last longer. A buck converter is a simple circuit with a transistor switch, a diode, an inductor, and a capacitor as shown in Fig. 3.152. The flywheel diode is used to stop the reverse inductive current. The transistor base current is a pulse-width modulated square wave which drives the transistor as a switch. The actual circuit and connections to the transistor are not shown here. The switch symbol in Fig. 3.152 means a PNP transistor whose output is either V_i or zero, depending on the base current. Here, a PNP transistor is used as a switch because of negative ground, for positive ground one can use NPN transistor.

The bond graph model of the buck converter is given in Fig. 3.153 where the transistor switch has been modeled as an ideal switch. Note that a transistor’s response time is usually a few nanoseconds which is much less than the buck converter’s response time. Thus, ideal switch assumption does not change the system response. The load is assumed to be a constant voltage V_o . The transformer modulus μ is switched between 1 (on) and 0 (off). The diode is modeled by element R_D which has an idealized constitutive relation

$$R_D = \begin{cases} R_{\text{High}} & \text{if } e > 0 \text{ (diode is reverse biased)} \\ R_{\text{Low}} & \text{if } e \leq 0 \text{ (diode is forward biased)} \end{cases}$$

Note that the diode could be modeled with its actual constitutive relations. However, it may be noted that the diode resistance does not appear in system equations because the effort at the 0-junction to which it is attached is determined by the source. The diode is simply there to complete the circuit when the transistor is switched off. Moreover, no current flows through the diode when the transistor switch is on and no voltage drop occurs across the diode (because it is assumed to be ideal) when the

Fig. 3.153 Bond graph model of buck converter assuming ideal switch behavior and constant voltage load



transistor switch is off. Thus, one factor of power (e or f) is always zero and the net power dissipation in the diode is zero. So, it can be removed from the model. If a real diode has to be actually modeled then we need to consider two bond graphs: one without the diode and the other without the voltage source and the switch. There would then be two sets of system equations and one of them would be active at one point of time. This kind of a system is then called a hybrid system (a system with discrete mode changes). It is possible to create one combined bond graph model for a hybrid system with variable causality and such a bond graph model is called a hybrid bond graph.

Let us assume that the square wave pulse operating the switch has a time period T and it is on for time duration κT and remains off for time duration $(1 - \kappa) T$ where $0 \leq \kappa \leq 1$ and κ decides the duty cycle. When the switch is closed, the diode is reverse biased ($R_D = R_{High}$ and $f = e/R_{High} = 0$) and no current flows through it. During this period, the inductor stores energy. From the bond graph, we find the effort in bond 6 during $\mu = 1$ as

$$\begin{aligned} e_6 &= e_5 - e_7 \\ &= \mu e_1 - e_9 \\ &= V_i - V_o \end{aligned} \tag{3.173}$$

Thus, the current in the inductor at $t = \kappa T$ is found to be

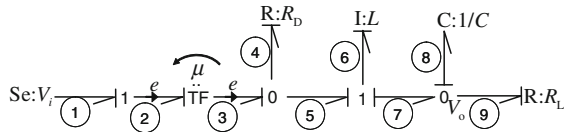
$$\begin{aligned} f_6 &= \frac{1}{L} \int_{-\infty}^{\kappa T} e_6 dt \\ &= I_0 + \frac{1}{L} \int_0^{\kappa T} e_6 dt \\ &= I_0 + \frac{(V_i - V_o) \kappa T}{L} \end{aligned} \tag{3.174}$$

where I_0 is the current at $t = 0$.

Let us now analyze what happens for the duration $t = \kappa T$ to $t = T$, i.e., when $\mu = 0$. The diode is forward biased and conducts freely to complete the circuit. During this period, the effort in bond 6

$$\begin{aligned} e_6 &= e_5 - e_7 \\ &= \mu e_1 - e_9 \\ &= -V_o \end{aligned}$$

Fig. 3.154 Bond graph model of buck converter assuming ideal switch behavior and resistive load



and the current in the inductor

$$\begin{aligned}
 f_6 &= \frac{1}{L} \int_{-\infty}^T e_6 dt \\
 &= I_{\kappa T} + \frac{1}{L} \int_{\kappa T}^T e_6 dt \\
 &= I_0 + \frac{(V_i - V_o)}{L} \kappa T - \frac{V_o}{L} (1 - \kappa) T
 \end{aligned} \tag{3.175}$$

where $I_{\kappa T} = I_0 + \frac{(V_i - V_o)}{L} \kappa T$ is the current at $t = \kappa T$.

In steady-state operation, the currents must be same at beginning and end of a cycle, i.e., at $t = 0$ and $t = T$. Thus, we must satisfy

$$I_0 = I_0 + \frac{(V_i - V_o)}{L} \kappa T - \frac{V_o}{L} (1 - \kappa) T \tag{3.176}$$

$$\Rightarrow \frac{(V_i - V_o)}{L} \kappa T = \frac{V_o}{L} T - \frac{V_o}{L} \kappa T \tag{3.177}$$

which gives

$$V_o = \kappa V_i \tag{3.178}$$

Because $0 < \kappa < 1$, the output voltage is always less than the input voltage and the buck converter acts as a DC step-down transformer.

Let us now consider a resistive load. The bond graph model of the circuit can now be given as shown in Fig. 3.154. In this case, the load voltage is decided by the current through the resistor and it is no more constant. Moreover, the C element modeling the capacitor in the circuit now appears in integral causality. The ideal diode is dropped from the model for simulation.

The simulation of the bond graph model given in Fig. 3.154 was performed with the following data: $V_i = 12\text{ V}$, $L = 0.01\text{ H}$, $C = 0.01\text{ }\mu\text{F}$, $R_L = 1\text{ k}\Omega$. This limits the peak collector current within 12 mA. The pulse time period and duty cycle were chosen as $T = 3\text{ }\mu\text{s}$ and $\kappa = 0.25$ (25% on time and 75% off time). As a result, the expected output voltage is $V_o = \kappa V_i = 0.25 * 12\text{ V} = 3\text{ V}$. The response of output voltage and the voltage across the inductor are shown in Fig. 3.155. It is found that the steady-state value of output voltage is indeed 3 V and it is reached fairly quick within 50 μs . Moreover, at all times during the transient when the transistor is off, the minimum value of the potential across the inductor is negative of the maximum output voltage at the previous instance when the transistor was on.

Fig. 3.155 Time response of buck converter with a resistive load

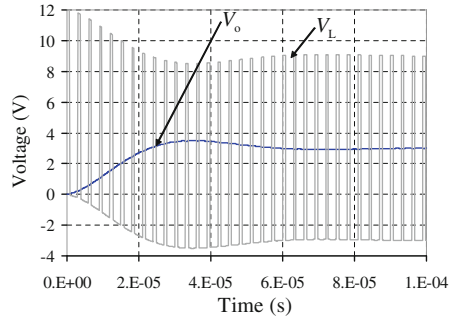
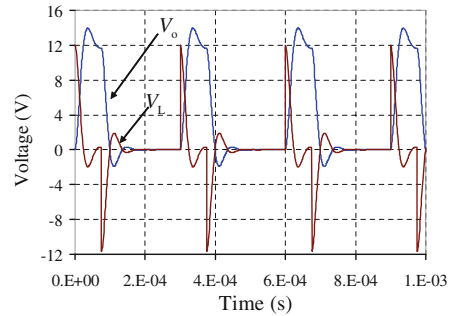


Fig. 3.156 Time response of buck converter with a resistive load and large switching time period



Note that the response settling time changes depending on the load resistance. For heavy load, it can take significant time to reach the steady state. For too small load resistance, the heavy current through the load during transistor off time may fully drain the energy stored in the circuit during the transistor on time and thus the step-down transformation fails. This is a critical issue that needs careful design. Figure 3.156 shows the response of the buck converter system with the same parameter values as chosen before, but with pulse time period taken as $T = 300 \mu\text{s}$. The response shows complete drain out of the energy during the transistor off time and thus the output voltage repeatedly falls to zero.

Although we are not discussing the hybrid bond graph in this book, the system equations from hybrid bond graph would look as follows:

$$\dot{P}_6 = \begin{cases} V_i - Q_8/C & \text{if } nT \leq t < (n + \kappa) T \\ -Q_8/C - R_D(P_6/L) & \text{if } (n + \kappa) T \leq t < (n + 1) T \end{cases} \quad (3.179)$$

$$\dot{Q}_8 = P_6/L - Q_8/(CR_L) \forall t \quad (3.180)$$

where function $R_D(i)$ with current $i = P_6/L$ models the voltage drop across the diode and $n = 0, 1, 2, \dots$ represents the number of elapsed time periods and is found as the truncated integer value of t/T , which can be modeled in C-language as $n = \text{floor}(t/T)$. Note that the simulation of hybrid model with a small potential drop across the diode gives the same result as before.

Transistors can switch very rapidly, but they cannot switch AC or high voltages. Transistors are also not good at switching large currents. In such cases, using relays is a better choice and a transistor can be used to switch the current in the relay's coil. However, relays cannot switch rapidly and usually require much more power.

For other applications of transistor and their bond graph models, one can see [7] for Colpitt's oscillator and Chua circuit simulation.

3.3.5.3 Linearization and Small-Signal Transistor Model

For small signal applications, the transistor is usually brought to a given operating point which is defined by a operating voltage V_{CE} and a base current I_B . The transistor is then operated by marginally fluctuating the base current around the operating point. The operating point lies in the linear zone (see Fig. 3.145). Thus, one can use a linearized model for transistor operation. In fact, one needs two models: the first is a full model which models the process of bringing the transistor to the operating point and the second is a small signal (AC signal superposed over a static DC or operating voltage) model. The linearized small signal model is also called an AC equivalent circuit. The additional impedances with zero-mean AC frequency input (assuming small amplitude and low frequency) are negligible for resistances as compared to inductances and capacitances in the circuit. Thus, resistances are removed from the AC equivalent circuit. For example, the amplifier circuit shown in Fig. 3.146 would contain only the transistor and three capacitors. In the model of this equivalent circuit, we can use an linearized description of the R field.

The linearization of the two-port R field depends on the causality on its two ports, i.e., what are the known signals and what are the unknown variables that have to be computed. Accordingly, one has to select the proper operating curve on which linearization has to be performed. For example, if we know V_{CE} and I_B then we can use the characteristic curve given in Fig. 3.145 to obtain I_C . However, we cannot use the same characteristic curve if I_B and I_C are known and V_{CE} and V_{BE} have to be computed. Therefore, different sets of characteristic curves are used for linearization depending upon the causality on the ports of the two-port R field. The description of those linearized models is shown in Fig. 3.157.

The y- and h-parameter models are most commonly used for small signal modeling of BJTs. In the h-parameter model (fourth item in Fig. 3.157) for common emitter configuration, input current I_B and output voltage V_{CE} are independent variables. In this model, parameters h_{11} and h_{22} are direct impedances (diagonal terms in the matrix). One can write

$$V_{BE} = h_{11}I_B + h_{12}V_{CE}$$

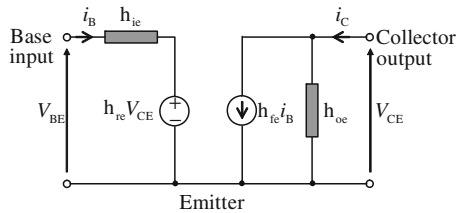
where h_{11} is a linear resistance and $h_{12}V_{CE}$ is voltage controlled voltage source (effort activated transformer). Likewise,

$$I_C = h_{21}I_B + h_{22}V_{CE}$$

Fig. 3.157 Two-port R field linearized model of BJT under different causal orientations

$$\begin{aligned} \left. \begin{array}{c} V_{BE} \\ I_B \end{array} \right\} R_T \left. \begin{array}{c} V_{CE} \\ I_C \end{array} \right\} & \left\{ \begin{array}{c} V_{BE} \\ V_{CE} \end{array} \right\} = \begin{bmatrix} z_{11} & z_{12} \\ z_{21} & z_{22} \end{bmatrix} \left\{ \begin{array}{c} I_B \\ I_C \end{array} \right\} \\ \left. \begin{array}{c} V_{BE} \\ I_B \end{array} \right\} R_T \left. \begin{array}{c} V_{CE} \\ I_C \end{array} \right\} & \left\{ \begin{array}{c} I_B \\ I_C \end{array} \right\} = \begin{bmatrix} y_{11} & y_{12} \\ y_{21} & y_{22} \end{bmatrix} \left\{ \begin{array}{c} V_{BE} \\ V_{CE} \end{array} \right\} \\ \left. \begin{array}{c} V_{BE} \\ I_B \end{array} \right\} R_T \left. \begin{array}{c} V_{CE} \\ I_C \end{array} \right\} & \left\{ \begin{array}{c} I_B \\ V_{CE} \end{array} \right\} = \begin{bmatrix} g_{11} & g_{12} \\ g_{21} & g_{22} \end{bmatrix} \left\{ \begin{array}{c} V_{BE} \\ I_C \end{array} \right\} \\ \left. \begin{array}{c} V_{BE} \\ I_B \end{array} \right\} R_T \left. \begin{array}{c} V_{CE} \\ I_C \end{array} \right\} & \left\{ \begin{array}{c} V_{BE} \\ I_C \end{array} \right\} = \begin{bmatrix} h_{11} & h_{12} \\ h_{21} & h_{22} \end{bmatrix} \left\{ \begin{array}{c} I_B \\ V_{CE} \end{array} \right\} \end{aligned}$$

Fig. 3.158 Equivalent circuit of h-parameter model of NPN BJT used for small signal AC analysis



where h_{22} is a linear conductance and $h_{21} I_B$ is a current controlled current source (flow activated transformer).

The equivalent circuit of the h-parameter model can be drawn as shown in Fig. 3.158.

In Fig. 3.158, input resistance $h_{ie}=h_{11}$, transconductances $h_{re}=h_{12}$ and $h_{fe} = h_{21}$, and output resistance $h_{oe} = 1/h_{22}$. The small letter subscripts indicate that the model is meant for AC analysis. Note that h_{re} represents the dependence of the transistor voltage-current characteristic curve on the value of V_{CE} . As can be seen from Fig. 3.145, I_C does not change much due to change in V_{CE} (in the flat linear regime where the slope is very small). The same is true for change in V_{BE} due to change in V_{CE} around the operating point. Thus, usually one neglects h_{re} (i.e., $h_{re} = 0$) from the model. Parameter h_{fe} is the current-gain (sometimes referred to as DC gain β_F or h_{FE}) of the transistor. As a further simplification, the output admittance can be considered to be infinite and thus $h_{oe} = 0$, i.e., it can be dropped from the model. The h-parameter model is very similar to hybrid-pi or Giacoletto model. Note that the h-parameter model is suitable for only small-signal low-frequency analysis. For high-frequency analyses, h-parameter model can be adapted with inclusion of inter-electrode capacitances and other parasitic elements.

3.3.5.4 Large Signal Model

The transport model for a BJT describes the three currents in the transistor. This transport model is similar to the constitutive relation of a diode with the addition for the diffusion of electrons through the base. These transport equations for a BJT,

called Ebers-Moll equations, are given as

$$I_C = I_S \left(\exp \left(\frac{V_{BE}}{V_T} \right) - \exp \left(\frac{V_{BC}}{V_T} \right) \right) - \frac{I_S}{\beta_R} \left(\exp \left(\frac{V_{BC}}{V_T} \right) - 1 \right) \quad (3.181)$$

$$I_B = \frac{I_S}{\beta_F} \left(\exp \left(\frac{V_{BE}}{V_T} \right) - 1 \right) + \frac{I_S}{\beta_R} \left(\exp \left(\frac{V_{BC}}{V_T} \right) - 1 \right) \quad (3.182)$$

$$I_E = I_B + I_C = I_S \left(\exp \left(\frac{V_{BE}}{V_T} \right) - \exp \left(\frac{V_{BC}}{V_T} \right) \right) + \frac{I_S}{\beta_F} \left(\exp \left(\frac{V_{BE}}{V_T} \right) - 1 \right) \quad (3.183)$$

where $V_T = kT/q = T/11600$ is the thermal voltage, I_S is the reverse saturation current, β_F (or h_{FE}) is the forward common emitter current gain, and β_R is the reverse common emitter current gain. Typically, I_S is in the range of 10^{-15} – 10^{-12} A, β_F is in the range of 20–500, and β_R is in the range of 0–20. The complete Ebers-Moll equations describe both forward and reverse mode operation. The first term in collector and emitter current expressions gives current transported completely through the base region.

Recall the definition of current gains. For forward active operation, they are

$$\begin{aligned} \alpha_F &= I_C/I_E \\ \beta_F &= I_C/I_B \\ &= \frac{I_C}{I_C - I_E} \\ &= \frac{\alpha_F}{1 - \alpha_F} \end{aligned}$$

where α_F is the common base forward short-circuit current gain whose value lies between 0.98 and 0.998.

The forward-active, reverse-active, and saturation characteristics are schematically shown in Fig. 3.159. Note that I_C is proportional to I_B in both forward and reverse active modes. The NPN BJT is in forward active mode for $V_{CE} > V_{BE}$ and $I_C = \beta_F I_B$ is a relation which holds for all values of V_{CE} . For $V_{CE} < V_{BE}$, the transistor is in saturation. In saturation regime, I_C is approximately proportional to V_{CE} as indicated by the dashed line in Fig. 3.159. Similar relations hold good for reverse active mode. The proportionality approximation does not hold for a very small range of operation between saturation and forward or reverse active mode operations (near knee points). Likewise, in the common base characteristic, $I_C = \alpha_F I_E$ is a relation which holds for all values of V_{CB} in forward-active mode operation and the similar conclusion can be drawn for reverse-active mode operation.

The equivalent circuit model of Ebers-Moll equations is shown in Fig. 3.160 where α_R is the reverse common base current gain with $\alpha_R = \beta_R/(1 + \beta_R)$.

The Ebers-Moll equations for forward active mode operation with $\alpha_F = \beta_F/(1 + \beta_F)$ are obtained by setting $V_{BC} = 0$ in full Ebers-Moll equations and are given

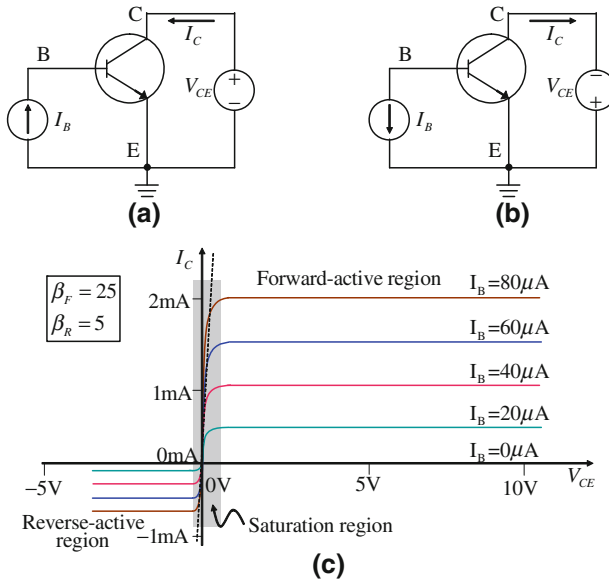
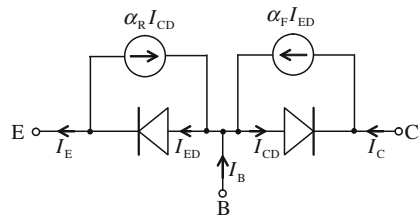


Fig. 3.159 **a** forward-active mode operation of NPN BJT, **b** reverse-active mode operation of NPN BJT, and **c** NPN BJT characteristic in saturation, forward and reverse active modes for $\beta_F = 25$ and $\beta_R = 5$

Fig. 3.160 Equivalent circuit of full Ebers-Moll NPN BJT model



as

$$I_C = I_F = I_S \left(\exp \left(\frac{V_{BE}}{V_T} \right) - 1 \right) \tag{3.184}$$

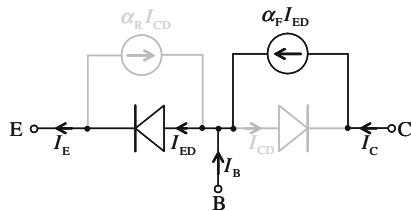
$$I_B = \frac{I_F}{\beta_F} = \frac{I_S}{\beta_F} \left(\exp \left(\frac{V_{BE}}{V_T} \right) - 1 \right) \tag{3.185}$$

$$I_E = I_B + I_C = \frac{I_S}{\alpha_F} \left(\exp \left(\frac{V_{BE}}{V_T} \right) - 1 \right) \tag{3.186}$$

The equivalent circuit obtained from the above equations (a simplified form of Fig. 3.160) is shown in Fig. 3.161.

The Ebers-Moll equations for reverse operation are

Fig. 3.161 Equivalent circuit of Ebers-Moll NPN BJT model for forward active mode operation



$$I_R = -I_E = I_S \left(\exp \left(\frac{V_{BC}}{V_T} \right) - 1 \right) \tag{3.187}$$

$$I_B = \frac{I_R}{\beta_R} = \frac{I_S}{\beta_R} \left(\exp \left(\frac{V_{BC}}{V_T} \right) - 1 \right) \tag{3.188}$$

$$I_C = -\frac{I_S}{\alpha_R} \left(\exp \left(\frac{V_{BC}}{V_T} \right) - 1 \right) \tag{3.189}$$

The forward and reverse active modes are different due to asymmetric doping. Thus, the parameter β_R has a significantly lower value compared to β_F . The complete Ebers-Moll equations are obtained by combining the forward and reverse currents. The internal base current is due to diffusion of charges which can be determined from Fick’s law. However, it is not required in this model.

Another modification is needed in the model to account for the Early effect, i.e., the variation in the extent of the depletion region. The collector–base depletion region width increases with increase in the collector–base voltage V_{CB} ($V_{CB} = V_{CE} - V_{BE}$) due to the increased reverse bias at the collector–base junction. As the depletion region width increases, the effective base width through which electrons diffuse reduces because electrons are sucked in or swept away to the collector as they reach the depletion region. The reduced effective base width reduces the recombination and increases the charge concentration and gradient within the base. This leads to increased collector current, i.e., the current amplification factor increases. The variation in effective base width can be incorporated into the Ebers-Moll model with a redefined forward common emitter current gain as a function of V_{CB} .

The Ebers-Moll equations define the constitutive relation of the bond graph two-port R-field used to model BJTs. Note that there are actually two independent Ebers-Moll equations, the third is deduced algebraic from the first two. The two Ebers-Moll relations (excluding equation for I_E) can be directly used when the R field is causalled such a way that it appears in conductive causality in both of its ports. Otherwise, recursive numerical solution of the equations to find the root (solution) is required.

3.3.5.5 Detailed Nonlinear Model

In this section, we will show how a bond graph model gives a clear picture of the Ebers-Moll model and the energy flow within the BJT. This bond graph model is

Fig. 3.162 Schematic cross-section of laterally diffused NPN

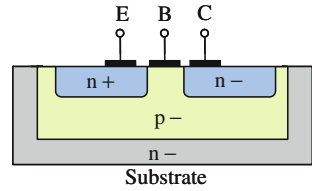
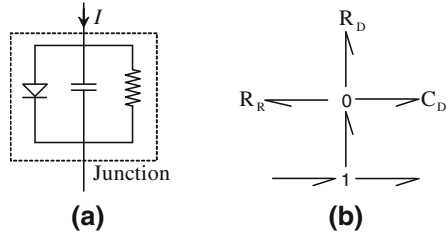


Fig. 3.163 BJT junction diode model: **a** equivalent circuit model and **b** bond graph model



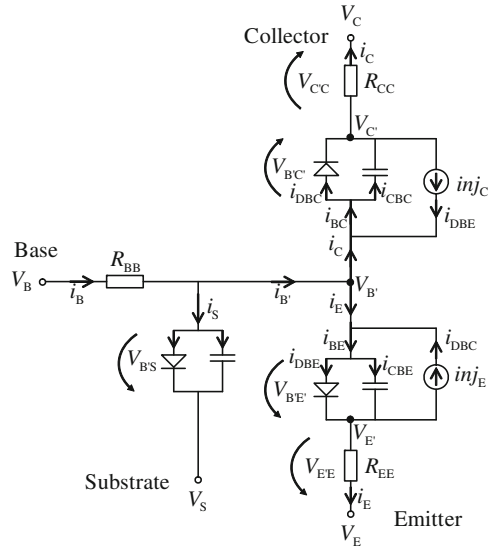
based on the one presented in [11, 26, 27]. This is a well-validated model of a BJT. We will discuss the bond graph model of a laterally diffused NPN BJT as shown in Fig. 3.162. Models of vertically diffused (parallel) NPN BJT and PNP BJTs can be consulted in [5, 10, 11].

In the model of the laterally diffused NPN BJT, we recognize three diode-like junctions: base-emitter junction, base-collector junction, and base-substrate junction. Each of these junctions can be modeled as an equivalent diode. The equivalent circuit model of diode-like junctions in a transistor and its bond graph representation are shown in Fig. 3.163. In the bond graph model, element R_D models the Shockley diode equation, element C_D models the junction capacitance (build up of holes and electrons near the junction) and element R_R models the recombination effect which causes slow discharge of the capacitor. Note that all the three elements in the junction diode model are highly nonlinear and they further depend on the operating temperature.

The equivalent circuit of the laterally diffused NPN BJT can be given as shown in Fig. 3.164. Note that in the diode models, R_R elements for diode models are dropped because the slow discharge is not relevant to the fast dynamics of the transistor being modeled here. At a later stage, these resistances can be separately included in the model. This model contains three junction diodes (with junction capacitances). The resistances R_{BB} , R_{CC} , and R_{EE} are input and output resistances. Various potential points, potential drops, and currents in branch are marked in the model. For example, $V_{B'E} = V_{B'E'} + V_{E'E}$. The flow injections or linking currents modeled as inj_C and inj_E are according to full Ebers-Moll model (see Fig. 3.160). Here, for lateral diode configuration, the substrate junction diode appears between the base and substrate potentials. For vertical diode configuration, the substrate junction diode would appear between the collector and substrate potentials.

One can see from Fig. 3.164 that $inj_C = I_{DBE}$, which is the current that passes through the diode between the base and the emitter. Likewise, $inj_E = I_{DBC}$, which is the current that passes through the diode between the base and the collector. Thus,

Fig. 3.164 Equivalent circuit model of laterally diffused NPN BJT



the injected current on one side of the base is actually equal to the current passing through the diode on the other side of the base. The linking current, i.e. the current that passes through the base between the collector and emitter, is $inj_E - inj_C$. The flow injections are given by diode equation. Thus we can write

$$inj_C = I_{DBE} = I_S \left(\exp \left(\frac{qV_{B'E'}}{kT} \right) - 1 \right) \tag{3.190}$$

$$inj_E = I_{DBC} = I_S \left(\exp \left(\frac{qV_{B'C'}}{kT} \right) - 1 \right) \tag{3.191}$$

and linking current

$$i_L = I_{DBE} = I_S \left(\exp \left(\frac{qV_{B'C'}}{kT} \right) - \exp \left(\frac{qV_{B'E'}}{kT} \right) \right) \tag{3.192}$$

The bond graph model of the lateral NPN BJT shown in Fig. 3.165 is drawn from the equivalent circuit. The diodes are modeled by nonlinear resistances R_{DBS} , R_{DBC} and R_{DBE} . The three junction capacitances give three states which when multiplied with inverse of the corresponding capacitances give the potentials across the junction capacitances. These potentials are used to compute the currents through the diodes. The flow injections are modeled as two modulated sources (MSf_C and MSf_E) which are the current returned by two junction diodes (R_{DBE} and R_{DBC}). The bond graph model also shows the link between the flow injections and current through the junction diodes on the opposite sides of the base.

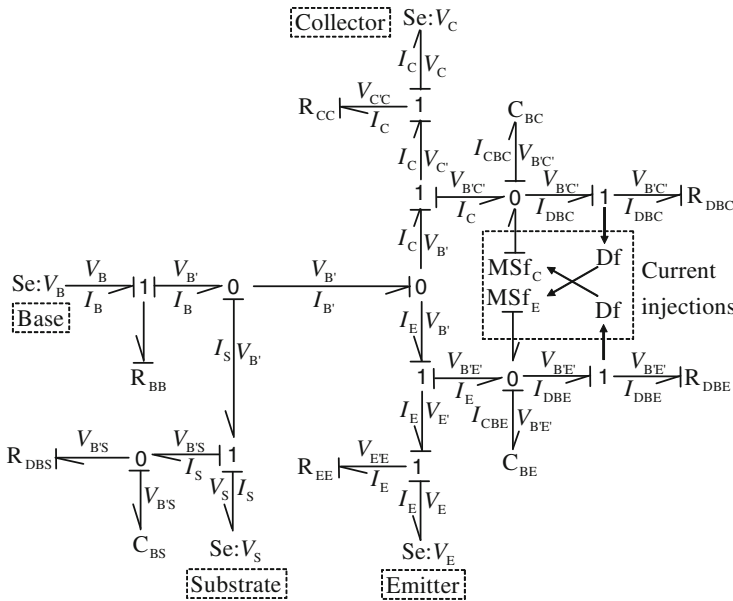


Fig. 3.165 Bond graph model of laterally diffused NPN BJT showing flow injections

Because the flow injection to emitter depends on potential difference across the collector–base junction diode and flow injection to collector depends on emitter–base junction diode, we can easily use an R field to model this cross coupling. Then the resulting model can be given as shown in Fig. 3.166 where the two-port field R_D models both the flow injections (given in Eqs. 3.190 and 3.191) and the direct diode resistances (R_{DBC} and R_{DBE}). The nonlinear R field receives two effort information and computes two flow information. For other causalities at the ports of the two-port R field, the constitutive relations can be appropriately written. The flow variables in two bonds of two-port R field are the resultant of the flow injection (MSf) and diode current at the corresponding 0-junctions in Fig. 3.165.

In [26, 27], the authors argued that the above-discussed bond graph models still use current sources (or R field) to describe the current injections and thus, the bond graph model does not provide any deeper intuition compared to the equivalent circuit model. The bond graph model being a portrayal of power exchange between subsystems has to explain where these current sources (injection currents) draw their power from. To remedy the problem with the circuit model, the authors of [26, 27] reformulated the Ebers-Moll equations in a different form with the help of the previously developed bond graph models.

The correct model showing the energetics of the problem must be able to explain the linking current. Thus, instead of modeling the individual current injections, one can model only the linking current.

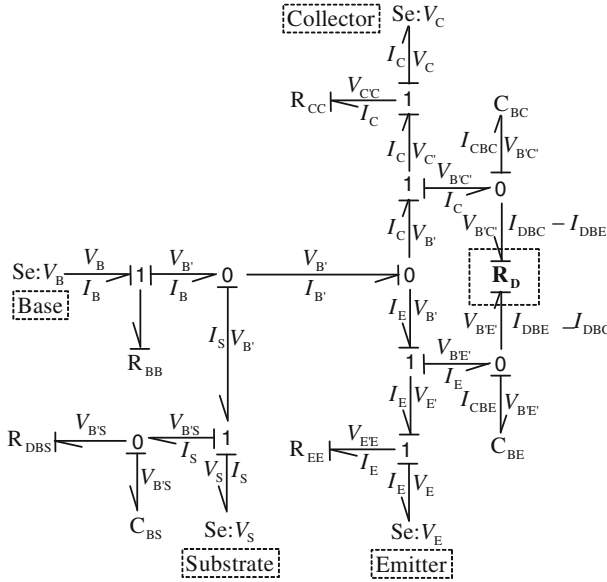


Fig. 3.166 Bond graph model of laterally diffused NPN BJT with two-port R field to model the flow injections

From Fig. 3.166, we find that the flow variables in the two ports of the R field are $I_{DBC} - I_{DBE}$ and $I_{DBE} - I_{DBC}$. The magnitude of these two flow variables being equal indicates the existence of a hidden 1-junction. The opposite signs can be adjusted through power directions. Thus, we can replace the R field by a 1-junction and one-port R element as shown in Fig. 3.167. The effort variable in the bond connected to the one-port R element becomes $V_{B'E'} - V_{B'C'} = V_{C'E'}$. The R element cannot use this effort information to compute the flow, which is the linking current $I_L = I_{DBE} - I_{DBC}$ because the constitutive relation for the linking current given in Eq. 3.192 requires values of $V_{B'E'}$ and $V_{B'C'}$. Therefore, the one-port R element is modulated by the required effort signals. The bond graph in Fig. 3.167 shows the path of linking current from the emitter to the collector and gives a better physical understanding of the power transfer in the system compared to a flow injection-based model.

In [27], the same model given in Fig. 3.167 was obtained differently. From Fig. 3.165, one can write the weak junction laws for the two 0-junctions (flow sum relations) connected to flow injection sources as follows:

$$\begin{aligned} I_C + I_{DBE} - I_{CBC} - I_{DBC} &= 0 \\ \Rightarrow I_C + (I_{DBE} - I_{DBC}) &= I_{CBC} \end{aligned} \tag{3.193}$$

and

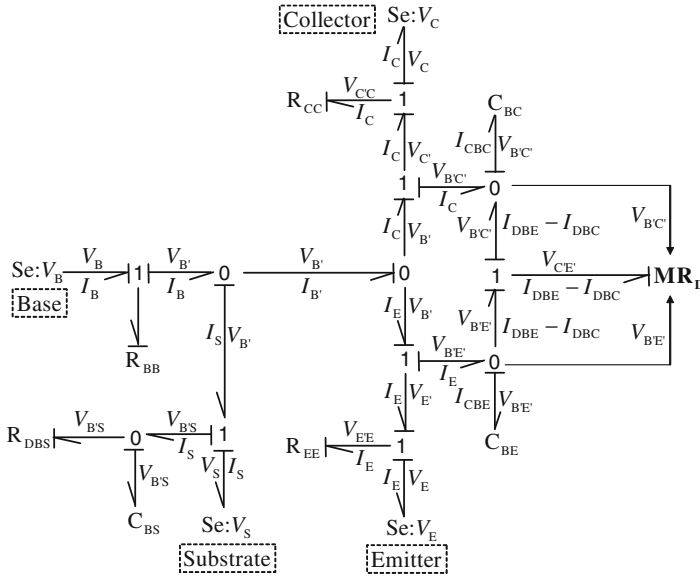


Fig. 3.167 Bond graph model of laterally diffused NPN BJT with linking current revealed in the model

$$\begin{aligned}
 I_E + I_{DBC} - I_{CBE} - I_{DBE} &= 0 \\
 \Rightarrow I_E &= (I_{DBE} - I_{DBC}) + I_{CBE}
 \end{aligned}
 \tag{3.194}$$

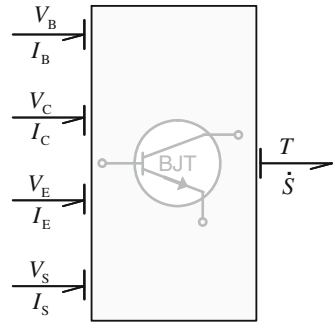
Moreover,

$$V_{C'E'} = V_{B'E'} - V_{B'C'}
 \tag{3.195}$$

Using the above three relations, the two-port R field in Fig. 3.166 can be decomposed into the one-port modulated R element.

In realistic transistor models, it is important to account for the operating temperature [8]. One can easily see that the junction diode characteristic (Eqs. 3.190–3.192) shows a strong dependence on the temperature. Likewise, junction capacitance and recombination resistances are also influenced by the temperature. Although it has not been shown in Figs. 3.165 to 3.167, temperature is always a modulating signal to all C and R elements in the bond graph model. We can neglect variation of the temperature across the transistor junctions and employ an average temperature. The temperature signal will actually be modeled as a passive bond instead of an active signal. This is due to the fact that the losses in various R elements contribute to increase the temperature of the transistor. Therefore, all R elements in the transistor model have to be in fact modeled as RS elements as discussed earlier (see Fig. 3.74). The power variables in the first port of the RS element are voltage (V) and current (I) whereas the power variables in the second port are temperature (T) and rate of entropy generation (\dot{S}). The voltage and current are related by a nonlinear constitutive relation like

Fig. 3.168 Encapsulated five-port submodel of laterally diffused NPN BJT



Eqs. 3.190–3.192 which in a general form can be given as $\Phi_R(V, I, T) = 0$. The rate of entropy generation is given as $\dot{S} = Q/T = VI/T$. Because we use a single average temperature as the effort variable for all RS elements, the total entropy output can be obtained at a 0-junction by summing individual entropy generation rates from all dissipative elements. Interested readers can look at the thermal modeling of PN junction behavior through bond graph approach presented in [8].

Thus, average temperature is an input to the lateral NPN BJT model and the total entropy flow rate is an output from the model. The sub-model for the lateral NPN BJT can be considered to have five passive interconnection ports as shown in Fig. 3.168.

Note that the entropy flow rate output from the model has to be used in a thermal model which should account for the heat generated by other electronic components, heat capacities of electronic items, substrate, etc., packaging details, conduction and radiation heat transfers, heat sinks (radiators), and the convection heat transfer through forced and/or natural cooling systems.

Transistors are integral parts of timer circuits. For example, a typical 555 timer IC can use about 25 transistors, 2 diodes, and 15 resistors on a silicon chip. Timers are essential to generate pulse-width modulation. Electronic timers use quartz clocks (tuning forks made of quartz or silicon-dioxide) and other electronic components. Timers are now mostly software implemented. Controllers in modern mechatronic systems use programmable logic controller (PLC) to implement timer. Timer circuits often implement some form of comparison logic to compare the timer value against a setpoint value and trigger some action when the timer count matches the setpoint. Examples of actions that can be triggered are pulse-width modulated waveform generation, buck converter duty-cycle regulation, etc.

3.4 Conclusions

In this chapter, we have developed models of various actuators, sensors, electronic circuits, and electronic devices. While modeling a mechatronic system, one often has to decide what level of details have to be considered. For example, while modeling the

op-amp integrator, it may not be useful to develop a full model of op-amp including its internal circuit elements. On the other hand, if one has to optimize the performance of an op-amp then the internal circuit has to be modeled with detailed models for transistors, diodes, and other elements. Likewise, while modeling the H-bridge circuit for pulse-width modulation, it is unnecessary to model the switches as transistor switches because the pulse width is usually hundreds or thousands of times more than the response time of transistors and thus, the idealized switch model (TF with modulus switching between 0 or 1) can be used. The decision on the details to be included in the model has to be made based on the time constants of the components in the system.

In mechatronic system design, most often we will use modulated sources (MSf and MSe) to represent actuators and detectors (De and Df) to represent sensors. An actuator model will be considered only when its response characteristic is comparable to the driven system's response characteristic or when the actuator output is significantly influenced by the system dynamics. For example, a DC motor driving a rotor system has to be modeled in details whereas a piezoactuator for a solenoid valve can be modeled as a modulated source.

Similarly, detailed sensor models should be considered when their response time is comparable to the system's response time. For example, a resistance thermometer and a regular strain gauge both have slow response time whereas infrared thermal sensor and piezo-type strain gauge both have fast response time. An accelerometer placed on a heavy gear box adds negligible mass whereas when it is placed at the tip of a thin beam, it can significantly change the system response due to the added mass. The key is to decide whether the sensor has to be modeled in details. Sensors like encoders and other non-contact sensors usually have very little energetic interaction with the system whereas a tachogenerator may load the system significantly.

A good modeling practice is to build simple sub-system models and then to compose the simple sub-system models to create further higher level sub-system models. The sub-system models can be thought of as objects in an object-oriented-modeling (OOM) framework. The final model of the system is obtained by integrating various sub-system models. This kind of modeling is called hierarchical modeling and it is a practice that is followed worldwide by system designers. This approach offers many advantages in product development lifecycle. It offers better maintainability of the model, reduces product design time and cost, and makes it easier to design future products. Bond graph modeling being a graphical level modeling approach is supported by dedicated software which can be used to maintain the model and derive the system equations.

Modeling is as much an art as it is science. Therefore, it needs a lot of practice, and with experience, one becomes a better modeler. Experienced designers know how to simplify their models to capture the essential dynamics that they are looking for. For example, when an experienced automotive designer is designing a suspension system, he/she would consider only a quarter of the vehicle and develop the suspension design by simulating the quarter-car model with one wheel and one suspension element. The same designer, when designing a steering system would most likely consider a bicycle handling model without suspensions. After the initial design to satisfaction,

the designer would consider the full vehicle model to validate the design and then go for field trials. As we understand from this discussion, it is not always ideal to include too much details in the model. The leaner is the model, the easier it is to understand its response, and correlate to the physical phenomena. At the same time, one should not over simplify the model so that essential dynamic parts are left out. There has to be a trade-off somewhere; this trade-off is a critical aspect of model building.

References

1. B. Allard, H. Morel, J-P. Chante, Reusing basic semiconductor region models in power device bond graph definition, in *Proceedings 5th European Conference on Power Electronics and Applications*, vol. 2 (IEE Conference Publication, Brighton, 1993), pp. 34–39
2. T.K. Bera, A.K. Samantaray, Consistent bond graph modeling of planar multibody systems. *World J. Model. Simul.* **7**(3), 173–178 (2011)
3. T.K. Bera, A.K. Samantaray, R. Karmakar, Bond graph modelling of planar prismatic joints. *Mech. Mach. Theory* **49**(12), 2–20 (2012)
4. T.K. Bera, A.K. Samantaray, R. Karmakar, Robust overwhelming control of a hydraulically driven three-degrees-of- freedom parallel manipulator through a simplified fast inverse model. *J. Syst. Control Eng.* **224**(2), 169–184 (2010)
5. K. Besbes, Modelling an insulated gate bipolar transistor using bond graph techniques. *Int. J. Numer. Model. Electron. Networks Devices Fields* **8**(1), 51–60 (1995)
6. F.E. Cellier, C. Clauss, A. Urquia, Electronic circuit modelling and simulation in Modelica, in *Proceedings of the Eurosim Congress on Modelling and Simulation*, vol. 2, pp. 1–10, 2007
7. W. Denman, M.H. Zaki, S. Tahar, Formal verification of bond graph modelled analogue circuits. *IET Circuits Devices Syst.* **5**(3), 243–255 (2011)
8. H. Garrab, B. Allard, H. Morel, S. Ghedira, K. Besbes, Role of the temperature distribution on the pn junction behaviour in the electro-thermal simulation. *Int. J. Numer. Model. Electron. Networks Devices Fields* **17**(6), 539–560 (2004)
9. B.C. Ghosh, S.N. Bhadra, Bond graph simulation of a current source inverter driven induction motor system. *Electron. Mac. Power Syst.* **21**, 51–67 (1993)
10. D.R. Hild, Circuit modeling in Dymola, Master’s thesis, Department of Electrical and Computer Engineering, University of Arizona, Tuscon, USA, 1993
11. D.R. Hild, F.E. Cellier, Object oriented electronic circuit modeling using Dymola, in *Proceedings of OOS Object Oriented Simulation Conference* (SCS Publishing, 1994), pp. 68–75
12. N. Idir, R. Bausiere, Circuit oriented simulation of GTO thyristors using bond-graphs, in *Proceedings of the IEEE International Conference on Systems, Man and Cybernetics*, vol. 1, pp. 579–582, 1993
13. K. Jongbaeg, M.D. Bryant, Bond graph model of a squirrel cage induction motor with direct physical correspondence. *J. Dyn. Syst. Meas. Contr.* **122**, 461–469 (2000)
14. D. Karnopp, Computer simulation of stick-slip friction in mechanical dynamic systems. *J. Dyn. Syst. Meas. Contr. Trans. ASME* **107**(1), 100–103 (1985)
15. D. Karnopp, Understanding magnetic and electrostatic actuators using bond graphs and a mechanical model. *J. Franklin Inst.* **317**, 227–234 (1984)
16. C.S. Kumar, A. Mukherjee, Robust control of a robot manipulator on a flexible foundation, in *Fourth International Conference on CAD/CAM, Robotics & Factories of Future* (TATA McGraw-Hill, New Delhi, India, 1989), pp. 727–742
17. H. Morel, B. Allard, S. Ghedira, A. Ammous. A bond graph model of the pn junction. in *Proceedings of the 3rd International Conference on Bond Graph Modeling and Simulation (ICBGM’97)*, vol. 29 (SCS Publishing, 1997), pp. 325–330

18. H. Morel, B. Allard, C. Lin, H. Helal, Semiconductor device modeling and simulation using bond graph, in *Proceedings of 2nd International Conference on Bond Graph Modeling and Simulation (ICBGM'95)*, vol. 27 (SCS Publishing, 1995), pp. 269–274
19. A. Mukherjee, R. Karmakar, A.K. Samantaray, *Bond Graph in Modeling, Simulation and Fault Identification* (CRC Press, Boca Raton, 2006). ISBN: 978-8188237968, 1420058657
20. A. Mukherjee, R. Karmakar, A.K. Samantaray, Modelling of basic induction motors and source loading in rotor-motor systems with regenerative force field. *Simul. Model. Pract. Theory* **7**(5), 563–576 (1999)
21. P.M. Pathak, A. Mukherjee, A. Dasgupta, Impedance control of space robots using passive degrees of freedom in controller domain. *Trans. ASME J. Dyn. Syst. Meas. Control* **127**, 564–578 (2005)
22. A.M. Pawlak, *Sensors and Actuators in Mechatronics: Design and Applications* (CRC Press, Boca Raton, 2007), pp. 33487–2742
23. P.Y. Richard, M. Morarescu, J. Buisson, Bond graph modelling of hard nonlinearities in mechanics: a hybrid approach. *Nonlinear Anal. Hybrid Syst.* **2**, 922–951 (2008)
24. J.M. Rodriguez-Fortun, J. Orus, F. Buil, J.A. Castellanos, General bond graph model for piezo-electric actuators and methodology for experimental identification. *Mechatronics* **20**, 303–314 (2010)
25. A.K. Samantaray, Modeling and analysis of preloaded liquid spring/damper shock absorbers. *Simul. Model. Pract. Theory* (special issue on bond graph modelling) **17**, 309–325 (2008)
26. M.C. Schweisguth, Semiconductor modeling with bondgraphs, Master's thesis, Department of Electrical and Computer Engineering, University of Arizona, Tucson, AZ, 1997
27. M.C. Schweisguth, F.E. Cellier, A bond graph model of the bipolar junction transistor, in *International Conference on Bond Graph Modeling (ICBGM'99)* (SCS Publication, San Francisco, CA, 1999), pp. 344–349
28. M. Sorli, L. Gastaldi, E. Codina, S. de las Heras, Dynamic analysis of pneumatic actuators. *Simul. Pract. Theory* **7**, 589–602 (1999)
29. C.H. Suh, C.W. Radcliffe, *Kinematics and mechanisms design* (Wiley, New York, 1978)
30. P. Vijay, Modelling, simulation and control of a solid oxide fuel cell system: a bond graph approach, Ph.D. thesis, Indian Institute of Technology, Kharagpur, India, 2009
31. P. Vijay, A.K. Samantaray, A. Mukherjee, Bond graph model of a solid oxide fuel cell with a C-field for mixture of two gas species. *Proc. IMechE Part I J Syst. Control Eng.* **222**(4), 247–259 (2008)
32. P. Vijay, A.K. Samantaray, A. Mukherjee, A bond graph model-based evaluation of a control scheme to improve the dynamic performance of a solid oxide fuel cell. *Mechatronics* **19**(4), 489–502 (2009)
33. P. Vijay, A.K. Samantaray, A. Mukherjee, On the rationale behind constant fuel utilization control of solid oxide fuel cells. *Proc. IMechE Part I J. Syst. Control Eng.* **223**(2), 229–252 (2009)

Chapter 4

Physical Model-Based Control

4.1 Introduction

An automatic control system refers to a set of devices which manipulate the output of a system by altering its inputs, in response to automatically generated commands. In manual control systems, the command is generated manually. In automatic control, a desired or prescribed system output is called the reference or a setpoint. The goal of the controller is to manipulate the inputs so as to obtain the desired effect on the outputs.

As an example, consider the speed control of a brush-less DC electric motor. The setpoint is prescribed as the desired motor speed irrespective of the load on the motor. The input variable is the voltage supplied to the motor, which generates certain armature current and thus regulates the driving torque. This supplied voltage can be varied manually or automatically through different means, such as by changing the resistance through a rheostat. The DC motor is modeled in a bond graph as a GY element. The GY element relates the armature current to the output torque and the motor speed to the back emf. At start-up, the motor angular velocity increases depending on the load and this causes development of back emf which reduces the torque applied on the load. As a consequence, at some point of time the back emf is exactly the same as the supplied voltage and no net torque is applied on the load. This describes the steady-state scenario. It is thus possible to precalculate the voltage that has to be supplied to achieve a certain output speed. If this exact voltage is applied by manually measuring and varying the input to the motor then it is a manual control system.

On the other hand, if a feedback system is developed which calculates the speed error, i.e., the difference between the desired motor speed and the actual motor speed (through measurement), and modifies the input voltage (through a regulator or controller) in proportion to the error, then we have an automatic control system. The constant of proportionality is called a gain. The connection between the output to the input is called a closed loop. Design of gains for stability of the system (including settling time or decay rate, overshoot minimization, ...) and controller algorithms

constitutes what is known as controller synthesis. Some control systems implement simultaneous closed-loop and open-loop (feed-forward) control, where the open-loop control helps improve the reference tracking performance.

A controller will have to behave correctly even when the connected physical system's parameter values are a little different from the nominal parameter values used during the controller design and when the controlled system is influenced by external factors (disturbances, noise in measurements, etc.). The controller has to be designed accordingly. Such a controller is then called a robust controller that is robust with respect to parameter uncertainties, external disturbances, and measurement uncertainties. Instead of a fixed controller design, one usually opts for an adaptive control scheme in which online system identification and estimation of the process parameters, or modification of controller gains, is performed so that strong robustness properties are obtained.

In intelligent mechatronic systems, the intelligence is embedded in the controller. For this intelligence to be of any use, the controller should receive some information. Just like our own sensory organs, which feed information to the brain, the sensors in a system feed information to the controller. The controller is the brain of the intelligent mechatronic system. In modern control systems, the controller is usually implemented in one or more microprocessors or computers. The controller processes sensed information and sends commands to actuators which may be likened to our muscles. The type of sensors needed for particular application varies according to the process type and environment. For example, in a dark room, our eyes are useless sensory organs; we need to instead rely on our ears and touch to navigate through that environment. Likewise, the number and kind of sensors needed and their placement within a system for a particular application is one of the initial design criteria in controller synthesis.

A well-developed system model is the primary requirement for development of its control system. In this chapter, we will concentrate on development of physical model-based control strategies. Physical model-based strategies are developed by exploiting the understanding of the dynamic behavior (physics) of the system. If a controller is developed from a mathematical (mostly numerical) model then these physical insights cannot be readily visualized from the mathematical model and thus the controller may turn out to be very complex and yield suboptimal performance. We will emphasize on the structural properties of the system which will be used to design the instrumentation architecture for specific control systems.

4.2 Model Conversions

4.2.1 Construction of Signal Flow Graph

A signal flow graph (SFG) is a linear graph which is used to derive transfer functions between the inputs and outputs of a system. The SFG of a system can be

systematically derived from the bond graph model of the system. First of all, let us define the terminologies associated with the SFG and their relation to the bond graph structure.

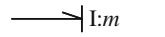
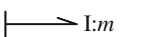
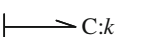
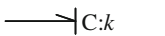

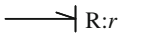
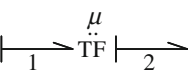
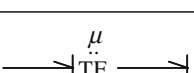
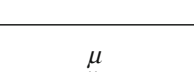
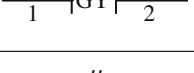
4.2.1.1 Nodes of SFG

- A signal flow graph is constituted of a set of nodes which are interconnected by a set of directed lines called branches or edges. A gain is associated with each edge. A node signifies an algebraic sum. The bond graph power direction (coordinate system) is represented in SFGs by gains $+1$ and -1 , whereas causality is portrayed by the direction of the edges. It is wrong to change the direction of edge and then take the negative of the gain. The SFG is a linear causal graph. Each branch in an SFG is associated with only one signal. Thus, each bond in a bond graph is represented by two nodes (effort and flow node) and two edges (with gains defined by element constitutive relations and/or strong or weak junction laws) in an SFG. Activated or signal bonds are associated with one power variable and thus they are represented by only one node and one edge.
- All bonds connected to a 1-junction have the same flow and thus may be represented by a single flow node. Similarly, all bonds connected to a 0-junction are represented by a single effort node. These are derived from the strong junction laws. If i, j, k, \dots are the bond numbers of bonds connected to a 1-junction then the common flow node is represented as $f_{i,j,k,\dots}$. Likewise, the common effort node for bonds at a 0-junction is similarly represented by $e_{i,j,k,\dots}$ when i, j, k, \dots are the bond numbers of bonds connected to the 0-junction.
- All bonds connected to a 1-junction contribute separate effort nodes (*viz.* e_i, e_j, \dots where i, j, \dots are bond numbers) and all bonds connected to a 0-junction contribute separate flow nodes (*viz.* $f_i, f_j \dots$ where i, j, \dots are bond numbers).

4.2.1.2 Branches and Gains

- The constitutive relation for an I-element in integral causality is $f = m^{-1} \int edt + f_0$. Note that initial conditions cannot be considered in the frequency domain. Thus, the term f_0 is neglected. Taking the Laplace transform of the two sides of the constitutive relation, $f(s) = e(s)/(ms)$ or $f(s)/e(s) = 1/(ms)$. This gives the gain associated with an integrally causalled I-element as $\frac{1}{ms}$ and the edge is directed from the effort to the flow node (cause to effect in bond graph term, input to output in SFG term). Likewise, for a differentially causalled I-element, the constitutive relation is $e = m \frac{df}{dt}$ or $e(s) = msf(s)$ which gives the gain as ms and the branch is directed from the flow node to the effort node.
- In an integrally causalled C-element, the constitutive relation is given by $e = K \int f dt + e_0$. Neglecting the initial condition e_0 and taking the Laplace transform of both sides, $e(s) = Ke(s)/s$ or $e(s)/f(s) = K/s$. Thus the gain associated with an integrally causalled C-element is K/s (or $\frac{1}{C_s}$) and the branch is directed from the

Table 4.1 Signal flow graph of bond graph elements

Bond graph	Signal flow graph
	$e(s) \xrightarrow{1/(ms)} f(s)$
	$f(s) \xrightarrow{ms} e(s)$
	$f(s) \xrightarrow{k/s} e(s)$
	$e(s) \xrightarrow{s/k} f(s)$
	$f(s) \xrightarrow{r} e(s)$
	$e(s) \xrightarrow{1/r} f(s)$
	$e_1(s) \xleftarrow{\mu} e_2(s)$ $f_1(s) \xrightarrow{\mu} f_2(s)$
	$e_1(s) \xrightarrow{1/\mu} e_2(s)$ $f_1(s) \xleftarrow{1/\mu} f_2(s)$
	$e_1(s) \xrightarrow{1/\mu} e_2(s)$ $f_1(s) \xrightarrow{1/\mu} f_2(s)$
	$e_1(s) \xleftarrow{\mu} e_2(s)$ $f_1(s) \xleftarrow{\mu} f_2(s)$

flow to the effort node (cause to effect). The gain become s/K for a differentially causalled C-element and the branch is directed from the effort to the flow node.

- The constitutive relationship for R-elements does not involve differentiation or integration. Thus the gain term does not contain the Laplace variable s . The gain for the R-element in resistive causality is $e(s)/f(s) = R$, whereas for conductive causality it is $f(s)/e(s) = 1/R$.
- Similar relationships can be established for two-port bond graph elements, i.e., TF and GY. The signal flow graph representations corresponding to various bond graph elements in different causal forms are shown in Table 4.1.

4.2.1.3 Receptor Nodes

- Receptor nodes represent weak junction laws, i.e., the summation constraints. At the 1-junction, flows in bonds are equal (strong law, which is used to represent a common flow node for all bonds connected to that junction) and signed (as decided by power directions) sum of efforts in the bonds is zero (weak junction

Fig. 4.1 SFG representation of 1-junction

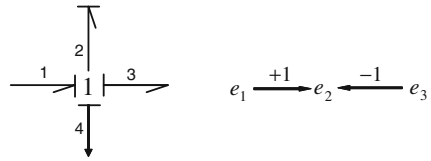
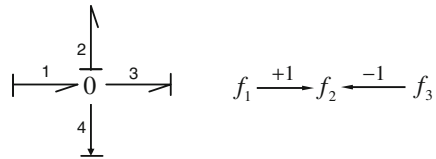


Fig. 4.2 SFG representation of 0-junction



law). The strong bond for the 1-junction is the bond that has causality away from the junction. The weak law for the junction is written in such a way that the variable associated with the strong bond appears on the left of the equation. The strong bond thus provides information of flow to the 1-junction. The weak variables of the 1-junction are efforts. The effort equation for the 1-junction is written for the weak variables (efforts), where the effort in the strong bond is expressed as signed sum of efforts in other bonds. This weak effort variable of the strong bond is called the receptor of the junction. For the 1-junction shown in Fig. 4.1 the junction algebra equation is $e_2 = e_1 - e_3$. The signal flow graph representation is shown on the right of Fig. 4.1.

In Fig. 4.1, bond number 2 is the strong bond and the weak variable e_2 is the receptor node. Signals from other nodes for weak variables are added to this node. The gain for all branches in SFG corresponding to bonds that are power directed in the opposite direction as compared to the strong bond (i.e., counter-oriented) is 1. Otherwise, i.e., for all co-oriented bonds (bonds having same power orientation as the strong bond as seen from the junction), the gain is -1 .

- Likewise, the receptor for an 0-junction is the weak flow variable of the strong bond of the junction (the bond that decides effort of the 0-junction, i.e., causalled near the junction). For the 0-junction shown in Fig. 4.2, the weak variable f_2 is the receptor node. The junction algebra can be represented at the receptor node f_2 as shown on the right of Fig. 4.2.

4.2.1.4 Example

Let us consider a mechanical system whose schematic diagram and bond graph model are shown in Fig. 4.3. The coupling is flexible with torsional stiffness K_t . In the first step, the leftmost 0-junction and elements connected to it in the bond graph model are considered. Node f_1 represents the input source, i.e., the motor speed. The part SFG is shown in Fig. 4.4.

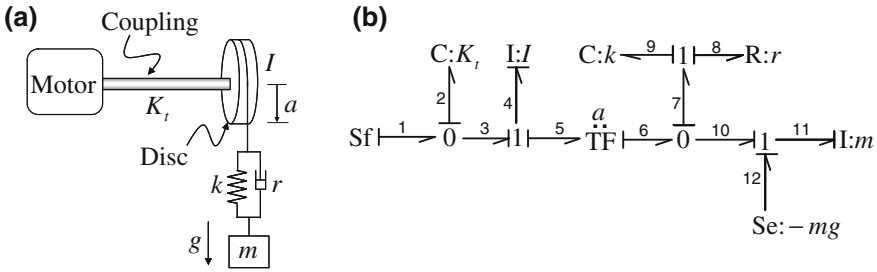


Fig. 4.3 A speed controlled motor with flexible coupling lifting a load

Fig. 4.4 First step in SFG construction

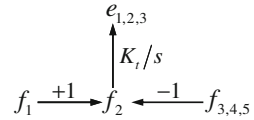


Fig. 4.5 Second step in SFG construction

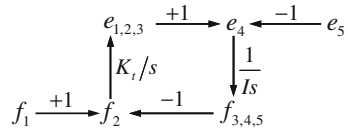
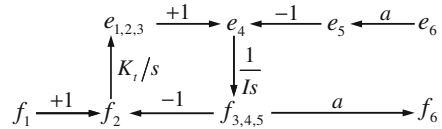


Fig. 4.6 Third step in SFG construction



The next junction considered is the 1-junction for disk’s angular velocity connected to bonds 3, 4, and 5. The resulting part of SFG is shown in Fig. 4.5.

The transformer between two 1-junctions is then represented in SFG (Fig. 4.6).

In this way, the entire signal flow graph may be constructed and represented as shown in Fig. 4.7. The inputs ($u(s)$) and outputs ($y(s)$) can now be identified in the SFG (see Fig. 4.8). The motor speed is the input and the vertical velocity of the mass is the output variable. The loops and paths may be lumped in a way very similar to that used with block diagrams: nodes with one input and one output may be eliminated by taking the product of the gains, and parallel branches between two nodes may be represented by a single branch with its gain as sum of gains in all parallel branches. This reduces the complexity of the SFG (see Fig. 4.9).

Now the linear system’s model has been completely represented as a compact signal flow graph. Let us now try to derive transfer function between the input and the output nodes. The transfer function from input to output is given by Mason’s gain rule as follows:

$$G(s) = \sum_i P_i \Delta_i / \Delta, \tag{4.1}$$

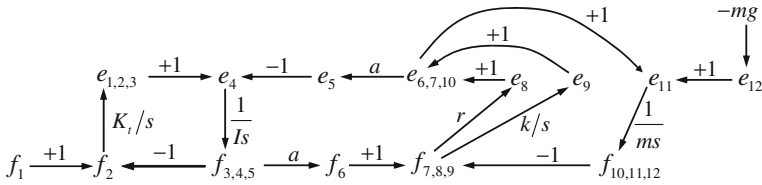


Fig. 4.7 Complete SFG of the system

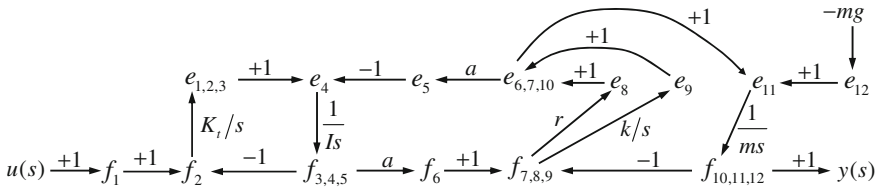


Fig. 4.8 SFG with input and output nodes

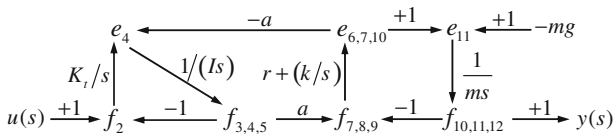


Fig. 4.9 Reduced signal flow graph model of the example system

where P_i = gain of the i th forward path, the graph determinant

$$\begin{aligned} \Delta = & 1 - \Sigma \text{all individual loop gains} \\ & + \Sigma \text{all possible gain products of two non-touching loops} \\ & - \Sigma \text{all possible gain products of three non-touching loops} \\ & + \dots \end{aligned}$$

and Δ_i = the Δ for the part of the SFG which does not touch i th forward path.

In the reduced SFG, there is one forward path from node $u(s)$ to node $y(s)$. The number of loops in the SFG is three: (1) $f_2 \rightarrow e_4 \rightarrow f_{3,4,5} \rightarrow f_2$, (2) $f_{3,4,5} \rightarrow f_7 \rightarrow e_{6,7,10} \rightarrow e_4 \rightarrow f_{3,4,5}$, and (3) $e_{6,7,10} \rightarrow e_{11} \rightarrow f_{10} \rightarrow f_7 \rightarrow e_{6,7,10}$, having corresponding loop gains L_1 to L_3 . These loop gains are

$$\begin{aligned} L_1 &= -K_t/(Is^2), \\ L_2 &= -a^2(rs + k)/(Is^2), \\ L_3 &= -(rs + k)/(ms^2), \end{aligned} \tag{4.2}$$

The forward path gain is

$$P_1 = aK_t(rs + k)/(Im s^4).$$

The forward paths touches all loops and hence $\Delta_1 = 1$. Gain product of two non-touching loops is L_1L_3 . There are no three or more non-touching loops.

Thus the numerator of the transfer function is $aK_t(rs + k)/(Im s^4)$.

The denominator is $1 + K_t/(Is^2) + a^2(rs + k)/(Is^2) + (rs + k)/(ms^2) + K_t/(Is^2) \times (rs + k)/(ms^2)$.

Multiplying both numerator and denominator by $Im s^4$, the transfer function is obtained as

$$\frac{y(s)}{u(s)} = \frac{aK_t(rs + k)}{Im s^4 + r(ma^2 + I)s^3 + (mK_t + ma^2k + kI)s^2 + K_t rs + K_t k}. \quad (4.3)$$

Once we have the transfer function with symbolic coefficients, we can apply Routh's criteria to obtain the stability domains for both the open- and closed-loop systems. This may be done in symbolic form through software like Reduce[®], Mathematica[®] and Matlab[®]. If one assigns the parameter values then the transfer function reduces to a ratio of two polynomials in s with numeric coefficients. Thereafter, usual control theoretical approaches in frequency domain (Bode, Nyquist, Nichols, and root loci plots) and time domain (through inverse Laplace transform) can be performed. The transfer function may be discretized by taking z-transforms and then digital control system analysis can be performed. Derivation of the correct transfer function is thus the stepping stone for all control-oriented analysis.

4.2.2 Transfer Function from State-Space Models

From the bond graph model, the state equations for a linear system can be written in state-space form. The process of deriving the state-space model follows the algorithm discussed in previous chapters. It can also be obtained using various software tools. The system model in state-space form is given as

$$\begin{aligned} \dot{x} &= \mathbf{A}x + \mathbf{B}u, \\ y &= \mathbf{C}x + \mathbf{D}u, \end{aligned} \quad (4.4)$$

where x is the vector of states (Ps and Qs), n is the number of states, \mathbf{A} is $n \times n$ square matrix, \mathbf{B} is $n \times m$ matrix, m is the number of sources, u is the vector of sources

(Se and Sf elements), y is the vector of outputs, l is the number of such outputs, \mathbf{C} is $l \times n$ matrix, and \mathbf{D} is $l \times m$ matrix. Taking Laplace transform of Eq. 4.4,

$$\begin{aligned} sx(s) &= \mathbf{A}x(s) + \mathbf{B}u(s) \text{ or } (s\mathbf{I} - \mathbf{A})x(s) = \mathbf{B}u(s), \\ y(s) &= \mathbf{C}x(s) + \mathbf{D}u(s), \text{ or } y(s) = \mathbf{C}(s\mathbf{I} - \mathbf{A})^{-1}\mathbf{B}u(s) + \mathbf{D}u(s), \end{aligned} \quad (4.5)$$

where \mathbf{I} is $n \times n$ identity matrix.

The transfer function matrix $\mathbf{G}(s)$ between input vector(s) $u(s)$ and output vector(s) $y(s)$ is defined as $\mathbf{G}(s) = y(s)/u(s)$:

$$\begin{aligned} \mathbf{G}(s) &= \mathbf{C}(s\mathbf{I} - \mathbf{A})^{-1}\mathbf{B} + \mathbf{D} \\ &= \frac{\mathbf{C} \text{Adjoint}(s\mathbf{I} - \mathbf{A})\mathbf{B} + \mathbf{D}}{|s\mathbf{I} - \mathbf{A}|} \\ &= \frac{\mathbf{N}(s)}{D(s)}, \end{aligned} \quad (4.6)$$

where $\mathbf{N}(s)$ is the matrix of the numerator polynomials and the common denominator polynomial for all elements in the transfer function matrix is $D(s) = |s\mathbf{I} - \mathbf{A}|$. The poles of the system are the roots of the equation $D(s) = 0$. Thus, they are the eigenvalues of matrix \mathbf{A} .

Let us consider the system and its bond graph model used in the earlier example (Fig. 4.3).

The state equations for the model are

$$\begin{aligned} \dot{P}_4 &= K_t Q_2 - a((aP_4/I - P_{11}/m)r + kQ_9), \\ \dot{P}_{11} &= (aP_4/I - P_{11}/m)r + kQ_9 - mg, \\ \dot{Q}_2 &= u(t) - P_4/I, \\ \dot{Q}_9 &= aP_4/I - P_{11}/m, \end{aligned} \quad (4.7)$$

where the state vector $x = [P_4 \ P_{11} \ Q_2 \ Q_9]^T$.

The output vector is the velocity of the hung-mass, or the variable f_{11} . From equations, $y = f_{11} = P_{11}/m$. Thus, the matrices in the state space quadruple are

$$\begin{aligned} \mathbf{A} &= \begin{bmatrix} -a^2r/I & ar/m & K_t & -ak \\ ar/I & -r/m & 0 & k \\ -1/I & 0 & 0 & 0 \\ a/I & -1/m & 0 & 0 \end{bmatrix}, \quad \mathbf{B} = \begin{bmatrix} 0 \\ 0 \\ 1 \\ 0 \end{bmatrix}, \\ \mathbf{C} &= [0 \ 1/m \ 0 \ 0] \quad \text{and} \quad \mathbf{D} = 0. \end{aligned} \quad (4.8)$$

Thus,

$$s\mathbf{I} - \mathbf{A} = \begin{bmatrix} s + a^2r/I & -ar/m & -K_t & ak \\ -ar/I & s + r/m & 0 & -k \\ 1/I & 0 & s & 0 \\ -a/I & 1/m & 0 & s \end{bmatrix} \quad (4.9)$$

and the characteristic polynomial is

$$|s\mathbf{I} - \mathbf{A}| = s^4 + r \left(\frac{a^2}{I} + \frac{1}{m} \right) s^3 + \left(\frac{K_t}{I} + \frac{a^2k}{I} + \frac{k}{m} \right) s^2 + \frac{K_t r}{mI} s + \frac{K_t k}{mI},$$

$$D(s) = \frac{Ims^4 + r(ma^2 + I)s^3 + (mK_t + ma^2k + kI)s^2 + K_t rs + K_t k}{mI}.$$

While calculating \mathbf{C} Adjoint($s\mathbf{I} - \mathbf{A}$) \mathbf{B} , we note that both matrices \mathbf{C} and \mathbf{B} are sparse and thus only one element in the second row and third column of the adjoint matrix of $s\mathbf{I} - \mathbf{A}$ is to be evaluated. This element turns out to be $aK_t(rs+k)/I$. So the numerator polynomial is $(1/m)(aK_t(rs+k)/I)$. After multiplying both numerator and denominator by mI , the transfer function obtained is

$$\frac{y(s)}{u(s)} = \frac{aK_t(rs+k)}{Ims^4 + r(ma^2 + I)s^3 + (mK_t + ma^2k + kI)s^2 + K_t rs + K_t k}. \quad (4.10)$$

Symbolically, deriving transfer functions of higher order systems is resource and time intensive. However, if numeric parameter values are assigned, the transfer function matrix can be easily obtained from numeric \mathbf{A} , \mathbf{B} , \mathbf{C} and \mathbf{D} matrices. Note that state-space models are used in advanced control theoretical analysis, some of which will be discussed in the later chapters.

4.2.3 Block Diagram Models

For linear systems, the block diagram representation is just another form of signal flow graph. A node in an SFG having more than one input represents a sum block in a block diagram. The branch gains in an SFG are represented as gain blocks in the block diagram form. This simple algorithmic procedure shown in Fig. 4.10 converts signal flow graph model into block diagram form.

However, an SFG can only represent a linear system model. On the other hand, a block diagram representation is more general; it can contain blocks that implement nonlinear constitutive relations. Leaving apart the nonlinear parts of the model, a backbone block diagram form can be constructed from an SFG and then the nonlinear part can be added to it.

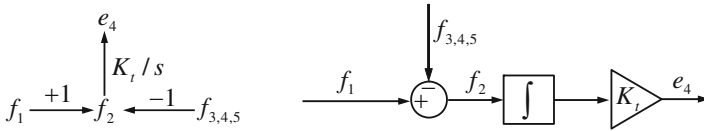


Fig. 4.10 Conversion of SFG into block diagram form

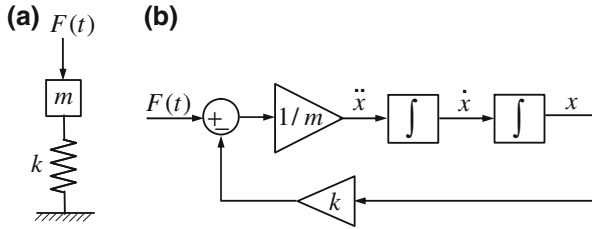


Fig. 4.11 A spring-mass system and its block diagram

Usually, block diagrams are constructed from the equations of motion of the system. We know that even a simple change in the system can greatly change the equations of motion. Therefore, the form of the block diagram may undergo radical changes while the user introduces or removes some element from the model. That is why, the block diagram form is not a suitable tool for conceptual prototype development; especially so when the model structure is not fixed a priori. In the following, we taken up an example to illustrate this point.

Consider the equation model for a spring mass system shown in Fig. 4.11a:

$$m\ddot{x} + kx = F(t).$$

The highest order differentiation in this equation of motion is two. Thus, the above equation may be written as

$$m\ddot{x} = F(t) - kx.$$

This equation may now be represented as a block diagram shown in Fig. 4.11b where the difference between input $F(t)$ and a feedback term kx is taken at a sum node and the result is $m\ddot{x}$. This result is then scaled by factor $1/m$ and double integrated to give x which is amplified by gain k and connected to the sum node to complete the circuit. The state variables in the block diagram model are the outputs of integration blocks, i.e., \dot{x} and x . The initial conditions can be applied on these state variables at the integration blocks.

If the system is modified by adding a damper in parallel to the spring (see Fig. 4.12a), then the equation of motion to be considered for block diagram model becomes

$$m\ddot{x} = F(t) - c\dot{x} - kx.$$

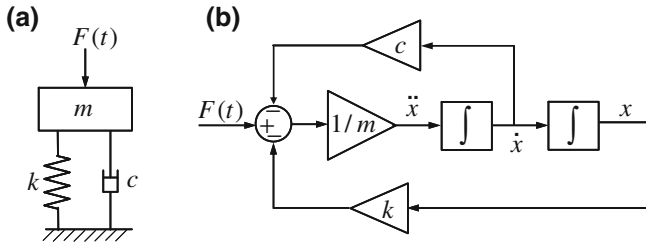
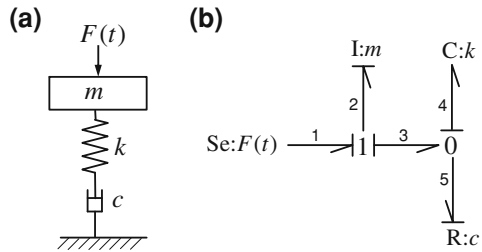


Fig. 4.12 A spring-mass-damper system and its block diagram

Fig. 4.13 One and a half degrees of freedom system and its bond graph model



Accordingly, a new feedback from the velocity point \dot{x} with gain c is introduced at the sum block as shown in Fig. 4.12b.

Thus, the additional damping resulted in just a small modification to the block diagram of the system without damping. Let us now consider a damper which is in series with the spring as shown in Fig. 4.13a. This kind of a system is said to have one and a half degrees of freedom although the number of state variables is still two.

The resulting equation of motion undergoes a big change: We can now take the help of the bond graph model shown in Fig. 4.13b to derive the equations of motion as follows:

$$\begin{aligned} \dot{P}_2 &= F(t) - kQ_4, \\ \dot{Q}_4 &= P_2/m_2 - kQ_4/c. \end{aligned} \tag{4.11}$$

The equations of motion in Eq. 4.11 can now be represented as the block diagram in Fig. 4.14 where \dot{x} is the velocity of the mass point and \dot{x}_1 is the velocity of the moving end of the damper.

The block diagram in Fig. 4.14 is radically different from Fig. 4.12b, although both of them correspond to addition of a damper to the spring-mass system. This is why, it is difficult to perform system design studies on a block diagram model; any change to system morphology means the equations of motion have to be re-derived and a new block diagram has to be constructed. We will now demonstrate how this block diagram form can be arrived at from the bond graph model itself without actually deriving the complete equations of motion.

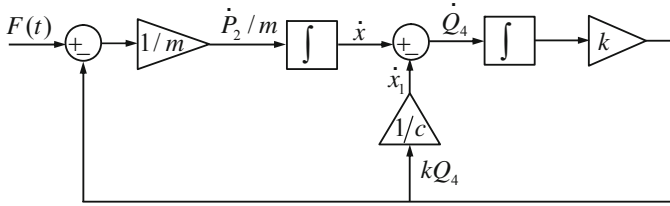


Fig. 4.14 Block diagram model of one and a half degrees of freedom system

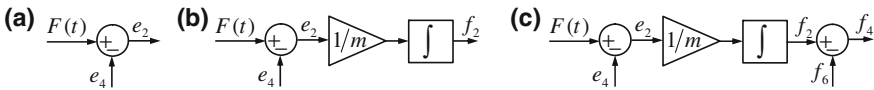
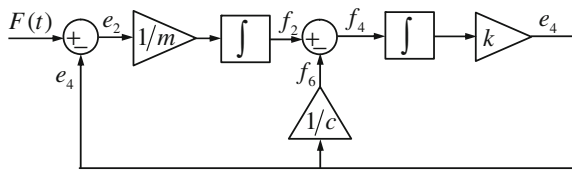


Fig. 4.15 Gradual build-up of block diagram of one and a half degrees of freedom system from its bond graph model

Fig. 4.16 Completed conversion from bond graph into block diagram form



The algorithmic procedure used to construct the block diagram model is similar to that used to construct the SFG. Each bond graph junction corresponds to a sum element in the block diagram where the weak junction law (effort sum at 1-junction and flow sum at 0-junction) is represented. The output of this sum element is the weak variable in the strong bond of that junction. The constitutive relations of elements are added as gain blocks between different sum elements.

Consider the 1-junction in Fig. 4.13b. From causality, the weak junction law gives $e_2 = e_1 - e_3 = F(t) - e_4$. This part of the equation is modeled in Fig. 4.15a.

The constitutive relation for the I element gives $f_2 = (1/m) \int e_2 dt$, which is added to the part block diagram in Fig. 4.15b.

Now consider the 0-junction where the weak junction law gives $f_4 = f_3 - f_6 = f_2 - f_6$. This can be represented in the part block diagram as shown in Fig. 4.15c.

In the part block diagram, all weak junction laws have been represented. Two open ports are remaining. These can be completed by considering the constitutive relations for the C and R elements, i.e., $e_4 = k \int f_4 dt$ and $f_6 = e_6/c = e_4/c$. This results in the block diagram shown in Fig. 4.16 which is the same as that given earlier in Fig. 4.14.

Now let us consider some nonlinearities in the model. The spring is assumed to have hardening characteristic so that the spring force $F_k = k|x|x$ where x is the

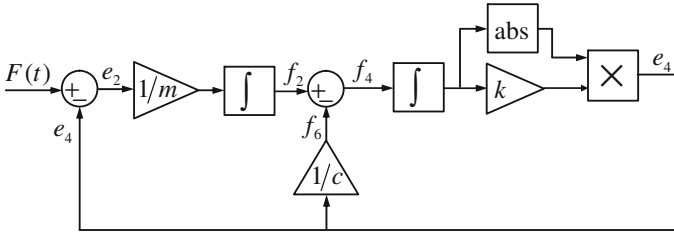


Fig. 4.17 Block diagram of a nonlinear system

deformation of the spring. This nonlinearity can now be included in the backbone block diagram model developed in Fig. 4.14. First of all, we introduce two blocks, one to take absolute value of a signal and the second to compute the product of two signals. Such blocks are available in Matlab Simulink. Then the block diagram of the nonlinear system is obtained as shown in Fig. 4.17.

4.3 Causal Paths

Understanding the information exchange taking place across the elements in the model is the key to design better control laws. This involves studying the graph to infer which elements are influencing which dynamics, how the information between different segments of the graph are coupled, and what is the order of influence of a disturbance in particular segment in the model on the other segments of the model. In other words, the objective is to find if the influence of dynamics of a particular segment of a particular model segment has strong (or significant) interaction or weak (or minor) interaction on the dynamics of another segment of that same model.

Definition 4.1 A causal path [4] tracks the progress of a signal through the model. In bond graph terms, a signal is one of the power variables, i.e., effort or flow. When the signal reaches a junction, it is either distributed (i.e., follows any one of the weak bonds if the signal is the strong variable of the junction) or goes to the strong bond (if it is the weak variable of the junction). When the signal reaches a passive element (I, C, or R), it returns back through it but undergoes a qualitative change (i.e., flow variable becomes effort variable and vice versa). Similarly, if the signal passes through a gyrator, then there is a qualitative change. When a signal reaches a source or a sensor, it is terminated there.

Definition 4.2 When a causal path starts from a particular variable in a particular bond and returns to the same variable in the same bond again, it is called a closed path and the path is terminated there.

Definition 4.3 A closed causal path in which no passive elements are encountered (i.e., no I, C, or R) is a causal loop [12, 25, 26].

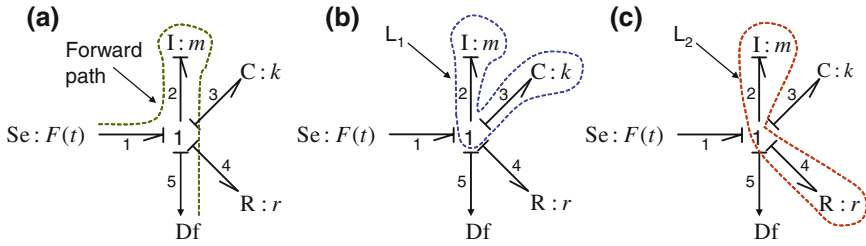


Fig. 4.18 Forward path (a) and loops (b and c) in a bond graph model

Definition 4.4 A closed causal path in which all passive elements encountered are either resistive elements or differentially causalled storage elements is an algebraic loop [3, 12].

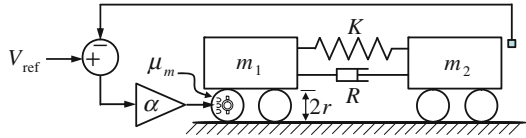
If the causal path from one segment reaches another segment by passing through many storage elements, then the interaction between the segments is said to be weak. This is because of the fact that integrally causalled storage elements in conjunction with dampers act like low-pass filters and thus a disturbance at one segment would be mildly felt at the other segment. The number of storage elements encountered between the segments decides the filter order, i.e., first order, second order, and so on.

4.3.1 Transfer Function from Causal Paths

The causal paths in a bond graph model can be directly used to derive the transfer function. We illustrate this with the help of two examples. Consider the spring-mass-damper system in Fig. 4.12a. Its bond graph model is shown in Fig. 4.18a. We need to derive transfer function between the input excitation and the displacement of the mass point.

From the bond graph model, the forward causal path from the source to the sensor can be determined as follows. The starting signal in this case is e_1 . The causal path now encounters the 1-junction and the effort signal goes to the I-element. As the effort signal passes through the passive I-element, the signal undergoes a qualitative change and is returned as a flow signal. The flow signal now reaches the sensor. The entire forward causal path (see Fig. 4.18a) is thus written as $u \rightarrow e_2 \rightarrow I : m \rightarrow f_2 \rightarrow y$. The forward path gain is multiplication of gains in each sub-path. For element $I : m$, the gain is $1/(ms)$. Note that when effort variable is traversed at 1-junction, if the power direction of the bond associated with the incident effort variable is the same as that of the bond associated with the output effort variable when seen from the junction, then the gain is $+1$; else it is -1 . For the 0-junction, when flow variable is traversed and the power direction of the bond associated with the incident flow variable is the same as that of the bond associated with the output flow variable when

Fig. 4.19 An articulated vehicle



seen from the junction, then the gain is +1; else it is -1. When flow variable is traversed between bonds at a 1-junction or effort variable is traversed between bonds at a 0-junction, the gain remains +1. With this rule, the gain between $e_1 \rightarrow e_2$ is +1. Thus the forward path gain is $P_1 = 1/(ms)$.

The loops in the model are due to closed causal paths. There are two such loops (see Fig. 4.18b, c) given by causal paths $e_2 \rightarrow I : m \rightarrow f_2 \rightarrow f_3 \rightarrow C : k \rightarrow e_3 \rightarrow e_2$ and $e_2 \rightarrow I : m \rightarrow f_2 \rightarrow f_4 \rightarrow R : r \rightarrow e_4 \rightarrow e_2$. The starting node and the terminating node of the loop are the same. In the first loop, the branch $e_3 \rightarrow e_2$ at the 1-junction involves a power direction change and its gain is -1. Likewise, the gain in branch $e_4 \rightarrow e_2$ is also -1. Thus the two loop gains are $L_1 = -k/(ms^2)$ and $L_2 = -r/(ms)$.

The forward path touches all the loops in the model (there are common nodes). Thus, $\Delta_1 = 1$. Also, the two loops touch each other. Thus, the open loop transfer function is $G(s) = P_1 \Delta_1 / (1 - L_1 - L_2)$ or

$$G(s) = \frac{1/(ms)}{1 + k/(ms^2) + r/(ms)} = \frac{s}{ms^2 + rs + k}.$$

4.3.2 Closed-Loop Transfer Function

As another example, we consider a closed-loop system. An articulated electrical vehicle as shown in Fig. 4.19 is considered. The wheels are assumed to roll without slip and the rolling friction is neglected. The vehicle speed is controlled in the following manner. The velocity of the front wagon is measured and it is compared with a reference velocity (setpoint). The error signal is amplified to regulate the actuator, which is a current controlled brush-less DC electric motor driving the rear wagon. This constitutes a proportional feedback closed-loop control system. The objective is to determine a suitable feedback gain such that (1) there is marginal steady-state error, (2) there is less response time, (3) there is not much overshoot, and (4) the vehicle has a smooth response.

The bond graph model of the system is shown in Fig. 4.20. The motor constant is μ_m , which is the constant of proportionality between the armature current and the torque produced at the driving wheel. The wheel radius is r . The motor is modeled by GY element and the conversion from motor torque into forward driving force is modeled as TF element. The consecutive GY and TF elements reduce to an equivalent GY element with modulus $\mu = \mu_m/r$.

Fig. 4.20 Bond graph model of articulated vehicle

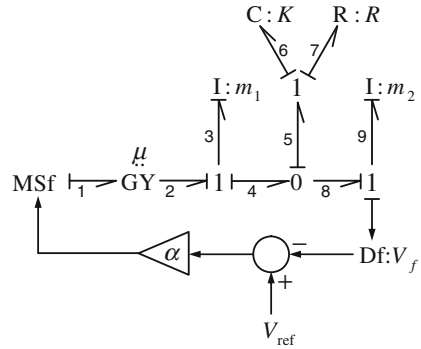
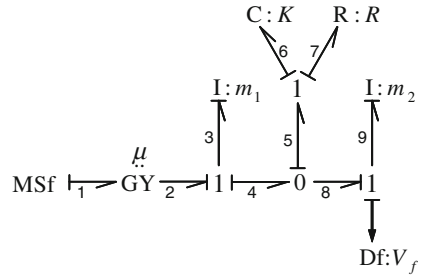


Fig. 4.21 Bond graph model of open-loop articulated vehicle

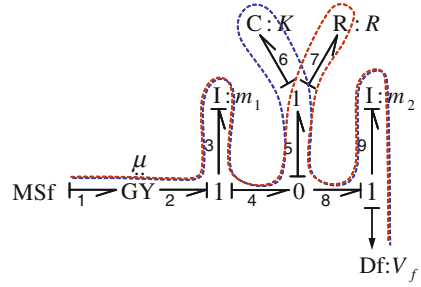


To determine the feedback gain, we consider the open-loop system shown in Fig. 4.21.

From the bond graph model, the forward causal path from the source to the sensor can be determined as follows. The starting signal in this case is f_1 . The causal path now encounters a gyrator element and hence it will further undergo a qualitative change as: $f_1 \rightarrow GY : \mu \rightarrow e_2$. Because e_2 is the weak variable in the next 1-junction, it goes to the strong bond, i.e., bond number 3. We will write this as $f_1 \rightarrow GY : \mu \rightarrow e_2 \rightarrow e_3$. In fact, this traversal can be visually done: bond number 2 has a causality towards the 1-junction and so it can take a path along any bond having causality away from the junction. In this case, because we have a 1-junction, there is only one bond having causality away from the junction. If it were a 0-junction, then all other bonds would have causality away from the junction and the causal path could have traversed along any one of them. All those possibilities are counted as different causal paths. In the next step, we encounter a passive element ($I : m_1$ at bond number 3 through which the causal path returns with a qualitative change. This is because the I-element in this case takes effort information and returns flow information. Thus the causal path will now be written as $f_1 \rightarrow GY : \mu \rightarrow e_2 \rightarrow e_3 \rightarrow I : m_1 \rightarrow f_3$.

The flow information f_3 is now distributed by the 1-junction: one goes back to the source through the gyrator and the causal path terminates there, i.e., $f_1 \rightarrow GY : \mu \rightarrow e_2 \rightarrow e_3 \rightarrow I : m_1 \rightarrow f_3 \rightarrow f_2 \rightarrow GY : \mu \rightarrow e_1$ (which is called a source loading) and the other path continues as $f_1 \rightarrow GY : \mu \rightarrow e_2 \rightarrow e_3 \rightarrow I : m_1 \rightarrow f_3 \rightarrow f_4 \rightarrow f_5$.

Fig. 4.22 Forward causal path in the bond graph model of open-loop articulated vehicle



Bond number 5 is the strong bond of the next 1-junction and the causal path is divided into two paths there (see Fig. 4.22), each one of them reaching e_5 as follows:

$$\begin{aligned} f_1 \rightarrow GY : \mu \rightarrow e_2 \rightarrow e_3 \rightarrow I : m_1 \rightarrow f_3 \rightarrow f_4 \rightarrow f_5 \rightarrow f_6 \\ \rightarrow C : K \rightarrow e_6 \rightarrow e_5 \end{aligned} \quad (4.12)$$

and

$$\begin{aligned} f_1 \rightarrow GY : \mu \rightarrow e_2 \rightarrow e_3 \rightarrow I : m_1 \rightarrow f_3 \rightarrow f_4 \rightarrow f_5 \rightarrow f_7 \\ \rightarrow R : R \rightarrow e_7 \rightarrow e_5 \end{aligned} \quad (4.13)$$

Because there are two paths between f_5 to e_5 , we can combine the above two paths as : $f_1 \rightarrow GY : \mu \rightarrow e_2 \rightarrow e_3 \rightarrow I : m_1 \rightarrow f_3 \rightarrow f_4 \rightarrow f_5 \rightarrow (C : K + R : R) \rightarrow e_5$. Signal e_5 is the strong variable at the 0-junction and thus it again has two branches. One branch returns to the source and the other proceeds as follows: $f_1 \rightarrow GY : \mu \rightarrow e_2 \rightarrow e_3 \rightarrow I : m_1 \rightarrow f_3 \rightarrow f_4 \rightarrow f_5 \rightarrow (C : K + R : R) \rightarrow e_5 \rightarrow e_8 \rightarrow e_9 \rightarrow I : m_2 \rightarrow f_9 \rightarrow V_f$. This is the forward path. In fact, if we consider appropriate element gains (R and $1/R$ for R-elements in resistive and conductive causality, respectively; $1/Is$ and K/s for integrally causalled I and C elements, respectively; and the transformer and gyrator moduli as are appropriate) and signs (due to power directions), we can arrive at the forward path gains. We can now consider gains of the elements and find the forward path gain as $P_1 = \mu \times 1/(m_1s) \times (K/s + R) \times 1/(m_2s)$. Note that we have only one forward path gain because we merged the causal paths from f_5 to e_5 , otherwise we would have had two forward paths.

Let us now investigate the loops in the model. Because we have combined gains of two branches between f_5 to e_5 , the closed causal paths are (1) $I : m_1 \rightarrow f_3 \rightarrow f_4 \rightarrow f_5 \rightarrow (C : K + R : R) \rightarrow e_5 \rightarrow e_4 \rightarrow e_3 \rightarrow I : m_1$ and (2) $I : m_2 \rightarrow f_9 \rightarrow f_8 \rightarrow f_5 \rightarrow (C : K + R : R) \rightarrow e_5 \rightarrow e_8 \rightarrow e_9 \rightarrow I : m_2$. While calculating loop gains, because the starting and terminating nodes are the same, we need to consider only one of them. From closed path (1), the loop gains is $L_1 = -1/(m_1s) \times (K/s + R)$; the minus sign comes due to change in effort signs between $e_4 \rightarrow e_3$ (power direction variation at the 1-junction). Likewise, due to

Fig. 4.23 Closed causal paths in the bond graph model of open-loop articulated vehicle

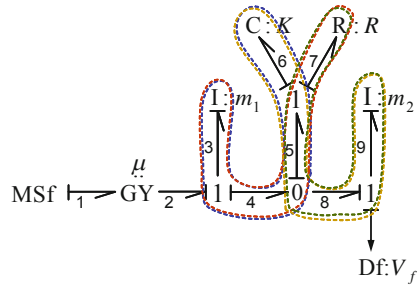


Fig. 4.24 Signal flow graph model of articulated vehicle

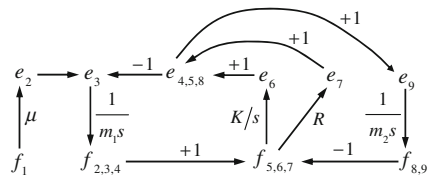
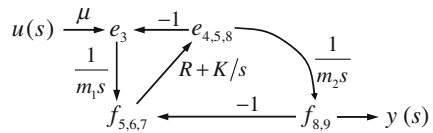


Fig. 4.25 Simplified SFG model of articulated vehicle



change in signs between $f_8 \rightarrow f_5$, the gain associated with closed loop (2) turns out to be $L_2 = -1/(m_2s) \times (K/s + R)$. The four closed causal paths (loops) and their reduction to two loops are shown in Fig. 4.23. Thus, Mason's rule can be applied directly on the bond graph model to arrive at the transfer function [2, 10].

The SFG of the open-loop system is shown in Fig. 4.24. This SFG can be further reduced to a form shown in Fig. 4.25. The forward path gain and the loop gains from the SFG can be determined and shown to be equal to those obtained from the bond graph model.

Consider the two loops with gains L_1 and L_2 . These loops are not non-touching. In the bond graph model, touching loops must pass through at least a common junction or element. The open loop transfer function is then given as $P_1 \Delta_1 / (1 - L_1 - L_2)$, where $\Delta_1 = 1$ because the forward path touches all loops. Thus, multiplying both numerator and denominator by $m_1 m_2 s^3$, the transfer function is given as

$$G(s) = \frac{y(s)}{u(s)} = \frac{\mu R s + \mu K}{m_1 m_2 s^3 + (m_1 + m_2) R s^2 + (m_1 + m_2) K s}. \quad (4.14)$$

One of the poles of the open-loop transfer function is at $s = 0$. This corresponds to the undamped rigid body mode of the vehicle. The other two poles are complex which are due to the mode associated with internal oscillations.

The order of the numerator polynomial is determined by the largest number of integrally causalled storage elements in the forward path. This also determines the relative degree (difference between the orders of the denominator and numerator polynomials) of the system. If a causal path from a source to an output does not contain any integrally causalled storage elements, then the input directly influences the output (the D matrix in state-space quadruple form is not null). In other words, this is called a direct input feedthrough, i.e., the relative degree of the system is zero.

Note that because of the gain appearing in the forward path, the closed-loop transfer function is given by

$$\begin{aligned} G_c(s) &= \frac{\alpha G(s)}{1 + \alpha G(s)} \\ &= \frac{\alpha(\mu R s + \mu K)}{m_1 m_2 s^3 + (m_1 + m_2) R s^2 + ((m_1 + m_2) K + \alpha \mu R) s + \alpha \mu K}. \end{aligned} \quad (4.15)$$

and the characteristic polynomial is

$$\Phi(s) = m_1 m_2 s^3 + (m_1 + m_2) R s^2 + ((m_1 + m_2) K + \alpha \mu R) s + \alpha \mu K. \quad (4.16)$$

For stability analysis, the Routh array may be constructed as

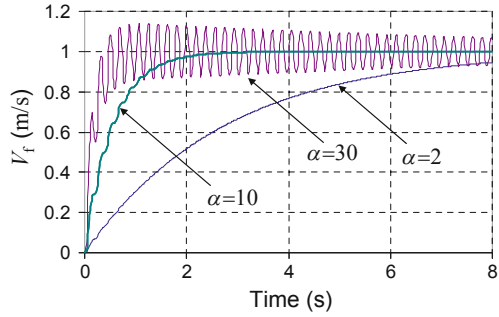
$$\begin{array}{r} s^3 : m_1 m_2 \qquad \qquad \qquad (m_1 + m_2) K + \alpha \mu R \quad 0 \\ s^2 : (m_1 + m_2) R \qquad \qquad \qquad \alpha \mu K \qquad \qquad 0 \\ s^1 : (m_1 + m_2) K + \alpha \mu R - \frac{m_1 m_2 \alpha \mu K}{(m_1 + m_2) R} \quad 0 \qquad \qquad \cdot \\ s^0 : \alpha \mu K \end{array} \quad (4.17)$$

We look for sign changes in the first column of the Routh array. The masses and stiffnesses are all positive. Then from the second row, the necessary conditions to stabilize this system is $R > 0$. From the fourth row, we observe that for $\mu > 0$, $\alpha > 0$ is required. Finally considering the third row, the overall stability domain is given by

$$R > 0 \quad \text{and} \quad 0 < \alpha < \frac{K R (m_1 + m_2)^2}{m_1 m_2 \mu K - \mu (m_1 + m_2) R^2}. \quad (4.18)$$

We chose a set of parameter values as $m_1 = 10$, $m_2 = 1$ kg, $K = 1,000$ N/m, $R = 5$ Ns/m, $\mu_m = 0.2$ and $r = 0.1$ m ($\mu = 2$), for which the stable gain range is found to be $0 < \alpha < 31.105$. We can now investigate the influence of different gain values. This may be easily done by plotting the root loci of the transfer function. For $\alpha = 0$, the poles of the system are 0 and $-2.75 \pm 33.05j$. For $\alpha = 2$, the poles of the

Fig. 4.26 Response of the articulated vehicle with different feedback gains



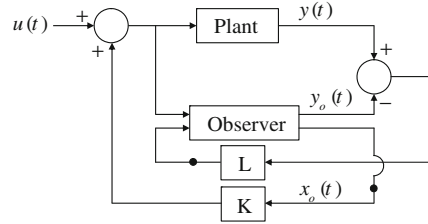
system are -0.363 and $-2.568 \pm 33.07j$. Thus, as the gain increases, the decay rate in rigid body mode increases (from 0 to 0.363) and the decay rate of oscillatory mode decreases (from 2.75 to 2.568). Thus, there exists a gain for which both the decay rates will be the same. At $\alpha = 10$, we have nearly such a configuration with the poles of the system at -1.812 and $-1.843 \pm 33.16j$. If we increase the gain further, the decay rate of oscillatory mode decreases and becomes zero at the stability threshold. For a value near the stability threshold, i.e., for $\alpha = 25$, the poles of the system are -4.46 and $-0.52 \pm 33.46j$.

The step responses of the system for the considered gain values are plotted in Fig. 4.26. The step response ($V_{ref} = 1$) is the plot of inverse Laplace transform of $G_c(s)/s$, because the Laplace transform of unit step is $1/s$. We observe from these step responses that when the feedback gain is low, the settling time is large, whereas when the feedback gain is on the higher side, there is some overshoot and the vehicle motion is not smooth. As a tradeoff, a gain value near 10 is proper for the considered system.

4.4 Controller and Observer Design

A full state-feedback control system uses an observer to estimate the unmeasured states of the system. These estimated states are then used in a feedback loop to control the actual system. The separation principle [1] allows independent designs for the controller and observer gains. These gains are so designed that the poles of the system and of the observer are placed at the desired locations. The general scheme of augmented controller-observer system is shown in Fig. 4.27, where $y(t)$ and $y_0(t)$ are, respectively, the plant and the observer outputs. The individual gains in this augmented controller and observer system (\mathbf{K} and \mathbf{L}) can be independently designed.

Fig. 4.27 General schematics for pole placement



4.4.1 Pole Placement

The full state feedback is implemented by modifying the input to the system as follows: $u' = u + \mathbf{K}\bar{x}$, where u' is the new input vector, u is the actual input vector, \mathbf{K} is a matrix of feedback gains, and \bar{x} is the state vector estimated from the observer. Because of separation principle, we will base our design on the assumption that $\bar{x} = x$. Then the state space form of the closed-loop system becomes

$$\begin{aligned}\dot{x} &= \mathbf{A}x + \mathbf{B}(u + \mathbf{K}x) = (\mathbf{A} + \mathbf{BK})x + \mathbf{B}u, \\ y &= \mathbf{C}x + \mathbf{D}(u + \mathbf{K}x) = (\mathbf{C} + \mathbf{DK})x + \mathbf{D}u.\end{aligned}\quad (4.19)$$

The new poles of the system are the eigenvalues of matrix $\mathbf{A} + \mathbf{BK}$. Finding a proper gain matrix such that eigenvalues of matrix $\mathbf{A} + \mathbf{BK}$ are the desired pole locations constitutes the pole placement problem. This problem can be solved in various ways. One of the commonly used methods is to bring the system to a controllable canonical form through similarity transformation, and the other commonly used method is the Ackermann's formula.

If there exists a matrix \mathbf{K} such that all poles of matrix $\mathbf{A} + \mathbf{BK}$ are sufficiently different from poles of matrix \mathbf{A} , then the system is said to be full state controllable. On the other hand, if the system is partially state controllable then only a few poles of $\mathbf{A} + \mathbf{BK}$ are sufficiently different from poles of matrix \mathbf{A} (those are called controllable poles) and the system is said to be partially controllable. Formally, controllability means the ability to move the internal states of a system by application of an external input to any final state from any initial state within a finite time interval.

To implement the feedback $\mathbf{K}x$, we need to know the states of the system. The observer is used to provide state estimates [18]. An observer is a model of the plant which receives the same input as the plant. The output of the actual plant and the observer is compared and the error is fed back through a gain such that the error dynamics is asymptotically stable.

For a system whose dynamics is described by

$$\begin{aligned}\dot{x} &= \mathbf{A}x + \mathbf{B}u, \\ y &= \mathbf{C}x + \mathbf{D}u;\end{aligned}\quad (4.20)$$

the corresponding observer dynamics is given by

$$\begin{aligned}\dot{x}_o &= \mathbf{A}x_o + \mathbf{B}u + \mathbf{L}(y - y_o), \\ y_o &= \mathbf{C}x_o + \mathbf{D}u;\end{aligned}\tag{4.21}$$

where subscript ‘o’ refers to observer. The observer design objective is that the observer states asymptotically converge to actual system states.

Then the state error dynamics is written as

$$\begin{aligned}\dot{x}_e &= \dot{x} - \dot{x}_o \\ &= \mathbf{A}x + \mathbf{B}u - \mathbf{A}x_o - \mathbf{B}u - \mathbf{L}(y - y_o) \\ &= \mathbf{A}(x - x_o) - \mathbf{L}(\mathbf{C}x + \mathbf{D}u - \mathbf{C}x_o - \mathbf{D}u) \\ &= (\mathbf{A} - \mathbf{L}\mathbf{C})(x - x_o) = (\mathbf{A} - \mathbf{L}\mathbf{C})x_e.\end{aligned}\tag{4.22}$$

If all eigenvalues of matrix $\mathbf{A} - \mathbf{L}\mathbf{C}$ lie on the left half of the complex plane, i.e., have negative real part, then the error between the plant and the observer states would decrease asymptotically. Thus, we need to choose a gain matrix \mathbf{L} such that the observer starts tracking the plant as soon as possible.

4.4.2 Controllability and Observability

If there exists an input $u(t)$ such that a linear system at any arbitrary initial state $x(t_0)$ can be brought to a final state $x(t_f)$, then the linear system is said to be controllable in the interval $[t_0, t_f]$. If the initial state $x(t_0)$ of a linear system can be calculated from the knowledge of inputs $u(t)$ and outputs $y(t)$ in the interval $[t_0, t_f]$, then the linear system is said to be observable in that interval. These two properties are important to design an integrated controller system. To place the controller poles, it is required that the system must be controllable. Likewise, observer poles can be placed at desired locations only when the system is observable.

Consider the state-space equations as

$$\dot{x} = \mathbf{A}x + \mathbf{B}u,\tag{4.23}$$

$$y = \mathbf{C}x + \mathbf{D}u.\tag{4.24}$$

By taking successive derivatives

$$\begin{aligned}\dot{x} &= \mathbf{A}x + \mathbf{B}u, \\ \ddot{x} &= \mathbf{A}\dot{x} + \mathbf{B}\dot{u} = \mathbf{A}^2x + \mathbf{A}\mathbf{B}u + \mathbf{B}\dot{u}, \\ &\vdots \\ x^{(n)} &= \frac{d^n x}{dt^n} = \mathbf{A}^n x + \mathbf{A}^{n-1}\mathbf{B}u + \mathbf{A}^{n-2}\mathbf{B}\dot{u} + \dots + \mathbf{B}u^{(n-1)}.\end{aligned}\tag{4.25}$$

We stop at n th derivative because we cannot obtain linearly independent equations thereafter. This is due to the Cayley–Hamilton theorem. Thus, from the available equations, we may write

$$\begin{aligned} \dot{x} &= \mathbf{A}x + \mathbf{B}u, \\ \ddot{x} &= \mathbf{A}\dot{x} + \mathbf{B}\dot{u} = \mathbf{A}^2x + \mathbf{A}\mathbf{B}u + \mathbf{B}\dot{u}, \\ &\vdots \\ x^{(n)}(t) - \mathbf{A}^n x(t) &= [\mathbf{B} \ \mathbf{A}\mathbf{B} \ \dots \ \mathbf{A}^{n-1}\mathbf{B}] \begin{bmatrix} u^{(n-1)}(t) \\ u^{(n-2)}(t) \\ \vdots \\ u(t) \end{bmatrix}. \end{aligned} \quad (4.26)$$

If the current state is known and controllability matrix $[\mathbf{B} \ \mathbf{A}\mathbf{B} \ \dots \ \mathbf{A}^{n-1}\mathbf{B}]$ is not singular, then we may specify our requirement for evolution of the system's response in terms of the derivatives of the state vector up to n th order (\dot{x} , \ddot{x} , ...) and obtain a solution in terms of the input and its derivatives up to $(n - 1)$ th order. This means, it is possible to create an input function for every desired evolution of the state vector at each point of time.

Another approach is to consider the solution of Eq. 4.23 as

$$x(t) = e^{\mathbf{A}(t-t_0)}x(t_0) + \int_{t_0}^t e^{\mathbf{A}(t-\tau)}\mathbf{B}u(\tau) d\tau.$$

If the system can be brought to a final state x_f in a finite time interval $[t_0, t_f]$, then

$$\begin{aligned} x_f &= e^{\mathbf{A}(t_f-t_0)}x(t_0) + \int_{t_0}^{t_f} e^{\mathbf{A}(t_f-\tau)}\mathbf{B}u(\tau) d\tau \\ \text{or } e^{-\mathbf{A}t_f}x_f - e^{-\mathbf{A}t_0}x(t_0) &= \int_{t_0}^{t_f} e^{-\mathbf{A}\tau}\mathbf{B}u(\tau) d\tau \end{aligned} \quad (4.27)$$

Now we may make use of the Cayley–Hamilton theorem and truncate the Taylor series expansion of $e^{-\mathbf{A}\tau}$ at $(n - 1)$ th power of matrix \mathbf{A} (because all higher powers of matrix \mathbf{A} can be expressed in terms of the lower powers). Thus,

$$e^{-\mathbf{A}\tau} = \sum_{k=0}^{n-1} \alpha_k(\tau) \mathbf{A}^k \quad (4.28)$$

where $\alpha_k(\tau)$ are some scalar time coefficients.

Then, Eq. 4.27 can be written as

$$e^{-\mathbf{A}t_f} x_f - e^{-\mathbf{A}t_0} x(t_0) = \sum_{k=0}^{n-1} \mathbf{A}^k \mathbf{B} \int_{t_0}^{t_f} \alpha_k(\tau) u(\tau) d\tau \quad (4.29)$$

$$= [\mathbf{B} \ \mathbf{A}\mathbf{B} \ \dots \ \mathbf{A}^{n-1}\mathbf{B}] \begin{bmatrix} \int_{t_0}^{t_f} \alpha_0(\tau) u(\tau) d\tau \\ \int_{t_0}^{t_f} \alpha_1(\tau) u(\tau) d\tau \\ \vdots \\ \int_{t_0}^{t_f} \alpha_{n-1}(\tau) u(\tau) d\tau \end{bmatrix} \quad (4.30)$$

If the final state and the finite time interval are specified, then

$$\begin{bmatrix} \int_{t_0}^{t_f} \alpha_0(\tau) u(\tau) d\tau \\ \int_{t_0}^{t_f} \alpha_1(\tau) u(\tau) d\tau \\ \vdots \\ \int_{t_0}^{t_f} \alpha_{n-1}(\tau) u(\tau) d\tau \end{bmatrix} = [\mathbf{B} \ \mathbf{A}\mathbf{B} \ \dots \ \mathbf{A}^{n-1}\mathbf{B}]^{-1} \left(e^{-\mathbf{A}t_f} x_f - e^{-\mathbf{A}t_0} x(t_0) \right) \quad (4.31)$$

The right-hand side terms of Eq. 4.31 are known quantities and the left-hand side contains functions of the input. These functions can be determined provided matrix $S = [\mathbf{B} \ \mathbf{A}\mathbf{B} \ \dots \ \mathbf{A}^{n-1}\mathbf{B}]$, called the controllability matrix, is invertible, i.e., it must be of full rank: $\text{rank}(\mathbf{S}) = n$. There are many procedures to compute the actual input sequence, such as by controllability Grammian.

Consider Eq. 4.23 with $\mathbf{D} = 0$. The derivatives of the output can be written as

$$\begin{aligned} \dot{y} &= \mathbf{C}\dot{x} = \mathbf{C}\mathbf{A}x + \mathbf{C}\mathbf{B}u, \\ \ddot{y} &= \mathbf{C}\mathbf{A}\dot{x} + \mathbf{C}\mathbf{B}\dot{u} = \mathbf{C}\mathbf{A}^2x + \mathbf{C}\mathbf{A}\mathbf{B}u + \mathbf{C}\mathbf{B}\dot{u}, \\ &\vdots \\ y^{(n-1)} &= \frac{d^{n-1}y}{dt^{n-1}} = \mathbf{C}\mathbf{A}^{n-1}x + \mathbf{C}\mathbf{A}^{n-2}\mathbf{B}u + \mathbf{C}\mathbf{A}^{n-3}\mathbf{B}\dot{u} + \dots + \mathbf{C}\mathbf{B}u^{(n-2)}. \end{aligned} \quad (4.32)$$

As discussed before, it is useless to take any higher order derivatives. If $y(t_0)$ and all its derivatives are known, and $u(t_0)$ and all its derivatives are also known, then it is possible to compute state $x(t_0)$ from

$$\begin{bmatrix} \mathbf{C} \\ \mathbf{C}\mathbf{A} \\ \vdots \\ \mathbf{C}\mathbf{A}^{n-1} \end{bmatrix} x(t_0) = \begin{bmatrix} y(t_0) \\ \dot{y}(t_0) - \mathbf{C}\mathbf{B}u(t_0) \\ \vdots \\ y^{(n-1)}(t_0) - \mathbf{C}\mathbf{A}^{n-2}\mathbf{B}u(t_0) - \dots - \mathbf{C}\mathbf{B}u^{(n-2)}(t_0) \end{bmatrix}. \quad (4.33)$$

if matrix $\mathbf{O} = [\mathbf{C} \ \mathbf{C}\mathbf{A} \ \dots \ \mathbf{C}\mathbf{A}^{n-1}]^T$, called the observability matrix, is invertible, i.e., $\text{rank}(\mathbf{O}) = n$.

Controllability and observability, together referred to as control properties, are fundamental properties which are to be determined before designing the controller for a system. The controllability and observability properties are stated in terms of Lie brackets for nonlinear systems. For large systems, whether linear or nonlinear, determining these control properties is a time-consuming task. First of all, the system equations have to be derived and written in state-space form. Then, numerical parameter values have to be considered and controllability and observability matrices have to be computed. Fortunately, there are structural approaches to quickly test controllability and observability of systems. The properties of the structure of the model (in graphical or equation form) are exploited in those approaches.

4.5 Structural Analysis of Control Properties

Structural properties relate to properties of the model structure. These properties do not depend on the actual values of the parameters. Structural analysis was first developed in [11] for SISO systems and was later extended to MIMO systems [21].

For a state-space description defined as

$$\begin{aligned}\dot{x} &= \mathbf{A}x + \mathbf{B}u, \\ y &= \mathbf{C}x + \mathbf{D}u,\end{aligned}\tag{4.34}$$

the structural control properties are related to matrix properties of 4-tuple (or quadruple) $\{\mathbf{A}, \mathbf{B}, \mathbf{C}, \mathbf{D}\}$. The structurally equivalent description of the 4-tuple is given as $\{\mathbf{A}^*, \mathbf{B}^*, \mathbf{C}^*, \mathbf{D}^*\}$. For every nonzero entry in the original 4-tuple, the corresponding entry in the structurally equivalent 4-tuple is 1 and the rest of the entries remain 0. The structurally equivalent 4-tuple $\{\mathbf{A}^*, \mathbf{B}^*, \mathbf{C}^*, \mathbf{D}^*\}$ is also termed interconnection matrices.

The structural control properties may be evaluated on the structurally equivalent 4-tuple $\{\mathbf{A}^*, \mathbf{B}^*, \mathbf{C}^*, \mathbf{D}^*\}$ [9]. The interconnection matrices may be derived in a straightforward manner from the bond graph model of a system by following the causal paths on the model. This does not require derivation of the complete state-space equations. In the following, we illustrate this approach by assuming that there is no direct feedthrough in the system ($\mathbf{D} = \mathbf{0}$). Let the elements of \mathbf{A}^* , \mathbf{B}^* and \mathbf{C}^* be defined as follows for a system of n states, m inputs, and p outputs:

$$\mathbf{A}^* = \begin{pmatrix} a_{11}^* & a_{12}^* & \dots & a_{1n}^* \\ a_{21}^* & a_{22}^* & \dots & a_{2n}^* \\ \vdots & \vdots & \vdots & \vdots \\ a_{n1}^* & a_{n2}^* & \dots & a_{nn}^* \end{pmatrix}, \quad \mathbf{B}^* = \begin{pmatrix} b_{11}^* & b_{12}^* & \dots & b_{1m}^* \\ b_{21}^* & b_{22}^* & \dots & b_{2m}^* \\ \vdots & \vdots & \vdots & \vdots \\ b_{n1}^* & b_{n2}^* & \dots & b_{nm}^* \end{pmatrix}, \quad \mathbf{C}^* = \begin{pmatrix} c_{11}^* & c_{12}^* & \dots & c_{1n}^* \\ c_{21}^* & c_{22}^* & \dots & c_{2n}^* \\ \vdots & \vdots & \vdots & \vdots \\ c_{p1}^* & c_{p2}^* & \dots & c_{pn}^* \end{pmatrix}.\tag{4.35}$$

Fig. 4.28 A two-degrees-of-freedom system with flow actuation

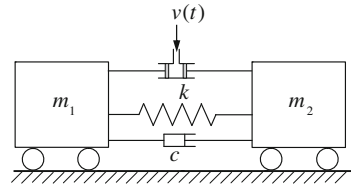
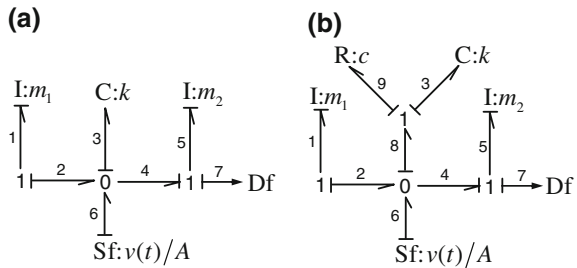


Fig. 4.29 Bond graph model of two-DOF system (a) without damper and (b) with damper



The elements are determined from partial causal path analysis. First of all, all elements of matrix \mathbf{A}^* , \mathbf{B}^* , and \mathbf{C}^* are initialized to 0. To determine element a_{ij} , one starts from the bond graph storage element associated with j th state and checks for existence of the shortest causal path (containing least number of storage elements) up to the bond graph storage element associated with i th state. If such a causal path exists and it does not pass through any other storage element in integral causality (i.e., the order of the shortest causal path is zero) then $a_{ij} = 1$. Moreover, if there are no activated bonds (signal bonds) involved during traversal of that causal path, it implies the existence of a direct causal path (traversal of complimentary power variable) from bond graph storage element associated with i th state to the bond graph storage element associated with j th state without passing through any other storage element in integral causality, i.e., $a_{ji} = 1$. Thus for a bond graph model composed of purely passive bonds, $a_{ij} = a_{ji}$, or in other words, matrix \mathbf{A}^* is symmetric (more detailed proof of this is given in [28]).

The elements of matrix \mathbf{B}^* are likewise determined. The element $b_{ij} = 1$ if there is a direct causal path from j th input to i th state. The direct causal path here means it does not pass through any other storage element. Likewise, if there is a direct causal path from i th state to j th output, the element $c_{ij} = 1$.

As an example, consider the two-degrees-of-freedom system shown in Fig. 4.28 where $V(t)$ indicates volume flow rate of an incompressible fluid. If the piston area is A , it translates into a linear velocity input of $V(t)/A$. The bond graph model of this system without considering the damper is given in Fig. 4.29a and that with damper is given in Fig. 4.29b.

From Fig. 4.29a, the state vector is defined as $x = [P_1 \ P_5 \ Q_3]^T$, the input vector is $u = SF_6$ and the output vector is $y = Df_7$. To determine element a_{11} , we start from the output variable associated with the I element at bond 1, i.e., from variable f_1 and

search for a direct causal path to input variable associated with the I element at bond 1, i.e., variable e_1 . Because no such path exists in Fig. 4.29a, $a_{11} = 0$. The causal path starting from variable f_1 is as follows: $f_1 \rightarrow f_2 \rightarrow f_3 \rightarrow C : k \rightarrow e_3 \rightarrow \dots$. Because the path cannot pass through an integrally causalled element, it has to be truncated as $f_1 \rightarrow f_2 \rightarrow f_3 \rightarrow C : k$. Thus, there is no direct causal path between f_1 to e_5 , which is the input variable associated with the second state. Thus, $a_{12} = 0$. However, there is a direct causal path ($e_3 \rightarrow e_2 \rightarrow e_1$) between output of the storage element associated with state 3 to the input of the storage element associated with state 1. Thus, $a_{13} = 1$.

Note that the symmetry of matrix \mathbf{A}^* demands that $a_{31} = 1$. This is easily visualized. The causal path from output of the storage element associated with state 3 to the input of the storage element associated with state 1 is as follows: $f_1 \rightarrow f_2 \rightarrow f_3$. This causal path is direct and thus $a_{31} = 1$. The elements of the second row of matrix \mathbf{A}^* may be similarly obtained. $a_{21} = a_{12} = 0$, $a_{22} = 0$ (similar to the way we found a_{11}) and $a_{23} = 1$ (similar to the way we found a_{13}). From symmetry, $a_{32} = 1$. The first two elements of the third row of matrix \mathbf{A}^* have already been determined. The last element $a_{33} = 0$ because there is no direct causal path from variable e_3 to f_3 .

To evaluate elements of matrix \mathbf{B}^* , we examine direct causal path(s) from variable f_6 to input variables of bond graph storage elements. The one direct causal path is $f_6 \rightarrow f_3$. Thus, $b_{11} = b_{21} = 0$ and $b_{31} = 1$. Likewise, the elements of matrix \mathbf{C}^* are evaluated from direct causal paths existing between output variables of bond graph storage elements to sensed variable f_7 , which gives $c_{11} = c_{13} = 0$, and $c_{21} = 1$.

Thus, from Fig. 4.29a, we find

$$\mathbf{A}^* = \begin{pmatrix} 0 & 0 & 1 \\ 0 & 0 & 1 \\ 1 & 1 & 0 \end{pmatrix}, \quad \mathbf{B}^* = \begin{pmatrix} 0 \\ 0 \\ 1 \end{pmatrix}, \quad \mathbf{C}^* = (0 \ 1 \ 0). \quad (4.36)$$

Let us now consider the bond graph model given in Fig. 4.29b. The state vector, the input vector, and the output vector remain the same as that in the earlier case. To evaluate element a_{11} , we have to find a direct causal path from the output variable associated with the I element at bond 1, i.e., from variable f_1 to the input variable associated with the I element at bond 1, i.e., variable e_1 . In this case, the causal path $f_1 \rightarrow f_2 \rightarrow f_8 \rightarrow f_9 \rightarrow R : c \rightarrow e_9 \rightarrow e_8 \rightarrow e_2 \rightarrow e_1$ does not involve any storage element and hence it is a direct path. Thus, $a_{11} = 1$. Similarly, direct causal path $f_5 \rightarrow f_4 \rightarrow f_8 \rightarrow f_9 \rightarrow R : c \rightarrow e_9 \rightarrow e_8 \rightarrow e_2 \rightarrow e_1$ indicates that $a_{12} = 1$ (also $a_{21} = 1$). The direct causal path ($e_3 \rightarrow e_2 \rightarrow e_1$) gives $a_{13} = a_{31} = 1$. Continuing in this way, the structurally equivalent matrices of the 4-tuple are found to be

$$\mathbf{A}^* = \begin{pmatrix} 1 & 1 & 1 \\ 1 & 1 & 1 \\ 1 & 1 & 0 \end{pmatrix}, \quad \mathbf{B}^* = \begin{pmatrix} 0 \\ 0 \\ 1 \end{pmatrix}, \quad \mathbf{C}^* = (0 \ 1 \ 0). \quad (4.37)$$

We now examine the state-space equations of motion. From Fig. 4.29a, we find

$$\begin{bmatrix} \dot{P}_1 \\ \dot{P}_5 \\ \dot{Q}_3 \end{bmatrix} = \begin{pmatrix} 0 & 0 & -k \\ 0 & 0 & k \\ \frac{1}{m_1} & -\frac{1}{m_2} & 0 \end{pmatrix} \begin{bmatrix} P_1 \\ P_5 \\ Q_3 \end{bmatrix} + \begin{pmatrix} 0 \\ 0 \\ 1 \end{pmatrix} V(t)/A,$$

$$y = \begin{pmatrix} 0 & \frac{1}{m_2} & 0 \end{pmatrix} \begin{bmatrix} P_1 \\ P_5 \\ Q_3 \end{bmatrix}. \quad (4.38)$$

The structurally equivalent form of the state equations in Eq. 4.38 are the same as those given in Eq. 4.36.

The state-space equations of motion from Fig. 4.29b are given as

$$\begin{bmatrix} \dot{P}_1 \\ \dot{P}_5 \\ \dot{Q}_3 \end{bmatrix} = \begin{pmatrix} -\frac{c}{m_1} & \frac{c}{m_2} & -k \\ \frac{c}{m_1} & -\frac{c}{m_2} & k \\ \frac{1}{m_1} & -\frac{1}{m_2} & 0 \end{pmatrix} \begin{bmatrix} P_1 \\ P_5 \\ Q_3 \end{bmatrix} + \begin{pmatrix} 0 \\ 0 \\ 1 \end{pmatrix} V(t)/A,$$

$$y = \begin{pmatrix} 0 & \frac{1}{m_2} & 0 \end{pmatrix} \begin{bmatrix} P_1 \\ P_5 \\ Q_3 \end{bmatrix}, \quad (4.39)$$

whose structurally equivalent form turns out to be the same as those given in Eq. 4.37.

Thus, to evaluate structural control properties of a system from its bond graph model, one need not derive the complete equations of motion. Simple causal path analysis is sufficient to derive the structurally equivalent matrices of the 4-tuple and they may then be used for control system analysis. This procedure is easily automated in a simple computer program and applied to study control properties of larger systems.

4.5.1 Structural Rank

Consider a linear time-invariant (LTI) system represented by the following state-space model:

$$\begin{aligned} \dot{x} &= \mathbf{A}x + \mathbf{B}u, \\ y &= \mathbf{C}x + \mathbf{D}u. \end{aligned} \quad (4.40)$$

If n is the number of states, then the characteristic polynomial of the system or the denominator of transfer functions from the control input to the observed outputs may be written as

$$D(s) = |s\mathbf{I} - \mathbf{A}| = s^p (s^q + a_{q-1}s^{q-1} + \cdots + a_1s + a_0), \quad (4.41)$$

where s is the Laplace operator, \mathbf{I} is an $n \times n$ identity matrix, $p + q = n$, and the coefficients $a_{q-1} \dots a_0$ are functions of the system parameters. The number of structurally null modes in the system is p , i.e., there are at least p number of eigenvalues which are zero. However, the actual null modes in the system may be higher owing to parameter dependence, e.g., when $a_0 = 0$, the number of null modes is $p+1$.

Since the term s^p can be separated out as a factor from $|s\mathbf{I} - \mathbf{A}|$, the $s\mathbf{I} - \mathbf{A}$ matrix contains p rows with diagonal elements containing s and other terms in those rows cancel out during determinant calculation. Thus for $s = 0$, or $s\mathbf{I} - \mathbf{A} = -\mathbf{A}$, these rows are linearly dependent on other rows. This implies that matrix \mathbf{A} can be brought to a form where p rows will contain all elements equal to zero. Thus, the structural rank of matrix \mathbf{A} is $n - p = q$.

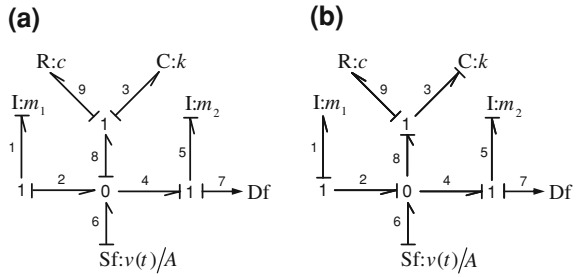
To find q , the system equations need not be derived and tested. They can be obtained by evaluating the rank of the structurally equivalent matrices:

As an example, the rank of structurally equivalent 3×3 matrix \mathbf{A}^* in Eqs. 4.36 and 4.37 is two. Thus, the system shown in Fig. 4.28, whether the damper is present or absent, has at least one null mode. This conclusion may be directly derived from the physical understanding of the system. The system null mode corresponds to a case when both the masses move with equal velocity so that neither the spring nor the damper is deformed. This null mode indicates 0 eigenvalue of matrix \mathbf{A} given in Eqs. 4.38 and 4.39. The other two eigenvalue matrices \mathbf{A} turn out to be complex conjugates of each other and are associated with the internal mode of vibration (deformation of the spring and the damper). These eigenvalues are complex conjugates with nonzero real part when the damper is present and purely imaginary when the damper is absent. These two non-null eigenvalues indicate the rank of matrix \mathbf{A} . Although it appears that a correct conclusion has been arrived at by considering structurally equivalent matrices in place of actual matrices of the state-space 4-tuple, it will be shown that the results obtained from structural equivalence may be misleading.

A more straightforward approach to determine the structural rank of the system from its bond graph model is given in [5, 19, 22–24]. It is based on re-causalling the base model as follows:

1. The order (n) of a system (dimension of matrix \mathbf{A} or number of states) is the number of integrally causalled storage elements (I and C) in the base model, i.e., the model causalled to maximize integral causality (a preferred integral causality model).
2. The structural rank of the model (rank of matrix \mathbf{A} without parameter dependence) is the number (q) of differentially causalled storage elements (I and C) in a preferred differential (or derivative) causality model which were in integral causality in the base model. This step comprises re-causalling of the model with a different preference and then comparing the causality of I and C with those in the base model.

Fig. 4.30 Bond graph model of two-DOF system in preferred (a) integral and (b) derivative causality



3. The number of structurally null modes is the number $(p = n - q)$.

Let us again consider the two-degrees-of-freedom system given in Fig. 4.28. Its bond graph model in the preferred integral causality is given in Fig. 4.30a. We find three storage elements in integral causality which means $n = 3$. The bond graph model may be assigned preferred derivative causality in many ways. The bond graph model in one such form is given in Fig. 4.30b. It is not possible to assign differential causality to both the I-elements because in that case there will be a violation of causality at the 0-junction. Thus, a maximum of two storage elements can be assigned derivative causality. This means that the structural rank of the system $q = 2$ and the number of null modes of the system $p = n - q = 1$. This is the same result that has been obtained earlier by analyzing the structurally equivalent matrices.

Caveat

If the rank of a system evaluated from structurally equivalent matrix \mathbf{A}^* turns out to be equal to the number of states then the system has full rank and does not contain null modes. However, when the rank of matrix \mathbf{A}^* is less than the number of states then it cannot be concluded that the system does not have full rank or that the system has null modes.

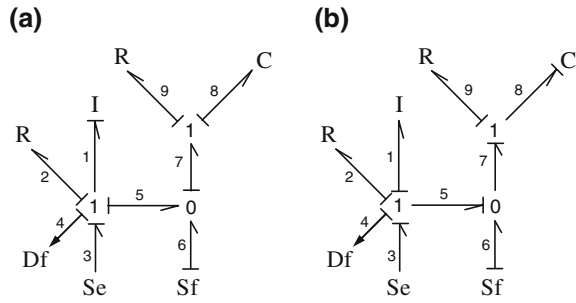
We can illustrate this conflict with a simple example.

Consider the bond graph model given in Fig. 4.31a for which the state vector $x = [P_1 \ Q_8]^T$, the input vector is $u = [Se_3 \ Sf_6]^T$ and the output vector is $y = Df_4$. Its structurally equivalent matrices in the 4-tuple describing the state-space equations are

$$\mathbf{A}^* = \begin{pmatrix} 1 & 1 \\ 1 & 1 \end{pmatrix}, \quad \mathbf{B}^* = \begin{pmatrix} 1 & 0 \\ 0 & 1 \end{pmatrix}, \quad \mathbf{C}^* = (1 \ 0). \tag{4.42}$$

The rank of the system, when evaluated from a structurally equivalent matrix, turns out to be $\text{rank}(\mathbf{A}^*) = 1$. Note that when the rank of the system is evaluated directly from matrix \mathbf{A} (after full equation derivation), it is found to be 2. The same result is obtained by assigning preferred derivative causality to the model (See Fig. 4.31b). Thus, rank evaluation based on structurally equivalent matrices can give

Fig. 4.31 Bond graph model of a certain system in preferred (a) integral and (b) derivative causality



wrong results, especially when it predicts that the system does not have full rank. Some makeshift solutions in this regard have been suggested. One of them is to replace some ones by zeroes and recheck the rank. Another approach is to replace all ones by some random numbers and re-evaluate the rank. If the new rank turns out to be more than the older rank, then the maximum rank obtained is the solution. However, this process too can give wrong results (for example, when applied on the 4-tuple given in Eq. 4.37, it may give rank of the system to be 3 whereas the actual rank is 2). Thus, these are all chance results which cannot be relied upon.

In conclusion, the approach presented in [28] (which in turn is based on [9]) may at best be a test to assure whether a system has full rank. If it gives positive results, then it is acceptable. But a negative result means one has to use alternative methods to test the structural rank, such as the one based on differential causality assignment on the bond graph model.

4.5.2 Structural Controllability

The numerical method to determine the controllability of a system is to check whether the controllability matrix has full rank n , where n is the number of states. The controllability matrix(\mathbf{S}) of a continuous time system is defined as

$$\mathbf{S} = [\mathbf{B} \ \mathbf{A}\mathbf{B} \ \dots \ \mathbf{A}^{n-1}\mathbf{B}]. \tag{4.43}$$

The rank of the controllability matrix depends on the numerical values of the parameters and hence it cannot be considered as a robust measure, i.e., it does not indicate whether there are some parameter values for which the system may be controllable and conversely, whether the system is uncontrollable for all combination of parameter values. Thus, one needs to study the structural properties rather than the numerical properties.

The structurally equivalent controllability matrix(\mathbf{S}^*) is defined as

$$\mathbf{S}^* = [\mathbf{B}^* \ \mathbf{A}^*\mathbf{B}^* \ \dots \ (\mathbf{A}^*)^{n-1}\mathbf{B}^*]. \tag{4.44}$$

It is easier to compute the rank of the structurally equivalent controllability matrix which indicates structural controllability of the system.

For the system considered in Fig. 4.28, the structurally equivalent controllability matrix is given as

$$\mathbf{S}^* = \left[\begin{array}{c|c|c|c|c} \begin{pmatrix} 0 \\ 0 \\ 1 \end{pmatrix} & \begin{pmatrix} 1 & 1 & 1 \\ 1 & 1 & 1 \\ 1 & 1 & 0 \end{pmatrix} & \begin{pmatrix} 0 \\ 0 \\ 1 \end{pmatrix} & \begin{pmatrix} 1 & 1 & 1 \\ 1 & 1 & 1 \\ 1 & 1 & 0 \end{pmatrix}^2 & \begin{pmatrix} 0 \\ 0 \\ 1 \end{pmatrix} \end{array} \right] \quad (4.45)$$

$$= \begin{bmatrix} 0 & 1 & 2 \\ 0 & 1 & 2 \\ 1 & 0 & 2 \end{bmatrix}. \quad (4.46)$$

We find that $\text{rank}(\mathbf{S}^*) = 2$ which is less than the order ($n = 3$) of the system. Thus, the system is structurally uncontrollable. Note that when one finds a system to be controllable by analyzing structurally equivalent matrices, it is the correct result. However, one cannot conclude that a system is uncontrollable when the analysis is based on structurally equivalent matrices.

The true structural controllability can be elegantly derived from causal analysis on the bond graph model [5, 19, 22–24]. This procedure neither requires derivation of state equations nor its structural equivalence 4-tuple. It is a procedure simply based on bond graph structure, which is robust and parameter independent. This procedure is remarkable in the sense that it also indicates the location of actuators and their type so as to make a system controllable with minimal number of actuators.

The conditions needed for a system to be structurally controllable are:

1. *Attainability/reachability condition (necessary condition)*: every storage element (integrally causalled I and C) in the bond graph model with preferred integral causality must have at least one causal path from a control source (MSe or MSf).
2. *Sufficient condition*: every integrally causalled storage element (I and C) in the bond graph model (with preferred integral causality) can be differentially causalled (assigned derivative causality) when preferred differential causality is assigned on the bond graph model. If some integrally causalled elements in preferred integral causality mode cannot be assigned differential causality in the preferred differential causality mode, then dualization of some or all control sources (control MSe to control MSf and vice versa) or inversion of their causalities may be performed to allow those storage elements to accept differential causality. Note that causalities of uncontrolled sources, e.g. force due to gravity, are not to be altered.

If the necessary and sufficient conditions are satisfied, then the rank of matrix \mathbf{S} is n . If matrix \mathbf{A} is of full rank, the system is controllable with a single actuator whose position is determined by the attainability condition (such that matrix $[\mathbf{B} \ \mathbf{A}]$ has full rank) and other design considerations.

If the sufficient condition is not satisfied and only q ($q < n$) number of storage elements, originally in integral causality, could be differentially causalled, then the

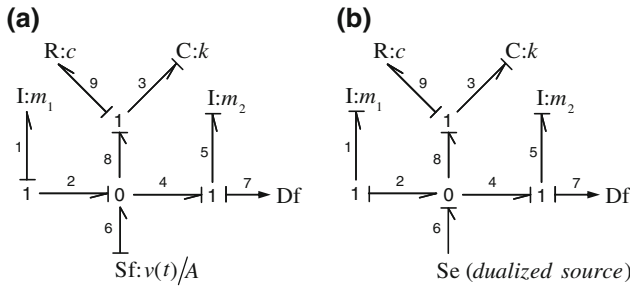


Fig. 4.32 Structural controllability test on bond graph model of two-DOF system with (a) no source dualization and (b) source dualization

rank of matrix S is q . Then for the model to be controllable, $p = n - q$ actuators are needed and their location has to be determined by attainability condition and their participation has to be determined by control source dualization.

In the bond graph model given in Fig. 4.30a, all storage elements are linked by causal paths from the source (here, causal path is complete and need not be direct, i.e., it may pass through storage elements). Thus, the model satisfies attainability condition.

When given preferred derivative causality, without changing the source, we find that one of the storage elements could not be differentially causalled (See Fig. 4.32a). When the control input is dualized, two storage elements could not be differentially causalled (See Fig. 4.32b). Thus, the maximal differential causality is given in Fig. 4.32a, from which we find that the system is uncontrollable. It is left to the reader to verify that the system becomes structurally controllable when the flow excitation is removed and an effort excitation is given at any of the mass points.

Structural controllability test requires maximal derivative causality assignment with/without dualization of sources. During structural controllability tests, one may dualize control sources (MSe and MSf elements) to assign differential causalities to storage elements. It is important to note that while some sources are dualized, some may not be. Solving this problem is difficult for large systems. However, allowing source dualization means that the ports attached to these elements can take up any causality. One of the alternative methods to check structural controllability is to replace all the control sources by R-elements, which can take any causality, and then complete the preferred differential causality assignment.

4.5.3 Structural Observability

The rank of the observability matrix depends on the numerical values of the parameters and hence it cannot be considered as a robust measure of full-state observability. This method also does not identify the modes of the system that are not observable.

Thus, analyzing the structurally equivalent observability matrix gives a better idea of the observability of the system. The structurally equivalent observability matrix (\mathbf{O}) is given as

$$\mathbf{O}^* = \begin{bmatrix} \mathbf{C}^* \\ \mathbf{C}^* \mathbf{A}^* \\ \mathbf{C}^* (\mathbf{A}^*)^2 \\ \vdots \\ \mathbf{C}^* (\mathbf{A}^*)^{n-1} \end{bmatrix}. \quad (4.47)$$

The full rank condition can be tested on the structurally equivalent observability matrix instead of the actual observability matrix (which needs full state equations).

For the considered example, the structurally equivalent observability matrix is found to be

$$\mathbf{O}^* = \begin{bmatrix} 0 \ 1 \ 0 \\ (0 \ 1 \ 0) \begin{pmatrix} 1 & 1 & 1 \\ 1 & 1 & 1 \\ 1 & 1 & 0 \end{pmatrix} \\ (0 \ 1 \ 0) \begin{pmatrix} 1 & 1 & 1 \\ 1 & 1 & 1 \\ 1 & 1 & 0 \end{pmatrix}^2 \end{bmatrix} = \begin{bmatrix} 0 & 1 & 0 \\ 1 & 1 & 1 \\ 3 & 3 & 2 \end{bmatrix}. \quad (4.48)$$

We find that $\text{rank}(\mathbf{O}^*) = 3$, which is the same as the number of states in the system. Thus, the system is observable with the given set of sensors. Here, the use of structurally equivalent matrices gives that the observability matrix has full rank. This is an acceptable (and true) result. However, if it were found that the rank of the structurally equivalent observability matrix is less than the number of states then it cannot be concluded for sure that the system is actually unobservable.

The structural observability is more elegantly tested by causal analysis of the bond graph model [5, 19, 22–24]. This procedure does not require construction of actual or equivalent 4-tuple and it is both robust and parameter independent. This procedure also indicates the location and type of sensor required to make a system observable with minimal number of sensors. It will be shown in later chapters that a system needs to be observable to be monitorable (i.e., detect abnormal changes to system as consequence of a fault). The bond graph causality-based structural observability test requires that the model satisfies the following conditions:

1. *Attainability/reachability condition (necessary condition)*: every storage element (integrally causalled I and C) in the bond graph model with preferred integral causality must have at least one causal path to a sensor (De or Df element).
2. *Sufficient condition*: every integrally causalled storage element (I and C) in the bond graph model with preferred integral causality can be differentially causalled (assigned derivative causality) when preferred differential causality is assigned

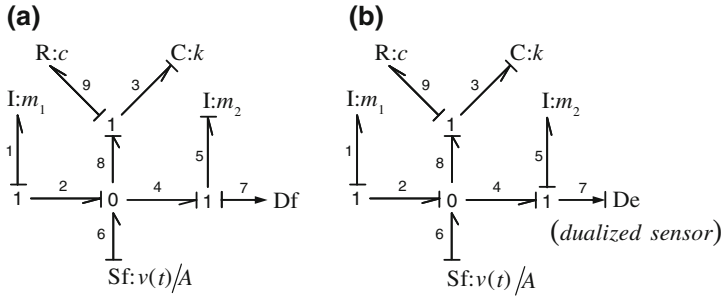


Fig. 4.33 Structural observability test on bond graph model of two-DOF system with (a) no sensor dualization and (b) sensor dualization

on the bond graph model. When some integrally caused elements in preferred integral causality mode cannot be assigned differential causality in the preferred differential causality mode, some or all sensors may be dualized (De to Df and *vice versa*) or their causalities may be inverted such that those storage elements can be differentially caused.

If the necessary and sufficient conditions are satisfied, then the rank of matrix \mathbf{O} is n . If rank of matrix \mathbf{A} is n , then only one suitably placed sensor, determined by attainability condition (so that matrix $[\mathbf{C}^T \mathbf{A}^T]^T$ has full rank), is sufficient to guarantee full-state observability. If the rank of \mathbf{O} is q , then $p = n - q$ number of additional sensors are needed to assure observability and the position of these sensors has to be determined by the attainability condition and design considerations.

For the considered example, maximal derivative causality assignment without sensor dualization and with sensor dualization are shown in Fig. 4.33. It is found that sensor dualization allows us to assign derivative causality to all three storage elements. Thus, the system is structurally observable with the given set of sensors.

During structural observability tests, one may dualize sensors (De and Df elements) so that the maximum number of storage elements are brought to differential causality. This process may require dualization of some sensors and keeping the rest in their original form. For large systems with many sensors, it is difficult to achieve maximal derivative causality in this process. However, allowing dualization of sensors means that the ports connected to sensors can be assigned any causality. Alternatively, one may simply replace all sensors by R-elements and then proceed with preferred differential causality assignment.

4.5.4 Infinite Zeroes and Relative Degree

While the controllability of a system is a desired property, one also needs to estimate the degree of controllability. In [6], two reasons are given for lower degree of con-

trollability (i.e., when a system is hard to control) of a linear system described by a rational transfer function. A system may be hard to control when

1. The relative degree of the transfer function is large.
2. The zeroes of the transfer function are lightly damped or have positive real parts.

For a SISO system, the relative degree of a transfer function is the number of poles (states)—number of zeroes. The actual zeroes of a transfer function are referred to as finite zeroes. The number of infinite zeroes of a system is the relative degree of the transfer function, i.e., the number of asymptotes in the root locus.

The number of poles of the transfer function is the number of storage elements in integral causality in the behavior model (also called forward model). On the other hand, the number of zeroes of the transfer function is the number of storage elements in integral causality in the inverse model [16, 17]. The inverse model of a system is described in the later chapters. The inverse model relates to computation of desired inputs for specified outputs. If the transfer function between a source and a sensor is $G_f(s)$, then in the inverse model the original source becomes the sensor and the original sensor becomes the source and the new source to new sensor transfer function is $G_i(s) = 1/G_f(s)$, meaning that the zeroes of $G_f(s)$ become poles of $G_i(s)$.

Naturally, the ease with which LTI systems can be controlled is related to the number and location of the system's zeroes. The reasons to study the relative degree of a system during a control system design is to choose the proper type of sensor and its location such that the relative degree of the obtained transfer function is minimized.

As an example, consider a certain system whose transfer function is given as

$$G(s) = \frac{s + 4}{(s + 1)(s^2 + 2s + 2)}.$$

The root loci of this system for positive gains is given in Fig. 4.34a, which shows two asymptotes (for two infinite zeroes) with the centroid at 0.5. The range of stable feedback gains for this system may be evaluated from Routh array and it is given as $-0.5 < K < 10$.

Because this system has a small relative degree ($3 - 1 = 2$), it is easily controllable. We may add a lead compensator so that the asymptotes lie in the left half of the complex plane. The lead compensator must move the centroid of the graph by -0.5 at the minimum. A lead compensator that moves the centroid by -1 may be given as $f(s) = (s + 5)/(s + 7)$.

The transfer function of the new system is then

$$G_c(s) = \frac{(s + 4)(s + 5)}{(s + 1)(s + 7)(s^2 + 2s + 2)}.$$

The root loci of the modified system is shown in Fig. 4.34b which shows that the system is stable for all positive feedback gains. From Routh array, one finds the range of stable feedback gains for the compensated system to be $K > -0.7$. This result

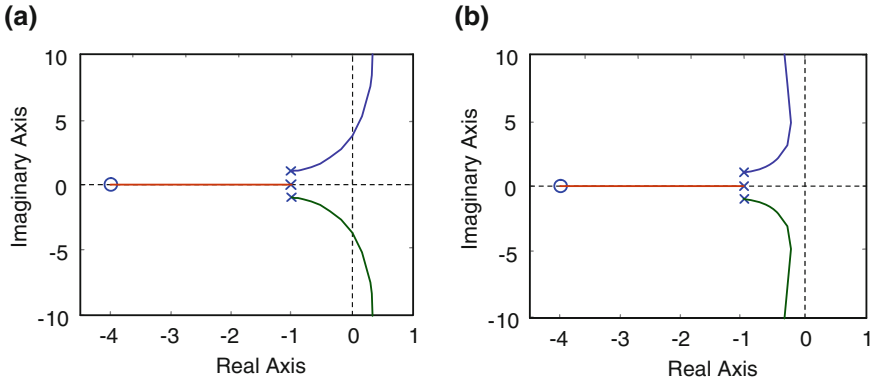


Fig. 4.34 Root loci of (a) $G(s)$ and (b) $G_c(s)$ for positive gains

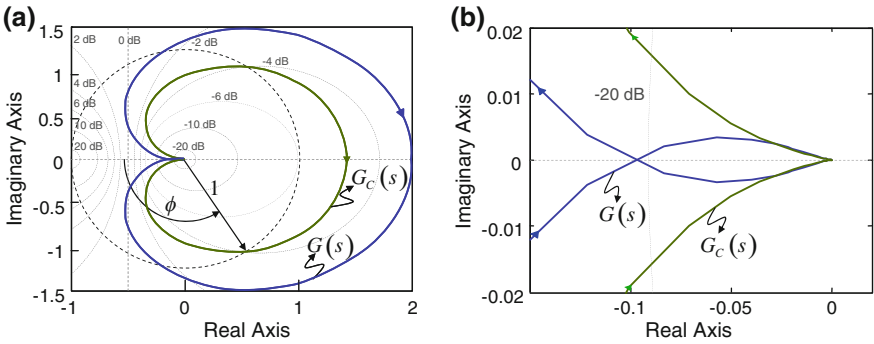


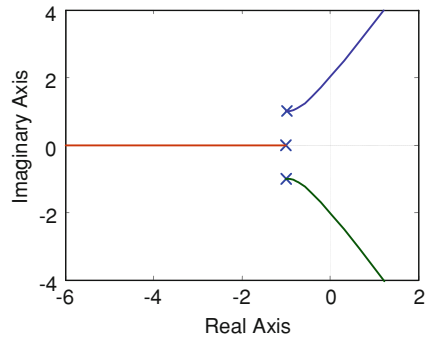
Fig. 4.35 a Nyquist plot of $G(s)$ and $G_c(s)$ and b their zoomed plots

may also be obtained from the Nyquist plot of the transfer functions (See Fig. 4.35). The original systems frequency response crosses real axis at two points (-0.1 and 2.0) which give the stable ranges as $k < -1/(-0.1)$ or $k < 10$ and $k > -1/2.0$ or $k > -0.5$. After the polar plot is turned due to phase addition, the frequency response of G_c crosses real axis at one point (1.4285) which gives the stable range as $k > -1/1.4285$ or $k > -0.7$. The gain margin and phase margin of the compensated system indicate that it is stable for all positive feedback gains.

It is worthwhile to note here that it was possible to include the compensator in the system because the original system had a small relative degree. Consider a variation of the transfer function as

$$G(s) = \frac{1}{(s + 1)(s^2 + 2s + 2)}$$

Fig. 4.36 Root loci of $G(s)$ with relative degree of 3



which has a relative degree of 3. The root loci of the transfer function is given in Fig. 4.36. It is natural to see that even if we shift the centroid of the asymptotes to the left by a large amount, the asymptotes would still cross the imaginary axis. In short, this system cannot be stabilized by any means for all positive values of feedback gain. This is due to the large number of asymptotes (relative degree) in the system.

The number of integrally causalled storage elements in the inverse bond graph model gives the number of zeroes in the transfer function obtained from the forward model. The inverse model is created by imposing both effort and flow information from the sensor and receiving both at the source. This procedure, where both information can be imposed on a bond cannot be done through normal causality. This is why, the notion of bicausality [6, 13–17] is introduced. Bicausality notation splits the causality assignment for the two factors of power, namely effort and flow. By separating the causal strokes, it allows imposing two complimentary information at one end of a bond.

In bicausality notation, the effort and flow causalities are split into two half-causal strokes. The side of the bond with the half-arrow for power direction is used to impose flow causality and the effort causality is imposed on the other side. When flow and effort causalities are counter-oriented, the two half-causal strokes appear at one end of the bond and merge to form a single causal stroke, which is called uncausality or normal causality that we know so far. When flow and effort information are co-oriented, their causal strokes appear at two different ends.

In Fig. 4.37, each bond has two half-causal strokes, one for effort and the other for flow. The causal stroke for the flow variable is shown on the side, where the half-arrow for power direction is present. On the other side of the power direction, the causality for effort variable is portrayed. When the effort and flow information paths are counter-oriented, as in Fig. 4.37a, b, the bond is called to be uncausalled. Uncausality corresponds to normal causality in bond graph modeling. The cases shown in Fig. 4.37c, d correspond to cases, when effort and flow information paths are co-oriented.

In the inverse model, the source element (Se or Sf) is replaced by a source sensor (SS) element [6, 14] and the sensor (De or Df) element is replaced by a sensor source (again SS) element. The difference between source sensor and sensor source lies in

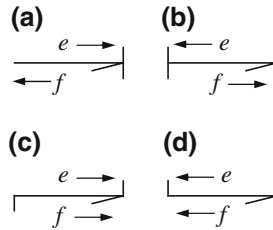


Fig. 4.37 Information exchange in bi-causal bonds

Table 4.2 Source-sensor causality assignment

Causal configuration	Nature of the SS element
SS \longrightarrow	Effort source, flow sensor (Se element)
SS \longrightarrow	Flow source, effort sensor (Sf element)
$\xrightarrow{f=0}$ SS	Zero flow source, effort sensor (De element)
$\xrightarrow{e=0}$ SS	Zero effort source, flow sensor (Df element)
SS \longleftarrow	Flow source, effort source
\longleftarrow SS	Flow sensor, effort sensor

the causality of the element: the source sensor element receives information of both power variables, whereas the signal source element supplies both. The causality of source sensor element is shown in Table 4.2.

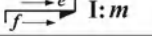
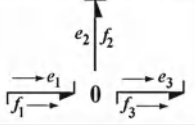
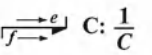
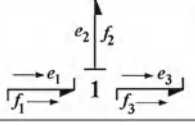
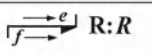
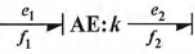
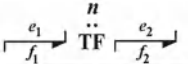
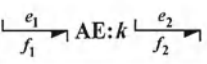
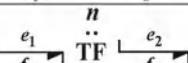
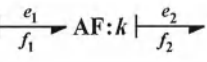
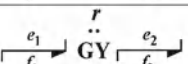
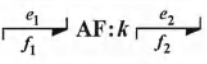
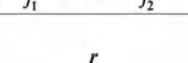
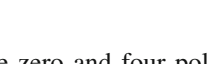
The rule for bicausal 0 (1)-junction is that only one bond can bring effort (flow) information and other bonds can bring the flow (effort) information. This means that at a bicausal junction, there must be one bond bringing in both effort and flow information while there must be another bond taking out both effort and flow information. Thus, at every junction, only two bonds must be bicausal (not more, not less). The different ways of information exchange in bi-causal bonds are shown in (Table 4.3).

To arrive at the inverse model, bicausality is propagated from the original sensor to the original source. In the process, some internal bonds in the model are assigned bicausality such that it is propagated to the receiving source sensor.

Let us reconsider the electromechanical system shown in Fig. 4.38a and suppose that the velocity of the mass being lifted is measured. The transfer function from the input (motor speed) to the output (velocity of lifted mass) can be shown to be

$$\frac{y(s)}{u(s)} = \frac{aK_t (rs + k)}{Ims^4 + r (ma^2 + I) s^3 + (mK_t + ma^2k + kI) s^2 + K_t rs + K_t k}. \quad (4.49)$$

Table 4.3 Bicausal configurations for bond graph elements

Bicausal configuration	Assignment statements	Causal configuration	Assignment statements
 I: m	$m = (\int e \cdot dt) / f$	 0	$e_2 = e_1$ $e_3 = e_1$ $f_3 = f_1 - f_2$
 C: $\frac{1}{C}$	$C = (\int f \cdot dt) / e$	 1	$f_2 = f_1$ $f_3 = f_1$ $e_3 = e_1 - e_2$
 R: R	$R = e / f$	 AE: k	$f_1 = 0$ $e_2 = k \cdot e_1$
 TF $\overset{n}{\dots}$	$e_2 = e_1 / n$ $f_2 = n \cdot f_1$	 AE: k	$f_1 = 0$ $e_1 = e_2 / k$
 TF $\overset{n}{\dots}$	$e_1 = n \cdot e_2$ $f_1 = f_2 / n$	 AE: k	$f_1 = 0$ $e_1 = e_2 / k$
 GY $\overset{r}{\dots}$	$e_2 = r \cdot f_1$ $f_2 = e_1 / r$	 AF: k	$e_1 = 0$ $f_2 = k \cdot f_1$
 GY $\overset{r}{\dots}$	$e_1 = r \cdot f_2$ $f_1 = e_2 / r$	 AF: k	$e_2 = 0$ $f_2 = k \cdot f_1$

This transfer function shows one finite zero and four poles. Thus, the relative degree (number of infinite zeroes) of the system is three. Let us now try to find this information without actually deriving the transfer function.

The forward bond graph model of the system is given in Fig. 4.38b. In the forward model, there are four storage elements in integral causality and hence the transfer function has four poles.

In the inverse model of the system given in Fig. 4.39, the sensor (Df) and source (Sf) have been replaced with source sensor (SS) elements. Note that fixed sources (those, which are not control inputs) are retained as they are, e.g., $Se: -mg$ at bond number 12. We try to maximize integral causality in the inverse model. The SS element in bond number 13 imposes both effort and flow information, thereby forcing differential causality in the I-element at bond number 11. Likewise, two more storage elements are forced to assume differential causality. The SS element at bond number 1 receives both flow and effort information. Consequently, the inverse model has only one integrally causalled element (C-element at bond 8) and then the number of poles of the inverse model is 1. This implies that the number of finite zeroes of the forward model is 1 and the relative degree of the system is $4 - 1 = 3$.

The results relating to relative degree of the system as derived from structural analysis is robust in the sense that it does not depend on the parameter values. The actual relative degree of the system may change under specific combination of parameter values. For example, if $r = 0$ in Eq. 4.49 then the relative degree of the transfer function will be 4. If we assume $r = 0$ at the outset and remove it from the bond graph model then we find from the inverse model in Fig. 4.40 that no element is

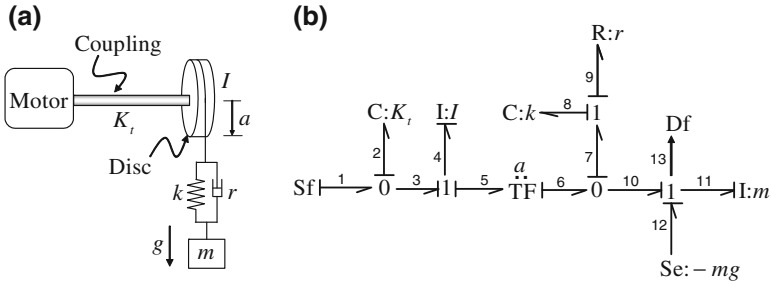
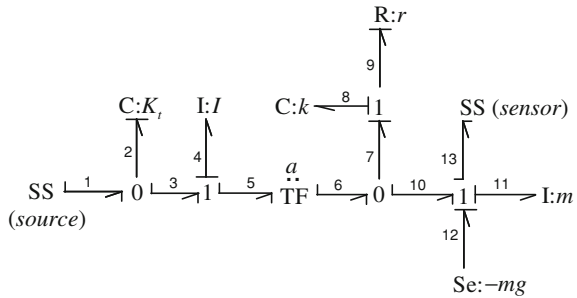


Fig. 4.38 A speed controlled motor with flexible coupling lifting a load

Fig. 4.39 Bicausal inverse model



in integral causality, thereby giving the correct number of zeroes as 0 and the relative degree of the transfer function as 4.

Another approach to determine relative degree is to find the shortest causal path. The shortest causal path links the input(s) to the output(s) in such a way that minimum number of storage elements appear in the causal path. The shortest causal path in the bond graph model given in Fig. 4.38b is marked in Fig. 4.41a. If damper is removed, then the shortest causal path is shown in Fig. 4.41b. From Fig. 4.41a, it is found that one of the storage elements (C-element at bond 8) does not appear on the shortest causal path. This means the order of the numerator polynomial of the transfer function is 1, or the relative degree is 3. On the other hand, it is found from Fig. 4.41b that all storage elements appear on the shortest causal path. Thus, the order of the numerator polynomial of the transfer function is 0, i.e., the relative degree is 4. These are the same results derived earlier through bicausality assignment on the inverse models.

4.5.5 Zero Dynamics

Zero dynamics relates to the numerator polynomial of a system’s transfer function. Therefore, zero dynamics cannot be influenced by feedback compensation or

Fig. 4.40 Bicausalised inverse model of system without damper

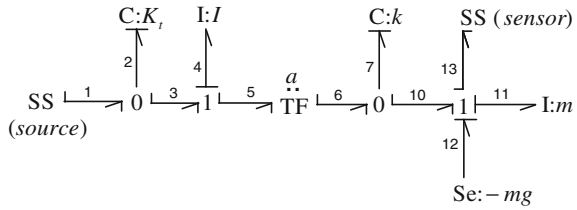
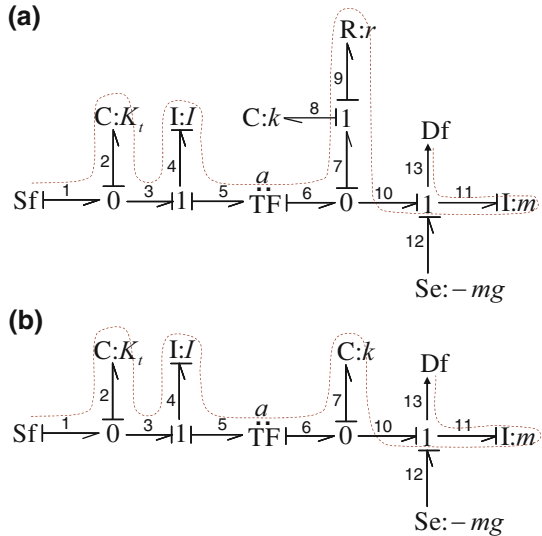


Fig. 4.41 Shortest causal path



pole-placement. Thus, it determines the performance limit of many feedback-control systems. A minimum-phase system is one whose forward and inverse dynamics are causal and stable. This means that the poles and zeroes of the system must lie on the left half of the complex plane. Note that even when a system is asymptotically stable (i.e., all its poles are stable), it may become non-minimum-phase if any of its zeroes lie on the right half of the complex plane. Then the inverse system, whose poles are the zeroes of the forward system, becomes unstable. This inverse system is necessary in many control applications (see Chaps. 9 and 13 on robust overwhelming control).

A physical system, and especially its sensor and actuator locations, must be designed in such a way that they possess the desired zero dynamics. Structural analysis of a graphical model often indicates different subsystems contributing to zero dynamics. Thus, it is possible to make prior structural-level design modifications to achieve the desired zero dynamics. Zero dynamics for SISO and MIMO can be elegantly determined from causal path analysis on the bond graph model of a system [7, 8, 27]. The zero dynamics arises out of the subsystems which do not appear in the shortest causal path. Thus, it is related to the relative degree of the transfer function of an SISO system. If the system is MIMO then the vector relative degree has to be considered [8].

Consider the system given in Fig. 4.38a and its bond graph model in Fig. 4.38b. The inverse system is obtained through bicausality assignment in Fig. 4.39 from which we have found that the relative degree of the system is three. The subsystems responsible for zero dynamics are those containing integrally causalled elements in the inverse model. It is identified as the R-C element pair at 1-junction connected to bond number 7 in Fig. 4.39. According to the causality, bond 7 receives flow information and returns effort information: $e_7 = k \int f_7 dt + r f_7$. Taking Laplace transform, the first-order transfer function resulting from this subsystem is $rs + k$, which decides the zeroes (roots of numerator polynomial) of the transfer function given in Eq. 4.49 and gives the system's finite zero at $s = -k/r$. Then for all positive values of k and r , the zero dynamics of the system is stable. Note that if $r = 0$ then the zero at $s = -k/r$ becomes an infinite zero, i.e., the relative degree of the system increases by 1. This may be found also from Fig. 4.40 where there are no subsystems containing integrally causalled elements. More details on zero dynamics may be consulted in [20].

4.6 Discrete-Time Models

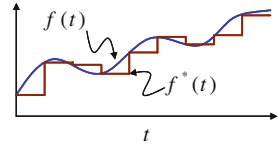
Modern control systems are generally implemented in digital computers which allows for implementation of efficient and complex control laws. Design of digital control systems is fundamentally different from that of continuous-time control systems. We start from the concept of a zero-order-hold (see sample and hold device in the previous chapter). A zero-order-hold (ZOH) samples an input signal at fixed intervals and retains the sampled value till the next sampling instance. Mathematically, the sampled output of an analog signal $f(t)$ when passed through a ZOH is given as

$$f^*(t) = \sum_{k=0}^{\infty} f(kT) (u_s(t - kT) - u_s(t - (kT + T))) \quad (4.50)$$

where $u_s(t)$ is the unit step function, T is the sampling time period or sampling interval, and k is the sample number. The term $u_s(t - kT) - u_s(t - (kT + T))$ models a pulse of unit amplitude during $kT \leq t < kT + T$. This is schematically shown in Fig. 4.42.

From the Shannon sampling theorem, the sampling frequency must be theoretically more than twice the largest frequency content (Nyquist frequency or cut-off frequency) in the signal. To avoid aliasing and frequency folding, the sampling frequency must be larger than the Shannon frequency which is twice that of the Nyquist frequency. However, to convert the sampled signal back into the analog signal, one needs to put a low-pass filter. No filter has an ideal low-pass characteristic with a perfectly sharp cut-off. Therefore, to accommodate the real filter, one actually samples a signal at much higher frequency. The frequency domain analysis of digital systems is carried out with z-transforms. In this book, we will deal with the state-space analysis

Fig. 4.42 Output of zero-order-hold (ZOH)



and thus consider the discretization of analog state space models to their discrete forms.

Let an analog system be described by the following state-space model

$$\dot{x} = Ax + Bu, \quad \text{and} \quad y = Cx + Du$$

with the parameters having their usual meaning. For an LTI system, the solution of this system at any time $t = t_f$ starting from an initial time $t = t_0$ may be written as

$$x(t_f) = e^{A(t_f-t_0)}x(t_0) + \int_0^{t_f} e^{A(t_f-\tau)} Bu(\tau) d\tau, \tag{4.51}$$

where the state-transition matrix $\Phi(t, \tau) = e^{A(t-\tau)}$ and $x(t_0)$ is the vector of initial conditions. If the system is sampled at intervals of T then $u(t)$ does not change during sampling intervals, i.e., $u(t) = u(kT) \forall kT \leq t < (k+1)T$ with a ZOH. Let us assume the initial state of the system is known at $t_0 = kT$ and the final state is required at $t_f = kT + T$. Then by putting $t_f = kT + T$ in Eq. 4.51, we can write

$$x(kT + T) = e^{A((k+1)T-kT)}x(kT) + \int_{kT}^{kT+T} e^{A((k+1)T-\tau)} Bu(kT) d\tau \tag{4.52}$$

$$= e^{AT}x(kT) + A^{-1}(e^{AT} - I)Bu(kT). \tag{4.53}$$

where I is an identity matrix of appropriate dimension. Dropping the fixed sampling time, we can write the final discretized version of Eq. 4.52 (called a difference equation) in a discrete-time state-space form as

$$\begin{aligned} x(k+1) &= A_d x(k) + B_d u(k), \\ y(k) &= C_d x(k) + D_d u(k), \end{aligned} \tag{4.54}$$

where $A_d = e^{AT}$, $B_d = A^{-1}(e^{AT} - I)B$, $C_d = C$ and $D_d = D$.

For sufficiently small sampling time, one can use the first two terms of Taylor series expansion and approximate $A_d = e^{AT} \approx I + AT$ and $B_d \approx A^{-1}(I + AT - AT)B = BT$. This approximation is good enough to simulate LTI systems through a small computer code.

Note that if an eigenvalue of matrix A is on the left half of complex plane, then the corresponding eigenvalue of matrix $A_d = e^{AT}$ appears inside a unit circle about the origin in the complex plane. In digital systems, the unit circle in the

complex plane acts as the stability boundary. Regular pole-placement and feedback-control system analysis methods can be applied on the discrete-time system models. One may need a bilinear transformation to convert the circular stability boundary (unit circle in complex plane) into the usual line boundary separating the positive and negative real sides of the complex plane and then apply the Routh stability criterion.

4.7 Actuator Sizing

In mechatronic systems, it is important to choose actuators of right capacity. If an actuator cannot give the desired output, it is said to be saturated. Saturation of actuator can be of three types: (1) actuator is unable to supply the desired effort, (2) unable to supply the desired flow, and (3) unable to output the desired power. For example, while a pump can give maximum flow Q_{\max} if working below a certain pressure head P_{\min} and can give minimum flow Q_{\min} while working above a certain pressure head P_{\max} , it may not be able to generate any flow Q at any pressure head P when $Q_{\min} < Q < Q_{\max}$ and $P_{\min} < P < P_{\max}$ due to the limits on the power $W = PQ$. In mechatronic systems such as robots, it is important to design the system and its actuator in such a way that the performance criterion of the device is maintained. Besides these limits, actuators also have a limited slew rate, i.e., how fast an actuator can move from one to another amount of output.

As an example, consider the word bond graph of an actuating system, along with its power modulator, given in Fig. 4.43 [14], in which different power variables are marked. Each of those power variables usually have a constraint as follows: $E_{mn} \leq e_m(t) \leq E_{mx}$, $F_{mn} \leq f_m(t) \leq F_{mx}$, $|e_m(t) \cdot f_m(t)| \leq W_m$, $E_{an} \leq e_a(t) \leq E_{ax}$, $F_{an} \leq f_a(t) \leq F_{ax}$, $|e_a(t) \cdot f_a(t)| \leq W_a$, $\forall t \in [0, T]$, where T is the time required to transit from the initial state to the final state.

Let us assume that the characteristics or specifications of a certain actuator is known. The objective is to find out an output profile (e.g. maximum allowable slew rate), and the corresponding input law, for which all the operating constraints are satisfied. A linear quadratic regulator (LQR) is one of the classical approaches to design control laws which can adjust the actuator output requirement. For LQR design, the optimal control problem can be solved with a heavy cost on excessive input size. However, the optimal control solution does not address the limits placed on the power. What one needs is a solution which accounts for the evolution of both the power variables (efforts and flows) in an actuator.

For an actuator with given specifications, a representative plot of the time evolution of different variables in the constraint space is shown in Fig. 4.44. The hyperbolic curves represent constraints on power (product of effort and flow) and the non-shaded area in the middle of each plot is the admissible operating regime. The paths p_1 to p_4 correspond to the way the power variables are required to change for four different control laws or controller parameters. One finds from these graphs that path p_1 violates the constraint on modulator output power, path p_2 violates the same

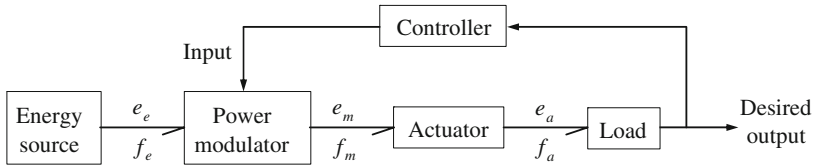


Fig. 4.43 Word bond graph of a feedback actuated system

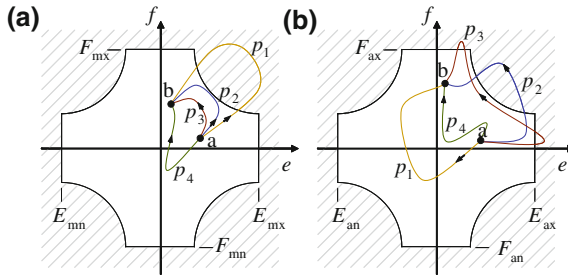


Fig. 4.44 Actuator sizing: **a** response trajectories for power modulator power variables and **b** actuator power variables

constraint on actuator output power, and path p_3 causes actuator saturation on both effort and flow requirements. As a result, path p_4 is found to be suitable and the corresponding controller can be used.

On a different note, if the profile of evolution of the power variables (efforts and flows) are known then one needs to find or design an actuator whose performance specifications would bound the response curves. This is called actuator sizing.

If the desired output of a given system is prescribed (e.g., the positions and end-effector velocities of a serial manipulator at various time instances) then one can actually perform a system inversion and simulate the system to determine the input sequences. In this way, one can determine the specifications for the actuators (link motors). Fortunately, bicausality gives a convenient solution to actuator sizing. For actuator sizing, one needs to convert all sensors into SS elements such that they impose the desired output of the actual system on the model. The sources are also replaced by SS elements such that they receive both effort and flow informations. In addition, the model is assigned preferred differential causality.

Let us take an example system shown in Fig. 4.45a where the load is to be lifted at some predefined speed profile by a controller. The speed profile is given as $v(t) = 1 - e^{-\alpha t}$ where the parameter α governs the actuator rating. The bicausalled bond graph model of the system in preferred derivative causality is shown in Fig. 4.45b.

Initially, let us ignore the damping for which the bicausalled bond graph model given in Fig. 4.40 can be used to size the motor. If the measured velocity of mass m is v then from Fig. 4.40 we can write the following from the constitutive relations of the rightmost 1-junction:

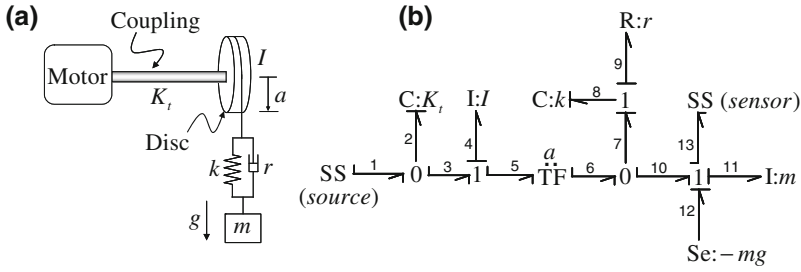


Fig. 4.45 Actuator sizing example: **a** the system and **b** its bicausal bond graph model in preferred differential causality

$$f_{10} = f_{13} = v, e_{13} = 0 \tag{4.55}$$

$$e_{10} = e_{11} - e_{12} = m\dot{v} + mg \tag{4.56}$$

For the neighboring 0-junction in Fig. 4.40, we can write

$$e_6 = e_7 = e_{10} = m\dot{v} + mg \tag{4.57}$$

$$f_6 = f_7 + f_{10} = \dot{e}_7/k + v = \frac{m\ddot{v}}{k} + v \tag{4.58}$$

Proceeding in the same way, one can express both source power variables e_1 and f_1 in terms of the prescribed response variable v and its derivatives up to a certain order (in this case, up to fourth derivative for four differentially caussed elements encountered in the causal path from the sensor to the source). The closed-form expression can be easily evaluated through a computer program to determine the actuator power variables and power output and thus an actuator of suitable specification can be chosen for the application.

However, it is not always possible to obtain a closed-form solution. If the damper is nonzero in Fig. 4.45a then we can see that a differential algebraic loop is present in the bicausal model given in Fig. 4.45b. Here, we can simulate a block diagram model derived from the bicausal bond graph model which is shown in Fig. 4.46.

In the block diagram model, the desired output is the input. The outputs of the block diagram model are the actuator power variables. The block diagram contains four derivative (du/dt) blocks. It was simulated for the following data: $m = 1$ kg, $I = 0.2$ kgm², $a = 0.5$ m, $k = 100$ N/m, $r = 5$ Ns/m, $K_t = 1,000$ Nm/rad, $g = 9.81$ m/s², and $\alpha = -0.2$. The calculated motor power variables are plotted in Fig. 4.47.

From these results, it is found that one should select a motor with a minimum of 40 W output power and capable of giving 21 Nm torque. If the demanded actuator slew rate is increased by selecting $\alpha = -5$ (i.e., a very quick response) then simulations show that the motor should be able to provide a minimum of 46 W output power and 25 Nm torque. As the actuator size is varied, one can assume that the rotary inertia I also varies. Thus, one needs some amount of iteration to match the actuator. The

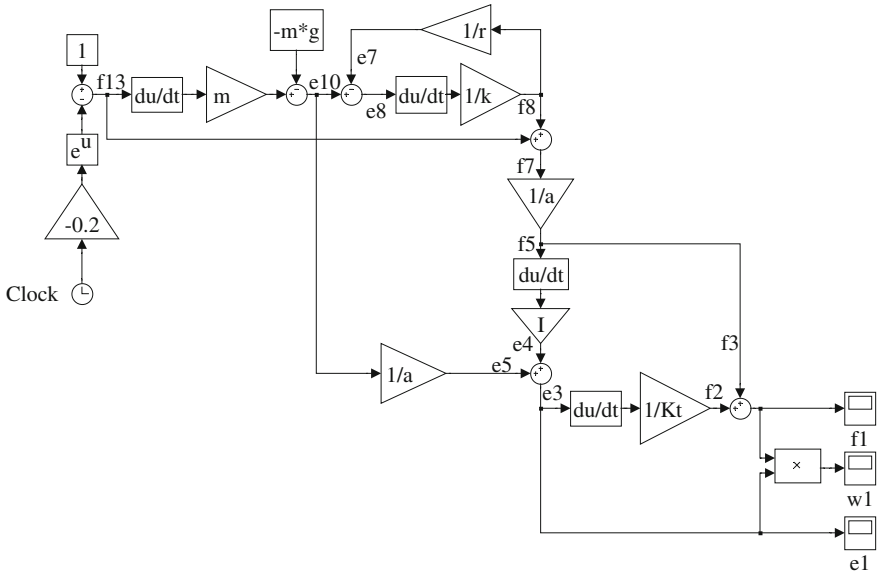
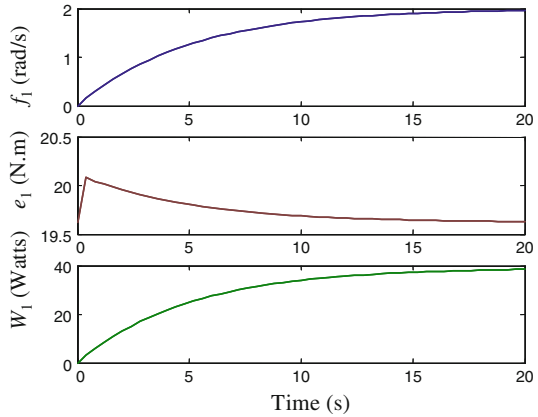


Fig. 4.46 Block diagram model derived from the bicausal bond graph model in preferred differential causality

Fig. 4.47 Time evolution of flow, effort, and power demanded from the actuator to drive the system along the specified trajectory



calculated specifications are useful to select a proper actuator (called a sized actuator) for the application.

References

1. J.S. Bay, *Fundamentals of Linear State Space Systems* (McGraw-Hill, Boston, 1999)
2. F.T. Brown, Direct application of loop rule to bond graphs. *J. Dyn. Syst. Meas. Control Trans. ASME* **94**(3), 253–261 (1972)

3. R. Cacho, J. Felez, C. Vera, Deriving simulation models from bond graphs with algebraic loops: the extension to multibond graph systems. *J. Frankl. Inst.* **337**(5), 579–600 (2000)
4. G. Dauphin-Tanguy, *Les Bond Graphs* (Hermès Science, Paris, 2000)
5. G. Dauphin-Tanguy, A. Rahmani, C. Sueur, Bond graph aided design of controlled systems. *Simul. Pract. Theory* **7**(5–6), 493–513 (1999)
6. P.J. Gawthrop, Physical interpretation of inverse dynamics using bicausal bond graphs. *J. Frankl. Inst.* **337**(6), 743–769 (2000)
7. S.Y. Huang, K. Youcef-Toumi, Zero dynamics of physical systems from bond graph models—part I: SISO systems. *J. Dyn. Syst. Meas. Control Trans. ASME* **121**(1), 10–16 (1999)
8. S.Y. Huang, K. Youcef-Toumi, Zero dynamics of physical systems from bond graph models—part II: MIMO systems. *J. Dyn. Syst. Meas. Control Trans. ASME* **121**(1), 18–26 (1999)
9. T. Kailath, *Linear Systems* (Prentice-Hall, Englewood Cliffs, 1980)
10. J.D. Lamb, G.M. Asher, D.R. Woodall, Causal loops and Mason’s rule for bond graphs, in *Proceedings of ICBGM’93*, Simulation series, vol. 25(2) (SCS publication, 1993), pp. 67–72, ISBN:1-56555-019-6
11. C.T. Lin, Structural controllability. *IEEE Trans. Autom. Control* **AC-19**, 201–208 (1974)
12. A. Mukherjee, R. Karmakar, A.K. Samantaray, *Bond Graph in Modeling, Simulation and Fault Identification* (CRC Press, Boca Raton, 2006), ISBN: 978-8188237968, 1420058657
13. R.F. Ngwompo, P.J. Gawthrop, Bond graph-based simulation of non-linear inverse systems using physical performance specifications. *J. Frankl. Inst.* **336**(8), 1225–1247 (1999)
14. R.F. Ngwompo, S. Scavarda, Dimensioning problems in system design using bicausal bond graphs. *Simul. Pract. Theory* **7**, 577–587 (1999)
15. R.F. Ngwompo, S. Scavarda, D. Thomasset, Inversion of linear time-invariant SISO systems modelled by bond graph. *J. Frankl. Inst.* **333**(2), 157–174 (1996)
16. R.F. Ngwompo, S. Scavarda, D. Thomasset, Physical model-based inversion in control systems design using bond graph representation—part 1: theory. *Proc. IMechE Part I J. Syst. Control Eng.* **215**, 95–103 (2001)
17. R.F. Ngwompo, S. Scavarda, D. Thomasset, Physical model-based inversion in control systems design using bond graph representation—part 2: applications. *Proc. IMechE Part I J. Syst. Control Eng.* **215**, 105–112 (2001)
18. J. O’Reilly, *Observers for Linear Systems* (Academic press, New York, 1983)
19. A. Rahmani, C. Sueur, G. Dauphin-Tanguy, Approche des bond graphs pour l’analyse structurelle des systèmes linéaires. *Linear Algebra Appl.* **259**, 101–131 (1997)
20. A.K. Samantaray, B. Ould Bouamama, *Model-Based Process Supervision—A Bond Graph Approach* (Springer, London, 2008)
21. R.N. Shields, J.B. Pearson, Structural controllability of multi-input linear systems. *IEEE Trans. Autom. Control* **AC-21**(2), 203–212 (1976)
22. C. Sueur, G. Dauphin-Tanguy, Structural controllability/observability of linear systems represented by bond graphs. *J. Frankl. Inst.* **326**(6), 869–883 (1989)
23. C. Sueur, G. Dauphin-Tanguy, Bond graph approach for structural analysis of MIMO linear systems. *J. Frankl. Inst.* **328**(1), 55–70 (1991)
24. C. Sueur, G. Dauphin-Tanguy, Controllability indices for structured systems. *Linear Algebra Appl.* **250**, 275–287 (1997)
25. J. Van Dijk, P.C. Breedveld, Simulation of system models containing zero-order causal paths-I. classification of zero-order paths. *J. Frankl. Inst.* **328**, 959–979 (1991)
26. J. Van Dijk, P.C. Breedveld, Simulation of system models containing zero-order causal paths-II. Numerical implications of class 1 zero-order paths. *J. Frankl. Inst.* **328**, 981–1004 (1991)
27. S.T. Wu, K. Youcef-Toumi, On relative degrees and zero dynamics from physical system modeling. *J. Dyn. Syst. Meas. Control Trans. ASME* **117**(2), 205–217 (1995)
28. X. Zhang, *Modeling, Control, Fault Detection and Isolation of Chemical Processes using a Bond Graph Framework*. Ph.D. Thesis, Texas Tech University, 2009

Chapter 5

Rigid Body, Flexible Body, and Micro Electromechanical Systems

5.1 Introduction

The application of multibody systems varies widely from terrestrial vehicle, air, and space applications, MEMS applications to biomechanical applications, etc. Multibody systems consist of rigid and elastic bodies, joint components, passive and active coupling elements. The four basic joint components are translational joint, revolute joint, double translational joint, and double translational-revolute joint [81]. The first step in the dynamic analysis of a real physical system is the modeling of its components. Multibody system dynamics is described by a set of equations of motion. We consider mechanisms whose configuration is characterized by many kinematic loops. The holonomic and nonholonomic constraints are analyzed to obtain a minimal number of generalized coordinates to represent motion. The equations of motion of a multibody system can be analyzed in different ways based on the principle used (Newton-Euler method, Principle of virtual work, Principle of virtual power, etc.), coordinating system used (Cartesian and Lagrangian coordinating systems), and the kinematic constraints of the system (Coordinate partitioning method and augmented Lagrange formulation) [46]. The dynamic equations for the multibody systems may be expressed by Jourdain's principle and the Lagrange multiplier method together with Baumgarte's stabilization [80]. The number of equations increases when Lagrange multipliers are used. Moreover, when there is a little change in the configuration, the aforementioned process has to be repeated again, i.e., the derivation process is not in a modular algorithmic form. This motivated Karnopp and Margolis [67] to develop a systematic approach to modeling of planar mechanisms by using bond graphs.

Large transient dynamic forces are often set up in multibody systems and they are often incorrectly neglected in the design stage due to improper modeling. These dynamic forces can be determined by simulation of a properly developed model of the actual system or by experimentation. While simple mass lumping methods provide compact models, they often give incorrect dynamic forces due to incorrect representation of rotary inertias and impact forces. On the other hand, variational

mass lumping method becomes too cumbersome when the mass distribution is time varying. In this chapter, we introduce a step-by-step approach to construct bond graph models of complex multibody and flexible body systems. Initially, we introduce bond graph modeling of planar systems and then move on to spatial systems. Flexible body systems are much more complex [149] and are only partially discussed to cover the requirements of the other chapters in this book.

5.2 Planar Multibody Systems

Modeling of mechanisms is not a trivial task because the goal is not only to obtain consistent kinematics but also to get proper dynamic loads. Ensuring the latter in a lumped parameter model needs proper allocation of lumped masses. In this section, we discuss bond graph modeling of planar mechanical systems. A planar mechanical system is considered to be composed of a set of rigid bodies, which are constrained together through a set of joints. The primary emphasis is given to development of bond graph models of revolute joints with clearance and of mass distribution in prismatic or slider joints. These so-called proper bond graph models are necessary in order to generate well-computable simulation models and also to accurately calculate the dynamic loads. We follow a pedagogical approach in our presentation. Various examples are chosen and their bond graph models are developed from the first principles using different formulations and approximations. Finally, two separate mechanisms are considered as illustrative examples.¹ Their bond graph models are validated through numerical simulations and comparison with analytical and simulation results available in the literature.

5.2.1 Bond Graph Modeling of Flexible Two-Force Members

Consider a massless two-force member, which will be analyzed in a fixed coordinate frame (x, y) , as shown in Fig. 5.1a. The contemporary length (L) between the two pin-jointed end points of the link (marked as 1 and 2) may be expressed as

$$L^2 = (x_1 - x_2)^2 + (y_1 - y_2)^2 \quad (5.1)$$

where numeric subscripts refer to the points in Fig. 5.1a. Differentiating Eq. 5.1 with respect to time, one obtains

$$\begin{aligned} 2L\dot{L} &= 2(x_1 - x_2)(\dot{x}_1 - \dot{x}_2) + 2(y_1 - y_2)(\dot{y}_1 - \dot{y}_2) \\ \Rightarrow \dot{L} &= \left(\frac{x_1 - x_2}{L}\right)(\dot{x}_1 - \dot{x}_2) + \left(\frac{y_1 - y_2}{L}\right)(\dot{y}_1 - \dot{y}_2) \end{aligned} \quad (5.2)$$

¹ A part of this section is adapted from these authors' previous work published in [7].

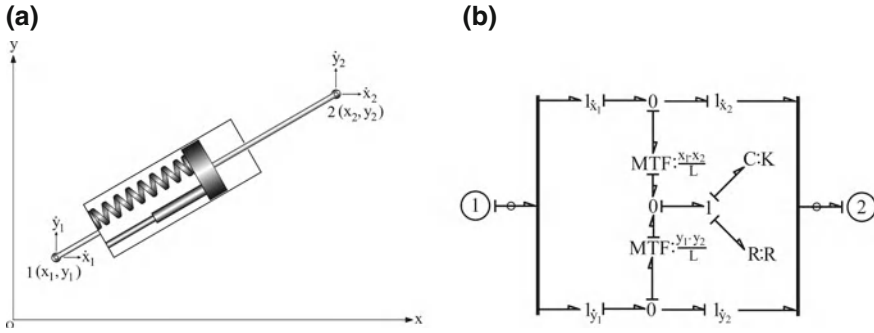


Fig. 5.1 a Schematic of a massless plane impedance and b its bond graph model

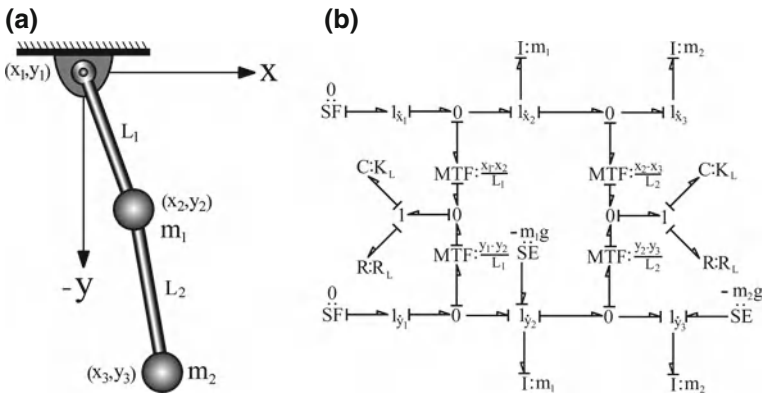


Fig. 5.2 a Schematic of a double pendulum and b its bond graph model

Equation 5.2 can be found in many standard books on finite element modeling. We then use the kinematic constraint in Eq. 5.2 to draw the bond graph model of a massless two-force member (we call it a plane impedance [91]) in Fig. 5.1b. The different transformer moduli used in the modulated transformer (MTF) elements in the model are $\mu_{x_1x_2} = (x_1 - x_2) / L$ and $\mu_{y_1y_2} = (y_1 - y_2) / L$. The power conserving junction structure of a bond graph ensures that this model also gives a proper representation of the dynamical constraints, i.e., the relations between the forces [66, 79].

5.2.1.1 Double Bob Pendulum

A double bob pendulum comprises two simple pendulums joined together, one of which is attached to the fixed point. Let us consider this double bob pendulum with masses m_1 and m_2 attached by two flexible massless links of lengths L_1 and L_2 , respectively, as shown in Fig. 5.2a. The bond graph model of it by considering the bob weights as sources of efforts is shown in Fig. 5.2b. The bond graph model of the double pendulum developed by Romero et al. [115, 116] in recent articles is improper

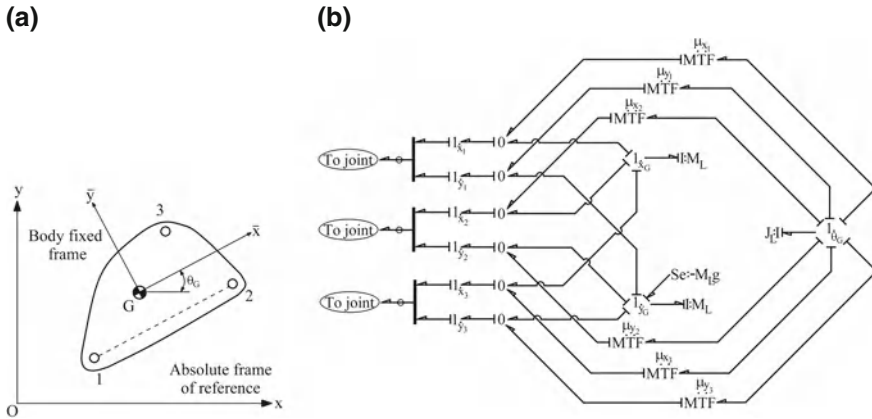


Fig. 5.3 a Schema for a three-port rigid link and b its bond graph model

in the sense that the model contains four inertia elements with differential causalities and a few causal loops. Moreover, those inertia elements were illogically replaced later by compliance elements. We would like to highlight the fact that a model of multiple simple pendulums is a cascaded representation of the model in Fig. 5.2b. It is always a causally consistent representation, i.e., there are no causal loops or differential causalities in the model. Moreover, when joint clearances are included we can model much complex problems, such as the dynamics of a falling chain. A further detailed bond graph model of a double pendulum with flexible wires is given in [104].

The same modeling principle can be used to model closed-loop chains such as determinate and indeterminate trusses where the mass of the members is usually neglected, and can thus be lumped at the ends of the members.

5.2.2 Model of Rigid Planar Links

We use a body-fixed frame on a rigid link and relate the motions to the absolute frame of reference through appropriate velocity transformation. The displacements of any point (i th point) on the rigid link, as shown in Fig. 5.3a, are expressed in terms of linear displacements (x_G, y_G) of the center of gravity in the x-y plane and angular position (θ_G) of the center of gravity about the z-axis as follows:

$$\begin{Bmatrix} x_i \\ y_i \end{Bmatrix} = \begin{Bmatrix} x_G \\ y_G \end{Bmatrix} + \begin{bmatrix} \cos\theta_G & -\sin\theta_G \\ \sin\theta_G & \cos\theta_G \end{bmatrix} \begin{Bmatrix} \bar{x}_i \\ \bar{y}_i \end{Bmatrix} \tag{5.3}$$

Differentiating Eq. 5.3 with respect to time, and noting that \bar{x}_i and \bar{y}_i are constant in a rigid body, one obtains

$$\dot{x}_i = \dot{x}_G + \mu_{x_i} \dot{\theta}_G, \tag{5.4}$$

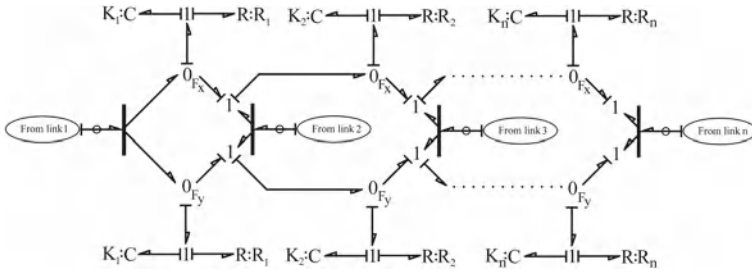


Fig. 5.4 Bond graph model of an ideal joint component with multiple shear and pin flexibility

$$\dot{y}_i = \dot{y}_G + \mu_{y_i} \dot{\theta}_G \tag{5.5}$$

where, $\mu_{x_i} = -(\bar{x}_i \sin \theta_G + \bar{y}_i \cos \theta_G)$ and $\mu_{y_i} = \bar{x}_i \cos \theta_G - \bar{y}_i \sin \theta_G$.

Equations 5.4 and 5.5 are sufficient to construct the augmented bond graph model of the rigid link as shown in Fig. 5.3b. We have considered a rigid link with three joints, but the model may be extended to connect to any number of body components by joint components. In Fig. 5.3b, the mass and rotary inertia are modeled by I-elements connected to the 1-junctions representing the velocities of the center of gravity in the inertial frame. The number of inertial ports does not depend on the configuration of the coordinate systems. The body weight may be neglected if the link lies in the horizontal plane. In the bond graph model given in Fig. 5.3b, a bond with a circle over it represents a vector bond and a thick vertical line is used to split a vector bond into scalar bonds or to merge scalar bonds to form a vector bond.

5.2.3 Modeling Revolute Joints

The joint component is one of the basic components in a mechanism-modeling library. The forces and moments are calculated in the joint component for connecting two body components. We initially assume that joints are flexible and frictionless. The bond graph model of the joint component in Fig. 5.4 can be used to fasten any number of body components. The C- and R-elements in Fig. 5.4, model the energy storage and dissipation due to relative motion between two rigid bodies.

To reduce the dynamic effects, higher values of pin stiffness and damping are generally taken into account. As a result, there exists almost the same generalized flow in all bonds connected to the joint element from the body components and the impedance coupling tends to become a plain coupling. Decreasing the value of compliance element can increase the joint flexibility. If the values of damping and compliance parameters are taken to be zero then the connected body components are decoupled. This is how the type of the joint can be changed as per requirement.

We did not consider joint clearance in the model given in Fig. 5.4. However, for the mobility and assemblage of the mechanisms, joint clearance is very much necessary. The effects of these clearances are rapid wear, undesired vibration, rattling, noise, etc.

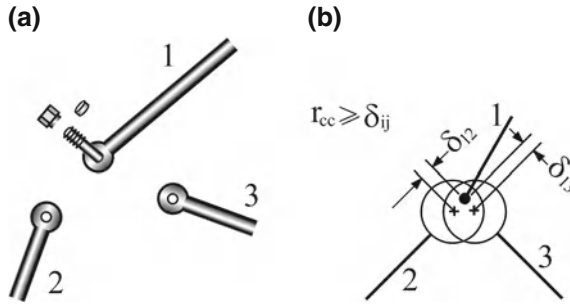


Fig. 5.5 **a** Schema for rigid links and joint components and **b** different clearances between two pair of rigid links

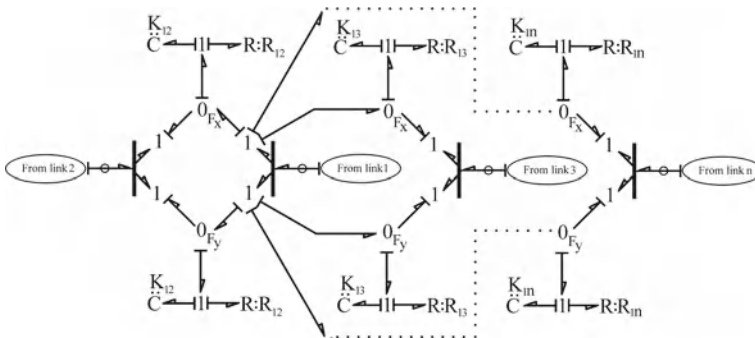


Fig. 5.6 Bond graph model of revolute joint with clearance between links

The elastic impact due to clearances gives rise to discontinuous forces in the joint. The flexibility of links reduces the impact forces at the joints with clearance. Three rigid links with joint components are shown in Fig. 5.5a. The clearances between two pairs (link 1 and link 2, and link 1 and link 3) of rigid links are shown in Fig. 5.5b, where r_{cc} is the radius of clearance circle. The parameter δ_{ij} (where i and j enumerate the links) is the instantaneous distance between the centers of the bolt and the hole in the respective link ends. If no clearance is provided between a pair of links, the corresponding value of r_{cc} is zero. When $\delta_{ij} > r_{cc}$, the impact between a pair of links is modeled by switching the values of stiffness K_{ij} and damping R_{ij} in Fig. 5.6 to large values from their nominal values of zero.

The friction between two links at the joint may be modeled by an R-element at a 0-junction where relative angular velocities between two links may be calculated. This R-element needs modulation, i.e., it should be active only when $\delta_{ij} > r_{cc}$. Various dissipation phenomena, e.g., viscous friction in a lubricated joint or dry friction can be modeled by this R-element. Likewise, torsional stiffness and damping at the joint may be modeled by a 1-C-R structure connected to the 0-junction. If the joint is actuated then the motor model with appropriate causalities to apply a torque (effort) may be connected to that 0-junction. The power directions in the bond graph model are set to calculate relative angular velocities at this 0-junction. This also ensures that a

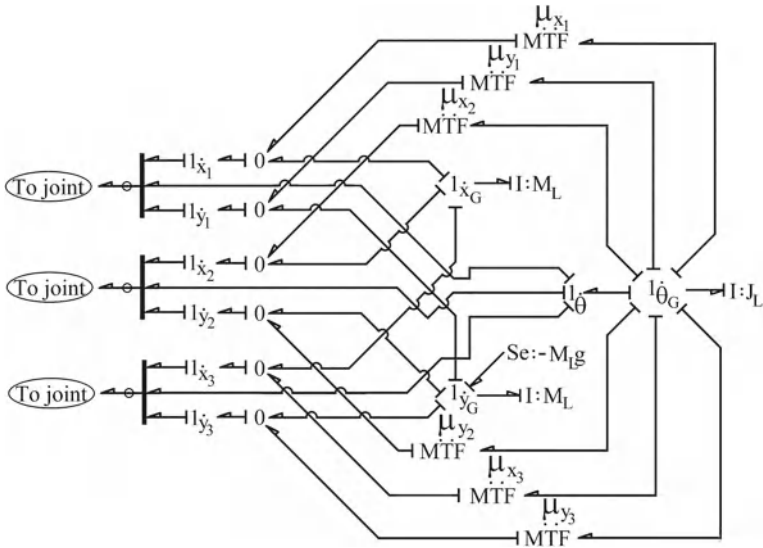


Fig. 5.7 Bond graph model of a three-port rigid link with angular velocity as an output variable

motor would apply a forward torque on the driven link and the reverse reactive torque on the driving link. Such models will be developed later for serial robotic manipulators. These are certain advantages of bond graph modeling that ensure proper model composition. Detailed bond graph models of various joints can be consulted in [157].

5.2.4 Detailed Model of Revolute Joint

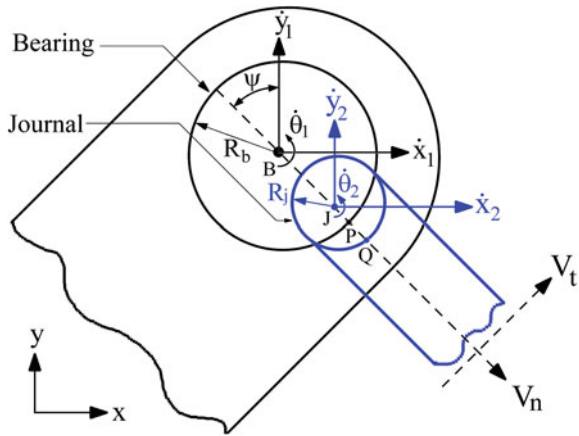
A detailed model of revolute joint requires information of angular positions of the rigid bodies joined together. This information is required to calculate the frictional forces and other joint forces, e.g., the hydrodynamic forces in a lubricated joint which acts like a journal bearing. Therefore, first of all, the submodel of the rigid planar link is modified so that the angular velocity of the rigid body becomes an output of that submodel. The revised model of the rigid planar link is shown in Fig. 5.7. It is similar to the model given in Fig. 5.3b. In the bond graph model given in Fig. 5.7, a bond with a circle over it represents a vector bond and a thick vertical line is used to split a vector bond into scalar bonds or to merge scalar bonds to form a vector bond.

When equations are derived from the bond graph model in Fig. 5.7, one obtains the force and moment balance equations as

$$F_{xG} = \sum_i F_{x_i}, \quad F_{yG} = \sum_i F_{y_i} \quad \text{and} \quad M_{zG} = \sum_i (\mu_{x_i} F_{x_i} + \mu_{y_i} F_{y_i}) \quad (5.6)$$

where F_{x_i} and F_{y_i} are the force components at i th joint, respectively, and F_{xG} , F_{yG} and M_{zG} represent the resultant forces acting in the x and y directions at the mass

Fig. 5.8 Schematic representation of a clearance joint



center and the resultant moment acting along z-axis at the mass center. These relations are output from the bond graph model.

The revolute clearance joint is shown in Fig. 5.8. Small joint clearance or flexibility (if shrunk-fit) is necessary for ease of assembling the links and also for smooth mobility of the mechanism with reduced friction when a change point configuration is reached. The latter is important in case of appreciable thermal expansion or contraction of the links. However, joint clearance also leads to impact forces, rapid wear, rattling, and noise [45]. Note that joints without clearance develop some amount of clearance over long use due to normal wear and tear.

The normal reaction acts along the attitude line (the line connecting bearing and journal centers in Fig. 5.8 and frictional forces act perpendicular to attitude line. Various authors have considered various formulations for these forces [1, 45, 139].

The normal and tangential velocities are

$$V_n = (\dot{x}_1 - \dot{x}_2) \sin \psi - (\dot{y}_1 - \dot{y}_2) \cos \psi \tag{5.7}$$

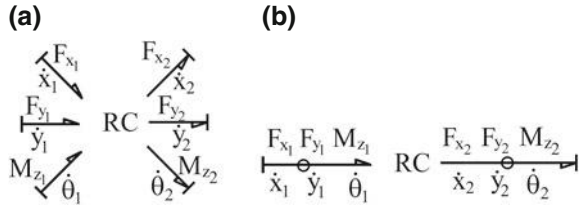
$$V_t = (\dot{x}_1 - \dot{x}_2) \cos \psi + (\dot{y}_1 - \dot{y}_2) \sin \psi + (\dot{\theta}_1 R_b - \dot{\theta}_2 R_j) \tag{5.8}$$

where the variables are defined in Fig. 5.8. The penetration depth due to impact between the two components is given as $\delta = (BJ - c)$ where the c is radial clearance. Note that δ is taken to be zero when $(BJ - c) < 0$. The normal contact force which is evaluated according to the relation given in [67] as

$$F_n = K \delta^\alpha + \left[\frac{3K \delta^\alpha (1 - C_e^2)}{4 \dot{\delta}^-} \right] \dot{\delta} \text{ for } \delta > 0, F_n = 0 \text{ otherwise.} \tag{5.9}$$

In Eq. 5.9, the first term denotes the elastic Hertzian contact force [67] where the stiffness is given as $K = \frac{4}{3(\eta_1 + \eta_2)} \sqrt{R_b R_j / (R_b + R_j)}$, with $\eta_i = (1 - \nu_i^2) / E_i$, $i = 1, 2$ are two material parameters, ν and E are the Poisson's ratio and Young's

Fig. 5.9 **a** Bearing and journal of a clearance revolute joint, **b** bond graph model and **c** its equivalent bond graph



modulus, respectively, α is usually taken as 1.5 for contact between metallic bodies, and C_e is the coefficient of restitution used to model impact. The second term in Eq. 5.9 is due to internal damping of the materials which introduces strain rate-dependent damping during impact with δ^- being the initial impact velocity and δ is the relative penetration rate. In some references, the instantaneous damping coefficient during impact has been considered to be a cubic step function of the penetration.

The tangential force is calculated from the modified Coulomb’s friction law as follows [45]

$$F_t = -C_f C_d F_n \cdot \text{sgn}(V_t) \tag{5.10}$$

where C_f is coefficient of friction, C_d is dynamic correction coefficient (see [45] for details), and $\text{sgn}(\cdot)$ is the signum function. Other forms of dry-friction formulations (e.g., stick-slip [64], honey-drop, and Stribeck friction model, etc.) may be used here. The formulation given in reference [1] uses Poisson’s hypothesis for the definition of the coefficient by first recognizing the correct mode of impact; i.e., sliding, sticking, and reverse sliding. If the clearance between the journal and the bearing is lubricated then fluid-film forces dictate the normal and tangential forces. Bond graph model of journal bearings can be consulted in [123]. However, only dry friction is considered in the models developed in this book.

The normal and tangential contact forces can be resolved into two components in x-y directions:

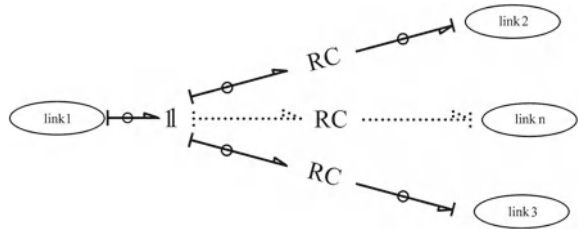
$$F_x = F_n \sin \psi + F_t \cos \psi \quad \text{and} \quad F_y = -F_n \cos \psi + F_t \sin \psi \tag{5.11}$$

The moments acting at the bearing and the journal center due to tangential forces are, respectively,

$$M_b = F_t R_b \quad \text{and} \quad M_j = F_t R_j. \tag{5.12}$$

The bond graph model of the revolute clearance joint is shown in Fig. 5.9a and its equivalent bond graph in compact form using vector bonds is shown in Fig. 5.9b. The constitutive relation for the RC-field element (a field element is connected to more than one bonds) is $\bar{e} = \varphi_{RC}(\bar{f}, \int \bar{f} dt, r)$ where r is a set of fixed parameters (geometric and material properties), $\bar{f} = [\dot{x}_1 \ \dot{y}_1 \ \dot{\theta}_1 \ \dot{x}_2 \ \dot{y}_2 \ \dot{\theta}_2]^T$ is the vector of generalized flow (velocity) variables, $\bar{e} = [F_{x1} \ F_{y1} \ M_{z1} \ F_{x2} \ F_{y2} \ M_{z2}]^T$ is the vector of generalized effort variables and $\varphi_{RC}(\cdot)$ function models Eqs. 5.7–5.12. Because the constitutive relation involves both the rate of deformation and deformation to

Fig. 5.10 Bond graph model of rigid planar links connected by revolute joint



compute the effort (force and moment) variables, the physical phenomenon involved is a combination of dissipation and potential energy storage, which together are represented by a defined bond graph element (RC-field). Note that the attitude angle ψ must be calculated using $\text{atan2}(\cdot)$ function such that the quadrant information is not lost during the process.

The model of rigid links joined together by a revolute joint (see Fig. 5.5) may now be developed easily. When $\delta_{ij} > r_{cc}$, the interaction forces between a pair of links are modeled by Eqs. 5.9 and 5.10 and are transformed into inertial frame forces and moments by Eqs. 5.11 and 5.12. The bond graph model of many links connected to the common reference link is shown in Fig. 5.10 where the bold 1-junction is drawn using vector bond graph notation and the dimension of effort and flow variable vectors in each bond is three.

The generalized model given in Fig. 5.10 can be simplified if the joints do not have clearance. Such joints without flexibility are referred to as kinematic joints. However, we will consider joint flexibility in our model. Note that if the joint stiffness is made large in a joint without clearance then the flexible joint behaves as an ideal kinematic joint.

For the flexible joint without clearance, $\delta = BJ$ (from Fig. 5.5a). Furthermore, since $R_b = R_j$, Hertzian contact theory is not applicable because the contact area is more than the characteristic radius of the bodies. The effective stiffness is then considered as K which has to be evaluated experimentally or numerically, e.g., from a finite element model. The damping is proportional to effective stiffness. The proportionality constants between stiffness and damping for various materials are tabulated in reference [43]. Note that without clearance, the stiffness and damping encountered in any radial direction is the same, i.e., the 2×2 stiffness and damping matrices are symmetric and rotationally invariant.

The normal force is then given as

$$F_n = K\delta + \lambda K\dot{\delta} \tag{5.13}$$

where λ is the material damping-related proportionality constant [43]. The tangential force F_t is still given by Eq. 5.10.

If dry friction is neglected and viscous friction is considered (which can be modeled with relative angular velocities) then $F_t = 0$. Consequently, the interaction

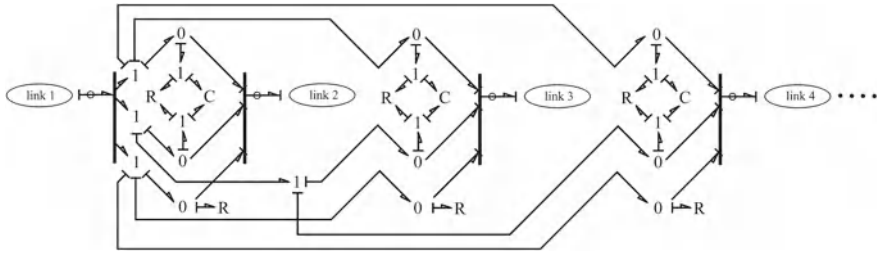


Fig. 5.11 General form of bond graph model of an ideal revolute joint component

forces in x-y reference frame between *i*th link and the reference link (link number 1) are given as

$$\begin{Bmatrix} F_x \\ F_y \end{Bmatrix} = \begin{bmatrix} K & 0 \\ 0 & K \end{bmatrix} \begin{Bmatrix} \int (\dot{x}_i - \dot{x}_1) dt \\ \int (\dot{y}_i - \dot{y}_1) dt \end{Bmatrix} + \begin{bmatrix} \lambda K & 0 \\ 0 & \lambda K \end{bmatrix} \begin{Bmatrix} (\dot{x}_i - \dot{x}_1) \\ (\dot{y}_i - \dot{y}_1) \end{Bmatrix} \quad (5.14)$$

Separation of the elastic and damping forces and their representation as separate fields (C-field and R-field) yield a simplified bond graph model for joints between several links as shown in Fig. 5.11. The viscous friction between two links at the joint is modeled by separate R-elements at 0-junctions where relative angular velocities between the links and the reference link are calculated. Likewise, torsional stiffness and damping at the joint may be modeled by 1-C-R structures connected to the 0-junction. If the joint is passive, i.e., actuated, then the motor model with appropriate causalities to apply a torque (effort) may be connected to that 0-junction. The power directions in the bond graph model are set to calculate relative angular velocities at this 0-junction. This also ensures that a motor would apply a forward torque on the driven link and the reverse reactive torque on the driving link.

When the values of joint stiffness and damping are large, there exists almost the same generalized flow in all bonds connected to the joint element from the body components and the impedance coupling tends to become a plain coupling or kinematic joint. Decreasing the value of compliance element can increase the joint flexibility. If the values of damping and compliance parameters are taken to be zero then the connected body components are decoupled. This is how the type of the joint can be changed as per requirement.

5.2.5 Model of the Slider Component

The slider is one of the most difficult multibody components which give rise to nonlinear equations of motion. Incorrect modeling of slider component generates improper inertial forces. The schematic view of a plane slider is shown in Fig. 5.12. The main advantage of a bond graph model is that the radial and tangential forces acting at different points of the model need not be calculated. Simulations supported by theoretical bond graph model of the actual system can determine these dynamic forces.

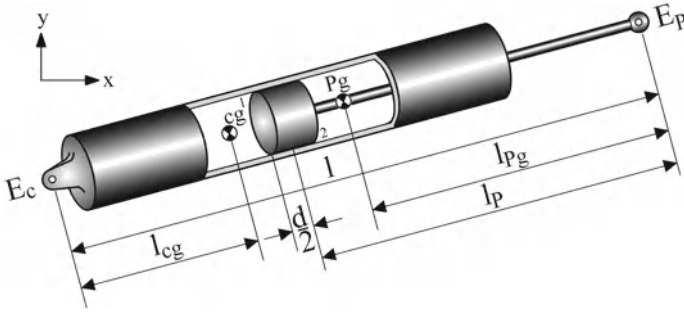


Fig. 5.12 Schema of a slider model

The velocities of the end points E_c and E_p of the plane slider are expressed as follows:

$$\begin{aligned}\dot{x}_1 &= \dot{x}_{cg} + l_{cg}\dot{\theta}_{cg}\sin\theta_{cg}, \\ \dot{y}_1 &= \dot{y}_{cg} - l_{cg}\dot{\theta}_{cg}\cos\theta_{cg},\end{aligned}\quad (5.15)$$

$$\begin{aligned}\dot{x}_2 &= \dot{x}_{Pg} - l_{Pg}\dot{\theta}_{Pg}\sin\theta_{Pg}, \\ \dot{y}_2 &= \dot{y}_{Pg} + l_{Pg}\dot{\theta}_{Pg}\cos\theta_{Pg}.\end{aligned}\quad (5.16)$$

The contemporary length (l) between two points E_c and E_p may be expressed as

$$l^2 = (x_1 - x_2)^2 + (y_1 - y_2)^2 \quad (5.17)$$

whose differentiation with respect to time yields

$$\dot{l} = \left(\frac{x_1 - x_2}{l}\right)(\dot{x}_1 - \dot{x}_2) + \left(\frac{y_1 - y_2}{l}\right)(\dot{y}_1 - \dot{y}_2) \quad (5.18)$$

The normal velocity at the contact point 1 on the cylinder by assuming a thin but long piston is

$$V_{c_1} = -\sin\theta_{cg}\dot{x}_{cg} + \cos\theta_{cg}\dot{y}_{cg} + (l - l_p - l_{cg} - d/2)\dot{\theta}_{cg} \quad (5.19)$$

At the same time, the normal velocity at the contact point 1 on the piston is

$$V_{p_1} = -\sin\theta_{Pg}\dot{x}_{Pg} + \cos\theta_{Pg}\dot{y}_{Pg} - (l_p - l_{Pg} + d/2)\dot{\theta}_{Pg} \quad (5.20)$$

Likewise, the normal velocity at the contact point 2 on the cylinder is

$$V_{c_2} = -\sin\theta_{cg}\dot{x}_{cg} + \cos\theta_{cg}\dot{y}_{cg} + (l - l_p - l_{cg} + d/2)\dot{\theta}_{cg} \quad (5.21)$$

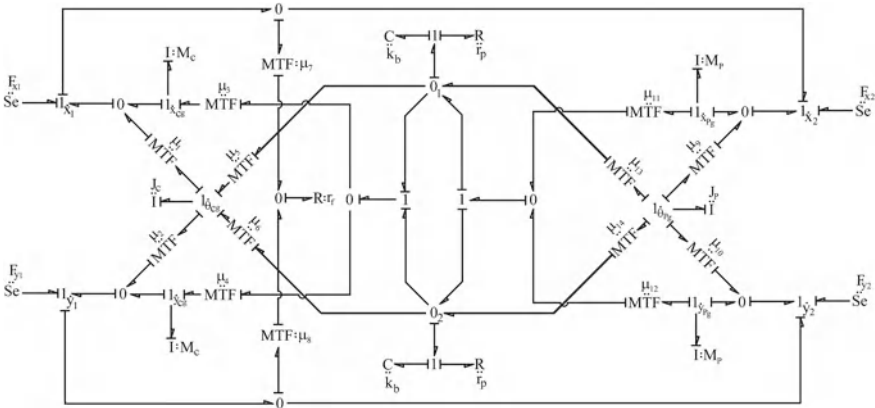


Fig. 5.13 Bond graph model of the slider component

and the normal velocity at the contact point 2 on the piston is

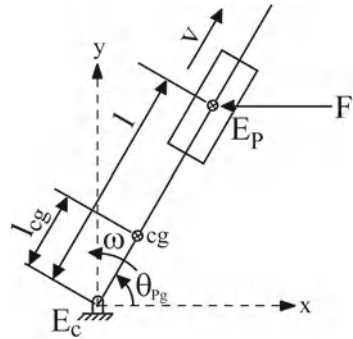
$$V_{P_2} = -\sin\theta_{Pg}\dot{x}_{Pg} + \cos\theta_{Pg}\dot{y}_{Pg} - (l_P - l_{Pg} - d/2)\dot{\theta}_{Pg} \tag{5.22}$$

The different multipliers in Eqs. 5.15–5.22 are used as transformer moduli of MTF-elements in the bond graph model. They are $\mu_1 = l_{cg}\sin\theta_{cg}$, $\mu_2 = -l_{cg}\cos\theta_{cg}$, $\mu_3 = -1/\sin\theta_{cg}$, $\mu_4 = 1/\cos\theta_{cg}$, $\mu_5 = 1/(l - l_P - l_{cg} - d/2)$, $\mu_6 = 1/(l - l_P - l_{cg} + d/2)$, $\mu_7 = (x_1 - x_2)/l$, $\mu_8 = (y_1 - y_2)/l$, $\mu_9 = -l_{Pg}\sin\theta_{Pg}$, $\mu_{10} = l_{Pg}\cos\theta_{Pg}$, $\mu_{11} = -\sin\theta_{Pg}$, $\mu_{12} = \cos\theta_{Pg}$, $\mu_{13} = -(l_P - l_{Pg} + d/2)$ and $\mu_{14} = -(l_P - l_{Pg} - d/2)$.

The augmented bond graph model of the system under consideration is shown in Fig. 5.13. In Fig. 5.13, the sources of efforts indicate the joint forces, labeled 1-junctions represent various velocity points, the masses (M_P , M_C) and the moment of inertias (J_P , J_C) of the slider and rod, respectively, are modeled by the I-elements connected to the 1-junctions representing the velocities of the center of gravity of the two in the inertial frame, the MTF-elements are used to synthesize the constraints and junctions 0_1 and 0_2 represent the forces at the contact points between the cylinder and the piston. MTF-elements with moduli μ_7 and μ_8 are used to calculate the relative velocity between the piston and the cylinder at a 0-junction and the friction between the piston and the cylinder is modeled by an R-element (r_f) at that junction. If the cylinder is actuated (e.g., a hydraulic/pneumatic cylinder driven by the pressure difference) then the actuating force should be modeled at this 0-junction (this case has been considered later in this chapter). Note that if there is dry friction at the piston and cylinder interfaces then the constitutive relation of the R: r_f -element should be modulated by the normal reactions given by 0_1 and 0_2 -junctions.

The models developed in the previous sections can be easily extended for three-dimensional systems by including modified versions of kinematic relations. We consider two benchmark problems in the following sections.

Fig. 5.14 Schema of Rapson slide



5.2.6 Case Study-I: Rapson Slide

In a Rapson slide, the slider replaces piston and rod replaces cylinder of the piston-cylinder model given in Fig. 5.12. The tiller is hinged at the point E_c . The block slides on the rod. We assume that horizontal force acts at the center of the slider and the mechanism lies in a horizontal plane (Fig. 5.14). The distance of the end point of the piston rod from the combined center of gravity of the piston and rod (Fig. 5.12) and the distance of the same point from the individual center of gravity of the piston, are set to zero so that the center of gravity of the piston and the end point of the piston rod E_p coincide with each other. With these boundary conditions, the Rapson slide model is equivalent to the piston-cylinder model as described above.

5.2.6.1 Bond Graph Model

The bond graph model of the Rapson slide [7], shown in Fig. 5.15, is obtained by slightly modifying the bond graph model of piston-slider model. As the end point of the rod E_c is fixed, there is no motion to it. This is shown in the bond graph model by putting two zero flow sources. Two coupling capacitors or pads [91] are used in conjunction with these zero flow sources for avoiding the differential causalities. Physically, these pads (1-C-R structures) indicate the joint stiffness and damping at the hinge.

5.2.6.2 Simulink Model

To validate the bond graph model of the Rapson slide, we develop a Matlab Simulink model of the same and compare the numerical results. With reference to Fig. 5.14, the forces acting on the slider of the Rapson slide are calculated.

Forces acting in the radial direction, including centrifugal force, at the point E_p are balanced as

$$M_p(\ddot{l} - \dot{\theta}_{pg}^2 l) + F \cos \theta_{pg} = 0 \tag{5.23}$$

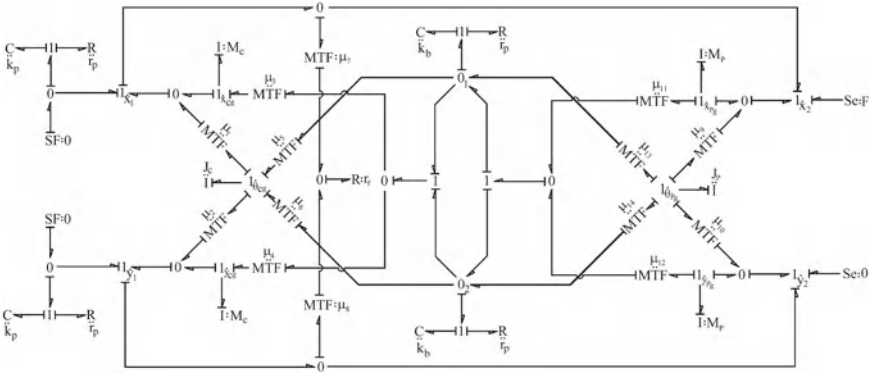


Fig. 5.15 Bond graph model of a Rapson slide

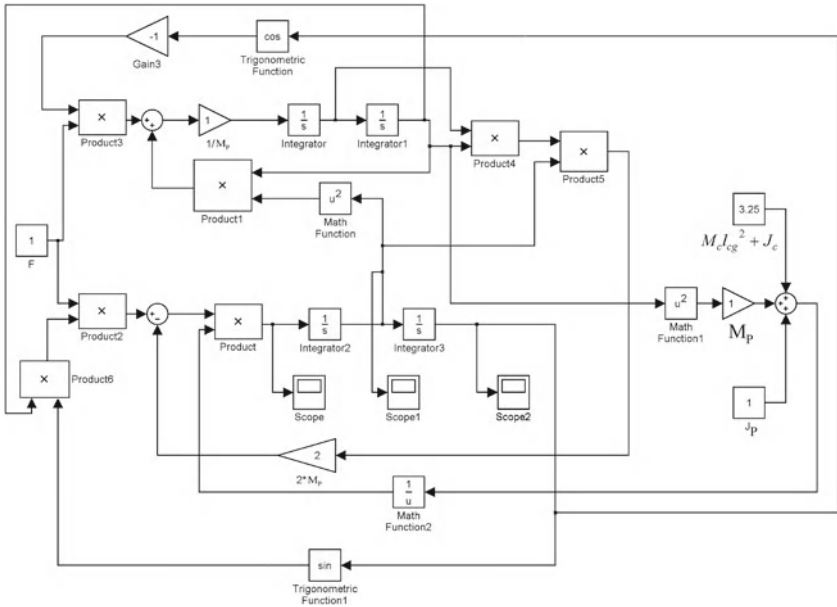


Fig. 5.16 Block diagram model of Rapson slide

The moment acting in the tangential direction, including Coriolis force, at the point E_P are balanced:

$$J_{eqv}\ddot{\theta}_{Pg} + 2M_P\dot{\theta}_{Pg}\dot{l} - Fl\sin\theta_{Pg} = 0 \tag{5.24}$$

where the total equivalent moment of inertia at point E_c is

$$J_{eqv} = M_P l^2 + J_P + M_c l_{cg}^2 + J_c \tag{5.25}$$

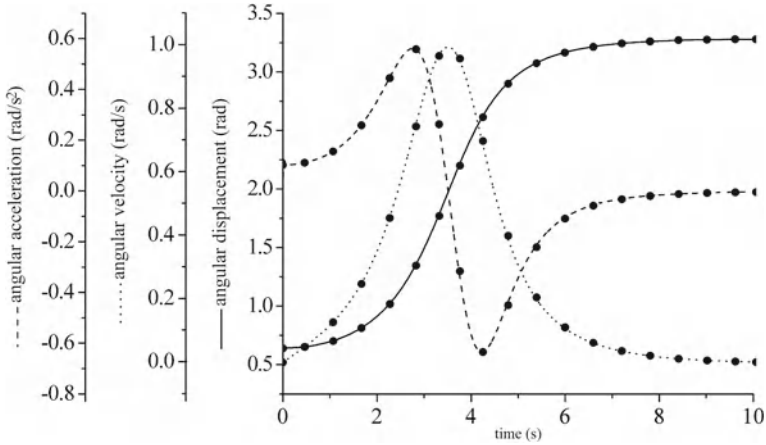


Fig. 5.17 Angular displacement, velocity, and acceleration for the center of the slider (*line* indicates bond graph model, and *scatter points* indicate Simulink model)

Equations 5.23–5.25 are used to construct the Simulink model given in Fig. 5.16. Note that Eqs. 5.23–5.25 give a very compact model of the Rapson slide mechanism with two degrees of freedom (DOF) but the contact dynamics and frictional forces are neglected.

5.2.6.3 Simulation Results and Validation of the Model

The parameter values are $d = 0.4$ m, $l = 5$ m, $l_{cg} = 1.5$ m, $l_p = 0.0$ m, $l_{Pg} = 0.0$ m, $k_b = 10^5$ N/m, $k_p = 10^5$ N/m, $r_p = 10^3$ N.s/m, $F = 1$ N, $J_c = 1$ kg.m², $J_p = 1$ kg.m², $M_c = 1$ kg, $M_p = 1$ kg, and $r_f = 0.0$ N.s/m. The initial conditions used in simulation are $x_c = 1.2$ m, $y_c = 0.9$ m, $x_p = 4$ m, $y_p = 3$ m, $x_1 = 0$ m, $y_1 = 0$ m, $\theta_c = 0.6435011$ rad, and $\theta_p = 0.6435011$ rad.

We consider that initially the Rapson slide lying in horizontal plane makes an angle of 36.87° with the reference x-axis. A horizontal force of constant magnitude 1 N acts at the center of gravity of the slider in a direction parallel to the reference x-axis. The distance between the points E_c and the center of gravity of the piston is 5 m. No other external force acts on the system.

The angular displacement, angular velocity, and the angular acceleration of the slider are shown in Fig. 5.17 where solid lines indicate results from the bond graph model and scattered points are results from the Simulink model.

Although not visible to the naked eye, the results for the angular velocity and angular acceleration from the two models differ slightly. These errors may be attributed to the extra dynamics (contact forces and pads) modeled in the bond graph model. Disregarding such marginal errors, we can safely state that the bond graph model of Rapson the slide is more accurate in the sense that it predicts joint flexibility effects.

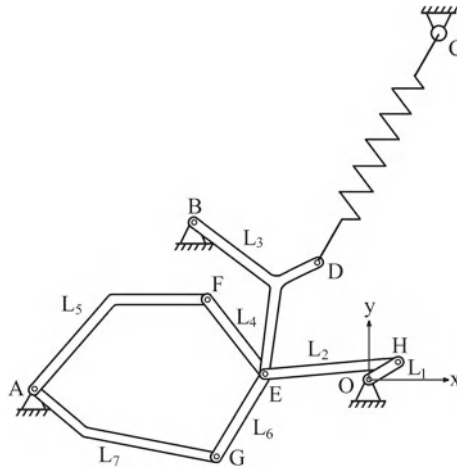


Fig. 5.18 Seven-body mechanism

5.2.7 Case Study-II: A Seven-Body Mechanism

5.2.7.1 Model

The seven-body mechanism (also called Andrew’s mechanism) in [129] is a benchmark problem adopted in the literature on different multibody simulation [7, 81]. It consists of seven irregular-shaped bodies, which are connected by frictionless revolute joints as shown in Fig. 5.18. This mechanism is driven by constant drive torque motor located at point O. The point D of link 3 is connected to the reference frame by a massless spring. The bond graph model for the rigid bodies ($L_1, L_2, L_4, L_5, L_6,$ and L_7) having an arbitrary centroid position was developed in Fig. 5.3b. Frictionless flexible joints, whose bond graph model was developed in Fig. 5.4, connect the seven links, spring, and ground. The spring is modeled according to Eq. 5.2 as a two-force member without inertia. Readers may also consult [132] where bond graph model of a planar 9-bar torque converting mechanism used for power transmission is discussed.

The connectivity among different components of the mechanism and with the reference frame at points A, B, C, and O are shown in a word bond graph model in Fig. 5.19. As the links 5 and 7 are hinged at the same point A through revolute joints, the grounded joints may be considered together or separately. Links 3, 5, and 7 are connected to the ground through separate revolute joints. Link 1 or the crank is directly connected to the ground. A torque, τ_M , is directly applied to the crankshaft. Bond graph models of the crank and the ground are shown in Fig. 5.20.

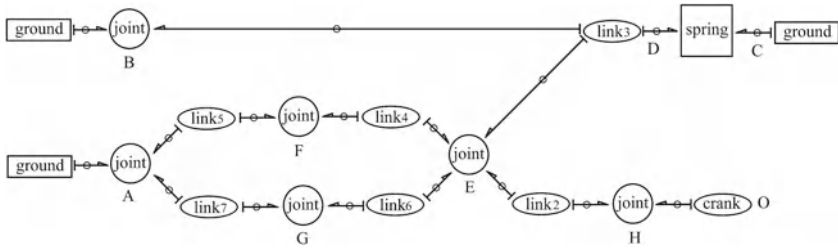


Fig. 5.19 Word bond graph of seven-body mechanism

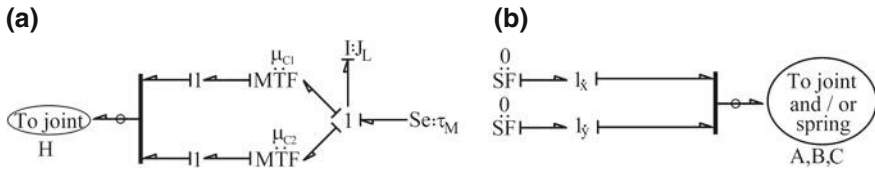


Fig. 5.20 Bond graph model of a crank and ground

5.2.7.2 Simulation Results

The geometric parameters, mass, rotational inertia about center of mass of the links, and initial positions of the fixed points A, B, C, and O are adopted from [129]. The constant drive torque τ_M given by the motor is 0.033 Nm. The spring coefficient and unstretched length for the spring are 4530 N/m and 0.07785 m, respectively. The initial positions of the different points in the mechanism are specified as $x_D = -0.010249641$ m, $y_D = 0.026190026$ m, $x_E = -0.0209593$ m, $y_E = 0.0012925$ m, $x_F = -0.033996$ m, $y_F = 0.01645968$ m, $x_G = -0.03163377$ m, $y_G = -0.01562066$ m, $x_H = 0.00698655$ m, and $y_H = 0.000433722$ m. These initial positions were calculated from the geometry specified in [129]. The joint stiffness and damping were considered as 10^{10} N/m and 10^3 N s/m, respectively.

The simulation was performed for a time duration of 0.030 s. The angular displacement, angular velocity, and the angular acceleration of link 1 or the crank are shown in Fig. 5.21. Link 1 or the crank completes just one revolution in 16.3 ms. The results for this seven-body mechanism presented in [81] show that the angular displacement of the link1 is below 16rad after 30ms whereas this result shows it exceeds 16rad after 0.029898 s. The present results totally agree with the results of different original simulation results presented in [129]. Moreover, the developed bond graph models are modular and it is easier to synthesize models of other planar mechanisms by appropriately assembling various submodels.

When joint clearance effect is considered in the model (see 5.2.4) the results change significantly. The impacts produce sharp change in the acceleration levels. The results given in Fig. 5.22 were obtained for clearance $c = 0.0001$ m at joint H.

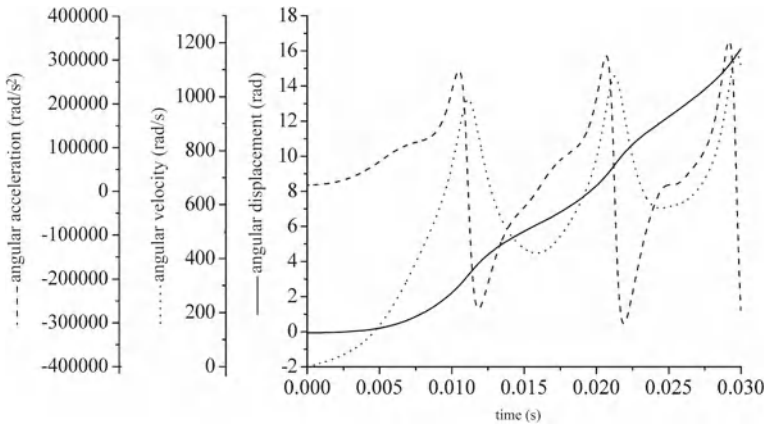


Fig. 5.21 Angular displacement, velocity, and acceleration for the crank

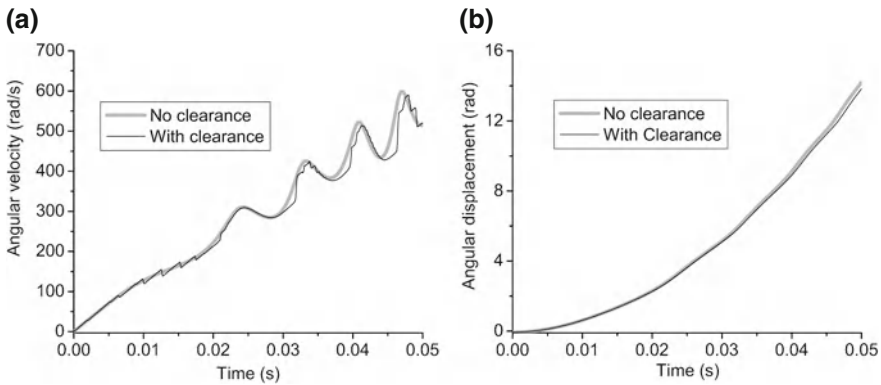
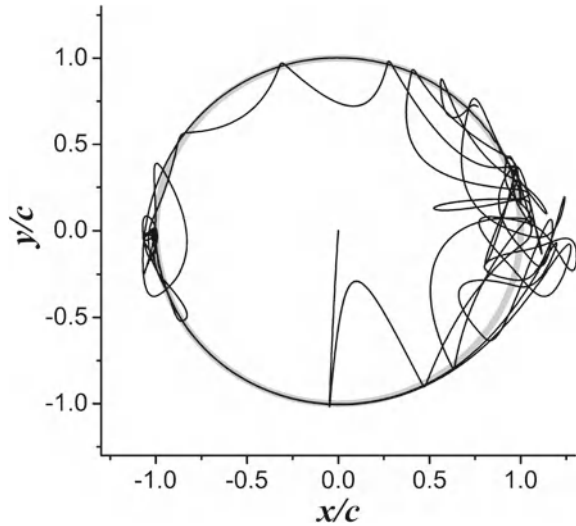


Fig. 5.22 **a** Angular velocity and **b** displacement of the crank with joint clearance

It is seen from Fig. 5.22 that the influence of clearance is prominently visible in angular velocity response (after one integration of the most affected response, acceleration) whereas the influence reduces on further integration, i.e., angular displacement response. Note that the sharp changes in velocity during impacts introduce dynamic loads which may severely damage the system and reduce its fatigue life. Therefore, correct modeling of impacts and other similar phenomena (e.g., backlash) is necessary during mechatronic system design. The motion of the journal center (end H of link OH) within the clearance circle is shown in Fig. 5.23 where the plotted variables are the normalized linear displacements. This result shows the impacts, joint flexibility (incursions outside the clearance circle), and grazing motion during which frictional forces act on the journal and the outer race. Any motion within the clearance circle is a free-flight inertial motion during which no power transmission takes place.

Fig. 5.23 Normalized journal center displacements in x and y directions (The normalized clearance circle is a unit circle which is shown in the background.)



5.2.8 Modeling Hydraulic Actuators

5.2.8.1 Model of Hydraulic Servo System

Hydraulic linear actuators are used in heavy-duty applications due to their capacity to produce large forces at high speeds, high durability and stiffness, and rapid response. One of the major uses of hydraulic actuators is in Stewart platforms. The hydraulic servo system consists of servo mechanism, servo cylinder, controller, loads, and hydraulic power supply. We will initially develop a model of a planar hydraulic actuator.

5.2.8.2 Four-Way Directional Control Valve Model

Four-way directional control valve, as shown in Fig. 5.24, is used to control the hydraulic system. The supply port and the return ports are connected with the pump and the tank, respectively. The load flow ports 1 and 2 are connected with the hydraulic cylinder.

The four-way three-land proportional spool valve has a symmetric underlap land L at the neutral position. The flows through the valve orifices of the spool valve are described by the orifice equations as given by [83].

The bond graph of the model of four-way directional control valve is shown in Fig. 5.25. The supply pressure p_s is represented by an Se-element. C- and R-elements connected with the 0_{p_1} junction, which determines the plenum pressure p_1 , indicate the bulk stiffness of fluid K_1 and outlet valve port resistance R_1 from port 1, respectively. Similarly, C- and R-elements connected with the 0_{p_2} junction

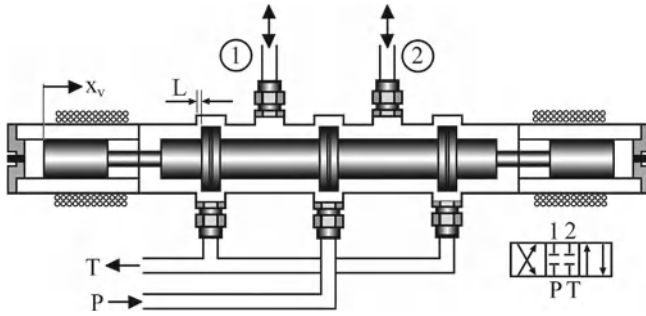
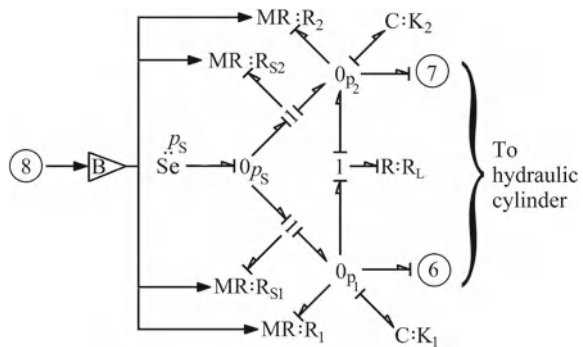


Fig. 5.24 Four-way directional control valve

Fig. 5.25 Bond graph model of the four-way directional control valve



(which determines the plenum pressure p_2) indicate bulk stiffness of fluid K_2 and outlet valve port resistance R_2 from port 2, respectively. The fluid flow through ports 1 and 2 from the supply are, respectively, modeled by resistive elements R_{s1} and R_{s2} . The numbers (6, 7, and 8) shown within the circles identify the ports for interfacing this submodel to other submodels. The current i is taken from the force controller through port 8 and it is amplified (gain parameter B) and imposed on the modulated resistances R_1, R_2, R_{s1} and R_{s2} . R_L represents the leakage resistance. The driving efforts produced by the servo mechanism are taken out through ports 6 and 7 and are to be applied on the piston of the hydraulic cylinder.

Depending upon the port opening areas ($w_v (x_v \mp L)$), the flow rates through the modulated resistances are given as follows:

$$\begin{aligned}
 Q_{R_1} &= \gamma (x_v - L) \text{sign}(p_1) \sqrt{|p_1|} \quad \forall x_v \leq L, \text{ else } Q_{R_1} = 0; \\
 Q_{R_{s1}} &= \gamma (x_v + L) \text{sign}(p_s - p_1) \sqrt{|p_s - p_1|} \quad \forall x_v \geq -L, \text{ else } Q_{R_{s1}} = 0; \\
 Q_{R_2} &= \gamma (x_v + L) \text{sign}(p_2) \sqrt{|p_2|} \quad \forall x_v \geq -L, \text{ else } Q_{R_2} = 0; \\
 Q_{R_{s2}} &= \gamma (x_v - L) \text{sign}(p_s - p_2) \sqrt{|p_s - p_2|} \quad \forall x_v \leq L, \text{ else } Q_{R_{s2}} = 0; \quad (5.26)
 \end{aligned}$$

where the subscripts indicate the respective resistances in the bond graph model.

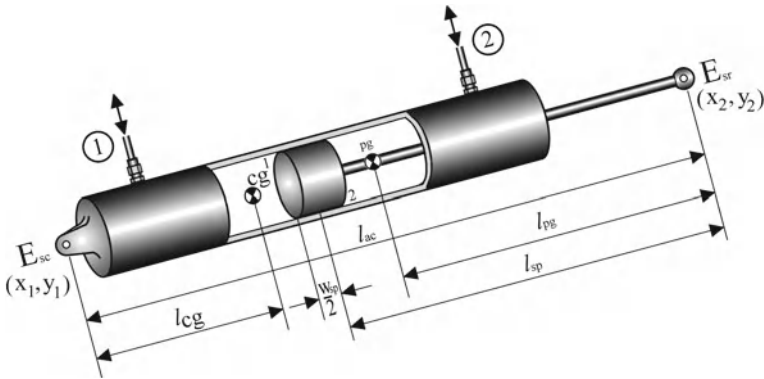


Fig. 5.26 Schema of the hydraulic piston-cylinder prismatic link

The C-elements determine the plenum pressures which are influenced by the motion of the hydraulic cylinder. Their constitutive relations are discussed in the following section.

5.2.8.3 Hydraulic Cylinder Model

The schematic drawing of the hydraulic actuator is shown in Fig. 5.26. The cylinder ports 1 and 2 are connected to the proportional valve which modulates the motion of the piston by modulating the fluid flow into and out of the piston chambers.

The end of the cylinder E_{sc} is assumed to be fixed to the ground and the other end, i.e., rod end, E_{sr} is connected to a moving object or load. The contemporary length l_{ac} of it is the distance between the two end points. The center of gravity (cg) of the cylinder is located at a distance of l_{cg} from the fixed end. The combined center of gravity (pg) of the piston and the rod is located at a distance of l_{pg} from the rod end E_{sr} . The width of the piston is w_{sp} . The center of the piston is located at a distance l_{sp} from the rod end.

5.2.8.4 Formulation of the Constitutive Model

The net external force acting at the piston is due to the hydraulic forces and friction force:

$$F_{sp} = p_1 A_{sp} - p_2 (A_{sp} - A_{sr}) - R_{fr} \dot{x}_{sp} \quad (5.27)$$

where F_{sp} denotes the load force on the piston, R_{fr} is the frictional damping, A_{sp} , and A_{sr} are the cross-sectional areas of the piston and the piston rod, and \dot{x}_{sp} is the relative velocity between the piston and the cylinder. It is assumed that the process is isothermal and that the pressure of fluid is uniform everywhere on each side of the piston.

The continuity equation for the piston chambers [42] is given as

$$\dot{p}_1 = \frac{\beta}{V_1} [-\dot{V}_1 - C_L(p_1 - p_2) + Q_1] \quad (5.28)$$

$$\dot{p}_2 = \frac{\beta}{V_2} [-\dot{V}_2 + C_L(p_1 - p_2) - Q_2] \quad (5.29)$$

where, $C_L = 1/R_L$ is the internal leakage coefficient of the piston. The total volumes of fluid in each control volume are

$$V_1 = V_{1lf} + A_{sp}x_{sp} \quad (5.30)$$

and

$$V_2 = V_{2lf} + (A_{sp} - A_{sr})(S - x_{sp}), \quad (5.31)$$

where S is the stroke of the piston, V_{1lf} and V_{2lf} are the volumes of fluid in the lines and fittings of the corresponding sides of the piston. Therefore,

$$\dot{V}_1 = A_{sp}\dot{x}_{sp} \quad (5.32)$$

and

$$\dot{V}_2 = -(A_{sp} - A_{sr})\dot{x}_{sp}. \quad (5.33)$$

Substituting the values of \dot{V}_1 and \dot{V}_2 in Eqs. 5.28–5.29, the following continuity equations in terms of piston movement are obtained:

$$\dot{p}_1 = \frac{\beta}{V_{1lf} + A_{sp}x_{sp}} [-A_{sp}\dot{x}_{sp} - C_L(p_1 - p_2) + Q_1], \quad (5.34)$$

$$\dot{p}_2 = \frac{\beta}{V_{2lf} + (A_{sp} - A_{sr})(S - x_{sp})} [(A_{sp} - A_{sr})\dot{x}_{sp} + C_L(p_1 - p_2) - Q_2]. \quad (5.35)$$

Thus, the stiffness parameters in Fig. 5.25 are $K_1 = \beta/V_1$ and $K_2 = \beta/V_2$, where V_1 and V_2 are the state variables associated with the respective C-elements.

5.2.8.5 Bond Graph Model

The bond graph model of the hydraulic cylinder is shown in Fig. 5.27. The movement of the piston depends upon the pressures p_1 and p_2 which are determined in the submodel for four-way directional control valve and are interfaced through ports 6 and 7. The information of the force due to pressure difference, which is required for implementation of the force controller, is taken out through port 5. The information of the rate of deformation (\dot{l}_{aci}) of the real actuator in the plant side is also taken out for development of an inverse system dynamics model, which is discussed in the final chapter of this book.

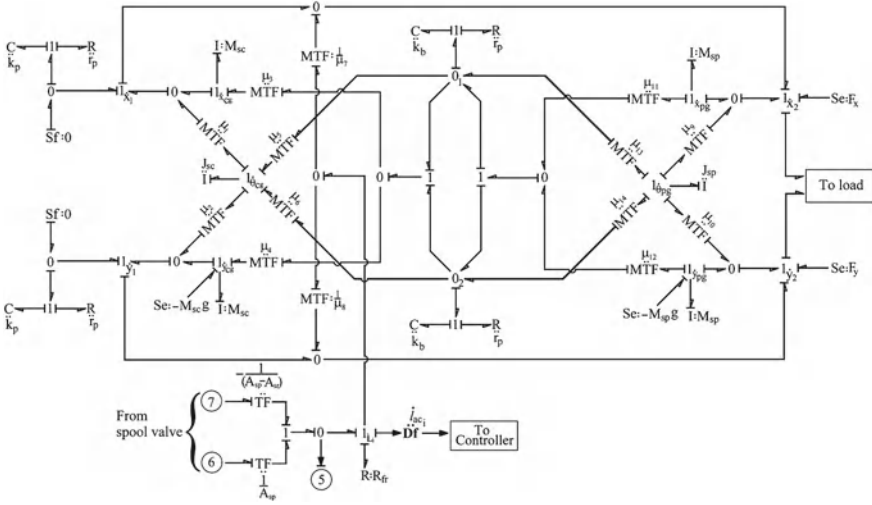


Fig. 5.27 Bond graph model of the hydraulic piston-cylinder prismatic link

The linear velocities (\dot{x}_{cg} , \dot{y}_{cg}) of the center of gravity of the cylinder in the x - y plane and rotational velocity ($\dot{\theta}_{cg}$) of the same about the z -axis are represented by the junctions ($1\dot{x}_{cg}$, $1\dot{y}_{cg}$) and $1\dot{\theta}_{cg}$, respectively. The linear and angular velocities of the center of gravity of the cylinder are transformed to obtain the velocities of the end point E_{sc} (x_1 , y_1) of the cylinder by using the transformers with moduli $\mu_1 = l_{cg} \sin \theta_{cg}$ and $\mu_2 = -l_{cg} \cos \theta_{cg}$. Similarly, the linear velocities (\dot{x}_{pg} , \dot{y}_{pg}) of the center of gravity of the piston and rod in the x - y plane and rotational velocity ($\dot{\theta}_{pg}$) of the same about the z -axis are represented by the junctions ($1\dot{x}_{pg}$, $1\dot{y}_{pg}$) and $1\dot{\theta}_{pg}$, respectively, and they are transformed to obtain the velocities of the rod end E_{sr} (x_2 , y_2) through transformers with moduli $\mu_9 = -l_{pg} \sin \theta_{pg}$ and $\mu_{10} = l_{pg} \cos \theta_{pg}$.

The masses (M_{sc} , M_{sp}) and the moment of inertias (J_{sc} , J_{sp}) of the cylinder and piston rod, respectively, are modeled by the I-elements connected to the corresponding 1-junctions representing the velocities of their center of gravity in the inertial frame. The end point of the rod E_{sc} is fixed by adding zero source of flows at the appropriate locations. Coupling capacitors [137] or pads [105], with stiffness k_p and damping r_p , are added to the model at appropriate locations for avoiding differential causalities. Additional forces acting at the end point E_{sr} (x_2 , y_2) of rod are modeled by source of efforts denoted as F_x and F_y .

The normal velocity at the contact point 1 (see Fig.5.26) on the cylinder by assuming a thin but long piston is

$$V_{c1} = -\sin \theta_{cg} \dot{x}_{cg} + \cos \theta_{cg} \dot{y}_{cg} + (l_{ac} - l_{sp} - l_{cg} - W_{sp}/2) \dot{\theta}_{cg} \tag{5.36}$$

At the same time, the normal velocity at the contact point 1 on the piston is

$$V_{p1} = -\sin \theta_{pg} \dot{x}_{pg} + \cos \theta_{pg} \dot{y}_{pg} + (l_{sp} - l_{pg} + W_{sp}/2) \dot{\theta}_{pg} \tag{5.37}$$

Likewise, the normal velocity at the contact point 2 on the cylinder is

$$V_{c_2} = -\sin \theta_{cg} \dot{x}_{cg} + \cos \theta_{cg} \dot{y}_{cg} + (l_{ac} - l_{sp} - l_{cg} + W_{sp}/2) \dot{\theta}_{cg} \quad (5.38)$$

and the normal velocity at contact point 2 on the piston is

$$V_{p_2} = -\sin \theta_{pg} \dot{x}_{pg} + \cos \theta_{pg} \dot{y}_{pg} + (l_{sp} - l_{pg} - W_{sp}/2) \dot{\theta}_{pg} \quad (5.39)$$

We impose constraints that the velocities of contact points 1 and 2 are the same as that of the corresponding points on the piston. This constraint is numerically/implicitly implemented by tying up the corresponding velocity points with stiff coupling capacitors (see O_1 and O_2 junctions in Fig. 5.27). In physical terms, this coupling capacitor represents the contact stiffness (k_b). We also introduce a contact damping term (r_p). The transformer elements with moduli $\mu_3, \mu_4, \mu_5, \mu_6, \mu_{11}, \mu_{12}, \mu_{13}$ and μ_{14} are used to synthesize the kinematic relations in Eqs. 5.36–5.39.

The contemporary length (l_{ac}) between two end points E_{sc} and E_{sr} may be expressed as

$$l_{ac}^2 = (x_2 - x_1)^2 + (y_2 - y_1)^2 \quad (5.40)$$

whose differentiation with respect to time yields

$$\dot{l}_{ac} = \left(\frac{x_2 - x_1}{l_{ac}} \right) (\dot{x}_2 - \dot{x}_1) + \left(\frac{y_2 - y_1}{l_{ac}} \right) (\dot{y}_2 - \dot{y}_1), \quad (5.41)$$

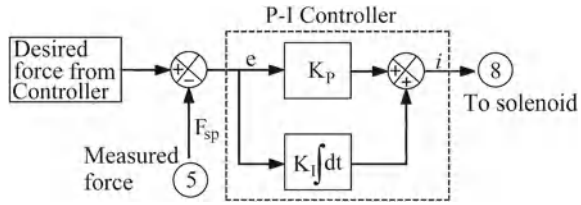
The rate of deformation of the prismatic actuator (measured as \dot{l}_{ac_i} in Fig. 5.27) is the relative velocity between two points E_{sc} and E_{sr} . Modulated transformer elements with moduli $1/\mu_7$ and $1/\mu_8$, where $\mu_7 = (x_2 - x_1)/l_{ac}$ and $\mu_8 = (y_2 - y_1)/l_{ac}$, are used to synthesize the kinematic constraint given by Eq. 5.41.

5.2.8.6 Force Controller Design

The force acting on the piston of the hydraulic cylinder is controlled through a feedback proportional-integral (PI) controller, as shown in Fig. 5.28. The information of the force acting on the piston (measured by incorporating pressure sensors in the actuator) is received from the model in Fig. 5.27 through port 5. The inverse dynamics model (developed in the final chapter of this book) prescribes the desired force (set point) for this controller. The controller output (through port 8) is used to activate the spool valve linear displacement in the bond graph model given in Fig. 5.25.

In the last chapter of this book, a vehicle simulator system will be developed. That simulator based on a Stewart platform uses hydraulic actuators. To complete the closed-loop control, force on the piston in each leg (hydraulic actuator of the platform) is fed back. The input to the controller is the force error e which is the difference between the reference force from the inversion controller and the current piston force. The output of the force controller is the current. This current controls the motion of the servo valve and actuates the legs so that desired force is applied on the platform.

Fig. 5.28 PI controller for the solenoid current in the four-way spool valve



5.3 Spatial Multibody Systems

The motion of a rigid body in space is described by six degrees of freedom. In a multibody system composed of many rigid/flexible bodies, it is easier to define velocities of different points on separate bodies in respective body-fixed frames. These velocities can be then transformed to corresponding inertia frame velocities. The constraints between various body motions are then implemented in a common reference frame called inertial reference frame. A body-fixed frame is termed a non-inertial reference frame. In a body-fixed frame, the velocities of various points on a rigid body are easily computed because the geometric distances remain constant. The similarities can be extended to flexible body systems, e.g., the deflection of a beam floating in water is described best with respect to a body-fixed frame with one of its axes aligned initially along the line connecting the two ends of the beam and then the computed results can be superposed on the rigid body translation and rotation of the beam. Noninertial frames are always preferred when modeling complex multibody or many-body systems.

5.3.1 Noninertial Reference Frame

Let X - Y - Z be an inertial coordinate system and x - y - z be a body-fixed or noninertial coordinate system on the rigid body with origin O' at the center of mass which translates and rotates with the rigid body. It is assumed that this body-fixed coordinate system shown in Fig. 5.29 is aligned along the principal axes of the rigid body.

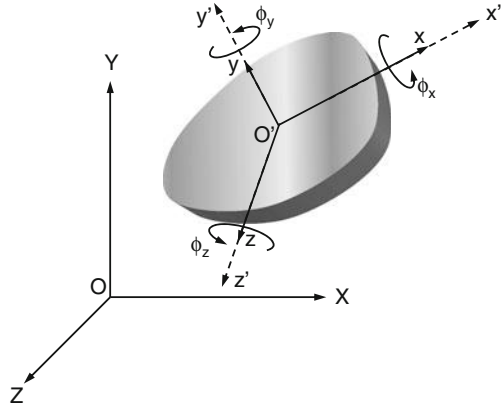
The velocity vector in the inertial frame is represented as \mathbf{V}_{XYZ} and in the body-fixed frame as \mathbf{V}_{xyz} . The angular velocity vector in the later frame is ω_{xyz} . Then, the acceleration vector in the inertial frame is given as

$$\mathbf{a}_{XYZ} = \mathbf{a}_{xyz} + \omega_{xyz} \times \mathbf{V}_{xyz} \tag{5.42}$$

where \mathbf{a}_{xyz} is the acceleration observed in moving frame. In terms of scalar components of acceleration,

$$\begin{aligned} \ddot{X} &= \ddot{x} + (\dot{z}\omega_y - \dot{y}\omega_z), \\ \ddot{Y} &= \ddot{y} + (\dot{x}\omega_z - \dot{z}\omega_x), \\ \ddot{Z} &= \ddot{z} + (\dot{y}\omega_x - \dot{x}\omega_y). \end{aligned} \tag{5.43}$$

Fig. 5.29 Body-fixed coordinate system



If F_x, F_y and F_z are the resultant force components along the body-fixed axes and acting at the center of mass of the rigid body and XYZ and xyz axes coincide then

$$\begin{aligned}
 m\ddot{X} &= m\ddot{x} + m(\dot{z}\omega_y - \dot{y}\omega_z) = F_x, \\
 m\ddot{Y} &= m\ddot{y} + m(\dot{x}\omega_z - \dot{z}\omega_x) = F_y, \\
 m\ddot{Z} &= m\ddot{z} + m(\dot{y}\omega_x - \dot{x}\omega_y) = F_z
 \end{aligned}
 \tag{5.44}$$

or

$$m\ddot{x} = F_x - m(\dot{z}\omega_y - \dot{y}\omega_z), \tag{5.45}$$

$$m\ddot{y} = F_y - m(\dot{x}\omega_z - \dot{z}\omega_x), \tag{5.46}$$

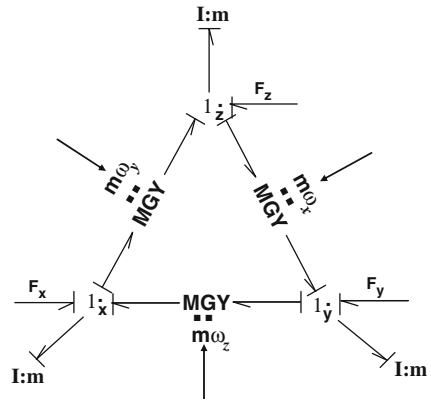
$$m\ddot{z} = F_z - m(\dot{y}\omega_x - \dot{x}\omega_y), \tag{5.47}$$

where $m(\dot{z}\omega_y - \dot{y}\omega_z)$, $m(\dot{x}\omega_z - \dot{z}\omega_x)$ and $m(\dot{y}\omega_x - \dot{x}\omega_y)$ are pseudo forces or fictitious forces acting on the rigid body in noninertial reference frame. Equations 5.45–5.47 are the Newton’s equations written in the noninertial frame. The bond graph model of the rigid body translational motion in noninertial coordinates is then given in Fig. 5.30 where GY elements model the pseudo forces. Note that each 1 junction is connected with two gyrators. The gyrator between 1-junctions representing motions along x-axis and y-axis has modulus $m\omega_z$ which applies a pseudo force $m\dot{y}\omega_z$ at $1_{\dot{x}}$ junction and $-m\dot{x}\omega_z$ at $1_{\dot{y}}$ junction. The other gyrators produce similar relations and thus only three gyrators completely represent all pseudo forces.

5.3.2 Euler Angles

The orientation or attitude of a body is given relative to a frame of reference. The position, as described just before, and the orientation together describe the body’s

Fig. 5.30 Bond graph model of Newton's equations in noninertial frame



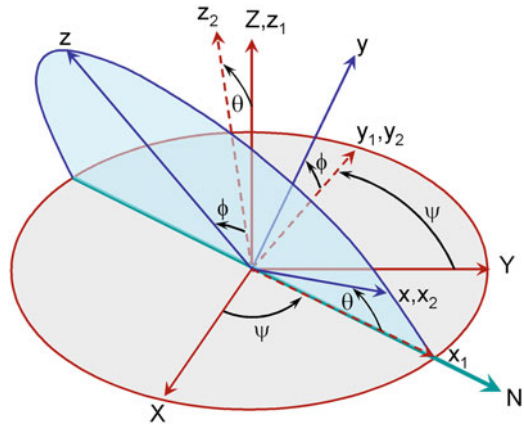
disposition in the space. Euler's rotation theorem states that two successive rotations about two different fixed axes is equivalent to a single rotation about a different fixed axis. Thus, three or more rotations about fixed axes are also equal to only one rotation, but about an axis which is complicated to calculate unless matrix or vector rotation approaches are used. Any orientation of the body can be represented by a rotation vector, which is a product of elementary rotation matrices representing rotations about fixed or rotated axes. In Cartesian coordinate system, these elementary rotations are represented as Euler angles.

If the reference frame is X-Y-Z and the body-fixed frame is x-y-z then the nodal line for Euler angles can be taken as an intersection of like or homologous planes (e.g., X-Y and x-y planes). The Euler angles are then called true or proper Euler angles. For a symmetric rigid body with a fixed point or a point moving with the center of mass and lying on the axis of symmetry, the Z-axis of the inertial coordinate system can be aligned with the axis of precession and then the rotations about the body-fixed axes represent precession, nutation, and spin of that rigid body. Such a frame is used in many engineering applications like gyroscopes, aircraft, and gyro pendulums [124].

In some applications, such as vehicle dynamics, robotics, aerospace vehicles, and computer graphics, it is preferable to use intersection of nonhomologous planes to define the nodal line. The Euler angles in this case are not proper. There are six possibilities to define improper Euler angles. There are different names for such angles: Cardan angles, nautical angles, roll-pitch-yaw (RPY) angles, etc. These angles are together referred to as Tait-Bryan angles. The three angles used in this formulation are defined as the roll angle, pitch angle, and yaw angle.

The angular orientation of the body-fixed coordinate system x-y-z with reference to the inertial coordinate system can be prescribed in different ways through Tait-Bryan angles. We will use Cardan angles in this book. The line of nodes is taken as intersection between X-Y and x-z planes. Let X-Y-Z axes be rotated by an angle ψ about the Z-axis as shown in Fig. 5.31 so that a coordinate system $x_1-y_1-z_1$ results where x_1 -axis is aligned with the line of nodes. Further, rotate the $x_1-y_1-z_1$ axes by

Fig. 5.31 Cardan angles or roll, pitch and yaw (RPY) Tait-Bryan angles



an angle θ about the y_1 axis so that the new rotated coordinate axes are x_2 - y_2 - z_2 and x_2 axis is aligned with x -axis. Finally, rotate x_2 - y_2 - z_2 axes by an angle ϕ about the x_2 axis or x -axis so that y_2 - z_2 axes align with y - z axes. These three rotations, ψ , θ , and ϕ in Z - Y - X convention are called Cardan angles and they, respectively, represent the body yaw, pitch, and roll. For vehicle dynamics applications, the body-fixed z -axis should be vertical to the ground and x -axis should be aligned along the length of the vehicle. For aircraft, space craft, and naval vessels, the x -axis should be aligned along the length and the z -axis should face toward the ground (also called local vertical direction).

Roll, pitch, and yaw angles are extensively used in robotics and rigid body mechanics.

Consider a nonrotating coordinate frame x - y - z whose axes are momentarily aligned with principal axes of the body. The moment of momentum vector about a moving frame x_p - y_p - z_p aligned with principal axes is given as

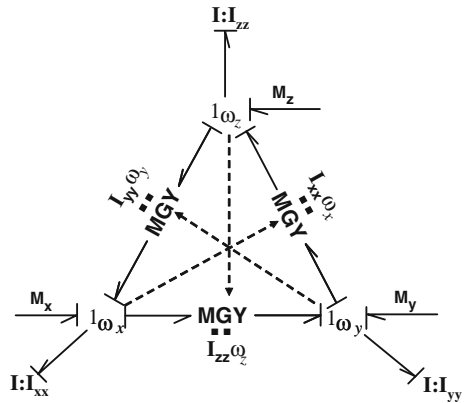
$$\mathbf{H}|_{x_p, y_p, z_p} = \begin{bmatrix} I_{xp} & 0 & 0 \\ 0 & I_{yp} & 0 \\ 0 & 0 & I_{zp} \end{bmatrix} \begin{Bmatrix} \omega_{xp} \\ \omega_{yp} \\ \omega_{zp} \end{Bmatrix} \quad (5.48)$$

where ω_{xp} , ω_{yp} and ω_{zp} are components of the angular velocity vector ω along the principal axes and I_{xp} , I_{yp} and I_{zp} are second moment of inertia about the principal axes.

The time derivative of moment of momentum vector in a given frame of reference gives the torques applied about the axes of that reference. The time derivative of moment of momentum vector in the nonrotating reference frame which is momentarily aligned with the principal axes is given as

$$\left. \frac{d\mathbf{H}}{dt} \right|_{x, y, z} = \left. \frac{d\mathbf{H}}{dt} \right|_{x_p, y_p, z_p} + \omega \times \mathbf{H}|_{x_p, y_p, z_p} \quad (5.49)$$

Fig. 5.32 Euler junction structure (subscript ‘p’ has been dropped from the figure)



This equation in component or scalar form can be written as

$$I_{xp}\dot{\omega}_{xp} - (I_{yp} - I_{zp}) \omega_{yp}\omega_{zp} = M_{xp}, \tag{5.50}$$

$$I_{yp}\dot{\omega}_{yp} - (I_{zp} - I_{xp}) \omega_{zp}\omega_{xp} = M_{yp}, \tag{5.51}$$

$$I_{zp}\dot{\omega}_{zp} - (I_{xp} - I_{yp}) \omega_{xp}\omega_{yp} = M_{zp}, \tag{5.52}$$

where M_{xp} , M_{yp} and M_{zp} are components of resultant moment due to external forces and couples about the nonrotating coordinate frame x-y-z whose axes are momentarily aligned with the principal axes of the body.

Equations 5.50–5.52 are the Euler equations and in combination with Eqs. 5.45–5.47, the whole set of six equations is referred to as Newton-Euler equations. Euler equations can be represented in bond graph form as shown in Fig. 5.32, which is often called a Euler junction structure (EJS).

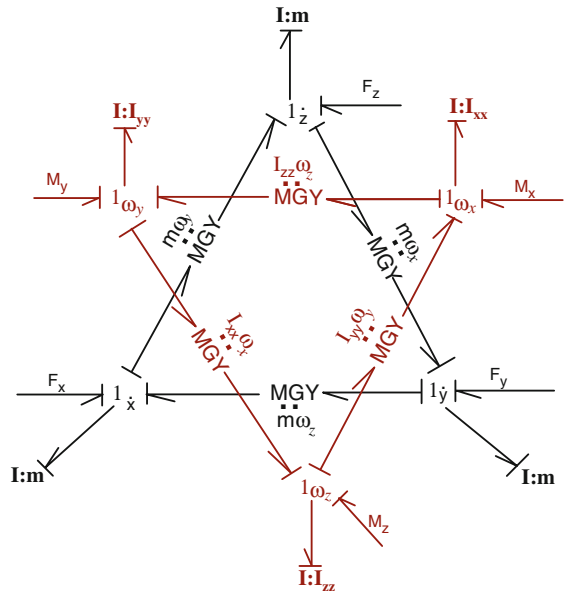
The Newton-Euler equations are represented in bond graph form by combining Figs. 5.30 and 5.32, which results in a star-shaped construct given in Fig. 5.33. Note that all MGY elements in Figs. 5.30 and 5.32 require information of angular velocity components. These modulations are not shown in Fig. 5.33.

5.3.3 Coordinate Transformation

The transformation from the moving frame to the inertial frame can be written using successive multiplication of rotation matrices as follows:

$$\begin{Bmatrix} \dot{X} \\ \dot{Y} \\ \dot{Z} \end{Bmatrix} = \mathbf{T}_{\psi,\theta,\phi} \begin{Bmatrix} \dot{x} \\ \dot{y} \\ \dot{z} \end{Bmatrix} \text{ and } \begin{Bmatrix} \omega_X \\ \omega_Y \\ \omega_Z \end{Bmatrix} = \mathbf{T}_{\psi,\theta,\phi} \begin{Bmatrix} \omega_x \\ \omega_y \\ \omega_z \end{Bmatrix} \tag{5.53}$$

Fig. 5.33 Bond graph model of Newton-Euler equations



where

$$\mathbf{T}_{\psi,\theta,\phi} = \underbrace{\begin{bmatrix} \cos \psi & -\sin \psi & 0 \\ \sin \psi & \cos \psi & 0 \\ 0 & 0 & 1 \end{bmatrix}}_{\mathbf{T}_\psi} \underbrace{\begin{bmatrix} \cos \theta & 0 & \sin \theta \\ 0 & 1 & 0 \\ -\sin \theta & 0 & \cos \theta \end{bmatrix}}_{\mathbf{T}_\theta} \underbrace{\begin{bmatrix} 1 & 0 & 0 \\ 0 & \cos \phi & -\sin \phi \\ 0 & \sin \phi & \cos \phi \end{bmatrix}}_{\mathbf{T}_\phi}, \quad (5.54)$$

and ψ , θ , and ϕ are the Z-Y-X Cardan angles defined in Fig. 5.31. The computation of Cardan angles will be shown later in this section.

This power conserving coordinate transformation (in short, CTF) is represented by the bond graph junction structure shown in Fig. 5.34.

The transformer moduli used in Fig. 5.34 are obtained from Eq. 5.54 as follows: $\mu_1 = \cos \psi \cos \theta$, $\mu_2 = \cos \psi \sin \theta \sin \phi - \sin \psi \cos \phi$, $\mu_3 = \cos \psi \sin \theta \cos \phi + \sin \psi \sin \phi$, $\mu_4 = \sin \psi \cos \theta$, $\mu_5 = \sin \psi \sin \theta \sin \phi + \cos \psi \cos \phi$, $\mu_6 = -\cos \psi \sin \phi + \sin \psi \sin \theta \cos \phi$, $\mu_7 = -\sin \theta$, $\mu_8 = \cos \theta \sin \phi$, $\mu_9 = \cos \theta \cos \phi$.

The CTF block represents this coordinate transfer. The bonds connected to the two-port CTF are vector bonds whose power variables are vectors. The power variables on one side of CTF are $\mathbf{f} = \{\dot{x}, \dot{y}, \dot{z}\}^T$ and $\mathbf{e} = \{F_x, F_y, F_z\}^T$, whereas they are $\mathbf{f} = \{\dot{X}, \dot{Y}, \dot{Z}\}^T$ and $\mathbf{e} = \{F_X, F_Y, F_Z\}^T$ on the other side. The same CTF-element is used to transform angular velocities from rotating to fixed frame where the corresponding power variables are $\mathbf{f} = \{\omega_x, \omega_y, \omega_z\}^T$ and $\mathbf{e} = \{M_x, M_y, M_z\}^T$ on one side and $\mathbf{f} = \{\omega_X, \omega_Y, \omega_Z\}^T$ and $\mathbf{e} = \{M_X, M_Y, M_Z\}^T$ on the other side of CTF.

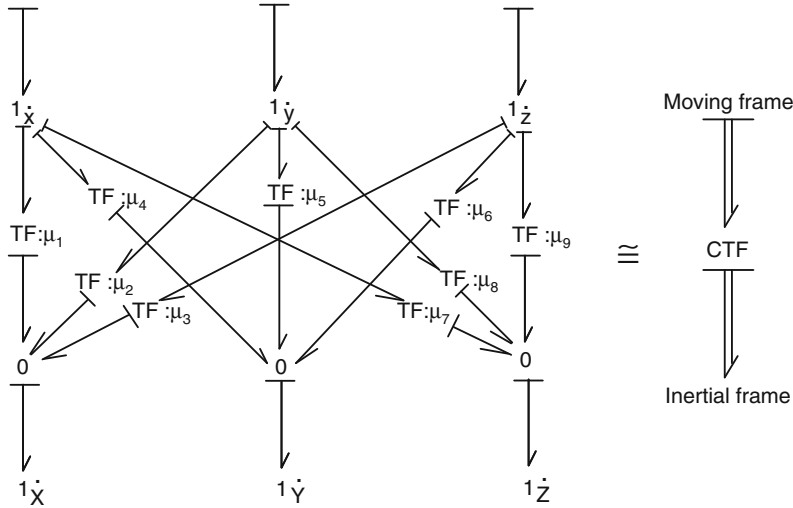


Fig. 5.34 Bond graph model of coordinate transformation from rotating to fixed frame

The transformation from the inertial frame to the moving frame is given as

$$\begin{Bmatrix} \dot{x} \\ \dot{y} \\ \dot{z} \end{Bmatrix} = \mathbf{T}_{\psi,\theta,\phi}^{-1} \begin{Bmatrix} \dot{X} \\ \dot{Y} \\ \dot{Z} \end{Bmatrix} \text{ and } \begin{Bmatrix} \omega_x \\ \omega_y \\ \omega_z \end{Bmatrix} = \mathbf{T}_{\psi,\theta,\phi}^{-1} \begin{Bmatrix} \omega_X \\ \omega_Y \\ \omega_Z \end{Bmatrix} \quad (5.55)$$

where

$$\begin{aligned} \mathbf{T}_{\psi,\theta,\phi}^{-1} &= \mathbf{T}_{\phi}^{-1} \mathbf{T}_{\theta}^{-1} \mathbf{T}_{\psi}^{-1} \\ &= \begin{bmatrix} 1 & 0 & 0 \\ 0 & \cos \phi & \sin \phi \\ 0 & -\sin \phi & \cos \phi \end{bmatrix} \begin{bmatrix} \cos \theta & 0 & -\sin \theta \\ 0 & 1 & 0 \\ \sin \theta & 0 & \cos \theta \end{bmatrix} \begin{bmatrix} \cos \psi & \sin \psi & 0 \\ -\sin \psi & \cos \psi & 0 \\ 0 & 0 & 1 \end{bmatrix}. \end{aligned} \quad (5.56)$$

The above transformation (another form of CTF) for linear velocities is represented in bond graph form as shown in Fig. 5.35. The same transformation works for rotational velocities.

The transformer moduli used in Fig. 5.35 are obtained from Eq. 5.56, as follows: $\lambda_1 = \cos \psi \cos \theta$, $\lambda_2 = \sin \psi \cos \theta$, $\lambda_3 = -\sin \theta$, $\lambda_4 = \cos \psi \sin \theta \sin \phi - \sin \psi \cos \phi$, $\lambda_5 = \sin \psi \sin \theta \sin \phi + \cos \psi \cos \phi$, $\lambda_6 = \cos \theta \sin \phi$, $\lambda_7 = \cos \psi \sin \theta \cos \phi + \sin \psi \sin \phi$, $\lambda_8 = \sin \psi \sin \theta \cos \phi - \cos \psi \sin \phi$, $\lambda_9 = \cos \theta \cos \phi$.

5.3.4 Transformation of Angular Velocities

The angular velocities ω_x , ω_y and ω_z used so far represent angular velocities about body-fixed axes. Except ω_x , which is the angular velocity about the body-fixed x-axis

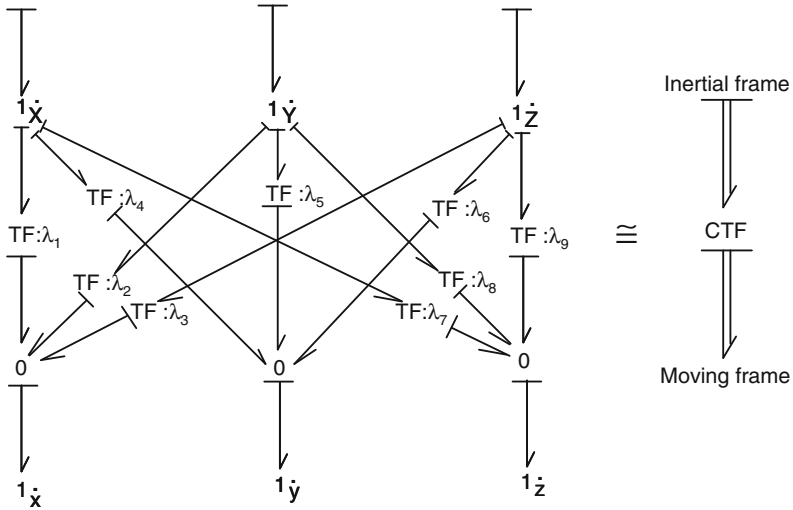


Fig. 5.35 Bond graph model of coordinate transformation from fixed to rotating frame

in Z-Y-X Cardan angle form and represents the rate of change of a Euler angle, the other are not related to Euler angle rates. This is because the rotations are given successively: rotation about z-axis followed by rotation about rotated y-axis and then about further rotated x-axis which means the x-axis does not change in the last step.

To avoid confusion, let us write Euler angle rates as $\dot{\psi}$, $\dot{\theta}$ and $\dot{\phi}$, respectively. The last rotation remains unchanged. The angular velocities in the body-fixed frame are denoted as ω_{xb} , ω_{yb} and ω_{zb} . They are related to the Euler angle rates as follows:

$$\begin{aligned} \begin{Bmatrix} \omega_{xb} \\ \omega_{yb} \\ \omega_{zb} \end{Bmatrix} &= \begin{bmatrix} 1 & 0 & 0 \\ 0 & \cos \phi & \sin \phi \\ 0 & -\sin \phi & \cos \phi \end{bmatrix} \begin{bmatrix} \cos \theta & 0 & -\sin \theta \\ 0 & 1 & 0 \\ \sin \theta & 0 & \cos \theta \end{bmatrix} \begin{Bmatrix} 0 \\ 0 \\ \dot{\psi} \end{Bmatrix} \\ &+ \begin{bmatrix} 1 & 0 & 0 \\ 0 & \cos \phi & \sin \phi \\ 0 & -\sin \phi & \cos \phi \end{bmatrix} \begin{Bmatrix} 0 \\ \dot{\theta} \\ 0 \end{Bmatrix} + \begin{Bmatrix} \dot{\phi} \\ 0 \\ 0 \end{Bmatrix} \end{aligned} \tag{5.57}$$

where the last rotation $\dot{\phi}$ is just an add-on term. As a result,

$$\begin{Bmatrix} \omega_{xb} \\ \omega_{yb} \\ \omega_{zb} \end{Bmatrix} = \begin{bmatrix} 1 & 0 & -\sin \theta \\ 0 & \cos \phi & \cos \theta \sin \phi \\ 0 & -\sin \phi & \cos \theta \cos \phi \end{bmatrix} \begin{Bmatrix} \dot{\phi} \\ \dot{\theta} \\ \dot{\psi} \end{Bmatrix} \tag{5.58}$$

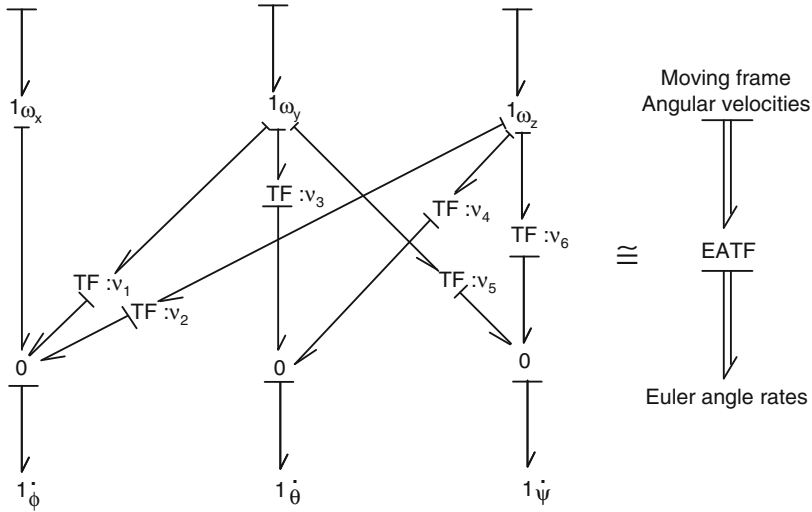


Fig. 5.36 Bond graph model for calculation of Euler angles

The inverse transformation from body-fixed angular velocities to Euler angle rates is given by

$$\begin{aligned}
 \begin{Bmatrix} \dot{\phi} \\ \dot{\theta} \\ \dot{\psi} \end{Bmatrix} &= \begin{bmatrix} 1 & 0 & -\sin \theta \\ 0 & \cos \phi & \cos \theta \sin \phi \\ 0 & -\sin \phi & \cos \theta \cos \phi \end{bmatrix}^{-1} \begin{Bmatrix} \omega_{xb} \\ \omega_{yb} \\ \omega_{zb} \end{Bmatrix} \\
 &= \begin{bmatrix} 1 & \tan \theta \sin \phi & \tan \theta \cos \phi \\ 0 & \cos \phi & -\sin \phi \\ 0 & \sin \phi / \cos \theta & \cos \phi / \cos \theta \end{bmatrix} \begin{Bmatrix} \omega_{xb} \\ \omega_{yb} \\ \omega_{zb} \end{Bmatrix} \quad (5.59)
 \end{aligned}$$

The transformation given in Eq. 5.59 is represented in bond graph form as a transformer junction structure shown in Fig. 5.36.

In serial robots, when the wrist axes used to control yaw, pitch, and roll pass through a common point, a gimbal lock takes place. Such a phenomenon is called a wrist flip in robotics. Gimbal lock is also a problem in inertial navigation and robotics.

Consider the transformation matrix

$$\mathbf{T}_{\psi, \theta, \phi} = \underbrace{\begin{bmatrix} \cos \psi & -\sin \psi & 0 \\ \sin \psi & \cos \psi & 0 \\ 0 & 0 & 1 \end{bmatrix}}_{\mathbf{T}_{\psi}} \underbrace{\begin{bmatrix} \cos \theta & 0 & \sin \theta \\ 0 & 1 & 0 \\ -\sin \theta & 0 & \cos \theta \end{bmatrix}}_{\mathbf{T}_{\theta}} \underbrace{\begin{bmatrix} 1 & 0 & 0 \\ 0 & \cos \phi & -\sin \phi \\ 0 & \sin \phi & \cos \phi \end{bmatrix}}_{\mathbf{T}_{\phi}}, \quad (5.60)$$

where all rotations (ψ , θ , and ϕ) are bounded within interval $[-\pi, \pi]$. Consider a special configuration where $\theta = \pi/2$. Then, the transformation matrix may be written as

$$\begin{aligned} \mathbf{T}_{\psi,\theta,\phi} &= \begin{bmatrix} \cos \psi & -\sin \psi & 0 \\ \sin \psi & \cos \psi & 0 \\ 0 & 0 & 1 \end{bmatrix} \begin{bmatrix} 0 & 0 & 1 \\ 0 & 1 & 0 \\ -1 & 0 & 0 \end{bmatrix} \begin{bmatrix} 1 & 0 & 0 \\ 0 & \cos \phi & -\sin \phi \\ 0 & \sin \phi & \cos \phi \end{bmatrix} \\ &= \begin{bmatrix} 0 & \cos \psi \sin \phi - \sin \psi \cos \phi & \cos \psi \cos \phi + \sin \psi \sin \phi \\ 0 & \cos \psi \cos \phi + \sin \psi \sin \phi & \cos \psi \sin \phi - \sin \psi \cos \phi \\ -1 & 0 & 0 \end{bmatrix} \\ &= \begin{bmatrix} 0 & \sin(\phi - \psi) & \cos(\phi - \psi) \\ 0 & \cos(\phi - \psi) & \sin(\phi - \psi) \\ -1 & 0 & 0 \end{bmatrix}. \end{aligned} \quad (5.61)$$

From the above rotation matrix, one finds that changing values of the rotation angles ϕ and ψ has the same effects: the rotation angle $\phi - \psi$ changes but ϕ and ψ cannot play different roles. However, the rotation's axis remains in the Z direction ($\omega_z = -\omega_x$) because the first column and the last row of the matrix cannot be changed by changing values of ϕ and ψ . This indicates loss of one degree of freedom. Thus, for ϕ and ψ to play different roles, θ must be deviated from $\theta = \pi/2$ position.

Note that gimbal lock takes place for both proper Euler angles and Tait-Bryan angles. Thus, it is a problem to use Euler angles in certain engineering applications especially when the rotations can be large. A quaternion representation does not suffer from gimbal lock problem. Quaternions are a number system that extends the complex numbers. The product of two quaternions is noncommutative. Bond graph models of rigid body mechanics based on quaternions can be consulted in [6, 40].

For a symmetric rigid body with a fixed point or a point moving with the center of mass and lying on the axis of symmetry, the z-axis of the body-fixed coordinate system can be aligned with the axis of spin. The axis of spin, thus, passes through a fixed point (e.g., geometric center of a disk or bearing support). Such a frame is called a gimbal frame which is used in many engineering applications like rotor dynamics and robotics.

5.3.5 Model of a Spinning Top

Let us consider a spinning top shown in Fig. 5.37. The root of the top does not move from its position, i.e., it does not slip away from its position. No aerial or root damping is considered in the model. The root damping (a rotating damping), which gives rise to circulatory forces/moments, is a much higher level topic. It is the basic reason for Tippe-top dynamics. Interested readers may consult [15, 28, 124] for further details on this amazing dynamical problem. Here, we consider a moving frame x,y,z engraved in the body of the top with its origin at the centroid of the top and the z-axis

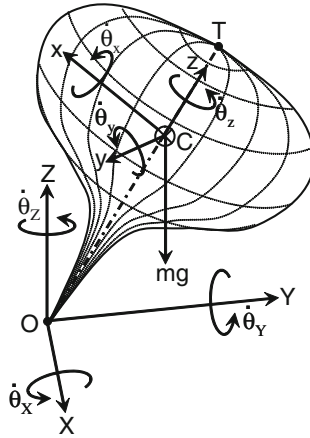


Fig. 5.37 Model of the spinning top using body-fixed frame and Cardan angles

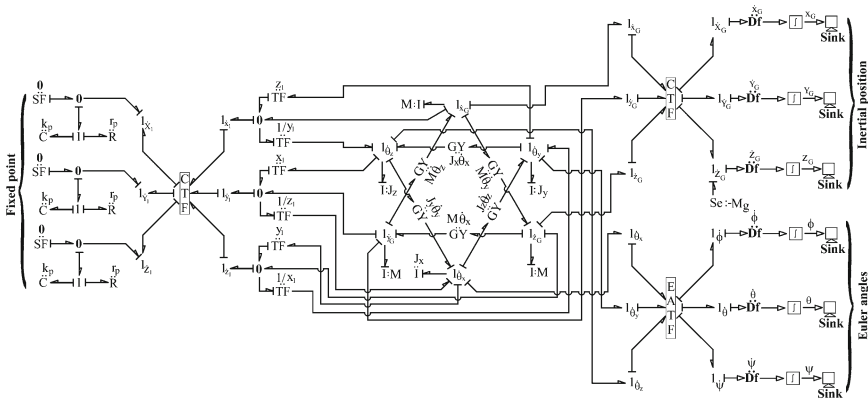


Fig. 5.38 Bond graph model of the spinning top using Cardan angles

aligned along the axis of symmetry. The origin of the inertial axes X, Y, Z coincide with the root of the top. These axes are schematically shown in Fig. 5.37.

The bond graph model of the top is shown in Fig. 5.38.

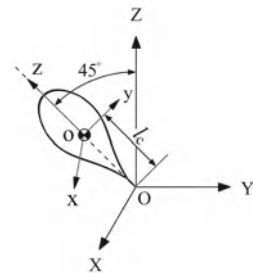
The Newton-Euler equations are represented by the double gyrator rings where the gyrators are modulated by the angular velocities in the body-fixed frame. The position of the fixed point in the body-fixed frame is x_1, y_1, z_1 . If the centroid of the top is at a distance l_C from the fixed point then $x_1 = 0, y_1 = 0$, and $z_1 = -l_C$. The velocity of the root of the top in the body-fixed frame is

$$\begin{aligned}
 \dot{x}_1 &= \dot{x} + z_1 \dot{\theta}_y - y_1 \dot{\theta}_z, \\
 \dot{y}_1 &= \dot{y} + x_1 \dot{\theta}_z - z_1 \dot{\theta}_x, \\
 \dot{z}_1 &= \dot{z} + y_1 \dot{\theta}_x - x_1 \dot{\theta}_y,
 \end{aligned}
 \tag{5.62}$$

Table 5.1 Parameter values used in simulation of the top model

Parameter	Description	Value
M	Mass of the top	0.007 kg
J_x	Moment of inertia about body-fixed x-axis	$2.03 \times 10^{-4} \text{ kg m}^2$
J_y	Moment of inertia about body-fixed y-axis	$2.03 \times 10^{-4} \text{ kg m}^2$
J_z	Moment of inertia about body-fixed z-axis	$2.4 \times 10^{-3} \text{ kg m}^2$
g	Acceleration due to gravity	9.81 m/s^2
k_p	Pad stiffness	10^6 N/m
r_p	Pad damping	10^3 N s/m
x_1	x position of fixed point in body-fixed frame	0 m
y_1	y position of fixed point in body-fixed frame	0 m
z_1	z position of fixed point in body-fixed frame	-0.08 m

Fig. 5.39 Definition of initial position and orientation of the spinning top



The velocity of the root in inertial frame is zero, i.e., it does not move. Thus, first of all, coordinate transformation (by CTF block) is performed to bring body-fixed velocities to inertial frame and then those velocities are constrained to be zero by zero valued flow sources. Three pad elements (with stiffness k_p and damping r_p) are used to implement implicit constraints.

To display the motion of the centroid of the top in inertial frame, another set of coordinate transformations are performed. The CTF blocks use Euler angles which are computed by the EATF (Euler Angle Transformation) block whose detailed model based on Eq. 5.59 is shown in Fig. 5.36.

The top model was simulated with the data given in Table 5.1.

The initial configuration of the top is shown in Fig. 5.39 from where initial conditions for Euler angles are given as $\phi = \pi/4 \text{ rad}$, $\theta = \psi = 0 \text{ rad}$ and the initial conditions for integration blocks to display inertial position of the top centroid are given as $X = 0 \text{ m}$, $Y = -l_C \sin(\pi/4)$, and $Z = l_C \cos(\pi/4)$. The initial spin rate of the top is taken to be 1.04 rad/s which is specified as initial angular momentum of $1.04 \times I_{zz} = 0.0025132 \text{ kg m}^2/\text{s}$ about the body-fixed z-axis.

The simulation result showing the motion of the centroid of the top in the inertial reference frame is plotted in Fig. 5.40 and the projection of that motion in the X-Y plane is also shown.

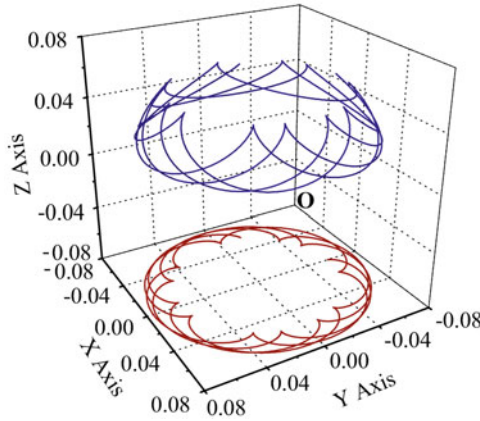


Fig. 5.40 Simulated motion of the top’s centroid and its projection on the horizontal plane

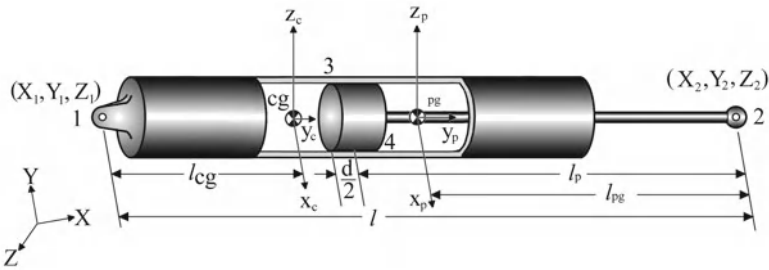


Fig. 5.41 Body-fixed coordinate systems and geometric dimensions used to model the three-dimensional prismatic joint

5.3.6 Model of Three-Dimensional Prismatic Joint

The planar model of prismatic joint model discussed in Sect. 5.2.5 can be easily extended to three-dimensional prismatic joint model. The three-dimensional cylinder–piston is modeled as two rigid bodies, each with six degrees of freedom. The local coordinate frame attached at the center of mass of each body is assumed to be aligned with the inertial principal axes. The rigid body motions are described with respect these body-fixed coordinate systems (see Fig. 5.41) which rotate and translate with the respective rigid bodies.

The Newton-Euler equations for the cylinder with attached body-fixed axes aligned with its principal axes of inertia are as follows:

$$\sum F_x = m_c \ddot{x}_c + m_c (\dot{z}_c \dot{\theta}_{cy} - \dot{y}_c \dot{\theta}_{cz}) \tag{5.63}$$

$$\sum F_y = m_c \ddot{y}_c + m_c (\dot{x}_c \dot{\theta}_{cz} - \dot{z}_c \dot{\theta}_{cx}) \tag{5.64}$$

$$\sum F_z = m_c \ddot{z}_c + m_c (\dot{y}_c \dot{\theta}_{cx} - \dot{x}_c \dot{\theta}_{cy}) \tag{5.65}$$

$$\sum M_x = J_{cx}\ddot{\theta}_{cx} + \dot{\theta}_{cz}\dot{\theta}_{cy}(J_{cz} - J_{cy}) \quad (5.66)$$

$$\sum M_y = J_{cy}\ddot{\theta}_{cy} + \dot{\theta}_{cx}\dot{\theta}_{cz}(J_{cx} - J_{cz}) \quad (5.67)$$

$$\sum M_z = J_{cz}\ddot{\theta}_{cz} + \dot{\theta}_{cy}\dot{\theta}_{cx}(J_{cy} - J_{cx}) \quad (5.68)$$

where F_x , F_y and F_z are external forces acting in body-fixed x, y, and z directions, respectively, M_x , M_y and M_z are external moments acting in body-fixed x, y, and z directions, respectively, M_c is the mass of the cylinder, J_{cx} , J_{cy} and J_{cz} are the moment of inertias about principal axes, \dot{x}_c , \dot{y}_c and \dot{z}_c are velocities of the mass center in the body-fixed frame, \ddot{x}_c , \ddot{y}_c and \ddot{z}_c are accelerations of the mass center in the body-fixed frame, $\dot{\theta}_{cx}$, $\dot{\theta}_{cy}$ and $\dot{\theta}_{cz}$ are angular velocities of the mass center in the body-fixed frame, and $\ddot{\theta}_{cx}$, $\ddot{\theta}_{cy}$ and $\ddot{\theta}_{cz}$ are angular accelerations of the mass center in the body-fixed frame.

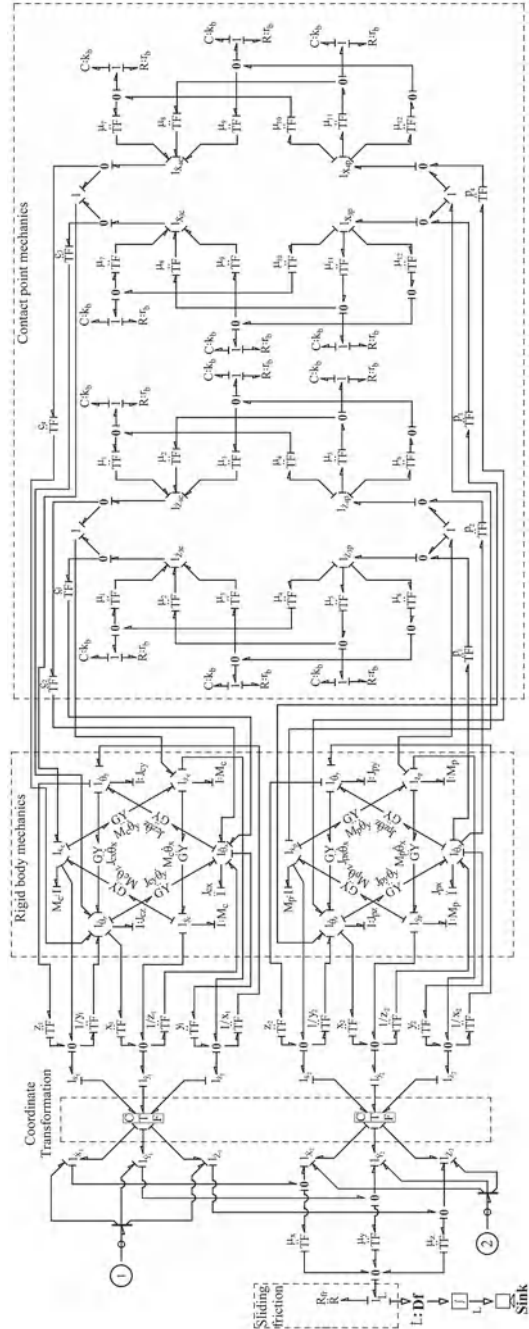
The backbone of the bond graph model of the slider shown in Fig. 5.42 is constructed from Eqs. 5.63–5.68. The linear and rotary inertias are coupled by a pair of gyrator rings (Euler junction structure) [59, 65, 91] one for translational and the other for rotational velocities, according to Eqs. 5.63–5.68. Each pair of gyrator rings introduces six degrees of freedom. Likewise, six more degrees of freedom are considered for the piston and the piston rod. They are represented by another pair of gyrator rings and the variables used in that part of the model are represented by similar nomenclature where subscript ‘p’ is used in place of ‘c’ to indicate that they are associated with the piston.

The rate of change of length (l) between the cylinder and piston ends is expressed as

$$\dot{l} = \left(\frac{X_1 - X_2}{l} \right) (\dot{X}_1 - \dot{X}_2) + \left(\frac{Y_1 - Y_2}{l} \right) (\dot{Y}_1 - \dot{Y}_2) + \left(\frac{Z_1 - Z_2}{l} \right) (\dot{Z}_1 - \dot{Z}_2) \quad (5.69)$$

where (X_1, Y_1, Z_1) , and (X_2, Y_2, Z_2) represent the coordinates of the cylinder and piston end points, respectively, in the inertial frame. The position of the cylinder end point with respect to the body-fixed frame at the mass center is given as (x_1, y_1, z_1) and that for the piston end point with respect to its body-fixed frame is given as (x_2, y_2, z_2) . The velocities of these points are represented in the bond graph model at 1-junctions with appropriate suffixes. The linear and angular velocities of the mass centers of the cylinder and piston are used to compute velocities of the end points in respective body-fixed frames and then they are transformed to inertial velocities to implement constraints in the inertial frame, i.e., Eq. 5.69 and external forces (joint forces) acting at the end points of the cylinder and the piston. The end point joint forces are inputs to the model given at ports (1) and (2) shown within circles. The coordinate transformation (CTF) block [40, 59] is required to transform body-fixed velocities to the inertial velocities of the cylinder and the piston. Note that CTF-block requires Euler angles for use as internal transformer moduli [59]. The calculation of Euler angles is not explicitly shown in the bond graph model.

Fig. 5.42 Bond graph model of three-dimensional prismatic joint



MTF-elements with moduli μ_x , μ_y and μ_z are used to calculate the relative sliding velocity between the piston and the cylinder at a 0-junction and the friction between the piston and the cylinder is modeled by an R-element (R: R_{fr}) at that junction. We consider constraints allowing local deformations so as to compute normal reactions at contact points and thus to dynamically compute the frictional forces. A set of transformers with moduli c_1 to c_4 and p_1 to p_4 are determined from kinematic analysis to compute the velocities of the contact points on the cylinder and the piston in respective body-fixed frames. These body-fixed velocities are transformed into inertial velocities (through a set of transformers with moduli μ_1 to μ_{12} , similar to expanded form of CTF-block) and are then implicitly constrained. The relative normal velocity between the contact point on the cylinder and the normal velocity at the contact point on the piston are implicitly constrained by contact stiffness and damping parameters, k_b and r_b , respectively. In comparison to other stiffness at the contact point, the bending stiffness of the piston rod is lowest and hence k_b and r_b are approximated to represent the bending stiffness and damping of the piston rod.

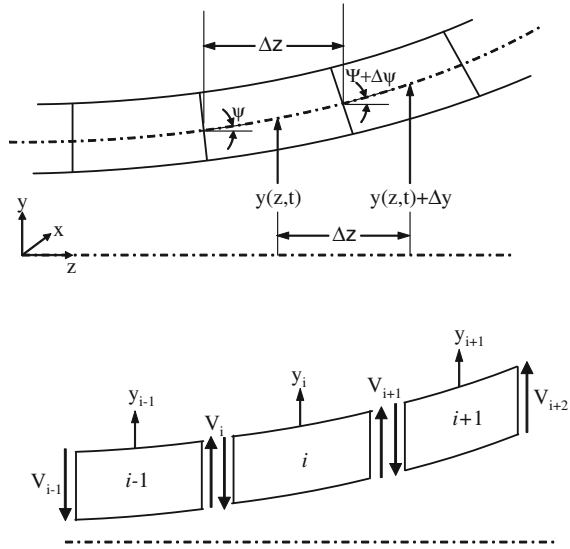
The model of the three-dimensional prismatic joint can be interfaced with other energy domains in exactly the same way as the planar prismatic joint model. One example where three-dimensional prismatic joints are used is a Stewart platform discussed in Chap. 13 of this book.

5.4 Flexible Body Systems

The rigid body assumption in modeling systems may fail when the internal forces within any massive member of the system cause significant deformations. For example, a slender beam, thin plate or membrane, beam column, flexible robotic manipulator, and rotor shaft usually shows appreciable amount of deformation upon application of external load. The steady-state configuration of such a member may be represented by a model with equivalent mass and stiffness. However, the transient motions within the body cannot be modeled in this way. A governing equation of a flexible body in which the mass cannot be neglected is given by partial differential equations. Such systems are called distributed parameter systems.

Modeling of distributed parameter systems in bond graph domain involves some approximations. One way is to consider small blocks within the flexible body where inertia effects are lumped and then the stiffness effect is added between these lumped inertias. This way of modeling through spatial discretization of the flexible system is called a finite element modeling. Another approach is to directly write the partial differential equation of the system in the form of a difference equation and then use the finite difference scheme to model the system. Besides spatial discretization, one may follow the so-called modal separation. In this approach, the mode shapes of the flexible system satisfying the governing equation and boundary conditions are predetermined and a finite number of modes are then modeled [12, 91, 117]. Each modal oscillation is represented by modal mass, stiffness, and damping parameters.

Fig. 5.43 Coordinate system used in Euler-Bernoulli beam model



5.4.1 Beams

In this book, we will only consider the spatial discretization scheme for slender beams. There are various levels of abstractions when beams are modeled. The Euler-Bernoulli beam model is the simplest form. It does not consider rotary inertia of the beam and its shear deformation. However, this approximation gives nearly accurate results for slender beams, i.e., when the depth of the beam is much smaller than its length. The Rayleigh beam formulation, which accounts for the rotary inertia of the beam, is an improvement over Euler-Bernoulli formulation. Rayleigh beam formulation gives better approximation of the natural frequencies of a slender beam than the Euler-Bernoulli formulation and it requires less number of discrete elements to create a model. The shear deformation effect becomes prominent when the beam thickness is large and the model of such system is constructed by accounting for the additional deformation of each element due to the shear force. Such a formulation leads to the Timoshenko beam model.

5.4.2 Euler-Bernoulli Beam Model

Consider a part of a beam shown in Fig. 5.43 where the neutral axis of the undeflected beam aligns with the horizontal z-axis. It is assumed that the neutral axis is the same as the beam geometric axis and the beam is subjected to pure bending (no axial or torsional loads). The deflection of the neutral axis is shown along the y-axis and the rotation of the neutral axis about the x-axis is denoted as ψ . The whole beam is then divided into a finite number of parts. Let each part have equal length Δz . Each of

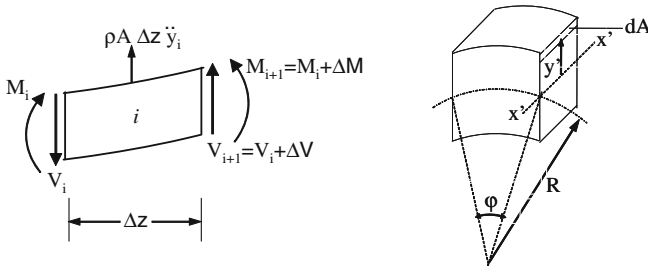


Fig. 5.44 Forces and moments acting on a small beam segment

these parts is called an element and a node lies between two adjacent elements. The elements and nodes are enumerated by following some consistent nomenclature and this enumeration is used as subscript to define various variables of interest such as the deflection y , rotation ψ , shear force V , bending moment M , and so on.

Consider a small segment of a slender vibrating beam shown in Fig. 5.44. The shear forces and bending moments on the two faces of the beam element are shown in the figure. With usual assumptions for Euler-Bernoulli beam formulation, i.e., slender beam, plane section remains plane, the slope of deflection curve is small, and so on, the radius of curvature R of the beam element is found from

$$\frac{1}{R} = \frac{\frac{\partial^2 y}{\partial z^2}}{\left(1 + \left(\frac{\partial y}{\partial z}\right)^2\right)^{3/2}} \simeq \frac{\partial^2 y}{\partial z^2}. \tag{5.70}$$

The strain in z direction at any fiber or elemental area dA at a distance y' from the neutral axis is given as

$$\varepsilon_z(y') = \frac{R\varphi - (R + y')\varphi}{R\varphi} = -\frac{y'}{R}. \tag{5.71}$$

In an elastodynamical problem, the total bending stress is given as

$$\sigma_z(y') = \sigma_{ze}(y') + \sigma_{zd}(y') \tag{5.72}$$

where σ_{ze} is the axial bending stress developed due to elastic deformations and σ_{zd} is the same due to rate of change of elastic deformations or internal damping: $\sigma_{ze} = E\varepsilon_z$ and $\sigma_{zd} = \mu_i \dot{\varepsilon}_z$ (internal/material damping induced stress is proportional to the strain rate), where E is the Young's modulus of the material and μ_i is another material property. It may be noted that μ_i is also proportional to E and is usually written as $\mu_i = \lambda_i E$ with λ_i being the proportionality constant.

The total bending moment about x-axis can be expressed as $M_x = M_{xe} + M_{xd}$ where M_{xe} and M_{xd} are the contributions from the elastic and dissipative stresses,

respectively. These components may be written as

$$\begin{aligned} M_{xe} &= - \int_A \sigma_{ze} y' dA = - \int_A E \left(\frac{\partial^2 y}{\partial z^2} \right) y'^2 dA \\ &= -E \left(\frac{\partial^2 y}{\partial z^2} \right) \int_A y'^2 dA = -EI \left(\frac{\partial^2 y}{\partial z^2} \right), \end{aligned} \quad (5.73)$$

$$\begin{aligned} M_{xd} &= - \int_A \sigma_{zd} y' dA = - \int_A \mu_i \frac{\partial}{\partial t} \left(\frac{\partial^2 y}{\partial z^2} \right) y'^2 dA \\ &= -\mu_i \frac{\partial}{\partial t} \left(\frac{\partial^2 y}{\partial z^2} \right) \int_A y'^2 dA = -\mu_i I \frac{\partial}{\partial t} \left(\frac{\partial^2 y}{\partial z^2} \right) \end{aligned} \quad (5.74)$$

where I is the second moment of area of the shaft cross-section about axis $x'-x'$ shown in the figure.

From the equilibrium consideration of the element shown in the left of Fig. 5.44, we find

$$V_{i+1} - V_i + \rho A \Delta z \ddot{y}_i = 0, \quad (5.75)$$

$$M_{i+1} + V_{i+1} \Delta z + \rho A \Delta z \ddot{y}_i \Delta z / 2 - M_i = 0, \quad (5.76)$$

where ρ is the density of the beam material, A is the cross-sectional area, and $\rho A \Delta z \ddot{y}_i$ is the inertial force. Neglecting second-order terms, i.e., $\Delta z^2 \simeq 0$, we obtain

$$\rho A \Delta z \ddot{y}_i = -\Delta V \text{ and } V = -\Delta M / \Delta z. \quad (5.77)$$

The governing equations for the model are then given as

$$\psi = \frac{\Delta y}{\Delta z}, \quad (5.78)$$

$$M = -EI \left(\frac{\partial^2 y}{\partial z^2} \right) - \mu_i I \frac{\partial}{\partial t} \left(\frac{\partial^2 y}{\partial z^2} \right) \simeq -EI \frac{\Delta \psi}{\Delta z} - \mu_i I \frac{\Delta \dot{\psi}}{\Delta z}, \quad (5.79)$$

$$V = -\frac{\Delta M}{\Delta z}, \quad (5.80)$$

$$\rho A \ddot{y} = -\frac{\Delta V}{\Delta z}. \quad (5.81)$$

The complete governing equation in partial differential equation form is

$$\rho A \ddot{y}(z, t) + EI \frac{\partial^4 y}{\partial z^4}(z, t) + \mu_i I \frac{\partial^4 \dot{y}}{\partial z^4}(z, t) = \frac{\partial}{\partial z} F(z, t) \quad (5.82)$$

where $F(z, t)$ is the distribution of the external forces.

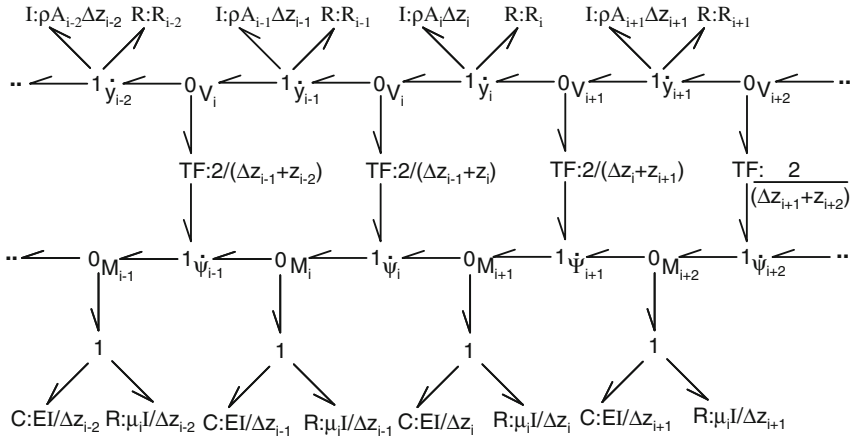


Fig. 5.45 Bond graph model of Euler-Bernoulli beam

The bond graph model of the beam may now be developed from Eqs. (5.78) to (5.81) as shown in Fig. 5.45.

Let us now concentrate on a specific segment of the model. In Fig. 5.45, $0V_i$ junction models the equation $\Delta \dot{y} = \dot{y}_i - \dot{y}_{i-1}$ and the TF-element then transforms $\Delta \dot{y}$ to $\Delta \dot{\psi}$ as follows: $\Delta \dot{\psi} = \Delta \dot{y} \times 2/(\Delta z_{i-1} + \Delta z_i)$. If each finite element has the same length Δz then the transformer modulus becomes $1/\Delta z$, i.e., $\Delta \dot{\psi} = \Delta \dot{y}/\Delta z$. Junction $0M_i$ models the equation $\Delta \dot{\psi} = \dot{\psi}_i - \dot{\psi}_{i-1}$, which is the flow variable used to model the total bending moment $M_x = M_{xe} + M_{xd} = K \int \Delta \dot{\psi} dt + R \Delta \dot{\psi}$. Comparing with Eq. 5.79, the bending stiffness and damping modeled at the 1-junction by C- and R-elements are found to be $K = EI/\Delta z$ and $R = \mu_i I/\Delta z$, respectively. If elements have unequal length then the local length has to be used. Likewise, for a beam of variable cross-section or material property, local values of I , E and μ_i should be used in the model.

Junction $1\dot{\psi}_i$ models the equation $\Delta M = M_{i+1} - M_i$, which produces the shear force by the transformation (modeled by the TF-element) as follows: $V = \Delta M \times 2/(\Delta z_{i-1} + \Delta z_i)$, which reduces to $V = \Delta M/\Delta z$ for elements of equal length. Finally, $1\dot{y}_i$ junction models the equation $\Delta V = V_{i+1} - V_i$ which acts on the mass of the beam segment $\rho A_i \Delta z_i$. Additionally, external damping offered by the medium in which the beam vibrates is modeled by the $R:R_i$ element. If external damping is uniformly distributed then its value may be expressed as $\xi \Delta z_i$ where ξ is the external damping per unit length of the beam.

It is evident from Fig. 5.45 that the bond graph model has a repeated structure. This bond graph model is not causalled at this time. First of all, one must apply the boundary conditions on this model which give fixed causalities to some ports and then the rest of the model can be causalled. As an example, let us consider a beam of length l with fixed-fixed boundary condition as shown in Fig. 5.46. Mathematically,

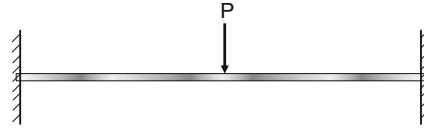


Fig. 5.46 A beam with both ends fixed and a concentrated load

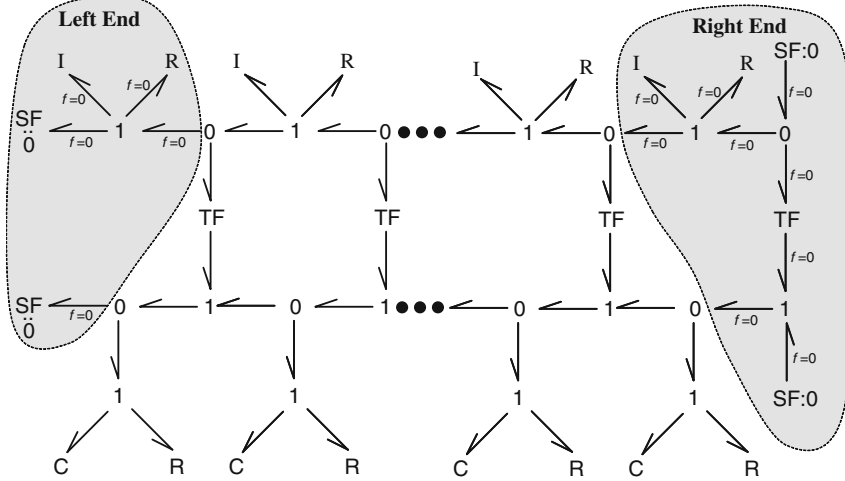


Fig. 5.47 Bond graph model of a beam with both ends fixed

the boundary conditions are

$$\begin{aligned}
 y(z, t)|_{z=0} = 0 \text{ and } \left. \frac{\partial y(z, t)}{\partial z} \right|_{z=0} = 0, \\
 y(z, t)|_{z=l} = 0 \text{ and } \left. \frac{\partial y(z, t)}{\partial z} \right|_{z=l} = 0,
 \end{aligned}
 \tag{5.83}$$

where $z = 0$ and $z = l$ indicate the two ends of the beam.

In bond graph terms, this signifies that the linear velocities and angular velocities are zero at the boundaries. These can be imposed on the bond graph model by zero flow sources appended to ends of the model as shown in Fig. 5.47. Not that imposition of boundary conditions at 0-junctions and 1-junctions (see the left and right sides of the model in Fig. 5.47) have almost the same effect on the dynamics of the system as long as the number of elements in the model is large.

Note that if the flow in any passive bond at a 1-junction is zero then the flows in the rest of the bonds is zero and if the flows in all but one of the bonds of a 0-junction are zero then the flow in the remaining bond is zero. With this consideration, when these boundary conditions are imposed on the model, the flows in some of the bonds of the bond graph model become zero and consequently they carry no power. Therefore,

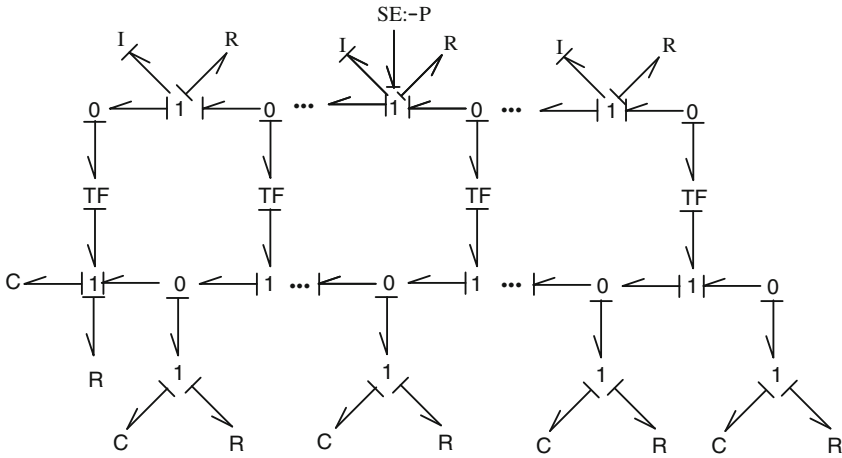


Fig. 5.48 Bond graph model of a beam with both ends fixed

Fig. 5.49 A cantilever beam with a part-span support



those bonds can be removed from the model. The reduced bond graph model of the system with causality assignment and application of the central concentrated load is then given in Fig. 5.48.

As another example, an overhang beam shown in Fig. 5.49 is considered. In this problem, the boundary conditions are

$$\begin{aligned}
 y(z, t)|_{z=0} &= 0 \text{ and } \left. \frac{\partial y(z, t)}{\partial z} \right|_{z=0} = 0, \\
 y(z, t)|_{z=a} &= 0, \\
 V(z, t)|_{z=l} &= 0 \text{ and } M(z, t)|_{z=l} = 0,
 \end{aligned}
 \tag{5.84}$$

where $z = 0$ and $z = l$ indicate the two ends of the beam, and $z = a$ defines the position of the roller support. These boundary conditions are imposed on the beam model as shown in Fig. 5.50.

Note that if the effort in any passive bond at a 0-junction is zero then the efforts in the rest of the bonds is zero and if the efforts in all but one of the bonds of a 1-junction are zero then the effort in the remaining bond is zero. Removal of the bonds carrying no power (i.e., either effort or flow in those bonds is zero), produces the reduced causalised bond graph model shown in Fig. 5.51.

The above two examples show how any general boundary condition can be applied to the Euler-Bernoulli beam model. If a subsystem is attached to the beam at a given

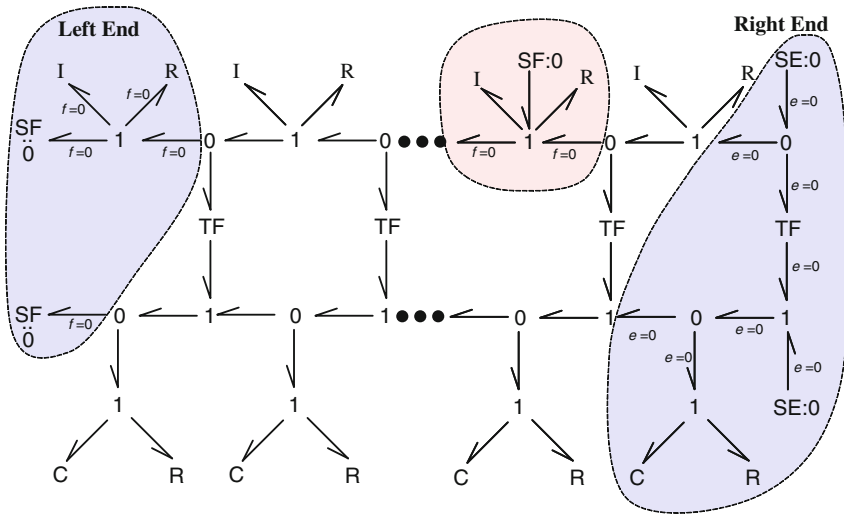


Fig. 5.50 Bond graph model of a cantilever beam with a part-span support

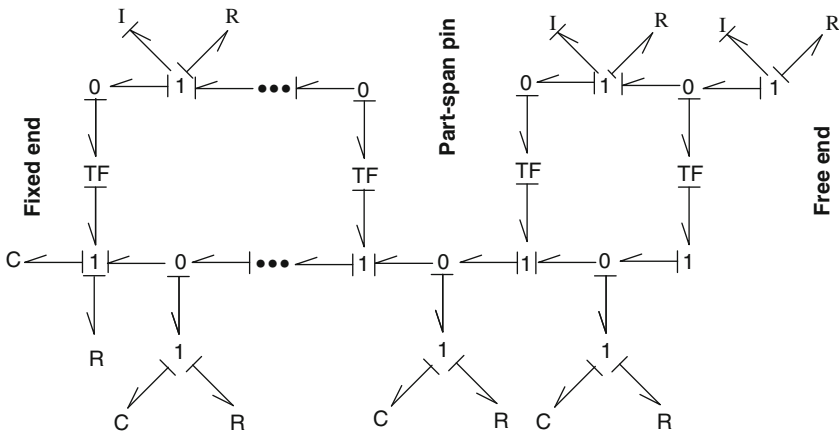


Fig. 5.51 Reduced bond graph model of a cantilever beam with a part-span support

point then it may be modeled at a specific 1-junction. Such an example is shown in Fig. 5.52 and its bond graph model is shown in Fig. 5.53.

5.4.3 Beam Columns

Design of beam columns is primarily governed by the buckling limit or buckling load, which is the single most important criterion in earthquake resistant structures. If a



Fig. 5.52 A cantilever beam with an appended system

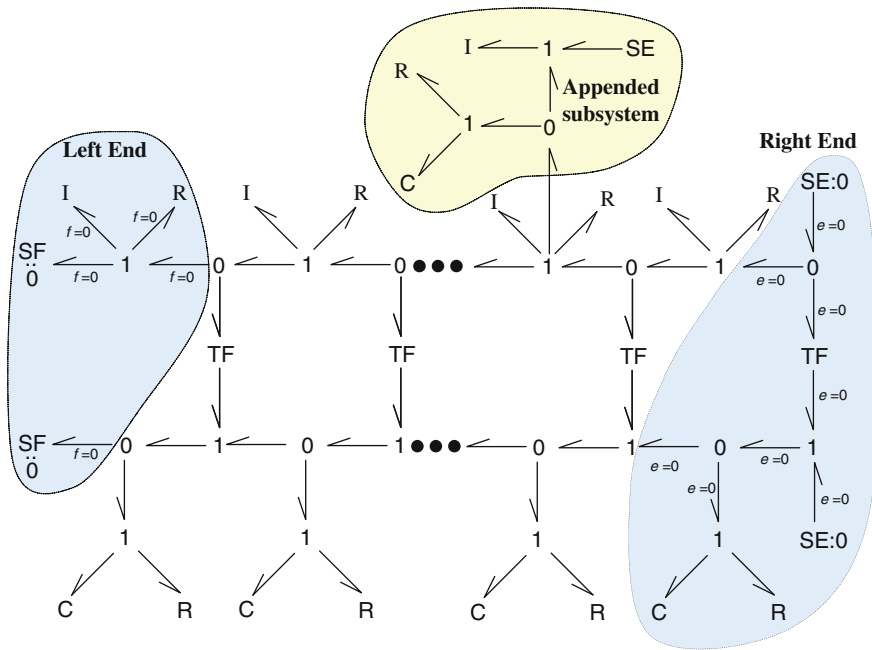


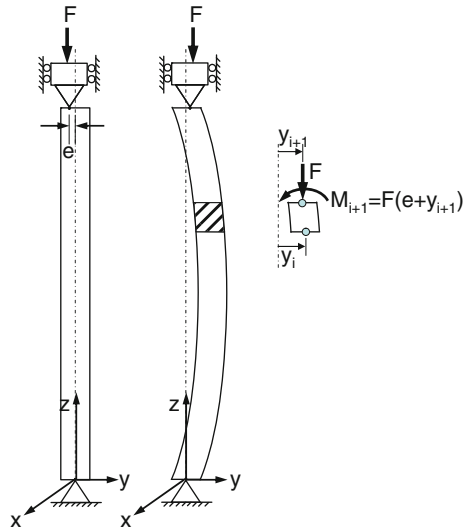
Fig. 5.53 Bond graph model of a cantilever beam with an appended system

column deflects laterally then the heavy load on it causes it to deflect more and then it may buckle under certain conditions. In this section, we will discuss the dynamics of a beam subjected to an axial compressive load (see Fig. 5.54).

Let us discretize the beam column into several segments. The i th segment from the bottom experiences additional bending moments due to the compressive axial load. The bending moment about x-axis is $M_{(i+1)x} = F(e + y_{i+1})$ and about y-axis is $M_{(i+1)y} = F(x_{i+1})$. The transverse vibrations in x- and y-directions of the beam column are independent. The applied bending moment changes from segment to segment. At the topmost position, say n th node, the lateral displacement is zero and the bending moment about x-axis and y-axis are $M_{nx} = Fe$ and $M_{ny} = 0$, respectively.

The beam column may now be modeled as shown in Fig. 5.55.

Fig. 5.54 A beam column with an offset compressive load



In Fig. 5.55, the applied axial force is modeled separately and its contributions to moments at different sections is introduced through transformers. Let us consider the bending moments about x-axis. Note that when $M_n = Fe$ is applied to the final node, the moment at the preceding node is $M_{n-1} = F(e + y_{n-1})$. The moment applied at n th node is already transferred to the preceding node by internal deformations. Thus, the incremental moment to be applied is $\Delta M_{n-1} = F(y_{n-1} - y_n) = F\Delta y_{n-1}$. The bond graph model, thus, incorporates the incremental moments and not the absolute moments. These incremental moments are given as $\Delta M_{ix} = F(y_i - y_{i+1}) = F\Delta y_i$. Likewise, incremental moments about y-axis are computed.

At the ground node (bottom node), the boundary conditions are given as zero displacement and zero rotation. The net shear force and bending moment acting at that node are generated as reactions to applied loads. The bending moment components at the root due to axial load only, i.e., excluding the contributions from inertial and other dynamical factors or when the beam assumes a steady deflection shape, are

$$\begin{aligned} \sum_{i=1}^n \Delta M_{ix} &= Fe + F((y_1 - y_2) + (y_2 - y_3) + \dots + (y_{n-1} - y_n)) \\ &= Fe + F(y_1 - y_n) = Fe, \end{aligned} \tag{5.85}$$

$$\begin{aligned} \sum_{i=1}^n \Delta M_{iy} &= F((x_1 - x_2) + (x_2 - x_3) + \dots + (x_{n-1} - x_n)) \\ &= F(x_1 - x_n) = 0. \end{aligned} \tag{5.86}$$

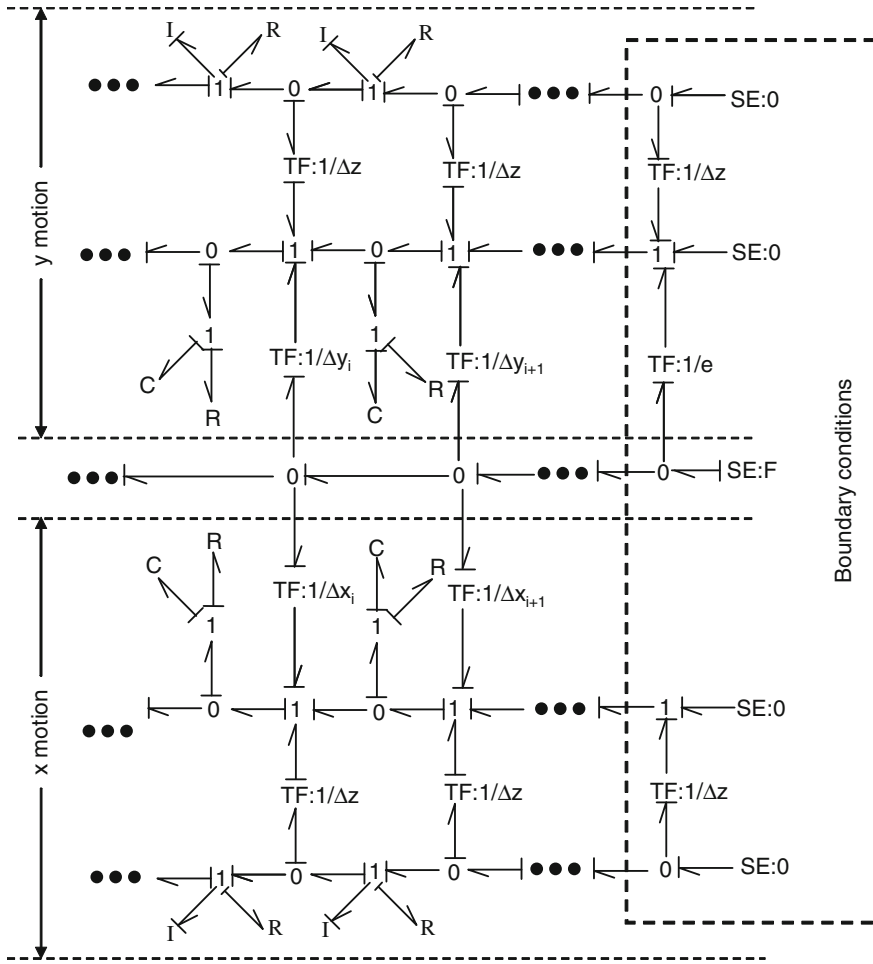


Fig. 5.55 Bond graph model of a beam column

5.4.4 Rayleigh Beam Model

The Rayleigh beam formulation is based on shear force and bending moment representations given in Newtonian convention. In Eulerian convention used to model the Euler-Bernoulli beam (see Fig. 5.44), the positive shear force and bending moments are in opposite directions at the two faces of the beam element. In Newtonian convention, a common reference is taken for both faces of the beam element: upward shear force is positive force and anticlockwise moment is positive moment (see Fig. 5.56). The rotation of the beam segment is explicitly modeled in Rayleigh beam formulation. The beam segment is assumed to store potential energy due to four distinct displacements: displacements of either end and rotations of either end.

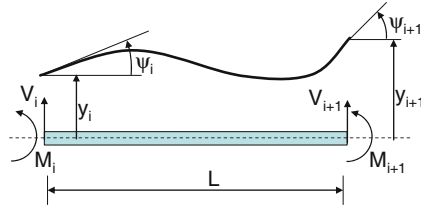


Fig. 5.56 Newtonian sign convention for Rayleigh beam model

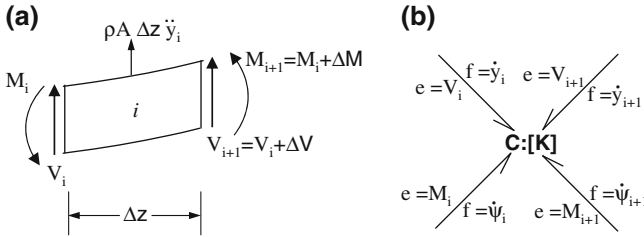


Fig. 5.57 **a** Forces and moments acting on a beam segment and **b** bond graph representation of element stiffness

In a bond graph formulation, the potential energy storage is represented as a four-port C-field (see Fig. 5.57). The i th beam element is influenced by displacements y_i and y_{i+1} , and rotations ψ_i and ψ_{i+1} . The flow variables in four ports of the C-field are the corresponding linear and rotational velocities. The effort variables are the shear forces and bending moments. They are related as follows:

$$\begin{Bmatrix} V_i \\ M_i \\ V_{i+1} \\ M_{i+1} \end{Bmatrix} = \begin{bmatrix} k_{11} & k_{12} & k_{13} & k_{14} \\ k_{21} & k_{22} & k_{23} & k_{24} \\ k_{31} & k_{32} & k_{33} & k_{34} \\ k_{41} & k_{42} & k_{43} & k_{44} \end{bmatrix} \begin{Bmatrix} y_i \\ \psi_i \\ y_{i+1} \\ \psi_{i+1} \end{Bmatrix}, \tag{5.87}$$

or $\mathbf{e} = \mathbf{K}_{4 \times 4} \mathbf{f}$, where $\mathbf{e} = [V_i \ M_i \ V_{i+1} \ M_{i+1}]^T$ and $\mathbf{f} = [y_i \ \psi_i \ y_{i+1} \ \psi_{i+1}]^T$ are the vectors of effort and flow variables, respectively.

The elements of the stiffness matrix \mathbf{K} may be derived in different ways. One of them is shown here. Let $y_i = 1$ and $y_{i+1} = 0$, $\psi_i = \psi_{i+1} = 0$. Then, we obtain $V_i = k_{11}$, $M_i = k_{21}$, $V_{i+1} = k_{31}$, $M_{i+1} = k_{34}$. Likewise, if another element of \mathbf{f} is unity and others are zero, we obtain the expressions for elements in another column of the stiffness matrix. In fact, the stiffness matrix is symmetric and one needs to evaluate only half of the elements of this matrix.

To determine the elements in the third column of \mathbf{K} , let us consider a beam with one end fixed and the other end moving in a slot (see Fig. 5.58a). The deflection at

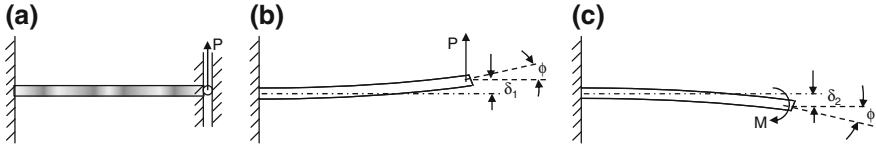


Fig. 5.58 One of the boundary conditions for evaluation of elements of beam stiffness matrix with equivalent superpositions

the slotted end can be found from superposition. A cantilever beam with a tip load P (see Fig. 5.58b) produces deflection and rotation, respectively, as follows:

$$\delta_P = PL^3 / (3EI) \text{ and } \phi_P = PL^2 / (2EI)$$

where $L = \Delta z$ is the length of the element. The superposition of an end moment is required to produce exactly the opposite amount of end rotation such that the superposed system's boundary condition is equivalent to that of a slot. The cantilever beam with a tip moment $-M$ (see Fig. 5.58c) produces deflection and rotation as follows:

$$\delta_M = -ML^2 / (2EI) \text{ and } \phi_M = -ML / (EI).$$

Setting $\phi_P + \phi_M = 0$, we find the required bending moment as $M = PL/2$. The net deflection at the slot end is then

$$\delta_P + \delta_M = PL^3 / (3EI) - PL^3 / (4EI) = PL^3 / (12EI).$$

Thus, if the tip deflection $y_{i+1} = PL^3 / (12EI)$, and $y_i = 0$, $\psi_i = \psi_{i+1} = 0$, then the shear forces and bending moments in Newtonian convention are $V_i = -P$, $M_i = -(PL - M) = -PL/2$, $V_{i+1} = P$, and $M_{i+1} = -PL/2$. The elements in the third column of the stiffness matrix are then found to be

$$\begin{aligned} k_{13} &= V_i / y_{i+1} = -12EI / L^3, \\ k_{23} &= M_i / y_{i+1} = -6EI / L^2, \\ k_{33} &= V_{i+1} / y_{i+1} = 12EI / L^3, \\ k_{43} &= M_{i+1} / y_{i+1} = -6EI / L^2. \end{aligned} \tag{5.88}$$

To evaluate the elements of the fourth column, we assume $y_i = y_{i+1} = 0$, $\psi_{i+1} = 1$, and $\psi_i = 0$. This condition is met if a tip load $-P$ and moment M are so applied that $\delta_P + \delta_M = 0$. The relation between P and M is then given as $M = 2PL/3$. The rotation of the right end of the beam is then

$$\begin{aligned} \phi_P + \phi_M &= -PL^2 / (2EI) + ML / (EI) = -3ML / (4EI) + ML / (EI) \\ &= ML / (4EI). \end{aligned}$$

Thus, if the tip rotation $\psi_{i+1} = ML/(4EI)$, and $y_i = y_{i+1} = 0$, $\psi_i = 0$, then the shear forces and bending moments are $V_i = P = 3M/(2L)$, $M_i = PL - M = M/2$, $V_{i+1} = -P = -3M/(2L)$, and $M_{i+1} = M$. The elements in the fourth column of the stiffness matrix are then found to be

$$\begin{aligned} k_{14} &= V_i/\psi_{i+1} = 6EI/L^2, \\ k_{24} &= M_i/\psi_{i+1} = 2EI/L, \\ k_{34} &= V_{i+1}/\psi_{i+1} = -6EI/L^2, \\ k_{44} &= M_{i+1}/\psi_{i+1} = 4EI/L. \end{aligned} \quad (5.89)$$

The first and second columns of the stiffness matrix can be derived similarly. Then, the final form of the stiffness matrix is given as

$$\mathbf{K} = \frac{EI}{L^3} \begin{bmatrix} 12 & 6L & -12 & 6L \\ 6L & 4L^2 & -6L & 2L^2 \\ -12 & -6L & 12 & -6L \\ 6L & 2L^2 & -6L & 4L^2 \end{bmatrix} \quad (5.90)$$

so that

$$\begin{Bmatrix} V_i \\ M_i \\ V_{i+1} \\ M_{i+1} \end{Bmatrix} = \frac{EI}{L^3} \begin{bmatrix} 12 & 6L & -12 & 6L \\ 6L & 4L^2 & -6L & 2L^2 \\ -12 & -6L & 12 & -6L \\ 6L & 2L^2 & -6L & 4L^2 \end{bmatrix} \begin{Bmatrix} y_i \\ \psi_i \\ y_{i+1} \\ \psi_{i+1} \end{Bmatrix}. \quad (5.91)$$

Note that the stiffness matrix is symmetric. This stiffness matrix can also be derived directly by taking partial derivatives of the strain energy with respect to the individual nodal displacements.

All material offer some kind of internal damping. You may notice that if a beam is bent both ways in quick succession then it heats up. This heating comes from material damping. The stiffness accounts for the elastic force proportional to the strain induced along the axial direction whereas the damping accounts for the restoring force proportional to the strain rate. Thus, the total shear force and bending moment due to flexure (in dynamic state) are given as

$$\begin{aligned} \begin{Bmatrix} V_i \\ M_i \\ V_{i+1} \\ M_{i+1} \end{Bmatrix} &= \mathbf{K}_{4 \times 4} \begin{Bmatrix} y_i \\ \psi_i \\ y_{i+1} \\ \psi_{i+1} \end{Bmatrix} + \mathbf{R}_{4 \times 4} \begin{Bmatrix} \dot{y}_i \\ \dot{\psi}_i \\ \dot{y}_{i+1} \\ \dot{\psi}_{i+1} \end{Bmatrix} \\ &= \mathbf{K}_{4 \times 4} \begin{Bmatrix} \int \dot{y}_i dt \\ \int \dot{\psi}_i dt \\ \int \dot{y}_{i+1} dt \\ \int \dot{\psi}_{i+1} dt \end{Bmatrix} + \mathbf{R}_{4 \times 4} \begin{Bmatrix} \dot{y}_i \\ \dot{\psi}_i \\ \dot{y}_{i+1} \\ \dot{\psi}_{i+1} \end{Bmatrix}. \end{aligned} \quad (5.92)$$

Fig. 5.59 Representation of element stiffness and damping in Rayleigh beam bond graph model

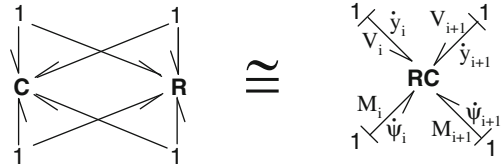
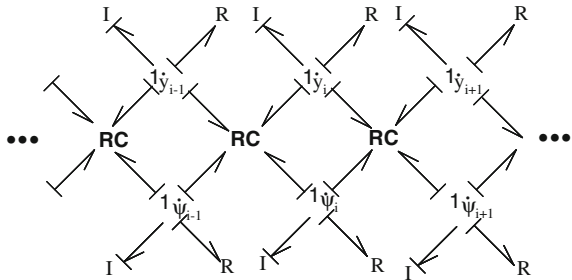


Fig. 5.60 Rayleigh beam bond graph model



The damping matrix is given as

$$\mathbf{R} = \frac{\mu_i I}{L^3} \begin{bmatrix} 12 & 6L & -12 & 6L \\ 6L & 4L^2 & -6L & 2L^2 \\ -12 & -6L & 12 & -6L \\ 6L & 2L^2 & -6L & 4L^2 \end{bmatrix} = \lambda \mathbf{K} \tag{5.93}$$

where μ_i is a material constant specified as $\mu_i = \lambda E$, with λ being the proportionality constant evaluated from experiments. The unit of λ is same as that of time.

The bond graph representation of the combined stiffness and damping of the beam element is then given as shown in Fig. 5.59.

Several such beam elements are then combined to model a finite length of the beam as shown in Fig. 5.60. The nodal masses and moment of inertias are included as lumped inertias at 1 junctions representing nodal linear and angular velocities, respectively. The inertia of linear motion at i th node is given as $I : \rho (A_{i-1} \Delta z_{i-1} + A_i \Delta z_i) / 2$ or if uniform elements are considered then as $I : \rho A \Delta z$, where A is the area of the beam cross-section. Likewise, the rotary at i th node is given as $I : \rho (I_{i-1} \Delta z_{i-1} + I_i \Delta z_i) / 2$ or if uniform elements are considered then as $I : \rho I \Delta z$. Likewise, the external dampings to linear and rotational motions are represented as lumped resistances at respective 1 junctions.

It may be noted that the nodal inertias can be represented more accurately by using an I-field (see [91] for details). However, when the number of elements considered to model the beam is sufficiently large, I-field representation does not give any added advantage.



Fig. 5.61 A cantilever beam with a part-span support and tip load

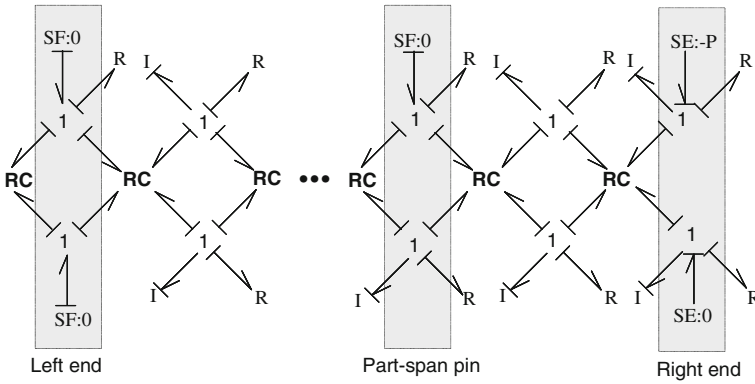


Fig. 5.62 Rayleigh beam bond graph model of a cantilever beam with a part-span support and tip load

The boundary conditions are applied to the Rayleigh beam model in a manner similar to the Euler-Bernoulli beam model. For example, consider the beam supported and loaded as shown in Fig. 5.61.

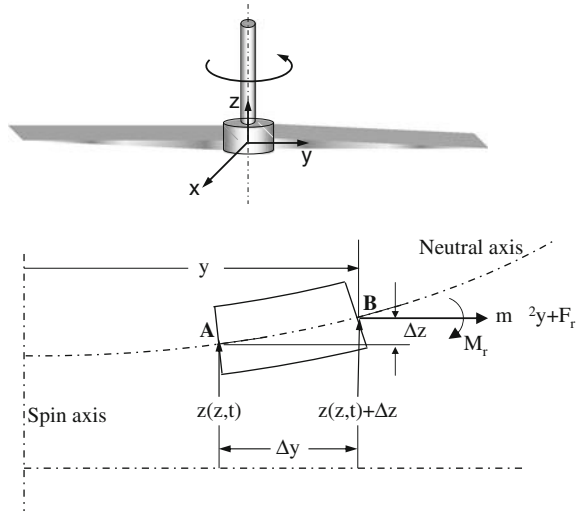
The boundary conditions for this beam are

$$\begin{aligned}
 y(z, t)|_{z=0} &= 0 \quad \text{and} \quad \left. \frac{\partial y(z, t)}{\partial z} \right|_{z=0} = 0, \\
 y(z, t)|_{z=a} &= 0, \\
 V(z, t)|_{z=l} &= -P \quad \text{and} \quad M(z, t)|_{z=l} = 0,
 \end{aligned}$$

where $z = 0$ and $z = l$ indicate the two ends of the beam, and $z = a$ defines the position of the roller support. These boundary conditions are imposed on the beam model as shown in Fig. 5.62.

Finite number of modes of a beam may be approximated by a modal bond graph (see [12, 78, 90, 91]). However, such a model requires that the mode shapes of the beam can be analytically determined from which one can obtain the modal inertia, stiffness and damping values, and the modal participation matrices. The modal parameters for an autonomous system are obtained by solving an eigenvalue problem and implementing the orthogonality conditions. However, solution of the eigenvalue problem cannot be obtained for any general kind of loading and boundary conditions. Therefore, use of modal bond graphs is restricted in some sense.

Fig. 5.63 A rotating fan with two blades



5.4.5 Centrifugal Stiffening

Rotating beams are often part of everyday machinery. When a beam spins about its axis along its length, it is called a shaft, e.g., a rotor shaft. There are other applications when the beam rotates about an axis normal to the beam axis, e.g., a fan, blades of a turbine rotor, helicopter blades, swing arms of a boom crane, robot arms, etc. The rotating beam is twisted in most of the cases. To simplify modeling, we will neglect the beam twist in this section.

The schematic representation of a fan with two blades is shown in Fig. 5.63. This is a symmetric system and it is enough to analyze the vibrations of one of the blades. A body-fixed coordinate system rotating with the fan is used for the modeling. The axial motions are neglected and thus the beam deflections are parallel to the rotation axis. Therefore, Coriolis forces are neglected. It is further assumed that the beam width is much larger than its thickness. Thus, the deflection of the beam is only in the body-fixed z -axis and a small twist is allowed about the body-fixed y -axis.

With these assumptions, the axial force acting at any section of the beam due to the centrifugal forces can be expressed as

$$F(y) = \Omega^2 \int_y^L \rho A(\zeta) \zeta d\zeta. \tag{5.94}$$

If the beam is deflected transversely then this axial force produces a bending moment. The forces and moments in this case are of distributed nature. The maximum axial force is at the root of the beam and so is the bending moment. Thus, we start calculating the forces and moments from the free end of the beam.

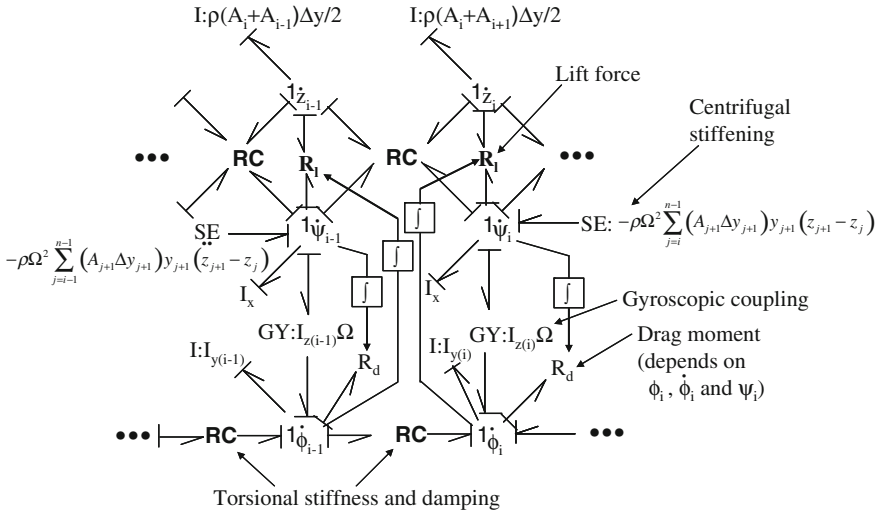


Fig. 5.64 Bond graph model of a rotating fan with two blades

Let us consider n finite elements to model this beam where the first element is at the root of the beam. Further, let the length of the element at the free end be Δy_n and the deflection of the free end at a time t be $z_n = z(L, t)$. If the variation of the cross-section area is neglected for a small segment of the beam then the axial force produced due to this element is $F_n = \rho A_n \Delta y_n \Omega^2 y_n$ where the average area of the section is A_n . This force produces a bending moment at the interface of n th and $(n - 1)$ th elements as $M_{n-1} = F_n (z_n - z_{n-1})$. The exact point of application of the force at the centroid of the element is not considered here because it does not matter if the number of the elements considered in the model is large.

The axial force produced due to rotation of the $(n - 1)$ th element is $F_{n-1} = \rho A_{n-1} \Delta y_{n-1} \Omega^2 y_{n-1}$. Thus, the total axial force acting at the interface of $(n - 1)$ th and $(n - 2)$ th elements is $F_n + F_{n-1}$ and the total bending moment may be approximated as $M_{n-1} + M_{n-2}$ where $M_{n-2} = F_{n-2} (z_{n-1} - z_{n-2})$.

The bond graph model of a segment of the rotating beam may now be developed using Rayleigh beam formulation as shown in Fig. 5.60 where bending is assumed to occur only in one direction. The bending moments are included in the model either incrementally or totally. This does not change the model equations because it is the difference between the bending moments applied at two ends of an element, i.e., the RC-element, that produces deformation of the element (this is evident from the first and third rows of the stiffness matrix). The bending moments due to centrifugal forces are applied in such a manner that they try to straighten the beam in a direction opposite to its local deflection.

The rotating beam model given in Fig. 5.64 also takes care of the torsional vibrations, i.e., the twist of the beam. The two-port RC-element models the torsional

stiffness and damping. The torsional stiffness of an element is given as $K_T = JG/\Delta y$ where G is the modulus of rigidity and $J = \beta ab^3$ is the effective polar moment of area for rectangular cross-section, a is the width, b the depth, and value of parameter β depends on the ratio a/b (here, we will assume $a/b = 10$ for which $\beta = 0.312$). The torsional damping is proportional to the stiffness, i.e., $R_T = \lambda K_T$.

A gyroscopic coupling is set up between the beam bending and twist. We do not need the full gyrotor ring structure here because the angular velocity Ω about the z -axis is assumed to be constant. Drag and lift forces act on a twisted beam rotating in a viscous medium. These forces (or moments) are velocity dependent and thus are modeled as R-elements. The lift force produces additional shear force and bending moment at an element and it primarily depends on the amount of the beam twist, fan speed Ω , and other geometric and environmental parameters. Thus, the information of the beam twist angle is supplied to R_l element that models the lift forces. Likewise, the drag force produces a twisting moment (modeled by R_d element) which depends on the fan speed Ω , the angle and rate of change of angle of twist, the rotation of the beam axis (although the later two have small influence) and other geometric and environmental parameters.

The full model of the rotating beam as shown in Fig. 5.64 is obtained after implementing the boundary conditions.

If the beam warping has to be considered in the model then Timoshenko beam theory is used to develop the model. The equations of motion for the basic nonrotating beam are given as

$$\rho A \frac{\partial^2}{\partial t^2} (z(y, t) - e\theta(y, t)) + EI \frac{\partial^4}{\partial y^4} z(y, t) + \lambda_i EI \frac{\partial^5}{\partial y^4 \partial t} z(y, t) = \frac{\partial}{\partial y} F(y, t), \tag{5.95}$$

$$EI_w \frac{\partial^4}{\partial y^4} \theta(y, t) + \lambda_i EI_w \frac{\partial^5}{\partial y^4 \partial t} \theta(y, t) - GJ \frac{\partial^2}{\partial y^2} \theta(y, t) - \lambda_i GJ \frac{\partial^2}{\partial y^2 \partial t} \theta(y, t) + \rho A \frac{\partial^2}{\partial t^2} \left((e^2 + r^2) \theta(y, t) + ez(y, t) \right) = \frac{\partial}{\partial y} Tz(y, t) \tag{5.96}$$

where $Fz(y, t)$ and $Tz(y, t)$ are the distribution of the external forces and torques, respectively. Here, t denotes time, z is the distance along the elastic axis of the beam, and z is the bending displacement of the shear center, the beam cross-section being assumed symmetrical about the plane O_{xz} . The quantity θ is the torsional rotation about y axis, e the position of the section centroid C relative to the shear center S , ρA is the mass per unit length, and r the polar radius of gyration of the cross-section about the centroid. The flexural rigidity in the O_{yx} plane is EI , while EI_w is the torsional rigidity associated with warping and GJ is the Saint-Venant torsional

rigidity [8]. The centrifugal effects are added to the equations of motion for modeling the rotating beam and the resulting equations of motion are

$$\begin{aligned} \rho A \frac{\partial^2}{\partial t^2} z(y, t) - \rho A e \frac{\partial^2}{\partial t^2} \theta(y, t) - \rho \Omega^2 \int_z^L A \xi d\xi \frac{\partial^2}{\partial t^2} z(y, t) \\ + \rho \Omega^2 e \int_z^L A \xi d\xi \frac{\partial^2}{\partial t^2} \theta(y, t) + EI \frac{\partial^4}{\partial y^4} z(y, t) + \lambda_i EI \frac{\partial^5}{\partial y^4 \partial t} z(y, t) = \frac{\partial}{\partial y} F(y, t), \end{aligned} \quad (5.97)$$

$$\begin{aligned} EI_w \frac{\partial^4}{\partial y^4} \theta(y, t) + \lambda_i EI_w \frac{\partial^5}{\partial y^4 \partial t} \theta(y, t) - GJ \frac{\partial^2}{\partial y^2} \theta(y, t) - \lambda_i GJ \frac{\partial^2}{\partial y^2 \partial t} \theta(y, t) \\ + \rho \Omega^2 e \int_z^L A \xi d\xi \frac{\partial^2}{\partial t^2} z(y, t) - \rho \Omega^2 (e^2 + r^2) \int_z^L A \xi d\xi \frac{\partial^2}{\partial t^2} \theta(y, t) \\ - \rho A e \frac{\partial^2}{\partial t^2} z(y, t) + \rho A (e^2 + r^2) \frac{\partial^2}{\partial t^2} \theta(y, t) = \frac{\partial}{\partial y} T(y, t), \end{aligned} \quad (5.98)$$

where Ω is the angular speed of rotation.

These equations can now be discretized to develop a Timoshenko beam bond graph model (see [91]) and then other effects such as drag and lift forces, and boundary conditions can be imposed on the developed model. A much more detailed bond graph model is developed in [152] where a multiport IC-field is used to model a rotating beam with large deflections. The co-rotational formulation used to develop bond graph models of beams with large deflection [31] can also be adapted to model rotating beams.

5.4.6 Beams Made of Two Layers

A beam made of two material layers is shown in Fig. 5.65. The difference in elastic modulus of the materials causes the neutral axis to shift from the geometric center to another location. The cross-section of the beam made by gluing or welding two dissimilar materials of equal width w and thickness $h/2$ is shown in Fig. 5.65. When the beam is bent by application of a bending moment, the strains (ε) and stresses on the beam cross-section develop as shown in the figure. Clearly, there is a stress discontinuity at the interface of the two materials.

To analyze the dynamics of such a beam, i.e., disregarding the internal stresses and strains, an equivalent beam cross-section may be used. One of the beam materials, say material 1, is taken as the reference material. Let $\alpha_{21} = E_2/E_1$, $\alpha_{31} = E_3/E_1$, etc. The equivalent width of other material layers can be expressed as $w_2 = \alpha_{21}w$, $w_3 = \alpha_{31}w$, etc. as shown in Fig. 5.66. The centroid of the resulting equivalent cross-section gives the location of the beam neutral axis and the resulting flexural rigidity

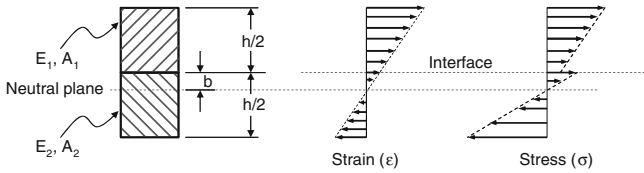


Fig. 5.65 Cross-section of a composite beam

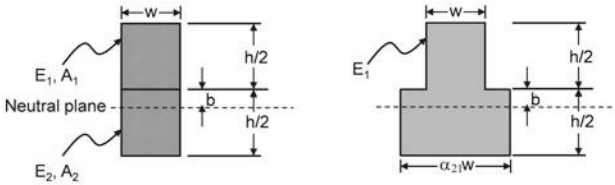


Fig. 5.66 Equivalent cross-section of a composite beam

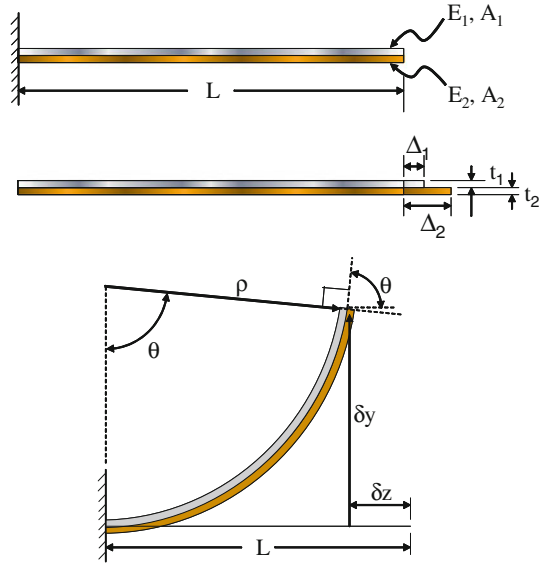
of the beam is defined as $EI = E_1 I_{eq}$ where I_{eq} is the second moment of area of the equivalent beam cross-section about the neutral axis of the beam. The beam modeling methodology remains the same as before.

5.4.7 Bimetallic Strip

A bimetallic strip is made of two strips of different metals which have different coefficients of thermal expansion. Usually steel, copper, and brass are the metals used in the bimetallic strip. The metal strips are joined together throughout their length by brazing or welding. The length of the two metal strips are equal at some initial temperature (top part in Fig. 5.67). When the flat strip is heated to a temperature above the initial configuration temperature, the difference in thermal expansion coefficients causes the strip to bend so that the metal with the higher coefficient of thermal expansion is on the outer side of the curve. The opposite happens when the strip is cooled below its initial configuration temperature.

The differences in thermal expansion of the two materials is schematically shown in the middle part of Fig. 5.67 where it is assumed that there is no connection between the two material layers. The parameters E , A , t , α , and Δ refer to the Young’s modulus, cross-section area, thickness, coefficient of thermal expansion (CTE), and elongation, respectively, and the subscripts 1 and 2 enumerate the materials. If the strips are joined together then the strip reaches a final configuration as shown in bottom part of Fig. 5.67. Timoshenko [140] suggested a simple and effective analytical model for evaluating the thermostat bow and the normal stresses in the cross-sections of the thermostat strips. Aleck [2] gave an improved formulation based on theory-of-elasticity treatment of the problem. The resulting curvature of the strip, assuming that the

Fig. 5.67 Thermal expansion induced curvature in bimetallic strip: normal configuration in *top*, unconstrained expansion in *middle* and actual constrained expansion in *bottom*



width of the strip could be considered as being very small, was given by Timoshenko [140] as

$$\rho_{th} = \frac{\frac{t}{2} + 2 \frac{(E_1 I_1 + E_2 I_2)}{wt} \left(\frac{1}{E_1 t_1} + \frac{1}{E_2 t_2} \right)}{(\alpha_2 - \alpha_1) (T - T_0)}, \quad (5.99)$$

where ρ_{th} is the thermally induced radius of curvature, $I_1 = wt_1^3/12$, $I_2 = wt_2^3/12$, $t = t_1 + t_2$, the width for both the strips is taken to be w , T is the current temperature, and T_0 is the initial temperature. The thermally induced bending moment is thus

$$M_{th} = \frac{-EI}{\rho_{th}} = -\frac{EI (\alpha_2 - \alpha_1) (T - T_0)}{\frac{t}{2} + 2 \frac{(E_1 I_1 + E_2 I_2)}{wt} \left(\frac{1}{E_1 t_1} + \frac{1}{E_2 t_2} \right)}. \quad (5.100)$$

Note that this bending moment is an externally applied moment in addition to other moments acting on the beam, i.e., the overall curvature is $\kappa = 1/\rho_{th} + 1/\rho_{ex}$ where ρ_{ex} is induced due to other loads or residual stresses. The term EI in Eq. 5.100 is the equivalent flexural rigidity computed from equivalent beam cross-section. If biaxial state of stress is assumed (when the beam thickness and width are of comparable dimension) then plane strain formulation should be used where for each material i (1 or 2) the modulus of elasticity E_i should be replaced by $E_i / (1 - \nu_i)$ and the CTE α_i should be replaced by $(1 + \nu_i) \alpha_i$. In addition, a force acts at the interface of the two materials. Timoshenko's formulation [140] gives the forces and moments on each layer of the strip. These are also detailed in [38]. Thus, it is possible to model the two layers separately and constrain them together at the interface. The end effect

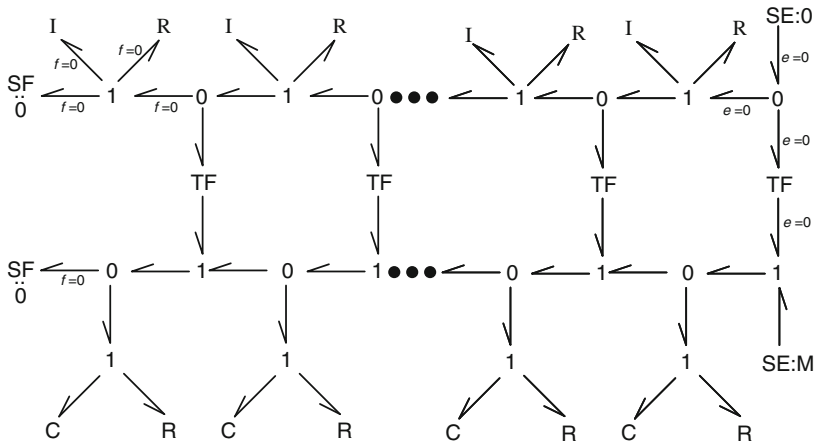


Fig. 5.68 Bond graph model of a bimetallic strip at uniform temperature

may be included through Hess solution [38]. Other formulations may be consulted in [113, 135].

The deflection of the tip of the beam at uniform temperature can be calculated directly from geometric analysis. If the temperature is uniform at all points in the beam then the radius of curvature is constant at all points taken along the neutral axis (see Fig. 5.67). Then, the tip angle $\theta = L/\rho$, $\delta z = L - \rho \sin \theta$ and $\delta y = \rho (1 - \cos \theta)$ where L is the original length of the strip.

The bond graph model of a uniformly heated cantilever bimetallic strip is shown in Fig. 5.68. The bond graph model is generated assuming that Euler-Bernoulli beam theory is valid. Thus, it suffices to include the temperature change effect as a external concentrated bending moment applied at the tip of the cantilever strip. The bending moments at all positions along the length of the strip remains the same because the end moment is transmitted to other locations through the beam compliance. Thus, the external moment is applied only at the tip and it may be modulated according to the temperature.

The original Euler-Bernoulli theory is valid only for infinitesimal strains and small rotations. For moderately large rotations where strain remains small, Euler-Bernoulli theory can be extended by using the von Karman strains [112]. Another approach is to use Timoshenko beam theory with a co-rotational formulation. Bond graph models of beams with large deformation may be consulted in [31].

Figure 5.69 shows a bimetallic strip with nonuniform temperature along its length. Thus, the curvature is different at different positions along the length of the strip. To account for this effect, the bending moments at different locations must be different, i.e., one needs to construct a bending moment diagram as a function of the position and temperature at that position. Thus, the thermal modeling of the system is required. Figure 5.70 shows the bond graph model of the system where beam mechanical model is coupled to its thermal model.

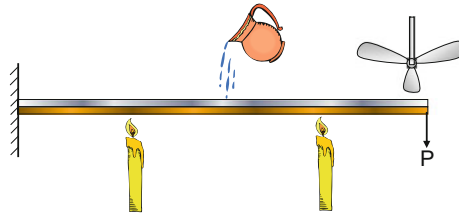


Fig. 5.69 A bimetallic strip at nonuniform temperature

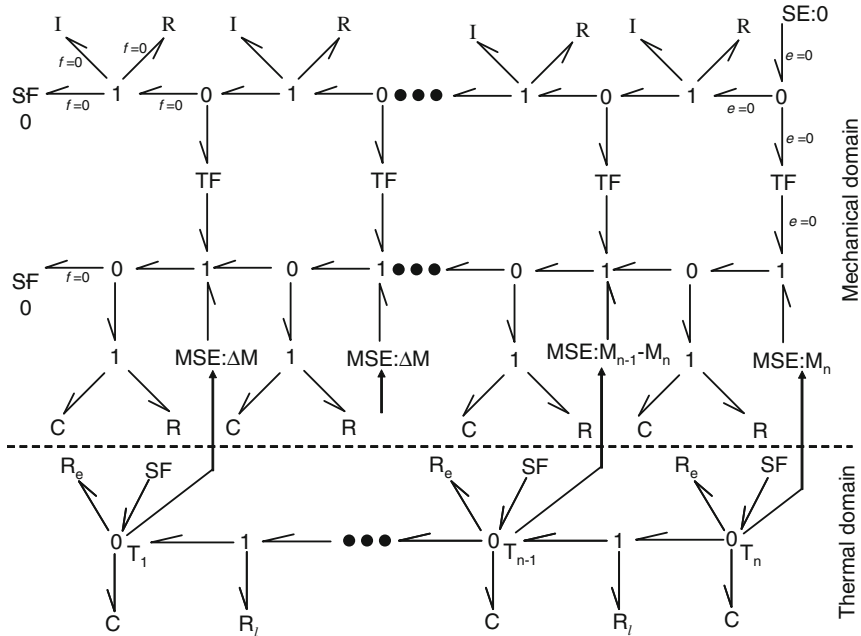


Fig. 5.70 Bond graph model of a bimetallic strip at nonuniform temperature

In the thermal part of the model, pseudo-bond graph is used with temperature (T) and heat transfer rate (\dot{Q}) as the power variables. Various SF-elements at nodes represent the external heating or cooling. The resistances model heat transfer: R_e models heat transfer from the metal to the environment and R_l models heat transfer along the beam axis. The two metals in the bimetallic strip may be separately modeled or lumped together as has been done in this case. The C-elements model the heat capacity of the segment of the strip between two adjacent nodes. The temperature at each node is used to compute the local curvature and local bending moment. If the bending moment at a particular node is different from the next node then the difference between the two bending moments (ΔM) is modeled at that node as an external concentrated bending moment acting at that node. Thus, the true bending moment diagram with variable temperature is approximated by step changes at the

nodes (much like a sample and hold approximation along the length of the strip). Note that if a beam is at uniform temperature then $\Delta M = 0$ at each node and the thermal model is no more relevant because the end moment M_n can be directly applied as a function of the uniform temperature.

Bimetallic strips are used for various applications such as compensation of temperature induced errors in mechanical clocks, on-off thermostats for regulation of heating and cooling, adjustable thermostats to change temperature set point in temperature control systems, recording thermometers, and miniature circuit breakers. Bimetallic strips have also been used in a variety of microelectromechanical systems (MEMS). A few of those applications are discussed later.

Beams made of shape memory alloys which show dependence of material properties with temperature can be modeled in a way similar to bimetallic strips. The local bending moments at nodes are expressed in terms of temperature (step changes at transition temperature) by coupling the mechanical and thermal models of a shape memory alloy beam.

5.4.8 Piezoelectric Effect

Piezoelectric effect refers to electrical polarization of the crystals in some crystalline materials when they are subjected to a mechanical force [61, 109]. Inverse piezoelectric effect refers to induced internal stresses leading to change in dimensions when such crystals are exposed to an electric field. Lead zirconate titanate (PZT) based ceramics are the most widely used piezoelectric materials. Some piezoceramic materials like Tourmaline show pyroelectricity effect, i.e., over and above the piezoelectric effect these materials also generate electrical signal in response to change in the temperature of the crystal.

Piezoceramic devices may be used as sensors, actuators, generators, and transducers. From an engineering point-of-view, a good piezoelectric material should exhibit greater sensitivity and linearity, and should be able to operate at higher temperatures.

Piezoelectric actuators convert electrical energy into controlled mechanical motion. Examples are precision machining tools, camera lens positioning, hydraulic valves in a micropump, mirrors such as the micromirrors discussed later, etc. Piezoelectric sensors are used in various applications: pressure sensor in the touch pads, combustion monitoring in internal combustion engines, displacement and acceleration sensors, etc. In an energy harvesting device, the electrical energy generated by a piezoelectric element is stored. When impact force is applied on piezoelectric ceramics, the generated voltage can create a spark across an electrode gap. This effect is used in electronic fuel lighters. Piezoelectric materials are increasingly being used in smart structures.

A transducer is a device that converts small amounts of energy from one kind into another. A piezoelectric transducer has very high DC output impedance. Therefore, it can be modeled as a transformer (TF) or a proportional modulated voltage source (MSe). Piezoelectric transducers convert electrical energy into mechanical energy in

form of vibration, sound, or ultrasound. They are useful in various microelectronic applications such as atomizing liquids, ultrasonic machining, and medical diagnostics. The piezoelectric acoustic transducer can be used to both generate ultrasound signal from electrical energy and vice versa. A piezoelectric transducer can convert electrical energy into extremely rapid mechanical vibrations (called ultrasound vibrations) which are inaudible for our ears. These ultrasound vibrations can be used for scanning, cleaning, etc. A piezoelectric microphone converts audible sound energy into electrical energy.

The elastic modulus of a common piezoelectric material exceeds that of many metals. Thus, they are used for precision measurements. In a piezoelectric sensor the sensing element shows almost negligible deflection. In piezoelectric pressure sensors, a thin membrane with a heavy base is used so that the applied pressure loads the elements in a specific direction. In piezoelectric accelerometer, a heavy seismic mass is attached to the crystal elements. The difference in the working principle between these two sensors is the way forces are applied to the sensing elements. In a pressure sensor, a thin membrane is used to transfer the force to the elements, whereas in an accelerometer the forces are applied by the inertial force induced in the attached seismic mass. The principle used in designing piezoelectric acceleration sensors can also be used to harvest energy from mechanical vibrations. Piezoelectric acoustic sensors use the same principle where the acoustical signal induces vibrations in a thin membrane in which the piezoelectric element is mounted. Piezoelectric ultrasound sensors are used in medical imaging and nondestructive testing (NDT) of industrial components.

Piezoelectric ceramics are anisotropic materials. Thus, each physical constant used to describe the behavior of a piezoelectric material is denoted with two subscripts which indicate the directions of the two related quantities. The commonly used piezoelectric constants are the piezoelectric charge constant, d , the piezoelectric voltage constant, g , and the permittivity, ϵ . These constants are temperature dependent. The electromechanical coupling factor, k , defines how electrical energy is converted into mechanical energy and *vice versa*. The electromechanical coupling factor has two subscripts in which the first denotes the direction along which the electric field is applied or developed and the second subscript denotes the direction along which the mechanical force is applied or developed.

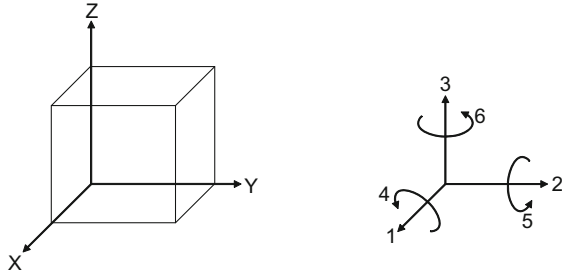
The strain–charge form of the so-called coupled equations describing the behavior of a piezoelectric material is given as

$$\{S\} = [s^E]\{T\} + [d^t]\{E\} \quad (5.101)$$

$$\{D\} = [d]\{T\} + [\epsilon^T]\{E\} \quad (5.102)$$

where S is strain, s is compliance, T is stress, D is the electric charge density displacement (electric displacement), ϵ is permittivity, E is electric field strength, $[d]$ is the matrix for the direct piezoelectric effect and $[d^t]$ is the matrix for the converse piezoelectric effect. The superscript E indicates zero or constant electric

Fig. 5.71 Voigt notation to represent piezoelectric tensors



field, the superscript T indicates zero or constant stress field and the superscript t denotes transpose of matrix.

In the piezoelectric material constitutive relations, D and E are vectors, permittivity ϵ is Cartesian tensor of rank 2, stress and strain are also rank-2 tensors. Because strain and stress are all symmetric tensors, the subscript of strain and stress can be relabeled in different ways (called Voigt notation). For example, $11 \rightarrow 1$; $22 \rightarrow 2$; $33 \rightarrow 3$; $23 \rightarrow 4$; $13 \rightarrow 5$; $12 \rightarrow 6$ (see Fig. 5.71).

After relabeling, S and T may be each represented as 6-component vectors, and s as a 6×6 matrix. The resulting form of the strain–charge form of the coupled equations describing the behavior of a piezoelectric material is

$$\begin{Bmatrix} S_1 \\ S_2 \\ S_3 \\ S_4 \\ S_5 \\ S_6 \end{Bmatrix} = \begin{bmatrix} s_{11}^E & s_{12}^E & s_{13}^E & 0 & 0 & 0 \\ s_{21}^E & s_{22}^E & s_{23}^E & 0 & 0 & 0 \\ s_{31}^E & s_{32}^E & s_{33}^E & 0 & 0 & 0 \\ 0 & 0 & 0 & s_{44}^E & 0 & 0 \\ 0 & 0 & 0 & 0 & s_{55}^E & 0 \\ 0 & 0 & 0 & 0 & 0 & s_{66}^E \end{bmatrix} \begin{Bmatrix} T_1 \\ T_2 \\ T_3 \\ T_4 \\ T_5 \\ T_6 \end{Bmatrix} + \begin{bmatrix} 0 & 0 & d_{31} \\ 0 & 0 & d_{32} \\ 0 & 0 & d_{33} \\ 0 & d_{24} & 0 \\ d_{15} & 0 & 0 \\ 0 & 0 & 0 \end{bmatrix} \begin{Bmatrix} E_1 \\ E_2 \\ E_3 \end{Bmatrix}$$

$$\begin{Bmatrix} D_1 \\ D_2 \\ D_3 \end{Bmatrix} = \begin{bmatrix} 0 & 0 & 0 & 0 & d_{15} & 0 \\ 0 & 0 & 0 & d_{24} & 0 & 0 \\ d_{31} & d_{32} & d_{33} & 0 & 0 & 0 \end{bmatrix} \begin{Bmatrix} T_1 \\ T_2 \\ T_3 \\ T_4 \\ T_5 \\ T_6 \end{Bmatrix} + \begin{bmatrix} \epsilon_{11} & 0 & 0 \\ 0 & \epsilon_{22} & 0 \\ 0 & 0 & \epsilon_{33} \end{bmatrix} \begin{Bmatrix} E_1 \\ E_2 \\ E_3 \end{Bmatrix} \quad (5.103)$$

In the revised formulation, s^E is a 6×6 symmetrical matrix called mechanical matrix of flexibility (the superscript E indicates that either the electrical field is zero or it is a constant), ϵ^T is a 3×3 symmetrical matrix called electrical permittivity of the material (the superscript T indicates that either the stress is zero or it is a constant), and d is a 3×6 matrix of piezoelectric coefficients (the superscript t refers to matrix transposition). In Eq. 5.103, the choice of (E, T) as independent variables instead of (D, S) is motivated by the device controlling techniques. When one is mainly dealing

with actuating function, (E, T) are the inputs and (D, S) are the outputs. However, the choice is made according to frequency domain response characteristics. When the device is used near its antiresonance frequency, the good independent variables choice is (D, S) and when it is used near the resonance frequency, the good choice is (E, T) .

Three main modes of operation of a piezoelectric material are transverse effect, longitudinal effect, and shear effect. The sensitivity to the applied force is more easily adjusted by using the transverse effect (this will be shown later when we discuss an energy harvesting device). There are two direct piezoelectric coefficients d_{ij} , and e_{ij} , which are defined as follows:

$$d_{ij} = \left(\frac{\partial D_i}{\partial T_j} \right)^E = \left(\frac{\partial S_j}{\partial E_i} \right)^T \quad (5.104)$$

$$e_{ij} = \left(\frac{\partial D_i}{\partial S_j} \right)^E = - \left(\frac{\partial T_j}{\partial E_i} \right)^S \quad (5.105)$$

The two converse or inverse coefficients g_{ij} and h_{ij} are defined as follows:

$$g_{ij} = - \left(\frac{\partial E_i}{\partial T_j} \right)^D = \left(\frac{\partial S_j}{\partial D_i} \right)^T \quad (5.106)$$

$$h_{ij} = - \left(\frac{\partial E_i}{\partial S_j} \right)^D = - \left(\frac{\partial T_j}{\partial D_i} \right)^S \quad (5.107)$$

The piezocrystal can generate high voltage across its faces. However, the charge developed is small and the potential difference is large because the width of the piezoelement is small, thus increasing the electrical capacitance of the element. Multilayer ceramics with thin layers with thickness in the order of 100 nm can generate high electric fields with manageable voltage. Such multilayer ceramics are used in direct and amplified piezoelectric actuators which can produce precise movements. Examples are high-precision piezoelectric motors which have much larger positioning accuracy as compared to conventional stepper motors (traveling wave motor used for autofocus in reflex cameras, Inchworm motors, stepping piezomotors using stick-slip motion). Piezomotors are used for micromirror positioning, atomic force microscopes, and scanning tunneling microscopes, precision fuel injection systems in diesel engines, and also for active vibration control.

A turntable for increasing the data density and read/write access time in a hard disk drive is modeled in [128]. The turn table is rotated using piezoelectric tubes by using the concept of Inertial Sliding Motion (ISM) as shown in Fig. 5.72. Stick-slip effect is used therein for ISM. The piezoelectric tubes used for the turntable are hollow cylinders made of PZT which are metallized on the inner and the outer surfaces and are poled in the radial direction (see Fig. 5.73).

The outside metal coating is further sectioned into four quadrants. This allows independent actuation of four quadrants. In the symmetric voltage mode, two voltages

Fig. 5.72 Schema of the turntable

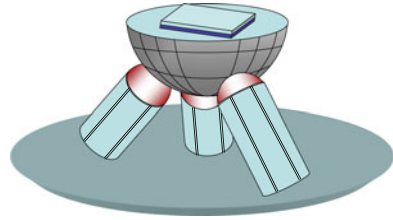
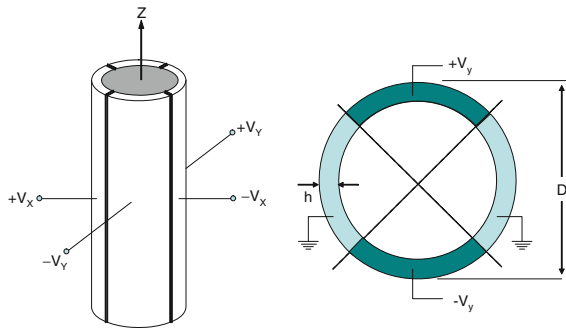


Fig. 5.73 Arrangement of the actuating patches in the tubes of the turntable



equal in magnitude and opposite in sign are applied to two opposite quadrants, while the remaining two quadrants are grounded. In the asymmetric voltage mode, a potential is applied to only one quadrant while the remaining three quadrants are grounded. The radius of curvature of the tube bending for symmetric actuation (for the case shown in the right half of Fig. 5.73) is derived as [128]

$$R_{bending} = \frac{\pi D h}{4\sqrt{2}d_{31} V} \tag{5.108}$$

and the radius of curvature of the tube bending for asymmetric actuation is twice that of the symmetric actuation [23].

A similar system used in Scanning Tunneling Microscopes (STMs) and Atomic Force Microscopes (AFMs) is discussed in [49], where two adjacent patches of the piezotube are used for actuation and the remaining two patches are used for sensing where high sensor impedance is equivalent to open electrode configuration. Under such asymmetric actuation, the deformation of the tube is superposition of two modes of motion: (1) the elongation of one side of the tube leads to elongation of the opposite side (called a piston mode) to balance axial stresses and (2) the bending induces elongation on one side and compression on the other side (called a bending mode). The piston mode has slow dynamics relative to the bending mode. The bending mode leads to the desired horizontal motion of the actuator tip in the STM or AFM. It has been shown in [49] that for low frequency applications, the bending mode can be modeled as a mass-spring-damper subsystem. The piston mode makes this collocated sensor/actuator system a nonminimum phase system which

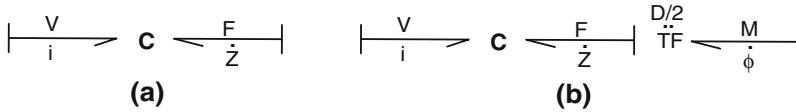


Fig. 5.74 **a** Two port C-field for modeling piezoelectric coupling of electrical and mechanical domains and **b** Two port C-field with transformer element for modeling bending of a piezotube

causes problems in controlling the positional accuracy near the resonant frequency. A physical-model-based control strategy for this system using bond graph model is developed in [49].

In this book, we will consider the symmetric actuation case. Let D be the diameter of the tube, L be its length, h be the wall thickness of the tube, $A_m = \pi Dh/4$ be the cross-section area of the elongated surface (one quadrant), $A_e = \pi DL/4$ be area of the actuated surface, $V = hE_1$ be the applied voltage, $z = LS_3$ be the expansion of the length of the tube, and $q = A_e D_1$ be the charge at the electrodes. For the piezotube, applying a voltage to the piezoelectric element in the 1-direction results in a strain $S_3 = d_{31}E_1 = d_{31}V/h$ in 3-direction where d_{31} is the relevant piezoelectric charge constant. This strain creates a stress $T_3 = S_3/s_{33}$ in 3-direction where s_{33} is the relevant compliance (reciprocal of stiffness). Likewise, application of a force F in 3-direction to the piezoelectric element creates an electric displacement $D_1 = d_{31}T_3 = d_{31}F/A_m$, which further creates an electric field $E_1 = D_1F/\epsilon_{11}$. Thus, the governing equations of a quadrant of the piezotube is a reduced form of Eq. 5.103 which is given as

$$\begin{Bmatrix} S_3 \\ D_1 \end{Bmatrix} = \begin{bmatrix} s_{33}^E & d_{31} \\ d_{31} & \epsilon_{11}^T \end{bmatrix} \begin{Bmatrix} T_3 \\ E_1 \end{Bmatrix} \tag{5.109}$$

or

$$\begin{Bmatrix} z \\ q \end{Bmatrix} = \begin{bmatrix} \frac{s_{33}^E L}{A_m} & \frac{d_{31} L}{h} \\ \frac{d_{31} L}{h} & \frac{\epsilon_{11}^T A_e}{h} \end{bmatrix} \begin{Bmatrix} F \\ V \end{Bmatrix}. \tag{5.110}$$

The above relation describes bending mode of a quadrant of the piezotube and may be written in a form

$$\begin{Bmatrix} F \\ V \end{Bmatrix} = \begin{bmatrix} \frac{s_{33}^E L}{A_m} & \frac{d_{31} L}{h} \\ \frac{d_{31} L}{h} & \frac{\epsilon_{11}^T A_e}{h} \end{bmatrix}^{-1} \begin{Bmatrix} z \\ q \end{Bmatrix} = \begin{bmatrix} \frac{s_{33}^E L}{A_m} & \frac{d_{31} L}{h} \\ \frac{d_{31} L}{h} & \frac{\epsilon_{11}^T A_e}{h} \end{bmatrix}^{-1} \begin{Bmatrix} \int \dot{z} dt \\ \int i dt \end{Bmatrix}. \tag{5.111}$$

Thus, we can represent the above relationship as a 2-port C-field shown in Fig. 5.74a. The axial force can now be multiplied with the moment arm (distance of

piezolayer from the neutral axis), which may be modeled by a TF-element, to generate the bending moment acting on the beam and the beam modeling part remains the same as that for the bimetallic strip. The TF-element, shown in Fig. 5.74b, simultaneously transforms elongation rate to rate of change of angle. Four such quadrants of the piezotube are modeled by four two-port C-elements and are then coupled to X- and Y-direction beam bending models.

The tube bending is modeled as a spatial spring in [128]. The tube consists of four quadrants and thus there should be four variable spatial springs. However, the tube is one flexible body and therefore the four spatial springs on each quadrant are merged into one spring, which is positioned in the center of the tube. The friction between the tube tip and the turntable are also modeled with stick-slip effect. The final bond graph model was then implemented in 20-sim software. It may be, however, noted that the model includes only the static characteristics. The mass matrix has to be additionally included to give the desired resonance and antiresonance frequencies. Instead of mass matrix, discrete lumped masses can as well be represented in the model.

Let us now consider pure piston mode or bar operating mode operation of a piezobar. The piezobar device is made by stacking up of thin elements from 100 to 300 μm . Conventionally, the z-axis is the poling axis. The bar elongates or contracts along z-axis and there is no bending. In this operating mode, one has: $D_1 = D_2 = 0$, $D_3 \neq 0$, $E_1 = E_2 = 0$, $E_3 \neq 0$, $T_1 = T_2 = 0$, $T_3 \neq 0$, $S_1 \neq 0$, $S_2 \neq 0$ and $S_3 \neq 0$. Thus, Eq. 5.103 reduces to

$$S_1 = s_{13}^E T_3 + d_{31} E_3$$

$$S_2 = s_{23}^E T_3 + d_{32} E_3$$

$$S_3 = s_{33}^E T_3 + d_{33} E_3$$

$$D_3 = d_{33} T_3 + \varepsilon_{11}^T E_3$$

If there are no lateral forces in bar mode operation, then the energy content in those directions is zero. Thus, one needs only the last two equations, i.e., the model constitutive relations are

$$S_3 = s_{33}^E T_3 + d_{33} E_3 \quad (5.112)$$

$$D_3 = d_{33} T_3 + \varepsilon_{11}^T E_3 \quad (5.113)$$

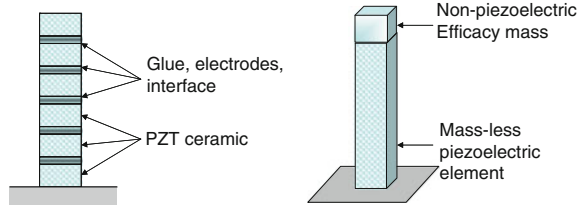
Let us now consider an elemental energy of the piezobar as

$$\delta U = [T]^\delta \delta[S] + [E]^\delta \delta[D] \quad (5.114)$$

which for the bar mode (i.e., substitution of expressions in Eqs. 5.112 and 5.113) gives

$$\delta U = T_3(s_{33}^E \delta T_3 + d_{33} \delta E_3) + E_3(d_{33} \delta T_3 + \varepsilon_{33}^T \delta E_3)$$

Fig. 5.75 Construction of a piezobar and its equivalent representation for the first mode motion



$$\begin{aligned}
 &= s_{33}^E T_3 \delta T_3 + d_{33} (T_3 \delta E_3 + E_3 \delta T_3) + \varepsilon_{33}^T E_3 \delta E_3 \\
 &= s_{33}^E T_3 \delta T_3 + d_{33} \delta (T_3 E_3) + \varepsilon_{33}^T E_3 \delta E_3
 \end{aligned} \tag{5.115}$$

Upon integration, one obtains

$$\begin{aligned}
 U &= \frac{1}{2} s_{33}^E (T_3)^2 + d_{33} T_3 E_3 + \frac{1}{2} \varepsilon_{33}^T (E_3)^2 \\
 &= U_M + 2U_C + U_E
 \end{aligned} \tag{5.116}$$

where the first term $U_M = \frac{1}{2} s_{33}^E (T_3)^2$ is purely mechanical potential energy, the last term $U_E = \frac{1}{2} \varepsilon_{33}^T (E_3)^2$ is a purely electrical potential energy across the piezoelement due to capacitive effect, and the middle term $2U_C = d_{33} T_3 E_3$ is an electromechanical energy coupling term. The electromechanical coupling factor κ is a nondimensional parameter which is defined as

$$\kappa = \frac{U_C}{\sqrt{U_M U_E}} = \frac{d_{33}}{\sqrt{s_{33}^E \varepsilon_{33}^T}}. \tag{5.117}$$

Model of piezobar device can be developed based upon continuum approximation or finite mode approximation. For first model, Boukari [16] developed a bond graph model using lumped mass approximation (see Fig. 5.75) and also presented its block-diagram model [17]. The model can be extended to include higher modes by breaking the piezoelement into more number of nonpiezoelectric massive elements and massless piezoelectric compliant elements. In Fig. 5.75, the efficacy mass m_e is so determined that the first natural frequency of the piezobar and the model are matched.

Starting from

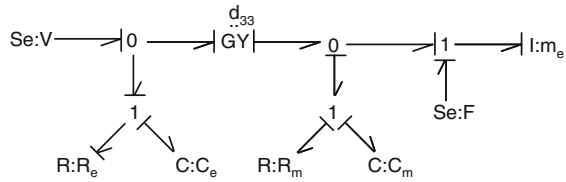
$$S_3 = s_{33}^E T_3 + d_{33} E_3 \tag{5.118}$$

$$D_3 = d_{33} T_3 + \varepsilon_{11}^T E_3 \tag{5.119}$$

and integrating over the massless piezoelement length, one obtains

$$u = \frac{F - m\ddot{u}}{K_m} + d_{33} V \tag{5.120}$$

Fig. 5.76 Bond graph model of a first mode dynamics of a piezobar with efficacy mass



$$q = d_{33} (F - m\ddot{u}) + C_e V \tag{5.121}$$

where u is the displacement of efficacy mass (elongation of the massless piezoelement), q is the charge developed, V is the applied potential, $K_m = 1/C_m$ is the mechanical stiffness of the piezoelement, and C_e is the equivalent electrical capacitance of the piezoelement. Every piezoelement has some mechanical damping (R_m) and electrical circuit resistance (R_e). Thus, the bond graph model derived from Eqs. 5.120 and 5.121 can be given as shown in Fig. 5.76.

The bond graph model in Fig. 5.76 does not include temperature influence, nonlinearities and hysteresis. Bond graph models of piezoelements with nonlinearities and hysteresis can be consulted in [128]. Similarly, bond graph model of a four-quadrant piezotube, where two adjacent sides are used as actuating patches and two sides opposite to the actuating patches are used as sensing patches, with first piston mode and first bending mode approximations is given in [49]. The temperature dependent distributed parameter bond graph model of a piezoelement is given in [85, 86].

Bond graph models of a piezoelectric layer polarized in a single axis under isothermal conditions are developed in [114]. Taking into account the direct and converse piezoelectric effects, the constitutive relations can be written as

$$T = c^D S - h D \tag{5.122}$$

$$E = -h S + \beta^S D \tag{5.123}$$

where D , T , E , and S are the electric displacement, stress, electric field and strain, respectively, c^D is stiffness under constant electric displacement, h is the piezoelectric constant and β^S is the impermittivity at constant strain. One may now assume that the electric field is perfectly perpendicular at the surface of the layer in the direction of polarization and the material is isotropic. Under these assumptions, $E \simeq V/l$ and $Q \simeq DA$ where V is the input voltage (in actuator mode), Q is the electric charge, l is the layer thickness, and A is the actuator area. If x is the actuator displacement and F is the actuator force then $S = x/l$ and $F = TA$. Equations 5.122 and 5.123 can now be written as

$$\begin{pmatrix} F \\ V \end{pmatrix} = \begin{bmatrix} c^D A/l & -h \\ -h & \beta^S l/A \end{bmatrix} \begin{pmatrix} x \\ Q \end{pmatrix} = \begin{bmatrix} c^D A/l & -h \\ -h & \beta^S l/A \end{bmatrix} \begin{pmatrix} \int \dot{x} dt \\ \int i dt \end{pmatrix} \tag{5.124}$$

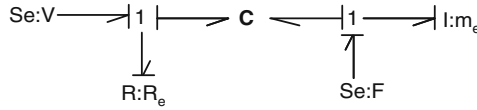


Fig. 5.77 Bond graph model of longitudinal dynamics of a piezolayer

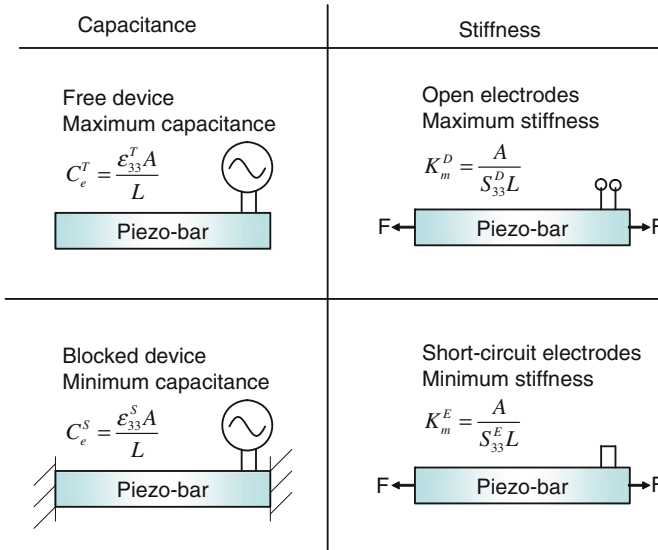


Fig. 5.78 Measurement of key piezoelectric constants

Equation 5.124 is the constitutive relation of a two-port bond graph C-field shown in Fig. 5.77 where R_e is the circuit resistance, m_e is the efficacy mass, and V and F are external effort inputs.

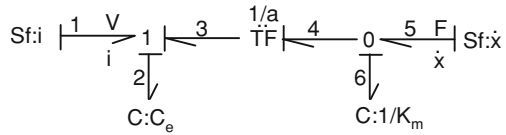
The C-field in Fig. 5.77 has a purely electrical capacitance, a mechanical stiffness, and an electromechanical coupling. These can be expressed in various ways depending upon the way the total energy is defined, which is equivalent to the way parameter measurements are taken (see Fig. 5.78). In Fig. 5.78, C_e and K_m are the electrical capacitance and mechanical stiffness, respectively, and A is the device cross-sectional area.

From Fig. 5.78, note that in a general case, $C_e^S \leq C_e \leq C_e^T$ and $K_m^E \leq K_m \leq K_m^D$.

The description used in most piezoelectric suppliers technical data defines the total energy as follows:

$$U = \frac{1}{2} K_m (x - aQ)^2 + \frac{1}{2C_e} Q^2. \tag{5.125}$$

Fig. 5.79 Bond graph model of a piezo-layer as per [114]



The terms force and voltage can be derived as $F = \frac{\partial U}{\partial x}$ and $V = \frac{\partial U}{\partial Q}$. The resulting constitutive relation in matrix form is then given as

$$\begin{pmatrix} F \\ V \end{pmatrix} = \begin{bmatrix} K_m & -K_m a \\ -K_m a & K_m a^2 + 1/C_e \end{bmatrix} \begin{pmatrix} x \\ Q \end{pmatrix} \tag{5.126}$$

where $a = -x/Q$ and $C_e = Q/V$ for $F = 0$, i.e., for free device measurement ($C_e = C_e^T$), and $K_m = -F/(aQ)$ with $x = 0$ ($K_m = K_m^S$, blocked device configuration). Thus, the stiffness matrix parameters can be experimentally determined. Most often, they are given in the piezoelectric supplier’s technical data.

The stiffness matrix in Eq. 5.126 can be used to create a bond graph model shown in Fig. 5.79 where in place of a C-field, two scalar C-elements and a coupling transformer (TF element) are used. The transformer modulus is the reciprocal of the electromechanical coupling factor, a .

From the bond graph given in Fig. 5.79,

$$\begin{aligned} F &= e_5 = e_6 \\ &= K_m \int f_6 dt = K_m \int (f_5 - f_4) dt \\ &= K_m \int (f_5 - a f_3) dt = K_m \int (\dot{x} - ai) dt \\ &= K_m (x - aQ) \\ &= K_m x - K_m aQ \end{aligned} \tag{5.127}$$

Likewise,

$$\begin{aligned} V &= e_1 = e_2 - e_3 = Q/C_e - ae_4 \\ &= Q/C_e - ae_6 \\ &= Q/C_e - aF \\ &= Q/C_e - aK_m(x - aQ) \\ &= -K_m ax + (K_m a^2 + 1/C_e)Q \end{aligned} \tag{5.128}$$

The above two relations are exactly the same as the constitutive relation of the C-field defined in Eq. 5.126.

Fig. 5.80 Bond graph model of a piezolayer as per [114] with mechanical and electrical losses

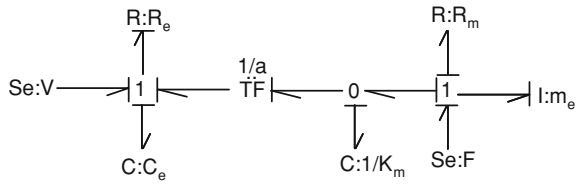
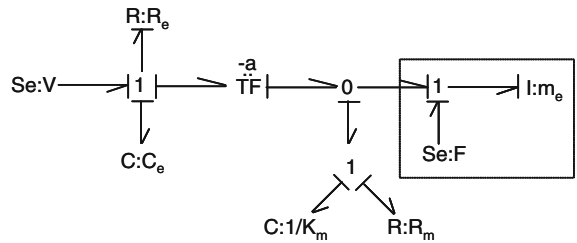


Fig. 5.81 Bond graph model of a piezolayer as per [94] with mechanical and electrical losses



The piezobar may be modeled as a lumped-mass system for first mode approximation by including the electrical and mechanical losses and the efficacy mass as shown in Fig. 5.80.

In a similar model created in [94], the mechanical losses are modeled in mechanical parallel with mechanical stiffness (see Fig. 5.81). Note that the efficacy mass and external forces shown in Fig. 5.81 are actually not present in [94], but the external flow in that work is the result of bending a piezopatch mounted on an asynchronously whirling rotor shaft.

In fact, the hysteretic damping is also included in the model developed in [114]. One of the approaches is to combine the linear capacitor $C:C_e$ and a hysteresis model so that the hysteresis model causes a perturbation in the average voltage value represented by the linear capacitor [29]. Another approach is to altogether eliminate the capacitor and substitute it with a hysteresis model, so that nonlinear phenomena like saturation, depolarization, or inverse polarization are included in the model. To maintain compatibility with the existing literature on ceramics, where constitutive relation for effective capacitance relates polarization density (P) to electric field (E), one may insert a transformer of modulus $1/l$ in all bonds around the 1 junction shown in Fig. 5.79. The resulting structure of the model then becomes the one shown in Fig. 5.82. This model is equivalent to the earlier model. The hysteresis can now be modeled by changing the constitutive relation of the C-element representing device capacitance. However, we will keep that aside at this moment.

In addition to hysteresis, piezoelements also show frequency dependent (rate-dependent) behavior and creep or relaxation, which may severely compromise positioning accuracy of the piezoactuator. These effects may be modeled in the mechanical domain by replacing the mechanical stiffness ($C : 1/K_m$) by a Kelvin–Voigt model (see Fig. 5.83) or a rate-dependent constitutive relation for the mechanical damper ($R : R_m$) between the layers [22]. Other types of bond graph models to

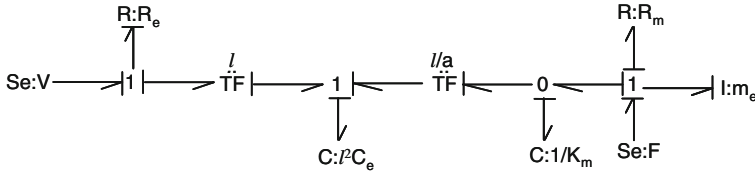


Fig. 5.82 Modified bond graph model of a piezolayer as per [114] with mechanical and electrical losses

Fig. 5.83 Bond graph model of frequency dependent relaxation and creep based on Kelvin–Voigt model

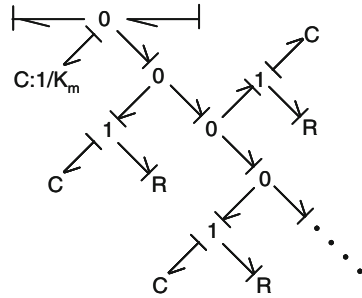
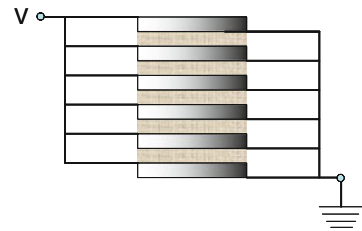


Fig. 5.84 Electrical actuation of a piezobar made from several piezoelement layers



represent hysteresis losses and frequency dependent damping can be consulted in [52, 128, 154].

Let us now consider the model of a piezobar made by stacking thin layers of piezoelectric elements as shown in Fig. 5.84.

Each layer is modeled as shown in Fig. 5.80 above. Because the layers are very thin, the efficacy mass in each layer can be considered as the sum of the layer’s mass and half the mass of the interface. The resulting model is a distributed parameter model as shown in Fig. 5.85 where R_{e1} , C_{e1} , a_1 , K_{m1} , R_{m1} , and m_1 are the parameters associated with layer 1. Likewise, subscripts 2 to n are used to defined parameters in respective layers where n is the total number of layers. As boundary conditions, the external force is applied in layer 1 ($Se:F$) and the bottom layer is fixed ($Sf:0$). The mechanical damping has been replaced by nonlinear interface dampers which model rate-dependent characteristics (this approach eliminates the need for Kelvin–Voigt model). Between the layers, the rate-dependent damping is modeled in a simplified manner at a 0-junction where the interlayer damping or loss is represented by element R_{L1} , R_{L2} , etc. with the subscripts enumerating the interfaces. The external circuit

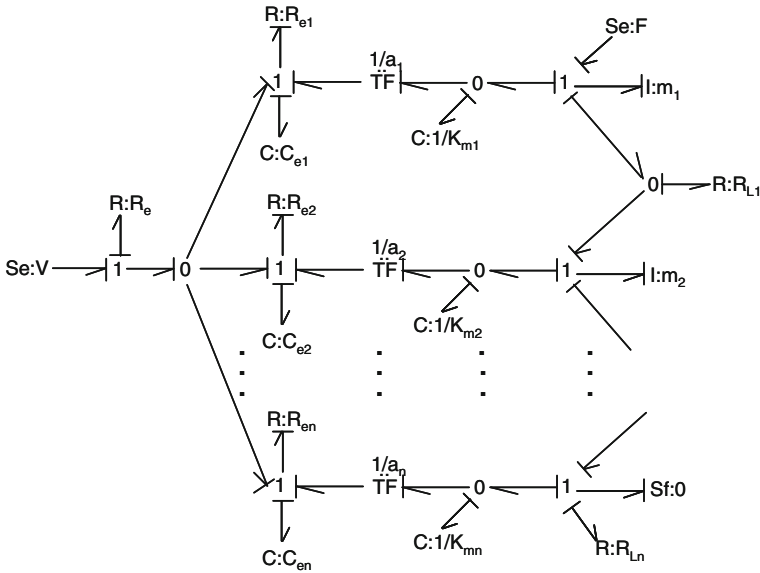


Fig. 5.85 Bond graph model of piston mode actuation of a piezobar made from several layers

resistance is modeled as a separate R-element ($R:R_e$). The element capacitances are assumed to have nonlinear constitutive relations (e.g., Ishlinkii’s backlash model [3]) to account for hysteresis. Extra states may be included at the capacitor interface to model hysteresis according to Bouc-Wen model [53].

Another form of the model in which the energy is defined in a different way is also discussed in [114]. The total energy is defined as follows:

$$U = \frac{1}{2} K_m x^2 + \frac{1}{2C_e} \left(\frac{x}{b} - Q \right)^2. \tag{5.129}$$

The force and voltage can be derived as $F = \frac{\partial U}{\partial x}$ and $V = \frac{\partial U}{\partial Q}$. The resulting constitutive relation in matrix form is then given as

$$\begin{pmatrix} F \\ V \end{pmatrix} = \begin{bmatrix} K_m + 1/(b^2 C_e) & -1/(b C_e) \\ -1/(b C_e) & 1/C_e \end{bmatrix} \begin{pmatrix} x \\ Q \end{pmatrix} \tag{5.130}$$

where $b = -V/F$ and $C_e = Q/V$ for $x = 0$, i.e., measured in blocked device configuration ($C_e = C_e^S$), and $K_m = F/x$ with $V = 0$ (i.e., $K_m = K_m^E$). Such stiffness matrix parameters can be experimentally determined and are often given in the supplier’s technical data. The stiffness matrix in Eq. 5.130 can be used to create a bond graph model shown in Fig. 5.86 where the transformer modulus is the electromechanical coupling factor, b . The extended model with electrical losses

Fig. 5.86 Alternative form of the bond graph model of a piezolayer as per [114]

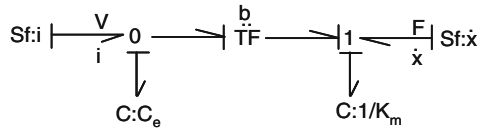


Fig. 5.87 Alternative form of the bond graph model of a piezolayer as per [114] with mechanical and electrical losses

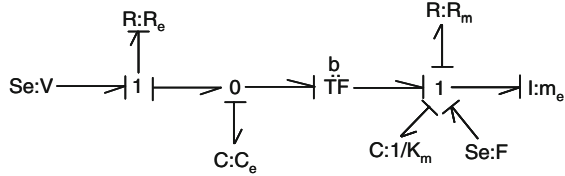
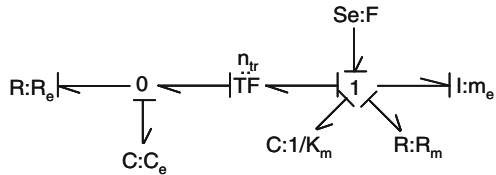


Fig. 5.88 Bond graph model of a piezostack force/pressure sensor as per [30]



(hysteresis), mechanical losses (rate-dependent damping), and efficacy mass is given in Fig. 5.87.

A similar bond graph model is used in [148]. However, their transformation factor (transformer moduli) is defined as $-Q/x$ with $F = 0$ which actually gives reciprocal of electromechanical coupling factor a (see Eq. 5.126). The coupling factor a is suitable for use in the bond graph structure presented earlier in Fig. 5.80. For the bond graph structure used in [148] and shown in Fig. 5.87, the correct transformer moduli should be b or the bond graph model structure should comply with Fig. 5.80 with transformer moduli $1/a$.

A self-powered wireless sensor system for pressure monitoring is modeled in [30]. A piezoceramic stack transduces mechanical energy to electrical form and the signal is then transmitted in the form of ultrasonic pulse trains to be received by an external receiver. Both the ultrasonic signal transmitter and receiver are piezo-based devices. The bond graph model of the transducer part that converts mechanical force (induced by pressure) to electrical domain is shown in Fig. 5.88. Note that this model can be derived from the piezobar actuator model given in 5.87 by setting the external voltage supply to be zero ($V = 0$) and changing the power directions so as to conform to the sensor mode application. The lumped elements in the model are assumed to account for the effective impedances at the ports. The electromechanical coupling transformer has a modulus n_{tr} which is given as

$$n_{tr} = \frac{nAd_{33}Y}{h} \tag{5.131}$$

where n is the number of elements in the piezostack, h is the thickness and A is the top area of each element, and Y is the Young's modulus of the material. In addition to the transducer, bond graph models of the piezo-based ultrasonic transmitter and receiver are developed and integrated in [30] and the simulated results therein have been very well matched with the experiments.

There are several other detailed models of piezoelectric sensors and actuators. Interested readers may refer to [52, 68, 75, 84–86, 145, 154].

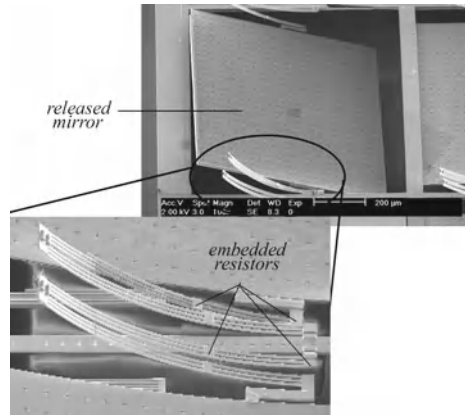
5.4.9 MEMS Devices

Microelectromechanical systems (MEMS) are micron level (0.001–0.1 mm size) mechanical devices which are operated by electricity. An MEMS device usually comprises a central processing unit, a microprocessor, and actuation and sensing parts. MEMS are fabricated using technologies used for fabrication of microelectronics components. The basic fabrication process includes deposition, patterning and etching. MEMS are generally used for sensing and actuation. MEMS technology uses integrated circuit fabrication techniques to build miniature systems with both electrical and nonelectrical components. MEMS devices provide low power consumption, space efficiency, and low weight. Examples of MEMS are microgyroscopes used in vehicle control systems, inkjet printer head, microaccelerometers used in game controllers, digital cameras, and cell phones, etc., micro pressure sensors used for blood or pneumatic tire pressure measurement, optical switches, microactuators in digital light projectors, nonvolatile computer memory or Millipede for data storage, scratch drive actuator that converts electrical energy into one-dimensional motion, electrostatic motor or capacitor motor, and biosensors and chemosensors used in medical and biological applications.

5.4.10 Micromirrors

MEMS micromirrors are used in optical systems to direct light from one position to another over a range of reflection angles. Optical MEMS are used for a variety of specialized applications such as medical imaging, projection displays, optical scanners, and optical communication systems. Texas Instrument's digital light processing (DLP) technology is based on optical MEMS. DLP technology is used in rear projection television, color projectors, digital cinema projectors, etc. In DLP projectors, microscopically small mirrors are laid out in a matrix on a semiconductor chip called digital micromirror device (DMD). Each mirror is used to represent one or more pixels in the projected image. The resolution of the projected image directly depends on the number of mirrors and their arrangement in the DMD. Each mirror can be positioned in two orientations and toggling between these two positions (on and off states) reflects light in two directions. In one orientation (on state), the light passes

Fig. 5.89 SEM of a single mirror pixel (Courtesy: Peter Gilgunn [51])



through a lens and in the other orientation (off state), the incident light is directed on to a heat sink where it is absorbed.

The reflection angle of a micromirror is controlled statically or dynamically through an actuation mechanism that rotates the mirror surface [143]. The different actuation possibilities are electrostatic, piezoelectric, electromagnetic, electrocapillary, and electrothermal actuations. Electrostatic and electrothermal actuations are the most common methods of optical MEMS actuation.

Micromirror devices can exhibit different motions: piston, rotation or a combination of both. Piston motion (displacement of mirror center perpendicular to the mirror surface without any rotation) is required to modify the phase of an optical wavefront without affecting its direction. Centroidal rotational motion is required to change the direction in which a beam of light is reflected while minimizing the effect on its phase. A combination of phase and direction modification is required in imaging applications.

The actuator selection is dependent on the type of application. Different actuation mechanisms lead to different results in terms of resonant frequency, maximum angle of rotation, energy efficiency, device size, power requirement, stability, and level of fabrication difficulty.

One example of DMD is a Complimentary Metal-Oxide-Semiconductor MEMS (CMOS-MEMS). The SEM image of single mirror pixel in a DMD fabricated at Carnegie Mellon university [51] is shown in Fig. 5.89. The mirror is connected to the actuators at its midpoint which minimizes linear (nonrotational) motion during operation. On each side of the mirror, there are two bimetallic actuators: one for positive angular motion and the other for negative angular motion. There is thermal insulation between the positive and negative actuators so that when one is flattened through heating, the other remains curled.

The arrangement of bimetallic elements (bimorphs) in a micromirror is shown schematically in Fig. 5.90. The heating elements are shown in Fig. 5.91. Two types of heating elements can be used: low resistivity polysilicon film embedded along

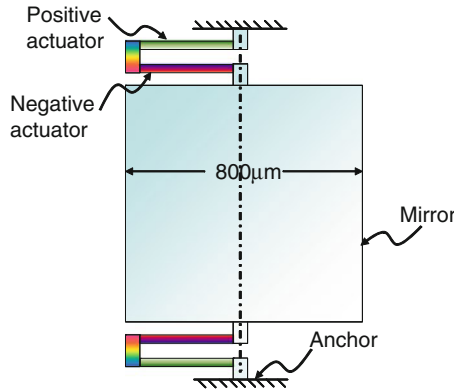


Fig. 5.90 Top view of micromirror [51] showing the mirror connection to anchor region through series connected electrothermal actuators

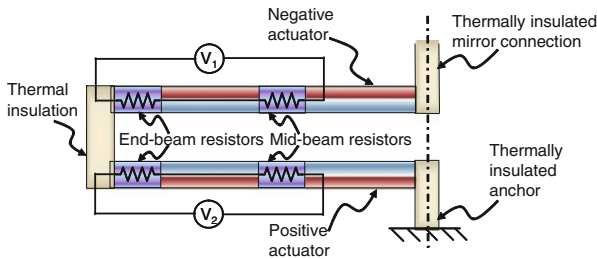
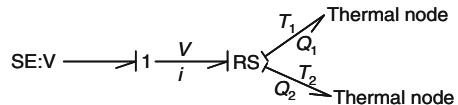


Fig. 5.91 Heating elements in CMOS-MEMS actuators

Fig. 5.92 Bond graph model of heater element in electrothermal actuators



the entire length of the actuator for distributed heat generation and high resistivity polysilicon resistors placed at discrete locations along the length of the actuators.

A lumped parameter one-dimensional model for thermal analysis has been developed in [51]. That equivalent model can be represented in a bond graph form. The bond graph model of the heating elements is shown in Fig. 5.92 where the three-port RS-element couples the electrical and thermal domains. The resistance of the heating element is assumed to be influenced by the temperature of the element. This temperature is determined from the thermal model of the corresponding layer of the bimetallic strip. The two thermal ports of the RS-field are connected to the respective nodes of the thermal models where the heat capacity of a finite element is modeled. The local temperatures tapped from the nodes of the thermal model modulate the effort sources representing nodal bending moments acting on the beam mechanical model.

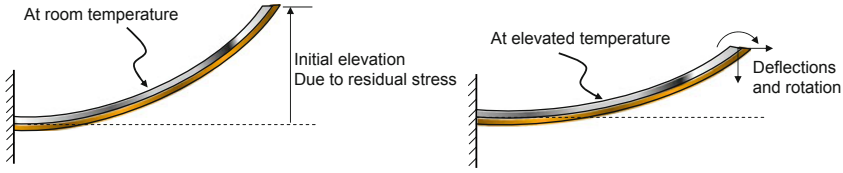


Fig. 5.93 Initial and deflected positions of the bimetallic strip used in [142] for micromirror positioning

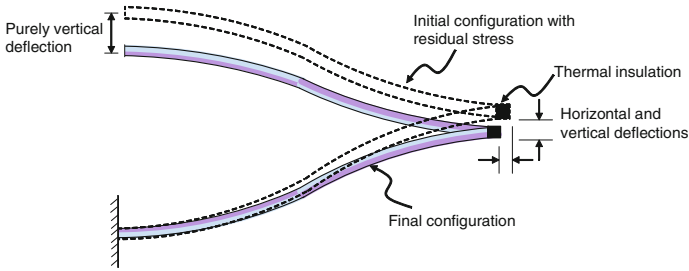


Fig. 5.94 Arrangement of bimorphs made in [142] to ensure actuator motion in one direction

The constitutive relations for the RS-element are

$$\begin{aligned}
 R &= R_1 (T_1) + R_2 (T_2) , \\
 i &= V/R , \\
 Q_1 &= i^2 R_1 (T_1) , \quad Q_2 = i^2 R_2 (T_2) , \\
 Q &= Q_1 + Q_2 .
 \end{aligned}
 \tag{5.132}$$

In this formulation, T_1 and T_2 are the temperatures in the two strips at the concerned node. If the temperature difference along the thickness direction can be neglected then the RS-element can be modeled as a two-port element with one electrical and one thermal port.

Todd et al. [142] developed a multi-degree-of-freedom electrothermal micromirror design that uses thermal inverted-series-connected (ISC) bimorph actuators. This micromirror can operate in one-dimensional piston mode and two-dimensional tilt mode. The basic building block of the ISC is a bimetallic strip with residual stress. At room temperature, the bimetallic strip is curved and shows some initial displacement. As the temperature is increased, its tip displacement decreases and the end face rotates as shown in Fig. 5.93.

Two such bimetallic strips are arranged in series where the curvatures of the two strips are opposite; thus forming a S-shape. Further, two such S-shapes are connected to form a tweezer-like shape as shown in Fig. 5.94. The benefit of such an arrangement is that when one end of this structure is fixed to the base (the substrate structure) the

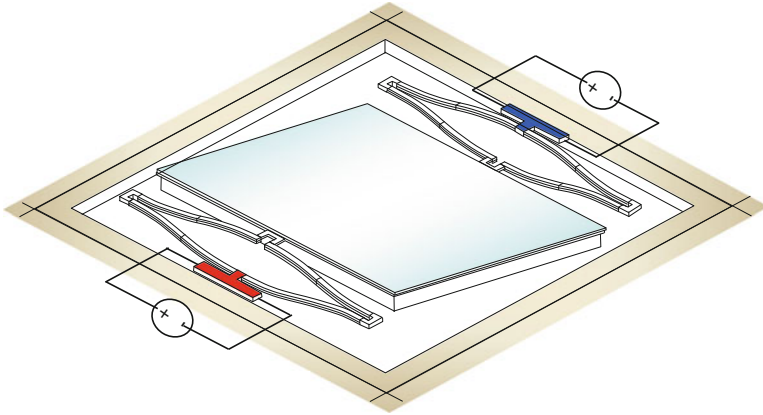


Fig. 5.95 Arrangement of ISC bimorph actuators in a single mirror pixel as developed in [142]

temperature induced displacement of the other free end of the tweezer-like shape is mostly in one direction.

This configuration allowed Todd et al. [142] to produce multi-degrees-of-freedom motion of a mirror in a micromirror array. One pixel of the array is schematically shown in Fig. 5.95. There are actually four actuator units, one attached to each side. Figure 5.95 shows two actuators. With this arrangement, the micromirror can be moved up (piston mode motion) and tilted both ways. This arrangement allows redirection of light in different angles. The electrical heating is controlled by the voltage sources connected to the thermal actuators.

5.4.11 Micromotors

Different types of micromotors use piezoelectric effect. Examples of piezoelectric motors are traveling wave motors which are used for autofocus in reflex cameras, inertial sliding motion (ISM) motors, stick-slip actuators, stepping piezo motor, etc.

5.4.11.1 Inertial Sliding Motion Motor

The inertial sliding motion motor [58] shown in Fig. 5.96 has a heavy mass M and a small mass m connected by a piezobar. The heavy mass M is in contact with ground where it encounters stick-slip friction. When the piezobar is elongated at a slow rate, the heavy mass M moves forward a little due to sticking effect whereas the smaller mass m moves backwards. The piezobar is then contracted to its initial length at a much faster rate which causes the heavy mass to move back by a much larger distance

Fig. 5.96 Schema of inertial sliding motion

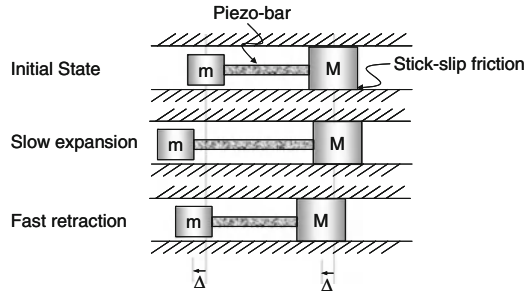
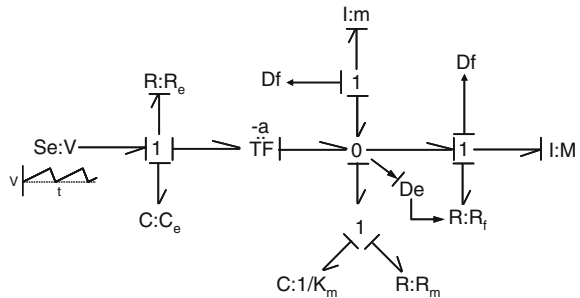


Fig. 5.97 Bond graph model of inertial sliding motion (ISM) motor



than it has moved forward during slow expansion. Repetition of this sequence causes the center of mass of the system to move backwards.

The bond graph model of the ISM device shown in Fig. 5.97 is based on the model structure of Fig. 5.81.

In the bond graph model, the relative velocity of the two masses are computed at the 0-junction in the mechanical side model. Two flow detectors (Df elements) are used to plot the results. The supply voltage is a triangular wave with a smaller slope in the first phase and a larger slope in the second phase. The stick-slip friction is modeled by R:Rf element which has the following simple constitutive relation:

$$e = \begin{cases} F, & \text{if } \dot{x} = 0 \text{ and } |F| \leq \mu_s Mg \\ \mu_s Mg * \text{sign}(F), & \text{if } \dot{x} = 0 \text{ and } |F| > \mu_s Mg \\ \mu_k Mg * \text{sign}(\dot{x}), & \text{otherwise.} \end{cases} \quad (5.133)$$

In the above equation, F is the force developed in the piezo element (i.e., the force at the 0-junction), μ_s and μ_k refer to static and kinematic friction coefficients, respectively, g is the acceleration due to gravity and $\text{sign}(\cdot)$ is the signum function. Therefore, the R-element is actually modulated by effort signal from the effort detector (De) at the 0-junction. The above equation imposes the constraint that as long as the mass is static and the applied force is below the critical force $\mu_s Mg$, the frictional forces exactly balance the applied forces. Other models of stick-slip friction can be consulted in [4, 19, 36, 64, 72, 100].

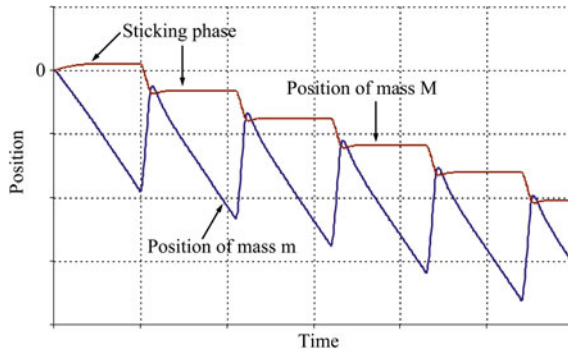


Fig. 5.98 Simulation results showing the response of inertial sliding motion (ISM) motor

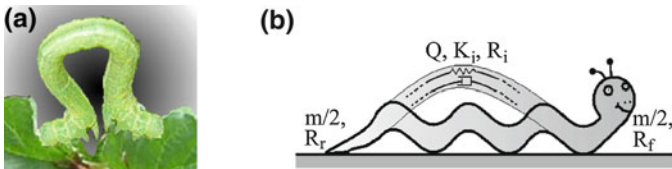


Fig. 5.99 a An inchworm, and its b schematic representation

The simulated motion of the device computed from the bond graph model is shown in Fig. 5.98. The results show clear sticking and sliding phases in the motion of the heavy mass.

5.4.11.2 Inchworm Motor

Another example of purely bar mode piezoelectric actuation is the Inchworm motor technology developed and patented by EXFO. Inchworm motor provides true linear motion with nanometer resolution. Inchworm motors use piezoelectric ceramic actuators to achieve nanometer-scale positioning steps over hundreds of millimeters and therefore, there are no backlash or mechanical drift problems encountered in such actuators. The inchworm motor is a *biologically inspired system*.

An inchworm, also called a geometrid caterpillar, is shown in Fig. 5.99a. It has a highly complex motion and for our modeling purpose, we will simplify the problem to a one-dimensional motion form as given in Fig. 5.99b. For movement, the worm bends and stiffens itself in a Ω -like shape and then lifts one of its ends to move in that direction. It then anchors the just moved end, relaxes its muscles, releases the other end, and finally pulls it to a location to again form the Ω -like shape. Thus, the worm follows two distinct steps during its motion, which constitute the two hybrid configurations of the system.

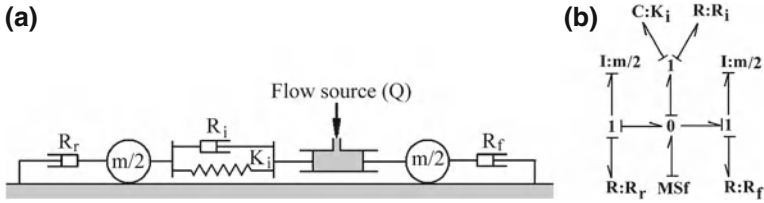


Fig. 5.100 **a** Equivalent mechanical model of an inchworm and **b** the corresponding integrally causal bond graph model

We will assume that the mass of the insect is equally lumped at its two ends. We further assume that there are two resistances (R_f and R_r) anchoring these masses to the ground and there is no ground resistance at any other place. These resistances should be modeled as stick-slip Coulomb friction, but we will show that a viscous damper gives reasonable results. The stiffening and relaxing of the muscles is assumed to be a flow source, Q , which charges a spring (bending stiffness) and damper combination (K_i and R_i). The equivalent mechanical system is then represented in Fig. 5.100a with the corresponding bond graph model in Fig. 5.100b.

Let us now evaluate the structural control properties for the inchworm system based on the theory presented in Chap. 4. We find that the control source (MSf) has causal paths to all three storage elements. We consider three separate cases here:

1. If there is no ground damping, i.e., if the surface is friction less or the worm cannot grip it properly, then we can drop the R-elements at two ends of the bond graph model. When the corresponding bond graph model is assigned preferred differential causality, as in Fig. 5.101a, we find that the system is uncontrollable. In fact, in this configuration the internal mode of vibration is controllable whereas the rigid body mode (translation of the worm as a whole) is uncontrollable. One can always verify through structural analysis that the system in Fig. 5.101a has a null mode.
2. If there is sufficient friction at the contact surface between the ground and the worm, then we can show that all the storage elements in the full bond graph model in Fig. 5.100b can be completely assigned differential causality and thus the system is controllable. However, the motion of an inchworm is hybrid in nature: in any given posture, it grips the ground at one of its ends and pulls/pushes the other end. Therefore, we should check controllability of the two hybrid modes, each one of them being represented as LTI system models. From Fig. 5.101b and c, we find that both hybrid modes of the system are controllable.
3. If we consider that the microgrippers on one end of the worm are damaged and the worm is able to grip only on its remaining end, then also the overall system remains controllable (either Fig. 5.101b or c, depending upon which end is damaged).

To validate these results, we consider that the pumping cycle (flow source) of the worm is a square wave having some amplitude q_m and a time period T . When the flow source is positive, the worm locks its rear end (i.e. modulates the damper R_r)

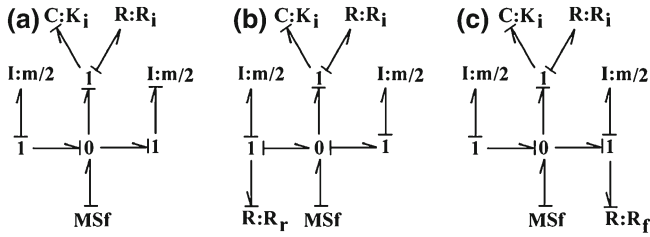
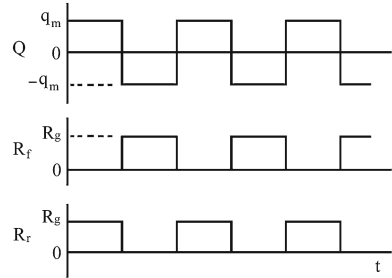


Fig. 5.101 Bond graph of inchworm model under different hybrid configurations

Fig. 5.102 Modulation of inchworm’s locomotion parameters



and keeps the front end free from ground; whereas when the flow source is negative, it locks its front end (i.e. a high damping value R_f) and releases its rear end. These periodic modulations are shown in Fig. 5.102 where R_g is the maximum value of damping.

We consider the following representative data: $m = 0.05 \text{ kg}$, $K_i = 10 \text{ N/m}$, $R_i = 0.01 \text{ N.s/m}$, $T = 10 \text{ s}$, $Q = 0.01 \text{ m/s}$, $R_g = 0.1 \text{ N.s/m}$. In the first case, we assume that both $R : R_f$ and $R : R_r$ are absent in the bond graph model. The corresponding simulation results are shown in Fig. 5.103a, where the displacement of the front end is given by the curve with \star marks and the displacement of the rear end is given by the plane curve. We find that when the front end of the worm goes ahead, the rear end goes back and vice versa; thereby meaning that the mass center of the worm does not move but the internal mode or relative displacement of the ends is controllable. This confirms our earlier results predicting overall uncontrollability of the system, which in this case refers to the uncontrollability of the rigid body mode. When we include damping at both ends of the worm and consider the modulations shown in Fig. 5.102, we find from the simulation results in Fig. 5.103b that the worm is able to move without appreciable slip.

As a special case, when we considered that the maximum damping between the worm and the ground is reduced to $R_g = 0.01 \text{ N.s/m}$, i.e., the surface became a bit slippery, then the simulation results revealed that the worm is able to move with heavy initial slip, which gradually reduces. Obviously, the worm traveled less distance in the same time. Furthermore, when we considered high damping in the rear end of the worm and assumed that the front end does not give damping then simulations revealed that the worm was able to move and cover slightly lesser distance than

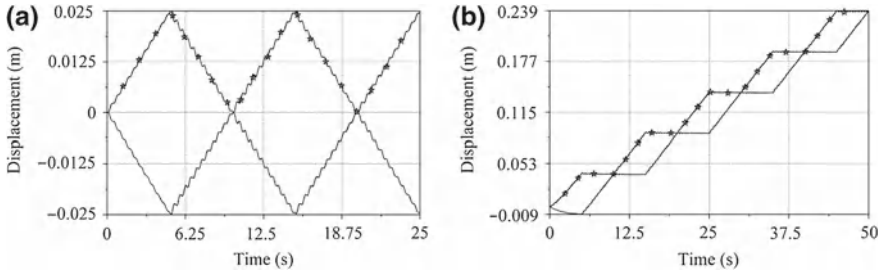


Fig. 5.103 **a** Motion of inchworm without grip and **b** motion of inchworm with proper grip

when it had damping at its both ends. This proves that the system is controllable with damping at one of its ends. When one interprets the simulation results, one finds that interestingly, when the flow source is negative and the rear end is being dragged forward (i.e. no damping at both ends during this phase), the front end does not retract significantly. This is attributed to the momentum gained by the front end during the previous half cycle of the motion. In this case, the motion of the worm is somewhat similar to inertial sliding motion (ISM).

The working principle of the inchworm motor is explained with Fig. 5.104. It is easy to find the similarities of this system and its sequence of actuation with the real inchworm’s mobility. The inchworm motor has six piezoactuators. Actuators 1 and 2 are for lateral motion and actuators 3–6 are for clutching, clamping, or gripping the shaft of the linear motor. The actuation process consists of a six step cyclical process after the initial relaxation and initialization phases. The motor can move the shaft along both directions. Depending upon the desired direction of motion, initialization phase involves gripping the motor shaft by clutching the piezo closest to the direction of desired motion (also called forward clutch piezo). In step 1, the lateral piezo is extended so that the shaft and the forward clutch piezo move forward and the backward piezo moves back. In the next step, the backward clutch piezo is engaged/extended and then in step 3, the forward clutch piezo is released/relaxed. Note that the lateral piezos are already in an extended state due to step 1. In step 4, the lateral piezos are contracted/relaxed back to their normal state as a consequence of which the motor shaft again moves forward. Steps 5 and 6 reinitialize the motor.

The inchworm motor can be modeled as shown in Fig. 5.105. due to symmetry, only one lateral actuator and two clamping actuators need to be modeled. The contact of the left and right clamping piezos with the motor shaft is modeled by $C:1/K_C$ element where K_C is the contact stiffness. This contact element is modulated by the clamping piezo displacement signal so that there is no clamping force when the piezo does not contact the shaft. The constitutive relation for $C:1/K_C$ element can be given as

$$e = \begin{cases} 0, & \text{if } y \leq \delta \\ K_C (y - \delta), & \text{if } y > \delta \end{cases} \quad (5.134)$$

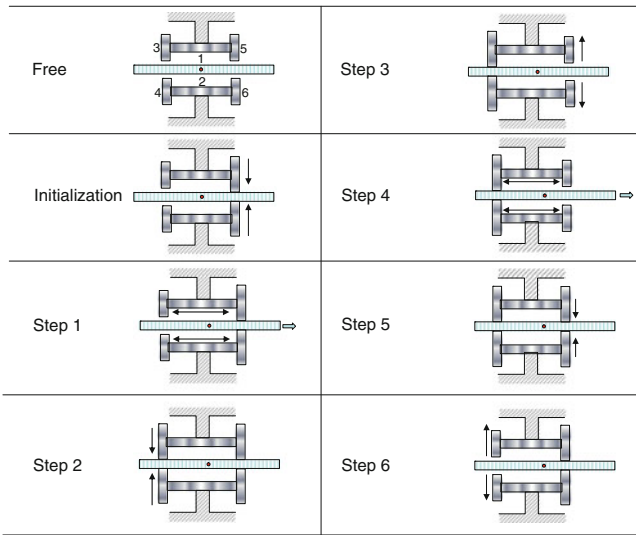


Fig. 5.104 Working principle of a biologically inspired inchworm motor

where y is the piezo displacement from its free length and δ is the initial gap. The clamping forces N_1 and N_2 modulate the friction modeled in elements $R:R_{f1}$ and $R:R_{f2}$, respectively, in addition to the longitudinal force F applied on the element. The critical force in these resistances modeling stick-slip friction are $\mu_S N_1$ and $\mu_S N_2$, respectively, where μ_S is the coefficient of static friction. The constitutive relation for these R-elements given in Eq. 5.133 is appropriately revised. The mass M refers to sum of the clutch piezo mass and half of the lateral piezo mass. The mass m refers to half of the clamping piezo mass or the corresponding efficacy mass. The supply voltages to the piezos are regulated as per the sequence described in Fig. 5.104 and they are shown to the right of the bond graph model in Fig. 5.105.

5.4.12 Energy Harvesting System

A micro piezoelectric energy harvesting system (see Fig. 5.106) is modeled in [48]. Such kind of energy extraction is useful to power sensor networks for process monitoring especially where it is difficult to change the batteries regularly, e.g., in an underwater monitoring system. The source from which the energy can be harvested can be vibration of mechanical structures, pressure gradient, wind, light, human motion, temperature gradient, etc. In cantilever type piezoelectric energy harnessing/harvesting applications, d_{31} mode (transverse effect) of electromechanical coupling is preferred over the d_{33} mode because it allows more energy recovery and the

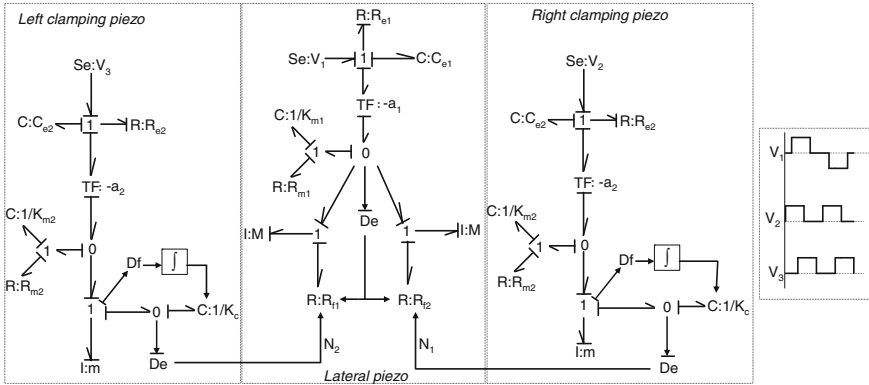
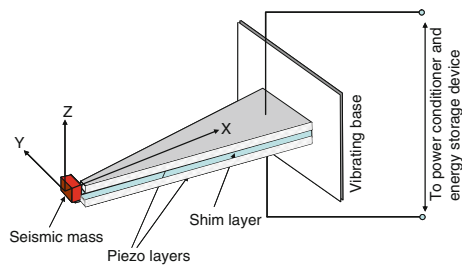


Fig. 5.105 Bond graph model of a biologically inspired inchworm motor

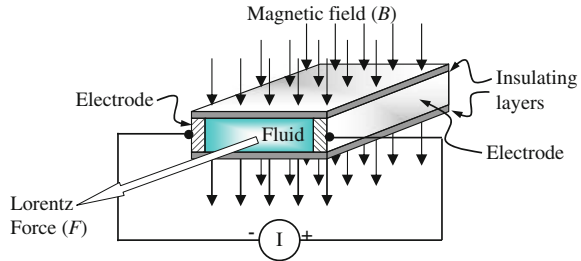
Fig. 5.106 A cantilever type energy harvesting system



resonant frequency (where maximum energy is transferred) is lower in this mode. The strain along X-axis is converted to potential along poling axis (Z-axis). By properly adjusting the seismic mass to create resonant frequency matching the base excitation frequency and appropriately tuning the power conditioner/rectifier parameters [47], good amount of energy can be harvested.

The bending mode operation of piezoelement should be ideally modeled as discussed earlier in this section, i.e., as per the model given in [128]. However, for thin beams, the model can be given in the form of the junction structure shown in Fig. 5.80 with the transformer modulus being the electromechanical coupling factor k_{31} . In [48], stress and strain are used as bond graph power variables in the mechanical domain and voltage and current are power variables in the electrical domain. Consequently, the multiplication of effort and flow variables in a bond in the mechanical domain is power per unit volume. The transformer modulus is thus multiplied with the volume of the piezoelement to couple the mechanical and electrical domains. However, such an ad hoc model can be improved to the full bending mode model, i.e., by including the two-port C-field representation given in Fig. 5.74a.

Fig. 5.107 Working principle of MHD micropump



5.4.13 Micropumps

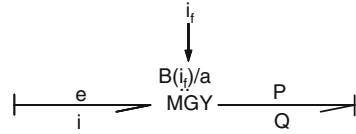
Micropumps are usually nonmechanical pumps which rely on electrokinetic effect, acoustic streaming, magnetohydrodynamic (MHD) effect and electrochemical (ECM) effect etc. for microscale fluid transport. Their major applications are found in medical diagnostics, genetic sequencing, chemistry production, drug discovery, and proteomics etc. Micropump is the most essential and important item of a microfluidic device. Although mechanical type micropumps based on electrostatic, electromagnetic, pneumatic, thermopneumatic, and piezoelectric force are available, they are less reliable due to high pressure drops across the check valves and mechanical fatigue of components with low mechanical strength. Therefore, nonmechanical micropumps are preferred. In this part, we will discuss an AC type micropump based on MHD principle which was successfully developed in [74] and fabricated using UV-LIGA (Lithography, Electroplating, and Molding with ultraviolet light source) fabrication.

The MHD principle drives the fluid due to Lorentz force. When an electrical current is supplied to a conductor in a magnetic field, Lorentz force orthogonal to both the electric current and magnetic field is generated on the current carrying conductor. When an electrical field is applied across an electrically conductive fluid filled between two facing electrodes in a channel, ionic transport leads to the transport of charges and hence to the flow of electrical current through the electrolyte solution. If an external magnetic field is applied perpendicular to the direction of the ionic current then Lorentz body force is generated on the fluid element which generates a pressure difference that drives the fluid to flow along the channel. This principle is schematically illustrated in Fig. 5.107.

DC supply to the electrodes leads to bubble generation problems caused by electrolysis of the working fluid (see discussions on fuel cells given in the next chapter). Therefore, AC supply with a sufficiently high frequency across the two facing electrodes of the micropump can be used. AC supply causes formation of a double layer (akin to a capacitor) at the metal electrodes. This way, the fluid can be pumped in the same manner without any electrolysis effect [74].

For one-dimensional fluid flow, under certain assumptions, the following relations hold good [74]:

Fig. 5.108 Bond graph of coupling between hydraulic and electrical domain in MHD micropump



$$\begin{aligned}
 P &= B(i_f) \frac{i}{a} \\
 e &= B(i_f) \frac{Q}{a}
 \end{aligned}
 \tag{5.135}$$

where P , Q , e , and i are, respectively, the fluid pressure difference, fluid volume flow rate, voltage across the electrodes and the current passing through the electrodes and fluid. The magnetic field B is a function of the current i_f through the coils of an electromagnet and a is the pump channel height or depth. If the effort and flow variables in the electrical side are e and i , respectively, and those in the hydraulic side are P and Q , respectively, Eq. 5.135 defines the constitutive relations of a modulated gyrator (MGY) as shown in Fig. 5.108.

If the current through the electromagnet $i_f = I_0 \sin(\omega t)$ with I_0 as current amplitude and ω as its frequency then the induced magnetic field is given as [74]

$$B(i_f) = \frac{\mu_i N}{2\sqrt{l^2 + r^2}} I_0 \sin(\omega t)
 \tag{5.136}$$

where l , r , μ_i , and N are the length, radius, and permeability of the magnetic core, and the number of turns, respectively.

The current supply to the electrodes is synchronous with the supply to the magnetic core. It is given as

$$i = \frac{a\sigma L}{b} E_0 \sin(\omega t)
 \tag{5.137}$$

where a , b , σ , L , and E_0 are the depth and width of the microchannel, conductivity of the fluid, channel length and the amplitude of input voltage signal, respectively. The current to the electrodes is directly modeled as a source of flow in [74].

For one-dimensional fluid flow modeling, the microchannel can be reticulated into a finite number of small elements. This way, lumped parameter modeling of a distributed parameter system is possible. The principle of reticulation has been already discussed while dealing with beam modeling. The one-dimensional fluid flow modeling has been extensively discussed in a book [91]. The fluid inertia is given as

$$I = \rho \int \frac{dl}{A(l)}
 \tag{5.138}$$

where ρ is the fluid density, dl is a length segment along the direction of flow, and A is the cross-sectional area of the tube. Note that the pressure momentum is $I Q$ and for a pipe segment of length ΔL with uniform area A , $I = \rho \Delta L / A$.

From definition of bulk modulus of a fluid $P = -\beta \Delta V / V$, the capacitance of a fluid element (see discussions on liquid springs in the next chapter) is given as

$$C = \frac{V}{\beta} = \frac{A \Delta L}{\beta} \text{ so that } -P = \Delta V / C \quad (5.139)$$

where β is the bulk modulus of the fluid, V is the volume of the considered element, A and ΔL are the cross-sectional area and length of the considered element.

The resistance to fluid flow is given as [74]

$$R = \frac{8\mu \Delta L (a + b)^2}{a^3 b^3} \quad (5.140)$$

where μ is the viscosity of the fluid and a and b are the channel dimensions mentioned earlier.

The fluid flow is thus modeled as an equivalent electrical circuit with inductance, capacitance and resistance. The pressure difference is imposed on the circuit through the modulated gyrator and the flow source. However, without modeling of the double layer capacitor, the model remains incomplete.

The double layer capacitor is usually modeled by Randles equivalent circuit [111] shown in Fig. 5.109a whose bond graph model is shown in Fig. 5.109b where e_s is the voltage applied across the electrodes. The resistance to current flow from electrode to the working fluid is an active electrolyte resistance R_s which is a kind of ohmic or uncompensated resistance. Note that, in our case, R_c is the ohmic resistance within the fluid, i.e., $\frac{b}{a\sigma L}$, as defined in Eq. 5.137 and can include other circuit losses. In addition, R_{ct} is the polarization resistance or charge transfer resistance at the interface between the electrode and the electrolyte. The electrode holds a charge density which arises from either an excess or deficiency of electrons at the electrodes. This phenomena is modeled as a double layer capacitor C_d . More details on these aspects are given in the next chapter during discussions on fuel cell systems. The resistances and capacitances in the Randles equivalent circuit model are determined from electrochemical impedance spectroscopy (EIS) [73].

The micropump channel model is given in Fig. 5.110 where the fluid line in the entire channel has been divided into two capacitive elements (C_h) and three nodes representing fluid inertia (I_h) and resistance (R_h). This model is based on the model given in [74] with some modifications. The constitutive relations for fluid inertia, capacity and resistance are given in Eqs. 5.138, 5.139 and 5.140, respectively. The driving Lorentz force (pressure difference) is applied through three gyrators which couple hydraulic and electromagnetic domains through three Randles equivalent circuit models. These gyrators are modulated by current signals (i_f). Two transformers with modulus n_1 and n_2 scale the voltage supplied to the electrodes and the coils of the electromagnet, respectively. The current passing through the electromagnet is

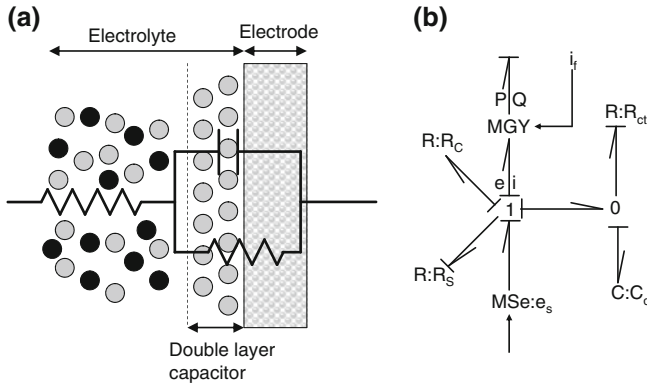


Fig. 5.109 a Randles equivalent circuit and b its bond graph model

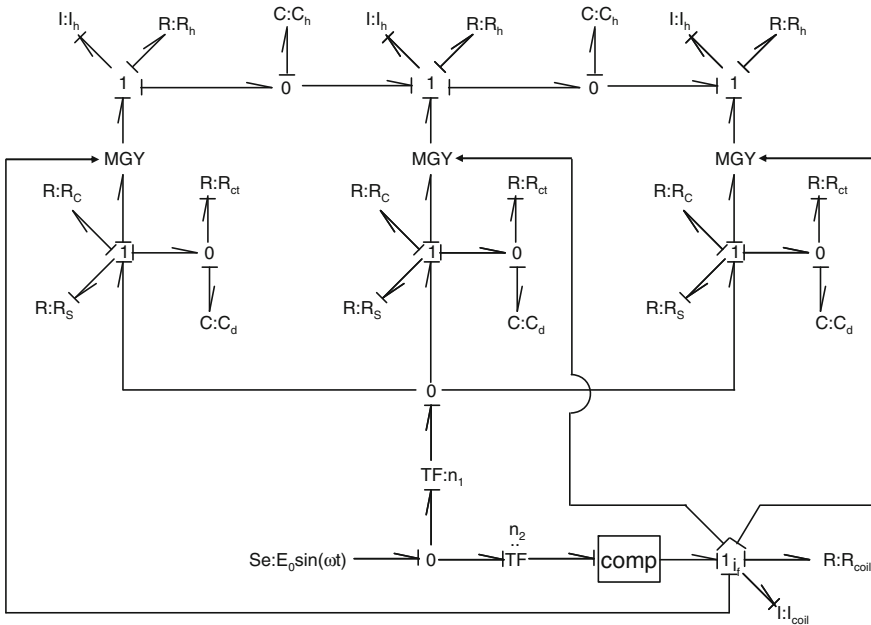


Fig. 5.110 Bond graph model of MHD micropump

synchronized with the current passing through the electrolyte by a phase-shift compensator (modeled in block ‘comp’). The coil inductance and resistance are modeled by elements $I:I_{coil}$ and $R:R_{coil}$, respectively. Note that the hydraulic circuit model given in [74] contains a C-element at the right most 1-junction. That C-element is removed here because it impedes fluid flow (i.e., hooks the fluid element to an inertial frame).

5.4.14 Shape-Memory Alloys

A shape-memory alloy (SMA) is an alloy metal that can remember an original shape to which it can return upon application of external stimuli like stress, temperature, electric, or magnetic fields. Thus, the shape-memory effect refers to the capacity of a material to trigger a predefined shape change when exposed to some particular external stimulus. The thermal shape-memory effect is caused by the changes of crystalline structure from austenite phase to stable martensite phase and vice versa as a consequence of heating or cooling. There are several types of shape-memory alloys among which the mostly used ones are the copper-zinc-aluminum-nickel, copper-aluminum-nickel, and nickel-titanium (NiTi) alloys. Nickel-titanium alloy, though expensive, is a biocompatible thermal SMA which offers good controllability, high work per unit volume, repeatability (number of cycles) and low current for activation. It is widely used and commercialized under trade name Nitinol (Nickel Titanium Naval Ordnance Laboratories).

A thermal SMA can be plastically deformed in low temperature martensite phase and when heated sufficiently to transform martensite to austenite, it returns to the cold-forged shape prior to the deformation. This kind of recovery of shape from large deformations is referred to as pseudoelasticity. At temperature below the transformation temperature, the crystalline structure of SMA changes to martensite where it can be easily deformed. In some SMAs, applied force or stress causes the transformation between martensite and austenite phases. When the material is reheated above the transformation temperature, the crystalline structure of SMA changes to austenite and the material recovers its memorized austenite shape. This process, under zero stress, is schematically shown in Fig. 5.111, where the martensite fraction R_m is plotted versus the temperature T . In cold state, the crystal structure of the material is pure martensite ($R_m = 1$). During heating, the temperatures at which the transformation from martensite to austenite starts and finishes are denoted by T_{AS} and T_{AF} , respectively. However, the transition temperatures are different when the material is cooled: martensite formation starts at T_{MS} and continues till the temperature is lowered to T_{MF} where all austenite is converted to stable martensite. Thus, $T_{MF} < T_{MS} < T_{AS} < T_{AF}$. Repeated use of the shape-memory effect can shift these characteristic transformation temperatures.

Phase transformation also takes place in SMA materials due to application of stress. The superelastic behavior of SMA material under uniaxial loading is schematically shown in Fig. 5.112. If stress is gradually increased in an initially austenite SMA material and the temperature is held constant then the phase transformation starts at a certain strain and thereafter the effective stiffness of material remains very small allowing large deformation till another limiting strain is reached. After this limiting strain, the material contains fully twinned martensite and the stiffness becomes large. However, when the material is in martensite form at large strain and the stress is gradually reduced (i.e., unloading phenomenon) then nature of the stress–strain curve is different from the one that describes the loading phenomenon. The loading and unloading cycles thus produce a hysteresis cycle.

Fig. 5.111 Phase transformation with change in temperature at constant stress in a shape-memory alloy

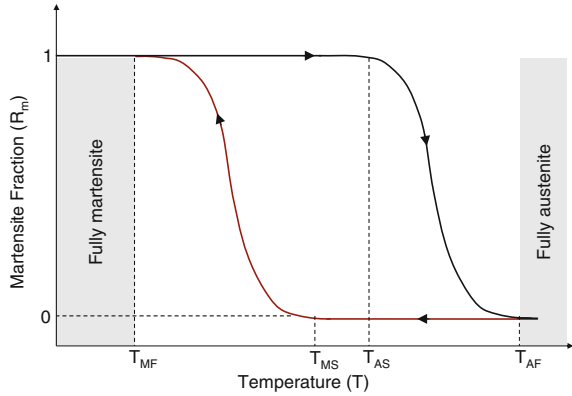
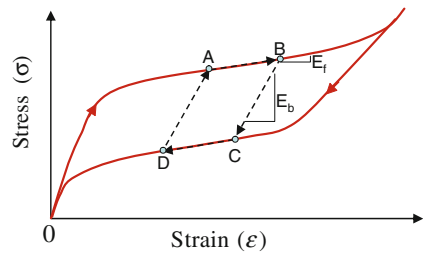


Fig. 5.112 Superelastic behavior in a shape-memory alloy under uniaxial loading and unloading

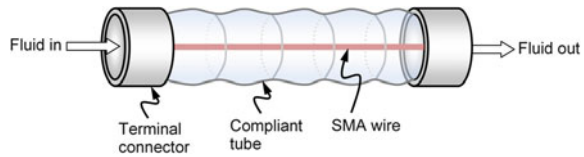


A partial loading and unloading curve is shown by points A, B, C, and D in Fig. 5.112. While loading from point A to B, the apparent modulus of elasticity is E_f . If one starts unloading from point B then the modulus of elasticity in the return path is $E_b > E_f$. Thus, at point B, the stiffnesses of the SMA element in forward and backward loading are different. The same happens at other points. This property of the SMA material is very useful in designing a variety of microactuators.

SMA material is lightweight. Thus, it is used as a solid-state alternative to conventional actuators. SMA actuators have compact design, high power-to-weight ratio, smooth noiseless operation and precise controllability. However, low efficiency, degradation, fatigue, and slow response time (or bandwidth) are some of its disadvantages. The later (slow response time) is primarily due to the slowness of thermal conduction (heating and cooling) and can be remedied by using magnetic field actuated SMAs. Shape-memory alloys belong to the group of smart or intelligent materials whose one or more properties can be significantly controlled in a predictable and useful manner. Thus, actuators made from SMA material are also called smart actuators.

Modern robots such as exoskeletons and haptic devices are becoming increasingly complex with large number of degrees-of-freedom (DOFs) and equally large number of actuators to control and power them. One needs compact and lightweight actuators with efficient control architecture and mechanism of power delivery so that hundreds

Fig. 5.113 A unit of wet SMA actuator



of actuators can be accommodated in limited space. This is why SMA actuators are gaining wide use in the field of microrobotics.

The human muscles are powered by the nutrition received from the circulating blood. Recently, development of biologically inspired artificial muscles has been inspired by the fluidic heating and cooling of the body through blood vessels. Robotic systems can function by circulating fluid to deliver power. There is a new concept of vasculated robotic flesh where a network of fluid vessels delivers power to embedded fluidic actuators.

The compliant vessels in these fluidic actuators contain thermal SMA wires, which are contracted and/or extended through combined fluidic and electric power (see Fig. 5.113). Such fluidic actuators, called wet SMA actuators, can be arranged in parallel or series to create artificial muscle bundles and arrays. Wet SMA actuator bundles and arrays implement networks of fluidic valves and electrical switches to direct hot and cold water to actuators and to control electric current to the actuators, respectively. Wet SMA actuators offer strength and compactness in excess of hundreds of times of that of human muscle and they can recover significant amount of strain (more than 0.06). The constituents of a wet SMA actuator are: the active SMA wire elements, the mechanical structure or the compliant vessel, the drive and control system, the power system, and the forced heating/cooling system. As is evident from the constituents, design of SMA actuators needs an interdisciplinary approach such as bond graph modeling.

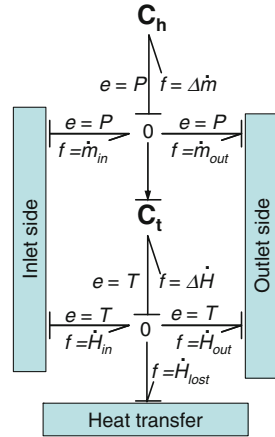
A unit wet SMA actuator is shown in Fig. 5.113. Several such actuators are connected either in series, parallel or both. The terminal connectors are rigid and the tube is flexible. Fluid enters and exits through the terminal connectors. A thin SMA wire is connected between the terminal connectors.

The bond graph model of the physical wet SMA actuator has five distinct parts: fluid flow, heat convection through the fluid, heat transfer from the fluid to the SMA wire and tube, mechanical contraction/extension of the SMA wire and the mechanical load on the actuator.

The thermofluid model of the fluid flow can be developed based on well-defined formalisms established in [82, 102, 103, 118, 137]. Usually, it is easier to model thermofluid systems using pseudobond graphs. In a pseudobond graph, the product of effort and flow variables does not give power; however, all the constraint relations remain the same. Power conservation is not guaranteed in a pseudobond graph and it has to be explicitly maintained by adding extra sources.

The pseudo power variables chosen for thermofluid system are as follows: in the hydraulic domain, pressure (P) is the effort variable and mass flow rate (\dot{m}) is the

Fig. 5.114 Bond graph model of thermo-fluid storage capacitor



flow variable; in the thermal domain, temperature of the fluid (T) is the effort variable and enthalpy flow rate (\dot{H}) is the flow variable. If the fluid is assumed to be single phase and incompressible then the rate of change of internal energy of a fluid of volume V can be written as $\dot{E} = \dot{H} - V\dot{P}$. Further assuming that the change in pressure in the fluid line of the wet SMA actuator is small, one can write $\dot{E} \simeq \dot{H}$. Under these assumptions, the bond graph model for hydraulic and thermal energy storage in a control volume is given as shown in Fig. 5.114.

In Fig. 5.114, C_h represents the hydraulic capacity whose constitutive relation is given as

$$P = \frac{1}{C_h} \int \dot{m} dt = \frac{1}{C_h} \int (\dot{m}_{in} - \dot{m}_{out}) dt \tag{5.141}$$

where \dot{m}_{in} and \dot{m}_{out} are, respectively, the inlet and outlet mass flow rates to/from the control volume.

Note that for the incompressible fluid, C_h is computed from the flexibility of the compliant tube of the wet SMA actuator. If the tube is assumed to be a thin-walled cylinder then neglecting thermal expansion of the tube, the hoop and tangential stresses in the tube walls can be used to compute the volume change of the tube for given internal pressure. This way, a theoretical value of hydraulic capacity relating change in pressure to change in volume (proportional to change in mass) can be derived. However, when bellows are used as tube, the easiest way to determine the hydraulic capacity is through experiments.

The temperature of the fluid element can be given as

$$T = \frac{H}{mc_v} = \frac{1}{mc_v} \int (\dot{H}_{in} - \dot{H}_{out} - \dot{H}_{lost}) dt = \frac{\int (\dot{H}_{in} - \dot{H}_{out} - \dot{H}_{lost}) dt}{c_v \int (\dot{m}_{in} - \dot{m}_{out}) dt} \tag{5.142}$$

where c_v is the specific heat of the fluid at constant volume, \dot{H}_{in} , \dot{H}_{out} , and \dot{H}_{lost} are, respectively, the inlet, outlet, and lost/gained enthalpy flow rates to/from the control volume. The enthalpy lost/gained is primarily due to heat transfer from the fluid to the tube and to the SMA wire.

From Eq. 5.142, it is found that the thermal capacity of the fluid is $C_t = mc_v$, which depends on the mass of the fluid in the control volume. One can write $C_t = (C_h P) c_v$. Therefore, the thermal energy storage shown in the bond graph model in Fig. 5.114 is represented by a modulated C-element in which fluid pressure P is a modulating signal from the 0-junction in the hydraulic part of the model.

Note that for single phase thermofluid energy storage, the hydraulic part of the model is assumed to influence the thermal part of the model, but the reverse influence (e.g., thermal expansion, variation of c_v with temperature, change in tube material constants like Young's modulus and Poisson's ratio due to temperature, etc.) is neglected. In a more complicated model, these could be included and the two scalar single-port C-elements in the hydraulic and thermal parts of the model can be merged to a two-port C-field representation.

The thermofluid transport is used to model flow through a pipe, valve, etc. It is assumed that all heat transfer takes place from the storage element and no heat loss/gain occurs during the transport. The fluid inertia is neglected. The mass flow rate through the pipe is modeled by the element R_h in the bond graph model given in Fig. 5.115. Its constitutive relation is given by accounting for the wall and viscous friction losses [13, 14, 137]. For laminar flow, it may be modeled as a linear damper with the constitutive relation

$$\dot{m} = \frac{\Delta P}{R_h} \quad (5.143)$$

The enthalpy flow through the pipe depends on the direction of flow. If the pressure and temperature of upstream side are denoted by P_u and T_u , respectively, and those for the downstream side are P_d and T_d , respectively, and the velocity of the fluid is assumed to be small then the enthalpy flow rate can be written as

$$\dot{H} = \begin{cases} \dot{m}c_v T_u & \text{if } \dot{m} > 0 \text{ or } P_u > P_d \\ \dot{m}c_v T_d & \text{if } \dot{m} < 0 \text{ or } P_u < P_d \\ 0 & \text{if } \dot{m} = 0 \text{ or } P_u = P_d \end{cases} \quad (5.144)$$

Equation 5.144 defines constitutive relation for the Coupling Element for Thermofluid (CETF) transport [103, 118, 119] as shown in Fig. 5.115.

The modeling of shape-memory wire requires proper accounting of the martensite fraction R_m which is the volume fraction of martensite in the metal. When cold, the crystalline structure is purely martensite, i.e., $R_m = 1$. When heated above recrystallization temperature, pure austenite phase is produced, i.e., $R_m = 0$. Thus, if the austenite volume fraction is denoted by R_a , at any time $R_a + R_m = 1$.

The slope of the martensite volume fraction versus temperature curve given in Fig. 5.111 can be approximated with a normal distribution [41] (see Fig. 5.116). Thus, one can write

Fig. 5.115 Bond graph model of thermofluid transport

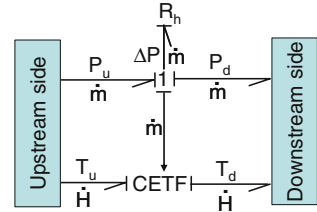
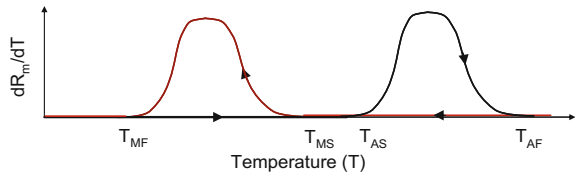


Fig. 5.116 Rate of martensite fraction with change in temperature of SMA material



$$\frac{dR_m}{dT} = \frac{1}{\sqrt{2\pi}\sigma_T} e^{-\left(\frac{T-T_a}{\sqrt{2}\sigma_T}\right)^2} \tag{5.145}$$

which upon integration gives

$$R_m = \frac{1}{2} \left(1 - \operatorname{erf} \left(\frac{T - T_a}{\sqrt{2}\sigma_T} \right) \right) \tag{5.146}$$

where $\operatorname{erf}(\cdot)$ is the error function, T is the wire temperature, T_a is the average temperature at which phase transformation occurs, and σ_T is the standard deviation of the temperature for phase transformation. From Fig. 5.116, it should be noted that the values of T_a and σ_T during phase transformation from martensite to austenite (i.e., heating) are different from those during phase transformation from austenite to martensite (i.e., cooling).

Thus, taking the hysteresis into account, the martensite fraction is written as

$$R_m = \begin{cases} \frac{1}{2} \left(1 - \operatorname{erf} \left(\frac{T - T_a^A}{\sqrt{2}\sigma_T^A} \right) \right) & \text{for forward transformation} \\ \frac{1}{2} \left(1 - \operatorname{erf} \left(\frac{T - T_a^M}{\sqrt{2}\sigma_T^M} \right) \right) & \text{for reverse transformation} \end{cases} \tag{5.147}$$

where T_a^A ($T_{AS} < T_a^A < T_{AF}$) and σ_T^A correspond to mean and standard deviation of the transformation temperature during phase transformation from martensite to austenite and T_a^M ($T_{MF} < T_a^M < T_{MS}$) and σ_T^M are the corresponding variables during reverse transformation, and the temperature in the previous time step is used to determine whether the SMA wire is being cooled or heated.

The phase transformation is also stress dependent. The transformation temperatures are influenced by the stress applied on the SMA element. However, transformation temperatures are assumed to be constants in [41] because the stresses on

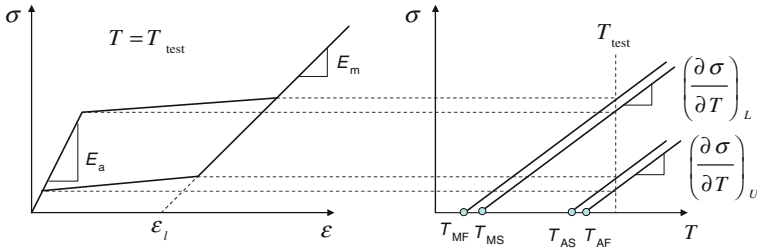


Fig. 5.117 Stress and temperature dependence of SMA material parameters and definition of stress influence coefficient

the SMA wire are small and the influence of small static load has been accounted for in calculation of average transformation temperature T_a . In reality, the relationship between transformation temperature and applied stress is linear, with different proportionality constants for forward and reverse transformations. These proportionality constants are called stress influence coefficients. The hysteretic loading of the SMA wire, the pseudoelastic behavior and the temperature dependence (stress influence coefficients) are shown in Fig. 5.117 where E_a and E_m are stiffness of the fully austenite and fully martensite phases, respectively, and ϵ_L is the total recovery strain. The stress influence coefficients, which are usually constant, are $\frac{\partial \sigma}{\partial T}$ during loading and unloading phases (indicated by subscripts L and U , respectively, in Fig. 5.117). Note that at zero stress, the transition temperatures are the ones shown in Fig. 5.111. As the applied stress increases, the transition temperatures change proportionally. Figure 5.117 shows the stress values at which phase transformations start and finish for a given temperature. Alternatively, it shows the temperature values at which the phase transformations start and end for a given stress. For time varying stress and temperature, the transition points have to be dynamically computed.

By using the so-called variable sublayer model [41] and neglecting the stress influence coefficients, the stress in the SMA wire can be written as

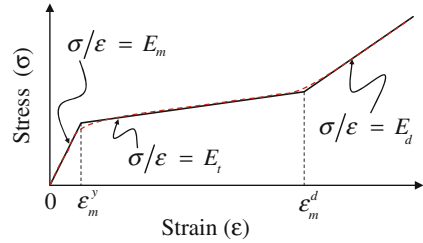
$$\sigma = R_a \sigma_a + R_m \sigma_m = (1 - R_m) \sigma_a + R_m \sigma_m \tag{5.148}$$

where the factored stresses σ_a and σ_m in austenite and martensite phases can be written in terms of respective stress–strain relationships.

The deformation in the high temperature austenite phase is assumed to be mostly elastic so that when $R_m = 0$, the material behaves in purely elastic manner (regains its shape). Thus, one can write $\sigma_a = \epsilon E_a$ where $\epsilon = \Delta L/L$ is the common strain for both the phases, ΔL is the elongation of the SMA wire and L is the free length of the wire, and E_a is the modulus of elasticity of the austenite phase.

The deformation of the martensite phase is nonlinear because the martensite phase is in a fully twinned state at low strains and becomes fully detwinned at high strains. In the in between regime, the martensite phase is partially twinned and has the least elastic modulus, i.e., allows large change in strain for small increment in stress.

Fig. 5.118 Stress in martensite sublayer versus the strain as per the variable sublayer model



There are no clear cut strain values at which these transitions take place. Therefore, averaged transition points are assumed to represent the stress–strain relationship. One such approximate representation [41] is shown in Fig. 5.118 where the martensite phase is fully twinned for $\epsilon < \epsilon_m^y$ and fully detwinned for $\epsilon > \epsilon_m^d$, and E_m , E_t and E_d are the averaged moduli of elasticity for $\epsilon < \epsilon_m^y$, $\epsilon_m^y \leq \epsilon \leq \epsilon_m^d$ and $\epsilon > \epsilon_m^d$, respectively.

Then, the stress in the martensite sublayer can be written as

$$\sigma_m = \begin{cases} \epsilon E_m & \text{for } \epsilon < \epsilon_m^y \\ \epsilon_m^y E_m + (\epsilon - \epsilon_m^y) E_t & \text{for } \epsilon_m^y \leq \epsilon \leq \epsilon_m^d \\ \epsilon_m^y E_m + (\epsilon_m^d - \epsilon_m^y) E_t + (\epsilon - \epsilon_m^d) E_d & \text{for } \epsilon > \epsilon_m^d \end{cases} \quad (5.149)$$

If the variation in wire diameter due to stress is neglected then for wire cross-section A and elongation $x = \Delta L$, one can write

$$\begin{aligned} F_x &= ((1 - R_m) \sigma_a + R_m \sigma_m) A \\ &= (1 - R_m(T)) E_a A x / L + R_m(T) \sigma_m(x/L, E_m, E_t, E_d) A \end{aligned} \quad (5.150)$$

where $R_m(T)$ is written as a function to show that the martensite fraction is a function of the temperature and $\sigma_m(x/L, E_m, E_t, E_d)$ is the constitutive relation defined in Eq. 5.149.

A somewhat improved equation depicting stress, strain, temperature, and martensite volume fraction is given by Tanaka [136] and Liang-Rogers [77] models which can be written as

$$\sigma - \sigma_S = E(R_m)\{\epsilon - \epsilon_S\} + \theta(T)\{T - T_S\} + \Omega(R_m)\{R_m - R_{mS}\} \quad (5.151)$$

with

$$E(R_m) = (1 - R_m)E_a + R_mE_m$$

and

$$\Omega(R_m) = -E(R_m)\epsilon_L$$

where Ω is thermoelastic constant of SMA, ε_L is the total recovery strain, $\theta(T)$ is a material function of temperature, and ε_S , T_S and R_{mS} indicate the initial strain, temperature, and martensite fraction, respectively. The term $\theta(T)\{T - T_S\}$ is usually negligible compared to the other terms and can be dropped.

In Tanaka model [136], the martensite fraction evolution is given as

$$R_m = \begin{cases} 1 - \exp(a_M(T_{MS} - T) + b_M\sigma) & \text{for austenite to martensite transformation} \\ \exp(a_A(T_{AS} - T) + b_A\sigma) & \text{for martensite to austenite transformation} \end{cases} \quad (5.152)$$

where the material constants a_M , b_M , a_A , and b_A are defined as

$$a_A = \frac{\ln(0.01)}{T_{AS} - T_{AF}}, \quad b_A = \frac{a_A}{C_A},$$

$$a_M = \frac{\ln(0.01)}{T_{MS} - T_{MF}}, \quad b_M = \frac{a_M}{C_M},$$

with the stress influence coefficients $C_A = \left(\frac{\partial\sigma}{\partial T}\right)_U$ and $C_M = \left(\frac{\partial\sigma}{\partial T}\right)_L$. The material parameters are evaluated through experiments. Liang-Rogers model [77] differs from Tanaka model [136] in the way the evolution of martensite volume fraction is defined. In Liang-Roger's model [77], the martensite volume fraction is defined as follows:

$$R_m = \begin{cases} \frac{(1 - R_{mS})}{2} \cos(a_M(T - T_{MF}) + b_M\sigma) + \frac{(1 + R_{mS})}{2} & \text{for A} \rightarrow \text{M} \\ \frac{R_{mS}}{2} (1 + \cos(a_A(T - T_{AS}) + b_A\sigma)) & \text{for M} \rightarrow \text{A} \end{cases} \quad (5.153)$$

where A \rightarrow M and M \rightarrow A indicate austenite to martensite transformation and martensite to austenite transformation, respectively, and the material constants a_M , b_M , a_A and b_A are defined as

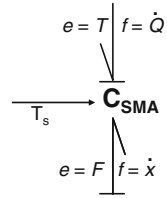
$$a_A = \frac{\pi}{T_{AF} - T_{AS}}, \quad b_A = -\frac{a_A}{C_A},$$

$$a_M = \frac{\pi}{T_{MS} - T_{MF}}, \quad b_M = -\frac{a_M}{C_M},$$

with C_A , C_M and R_{mS} being the stress influence coefficients and the initial martensite temperature in respective phase transformations. Usually, the stress influence coefficients are assumed to be same, i.e., $C_A \simeq C_M$. There are many advanced models such as Ikeda model [62], Brinson model and Boyd-Lagoudas model, etc. whose details can be consulted in [39, 108], and detailed thermomechanical behavior models in one and three dimensions can be consulted in [87, 88, 156].

The bond graph model of the SMA wire can now be given as shown in Fig. 5.119 where a two-port modulated C-field (C_{SMA}) represents the coupling between thermal and mechanical domains. The modulating signal T_s is the temperature of supply fluid which can be used to determine if the SMA wire is being cooled ($T_s < T$) or heated

Fig. 5.119 Bond graph model of SMA wire



($T_s > T$) and thus a simplified logic can be used in the constitutive relation given in Eq. 5.147. One of the bonds in the C-field is differentially causalled. The constitutive relation of the C-field in a general form can be given as

$$\begin{Bmatrix} \dot{Q} \\ F \end{Bmatrix} = \Phi_{CSMA} \left(T, \int \dot{x} dt, T_s \right)$$

where the function Φ_{CSMA} is combined form of Eqs. 5.150 and 5.147, and \dot{Q} is the rate of heat liberation or absorption during the phase transformation. The C-field shows that the mechanical force is a function of temperature (consequently R_m and T_s) but the thermal domain is not influenced by mechanical domain due to our assumptions.

Any phase transformation process involves liberation or absorption of heat. For example, the latent heat of vaporization is absorbed during steam generation from under saturated liquid water and the latent heat is released during condensation. In metallurgy, the phase transformation process is ideally modeled by the Time-Temperature-Transformation (TTT) diagram. However, we have not used the time information in computation of the martensite volume fraction R_m . Without a finite rate of phase transformation, it is impossible to determine the rate of heat liberation or absorption during phase transformation. Moreover, for a thin SMA wire, the heat liberated or absorbed during phase transformation is so small with respect to the heat content in the flowing fluid that it can be neglected. It is, thus, presumed that the phase transformation is instantaneous and the heat generated/absorbed in the process is negligible $\dot{Q} = 0$. In that case, the two-port C-field reduces to a scalar single port C-element modulated by two temperature signals. However, we will retain the two-port C-field form and leave the heat liberation/absorption part for future development.

The wet SMA array considered in [41] consists of a series connection of wet SMA units. The inertia of the actuator (or its equivalent inertia) is lumped at its free end. A part of the bond graph model of the wet SMA array showing model of three actuator units connected in series is shown in Fig. 5.120 where $Sf : \dot{m}$ is the rate of fluid pumping, $Sf : \dot{m}c_v T_i$ is the rate of enthalpy pumping and $T_i = T_s$ is the inlet temperature of the pumped fluid.

The heat capacity of the flexible tube in a unit is $m_t c_{vt}$ with m_t and c_{vt} being the mass and specific heat capacity of the unit tube. It is modeled by C_{tt} element. The resistance to heat transfer from the fluid to the tube and from the tube to the environment are modeled by resistor elements R_{ft} and R_{he} , respectively.

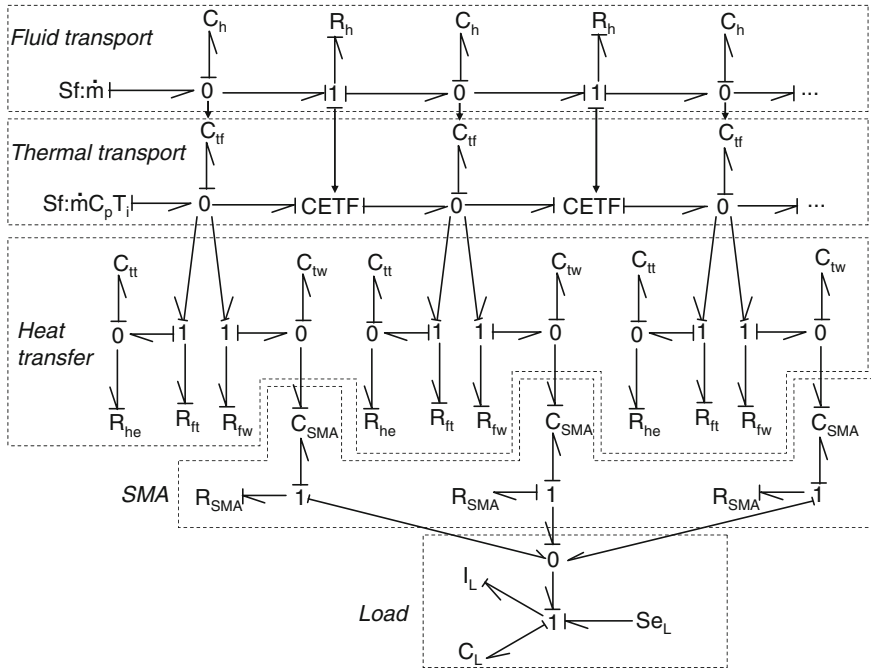


Fig. 5.120 Bond graph model of wet SMA actuator

The heat capacity of the SMA wire in a unit is $m_w c_{vw}$ with m_w and c_{vw} being the mass and specific heat capacity of the SMA wire in a unit. This heat capacity is modeled by C_{tw} element and the resistance to heat transfer from the fluid to the SMA wire is modeled by resistor element R_{fw} .

The SMA wire is modeled by two-port C-field (C_{SMA}) where the modulating signal has not been shown. However, the hysteresis in the phase transformation temperatures is assumed to be implemented in the constitutive relations. Note that the heat capacity of the wire can be modeled together with C_{SMA} and this would avoid the differential causality in the model. The material or internal damping offered by the wire is modeled by resistance R_{SMA} . Due to the series connection of SMA actuator units to form the SMA array, the axial force in all units is same. Therefore, the SMA wire models are connected to a 0-junction. The effective mass, effective mechanical stiffness of the tube, and external load on the SMA array are modeled by bond graph elements I_L , C_L and Se_L , respectively.

Note that the SMA wire resistance, like its stiffness, is also nonlinear [41], but can be approximated as a piece-wise linear resistance. The resistance comes from stress rate of austenite phase ($\dot{\sigma}_a = E_a \dot{\epsilon}$) and stress rate of martensite phase ($\dot{\sigma}_m = E_m \dot{\epsilon}$, $E_t \dot{\epsilon}$ or $E_d \dot{\epsilon}$, depending on value of strain). Therefore, although not shown in the bond graph model, the resistance R_{SMA} is also modulated by strain or equivalently, the

deformation of the wire segment. This modulation has to be shown from an integration block connected to the 1-junction to which the R_{SMA} element is connected.

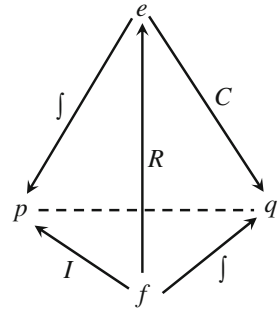
The above developed model does not consider heat transfer along the length of the actuator, the thermal expansion, the details of elastic deformation of the bellow structured tube, the rate of phase transformation, the actual phase transformation curve, the pressure–volume work, the change of tube dimensions due to pressure, the change in wire diameter due to Poisson’s ratio, the plastic deformation of the wire in martensite phase, etc. Therefore, there is considerable scope for improvement of this model. The SMA wire is essentially a spring with variable stiffness and internal source (energy import or export). To account for these complexities, the neuronal or neural bond graph (NBG) concept has been proposed in [21]. In a neuronal bond graph, a neuronal or neural bond graph element is represented by generic variable impedance Z (e.g. SMA stiffness and damping) whose constitutive relation is determined from a Memory Neural Network (MNN). A MNN can change its structure based on the input–output task history and can learn during simulation. Authors of [21] have used NBG to model SMA wire actuated cooperative microrobots. The variable stiffness models developed in [128, 150] are also possible approaches to model the SMA wire. The network of wet SMA units to form the actuator array can be very complex. Usually, fluid flow in SMA array is controlled through Matrix Manifold and Valve system (MMV) or Matrix Vasoconstriction Device (MVD). In addition to the usual switches and on–off control valves to control the flow, usually diodes and check valves are used in the SMA array to stop backflow of current and fluid. In a networked fluidic system, the impedance of the network does not decrease in proportion to the number of actuators that are open. The fluidic inertia and storage greatly influence the effective impedance depending on the number of actuators in open state, and thus it is complicated to develop control systems for the system. Bond graph models for the fluidic MMV and MVD systems in wet SMA arrays have been developed in this context in [44].

Electroactive polymers (EAP) are another category of material that exhibit variations in stiffness, conductivity and coloration under influence of electrical and/or chemical loading. Their ability to change shape under electrical or chemical loading and also their ability to recover large strains makes them suitable for use in microactuators. These materials are especially suitable for development of artificial muscles. A detailed bond graph model of EAP actuator and experimental results are given in [18].

5.4.15 A Note on Memristor and Memcapacitance

These authors feel that the hysteretic behavior SMA can be modeled in a better way by using bond graph elements which have some kind of memory. In fact, the father of bond graph modeling, H.M. Paynter, had hinted at existence of such an element with memory as far back as 1961. Paynter drew the tetrahedron of state (Fig. 5.121) [106] linking the two power variables, namely effort (e) and flow (f), and the two

Fig. 5.121 Paynter's tetrahedron of state showing relation of state variables and constitutive relations [106]



state variables. He drew five directed edges out of which two are definition of the states given as

$$p = \int e dt \quad \text{and} \quad q = \int f dt \quad (5.154)$$

and the other three define the constitutive relations for I-, C-, and R-elements as follows:

$$\begin{aligned} \Phi_I(p, f) &= 0, \\ \Phi_C(q, e) &= 0, \\ \Phi_R(e, f) &= 0. \end{aligned} \quad (5.155)$$

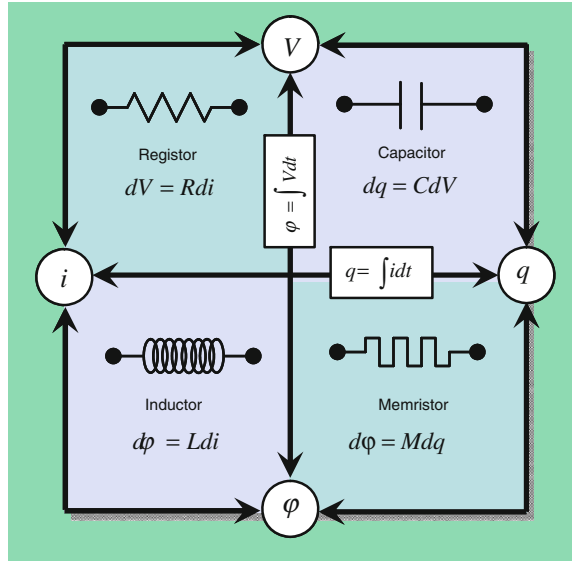
The sixth edge of the tetrahedron of state is undefined. Paynter drew an undirected hidden line as shown in Fig. 5.121 to highlight this missing relation.

In 1971, Leon Chua, an electrical engineer, was trying to derive a rigorous mathematical foundation for electronics. From symmetry arguments, he reasoned that for the sake of the logical completeness of circuit theory, there should be a fourth passive element in addition to the already known inductance, capacitance, and resistance. The complete quartet of elements adapted from [25, 133] is shown in Fig. 5.122. The fourth element, linking the charge q and flux φ was termed a memristor (shorthand for memory resistor) by Chua [25]. The memristor would behave as a resistor that could remember what current had flowed through it before. It is evident that the memristor is the element that Paynter has indicated by the hidden line in the tetrahedron of states [106].

Memory of a single variable means introduction of a state. This state is an internal state of the memristor. The one-port or two-terminal memristor constitutive relation for electrical network is then defined as

$$\begin{aligned} \varphi &= M(q) \\ \Rightarrow \frac{d\varphi}{dt} &= \frac{dM(q)}{dq} \frac{dq}{dt} \\ \Rightarrow V &= R(q) i \end{aligned} \quad (5.156)$$

Fig. 5.122 The fundamental two-terminal circuit elements [25, 133]



where $R(q) = dM(q)/dq$ is a charge modulated resistor and the internal state $q = \int i dt$. As we can understand, the memristor in this case is a charge modulated resistance. The value of resistance can become positive and negative depending upon the definition of the function, and hence it can act as a dissipater or as an internal energy source.

Chua and Kang [26] generalized the memristor concept to a much broader class of nonlinear dynamical systems which they called memristive systems. The constitutive relation for a memristive element is defined as

$$\begin{aligned} V &= R(q, i, t) i \\ q &= \int f(q, i, t) dt \end{aligned} \tag{5.157}$$

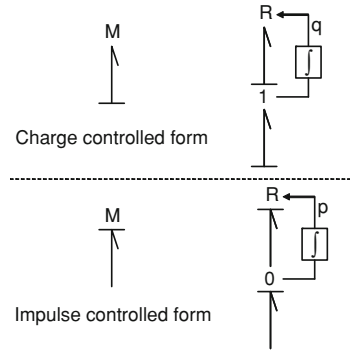
As is evident from Eq. 5.157, a memristive element is no more a charge modulated resistance. In most physical systems, the functions $R(\cdot)$ and $f(\cdot)$ do not explicitly involve time in case where we obtain a time invariant nonlinear memristive system.

Oster and Auslander [101] formally introduced the memristor as a one-port element in bond graph theory. The memristor is denoted by symbol M and its constitutive relation is defined as

$$\Phi_M(p, q) = 0 \tag{5.158}$$

Depending on which form is required for modeling, Eq. 5.158 can be written, respectively, in impulse controlled form and charge controlled form as

Fig. 5.123 Equivalent representation of memristor in a bond graph



$$q = F(p) \text{ or } p = G(q) \tag{5.159}$$

Taking time derivatives, one can write

$$\frac{dq}{dt} = \frac{dF(p)}{dp} \frac{dp}{dt} \Rightarrow f = W(p) e \text{ with } p = \int e dt \tag{5.160}$$

or

$$\frac{dp}{dt} = \frac{dG(q)}{dq} \frac{dq}{dt} \Rightarrow e = M(q) f \text{ with } q = \int f dt \tag{5.161}$$

Thus, the internal states in impulse controlled form and charge controlled forms of memristor are impulse and charge, respectively. The function $M(q)$ is called incremental memristance and function $W(p)$ is called incremental memductance. If $M(q)$ or $W(p)$ is constant then one obtains an ordinary resistor (which has no memory). It is also seen that a memristor, like a resistor, is causally neutral, i.e., it can receive either effort or flow as the input variable. However, from modeling point-of-view, one can always impose a preferred causality.

A memristor can be always modeled as a displacement or impulse modulated resistance by using an available state of the system or an added state (see Fig. 5.123). However, an added state is always required when we have a memristive element as defined in Eq. 5.157.

Oster and Auslander [101] gave some examples of physical systems where a memristor element is present. A tapered dashpot (an airplane strut) can be modeled as a memristor or as a displacement modulated resistance. They also show that an electrochemical system containing a membrane rectifier, i.e., an electrolytic cell whose electrical resistance depends on the electrolyte concentration between two charged membranes, is better modeled with a memristor element.

It has been shown in [26] that the current–voltage characteristics of some devices like thermistors, Josephson junctions and neon bulbs can be modeled using the memristive element. Recently, electrical switching in thin-film devices has attracted a lot of attention because such a technology can increase the speed of memory circuits many

fold as compared to conventional switches made of complementary metal-oxide-semiconductors. The resistance switching and charge transport in such devices is argued to be due to atomic rearrangement. Such behavior has also been experimentally observed in various material systems, organic films containing charged dopants, metal oxides like titanium dioxide (TiO₂), and various perovskites. It has been stated in [133] that multistate and binary switching do indeed show dynamical negative differential resistance in some cases, i.e., the memristive element can act like an energy source under certain conditions.

A fast low-power switch was created in early 2000s at Hewlett-Packard (HP) Laboratories in which two nanoscale titanium dioxide resistor layers were placed together and the current through one was used to toggle the resistance of the other layer. Titanium dioxide in its pure state is a semiconductor. However, when it is heated, some oxygen escape leaving electrically charged bubbles that make it behave like a metal. In the low-power switch developed at HP, the upper layer was made from pure titanium dioxide and the lower layer was made from oxygen depleted metal. When a positive voltage is applied across the switch, the charged bubbles are pushed up from the metal into the upper semiconductor layer which reduces the electrical resistance and makes the switch behave as a conductor. When the voltage is applied in opposite polarity, the charged bubbles are pushed back to the lower layer and the switch behaves as a high-resistant semiconductor. The interesting part of this device was that if the voltage is switched off at any time, the oxygen bubbles remain trapped where they were and the resistance remains frozen till the voltage is reapplied. The instant the voltage is reapplied, the device wakes up remembering its past resistance. This is exactly a memristor. Other similar behaviors are observed where atomic scale movements are involved. Therefore, memristor and memristive elements are usually associated with dynamics in the nanoscale. It has also been shown that a single-celled organism like *P. polycephalum* can memorize a specific pattern of events it faces and change its behavior to anticipate a future event [95].

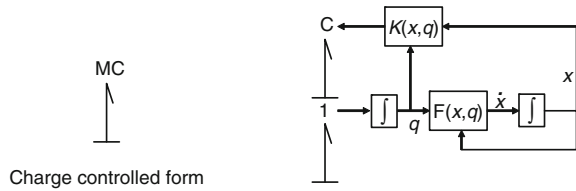
Chua had already speculated that the behavior of synapses, which are the gaps between nerve cells across which impulses must pass, looked similar to memristor. In fact, the impulses pass through an ion channel where potassium and sodium ion pass through membranes of cells and thus the synapses can alter their response according to the frequency and strength of the signals. Memristors are almost always present where micro- or nanoscale ionic transport phenomena are involved. Research in memristor suggests it might be possible to exponentially increase the computing power and even create an artificial or electronic brain.

The success of memristors has motivated the search for new devices like memcapacitors and meminductors [33, 34]. A memcapacitor can store data without dissipating any energy. There has been already some success in making physical memcapacitors [71].

The charge-controlled form of the constitutive relation of a memcapacitor is defined as [10]

$$V = D_M(x, q, t) q \quad (5.162)$$

Fig. 5.124 Equivalent representation of memcapacitor in a bond graph



where V is voltage, D_M is inverse of capacitance C_M , q is charge and the internal state is governed by the differential equation

$$\dot{x} = F(x, q, t). \tag{5.163}$$

In terms of bond graph, we can write the time invariant charge-controlled form of the constitutive relation as

$$e = K_M \left(x, \int f dt \right) \int f dt \text{ with } x = \int F \left(x, \int f dt \right) dt \tag{5.164}$$

where K_M is inverse of capacitance or equivalent stiffness. If we consider a case where the current through the capacitor is switched off then not only the potential across the capacitor stays frozen but also the capacitance till the current again starts flowing through the capacitor.

A physical equivalent system for a memcapacitor is a usual parallel plate capacitor in which the distance between the plates is modulated through an exogenous state (memory variable).

The equivalent bond graph model of the memcapacitors derived from the SPICE model given in [10, 69] is shown in Fig.5.124 where MC denotes the one-port memcapacitor element. Note that the first integral used to compute the charge is not essential because the charge is a state variable associated with the integrally causalem C-element. Thus, in essence, there is one added internal state. The usual hysteretic behavior of the memcapacitors has been simulated with this model in [10].

In contrast to the quasistatic phase transformation model used to develop the SMA wire bond graph model, a dynamic model should ideally contain a few memory variables or internal states. The first internal state should remember the history of temperature change (to determine the direction of temperature change) and the second should remember the martensite fraction. For example, consider that the temperature has been gradually increased to $T = T_x$ ($T_{AS} < T_x < T_{AF}$) and martensite is being transformed to austenite. If the temperature T is suddenly reduced before the phase transformation to austenite is complete then the martensite or austenite fraction should remain frozen till the lower reverse transformation temperature is reached ($T < T_{MS}$) or the temperature is increased above the previous highest temperature ($T > T_x$). This is the case of a partial hysteresis cycle. Thus, one needs a memory variable for martensite fraction and also for direction of transformation. Since martensite fraction influences the stiffness of the SMA wire, the memory variables

are to be modeled as part of a memcapacitor. In the same vein, if the heat liberation or absorption during the phase transformation is to be modeled then one needs the rate of change of martensite fraction or rate of phase transformation with respect to time. Phase transformation is never instantaneous; it is dependent on how much time the material has been held at a temperature. Thus, time explicitly enters into the picture. As a consequence, use of a memristor (more specifically, a memristive element), with its constitutive relations expressed in terms of martensite fraction rate and time, seems appropriate. Although we are not going to develop such a model at this stage, we encourage the readers to think about it and other similar models where internal or dummy memory variables (e.g. Bouc-Wen model) are needed.

5.5 Bearings and Rotors

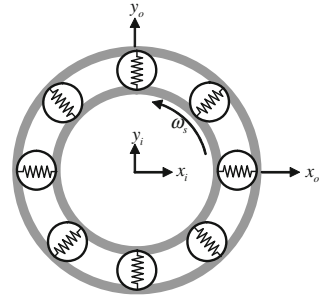
Bearings allow constrained relative motion between two or more parts. Bearings are usually classified according to the type of relative motion, the principle of operation, and the type of load that can be supported. In this book, we will model two very commonly used bearings, namely rolling element bearings and journal bearings. We will also model an active magnetic bearing which eliminates friction between the constrained parts.

5.5.1 *Rolling Element Bearings*

In a rolling element bearing, round elements are placed between the two pieces. The relative motion between the two pieces causes the round rolling elements to roll. This way, the only friction is encountered as the rolling resistance at the contact of the rolling element with the pieces. A ball bearing is a common type of rolling element bearing. The constrained pieces are called inner and outer races between which there are a set of balls. There is a groove in each race and the balls rest and roll within these grooves. In addition, the balls are kept inside a cage which maintains the distance between the balls as they roll. Under load, a ball deforms or flattens at its points of contact with the races which causes the contact zone to be a patch rather than a point. Roller bearings use rollers or cylinders in place of balls so that the bearing can carry higher load at the cost of more friction. A typical rolling element bearing is shown in Fig. 5.125 where some balls or rollers are placed between the rolling elements. Under load in a particular direction, the rolling elements are either compressed or released from compression. The rolling elements cannot be under tension even when the gap between the inner and outer races at the location of the ball is larger than the ball diameter.

Each ball/roller can be modeled as a spring with some material damping. The spring forces can be decomposed into orthogonal components (x and y components)

Fig. 5.125 General schema of a rolling element bearing



and summed up. The resultant force acts in opposite directions on the inner and the outer races.

The cage frequency is calculated as

$$\omega_c = \frac{\omega_s}{2} \left(1 - \frac{D_b}{D_p} \right) \tag{5.165}$$

where ω_s is the shaft speed, D_p is the pitch circle diameter and D_b is the ball diameter.

If there are n_b number of balls then the position of j th ball ($j = 1..n_b$) is

$$\phi_j = \frac{2\pi (j - 1)}{n_b} + \omega_c t + \phi_0 \tag{5.166}$$

where ϕ_0 is the initial position of the first ball at $t = 0$.

The contemporary compression of j th ball is then given by

$$\delta_j = (x_i - x_o) \cos \phi_j + (y_i - y_o) \sin \phi_j - c \tag{5.167}$$

where c is the radial clearance, and position variables are as shown in Fig. 5.125. If balls are precompressed, then c should be negative.

The force due the compression of the j th ball is given by Hertzian contact theory:

$$f_j = k_b \delta_j^n, \tag{5.168}$$

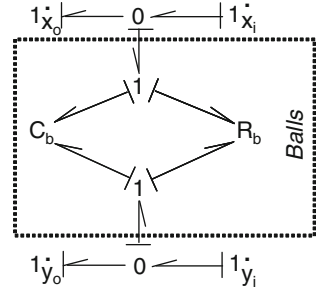
where the usual value of $n = 1.5$ for ball bearings and 1.1 for roller bearings.

Note that the force is directed toward the center of the shaft. Therefore, the net forces in x and y directions due to contact of all the balls is given as

$$f_x = k_b \sum_{j=1}^{n_b} \delta_j^n \gamma_j \cos \phi_j, \tag{5.169}$$

$$f_y = k_b \sum_{j=1}^{n_b} \delta_j^n \gamma_j \sin \phi_j, \tag{5.170}$$

Fig. 5.126 General bond graph model of a rolling element bearing



where γ_j is a switched variable which takes care of the loss of contact or looseness of the j th ball. It is defined as

$$\gamma_j = \begin{cases} 1 & \text{if } \delta_j > 0, \\ 0 & \text{otherwise.} \end{cases} \tag{5.171}$$

Thus, the total ball elastic force can be written as

$$\begin{Bmatrix} F_{xs} \\ F_{ys} \end{Bmatrix} = \phi_{bs} (x_i - x_o, y_i - y_o) \tag{5.172}$$

where F_{xs} and F_{ys} are force components in x and y directions, respectively, x and y represent displacements of the races denoted by subscripts i and o for inner and outer races, respectively, and ϕ_{bs} is a function described in Eqs. 5.169 and 5.170.

The damping forces can be determined by selecting a damping coefficient for each ball as $\lambda_i K_b$ where λ_i is a material constant and K_b is the ball stiffness. The damping force components in x and y directions are given as

$$\begin{Bmatrix} F_{xd} \\ F_{yd} \end{Bmatrix} = \phi_{bd} (\dot{x}_i - \dot{x}_o, \dot{y}_i - \dot{y}_o). \tag{5.173}$$

The elastic forces and damping forces can be modeled in a bond graph as two-port C- and R-fields, respectively, as shown in Fig. 5.126.

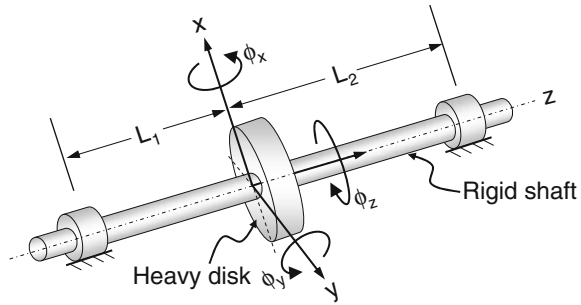
If the constitutive relations for the C- and R-fields are combined together as follows

$$\begin{Bmatrix} F_x \\ F_y \end{Bmatrix} = \phi_b \left(\int (\dot{x}_i - \dot{x}_o) dt, \int (\dot{y}_i - \dot{y}_o) dt, \dot{x}_i - \dot{x}_o, \dot{y}_i - \dot{y}_o \right) \tag{5.174}$$

then the ball forces can be represented by a two-port RC-field which offers both stiffness and damping.

A better model of the rolling element bearing with inclusion of various faults is given in [97] where multibody dynamics of healthy and faulty rolling element bearings were modeled using vector bond graphs.

Fig. 5.127 A rigid rotor mounted symmetrically on two bearings



As an example, let us consider a rigid rotor system shown in Fig. 5.127 where it is assumed that the rotor shaft is massless and rigid and the rotor disk is thin and massive (a point mass). The shaft is supported on ball bearings on its two sides.

For ease of modeling, an inertial coordinate frame x, y, z is chosen whose origin is at the mass center of the disk at its undeflected position. Note that the coordinate frame is not moving. The deflections of the rigid shaft in x and y directions at the left bearing support are, respectively, given as

$$\dot{x}_l = \dot{x} - \phi_y L_1 \tag{5.175}$$

$$\dot{y}_l = \dot{y} + \phi_x L_1. \tag{5.176}$$

Likewise, the deflections of the rigid shaft at the right bearing support are

$$\dot{x}_r = \dot{x} + \phi_y L_2 \tag{5.177}$$

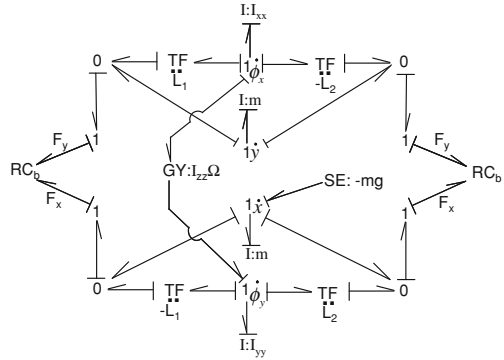
$$\dot{y}_r = \dot{y} - \phi_x L_2. \tag{5.178}$$

Let the rotor spin velocity $\dot{\phi}_z = \Omega$ be constant and externally governed by the drive. We assume that the drive is not influenced by the motion of the load (i.e., lateral and rotational motions of the disc). From symmetry of the circular disc, $x, y,$ and z axes are principal axes. The rotary inertias of the disk about these principal axes $x, y,$ and z are I_{xx}, I_{yy} and I_{zz} , respectively. Note that $I_{xx} = I_{yy}$ and this relation does not change even if the disk is rotated by any amount about the z -axis.

The boundary conditions are important in modeling of a rotor system. For ball bearings with a single row of balls, the shaft is free to rotate about x -axis and it is also free to rotate by the other two axes by small amounts. This is equivalent to a pin joint. For small rotations about x - and y -axes, the bearings offer no restraining force. However, the bearings restrain lateral motions in x and y directions. Note that in case of roller bearings, the bearings also restrain rotations about x - and y -axes.

Assuming the outer race of the bearing to be rigid and fixed to the ground, the bond graph model of the rotor shaft system can be given as shown in Fig. 5.128. Kinematic relations derived in Eqs. 5.175–5.178 are used in the model to determine the relative velocities of the shaft with respect to the outer races at left and right bearing supports.

Fig. 5.128 Bond graph model of a rigid rotor mounted symmetrically on two bearings



The bearings are modeled by RC fields whose constitutive relations are defined in Eq. 5.174.

Note that in addition to inertial forces at the disk and support forces at the bearings, a gyroscopic coupling exists between the two rotational motions. Letting \hat{x} , \hat{y} , and \hat{z} be the unit vectors, the gyroscopic moments are derived as

$$M_x \hat{x} + M_y \hat{y} = I_{zz} \Omega \hat{z} \times (\dot{\phi}_x \hat{x} + \dot{\phi}_y \hat{y}) = -I_{zz} \Omega \dot{\phi}_y \hat{x} + I_{zz} \Omega \dot{\phi}_x \hat{y}$$

$$\Rightarrow M_x = -I_{zz} \Omega \dot{\phi}_y \text{ and } M_y = I_{zz} \Omega \dot{\phi}_x.$$

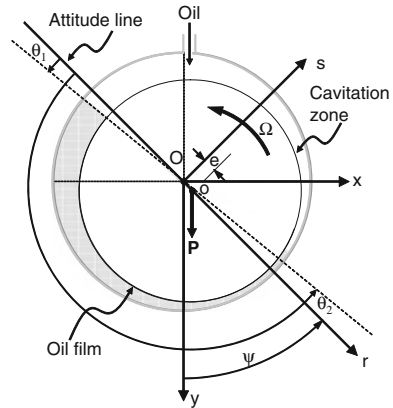
These conservative moments are represented by the GY element in the bond graph. Note that the bond graph model appropriately transforms the bearing forces to the forces and moments acting on the rotor disk mass center.

Several detailed models of rotor dynamic systems are available in the literature. A pendulous flywheel's model based on rigid body dynamics is given in [60]. Bond graph models of some basic rotor dynamic systems like Jeffcott rotor and Stodola-Green rotor can be found in [107]. Another model of Jeffcott is given in [27].

5.5.2 Journal Bearing

Journal bearing is the most common type of plain bearing in which a shaft or journal rotates in a slightly larger bore of a bearing, usually with some form of lubricant. In fluid lubrication bearings, fluid dynamic effect eliminates surface-to-surface contact between the journal and the bearing and thus reduces friction. If the lubricant fluid is supplied by an external pump to maintain fluid pressure inside the bearing and thus supports the journal then the bearing is said to be hydrostatically lubricated. If there is no external pump and the fluid pressure is maintained by the rotation of the journal then the bearing is said to be hydrodynamically lubricated. As the journal rotates within the bearing, a wedge is formed between the journal and the bearing. When the lubricant is forced through this wedge, the fluid pressure produces the force to

Fig. 5.129 Schema of a journal bearing and the fluid film in it



support the journal. After passing through the wedge, the fluid expands which causes a drop in pressure and possible cavitation (at below atmospheric pressure). At this zone, the low pressure is utilized to suck in lubricant from the supply line so that the lubricant leaking from the bearing sides can be replenished.

While the hydrodynamic force lifts the journal, the journal center also shifts horizontally in the direction of rotation (see Fig. 5.129). The line that passes through the journal center ‘o’ and bearing center ‘O’ is called the attitude line and the angle made between the attitude line and the vertical line is called attitude angle (ψ). The distance between the journal and bearing centers is called eccentricity (e). In steady operation of a rotor with static load and no dynamic forces like unbalance forces, the attitude angle and eccentricity are fixed. In Fig. 5.129, the extent of oil film with positive pressure is measured from the attitude line and is given by angles θ_1 and θ_2 .

The pressure distribution along the bearing length and circumferential directions changes depending upon bearing geometric features. For a perfectly circular bearing, if the bearing length B to diameter D ratio is less than 1, i.e., $B/D < 1$, then the so-called short bearing assumptions are applicable. Otherwise, the so-called long bearing or finite bearing assumptions are taken. Most of the common journal bearings are usually short. In a short bearing, it is assumed that the fluid pressure at both ends along the length of the bearing is the atmospheric pressure. Moreover, it is assumed that the extent of positive pressure fluid-film zone is $\theta_2 - \theta_1 = \pi$ and in the remaining part or the cavitations region, the fluid pressure is same as the atmospheric pressure. On the other hand, for a long bearing, the variations in fluid pressure along the bearing length is neglected and the fluid film is assumed to be full, i.e., devoid of cavitations. A finite bearing approximation combines both short and long bearing assumptions. Thus, the boundary conditions have to be suitably selected for the bearing under consideration. In this book, we will consider that short bearing approximation is applicable. A schematic representation of pressure distribution with short bearing approximation is shown in Fig. 5.130.

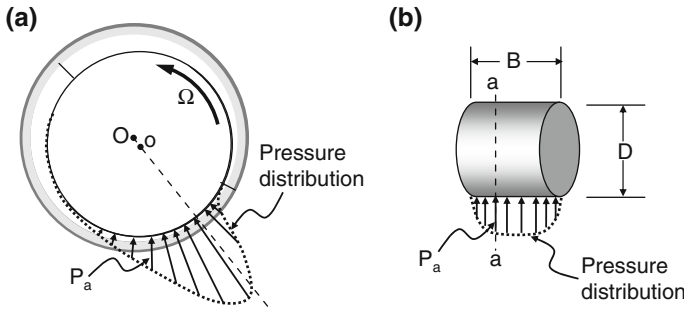


Fig. 5.130 Pressure distribution in a journal bearing in **a** circumferential and **b** axial directions.

If Ω is the journal angular speed, z is the position measured along the bearing axis (or length), B is the bearing length, μ is the dynamic coefficient of viscosity of the lubricant, θ is an angular position measured from the attitude line as shown in Fig. 5.129, ψ is the attitude angle, and $\varepsilon = e/c$ is the eccentricity ratio, where c is the bearing clearance (difference between bearing and journal radius), then the pressure distribution under short bearing assumption is as

$$p(z, \theta) = \frac{(z - B)}{2} (12\mu c \dot{\varepsilon} \cos \theta - 6\mu (\Omega - 2\dot{\psi}) c \varepsilon \sin \theta) (c(1 + \varepsilon \cos \theta))^{-3} \tag{5.179}$$

where the attitude angle is given by

$$\psi = \tan^{-1} \left(\frac{\pi}{4} \frac{\sqrt{1 - \varepsilon^2}}{\varepsilon} \right). \tag{5.180}$$

The forces acting on the journal are found as $\int p dA$ where the integration is taken over the extent of the positive pressure zone defined by angles θ_1 and θ_2 (see Fig. 5.129) as follows:

$$\theta_1 = \tan^{-1} \frac{2\dot{\varepsilon}}{\varepsilon (\Omega - 2\dot{\psi})}, \theta_2 = \theta_1 + \pi. \tag{5.181}$$

The force components along r -direction (attitude line, as shown in Fig. 5.129) and s -direction are

$$F_r = \frac{D}{2} \int_0^b \int_{\theta_1}^{\theta_2} p(z, \theta) \cos \theta d\theta dz \tag{5.182}$$

$$F_s = \frac{D}{2} \int_0^b \int_{\theta_1}^{\theta_2} p(z, \theta) \sin \theta d\theta dz \tag{5.183}$$

For steady operation, Holmes [57] linearized Eqs. 5.182 and 5.183 about the equilibrium point defined by $\varepsilon = \varepsilon_0$ and

$$\psi = \psi_0 = \tan^{-1} \left(\frac{\pi}{4} \frac{\sqrt{1 - \varepsilon_0^2}}{\varepsilon_0} \right).$$

At steady operation of a journal bearing with constant shaft load P (mostly self-weight) and constant speed Ω , the relation between the load (called load bearing capacity) and the eccentricity is given as

$$P = \frac{\mu \Omega (D/2) B^3 \varepsilon}{4c^2 (1 - \varepsilon^2)^2 \sqrt{\pi^2 (1 - \varepsilon^2) + 16\varepsilon^2}}. \quad (5.184)$$

The equilibrium point $\varepsilon = \varepsilon_0$ is found by solving Eq. 5.184. Because $\dot{\varepsilon} = 0$ and $\dot{\psi} = 0$ in steady operation, one finds $\theta_1 = 0$ and $\theta_2 = \pi$. Then, the fluid-film forces are shown to be

$$\begin{Bmatrix} F_s \\ F_r \end{Bmatrix} = \begin{bmatrix} K_{ss} & K_{sr} \\ K_{rs} & K_{rs} \end{bmatrix} \begin{Bmatrix} r \\ s \end{Bmatrix} + \begin{bmatrix} R_{ss} & R_{sr} \\ R_{rs} & R_{rs} \end{bmatrix} \begin{Bmatrix} \dot{r} \\ \dot{s} \end{Bmatrix} \quad (5.185)$$

where

$$K_{ss} = 4 \frac{P}{c} \varphi(\varepsilon_0), \quad K_{sr} = -\pi \frac{P}{c} \frac{1 + 2\varepsilon_0^2}{\varepsilon_0 \sqrt{1 - \varepsilon_0^2}} \varphi(\varepsilon_0),$$

$$K_{rs} = \pi \frac{P}{c} \frac{\sqrt{1 - \varepsilon_0^2}}{\varepsilon_0} \varphi(\varepsilon_0), \quad K_{rr} = 8 \frac{P}{c} \frac{1 + \varepsilon_0^2}{1 - \varepsilon_0^2} \varphi(\varepsilon_0),$$

and

$$R_{ss} = 2K_{rs}/\Omega, \quad R_{sr} = R_{rs} = -2K_{ss}/\Omega, \quad \text{and} \quad R_{rr} = -2K_{sr}/\Omega.$$

The stiffness and damping matrices along fixed x-y axes are obtained after planar rotational transformation. The transformation of stiffness matrix is given as

$$\begin{bmatrix} K_{xx} & K_{xy} \\ K_{yx} & K_{yy} \end{bmatrix} = \begin{bmatrix} \cos \psi & -\sin \psi \\ \sin \psi & \cos \psi \end{bmatrix} \begin{bmatrix} K_{ss} & K_{sr} \\ K_{rs} & K_{rs} \end{bmatrix} \begin{bmatrix} \cos \psi & \sin \psi \\ -\sin \psi & \cos \psi \end{bmatrix} \quad (5.186)$$

and the damping matrix is similarly transformed under assumption that $\dot{\psi} = 0$.

The stiffness and damping matrices are used to define the constitutive relations for a linear bond graph C-field and a linear R-field with constant parameters.

For dynamic simulation, neither the load nor the speed can be assumed to be constant. The integrations of Eqs. 5.182 and 5.183 can be performed under certain assumptions to yield closed form expressions for fluid-film forces [89] which when transformed to x-y frame are expressed as follows:

$$P_x = \frac{\mu DB^3}{4c^2} ((\Omega - 2\dot{\psi}) \varepsilon F_2 - 2\dot{\varepsilon} F_1), \quad (5.187)$$

$$P_y = \frac{\mu DB^3}{4c^2} ((\Omega - 2\dot{\psi}) \varepsilon F_3 - 2\dot{\varepsilon} F_2), \quad (5.188)$$

with

$$F_1 = \frac{1}{(1 - \varepsilon^2)^{5/2}} \left[\frac{\bar{\psi}}{2} + \frac{\sin 2\bar{\psi}}{4} - 2\varepsilon \sin \bar{\psi} + \varepsilon^2 \bar{\psi} \right] \Big|_{\psi_1}^{\psi_2}$$

$$F_2 = \frac{1}{(1 - \varepsilon^2)^2} \left[\frac{1}{2} \sin^2 \bar{\psi} + \varepsilon \cos \bar{\psi} \right] \Big|_{\psi_1}^{\psi_2}$$

$$F_3 = \frac{1}{(1 - \varepsilon^2)^{3/2}} \left[\frac{\bar{\psi}}{2} - \frac{\sin 2\bar{\psi}}{4} \right] \Big|_{\psi_1}^{\psi_2}$$

where $\bar{\psi}$ is a dummy variable with its limits ψ_1 and ψ_2 expressed as functions of eccentricity ratio and the extent of fluid film (θ_1 and θ_2) as follows:

$$\psi_i = \tan^{-1} \frac{\sqrt{1 - \sigma_i^2}}{\sigma_i}, \quad \sigma_i = \frac{1}{\varepsilon} \left(1 - \frac{1 - \varepsilon^2}{1 + \varepsilon \cos \theta_i} \right), \quad \text{for } i = 1, 2.$$

The above-derived fluid-film forces are nonlinear and it is no more possible to separate the stiffness and damping parts in it. In a general form, the forces are expressed as

$$\begin{Bmatrix} F_x \\ F_y \end{Bmatrix} = \Phi_{RC} (\varepsilon, \dot{\varepsilon}, \psi, \dot{\psi}, \Omega), \quad (5.189)$$

where Φ_{RC} is a function which defines the constitutive relations of a nonlinear two-port RC-field element with Ω as a modulating signal.

Note that

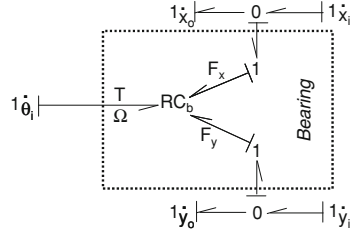
$$e = \sqrt{x^2 + y^2}, \quad \varepsilon = e/c, \quad \dot{\varepsilon} = \frac{x\dot{x} + y\dot{y}}{\varepsilon c^2},$$

$$\psi = \tan^{-1} \left(\frac{\pi}{4} \frac{\sqrt{1 - \varepsilon^2}}{\varepsilon} \right) \quad \text{and} \quad \dot{\psi} = \frac{x\dot{y} + y\dot{x}}{\varepsilon^2 c^2}.$$

Thus, if drag moment M_z or T is also included in the formulation, one can rewrite Eq. 5.189 as

$$\begin{Bmatrix} F_x \\ F_y \\ M_z \end{Bmatrix} = \Phi_{RC} (x, \dot{x}, y, \dot{y}, \Omega_z) \quad (5.190)$$

Fig. 5.131 General bond graph model of a journal bearing



which is represented in bond graph form as a three-port nonlinear RC-field in Fig. 5.131. The calculation of drag moment can be consulted in [20]. Note that if drag forces or rotational dynamics are neglected then the model reduces to a two-port modulated RC-field [123].

Bond graph modeling has been used in [54] to study a rotor system stabilizing scheme using a combination of a squeeze film damper and a plane journal bearing. A further detailed bond graph model of journal bearings is given in [20] where a 3-port R-field element is used to represent hydrodynamic bearing constitutive relations in $r-s$ coordinate frame and a transformation matrix is used to convert $x-y$ frame motions to $r-s$ coordinate frame. The developed bond graph model is good enough to simulate most key phenomena in dynamics of rotors supported on journal bearings like half-frequency whirl and resonant oil whirl (or whip).

5.5.3 Magnetic Bearing

A magnetic bearing supports the load using magnetic levitation and there is no physical contact between the bearing and the load. Due to lack of physical contact or friction, there is no mechanical wear in a magnetic bearing. Magnetic bearings can operate at very high speeds. Magnetic bearing are maintenance free because they run without lubrication. They can also operate in a vacuum such as in flywheel energy storage systems used in space applications. Magnetic bearings usually require backup bearings during initial startup conditions. Backup bearings also guard against unforeseen power or control system failures. In a maglev system, magnetic propulsion is used in addition to supporting or levitating a load.

A magnetic bearing requires continuous power input and an active control, and thus it is also called an Active Magnetic Bearing (AMB). Permanent magnets may be used in a magnetic bearing to carry the static load and additional electromagnets are activated only when the levitated object deviates from its static equilibrium position. The equilibrium of an open loop magnetic bearing is intrinsically unstable (proof given by Earnshaw’s theorem) because the attractive force increases as the load is brought closer to the magnet. This is equivalent to a negative mechanical stiffness. In addition, the electromagnetic domain is mostly conservative and there is almost no damping in the system (except for eddy current losses in the magnetic domain). Thus,

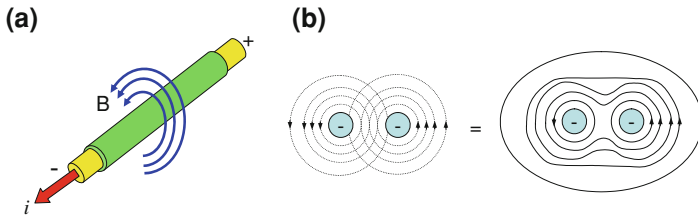
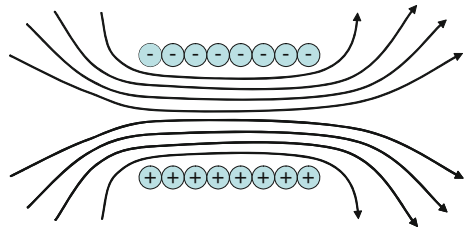


Fig. 5.132 Magnetic field around **a** a current carrying wire and **b** two wires carrying current in same direction

Fig. 5.133 Magnetic field around a solenoid



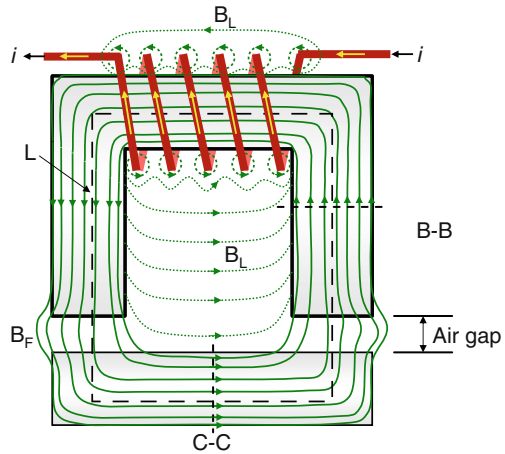
any oscillation set in the system (say, due to unbalance in a rotor) tends to remain undamped. The goal of the control system is thus twofold: counter the negative mechanical stiffness and introduce damping into the levitating force.

When two magnetic bearings are used at two ends of the shaft to levitate a rotor mounted on the shaft, similar bearing forces can be actively generated to control the cylindrical mode of vibration of the rotor whereas oppositely directed active forces can control the conical mode of vibration. In hybrid force and moment control approach, it is possible to generate couple moments by placing two closely spaced magnetic bearings at each end of the shaft and thus control the second and higher bending modes. In this book, we will discuss on modeling the magnetic levitation. Based upon this model, one can build models of different magnetically levitated rotor-bearing systems and interface suitable control algorithms.

A magnetic bearing used to support a rotor contains several electromagnets placed along the periphery of the bearing. A simple electromagnet consists of a coil of insulated wire wrapped around an iron core. When an electric current (i) flows in a wire it creates a magnetic field (B , also called magnetic flux density) around the wire where the field is oriented according to the right-hand rule as shown in Fig. 5.132a. When current flows through two closely spaced current carrying wires, the magnetic fields add up as shown in Fig. 5.132a. This principle is used to augment the strength of the magnetic field.

If a current carrying wire is wound into a coil with many turns of wire compacted side by side then the magnetic field is concentrated along the center of the coil and creates a strong magnetic field there as shown in Fig. 5.133. A coil resembling the shape of a straight tube is called a solenoid and if this straight tube is bent into a donut shape then it is called a toroid.

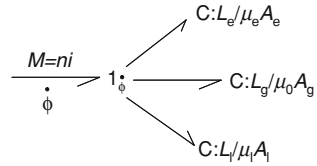
Fig. 5.134 Magnetic field in an electromagnet



In an iron-core electromagnet, a core of ferromagnetic material is placed inside the coil. This produces much stronger magnetic fields (many thousands of times of the strength of the field generated by the coil alone) due to the high magnetic permeability of the ferromagnetic material. In most applications of electromagnets, the iron core is in the form of a loop (or magnetic circuit) and the loop is sometimes broken by small air gaps. One such field through an iron-core electromagnet and a ferromagnetic bar placed near it is shown in Fig. 5.134. The iron core reduces the resistance (or reluctance in magnetism) to the magnetic field, and thus a stronger magnetic field can be sustained if most of the magnetic field's path is within the iron core. Such types of electromagnets are widely used in many electric and electromechanical devices, e.g. electric motors and generators, electrical transformers, relays, magnetic locks, electric bells, loudspeakers, magnetic data storage and recording equipment, MRI machines, mass spectrometers, particle accelerators, maglev trains, and magnetic bearings.

In the kind of electromagnet shown in Fig. 5.134, the magnetic field strength B is almost constant around the magnetic circuit (sections B-B and C-C) and almost zero outside it. If the core has more or less constant cross-section area throughout its length then the field in the core is roughly constant. Some of the magnetic field lines do not pass through the entire ferromagnetic core (they are called leakage flux B_L) and they do not contribute to the force generated by the electromagnet. In the air gaps, the magnetic field lines spread out and then curve back (together called fringing fields B_F), respectively, when leaving and entering the next core material. Thus, the field strength reduces in the air gap. However, if the length of the air gap is small then the field in the air gap can be approximated to be the same as that in the core. The B field increases with increase in the electric current through the coil. However, it saturates at a certain value and further increase in current through the windings does not increase the field strength.

Fig. 5.135 Bond graph model of the magnetic field in an electromagnet



If the number of turns of the winding is n and current is i then the magnetomotive force generated (unit in Ampere turns) is given by

$$M = ni. \tag{5.191}$$

Let us break the magnetic circuit shown in Fig. 5.134 into three distinct parts: electromagnet with mean core length L_e and magnetic permeability μ_e , air gap with fixed gap length L_g and magnetic permeability μ_0 , and the levitated part with mean core length L_l and magnetic permeability μ_l . Let us assume the cross-section areas of the electromagnet, the air gap, and the levitated object are different and are given by A_e , A_g and A_l , respectively. If the Ampere’s law is applied with assumption of negligible leakage flux and fringing flux then one obtains

$$ni = \left(\frac{L_e}{\mu_e A_e} + \frac{L_g}{\mu_0 A_g} + \frac{L_l}{\mu_l A_l} \right) \phi. \tag{5.192}$$

where ϕ is the constant magnetic flux through the core and the air gap and $L = L_e + L_g + L_l$. If $A_e = A_g = A_l = A$ then we have constant flux density $B = \phi/A$ which is uniformly distributed over any cross-section. Then, one obtains

$$ni = B \left(\frac{L_e}{\mu_e} + \frac{L_g}{\mu_0} + \frac{L_l}{\mu_l} \right) = (H_e L_e + H_g L_g + H_l L_l). \tag{5.193}$$

where the magnetic field intensity H is related to the flux density B as follows: $\mu = B/H$. Note that the permeability (μ) of the core material (electromagnet and the levitated object) varies with the magnetic field and its value must be obtained from the core material B – H hysteresis curve.

For bond graph modeling of the magnetic circuit, we can choose the magneto motive force ni as the effort variable and the rate of change of magnetic flux $\dot{\phi}$ as the flow variable. In that case, Eq. 5.192 defines the constitutive relation of three C-elements as shown in Fig. 5.135 where terms $\frac{L_e}{\mu_e A_e}$, $\frac{L_g}{\mu_0 A_g}$ and $\frac{L_l}{\mu_l A_l}$ are reluctances of different segments of the magnetic circuit.

Let us now consider model of an electrical transformer as shown in Fig. 5.136 where E is an externally applied voltage, R_E is the circuit resistance on the primary side and R_L is the load on the secondary side.

Fig. 5.136 Schematic representation of an electrical transformer circuit

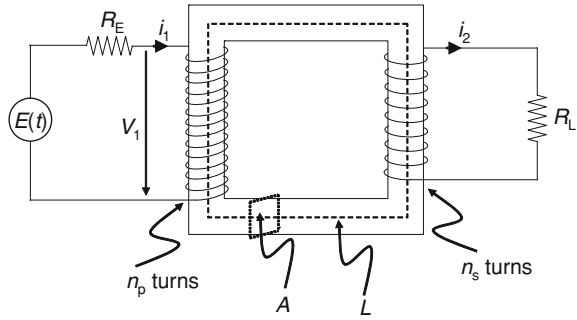
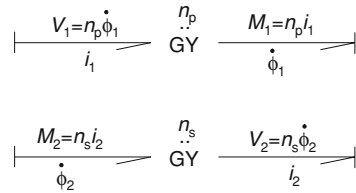


Fig. 5.137 Bond graph model of magnetic induction



For primary side, from Faraday’s law of induction, we can write

$$V_1 = -n_p \frac{d\phi_1}{dt} = -n_p \dot{\phi}_1. \tag{5.194}$$

Combining the above equation with that for the magnetomotive force $M_1 = n_p i_1$, we obtain a conservative equation where $V_1 i_1 = M_1 \dot{\phi}_1$ which can be modeled as a gyrator in bond graph form. Interested readers may see [144] for example of bond graph modeling of eddy current devices where the electromagnetic induction has been discussed in details. The negative sign is adjusted in power direction, as shown in Fig. 5.137.

Likewise, we can write the following relations for the secondary side:

$$V_2 = n_s \frac{d\phi_2}{dt} = n_s \dot{\phi}_2 \tag{5.195}$$

and $M_2 = -n_s i_2$. Note that contrary to the primary side where V_1 is an applied voltage, V_2 is the generated voltage in the secondary side (i.e., the sense of measurement are different). If both these are treated in a single reference frame (e.g., supplied voltage) then the sign change between Eqs. 5.194 and 5.195 is not necessary.

The difference between the magnetomotive forces in the primary and the secondary side is responsible in driving the magnetic flux through the iron core. This can be represented in bond graph form as shown in Fig. 5.138 where the reluctance is taken to be $\frac{L}{\mu A}$ with L , μ and A being the mean core length, magnetic permeability of the core and the constant core cross-section area, respectively. Further note that continuity of flux means $\dot{\phi}_1 = \dot{\phi}_2 = \dot{\phi}$ which is why a 1-junction is used in Fig. 5.138.

Fig. 5.138 Bond graph model of flux storage in iron core

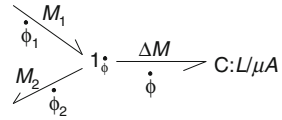


Fig. 5.139 Bond graph model of electrical transformer

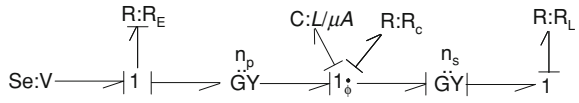


Fig. 5.140 Equivalence of two consecutive gyrator elements

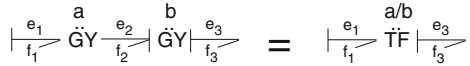
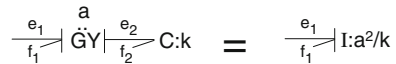


Fig. 5.141 Equivalence of a gyrator element combined with C-element



In addition to the conservative transformation of electrical energy to magnetic domain and its conservative storage in the core in the form of magnetic flux, one also needs to model the losses in the electrical and magnetic circuits. The electrical losses due to ohmic heating can be assumed to be modeled with the resistances in the primary and the secondary sides. The magnetic losses due to flux leakage, and effects such as eddy current and hysteresis for AC supply also have to be included. For the time being, we will simply represent all these core losses as a simple resistor R_C which will be detailed further as we proceed. We further assume that the coils are suitably clamped so that they are not displaced by Lorentz force. The bond graph model of the transformer can now be developed as shown in Fig. 5.139.

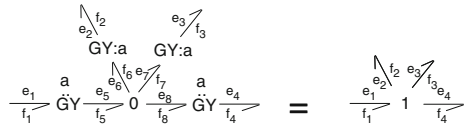
One often finds equivalent circuits of electrical transformers in electrical engineering text books. Let us now see how we can obtain an equivalent electrical circuit of the system through bond graph method. For this purpose, we introduce some generally known equivalence (called transformer and gyrator equivalence) in bond graph theory [91].

When two gyrators appear one after the other, as shown in Fig. 5.140, we can readily see that

$$\begin{aligned}
 e_2 &= af_1, e_1 = af_2, \\
 f_3 &= e_2/b, f_2 = e_3/b \\
 \Rightarrow f_3 &= (a/b) f_1, e_1 = (a/b) e_3
 \end{aligned}
 \tag{5.196}$$

Thus, two gyrators combine to produce the effect of a transformer (TF) element. Likewise, two transformers combine to a single transformer and a transformer and a gyrator combine to a single gyrator.

Fig. 5.142 Equivalence of a 0-junction surrounded by gyrators elements with same moduli



Let us now see how a gyrator combines with a C-element as shown in Fig. 5.141. For the given causality,

$$\begin{aligned}
 f_2 &= e_1/a, \\
 e_2 &= k \int f_2 dt = \frac{k}{a} \int e_1 dt \\
 \Rightarrow f_1 &= e_2/a = \frac{k}{a^2} \int e_1 dt.
 \end{aligned}
 \tag{5.197}$$

Thus, the relation between variables f_1 and e_1 is that for an integrally causalled I-element with inertia a^2/k . In fact, this equivalence is true if other causal form is used. We leave the reader to prove it. Likewise, it can be proved that a gyrator combined with an I-element yields a C-element and a gyrator combined with an R-element yields an R-element.

Finally, let us see what happens when a gyrator is present in all bonds connected to a junction element (1 or 0). From Fig. 5.142, we can derive the following relations:

For 0 junction:

$$e_5 = e_6 = e_7 = e_8, \tag{5.198}$$

$$f_5 - f_6 - f_7 - f_8 = 0. \tag{5.199}$$

For gyrators:

$$e_5 = af_1, e_6 = af_2, e_7 = af_3, e_8 = af_4 \tag{5.200}$$

$$e_1 = af_5, e_2 = af_6, e_3 = af_7, e_4 = af_8 \tag{5.201}$$

From Eqs. (5.198) and (5.200),

$$f_1 = f_2 = f_3 = f_4, \tag{5.202}$$

and from Eqs. (5.199) and (5.201),

$$e_1 - e_2 - e_3 - e_4 = 0. \tag{5.203}$$

As a result, the relationships between external ports satisfy the constraints imposed by a 1-junction. Thus, a 0-junction with gyrators of same modulus all around it is effectively a 1-junction. It can be likewise shown that a 1-junction with gyrators of

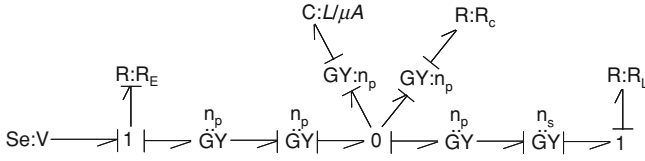


Fig. 5.143 Bond graph model of electrical transformer with gyrators inserted around 1-junction

Fig. 5.144 Reduced bond graph model of electrical transformer obtained using gyrator equivalence

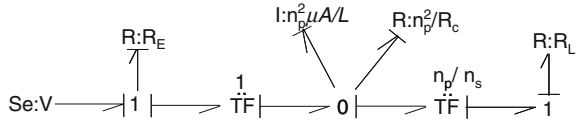


Fig. 5.145 Bond graph model of equivalent circuit of the electrical transformer

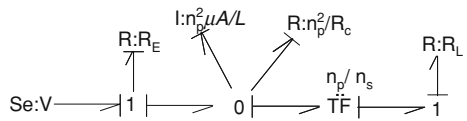
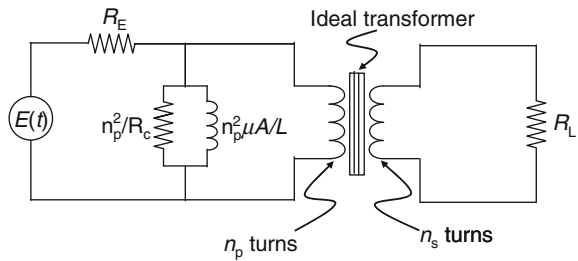


Fig. 5.146 Equivalent circuit of the electrical transformer with magnetic circuit referred to the primary side



same modulus all around it is effectively a 0-junction. More such equivalences and their use in system modeling can be consulted in [91].

Once these equivalences have been established, let us modify the bond graph model of the transformer given in Fig. 5.139 by replacing the 1_ϕ junction by a 0-junction with gyrators of equal modulus n_p in all bonds connected to the 0-junction. The resulting model is shown in Fig. 5.143.

We can now combine two consecutive gyrators to transformers and combine the remaining gyrators with C- and R-elements and obtain a revised bond graph model as shown in Fig. 5.144 and then to a further reduced form as shown in Fig. 5.145.

The equivalent electrical circuit whose bond graph model can be given as in Fig. 5.145 is shown in Fig. 5.146. In fact, this is the equivalent circuit of a real transformer when the magnetic circuit has been referred to the primary side electrical circuit.

Let us now turn our attention back to the basic problem, i.e., the magnetic bearing. We have so far established the framework to model the magnetic domain.

Fig. 5.147 Schema of a single-sided magnetic bearing

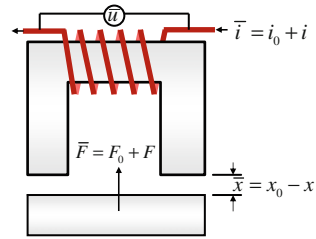
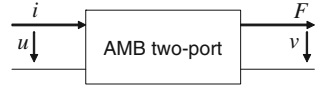


Fig. 5.148 AMB two-port model



To start with, let us consider a single-sided magnetic bearing as shown in Fig. 5.147 and develop its model. This model can be extended for two-sided interaction. It is assumed that in the equilibrium configuration, x_0 , i_0 and F_0 are the nominal air gap, current and force (self weight), respectively, and \bar{u} is the potential across the coil. Variables x , i , and F represent the deviations from the operating (nominal) values.

In [147], a simplified two-port model (see Fig. 5.148) was developed based on the assumption that core losses and leakage flux are negligible. Further to that, it can be seen from Eq. 5.192 and the bond graph model in Fig. 5.135 that the reluctance of the iron core can be neglected in comparison to that of the air gap.

From Fig. 5.147, the effective mean length of the flux path through the air gap is $2\bar{x}$ because the flux passes through the air gaps on the left and on the right. Thus,

$$n\bar{i} = \frac{2\bar{x}}{\mu_0 A} \bar{\phi} \tag{5.204}$$

where μ_0 is the magnetic permeability of air. In another form,

$$\bar{B} = \frac{\bar{\phi}}{A} = \left(\frac{n\mu_0}{2}\right) \frac{\bar{i}}{\bar{x}}. \tag{5.205}$$

The coil voltage

$$\bar{u} = n \frac{d\bar{\phi}}{dt} = nA \frac{d\bar{B}}{dt}. \tag{5.206}$$

The force developed is then given as

$$\bar{F} = \frac{A}{\mu_0} \bar{B}^2 = \frac{n^2 \mu_0 A}{4} \frac{\bar{i}^2}{\bar{x}^2}. \tag{5.207}$$

Fig. 5.149 Equivalent linearized AMB two-port model

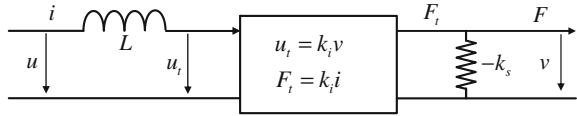
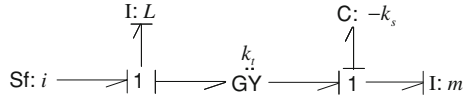


Fig. 5.150 Linearized bond graph model of one-sided AMB



In [147], the above equations were linearized about the operating point with variables x , i , u , and F representing the deviations from the operating (nominal) values. This yields the linearized equations of the form

$$F = k_i i + k_s x \tag{5.208}$$

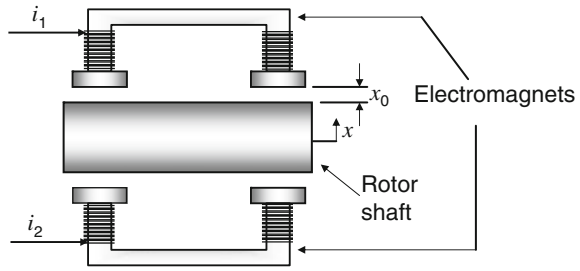
$$u = L \frac{di}{dt} + k_i \dot{x} \quad (\dot{x} = v) \tag{5.209}$$

Note that in the first equation, the term k_s introduces a negative stiffness because variable x is defined in $\bar{x} = x_0 - x$ with a negative sign. This is consistent with the dynamics of magnetic bearings where the attractive force increases as the gap reduces. In Eqs. 5.208 and 5.209, $L = n^2 A \mu_0 / (2x_0)$ is the inductance, $k_i = Li_0/x_0$ is the force–current factor and $k_s = k_i i_0/x_0$ is the force–displacement factor. Note that the term $k_i \dot{x}$ in Eq. 5.209 is the back EMF and the term $k_i i$ in Eq. 5.208 is the current induced force. Thus, the parameter k_i is actually a transduction factor and it can be modeled as the modulus of a gyrator (GY) element. The equivalent representation of Eqs. 5.208 and 5.209 can be given as shown in Fig. 5.149 [147] in which the left part is the electrical side and the right part is the mechanical side where the force due to transduction (F_i) is added with the force due to force-displacement factor to yield the total magnetic pulling force.

In bond graph form, the linearized model of one-sided magnetic bearing can be given as shown in Fig. 5.150. Note that the self-weight or gravity force is not modeled because it is assumed to be equal to F_0 and they cancel out each other in nominal or equilibrium configuration around which the model has been linearized. Note that for $u = 0$ and all other states initialized to zero ($i = x = \dot{x} = 0$), the system remains in static equilibrium. Note that the inputs and states here are deviations from the nominal operating values. If the system is disturbed from this equilibrium configuration (by giving an input disturbance or some nonzero initial values to states) then it becomes unstable due to the negative mechanical stiffness. Therefore, the input voltage has to be controlled to maintain equilibrium.

The two-sided active magnetic bearing schematic is shown in Fig. 5.151 where x_0 is the nominal air gap and the currents through the two magnets are i_1 and i_2 . It is assumed that both the magnets have same geometric dimensions and same number of turns in the coil. It is further assumed that the rotor does not tilt. The electromagnets are assumed to be current controlled.

Fig. 5.151 Schema of a two-sided AMB



Then, the force from the top and bottom magnets, respectively, can be written as

$$F_1 = \frac{\phi_1^2}{\mu_0 A}, \tag{5.210}$$

and

$$F_2 = \frac{\phi_2^2}{\mu_0 A}, \tag{5.211}$$

with the corresponding magneto motive forces (MMFs) given as

$$M_1 = \frac{2(x_0 - x)\phi_1}{\mu_0 A}, \tag{5.212}$$

and

$$M_2 = \frac{2(x_0 + x)\phi_2}{\mu_0 A}. \tag{5.213}$$

The forces can be written in terms of the currents as

$$F_1 = \frac{n^2 \mu_0 A}{4} \frac{i_1^2}{(x_0 - x)^2} \tag{5.214}$$

and

$$F_2 = \frac{n^2 \mu_0 A}{4} \frac{i_2^2}{(x_0 + x)^2}. \tag{5.215}$$

Thus, the equation of motion for the rotor is obtained from force balance and it is given as [153]

$$m\ddot{x} = \frac{n^2 \mu_0 A}{4} \frac{i_1^2}{(x_0 - x)^2} - \frac{n^2 \mu_0 A}{4} \frac{i_2^2}{(x_0 + x)^2} - mg. \tag{5.216}$$

The bond graph model of the system [153] can be drawn as shown in Fig. 5.152 where the constitutive relations for the two-port C-fields are defined in Eqs. 5.214

Fig. 5.152 Bond graph model of a lossless two-sided AMB

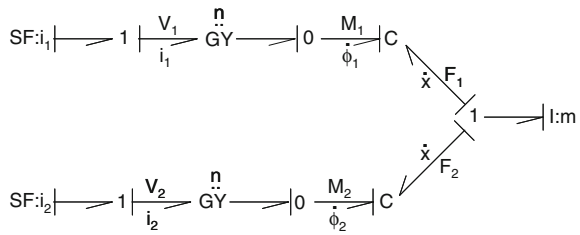
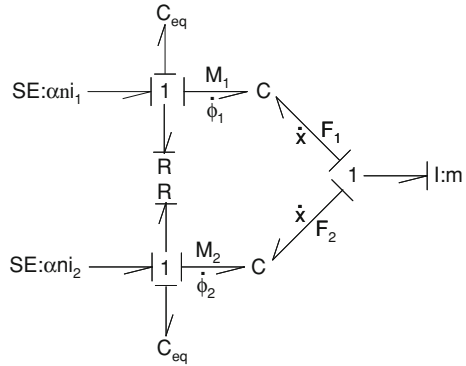


Fig. 5.153 Bond graph model of a two-sided AMB including the losses and secondary effects as equivalent capacities and resistances



and 5.215 using which the output power variables (F_1 , F_2 and then $\dot{\phi}_1$ and $\dot{\phi}_2$) can be computed in terms of input power variables (\dot{x} , ni_1 and ni_2). Note that one port of each C-field is differentially causalled because we are considering a current controlled configuration. Further note that losses have not been modeled.

However, the secondary effects such as flux leakage, fringing flux, reluctance of the core material, and eddy current loss etc. cannot be neglected in practice and they should be included in the model for design of reliable and robust controllers. The secondary effects have been characterized in a structural manner in [153] and then the resultant reduced model has been used to devise a sliding control algorithm. Although the authors of [153] consider a discretized model of the core, flux leakage and the fringing losses, they finally reduce the model to structure with a lumped capacitance C_{eq} (containing core compliance, fringing compliance, etc.) and a lumped resistance R that models eddy current and other losses. In addition, they consider the transduction between electrical and magnetic domains to be nonideal and introduce an efficiency factor α which is 1 under the ideal case. Thus, this nonideal transduction cannot be represented by a GY element and rather, the MMF αni is modeled as an effort source. The model of the magnetic bearing-rotor system is then given as shown in Fig. 5.153.

Note that in this model containing the losses, all ports of the C-fields and other storage elements are integrally causalled. In fact, the resistance R introduces a time constant (time constant for eddy current losses) into the system and thus avoids

the differential causalities present in the previous model (Fig. 5.152). The magnetic fluxes are state variables in the revised model whereas they were not so in the previous model that did not include losses. The time constant of the system is also influenced by the value of the C_{eq} parameter.

From the bond graph model given in Fig. 5.153, we obtain

$$\dot{\phi}_1 = \frac{\alpha n i_1 - M_1}{R} = \frac{\alpha n}{R} i_1 - \frac{2(x'_0 - x)}{\mu_0 A R} \phi_1, \quad (5.217)$$

$$\dot{\phi}_2 = \frac{\alpha n i_2 - M_2}{R} = \frac{\alpha n}{R} i_2 - \frac{2(x'_0 + x)}{\mu_0 A R} \phi_2, \quad (5.218)$$

where

$$x'_0 = \frac{\mu_0 A}{2C_{eq}} + x_0.$$

The force balance equation on the mass point yields

$$m\ddot{x} = \frac{\phi_1^2}{\mu_0 A} - \frac{\phi_2^2}{\mu_0 A} - mg. \quad (5.219)$$

If the core losses like fringing flux and the flux leakage are neglected (i.e., $\alpha = 1$) and the magnetic permeability of the core is assumed to be much larger than μ_0 then $C_{eq} = \infty$ and as a consequence $x'_0 = x_0$. In addition, if the control system bandwidth is much less as compared to the bandwidth of eddy current dynamics (see [153] for details) then the eddy current losses can be neglected ($R = 0$). Under these conditions, Eqs. 5.217–5.219 can be combined and reduced to Eq. 5.216 which was derived previously for the idealized active magnetic bearing.

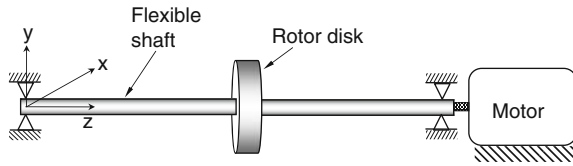
5.5.4 Source Interaction in Rotor Dynamics

A mechatronic system needs a holistic design approach [24]. Rotors used in mechatronic systems need to be designed along with the driving motor. This constraint is more important in systems with low power supply, which is usual as we move toward miniaturization of products.²

In an ideal vibrating system, excitation (energy source) is not influenced by the response of the system. On the contrary, when the excitation is influenced by the response of the system, the excitation is said to be a nonideal source and overall system is a nonideal vibrating system. All dynamic systems are inherently nonideal [5]. However, we rarely study nonideal system dynamics and usually, we idealize the system models. This approach is fine as long as the drives or actuators in the system have access to sufficient input power. However, if power supply is limited

² A part of this section is taken from these authors' previous work published in [121, 126].

Fig. 5.154 A heavy rotor mounted on a flexible shaft which is supported on two ideal bearings and is driven by a nonideal (DC) motor

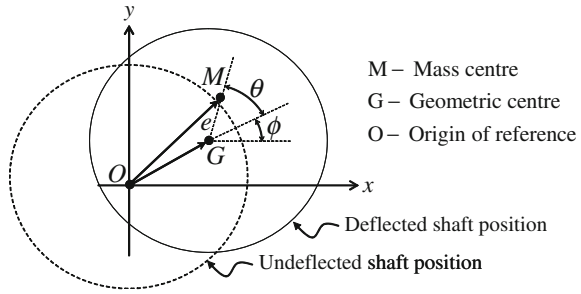


then neglecting the source–system interaction (i.e., not performing a holistic design) can lead to major design problems. Modern micromechanical systems usually contain small power sources and thus it is important to consider them as nonideal systems. In emerging application areas such as medical robotics and flexible space manipulators, rotating tools supported on flexible shafts are used as end effectors to perform a variety of tasks such as grinding, drilling, blowing, gyro stabilizing, etc. If improperly designed, these devices may produce undesirable performance. We will show one such application here.

In terms of mathematical modeling of a nonideal system as compared to the corresponding ideal system, an additional equation is required to describe how the energy source interacts with the rest of the dynamic system [122]. More precisely, to describe a nonideal dynamic system model one needs to have an additional degree of freedom compared to its ideal counterpart. Arnold Sommerfeld [131] discovered a phenomenon, better known as the Sommerfeld effect [11, 99], which is characterized by the jumps in the system response at critical values of power input to the source. He conducted an experiment consisting of an unbalanced rotor driven by a DC motor which was connected with a nonideal energy source and supported on an elastic foundation. Sommerfeld's observation was that the structural response of the system to which a nonideal electrical motor is connected may act like energy sink under certain conditions so that a part of the energy supplied by the source is spent to vibrate the structure rather than increasing the drive speed [37]. The same problem is also encountered in unbalanced rotor systems with flexible shaft and it requires great deal of control action to increase the spin speed of the rotor beyond its transverse vibration natural frequencies [35, 126]. Sommerfeld effect is also encountered near stability thresholds [120, 122]. Note that any drive with limited power supply or without feedback compensation is nonideal. Even a three-phase induction motor is a nonideal drive [92].

As an example, we consider a simple rotor model shown in Fig. 5.154 and assume that the flexible shaft is massless and it is supported on two identical rigid bearings. Furthermore, following assumptions are taken: a rigid rotor disk is fixed at the middle of the shaft, the rotor-shaft system is driven by a DC motor, the shaft has a uniform circular cross-section, the disk is mounted with its plane perpendicular to the shaft axis, the center of mass of the rotor disk has an eccentricity, and the torsional vibration of the rotor shaft are neglected. The stiffness of the shaft, the internal (material damping) and the aerial (external damping) are referred to the disk center which yields a regular Jeffcott/Laval rotor model.

Fig. 5.155 Mass center of the rotor disk in deflected and undeflected shaft position



Let us consider the original and deflected positions of the rotor disk as shown in Fig. 5.155 where e is the eccentricity of the mass center.

The coordinates of the mass center (x_m, y_m) of the disk can be obtained from the coordinates of the geometric center (x, y) of the disk as follows:

$$x_m = x + e \cos(\theta + \phi), \quad y_m = y + e \sin(\theta + \phi), \quad (5.220)$$

where θ is the angle of rotation of the rotor disk, e is the constant eccentricity, and ϕ is a constant phase corresponding to the initial position of the mass center of the disk. The velocity and acceleration relations are obtained by successive differentiation of Eq. 5.220 with respect to time as follows:

$$\dot{x}_m = \dot{x} - e\dot{\theta} \sin(\theta + \phi), \quad \dot{y}_m = \dot{y} + e\dot{\theta} \cos(\theta + \phi), \quad (5.221)$$

$$\ddot{x}_m = \ddot{x} - e\ddot{\theta} \sin(\theta + \phi) - e\dot{\theta}^2 \cos(\theta + \phi), \quad (5.222)$$

$$\ddot{y}_m = \ddot{y} + e\ddot{\theta} \cos(\theta + \phi) - e\dot{\theta}^2 \sin(\theta + \phi). \quad (5.223)$$

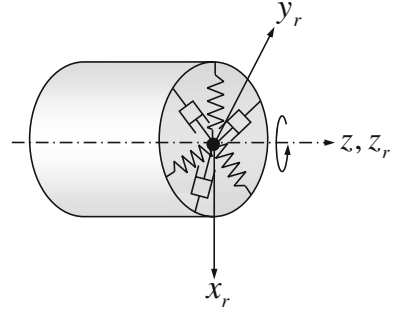
Multiplying both sides of Eqs. 5.222 and 5.223 by mass of the element, the inertial forces referred to the geometric center can be written as

$$m\ddot{x} = m\ddot{x}_m + me\ddot{\theta} \sin(\theta + \phi) + me\dot{\theta}^2 \cos(\theta + \phi), \quad (5.224)$$

$$m\ddot{y} = m\ddot{y}_m - me\ddot{\theta} \cos(\theta + \phi) + me\dot{\theta}^2 \sin(\theta + \phi). \quad (5.225)$$

Let us now consider the material or internal stiffness and damping in a shaft segment. In Fig. 5.156, x_r, y_r and z_r represent a body-fixed coordinate system, and x, y and z represent an inertial coordinate system with same origin. Note that for symmetric stiffness, frame rotation has no influence. If R_i is the coefficient of internal damping then the force due to it may be calculated by coordinate transformation from rotating to fixed frame as follows [9, 127]:

Fig. 5.156 Material or internal damping in rotating frame



$$\begin{Bmatrix} F_x \\ F_y \end{Bmatrix} = R_i \begin{Bmatrix} \dot{x}_r \\ \dot{y}_r \end{Bmatrix} = R_i \left(\begin{Bmatrix} \dot{x} \\ \dot{y} \end{Bmatrix} - \dot{\theta} \times \begin{Bmatrix} x \\ y \end{Bmatrix} \right) = R_i \begin{Bmatrix} \dot{x} \\ \dot{y} \end{Bmatrix} + \begin{bmatrix} 0 & R_i \dot{\theta} \\ -R_i \dot{\theta} & 0 \end{bmatrix} \begin{Bmatrix} x \\ y \end{Bmatrix}. \tag{5.226}$$

The first part of the force generated due to internal damping is dissipative (i.e., it adds to external damping, R_e); whereas the second part is a nonpotential positional force field called circulatory force [50]. Such circulatory forces (and its equivalent form called a follower force) appear in variety of other dynamic problems [28, 70, 124]. Note that the last term in Eq. 5.226 gives circulatory forces which is a position dependent restoring force [134], but the stiffness matrix is asymmetric. The stiffness matrix in linearized model of journal bearing given in Eq. 5.185 is anti-symmetric, which means it has a symmetric and an asymmetric part. Thus, journal bearings also give rise to circulatory forces and these circulatory forces are indeed responsible for hydrodynamic instability in journal bearings. More details on this can be found in [9, 123].

Because the rotor disk is at middle of the shaft and the shaft is symmetrically mounted on rigid or ideal bearings, it can be assumed that the disk does not rotate about its diameters under action of unbalance induced centrifugal forces. Thus, we can neglect the rotary inertia of the disk about its diametral axis and the associated degrees of freedom. The equations of motion can finally be written in inertial coordinates as follows:

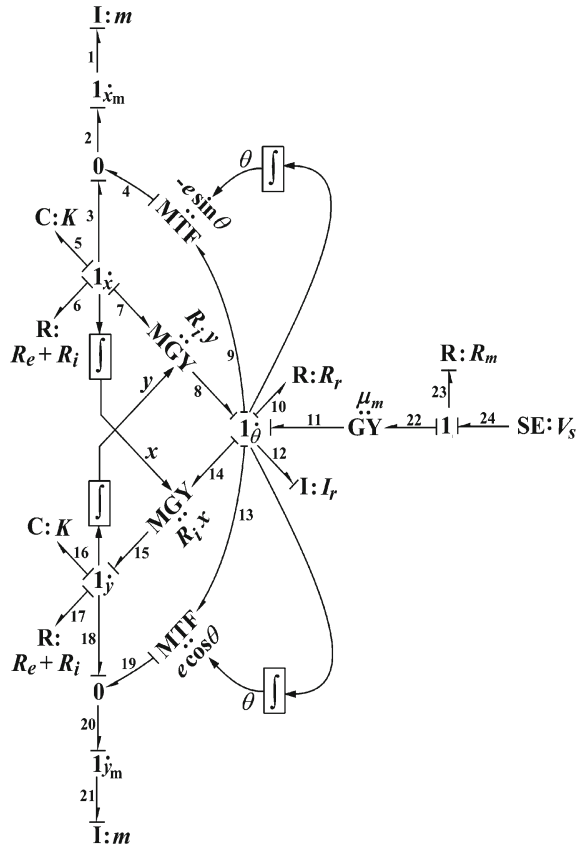
$$m\ddot{x} + (R_e + R_i)\dot{x} + R_i\dot{\theta}y + Kx = me\ddot{\theta}\sin(\theta+\phi) + me\dot{\theta}^2 \cos(\theta+\phi), \tag{5.227}$$

$$m\ddot{y} + (R_e + R_i)\dot{y} - R_i\dot{\theta}x + Ky = me\ddot{\theta}\cos(\theta+\phi) - me\dot{\theta}^2 \sin(\theta+\phi), \tag{5.228}$$

$$I_r\ddot{\theta} + R_r\dot{\theta} = \tau_m - \tau_l \tag{5.229}$$

where m is the mass of the disk, I_r is the rotary inertia of the shaft–disk system about the spinning axis, R_e is the external damping, and R_i is the internal damping referred to the geometric center of the disk, R_r is the damping to the spinning shaft (due to bearings and medium), K is the shaft stiffness referred to disk geometric center, τ_m is the torque developed by the DC motor, and τ_l is the torque due to source loading by

Fig. 5.157 Bond graph model of the shaft–disk system coupled with DC motor



the nonconservative (circulatory) forces. The last equation models the rotor-motor interaction and is present due to the nonideal source assumption. Note that these equations of motion are same as that for a rigid unbalanced rotor mounted on a soft foundation or bearing. The circulatory force (internal damping induced force) in this case can be generated due to the antisymmetric bearing stiffness matrix [9, 123].

The source loading torque can be determined from the bond graph model of system as has been presented later. It is given as

$$\begin{aligned} \tau_L = & R_i (x \dot{y} - y \dot{x}) + ((R_e + R_i) \dot{x} + Kx) e \sin(\theta + \phi) \\ & - ((R_e + R_i) \dot{y} + Ky) e \cos(\theta + \phi). \end{aligned} \tag{5.230}$$

The caussed bond graph model of the rotor-motor system shown in Fig. 5.157 is synthesized from the velocity relations given in Eq. 5.221 and the internal damping induced forces given in Eq. 5.226. The subscripts labeling 1-junctions describe various velocity points.

In the bond graph model, R_r is the external torsional damping offered to the spinning shaft (due to bearings and the medium), I_r is the rotary inertia of the shaft–disk system about the spinning axis, V_s is the voltage supply to the DC motor, μ_m is the motor characteristic constant, and R_m is the armature resistance of the motor. The two modulated gyrators model the circulatory forces as per Eq. 5.226 and the two modulated transformers model the eccentricity effect as per Eq. 5.221. The rest of the bond graph model is self-explanatory.

The state variables associated with the integrally causalled storage elements I and C are p and Q , respectively, with the subscripts indicating the bond numbers in the model given in Fig. 5.157. The state equation for the rate of angular momentum (i.e., torque) of the shaft derived from the bond graph is

$$\begin{aligned} \dot{p}_{12} = & \left(\frac{V_s \mu_m}{R_m} - \frac{\mu_m^2 p_{12}}{I_r R_m} \right) - R_r \frac{p_{12}}{I_r} - (R_e + R_i) e^2 \frac{p_{12}}{I_r} \\ & - \left(K Q_5 + (R_e + R_i) \frac{p_1}{m} \right) e \sin \theta + \left(K Q_{16} + (R_e + R_i) \frac{p_{21}}{m} \right) e \cos \theta \\ & + R_i y \left(\frac{p_1}{m} \right) - R_i x \left(\frac{p_{21}}{m} \right) \end{aligned} \quad (5.231)$$

The torque supplied by the motor is

$$e_{24} = \left(\frac{V_s \mu_m}{R_m} - \frac{\mu_m^2 p_{12}}{I_r R_m} \right). \quad (5.232)$$

The drive is loaded by contributions from various components [121]: the load due to damping on the rotation is $R_r \frac{p_{12}}{I_r}$, the couple moment due to shifting of elastic and damping forces from geometric center of the shaft to the mass center of the rotor is $\left(K Q_5 + (R_e + R_i) \frac{p_1}{m} \right) e \sin \theta - \left(K Q_{16} + (R_e + R_i) \frac{p_{21}}{m} \right) e \cos \theta$, the additional damping load due to rotation of the mass center of the rotor with respect to the geometric center is $(R_e + R_i) e^2 \frac{p_{12}}{I_r}$ and the source loading due to circulatory forces is $R_i x \left(\frac{p_{21}}{m} \right) - R_i y \left(\frac{p_1}{m} \right)$.

Therefore, the source loading torque, excluding that from rotational damping, is given as

$$\begin{aligned} \tau_L = & \left(K Q_5 + (R_e + R_i) \frac{p_1}{m} \right) e \sin \theta - \left(K Q_{16} + (R_e + R_i) \frac{p_{21}}{m} \right) e \cos \theta \quad (5.233) \\ & + (R_e + R_i) e^2 \frac{p_{12}}{I_r} - R_i y \left(\frac{p_1}{m} \right) + R_i x \left(\frac{p_{21}}{m} \right) \end{aligned}$$

which can be written in a form given earlier in Eq. 5.230 with the assumption that the term e^2 is negligible for small eccentricity. Otherwise, $(R_e + R_i) e^2 + R_r$ can be considered as the effective rotational damping in Eq. 5.230.

The overall unbalance response of the rotor system is superposition of free and forced vibration responses. For free vibration response, it will be assumed that $e = 0$ in Eqs. 5.227, 5.228 and 5.230. Use of a complex variable $q = x + iy$ converts Eqs. 5.227 and 5.228 to a compact form

$$m\ddot{q} + (R_e + R_i)\dot{q} + (K - iR_i\dot{\theta})q = 0. \quad (5.234)$$

At steady state, the shaft speed is constant given as $\dot{\theta} = \omega_r$. Let us assume a nondecaying solution of the form $q = q_0 e^{i\omega t}$ existing at the exact stability threshold (i.e., at the marginal stability condition), where q_0 is the complex amplitude of the free response and ω is the whirl frequency. Substitution of the assumed solution into Eq. 5.234 and separation of the real and the imaginary parts gives

$$-m\omega^2 + K = 0, \quad (5.235)$$

$$(R_e + R_i)\omega = R_i\omega_r. \quad (5.236)$$

From Eqs. 5.235 and 5.236,

$$\omega = \omega_n = \pm\sqrt{K/m}, \quad (5.237)$$

$$\omega_r = \omega_n (1 + R_e/R_i), \quad (5.238)$$

where, ω_n is the critical speed of the undamped shaft. The marginal stability at $\dot{\theta} = \omega_r$ yields the stability threshold speed, ω_{th} of shaft as follows:

$$\omega_{th} = \omega_n (1 + R_e/R_i) \quad (5.239)$$

where the system is stable for $\dot{\theta} < \omega_{th}$ and unstable for $\dot{\theta} > \omega_{th}$.

The Sommerfeld effect is primarily observed during passage through resonance [35, 126]. It is readily seen from Eq. 5.239 that the stability threshold is higher than the critical speed of the system for external damping parameter $R_e > 0$. Thus, the passage through resonance occurs in a stable operating regime. The steady-state response of the system in a stable regime ($\omega_r < \omega_{th}$) is the pure forced vibration response (the transients die out with time).

The steady-state unbalance response of a discrete rotor-disk system is a synchronous circular motion about the stable equilibrium [138] which is given as $x = B\cos(\omega_r t + \psi_1)$ and $y = B\sin(\omega_r t + \psi_1)$, where ψ_1 is an arbitrary phase and

$$B = \frac{m\epsilon\omega_r^2}{\sqrt{(K - m\omega_r^2)^2 + R_e^2\omega_r^2}} \quad (5.240)$$

The mechanical power drawn from the motor during steady-state synchronous whirl is expressed as

$$W_m = \tau_m \omega_r = \frac{\mu_m (V_s - \mu_m \omega_r) \omega_r}{R_m}, \quad (5.241)$$

and the mechanical power dissipated during the steady-state synchronous whirl (at any point on the circular orbit of radius B) is given by the sum of the product of the effort and flow variables in bonds connected to R-elements in the bond graph model as

$$W_d = (R_e + R_i) B^2 \omega_r^2 + R_r \omega_r^2. \quad (5.242)$$

Under steady whirl and spin, the supplied mechanical power has to be equal to the dissipated power [126]. This leads to

$$\frac{\mu_m (V_s - \mu_m \omega_r) \omega_r}{R_m} = (R_e + R_i) B^2 \omega_r^2 + R_r \omega_r^2, \quad (5.243)$$

which with use of Eq. 5.240 can be further simplified into a fifth-order polynomial equation in ω_r as follows:

$$\begin{aligned} m^2((\mu_m^2 + R_m R_r) + R_m e^2 (R_e + R_i)) \omega_r^5 - m^2 \mu_m V_s \omega_r^4 \\ - (\mu_m^2 + R_m R_r)(2mK - R_e^2) \omega_r^3 + V_s \mu_m (2mK - R_e^2) \omega_r^2 \\ + K^2 (\mu_m^2 + R_m R_r) \omega_r - K^2 V_s \mu_m = 0. \end{aligned} \quad (5.244)$$

All real positive roots of Eq. 5.244 which when substituted into Eq. 5.240 result in real positive whirl orbit amplitudes are admissible solutions. Some of the possible roots of Eq. 5.244 correspond to stable solutions whereas others are unstable (saddles). The stable solutions satisfy

$$\left. \frac{d}{d\omega_r} (W_m - W_d) \right|_{\omega_r = \varpi_r} < 0, \quad (5.245)$$

where ϖ_r is an admissible solution obtained from Eq. 5.244. Use of Eqs. 5.241 and 5.242 in inequality 5.245 and subsequent substitution of B from Eq. 5.240 yields

$$\left. \frac{d}{d\omega_r} \left(\left(\frac{V_s \mu_m}{R_m} - \frac{\mu_m^2}{R_m} \omega_r \right) \omega_r - R_r \omega_r^2 - \frac{(R_e + R_i) m^2 e^2 \omega_r^6}{(K - m \omega_r^2)^2 + R_e^2 \omega_r^2} \right) \right|_{\omega_r = \varpi_r} < 0, \quad (5.246)$$

which must be satisfied by every solution lying on the stable branch [126].

All real positive roots of Eq. 5.244 are allowable solutions, which may be substituted into Eq. 5.240 to obtain the corresponding whirl orbit amplitudes. Equation 5.244 has odd number of real roots and at least one of the roots is real and nonzero. By applying Descartes's rule of signs, with $2mK > R_e^2$, the number of positive roots is either 3 or 1. Multiple solutions of this kind lead to the highly complex nonlinear

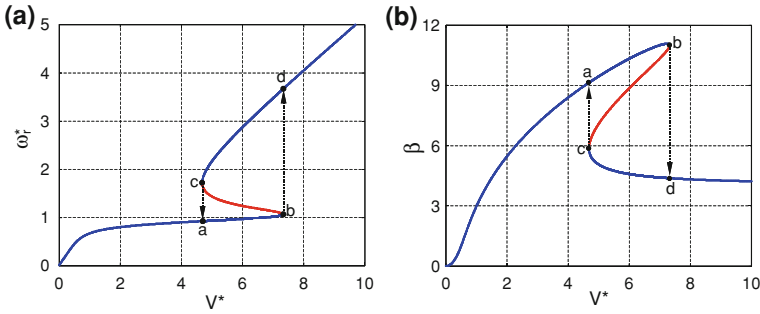


Fig. 5.158 Variations in steady-state **a** rotor spin rate and **b** flexural vibration or whirl amplitude with supply voltage

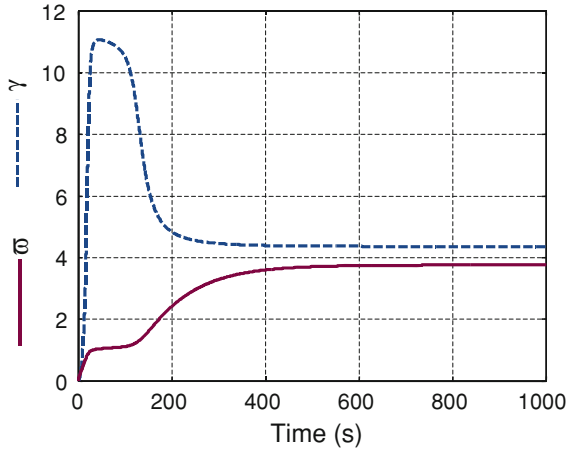
phenomenon called the Sommerfeld effect, which is a kind of jump phenomena [126].

Following representative values are considered for numerical studies: $m = 2 \text{ kg}$, $K = 8 \times 10^4 \text{ N/m}$, $e = 10^{-3} \text{ m}$, $R_e = 150 \text{ N.s/m}$, $R_i = 50 \text{ N.s/m}$, $R_r = 2 \times 10^{-5} \text{ Nms/rad}$, $\mu_m = 0.1 \text{ Nm/A}$, $R_m = 40 \Omega$ and $I_r = 0.004 \text{ kg.m}^2$. For the chosen values of m and K , Eq. 5.237 gives $\omega_n = 200 \text{ rad/s}$. The steady-state characteristic is defined by the following nondimensional quantities: the nondimensional voltage $V^* = V_s / (\mu_m \omega_n)$, the nondimensional rotor spin speed $\omega_r^* = \omega_r / \omega_n$, the nondimensional whirl amplitude $\beta = B \omega_n^2 / g$, and the nondimensional branch stability indicator (see L.H.S of the inequality 5.246.) $\lambda = (\omega_n^2 / (m g^2)) d(W_m - W_d) / d\omega_r$, where g is the acceleration due to gravity. For the given data, the domain of stability of free vibrations obtained from Eq. 5.239 [9] is $\omega_r^* < (1 + R_e / R_i) = 4$.

The nondimensional rotor spin speed (positive real roots of Eq. 5.244) is plotted against the nondimensional supply voltage in Fig. 5.158a where the branch between points marked as ‘b’ and ‘c’ is unstable. In the coast-up operation (i.e., while voltage is gradually increased to increase the rotor speed), the rotor spin speed is entrained at values near the natural frequency ($\omega_r^* = 1$) for a considerable range of voltage (points ‘a’ to ‘b’ in Fig. 5.158a). As the supply voltage is gradually increased further, the rotor spin speed suddenly jumps to a much higher value (to point ‘d’). In the coast-down (i.e., while voltage is gradually decreased to reduce the rotor speed) operation, a similar jump from point ‘c’ to point ‘a’ is observed.

The amplitudes are calculated from Eq. 5.240 and are plotted against the supply voltage in Fig. 5.158b. Points ‘a’ to ‘d’ in Fig. 5.158a are mapped to corresponding locations in Fig. 5.158b. As the rotor spin rate jumps from a lower value to a higher value, the amplitude jumps from a higher value to a lower value. The opposite occurs when the rotor speed jumps from a higher value to a lower value. From Fig. 5.158a, we find that some speeds (between points ‘b’ and ‘c’) are never reached in steady state, neither during coast-up nor during coast-down operation. This is the distinct characteristics of the Sommerfeld effect.

Fig. 5.159 Time evolution of the rotor spin speed and whirl amplitude during coast-up operation



Let us now have a look at the transient response of the system and investigate the passage through resonance phenomenon. We introduce nondimensional variables $\gamma = \omega_n^2 \sqrt{x^2 + y^2} / g$ and $\varpi = \dot{\theta} / \omega_n$ for plotting the results. In steady state, $\lim_{t \rightarrow \infty} \gamma = \beta$ and $\lim_{t \rightarrow \infty} \varpi = \omega_r^*$. All simulation results are obtained with common arbitrarily selected initial values as $x = 0.001\text{m}$, $y = 0$, $\theta = 0$, $\dot{x} = \dot{y} = 0$ and $\dot{\theta} = 0$.

For simulation, the supply voltage was chosen as $V_s = 150\text{ V}$ (i.e., $V^* = 7.5$). For this supply voltage, the rotor has to spin through the resonance to a higher speed slightly beyond point ‘d’ as shown in Fig. 5.158 and the predicted steady-state whirl frequency and amplitude of synchronous whirl are $\omega_r^* = 3.757$ and $\beta = 4.363$, respectively. The stability boundary for this data (i.e., $R_e = 150\text{ N/s/m}$ and $R_i = 50\text{ N/s/m}$) is at $\omega_r^* = 4$. Naturally, stable capture in the steady state is expected. The corresponding simulation results plotted in Fig. 5.159 show convergence of the transient response to the predicted steady-state values.

In initial phases shown in Fig. 5.159, higher whirl amplitude region corresponds to the passage through resonance [35], i.e., the period during which $\omega_r^* \approx 1$. Because the supply voltage is higher than the threshold required to pass through the resonance (i.e., point ‘b’ in Fig. 5.158), the spin rate increases to a stable value and consequently the whirl amplitude reduces.

Often the mass of the shaft cannot be neglected. Moreover, there can be more than one rotor disks. In these cases, distributed parameter rotor-shaft models are required. A finite element bond graph model of rotor-shaft system has been developed in [98]. The models are derived from the beam model with additional parts to include gyroscopic, rotating material damping, centrifugal, and other forces. Sommerfeld effect is also observed in such systems. Readers may consult [32, 93, 125] for further details.

5.5.5 Shape-Memory Alloy Based Control of Passage Through Resonance

The resonance conditions must be avoided in startup and rundown operations of a rotating machine working beyond the critical speed [63]. The large transverse vibration amplitudes during passage through resonance can damage the rotor shaft, the bearings and other equipment like turbine blades, couplings, etc. When the drive motor has sufficient power one can accelerate through the resonant frequencies during coast-up operation. However, when the motor has limited power then there is a possibility of getting caught in the resonant regime for a considerable time because near the resonance the drive energy is spent to increase the transverse vibration amplitudes rather than to increase the spin speed [110, 141]. As can be see from Fig. 5.158, the amplitudes are much higher during passage through critical speeds in spin-up (coast-up) operation as compared to that during coast-down operation.

One of the approaches to solve this problem is to modulate the resonant frequencies themselves. In coast-up operation, if the rotor is brought to a speed somewhere below the first critical speed and suddenly the first critical speed is lowered below the current rotor speed then the rotor has passed through its modified critical speed and its speed can be smoothly increased further to the desired operating speed. In the rundown operation, as the rotor speed approaches the modified critical speed, the critical speed can be switched to a value higher than the current rotor speed. The easiest approach to change the critical speeds is to switch the stiffnesses of the rotor shaft or the bearings or foundations. The shaft stiffness switching was investigated in [151] and the foundation or suspension stiffness switching was studied in [35, 55, 56]. However, switching the stiffness through conventional means such as with a hydraulic suspension is complicated because of the slow response time, large space requirement and difficulty in control, etc.

Use of memory materials for controlling the response at critical speed was proposed in [96, 146]. In [96], use of SMA wires was proposed to change the stiffness of a rotor support or the bearing stiffness during runup and rundown so that passage through critical speeds can be avoided. Similar stiffness scheduling schemes to pass through critical speeds have also been considered in [130] and demonstrated through experiments in [155].

In the experimental implementation made in [76], the effective stiffness of the support is controlled by varying the loading on a pair of elastomer O-rings which support the rolling element bearings as shown in Fig. 5.160. The stiffness of the O-rings is strongly influenced by the loading on the elastomer which is applied by a set of multiloop SMA wires on two sides of the bearing which provide the clamping force. The temperature of the SMA wires is controlled through Ohmic heating and measurements from thermocouples are used to modulate the power supply to the heating elements.

A laboratory test rig shown in Fig. 5.161 was designed at Swansea University based on the above-discussed principle [76]. It was found from impact testing that

Fig. 5.160 The schema of the rotor-bearing test rig at Swansea University

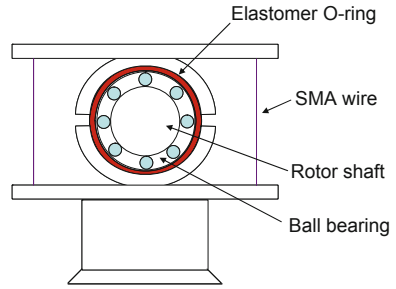
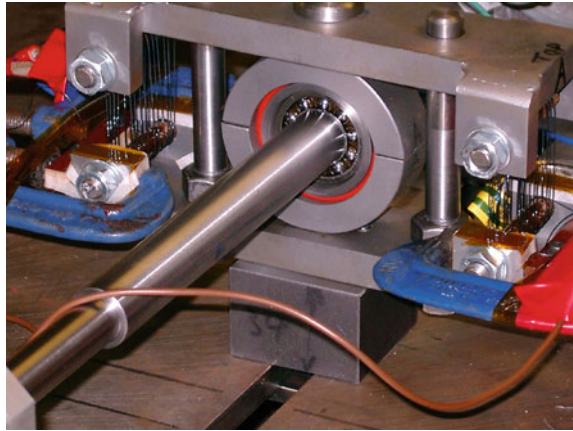


Fig. 5.161 Photograph of the rotor-bearing test rig at Swansea University (Courtesy: Dr. S. Jana [76])



there is significant shift in the natural frequency of the shaft and bearing assembly upon activation of the SMA wires.

Some sample results showing passage through resonance during coast/run-up operation with and without stiffness modulation are shown in Figs. 5.162 and 5.163. These results are obtained from the bond graph model given in Fig. 5.157 which is also a valid model for an eccentric rotor on rigid shaft mounted symmetrically on flexible supports or bearings. The rotor system considered for these results is driven by a DC motor (nonideal source) and the first critical speed of transverse vibrations is about 200 rad/s when the SMA wires are hot. In cold state, the first critical speed of transverse vibrations is 150 rad/s. The stiffness is switched through forced cooling of the SMA wires as the rotor speed reaches about 160 rad/s.

Although results do not show it, the rotor speed may be held constant at 175 rad/s for some time to allow the SMA wires to cool by switching off the power to the heating elements so that the austenite phase is fully transformed to martensite phase. The inset in Fig. 5.162 shows that for the system without stiffness switching, the rotor speed gets stuck at the resonance conditions (at spinning speed of about 200 rad/s) for considerable duration of time and the vibration amplitudes are large during that period. The stiffness switching produces smooth passage through resonance.

Fig. 5.162 Variation in rotor speed during passage through resonance with and without pedestal stiffness modulation

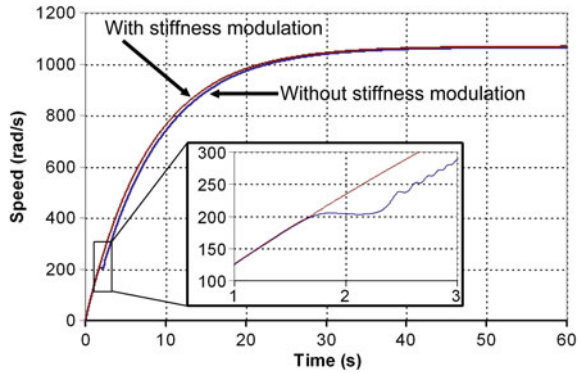


Fig. 5.163 Variation in rotor flexural vibration amplitude during passage through resonance with and without pedestal stiffness modulation

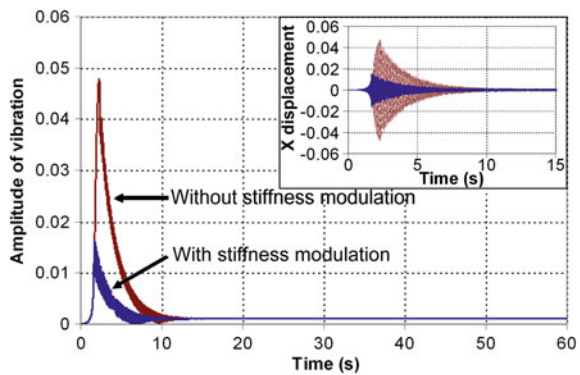


Figure 5.163 shows that the stiffness modulation significantly reduces the magnitude and duration of high amplitude transverse vibrations. The inset in Fig. 5.163 shows the transverse vibration displacements during the passage through resonance with and without stiffness modulation.

During runup operation, the bearing stiffness reduction just before the resonance condition also lowers the rotor stability threshold speed (see Eq. 5.239). Thus, it is required to switch the rotor stiffness back to the higher value (i.e., reheat the SMA wires) as soon as the rotor speed has crossed the critical speed. Note that when springs are connected in mechanical series, the overall stiffness is lower than the lowest stiffness of all the springs. As a consequence, the elastomer layer reduces the overall support stiffness and, consequently, the stability threshold. This is a price that has to be paid for achieving smooth passage through resonance.

References

1. S. Ahmed, H.M. Lankarani, M.F.O.S. Pereira, Frictional impact analysis in open-loop multi-body mechanical systems. *Trans. ASME J. Mech. Des.* **121**(1), 119–127 (1999)
2. B.J. Aleck, Thermal stresses in a rectangular plate clamped along an edge. *ASME J. Appl. Mech.* **16**, 118–122 (1949)
3. W.T. Ang, F.A. Garmn, P.K. Khosla, C.N. Riviere, Modeling rate-dependent hysteresis in piezoelectric actuators, in *Proceedings of the IEEE/RSJ International Conference on Intelligent Robots and Systems*, Las Vegas, Nevada, 2003
4. K.J. Astrom, C. Canudas de Wit, H. Olsson, P. Lischinsky, A new model for the control of systems with friction. *IEEE Trans. Autom. Control* **40**(3), 419–425 (1995)
5. J.M. Balthazar, D.T. Mook, H.I. Weber, R.M.L.R.F. Brasil, A. Fenili, D. Belato, J.L.P. Felix, An overview on non-ideal vibrations. *Meccanica* **38**, 613–621 (2003)
6. S. Behzadipour, A. Khajepour, Causality in vector bond graphs and its application to modeling of multi-body dynamic systems. *Simul. Model. Pract. Theory* **14**(3), 279–295 (2006)
7. T.K. Bera, A.K. Samantaray, Consistent bond graph modeling of planar multibody systems. *World J. Model. Simul.* **7**(3), 173–178 (2011)
8. A.N. Bercin, M. Tanaka, Coupled flexural-torsional vibrations of Timoshenko beams. *J. Sound Vib.* **207**(1), 47–59 (1997)
9. R. Bhattacharyya, A. Mukherjee, A.K. Samantaray, Harmonic oscillations of non-conservative, asymmetric, two-degree-of-freedom systems. *J. Sound Vib.* **264**, 973–980 (2003)
10. D. Birolek, Z. Birolek, V. Biolkova, Spice modelling of memcapacitor. *Elect. Lett.* **46**(7), 520–522 (2010)
11. I.I. Blekhman, *Vibrational Mechanics: Nonlinear Dynamic Effects, General Approach, Applications* (World Scientific, Singapore, 2000)
12. W. Borutzky, *Bond Graph Methodology—Development and Analysis of Multidisciplinary Dynamic System Models* (Springer, Heidelberg, 2010)
13. W. Borutzky, B. Barnard, J. Thoma, Describing bond graph models of hydraulic components in Modelica. *Math. Comput. Simul.* **53**, 381–387 (2000)
14. W. Borutzky, B. Barnard, J. Thoma, An orifice flow model for laminar and turbulent conditions. *Simul. Model. Pract. Theory* **10**, 141–152 (2002)
15. N.M. Bou-Rabee, J.E. Marsden, L.A. Romero, Tippe top inversion as a dissipation-induced instability. *SIAM J. Appl. Dyn. Syst.* **3**(3), 352–377 (2004)
16. A. Boukari, Piezoelectric actuators modeling for complex systems control. Ph.D. thesis, Arts et Mtiers ParisTech, 2010
17. A.F. Boukari, G. Moraru, J.C. Carmona, Malburet F, User-oriented simulation models of piezo-bar actuators: part I and part II, in *Proceedings of IDETC/CIE 2009, ASME 2009 International Design Engineering Technical Conferences & International Conference on Mechanical and Embedded Systems and Applications*, San Diego, USA, 2009
18. T.A. Bowers, Modeling, simulation and control of a polypyrrole-based conducting polymer actuator. Master's thesis, Arizona State University, 2004
19. P.C. Breedveld, An alternative model for static and dynamic friction in dynamic system simulation, in *IFAC-Conference on Mechatronic Systems*, vol. 2, pp. 717–722, 2000
20. M.D. Bryant, S. Lee, Resistive field bond graph models for hydrodynamically lubricated bearings. *Proc. IMechE Part I: J. Syst. Control Eng.* **218**(8), 645–654 (2004)
21. M. Calin, N. Chaillet, J. Agnus, A. Bourjault, Design of cooperative microrobots with impedance optimization, in *IEEE International Conference on Intelligent Robots and Systems*, pp. 1312–1317, 1997
22. R. Changhai, S. Lining, Hysteresis and creep compensation for piezoelectric actuator in open-loop operation. *Sens. Actuator A* **122**, 124–130 (2005)
23. C.J. Chen, *Introduction to Scanning Tunneling Microscopy* (Oxford University Press, Oxford 1993)

24. R. Chhabra, M. Reza Emami, Holistic system modeling in mechatronics. *Mechatronics* **21**(1), 166–175 (2011)
25. L.O. Chua, Memristor—the missing circuit element. *IEEE Trans. Circ. Theory* **18**, 507–519 (1971)
26. L.O. Chua, S.M. Kang, Memristive devices and systems. *Proc. IEEE* **64**(2), 209–223 (1976)
27. J. Compos, M. Crawford, R. Longoria, Rotordynamic modeling using bond graphs: modeling the jeffcott rotor. *IEEE Trans. Magn.* **41**(1), 274–280 (2005)
28. S.H. Crandall, The effect of damping on the stability of gyroscopic pendulums. *Zeitschrift für Angewandte Mathematik und Physik* **46**, S761–S780 (1995)
29. D. Croft, G. Shed, S. Devasia, Creep, hysteresis, and vibration compensation for piezoactuators: atomic force microscopy application. *ASME J. Dyn. Syst. Meas. Control* **123**, 3543 (2001)
30. Y. Cui, R.X. Gao, D. Yang, D.O. Kazmer, A bond graph approach to energy efficiency analysis of a self-powered wireless pressure sensor. *Smart Struct. Syst.* **3**(1), 1–22 (2007)
31. V. Damic, Modelling flexible body systems: a bond graph component model approach. *Math. Comput. Model. Dyn. Syst.* **12**(2–3), 175–187 (2006)
32. S.S. Dasgupta, A.K. Samantaray, R. Bhattacharyya, Stability of an internally damped non-ideal flexible spinning shaft. *Int. J. Non-Linear Mech.* **45**(3), 286–293 (2010)
33. M. Di Ventra, Y.V. Pershin, L.O. Chua, Circuit elements with memory: memristors, memcapacitors, and meminductors. *Proc. IEEE* **97**(10), art. no. 5247127:1717–1724 (2009)
34. M. Di Ventra, Y.V. Pershin, L.O. Chua, Putting memory into circuit elements: memristors, memcapacitors, and meminductors. *Proc. IEEE* **97**(8), art. no. 5109686:1371–1372 (2009)
35. M.F. Dimentberg, L. McGovern, R.L. Norton, J. Chapdelaine, R. Harrison, Dynamics of an unbalanced shaft interacting with a limited power supply. *Nonlinear Dyn.* **13**, 171–187 (1997)
36. P. Dupont, V. Hayward, B. Armstrong, F. Altpeter, Single state elasto-plastic friction models. *IEEE Trans. Autom. Control* **47**(5), 187–192 (2002)
37. M. Eckert, The Sommerfeld effect: theory and history of a remarkable resonance phenomenon. *Eur. J. Phys.* **17**(5), 285–289 (1996)
38. J.W. Eischen, C. Chung, J.H. Kim, Realistic modeling of edge effect stresses in bimaterial elements. *ASME J. Elect. Packag.* **112**, 16–23 (1990)
39. J.J. Epps, I. Chopra, Comparative evaluation of shape memory alloy constitutive models with test data, in *Collection of Technical Papers—AIAA/ASME/ASCE/AHS/ASC Structures, Structural Dynamics and Materials Conference*, vol. 2, pp. 1425–1437, 1997
40. T. Ersal, H.K. Fathy, J.L. Stein, Structural simplification of modular bond-graph models based on junction inactivity. *Simul. Model. Pract. Theory* **17**(1), 175–196 (2009)
41. J.D. Ertel, S.A. Mascaró, Dynamic thermomechanical modeling of a wet shape memory alloy actuator. *J. Dyn. Syst. Meas. Control Trans. ASME* **132**(5), 1–9 (2010)
42. B. Eryilmaz, B.H. Wilson, Unified modeling and analysis of a proportional valve. *J. Franklin Inst.* **343**, 48–68 (2006)
43. A.P. Filippov, *Vibrations of Mechanical Systems* (National Lending Library for Science and Technology, Boston Spa, Yorkshire, England, 1971)
44. L. Flemming, S. Mascaró, Wet SMA actuator array with matrix vasoconstriction device, in *Proceedings of the 2005 ASME International Mechanical Engineering Congress and Exposition*, pp. 1751–1758, 2005
45. P. Flores, Modeling and simulation of wear in revolute clearance joints in multibody systems. *Mech. Mach. Theory* **44**(6), 1211–1222 (2009)
46. P. Flores, J. Ambrosio, J.C. Pimenta Claro, H.M. Lankarani, *Kinematics and Dynamics of Multibody Systems with Imperfect Joints: Models and Case Studies* (Springer, Berlin, 2008)
47. A.M. Flynn, S.R. Sanders, Fundamental limits on energy transfer and circuit considerations for piezoelectric transformers. *IEEE Trans. Power Electr.* **17**(1), 8–14 (2002)
48. R.X. Gao, Y. Cui, Vibration-based sensor powering for manufacturing process monitoring. *Trans. North Am. Manuf. Res. Inst. SME* **33**, 335–342 (2005)
49. P.J. Gawthrop, B. Bhikkaji, S.O.R. Moheimani, Physical-model-based control of a piezoelectric tube for nano-scale positioning applications. *Mechatronics* **20**, 74–84 (2010)

50. G. Genta, *Dynamics of Rotating Systems* (Springer, Heidelberg, 2005)
51. P.J. Gilgunn, Large angle micro-mirror arrays in CMOS-MEMS. Master's thesis, Carnegie Mellon University, 2006
52. M. Goldfarb, N. Celanovic, A lumped parameter electromechanical model for describing the nonlinear behavior of piezoelectric actuators. *J. Dyn. Syst. Meas. Control Trans. ASME* **119**(3), 478–485 (1997)
53. O. Gomis-Bellmunt, F. Ikhouane, P. Castell-Vilanova, J. Bergas-Jan, Modeling and validation of a piezoelectric actuator. *Electron. Eng.* **89**, 629–638 (2007)
54. B. Halder, A. Mukherjee, R. Karmakar, Theoretical and experimental studies on squeeze film stabilizers for flexible rotor-bearing systems using newtonian and viscoelastic lubricants. *Trans. ASME J. Vib. Acoust. Stress Reliab. Des.* **112**(4), 473–482 (1990)
55. Y.-Y. He, S. Oi, F.-L. Chu, H.-X. Li, Vibration control of a rotor-bearing system using shape memory alloy: I. Theory. *Smart Mater. Struct.* **16**(1), 114–121 (2007)
56. Y.-Y. He, S. Oi, F.-L. Chu, H.-X. Li, Vibration control of a rotor-bearing system using shape memory alloy: II. Experimental study. *Smart Mater. Struct.* **16**(1), 122–127 (2007)
57. R. Holmes, The effect of sleeve bearings on the vibration of rotating shafts. *Tribology* **5**(4), 161–168 (1972)
58. L. Howald, H. Rudin, H.J. Guentherodt, Piezoelectric inertial stepping motor with spherical rotor. *Rev. Sci. Instrum.* **63**(8), 3909–3912 (1992)
59. D. Hrovat, J. Asgari, M. Fodor, in *Automotive Mechatronic Systems*, Mechatronic Systems Techniques and Applications: Transportation and Vehicular Systems, vol. 2 (Gordon and Breach Science Publishers, Amsterdam, 2000), pp. 1–98
60. M. Hubbard, Whirl dynamics of pendulous flywheels using bond graphs. *J. Franklin Inst.* **308**(4), 505–521 (1979)
61. T. Ikeda, *Fundamentals of Piezoelectricity* (Oxford Science Publications, Oxford, 1996)
62. T. Ikeda, F.A. Nae, H. Naito, Y. Matsuzaki, Constitutive model of shape memory alloys for unidirectional loading considering inner hysteresis loops. *Smart Mater. Struct.* **13**, 916–925 (2004)
63. T. Iwatsubo, H. Kanki, R. Kawai, Vibration of asymmetric rotor through critical speed with limited power supply. *J. Mech. Eng. Sci.* **14**(3), 184–194 (1972)
64. D. Karnopp, Computer simulation of stick-slip friction in mechanical dynamic systems. *J. Dyn. Syst. Meas. Control Trans. ASME* **107**(1), 100–103 (1985)
65. D.C. Karnopp, D.L. Margolis, R.C. Rosenberg, *System Dynamics: Modeling and Simulation of Mechatronic Systems* (Wiley, New York, 2000)
66. D.C. Karnopp, Power-conserving transformations: physical interpretations and applications using bond graphs. *J. Franklin Inst.* **288**(3), 175–201 (1969)
67. D.C. Karnopp, D.L. Margolis, Analysis and simulation of planar mechanism systems using bond graphs. *J. Mech. Des.* **101**, 187–191 (1979)
68. S. Karunanidhi, M. Singaperumal, Mathematical modelling and experimental characterization of a high dynamic servo valve integrated with piezoelectric actuator. *Proc. Inst. Mech. Eng. Part I: J. Syst. Control Eng.* **224**(4), 419–435 (2010)
69. O. Kavehei, A. Iqbal, Y.S. Kim, K. Eshraghian, S.F. Al-Sarawi, D. Abbott, The fourth element: characteristics, modelling and electromagnetic theory of the memristor. *Proc. R. Soc. A* **466**(2120), 2175–2202 (2010)
70. O.N. Kirillov, Destabilization paradox due to breaking the hamiltonian and reversible symmetry. *Int. J. Non-Linear Mech.* **42**, 71–87 (2007)
71. M. Krems, Y.V. Pershin, M. Di Ventra, Ionic memcapacitive effects in nanopores. *Nano Lett.* **10**(7), 2674–2678 (2010)
72. V. Lampaert, Modelling and control of dry sliding friction in mechanical systems. Ph.D. thesis, Katholieke Universiteit Leuven, 2003
73. A. Lasia, *Electrochemical Impedance Spectroscopy and Its Applications*. Modern Aspects of Electrochemistry, vol. 32, chapter 2 (Kluwer Academic/Plenum Pub, New York, 1999), p. 143

74. D.E. Lee, Development of micropump for microfluidic applications. Ph.D. thesis, Louisiana State University, 2007
75. F.-S. Lee, T.J. Moon, G.Y. Masada, Extended bond graph reticulation of piezoelectric continua. *J. Dyn. Sys. Meas. Control* **117**(1), 1–7 (1995)
76. A.W. Lees, S. Jana, D.J. Inman, M.P. Cartmell, The control of bearing stiffness using shape memory. in *4th International Symposium on Stability Control of Rotating Machinery (ISCORMA-4)*, Calgary, Alberta, Canada, 27–30 August 2007
77. C. Liang, C.A. Rogers, One dimensional thermomechanical constitutive relations for shape memory material. *J. Intell. Mater. Struct.* **1**, 207–234 (1990)
78. D.L. Margolis, G.E. Young, Reduction of models of large scale lumped structures using normal modes and bond graphs. *J. Franklin Inst.* **304**(1), 65–79 (1977)
79. D.L. Margolis, Bond graphs and the exploitation of power conserving transformations. *Comput. Programs Biomed.* **8**(3–4), 165–170 (1978)
80. W. Marquis-favre, E. Bideaux, S. Scavarda, A planar mechanical library in the AMESIM simulation software. Part I: Formulation of dynamics equations. *Simul. Model. Pract. Theory* **14**, 25–46 (2006)
81. W. Marquis-favre, E. Bideaux, S. Scavarda, A planar mechanical library in the AMESIM simulation software. Part II: Library composition and illustrative example. *Simul. Model. Pract. Theory* **14**, 95–111 (2006)
82. K. Medjaher, A.K. Samantaray, B. Ould Bouamama, Bond graph model of a vertical U-tube steam condenser coupled with a heat exchanger. *Simul. Model. Pract. Theory* **17**(1), 228–239 (2009)
83. H.E. Merrit, *Hydraulic Control Systems* (Wiley, New York, 1967)
84. W. Moon, I.J. Busch-Vishniac, Finite element equivalent bond graph modeling with application to the piezoelectric thickness vibrator. *J. Acoust. Soc. Am.* **93**, 3496–3506 (1993)
85. W. Moon, I.J. Busch-Vishniac, Modeling of piezoelectric ceramic vibrators including thermal effects: Part III. Bond graph model for one dimensional heat conduction. *J. Acoust. Soc. Am.* **101**, 1398–1407 (1997)
86. W. Moon, I.J. Busch-Vishniac, Modeling of piezoelectric ceramic vibrators including thermal effects. Part IV: development and experimental evaluation of a bond graph model of the thickness vibrator. *J. Acoust. Soc. Am.* **101**, 1408–1429 (1997)
87. C. Morin, Z. Moumni, W. Zaki, A constitutive model for shape memory alloys accounting for thermomechanical coupling. *Int. J. Plast.* **27**, 748–767 (2011)
88. C. Morin, Z. Moumni, W. Zaki, Thermomechanical coupling in shape memory alloys under cyclic loadings: Experimental analysis and constitutive modeling. *Int. J. Plast.* **27**, 1959–1980 (2011)
89. A. Mukherjee, Effect of bi-phase lubricants on dynamics of rigid rotors. *Trans. ASME J. Lubr. Tech.* **105**, 29–38 (1983)
90. A. Mukherjee, R. Karmakar, *Modelling and Simulation of Engineering Systems through Bond Graphs* (Alpha Sciences International, Pangbourne, UK, 2000)
91. A. Mukherjee, R. Karmakar, A.K. Samantaray, *Bond Graph in Modeling, Simulation and Fault Identification* (CRC Press, Boca Raton, 2006) ISBN: 978-8188237968, 1420058657
92. A. Mukherjee, R. Karmakar, A.K. Samantaray, Modelling of basic induction motors and source loading in rotor-motor systems with regenerative force field. *Simul. Pract. Theory* **7**(5), 563–576 (1999)
93. A. Mukherjee, V. Rastogi, A. Dasgupta, Extension of lagrangian-hamiltonian mechanics for continuous systems-investigation of dynamics of a one-dimensional internally damped rotor driven through a dissipative coupling. *Nonlinear Dyn.* **58**(1–2), 107–127 (2009)
94. A. Mukherjee, S. Sengupta, Active stabilization of rotors with circulating forces due to spinning dissipation. *J. Vib. Control* **17**(10), 1509–1524 (2011)
95. J. Mullins, Memristor minds. *New Sci.* **4**, 42–45 (2009)
96. K. Nagaya, S. Takeda, Y. Tsukui, T. Kumaido, Active control method for passing through critical speeds of rotating shafts by changing stiffnesses of the supports with use of memory metals. *J. Sound Vib.* **113**(2), 307–315 (1987)

97. M. Nakhaeinejad, M.D. Bryant, Dynamic modeling of rolling element bearings with surface contact defects using bond graphs. *J. Tribol.* **133**(1) art. no. 011102 (2011)
98. M. Nakhaeinejad, S. Lee, M.D. Bryant, Finite element bond graph model of rotors, in *2010 Spring Simulation Multiconference (SpringSim'10)*, art. no. 213 (2010)
99. A. Nayfeh, D. Mook, *Nonlinear Oscillations* (Wiley-Interscience, New York, 1979)
100. H. Olsson, K.J. Astrom, C. Canudas de Wit, M. Gaefvert, P. Lischinsky, Friction models and friction compensation. *Eur. J. Control* **4**(3), 176–195 (1998)
101. G.F. Oster, D.M. Auslander, Memristor: a new bond graph element. *Trans. ASME Dyn. Syst. Meas. Contr.* **94**(3), 249–252 (1972)
102. B. Ould Bouamama, Bond graph approach as analysis tool in thermofluid model library conception. *J. Franklin Inst.* **340**(1), 1–23 (2003)
103. B. Ould Bouamama, K. Medjaher, A.K. Samantaray, M. Staroswiecki, Supervision of an industrial steam generator. Part I: Bond graph modelling. *Control Eng. Pract.* **14**(1), 71–83 (2005)
104. D.A. Palmer, Modelling and control of suspensions as used in interferometric gravitational wave detectors. Ph.D. thesis, University of Glasgow, 2003
105. P.M. Pathak, A. Mukherjee, A. Dasgupta, Impedance control of space robots using passive degrees of freedom in controller domain. *Trans. ASME: J. Dyn. Syst. Meas. Control* **127**(4), 564–578 (2005)
106. H.M. Paynter, *Analysis and design of Engineering Systems* (M.I.T. Press, Cambridge, 1961)
107. E. Pedersen, Rotordynamics and bondgraphs: basic model. *Math. Comput. Model. Dyn. Syst.* **15**(4), 337–352 (2009)
108. H. Prahlad, I. Chopra, Comparative evaluation of shape memory alloy constitutive models with experimental data. *J. Int. Mater. Syst. Struct.* **12**(6), 383–395 (2001)
109. A. Preumont, *Mechatronics: Dynamics of Electromechanical and Piezoelectric Systems* (Springer, Heidelberg, 2006)
110. R.H. Rand, R.J. Kinsey, D.L. Mingori, Dynamics of spinup through resonance. *Int. J. Non-Linear Mech.* **27**(3), 489–502 (1992)
111. J.E.B. Randles, Kinetics of rapid electrode reactions. *Discuss. Faraday Soc.* **1**, 11 (1947)
112. J.N. Reddy, *Nonlinear Finite Element Analysis* (Oxford University Press, Oxford, 2007)
113. T.A. Rich, Thermo-mechanics of bimetal. *Gen. Electr. Rev.* **37**(2), 102–105 (1934)
114. J.M. Rodriguez-Fortun, J. Orus, F. Buil, J.A. Castellanos, General bond graph model for piezoelectric actuators and methodology for experimental identification. *Mechatronics* **20**, 303–314 (2010)
115. G. Romero, J. Felez, J. Maroto, M.L. Martinez, Kinematic analysis of mechanism by using bond-graph language, in *Proceedings 20th European Conference on Modelling and Simulation*, 2006
116. G. Romero, J. Felez, J. Maroto, J.M. Mera, Efficient simulation of mechanism kinematics using bond graphs. *Simul. Model. Pract. Theory* **17**, 293–308 (2009)
117. B. Samanta, A. Mukherjee, Analysis of acoustoelastic systems using modal bond graphs. *Trans. ASME J. Dyn. Syst. Meas. Control* **112**(1), 108–115 (1990)
118. A.K. Samantaray, K. Medjaher, B. Ould Bouamama, M. Staroswiecki, G. Dauphin-Tanguy, Component based modelling of thermo-fluid systems for sensor placement and fault detection. *SIMULATION: Trans. Soc. Model. Simul. Int.* **80**(7–8), 381–398 (2004)
119. A.K. Samantaray, B. Ould Bouamama, *Model-based Process Supervision—A Bond Graph Approach* (Springer, London, 2008)
120. A.K. Samantaray, A note on internal damping induced self-excited vibration in a rotor by considering source loading of a DC motor drive. *Int. J. Non-Linear Mech.* **43**(9), 1012–1017 (2008)
121. A.K. Samantaray, On the non-linear phenomena due to source loading in rotor-motor systems. *Proc. IMechE Part-C: J. Mech. Eng. Sci.* **223**(4), 809–818 (2009)
122. A.K. Samantaray, Steady state dynamics of a non-ideal rotor with internal damping and gyroscopic effects. *Nonlinear Dyn.* **56**(4), 443–451 (2009)

123. A.K. Samantaray, R. Bhattacharyya, A. Mukherjee, An investigation into the physics behind the stabilizing effects of two-phase lubricants in journal bearings. *J. Vib. Control* **12**(4), 425–442 (2006)
124. A.K. Samantaray, R. Bhattacharyya, A. Mukherjee, On the stability of Crandall gyropendulum. *Phys. Lett. A* **372**, 238–243 (2008)
125. A.K. Samantaray, S.S. Dasgupta, R. Bhattacharyya, Bond graph modeling of an internally damped nonideal flexible spinning shaft. *J. Dyn. Syst. Meas. Control Trans. ASME* **132**(6), art. no. 061502 (2010)
126. A.K. Samantaray, S.S. Dasgupta, R. Bhattacharyya, Sommerfeld effect in rotationally symmetric planar dynamical systems. *Int. J. Eng. Sci.* **48**(1), 21–36 (2010)
127. A.K. Samantaray, A. Mukherjee, R. Bhattacharyya, Some studies on rotors with polynomial type non-linear external and internal damping. *Int. J. Non-Linear Mech.* **41**(9), 1007–1015 (2006)
128. M. Schepers, Modeling a piezoelectric inertial stepping turntable using bond graphs. Master's thesis, University of Twente, 2004
129. W. Schiehlen, *Multibody Systems Handbook* (Springer, Berlin, 1990)
130. D.J. Segalman, G.G. Parker, D.J. Inman, in *Vibration Suppression by Modulation of Elastic Modulus Using Shape Memory Alloy*, ed. by M. Shahinpoor, H.S. Tzou. Intelligent Structures, Materials and Vibration, vol. 58, pp. 1–5. ASME, 1993
131. A. Sommerfeld, Beitrge zum dynamischen ausbau der festigkeitslehe. *Physikal Zeitschr* **3**, 266–286 (1902)
132. J.S. Stecki, Bond graph modelling of power transmission by torque converting mechanisms. *J. Franklin Inst.* **311**(2), 93–110 (1981)
133. D.B. Strukov, G.S. Snider, D.R. Stewart, R.S. Williams, The missing memristor found. *Nature* **453**, 80–83 (2008)
134. Y. Sugiyama, M.A. Langthjem, Physical mechanism of the destabilizing effect of damping in continuous non-conservative dissipative systems. *Int. J. Non-Linear Mech.* **42**, 132–145 (2007)
135. E. Suhr, Predictive analytical thermal stress modeling in electronics and photonics. *Appl. Mech. Rev.* **62**, 040801 (2009)
136. K. Tanaka, A thermomechanical sketch of shape memory effect; one dimensional tensile behavior. *Res. Mech.* **18**, 251–263 (1986)
137. J.U Thoma, B. Ould Bouamama, *Modelling and Simulation in Thermal and Chemical Engineering. Bond Graph Approach* (Springer, Telos, 2000)
138. W.T. Thomson, M.D. Dahleh, *Theory of Vibration with Applications* (Prentice Hall, Upper Saddle River, 1998)
139. Q. Tian, Y. Zhang, L. Chen, J. Yang, Simulation of planar flexible multibody systems with clearance and lubricated revolute joints. *Nonlinear Dyn.* **60**, 489–511 (2010)
140. S. Timoshenko, Analysis of bi-metal thermostats. *J. Opt. Soc. Am.* **11**(3), 233–255 (1925)
141. S. Timoshenko, *Vibration Problems in Engineering* (Van Nostrand, Princeton, 1961)
142. S.T. Todd, A. Jain, H. Xie, A multi-degree-of-freedom micromirror utilizing inverted-series-connected bimorph actuators. *J. Opt. A: Pure Appl. Opt.* **8**, S352–S359 (2006)
143. S.T. Todd, Electrothermomechanical modeling of a 1-D electrothermal MEMS micromirror. Master's thesis, University of Florida, 2005
144. A. Tonoli, N. Amati, Dynamic modeling and experimental validation of eddy current dampers and couplers. *J. Vib. Acoust.* **130** article no. 021011, 1–9 (2008)
145. N. Vahdati, S. Heidari, Bond graph model of a multi-layer piezoelectric (pzt) beam and its application in semi-active hydraulic mounts, in *ASME 2009 Dynamic Systems and Control Conference (DSCC2009)*, Paper no. DSCC2009-2786, pp. 347–354, Hollywood, California, USA, 12–14 October 2009
146. Z. Videman, I. Porat, An optimal-control method for passage of a flexible rotor through resonances. *Trans. ASME J. Dyn. Syst. Meas. Control* **109**(3), 216–223 (1987)
147. D. Vischer, H. Bleuler, Self-sensing active magnetic levitation. *IEEE Trans. Magn.* **29**(2), 1276–1281 (1993)

148. W. Wang, D. Shin, C. Han, H. Choi, Modeling and simulation for dual stage system using bond graph theory, in *ISOT 2009—International Symposium on Optomechatronic Technologies*, art. no. 5326087, pp. 197–202, 2009
149. T.M. Wasfy, A.K. Noor, Computational strategies for flexible multibody systems. *Appl. Mech. Rev.* **56**(6), 553–613 (2003)
150. M. Wassink, R. Carloni, S. Stramigioli, Port-hamiltonian analysis of a novel robotic finger concept for minimal actuation variable impedance grasping, in *Proceedings—IEEE International Conference on Robotics and Automation*, number art. **5509871**, 771–776 (2010)
151. J. Wauer, S. Suherman, Vibration suppression of rotating shafts passing through resonances by switching shaft stiffness. *J. Vib. Acoust.* **120**, 170–180 (1997)
152. Y. Xing, E. Pedersen, T. Moan, An inertia-capacitance beam substructure formulation based on the bond graph method with application to rotating beams. *J. Sound Vib.* **330**(21), 5114–5130 (2011)
153. T.-J. Yeh, Y.-J. Chung, W.-C. Wu, Sliding control of magnetic bearing systems. *J. Dyn. Syst. Meas. Control* **123**, 353–362 (2001)
154. T.-J. Yeh, H. Ruo-Feng, L. Shin-Wen, An integrated physical model that characterizes creep and hysteresis in piezoelectric actuators. *Simul. Model. Pract. Theory* **16**(1), 93–110 (2008)
155. A.J. Zak, M.P. Cartmell, W.M. Ostachowicz, Dynamics and control of a rotor using an integrated SMA/composite active bearing actuator, in *5th International Conference on Damage Assessment of Structures*, pp. 233–240, University of Southampton, UK, 2003
156. W. Zaki, Z. Mounni, A three-dimensional model of the thermomechanical behavior of shape memory alloys. *J. Mech. Phys. Solids* **55**, 2455–2490 (2007)
157. A. Zeid, C.H. Chung, Bond graph modeling of multibody systems: a library of three-dimensional joints. *J. Franklin Inst.* **329**(4), 605–636 (1992)

Part II

Advanced Topics and Applications

“Experiment without theory is blind; theory without experiment is lame.”

–Immanuel Kant

This part discusses some of the intelligent mechatronic system applications. Most innovations in the mechatronics field have been done by automobile and aerospace industries. We have dedicated a chapter on vehicle mechatronic systems where we discuss advanced applications like antilock and regenerative braking systems, automatic transmission, and hybrid vehicles with fuel cells.

An intelligent mechatronic system can adjust itself with the changing environment, e.g. when some of its components fail or the system parameters change. This requires online fault detection, its isolation, parameter estimation, and then taking re-medial measures according to the identified situation. Such systems are safe and robust. The second chapter in this part deals with fault detection, isolation and system reconfiguration.

Mechatronics is an integral part of robotics. Three chapters of this part are devoted to modeling and control of robotic systems: two of them introduce the basic concepts of robot kinematics, dynamics, and controller development, and the third discusses space robot modeling and controller design.

An intelligent transportation system comprising a set of intelligent autonomous vehicles is discussed in one of the chapters. Fault tolerant control laws for vehicle operation in healthy and faulty situations are developed. Bond graph approach is used for modeling, monitoring, and controlling the vehicle. Furthermore, modes of operation of a train of vehicles forming a platoon are studied to obtain the reconfiguration scenarios under different fault conditions.

One chapter of this part addresses model-based fault detection and isolation of networked control systems. A telerobotics system is considered, whose behavior is represented by a hybrid model, including the continuous, discrete, and stochastic aspects of the system components.

The last chapter concerns a virtual reality application. A basic vehicle driving simulator system is developed therein with the controlled Stewart platform, vehicle model, human-machine interface for human-in-the-loop simulation, and graphics display for visual feedback.

Chapter 6

Vehicle Mechatronic Systems

Vehicle, aircraft, and spacecraft industries lead the innovations in mechatronics research. Mechatronization of vehicles has been one of the major developments of our time [25]. Mechatronized vehicles use increasing numbers of mechatronic components (sensors, actuators, controllers) as replacement for mechanical, electrical, hydraulic, and electronic units or act to integrate their functions in a more useful and coordinated manner. Designing such mechatronic components and evaluating their performance in real vehicle applications is a challenging task. These systems need a high degree of reliability and hence the integration of electrical, mechanical, control engineering, and software technologies must be thoroughly designed and tested. This is the reason why hardware-in-the-loop systems (HIL systems) are being used throughout the development process for complex vehicle mechatronic systems. Systematic and automated testing of all electronic control units (ECUs) both as individual components and within the overall system can be performed through the HIL system. Modern automobile systems are using intelligent sensors and actuators. These intelligent units perform various additional tasks such as communication and decision making. The reliability of these intelligent systems needs thorough testing before commercialization. In hardware-in-the-loop simulation (HIL simulation or HILS) the behavior of the vehicle is simulated by software and hardware models. Real vehicle components (ECUs and other electronic/control units) are then connected via their electrical interfaces, to a vehicle dynamics simulator (virtual vehicle), which reproduces the behavior of the real-time environment. One such case has been illustrated in the final chapter of this book.

HILS allows early testing of ECU control algorithms and circuits even before a prototype vehicle has been produced or while the vehicle is being simultaneously developed. This cuts the total development time. Moreover, HILS reduces the number of expensive field trials, allows testing under simulated extreme or hazardous conditions and simulation of faults (e.g., brake failure) and environmental effects (e.g., skidding on snow), and maintains repeatability/reproducibility of tests. Software-in-the-loop simulation (SILS) is a precursor to HILS. It is a virtual prototyping step,

i.e., it allows one to test the control logic by plugging in the control software code to the vehicle model. At this time, it is important to note that the accuracy of the SILS/HILS, and consequently the prototype development, is highly dependent on the accuracy of the vehicle model along with the control architecture. SIMPACK Automotive and Saber are two well-known software suites for HIL and SIL simulation. This chapter is devoted to modeling and simulation of complex vehicle mechatronic systems individually and integrated with the full vehicle dynamics model.

Some of the vehicle mechatronic systems are so simple that we often overlook them, e.g., speed, fuel and other indicators, central locking system, automatic door closure system, rear and side view mirror positioning systems, headlight positioning system, warning buzzer, heating/air-conditioning regulation system, electronic massage system at lumbar support, power seat adjuster, power window regulator, communication with traffic routing systems, etc. And then there are complex mechatronic systems like multi-point fuel injection systems, air–fuel ratio control system, microprocessor controlled catalytic converter system for emission control, power assisted steering, active and semi-active suspension systems, automatic transmission system, hybrid drive systems and power trains, anti-lock and regenerative brakes, cruise control or automatic navigation system, self-diagnostic (early troubleshooting and warning) system, voice command system, driver alarm at low coefficient of friction and risk of aquaplaning, counter-steering by active bearing kinematics in case the friction coefficient is different on wheels on opposite sides, fault accommodation (load, side wind, brake squeal, crossfall of road), etc.

Most of these vehicle mechatronic systems are simple electronic or electro-mechanical systems which do not require much of control action. On the other hand, critical vehicle mechatronic systems use microprocessors to carry out complex processing. Bond graph modeling allows easy integration of vehicle model with mechatronic systems [31, 45–47]. We will discuss a few of those complex systems in this chapter.

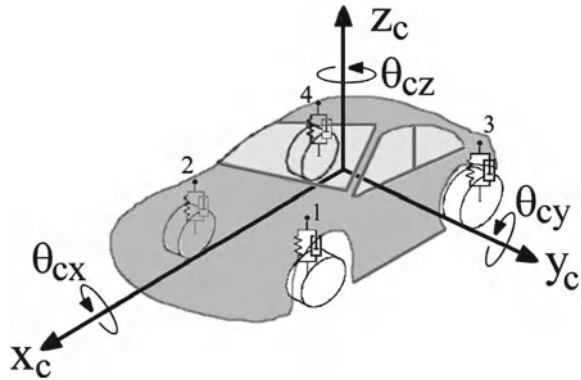
6.1 Model of a Four Wheel Vehicle

A road vehicle constitutes a multibody system. The vehicle body, each wheel, each axle, gear box, differential, etc. can be each considered as a 6 DOF rigid body. These rigid bodies are constrained by means of various joints. In the present case, we reduce the degrees of freedom of the system by neglecting trivial dynamics. We assume that the engine, differential, etc. are rigidly mounted on the vehicle body. Wheels are rigidly fixed to the axles which are attached to the body through suspension systems.

The schematic representation of the full vehicle model¹ is shown in Fig. 6.1.

¹ This section is partly adapted from these authors' previous works published in [6, 8].

Fig. 6.1 Four wheel vehicle model



6.1.1 Word Bond Graph Representation

The word bond graph representation of the full vehicle model is shown in Fig. 6.2 where bonds represented by two parallel lines are multi-bonds. In the word bond graph, the global system is decomposed into six subsystems. These are: vehicle body, suspension, wheel, steering, antilock braking system, and differential. The flow variables at the interface of different subsystems are marked in Fig. 6.2. The complementary power variables or generalized effort variables (force for linear velocity and torque for angular velocity) are not shown in Fig. 6.2 to maintain clarity of the figure. The four wheels are connected to the vehicle body through suspensions. The steering and ABS (a brake system) are coupled with the axle by scalar bonds.

Likewise, scalar bonds connect the differential to the rear wheels and the vehicle body. The model architecture and its submodels are developed in line with those presented in [19, 28, 57].

6.1.2 Tire Slip Forces and Moments

The tire forces and moments from the road surface act on the tire as shown in Fig. 6.3. The tire characteristics play an important role in the dynamic behavior of vehicles. The forces acting along x , y , and z axes are longitudinal force F_x , lateral force F_y and normal force F_z , respectively. Similarly, the moments acting along x , y , and z axes are overturning moment M_x , rolling resistance moment M_y and the self-aligning moment M_z , respectively [62].

The longitudinal slip arises due to application of torque about the wheel spin-axis. In actual case, as the vehicle speed cannot be measured, the longitudinal slip is calculated by measuring the wheel speed and acceleration [56]. The longitudinal slip

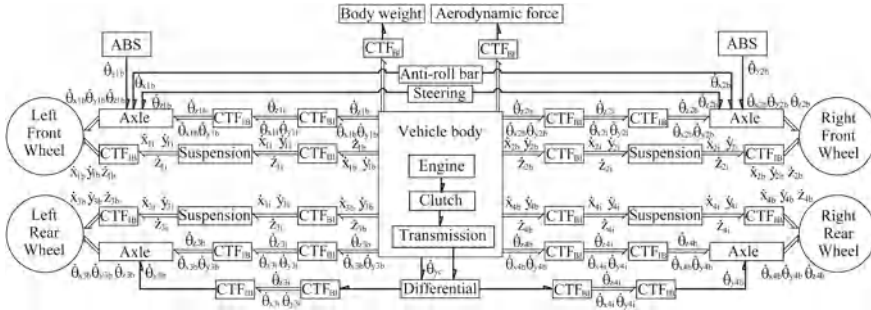
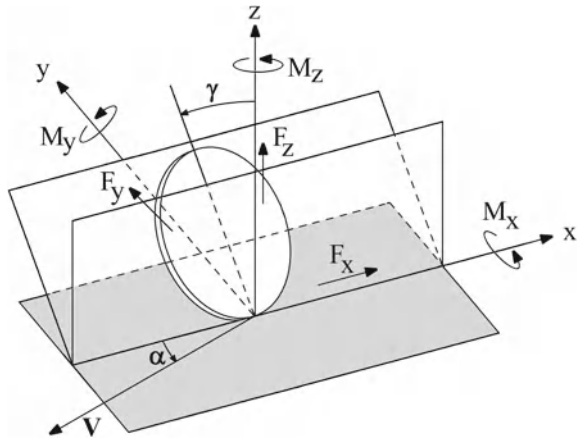


Fig. 6.2 Word bond graph of four wheel vehicle model

Fig. 6.3 Tire forces and moments



ratio is defined as the normalized difference between the circumferential velocity and the translational velocity of the driven wheel [40]. It is expressed as:

$$\sigma_x = \begin{cases} \frac{\dot{\theta}_{wy}r_w - \dot{x}_w}{\dot{\theta}_{wy}r_w} & \text{(during traction, assuming } \dot{\theta}_{wy} > 0) \\ \frac{\dot{x}_w - \dot{\theta}_{wy}r_w}{\dot{x}_w} & \text{(during braking, assuming } \dot{x}_w > 0) \end{cases} \quad (6.1)$$

Lateral wheel slip is the ratio of lateral velocity to the forward velocity of wheel [58]. It is given as:

$$\sigma_y = \tan \alpha = \frac{\dot{y}_w}{\dot{x}_w} \quad (6.2)$$

If the longitudinal slip ratio σ_x and lateral slip ratio σ_y are known then for small slip ratios, the longitudinal force F_x and lateral force F_y can be, respectively, approximated as $F_x = \sigma_x C_x$ and $F_y = \sigma_y C_y$ where, C_x and C_y are longitudinal tire stiffness

(coefficient) and cornering coefficient, respectively. However, these linear relations are invalid for large slip ratios.

The empirical magic formula based on experimental data is adopted for the development of tire–road friction model. It gives more accurate results for larger slip angles. It is also applicable to a wide range of operating conditions. Longitudinal slip velocity develops longitudinal force F_x , whereas side slip velocity and camber angle γ generate side force F_y and self-aligning moment M_z . Pacejka’s magic formula states that longitudinal force, side force, and the self-aligning moment are functions of longitudinal slip and side slip, respectively. Though this formula does not consider the velocity dependence of friction, it is used here for its simplicity. It is given as:

$$y_o = D \sin \left[C \tan^{-1} \left\{ Bx_i - E \left(Bx_i - \tan^{-1} (Bx_i) \right) \right\} \right] \quad (6.3)$$

where output variable, $y_o : F_x, F_y$ or M_z and input variable, $x_i : \sigma_x$ or σ_y .

Ply-steer, rolling resistance, and conicity effects may cause slight variation in the function in Eq. 6.3, but these variations may be neglected. The constant parameters (B, C, D, E) can be determined by measuring the tire forces and moments by sophisticated equipments. This formula is unsuitable when snow and ice start significantly affecting the vehicle performance.

The tire friction models are generally nonlinear in nature. The coefficient of friction (Fig. 6.4) is

$$\mu = \frac{\sqrt{F_x^2 + F_y^2}}{F_z}$$

where longitudinal force F_x and side force F_y can be found out under particular conditions of constant value of linear and angular velocity from the most widely used static magic formula (Eq. 6.3) given by Pacejka [58] and F_z is the normal force. However, one main disadvantage of this model is its inability to describe low slip effects and large forward and side slip effects during wheel lockup.

Another friction model often used to model tire forces is given by Burckhardt as follows [55]:

$$\mu(\sigma_x, \dot{x}_c) = \left[C_1 \left(1 - e^{-C_2 \sigma_x} \right) - C_3 \sigma_x \right] e^{-C_4 \sigma_x \dot{x}_c} \quad (6.4)$$

where constant parameters $C_1, C_2, C_3,$ and C_4 are determined from experiments. These parameters for asphalt dry road conditions are given in [55]. The normal load at the tire is kept constant for using this model. This model considers the velocity dependence of friction force. The main drawback of this model is the nonlinearity of its parameters which are difficult to estimate.

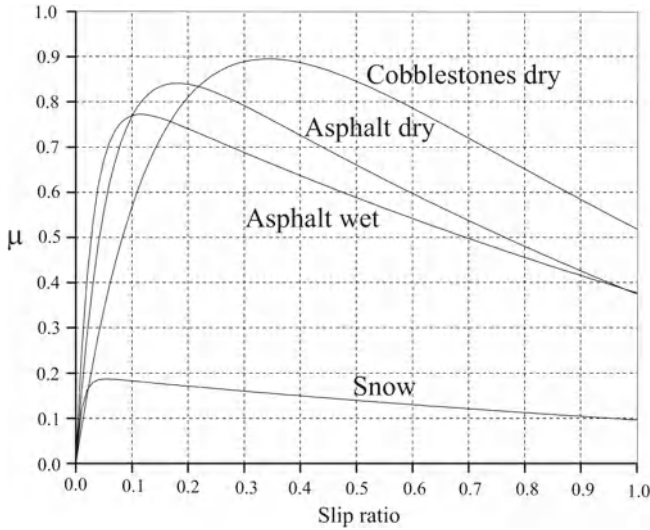


Fig. 6.4 Friction coefficient versus slip ratio curves for different road surfaces

6.1.3 Vehicle Body

The vehicle body is considered a 6 DOF rigid body. Wheel axles and wheels are attached to the body. Wheel axles are attached to the body through suspension systems. The vehicle body motion is described by three linear displacements along body-fixed x , y , and z axes and the rotational motion of the body can be defined by the three Cardan angles. The Newton–Euler equations of the vehicle body with attached body fixed axes aligned with the principal axes of inertia are as follows:

$$\sum F_x = m_c \ddot{x}_c + m_c (\dot{z}_c \dot{\theta}_{cy} - \dot{y}_c \dot{\theta}_{cz}), \tag{6.5}$$

$$\sum F_y = m_c \ddot{y}_c + m_c (\dot{x}_c \dot{\theta}_{cz} - \dot{z}_c \dot{\theta}_{cx}), \tag{6.6}$$

$$\sum F_z = m_c \ddot{z}_c + m_c (\dot{y}_c \dot{\theta}_{cx} - \dot{x}_c \dot{\theta}_{cy}), \tag{6.7}$$

$$\sum M_x = J_{cx} \ddot{\theta}_{cx} + \dot{\theta}_{cz} \dot{\theta}_{cy} (J_{cz} - J_{cy}), \tag{6.8}$$

$$\sum M_y = J_{cy} \ddot{\theta}_{cy} + \dot{\theta}_{cx} \dot{\theta}_{cz} (J_{cx} - J_{cz}), \tag{6.9}$$

$$\sum M_z = J_{cz} \ddot{\theta}_{cz} + \dot{\theta}_{cy} \dot{\theta}_{cx} (J_{cy} - J_{cx}). \tag{6.10}$$

The equations for three linear velocities of left-front suspension reference point (point 1 in Fig. 6.1) in the moving system of axes are

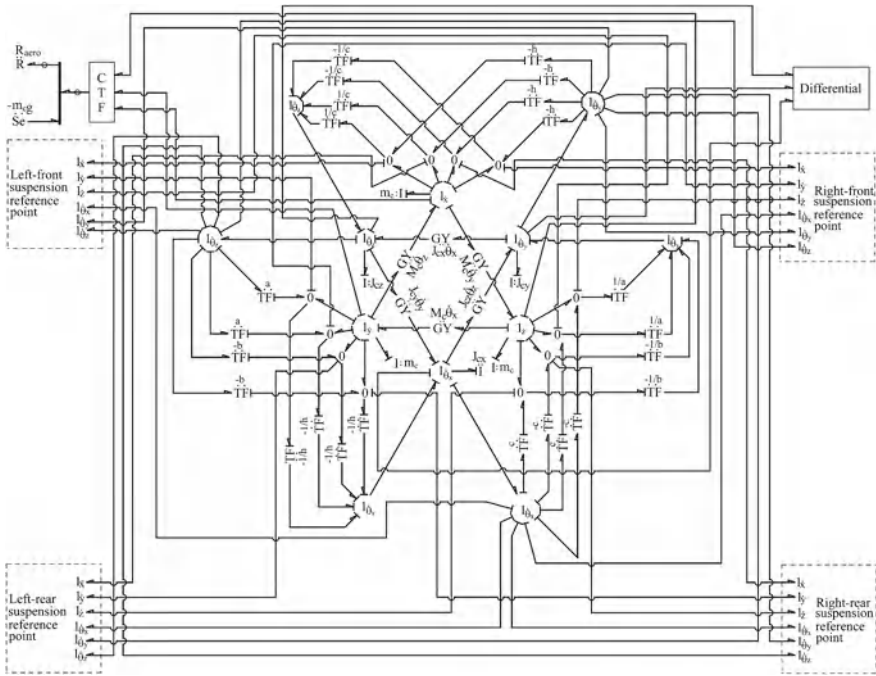


Fig. 6.5 Bond graph model of vehicle body

$$\begin{aligned}
 \dot{x}_1 &= \dot{x}_c + z_1 \dot{\theta}_{cy} - y_1 \dot{\theta}_{cz}, \\
 \dot{y}_1 &= \dot{y}_c + x_1 \dot{\theta}_{cz} - z_1 \dot{\theta}_{cx}, \\
 \dot{z}_1 &= \dot{z}_c + y_1 \dot{\theta}_{cx} - x_1 \dot{\theta}_{cy}.
 \end{aligned}
 \tag{6.11}$$

The equations for the three angular velocities of left front suspension reference point are similarly expressed. Likewise, the equations for three linear velocities and three angular velocities of other suspension reference points can be derived.

It is assumed that the aerodynamic effects, although considered in the model, are not very significant and that the vehicle is symmetrical with respect to its longitudinal axis. The bond graph in Fig. 6.5 models the vehicle body inertia and transformations of the three linear and three angular velocities into velocities at relevant suspension reference points. The vehicle body is modeled as a rigid body with six degrees of freedom, i.e., pitch, roll, yaw, heave, surge, and sway motions. The rigid body motion is described with respect to a coordinate system rotating and translating with it. This local coordinate frame attached at the center of mass of the body is assumed to be aligned with the inertial principal axes. The inertias are coupled by a pair of gyration rings (Euler junction structure), one for translational and the other for rotational velocities, according to Eqs. 6.5–6.10.

Three sets of forces and moments act on the body. First, the weight of the body and the aerodynamic forces (modeled by R_{aero} element) in the inertial frame act on the vehicle body model in non-inertial frame through coordinate transformation (CTF) [21]. Second, engine torque which is in a different body-fixed frame (wheel frame) is transformed twice to act on the body (through the differential). Lastly, the suspension forces and moments (constraint forces) acting in the inertial frame are transformed to get forces in the body-fixed direction. Then these forces are multiplied with the moment arms. The forces at all the four corners of the body are added together to get the suspension force acting at the center of gravity of the body. For display purposes, the angles of rotation in the inertial frame are obtained by integration of the angular velocities in the body-fixed frame after CTF.

6.1.4 Suspension System

Depending on the desired behavior of the vehicle, various types and forms of suspensions are used. Single wheel suspension system is the only option when an independent suspension system is required. Suspensions which can damp the vertical motion only slightly, due to the axle stiffness or axle fixed in a hinge point, are some typical single wheel suspension system arrangements. In real vehicles, the wheels are not connected to the car body only by an axle but through suspension systems which form a link between the vehicle body and the wheels. Suspension systems contribute to a car's smooth running and safe acceleration or braking. There are several suspension systems, e.g., McPherson, pseudo-McPherson, trailing arms, multi-arms, etc. [49]. A suspension system can be approximated by simple linear spring-damper suspension system which corresponds to energy storage and energy dissipation at each corner of the vehicle body while allowing free rotation of the wheel about the axle (y -axis).

The suspension system is used for the attachment of car body and wheel in a vehicle. The forces are calculated in the suspension for connecting two body components. In the bond graph model [6] given in Fig. 6.6, the C- and R-elements, which are in parallel, model the energy storage and dissipation due to relative motion between the car body and the wheel. The values of the stiffness and damping in the z -direction are the actual suspension stiffness and damping parameters, whereas much higher values of stiffness and damping in the longitudinal and lateral directions are considered to implement the constraints which limit the relative motions in x and y directions.

6.1.5 Wheels

The wheels are modeled by their mass, rotary inertia, radius, and tire stiffness. The tire is the most important of the wheel components. So tire forces and moments play an important role in vehicle dynamics. Tire forces are necessary to control the vehicle. As the tires are the only means of contact between the road and the vehicle, they

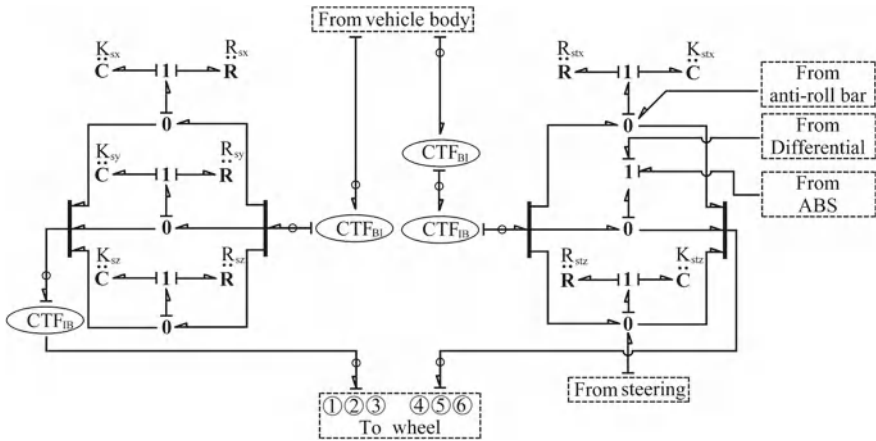


Fig. 6.6 Bond graph model of suspension system (Linear motion is on left and angular motion on right)

are the key factors determining the vehicle handling performance. Tire models are broadly classified as physical, analytical, and empirical models. The physical models are constructed to predict tire elastic deformation and tire forces. In such models, complex numerical methods are required to solve the equations of motion. Analytical models are not useful at large slip and at combined slip. Empirical models based on experimental correlations are generally more accurate. Here, both longitudinal and cornering forces and self-aligning moment are modeled empirically as per Pacejka’s magic formula [58].

The bond graph model of wheel is shown in Fig. 6.7. The wheel is modeled as a rigid body with six degrees of freedom. Similar to vehicle body, the inertias are coupled by a pair of gyrator rings, one for the translational and the other for the rotational velocities.

The wheel vertical dynamics is decoupled from longitudinal and cornering dynamics. The suspension force (F_z) and wheel radius (r_w) are used to modulate longitudinal and cornering dynamics. K_t and R_t represent the vertical stiffness and damping of tire. The MR-element which is used for modeling road–tire interactions is modulated by the normal reaction, i.e., the suspension force (F_z). Kinetic phenomenon and weight of the wheel are considered for the unsprung mass vertical dynamics. The tire–road interactions and braking action are considered for wheel longitudinal and cornering dynamics. The cornering force and self-aligning moment are dependent on vertical load and lateral slip angle, while the longitudinal force is dependent on vertical load and longitudinal slip rate. The characteristic relations for the MR-element are given according to Pacejka’s magic formulae (Eq. 6.3) or the composite slip based formulation [68].

In Fig. 6.7, the numbers shown within the circles identify the ports for interfacing this submodel to other submodels. Ports 1–6 are connected to the corresponding

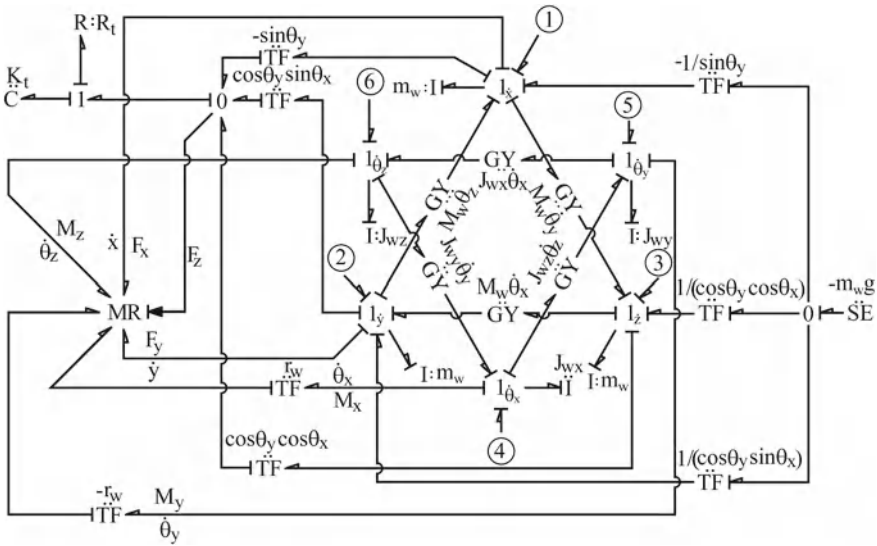


Fig. 6.7 Bond graph model of a wheel

velocities of the suspension reference point. The braking torque is applied on the front wheel through port 7 and the engine torque is transmitted to the rear wheel through the same port (port 7). Port 8 (shown as a dotted bond) is present only for front wheels. This port is used to interface the front wheel model to the anti-roll bar model, which constrains the relative roll between two front wheel axles.

6.1.6 Steering System

One basic feature of a good vehicle is its directional stability, which is the ability to steer smoothly. The steering action is achieved by rotating the front wheels of the vehicle around the vertical axis. Vehicles do not steer both the front wheels by an equal amount. While negotiating a curve the inner tires of the car will follow a circle with smaller radius than the outer tires. This distinction comes from the Ackermann steering concept. If a and b are the distances of front and rear wheels from vehicle c.g., c is half track width, θ is wheel angle, δ is steering angle and subscripts st, l and r refer to steering, left and right wheels respectively, then the rates of change of wheel steering angles in terms of steering input at the center are

$$\dot{\theta}_1 = \left[\frac{(a + b) \cos^2 \theta_1 + c \tan \theta_1 \cos^2 \theta_1}{(a + b) \cos^2 \theta_{st} - c \tan \theta_{st} \cos^2 \theta_{st}} \right] \dot{\theta}_{st} \tag{6.12}$$

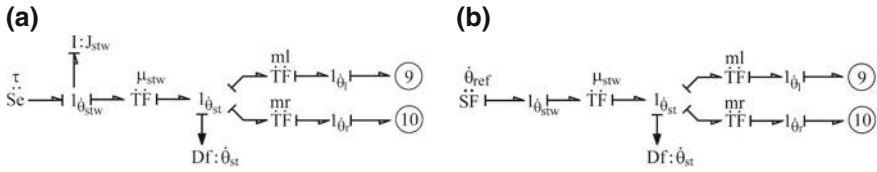


Fig. 6.8 Bond graph model of steering system with (a) torque input and (b) angular velocity input

$$\dot{\theta}_r = \left[\frac{(a + b) \cos^2 \theta_r - c \tan \theta_r \cos^2 \theta_r}{(a + b) \cos^2 \theta_{st} + c \tan \theta_{st} \cos^2 \theta_{st}} \right] \dot{\theta}_{st} \quad (6.13)$$

We are directly modeling the input from the human operator. The moment applied on the steering wheel about the z-axis is supplied as shown in Fig. 6.8a. The actual rate of rotation of the steering wheel is measured by a yaw rate sensor. It is assumed that the human vision system prescribes the desired rate of rotation. A feedback yaw rate controller may be developed where the controller action can mimic the driver’s response to the consequences of steering. The steering model output is used to rotate the front wheels by applying torques on the front axle (and reactive torques on the vehicle body). The rotary inertia J_{st} of the steering wheel is represented by I-element. The remainder of the system comprises mechanical transmission to the front axle. The rate of rotations of left and right wheels about the z-axis are represented at $I_{\dot{\theta}_l}$ and $I_{\dot{\theta}_r}$ junctions. These are interfaced to the front axle model through ports 9 and 10. The modulated transformer (MTF) moduli are determined from Ackermann’s formulae given in Eqs. 6.12–6.13 (see ref. [8] for details).

In experimental investigations, steering wheel rotations (driver inputs) are measured. The model in Fig. 6.8a may be modified to the form shown in Fig. 6.8b to take the rate of steering wheel rotation as the input. The transformer with modulus μ_{stw} is used to scale steering wheel rotation to steering rotation.

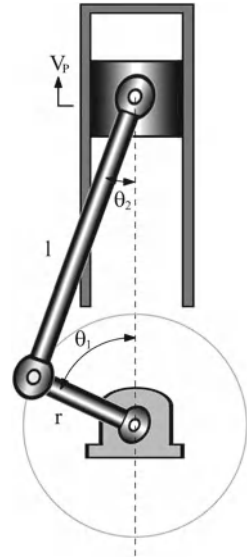
6.1.7 Slider-Crank System

An internal combustion engine with crank shaft and connecting rod is shown in Fig. 6.9. The thermodynamic process of the engine transforms heat into mechanical power.

The inertia of the slider, crank, and piston are negligible with respect to that of the rest of the system, i.e., flywheel, transmission shaft, gears, vehicle mass, and tires. Thus, a simple kinematic model may be developed by neglecting the inertias of the slider, crank, and piston. Note that it is possible to develop a full model of the slider-crank system along the lines of the model developed for the seven-body mechanism (Andrew’s mechanism).

For the simplified model, the relationship between angular velocity of crank shaft and linear velocity of piston as well as the relationship between torque and force are

Fig. 6.9 An internal combustion engine with crank shaft and connecting rod



obtained from the kinematic relations. The velocity of the piston is given as

$$\dot{x}_p = r \sin \theta_1 \dot{\theta}_1 + l \sin \theta_2 \dot{\theta}_2, \tag{6.14}$$

where θ_1 (angular position of the crank) and θ_2 are the angles shown in the figure, r is the crank radius, and l is the length of the connecting rod. From kinematic analysis, it follows that

$$r \sin \theta_1 = l \sin \theta_2 \quad \text{and} \quad \dot{\theta}_2 = \frac{(r/l) \cos \theta_1}{[1 - (r/l)^2 \sin^2 \theta_1]^{1/2}} \dot{\theta}_1. \tag{6.15}$$

Substitution of θ_2 and $\dot{\theta}_2$ from Eq. 6.15 into Eq. 6.14 yields the angular velocity of crank shaft $\dot{\theta}_1$ in terms of velocity of piston as

$$\dot{\theta}_1 = \frac{1}{r} \left[\frac{(r/l) \sin 2\theta_1}{2[1 - (r/l)^2 \sin^2 \theta_1]^{1/2}} + \sin \theta_1 \right]^{-1} \dot{x}_p. \tag{6.16}$$

This relation between two flow variables (\dot{x}_p and $\dot{\theta}_1$) is represented by a MTF element in bond graph model, with the angular position of the crank shaft as the modulating variable. The transformer modulus is

$$\mu_T = \frac{1}{r} \left[\frac{(r/l) \sin 2\theta_1}{2[1 - (r/l)^2 \sin^2 \theta_1]^{1/2}} + \sin \theta_1 \right]^{-1}. \tag{6.17}$$

6.1.8 Engine

The engine model comprises different energy domains: thermal, hydraulic, mechanical, and chemical. In the following, each energy domain is separately considered to develop the engine model in a step-by-step manner.

6.1.8.1 Engine Thermodynamics

We will first derive the thermodynamic relations for a collapsible chamber. It is convenient to consider pseudo-power variables in thermodynamic formulations [20, 32, 39, 48]. In a pseudo-bond graph, the product of the effort and flow variables does not yield a power variable. However, all rules for true bond graphs are applicable to pseudo-bond graphs and the energetic consistency is maintained by including additional sources (this part is tricky and should be properly handled). On the other hand, true bond graphs of thermodynamic systems are inherently energetically consistent (and preferred) but may lead to very complex model structure and constitutive relations [70–73] (See the section on solid oxide fuel cell modeling at the end of this chapter).

The control volume contains mass m in a variable volume V and with energy E . At this time, we assume that ideal gas law is applicable. Note that this approximation can represent the real case with the use of virial coefficients. The gas pressure, temperature, and enthalpy are denoted by P , T , and H , respectively.

When heat δQ is introduced into a thermodynamic system containing unit mass,

$$dE \text{ or } dU = \delta Q - pdV, \quad (6.18)$$

where U is the internal energy. From definition of specific heat at constant volume, $C_v = \left. \frac{\partial u}{\partial T} \right|_V = \left. \frac{\delta Q}{dT} \right|_V$ where u is the specific internal energy. The temperature of the gas can be written as (U and E are given the same status)

$$T = \frac{E}{mC_v}. \quad (6.19)$$

From ideal gas law,

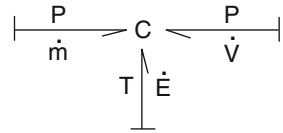
$$PV = mRT \quad (6.20)$$

which can be written in the form

$$P = \frac{RE}{VC_v}, \quad (6.21)$$

where R is the characteristic gas constant.

Fig. 6.10 Pseudo-bond graph model of a collapsible gas chamber with mass and heat transfer ports



We define \dot{m} , \dot{V} and \dot{E} as the flow variables and P , P , and T as the corresponding effort variables. Obviously, the product of complementary power variables (effort times flow) is not power. Thus, we have pseudo-power variables with which we can construct a pseudo-bond graph.

The pseudo-bond graph given in Fig. 6.10 is a three-port C -field in which the power variables are labeled in the bonds. This C -field was introduced initially in [34] and later used in [7, 26] to simulate an engine. In integral causality, this C -field receives information of three flow variables (\dot{m} , \dot{V} and \dot{E}) and computes the effort variables as follows:

$$T(t) = \frac{\int_0^t \dot{E}(\tau) d\tau + E_0}{\left(\int_0^t \dot{m}(\tau) d\tau + m_0\right) C_v}, \tag{6.22}$$

$$P(t) = \frac{R \left(\int_0^t \dot{E}(\tau) d\tau + E_0\right)}{\left(\int_0^t \dot{V}(\tau) d\tau + V_0\right) C_v}. \tag{6.23}$$

The state variables are time integrals of flow variables m , V , and E , for which corresponding initial values at $t = 0$ are prescribed as m_0 , V_0 , and E_0 , respectively. For a given position of the crank shaft, the volume of the chamber is known. For example, if at $t = 0$ the piston is at top dead center with $\theta = 0$, then the initial condition may be prescribed as $V_0 = V_c$, where V_c is the clearance volume. At start-up, the pressure and temperature inside the chamber are the same as that of the atmosphere, i.e., $P = P_0$ and $T = T_0$. Then, the other initial values for state variables are obtained from back calculation as

$$m_0 = \frac{P_0 V_0}{RT_0} \quad \text{and} \quad E_0 = m_0 C_v T_0. \tag{6.24}$$

Note that it is possible to create a true bond graph model of the collapsible chamber. Although the true bond graph model is slightly complicated, it gives the right physics

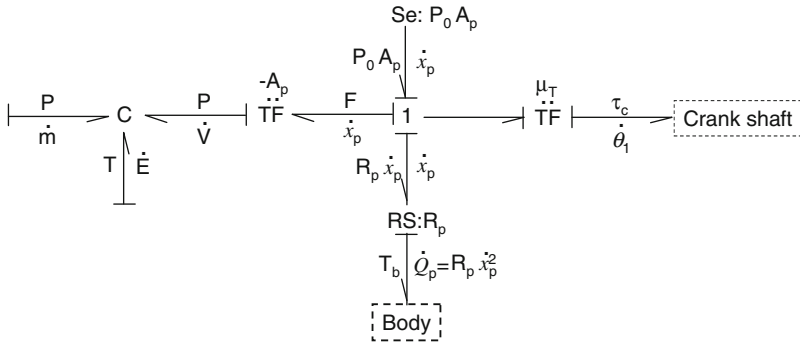


Fig. 6.11 Bond graph model of the piston and crank shaft connected to the engine

of the system (the growth of entropy, irreversibility of the system, entropy of mixing, and so on). The true bond graph model of the collapsible chamber is given at the end of this chapter where it is used to model the cathode and anode channels of a solid oxide fuel cell.

6.1.8.2 Mechanical Work

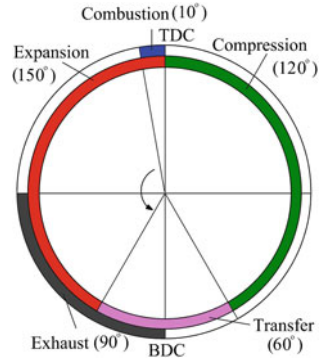
The mechanical work output from the engine is used to rotate the crank shaft which is in turn connected through the transmission system to the end load (wheels in contact with ground). The force balance equation for the piston is

$$P_0 A_P - P A_P - R_P \dot{x}_P - \mu_T \tau_c = 0, \tag{6.25}$$

where A_P is the cross-sectional area of the piston, P_0 is the atmospheric pressure acting on the free side of the piston, R_P is the resistance between the piston and the cylinder, μ_T is the transformer modulus defined in Eq. 6.17, and τ_c is the load torque. The bond graph model of mechanical coupling with the engine is given in Fig. 6.11. Note that the left side TF-element scales effort variable pressure P to force $F_P = -P A_P$ (positive force is in upward direction) and at the same time, it scales flow variable \dot{x}_P to another flow variable $\dot{V} = -A_P \dot{x}_P$ (positive piston velocity reduces gas volume).

The heat generated due to friction should be ideally added to the metallic body. This calls for the use of RS-element (the name suggests resistance + source [69]) in place of R-element. The two-port RS-element shown in Fig. 6.11 receives two information: flow variable \dot{x}_P and body temperature T_b . The resistance between the piston and the cylinder depends upon many factors such as the body temperature, level of lubrication, age of the piston rings and engine unbalance forces. If temperature is too high, then the resistance increases and engine seizure may take place. The

Fig. 6.12 Valve timing diagram for a two-stroke engine



RS-element uses the two input information to compute two outputs: the resistance force ($R_p \dot{x}_p$) and the rate of heat generation ($R_p \dot{x}_p^2$) due to the resistance.

6.1.8.3 Mass and Heat Transfer

The mass transfer into the chamber takes place during the suction phase and mass transfer out of the chamber takes place during the discharge phase. These phases are governed by the cam position which in turn depends on the angular position of the crank shaft. A typical valve timing diagram is shown in Fig. 6.12 in which TDC and BDC refer to top and bottom dead centers, respectively. The timings may change for different engines. In four stroke engines, intake, compression, combustion, and exhaust strokes complete during two crankshaft rotations, i.e., two crankshaft rotations are needed per working cycle of the engine. This is the commonly used cycle in vehicles. The exhaust and intake durations are comparatively large in a four-stroke cycle and thus the engine efficiency increases and the pollution level falls. Consequently, the valve timing diagram is different for the four-stroke engine.

For the flows to take place, it is not just enough to have the valve open. The pressure difference must be so that the flow takes place in the desired direction (into or out of the chamber). Nozzle flow equation [26, 34] is used to model flow through the valves.

The critical pressure ratio in Nozzle flow equation is given as

$$P_{cr} = \left(\frac{2}{\gamma - 1} \right)^{\gamma/(\gamma-1)}, \tag{6.26}$$

where γ is the ratio of specific heat at constant pressure and specific heat at constant volume. This critical pressure determines the flow choking condition (or the so-called von mises asymptote). The pressure ratio is considered as

$$P_r = \begin{cases} P_d/P_u & \text{if } P_d/P_u > P_{cr}, \\ P_{cr} & \text{if } P_d/P_u < P_{cr}, \end{cases} \quad (6.27)$$

where P_u and P_d refer to pressures in the upstream and downstream sides, respectively.

The mass flow rate of air fuel mixture through the suction valve is given as

$$\dot{m}_i = \frac{A_{v_i} C_{d_i} P_0}{\sqrt{T_0}} \sqrt{\frac{2\gamma}{R(\gamma-1)} \left[P_r^{2/\gamma} - P_r^{(\gamma-1)/\gamma} \right]}, \quad (6.28)$$

where $P_r = P/P_0$ or P_{cr} (as defined in Eq. 6.27), A_{v_i} is the full valve opening area of the inlet valve and C_{d_i} is the coefficient of discharge of the inlet valve (a function of the cam position or crank shaft position θ). The fuel mass flow rate is $\dot{m}_f = \alpha \dot{m}_i$ where α the fuel-air ratio, and $\dot{m}_i = \dot{m}_f + \dot{m}_a$ where \dot{m}_a is the air mass flow rate. The fuel air ratio α is controlled by the throttle valve position, i.e., the pressure on the accelerator or gas pedal. It is necessary to separately keep track of the fuel intake to model the combustion phenomenon.

The discharge mass flow rate is governed by a similar equation:

$$\dot{m}_o = \frac{A_{v_o} C_{d_o} P}{\sqrt{T}} \sqrt{\frac{2\gamma}{R(\gamma-1)} \left[P_r^{2/\gamma} - P_r^{(\gamma-1)/\gamma} \right]}, \quad (6.29)$$

where the chamber is the upstream side and atmosphere is the downstream side ($P_r = P_0/P$ or P_{cr}), A_{v_o} is the full valve opening area of the exhaust valve and C_{d_o} is the coefficient of discharge of the exhaust valve which is again a function of the cam position.

From definition of enthalpy,

$$H = U + PV, \quad (6.30)$$

which gives

$$dH = dU + PdV + Vdp. \quad (6.31)$$

For unit mass of gas at constant pressure, $dH = dU + PdV = \delta Q$, from which the specific heat at constant pressure is defined as

$$C_P = \left. \frac{\partial H}{\partial T} \right|_P = \left. \frac{\delta Q}{dT} \right|_P. \quad (6.32)$$

The mass transfer also introduces energy convection into or out of the chamber. The rate of heat convected into the chamber is given as

$$\dot{Q}_i = \dot{m}_i C_P T_0. \quad (6.33)$$

Note that the specific heat at constant pressure, C_P , used in the above expression changes depending upon the air–fuel ratio. Likewise, the rate of heat taken out with exhaust is

$$\dot{Q}_o = \dot{m}_o C_P T. \quad (6.34)$$

Further noting that $\delta Q = dU + PdV$,

$$dU = \delta Q - PdV \text{ or } \dot{E} = \dot{Q} - P\dot{V}. \quad (6.35)$$

The total energy balance equation is then given as

$$\dot{E} = \dot{Q}_c + \dot{Q}_i - \dot{Q}_o - P\dot{V} - \lambda_{gb}(T - T_b), \quad (6.36)$$

where \dot{Q}_c is the heat released due to combustion, λ_{gb} is the overall heat transfer coefficient between the gas and body (cylinder + piston), and $\lambda_{gb}(T - T_b)$ is the heat transferred to the body.

The metallic body also exchanges heat with the environment. The heat balance equation for the metallic body is given as

$$m_b C_{pb} T_b(t) = m_b C_{pb} T_0 + \int_0^t (\lambda_{gb}(T(\tau) - T_b(\tau)) - \lambda_{ba}(T_b(\tau) - T_0)) d\tau, \quad (6.37)$$

$$\text{or } T_b(t) = T_0 + \frac{1}{m_b C_{pb}} \int_0^t (\lambda_{gb}(T(\tau) - T_b(\tau)) - \lambda_{ba}(T_b(\tau) - T_0)) d\tau,$$

where m_b is the mass of the body, C_{pb} is the specific heat capacity of the body and λ_{ba} is the overall heat transfer coefficient between the body and the environment.

The bond graph model of the heat and mass transfer part of engine model is shown in Fig. 6.13. The two modulated R-elements (MR-elements) model the inlet and outlet flows (as per Eqs. 6.28 and 6.29) and the 0_H junction models the material balance. The heat balance, given in Eq. 6.36, is modeled at 0_T junction. The model of heat transfer to body and then to environment is marked in the figure wherein 0_{Tb} junction models the heat balance in the metallic body, the C-element represents the heat capacity of the metallic body, and resistances R_{gb} and R_{ba} model the heat transfers between gas–body and body–atmosphere, respectively.

6.1.8.4 Combustion

Combustion of fuel takes place through ignition. In gasoline or Otto cycle engines, the air–fuel mixture is ignited through a spark-plug. In diesel cycle or compression ignition engine, the gas pressure and temperature are tremendously high at the

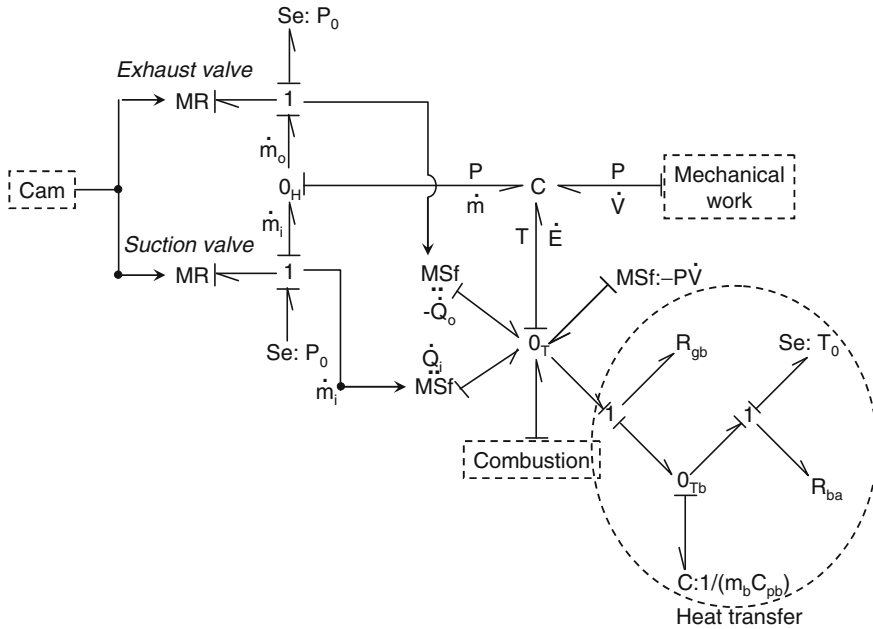


Fig. 6.13 Bond graph model of heat and mass transfer in the engine

top-dead center after the compression stroke and spontaneous ignition takes place. Combustion causes sudden increase in pressure which drives the piston towards the bottom dead center. This phase is known as the power stroke.

The combustion of fuel releases energy into the gas. The amount of energy released depends upon many factors, e.g., type of the fuel (its calorific value), pressure and temperature of the air fuel mixture, mixture quality, spatial uniformity in distribution, engine speed, and so on. The heat of combustion is the energy released as heat when a hydrocarbon is completely combusted with oxygen under standard conditions. Usually, complete combustion never takes place. Some part of the hydrocarbon fuel is fully combusted to form CO_2 , whereas some part is partially combusted to CO and some fuel remains unburnt. Other parasitic reactions also happen during this time. The combustion phenomenon occurs so fast that it is difficult to model it with other dynamics. The time constant difference is so severe that one needs a multi-scale simulation approach. However, an approximate model can be developed by considering experimental values of combustion efficiency. We assume that an efficiency map is available and decides the combustion efficiency η based on the state of the system. Note that combustion efficiency is different from engine efficiency.

We assume that the air–fuel mixture is dry, but some amount of water forms as a by-product of combustion process. Then, the lower heating value (LHV) of the fuel is considered as the heat of combustion. For gasoline, it is typically 44.40 MJ/kg. If q_{hc} is the heat of combustion or the calorific value, the heat released during the

combustion process is

$$\dot{Q}_c = \eta m_f q_{hc}, \quad (6.38)$$

where η is determined from the efficiency map [24] and $m_f = \int \dot{m}_f dt = \int \alpha \dot{m}_i dt$ is the mass of the fuel contained in the control volume. A detailed model of fuel injection system can be consulted in [1].

Although the combustion process is extremely fast, we still need to introduce a rate of combustion so that we can model it using a bond graph. The rate of combustion is determined by chemical kinetics, i.e., the spontaneity of reactions. The difference between the Gibb's free energy of the reactants and the products decides the reaction progression rate. There are many substeps involved in a chemical reaction and usually a few of those substeps are the rate determining factors [75]. This issue will be addressed at the end of this chapter. In any case, whatever way the combustion rate is modeled, it makes little change to the overall dynamics of the vehicle. We assume that the reaction rate is constant and it takes place during an extremely small time interval Δt (close to an impulse function) so that

$$\dot{Q}_c = \begin{cases} \frac{\eta m_f q_{hc}}{\Delta t} & \text{for } \theta_t < \theta < \theta_t + \Delta t \dot{\theta}, \\ 0 & \text{otherwise,} \end{cases} \quad (6.39)$$

where θ_t is the crank angular position when the piston has just passed the top dead center.

The bond graph model of combustion phenomenon along with the heat and mass transfer is given in Fig. 6.14. The part used to model combustion is given in a block diagram form. The accelerator pedal pressure modifies the α parameter value (fuel-air ratio) and the total fuel inlet during suction is obtained by integrating (\int block) the fuel mass flow rate (\dot{m}_f). This information is then used to model the heat input rate due to combustion (MSF: \dot{Q}_c) as per Eq. 6.39. Note that the fuel efficiency map is also used in determination of \dot{Q}_c . It is assumed that any unburnt fuel is discarded completely with the exhaust. This is why, the state associated with the \int block is initialized to zero at the start of the simulation and every time after the exhaust is completed.

6.1.8.5 Integrated Model

The complete model of the single cylinder engine is given in Fig. 6.15. It is possible to change the valve timings and convert this model into a four-stroke engine. The engine output is torque applied onto the crank shaft.

The crank shaft is connected to the flywheel and the transmission shaft through a clutch. The torque output from engine blocks can be applied on the crank shaft. A V8 engine configuration has been developed later in this section.

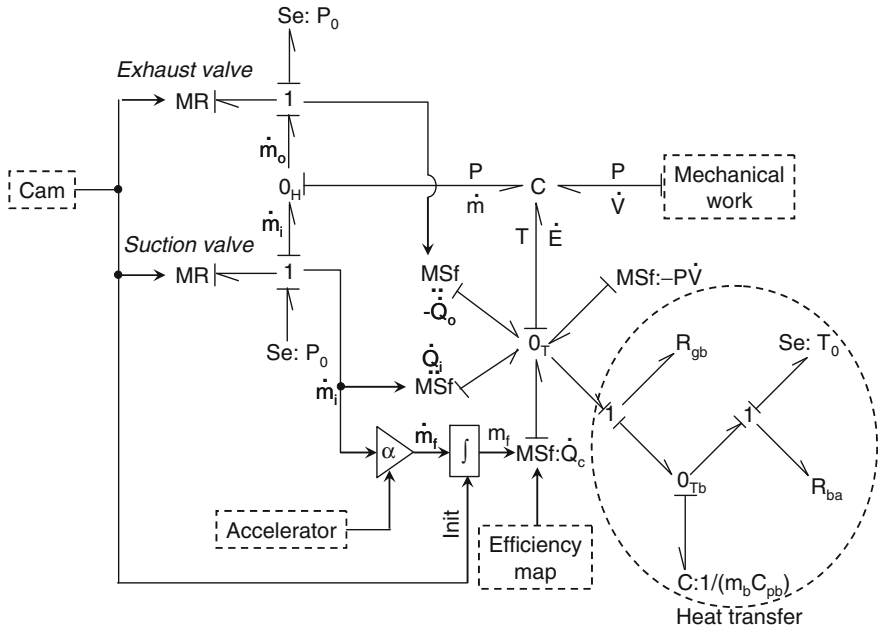


Fig. 6.14 Bond graph model of heat and mass transfer, and combustion phenomenon in the engine

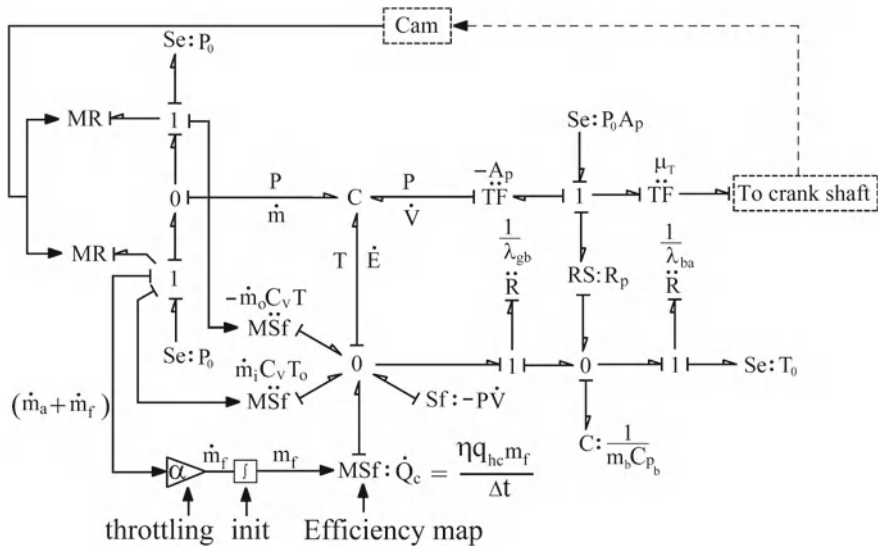
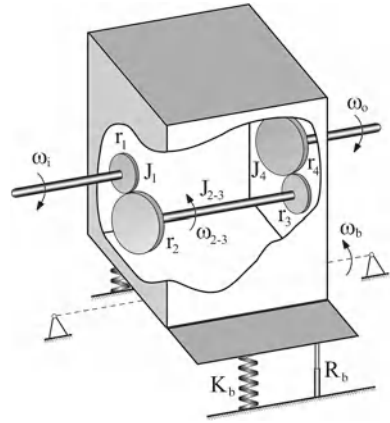


Fig. 6.15 Integrated bond graph model of the single cylinder internal combustion engine

Fig. 6.16 A cut-out of a single lay shaft transmission gearbox



6.1.9 Gearbox

A typical transmission gearbox for the rear wheel drive vehicle is shown in Fig. 6.16. The input shaft, output shaft, and lay shaft rotate with angular speeds ω_1 , ω_o and ω_{2-3} , respectively. The housing block is mounted on the vehicle body with suspensions and it can roll with angular velocity of ω_b (although this small rotation can be neglected, it is still included in the model). The roll stiffness and roll damping to the block are K_b and R_b , respectively.

The bond graph model of gearbox is shown in Fig. 6.17. It is adopted from the model developed in [28]. The engine torque from the crank shaft acts on the gear inertia J_1 and on the housing block as a reaction torque. The frictional resistances at the input and output shafts are R_i and R_o , respectively. The total reaction torque acting on the housing is summation of reaction torque due to two pairs of gears, reaction torque of input and output torques, and reaction torque due to relative rotation of lay shaft with respect to block housing. All the reaction torques are summed up at the I_{ω_b} junction (which has multiple copies so as to maintain the clarity of the figure, but can be merged to a single junction) where the rotary inertia of the housing block is modeled.

The roll of the gear box housing and vehicle body roll are constrained by the gear box housing suspension. The linear stiffness and damping of this suspension can be expressed as an effective torsional stiffness and damping, which is modeled by C: K_{be} and R: R_{be} elements at the 1-junction representing the relative roll velocity between the vehicle body and the gear box housing.

The relative angular speed of gear1 (ω_1) with respect to housing (ω_b) is transformed to obtain the angular speed of the lay shaft ω_{2-3} by using the transformer with modulus $-r_2/r_1$. Similarly, the relative angular speed of the lay shaft with respect to housing ($\omega_{2-3} - \omega_b$) is transformed to obtain the angular speed of the output shaft ω_o by using the transformer with modulus $-r_3/r_4$. The backlash (see Chap. 3) and gear-mesh stiffness and damping between two pair of gears are modeled

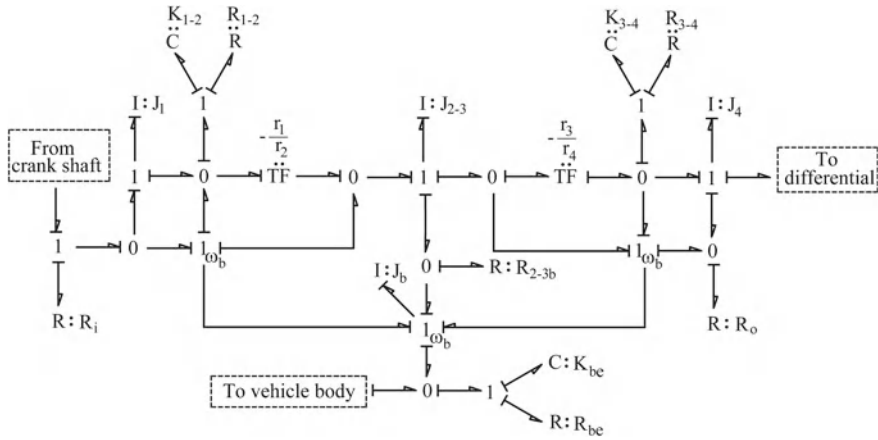


Fig. 6.17 Bond graph model of transmission gearbox

as torsional spring and damper in series connection (C: K_{i-j} and R: R_{i-j} , where i and j enumerate the gears). Moreover, the element R: R_{2-3b} models the reaction from lay shaft bearings. The bearing generates torque due to torsional damping depending on the relative angular velocity between the lay shaft and the gear box housing. More detailed models of the bearings (rolling element bearings and journal bearings) are given in the previous chapter.

6.1.10 Differential

The power transmission to the wheel axles is achieved through different mechanisms such as fluid coupling (discussed later in this chapter), locked differential, planetary gear set with bypass clutches (also detailed later in this chapter), and controlled clutch modulations. The planetary gear set and differential are the most widely used.

The schematic representation of a planetary gear set or epicyclic differential is shown in Fig. 6.18. The angular velocities are denoted by symbol ω , the radii by r and the subscripts s, c, p, and r, respectively, indicate sun, carrier, planet, and ring gears.

The angular velocity of the planet as seen from a fixed frame fixed to the ring gear is the sum of the angular velocity of the carrier and the angular velocity of the planet as seen from a frame fixed to the carrier. The relative angular velocity between the carrier and the sun gear is related to the planet’s angular velocity as follows:

$$\frac{\omega_c - \omega_s}{\omega_c + \omega_p} = -\frac{r_p}{r_s} \tag{6.40}$$

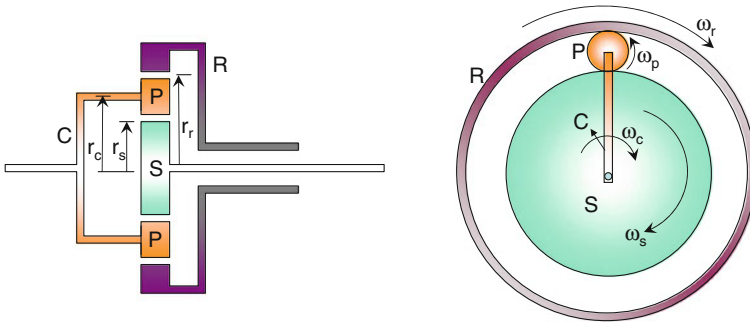


Fig. 6.18 Schematic representation of a planetary gear set

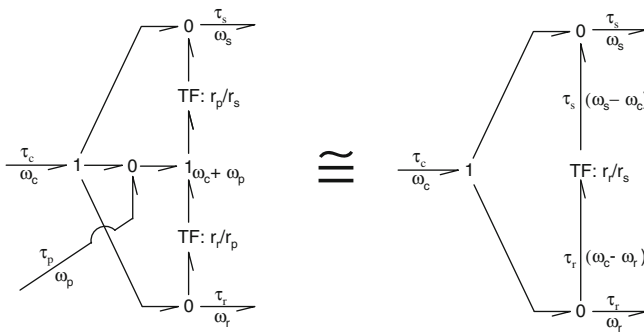


Fig. 6.19 Bond graph model of planetary gear set

Likewise,

$$\frac{\omega_c + \omega_p}{\omega_c - \omega_r} = \frac{r_r}{r_p}. \tag{6.41}$$

From these kinematic relations, the bond graph model of the planetary gear set is constructed as shown on the left of Fig. 6.19. The planets are not separately powered and their inertia and resistance to rotation may be neglected. Thus, the 0_P junction may be omitted from the model and the reduced model is shown on the right of Fig. 6.19. This model may be arrived at in a straightforward manner by combining Eqs. 6.40 and 6.41 so that the kinematic relation used to create the model becomes

$$\frac{\omega_c - \omega_s}{\omega_c - \omega_r} = -\frac{r_r}{r_s} \text{ or } \frac{\omega_s - \omega_c}{\omega_c - \omega_r} = \frac{r_r}{r_s}. \tag{6.42}$$

The negative sign in the TF modulus may be explained as follows: assume that the carrier is locked ($\omega_c = 0$). Then the planets will rotate opposite to the sun. The ring gear has internal gear teeth which means it will also rotate in the opposite direction to the sun gear's rotation.

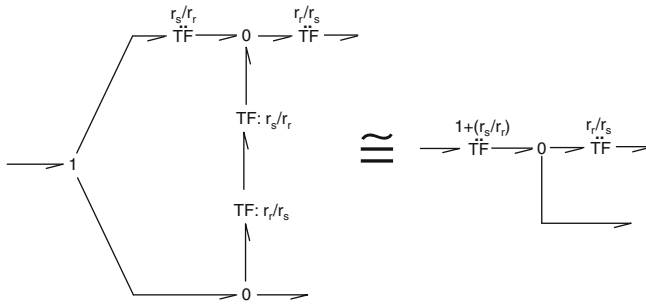


Fig. 6.20 Equivalent bond graph model of planetary gear set

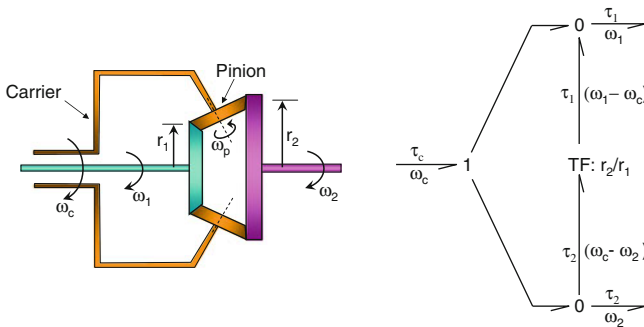


Fig. 6.21 Differential and its bond graph model

The bond graph model shown in Fig. 6.19 can be drawn in various forms by using transformer equivalences. For example, if TF-elements are introduced all around the topmost 0-junction, the resulting equivalent model assumes the form shown in Fig. 6.20.

The bevel gear differential or conventional differential is similar to the planetary gear system. The sun and the ring gears are the two bevel gears and the carrier holds the planets. A general schematic representation of the differential with unequal bevel gears and its bond graph model are shown in Fig. 6.21. The bond graph model is derived from the kinematic relation

$$\frac{\omega_c - \omega_1}{\omega_c - \omega_2} = -\frac{r_2}{r_1} \text{ or } \frac{\omega_1 - \omega_c}{\omega_c - \omega_2} = \frac{r_2}{r_1}. \tag{6.43}$$

In most differentials, $r_1 = r_2$ which gives $\omega_1 - \omega_c = \omega_c - \omega_2$ or $\omega_1 + \omega_2 = 2\omega_c$. Thus, the bond graph model of symmetric differential reduces to the form shown in Fig. 6.22.

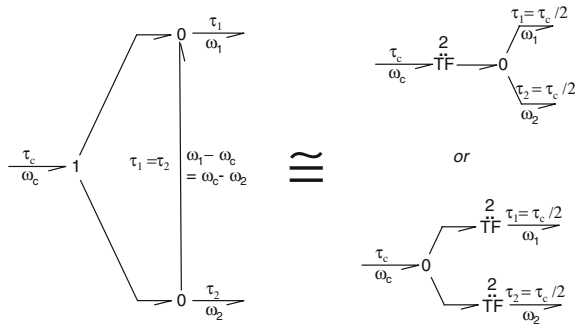


Fig. 6.22 Reduced bond graph model of a symmetric differential

This bond graph model explains a lot of physics of the differential. It is understood from the model that half of the engine torque is transmitted to each wheel. Furthermore, if any of the wheels are free to rotate (e.g., slips on an icy road) then the reaction torque from that wheel becomes zero, i.e., the torque on the other wheel also becomes zero. Consequently, the other wheel does not spin and the slipping wheel spins at the same speed as that of the input shaft.

From the preceding discussion, we find that if one wheel of a vehicle does not develop any frictional tire force then the other wheel which may be on a surface with very good grip cannot develop any driving force. As a result, the vehicle cannot move. To remedy this problem, some differentials have a clutching mechanism. If any wheel slips beyond a threshold value, the corresponding bevel gear in the differential is clutched to the carrier. Thus, the differential is controlled by the wheel slip. Such type of differential is called a limited-slip differential.

6.1.11 Transmission Line

The bond graph model of a complete vehicle with V8 engine is shown in Fig. 6.23. Engines E_1 to E_8 are connected to the crank shaft. The crank shaft drives the cam which is assumed to consume little power and hence is modeled in the signal domain.

The state vectors associated with the eight engines are to be initialized appropriately. If the piston of the first engine is assumed to be at top dead center at the start-up then the position for successive engines has to be changed accordingly so as to correspond with 45° crank rotation. The initial volumes are calculated from piston positions and then the initial gas mass and energy are calculated.

All vehicles require some kind of start-up device to rotate the engine. Usually, there is a start-up electric motor (called self-motor) which draws power from the electric battery. We have considered that the self-motor initially supplies a fixed angular velocity (ω_{st}) for a few cycles of engine rotation. The detailed model of self-motor can be developed and appended to the model given in Fig. 6.23. A flywheel

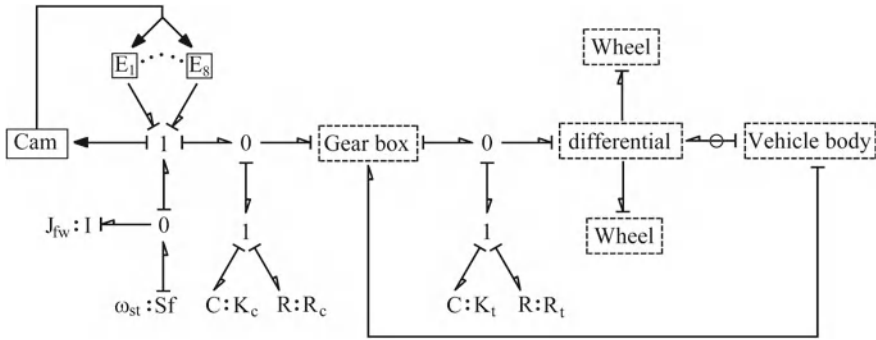


Fig. 6.23 Integrated model of a vehicle with engine and transmission line

is used on the crank shaft to maintain constant output speed. Without the flywheel, the engine would fail to rotate when the self-motor is turned off. The flywheel is an accumulator of energy which allows the engine to rotate through the bottom and top dead centers without getting locked there. The flywheel rotary inertia is modeled in Fig. 6.23 by I: J_{fw} element.

The engine is coupled to the gear box through a clutch. The gear box and the differential are suspended from the vehicle body. The clutch may be of different types and it may be absent in some designs (see the fluid-coupling and power-split device in this chapter). In mechanical friction clutch, usually dry-friction and stick-slip friction models [33] are used. The clutch torsional stiffness and damping are modeled by C: K_c and R: R_c elements in the bond graph model. The values of parameters K_c and R_c depend upon the pressure on the clutch pedal (unclutched, partially clutched, or fully clutched state). In a detailed friction model, the clutch force is modeled according to the normal pressure and the effective coefficient of friction which is a function of the slip ratio (the ratio of output to input speed). Details of such friction models are given earlier in this chapter during discussions on tire forces.

In Fig. 6.23, C: K_t and R: R_t elements model the torsional stiffness and damping offered by the long transmission shaft between the gear box (usually located at the front of the vehicle) and the differential. The universal coupling and other minor components have been neglected in this model.

6.1.12 Engine Dynamics Simulation

The engine is simulated at 30% throttle position when the engine is disengaged from the driveline. The fuel injected is high at the engine start-up and then it is regulated as per the throttle position. The self-motor is operated for first three engine cycles at

Table 6.1 Parameter values used in simulation of the V-8 engine model

Sub-system	Parameter values		
Engine	$A_p = 5 \times 10^{-3} \text{ m}^2$	$R_p = 0 \text{ N s/m}$	$r = 0.08 \text{ m}$
	$l = 0.2 \text{ m}$	$C_{d_i} = 0.01155$	$C_{d_o} = 0.01$
	$A_{v_o} = 0.008 \text{ m}^2$	$A_{v_i} = 0.008 \text{ m}^2$	$C_{p_b} = 459.8 \text{ J kg}^{-1} \text{ K}^{-1}$
	$m_b = 10 \text{ kg}$	$\lambda_b = 1 \text{ W m}^{-2} \text{ K}$	$\lambda_{b_a} = 0.04 \text{ W m}^{-2} \text{ K}$
	$J_{f_w} = 10 \text{ kg m}^2$	$\omega_{st} = 5 \text{ rad/s}$	
Clutch	$\bar{K}_c = 10^6 \text{ N m/rad}$	$R_c = 0.1 \text{ N m s/rad}$	
Gear box	$r_1 = 0.05 \text{ m}$	$r_2 = 0.1 \text{ m}$	$r_3 = 0.05 \text{ m}$
	$r_4 = 0.1 \text{ m}$	$J_1 = 1 \text{ kg m}^2$	$J_{2-3} = 2 \text{ kg m}^2$
	$J_4 = 2 \text{ kg m}^2$	$J_b = 100 \text{ kg m}^2$	$K_b = 10^5 \text{ N m/rad}$
	$R_b = 10^3 \text{ N m s/rad}$	$R_{2-3b} = 0.01 \text{ N m s/rad}$	$R_o = 0.01 \text{ N m s/rad}$
	$R_i = 1 \text{ N m s/rad}$	$K_{1-2} = 10^6 \text{ N m/rad}$	$R_{1-2} = 10^3 \text{ N m s/rad}$
	$\bar{K}_{3-4} = 10^6 \text{ N m/rad}$	$R_{3-4} = 10^3 \text{ N m s/rad}$	
	$\bar{K}_t = 10^6 \text{ N m/rad}$	$R_t = 10^3 \text{ N m s/rad}$	
Propeller shaft			
Atmosphere	$P_{atm} = 10^5 \text{ N/m}^2$	$T_{atm} = 300 \text{ K}$	
Gas properties	$C_v = 720 \text{ J kg}^{-1} \text{ K}$	$R = 287.05 \text{ J kg}^{-1} \text{ K}$	$\gamma = 1.41$
Fuel	$\dot{m}_f = 0.01 \text{ kg/s}$	$q_{hc} = 4.73 \times 10^7 \text{ J kg}^{-1}$	

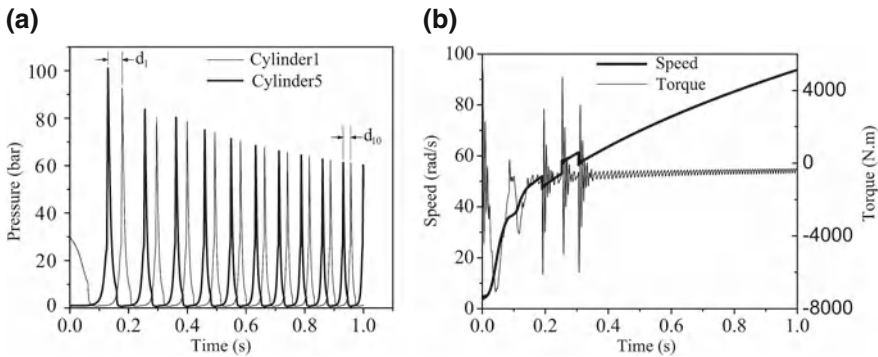


Fig. 6.24 Simulated dynamics of engine start-up

high fuel load. The crank shaft is connected to a large flywheel and clutches separate the engine from any other load. The engine parameters [7] are given in Table 6.1.

The time evolution of gas pressure in two engines is shown in Fig. 6.24a. The variation in crank shaft speed and torque during the initial start-up stage is shown in Fig. 6.24b. The time gap between the two pressure responses in the first cycle (d_1) is large. As the engine speed increases, this phase gap reduces. Gradually, a steady engine speed is reached.

The spikes in the crank-shaft speed and torque seen in the initial phase are due to the self-motor action. Once the crank-shaft has started rotating at a sufficient speed, the kinetic energy stored in the flywheel or other components of the transmission

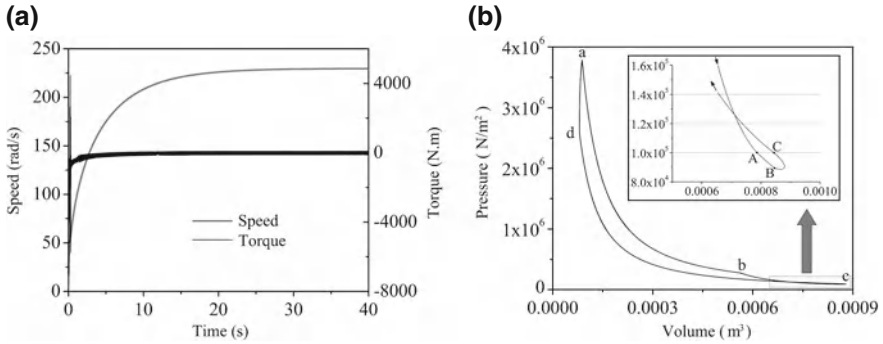


Fig. 6.25 a Engine steady-state results and b P-V diagram

line are sufficient to sustain the engine revolution. The self-motor is then switched off.

The steady crank-shaft speed and torque are shown in Fig. 6.25a. Because only an inertia load is there, at steady state the engine torque is nearly zero (except some little torque required for overcoming damping forces). This is a no-load engine simulation.

The pressure–volume (P-V diagram) curve for one of the engines is shown in Fig. 6.25b where the path between a to b is the expansion stroke, path b to c is the suction and discharge phase, path c to d is the compression stroke, and path d to a is combustion phase. The inset in Fig. 6.25b shows the details during suction and exhaust phases taking place around 1bar cylinder pressure. The exhaust takes place in the path between point B and point A in the inset. During the path between points A and B in the inset, the pressure difference is not conducive to either exhaust or suction. From point B to point C in the inset, suction takes place.

The steady-state P-V diagram for all engines is the same. Note that the steady-state maximum pressure is only about 40 bars because the engine is running unloaded. Moreover, the thermodynamic efficiency is less in this condition. The maximum cylinder pressure increases to around 80–100 bars under full throttle (first gear) and load.

If a 4-stroke engine is simulated then the PV-diagram becomes different. The expansion stroke is from point a (TDC or top dead center) to point c (BDC or bottom dead center). Then in the exhaust stroke, the piston moves from BDC to TDC with little change in pressure (marginally above atmospheric). The suction stroke takes the cylinder from TDC to BDC where the pressure also remains more or less constant (a little above atmospheric) and it is then followed up by compression stroke (BDC to TDC) and combustion. Thus the four-stroke engine’s PV-diagram has a smooth path between points a to c followed by two approximately constant pressure lines from BDC to TDC and back to BDC and finally the path from points c to a via point d.

6.1.13 Clutch

A clutch is used to connect the driving shaft to a driven shaft, so that the driven shaft may be started or stopped at will, without stopping the driving shaft. Thus, a clutch provides an interruptible connection between two rotating shafts. A clutch allows a high inertia load to be started with a small power. The clutch allows disengagement of the drive when brakes are applied on the driven shaft and thus continue the engine to run at no load. Clutches are also used during gear change so that sudden transient loads on the engine are avoided.

Clutches are of various kinds: friction clutch, dissipative viscous coupling, torque converter, etc. The detailed modeling of torque converter will be discussed later in this chapter. For the time being, a clutch can be modeled as a device which produces slip-dependent torque. The basic bond graph model of a clutch is a modulate R-element where the modulating signal indicates the pressure applied on the clutch. In a dry friction clutch, the friction pad is made of cotton and asbestos fibers woven or molded together and impregnated with resins or other binding agents. In many friction discs, copper wires are woven or pressed into the facings to give them added strength. Some friction discs use ceramic-metallic facings. Grooves are cut on the disk to assist cooling and also to avoid vacuum creation at high speeds such that disengagement is not hampered.

The schematic drawing of a friction clutch (a single plate dry clutch) is shown in Fig. 6.26 where the clutch plate is interposed between the flywheel surface of the engine and pressure plate. The engine flywheel, a friction disc called the clutch plate and a pressure plate are the basic components of a clutch. When the pressure plate is attached to the flywheel it rotates at the same speed as the crankshaft. When the driver pushes down the clutch pedal the pressure plate moves away from the friction disk and power transmitted through the clutch is interrupted. When the driver releases the clutch pedal, power is transmitted through the clutch. Springs in the clutch push the pressure plate against the friction disk. This pushing force determines the maximum frictional force between the friction disk and the flywheel, and determines the slip between the two. In separate arrangements, more number of mating surfaces are used for transmitting the torque.

Two basic types of clutch are the coil-spring clutch and the diaphragm-spring clutch. The coil spring clutch, which has a series of coil springs set in a circle, uses coil springs as pressure springs. At high rotational speeds, centrifugal forces on the coil springs and the lever of the release mechanism cause problems in the operation of this kind of clutch. Diaphragm type springs are used to avoid such problems. In diaphragm type design, the centre plate, on which the friction facings are mounted, consists of a series of cushion springs. These cushion springs are radially crimped (wavy) so that the crimping is progressively squeezed flat as the clamping force is applied to the facings. This arrangement enables gradual transfer of the force. When the clamping force is released, the plate springs back to its original crimped state. The power is transmitted from the plate to the hub through coil springs interposed between them. These springs are carried within rectangular holes or slots in the hub

Fig. 6.26 Schema of a friction clutch

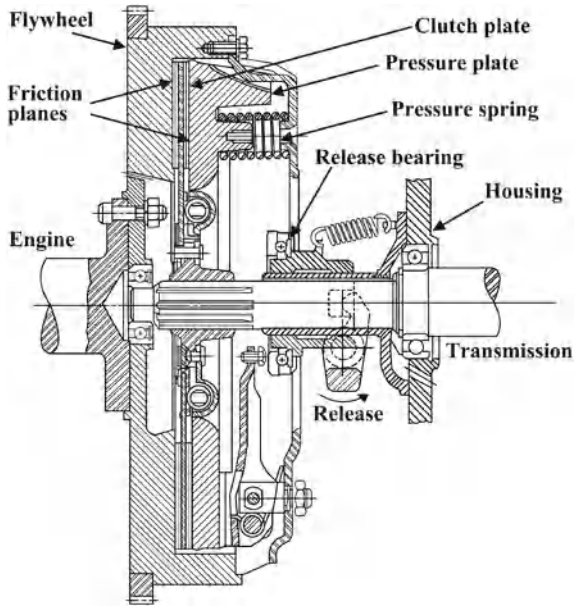
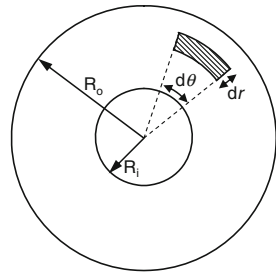


Fig. 6.27 Elemental area on friction plate



and plate. These heavy coil springs set in a circle around the hub smooth out the torsional vibrations and reduce transient loading of the plate and the engine.

Two basic formulations are followed to model friction clutches. Uniform pressure assumption is made for a new clutch whereas uniform wear is assumed for a worn out clutch.

If the friction disk is an annulus with external radius R_o and the internal radius is R_i (Fig. 6.27) then the uniform pressure distribution yields $p_0 = N / (\pi (R_o^2 - R_i^2))$ where N is the force applied on the clutch. The maximum transmissible torque is then given as

$$T_{\max} = \int_{R_i}^{R_o} \int_0^{2\pi} \mu_s p_0 r^2 d\theta dr = \frac{2\mu_s}{3} \left(\frac{R_o^3 - R_i^3}{R_o^2 - R_i^2} \right) N. \quad (6.44)$$

where μ_s is the coefficient of static friction. For dynamic modeling, a stick slip formulation is used or Stribeck effect is separately included. A better way is to use empirical models (like tire force calculation with Pacejka or Burckhardt formulations given in Eqs. 6.3 and 6.4, respectively). Thus, the clutch model is given by slip ratio instead of absolute value of the slip. As a consequence, the bond graph model is a two-port modulated R-field where the modulating signal is the applied force. The slip at any point at distance r away from the center of the annulus and angle θ from a reference radial line is given as $\sigma = (\omega_i r - \omega_o r) / \omega_i r = (\omega_i - \omega_o) / \omega_i$, where ω_i is the input shaft speed and ω_o is the output shaft speed. Thus, the slip ratio is constant at all points on the surface, which means the instantaneous coefficient of friction at a given slip ratio is also constant. Thus, the instantaneous torque transmitted is in given as

$$T(\sigma) = \frac{2\mu(\sigma)}{3} \left(\frac{R_o^3 - R_i^3}{R_o^2 - R_i^2} \right) N. \quad (6.45)$$

In uniform wear assumption, the wear rate is given according some established theories for the wear in a mechanical system. It is assumed that the wear rate R_w is proportional to the pV factor where p refers the contact pressure and V the sliding velocity. Then

$$R_w = kpV \quad (6.46)$$

where k is a constant of proportionality. If the relative angular velocity between the drive and driven shaft $\omega = \omega_i - \omega_o$ then the relative linear velocity at any point on the face of the clutch at distance r from the centre of the annulus is $V = \omega/r$. Thus, combining these equations and assuming a constant angular velocity ω

$$R_w = kp\omega r \Rightarrow pr = R_w / (k\omega) = K \quad (6.47)$$

where K is another constant. The largest pressure P_{\max} occurs at the smallest radius R_i and thus $K = p_{\max} R_i$. The pressure at any point at a distance r from the centre of the annulus is, thus,

$$p = p_{\max} \frac{R_i}{r}. \quad (6.48)$$

The axial force N is obtained as

$$N = \int_{R_i}^{R_o} \int_0^{2\pi} p_{\max} \frac{R_i}{r} r d\theta dr = 2\pi p_{\max} R_i (R_o - R_i) \quad (6.49)$$

$$\Rightarrow p_{\max} = \frac{N}{2\pi R_i (R_o - R_i)}.$$

The maximum transmissible torque is calculated as

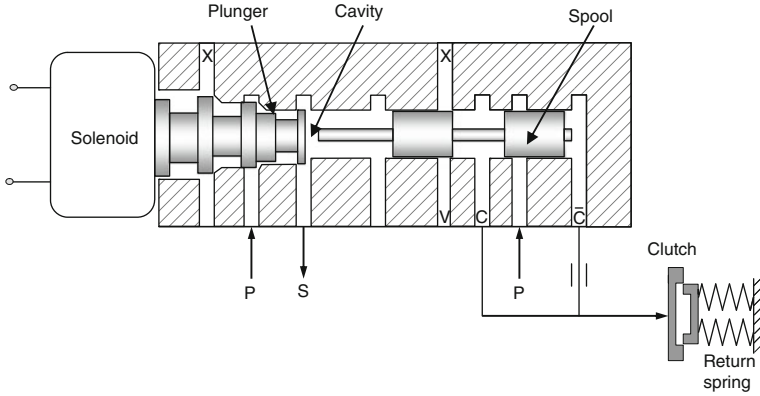


Fig. 6.28 Cut-out of an amplifier valve

$$T_{\max} = \int_{R_i}^{R_o} \int_0^{2\pi} \mu_s p_{\max} \frac{R_i}{r} r^2 d\theta dr = \mu_s \pi p_{\max} R_i (R_o^2 - R_i^2) \tag{6.50}$$

$$\Rightarrow T_{\max} = \mu_s N \left(\frac{R_i + R_o}{2} \right) = \mu_s N R_{av}$$

where R_{av} is the average radius of the friction pad annulus.

Because the slip ratio is constant, the formulation based on slip ratio yields instantaneous torque transmission as

$$T(\sigma) = \mu_s(\sigma) N R_{av}. \tag{6.51}$$

6.1.13.1 Clutch Pressure Control

The pressure plate (See Fig. 6.26) is moved in appropriate direction to control the normal reaction at the friction planes. This actuation is usually performed through electro-hydraulic valve actuator, which is also called an amplifier valve. The schema of an amplifier valve is shown in Fig. 6.28. In this figure, the clutch model has been simplified to include only the essential dynamical parts [28].

The solenoid is controlled through pulse width modulated (PWM) current signal. In some recent designs of amplifier valves used in direct electronic shift control, which use more powerful solenoid to provide more flow throughput, the spool is not required. Such designs are used in active suspensions and antilock brake systems (ABS), which are described in details in later sections of this chapter.

The model of the solenoid has been already developed in Chap. 3. Suitable control of the duty cycle of the PWM solenoid valve sets the plunger displacement which causes variations in the solenoid cavity pressure. When the spool valve is moved to

extreme right position in Fig. 6.28, the resistance to flow between the line (port P or pump) and the clutch (port C) becomes small and thus maximum pressure is applied on the clutch. When the spool valve moves to extreme left position in Fig. 6.28, the flow path between the line and the clutch is closed, but the flow path between the line (port P) and the vent (V) is fully open. This causes minimum pressure on the clutch and disengages the clutch. In intermediate positions, the leakage resistances decide the amount of pressure applied on the clutch. The position of the spool valve is controlled by the plunger.

The bond graph model of this electro-hydraulic actuator [28] is given in Fig. 6.29. The plunger/solenoid displacement and line pressure are the inputs to this model. The solenoid displacement is obtained from the model of the solenoid's electro-magnetic domain (See Chap. 3). The plunger position controls the passage resistances (modulated R-elements) between the pump and the cavity and the cavity and the sump. The cavity fluid compliance is modeled by element C_s . The pump (line) and sump pressures are denoted by P_l and P_0 , respectively. The transformers with moduli A and $1/A$, where A is the exposed cross-sectional area of the spool where the pressure acts, transform the pressure to force on the spool. The spool inertia, compliance and frictional resistance are modeled for the spool dynamics. The pressure of the fluid in the spool chamber (between line, clutch and vent) is represented at junction 0_c , where C_c models the fluid compliance. Two modulated R-elements control the passage resistances between the spool chamber and the clutch cavity and between the spool chamber and the vent. The modulating signal is the position of the spool. The flow through the hydraulic line (pipe) between the spool chamber and the clutch cavity is modeled by accounting for the fluid inertia and damping (skin-friction and viscous losses). The fluid compliance in clutch cavity is modeled by C_c element and R_l represents leakage resistance. The pressure in the clutch cavity applies force on the clutch plate. In the bond graph model, A_p is the effective frontal area of the pressure plate, and the I-, C-, and R-elements used to model the clutch plate represent the clutch or piston inertia, effective structural compliance (including the return spring) and the structural damping, respectively.

An actively controlled wet clutch allows easier control of torque transfer. It is a key part of active limited slip differential which significantly improves the vehicle dynamics and traction control. A detailed bond graph model of active limited slip differential can be consulted in [30].

6.1.13.2 Automatic Clutch During Gear Shift Process

Manual clutching is required during gear shifting. An automatic transmission system uses a torque converter whose details are given later in this chapter. A schematic of a four-speed automatic transmission system is shown in Fig. 6.30a (torque converter is excluded). It consists of reverse, low and high range clutches. A single shift actuator called a dog actuator is used in this design [28]. This type of design is simple, easy to maintain and does not require synchronizers. The turbine of the torque converter effectively acts as the synchronizer. The dog actuator is positioned appropriately (on

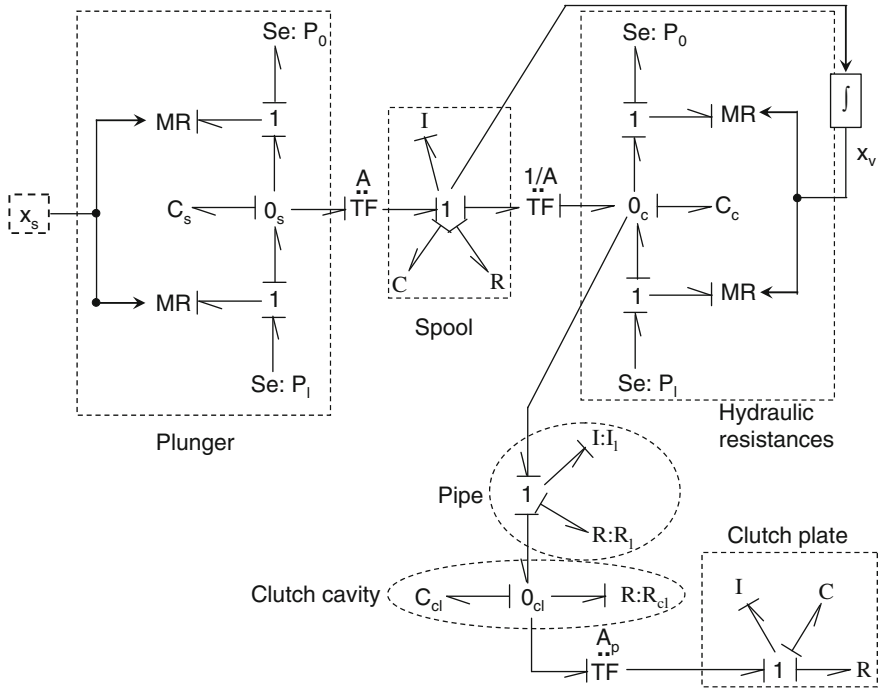


Fig. 6.29 Bond graph model of clutch pressure control

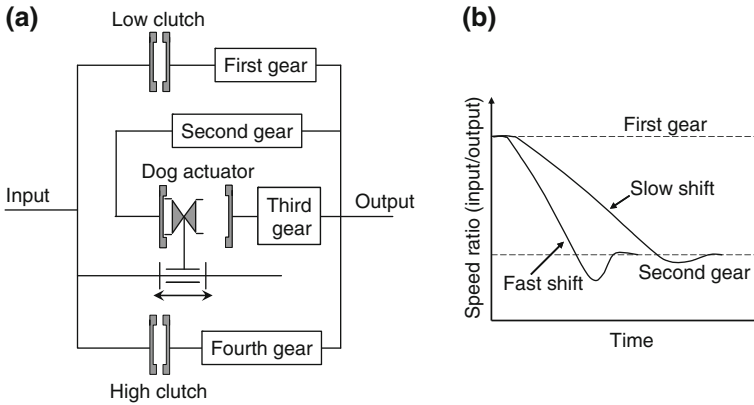


Fig. 6.30 a Clutch actuator in automatic transmission and b torque and speed drop transients during shifting process

the splined shaft) to either engage with the second or the third gear or with none of them. The first and fourth gear operations are performed by engaging the respective clutches. The output is then connected to the differential.

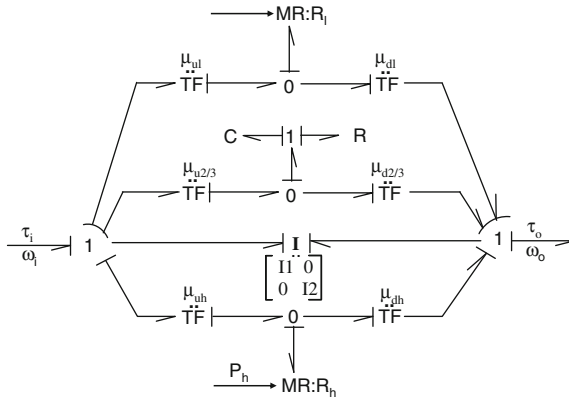


Fig. 6.31 Bond graph of clutch actuator in automatic transmission

In this type of design, the torque drop can be significant during a slow shift process. That is why electronic (microcomputer controlled) shifting mechanisms are used. These shifting mechanisms ensure quick gear shift with minimal torque-drop (See Fig. 6.30b). Moreover, it can be tuned to adapt the shift execution and shift scheduling according to different driving conditions. Faster shift is recommended to improve fuel efficiency whereas slower shift gives better drivability.

The bond graph model of the shift system in an automatic transmission system shown should include the inertias at the input and output of the transmission system and should also include the hydraulic control systems required to engage the clutches and the dog actuator. The effective inertia between the input and output of the transmission system can be represented as a two-port I-field. In this case, there is no inertia cross-coupling and hence the off-diagonal terms in the mass matrix are zero (in effect, we have two independent single port I-elements). In the bond graph model given in Fig. 6.31, the transformers model various gear ratios (indicated by first subscripts u and d for up and down sides, respectively, and second subscripts h, l and 2/3 for low, high and second/third gears, respectively). The gear mesh stiffness and damping are modeled for second and third gears (dog actuator part) so that the model remains in integral causality. Note that transformer moduli $\mu_{u2/3}$ and $\mu_{d2/3}$ have to be switched suitably depending upon the dog actuator position, e.g., to zero when the dog actuator does not engage with either second or third gears. The modulated R-elements model the clutches where the pressures applied on the clutches are the modulating variables. The clutches thus allow different amounts of slip between the up and the down sides of the automatic transmission device depending upon the pressure applied by the amplifier valves. The bond graph model given in Fig. 6.31 is applicable to both layshaft automatics and planetary automatic transmission (see later sections for details) with clutches and bands [12].

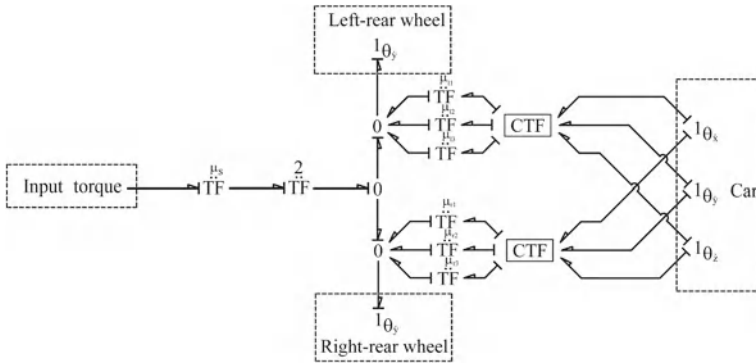


Fig. 6.32 Bond graph model of differential

6.1.14 Integrated Four Wheel Vehicle Model

The post-clutch section of a rear-wheel driven vehicle is modelled in Fig. 6.32 as a source of effort. The input torque is applied at a 0-junction representing the differential, which implies same torque but different velocities in the two traction wheels. The main gear box and differential gearbox (two MTFs) are not modeled here.

Note that the modular model developed here keeps the option open to include detailed engine and transmission system models.

6.1.15 Simulation Results for Four Wheel Model

The normal loads or load transfer on the wheels vary due to pitch, yaw and roll motions. At high speeds, aerodynamic forces can as well affect the load transfer. Therefore, the load on each wheel, which is the deciding factor of maximum braking and driving torques, is influenced by various factors; broadly the operational conditions (speed, steering angle, . . .) and the environmental conditions (wind speed, road condition, . . .). Initially, to get an idea about the handling dynamics of the vehicle, vehicle centre of mass trajectory in inertial frame and variation of normal loads on the wheels are studied. The parameter values used in the simulation of full vehicle model are taken from [6]. The developed vehicle model is further validated by comparing the results with experimental manoeuvre data available in literature [8].

6.1.15.1 Steering Response of the Vehicle

It is fundamental requirement that a vehicle should show under-steer characteristics above a certain value of linear speed. This would help the driver in safe maneuvering

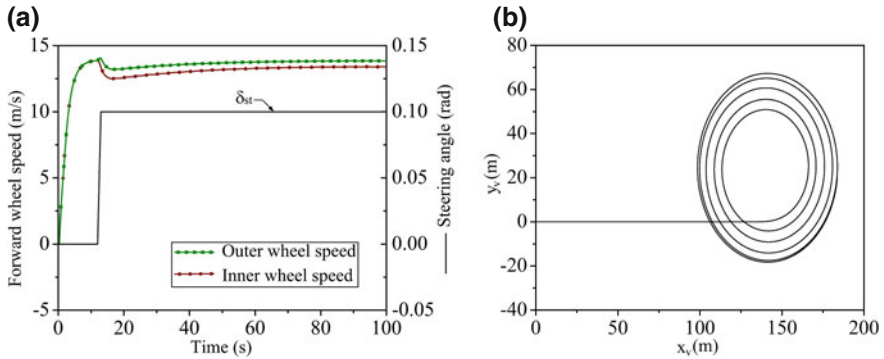


Fig. 6.33 **a** Speeds for left and right front wheels; and **b** Vehicle centre of mass trajectory in inertial frame

of the vehicle at high speeds. On the contrary, if a vehicle starts over-steering then the driver needs to quickly make clockwise and anticlockwise steering wheel rotations, which is both uncomfortable and unstable. Here, the vehicle operating speed is chosen as 50 km/h (13.88 m/s) and we desire the vehicle to under-steer at this speed.

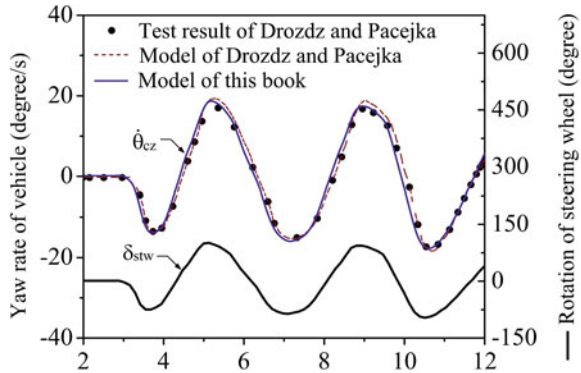
For simulating the steering response, the vehicle is steered with a fixed steering angle of 0.1 rad after an initial straight run for 12 s by which time the vehicle has reached a steady speed of 13.88 m/s. The variations in wheel speeds during maneuvering are shown in Fig. 6.33a. The result shows under-steer characteristics (Fig. 6.33b) with steady mean speed of 13.67 m/s and 0.446 m/s difference in speeds between inner and outer wheels. At steady turning radius of $r = 42.9$ m, kinematic analysis with half track width $c = 0.7$ m gives difference in wheel speeds as $2c\sqrt{\dot{x}_v^2 + \dot{y}_v^2}/r = 2 \times 0.7 \times 13.67/42.9 = 0.446$ m/s which matches the simulated results.

6.1.15.2 Slalom Manoeuvre

The test data of [19] are used to validate the developed four wheel model. In [19], slalom manoeuvre test was carried out on the vehicle at fixed vehicle speed of 50 km/h (13.88 m/s) and the steering wheel angle and the yaw rate were measured. The steering wheel angle was maintained between $\pm 100^\circ$ and the gear ratio between the steering wheel and axle rotation was 25:1. With this small change in axle orientations, the under-steered vehicle's linear speed remains almost constant at 50 km/h.

The experimental steering angle values (δ_{stw} in Fig. 6.34) at fixed time intervals were obtained from the graphs in [19] and were used as input ($\dot{\theta}_{ref} = d\delta_{stw}/dt$) in the developed four wheel bond graph model. The simulated yaw rates are compared with the experimentally obtained yaw rates of [19] in Fig. 6.34. Moreover, the results obtained in [19] from a reduced order vehicle model are also plotted in Fig. 6.34 for comparison. It is found that the two models accurately predict the actual handling behavior of the vehicle.

Fig. 6.34 Comparison of vehicle's yaw rate during slalom maneuver at vehicle speed of 50km/h with the test and simulation results of Drozdz and Pacejka

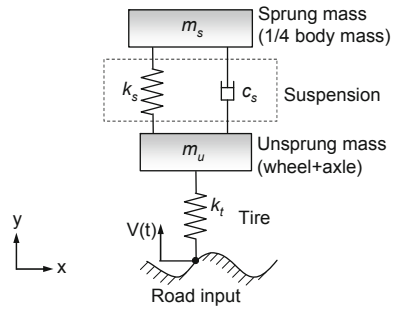


6.2 Suspension Systems

Vehicle suspension systems are designed to provide good riding comfort and manoeuvrability which means reduction of the force transmitted to the driver/vehicle while maintaining good tire contact with the ground. Better riding comfort requires a suspension system with a low natural frequency. On the other hand, to have good handling, a suspension system should have high natural frequency. In order to have a comfortable ride, the suspension system should have a low natural frequency which would filter out the high frequency inputs on rough roads. But to have good handling, the vehicle should have a suspension system with a high natural frequency, so as to filter out the relatively low-frequency cornering motions. Weight or load transfer under braking or acceleration, which causes pitching movements, known as dive or squat depending on their direction, is another point to consider during a suspension design. The load transfer between the inner and outer wheels while negotiating a curve also influences suspension performance. These contrasting requirements have been addressed from many angles to develop various advanced passive, active and semi-active suspension systems. Various solutions to the conflicting requirements have been proposed. The development of vehicles with a lower centre of gravity, springs with rising stiffness, added springs to increase stiffness in roll without increasing it too much in bump, all have led to much improved ride and handling of vehicles. But as the demand for improved fuel economy, greater payload, better on- and off-road ability, higher speed and for greater comfort, continue to increase in a competitive automobile market, the designer needs to continually optimize the suspension performance and find a solution to the ride/handling constraint according to the prevailing market demand.

Vehicle suspensions are designed not only to reduce the shock fed back to the rider and machine, but also to keep the wheels in better contact with the ground. A pneumatic tire acts like an air spring and little damping is offered due to the deformation of the rubber. Therefore, entire effective damping to road inputs is provided by the

Fig. 6.35 Elements of passive suspension system

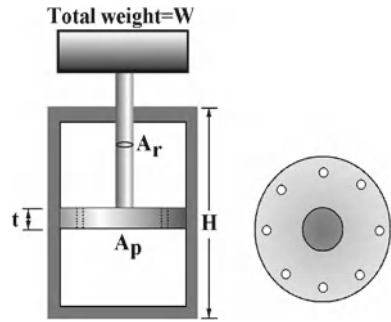


suspension system between the axle and the vehicle body. Consider a vehicle suspension without dampers. When the wheel goes over a bump, the suspension spring is compressed and then it causes the vehicle body to go up. The vehicle body continues to go up and pulls the wheels up with it, even when the wheel has crossed over the bump. Then the vehicle body falls under its own weight from the peak height and the up-down motion continues. Thus, tire-road contact is lost in some periods which means loss of traction and steerability. The suspension damper is used to absorb the potential energy stored in the suspension spring when the vehicle encounters a bump so as to avoid excessive vertical motion of the vehicle body and also loss of tire contact with the ground. However, dampers and springs must be correctly matched to each other. If the damping is too little then the wheel continues bouncing for long durations. On the other hand, too much damping reduces the ride comfort because the damper acts as a rigid strut when excitation frequencies are large and transmits the entire road disturbance to the vehicle body.

Suspension systems may be broadly divided into two categories: passive systems composed of springs and dampers where the stiffness and damping may be controlled with little use of external power and active systems where suspension forces are completely generated by actuators requiring large amounts of power from an external source. Some suspension systems are mixed in the sense that large amount of power from the external source may be needed for shorter time durations and very little power is required to operate the suspension at other times.

Passive suspension is composed of springs, shock absorbers and linkages that connects the wheels (or axles) to the vehicle. There are various types of passive suspensions constructions. The spring may be a coil spring, leaf spring, torsion beam, air/liquid spring, etc. The shock absorber gives damping to the system and usually, the energy is dissipated by forcing hydraulic fluid through orifices. The suspension configuration may be dependent type or independent type. In independent suspensions, motion of the wheels on opposite sides are not coupled. Examples of dependent suspension type are Watt's linkage and Panhard rod. Examples of independent suspension type are MacPherson strut, double wishbone suspension, multi-link suspension, swinging arm suspension, etc. The general schematic model of a suspension system is shown in Fig. 6.35, which is often called a quarter car

Fig. 6.36 Liquid spring schematic diagram



model. In this model, the sprung mass refers to one fourth of the vehicle body mass (including passengers and other loads) and unsprung mass refers to the mass of the wheel and the axle. The pneumatic tire usually has a much larger stiffness and low damping coefficient. Therefore, only tire stiffness is considered in the quarter car model.

Designers have been continuously striving to optimize the suspension performance for better handling and rider comfort, and higher payload. There is a considerable body of literature related to the design of vehicle suspension systems in both passive and active modes. Passive systems can be non-adjustable and non-controllable, or adjustable and non-controllable. Active systems provide a range of adjustment and controllability that provide a quality ride over a wide range of road conditions. These systems can be mechanical, hydro-mechanical, hydro/pneumatic-mechanical, and pure hydraulic in various configurations. Active suspension technology allows to change the suspension's natural frequency and damping in real time depending upon user preferences and thereby it provides a solution to the ride/handling constraint. Active components consume very little power, which is spent in driving control mechanisms for stiffness and damping selection. Usually, auxiliary stiffness and damping chambers are provided in air and liquid springs and the stiffness / damping selection mechanism consists of a set of controlled valves.

6.2.1 Passive Liquid-Spring Shock Absorber

Liquid shock absorbers are compact, light weight suspension struts which reduce the suspension play and they are generally used in very heavy load applications, such as heavy military vehicles, landing gear suspension in aircrafts and space shuttles. The schematic diagram ² of a liquid spring is shown in Fig. 6.36. The liquid flow through orifices produces damping, whereas; the cushioning effect comes from the fluid's compressibility.

² A part of this section is taken from these authors' previous work published in [65].

Silicone based fluids, which have smaller bulk modulus, are non-corrosive, and are considered stable, are considered suitable for liquid springs.

6.2.1.1 Mathematical Model

It is usually sufficient to assume that the thermodynamics plays a very minor role in liquid spring dynamics. Therefore, one may assume isothermal operation. The internal damping in compressible liquids is dependent on the strain-rate. This leads to the direction dependent instantaneous anisotropic pressure. The resultant force on the piston is a superimposition of force due to isotropic fluid pressure (P) and rate dependent pressure (P_d). The isotropic pressure leads to elastic force and the anisotropic pressure leads to damping force on a surface.

Change in isotropic pressure developed due to change of volume is given by

$$\Delta P = -\beta \left(\frac{\Delta V}{V_0} \right) = -\beta \frac{\left(\frac{m}{\rho_0} - V \right)}{\left(\frac{m}{\rho_0} \right)} = -\beta \left(1 - \frac{\rho_0 V}{m} \right) = -\beta \left(1 - \frac{\rho_0}{\rho} \right), \quad (6.52)$$

where ΔV is the reduction in volume with respect to free space volume V_0 , ρ is the instantaneous fluid density, ρ_0 is the free space fluid density, m is the mass contained within the control volume, and β is the fluid's Bulk modulus. Taking free space pressure as reference, the gage isotropic pressure (compression is taken as positive pressure) $P = -\Delta P$.

From classical fluid mechanics, we know that

$$(2\mu + 3B) \nabla \cdot q = \sigma_{xx} + \sigma_{yy} + \sigma_{zz} + 3P, \quad (6.53)$$

$$\nabla \cdot q = \dot{\epsilon}_{xx} + \dot{\epsilon}_{yy} + \dot{\epsilon}_{zz}, \quad \text{and} \quad B = -\frac{2}{3}(\mu - \mu_1),$$

where q is the velocity vector of stream lines, μ is the coefficient of viscosity, μ_1 is referred to as the second viscosity coefficient or elongational viscosity, B is a dependent parameter, σ_{xx} , σ_{yy} , σ_{zz} are the normal stresses in Cartesian coordinate, ϵ_{xx} , ϵ_{yy} , ϵ_{zz} are the linear strains in Cartesian coordinate, and superposed '.' denotes time derivative, i.e. $\dot{\epsilon}_{xx}$, $\dot{\epsilon}_{yy}$, $\dot{\epsilon}_{zz}$ are rate of linear strains. For isotropic case, i.e. incompressible fluids,

$$\sigma_{xx} + \sigma_{yy} + \sigma_{zz} = -3P. \quad (6.54)$$

The anisotropic pressure or stress on an infinitesimal element is given by

$$\sigma_{ij} = \mu \left(\frac{\partial q_i}{\partial x_j} + \frac{\partial q_j}{\partial x_i} \right) + \mu_1 \delta_{ij} \nabla \cdot q, \quad (6.55)$$

where δ is the Kronecker delta. The component of the viscous force (F_i) per unit volume (total volume V) in the direction of the rectangular coordinate x_i in a small cubical fluid element is given by

$$\frac{F_i}{V} = \frac{\partial}{\partial x_j} \left[\mu \left(\frac{\partial q_i}{\partial x_j} + \frac{\partial q_j}{\partial x_i} \right) + \mu_1 \delta_{ij} \nabla \cdot q \right]. \quad (6.56)$$

Note that $\nabla \cdot q = \partial \dot{x} / \partial x = \partial \dot{V} / \partial V$, where x is the position of the fluid element, and $\partial \dot{V} / \partial V$ is the local volumetric strain rate. For unidirectional flow without shear (due to movement of piston) in direction x , Eq. 6.55 is written as

$$\sigma_{xx} = \mu_1 \frac{\partial \dot{x}}{\partial x}. \quad (6.57)$$

A linear velocity gradient for the flow stagnation inside the chamber is assumed with boundary conditions $\dot{x}(0) = 0$ and $\dot{x}(x_p) = \dot{x}_p$, where the position of the piston with respect to the casing is x_p and the velocity of the piston is \dot{x}_p . Assuming Newtonian fluid, Eq. 6.57 reduces to

$$P_d = -\sigma_{xx} = -\mu_1 \left(\frac{\dot{x}_p}{x_p} \right) = -\mu_1 \left(\frac{\dot{V}_p}{V_p} \right), \quad (6.58)$$

where V_p is the control volume. Similar integer and non-integer order non-linear relations can be derived for Stoksian fluids. For the liquid-spring, Eq. 6.58 can be represented in a bond graph model as a state dependent damper (R -element) with damping coefficient equal to μ_1 / V_p , $p = 1, 2$. Note that $\mu_1 = \mu B - \frac{2}{3} \mu$, where μB is the bulk viscosity, and μ_1 is a non-linear function of density, ρ_p (ratio of the two state variables, i.e. m_p / V_p , $p = 1, 2$).

6.2.1.2 Spring Stiffness

When the pressure on both sides of the piston is same, the net resultant force (F) is the difference between the forces acting on the top and bottom surfaces of the piston. Thus,

$$F = P A_p - P (A_p - A_r) = P A_r. \quad (6.59)$$

For a single liquid spring (see Fig. 6.36), the equilibrium condition is defined by $P A_r = W$, where P is the equilibrium pressure. Consider the unloaded liquid spring, in which the charging pressure is P_c and the piston rests at one end. When the load W is applied, and $P_c < P$, then the piston moves down (or the cylinder moves up, depending upon whether the piston or the cylinder is fixed) so that the resultant volume of fluid inside the cylinder reduces and thereby increases the pressure to P from P_c . The amount of required displacement, y , is obtained from

$$P = \beta \left(1 - \frac{\rho_0}{\rho} \right),$$

which gives what should be the value of ρ , i.e. what should be fluid volume V for a constant charged mass m . Note that initial volume is $A_p (H - t)$ and hence

$$m = A_p (H - t) \frac{\beta \rho_0}{(\beta + P_c)} \quad (6.60)$$

The stiffness of the spring is given as

$$K = -\frac{\partial F}{\partial x} \quad (6.61)$$

If x is the current displacement of the spring given in quasistatic fashion then the net restoring force acting on the piston is

$$F = P A_r = -\beta A_r \left(\frac{V_0 - V}{V_0} \right). \quad (6.62)$$

For any additional displacement dx , the volume change is $\Delta V = A_r dx$ which results in restoring force

$$F + dF = -\beta A_r \left(\frac{V_0 - (V - A_r dx)}{V_0} \right) = -\beta A_r \left(\frac{V_0 - V}{V_0} \right) - \beta A_r \left(\frac{A_r dx}{V_0} \right). \quad (6.63)$$

Thus,

$$K = -\frac{\partial F}{\partial x} = -\frac{\beta A_r^2}{V_0}. \quad (6.64)$$

Equation 6.64 indicates that the stiffness of the liquid spring can be changed on the fly by varying the fluids bulk modulus or the volume being strained. This insight will be used later to develop a semi-active suspension.

6.2.1.3 Bond Graph Model of Elementary Liquid Spring

The bond graph model of the isothermal liquid spring is given in Fig. 6.37a, in which the relations for C-fields are governed by Eq. 6.52, isotropic and anisotropic pressures are denoted with subscripts i and d , respectively. Each two-port C-field receives two flow informations, $f = [\dot{m} \ \dot{V}]^T$ from which it calculates to effort variables $e = [P \ P]^T = \Phi_C \left(\int \dot{m} dt, \int \dot{V} dt \right)$, where function $\Phi_C(\cdot)$ represents Eq. 6.52.

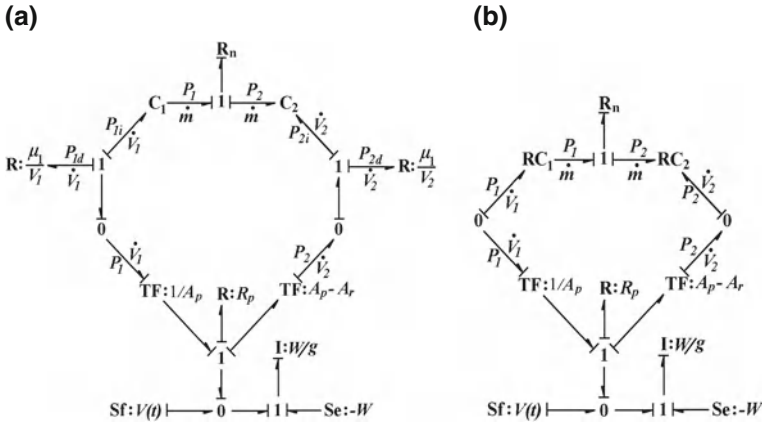


Fig. 6.37 a Isothermal liquid-shock absorber model and b its compact form

The R-elements on the left and right side of the model in Fig. 6.37a represent strain rate dependent damping according to Eq. 6.58. The TF-elements model the resultant force acting on the piston due to the pressure on both sides of the piston according to Eq. 6.59.

The flow through the orifices is modelled by R_n element in the bond graph model. The wall friction is modelled by R_p element, the input excitation is given by $Sf: V(t)$ element and the I-element models the mass of the piston.

Note that the flow through the orifice is assumed to be dependent on only the difference of isotropic pressures in the two control volumes. However, the exact volume being strained is less than that contained in the control volume. On the expanding side, some volume is being filled by the liquid flowing through orifices whereas on the compressing side, some liquid is being squeezed out through the orifice. Therefore, considering the effective volumetric strain rate,

$$P_d = -\mu_1 \left(\frac{\rho_p \dot{V}_p - \dot{m}_p}{\rho_p V_p} \right) = -\mu_1 \left(\frac{\rho_p \dot{V}_p - (\rho_p \dot{V}_p + \dot{\rho}_p V_p)}{\rho_p V_p} \right) = \mu_1 \left(\frac{\dot{\rho}_p}{\rho_p} \right). \tag{6.65}$$

Note that for a control volume with no mass transfer ($\dot{m}_p = \rho_p \dot{V}_p = \text{constant}$),

$$\frac{\dot{\rho}_p}{\rho_p} = -\frac{\dot{V}_p}{V_p},$$

i.e. Eqs. 6.58 and 6.65 give identical results. Furthermore, it is assumed that the shear flow losses due to the coefficient of viscosity, μ , and wall friction losses in the orifice are included in evaluating the orifice discharge coefficient, C_d , which is usually a nonlinear function of the average coefficient of viscosity and the fluid density. Then the isothermal liquid spring model considering the strain relaxation due to orifice

flow is given in Fig. 6.37b, where the RC-field elements are used to represent the combined pressure given by Eqs. 6.52 and 6.65. The constitutive relation for the RC-fields is given by

$$P_i = \beta \left(1 - \frac{\rho_0}{\rho} \right) + \mu_1 \left(\frac{\dot{\rho}_p}{\rho_p} \right) = \beta \left(1 - \frac{V_i \rho_0}{m_i} \right) - \mu_1 \left(\frac{\dot{V}_i}{V_i} \right) + \mu_1 \left(\frac{\dot{m}_i}{m_i} \right), \quad (6.66)$$

where m_i and V_i are state variables and $i = 1, 2$ represents the two control volumes. In Eq. 6.66, rate of states appearing in the right-hand side, which represent damping, lead to an implicit form and consequently an appropriate integration scheme is required for simulation.

The flow through the orifices, modelled by R_n element, is assumed to be governed by Bernoulli damping relation. It leads to a flow characteristics

$$f = C_d \sqrt{|\Delta P|} \text{sign}(\Delta P), \quad (6.67)$$

where the coefficient of discharge $C_d = n \cdot \Phi_o(d, L, \rho, T)$, Φ_o is a non-linear function, d is orifice diameter, n is number of orifices, L is the length of each orifice, ρ is average density of fluid (a constant here), and T is the fluid temperature. There are various expressions for Φ_o available in literature for sharp orifices and small bore orifices.

6.2.1.4 Model Initialization

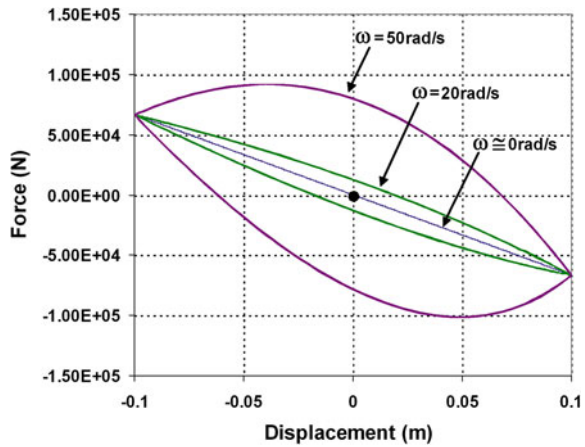
The change in average density of fluid in shock absorber is only due to change in intrusion of the piston rod. Therefore, coefficient of discharge in orifices remains almost constant and the total discharge coefficient including number of orifices and their dimensions can be used in the model.

The model states need to be initialized appropriately before simulation. From the given piston rod area (A_r), the steady state pressure may be calculated as $P_0 = W/A_r$. Then, one may assume an initial piston position (say, in middle of the suspension) and prescribe the initial volumes in two chambers (states associated with C-fields). Using Eq. 6.52, determine the initial volumetric strain at the given equilibrium pressure P_0 and then determine charging or initial density, ρ , of the fluid as follows:

$$\left(\frac{\Delta V}{V_0} \right) = \left(1 - \frac{\rho_0}{\rho} \right),$$

where ρ_0 is the free space density of the fluid. Once the charging fluid density is known, multiply with initial volumes to calculate the initial mass of fluid in each chamber (other states of the C-fields).

Fig. 6.38 Liquid spring damping characteristic



6.2.1.5 Damping Characteristic

The bond graph model given in Fig. 6.37b is modified to study the damping characteristics of the liquid-spring. First of all, the ground excitation is set to zero, i.e., $V(t) = 0$. Thereafter, the load inertia ($I:W/g$) is substituted by a source of flow. The cyclic displacement is given as $x = A \sin(\omega t)$. Taking derivative with time, we get the expression for the source of flow as $\dot{x} = A\omega \cos(\omega t)$. This cyclic velocity is given at the source of flow which substituted the load inertia.

The parameter values chosen for the liquid spring are as follows: piston diameter is 10 cm, piston rod diameter is 5 cm, internal height of the spring (excluding piston height) is 80 cm, orifice discharge coefficient is $10^{-2} \text{ kg}\cdot\text{Pa}^{-1/2}$, $\beta = 10^9 \text{ Pa}$, and the fluid density is 970 kg/m^3 .

We consider $\pm 10 \text{ cm}$ displacement ($A = 0.1 \text{ m}$) cyclic loading at various frequencies to evaluate damping performance. The results for 2cst viscosity silicone fluid are given in Fig. 6.38. The stiffness characteristics is obtained by choosing a very small value of frequency, $\omega = 0.01 \text{ rad/s}$. This is a quasi-static analysis where damping effects are almost absent. The stiffness characteristics is found to be linear within the considered range of deflections. As the frequency of excitation increases, more and more energy (the area enclosed by the hysteresis curve) is dissipated by the damper. Note that the energy dissipated for positive velocities and negative velocities is not the same because of the asymmetry in volumetric strain in the two control volumes.

6.2.2 Active Suspensions

Active suspensions use separate actuators and sensors for each wheel. Usually, these suspensions consume great deal of power to provide near perfect shock isolation. The actuators provide independent force on the suspension to improve the riding/handling characteristics. An active or semi-active suspension must perform the following tasks:

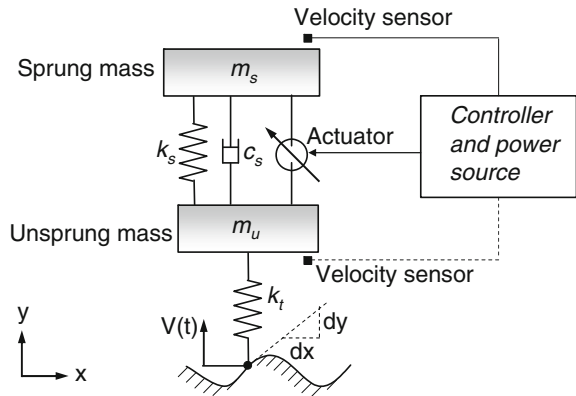
(a) support the vehicle body at the desired ride height, (b) minimize vertical shock transfer to the sprung mass, (c) correct the suspension level when the vehicle is cornering during a curve negotiation, and (d) provide pitch control when the vehicle accelerates or brakes. For example, when the front wheels of the vehicle go over a bump, the actuators on the front suspension act in such a way that the vehicle does not heave or pitch; the distance between the axle and the vehicle is changed appropriately by the actuator force. When the rear wheels pass over the same bump, the actuators on the rear suspension act the same way. Modern active suspension designs include self-levelling suspension and height adjustable suspension features. In racing cars operating at high speeds, the vehicle is lowered to improve its aerodynamic performance by using the adjustable suspension feature. Such activities require a properly programmed microprocessor or microcomputer to decide on the state of the vehicle from available measurements.

However, achieving all these also requires significant amount of energy, say to operate the pump continuously in a hydraulic/pneumatic active suspension system. Active suspensions are expensive and are thus found in high-end luxury vehicles. Moreover, they require frequent maintenance and the fuel efficiency of the vehicle is reduced due to the added mass and other complications. However, the pitch, cornering and weight change effects may be accommodated slowly because one has sufficient time at hand. On the other hand, controller response to ground excitation needs to be very fast. Thus, it is useful to separate these tasks and provide a fast acting (and large power consuming) actuator and a slow acting actuator. Further note that the large power consuming fast acting actuator (if electrical) can be made regenerative, i.e., generate some power to compensate for the power consumed at other times.

Dampers maintain contact between the wheel with the road by preventing the wheel from continuing upward motion at the crest of a bump. The stiffness and damping of the suspension must be properly matched to obtain the desired suspension response. If damper is offers too little damping then the suspension continues to bounce long after the actual ground excitation. On the other hand, too much suspension damping causes the damper to act as a rigid strut to high-frequency excitations and thus transmits the shock input to the vehicle body which reduces the ride comfort.

In a high bandwidth or fully active suspension system (See Fig. 6.39), an actuator is connected between the sprung and unsprung masses of the vehicle. Such a system aims to control the suspension over the full bandwidth of the system, which may be broadly divided into two resonant frequency ranges of a typical vehicle, namely the rattle-space frequency (10–12 Hz) and tire-hop frequency (3–4 Hz). The fully active suspension system requires actuators with a wide bandwidth which consume large amounts of power. When low band-width actuators (typically around the rattle space frequency) are used, the actuator is placed in series with the spring and the damper shown in Fig. 6.39. Such systems are known as slow-active or band-limited suspensions. Under high frequency input (corresponding to wheel-hop frequency), the actuator acts as a rigid strut and reduces the system to a stiff passive suspension. Thus, one achieves significant reduction in body roll and pitch during cornering and braking manoeuvres. Moreover, the energy consumption is lower than a high bandwidth system.

Fig. 6.39 Schematic representation of an active suspension system



6.2.2.1 Hydraulic Active Suspension

Hydraulic servo-mechanisms are often used to control active suspensions. Hydraulic power generated by a pump is easily distributed to the suspensions from a common source. On board sensors continually monitor the vehicle motion (ride level) and a computer or microprocessor operates the hydraulic servos of each wheel's suspension. This feedback mechanism generates suspension forces to regulate body lean, dive, and squat during various driving maneuvers.

The power required to drive the pump reduces the overall fuel efficiency of the vehicle. Moreover, hydraulic systems have slow response and thus the feedback system may become unstable under certain conditions.

6.2.2.2 Regenerative Electromagnetic Suspension

Electronically controlled active suspension system (ECASS) technology has been developed by L-3 Electronic Systems based on the 1990s design made at the University of Texas Center for Electromechanics. The ECASS-equipped vehicle provides exceptional performance in terms of absorbed power (comfort) and directional stability during tough maneuvering conditions. In this design, linear electromagnetic motors are used in place of hydraulic cylinders. Electromagnetic motors have fast response time than conventional fluid-based damper suspension systems and thus produce smooth variation of suspension force. This quick response aids to virtually eliminate all unwanted movement the body of a car such as roll elimination by automatic stiffening of the suspension when cornering. Therefore, ECASS technology gives the driver a greater sense of control.

Moreover, when the suspension is withdrawing power, the motor can be used as a generator (See discussions on regenerative braking in later sections of this chapter).

The power produced through the regeneration action is stored in the battery pack, which improves the overall fuel efficiency of the vehicle.

6.2.2.3 MR-Fluid Damper

Active hydraulic suspensions implement some kind of control over the suspension stiffness and damping. As far as liquid springs are concerned, they use Silicone fluid which is also a good carrier for synthesis of Magneto-Rheological fluids (MR-fluids). In MR-fluids with Silicone base, variable percentage of micron sized iron particles coated with anticoagulants is used as an additive. The viscosity of the MR-fluid and consequently the fluid flow through orifice is controlled through actuation of magnetic fields in semi-active liquid-spring suspensions. In some recent designs, the damper has a cylinder containing an MR fluid and a sliding piston assembly with a number of concentric annular flow gaps formed between concentrically mounted flux-rings positioned on the piston core. The sliding piston forms a chamber at either end of the assembly. Information from different sensors measuring suspension extension, steering angle, vehicle acceleration and road profile is used to calculate the optimum stiffness for the instantaneous state. The damper increases the overall MR damping and turn-up ratio for a given piston size by utilizing multiple flow gaps. Although the direction of the suspension force cannot be controlled by using MR-fluids, the heavy power requirement to sustain the magnetic field means such dampers fall in the active suspension category.

6.2.2.4 Design Guidelines

In [38], Karnopp reasons that the conventional damping element between the sprung and unsprung masses in a conventional suspension is in the wrong place because it produces a suspension force depending upon the relative velocities between the sprung and unsprung masses. An optimal suspension should apply a damping force on the sprung mass proportional to the velocity of the sprung mass. The control architecture of the suspension system is shown in the quarter car model given in Fig. 6.40a. In the quarter car suspension model, one usually assumes a constant linear vehicle velocity \dot{x} and from the road profile, the vertical excitation is calculated as $V(t) = \dot{y} = \dot{x} \frac{dy}{dx}$. An equivalent passive configuration of the controlled system in Fig. 6.40a is shown in Fig. 6.40b where a damper attached to the inertial frame applies the feedback force. However, in reality, when one end of the damper is attached to the vehicle body (sprung mass), there is no place to attach the other end of the damper to the inertial frame with zero inertial velocity or the ground. Thus, such a conceptual damper is termed a sky-hook damper.

The sky-hook damper is just a conceptual notion; it means that an equivalent force resulting from this conceptual damper should be applied on the sprung mass. However, the force cannot be supplied by an external actuator; the actuator itself must

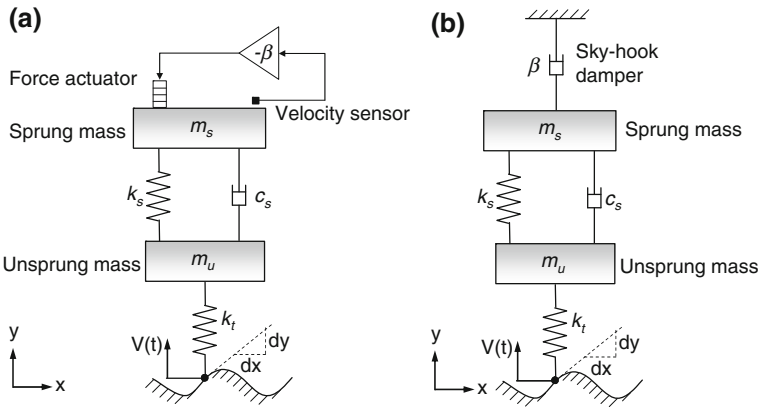


Fig. 6.40 Concept of shy-hook damper

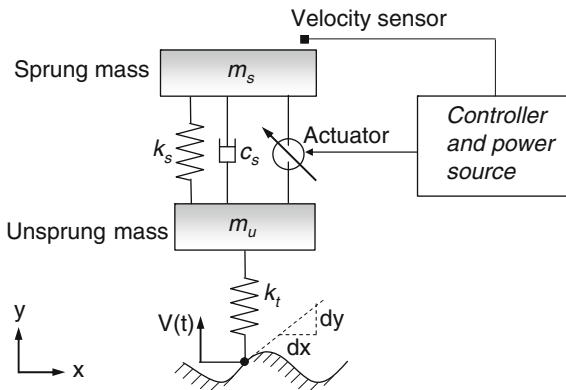


Fig. 6.41 Implementation of shy-hook damper

be carried by the vehicle. Thus, if the actuator is an integral part of the vehicle, it has to be mounted between the sprung and unsprung masses. This actuator generates a damping force proportional to the absolute velocity of the sprung mass, but applies it both to the sprung and the unsprung masses (See Fig. 6.41).

The bond graph model of the quarter car model of the active suspension system is shown in Fig. 6.42a. The bond graph model has four state variables, one controlled source and one sensor.

We can test the structural controllability of this system by assigning preferred derivative causalities to storage elements while allowing both direct and inverse causalities for controlled sources. The resulting bond graph in preferred derivative causality is shown in Fig. 6.42b. It is found that all storage elements can be assigned derivative causality and hence the system is structurally controllable when the actuation is made between the sprung and unsprung masses. However, note that if the

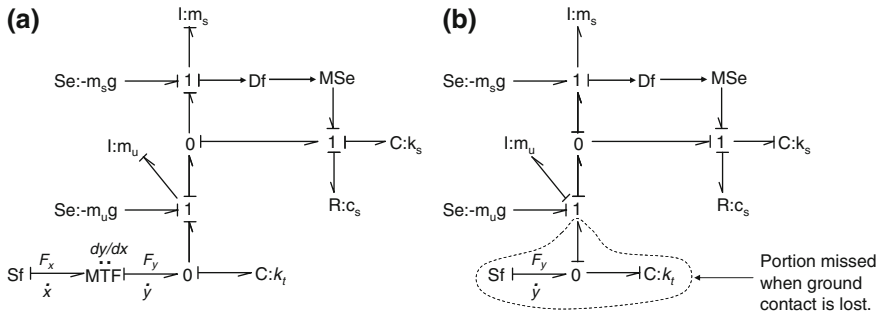


Fig. 6.42 Bond graph model of active suspension system in (a) preferred integral causality and (b) preferred derivative causality

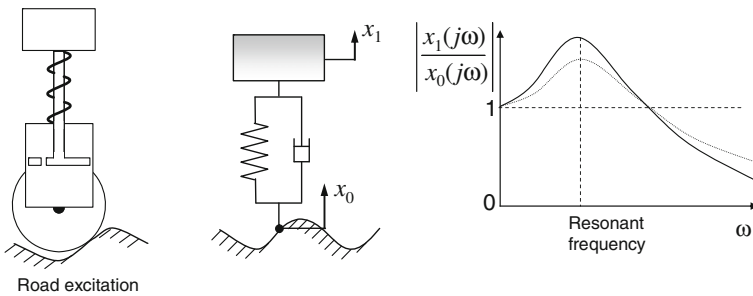


Fig. 6.43 Configuration and frequency response of passive suspension

wheel loses contact with the ground, the portion within the dotted lines shown in Fig. 6.42b should be removed. In that case, the I-element representing inertia of the unsprung mass would be integrally causalled and thus the system becomes structurally uncontrollable. Thus, the active suspension system is controllable as long as the wheel remains in contact with the ground and that must be ensured by the controller under normal operation. It is left to the reader to evaluate that the system remains observable when the wheel is in and not in contact with the ground.

The suspension performance undergoes significant improvements with implementation of sky-hook damper concept. Figure 6.43 schematically shows the conventional suspension system with a rigid wheel and a sprung mass, its equivalent mechanical system and its frequency response. The adjustment of damper parameter can change the frequency response from the curve shown in solid lines to the curve shown in dotted lines. However, as amplitudes at low-frequency excitation (most notably at the resonant frequency) reduce, the amplitudes grow for high frequency excitations.

The schematic representation of the active damper with solid wheels, its equivalent mechanical model with sky-hook damper, and the frequency response are shown in Fig. 6.44. The active damping with sky-hook damper concept greatly reduces the low-frequency amplitudes (including at the resonant frequency) and also the high

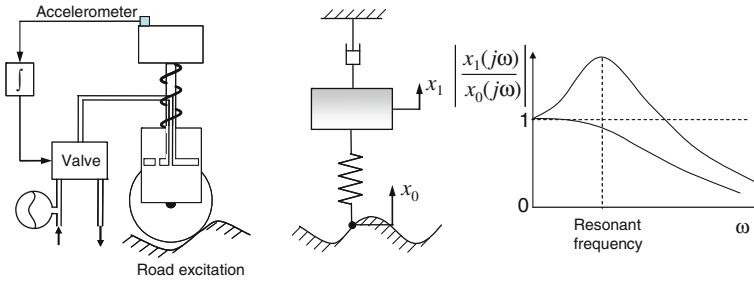


Fig. 6.44 Configuration and frequency response of active suspension

frequency amplitudes, although this reduction becomes marginal for much higher frequencies.

To compare the performance of fully active and passive suspension systems, the parameter values of the suspension are taken from [17] as follows: $m_s = 240$ kg, $m_u = 36$ kg, $k_s = 16,000$ N/m, $c_s = 980$ Ns/m and $k_t = 160,000$ N/m (See Fig. 6.41). The transfer function between the input velocity and output velocity (of the sprung mass) is found to be

$$H(s) = \frac{18,148s + 29,629}{s^4 + 31.3s^3 + 4,955s^2 + 18,148s + 296,296}. \tag{6.68}$$

The fully active system generates a suspension force $F_s = \alpha_s x + \alpha_d \dot{x} - \alpha_{sky} x_s$ where $x = (x_s - x_u)$, x_s is the deflection of the sprung mass, x_u is the deflection of the unsprung mass, α_s is the stiffness coefficient that leads to a force proportional to relative displacement of sprung and unsprung masses, α_d is a direct damping coefficient that leads to relative velocity-dependent force, and α_{sky} is the sky-hook damping coefficient that leads to a force proportional to absolute velocity of the sprung mass. For the fully active suspension with $\alpha_s = k_s$, $\alpha_d = c_s$ and $\alpha_{sky} = 2,000$ Ns/m, the transfer function between the input velocity and velocity of the sprung mass is found to be

$$H(s) = \frac{18,148s + 29,629}{s^4 + 39.64s^3 + 4,955s^2 + 5,5185s + 29,6296}. \tag{6.69}$$

Note that the suspension system model has four state variables. However, only three of them (partial state feedback) are used for establishing the suspension feedback force $u = F_s$. Chalasani [17] proposed a full state feedback of the form $u = -4,800X_1 - 1,524X_2 + 1,248X_3 + 958X_4$ and compared the frequency responses of the fully active and passive suspension systems. Karnopp [36, 38] showed that the sky-hook damper configuration (with the suspension force as a function of three state variables) produced remarkably similar response to the active configuration of [17]. The frequency response of passive and active suspension systems are compared in Fig. 6.45. Note that in Fig. 6.45, $G(s) = H(s)s$, which is

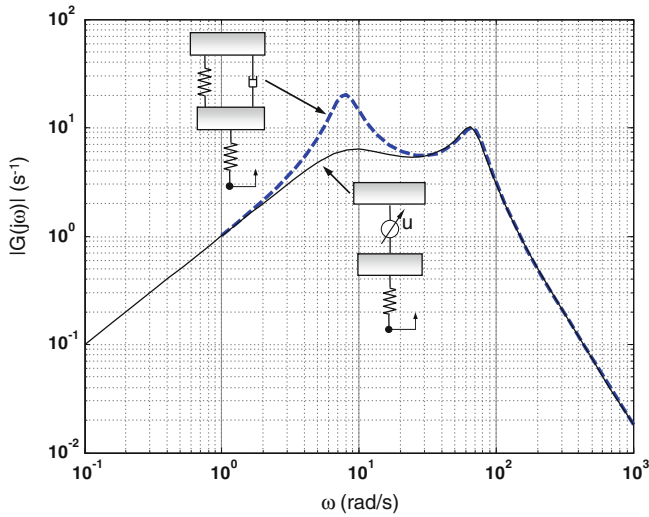


Fig. 6.45 Frequency response for acceleration of sprung mass

the transfer function between the ground excitation velocity and acceleration of the sprung mass. It is found that the active suspension suppresses the shock transmission around the dominant resonant frequency.

The frequency response in Fig. 6.46 shows the shock velocity transmission to the sprung mass. In the active suspension, the input velocity is directly transmitted to the sprung mass (gain = 1) in the complete low frequency range and there is significant attenuation immediately after the first resonant frequency of the corresponding passive system. It shows that the controller developed from a physical idea (sky-hook concept) gives as good a performance as a full-state feedback system developed from pole-placement.

Based on these ideas, Karnopp [38] proposed two contrasting versions of active suspensions shown in Fig. 6.47. The controller of the first one utilizes only the sprung mass velocity measurement while that of the second one uses velocity measurements of both the sprung and unsprung masses. The first configuration combines a slow-active or low-bandwidth load leveling system with semi-active force generator for high-frequency content absorption. The second configuration uses a single broadband actuator for absorption of both low-frequency and high-frequency excitations. Karnopp [38] suggests that the first configuration results in more practical systems than the second one.

The fully active second configuration can be achieved by a hydraulic contraction shown in Fig. 6.48a. Note that although this contraction can be used to provide any desired suspension force, the hydraulic actuation of valve positioning means slow response. We will have a further look at the hydraulic actuation later in this section. The bond graph model of the hydraulic actuation is given in Fig. 6.48b. In the bond graph model shown in Fig. 6.48b, the MR-element models the valve. It receives the

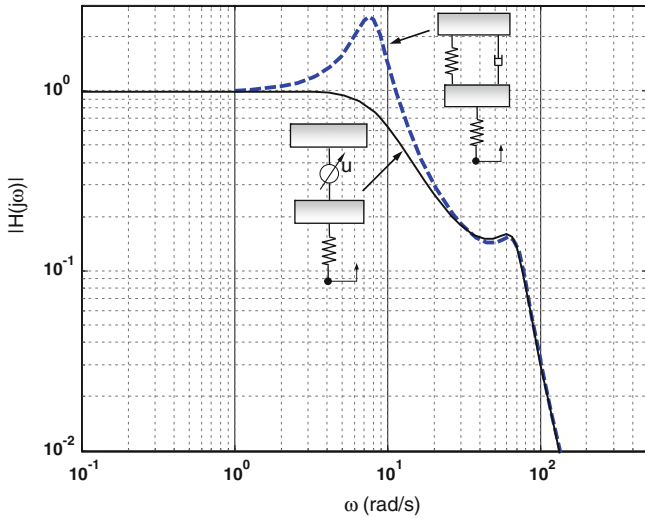


Fig. 6.46 Frequency response for velocity of sprung mass

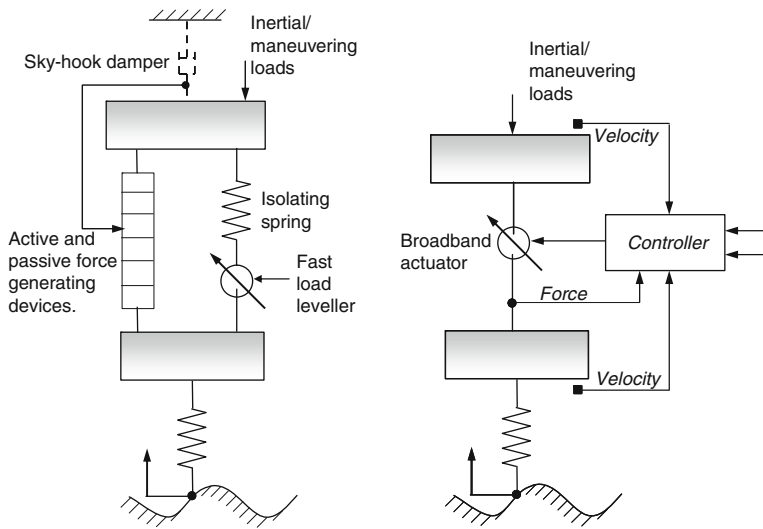


Fig. 6.47 Two configurations for active suspensions

velocity of the sprung mass as the modulating term and accordingly channels the flow through the valve (see the spool valve and hydraulic actuator models given in the previous chapter).

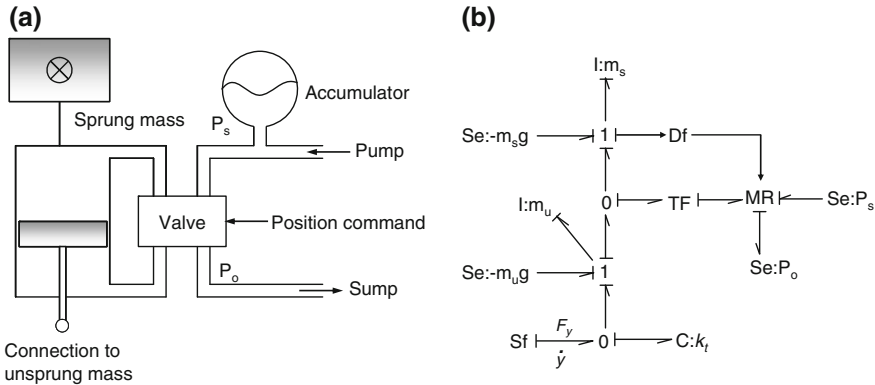


Fig. 6.48 **a** Active hydraulic force generation device and **b** its bond graph model

6.2.3 Semi-active Suspensions

Semi-active systems can only change the parameters of the shock absorber (e.g., viscous damping coefficient, spring stiffness), and do not add energy to the suspension system. The regulation of the suspension force is through passive interaction, e.g., with a spring or a dashpot. Thus, the line of action of the control force is fixed. Semi-active suspensions are less expensive to design and manufacture. They usually consume negligible amount of energy and thereby do not compromise with the fuel efficiency of the vehicle. Recent developments in semi-active suspension design has narrowed the performance gap between semi-active and fully active suspension systems.

6.2.3.1 Solenoid/Valve Actuated Semi-active Suspension

The basic semi-active suspension consists of a solenoid valve which manipulates the fluid flow inside the hydraulic damper. The solenoids are computer controlled. The control algorithm is developed by using the Sky-Hook damper technique of Karnopp [38]. It is also possible to control the stiffness of the suspension through a switched connection to an auxiliary volume.

In semi-active suspensions, the full suspension force is not generated by an actuator. Usually, hydraulic semi-active suspensions use control valves to channel hydraulic fluid flow in the proper direction by modulating control valves. The main idea is to modulate the energy dissipation in a passive damper through the sensed variables. The power dissipated by the hydraulic damper is given as $P_d = F_d (\dot{x}_u - \dot{x}_s) = F_d V_r$ where V_r is the relative velocity between the sprung and unsprung masses. For the power dissipation to be positive, which is what the suspension is meant to do, it is required that the instantaneous values of F_d and V_r must be of the same sign. However, all control systems have some feedback delay

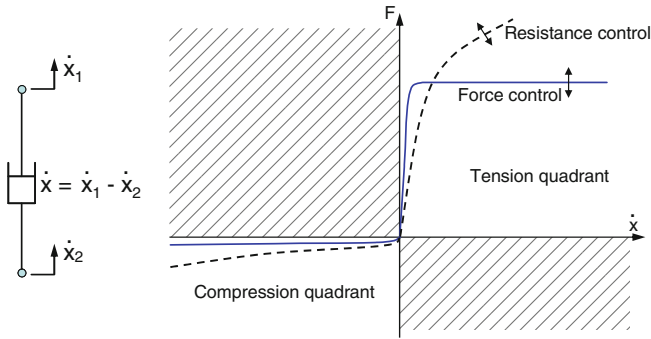


Fig. 6.49 Damper force generation for tension command

and actuation delay. Therefore, it is highly possible that the relative velocity may become of wrong sign than what is required to dissipate power. Thus, hydraulic semi-active suspension systems reduce the active component of force to near zero-value whenever the relative velocity is of wrong sign. Two different control laws are used depending upon whether the command is to generate tension or compression. When tension command is required, the control law should produce near-zero compression for wrong sign (negative values) of relative velocity. Likewise, when compression command is required, the control law should produce near-zero tensile force for wrong sign of velocity. This fact is schematically illustrated in Fig. 6.49. The forces and velocities must lie in the first and third quadrants such that the power is dissipated.

Two kinds of damper force generation schemes are shown in Fig. 6.49. In one of the cases, the damping force is independent of relative velocity (except around zero velocity). Such forces can be generated by electromagnetically loaded pressure control valves which open or close at pre-designed pressure differences. The second form considers that the generated damping force is strongly related to the relative velocity. Such force generation may be produced by varying valve openings (effectively, valve resistance) through electromagnetic actuation. Although these two forms of force generation seem radically different from each other, it has been shown [36] that the overall suspension performance remains similar.

It is seen from Fig. 6.49 that if the system is designed to switch at $\dot{x} = 0$ (from tension to compression command) then it is possible that the force may change sign and instead of dissipating power, power will be imported into the system. Thus, designing a control system for semi-active hydraulic systems is not so trivial. It is usually advisable to shift the switching point from $\dot{x} = 0$. In the literature, one finds numerous examples of force control, resistance control, and switching control (between two resistance laws). These kinds of semi-active systems with limited force regulations have been found to yield comparable performance to fully active suspensions.

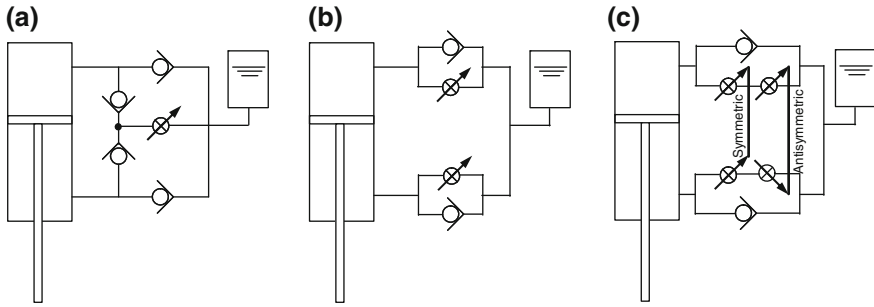


Fig. 6.50 Different configurations for generating hydraulic semi-active damper forces

There are many configurations to produce controllable forces in semi-active hydraulic suspensions. The principal goal is to dissipate energy as the hydraulic fluid is forced through a controlled valve. Some configurations can use multiple valves. A few basic configurations given in [36] are shown in Fig. 6.50.

In the first configuration (Fig. 6.50a), check valves regulate flow through a single controlled valve used for both tensile and compressive force generation. The minimum pressure in either cylinders of the damper is the reservoir pressure. The check valve may be an electromagnetic poppet valve used for pressure regulation or a position controlled spool valve. The use of a single valve to control both tensile and compressive damper forces requires the actuator to respond fast enough so that the relative velocity does not change sign in between command generation process and thus import energy into the system. To overcome this issue, the other two configurations were proposed.

The second configuration shown in Fig. 6.50b uses separate control valves for controlling tensile and compressive forces. This configuration has the added advantage that the actuators need not have fast response time; the check valves being fast passive systems provide quick switching around $\dot{x} = 0$. The third configuration (Fig. 6.50c) is a step ahead with two more control valves and the control valves used to control tension and compression forces are mechanically coupled. The coupling has a symmetric part (i.e., when one control valve position is increased in tension control part, the corresponding control valve position in compression control part increases) and an anti-symmetric part (i.e., when one control valve position is increased in tension control part, the corresponding control valve position in compression control part decreases). The symmetrically coupled control valves change the slope of the force versus velocity curve (i.e., stiffen or soften the damping) and the anti-symmetrically coupled control valves shift the force versus velocity curve to tension or compression side.

More details on design of active and semi-active suspensions can be consulted in [37, 38]. It is noteworthy that semi-active suspensions, which seem to have many limitations, indeed produce comparable performance to much costlier and resource

intensive fully active suspension systems. The so-called adaptive suspension, which uses a single control valve, is discussed next in detail.

6.2.3.2 Adaptive Suspension

Passive liquid spring suspensions belong to the pure hydraulic category. They differ from other hydraulic suspensions in the fact that a conventional hydraulic fluid is not generally used and separate subsystems are not used to control stiffness and damping. Passive liquid springs for sensitive military equipment use check valves instead of orifices in the piston, which allow flow only when designed preload shock is exceeded, and perform as rigid mountings under normal operations. Thus, the design of passive systems is fixed with respect to specific objectives. On the other hand, active and semi-active suspension technologies provide the ability to change the suspension's natural frequency in real time, in response to the operating environment and control inputs. Hence, it is possible to produce a suspension with low natural frequency when the ride quality is of primary concern and increase the suspension natural frequency when the operating conditions require it. With the ability to change natural frequency on the fly, the vehicle designer can confront the conflicting requirements of a soft compliant ride and a stable safe-handling vehicle with high-load-capacity.

An adaptive suspension allows reconfiguration of the device to suite required bounce and jounce behavior. One may select a compliant suspension configuration on rough roads, whereas a hard suspension behavior can be selected for high-speed maneuvers on smooth highway roads. The reconfiguration of the suspension components may be automatic or manual.

The components and configuration of a compressible liquid adaptive suspension system are shown in Fig. 6.51. We consider a quarter car model in which $M_V/4$ (one-fourth of the vehicle body mass M_V) is the sprung mass, M_{ax} is the unsprung mass (axle and wheel mass taken together), K_t is the tire stiffness, V_{c1} and V_{c2} are volumes of two small surge protection accumulators, and V_A is the volume of a properly designed large accumulator. The Rate and Damping valves are ON/OFF type, i.e., two position 2-way valves. The external valve is always open; however, no flow takes place through it as long as the damping valve is closed.

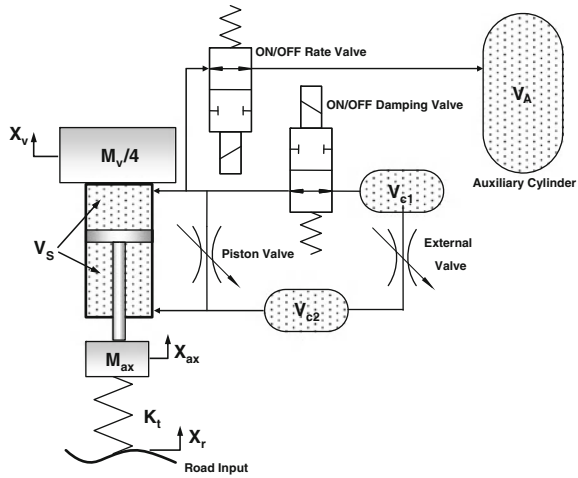
The liquid spring shown in Fig. 6.51 does not have holes or annular gaps in the piston. The damping is achieved by a regulated piston valve which connects the control volumes between the two sides of the piston. The working principle is exactly similar to that of the passive liquid spring.

As we know from the preceding section, the liquid spring's stiffness depends on the volume of liquid. The total liquid volume is given as

$$V = V_s + V_{c1} + V_{c2} + V_A \delta_r, \quad (6.70)$$

where δ_r is a binary variable. When the rate valve is open, $\delta_r = 1$, otherwise $\delta_r = 0$. Thus, the rate valve is used to govern the stiffness of the suspension system. Note

Fig. 6.51 Adaptive liquid spring suspension system



that several auxiliary volumes and rate valves may be used to obtain a wide range of stiffness selection.

The flow between the control volumes is given as

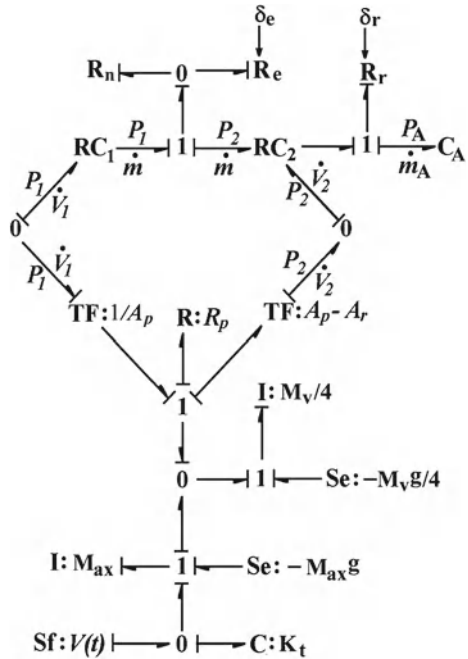
$$f = (C_{dp} + \delta_e C_{de}) \sqrt{|\Delta P|} \text{sign}(\Delta P), \tag{6.71}$$

where C_{dp} is the coefficient of discharge through the piston valve, C_{dd} is the coefficient of discharge through the external damping valve, and δ_e is a binary variable governed by the On/OFF state of the damping valve: $\delta_e = 1$ when the damping valve is open, otherwise $\delta_e = 0$.

The bond graph model of the adaptive liquid spring suspension is shown in Fig. 6.52. Two modulated R-elements in the model represent the external valve (R_e) and the rate valve (R_r). The rate valve must be properly controlled such that the spring stiffness does not vary suddenly because it would then suddenly change the equilibrium position of the piston. The new C-element (C_A) models the auxiliary volume. There is no pressure volume flow rate port in this new C-element because it has a constant volume. The bottom part of the model includes representations for the tire stiffness and the unsprung mass.

The damping valve in combination with the external and piston valves selects the damping level depending on the stiffness of the system (i.e. whether the rate valve is open or closed). The piston and external valves are used to dissipate energy (i.e. provide damping). The flow-pressure gains of the valve (if the flow is governed by linear relation) or coefficients of discharge, and the pressure differential breakpoints (where δ_e and δ_r are modulated) can be adjusted to achieve desired jounce and bounce. This is accomplished without the fuel-consuming power requirements of active suspension technology, since the compressible liquid spring is always reacting passively to road inputs at whatever stiffness has been selected for the moment. The

Fig. 6.52 Bond graph model of adaptive liquid spring suspension

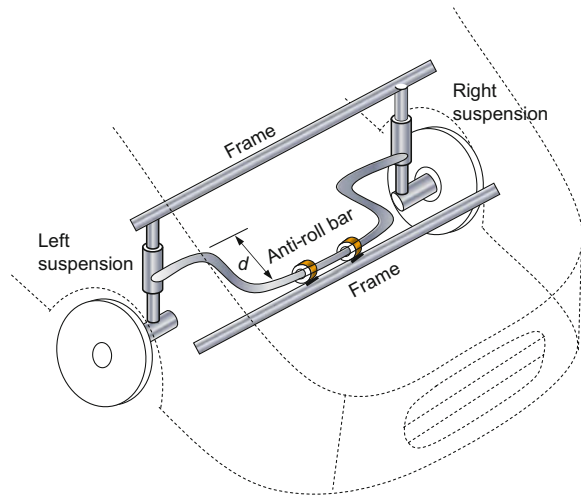


only power consumed is the small amount required by the stiffness selection control mechanism.

6.3 Anti-Roll Bar and Ride Height Management

When a vehicle takes a sharp turn at high speed, the inertial and centrifugal forces push down the part of the vehicle on the outside of the turn and lift up the part of the vehicle on the inside of the turn. Under severe conditions, the wheels on the inside of the turn may completely lift up from the road. The body roll or lean causes positive camber of the wheels on the outside of the turn and negative on the inside. Whether the wheels completely lift up or not, the normal reaction distribution on the wheels and camber angles change. These changes lead to loss of traction/braking (road holding) and steering during sharp turns. To avoid this, the suspensions' roll stiffness should be increased. Increasing roll stiffness of the suspension also increases the stiffness of the suspension in the vertical directions and results in uncomfortable drive. Thus, some sort of mechanism is required which would increase the effective roll stiffness[27] of the suspension while maintaining save level of compliance in vertical direction.

Fig. 6.53 Schematic diagram of anti-roll bar and its mounting



6.3.1 Passive Anti-Roll Bar

The mechanism in question, called an anti-roll bar, turns out to be very simple. Anti-roll bar, also called stabilizer bar and anti-sway bar, is part of the vehicle suspension system designed to reduce the roll of the vehicle while it takes a sharp turn. Anti-roll bar is normally a U-shaped round bar which connects the two front or two rear suspensions of the vehicle. Some vehicles have anti-roll bars for front and rear wheels. The bar is hinged to the vehicle frame using pivoting rubber mounts such that it can rotate about its own axis. Figure 6.53 shows the scheme of the anti-roll bar and its mounting on the vehicle frame.

When the vehicle takes a turn, the front (and rear) suspension strut on the outside of the turn is pushed up, i.e., it compresses. This applies a torsion moment on the anti-roll bar (the moment or lever arm d is shown in Fig. 6.53) which also pushes down the suspension on the inside of the turn. As a result, the vehicle body remains parallel to the road. In this way, the weight on the wheels of the vehicle is evenly distributed and the vehicle's tracking performance remains comparable to that while the vehicle runs on a straight path. Improved tracking performance also means comfortable handling and safety during cornering.

Anti-roll bar configuration influences the understeer or oversteer behavior of the vehicle. It is known that the slip angles (the simplest form of tire side force representation) determine whether a vehicle understeers or oversteers. If the cornering coefficient of the front wheels is lower than that of the rear wheels, then the rear wheels stick more to the road and the vehicle understeers. On the other hand, if the cornering coefficients of the front wheels are larger than that of the rear wheels, then under action of the same centrifugal force, the rear wheels slip more to the outside of the turn and the vehicle oversteers. Usually, for better handling of the car, understeer

characteristic is required because it gives the driver enough time to adjust steering in one particular direction. If a vehicle oversteers, then this adjustment is uncomfortable because the driver has to turn the steering wheel in reverse directions (clockwise and anticlockwise) in quick succession. The load distribution on the wheels also affects the cornering force. The proportion of the total roll stiffness (from the combined effective stiffness offered by the suspension springs and the anti-roll bar on both the axles) offered by the front and rear axles determines the loads transferred to the inside and outside wheels in a turn. If the roll stiffness on the front wheel is large, then the load distribution on the left and right front wheels would be more even whereas it would be uneven on the rear wheels. Because the linear velocity of the wheel on the inner side of the turn is smaller than that of the wheel on the outer side of the turn, the slip angle for the front wheel on the outer side of turn becomes larger than that of the wheel on the inner side and the vehicle understeers. On the other hand, if the roll stiffness on the front wheel is small compared to that of the rear wheel, the vehicles' understeer is reduced.

Note that the anti-roll bar is an absolute necessity in any vehicle because without it, the driver will have a lot of difficulty to take a turn. At the same time, if the suspension level equalizing effect is too much then the independence between the suspension members on both sides of the vehicle is lost. For example, if one wheel of the vehicle falls into a pit due to which the suspension on that side extends temporarily, then the anti-roll bar transmits the same effect to the suspension on the other side of the vehicle and results in unwanted extra pitch. Likewise, a wheel hitting a bump causes the wheel on the other side to lift up. Thus, there must be a balance between the level of body roll control offered by the anti-roll bar and independence of the suspensions. It is usually difficult to do much about this issue while using a passive anti-roll bar system. This is why, active and semi-active anti-roll systems have been developed which retain full independence between the suspensions on the two sides of the vehicle.

6.3.2 Active Anti-Roll and Ride Height Management System

The basic layout of a semi-active anti-roll system developed by Automotive Products is shown in Fig. 6.54. This system has a very fast response time. It effectively eliminates braking dive (forward pitch) and cornering roll by independently controlling all four suspensions. Moreover, this design allows the use of very soft suspension springs and thus, significantly improves the ride comfort. It also provides the self-leveling capability which adjusts the vehicle height upon load change, such as extra passengers boarding or leaving the vehicle.

The Automotive Products anti roll system has a damper valve between a gas spring and the piston. There are four such suspension systems, each for a wheel. All of these suspension struts are connected to a common high pressure hydraulic pump, which is driven by the engine. The high pressure reservoir is the same one used to operate other hydraulic systems such as the brakes. Each suspension unit

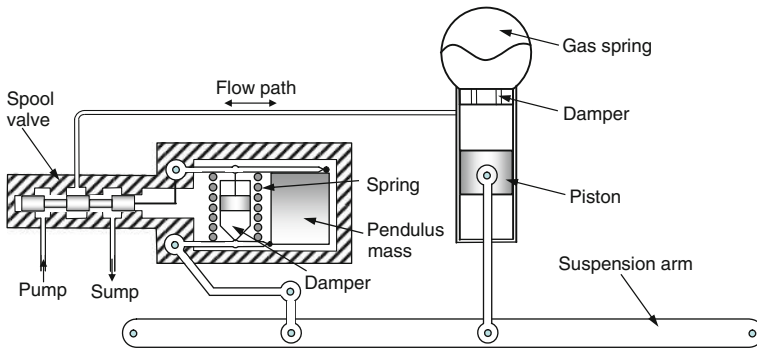


Fig. 6.54 Schema of anti-roll system developed by Automotive Products

has a ride-height sensing control valve through which fluid flows in or out to adjust the suspension length and thus, vehicle's ground clearance. The level correction is a slow process, i.e., it has a long response time. This is not a problem because the load change only takes place few times at considerably larger intervals. On the other hand, adjustments to road irregularities and inertia-induced loads (braking, cornering) require quick response. The Automotive Products anti-roll system acts as purely passive suspension (provided by the pneumatic parts) for such fast load changes. The active part (hydraulic part) is only used for level adjustment and thus the power and fast response time requirements are reduced.

The pendulous mass allows the device to determine whether the suspension motion is due to inertial effects (pitch, roll) or due to road unevenness. The inertia effects cause the suspension arm tilt and the spool valve is actuated through the linkages to force hydraulic fluid into/ out of the cylinder. Road unevenness moves the suspension arm vertically and thus the hydraulic part is not actuated. Then the gas spring and the valve damper provide the suspension damping.

In some forms of semi-active suspensions, the power required to pump the hydraulic fluid is generated from wheel movement due to road shocks. To harness the required power through regeneration, the vehicle must be run for some distance. As the vehicle encounters road unevenness, the suspension damping action is provided by charging a high-pressure chamber through fast acting check valves. Thus, the correct ride-height is obtained only when the vehicle has traveled some distance.

A fully active ride height adjustment system uses many sensors and actuators with a microprocessor-based control system. The load on the vehicle, velocity, accelerations in three linear axes, and angular accelerations (pitch and roll) are the sensed variables. In such a design, the vehicle weight is entirely supported by actuator generated forces. These actuators, besides providing compliant ride and good maneuverability, also manage roll, pitch and ride-height variations. However, supporting the entire vehicle on actuators consumes a lot of power. More details on such active suspension systems are already given in the previous sections of this chapter.

6.4 Power Steering

In a vehicle with manual steering, the driver has to supply the required steering moment to orient the steerable wheels in the desired direction. To overcome the huge force required to turn the wheels, mechanical advantage is provided in the form of steering gear and linkage. Still, the driver has to apply significant effort especially when the vehicle speed is low and the load is heavy.

Modern vehicles being bigger and heavier require huge traction and braking force. Therefore, the contact patch between the wheel and the road needs to be increased. This is why such vehicles use wider and low-pressure tires. However, as the vehicle gains more grip on the ground, it requires more effort to steer it. The huge physical strength required to drive such vehicles with manual steering is an impediment to older, handicapped, and other less-able drivers. Power-assisted steering (PAS) was introduced for this purpose. In PAS, an auxiliary actuator adds on power to the driver supplied power on the steering wheel. The auxiliary actuator may be pneumatic, hydraulic, or electric.

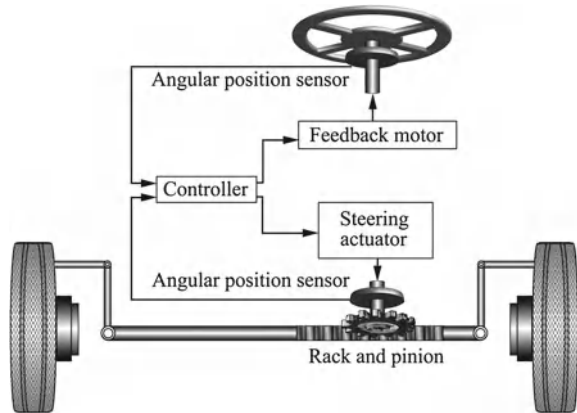
6.4.1 Drive-by-Wire System

In a drive-by-wire or steer-by-wire power steering system, the auxiliary actuator provides the full force to move the wheels and the driver power is not used in the process (See Fig. 6.55). The actual rotation of the steering wheel and the wheel rotation are measured and compared in a controller which then commands the electric or hydraulic actuator to generate the torque required to steer the wheels. Moreover, the controller also commands a feedback motor to generate a much smaller reaction torque which is felt by the driver. In essence, the driver gets the feeling of being actually able to steer the wheels with much reduced effort. Note that a simple torsion spring does not give the correct feedback moment to the driver. The controller has to take additional factors, such as the load on the wheels and the vehicle speed, into account to calculate the correct moment feedback to the driver.

6.4.2 Integral Power Steering

In integral power steering systems, a torsion bar is attached to the end of the worm shaft. When the driver rotates the steering wheel, the torsion bar twists. This twist may be used as a torque sensor. In power assisted hydraulic/pneumatic steering systems, as the torsion bar twists, it moves a spool valve slightly away from its neutral position. This allows fluid flow from a high-pressure fluid reservoir into the hydraulic actuator or power cylinder. The piston in the power cylinder moves and adds power to the steering axle. The power cylinder is connected to the steering linkage in linkage-type

Fig. 6.55 Drive-by-wire or Steer-by-wire fully active power steering system



power steering systems. In rack and pinion-type power steering systems, the power cylinder is a part of the rack, i.e., the rack motion is due to the force applied by the driver and the hydraulic piston.

The hydraulic cylinder and its control through spool valves have been already discussed in the previous chapter. The only difference is that in the previous chapter the spool valve is actuated by a solenoid with current control whereas in power steering applications, it is moved in proportion to the steering wheel rotation by mechanical means. Note that hydraulic actuators have slow response time. Therefore, electrical actuators are the better option. In this chapter, we will deal with electric power assisted steering (EPAS) systems. Note that the bond graph models for EPAS systems developed in this chapter can be readily changed to hydraulic power assisted systems by suitable replacement of the actuator component model by the hydraulic cylinder and spool valve bond graph models of the previous chapter.

6.4.3 Differential-Type Power Steering

A simple configuration of an EPAS, as shown in Fig. 6.56a, has been proposed in [47]. This EPAS system uses a differential which allows an electric motor to add power to the power provided by the driver without forcing the wheel from the driver's hands. Such a system has also been developed in [53].

The forces resisting the steering motion are the self-aligning moments (M_z) on the two wheels and the moments created by the cornering forces (F_c) and the mechanical trail of the contact patch (ϵ). The contact patch trails the vertical axis of rotation of the wheel as shown in Fig. 6.56b. The mechanical trail is due to the elastic deformation of the tire by hydrodynamic forces (and elastic waves) at tire road interface [50]. The bond graph model of the EPAS system with the differential is shown in Fig. 6.57.

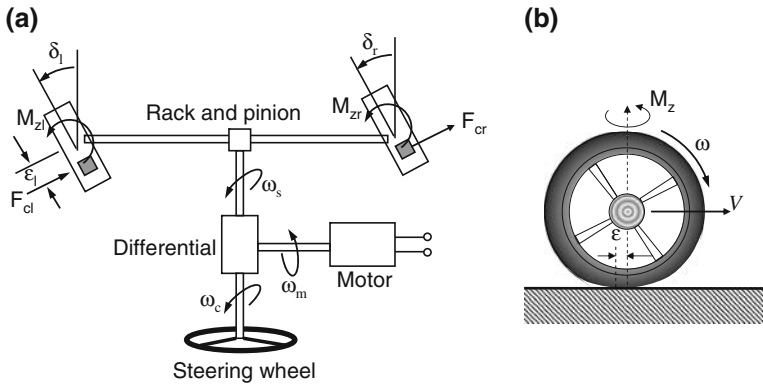
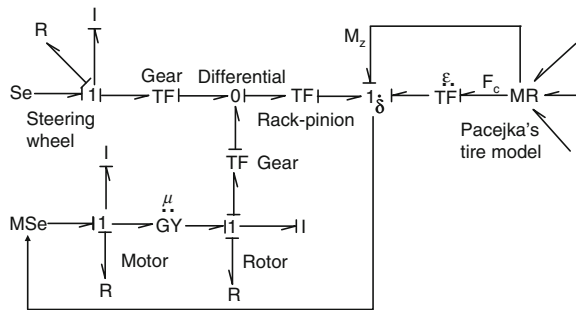


Fig. 6.56 Schematic representation of (a) differential type power steering system and (b) mechanical trail

Fig. 6.57 Bond graph model of differential type EPAS



The top left part of the bond graph model represents the torque applied on the steering wheel, and the rotary inertia and damping offered by the steering column. The rotation of the steering wheel is scaled by a reduction wheel. The bottom left part of the model concerns the assistance provided by an electric motor, whose input voltage is modulated depending upon the rotation of the wheel about the vertical axis (δ). This modulation may be done through various means, the most common of them being the scheme for pulse-width-modulation control of geared DC motors. This simple model does not consider separate values of δ for the two wheels. The differential is represented by the 0-junction. Pacejka's magic formula is used as the constitutive relation for the MR-element which generates the tire's self-aligning moment, cornering forces, and other forces as has been discussed during the wheel model development given previously.

Fig. 6.58 Schematic representation of the EPAS system

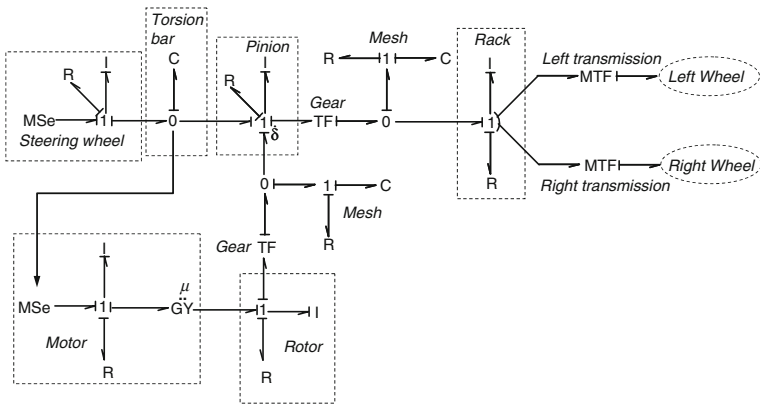
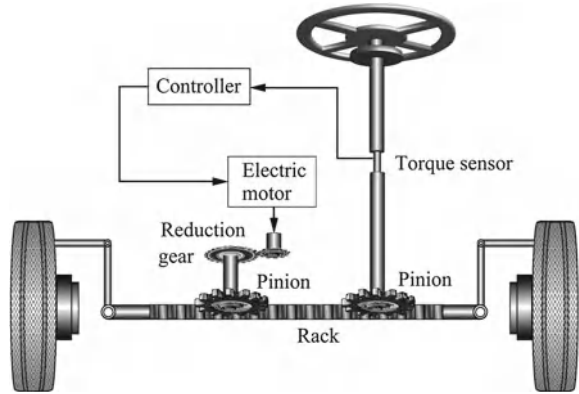


Fig. 6.59 Bond graph model of the EPAS system

6.4.4 Electric Power-Assisted Steering Model

A more accurate bond graph model of the EPAS system is given in [49]. The schematic representation of the considered EPAS is shown in Fig. 6.58. Such systems are now in use in many hybrid electric vehicles.

The EPAS system consists of a principal actuating line (steering wheel, steering column, torsion bar and the pinion), and a secondary actuating line (electric motor, reduction gears, drive column, and another pinion). The bond graph model of this system is shown in Fig. 6.59.

The steering wheel torque input, steering wheel and column inertia, and the resistance are modeled at the 1-junction in the top left part of the bond graph model. Likewise, both the pinions are assumed to be of the same size and thus their rotations must be the same. They are modeled at a 1-junction with a combined rotary inertia and damping. The torsion bar is modeled by a C-element representing the stiffness of

the torsion bar. The twist of the torsion bar is fed to the controller (not shown in the model) which modulates the voltage supply (MSe-element) to a DC motor. The DC motor model includes coil inductance, resistance, motor characteristics ($GY:\mu$), rotor inertia and damping, and the reduction gear. The model given in [49] also includes transmission efficiency, which is modeled by an MR-element. Here, we use a gear mesh coupling for that purpose. This coupling may be used to simulate backlash in the transmission.

The rack and pinion gear ratio (combined for both the pinions) is modeled by a TF-element. The rack inertia and linear resistance are modeled at a 1-junction and two MTF-elements modulated by the pinion rotation angle (See steering model) are used to couple the rack motion to the motion of the wheels. The modulation law for the two MTF-elements should take into account the steering linkage geometry, camber angle, and steering axle inclination [18]. The wheel model has been already developed in this chapter and it gives the reaction forces to the rack motion. Note that some of the inertias and resistances considered in this detailed model are so small with respect to the stiffness of the coupling elements that they may be lumped together to create a much simplified (or reduced order) model of the EPAS system.

6.5 Antilock Braking System

The tire, suspension, and brake system interaction is the most important from the point of vehicle safety. Therefore, suspension and brake systems are the major and critical areas of mechatronization.³

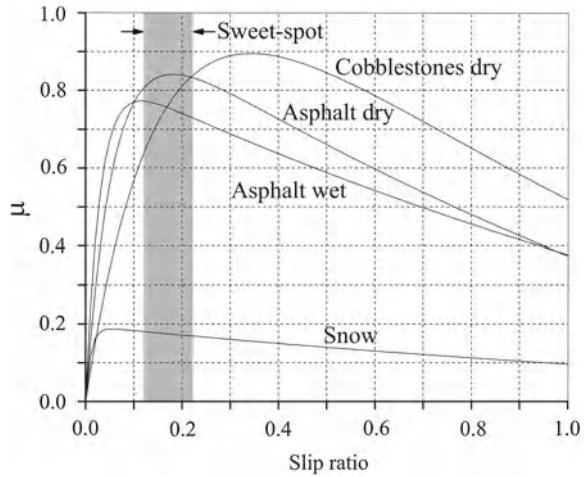
From the slip–friction curve discussed previously in this chapter, it is known that coefficient of friction increases with the increase of slip to a maximum value and then decreases to a minimum value. The longitudinal slip ratio is defined as the normalized difference between the circumferential velocity and the translational velocity of the driven wheel,

$$\sigma_x = \begin{cases} \frac{\dot{\theta}_{wy}r_w - \dot{x}_w}{\dot{\theta}_{wy}r_w} & \text{(during traction, assuming } \dot{\theta}_{wy} > 0) \\ \frac{\dot{x}_w - \dot{\theta}_{wy}r_w}{\dot{x}_w} & \text{(during braking, assuming } \dot{x}_w > 0) \end{cases} \quad (6.72)$$

where \dot{x}_w is the linear speed of the wheel, $\dot{\theta}_{wy}$ is its angular speed, and r_w is the radius of the wheel. The tire friction force (or the coefficient of friction) are obtained from the empirical formulas by Pacejka [58] or Burckhardt [14, 15], as has been discussed in this chapter. It is easily seen from the slip–friction curve shown in Fig. 6.60 that if the wheel gets locked ($\sigma_x = 1$) then the coefficient of friction becomes small and the wheel starts sliding. Consequently, the steering control is lost, which is totally undesirable. Hence, to increase steerability and lateral stability of the vehicle and

³ A part of this section is taken from these authors' previous work published in [6, 8].

Fig. 6.60 Friction coefficient versus slip ratio curves for different road surfaces



to decrease the stopping distance during braking, the slip value must be maintained within a range to get the high value of friction force. As the slip dynamics is very fast and at any value after the peak of the friction curve is open loop unstable, the slip value is kept within a certain range which is also called sweet-spot. The sweet-spot varies for different reasons such as tire type, tire pressure, tire temperature, road conditions.

ABS as a vehicle autonomous system can be used to improve stability and to reduce longitudinal stopping distance while maneuvering under braking condition. Antilock braking system is suitable for dangerous braking conditions such as braking on icy or wet asphalt roads or for panic braking situations. Upon braking, when the wheel starts slipping, i.e., the slip ratio increases to a maximum desired value, the braking torque is to be reduced and consequently, the speed of the wheel increases, i.e., the slip ratio decreases. Again when the slip ratio meets a minimum desired value, the braking torque is increased and the process continues. The control of ABS is a combination of slip and wheel acceleration control. In wheel acceleration control, the wheel angular velocities are measured and slip is controlled indirectly by changing the speed of the wheels. Slip cannot be kept in an acceptable range for conventional ABS. This is the main drawback for this system. Lots of testing and tuning are required for every ABS algorithm.

Some brake controllers receive direct, fast, and continuous information about dynamic events in the tire contact area from a tire sensor, which is generally embedded inside the tire tread and measures tread deformation, tire pressure, tire temperature, etc. The tire sensor output is used to distinguish between straight line driving or cornering and to determine the μ -split conditions (i.e., differential grip on opposing wheels as a function of road condition and normal load transmitted from the suspension). For example, tire sensors can identify if one of the wheel is offering higher grip as opposed to the wheel on the opposite side. This allows independent brake control for each wheel.

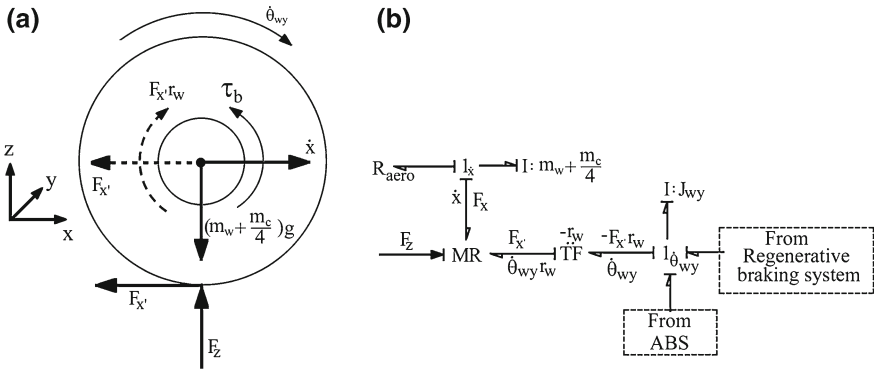


Fig. 6.61 a Schema of wheel under braking condition and b its bond graph model

The schema of a quarter car model and its bond graph model are shown in Fig. 6.61a,b, respectively. The equations of motion for rotational and linear dynamics of the quarter car model during braking are given by

$$\left(m_w + \frac{m_c}{4}\right) \ddot{x} = -F_{x'} - C_{aero} \dot{x}^2 \tag{6.73}$$

$$J_{wy} \ddot{\theta}_{wy} = F_{x'} r_w - \tau_b \tag{6.74}$$

where m_w is the mass of the wheel, m_c is the mass of the car body, $F_{x'}$ is the braking force due to friction, C_{aero} is the aerodynamic drag coefficient, J_{wy} is the rotary inertia of wheel and the axle, τ_b is the brake torque applied on the axle by brake pedal force, and r_w is the radius of the wheel.

In the bond graph model, the inertia (m_w) of the wheel and the vehicle body (m_c) is modeled by I-element at a 1-junction. Similarly, the rotary inertia (J_{wy}) is modeled at another 1-junction. The three-port modulated R-field implements Burckhardt’s formulae, i.e., $F_{x'} = \mu(\sigma_x, \dot{x}_c) F_z$, where the friction coefficient varies as shown in Fig. 6.60. The normal reaction force on the wheel, $F_z = (m_w + m_c/4) g$, modulates the R-field as an external signal input. The regenerative braking force modeled in the bond graph will be discussed in later sections of this chapter. For the time being, it may be assumed to be zero source of effort.

6.5.1 Antilock Braking Algorithm

The main components of ABS are brake servo, lever arm, cable, return spring, rod, cam, rotors, and brake pads. The schema of an ABS is shown in Fig. 6.62a. The ABS controller controls the voltage that is fed to the motor. The resistance is in series with the motor. The lever arm is connected to the motor. The cable is connected to the arm at one end and to the lever with cam at the other end. The return spring is

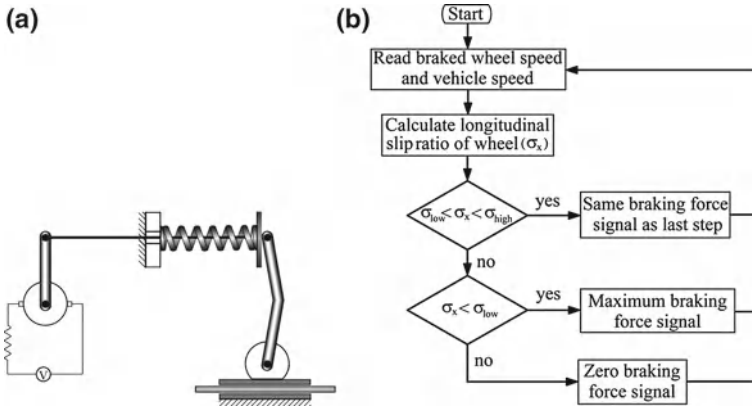


Fig. 6.62 a) Schema of an ABS and b) the flow diagram for ABS algorithm

used to bring back the brake shoes to their parked state. The flowchart for the ABS algorithm is shown in Fig. 6.62b.

The longitudinal slip is controlled between maximum and minimum values and accordingly brake force signal (and ultimately braking torque) varies as follows:

$$\tau = \begin{cases} \tau_{\text{previous}} & \text{if } \sigma_{\text{low}} \leq \sigma_x \leq \sigma_{\text{high}} \\ \tau_{\text{max}} & \text{if } \sigma_x < \sigma_{\text{low}} \\ 0 & \text{if } \sigma_x > \sigma_{\text{high}} \end{cases} \quad (6.75)$$

A comparison between the bond graph model of mechanical equivalent braking system (Fig. 6.62a) and the conventional hydraulic braking system is shown in Fig. 6.63. In hydraulic braking system, the pedal force F_{pedal} is represented by the Se-element (Fig. 6.63b). The fluid flow through supply or hold valve is modeled by a resistive element R_{sv} . The C-element connected with 0 junction, which determines pressure of brake cylinder, indicates the brake fluid compressibility K_{β} (a function of bulk modulus and fluid volume). R_{rv} is the resistance in the pressure relief valve and atmospheric pressure is indicated by the zero-valued Se-element. Braking torque depends on the area of the brake cylinder and the radius of the brake drum.

In the bond graph model (Fig. 6.63a) of the mechanical equivalent braking system [42] shown in Fig. 6.62a, the controlled voltage from the ABS controller is fed to the motor. The motor torque (τ_m) generated is represented by an Se-element. The resistive element connected to the 1-junction denotes mechanical losses (R_{lm}). The cable stiffness is represented by C-element connected to the 0-junction. The return spring having stiffness K_{re} is represented by a C-element. The other end of the return spring is anchored to the ground by a zero-valued source of flow. The output braking torque is applied on the wheel.

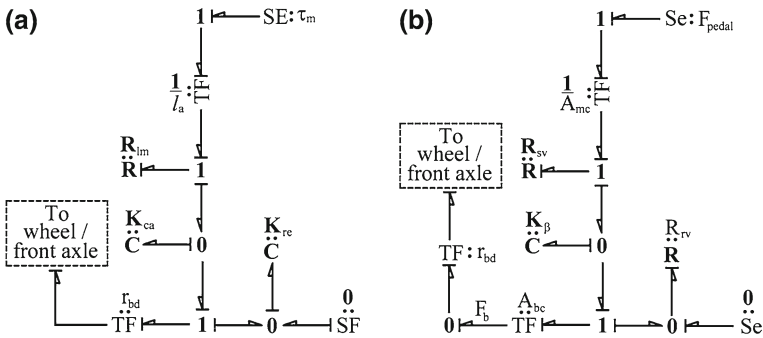
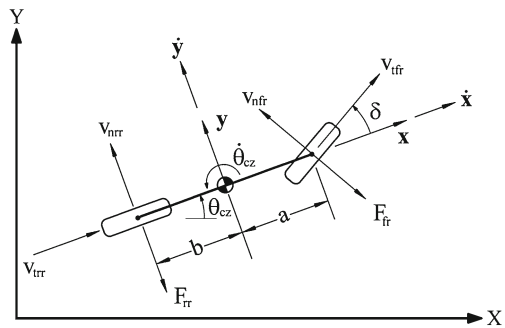


Fig. 6.63 Bond graph models of (a) mechanical equivalent braking system; and (b) hydraulic braking system

Fig. 6.64 Schema of the bicycle vehicle model



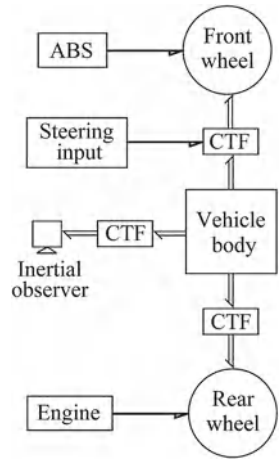
6.5.2 Bicycle Vehicle Model

A bicycle model of the vehicle is an improvement over the quarter car model because it includes the steering and cornering dynamics. The bicycle model works perfectly well when the turning radius is large in comparison to the wheel base length. This model does not take into account the roll, pitch, and heave motions and the suspension dynamics is neglected. Thus, the load transfer during maneuvering and braking cannot be included in this model. As the road is considered to be flat, the motion of the vehicle is planar. A schematic of the considered vehicle is shown in Fig. 6.64.

6.5.2.1 Kinematic Relations

The kinematic relations may be used to construct the backbone of the bond graph model of the bicycle [8]. Thereafter, the wheel rotations and longitudinal and lateral slip calculations may be inserted into the backbone model. It is assumed that only the front wheel is steered (by steering angle δ). The word bond graph of the bicycle model is shown in Fig. 6.65.

Fig. 6.65 Word bond graph of bicycle model



The model has to be developed in non-inertial frame. Note that a steered vehicle (bicycle in this case) is a nonholonomic system, i.e., the constraints on the motion are not integrable. This means, it is not possible to explicitly write down constraint relations as functions of displacements. However, the constraints are expressed in terms of velocities.

Let inertial reference frame be given by X-Y axes in Fig. 6.64 and x-y axes are body fixed (at the center of mass of the bicycle and aligned with the principal axes of the vehicle body). The velocity components along normal and tangential directions to the plane of rotation of the front wheel are

$$v_{nfr} = (\dot{y} + \dot{\theta}_{cz}a) \cos \delta - \dot{x} \sin \delta \tag{6.76}$$

$$v_{tfr} = (\dot{y} + \dot{\theta}_{cz}a) \sin \delta + \dot{x} \cos \delta \tag{6.77}$$

where \dot{x} , \dot{y} and $\dot{\theta}_{cz}$ are the two linear and angular velocities in the body-fixed frame, a and b are geometrical dimensions shown in Fig. 6.64, and δ is the front wheel steering angle.

Likewise, velocities normal and tangential to the plane of rotation of the rear wheel are

$$\begin{aligned} v_{nrr} &= (\dot{y} - \dot{\theta}_{cz}b) \\ v_{trr} &= \dot{x} \end{aligned} \tag{6.78}$$

From Newton-Euler equations (Eqs. 6.5–6.10) with $\dot{z} = \dot{\theta}_{cx} = \dot{\theta}_{cy} = 0$, one obtains

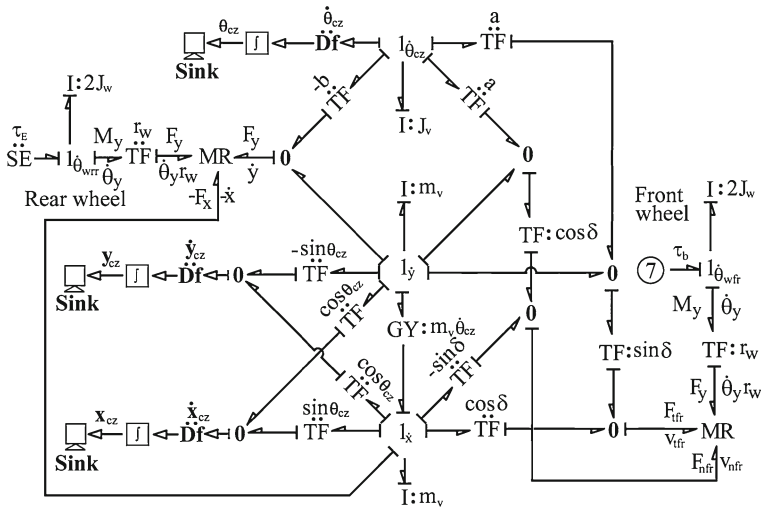


Fig. 6.66 Bond graph model of bicycle vehicle model

$$m_v \ddot{x} = m_v \dot{\theta}_{cz} \dot{y} + \sum F_x \tag{6.79}$$

$$m_v \ddot{y} = -m_v \dot{\theta}_{cz} \dot{x} + \sum F_y \tag{6.80}$$

where $\sum F_x$ and $\sum F_y$ are the external forces acting on the vehicle body in respective directions (aerodynamics forces, and cornering and longitudinal forces due to tire-road interaction) and $m_v = m_c + 4m_w$.

6.5.2.2 Bond Graph Model

In the word bond graph of the bicycle vehicle model shown in Fig. 6.65, CTF blocks represent necessary coordinate frame transformations. Maintaining the model structure defined in the word bond graph, the complete bond graph model as shown in Fig. 6.66 can be drawn using Eqs. 6.76–6.80.

The vehicle inertia ($I: m_v$) is modeled in the moving frame at $1_{\dot{x}}$ and $1_{\dot{y}}$ junctions. The rotary inertia ($I: J_v$) is modeled at another 1-junction. The transformer elements (TF) are used to calculate the tangential and normal velocities at tires according to Eqs. 6.76–6.78. The terms $m_v \dot{\theta}_{cz} \dot{y}$ and $-m_v \dot{\theta}_{cz} \dot{x}$ in Eqs. 6.79 and 6.80 are conservative pseudo-forces which can be implemented by a gyrator (GY) element in the bond graph model. The flow detectors (Df) connected to velocity points in the inertial frame are not present in the actual system, i.e., the actual system is not instrumented with an inertial sensor. These flow detectors are simply added to plot the positions of the vehicle center of mass in the inertial frame and also to modulate the MTF elements in the part of the junction structure. The external source of effort (SE: τ_E)

supplies the engine torque after passing through reduction gears to the rear wheel (differential is not included in bicycle model). The rotary inertia of the two wheels on the rear axle and that of the axle itself ($2J_w$) are modeled by I-element at $1_{\dot{\theta}_{wrr}}$ junction. Similarly, the rotary inertia of wheels and axle are modeled at $1_{\dot{\theta}_{wfr}}$ junction. The port number 7 shown within a circle is used to interface this model to the model of the brake system (see Fig. 6.63). The engine is assumed to be fully disengaged from the rear wheel during braking.

The two modulated 3-port R-fields (MR-elements) implement Pacejka's magic formulae for tangential and cornering tire forces. The normal forces (F_z) on front and rear wheels are assumed to be constant because roll, pitch, and heave motions due to suspension dynamics are not included in bicycle model. The constant normal forces on the front and rear wheels are $m_v g b / (a + b)$ and $m_v g a / (a + b)$, respectively. First of all, the velocity of the contact patch on the tire, the longitudinal velocity of the tire, and the lateral velocity are used to compute the longitudinal and lateral slip ratios. Thereafter, Pacejka's magic formula is used to compute the longitudinal and lateral tire forces and the reaction moment on the drive. The self-aligning moment is not included in the bicycle model. Thus, the MR-element, as causal in the model, receives the information of three generalized flow variables, and computes three generalized effort variables.

The CTF block (set of TF-elements modulated by trigonometric functions of θ_{cz} in Fig. 6.66) transforms velocities in the body-fixed frame to the inertial frame and then the velocities in the inertial frame are integrated to plot the vehicle position as seen by an inertial observer. This transformation is given by

$$\begin{Bmatrix} \dot{X} \\ \dot{Y} \end{Bmatrix} = \begin{bmatrix} \sin \theta_{cz} & \cos \theta_{cz} \\ \cos \theta_{cz} & -\sin \theta_{cz} \end{bmatrix} \begin{Bmatrix} \dot{x} \\ \dot{y} \end{Bmatrix}. \quad (6.81)$$

6.5.3 ABS Performance Simulation

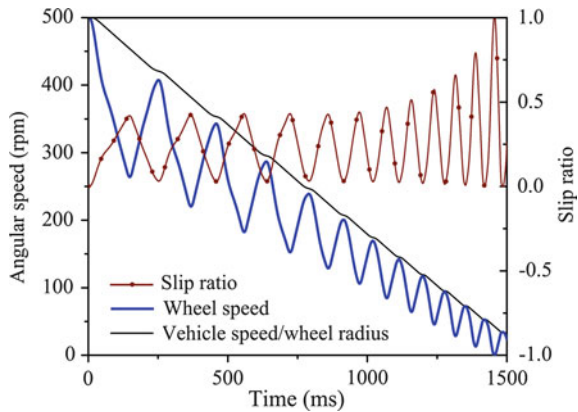
It has been mentioned before that a lot of trial and testing is required before finalizing an ABS controller. Implementation of ABS on the planar bicycle model should be tested to fine-tune and test the ABS control algorithm. Once the controller implementation (program) is found to be satisfactory, it can be ported to a full four-wheel vehicle model. The controller testing may be performed on a simulation model. The model parameters to be used in the simulation of the bicycle vehicle model are given in Table 6.2 where C_1 to C_4 are Burckhardt formula parameters. These parameters are used to compute the tire-road friction coefficient μ during braking and the parameter D of the Pacejka formulae is taken as $D = \mu F_z$. The table lists the nominal value of parameter D , which varies according to the slip ratio as the brakes are applied. Subscripts fr and rr are used to identify the front and rear wheels, respectively.

Some simulation and test results for ABS system are available in [42]. Considering the fact that steering effect was not considered in [42], the steering angle in the bicycle model was kept zero. The vehicle weight and the initial linear and angular velocities

Table 6.2 Parameter values of bicycle vehicle model.

Subsystem	Parameter values			
Vehicle body	$m_v = 1,600 \text{ kg}$	$J_v = 100 \text{ kg m}^2$	$a = 1.0 \text{ m}$	$b = 1.0 \text{ m}$
Wheel	$J_w = 15 \text{ kg m}^2$	$r_w = 0.3 \text{ m}$	$B_{fr} = 8.33$	$C_{fr} = 1.2$
	$D_{fr} = 6278.4$	$E_{fr} = -2$	$B_{rr} = 10.19$	$C_{rr} = 1.2$
	$D_{rr} = 6278.4$	$E_{rr} = -2$	$C_1 = 1.029$	$C_2 = 17.16$
	$C_3 = 0.523$	$C_4 = 0.03$		
Antilock brake	$\sigma_{low} = 0.04$	$\sigma_{high} = 0.5$	$K_{ca} = 10^4 \text{ N/m}$	$K_{re} = 10^6 \text{ N/m}$
	$r_{bd} = 0.15 \text{ m}$	$R_{lm} = 0.04 \text{ N s/m}$	$l_a = 1 \text{ m}$	$\mu_m = 0.4 \text{ N m/A}$
	$R_{aero} = 0.1 \text{ kg/s}$			

Fig. 6.67 Vehicle speed, wheel speed, and wheel slip ratio as obtained from the bicycle model during full braking by ABS



of the wheels are taken to be the same as those in [42] and the rear wheel of the vehicle is considered to be freely rolling. With these adjustments to match the scenarios, the ABS bicycle model developed in this section is nearly equivalent to that given in [42].

Figure 6.67 shows the results obtained from the developed ABS bicycle model. One observes almost linear variations in the forward linear wheel speed and a regular pattern of deceleration and acceleration of the wheel angular speed. The slip ratios are initially maintained within a bound and as the vehicle slows down, their maximum values approach unity (i.e., wheel locking). However, the maneuverability is important when the vehicle speed is sufficiently high immediately after panic braking. The low slip ratios during this time allow the driver to steer the vehicle while the brake pedal is still fully pressed.

6.5.4 ABS Performance While Braking and Maneuvering

The ABS is meant to provide better maneuverability while brakes are applied on the steered wheel. To evaluate the maneuverability of the vehicle under braking situation,

a particular scenario has been considered here. First of all, the vehicle starts from rest and it is brought to a steady linear speed of 50 km/h over a straight path. Then it is steered at $t = 12$ s to follow a circular path with a constant steering angle of 0.1 radians (about 5.6°). The steering action causes a decrease in the vehicle linear speed. Once the vehicle linear speed is stabilized and it moves at constant speed over the circular path, front wheel brakes are applied at $t = 17$ s. The ABS tries to control the slip ratio between 0.2 and 0.25, i.e., $\sigma_{\text{low}} = 0.2$ and $\sigma_{\text{high}} = 0.25$. Note that to handle large side and forward slips during wheel lockup, a composite slip-based formulation [68] developed by the U.S. department of transportation (DOT) has been used to compute tire forces. We encourage the readers to see [68] and appreciate how important it is to correctly model tire–road interaction forces. Note that the results obtained by using Pacejka’s magic formula are not very far away from the results obtained by using composite slip-based formulation.

Figure 6.68a shows the predefined path (2.5 m wide lane) over which the vehicle is supposed to move and the actual paths taken by the vehicle under two different braking conditions: the first when ABS is used and the second when a conventional mechanical brake is used. In the ABS, slip control strategy to keep the slip ratios between 0.2–0.25 (i.e., the sweet-spot) is applied. Initially, a sustained brake force is applied till the slip ratio becomes 0.2 and then the slip control algorithm takes over. The result shows that the vehicle veers off from the lane due to application of the conventional brake, whereas it stays within the lane till it stops when ABS is used.

The results in Fig. 6.68b show the change in slip ratios due to braking. The slip ratios for ABS remain within 0.2–0.25 and thus the vehicle is able to follow the steering. On the other hand, the slip ratio quickly approaches a value of 1.0 due to application of conventional brake. This causes the wheels to lock up and thus the vehicle cannot steer. Any rotation of the vehicle after the steered wheels are locked is purely due to the initial yaw momentum at the time of braking.

Figure 6.68c shows the vehicle speed variations due to steering and braking and Fig. 6.68d shows the angular velocity of the front wheel under the same condition. The wheel locks up due to application of conventional brake as soon as the wheel speed becomes zero. However, on application of ABS there is an initial sudden drop in wheel speed (till the slip ratio becomes 0.2) and then the wheel speed decelerates and accelerates much like the results shown in Fig. 6.67. The linear speed of the vehicle reduces almost linearly to zero in both case; the deceleration (see Fig. 6.68c) being slightly faster for ABS compared to the conventional brake. This deceleration almost doubles when brakes are applied both on the front and the rear wheels. With the ABS based on slip control mechanism, the vehicle stops faster and at a shorter distance.

6.5.5 Sliding Mode ABS Control

Pulsating effect (see wheel angular speed in Fig. 6.68d) is one of the major issues in Anti Lock Braking system while in operation. This leads to passenger discomfort

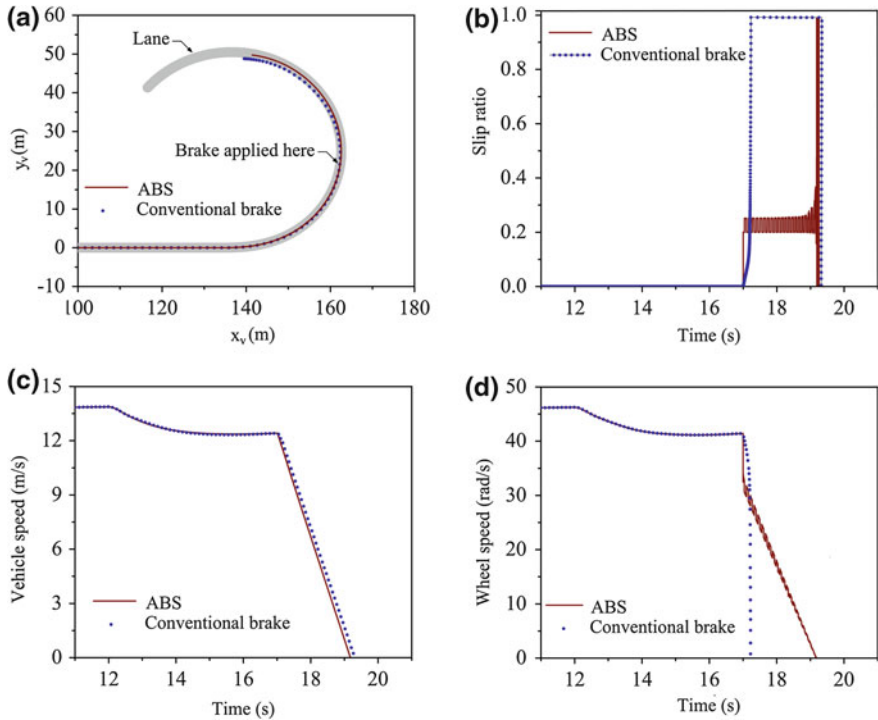


Fig. 6.68 **a** Vehicle center of mass trajectory in inertial frame; **b** wheel slip ratio; **c** vehicle speed; and **d** wheel speed for ABS and conventional braking system

during braking. To reduce this pulsating effect and yet maintain the same performance parameters, sliding mode ABS controllers have been proposed. Sliding Mode Control (SMC) is a high-speed switching feedback control that switches between two values based upon some rule. Sliding-mode ABS controllers are designed knowing the optimal value of the desired slip ratio. Brake pressure is increased, decreased, or held during the operation. A problem of concern here is the lack of direct slip measurements. The goal is to obtain a control algorithm which allows the maximal value of the tire–road friction force to be reached during emergency braking and to maintain the friction level around the sweet-spot in the friction-slip curve without variation.

The sliding surface may be described as

$$S = (\sigma_x - \sigma_{des}) \tag{6.82}$$

where σ_{des} is the desired slip ratio.

We can design the controller based on the quarter car model of the vehicle. Then taking $\dot{x}_w \cong \dot{x}$, differentiation of Eq. 6.72 with respect to time during braking period

gives

$$\dot{\sigma}_x = \frac{\dot{x}_w (\ddot{x}_w - \ddot{\theta}_w r_w) - (\dot{x}_w - \dot{\theta}_w r_w) \ddot{x}_w}{\dot{x}_w^2} = \frac{r_w (\dot{\theta}_w \ddot{x}_w - \ddot{\theta}_w \dot{x}_w)}{\dot{x}_w^2}. \quad (6.83)$$

Substituting expressions for \ddot{x}_w and $\ddot{\theta}_w$ from Eqs. 6.73 and 6.74 in the above equation gives

$$\begin{aligned} \dot{\sigma}_x &= -\frac{1}{\dot{x}_w} \left[\frac{(F_{x'} + C_{\text{aero}} \dot{x}_w^2) (1 - \sigma_x)}{m_e} + \frac{F_{x'} r_w^2}{J_{wy}} \right] + \frac{r_w \tau_b}{\dot{x}_w J_{wy}} \\ &= f(\dot{\theta}_{wy}, \dot{x}_w) + g(\dot{x}_w) \tau_b. \end{aligned} \quad (6.84)$$

To evaluate stability, the Lyapunov function can be written as

$$V_L = \frac{S^2}{2} = \frac{(\sigma_x - \sigma_{\text{des}})^2}{2}.$$

For stability of the sliding motion, the first derivative of the Lyapunov function has to be negative definite and the second derivative must be positive definite. \dot{V}_L is negative definite iff

$$[f(\dot{\theta}_{wy}, \dot{x}_w) + g(\dot{x}_w) \tau_b] \begin{cases} < 0 \quad \forall S > 0, \\ = 0 \quad \forall S = 0, \\ > 0 \quad \forall S < 0. \end{cases} \quad (6.85)$$

which is satisfied if a controller gain $\eta > 0$ is defined such that

$$\dot{S} = -\eta \cdot \text{sgn}(S) \quad (6.86)$$

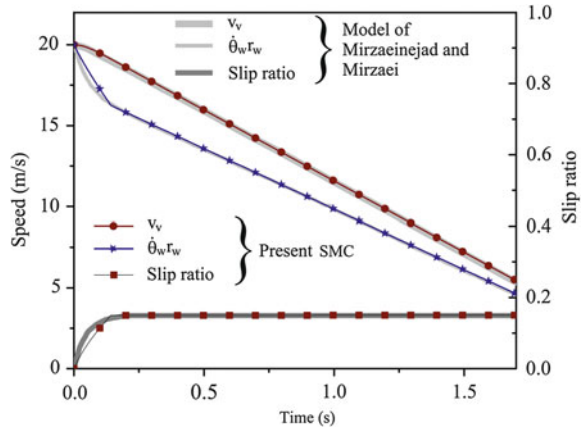
where $\text{sgn}(\cdot)$ is the signum function.

Using Eqs. 6.85 and 6.86, and noting that $F_{x'} = \mu(\sigma_x, \dot{x}_c) F_z$, $m_e = m_c/4 + m_w$ and $\dot{x}_c \cong \dot{x}_w$ (as the suspension stiffness in the longitudinal direction is very high),

$$\begin{aligned} \tau_b &= \frac{J_{wy}}{r_w} \left[\frac{(\mu(\sigma_x, \dot{x}_c) F_z + C_{\text{aero}} \dot{x}_w^2) (1 - \sigma_x)}{m_e} + \frac{\mu(\sigma_x, \dot{x}_c) F_z r_w^2}{J_{wy}} \right] - \frac{J_{wy}}{r_w} \eta \dot{x}_c \text{sgn}(S) \\ &= q(\dot{\theta}_{wy}, \dot{x}_c) - k_g \dot{x}_c \text{sgn}(S), \end{aligned} \quad (6.87)$$

where $k_g = \eta J_{wy}/r_w$. Sliding motion occurs when states $(\dot{\theta}_{wy}, \dot{x}_c)$ reach the sliding surface. Equation 6.87 defines the simplest sliding mode controller which calculates the braking torque to be applied on the axle so that the desired slip ratio is maintained at the tire-road interface.

Fig. 6.69 Comparison of sliding mode ABS controller results in [51] with the present model



A sliding mode ABS controller with integral feedback has been proposed very recently in [51]. Although the sliding mode controller developed therein has a different structure, it can be used to validate the controller developed in this section. A quarter car model with the wheel weight and one-fourth of the vehicle weight as the load on the wheel is used in [51] to test the controller. Moreover, Dugoff’s tire model is used therein with dry asphalt road condition and the wheel slip is maintained at 0.15 on the sliding surface.

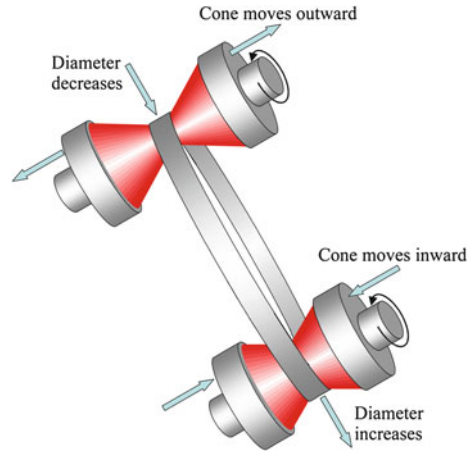
By considering zero steering angle, half-vehicle weight and freely rolling rear wheel, the bicycle model developed in this chapter becomes equivalent to that of a quarter car model. The vehicle weight and the initial linear and angular velocities of the wheels are taken to be the same as those in [51] and the parameters reported in [51] were used to simulate the bicycle model of the vehicle. In [51], the initial linear velocity is taken to be 20 m/s (72 km/h) and the results are plotted for 1.7 s duration. The same settings have been used in our simulations. An initial brake force is applied until the slip ratio reaches 0.15 and then SMC takes over. A comparison of the simulation results is given in Fig. 6.69.

The result shows that the vehicle linear velocity reduces linearly. After initial increase in slip ratio due to mechanical braking action, the SMC controls the slip ratio at the desired value of 0.15. As a consequence, after the initial drop in wheel angular speed due to mechanical braking, the wheel angular speed reduces linearly. Thus, the passenger feels a smooth braking action instead of the pulsating effect felt due to standard ABS application.

6.6 Regenerative Braking System

With mechanical friction brakes, the kinetic energy turns into heat energy and gets dissipated into the environment. Hybridization of vehicle driveline has led to the possibility of accumulating energy due to decrease in vehicle’s momentum during

Fig. 6.70 Schematic representation of a cone and belt CVT



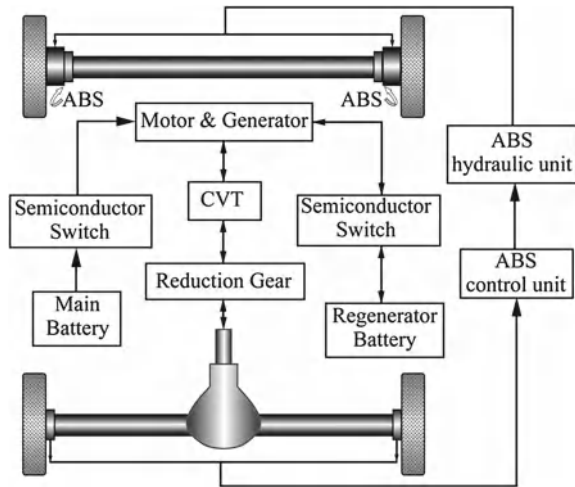
braking and consequently make use of that accumulated energy to drive/accelerate vehicle whenever it is intended. This type of a braking process is called regenerative braking. Regenerative braking improves vehicle's fuel economy, especially in city driving conditions, where frequent braking is required. To apply regenerative braking, an algorithm has to be designed to distribute the braking force into regenerative braking force and frictional braking force.

The main drawback of regenerative braking is that the generated electricity must be closely matched with the supply. Thus, the voltage developed by the generator must be closely controlled. By comparing the estimated regenerative brake torque with the maximum braking torque required to stop the vehicle, decisions are taken on the use of the type of braking in different situations. A continuously variable transmission (CVT), which is an automatic, step-less, smooth transmission system from which infinite number of gear ratios can be obtained within the limits (Fig. 6.70), is required to maintain constant speed at the generator input for various output velocities during regenerative braking process. Alternatively, a power-split device may be used. The regenerative braking force is usually insufficient during panic braking which is why additional braking force has to be provided by mechanical brakes. Pure mechanical brakes can lock up the wheels and thus compromise vehicles' directional stability. Thus, to ensure quick braking while maintaining vehicle maneuverability, the mechanical braking part can be performed by an ABS.

Note that standard ABS schemes cannot be used in conjunction with regenerative braking because that would require fast switching of the CVT ratio during braking and reduce the life of CVT. However, a sliding mode ABS control can be interfaced in parallel with regenerative braking and thus the advantages offered by both can be harnessed.

The schema of regenerative braking system is shown in Fig. 6.71. An electric vehicle setup is considered for this analysis on regenerative braking. The vehicle is considered to have rear wheel drives. The drive torque is applied to the differential

Fig. 6.71 Schema of regenerative braking



through motor, CVT, and final reduction gear. The electric motor itself acts as the generator during regenerative braking. The semiconductor switch in the transmission line behaves like a clutch. CVT is used to maintain the generator input speed constant during regeneration. During regenerative braking, the vehicle uses the motor as generator and its output is used to charge the regenerative battery. The braking of the vehicle is performed by using both regenerative and ABS for the present study. Pedal input, vehicle’s longitudinal velocity and CVT ratio are used as input for calculation of regenerative braking and maximum braking torque. When the brake is applied, the controller unit calculates the required torque and its distribution.

6.6.1 Regenerative Braking Algorithm

An algorithm is required to decide on how to distribute the braking force between regenerative braking and friction or antilock braking in an emergency braking situation. The emergency braking is differentiated from normal or slow braking from the brake pedal position or force. The flow diagram as shown in Fig. 6.72 is used here to decide on distribution of braking forces depending on various input parameters. If the regenerative braking force F_{reg} is less than the required maximum braking force F_{bf} then both regenerative and antilock braking will work in union. If regenerative braking force F_{reg} is more than the required maximum braking force F_{bf} , then regenerative braking alone will carry out the job.

In the present study, the regenerative braking torque applied at the wheels with final reduction gear ratio G is calculated as

$$T_w = iGT_{reg}W = F_{reg}r_w \tag{6.88}$$

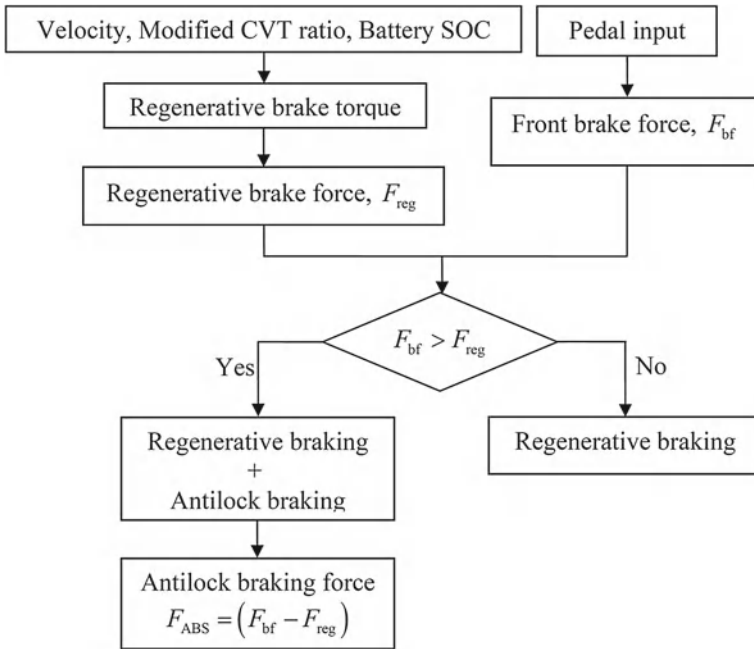


Fig. 6.72 Flow diagram of regenerative braking

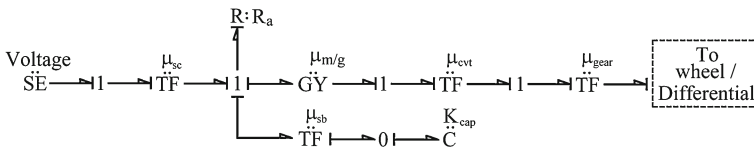


Fig. 6.73 Bond Graph model of regenerative braking

where W is the weight factor for state of charge (SOC) whose value is constant up to a certain percentage of SOC and after that value of SOC it decreases linearly [76]. The value of the regenerative torque T_{reg} is a constant determined from the motor characteristics curve. The CVT ratio is modulated as $i = \omega_m r_w / (\dot{x}_v G)$, where ω_m is the desired generator speed. The desired generator speed is a fixed value such that the voltage developed is the required charging voltage, e.g., about 13.8–14.4 V charging voltage for a 12 V (12.6 V open-circuit voltage at full charge) battery. The CVT ratio is accordingly modulated to maintain constant input speed at the generator end. When the vehicle is driven at constant speed, the CVT ratio is maintained constant as 0.58 (as per data in [76]) so that it works like a simple reduction gear and during regeneration process, the CVT ratio is varied within the range 0.58–2.47.

The bond graph developed for the regenerative module is shown in Fig. 6.73. Voltage of the main battery, represented by SE-element, is used to drive the vehicle.

The semiconductor switch denoted by TF-element (μ_{sc}) is modulated and it acts like a clutch. This is also used as a means to model the pulse width modulation-based control of input power. The power supply is disconnected ($\mu_{sc} = 0$) when brakes are applied. The R-element at the 1-junction represents armature resistance, which decides the current required for driving the vehicle and for charging the battery in the regeneration process. Here the regenerator-battery is modeled as a bank of high-capacity capacitors represented as a single equivalent capacitor. The motor or generator is modeled as a modulated gyrator. The TF-element used to modulate the CVT ratio (μ_{cvt}) has a constant value in the forward path (i.e., motor mode) and its value is modulated continuously during regeneration process (generator mode) to maintain constant speed at the generator input. During charging and boosting (i.e., when additional power is required, the capacitor is connected to the main energy source), the charging capacitor or battery is connected to the armature by a semiconductor switch represented by a modulated TF-element (μ_{sb}). This semiconductor switch also protects the battery against loss of charge (when charging voltage is below a certain limit) and overcharging (when charging voltage is above a certain limit).

6.6.2 Validation of Regenerative Braking

The model parameters used in the simulation of the quarter vehicle model are taken from [76]. The validation of the regenerative braking has been performed by comparing the results with those reported in [76]. The vehicle weight and the initial linear and angular velocities of the wheels are taken to be the same as those in [76]. With these adjustments to match the scenarios, the quarter vehicle model with regenerative braking system developed here is nearly equivalent to that presented in [76].

Figure 6.74 shows a comparison of the results reported in [76] with those obtained from the developed regenerative quarter car model. The vehicle speed (Fig. 6.74a) almost matches with the simulation and experimental test results given in [76]. The CVT ratio and battery SOC with conventional CVT control and CVT REGEN control are compared with results from the same source in Fig. 6.74b,c, respectively. The CVT ratio with REGEN control increases much faster than the conventional CVT control process. The battery SOC increases during regeneration process. The battery SOC increases marginally more with CVT REGEN control than that with conventional CVT control.

It is seen from Fig. 6.60 that coefficient of friction between the road and the wheel increases with the increase in slip ratio. Yeo et al. [76] showed that the time taken to stop the vehicle is nearly 13.6 s. As a result of this, the distance covered after applying brake is nearly 74.3 m. The time and stopping distance are higher as the value of slip ratio is only 0.01, i.e., the slip ratio is not controlled and the coefficient of friction value between the road and the wheel is very less. In order to avoid this problem, we consider regenerative antilock braking in the next step.

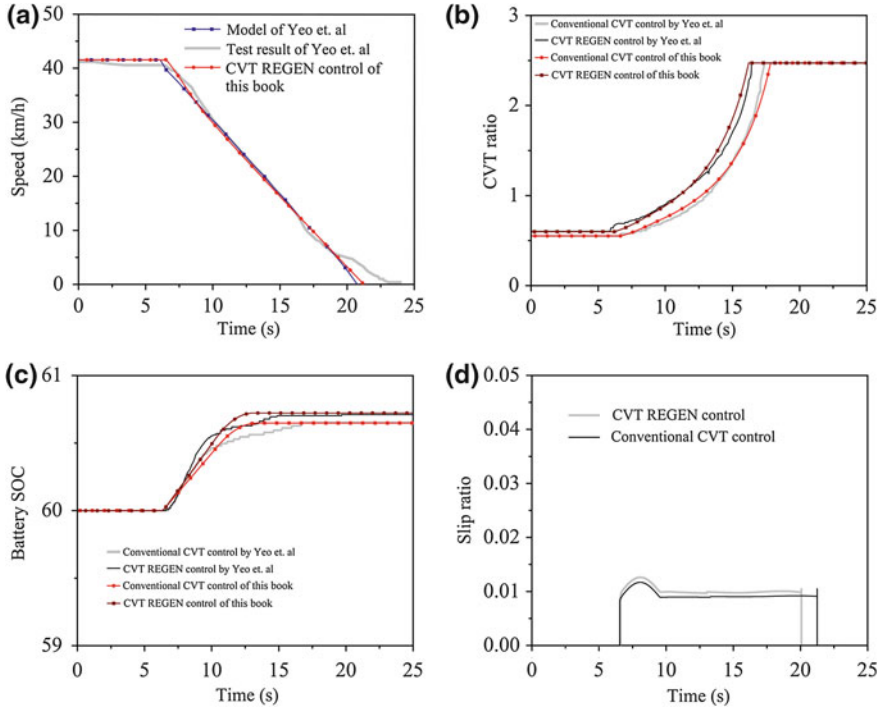


Fig. 6.74 Comparison of (a) vehicle speed, (b) CVT ratio, (c) battery SOC and (d) slip ratio for conventional CVT control and CVT REGEN control with the results of [76]

6.6.3 Modified Full Vehicle Model

The word bond graph representation of the full vehicle model is shown in Fig. 6.75. Some of the bonds in the word bond graph are multi bonds[10]. In the word bond graph, the global system is decomposed into eight subsystems. These are: vehicle body, suspension, wheel, steering, antilock braking system, differential, drive, and regenerative braking system. The four wheels are connected with the vehicle body through suspensions. The steering, anti roll bar, and ABS are coupled with the axle by scalar bonds. Likewise, scalar bonds connect the differential to the rear wheels and the vehicle body. Body weight and aerodynamic forces are connected to the vehicle body by vector bonds. Scalar bonds connect the main battery and the regenerative battery to the differential through motor/generator, CVT, and reduction gear. CTF blocks [49] indicate coordinate frame transformations.

Following static analysis, the normal loads acting on the front and rear wheels when the vehicle is moving in a straight path are given by

$$N_{fr,rr} = \frac{m_c}{4} g + m_w g \pm \frac{h}{4a} F_d \tag{6.89}$$

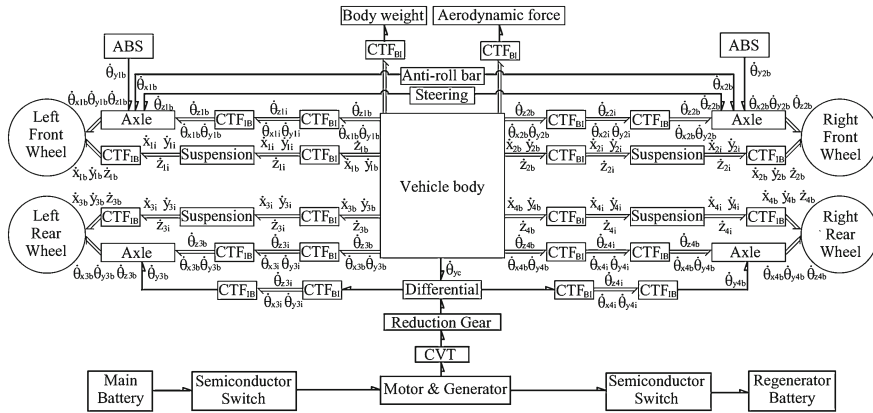


Fig. 6.75 Word bond graph model of full vehicle with regenerative braking

where, $F_d = m_c \ddot{x} + C_{aero} \dot{x}^2$, a is the half-wheel base length (considering mass center is at middle), h is the height of the mass center, and C_{aero} is the aerodynamic drag coefficient. In dynamic analysis, the normal reaction at any wheel is obtained from the values of the tire stiffness and deflection.

6.6.4 Performance of SMC-Based ABS with Regeneration

The sliding mode ABS control produces smoother variations in wheel rotational speed as compared to the conventional ABS system, thereby improving passenger comfort. This also means it is possible to obtain almost constant input speed at the generator input while smoothly varying CVT ratio. This concept was verified through simulation of the quarter car model. Because the wheel speed varies smoothly with SMC-based ABS, the CVT ratio is calculated from the expression $i = \omega_m / (\dot{\theta}_w G)$ for all values of slip ratio. The vehicle was brought to a steady longitudinal speed of 25 m/s (90 km/h) and then SMC ABS brake with regeneration was applied to the front wheels. The SMC tries to keep the slip ratio at the optimal value 0.2 while keeping the braking force bounded within an upper and a lower force limits till the sliding surface is reached around 0.04 s after application of brakes. The initial action of SMC ABS is similar to conventional braking till the vehicle slip ratio reaches 0.2 after which the sliding mode controller truly takes over.

The results in Fig. 6.76a show the variation of vehicle speed and wheel slip ratio during braking by combined SMC based ABS and regenerative braking. Slip ratio plot shows that the SMC algorithm is able to maintain the slip ratio at 0.2. It is seen from Eq. 6.89 that there will be no load transfer between the wheels if the term h vanishes. To compare the actual results with those obtained without considering load transfer, the value of h was artificially taken to be zero for the later simulation. It is

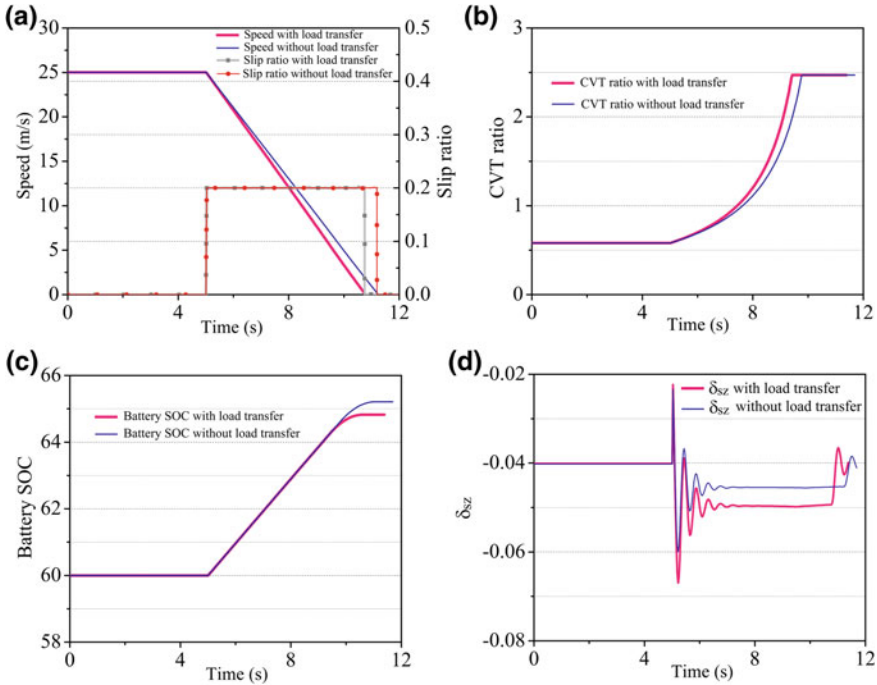


Fig. 6.76 a Vehicle speed, wheel speed, slip ratio, b CVT ratio, c battery SOC and d vertical deflection of front suspension for CVT REGEN control during load transfer

observed that the vehicle stops 0.4882s earlier due to load transfer effect than that obtained from a model which neglects load transfer. Figure 6.76b shows the variation of CVT ratio during regeneration process.

The variation of CVT ratio with load transfer consideration is somewhat steeper than that without load transfer consideration. Figure 6.76c shows the variation of battery SOC. The change in battery SOC is less when load transfer is considered. The deflection of front suspension in the vertical direction with and without load transfer is shown in Fig. 6.76d. Note that there is some additional deflection of the suspension even when load transfer is neglected. This is due to the fact that the brake torque applied on the wheels to stop its forward movement is applied in the reverse sense on the vehicle and this reactive couple moment being a free vector is translated to the center of gravity; thereby producing forward pitching of the vehicle. The 4.02 cm initial deflection of the suspension is due to the static load. The load transfer causes extra deflection of 4.2 mm during braking and once the vehicle stops, the suspensions regain their initial configuration.

6.7 Hybrid Vehicles

A hybrid vehicle uses two or more different power sources. The most used type called hybrid electric vehicle (HEV) combines an internal combustion (IC) engine with electric motors. In hybrid vehicles, the mechanical separation of the motor from the drive train offers various design innovations.

Some pollution-free green vehicles use propulsion by compressed air. An IC engine is used to compress the air when the pressure in the cylinder falls below a certain limit. Because the IC engine is not directly coupled with the drive, it is possible to operate it at full efficiency during compression of the air. Such systems are much more efficient than battery charged hybrid vehicles.

6.7.1 Classification of Hybrid Vehicles

Hybrid vehicles may be classified according to their power train configuration, fuel type, and mode of operation. In a parallel HEV, the electric motor and the internal combustion engine can individually or together drive the vehicle. The internal combustion engine may be operating on petroleum, diesel, bio-fuels, alcohol, etc. We will not go into the details of fuel types but rather concentrate on the drive train types and operation models.

A full hybrid or strong hybrid vehicle can run by drawing power from just the engine, just the batteries, or from both. Thus, high-capacity battery pack is needed to provide sufficient power for battery only operation. The usual approach while both power sources are driving the vehicle is to use a PSD. Alternatively, automatically controlled clutches may be used so that the appropriate clutch is engaged when power is drawn from one source. However, when there is no power-split device and both the sources are driving the vehicle, the electric motor must run at the same speed as that of the IC engine.

Some HEVs use regenerative braking (and regenerative suspensions) or kinetic energy recovery system (KERS) to store energy in a battery pack and then use that energy for boosting the vehicle speed under demand, such as assist during overtaking. These types of vehicles are termed mild parallel hybrids. Due to lack of sufficient motor power, a mild hybrid vehicle cannot be driven solely by the electric motor.

A series-parallel HEV uses a PSD to draw the power from an IC engine and one or more electric motors in any desired ratio. The IC engine is the primary power source. The power-split device is akin to a planetary gear set. The electric motor acts as a generator to charge the batteries during braking. When vehicle requires a speed boost, the electric motor is operated and engaged to the power-split device. The IC engine can be automatically shut down when the vehicle is not moving (such as at traffic signals) and later it may be restarted by the electric motor. This reduces fuel consumption and emissions.

Series-hybrid vehicles are driven by the electric motor which draws power from a battery pack. Although there is an engine, the vehicle power train has no mechanical connection with it. The engine runs a generator when the charge in the battery pack depletes due to use. Because the series-hybrid vehicle is purely driven by electric energy, the battery must be powerful enough to store and deliver large power on demand. Cyclic charging and discharging batteries reduces their life. Therefore, super-capacitors have been developed and combined with battery bank for use in series-hybrid vehicles. A variant of series-hybrid or parallel-hybrid vehicle is called plug-in hybrid electrical vehicle which has much larger energy storage capacity. The batteries of a plug-in HEV may be charged from the mains electricity supply at home to minimize the fuel consumption by the IC-engine.

The fuel cell hybrid vehicle is an electric vehicle where a fuel cell and a battery pack are together used as the power source. The fuel cell uses hydrogen as fuel. Any other fuel, such as methane, that can be reformed to hydrogen may be used in some fuel cells. More details of fuel cells are given in the previous chapter. The fuel cell voltage and power output varies with the load (current drawn). Thus, it is seldom used to directly drive the electric motors. Instead, it is used to charge the electric battery when it is depleted.

6.7.2 Power-Split Device

The PSD distributes the power produced by two separate sources. To divide the power efficiently, a planetary gear system is used (Fig. 6.77). The size of PSD used in modern vehicles is typically smaller than a soccer ball. The three basic components of the epicyclic planetary gear are: the central Sun gear, the Planet carrier which holds one or more peripheral planet or pinion gears that mesh with the sun gear, and an outer ring gear with inward-facing teeth that mesh with the planet gears. Each of the gears (or carriers) can rotate in different ways and thus provide a wide range of power options. In hybrid vehicle transmissions, the planetary carrier is connected to the IC engine and rotates the ring gear and transmits power to the sun gear through the planet gears (Fig. 6.78). At the same time, the electrical motor is connected to the ring gear which drives the vehicle. When braking, the ring gear drives the electrical motor as a generator. Series arrangement of these units can be used to increase the gear ratio.

The power-split device allows the vehicle to operate like a parallel hybrid because the electric motor can power the car by itself, the IC engine can power the car by itself, or both can power the car together. At the same time, the PSD also allows the car to operate like a series hybrid because the IC engine can operate at its peak efficiency independent of the vehicle speed and the excess power can be used to charge the batteries. The power-split device also behaves like a CVT, as has been discussed previously in the context of regenerative braking. It may also be noted that when the sun gear is held fixed, the electric motor connected to the ring gear

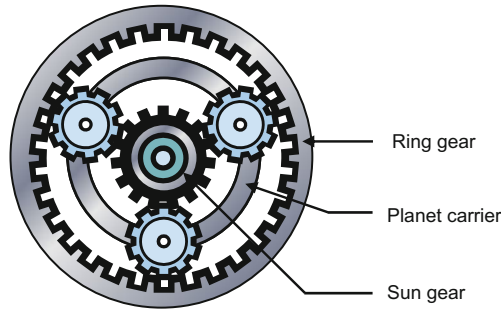


Fig. 6.77 Schematic representation of power-split device (PSD)

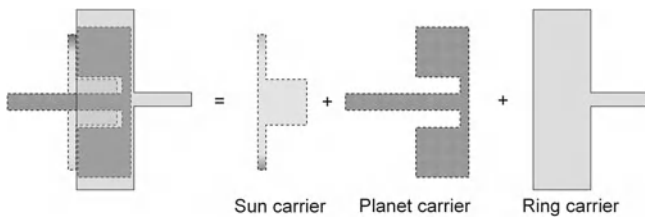
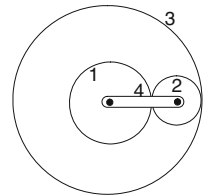


Fig. 6.78 Dissociation of the drive train: sun gear connected to generator, planet carrier connected to engine, and ring gear connected to motor

Fig. 6.79 Schematic representation of the links in the power-split device



transmits power to the planet carrier thereby powering to start the IC-engine, which means the vehicle does not need a separate starter motor.

The schematic representation of a planetary gear system is shown in Fig. 6.79 where links 1–4, respectively represent the sun gear, planet gear(s), ring gear, and planet carrier or arm.

From Fig. 6.79, the angular velocities may now be written as [3]

$$\begin{aligned} \omega_{1/4} &= \omega_1 - \omega_4, \\ \omega_{3/4} &= \omega_3 - \omega_4, \end{aligned} \tag{6.90}$$

where ω_i is the absolute angular velocity of the i -th link and $\omega_{i/j}$ is the angular velocity of the i -th link with respect to j -th link. Rearrangement of Eq. 6.90 yields

$$\frac{\omega_1 - \omega_4}{\omega_3 - \omega_4} = \frac{\omega_{1/4}}{\omega_{3/4}} = -\frac{N_3}{N_1}, \quad (6.91)$$

where N_1 is the number of teeth in link 1 and N_3 is the number of teeth in link 3. Note that the velocity ratios $\omega_{1/4}/\omega_{3/4} = -N_3/N_1$ because of the reversal in direction of rotation between link 1 and planet gears.

Using subscripts ‘s’ for sun, ‘r’ for ring, ‘p’ for planet gear, and ‘a’ for arm or planet carrier, we can write from Eq. 6.91

$$\begin{aligned} \frac{\omega_s - \omega_a}{\omega_r - \omega_a} &= -\frac{N_r}{N_s}, \\ \Rightarrow N_r \omega_r + N_s \omega_s &= (N_s + N_r) \omega_a. \end{aligned} \quad (6.92)$$

Let us define the form factor as

$$n = N_s/N_p.$$

To ensure that the gears mesh properly, their pitch circle diameters must match properly, i.e., $p_s + 2p_p = p_r$, where p indicates pitch circle diameter and subscripts identify the gears. From this geometric constraint, we can write

$$N_s + 2N_p = N_r. \quad (6.93)$$

Combining Eqs. 6.92 and 6.93, we obtain a kinematic constraint

$$n\omega_s + (2 + n)\omega_r - 2(1 + n)\omega_a = 0. \quad (6.94)$$

This kinematic constraint can be used to construct the bond graph model of the PSD given in Fig. 6.80.

In hybrid synergy drive (HSD) technology developed by Toyota motors, power-split devices are arranged to form series and parallel hybrid configurations. These two configurations are schematically illustrated in Fig. 6.81, where sun, planet carrier, and ring gears are marked as S, C, and R respectively. MG1 and MG2 are two electrical motors/generators and IC is the internal combustion engine. The load is transferred to the driven wheels through the differential.

Usually, MG1 is used as a starting boost device and charger for electric batteries. MG2 drives the vehicle. While braking, MG2 acts as generator (regenerative braking). This configuration allows the IC engine to operate at its peak efficiency speed. The third generation Toyota HSD uses Ravigneaux gearset (having a small and a large sun gear, and a common carrier gear with two independent planetary gears) which is also commonly used in automatic transmission systems. The bond graph model

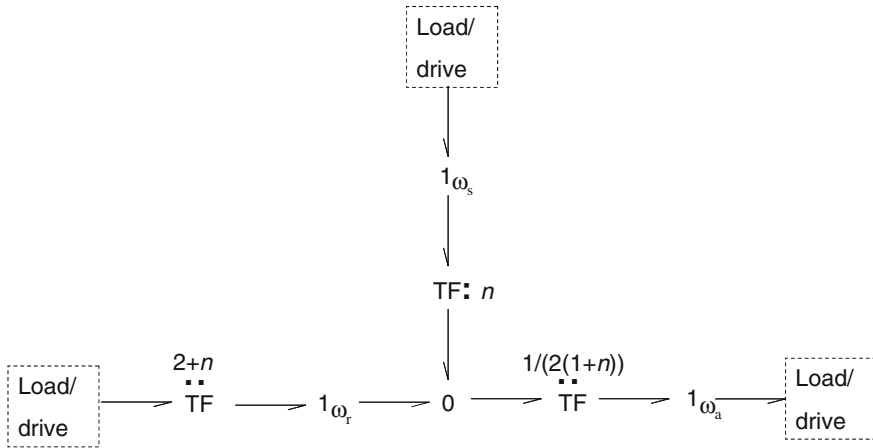


Fig. 6.80 Bond graph model of power split device

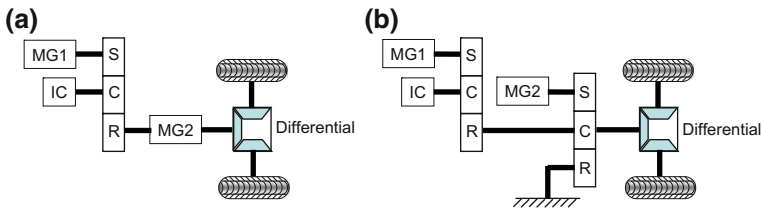


Fig. 6.81 a Toyota serial hybrid system and b Toyota parallel hybrid HSD configuration for four wheel drive system

of the parallel hybrid configuration (Fig. 6.81b) is given in Fig. 6.82. It combines the models for engine, regenerative braking, PSD, differential (gear box may as well be included), wheels and the vehicle body with suspensions. The model of the series hybrid configuration can be drawn in the same way.

6.8 Automatic Transmission

Automatic and semi-automatic transmissions free the driver from working on the clutch and gears so that the driver can concentrate more on the traffic. This greatly reduces stress on the driver especially on long drives and congested roads. A semi-automatic transmission is partly a manual transmission in which there is no clutch. It is also known as clutch-less manual transmission or automated manual transmission. In this system, there is no clutch pedal. Sensors, actuators, and microprocessor-

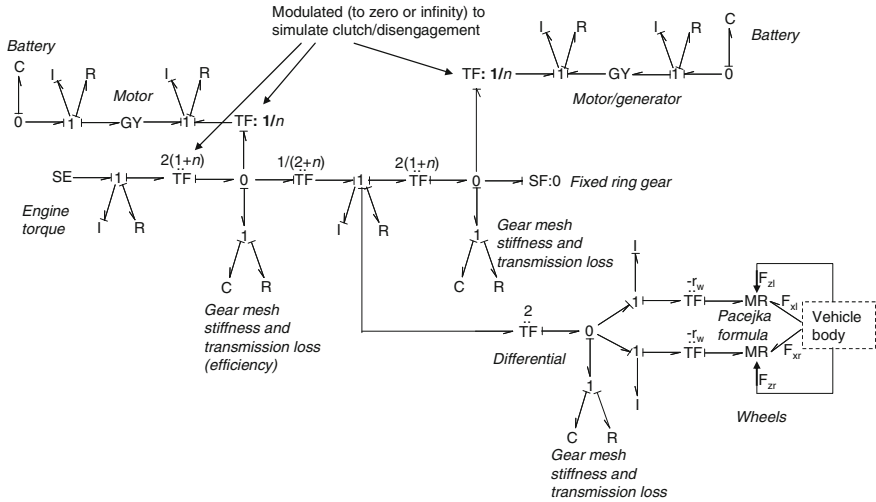


Fig. 6.82 Bond graph model of the power train in parallel hybrid vehicle configuration

based controllers are used to engage the drive with the transmission. The automatic clutching is quick and smooth.

A fully automatic transmission further relieves the driver from the job of changing gears. Such vehicles have only the brake pedal and accelerator pedals. Using sensed inputs from these pedals, gear ratios are automatically changed. The controller automatically selects the gear based on vehicle speed and throttle pedal position. A schematic diagram of the automatic transmission and its basic bond graph model are given in Fig. 6.83.

6.8.1 Components of Automatic Transmission System

The key feature of an automatic transmission is a set of planetary gear sets. Auxiliary devices are used to engage these planetary gear sets. Those are a torque converter, a set of bands, and wet-plate clutches to lock parts of the gear set, hydraulic systems to control the clutches and bands, and a gear pump to pressurize the hydraulic fluid.

To achieve more gear ratio options, compound planetary gears are used. A compound planetary gear set usually has one common ring gear connected to the transmission and two sun gears and two sets of planets on two planet carriers. This combination produces four forward gear ratios and one reverse gear ratio. To achieve these gear ratios, some of the gears have to be held fixed and some are to rotate at same speed. Clutches and bands are used to engage gears so that they can be fixed or connected serially. The bands wrap around sections of the gear train and connect to the housing. The bands are actuated by hydraulic cylinders to shift clutches.

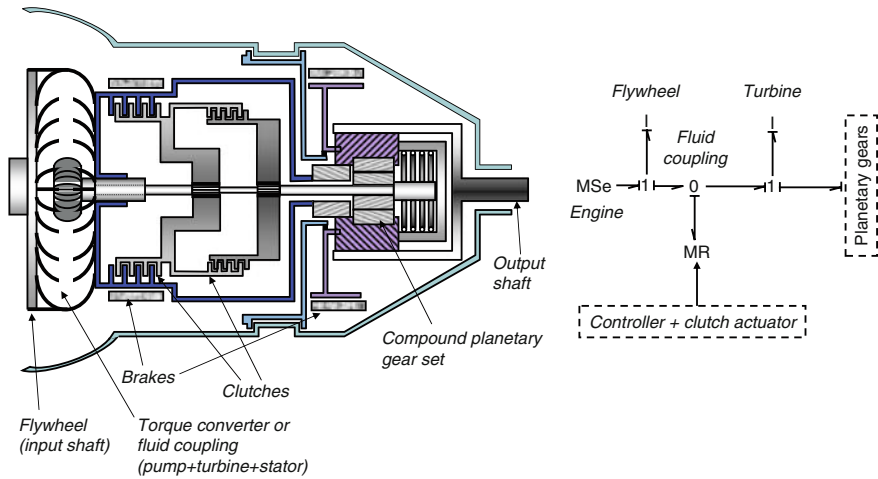
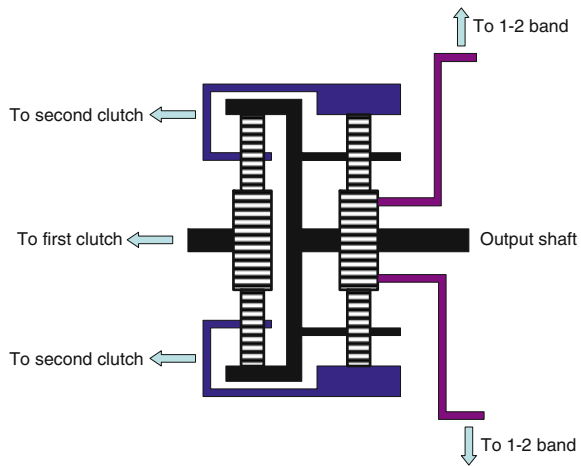


Fig. 6.83 Cut-away of an automatic transmission

Fig. 6.84 Clutches, bands, and planetary configuration of the automatic transmission system



A gear pump supplies fluid to the transmission cooler and the torque converter. A spring loaded valve is operated by a governor. The governor rotates at the same speed as the transmission shaft and thus the valve opening is proportional to the vehicle speed. The fluid flow from the pump to the turbine is thus passively controlled by the vehicle speed.

The transmission line contains several shift valves which supply hydraulic pressure to the clutches and bands to engage each gear. The shift valve determines when to shift from one gear to the next or previous gear. One arrangement of the clutches and bands in the compound planet configuration is shown in Fig. 6.84.

Electronically controlled transmissions monitor vehicle speed, engine speed, throttle position, pressure on the brake pedal, and accelerator pedal and control variety of peripheral devices such as regenerative and antilock braking system, active suspension system, etc. Usually, a fuzzy logic controller is used to correlate the inputs to outputs in predefined zones.

The torque converter is a fluid coupling which can introduce slip between the engine and the transmission. This allows the engine to operate independently of the transmission. The amount of slip depends on the resistance offered by the fluid coupling. If the resistance is large, there will be no slip whereas if the resistance is small, there will be appreciable slip. This resistance is changed by changing the fluid pressure in the coupling (much like the pressure in a mechanical friction clutch). Conventional fluid couplings are inefficient. Therefore, the torque converter is composed of a centrifugal pump, a turbine and a stator. The centrifugal pump is connected to the flywheel of the engine. As it turns, it draws fluid at its center and this fluid impinges on the blades of the turbine and flows along its blades to exit at turbine center. The turbine is connected to the transmission. The stator blades redirect the fluid returning from the turbine so that it does not enter the centrifugal pump. In this way, the efficiency of the torque converter is increased. When the pump and turbine rotate at the same speed, there is no torque transmission because the relative velocity of impinging jet on turbine blades is zero. Thus, the engine power is wasted. Some vehicles use a lockup clutch which locks the turbine and the pump of the torque converter to eliminate the slip.

6.8.2 Bond Graph Model of Automatic Transmission

A complete model of the NAVISTAR 4700 series 4x2 rear wheel driven truck, powered by a turbocharged, inter-cooled engine, and equipped with a four speed automatic transmission is given in [44]. This model considers the pitch-plane dynamics of the vehicle with tire forces, aerodynamic loading, suspension dynamics, and slope of the road profile [43]. The global or top-level view of the model is given in Fig. 6.85. The driver sends commands to the engine by varying the throttle/accelerator position and the mode of drive (parking, overdrive, normal. . .). The brake pedal position is also sensed. These commands influence the engine output and the gear selection in the drive train. The driver can also directly influence the vehicle dynamics through steering (which is not included in pitch-plane model) and selection of compliance level (active suspension parameters).

The drive train is composed of the pump, torque converter, planetary gears, transmission shaft and the differential. The word bond graph model of the transmission system is shown in Fig. 6.86. The speed of the transmission shaft is measured. This information along with the measured engine speed and throttle position decide the gear shift logic according to which the transmission ratio of the compound planetary gear is selected. Clutches and bands of the compound planetary gear are actuated to realize the desired transmission ratio.

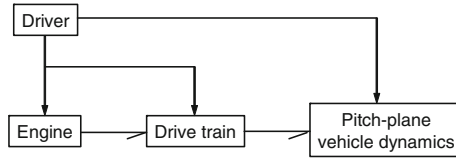


Fig. 6.85 Overall model of vehicle transmission system

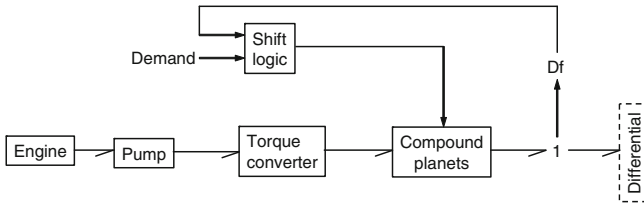
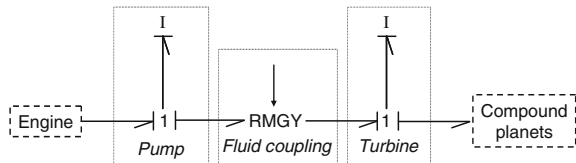


Fig. 6.86 Word bond graph model of the drive train

Fig. 6.87 Bond graph model of the torque converter



6.8.3 Torque Converter Model

The bond graph model of the torque converter is shown in Fig. 6.87. The engine power is controlled by the fuel injection controller and modeled according to [4]. The engine torque is applied on the pump where the rotary inertia of the impeller and the flywheel are modeled together. The RMGY-element couples the pump to the turbine. RMGY is a defined bond graph element which has been used in [44]. The power scaling gyrator (PGY) element defined in [41] is similar to RMGY. This element acts like a modulated gyrator in which power is not conserved (the R in RMGY signifies loss of power). A linear RMGY-element has thus two gyrator moduli (μ_1 and μ_2) which are defined in its constitutive relation:

$$\begin{aligned}
 e_1 &= \mu_1 f_1 \text{ and } e_2 = \mu_2 f_2, \\
 e_1 f_1 &\neq e_2 f_2 \text{ if } \mu_1 \neq \mu_2.
 \end{aligned}
 \tag{6.95}$$

In the torque converter, the stator is connected to the casing by a one-way clutch. The stator design ensures that the torque converter acts as torque multiplication device at low turbine speeds. The fluid coupling applies forward and reactive torques on

the turbine and the pump, respectively. These torques are functions of the pump and turbine speeds which is why the coupling is represented by a GY element. The non-power conserving RMGY-element used to model the losses in the fluid coupling has a nonlinear constitutive relation which is adopted from the static modeling methodology proposed in [3, 27, 64]. The parameters in this relation are empirically obtained by curve-fitting the quasi-static experimental data. The curve fitting is performed between the torque ratio and the speed ratio during steady operation. Likewise, the capacity factor is another parameter used in the constitutive relation and it is also curve fitted with the speed ratio as a free variable. The functional relationships thus obtained through curve-fitting are valid for quasi-static operation, i.e., these functions do not model the influence of large transients due to sudden variations in the input (engine speed) or the load.

The capacity factor or the coefficient of absorption in torque [3] is defined as

$$\begin{aligned} K &= \frac{\omega_i}{\sqrt{T_i}} \\ &= \Phi_k \left(\frac{\omega_T}{\omega_i} \right) = \Phi_k (\bar{\omega}) \end{aligned} \quad (6.96)$$

where ω_i is the angular speed of the input shaft (impeller pump or engine speed), T_i is the input torque on the impeller, ω_T is the output (turbine or transmission shaft) speed, Φ_k is the fitting function and the non-dimensional number $\bar{\omega} = \omega_T/\omega_i$ is called the sliding velocity.

The torque ratio[44] is defined as

$$\begin{aligned} \lambda &= \frac{T_T}{T_i} \\ &= \Phi_T \left(\frac{\omega_T}{\omega_i} \right) = \Phi_T (\bar{\omega}) \end{aligned} \quad (6.97)$$

where Φ_T is the fitting function. When the sliding velocity approaches 1, the lock-up clutch interlocks the impeller and turbine. In this case, the torque ratio and sliding velocity are both taken to be 1.

The constitutive relation of the nonlinear RMGY-element [44] representing the fluid coupling is given as follows:

$$T_i = \left(\frac{\omega_i}{\Phi_K (\bar{\omega})} \right)^2 \quad (6.98)$$

$$T_T = \Phi_T (\bar{\omega}) \left(\frac{\omega_i}{\Phi_K (\bar{\omega})} \right)^2 \quad (6.99)$$

where the input variables are ω_i and ω_T and the computed variables are T_i and T_T . A block diagram representation of the calculations needed in the RMGY-element is shown in Fig. 6.88.

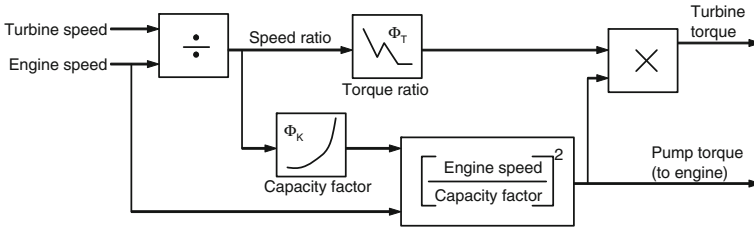


Fig. 6.88 Block diagram model of RMGY-element's constitutive relation

6.8.4 Gear Shift Logic and Transmission System Model

The bond graph model of the transmission system is shown in Fig. 6.89. The turbine model (see bond graph model of torque converter in Fig. 6.87) is connected to a 1-junction where two modulated R-elements model the losses. One of the R-elements represents power loss incurred in charging the pump and the second one represents the loss due to churning of transmission fluid. The torque loss due to churning depends on the gear number (how many clutches and bands are involved and in what configuration) and is a nonlinear expression with linear and quadratic terms.

Gear inertias are lumped with inertias of shaft segments. The springs and dampers in parallel model the gear mesh stiffness and damping along with the torsional stiffness and damping of lay shafts. The RMTF-element is a non-power-conserving transformer which includes internal dissipation [44]. The power scaling transformer (PTF) element defined in [41] is similar to RMTF. The name RMTF suggests it is a MTF with resistance which receives a pair of flow and effort information in two bonds to compute the complementary power variables in those bonds. This defined two-port element (see power variables in Fig. 6.89) has a separate torque ratio and speed ratio:

$$\omega_2 = \mu_\omega \omega_1 \text{ and } \tau_1 = \mu_\tau \tau_2, \tag{6.100}$$

where μ_ω and μ_τ are two scaling constants termed speed ratio and torque ratio, respectively. If $\tau_1 \omega_1 \geq \tau_2 \omega_2$, one introduces power loss into the model. The inputs to the RMTF-element are the turbine speed and the load torque and its outputs are the load on the turbine and the speed of the output shaft.

The power loss takes care of loss of efficiency during gear shifts. In the model developed by [44], it is assumed that the speed ratio varies linearly during a gear shift. The efficiency loss is modeled by varying the torque ratio. Before the gear shift and after completion of the gear shift, the speed and torque ratios are the same, i.e., $\mu_\omega = \mu_\tau$. During the gear shift, $\mu_\tau \leq \mu_\omega$. A blending function (see Fig. 6.90 for a gear downshift) is thus used to implement this feature. Note that the shift duration is typically less than 0.08 s.

In automatic transmissions, the decision regarding gear shift is taken according to the driver demand (accelerator pedal position, brake pedal position) and the current speed of the vehicle. Usually, a shift-logic chart (included in the code embedded in

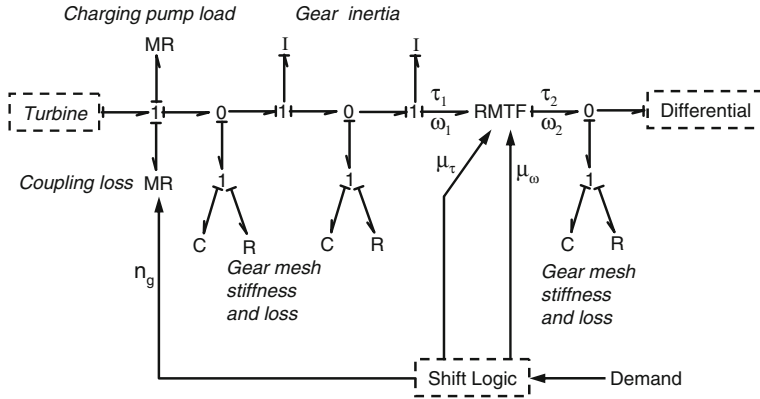
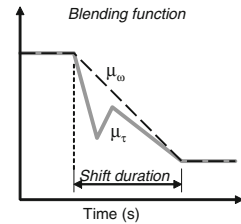


Fig. 6.89 Bond graph model of the transmission system

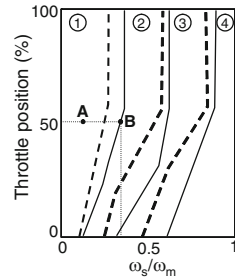
Fig. 6.90 Blending function to account for efficiency loss during gear shift



the microprocessor) is used to take this decision. One such chart is shown in Fig. 6.91 where solid lines indicate the up-shift and dashed lines indicate downshift margins, respectively, and ω_s and ω_m , respectively, represent the output shaft speed and a reference maximum output speed. For example, if the drive shaft connected to the differential rotates at 10% of the peak speed ($\omega_s/\omega_m = 0.1$) and the throttle position (accelerator pedal) is held fixed at 50%, which corresponds to point A in Fig. 6.91, then the compound planet is engaged in a way to produce the lowest forward gear ratio (1st gear). If the throttle position is not changed then the transmission ratio is held at 1st gear till the vehicle accelerates and its speed increases to a value so that $\omega_s/\omega_m > 0.35$ (point B in Fig. 6.91) at which point the gear up-shift from 1st to 2nd gear is automatically effected. A detailed experimental automatic shift logic map may be consulted in [27].

The transmission efficiency has also been included in the differential model given in [44]. Like the transmission system, ideal speed reduction and non-ideal torque multiplication based on a predefined gear efficiency map has been considered. Although we do not go through the entire model development process given in [44], it is worth mentioning here that the authors of that paper could validate their model with experimental results and produced a reduced order model (mostly removal of small rotary inertias of gears and gear mesh stiffness and damping) which produced comparable results to the full model. Note that a much complete and accurate model of the drive

Fig. 6.91 Schematic representation of gear shift logic



train components is developed in [3] in library form by using AMESim software, which also supports bond graph modeling.

6.9 Fuel Cells

The heat engine is highly polluting and responsible for effects such as ozone layer depletion and greenhouse effect. In this context, fuel cells, which are efficient and environmentally friendly power-generating systems that produce electrical energy by combining fuel and oxygen electrochemically, are being used as alternative energy sources.

A battery is an energy storage device, which contains the reactant chemicals. The electrodes in a battery take part in the chemical reaction. A battery must be discarded once the reactants are depleted (unless the battery is rechargeable). On the other hand, a fuel cell is an energy conversion device where the reactants are continuously supplied and the products are continuously removed. The electrodes and electrolyte do not participate in the chemical reaction but they provide the surfaces on which the reactions take place and they also serve as conductors for the electrons and ions. Therefore, a fuel cell is a thermo-electrochemical device, which converts chemical energy from the reaction of a fuel with an oxidant directly and continuously into electrical energy.

The basic components of a general fuel cell are two porous electrodes, i.e., anode and cathode, which are separated by a solid or liquid electrolyte. The electrolyte is impervious to gases. Fuel is supplied to the anode side and air is supplied to the cathode side. The oxidation reaction is made possible by conduction of ions through the electrolyte. Many challenges have to be overcome before its successful implementation of a fuel cell. Many issues regarding suitable materials for the electrolyte, interconnects, gas seals, and electrodes have to be addressed. There are also issues regarding cell stack design and life span improvement that warrant immediate attention. Computer control of fuel cell stack for load variation with minimum response time, better stack design, cyclic endurance, and power conditioner for utility services are other issues involved in a fuel cell design. Developing robust controller for integrated fuel cell systems is also a major challenge.

Table 6.3 Different types of fuel cells and their application areas.

Application Area	Power requirement (W)	Advantages	Type of fuel cell	Power scale
Portable electronic equipment	<100W	High energy density, fast recharging	PEMFC	1W
Small vehicles, home applications	1 kW to 100 kW	Zero emission, high efficiency	AFC, SOFC	1kW
Power generation, Heavy vehicles	100 kW to 10 MW	High efficiency, non-polluting, quiet operation	PAFC, MCFC	100kW 10MW

6.9.1 Classification of Fuel Cells

There are many types of fuel cells currently under research and development. Fuel cells are classified according to the electrolyte used. The major types of fuel cells are Molten carbonate fuel cells (MCFCs) where electrolyte is a mixture of molten alkali carbonates that conducts carbonate ions, low temperature (80–100° C) Proton exchange membrane fuel cells (PEMFCs) where a polymer membrane that conducts protons (or hydrogen ions) is used as an electrolyte, phosphoric acid fuel cells (PAFCs) where phosphoric acid is used as electrolyte that conducts protons, Alkaline fuel cells (AFCs) where the electrolyte is an aqueous solution of alkaline hydroxide which conducts hydroxyl ions and solid oxide fuel cells (SOFCs) where the electrolyte is a ceramic that conducts ions at high temperatures (800–1,000° C).

The electrolyte substance is specifically designed so that it is an electrical insulator (electrons cannot pass through it) and specific ions can pass through it (e.g., protons for PEMFC and oxygen ions for SOFC). The electrons freed during ionization are forced to travel through the external load and upon reaching the cathode side, they reunite with the ions which have passed through the electrolyte to complete the reaction.

Different types of fuel cells produce different amounts of power. Their suitability to specific applications is governed by the power requirement by the target application and operational constraints. The suitability of different fuel cell types for different application areas are given in Table 6.3. PEMFC and SOFC are the most important types because they can cater to wider ranges of application areas. Thus, we will specifically consider these two fuel cell types in this chapter. Other bond graph models of fuel cells can be consulted in [13].

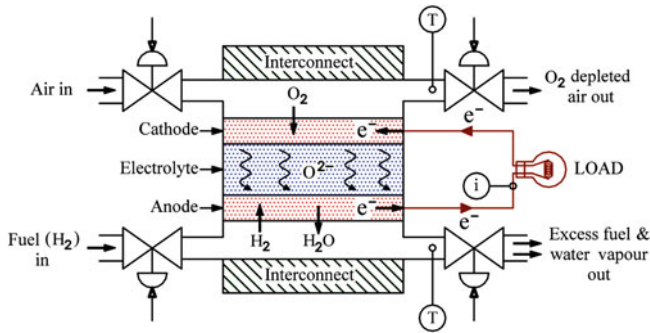


Fig. 6.92 Schematic diagram of a single cell of SOFC

6.9.2 Solid Oxide Fuel Cell

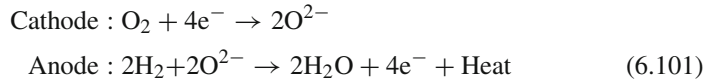
SOFC provides considerably high system efficiency in comparison to other fuel cell systems with cogeneration [67]. Expensive catalysts, which are needed in the case of proton-exchange fuel cells (platinum) and most other types of low temperature fuel cells, are not needed in SOFCs. Moreover, light hydrocarbon fuels, such as methane, propane, and butane, can be internally reformed within the anode because of the high operating temperature. SOFCs have a wide variety of applications from use as auxiliary power units in vehicles to stationary power generation with outputs ranging from 100 W to 2 MW. SOFCs are also coupled with gas turbines in order to improve their efficiencies. The SOFC is also used in combined heat and power systems.⁴

An SOFC is made up of four layers, three of which are ceramics (see Fig. 6.92). A single cell consisting of these four layers stacked together is typically only a few millimeters thick. Hundreds of these cells are then stacked together in series to form a stack. The ceramics used in SOFCs do not become electrically and ionically active until they reach very high temperature. The electrolyte represents the media through which ions migrate from one electrode to the other; thus causing a voltage difference between the anode and the cathode, and consequently an electric current through an external load. Ytria stabilized zirconia (YSZ), which is a ceramic material, is usually used as the electrolyte material.

In the cathode side of the SOFC, oxygen molecules can diffuse to the catalyst and combine with free electrons to form negatively charged oxygen ions. The electrolyte membrane is an electrical insulator. Only the negatively charged oxygen ions can conduct through the membrane. The conducted oxygen ions combine with hydrogen on the anode side to form water and liberate the electrons. These electrons in the anode side travel through the external circuit to the cathode side to complete the cycle.

The reaction taking place in a SOFC is given as

⁴ A part of this section is taken from these authors' previous work published in [71–73].



The reaction takes place at the so-called triple phase boundary (TPB), where electrons, ions, and gas phase coexist. The typical material of the anode is Nickel-Yttria stabilized Zirconia cermet. The cathode must be porous in order to allow oxygen molecules to reach the electrode/electrolyte interface. The most commonly used cathode material is lanthanum manganite. It is often doped with strontium and referred to as lanthanum strontium manganite (LSM). The interconnect serves the purpose of connecting cells together to form a stack and it also acts as a collector of the electrical current. It functions as the electrical contact to the cathode while protecting it from the reducing atmosphere of the anode.

6.9.3 Chemical Equilibrium

For any isolated thermodynamic system undergoing a general process which does not have any particular restrictions, the sign of the change in entropy of the universe given by the second law of thermodynamics determines its spontaneity. However, many practical processes occur under the conditions of constant temperature and pressure. For reactions occurring at isothermal and isobaric conditions, the sign of the change in Gibbs function of the reaction gives the information about the spontaneity of the reaction.

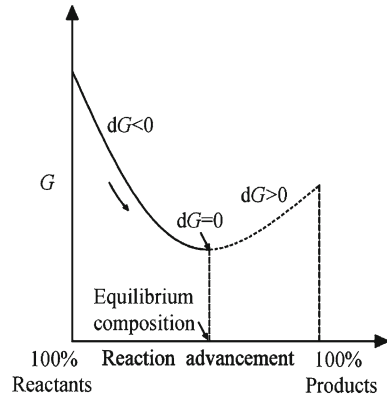
Consider a hydrostatic system in mechanical and thermal equilibrium but not in chemical equilibrium. Suppose that the system is in contact with a reservoir at temperature T and undergoes an infinitesimal irreversible process involving an exchange of heat δQ from the reservoir. The process may involve a chemical reaction. Therefore, the entropy change of the universe is $dS_0 + dS$, where the entropy change of the reservoir is dS_0 and the entropy change of the system is dS . During the infinitesimal irreversible process, the internal energy of the system changes by an amount dU , and an amount of work pdV is performed by the system. Therefore, according to the first law,

$$dQ = dU + pdV. \quad (6.102)$$

According to the second law of thermodynamics, an irreversible process leads to the increase in the entropy of the universe. Thus, we may write $dS_0 + dS > 0$. Since $dS_0 = -\delta Q/T$, we have

$$\begin{aligned} -\frac{dQ}{T} + dS > 0 \text{ or } dQ - TdS < 0 \\ \Rightarrow dU + pdV - TdS < 0. \end{aligned} \quad (6.103)$$

Fig. 6.93 Variation of the Gibbs function of the reaction with the reaction advancement



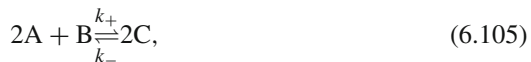
By definition, the Gibbs function G is given as $G = U + pV - TS$, which on differentiation gives $dG = dU + pdV + Vdp - TdS - SdT$. When the conditions of constant temperature and pressure are imposed, the change in Gibbs function is given by

$$dG = dU + pdV - TdS \quad (6.104)$$

From Eqs. 6.103 and 6.104, it is clear that the condition for the process to be irreversible and occur spontaneously is $dG < 0$. Conversely, the non-spontaneity of an isothermal and isobaric process can be identified by the condition $dG > 0$. Therefore, if dG for a isothermal and isobaric chemical reaction system is negative, it means that the process will occur irreversibly until the equilibrium is reached at which, the Gibbs function G will become minimum, i.e. $dG = 0$ (refer to Fig. 6.93).

6.9.4 Bond Graph Model of Chemical Reaction Kinetics

Consider two reactants and product in the example reaction



where k_+ is the forward reaction rate coefficient and k_- is the reverse reaction rate coefficient. The progress or advancement of a reaction can be represented in terms of mole numbers as $n_i(t) = n_i(0) + \nu_i \xi(t)$, where $\xi(t)$ is the reaction advancement coordinate with $\xi(0) = 0$ and ν_i is the stoichiometric coefficient of the i th species. The stoichiometric coefficients of the species in this example reaction (refer to Eq. 6.105) are $\nu_A = 2$, $\nu_B = 1$ and $\nu_C = 2$.

The time variation of the number of moles of the three species are related as $dn_A = -\nu_A d\xi$, $dn_B = -\nu_B d\xi$ and $dn_C = \nu_C d\xi$. As these quantities are perfect differentials, their integrations give the following:

$$\begin{aligned}n_A(t) &= n_A(0) - \nu_A \xi(t), \\n_B(t) &= n_B(0) - \nu_B \xi(t), \\n_C(t) &= n_C(0) + \nu_C \xi(t),\end{aligned}$$

where $\xi(0) = 0$.

The reaction advancement coordinate may be thought of as a generalized displacement whose time derivative defines the reaction rate [35]. The corresponding effort, which drives the reaction, is called affinity. The Gibbs free energy is the maximum amount of non-expansion work that can be extracted from a closed system through a completely reversible process. The change in Gibbs free energy of a system which is maintained at constant temperature and pressure is given as

$$dG = \left(\sum_{i \in P} \mu_i \nu_i - \sum_{i \in R} \mu_i \nu_i \right) d\xi, \quad (6.106)$$

where subscript i is used to represent the sums over the product and the reactant components and μ is the chemical potential. In this example, $P = [A \ B]$ and $R = [C]$.

The affinity of the reaction is given by

$$A = \sum_{i \in R} \mu_i \nu_i - \sum_{i \in P} \mu_i \nu_i, \quad (6.107)$$

where the quantity $A_F = \sum_{i \in R} \mu_i \nu_i$ is defined as the forward affinity and the quantity $A_R = \sum_{i \in P} \mu_i \nu_i$ is defined as the reverse affinity. Therefore, Eq. 6.106 can be written as

$$\frac{dG}{d\xi} = -A. \quad (6.108)$$

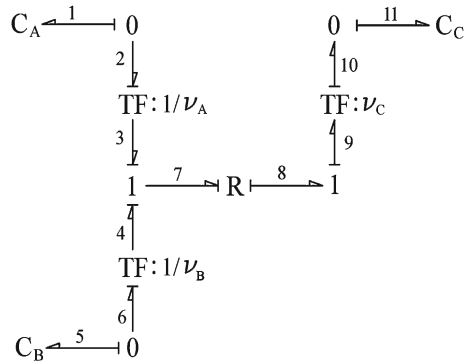
The affinity may be defined as a generalized effort variable in the bond graph model. At the equilibrium, the affinity of the reaction is zero, i.e., $dG/d\xi = 0$ or $A = 0$ and $A_F = A_R$.

The reaction rates are defined by the law of mass action. The law of mass action states that the rate of an elementary reaction (a reaction that proceeds through only one mechanistic step) is proportional to the product of the concentrations of the participating molecules. Therefore, the net rate of the reversible chemical reaction considered in Eq. 6.105 is given as

$$\dot{\xi} = k_+ c_A^2 c_B - k_- c_C^2, \quad (6.109)$$

where c refers to the concentration of the species ' i '. The concentration of a specific component is defined as the ratio of the number of moles of that component to the total number of moles of products and reactants.

Fig. 6.94 The bond graph model of an isothermal and isobaric chemical reaction



The true bond graph model for the kinetics of the reaction (refer to Eq. 6.105) is shown in Fig. 6.94. The effort and flow variables in the model are chemical potential and mole flow rate, respectively. The chemical potential of the component ‘*i*’ is given as

$$\mu_i = \mu_{i,0}(T, p) + RT \ln \left(\frac{c_i}{c_\Sigma} \right), \tag{6.110}$$

where c_i is the concentration of the component ‘*i*’, c_Σ is the reference concentration (usually taken as unity) and $\mu_{i,0}$ is the standard chemical potential. Equation 6.110 can be written in terms of number of moles ‘*n*’ as

$$\mu_i = \mu_{i,0}(T, p) + RT \ln \left(\frac{n_i}{n_\Sigma} \right), \tag{6.111}$$

which forms the constitutive relation for the C-elements of the bond graph model.

From Eq. 6.110, the concentrations of the reacting species can be represented in terms of their chemical potentials as

$$c_i = \exp \left(\frac{\mu_i - \mu_{i,0}(T, p)}{RT} \right). \tag{6.112}$$

The effort in the bond number 7 shown in Fig. 6.94 denotes the forward affinity of the reaction and is given by $e_7 = A_F = 2\mu_A + \mu_B$. Similarly, the effort in bond number 8 denotes the reverse affinity of the reaction and is given by $e_8 = A_R = 2\mu_C$.

The non-equilibrium part of the chemical reaction kinetics is represented as an R-field whose inputs are the forward and reverse affinities and the output is the reaction rate. The constitutive relation of the R-field is formulated using the mass action law. From Eqs. 6.109 and 6.112, the flows in the bonds numbered 7 and 8 are given as

$$\begin{aligned}
 f_7 = f_8 = \dot{\xi} &= k_+ \exp\left(\frac{2\mu_A - 2\mu_{A,0}}{RT}\right) \exp\left(\frac{\mu_B - \mu_{B,0}}{RT}\right) - k_- \exp\left(\frac{2\mu_C - 2\mu_{C,0}}{RT}\right) \\
 &= k_+ \exp\left(\frac{-2\mu_{A,0} - \mu_{B,0}}{RT}\right) \exp\left(\frac{A_F}{RT}\right) - k_- \exp\left(\frac{-2\mu_{C,0}}{RT}\right) \exp\left(\frac{A_R}{RT}\right),
 \end{aligned}$$

where, $\dot{\xi}$ has the unit of mol s⁻¹. This resistance field satisfies the Onsager reciprocity requirements [54]. Moreover, the network representation [61] of the chemical reactions helps in integrating the kinetic (rate laws defined by Eq. 6.109) and thermodynamic (affinities as defined in Eq. 6.107 as driving forces) points of view.

6.9.5 SOFC Modeling

Different levels of modeling of the SOFC system are possible. One has to consider spatial distribution of pressure, temperature and concentration. Such models are complex to solve and usually need a combined thermal and computational fluid dynamics (CFD) model. A full model involves slow (hydraulic and thermal) and fast (reaction, diffusion, ...) phenomena and therefore, multi-scale models are needed [23]. Fast dynamics is generally related to microscopic level. Let us consider a so-called zero-dimensional macroscopic model of the SOFC system. Such a model is good enough to develop the SOFC control system.

The assumptions for the model are

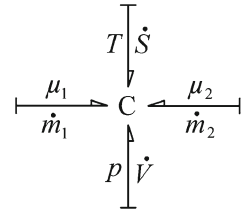
- The water formed due to the reaction is in the vapor form. All the gases involved are assumed to be ideal. This assumption is valid because of the low pressure and high operating temperatures.
- The fuel considered in this model is pure hydrogen. The oxidant is air with oxygen and nitrogen as its primary constituents.
- As the cell is well insulated, the heat loss to the surrounding is neglected.
- As the fast dynamics are irrelevant from the control perspective, the diffusion process is modeled through an approximation.

6.9.5.1 Storage of a Two-Species Gas Mixture

The SOFC channels on the anode side contain the hydrogen and water vapor, while the cathode side has nitrogen and oxygen. On the anode side hydrogen is consumed in the electrochemical reaction and the water vapor is produced, while on the cathode side oxygen is consumed. The nitrogen on the cathode side does not participate in the reaction. A storage element capable of representing the energy storage in a two-species gas mixture is necessary for modeling this scenario.

Consider that a mixture of two gases is contained in a collapsible chamber, which allows heat transfer from and to the surroundings. It is assumed that individual gases

Fig. 6.95 Two species of gases represented in a C-field



can independently flow either into or out of the chamber. Allowing the individual gas mass flow rates in proportion to their mass fractions in the mixture can also incorporate the mass flow of the mixture as a whole. The change of internal energy of the two gases in the mixture in terms of time derivatives is given by

$$\dot{U} = \frac{\partial U}{\partial V} \dot{V} + \frac{\partial U}{\partial S} \dot{S} + \frac{\partial U}{\partial m_1} \dot{m}_1 + \frac{\partial U}{\partial m_2} \dot{m}_2, \tag{6.113}$$

where subscripts 1 and 2 identify the species, U , V , and S are the total internal energy, common volume occupied by the species, and total entropy, respectively, m is the mass and superposed ($\dot{}$) indicates time derivative.

From the well-known thermodynamic relations, $\partial U/\partial V = -p$, $\partial U/\partial S = T$, $\partial U/\partial m_1 = \mu_1$ and $\partial U/\partial m_2 = \mu_2$, it is evident that the internal energy of the volume of the gases change due to four distinct power exchanges which can be represented by the products of the corresponding effort and flow variables. Therefore, the energy storage in the gas mixture can be represented as a four-port C-field as shown in Fig. 6.95. This C-field (an extension of the model in [11]) has four power ports: the flow and effort variables for the mechanical port are \dot{V} and p , respectively; those for the thermal port are \dot{S} and T , respectively; and those for the material ports are \dot{m} 's and μ 's, respectively.

We start from the ideal gas equation of state ($p v = RT$, v being the specific volume and R being characteristic gas constant) and the definition of specific heat capacity at constant volume ($du = c_v dT$, c_v being the specific heat at constant volume). According to the fundamental thermodynamic relation [77], the change in the specific entropy (s) of an ideal gas (gas species #1) in terms of the specific internal energy (u), the specific volume (v), the partial pressure (p_i , $i = 1, 2$) and the equilibrium temperature (T) is given by

$$ds_1 = \frac{du_1}{T} + \frac{p_1 dv_1}{T} = \frac{c_{v1} dT}{T} + \frac{R_1 dv_1}{v_1}. \tag{6.114}$$

Integrating Eq. 6.114 from an initial state (indicated by superscript 0) to a final state with the assumption of constant specific heat capacities and then writing the specific quantities in terms of the absolute quantities gives

$$s_1 = \frac{S_1^0}{m_1^0} + \ln \left\{ \left(\frac{T}{T^0} \right)^{c_{v1}} \left(\frac{Vm_1^0}{V^0 m_1} \right)^{R_1} \right\}. \quad (6.115)$$

Similarly, for gas species #2, which occupies the same volume and is at same temperature, we obtain

$$s_2 = \frac{S_2^0}{m_2^0} + \ln \left\{ \left(\frac{T}{T^0} \right)^{c_{v2}} \left(\frac{Vm_2^0}{V^0 m_2} \right)^{R_2} \right\}. \quad (6.116)$$

Multiplying Eq. 6.115 with m_1 and Eq. 6.116 with m_2 , we get the following expressions for the entropies of the gas species #1 and #2.

$$\begin{aligned} S_1 - \frac{S_1^0 m_1}{m_1^0} &= \ln \left\{ \left(\frac{T}{T^0} \right)^{m_1 c_{v1}} \left(\frac{Vm_1^0}{V^0 m_1} \right)^{m_1 R_1} \right\}, \\ S_2 - \frac{S_2^0 m_2}{m_2^0} &= \ln \left\{ \left(\frac{T}{T^0} \right)^{m_2 c_{v2}} \left(\frac{Vm_2^0}{V^0 m_2} \right)^{m_2 R_2} \right\}. \end{aligned} \quad (6.117)$$

The total entropy of a mixture of gases is given by the sum of the entropies of the individual gases: $S = (S_1 + S_2)$. Then, the temperature of the gases can be written as a function of the four state variables (m_1, m_2, V and S):

$$\begin{aligned} T &= T^0 e^{\alpha} \left(\frac{V}{V^0} \right)^{-\left(\frac{m_1 R_1 + m_2 R_2}{m_1 c_{v1} + m_2 c_{v2}} \right)} \\ &\times \left(\frac{m_1}{m_1^0} \right)^{\left(\frac{m_1 R_1}{m_1 c_{v1} + m_2 c_{v2}} \right)} \left(\frac{m_2}{m_2^0} \right)^{\left(\frac{m_2 R_2}{m_1 c_{v1} + m_2 c_{v2}} \right)}, \end{aligned} \quad (6.118)$$

$$\text{where } \alpha = \frac{S}{m_1 c_{v1} + m_2 c_{v2}} - \frac{m_1 S_1^0}{m_1 m_1^0 c_{v1} + m_1^0 m_2 c_{v2}} - \frac{m_2 S_2^0}{m_1 m_2^0 c_{v1} + m_2^0 m_2 c_{v2}}.$$

The internal energy of the gas mixture is obtained as the sum of the internal energies of both the gases in the chamber, i.e., $U = m_1 c_{v1} T + m_2 c_{v2} T$. The total pressure in the chamber is then obtained by summing the partial pressures, i.e., $p = m_1 R_1 T / V + m_2 R_2 T / V$, where T is given by Eq. 6.118. The same result can also be obtained by taking the partial derivative of the total internal energy with respect to the total volume.

$$\begin{aligned}
 p = T^0 & \left(\frac{m_1 R_1 + m_2 R_2}{V} \right) e^{\alpha} \left(\frac{V}{V^0} \right)^{-\left(\frac{m_1 R_1 + m_2 R_2}{m_1 c_{v1} + m_2 c_{v2}} \right)} \\
 & \times \left(\frac{m_1}{m_1^0} \right)^{\left(\frac{m_1 R_1}{m_1 c_{v1} + m_2 c_{v2}} \right)} \left(\frac{m_2}{m_2^0} \right)^{\left(\frac{m_2 R_2}{m_1 c_{v1} + m_2 c_{v2}} \right)}. \quad (6.119)
 \end{aligned}$$

Likewise, the chemical potentials of the gases can be obtained by taking the partial derivative of U with respect to their corresponding masses. Alternatively, the chemical potential of gas #1 can be given as $\mu_1 = u_1 + p_1 v_1 - T s_1 = c_{v1} T + R_1 T - T s_1 = h_1 - T s_1$. Noting that the specific enthalpy $h_1 = h_1^0 + \int c_p dT$ and $s_1 = s_1^0 + \int (c_p/T) dT - R_1 \ln(p_1/p_1^0)$, we get

$$\mu_1 = \mu_1^0(T) + R_1 T \ln \left(\frac{p_1}{p_1^0} \right), \quad (6.120)$$

where $\mu_1^0(T)$ is purely a function of the temperature. The partial pressure of the gas species #1 and the temperature of the mixture in Eq. 6.120 are written in terms of the state variables using the earlier expressions (refer to Eqs. 6.118 and 6.119). The chemical potential of gas #2 is obtained in a similar fashion as $\mu_2 = \mu_2^0(T) + R_2 T \ln(p_2/p_2^0)$. Equations 6.118– 6.120 are the constitutive relations of the four-port C-field as they give the effort variables (μ_1 , μ_2 , p and T) in terms of the four state variables (m_1 , m_2 , V and S), which are obtained by integrating the flow variables in the bonds of the four-port C-field shown in Fig. 6.95.

6.9.5.2 Bond Graph Model for Convection of a Gas Mixture

An R-field represents the convection of a two gas mixture [22]. The most important element in the expanded model of the MR-element is the RS-field element (see Fig. 6.96). This element receives the downstream side temperature and the information of the valve position (x), the upstream side chemical potentials and temperature, and the downstream side chemical potentials to calculate the mass and entropy flow rates. Note that all these variables are inputs to the MR-element. To maintain the clarity of the figure, the connections needed to explicitly show these modulations are not drawn. In Fig. 6.96, subscripts u and d refer to upstream and downstream sides, respectively.

The submodel in Fig. 6.96 receives information of six effort variables and computes six flow variables without the use of integration and/or differentiation. Therefore, this submodel can be represented as an encapsulated R-field (a six-port element MR in Fig. 6.96). From the continuity equation, the mass flow rate of a particular gas is the same for the inlet and the outlet side. This reduces the total number of independent flow variables to four (see Fig. 6.96). Then the constitutive relation of the nonlinear resistive field element is given as

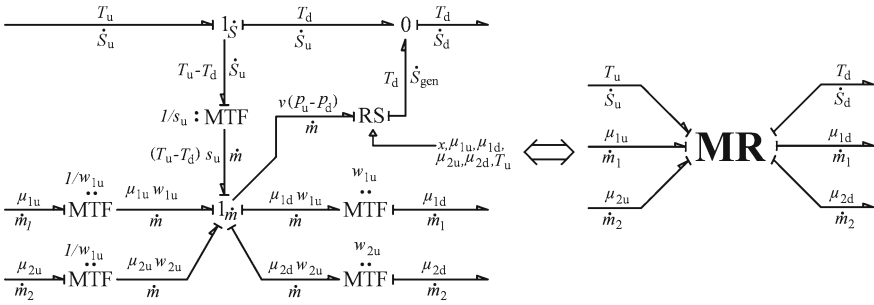


Fig. 6.96 Bond graph representation for convection of a two-component gas mixture

$$\{\dot{S}_u, \dot{S}_d, \dot{m}_1, \dot{m}_2\}^T = \Phi_R \left\{ (T_u, T_d, \mu_{1u}, \mu_{1d}, \mu_{2u}, \mu_{2d})^T \right\}. \tag{6.121}$$

where, $\Phi_R(\cdot)$ is a vector-valued function.

The overall mass flow rate (\dot{m}) of the mixture is imposed at the 1_m junction by the modulated RS-field element in Fig. 6.96 and it is given by the linear nozzle equation:

$$\dot{m} = K (p_u - p_d). \tag{6.122}$$

Although the total upstream and downstream side pressures are needed to calculate mass flow rate, they can indeed be calculated from the chemical potentials and temperatures. The individual mass flow rates of the two gases are then realized through the MTF elements shown in Fig. 6.96 as $\dot{m}_1 = \dot{m}w_{1u}$ and $\dot{m}_2 = \dot{m}w_{2u}$. The upstream mass fractions w_{1u} and w_{2u} are obtained from the upstream side storage element (the C-field in Fig. 6.95), i.e., $w_{1u} = m_{1u}/(m_{1u} + m_{2u})$, $w_{2u} = m_{2u}/(m_{1u} + m_{2u})$ and $w_{1u} + w_{2u} = 1$, where m_{1u} and m_{2u} are the contemporary masses (state variables) in the upstream side control volume.

The entropy flow rate associate with the mass flow rate is calculated by means of a transformer element (between junctions 1_s and 1_m), which is modulated by the specific entropy of the upstream side gases. This information of the upstream side specific entropy can either be obtained directly from the upstream side storage element or if a standalone scheme is required, it can be calculated from the upstream side μ 's and T 's (which are inputs of the MR-element) as

$$s_u = c_{p1}w_{1u} + c_{p2}w_{2u} - \frac{(\mu_{1u}w_{1u} + \mu_{2u}w_{2u})}{T_u}, \tag{6.123}$$

where c_p is the specific heat at constant pressure.

The entropy flow rate from the upstream side is given as $\dot{S}_u = \dot{m}s_u$. The R-field represents the change in the intensive variables between the upstream and the downstream sides. The temperatures, pressures, and the chemical potentials of the gas mixture in the upstream and the downstream sides are imposed by the storage elements on the corresponding sides. Due to this, there is an enthalpy difference between the

upstream and downstream sides, which can be represented as the relation between the changes in the intensive variables by using the Gibbs-Duhem equation [16] as

$$v (p_u - p_d) = s_u (T_u - T_d) + w_{1u} (\mu_{1u} - \mu_{1d}) + w_{2u} (\mu_{2u} - \mu_{2d}). \quad (6.124)$$

This relation is enforced by the $1_{\dot{m}}$ -junction in Fig. 6.96. Due to the enthalpy difference between the upstream and downstream side gases, entropy is generated in the resistive field. Using the principle of power conservation, the irreversible entropy generated \dot{S}_{gen} can be given as

$$\dot{S}_{\text{gen}} = \frac{\dot{m}v (P_u - P_d)}{T_d} = \frac{\dot{m} (s_u (T_u - T_d) + w_{1u} (\mu_{1u} - \mu_{1d}) + w_{2u} (\mu_{2u} - \mu_{2d}))}{T_d}, \quad (6.125)$$

where $s_u (T_u - T_d) + w_{1u} (\mu_{1u} - \mu_{1d}) + w_{2u} (\mu_{2u} - \mu_{2d})$ and T_d are effort inputs to the RS-element and \dot{m} is calculated internally from the constitutive relation of the RS-element (see Eq. 6.122). The downstream side entropy flow rate is the sum of the upstream side entropy flow rate (\dot{S}_u imposed at $1_{\dot{S}}$ -junction by the MTF-element) and the irreversible entropy generated (Eq. 6.125). This sum is realized by means of the zero-junction shown in Fig. 6.96.

The upstream and downstream pressures, which are needed in Eq. 6.122, can either be read directly from the upstream and downstream side storage elements (C -fields) or can be calculated as functions of μ 's and T 's (the input variables to the MR-element) as

$$\begin{aligned} p_{1u} &= \frac{R_1 T_u}{v_{u1}} = p_{u1}^0 \exp\left(\frac{\mu_{1u}}{T_u R_1} - \frac{\mu_{1u}^0}{T_u^0 R_1}\right) \left(\frac{T_u}{T_u^0}\right)^{\frac{c_{v1}}{R_1}}, \\ p_{2u} &= \frac{R_2 T_u}{v_{u2}} = p_{u2}^0 \exp\left(\frac{\mu_{2u}}{T_u R_2} - \frac{\mu_{2u}^0}{T_u^0 R_2}\right) \left(\frac{T_u}{T_u^0}\right)^{\frac{c_{v2}}{R_2}}. \end{aligned} \quad (6.126)$$

The total upstream side pressure is $p_u = p_{1u} + p_{2u}$. The total downstream side pressure can also be expressed similarly.

6.9.5.3 True Bond Graph Model of the SOFC

The true bond graph model of the SOFC is shown in Fig. 6.97. It uses the four-port C -field for representing the energy storage of the gases inside the anode and cathode flow channels. It also uses the R -field representation discussed in the last section for modeling the convection at the inlet and the outlet of the SOFC channels. The subscripts labeling various elements and power variables are as follows: an (anode), ca (cathode), H (hydrogen), O (Oxygen), N (nitrogen), W (water), AS (air source), HS (hydrogen source), M (Membrane electrode assembly or MEA), ai (anode inlet),

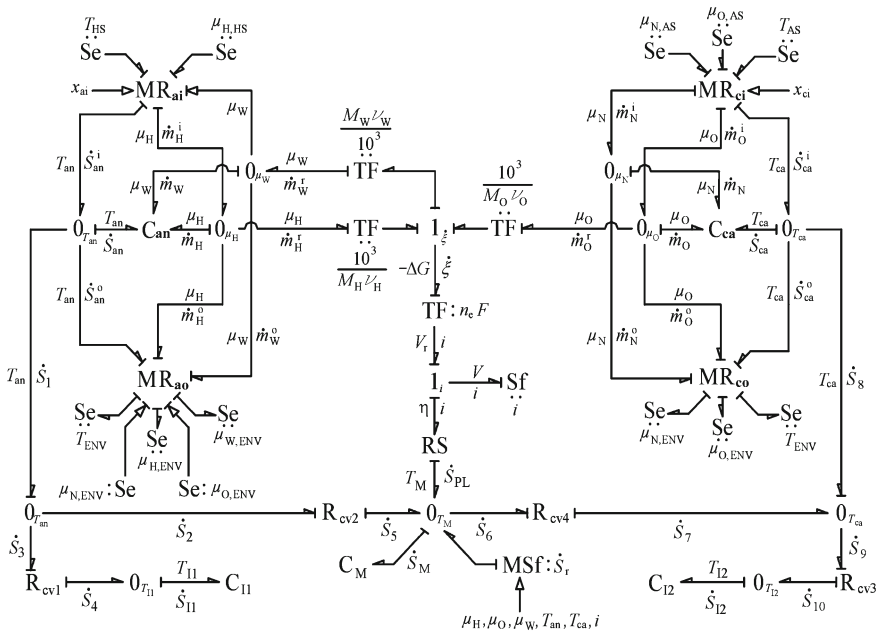


Fig. 6.97 True bond graph model of the SOFC

ci (cathode inlet), ao (anode outlet), co (cathode outlet), I1 (Interconnect on anode side), I2 (Interconnect on cathode side), PL (polarisation losses), r (reaction), and ENV (environment).

As the volumes of both the channels remain constant, the mechanical ports of the C-fields ($p\text{-}\dot{V}$ port of Fig. 6.95) are not shown in Fig. 6.97. The mass and entropy balances of the anode and cathode channel control volumes are given by the corresponding zero junctions in Fig. 6.97. The $0_{T_{an}}$ and the $0_{T_{ca}}$ junctions give the entropy balances for the anode channel and the cathode channel control volumes, respectively. The 0_{μ_H} , 0_{μ_W} , 0_{μ_O} and 0_{μ_N} junctions give the mass balances for the hydrogen, water vapor, oxygen, and nitrogen gases, respectively, in the control volumes. The 0_{T_M} junction gives the entropy balance at the MEA solid control volume.

The capacitive elements and fields in the model represent equilibrium thermodynamics part of the model. As the simulation precedes, the matter inside the control volume represented by these elements changes reversibly from one equilibrium state to the next, i.e., the process is assumed to be quasi-static. The R-fields represent the non-equilibrium parts of the model and they introduce the irreversibilities into the system. The MR-elements introduce the irreversibility due to mass convection into the system. The R-field element represented by ‘RS’ in Fig. 6.97 introduces the irreversibility due to the over-voltage phenomena (ohmic, concentration and activation losses). The other R-field elements introduce the irreversibilities due to the heat transfer phenomena.

The inlet and outlet valve resistances are modeled by the MR-fields described in Fig. 6.96, where subscripts are used to identify them. The valve resistances in the MR-fields may be controlled by modifying the variables for the stem positions. Note that although only hydrogen gas flows through the anode side inlet valve, the information of chemical potential of water vapor (μ_W) inside the anode channel is required for computing the downstream side pressure, which is supplied by an information bond in Fig. 6.97. Similarly, the additional information of the chemical potentials of nitrogen and oxygen in the atmosphere are required in the anode channel outlet valve model to calculate the downstream side pressure, which is provided by the source of efforts as shown in Fig. 6.97. The downstream side entropy flow is the sum of the upstream side entropy flow and the entropy generated due to the enthalpy difference between the upstream and downstream sides (Eq. 6.125).

In this model, the chemical potentials of the gases not only drive the electrochemical reaction but also, along with temperatures, determine the flow of the gases in and out of the channels. The transformation of power from the chemical domain into the electrical domain is implemented by the I_ξ junction and the transformers surrounding it as shown in Fig. 6.97.

The change in the Gibbs free energy of the system is given as

$$dG = Vdp - SdT + \mu dm. \quad (6.127)$$

Assuming constant temperature and pressure, the change in the Gibbs free energy of the reaction is obtained as

$$dG = \frac{\partial G}{\partial n_W} dn_W - \frac{\partial G}{\partial n_H} dn_H - \frac{\partial G}{\partial n_O} dn_O. \quad (6.128)$$

Note that the temperature and the pressure of the system may change during the system's dynamics. However, Eq. 6.128 is assumed to be valid for each instantaneous values of pressure and temperature of the system. The reaction coordinate (ξ) is defined such that $dn_H = -\nu_H d\xi$, $dn_O = -\nu_O d\xi$ and $dn_W = \nu_W d\xi$. Using these relations and the definition of the chemical potential, Eq. 6.128 can be written as

$$\Delta G = (\mu_W \nu_W - \mu_H \nu_H - \mu_O \nu_O) \Delta \xi. \quad (6.129)$$

If unit mole of fuel (hydrogen) is considered then $\Delta \xi = 1$. Therefore, the change in the Gibbs free energy per mole of fuel is given by

$$\Delta G = \mu_W \nu_W - \mu_H \nu_H - \mu_O \nu_O. \quad (6.130)$$

Note that the chemical potentials are in $\text{J}\cdot\text{mol}^{-1}$ in Eq. 6.130. Under reversible conditions, this change in the Gibbs free energy is converted entirely into electrical energy. Therefore, from the energy balance, the reversible cell voltage can be obtained as

$$V_r = -\frac{\Delta G}{n_e F}, \quad (6.131)$$

where the denominator gives the charge of the total number of electrons participating in the reaction per mole of the fuel and F is the Faraday's number. Equation 6.131 can further be written in terms of the partial pressures of the reactant and the product gases and is called the Nernst equation. The Nernst equation is used to calculate the effect of the change in the partial pressures of the reacting species on the reversible cell voltage. Note that the minus sign in Eq. 6.131 is required to obtain a positive value of voltage because the change in the Gibbs free energy per mol as defined in Eq. 6.130 is negative (as the free energy of the products is less than the free energy of the reactants).

The chemical potentials are calculated in J.kg^{-1} in the anode and cathode channel C-fields of the model. The three transformers shown in the effort activated bonds around the 1_{ξ} junction have factors of ' $1,000/M_i$ ' in order to convert the chemical potentials into J.mol^{-1} . The 1_{ξ} junction shown in Fig. 6.97 enforces the following relationship, which defines the negative of the change in Gibbs free energy per mol of fuel for the reaction.

$$-\Delta G = \frac{\nu_H M_H \mu_H + \nu_O M_O \mu_O - \nu_W M_W \mu_W}{1,000} \quad (6.132)$$

The reversible cell voltage, which is defined by the Nernst equation, is realised by means of a transformer element (with modulus $n_e F$) in Fig. 6.97. When the reaction system is in equilibrium, the change in the molar Gibbs free energy (ΔG) is zero. Therefore, the reversible voltage as predicted by the Nernst equation is also zero. When the reaction system is forced out of equilibrium (i.e., when the concentrations of the reactants and the products differ from the equilibrium concentrations), the reversible open circuit voltage (V_r) can be calculated by using the Nernst equation. However, the reaction cannot proceed as the circuit is not closed. But once the circuit is closed (as we try to draw current from the cell), the irreversibilities come into play and result in voltage losses.

The mole flow rate of the reaction ($\dot{\xi}$), which can be considered as the reaction rate, is related to the mole flow rates of consumption and production of the reactants and products, respectively, as

$$\dot{\xi} = \frac{\dot{n}_W^r}{\nu_W} = -\frac{\dot{n}_H^r}{\nu_H} = -\frac{\dot{n}_O^r}{\nu_O}. \quad (6.133)$$

The reaction mole flow rate and the current (i) are related as

$$i = \dot{\xi} n_e F. \quad (6.134)$$

Therefore, the relations between the mass-flow rates (in kg.s^{-1}) of hydrogen, oxygen, and water vapor taking part in the reaction and the current drawn by the load

are given as

$$i = \frac{1,000n_e F \dot{m}_W^r}{\nu_W M_W} = -\frac{1,000n_e F \dot{m}_H^r}{\nu_H M_H} = -\frac{1,000n_e F \dot{m}_O^r}{\nu_O M_O} \quad (6.135)$$

and they are realized through the $1_{\dot{g}}$ junction and the set of transformers in the bonds surrounding it as shown in Fig. 6.97. The current, i , drawn by an un-modeled external load is represented by a source of flow.

The theoretical open-circuit voltage (V_r) is the maximum voltage that can be achieved by a fuel cell under specific operating conditions. However, the voltage of an operating cell, which is equal to the voltage difference between the cathode and the anode, is generally lower than this. As current is drawn from a fuel cell, the cell voltage falls due to the internal resistances and overvoltage losses. The electrode overvoltage (η) losses are associated with the electrochemical reactions taking place at the electrode/electrolyte interfaces and can be divided into concentration (η_{act}) and activation (η_{conc}) over-voltages. The actual cell voltage is generally obtained by subtracting all the voltage losses from the open circuit voltage.

Three different kinds of voltage losses or overvoltages contribute to the cell irreversibility. Activation overvoltage refers to the overpotential required to exceed the activation energy barrier so that the electrode reactions proceed at the desired rate. The anodic and the cathodic activation overvoltages are governed by the Butler-Volmer equation [9], which for a transfer coefficient value of 0.5 are given as

$$\eta_{act,an} = \frac{2RT_M}{n_e F} \sinh^{-1} \left(\frac{0.5i}{i_{0,an}} \right) \quad (6.136)$$

$$\text{and } \eta_{act,ca} = \frac{2RT_M}{n_e F} \sinh^{-1} \left(\frac{0.5i}{i_{0,c}} \right). \quad (6.137)$$

It is clear from Eqs. 6.136 and 6.137 that the contribution of the activation overvoltage to the overall voltage loss is significant at low currents.

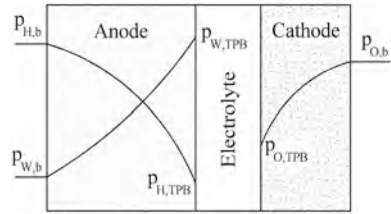
The Ohmic overvoltage (η_{ohm}) is due to the resistance to the transport of ions in the electrolyte and to the flow of electrons through the electrodes and current collectors. It is governed by the Ohm's law:

$$\eta_{ohm} = i R_{ohm}. \quad (6.138)$$

where R_{ohm} is the resistance per unit area. The ohmic overvoltage comes into play typically at the middle range of current densities within which the fuel cell is usually designed to operate.

The reactants, i.e., hydrogen and oxygen, in the flow channels have to diffuse through the porous anode and cathode, respectively, to reach the electrode-electrolyte interface where the reaction occurs. Similarly, the product of the reaction, i.e., water vapor, which is formed at the anode electrolyte interface, has to diffuse through the porous anode so as to reach the flow bulk in the anode channel. If the cell is functioning

Fig. 6.98 Schematic representation of the variation of the partial pressures of hydrogen and water vapor through the anode, and oxygen through the cathode



reversibly, the partial pressures of the reactant and the product gas species are the same at the flow bulk in the gas channels and at the TPB where the actual reaction takes place. But when current is drawn from the cell, the partial pressures of the gas species at the TPB differ from their corresponding partial pressures in the bulk due to limitations imposed by the diffusion process (refer to Fig. 6.98). The voltage lost due to this pressure difference between the bulk and the TPB is called the concentration overvoltage.

The concentration overvoltage is obtained by subtracting the Nernst voltage obtained by using the partial pressures at the flow bulk and those at the TPB. It is assumed that the pressure loss of hydrogen alone is significant and is responsible for the concentration overvoltage. With this assumption

$$\eta_{\text{conc}} = \frac{RT_M}{n_e F} \ln \left(\frac{p_{H,b}}{p_{H,TPB}} \right), \quad (6.139)$$

which may be further simplified [70] to a form

$$\eta_{\text{conc}} = \frac{RT_M}{n_e F} \ln \left(\frac{i_L}{i_L - i} \right) = -\frac{RT_M}{n_e F} \ln \left(1 - \frac{i}{i_L} \right), \quad (6.140)$$

where i_L is the limiting current. The concentration overvoltage is significant only at high currents. From Eq. 6.140, it can be understood that the concentration overvoltage is very less when $i \ll i_L$. It becomes significantly high when the value of the current approaches the limiting current. Note that Eq. 6.140 is not valid for $i = i_L$.

All these overvoltages are modeled by the RS-field shown in Fig. 6.97. The effort output (for the port with current as the flow input) of the RS-field is given as

$$\eta = \frac{RT_M}{n_e F} \left(2 \sinh^{-1} \left(\frac{0.5i}{i_{0,a}} \right) + 2 \sinh^{-1} \left(\frac{0.5i}{i_{0,c}} \right) - \ln \left(1 - \frac{i}{i_L} \right) \right) + i R_{\text{ohm}} \quad (6.141)$$

and the flow output (for the port with temperature as the effort input), i.e., the entropy flow rate which goes to the heat transfer part of the model, is given as

$$\dot{S}_{\text{PL}} = \frac{iR}{n_e F} \left(2 \sinh^{-1} \left(\frac{0.5i}{i_{0,a}} \right) + 2 \sinh^{-1} \left(\frac{0.5i}{i_{0,c}} \right) - \ln \left(1 - \frac{i}{i_L} \right) \right) + \frac{i^2 R_{\text{ohm}}}{T_M}. \quad (6.142)$$

The 0_{T_M} junction shown in Fig. 6.97 represents the temperature of the MEA solid. Convection is an important means of heat transfer in an SOFC as the gases flow through the anode and the cathode channels. Due to the ideal gas assumption and the low velocities, the flow in a fuel cell is usually laminar. The bond graph model shown in Fig. 6.97 includes the convective heat transfers between the anode and cathode channel gases, the MEA, and the interconnects. The R-fields, R_{cv2} and R_{cv4} , model the convective heat transfers between the gases and the MEA and the R-fields, R_{cv1} and R_{cv3} , model the convective heat transfers between the gases and the interconnects denoted by I1 and I2, respectively, in Fig. 6.97. The constitutive relations of the R-field, R_{cv1} , is given as [52]

$$\dot{S}_3 = \frac{\lambda_{\text{an}} A_c (T_{I1} - T_{\text{an}})}{T_{\text{an}}} \quad \text{and} \quad \dot{S}_4 = \frac{\lambda_{\text{an}} A_c (T_{I1} - T_{\text{an}})}{T_{I1}}. \quad (6.143)$$

The constitutive relations for the other R-field elements defining the convection heat transfer (R_{cv2} , R_{cv3} and R_{cv4}) are defined in a similar fashion. The thermal capacity of the MEA is represented by the compliance element C_M in Fig. 6.97. The constitutive relation of thermal capacity [69] of C_M element is given as:

$$T_M = T_M^0 \exp \left(\frac{S_M - S_M^0}{m_{MCM}} \right). \quad (6.144)$$

The thermal capacitance of the interconnect plates are represented by the two capacitive elements C_{I1} and C_{I2} which are governed by the same constitutive relation given in Eq. 6.144.

The enthalpy of the reaction is given as

$$\Delta H = \Delta G + T \Delta S. \quad (6.145)$$

where the part $T \Delta S$ is released as heat when the fuel cell operates reversibly. Under irreversible operation (under all realistic circumstances), the change in the Gibbs free energy of the reaction (ΔG) is not completely converted into useful electrical work. Rather, some of it ends up as heat energy. These irreversibilities, which are called overvoltages, give rise to entropy generation and are taken care by the RS-field element in the model. In order to account for the entropy change of the reaction, the entropy flow rate is added to the MEA by means of a modulated source of flow in Fig. 6.97:

$$\dot{S}_r = \frac{\dot{m}_H^r (h_H - \mu_H)}{T_{an}} + \frac{\dot{m}_O^r (h_O - \mu_O)}{T_{ca}} - \frac{\dot{m}_W^r (h_W - \mu_W)}{T_{an}}. \quad (6.146)$$

where the specific enthalpies are expressed as follows [5]:

$$h = R \left(a_1 T + a_2 T^2 + a_3 T^3 + a_4 T^4 + a_5 T^5 \right) + h_0. \quad (6.147)$$

The values of the coefficients $a_1 \cdots a_6$ and h_0 for the different gases are available in thermodynamics handbooks. The source of flow MSf: derivative of \dot{S}_r is modulated with signals i (to calculate \dot{m}_H^r , \dot{m}_O^r and \dot{m}_W^r according to Eq. 10.54), μ_W , μ_H , μ_O , T_{an} and T_{ca} (the latter five are calculable from state variables). Note that these modulating signals are not shown in Fig. 6.97 to maintain the visual clarity of the figure.

Unlike the pseudo-bond graphs, the energetic consistency of the true bond graph presented in Fig. 6.97 is apparent. The continuity of energy flows across different domains and across different interfaces is ensured because the effort and the flow variables correspond to the power variables in the corresponding energy domains throughout the bond graph model. All the storage elements in the global model given in Fig. 6.97 are in integral causality. There is no causality violation at any place in the junction structure. This ensures the energy consistency in the model. Moreover, this integrally causalled model does not have algebraic or causal loops, which ensures that this model is well computable.

6.9.5.4 Static Characteristics

The model needs extensive initialization before simulation. Readers may refer to [70–72] for the parameters used in the simulations and the procedure to calculate initial values of state variables. The fuel utilization (FU) and oxygen utilization (OU) are two of the most important control variables of the fuel cell. Fuel utilization (ζ_f) is defined as the ratio of the mass flow rate of the fuel taking part in the reaction to the mass flow rate of the fuel supplied to the cell. Oxygen utilization (ζ_o) is defined as the ratio of mass flow rate of oxygen consumed by the reaction to the mass flow rate of oxygen supplied to the cell. According to the operational requirement of the SOFC, FU must be maintained constant. Normally, FU of 0.8–0.9 is desired. Usually, a value of 0.8 is chosen for the FU and a value of 0.125 is chosen for the OU.

Figure 6.99 shows the reversible cell voltage as a function of the fuel utilization (FU) with the system pressure as the parameter. The FU is defined as the ratio of fuel mass consumed in the reaction to the supplied fuel mass. From these curves, it is evident that the reversible cell voltage decreases with the increase in the FU and also that increasing system pressure results in increased Nernst voltage. However, this increase is quite small compared to the added complications of operating the cell at high pressure and temperature. Therefore, the cell pressure is usually kept slightly above the atmospheric pressure. For economical viability the cell is operated

Fig. 6.99 Characteristic curves showing the variation of Nernst voltage as a function of FU

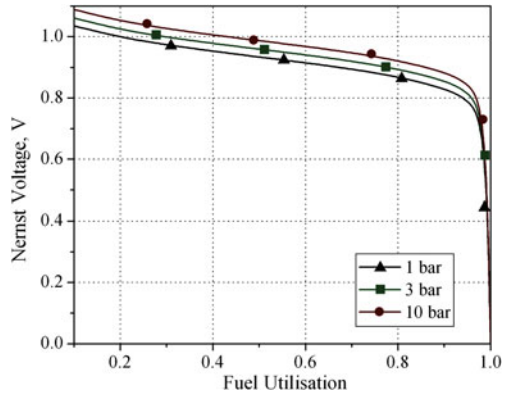
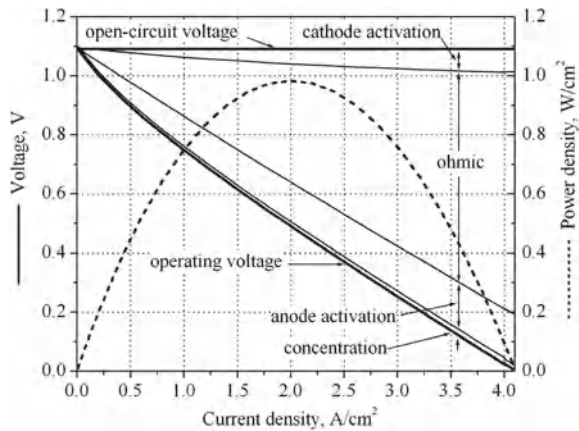


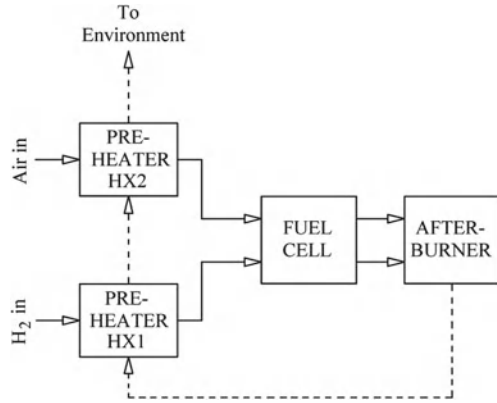
Fig. 6.100 The polarisation curve showing the contribution of various voltage losses



below 0.9 FU value. Note that a low FU is economically unviable. Some other static characteristic curves of the SOFC can be referred to in [70–72].

The power density and the polarization curves for a cell operating at 1,073 K and 1 bar with undepleted air (zero OU) and FU of 0.03 are shown in Fig. 6.100, where the various internal cell voltage losses are also indicated. For the cell under consideration, it can be seen from Fig. 6.100 that the ohmic and the activation losses are the major losses while the concentration voltage loss is minimum. Concentration losses cause the cell potential to drop to zero sharply with a concave curvature at a current density called the limiting current density [2]. For the cell and the operating conditions chosen in this work, no concave curvature is observed as high ohmic and activation losses cause the cell voltage to drop to zero much before the limiting current density ($i_L = 10 \text{ A/cm}^2$) is reached.

Fig. 6.101 A Schema of the SOFC System with heat exchangers



6.9.5.5 Fuel Cell Control

In a hydrogen-fed SOFC system, the anode and cathode outlet gases go to an after-burner, where all the remaining hydrogen is combusted, from where they pass through two pre-heaters which are used for heating the inlet hydrogen and air streams. A schematic representation of the full SOFC system is shown in Fig. 6.101. The exhaust gases from the anode and the cathode sides are fed to an afterburner where all the remaining hydrogen is combusted. The exhaust gases from the afterburner first pass through a hydrogen heat exchanger, HX1, where they lose some of their heat energy to the fuel cell inlet hydrogen stream and then they enter another heat exchanger, HX2, where they heat up the fuel cell inlet air and are then released into the atmosphere.

The afterburner and the heat exchangers are modeled using the pseudo-bond graph approach (the effort and flow variables are T and \dot{H} , respectively) as shown in Fig. 6.102. As a usual assumption, the hydraulic storage is neglected in heat-exchanger design [29]. It may be assumed that the hydraulic resistance has been already modeled at the fuel cell exit. As the afterburner and the heat exchanger models are obtained from the first law analysis, it is convenient to represent their dynamics in terms of pseudo-bond graphs. The energy balance equations used in the afterburner modeling are represented in a pseudo-bond graph. To maintain compatibility, the heat exchanger is also modeled as a pseudo-bond graph.

The C_{AB} element in the afterburner section marked in Fig. 6.102 represents the thermal capacitance of the afterburner gases. The two modulated sources of flows to the left of the C_{AB} element give the afterburner inlet enthalpy flow rate (\dot{H}_{abi}) and the enthalpy flow rate due to the hydrogen combustion reaction in the afterburner (\dot{H}_r). These flow sources are modulated by the signals of the fuel cell outlet gas species mass flow rates and the cathode gas temperature (which come from the true bond graph model of the fuel cell shown in Fig. 6.97). All the hydrogen gas coming out of the fuel cell is consumed in the instantaneous combustion reaction taking place at the afterburner, which is justified from the fact that the combustion reaction time constant is sufficiently small compared to the other dynamics in the system.

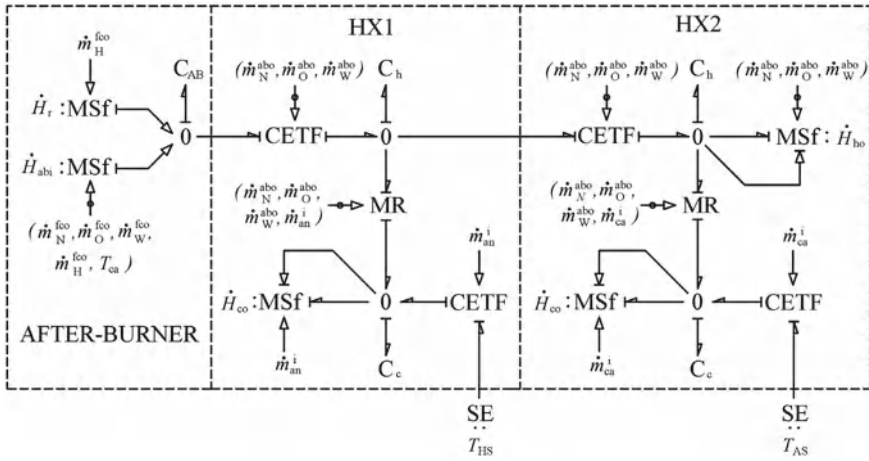


Fig. 6.102 Pseudo-bond graph models of the afterburner and heat exchangers

The coupling element for thermo-fluid (CETF) systems is used to describe convection of multi-component gas mixture (Fig. 6.103). The afterburner outlet enthalpy flow rate, which is also the hot fluid inlet enthalpy flow rate of the hydrogen heat exchanger (HX1), is given by the CETF element. The CETF element is modulated by the afterburner outlet species mass flow rates. The heat exchanger is assumed to be an ideal one in which the pressure and the mass flow rates do not change between the inlet and outlet sides. The thermal capacitances of the hot and cold fluids of the heat exchanger, HX1, are represented by C_h and C_c elements, respectively, in Fig. 6.102. The capacitance of the solid wall separating the two fluids may be included later in the model. The cold fluid inlet enthalpy flow rate is given by the CETF element which is modulated by the anode inlet mass flow rate signal (\dot{m}_{an}^i), whereas the cold fluid outlet mass flow rate is given by the MSf element which is modulated by the signals of the anode inlet mass flow rate (\dot{m}_{an}^i) and the temperature of the cold fluid. The heat transfer rate between the hot and the cold fluids of the hydrogen heat exchanger (HX1) is modeled by the MR-element (modulated with mass flow rate signals) using the NTU formulation as the constitutive relation. The air heat exchanger (HX2) is also modelled in a similar fashion. The temperatures defined by the cold fluid thermal capacitances (C_c) of the heat exchangers HX1 and HX2 are given as those of the anode and the cathode inlet temperatures (T_{ai} and T_{ci} , respectively) to the SOFC bond graph model shown in Fig. 6.97. The chemical potentials of the gas species at the channel inlets ($\mu_{H,ai}$, $\mu_{N,ci}$ and $\mu_{O,ci}$) are represented as functions of these temperatures.

In addition to the constant FU requirement, another requirement for the fuel cell operation is to maintain constant cell temperature despite the changes in the load so as to prevent thermal cracking of the membranes. This is usually achieved by manipulating the cathode inlet mass flow rate (i.e., manipulating the OU). In this work, the constant cell temperature requirement is achieved by means of introducing

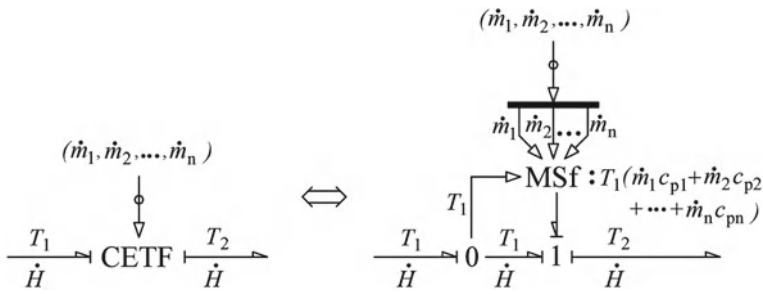


Fig. 6.103 Expanded form of CETF element for multi-component gas mixtures

a PI controller, which manipulates the cathode inlet mass flow rate around a preset value.

6.9.5.6 SOFC Bond Graph Model with Control System

The true bond graph model discussed before is further improved to include more detailed representation of the overvoltages, inclusion of the conduction and radiation heat transfer effects in the cell, and representation of the flow resistance by isentropic nozzle flow equation rather than a linear flow relation.

The MEA solid is represented by three control volumes; one each for the anode, the cathode, and the electrolyte. The temperatures of the solid anode, cathode, and electrolyte control volumes are represented by the junctions ‘ $0_{an,s}$ ’, ‘ $0_{ca,s}$ ’, and ‘ 0_{el} ’, respectively.

It is assumed that the entropy generated due to the ohmic resistance is added to the solid electrolyte. The ohmic resistance is modeled by the resistive field RS_O between the 1_i junction and the 0_{el} -junction in Fig. 6.104. The inputs to this field are the current (i) and the electrolyte temperature (T_{el}). The outputs are the overvoltage (η_{ohm}) and the entropy flow rate (\dot{S}_{el}), which are calculated as

$$\eta_{ohm} = i R_{ohm}$$

$$\text{and } \dot{S}_{el} = \frac{i^2 R_{ohm}}{T_{el}} \tag{6.148}$$

The activation and the concentration overvoltages at the anode are modeled by the resistive field element $RS_{A,C}^{an}$ between the 1_i -junction and the $0_{an,s}$ -junction in Fig. 6.104. The inputs to the resistive field are the current and the anode temperature. In addition, this element is modulated with the signals of gas species partial pressures. These signal bonds are not shown in the figure for maintaining the visual clarity. The outputs of the field are the total anodic overvoltage (η_{an}) and the entropy generated ($\dot{S}_{act,conc,an}$) due to the anodic overvoltages.

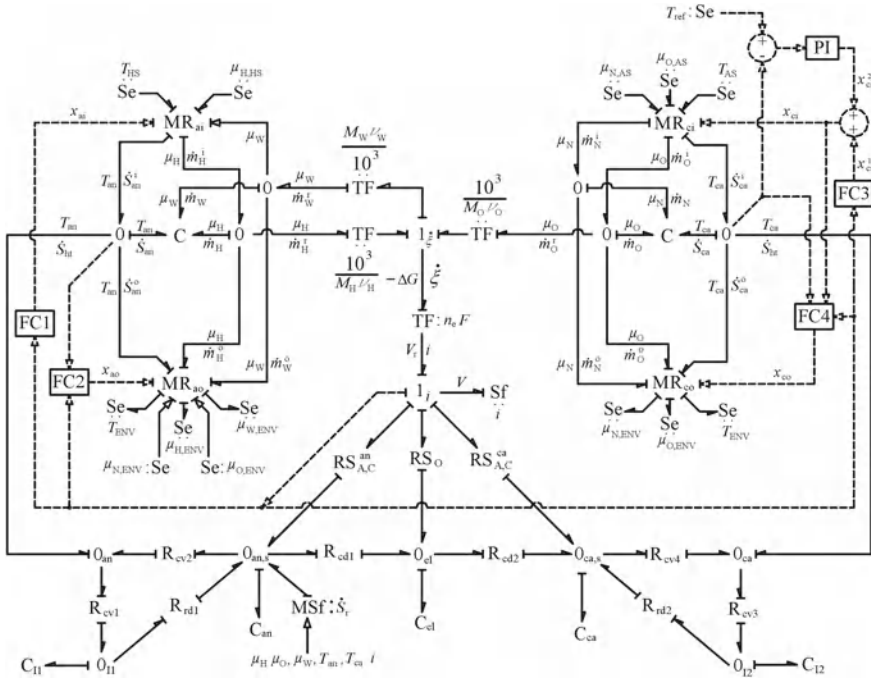


Fig. 6.104 True bond graph model of the closed-loop SOFC System

Similarly, the activation and the concentration overvoltages at the cathode are modeled by the resistive field element between the 1_i -junction and the $0_{ca,s}$ -junction in Fig. 6.104, where the $0_{ca,s}$ -junction represents the common temperature of the cathode solid.

As the SOFC operates at high temperatures, thermal radiation is a significant mode of heat transfer. The radiation heat transfer between the solid anode and the interconnect is modeled by the field element R_{rd1} and that between the solid cathode and the interconnect is modeled in Fig. 6.104 by the field element R_{rd2} . The constitutive relations of the field element R_{rd1} are given as

$$\dot{S}_{rd1,an,s} = \frac{(\sigma A_c / T_{an,s}) (T_{an,s}^4 - T_{I1}^4)}{((1/\epsilon_{an}) + (1/\epsilon_{in}) - 1)} \tag{6.149}$$

$$\text{and } \dot{S}_{rd1,I1} = \frac{(\sigma A_c / T_{I1}) (T_{an,s}^4 - T_{I1}^4)}{((1/\epsilon_{an}) + (1/\epsilon_{in}) - 1)}, \tag{6.150}$$

where $\dot{S}_{rd1,an,s}$ and $\dot{S}_{rd1,I1}$ are the entropy flow rates at the solid anode and the interconnect sides, respectively. The constitutive relations of the R-field element R_{rd2} are similar.

The mass flow rates through the valve resistances are given by the isentropic nozzle flow equations. The overall mass flow rate of the gas mixture is given by the

formulae for the mass flow through an isentropic nozzle as

$$\dot{m} = A(x) \frac{p_u}{\sqrt{T_u}} \sqrt{\frac{2\gamma}{R(\gamma-1)}} \sqrt{\left(\frac{p_d}{p_u}\right)^{2/\gamma} - \left(\frac{p_d}{p_u}\right)^{(\gamma+1)/\gamma}}, \quad (6.151)$$

where the valve areas are given by $A(x) = Ax$ by assuming linear valve characteristic, i.e., the coefficient of discharge varies linearly with the valve stem displacement.

6.9.6 SOFC Control

If all the valve displacements are varied proportionally to the current (in the case of a change in load current) then the steady-state operation with the desired values of OU, FU, and channel pressures can be maintained [72]. Note that the reaction mass flow rates are functions of current only. But the temperature of the gases in the channels will not remain constant, i.e., they would vary from their initial steady-state values when the load current changes. Hence, it is necessary to measure both the chamber gas temperatures. The control strategy proposed in this work consists of a primary controller, which simultaneously controls the four valves by varying their valve displacements in order to maintain constant FU and OU.

However, the above-mentioned control action does not ensure constant cell temperature. The usual method followed for controlling the SOFC temperature is the manipulation of the excess air supplied to the cell. For this purpose, a secondary PI temperature controller, which manipulates the air ratio around the value set by the primary controller, is added. The cathode chamber gas temperature is compared with the set point value of the temperature and the objective of the PI controller is to reduce the temperature error signal by manipulating the flow through cathode chamber inlet and outlet valves by means of varying their valve displacements. It is assumed that the economic cost of increased airflow is insignificant with respect to other operational costs.

The outputs of the primary controller are the four valve displacements (see [72] for details). The secondary controller acts only on the cathode inlet and outlet valves by means of manipulating their valve displacements (x_{ci} and x_{co}) in order to vary the OU. The modified expression for the cathode inlet valve displacement is given by the sum of the displacements due to the primary controller (x_{ci}^1) and the output of the PI controller.

The block diagram of the above control strategy, with both the primary and secondary controllers, is shown in the model given earlier in Fig. 6.104, where the control logic for the blocks FC1, FC2, FC3, and FC4 are given in [72].

The dynamic response (see [70, 71, 73–75] for parameter values and other details) of the open-loop fuel cell to step changes in the load is shown in Fig. 6.105. The load current changes from 100 A to 80 A after 500 s (0 s indicates a reference time in steady-state operation) and again to 90 A after 2,000 s. The open-loop response shows

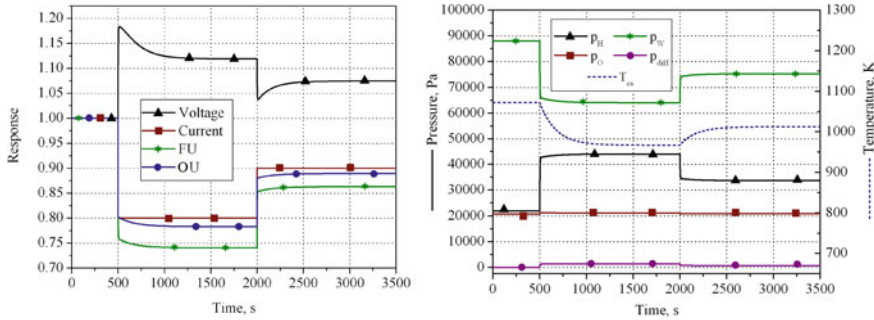


Fig. 6.105 Response of the open-loop SOFC System

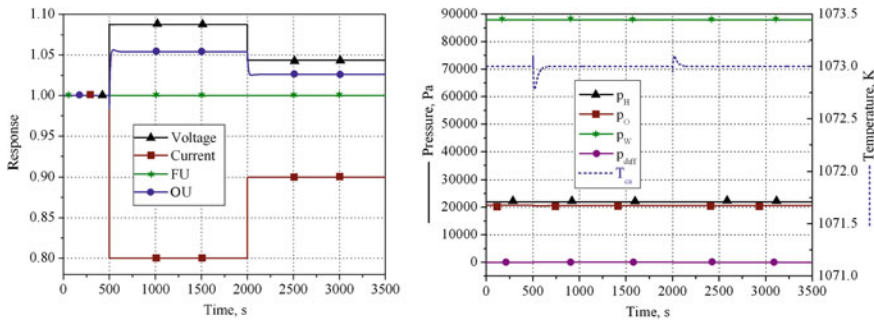


Fig. 6.106 Response of the closed-loop SOFC System

sharp variations in cell temperature and differential pressure (pressure difference between anode and cathode channels). These are detrimental to cell life. Moreover, the FU drops and compromises the cell efficiency. The dynamic response of the closed-loop fuel cell to the same step changes in the load is shown in Fig. 6.106. The OU is varied by the controller so as to bring back the cell temperature to the initial steady-state value. The results show that there is very little change in the partial pressures of the reactants and the product. The voltage increase in this case can be attributed to the decrease in the cell losses due to the lower current density. The pressure difference between the anode and the cathode chambers is small (about 62 Pa). In fact, the pressure difference cannot be made absolutely zero.

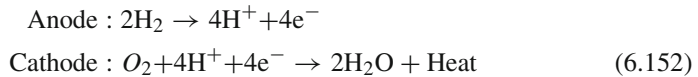
From these results, it is evident that the temperature and the pressure control requirements are conflicting and some tradeoff between them may be required. The maximum allowable pressure difference value depends on the strength of the membrane support and the age of the fuel cell. In the considered design, the pressure difference, obtained from the simulations (62 Pa) is small. If, in some case, the pressure difference turns out to be large enough then a third controller which resets the temperature set point of the PI controller when the chamber pressure crosses a certain limit may be added in order to retain the pressure difference within the allowable

limits. Additionally, the temperature control can also be accomplished by varying the temperature of the input fuel and the air by controlling cold air flow rate to external heat exchangers.

6.9.7 Proton Exchange Membrane Fuel Cell

The general schematic diagram of a PEMFC is given in Fig. 6.107. The hydrogen diffuses to the anode catalyst (usually, platinum) and it breaks into protons and electrons (zone 6 in Fig. 6.107). The polymer electrolyte (ionomer) membrane is electrical insulator. Only the protons conduct through the membrane to the cathode. The electrons travel through the external circuit to reach the cathode catalyst (diffusion zone) where oxygen reacts with the electrons and the protons conducted through the electrolyte to form water.

The reaction taking place in a PEMFC is given as



PEMFC is fundamentally different from SOFC due to the type of the reaction and the operating temperature. In a PEMFC, hydrogen ions (protons) diffuse and conduct through the membrane electrode assembly (MEA, which is anode+membrane+cathode) whereas in an SOFC, oxygen ions conduct. Thus, the MEA material and properties are fundamentally different. Moreover, PEMFC is a low temperature cell whereas SOFC is a high temperature cell (requires initial heating to start the reactions). The typical PEMFC operating temperature range is 50–120°C with nafion membrane and 120–200° C with polybenzimidazole (PBI) membrane, the later normally referred to as high-temperature PEMFC. The platinum catalyst is intolerant to impurities like carbon monoxide which is why PBI membranes are being used. PBI membrane allows use of impure hydrogen supply and reduces the operating cost. Depending on the temperature range, the water supplied/produced to/in the cell can be liquid or vapor form.

Each cell of a PEMFC produces around 1.1 volts (open circuit voltage). Several cells are stacked together to form a PEMFC stack which develops sufficient voltage. Bipolar plates (zone 1 in Fig. 6.107) are used to separate the cells, provide hydrogen and oxygen distribution channels, and are used as terminals to extract the current for the external load.

PEM fuel cells have the highest energy density (see Table 6.3). They also have very fast start-up time (fraction of a second). Thus, they are suitable for use in hybrid electric vehicles, portable power (electronic equipment), and backup power applications.

It may also be noted that a PEMFC has comparable cell efficiency (about 50–70%) with an SOFC (about 60–70%). However, PEMFC control requires additional energy.

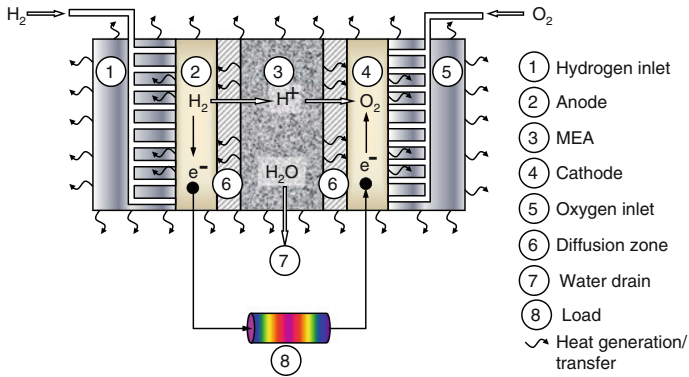


Fig. 6.107 Schematic diagram of a cut-away of a single PEMFC

SOFC on the other hand allows recuperation of energy from the high temperature exhaust. When overall efficiency is calculated, it turns out to be about 30–50 % for PEMFC system and about 50–60 % for SOFC system.

6.9.8 PEMFC Control

Water is not just a product of the reactions in a PEMFC but a necessity to start the reaction. A PEMFC fails to function when the hydration level falls below a minimum threshold and it also fails (efficiency drops) when hydration levels become too high (called flooding of the cell). Thus, water and air management is a key feature of PEMFC control. The membrane must be hydrated to control the rate of protons conducting through the electrolyte. At the same time, water is produced as the product of the reaction. Thus, the water must be evaporated and drained at precisely the same rate as it is produced by the reaction.

If water is removed in excess then the membrane dries up which increases the resistance to flow and eventually may lead to formation of cracks in the membrane. Any crack in the membrane leads to direct contact between hydrogen and oxygen molecules (called a gas "short circuit") and the heat generated by the uncontrolled exothermic reaction would damage the fuel cell. On the other hand, if the water is removed too slowly then the electrodes will flood which would prevent the flow of reactants to the catalyst and stop the reaction. Thus, water content management is the most crucial control parameter in PEMFC operation. To do so, water vapor is usually added to the feed (hydrogen) stream and the air (oxygen) flow rate is changed to remove water vapors. This is a tricky task to achieve properly, because of the limitations of the sensors and actuators. Relative humidity sensors measure the inlet/outlet humidity and it is not possible to obtain the right estimate of the hydration level in the membrane electrode assembly from these measurements. Moreover, actuators such as enthalpy wheel and gas/gas or water/gas membrane humidifier are

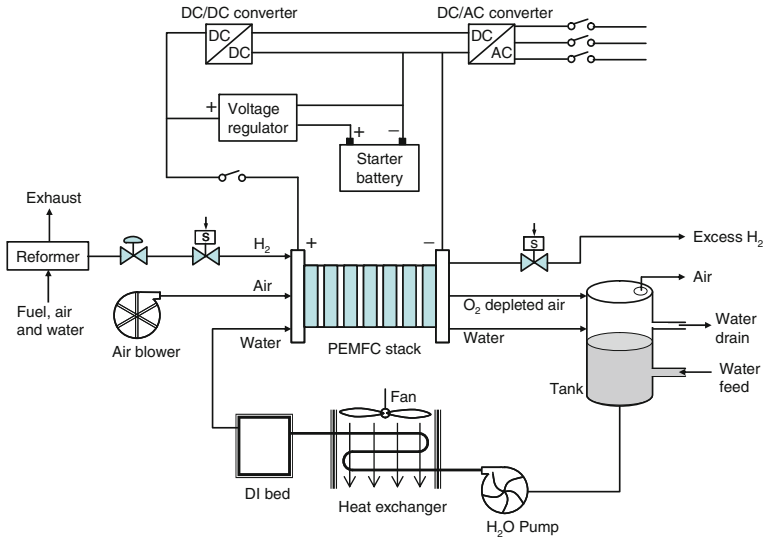


Fig. 6.108 Schematic diagram of PEMFC stack control and input/output conditioning

slow and/or inaccurate. Electroosmotic pumps are found to be somewhat efficient in this regard. Thus, it is not possible to obtain correct measurements (sensor limitation) and at the same time, it is not possible to apply correct corrective action (actuator limitation). This is why, fuzzy-logic controllers are found to be more suitable for PEMFC systems.

Maintaining the right cell temperature is also an important factor in the PEMFC system. The reaction between hydrogen and oxygen is highly exothermic and a large quantity of heat is generated at the reaction site. At the same time, if temperature is not correct, protons do not conduct and reactions do not start. Once the reaction starts, locally high temperatures develop at the reaction sites. However, the same temperature must be maintained throughout the cell. Any difference in temperature across the cell can lead to thermal cracking of the membrane and lead to gas short circuit. This is the same for all kinds of fuel cells. More information on this aspect has been given during discussions on SOFC control. Thus, the cell temperature must be above some minimum value and it must be kept constant to avoid large thermal transients. If there is sudden load change, then the thermal transients must be controlled and the system should transit to new uniform temperature operation as slowly as possible.

The start-up and control circuit for a PEMFC system is shown in Fig. 6.108. The starter battery is used to raise the cell temperature to the operating temperature. The reformer receives some hydrocarbon fuel and supplies hydrogen (may be impure if PBI membrane is used) to the PEMFC stack. The air blower and water supply to the stack perform to tasks: control the cell temperature and control the hydration level.

The feed water to the PEMFC stack must be pure and free from ions. The purest form of water is called DI (de-ionized) water. DI process at the DI bed removes organic and inorganic ionizable particles from water by a two-phase ion exchange process. Cation and anion resins are used to remove, respectively, the positive and negative ions and replace them with H^+ ions and OH^- (hydroxyl) ions. These ions then combine to form pure water. Resistivity (the level of difficulty for a solution to carry an electrical charge) of the water is used to measure the quality of DI water.

The heat exchanger is used to maintain the cell temperature. The cooling rate depends upon the temperature of the supplied water and the air flow from the air blower.

6.9.9 PEMFC Bond Graph Model

We will develop a static one-dimensional model of the PEMFC. This static model is based on the models developed in [63] and [60]. The following assumptions are made to develop a simple one-dimensional PEMFC model: the input gases are pure hydrogen and oxygen, the gasses in the anode and cathode channels are in homogeneous distribution (no spatial variation in concentration, pressure, and temperature), the pressure in the cell is constant (entry and exit cell pressures are constant and equal), the gas diffusion is solved in steady state and there are no parasitic reactions. This model is much simpler from the SOFC model developed before in the sense that variations in the cell pressure (and thus, partial pressures), mass (concentration), etc. are not considered. The variation in hydration level occurs very slowly and thus has been neglected in model formulation. The model only considers thermal transients and can be used for obtaining static characteristics of the cell. A model for full transient analysis has to be based on the true bond graph formulation developed for the SOFC model.

Pseudo-power variables are used in the model developed in [63] and [60]. We will keep the model structure almost similar to the cited sources and make minor changes wherever necessary.

6.9.9.1 Thermochemical Submodel

The hydraulic effort variable pressure (p) is considered in bars and the flow variable volume flow rate (D) is considered in m^3/s . Note that the product of effort and flow variables does not yield power due to inconsistency in units. The gas molar flow (J_{igas} considered in mol/s) and molar volume (V_m in m^3/mol) are used to compute the volume flow rate as follows:

$$D_{gas} = J_{igas} V_m, \quad (6.153)$$

where $V_m = 10^{-5} RT/P_{gas}$ and the factor 10^{-5} is used to convert the pressure unit from bar into Pa. Note that the subscript ‘gas’ may refer to H_2 or O_2 .

The theoretical or reversible cell voltage is given as the potential difference developed between the anode and cathode sides which is given by Nernst equation as

$$E = E_c - E_a = -\frac{\Delta G}{n_e F} = \frac{\Delta G_c - \Delta G_a}{n_e F}, \quad (6.154)$$

where subscripts c and a, respectively, refer to the cathode and anode, G is the Gibbs free energy, n_e is number of electrons participating in the reaction per mole of fuel and F is the Faraday’s number. The current generated by the reactions is given as

$$i = n_e F J_i. \quad (6.155)$$

In SOFC model, the change in Gibb’s free energy has been expressed in terms of specific volumes (in gas mixture because pure gases were not considered), molecular weights and chemical potentials (See Eq. 6.130) and the chemical potentials were evaluated from reference chemical potential (a polynomial function of temperature), temperature and pressure ratio between the current and reference state (See Eq. 6.120). The Gibb’s free energies may be alternatively calculated from the standard reference values as follows:

$$\begin{aligned} \Delta G_c &= \Delta G_c^0 - \frac{RT}{2} \ln(P_{O_2}) \\ \Delta G_a &= \Delta G_a^0 - RT \ln(P_{H_2}) \end{aligned} \quad (6.156)$$

Note that in the SOFC model, we have used $\ln(P_{O_2}/P_{O_2}^0)$ and $\ln(P_{H_2}/P_{H_2}^0)$ which have been simplified here because the pressure is considered in bars and the reference pressure is 1bar. The Gibb’s free energy at the reference state is calculated from the enthalpy and entropy at the reference state as

$$\Delta G^0 = \Delta H^0 - T \Delta S^0, \quad (6.157)$$

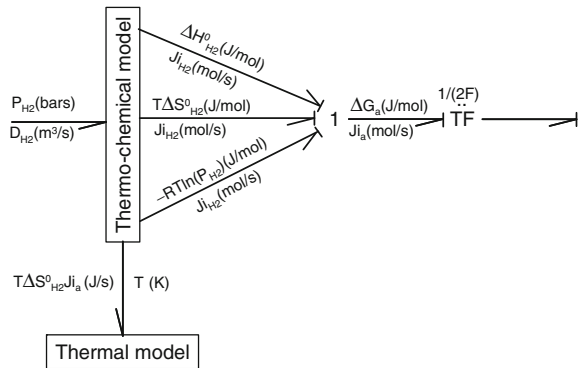
where the enthalpy difference is the theoretically maximum recoverable energy and $T \Delta S^0$ is the reaction heat (loss from theoretical maximum). ΔH^0 and ΔS^0 represent changes from the initial state and the final state of the reaction. Therefore,

$$\Delta H^0 = \Delta H_{\text{products}}^0 - \Delta H_{\text{reactants}}^0. \quad (6.158)$$

The reference enthalpies and entropies can be calculated from

$$\Delta H^0(T) = \Delta H^0(T_0) + \int_{T_0}^T \Delta c_p(\theta) d\theta \quad (6.159)$$

Fig. 6.109 Sub-model of thermochemical processes in the anode channel



and

$$\Delta S^0(T) = \Delta S^0(T_0) + \int_{T_0}^T \frac{\Delta c_p(\theta)}{\theta} d\theta, \tag{6.160}$$

where $c_p(\theta)$ defines the specific heat at constant pressure as a polynomial function of the temperature with virial coefficients as parameters.

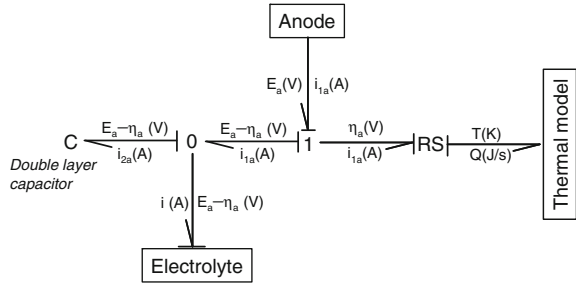
The bond graph submodel of the thermochemical phenomena in anode channel is given in Fig. 6.109. The model incorporates Eqs. 6.154–6.160 in a block and its effort outputs are summed at a 1-junction to produce the Gibb’s free energy change in the anode side. The 1-junction supplies the information of the rate of moles consumed in the reaction to the thermochemical model block. A TF-element is used to convert the change in Gibb’s free energy into the electric potential according to Nernst equation (Eq. 6.154). The thermochemical reaction block also outputs the reaction heat ($T\Delta S^0$) from Eq. 6.157 which produces heating of the anode material. The thermal model supplies the information of local temperature to the thermochemical model block.

The bond graph submodel of the thermochemical phenomena in anode channel is given in the similar manner. Because both oxygen and water vapors are involved in the reactions, there are five power output ports from the thermochemical block model of the cathode side. According to the reaction given in Eq. 6.152, half mole of oxygen is consumed per consumption of one mole of hydrogen to produce one mole of water. Thus, TF-elements with transformer moduli of $\frac{1}{2}$ are used to implement this scaling of variables at the interface to thermochemical model block for cathode channel.

6.9.9.2 Submodel for Double Layer Capacitor and Overvoltages

In the PEMFC model, the activation, diffusion, and concentration over voltages are modeled in the same way as the SOFC model. In addition, at the interface between

Fig. 6.110 Submodel of double layer capacitor and overvoltages for the anode channel



electrode and electrolyte, the double layer phenomenon is observed. The double layer phenomenon is modeled by a capacitor which fixes the dynamics of the activation phenomena.

The submodel for electrochemical field is shown in Fig. 6.110 where the C-element models the double layer capacitor and the RS-element models all over-voltages ($\eta_a = \eta_{act} + \eta_{conc} + \eta_{diff}$) together. The overvoltages produce heat which is taken as an output of the RS-element to the thermal part submodel. The constitutive relation for the RS-element has been already discussed during the development of SOFC model.

6.9.9.3 Overall Bond Graph Model

The overall model of the PEMFC system are shown in Fig. 6.111. In the bond graph model, the anode chamber thermochemical process submodel is connected to the double-layer capacitor submodel for anode and membrane (electrolyte) boundary. Likewise, thermochemical process submodel for the cathode channel (note the TF-elements with $\frac{1}{2}$ moduli) is connected to the double-layer capacitor submodel for cathode and membrane boundary. The reaction heat from anode and cathode channels and the heat generated due to overvoltages at anode-membrane and cathode-membrane segments (activation, concentration and diffusion losses) are interfaced with the thermal domain submodel given at the right of the figure.

The potential difference between cathode and anode potentials (taken between two double layer capacitors) minus the ohmic losses ($i^2 R$ loss) due to internal electrical resistance of the cell is the net potential applied across the external electrical load. This electrical load in turn decides the current drawn from the cell and thus the rate of reaction. The ohmic loss produces heating of the electrolyte which is modeled by another RS-element and the heat generated is interfaced with the thermal domain submodel.

The thermal domain submodel is a simple equivalent network model with lumped capacitances (heat capacity is mass times specific heat) and overall heat transfer coefficients. Heat transfer to the environment through conduction, forced convection (cooling), and radiation takes place at the end plates. The environment temperature (T_0) is modeled by sources of effort. Each 0-junction in the thermal domain submodel

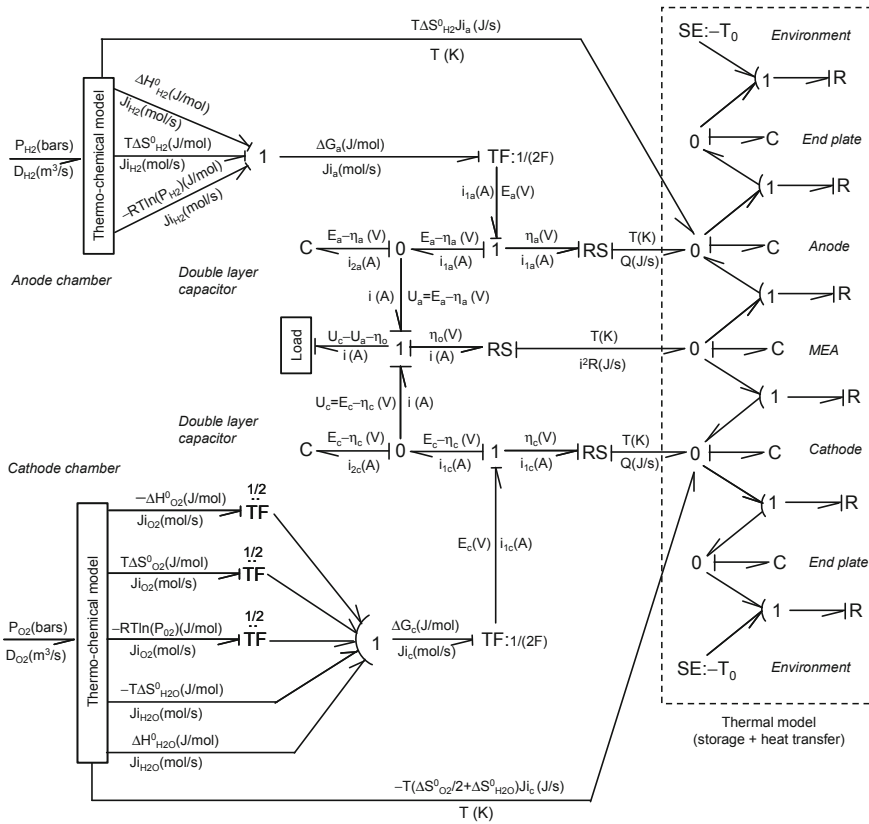


Fig. 6.111 Overall bond graph model of the PEMFC without control components

corresponds to a common temperature point. It is assumed that temperatures in local segments (e.g., anode, cathode, electrolyte) are uniform. The temperature information from these 0-junctions are used by RS-elements (see causality of the S bonds) to compute the resistances (overvoltages) as functions of temperature. Likewise, the temperature information are also fed to anode and cathode channel thermochemical block models to compute the components of Gibb’s free energy on the respective sides. The temperature difference between local segments drives heat flow between segments of the cell.

References

1. V. Aesoy, H. Engja, L.A. Skarboe, Fuel injection system design, analysis and testing using bond graph as an efficient modelling tool. SAE Spec. Publ. **1205**, 159–168 (1996)
2. P. Aguiar, C.S. Adjiman, N.P. Brandon, Anode-supported intermediate-temperature direct internal reforming solid oxide fuel cell I. model-based steady-state performance. J. Power Sources

- 138**, 120–136 (2004)
3. M. Alirand, F. Gallo, Development of a powerful drive line library in amesim to model transmission systems. in *Global Powertrain Congress, Advanced Transmission Design and Performance* (Stuttgart, Germany, 1999), pp. 66–74
 4. D. Assanis, W. Bryzik, N. Chalhoub, Z. Filipi, N. Henein, D. Jung, X. Liu, L. Louca, J. Moskwa, S. Munns, J. Overholt, P. Papalambros, S. Riley, Z. Rubin, P. Sendur, J. Stein, G. Zhang, Integration and use of diesel engine, driveline and vehicle dynamics models for heavy duty truck simulation. SAE Paper 1999-01-0970 (1999)
 5. R.S. Benson, *Advanced Engineering Thermodynamics*, 2nd ed. (Pergamon Press, Oxford, 1977)
 6. T.K. Bera, K. Bhattacharyya, A.K. Samantaray, Bond graph model based evaluation of a sliding mode controller for combined regenerative and antilock braking system. Proc. ImechE Part I J. Syst. Contr. Eng. **225**(7), 918–934 (2011)
 7. T.K. Bera, A.K. Samantaray, R. Karmakar, Bond graph modelling of planar prismatic joints. Mech. Mach. Theor. **49**(12), 2–20 (2012)
 8. T.K. Bera, K. Bhattacharyya, A.K. Samantaray, Evaluation of antilock braking system with an integrated model of full vehicle system dynamics. Simul. Model. Pract. Theor. **19**(10), 2131–2150 (2011)
 9. J.O'M Bockris, A.K.N. Reddy, M. Gamboa-Aldeco, *Modern Electrochemistry: Fundamentals of Electrodeics*, 2nd edn, (Kluwer Academic/Plenum Publishers, New York, 1998)
 10. A.M. Bos, *Modelling Multibody Systems in Terms of Multibond Graphs*. Ph.D. thesis, University of Twente, 1986
 11. P.C. Breedveld, *Physical Systems Theory in terms of Bond Graphs*. Ph.D. thesis, Twente University, Enschede, 1984
 12. L.T. Brown, D. Hrovat, Transmission clutch loop transfer control. U.S. Patent 4,790,419, 1988
 13. K. Bruun, *Bond Graph Modelling of Fuel Cells for Marine Power Plants*. Ph.D. thesis, Norwegian University of Science and Technology, Department of Marine Technology, 2009
 14. M. Burckhardt, Antiskid systems compared. Oelhydraul. Pneum. **28**(8), 489–491 (1984)
 15. M. Burckhardt, E.C. Glasner von Ostenwall, H. Krohn, Capabilities and limits of antilock systems (moeglichkeiten und grenzen von antiblockiersystemen). ATZ Automobiltechnische Zeitschrift **77**(1), 13–18 (1975)
 16. H.B. Callen, *Thermodynamics and an Introduction to Thermostatistics* (Wiley, New York, 1985)
 17. R.M. Chalasani, Ride performance potential of active suspension systems—part I: Simplified analysis based on a quarter-car model. in *Proceedings of 1986 ASME Winter Annual Meeting* (Los Angeles, CA, 1986), p. 1986
 18. W.H. Crouse, D.L. Anglin, *Automotive Mechanics* (TATA McGraw-Hill, New Delhi, 1995)
 19. W. Drozd, H.B. Pacejka, Development and validation of a bond graph handling model of an automobile. J. Franklin Inst. **328**(5/6), 941–957 (1991)
 20. Hallvard Engja, Bond graph model of a reciprocating compressor. J. Franklin Inst. **319**(1–2), 115–124 (1985)
 21. Tulga Ersal, Hosam K. Fathy, Jeffrey L. Stein, Structural simplification of modular bond-graph models based on junction inactivity. Simul. Model. Pract. Theor. **17**(1), 175–196 (2009)
 22. P.J. Feenstra, A library of port-based thermo-fluid submodels, MS thesis, University of Twente, 2000
 23. A.A. Franco, P. Schott, C. Jallut, B. Maschke, Multi-scale bond graph model of the electrochemical dynamics in a fuel cell. in *Proceedings of 5th MATHMOD Conference* (Vienna, Austria, 2005)
 24. W. Gao, C. Mi, A. Emadi, Modeling and simulation of electric and hybrid vehicles. Proc. IEEE **95**(4), 729–745 (2007)
 25. T.D. Gillespie, Fundamentals of vehicle dynamics. Soc. Automot. Eng. 1361–1370 (1992). ISBN: 1560911999
 26. J.J. Granda, The role of bond graph modeling and simulation in mechatronics systems: an integrated software tool: CAMP-G. MATLAB-SIMULINK. Mechatron. **12**, 1271–1295 (2002)

27. G.J. Heydinger, M.K. Salaani, W.R. Garrott, P.A. Grygier, Vehicle dynamics modelling for the national advanced driving simulator. *Proc. Inst. Mech. Eng. Part D J. Automobile Eng.* **216**(4), 307–318 (2002)
28. D. Hrovat, J. Asgari, M. Fodor, *Mechatronic Systems Techniques and Applications of Transportation and Vehicular Systems*, vol. 2, chapter Automotive Mechatronic Systems, (Gordon and Breach Science Publishers, Amsterdam, 2000), pp. 1–98
29. F.P. Incropera, D.P. Dewitt, *Fundamentals of Heat and Mass Transfer*, 4th edn. (Wiley, New York, 1996)
30. V. Ivanovic, J. Deur, Z. Herold, M. Hancock, F. Assadian, Modelling of electromechanically actuated active differential wet-clutch dynamics. *Proc. IMechE Part D J. Automobile Eng.* **226**, 433–456 (2012)
31. D. Karnopp, Bond graph for vehicle dynamics. *Veh. Syst. Dyn.* **5**, 171–184 (1976)
32. D. Karnopp, Pseudo bond graphs for thermal energy transport. *Trans. ASME J. Dyn. Syst. Meas. Contr.* **100**(3), 165–169 (1978)
33. D. Karnopp, Computer simulation of stick-slip friction in mechanical dynamic systems. *J. Dyn. Syst. Measur. Contr. Trans. ASME* **107**(1), 100–103 (1985)
34. D. Karnopp, Modelling and simulation of adaptive vehicle air suspensions with pseudo bond graphs in CAMP and ACSL. in *Proceedings of 11th IMACS World Congress on System Simulation and Scientific Computation* (Oslo, Norway, 1985)
35. D. Karnopp, Bond graph models for electrochemical energy storage: electrical, chemical and thermal effects. *J. Franklin Inst.* **327**(6), 983–992 (1990)
36. D. Karnopp, Design principles for vibration control systems using semi-active dampers. *Trans. ASME J. Dyn. Syst. Measur. Contr.* **112**(3), 448–455 (1990)
37. D. Karnopp, Power requirements for vehicle suspension systems. *Veh. Syst. Dyn.* **21**(2), 65–71 (1992)
38. D. Karnopp, Active and semi-active vibration isolation. *J. Mech. Des.* **117B**, 177–185 (1995)
39. D.C. Karnopp, State variables and pseudo-bond graphs for compressible thermo-fluid systems. *J. Dyn. Syst. Measur. Contr.* **101**(3), 201–204 (1979)
40. K. Li, J.A. Misener, K. Hedrick, On-board road condition monitoring system using slip-based tyre-road friction estimation and wheel speed signal analysis. *Proc. IMechE J. Multi-body Dyn.* **221**, 129–146 (2007)
41. P.Y. Li, R.F. Ngwompo, Power scaling bond graph approach to the passification of mechatronic systems—with application to electrohydraulic valves. *J. Dyn. Syst. Measur. Contr.* **127**(4), 633–641 (2005)
42. R.G. Longoria, A. Al-Sharif, C.B. Patil, Scaled vehicle system dynamics and control: a case study in anti-lock braking. *Int. J. Veh. Auton. Syst.* **2**(1/2), 18–39 (2004)
43. L.S. Louca, D.G. Rideout, J.L. Stein, G.M. Hulbert, Generating proper dynamic models for truck mobility and handling. *Int. J. Heavy Veh. Syst.* **11**(3–4), 209–236 (2004)
44. L.S. Louca, J.L. Stein, D.G. Rideout, Integrated proper vehicle modeling and simulation using a bond graph formulation. in *Proceedings of the 2001 International Conference on Bond Graph Modeling (ICBGM'01)*, vol. 33, No. 1, pp. 339–345 (2010)
45. D. Margolis, Bond graph for vehicle stability analysis. *Int. J. Veh. Des.* **5**, 427–437 (1984)
46. D. Margolis, J. Asgari, Multipurpose models of vehicle dynamics for controller design. SAE Technical Paper 911927 (1991). doi:[10.4271/911927](https://doi.org/10.4271/911927)
47. D. Margolis, T. Shim, A bond graph model incorporating sensors, actuators, and vehicle dynamics for developing controllers for vehicle safety. *J. Franklin Inst.* **338**(1), 21–34 (2001)
48. D.L. Margolis, Modeling of two-stroke internal combustion engine dynamics using the bond graph technique. SAE Technical Paper 750860, 2263–2275 (1975). doi:[10.4271/750860](https://doi.org/10.4271/750860)
49. W. Marquis-Favre, E. Bideaux, O. Mechin, S. Scavarda, F. Guillemard, M. Ebalard, Mechatronic bond graph modelling of an automotive vehicle. *Math. Comput. Model. Dyn. Syst.* **12**(2–3), 189–202 (2006)
50. R. Merzouki, B. Ould Bouamama M.A. Djeziri, and M. Bouteldja., Modelling and estimation of tire-road longitudinal impact efforts using bond graph approach. *Mechatronics* **17**(2–3), 93–108 (2007)

51. H. Mirzaeinejad, M. Mirzaei, A novel method for non-linear control of wheel slip in anti-lock braking systems. *Constr. Eng. Pract.* **18**(8), 918–926 (2010)
52. A. Mukherjee, R. Karmakar, A.K. Samantaray, *Bond Graph in Modeling, Simulation and Fault Identification* (CRC Press, USA, 2006), ISBN: 978-8188237968, 1420058657
53. T. Nakayama, E. Suda, The present and future of electric power steering. *Int. J. Veh. Des.* **15**(3–5), 243–254 (1994)
54. L. Onsager, Reciprocal relations in irreversible processes. I. *Phys. Rev.* **37**, 405–426 (1931)
55. M. Oudghiri, M. Chadli, A.E. Hajjaji, Robust fuzzy sliding mode control for antilock braking system. *Int. J. Sci. Tech. Autom. Contr.* **1**(1), 13–28 (2007)
56. B. Ozdalyan, Development of a slip control anti-lock braking system model. *Int. J. Automot. Technol.* **9**(1), 71–80 (2008)
57. H.B. Pacejka, Modelling complex vehicle systems using bond graphs. *J. Franklin Inst.* **319**(1/2), 67–81 (1985)
58. H.B. Pacejka, *Tyre and Vehicle Dynamics* (Butterworth-Heinemann, Elsevier, UK, 2006)
59. P.M. Pathak, A.K. Samantaray, R. Merzouki, B. Ould-Bouamama, Reconfiguration of directional handling of an autonomous vehicle. in *IEEE Region 10 Colloquium and 3rd International Conference on Industrial and Information Systems, ICIIS 2008*, Art. no. 4798408 (2008). doi:[10.1109/ICIINFS.2008.4798408](https://doi.org/10.1109/ICIINFS.2008.4798408)
60. C. Peraza, J.G. Diaz, F.J. Arteaga-Bravo, C.C. Villanueva, F. Gonzalez-Longatt, Modeling and simulation of PEM fuel cell with bond graph and 20sim. in *Proceedings of the American Control Conference*, Art. no. 4587303, pp. 5104–5108 (2008)
61. A.S. Perelson, Network thermodynamics, an overview. *Biophys. J.* **15**, 667–685 (1975)
62. R. Rajamani, *Vehicle Dynamics and Control* (Springer, New York, 2006)
63. R. Saisset, G. Fontes, C. Turpin, S. Astier, Bond graph model of a PEM fuel cell. *J. Power Sources* **156**(1), 100–107 (2006)
64. M.K. Salaani, G.J. Heydinger, Powertrain and brake modeling of the 1994 Ford Taurus for the national advanced driving simulator. *SAE Special Publ.* **1361**, 131–143 (1998)
65. A.K. Samantaray, Modeling and analysis of preloaded liquid spring/damper shock absorbers. *Simul. Model. Pract. Theor.* **17**(1), 309–325 (2009)
66. A.K. Samantaray, B. Ould Bouamama, *Model-Based Process Supervision—A Bond Graph Approach* (Springer, London, 2008)
67. S.C. Singhal, K. Kendall, *High Temperature Solid Oxide Fuel Cells: Fundamentals, Design and Applications* (Elsevier, Oxford, 2003)
68. H.T. Szostak, W.R. Allen, T.J. Rosenthal, Analytical modeling of driver response in crash avoidance maneuvering. volume II: An interactive model for driver/vehicle simulation. Technical Report, U.S. Department of Transportation Report NHTSA DOT HS-807-271, 1988
69. J.U. Thoma, B. Ould Bouamama, *Modelling and Simulation in Thermal and Chemical Engineering. Bond Graph Approach* (Springer, Telos, 2000)
70. P. Vijay, *Modelling, Simulation and Control of a Solid Oxide Fuel Cell System: A Bond Graph Approach* Ph.D. thesis, (Indian Institute of Technology, Kharagpur, India, 2009)
71. P. Vijay, A.K. Samantaray, A. Mukherjee, Bond graph model of a solid oxide fuel cell with a C-field for mixture of two gas species. *Proc. IMechE Part I J. Syst. Contr. Eng.* **222**(4), 247–259 (2008)
72. P. Vijay, A.K. Samantaray, A. Mukherjee, A bond graph model-based evaluation of a control scheme to improve the dynamic performance of a solid oxide fuel cell. *Mechatronics* **19**(4), 489–502 (2009)
73. P. Vijay, A.K. Samantaray, A. Mukherjee, On the rationale behind constant fuel utilization control of solid oxide fuel cells. *Proc. IMechE Part I J. Syst. Contr. Eng.* **223**(2), 229–252 (2009)
74. P. Vijay, A.K. Samantaray, A. Mukherjee, Constant fuel utilization operation of a SOFC system: An efficiency viewpoint. *Trans. ASME J. Fuel Cell Sci. Technol.* **7**(4), 041011 (7 pages) (2010)
75. P. Vijay, A.K. Samantaray, A. Mukherjee, Parameter estimation of chemical reaction mechanisms using thermodynamically consistent kinetic models. *Comput. Chem. Eng.* **34**(6), 866–877 (2010)

76. H. Yeo, S. Hwang, H. Kim, Regenerative braking algorithm for a hybrid electric vehicle with CVT ratio control. *IMechE J. Automobile Engineering* **220**, 1589–1600 (2006)
77. M.W. Zemansky, D.H. Dittman, *Heat and Thermodynamics* (McGraw-Hill, Singapore, 1997)

Chapter 7

Model-Based Fault Diagnosis and Fault Tolerant Control

7.1 Introduction

Mechatronic systems are complex equipment containing mechanical and electrical subsystems, electronic components, control systems, sensors, and actuators. The complexity of these systems arises from integration of several components belonging to different engineering domains. Failure of any component can lead to complete malfunctioning of the mechatronic device. Failure in some mechatronic systems, such as autonomous vehicles, can lead to serious accidents and severe economic loss. Moreover, some faults can occur suddenly without any prior symptom or warning. Modern mechatronic systems have to ensure improved reliability, availability, maintainability, and safety (RAMS). Thus, the design of a complex mechatronic system has to integrate engineering design with additional functionality such as maintenance, management, and supervision facilities. In such integrated designs, real-time fault detection and diagnosis algorithms are often embedded into smart or intelligent mechatronic systems, which provide prompt or early fault detection, classification of any abnormal system behavior, and prediction of the likely faults (also called prognostics), and thereby, they minimize the chances of total failure.

Real-time supervision means monitoring the condition of a system at each and every instant. Automated Fault Detection and Isolation (FDI) procedures are implemented in the supervision platform to ensure the safe operation of the system at all times. The diagnostic system in an FDI framework has to quickly detect any fault which can seriously degrade the performance of the system.

A fault is defined as a departure from an acceptable range of an observed variable or a calculated parameter associated with a system. A fault in a system can lead to undesired and/or uncontrollable sequence of events which can be catastrophic. Note that there is a difference between fault and failure: a failure means an irrecoverable structural change to the system, whereas a fault is a less severe malfunction which can be tolerated or controlled without requiring immediate replacement of the faulty component. Faults are of different types which are usually classified according to the cause of the fault. They are:

- Gross parameter changes or parametric faults.
- Structural changes or hard failures.
- Malfunctioning of sensors, actuators, and controllers.

A set of tools and methods are used in real-time supervision. These ensure safe operation of the system in normal situations as well as in the presence of failures or undesired disturbances. Each tool in a supervision environment is specifically designed for a specific activity. These activities are:

- Fault detection/monitoring level where deviation from nominal system behavior is detected and then an alarm state is declared.
- Fault isolation level where one or more faulty component(s) which led to abnormal system behavior are identified.
- Fault quantification/identification level where the severity of the fault and its type are determined.
- Fault accommodation level where it is decided whether a fault can be accommodated (tolerated or bypassed by some means) or not and the sequence of events to be followed based on that decision.

The activities discussed above are sequentially executed. The existence of a fault (an alarm) is detected at the monitoring level and the other activities are performed when an alarm is detected at the monitoring level. The steps executed after fault detection are termed alarm interpretation which classify the actual fault, its characteristics (occurrence time, fault size, consequences, etc.), and the root cause. Fault characterization and quantification gives the state of the system or severity of the fault (safe, marginally safe, dangerous, etc.) based on which the decision regarding whether the fault can be safely accommodated is taken. Fault accommodation may be performed in two different ways: (1) reconfiguration, i.e., changing the control laws to activate healthy standby devices offering the same services as the faulty devices and deactivate the faulty devices, or (2) fault tolerant control (FTC), i.e., continuing to use the partially malfunctioning devices by changing the control laws and the associated control problems on-the-fly so that the desired system state is maintained.

Type of fault occurrence is also a factor that influences diagnosis. When a normally operating system suddenly starts behaving abnormally, it is called an abrupt fault. When there is gradual drift in the behavior of a system away from its normal behavior, it is called a progressive fault. In an intermittent fault scenario, the system shows abnormal behavior for a small duration of time which is repeated arbitrarily and when the system behavior is in the borderline between normal and abnormal behavior, it is called an incipient fault.

The design of a fault diagnostic system must satisfy a set of guidelines. These guidelines may change depending upon the application at hand. Usually, the common standards that a diagnostic system must satisfy are as follows:

- It should be able to detect and diagnose the fault quickly after or just before the onset of the abnormal behavior.
- It should be able to differentiate between various failures, classify them, and isolate the faulty component(s).

- It should be robust to various disturbances and uncertainties.
- It should be able to adapt to newer situations and operating conditions, e.g., changing environmental conditions, normal degradation of components due to wear and tear, etc.
- It should be able to determine the origin or root cause of the fault, and catalog the sequence of the fault propagation from the root cause to the detected malfunction, and provide clear reasons for its actions.
- It should be economical, i.e., should not be requiring heavy resources, should be easy to implement, and adapt to various situations.

Most of the early approaches for FDI were rule based, where simple prediction rules are used to determine possible faults in a system and their causes. Rule-based methods are often incomplete and inflexible. Modern FDI methods are based on analysis of the underlying model structures and behavior of a system. These are called model-based FDI methods. Models serve as knowledge representation. A model represents a large amount of structural, functional, and behavioral information and their relationship [6, 10, 15, 36, 58, 76, 77, 95, 96]. This knowledge representation is used to create complex cause-effect reasoning leading to construction of powerful and robust automatic diagnosis and isolation systems [1, 31, 40, 41, 49, 50, 104, 107]. The model of a system may be qualitative, quantitative, or statistical. Accordingly, three different groups of model-based diagnosis approaches can be identified [105–107].

A bond graph model represents the model structure (kinematic and dynamic constraints), constitutive relations (device functions), sensors, actuators, and control loop, etc., and the structural, functional and behavioral relationship is established through causal paths linking the various parts of the model. Thus, a bond graph model gives an integrated representation of structural, behavioral, and functional knowledge of a physical system. Conceptual design is a two-step process: (1) transformation of functional requirements to a behavioral description and (2) matching the physical artifacts or devices to this desired behavioral description. In [113], it has been argued that “behavioral reasoning breaks preconceived links between functions and artefacts, allowing for innovative solutions to be found”. The fault diagnosis is based on the analysis of the underlying structure and behavior of a system [97]. Bond graph representation is used to create complex cause-effect reasoning leading to construction of powerful and robust automatic diagnosis and isolation systems. The causal paths yield the interdependency between different dynamic parts of the system. The causality can be used for qualitative or quantitative reasoning. Various bond graph-based qualitative FDI methods have been developed, e.g., intelligent supervisory control systems developed in [61, 110] by integrating bond graph causal knowledge with artificial intelligence, tree graphs [57, 56], temporal causal graph (TCG) [28, 29, 65], etc. Bond graph model-based quantitative FDI methods are analytical redundancy relations (ARRs) [62, 63, 68–70, 83, 84, 86, 87, 100, 101, 117] parameter estimation [38, 82], trend analysis [85], observer-based methods [88], unknown input observers [39], etc. A comprehensive coverage of these bond graph model-based diagnosis methods is available in [88].

7.2 Quantitative Fault Detection

Formally, model-based fault diagnosis is based on quantitative or qualitative comparison of the available system measurements with a priori information represented by the mathematical model of the system. Quantitative FDI methods check the consistency between the actual process and its model. They check the differences generated from the comparison of different model variables with those of the process. These differences are called residuals or symptom signals [6, 10, 15, 36, 58, 76, 77, 95, 96].

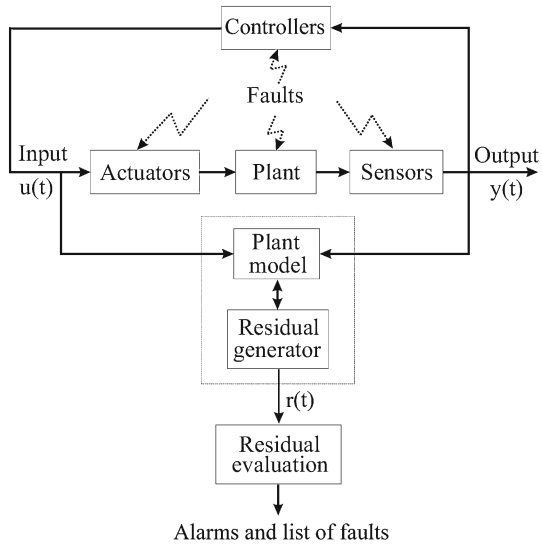
Generally, a residual is the result of comparison between the measured signals with their estimations obtained from a mathematical model of the considered system. At times, observers are used with the system model. However, it is possible to compare other quantities in place of the measurements and their estimates.

Every residual should be normally zero or close to zero when no fault is present, but should be distinguishably different from zero when a fault occurs. This is sometimes referred to as the *fundamental problem of residual generation*. However, in reality, it is impossible to fully satisfy the fundamental problem of residual generation because (1) it is impossible to create a perfect mathematical model of a system (usually, engineering assumptions are necessary in model development), (2) there are invariably some disturbances to the system, (3) the parameters of the system vary over time due to normal degradation or wear and tear, and (4) the measurements are never exact and contain noise. Thus, determination of fault symptoms from residuals needs various post-processing steps called decision procedure.

The objective of the decision procedure is to minimize the number of false alarms (i.e., detecting a fault while it is not there) and misdetections (i.e., not detecting a fault while there is actually a fault). These are two contrasting requirements which have to be simultaneously satisfied by the decision system. Towards this end, the model-based FDI scheme needs to be insensitive to modeling uncertainties. However, reducing the residuals' sensitivity to modeling uncertainties also reduces their sensitivities to faults. The right approach is to increase insensitivity to modeling uncertainties while simultaneously increasing sensitivity to faults. Two approaches followed in this regard are (1) Active approach, where fault sources are decoupled from modeling uncertainties and disturbances right during the model development [8, 11, 35, 37, 44, 60, 74, 79, 93, 109] and (2) passive approach, where residuals are bounded by varying thresholds.

The primary requirements of the FDI system are a residual generator [32–34, 55, 59] and a residual evaluator or decision support system. Residual generators can be developed using different methods, e.g., observers or bank of observers [14, 16, 17, 27, 30, 33, 54, 60, 75, 109, 111], parity relations [35, 37, 79], analytical redundancy relations [88, 97, 98] and parameter estimation [11, 13, 47, 49, 99, 116] based methods. The residual evaluator determines occurrences or the likelihood of faults. The decision rules are usually tuned for a specific system. The decision rule may be based on a geometric method such as a simple threshold test on the instantaneous residual values or moving averages of the residuals, adaptive thresholds [26, 81, 91], interval models [5, 4, 19, 42, 64, 80, 102, 103], cumulative sums [9],

Fig. 7.1 A general scheme of model-based FDI



and statistical methods like generalized likelihood ratio test or sequential probability ratio test [12, 112]. If residuals are well-designed then the decision-making becomes easier.

The general schematics of a model-based FDI system architecture is shown in Fig. 7.1. The FDI procedure compares the actual output from a system with reference output from an analytical model and the difference between the predicted and observed values, or the residual, which should be ideally zero during normal operation of the actual system, is monitored at every time. In this book, analytical redundancy-based approach is used for residual generation.

7.2.1 Analytical Redundancy Relations

Analytical Redundancy Relations (ARRs) are symbolically written constraints which are expressed in terms of known variables (measurements and inputs). They represent various compatibility conditions or constraints between a set of known process variables [98]. ARR are static or dynamic constraints which link the time evolution of the known variables when a system operates according to its normal operation model. The error or deviation from the constraint model is a residual. The objective of quantitative diagnosis is to evaluate the residuals and associate the fault symptoms with deviations of the residuals. In this book, ARR are derived from physical constraint laws expressed in the form of a bond graph model. Thus, the bond graph methodology has been exploited in this book as a tool for modeling, simulation, control analysis, and also for diagnosis.

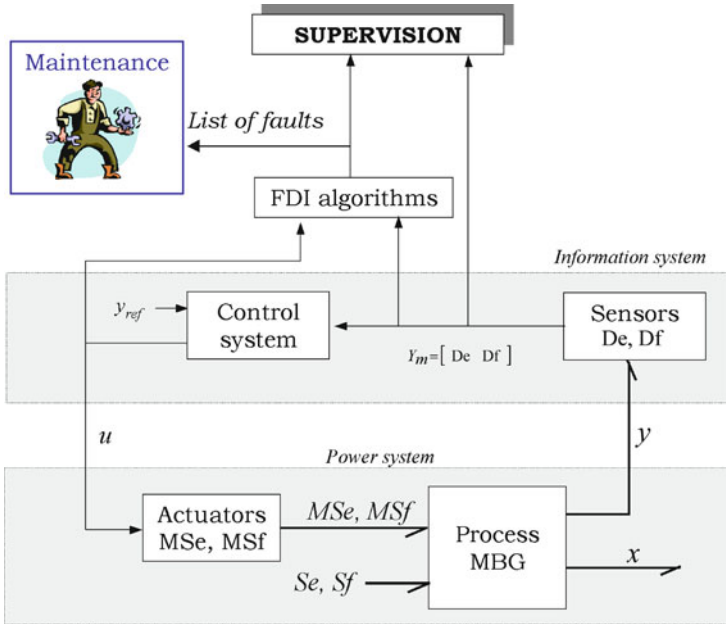


Fig. 7.2 Bond graph model-based supervision

The general schematics of bond graph model-based supervision system [88] is shown in Fig. 7.2. In a bond graph-based approach, the known or measured system variables are the sources (Se and Sf), the modulated sources (MSe and MSf), the measurements from sensors (De and Df), the model parameters (θ), and the controller outputs (u). An ARR is a constraint written as

$$ARR : f(De, Df, Se, Sf, MSe, MSf, u, \theta) = 0. \tag{7.1}$$

Usually, an ARR derived from a bond graph model represents some sort of physical law, e.g., Bernoulli equation in hydraulic domain; Newton’s law in mechanical domain; Kirchoff’s law in electrical domain. However, ARRs may not always have some physical meaning.

An ARR is an expression. When values such as parameter values and other measurements are put into this expression, the resulting numerical value of the LHS of the ARR is a residual. Thus, a residual, r , is obtained from numerical evaluation of an ARR, i.e.,

$$r = Eval[f(De, Df, Se, Sf, MSe, MSf, u, \theta)]. \tag{7.2}$$

Thus, for reliable fault detection, ARRs should be well designed. This depends on the choice and placement of sensors [88]. Well-designed ARRs should be robust (i.e., insensitive to disturbances), sensitive to faults and structured (i.e., only a subset of the

ARRs is not satisfied for a specific fault and thus allowing recognition of its origin). Structurally independent ARR's are those which cannot be algebraically constructed from other ARR's. Each structurally independent ARR has a unique (fault) signature.

7.2.2 Fault Signature Matrix

A Fault Signature Matrix (FSM), S , describes the structural sensitivity of each residual to various faults in physical devices, sensors, actuators, and controllers [97, 114]. Thus, matrix S forms a structure that links the discrepancies in components to changes in the residuals. The elements of matrix S are determined from the following analysis:

$$S_{ji} = \begin{cases} 1, & \text{if the } i\text{th residual is sensitive to faults in the } j\text{th component;} \\ 0, & \text{otherwise.} \end{cases} \quad (7.3)$$

A component's fault is monitorable (in other words its monitorability index $M_b = 1$) if at least one residual is sensitive to it. The alarm interpretation or fault isolation is done using the binary FSM. A fault in a component/variable can be isolated (or its isolatability index $I_b = 1$) only when it is monitorable and its fault signature is different from fault signatures of all other variables/components.

7.2.3 Coherence Vector

The residuals (evaluation of the ARR's by using the actual sensor data and the process parameters) are used to detect the faults in the process. The signal treatment and feature extraction followed to decide which residuals have deviated from normal operation is called the decision procedure. The type of decision procedure used to supervise a system is usually system specific. At any point of time, evaluation of ARR's gives values of residuals at that time. These residual values are then passed through a decision procedure. The decision procedure may be different for different residuals, e.g., function Θ_i for the i th residual. The output of Θ_i function is a binary number c_i , i.e., 1 (TRUE) or 0 (FALSE), where 0 indicates normal behavior and 1 indicates abnormal system behavior. This binary number is called the alarm state. The elements, c_i ($i = 1 \dots n$) of the binary coherence vector $C = [c_1, c_2, \dots, c_n]$ are determined periodically (as per sampling frequency) and are used to generate the alarm conditions. Thus, $C = [\Theta_1(r_1), \Theta_2(r_2), \dots, \Theta_n(r_n)]$. Robust decision procedures minimize misdetection and false alarms by treating the residual noises. In the simplest of cases, a common decision procedure called fixed threshold test (Θ) can be applied on each residual, r_i , as follows:

$$c_i = \Theta(r_i) = \begin{cases} 1, & \text{if } |r_i| > \delta_i; \\ 0, & \text{otherwise.} \end{cases} \quad (7.4)$$

where the threshold, δ_i , is fixed a priori through experience. Note that to account for modeling uncertainties, process and measurement noises, etc. these thresholds may be adaptive, i.e., functions of inputs, measurements and time [4, 5, 19, 21, 22, 26, 42, 81, 91, 102, 103].

The coherence vector C is calculated at every step and a fault is detected when $C \neq [0, 0, \dots, 0]$, i.e., at least one residual indicates abnormal system behavior. The coherence vector C is then matched with the rows of the binary fault signature matrix S to isolate the fault.

7.3 Bond Graph Model-Based Diagnosis

Obtaining ARR_s in closed symbolic form, even when they are well-known physical laws, is difficult because the elimination of unknown variables from the mathematical model of the system is not a trivial task [20, 90]. The causal path in a bond graph model offers a convenient approach to solution of this problem. The procedure for deriving ARR_s from bond graph models is well detailed in the literature [71]. In the following, we briefly explain that procedure.

In bond graph terminology, we have two kinds of sensors: effort sensor or detector of effort (De element) and flow sensor or detector of flow (Df element). We further introduce a sensor element, Ds, which measures a signal without qualitatively assigning the nature of signal, i.e., effort or flow, to the device. The process of deriving constraints or ARR_s is based on inversion of sensor causalities, i.e., the measurements which are outputs in a normal bond graph model used for simulation become inputs to the constraint model used for diagnosis, i.e., the inputs to the diagnosis model are the measured signals from the actual plant. The ARR_s are the conjugate power variables of the measured variables in the bonds connected to sensors [71]. This is schematically illustrated in Fig. 7.3. There are three sensors (two De elements and one Df element) in the model given in Fig. 7.3a and the measurements are y_1 , y_2 and y_3 . The causality of those sensor elements are inverted in Fig. 7.3b and the signal bonds connected to the sensors have been changed to power bonds. This is equivalent to replacement of De elements by Se elements and Df elements by Sf elements. The former model is called a behavioral or forward model and the latter model is called a diagnostic model. From Fig. 7.3b, the ARR_s are derived as the equations for power variables f_1 , f_2 and e_3 . Note that all storage elements (I- and C-elements) in Fig. 7.3b are in derivative causality and hence no integration appears in any of the ARR_s. Furthermore, the number of ARR_s is equal to the number of sensors in the model.

Sometimes, sensor causalities cannot be inverted because that would cause violation of the causality rules at a junction. A sensor whose causality cannot be inverted is usually a hardware redundancy, i.e., there is/are one or more sensor(s) whose output can be used to obtain the measurement of the redundant sensor [88]. A formal framework for derivation of ARR_s and evaluation of residual structures is given in [83]. In a diagnostic bond graph [87], a set of substitutions is performed in the bond graph

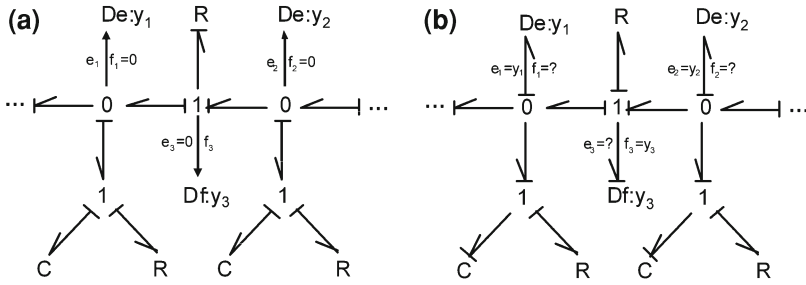


Fig. 7.3 **a** A part of a bond graph model with three sensors and **b** the bond graph model with inverted sensor causality

model after inverting the sensor causality. Such a bond graph model can be used for direct evaluation of residuals.

7.4 Example Application: An Autonomous Vehicle

Autonomous vehicles [3, 94] have been used for various applications such as material transfer in industries and ports. There is significant ongoing research focused on autonomous vehicles with additional sensory system to develop autonomous guidance systems on general terrains [92]. These systems use sophisticated sensors that can evaluate the surroundings and plan their path. The reconfigurability of autonomous vehicle is an important issue, as a faulty vehicle may hamper the continuous flow of material in an industry. Therefore, active research is going on in developing hybrid fault adaptive control of mobile robots [51]. This example concerns a model-based approach for fault detection and fault tolerant control (reconfiguration) of an autonomous vehicle.¹

7.4.1 System Description

An autonomous vehicle called RobuCar is shown in Fig. 7.4. It is an overactuated vehicle with four actuated traction wheels and two actuated steering systems. The vehicle length is 1.836 m, width is 1.306 m, and height is 0.616 m. It has weight of approximately 310 kg including the batteries. It can have maximum velocity of 18 km/h (5 m/s). Each wheel is driven by a switched DC motor with a power rating of 900 W, internal resistance of 1.6 Ω, and the input is 48 V. The output is coupled with a planetary gear system with a gear ratio of 1:13.

¹ This example is taken from these authors' previous work published in [73].

Fig. 7.4 The RobuCar at LAGIS, University of Lille1

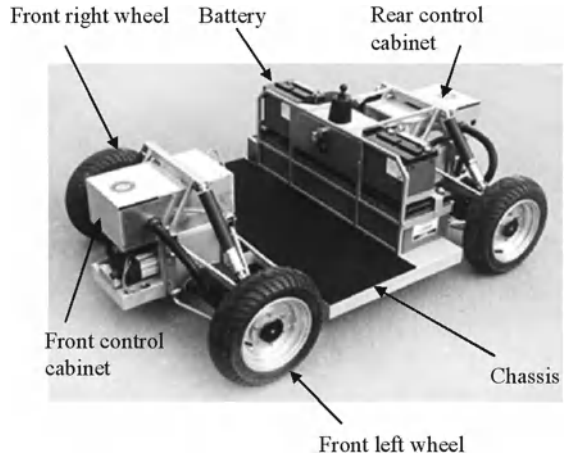
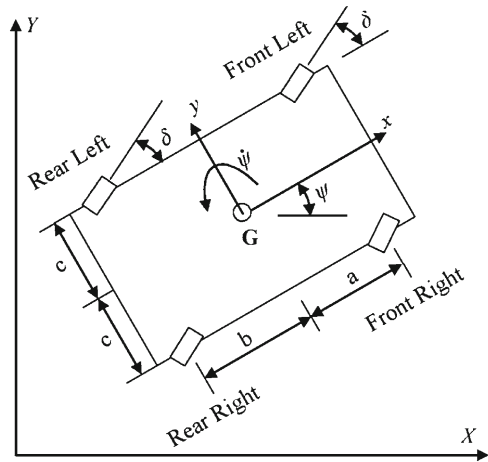


Fig. 7.5 Planar schematic (top view) of autonomous vehicle



The vehicle is equipped with an inertial sensor to measure its longitudinal, lateral, and yaw velocities. Moreover, the current drawn by each motor is measured by a Hall-effect sensor and each wheel’s rotation is measured through an encoder.

A two-dimensional model of the autonomous vehicle is shown in Fig. 7.5 where $X-Y$ is the inertial frame and $x-y$ is the body fixed frame attached to the autonomous vehicle. Point G is the center of mass (CM) of the vehicle. The locations of the wheels from the CM of the vehicle are shown in Fig. 7.5. The wheel coordinates with respect to body fixed frame $x-y$ are: (a, c) for front left, $(a, -c)$ front right, $(-b, c)$ for rear left, and $(-b, -c)$ for rear right. At any instant the orientation of body-fixed x -axis with respect to the inertial X -axis is ψ , and δ_j is the steering angle of the j th wheel. The following modeling assumptions are made: (i) the vehicle moves in a plane surface, (ii) the vehicle is controlled using steering, (iii) each wheel of autonomous vehicle is independently driven.

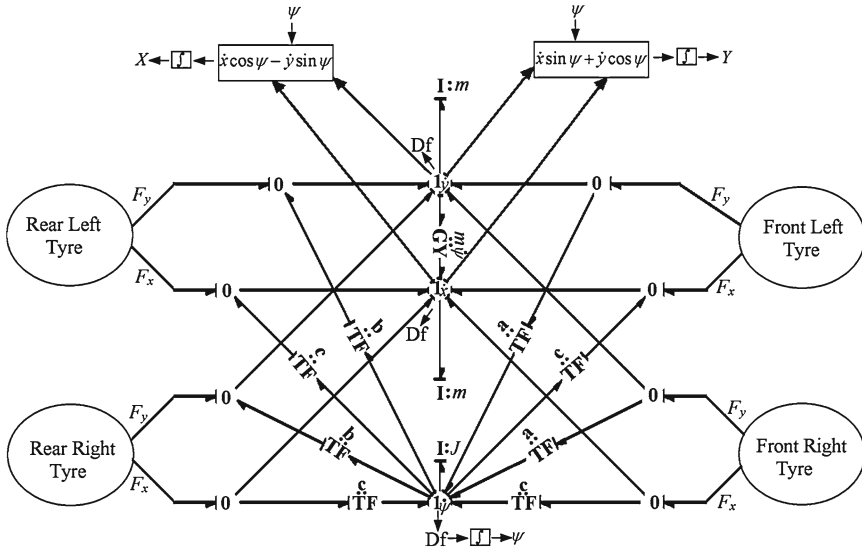


Fig. 7.6 Bond graph model of the autonomous vehicle

7.4.2 Bond Graph Model

The bond graph model of the autonomous vehicle (RobuCar) for directional handling is shown in Fig. 7.6. It is constructed directly from kinematic relations. Note that bond graph junction structure is power conservative because of which the dynamics is automatically represented correctly. The bond graph model in Fig. 7.6 is constructed in line with the model given by Hrovat [45]. In Fig. 7.6, m is the mass of the vehicle and J is the polar moment of inertia of the vehicle. \dot{x} and \dot{y} are the longitudinal and lateral velocities of the vehicle CM in the body-fixed frame, and $\dot{\psi}$ is the angular velocity of the vehicle. The longitudinal, lateral, and yaw motion of the CM of the vehicle are appropriately transformed to generate the longitudinal and lateral velocities of the wheel axles. The vehicle's motion is also transformed to the inertial frame for plotting purposes. F_x and F_y represent, respectively, the force transmitted to wheels in the x and y directions. The GY element appears due to modeling in non-inertial frame. More details on the bicycle model are given in Chap. 6.

The bond graph model of the motor and the wheel is shown in Fig. 7.7, where i represents the current through rotor of motor, μ is the torque constant of motor, J_w is the polar moment of inertia of wheel about its rotational axis, and r is the radius of wheel. The longitudinal and lateral velocities of the wheel axle in conjunction with wheel's spinning speed generate the longitudinal and lateral slip velocities.

An R field, as shown in Fig. 7.7, then generates the cornering and driving forces which are further transformed through the same bond graph junction structure to

Fig. 7.7 Bond graph model of actuated wheels

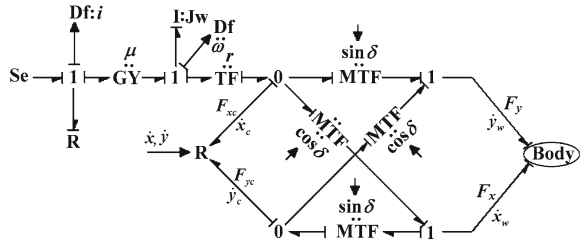


Table 7.1 Parameter values of RobuCar

Symbol	Parameter	Value
m	Mass of vehicle	390 kg
J	Polar moment of inertia of vehicle	160 kg m ²
a	Distance as shown in Fig. 7.5	0.96 m
b	Distance as shown in Fig. 7.5	0.88 m
c	Distance as shown in Fig. 7.5	0.65 m
V_s	Motor supply voltage	48 V
i_m	Motor torque constant	0.106 Nm/A
J_w	Polar moment of inertia of wheel axle	1.85 kg m ²
R_m	Motor resistance	1.6 Ω
r	Wheel radius	0.22 m
C	Cornering coefficient	1000 N
K_{p1}	Gain parameter in Eq. 7.6	0.2
K_{d1}	Gain parameter in Eq. 7.6	1.0
K_{p2}	Gain parameter in Eq. 7.6	0.1
K_{d2}	Gain parameter in Eq. 7.6	0.001

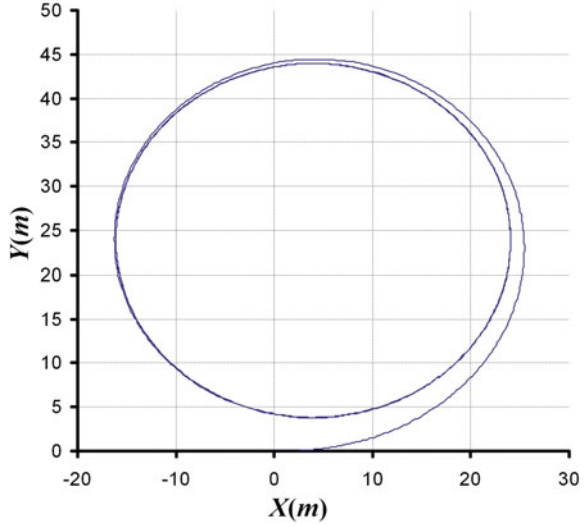
generate the forces and moments on the vehicle body. Assuming small side slip, the constitutive relation for the R field is given as [66, 67, 89]

$$\begin{aligned}
 F_{cx} &= \Phi_T(\dot{x}_c, \dot{x}, N) = \Phi_T(\omega r - \dot{x}_w \cos \delta - \dot{y}_w \sin \delta, \dot{x}, N), \\
 F_{cy} &= C\alpha = (C/\dot{x})\dot{y}_c = (C/\dot{x})(-\dot{x}_w \sin \delta + \dot{y}_w \cos \delta),
 \end{aligned}
 \tag{7.5}$$

where F_{cx} is the generated driving force, F_{cy} is the cornering or lateral force, N is the normal reaction at the wheel, δ is the steering angle, ω is the wheel spinning speed, C is the cornering coefficient [66, 67, 89] for a pneumatic tyre with small side slip, \dot{x}_w and \dot{y}_w are, respectively, the longitudinal and lateral velocities of the wheel axle, \dot{x}_c and \dot{y}_c are, respectively, the longitudinal and lateral velocities of the wheel contact patch with the road, and Φ_T is a function, which is experimentally determined in line with Pacejka’s formulation [25, 72].

This model is validated through simulation with the parameter values given in Table 7.1. It is found from the results shown in Fig. 7.8 that at the peak vehicle operating speed (5 m/s) and a constant front steering angle of 0.1 rad, the vehicle moves in a steady circular path of radius of 20m, which means that there is an understeering characteristic because the vehicle should move on a circle of radius of 18.4m under neutral steer. Therefore, the vehicle cannot be controlled by developing

Fig. 7.8 Vehicle CM trajectory for steering angle of 0.1 rad



a control law from purely kinematic considerations, e.g., from instantaneous center of rotation formulation [51, 108]. This is why a control law given in [53] for hybrid positional and directional control is used. The control law adjusts the steering angle as follows:

$$\delta = K_{p1}(y_{ref} - y_{act}) + K_{d1}(\dot{y}_{ref} - \dot{y}_{act}) + K_{p2}(\psi_{ref} - \psi_{act}) + K_{d1}(\dot{\psi}_{ref} - \dot{\psi}_{act}) \tag{7.6}$$

7.4.3 Generation of Fault Indicators

First of all, the sensors in the bond graph models shown in Figs. 7.6 and 7.7 are dualized into sources (i.e., sensor causalities are inverted) and the model is assigned preferred differential causality. The bond graph model of the wheel with inverted sensor causalities is shown in Fig. 7.9. There are two flow sensors in each wheel model: one measures motor current and the other measures wheel angular velocity. The effort variables in the bonds connected to these sensors in inverted causality are the ARR for this part of the system.

Let us consider the left rear wheel. For the current sensor in inverted causality, the effort in the bond is given as

$$e = (Se : V_s) - R_m (Df : i_m) - \mu (Df : \omega) . \tag{7.7}$$

The above relation is expressed in terms of known system variables, i.e., sources, measurements, and parameters of the system. Thus, it is an ARR which is formally written as

Table 7.2 Fault signature matrix (FSM) of RobuCar

Component	Residuals											M_b	I_b
	r_1	r_2	r_3	r_4	r_5	r_6	r_7	r_8	r_9	r_{10}	r_{11}		
Rear left motor	1	1	0	0	0	0	0	0	0	0	0	1	1
Rear left wheel	0	1	0	0	0	0	0	0	0	0	0	1	1
Rear right motor	0	0	1	1	0	0	0	0	0	0	0	1	1
Rear right wheel	0	0	0	1	0	0	0	0	0	0	0	1	1
⋮	⋮	⋮	⋮	⋮	⋮	⋮	⋮	⋮	⋮	⋮	⋮	⋮	⋮
Vehicle body	0	0	0	0	0	0	0	0	1	1	1	1	1

subscript j enumerates the wheels, $F_{x,j}$ and $F_{y,j}$ are the forces acting in x and y directions on the j th wheel center, Φ_T is a function defining the experimentally obtained longitudinal slip forces, d_j and e_j are the moment arms of the forces about the mass-center of the vehicle taken with appropriate signs, e.g., $d_1 = c$ and $e_1 = b$ where the rear left wheel is enumerated as wheel number 1. These 11 ARR are evaluated with sensor data for FDI and if any one of the ARRs is abnormal, then an alarm is generated.

7.4.4 Fault Isolation

Some form of technological specifications are always provided while designing the FDI system. One of them is the robustness of the components. Here, we will assume that the sensors in the RobuCar are robust, i.e., they do not fail. Then, the faults in all other items other than the sensors will be monitored. Another technological specification is that only a single component may fail at a time, i.e., the chances of failure of two components at the same time is nearly zero. This is referred to as the single fault hypothesis. If more than one component faults have to be detected and isolated at a time, the FDI procedure has to be designed differently, e.g., structured residual approach, trend analysis [85], parameter estimation [82], etc.

The ARRs given in Eqs. (7.8–7.10) are structurally analyzed to generate the FSM or the binary fault sensitivity table as shown in Table 7.2. For example, the variables appearing in ARR1 given in Eq. 7.8 are V_s, R_m, i, μ and ω . Out of these variables, V_s, i and ω are measured variables associated with sensors and sources. Thus, the monitored variables are R_m and μ both of which belong to component motor. Thus, motor fault (any fault, either in R_m or μ) influences residual r_1 . No other faults influence residual r_1 . Likewise, parameters associated with motor also appear in ARR2 given in Eq. 7.9. In addition, ARR2 also contains wheel and steering parameters $J_w, r, C,$ and δ . Thus, residual r_2 is influenced by fault in wheel (tire pressure), wheel road interface (change in cornering coefficient), and the motor. Likewise, fault symptoms for all other components is determined and represented in the FSM.

The sensitivity of a residual to a component fault is shown as 1 in Table 7.2 and insensitivity is shown as 0. When a components fault influences at least one residual then that fault is said to be monitorable (indicated by monitorability index $M_b = 1$),

i.e., at least one residual will show abnormal deviation upon occurrence of that fault. A specific fault is isolatable (indicated by isolatability index $I_b = 1$) when the deviation patterns in residuals are unique in response to that specific fault. This is equivalent to uniqueness of the fault signature, i.e., the entries in a row of Table 7.2 corresponding to a fault is different from all other rows in the FSM.

From Table 7.2, it is found that each fault has a unique fault signature and thus all faults are both monitorable and isolatable. However, note that we have not considered sensor faults in our technological specification. If sensor faults are also included in the FSM then we cannot isolate any fault. In fact, if sensor faults are to be isolated then redundant sensors should be added to the system. Such sensor placement problems are discussed in [85, 88].

7.4.5 Fault Accommodation Through Reconfiguration

A process may continue to operate as long as all of its critical faults can be detected and it remains observable and controllable. A reconfigurable system usually has more number of sensors and actuators than desired. The ARRs and the FSM must be modified every time a system is reconfigured. Moreover, the functional services offered by the components are organized into coherent subsets, called Operating Modes (OM), where each OM is associated to a bond graph model [68]. An automaton specifies the conditions to change from one OM to another [88].

Reconfiguration is possible, only when for failure of one or more base device(s), there are corresponding redundant devices available in good health. When two or more devices are redundant with a common base device, they are mutually redundant. The coupling between the supervisory layer and the base devices of the Robu-Car, considering only the actuator inventory, is represented by the tree-structure in Fig. 7.10.

In Fig. 7.10, basic functionalities required for system operation are listed and the associated devices needed to perform those functions are linked in a tree-structure. Where more than one device is available to perform the same task, branches are numbered indicating a weight or a hierarchical preference.

Theoretically, a process can operate normally, as long as at least one device is available for each basic function. When a device fails, the branch associated with it is removed and the system is reconfigured using the next device, according to the defined hierarchy, e.g., when rear left motor fails (see the \times marks in Fig. 7.10) during a lane change mission, the control law is reconfigured to the next preferred operating mode ($OM = 3$), i.e., a front wheel drive system with rear wheel steering.

7.4.6 Fault Tolerant Control

Fault Tolerant Control (FTC) relates to recovery from fault such that the system is controlled under actual constraints without replacing part(s) of the faulty system

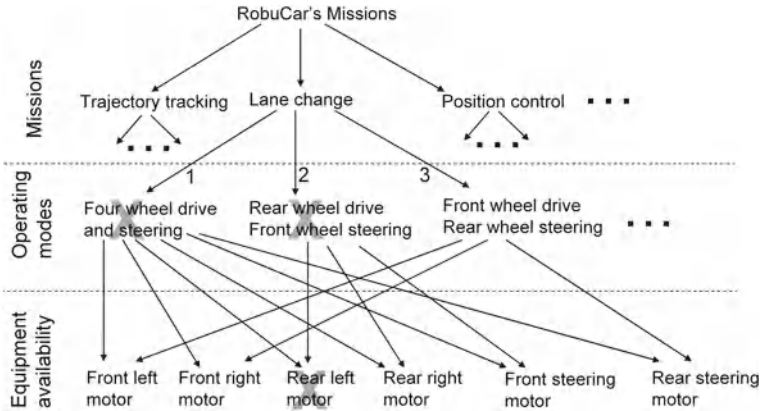


Fig. 7.10 Management of operating mode and equipment availability

[10, 48]. FTC approaches can be classified into two categories: passive approach (e.g. robust control) and active approach (e.g. adaptive control). Active FTC, where plant faults are diagnosed and estimated and subsequently the controller is redesigned for fault accommodation [88], and passive FTC through robust overwhelming control can be both implemented very elegantly by using bond graph model-based approach [88]. However, in this section, we will limit our attention to fault accommodation through reconfiguration.

7.4.7 Simulation Results

Two fault scenarios are considered here. The initial control configuration is chosen as rear wheel drive with front wheel steering and a pre-existing fault in the rear wheel steering (this information is stored in equipment availability database). In the first fault scenario, the RobuCar starts from the rest and is supposed to accelerate till it attends its peak speed while traveling along a straight line. A fault is simulated by disconnecting the power supply to the rear left wheel motor. This causes the vehicle to deviate from its straight line trajectory.

The fault detection is done by looking at the residuals. In Fig. 7.11, only the first two residuals which are sensitive to this fault are shown. Other residuals are insensitive to rear left wheel motor fault. During the fault, a non-null fault signature $C = [1 \ 1 \ 0 \ \dots \ 0]$ is generated. This fault signature has a unique match in Table 7.2, from which the rear left wheel motor fault is isolated.

Once this fault is isolated, the equipment availability database is searched and the reconfiguration automata changes the control law to a new configuration with front wheel drive and front wheel steering. Simultaneously, both the rear wheels are disengaged from the drive. Once all these actions are performed, the vehicle starts

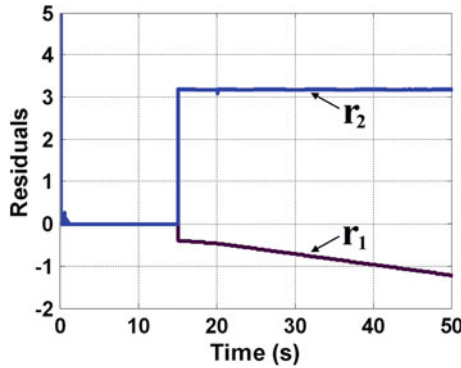


Fig. 7.11 Variation of residuals with time for the first fault scenario

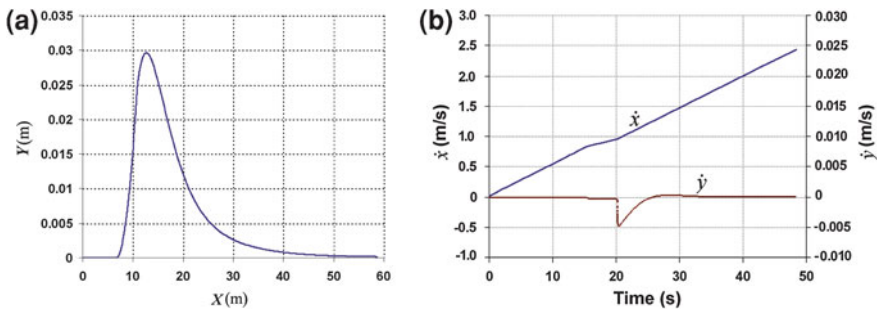


Fig. 7.12 Results of the first fault scenario. **a** Center of mass position of autonomous vehicle in X and Y frames in the *top view*. **b** Vehicle center of mass velocity in x and y frames versus the time

to follow its desired path as shown in Fig. 7.12a. The corresponding velocities are shown in Fig. 7.12b. The lateral shift due to the locked-up wheel is recovered in this process.

In the second fault scenario, a lane change operation is simulated with rear wheel drive and front wheel steering as the initial control configuration and it is assumed that all the components are in good health. The vehicle starts from rest and is supposed to move to a lane 0.5 m to the left of its initial path. During this operation, we simulated a fault in the rear left wheel motor. By following the aforementioned structural fault detection and isolation methods, the fault is isolated and a new control configuration with front wheel drive and rear wheel steering was selected. From the results shown in Fig. 7.13a, it is evident that the vehicle performs the lane change operation without any gross anomalies if the time lag between the occurrence of the actual fault and reconfiguration is within acceptable limits. The actual fault is introduced at 15 s which is not evident from the vehicle position given in Fig. 7.13a. However, the sharp change in the acceleration is clearly evident in Fig. 7.13b. The RobuCar is reconfigured at 20 s which causes a sharp change in the lateral velocities. The reconfigured system

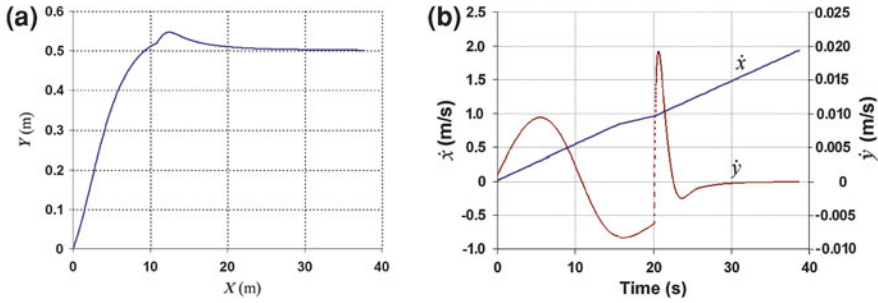


Fig. 7.13 Results of the second fault scenario. **a** Center of mass position of autonomous vehicle in X and Y frame in the *top view*. **b** Vehicle center of mass velocity in x and y frame versus the time

follows the given control set-points with a slightly higher overshoot in the lateral direction.

The overactuated RobuCar vehicle considered here offers many reconfiguration options. The directional handling performance of the vehicle under different actuator combination situations is used to rank the reconfiguration options in a hierarchical order of preference. This information is then stored in a decision support system (a knowledgebase) as a tree-structure and upon detecting and isolating fault(s) in component(s) of the vehicle, an automata selects the appropriate reconfiguration option. The fault detection and isolation is implemented by structural analysis of the residuals, which are evaluated with the ARRs generated from the bond graph model of the vehicle.

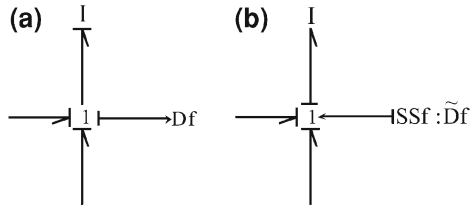
7.5 Diagnosis of Uncertain Systems

Mechatronic systems are composed of elements belonging to multiple energy domains (mechanical, electrical, etc.). The improvement of their safety depends on the fault detection and isolation (FDI) procedures, which mainly consist of the comparison of the actual system behavior with the reference describing the normal operation for the case of fault detection, or describing different kinds of faults for the case of fault isolation. The fault diagnosis scheme is composed of characterization and decision steps. The presence of false alarm, non-detection, and delay in fault detection, cause degradation of FDI performances. This latter is principally due to imperfect knowledge of the real value of the system parameters and their random variations.

Diagnosis of uncertain systems has been the subject of several recent research works [21, 24, 43, 46, 78]. This interest is reflected by the fact that physical systems are complex and non-stationary and require more robust and precise diagnosis.

This section deals with the generation of fault indicators and residual thresholds in the presence of parameter uncertainties by using a bond graph representation in

Fig. 7.14 **a** BG model in integral causality with a flow sensor. **b** BG model in derivative causality with a dualized flow sensor



linear fractional transformation (LFT) form (as developed in the second chapter). The bond graph model in LFT form allows the generation of Analytical Redundancy Relations (ARRs) composed of two completely separated parts: a nominal part, which represents the residuals, and an uncertain part which serves both for the calculation of adaptive thresholds and sensitivity analysis. The residuals' sensitivity analysis, which is based on the fault detectability indices, is used for residual evaluation. The developed algorithms are applied on an electromechanical test bench system for online fault detection and isolation. The research results have been developed in the PhD thesis supervised by two of authors: Ould Bouamama and Merzouki [23].

7.5.1 LFT Bond Graphs for Robust FDI

In a BG (as in a bipartite graph) can be defined as a set of variables $Z = K \cup X$, composed of known variables (K) associated with measured variables (De and Df) and input ones (Se, Sf, MSe, MSf), and of unknown variables $X = x_a \cup x_d \cup \dot{x}_d \cup x_i \cup \dot{x}_i$ (variables associated with all the elements of a BG). a, d, i refer respectively to algebraic, derivative and integral constraints.

The determination of ARRs on a bond graph model is done by elimination of unknown variables contained in the structural constraints of junctions 0 and 1. The equations of power balance on the junctions constitute the candidate ARRs [69, 87].

To avoid initial conditions problem which are not known in real processes, ARRs are directly generated from the BG model in derivative causality. Dualizing effort (or flow) detector transforms it into a signal source $SSe = \tilde{De}$ (or $SSf = \tilde{Df}$) modulated by the measured value, as illustrated in Fig. 7.14. This imposed signal is the starting point for the elimination of unknown variables. Thus, models in integral causality of Figs. 7.14a and 7.15a are aimed at physical simulation while those in derivative causality of Figs. 7.14b and 7.15b are used for ARRs generation.

From the BG model of Figs. 7.14b and 7.15b we can write:

$$SSf + \sum b_i \cdot e_i = 0 \tag{7.13}$$

$$SSe + \sum b_i \cdot f_i = 0$$

Fig. 7.15 **a** BG model in integral causality with an effort sensor. **b** BG model in derivative causality with a dualized effort sensor

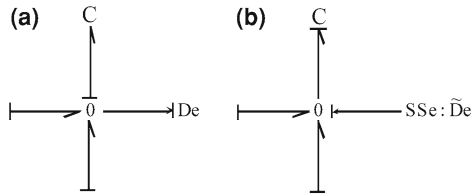
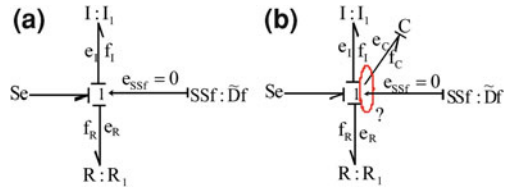


Fig. 7.16 **a** Bond graph model causally correct after dualizing the sensor. **b** Bond graph model with a conflict of causality (under-constrained)



with i the number of the bonds connected to the junction and $b_i = \pm 1$ following the half-arrow orientation.

ARRs generation consists in eliminating unknown variables e_i and f_i by following the causal path from a known variable to an unknown one. However, the elimination of the unknown variable on the considered causal constraint is not always possible. In the algebraic case where the equation is nonlinear, calculating the variable can be done only in one way.

Consider first a junction with I and R elements (Fig. 7.16a).

By dualizing the flow detector (on the model of Fig. 7.16a) which becomes a flow source SSf , I element can be assigned with derivative causality. The ARR of Eq. (7.14) is then derived by eliminating the unknown variables in junction 1 using causal paths from known variable SSf (imposed) to the unknown variables

$$Se - I \frac{dSSf}{dt} - R \cdot SSf = 0 \tag{7.14}$$

In the presence of a C element (Fig. 7.16b), a conflict of causality appears on the bond graph when trying to put both dynamic elements in derivative causality. It means that C -element has to stay in integral causality. ARR will depend on initial effort $e_{C(0)}$.

7.5.2 Generation of Robust Residuals

7.5.2.1 General Form of Uncertain ARR

The generation of robust analytical redundancy relations from a bond graph model proper and observable is summarized by the following steps:

1st *step*: Try to assign a preferred derivative causality on the nominal BG; if it is possible (the model is over-constrained), then continue the following steps;

2nd *step*: Build the LFT BG model;

3rd *step*: Derive ARR_s by writing junction equations, as:

$$\sum b_i \cdot f_{i_n} + \sum Sf + \sum w_i = 0$$

for a junction 0 and:

$$\sum b_i \cdot e_{i_n} + \sum Se + \sum w_i = 0$$

for a junction 1.

The unknown variables are e_{i_n} and f_{i_n} .

4th *step*: Eliminate the unknown variables by following the causal paths from sensors and sources to unknown variables;

5th *step*: Write the uncertain ARR_s as follows:

$$RRA : \Phi \left(\sum Se, \sum Sf, De, Df, \tilde{De}, \tilde{Df}, \sum w_i, R_n, C_n, I_n, TF_n, GY_n, RS_n \right) = 0 \quad (7.15)$$

where TF_n and GY_n are respectively the nominal values of TF and GY moduli. R_n , C_n , I_n and RS_n are the nominal values of elements R , C , I , and RS . $\sum w_i$ is the sum of modulated inputs corresponding to uncertainties on the elements (See Chap. 2) related to the considered junction.

7.5.2.2 Generation of Adaptive Thresholds

The generated ARR consists of two parts well separated due to the use of LFT model, a nominal part noted r :

$$r = \Phi \left(\sum Se, \sum Sf, De, Df, \tilde{De}, \tilde{Df}, R_n, C_n, I_n, TF_n, GY_n, RS_n \right) \quad (7.16)$$

and an uncertain part noted $b = \sum w_i$ with:

$$w_i = \Phi \left(De, Df, \tilde{De}, \tilde{Df}, R_n, C_n, I_n, TF_n, GY_n, RS_n, \delta_R, \delta_I, \delta_C, \delta_{RS}, \delta_{TF}, \delta_{GY} \right) \quad (7.17)$$

where $\delta_R, \delta_I, \delta_C, \delta_{RS}, \delta_{TF}, \delta_{GY}$ are respectively the values of multiplicative uncertainties on the elements (See Chap. 2) $R, I, C, RS, TF,$ and GY .

The uncertain part of the ARR is used to generate adaptive thresholds under an envelope form that contains residuals in absence of faults.

Parameter uncertainty can be defined as a slight deviation of the parameter from its nominal value, without any effect on the functioning of the system. It may be constant or variable and may vary randomly in a positive or in a negative sense.

From Eqs. (7.15–7.17), it gives

$$r + \sum w_i = 0 \Rightarrow r = - \sum w_i$$

Let us define a threshold of the residual noted a as:

$$a = \sum |w_i| \quad (7.18)$$

with $r \leq a$.

Thus an adaptive threshold of the residual is generated in the form of an envelope (Eq. 7.19):

$$-a \leq r \leq a \quad (7.19)$$

The use of absolute values to generate the thresholds of normal operation ensures the robustness of this algorithm to false alarms. To control the non-detections and delays in the detection of the faults, sensitivity analysis of the residuals to faults and uncertainties allows the estimation of the detectable fault values.

7.5.3 Sensitivity Analysis

Several methods of model-based robust FDI have been developed in recent years [2, 8, 43, 52, 115], for residual generation and evaluation. Evaluation methods depend on the approaches used for residual generation, and assumptions on the nature and type of uncertainties in the model. If we assume that uncertainties are not involved at the same frequency as faults, filtering methods are well suited. In the case where the variation of the residual is assumed normally distributed around a known mean value, statistical methods are used to generate normal operating thresholds. After a judicious choice of a confidence degree, it is possible to calculate the probability of false alarms and non-detections [7]. Parity space is used for the fault detection of sensors and actuators, where the evaluation of the residuals is performed by considering uncertainties bounded by a norm or an interval. With this method, it is difficult to find a good compromise between robustness to uncertainty and sensitivity to faults, since the elimination of the influence of uncertainties in the residual may cause insensitivity to faults, especially actuators faults [43]. Since it is often difficult to reduce or eliminate the impact of uncertainties on the residuals using the space

parity, it is useful to exploit the uncertain part of the model to derive thresholds for normal operation. Unfortunately, in case of parameter dependency, the thresholds are overvalued and likely differ, then they are usually generated by neglecting the parameter correlation.

LFT bond graph model allows to generate automatically residuals and adaptive thresholds; these thresholds provide robustness to uncertainties and are automatically adapted to changes in the operating modes of the system. The bond graph tool provides a practical solution to the problem of parameter dependency, because it is possible to track the spread of the influence of uncertainties in terms of effort or flow across the model through causal paths.

The sensitivity analysis of residuals to uncertainties and faults depends on sensitivity indices and fault detectability indices, to be defined. They allow control and improvement of diagnosis performance. In practice, the knowledge of fault detectable value allows the user to measure the damage that this fault can cause on the system, and the knowledge of uncertainties that could mask the appearance of faults may induce additional measurements to control their changes and achieve the desired performance.

7.5.3.1 Normalized Sensitivity Index

Sensitivity analysis of a residual to a parameter uncertainty can be done by deriving the uncertain part a of the ARR according to uncertainty δ_i as shown by Eqs. (7.20) and (7.21). The result is a power variable (effort or flow), derived using the nominal value of the parameter. The sensitivity of the ARRs generated from 1-junction and 0-junction are:

$$S_{\delta_i} = \frac{\partial a}{\partial |\delta_i|} = \frac{\partial (\sum |w_i|)}{\partial |\delta_i|} = \frac{\partial (\sum |\delta_i \cdot e_{i_n}|)}{\partial |\delta_i|} = |e_{i_n}| \quad (7.20)$$

$$S_{\delta_i} = \frac{\partial a}{\partial |\delta_i|} = \frac{\partial (\sum |w_i|)}{\partial |\delta_i|} = \frac{\partial (\sum |\delta_i \cdot f_{i_n}|)}{\partial |\delta_i|} = |f_{i_n}| \quad (7.21)$$

$i \in \{R, C, I, RS, TF, GY\}$ · δ_i is the multiplicative uncertainty on parameter i .

The normalized sensitivity index of the residual to a parametric uncertainty δ_i is the ratio between effort (or flow) given by the uncertainty δ_i and the effort (or flow) contributed by all the parameter uncertainties a . Thus, the sum of these indices gives:

$$\sum SI_{\delta_i} = \sum \frac{|w_i|}{a} = \frac{\sum |w_i|}{a} = 1 \quad (7.22)$$

The residual sensitivity to parameter uncertainty is proportional to the normalized sensitivity indices, i.e., the residual is most sensitive to the uncertainty that has the greatest normalized sensitivity index.

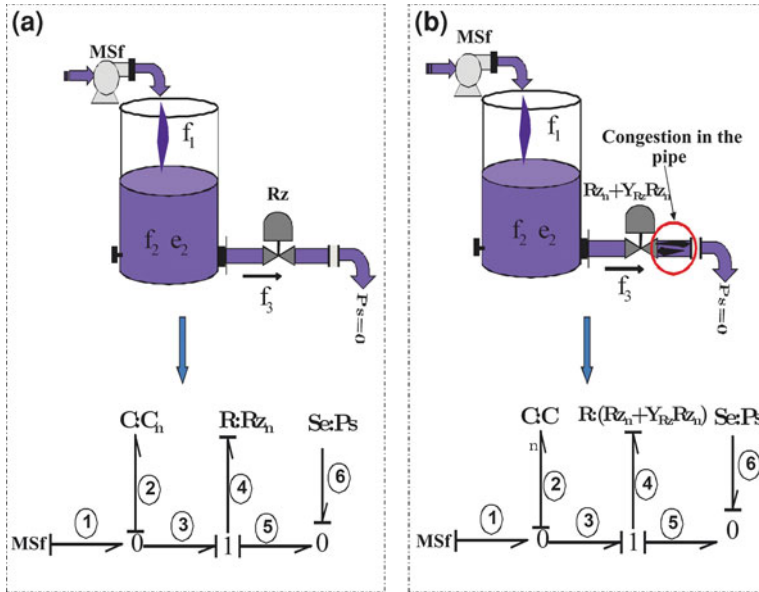


Fig. 7.17 **a** Bond graph model of a system without fault. **b** Bond graph model of a system with a parameter fault

7.5.3.2 Fault Detectability Index

In this section, we focus on two types of faults, parameter fault noted Y_i and structural fault noted Y_s . The parameter fault Y_i represents a rate of abnormal deviation of the parameter i of the system from its nominal value. It differs from the multiplicative parameter uncertainty noted δ_i , which is a slight deviation rate of the parameter from its nominal value, without any influence on the normal operating of the system. A parameter fault causes a degradation of system performances, and may cause its total failure.

An example of parameter fault is given in Fig. 7.17. The system consists of an hydraulic system: a tank filled by an external source (a pump). The fluid passes through a pipe to the outside. The bond graph model of the system without fault is given in Fig. 7.17a. Figure 7.17b shows the system with a plug in the pipe, considered as parameter fault because it changes the value of the element $R : R_z$, but does not modify the model structure. It is modeled in the same way as a multiplicative uncertainty, as a percentage of the nominal value of the parameter.

A structural fault noted Y_s corresponds to a new effort (or flow) source that causes a change in the structure of the model (leads to a leakage). Thus, the nominal model of the system is not conserved and its dynamic is altered by the presence of the fault. This difference between the system and the model generates an unbalance in the flow, mass, and energy conservation laws, calculated from junctions 0 and 1 of the bond graph model. For example, a water leakage in the tank of Fig. 7.18b is a structural

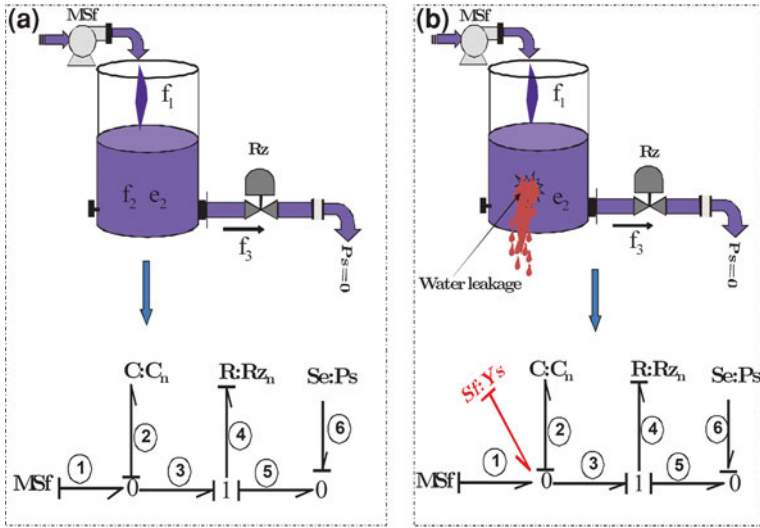


Fig. 7.18 **a** Bond graph model of a system without fault. **b** Bond graph model of a system with a structural fault

fault. It can be modeled by a flow source $Sf : Y_s$. The model structure has changed from the bond graph model of the system without fault of Fig. 7.18a.

The fault detectability index DI is defined as follows:

Definition 7.1 The fault detectability index DI is the difference in absolute value between the effort (or flow) provided by faults and those granted by all the uncertainties.

$$\begin{aligned}
 DI &= |Y_i| \cdot |e_{i_n}| + |Y_s| - a \text{ in a junction 1} \\
 DI &= |Y_i| \cdot |f_{i_n}| + |Y_s| - a \text{ in a junction 0}
 \end{aligned}
 \tag{7.23}$$

where $(|Y_i| \cdot |e_{i_n}| + |Y_s|)$ corresponds to the contribution of all faults. Y_i is the rate of detectable fault on the parameter i , Y_s is detectable value of a structural fault, and a is deducted from the uncertain part of the ARR. e_{i_n} is the effort brought by element with nominal parameter value i_n .

Proposition 7.1 *Fault detectability condition*

$$\begin{cases}
 \text{if } DI \leq 0 : \text{The fault is not detectable} \\
 \text{if } DI > 0 : \text{The fault is detectable}
 \end{cases}$$

Assumption: The effort (or flow) provided to the residual by the occurrence of multiple faults is greater than the effort (or flow) contributed to the residual by the occurrence of a single fault.



Fig. 7.19 Overview of the test bench

Given this assumption, detectable value of a fault can be calculated assuming that this fault is the only one present in the system. The detectable rate Y_i of the fault on the parameter i can be defined by one of the inequalities (7.24) and (7.25), assuming $Y_s = 0$.

- From the ARR generated from a junction 1, we deduce:

$$|Y_i| > \frac{a}{|e_{i_n}|} \tag{7.24}$$

- From the ARR generated from a junction 0, we deduce:

$$|Y_i| > \frac{a}{|f_{i_n}|} \tag{7.25}$$

Given Definition 3.1, Proposition 3.3, and Assumption 3.1, the detectable value of a structural fault Y_s can be defined by the inequality (7.26), assuming $Y_i = 0$.

$$|Y_s| > a \tag{7.26}$$

7.5.4 Application to a Mechatronic System

The mechatronic test bench of Fig. 7.19, consists of a computer, communicating with the power part of the system through DSpace acquisition card. The system consists of a DC motor which delivers a maximum power of 900 W, and equipped with an incremental encoder on its main axle.

The mechanical part of the system consists of a transmission mechanism (Fig. 7.20), defined by two moving parts linked to the engine axle by means of springs of different stiffness. The two parts can communicate through a dead zone varying between 0 and 0.5 rad. The position of the output axle is measured by an incremental encoder, which gives the relative position of the external load.

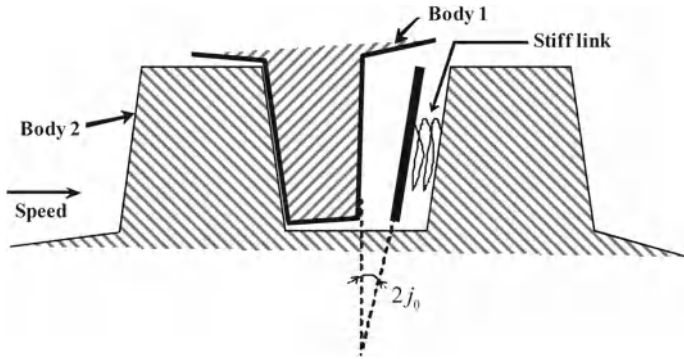


Fig. 7.20 The backlash mechanism

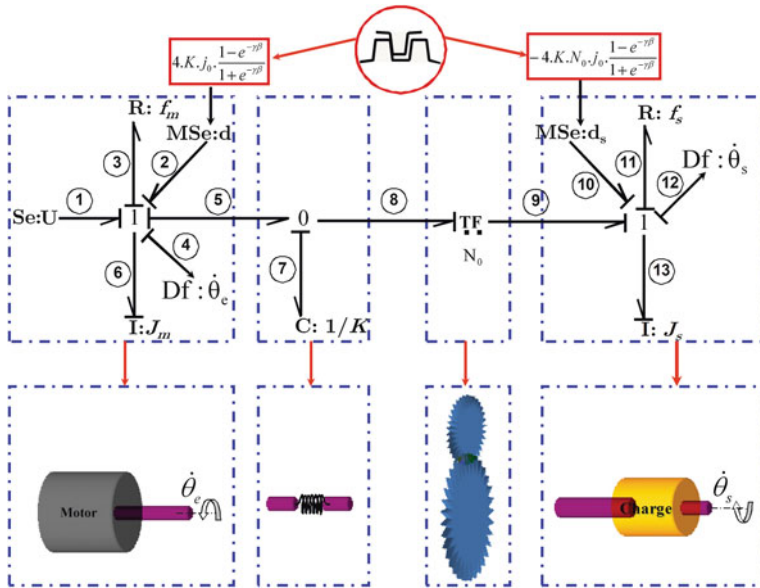


Fig. 7.21 Bond graph model of the nominal system in preferred integral causality

The bond graph model of the nominal system in integral causality is given in Fig. 7.21. The mechanical part of the engine is characterized by the viscous friction f_m and inertia J_m . Load part is characterized by friction f_s and inertia J_s . Reducer part is represented by TF , and the axles stiffness at the input and output of the reducer is represented by $C: \frac{1}{K}$ element. Modulated effort sources d and d_s are the disturbing torques caused by the presence of the backlash. Axle velocities are represented on the bond graph model of Fig. 7.21 by two flow sensors $Df: \dot{\theta}_e$ and $Df: \dot{\theta}_s$.

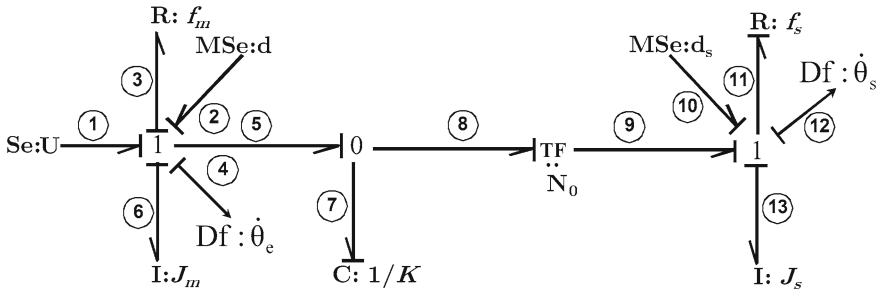


Fig. 7.22 Nominal bond graph model of the system in derivative causality

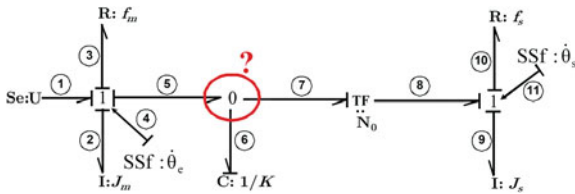


Fig. 7.23 Bond graph model of the system in derivative causality with dualized flow sensors

7.5.5 Robust FDI Procedure

1st step: Verification of structural properties of the system on the nominal bond graph model of Fig. 7.21.

On the bond graph model of Fig. 7.22, all dynamic elements are linked by causal paths to at least one detector, and all the dynamic elements I and C admit derivative causality on the bond graph model in preferred derivative causality. The model is thus proper and observable [18].

Dualization of the two sensors (Fig. 7.23), causes a problem of causality on the part of the system located before the transformer TF .

Since initial conditions are known as the real system is equipped with position detectors, we can generate two ARR from both 1-junctions, by keeping the element $C : \frac{1}{K}$ in integral causality.

2nd step: The LFT bond graph model of the test bench is given in Fig. 7.24.

Fictive inputs $w_i (i = 1 \dots 7)$ (See LFT BG modelling in Chap. 2) are linked to fictive outputs $z_i (i = 1 \dots 7)$ by the following relations:

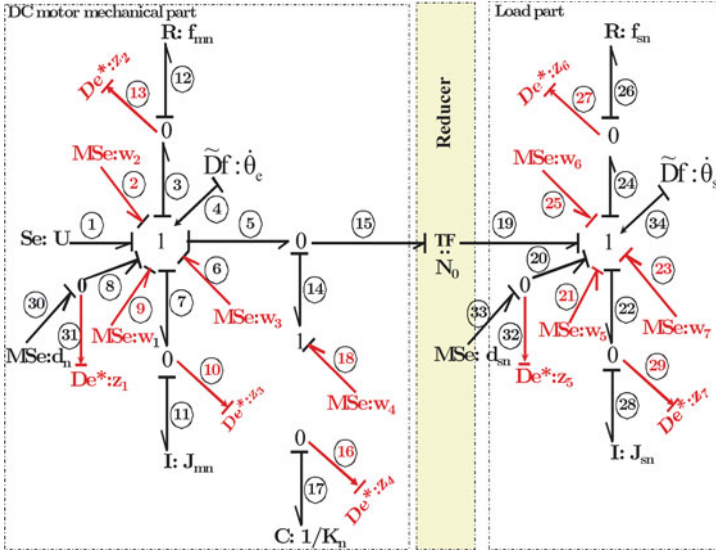


Fig. 7.24 LFT BG model of the test bench

$$\begin{cases} w_1 = (\delta_K \cdot \delta_{j_0} + \delta_K + \delta_{j_0}) \cdot z_1; z_1 = d_n \\ w_2 = -\delta_{f_m} \cdot z_2; z_2 = f_{m_n} \cdot \dot{\theta}_e \\ w_3 = -\delta_{J_m} \cdot z_3; z_3 = J_{m_n} \cdot \ddot{\theta}_e \\ w_4 = -\delta_K \cdot z_4; z_4 = K_n \cdot (\theta_e - N \cdot \theta_s) \\ w_5 = (\delta_K \cdot \delta_{j_0} + \delta_K + \delta_{j_0}) \cdot z_5; z_5 = d_{s_n} \\ w_6 = -\delta_{f_s} \cdot z_6; z_6 = f_{s_n} \cdot \dot{\theta}_s \\ w_7 = -\delta_{J_s} \cdot z_7; z_7 = J_{s_n} \cdot \ddot{\theta}_s \end{cases}$$

where δ_{J_m} , δ_{f_m} , δ_{J_s} , δ_{f_s} represent, respectively, the multiplicative uncertainties on the inertia and viscous friction of the engine and the load. δ_K is the multiplicative uncertainty on the stiffness constant.

Disturbing torques d and d_s are considered as known inputs, estimated by Eq.(7.27), and represented on the bond graph model of Fig.7.24 by two modulated inputs, with multiplicative uncertainties $\delta_d = \delta_K \cdot \delta_{j_0} + \delta_K + \delta_{j_0}$ and $\delta_{d_s} = N \cdot (\delta_K \cdot \delta_{j_0} + \delta_K + \delta_{j_0})$. The torque U and the reduction constant N_0 are considered well known.

$$\begin{cases} d = -4 \cdot K \cdot j_0 \cdot \frac{1-e^{-\gamma\beta}}{1+e^{-\gamma\beta}} \\ d_s = N \cdot d \end{cases} \quad (7.27)$$

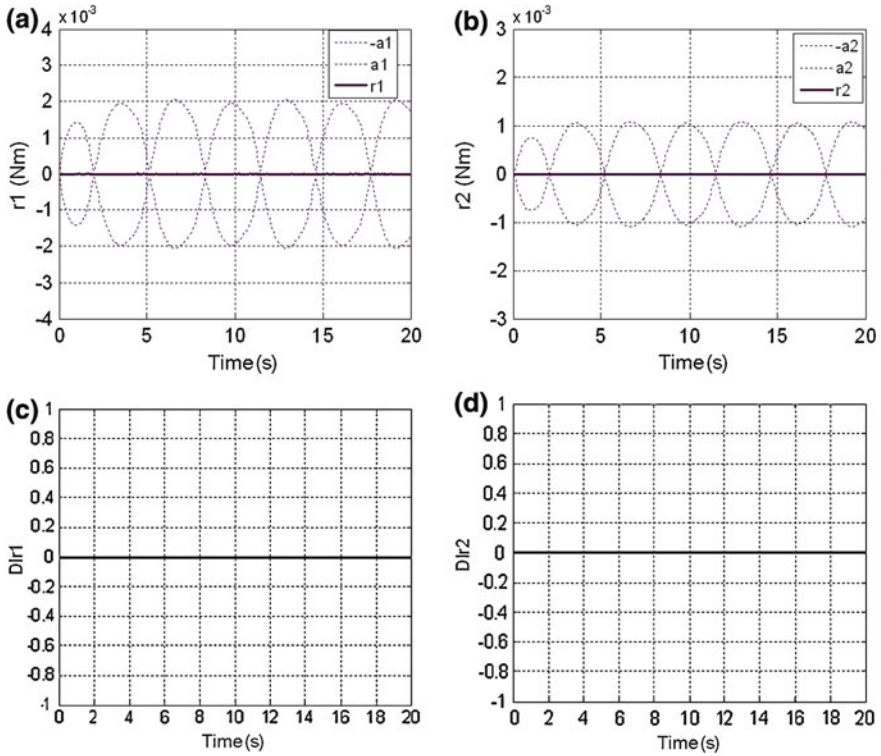


Fig. 7.25 Residuals and fault detectability indices in absence of faults and uncertainties. **a** Residual r_1 , **b** residual r_2 , **c** fault detectability index of r_1 and **d** fault detectability index of r_2

3rd step:

On the bond graph model of Fig. 7.24, ARR_s of Eq. (7.28) are generated from the energy balance on the two I-junctions.

$$ARR_1 : U - f_{m_n} \cdot \dot{\theta}_e - J_{m_n} \cdot \ddot{\theta}_e - K_n \cdot (\theta_e - N_0 \cdot \theta_s) + w_1 + w_2 + w_3 + w_4 = 0 \quad (7.28)$$

$$ARR_2 : N_0 \cdot K_n \cdot (\theta_e - N_0 \cdot \theta_s) + d_{s_n} - f_{s_n} \cdot \dot{\theta}_s - J_{s_n} \cdot \ddot{\theta}_s - N_0 \cdot w_4 + w_5 + w_6 + w_7 = 0$$

4th step: The ARR_s obtained in the previous step are composed of two separated parts, given in Eq. (7.29):

$$r_1 = U - f_{m_n} \cdot \dot{\theta}_e - J_{m_n} \cdot \ddot{\theta}_e - K_n \cdot (\theta_e - N \cdot \theta_s) \quad (7.29)$$

$$a_1 = |w_1| + |w_2| + |w_3| + |w_4| + |d_n|$$

$$r_2 = N \cdot K_n \cdot (\theta_e - N \cdot \theta_s) - f_{s_n} \cdot \dot{\theta}_s - J_{s_n} \cdot \ddot{\theta}_s$$

$$a_2 = |N \cdot w_4| + |w_5| + |w_6| + |w_7| + |d_{s_n}|$$

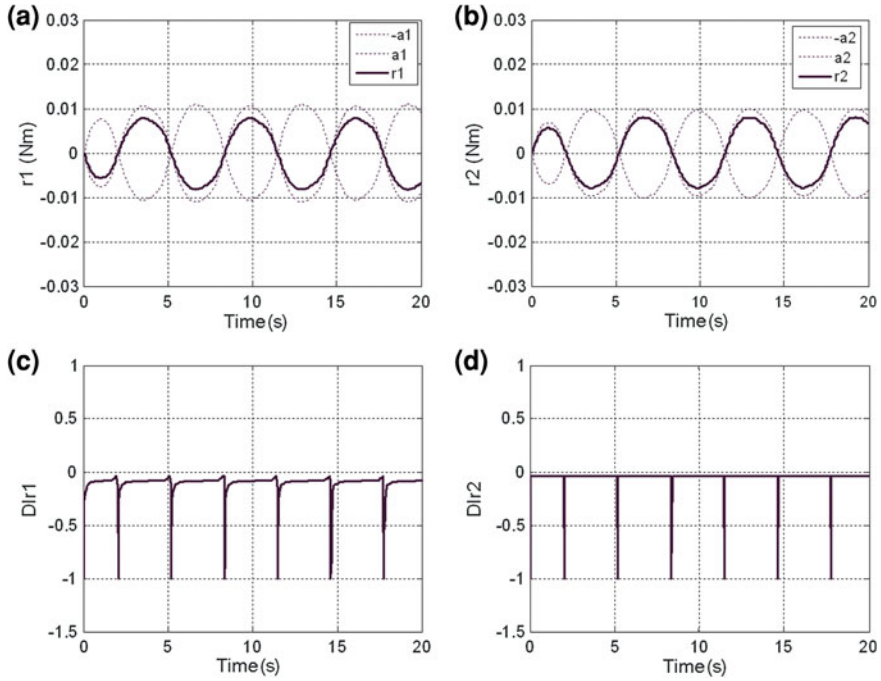


Fig. 7.26 Residuals and fault detectability indices in absence of faults and in presence of uncertainties. **a** Residual r_1 , **b** residual r_2 , **c** fault detectability index of r_1 and **d** fault detectability index of r_2

7.5.6 Simulation Results

The original backlash is considered as a model uncertainty, whose contributed efforts are estimated using the equations set (7.27), its variation cannot be associated with the variation of one of element R , I , and C of a BG model. An abnormal variation of the backlash is treated as a structural fault, its detectable value is determined using Eq. (7.23):

- Detectability index DIr_1

$$\begin{aligned}
 DIr_1 &= |Y_s| - \sum |w_i| \\
 &= |Y_s| - (|w_1| + |w_2| + |w_3| + |w_4| + |d_n|)
 \end{aligned}$$

$$DIr_1 > 0 \implies |Y_s| > (|w_1| + |w_2| + |w_3| + |w_4| + |d_n|)$$

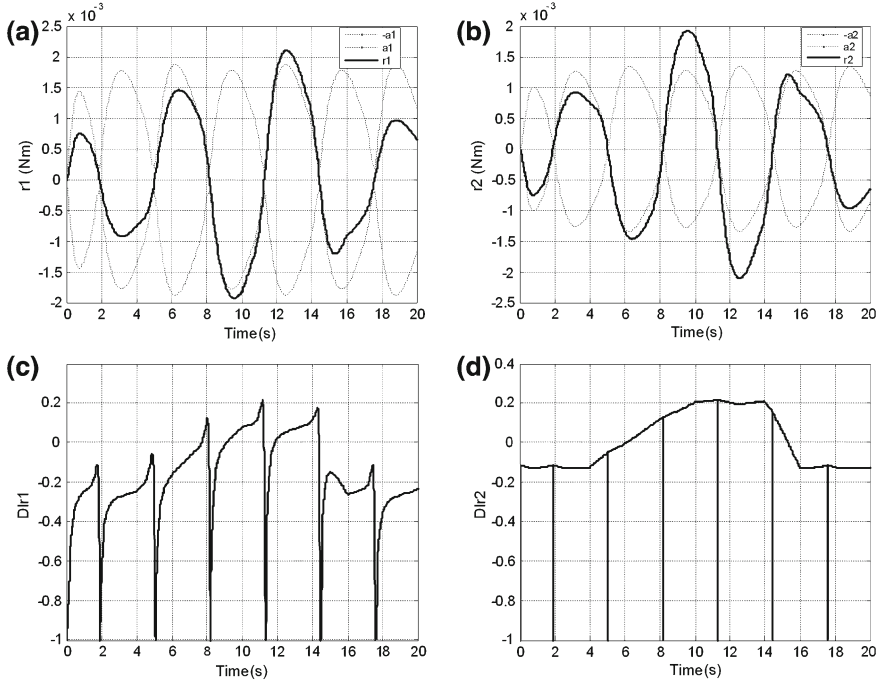


Fig. 7.27 Residuals and fault detectability indices in presence of fault. **a** Residual r_1 , **b** residual r_2 , **c** fault detectability index of r_1 , **d** fault detectability index of r_2

• Detectability index DIr_2

$$\begin{aligned}
 DIr_1 &= |Y_s| - \sum |w_i| \\
 &= |Y_s| - (|N.w_4| + |w_5| + |w_6| + |w_7| + |d_{s_n}|)
 \end{aligned}$$

$$DIr_2 > 0 \implies |Y_s| > (|N.w_4| + |w_5| + |w_6| + |w_7| + |d_{s_n}|)$$

with

$$|Y_s| = \left| -4.K. (j_0 + Y_{J_0}) \cdot \frac{1 - e^{-\gamma\beta}}{1 + e^{-\gamma\beta}} \right| \tag{7.30}$$

where Y_{J_0} is the fault. In absence of fault Y_{J_0} is equal to zero.

Figure 7.25 shows the residuals and fault detectability indices without any fault and any uncertainty. Figure 7.26 presents the residuals in presence of modeling uncertainties ($j_0 = 0.2$ rad which is the maximum backlash allowed on the system in normal operation) and parameter uncertainties, and in absence of fault ($Y_{J_0} = 0$).

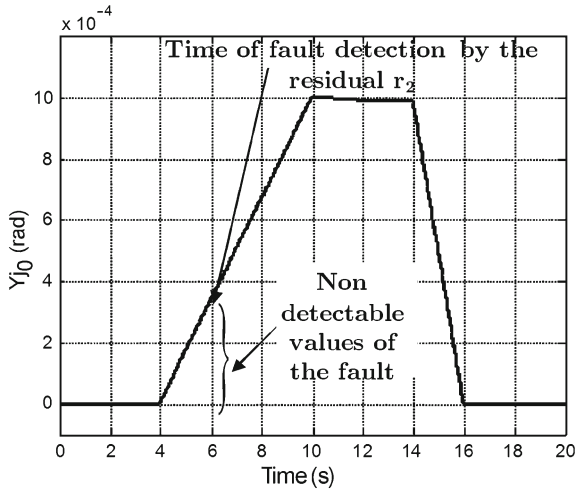


Fig. 7.28 Profile of the fault Y_j

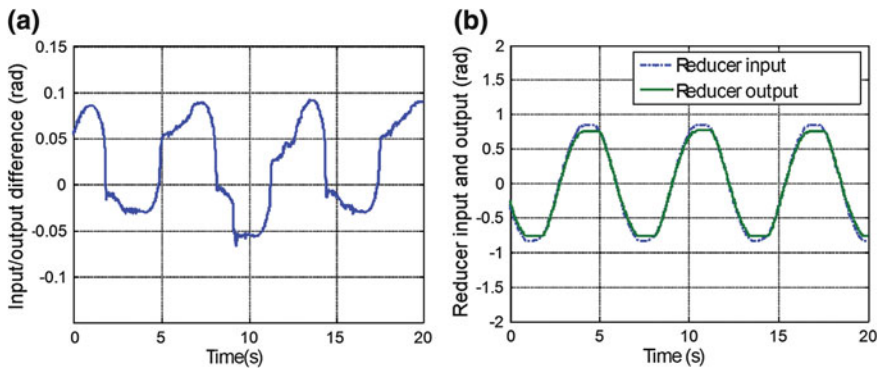


Fig. 7.29 **a** Position difference between θ_e and θ_s . **b** Reducer input θ_e and output θ_s

The fault detectability indices DIR_1 and DIR_2 are negative as shown in Fig. 7.26c and d. The residual values are equal to the torque provided by the initial disturbing torque, estimated by Eq. (7.27).

Figure 7.27 represents the residuals r_1 and r_2 in presence of fault. The fault is gradually added to the original backlash j_0 (Eq. 7.30) between time $t = 4$ and 16s as shown in Fig. 7.28. The fault detectability index DIR_2 becomes positive at the time $t = 6$ s (Fig. 7.28d), the fault amplitude at this time is 0.00038 rad (Fig. 7.28). Indeed, residual r_2 begins to detect the presence of the fault at time $t = 6$ s. The fault detectability index DIR_1 becomes positive at the time $t = 7.8$ s (Fig. 7.27c), at this time the residual r_1 detect the presence of the fault. So we conclude that the fault

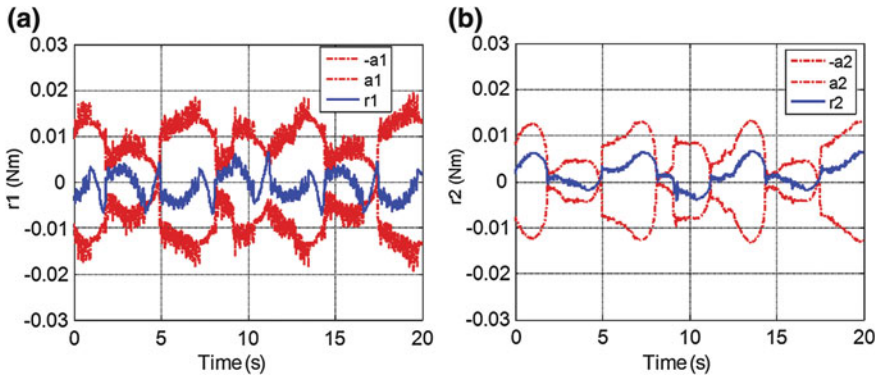


Fig. 7.30 Residuals and thresholds in normal operation. **a** Residual r_1 . **b** Residual r_2

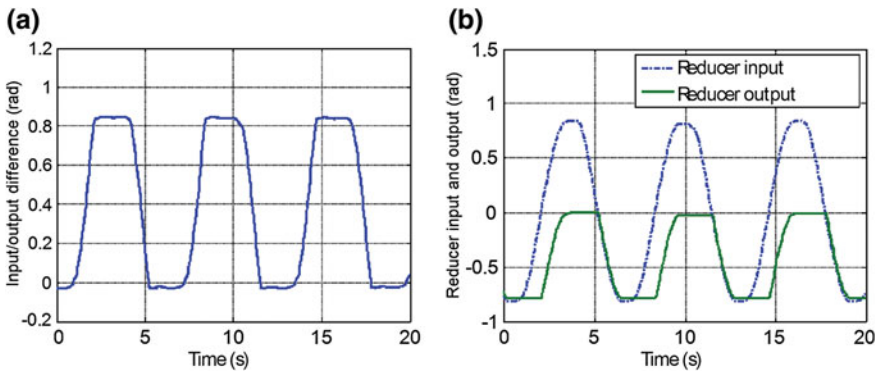


Fig. 7.31 **a** Position difference between θ_e and θ_s . **b** Reducer input θ_e and output θ_s

detectable value is 0.00038 rad, and it will be detected by the residual r_2 with a slight lead over the residual r_1 .

7.5.7 Experimental Results

On the real system, the residual values in normal operation are not equal to zero because of parameter uncertainties and the value of the model uncertainty corresponding to an initial backlash j_0 . The latter causes a slight difference between the input and output of the reducer as shown in Fig. 7.29a, b. The system being in normal operation, the residuals (Fig. 7.30) remain inside thresholds and no alarm is generated.

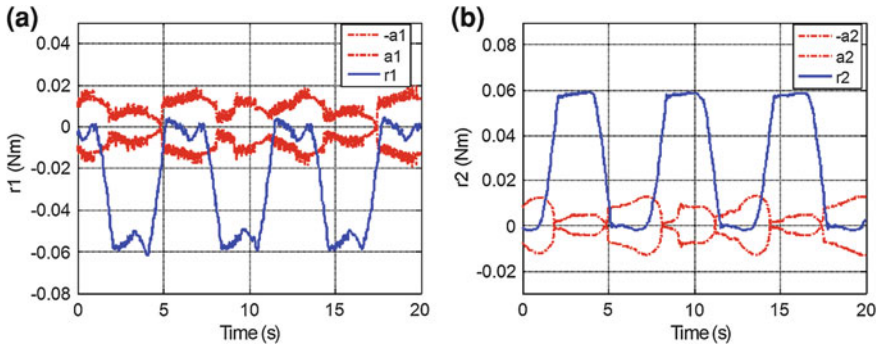


Fig. 7.32 Residuals and thresholds in faulty situation. **a** Residual r_1 . **b** Residual r_2

The structure of the test bench does not allow introducing a progressive fault to accurately reproduce the previous simulation. The fault is introduced by removing a metal plate at the reducer level.

The backlash variation causes a large difference between the reducer input and output as shown in Fig. 7.31a, b. Overlaying Fig. 7.31a with Fig. 7.32a, b, shows that the residuals begin to detect the fault as soon as its amplitude becomes slightly higher 0.2 rad, which correspond to the estimated value by the fault detectability indices.

7.6 Conclusion

Modeling is an important step in fault diagnosis scheme design, because the desired performances depend heavily on the model accuracy. The choice of the bond graph tool for FDI and robust FDI of uncertain systems is due to its multi-energy aspect, its causal and structural properties. The bond graph model allows easy derivation of ARRs and their implementation in real-time supervision [62, 69]. The LFT BG modeling does not introduce new bond graph elements on the model; therefore, no change occurs in the order of the model and its structural properties. Structural analysis can thus be done directly on the deterministic model. The transformation from the deterministic to LFT bond graph model is easily made by just replacing the deterministic elements R, I, C, TF, GY and RS by their corresponding LFT parts.

The presented FDI method allows the use of a bond graph model in LFT form to generate residuals and adaptive thresholds. To improve and monitor the performance of the diagnosis, a method of residual sensitivity analysis is proposed to estimate the detectable values of the faults.

The proposed application shows the robustness of the FDI algorithm on mechatronic systems. Indeed, simulation and experimental results show that the algorithm is robust to false alarms, because residuals remain inside the thresholds when the system is in normal operation. The performance of the algorithm against the non-detections and delays in fault detection is controlled by accuracy in estimation of the system parameters and their uncertainties.

References

1. G. Acosta, C.A. González, B. Pulido, Basic tasks for knowledge-based supervision in process control. *Eng. Appl. Artif. Intell.* **14**(4), 441–455 (2001)
2. O. Adort, D. Maquin, J. Ragot, Fault detection with model parameter structured uncertainties, in *European Control Conference ECC'99*, 1999
3. A. Albagul, M. Wahyudi, Dynamic modelling and adaptive traction control for mobile robots. *Int. J. Adv. Robot. Syst.* **1**(3), 149–154 (2004)
4. J. Armengol, L. Travé-Massuyès, J. Vehí, J.L. De la Rosa, A survey on interval model simulators and their properties related to fault detection. *Annu. Rev. Control* **24**, 31–39 (2000)
5. J. Armengol, J. Vehí, M.A. Sainz, P. Herrero, Fault detection in a pilot plant using interval models and multiple sliding windows, in *SAFEPROCESS 2003*, ed. by N. Eva Wu (IFAC, Washington DC) June 2003, pp. 729–734
6. K. Åström, P. Albertos, M. Blanke, A. Isidori, *Control of Complex Systems* (Springer, London, 2001)
7. M. Basseville, On-board element fault detection and isolation using the statistical local approach. *Automatica* **34**(11), 1359–1373 (1998)
8. M. Basseville, G. Benveniste, G. Moustakides, A. Rougée, Detection and diagnosis of changes in the eigenstructure of nonstationary multivariable systems. *Automatica* **23**, 479–489 (1987)
9. M. Basseville, I.V. Nikiforov, *Detection of Abrupt Changes: Theory and Application* (Prentice Hall, Englewood Cliffs, 1993), ISBN 0-13-126780-9
10. M. Blanke, M. Kinnaert, J. Lunze, M. Staroswiecki, *Diagnosis and Fault Tolerant Control* (Springer, Berlin, 2003)
11. G. Bloch, M. Ouladsine, P. Thomas, On-line fault diagnosis of dynamic systems via robust parameter estimation. *Control Eng. Pract.* **12**(3), 1709–1717 (1995)
12. G.E. Box, G.C. Tiao, *Bayesian Inference in Statistical Analysis* (Addison-Wesley, Reading, 1973)
13. P. Castaldi, W. Geri, M. Montanari, A. Tilli, A new adaptive approach for on-line parameter and state estimation of induction motors. *Control Eng. Pract.* **13**, 81–94 (2005)
14. J. Chen, R. Patton, H. Zhang, Design of unknown input observers and robust fault detection filters. *Int. J. Control* **63**, 85–105 (1996)
15. J. Chen, R.J. Patton, *Robust Model-Based Fault Diagnosis for Dynamic Systems* (Kluwer Academic Publisher, Dordrecht, 1999)
16. C. Commault, J.M. Dion, O. Sename, R. Motyeian, Observer-based fault detection and isolation for structured systems. *IEEE Trans. Autom. Control* **47**(12), 2074–2079 (2002)
17. M. Darouach, M. Zasadzinski, S.J. Xu, Full-order observers for linear systems with unknown inputs. *IEEE Trans. Autom. Control* **39**(3), 606–609 (1994)
18. G. Dauphin-Tanguy, C. Siè Kam, How to model parameter uncertainties in a bond graph framework. *ESS 99*, pp. 121–125, 1999
19. L. Dinca, T. Aldemir, G. Rizzoni, Fault detection and identification in dynamic systems with noisy data and parameter/modeling uncertainties. *Reliab. Eng. Syst. Saf.* **65**(1), 17–28 (1999)
20. S. Diop, Elimination in control theory. *Math. Control Signals Syst.* **4**, 17–32 (1991)
21. M.A. Djeziri, R. Merzouki, B. Ould Bouamama, Robust monitoring of an electric vehicle with structured and unstructured uncertainties. *IEEE Trans. Veh. Technol.* **58**, 4710–4719 (2009)
22. M.A. Djeziri, R. Merzouki, B. Ould Bouamama, G. Dauphin-Tanguy, Fault detection of backlash phenomenon in mechatronic system with parameter uncertainties using bond graph approach, in *Proceedings of IEEE International Conference on Mechatronics and Automation* (Luoyang, China, 2006), pp. 600–605
23. M.A. Djeziri, *Diagnostic des Systèmes Incertains par l'Approche Bond Graph*. Ph.D. thesis, Ecole Centrale de Lille, France, 2007
24. M.A. Djeziri, R. Merzouki, B. Ould-Bouamama, G. Dauphin-Tanguy, Robust fault diagnosis using bond graph approach. *IEEE/ASME Trans. Mechatron.* **12**(6), 599–611 (2007)
25. W. Drozd, H.B. Pacejka, Development and validation of a bond graph handling model of an automobile. *J. Frankl. Inst.* **328**(5/6), 941–957 (1991)

26. A. Emami-Naeini, M.M. Akhter, S.M. Rock, Effect of model uncertainty on failure detection: the threshold selector. *IEEE Trans. Autom. Control* **AC 33**, 1106–1115 (1988)
27. F.W. Fairman, S.S. Mahil, L. Luk, Disturbance decoupled observer design via singular value decomposition. *IEEE Trans. Autom. Control* **AC-29**(1), 84–86 (1984)
28. J. Feenstra, P.J. Mosterman, G. Biswas, P.C. Breedveld, Bond graph modeling procedures for fault detection and isolation of complex flow processes, in *International Conference on Bond Graph Modeling and Simulation (ICBGM'01)*, Simulation Series, vol. 33, No. 1, pp. 77–82, 2001, ISBN 1-56555-103-6
29. P.J. Feenstra, E.J. Manders, P.J. Mosterman, G. Biswas, R.J. Barnett, Modeling and instrumentation for fault detection and isolation of a cooling system, in *Proceedings of IEEE South East Conference*, Nashville, TN USA, 2000, pp. 365–372
30. P. Frank, Enhancement of robustness in observer-based fault detection. *Int. J. Control* **59**, 955–981 (1994)
31. P.M. Frank, Fault diagnosis in dynamic systems using analytical and knowledge-based redundancy—a survey and some new results. *Automatica* **26**(3), 459–474 (1990)
32. P.M. Frank, X. Ding, Frequency domain approach to optimally robust residual generation and evaluation for model based fault diagnosis. *Automatica* **30**, 789–904 (1994)
33. P.M. Frank, X. Ding, Survey of robust residual generation and evaluation methods in observer-based fault detection systems. *J. Process Control* **7**(6), 403–424 (1997)
34. J. Gertler, Residual generation in model-based fault diagnosis. *Control Theory Adv. Technol.* **9**(1), 259–285 (1993)
35. J. Gertler, Fault detection and isolation using parity relations. *Control Eng. Pract.* **5**(5), 653–661 (1997)
36. J. Gertler, *Fault Detection and Diagnosis in Engineering Systems* (Marcel Dekker, New York, 1998)
37. J. Gertler, D. Singer, A new structural framework for parity equation-based failure detection and isolation. *Automatica* **26**(2), 381–388 (1990)
38. S.K. Ghoshal, A.K. Samantaray, Multiple fault disambiguations through parameter estimation: a bond graph model-based approach. *Int. J. Intell. Syst. Technol. Appl.* **5**(1/2), 166–184 (2008)
39. S.K. Ghoshal, A.K. Samantaray, Wolfgang Borutzky (ed.) *Bond graph model-based fault diagnosis*, in *Bond Graph Modelling of Engineering Systems*, ed. by W. Borutzky (Springer, New York, 2011), pp. 227–265
40. C.A. González, G. Acosta, C. De Prada, Knowledge based process control supervision and diagnosis: the AEROLID approach. *Expert Syst. Appl.* **14**, 371–383 (1998)
41. C.A. González, B.P. Junquera, G.A. Lazo, C.L. Bello, On-line industrial supervision and diagnosis, knowledge level description and experimental results. *Expert Syst. Appl.* **20**(2), 117–132 (2001)
42. F. Hamelin, D. Sauter, Robust fault detection in uncertain dynamic systems. *Automatica* **36**(11), 1747–1754 (2000)
43. Z. Han, W. Li, S.L. Shah, Fault detection and isolation in the presence of process uncertainties, in *15th IFAC World Congress*, Barcelona, 2002, pp. 1887–1892
44. D.T. Horak, Failure detection in dynamic systems with modelling errors. *J. Guid. Control Dyn.* **11**(6), 508–516 (1998)
45. D. Hrovat, J. Asgari, M. Fodor, Automotive mechatronic systems, in *Mechatronic systems techniques and applications*, Transportation and Vehicular Systems, vol. 2 (Gordon and Breach Science Publishers, Amsterdam, 2000), pp. 1–98
46. K. Hsing-Chia, C. Hui-Kuo, A new symbiotic evolution-based fuzzy-neural approach to fault diagnosis of marine propulsion systems. *Eng. Appl. Artif. Intell.* **17**, 919–930 (2004)
47. R. Isermann, Process fault detection based on modelling and estimation methods: a survey. *Automatica* **20**, 387–404 (1994)
48. R. Isermann, *Fault-Diagnosis Systems: An Introduction from Fault Detection to Fault Tolerance* (Springer, London, 2005)

49. R. Isermann, B. Freyermuth, Process fault detection based on process model knowledge. Part I: Principles for fault diagnosis with parameter estimation. *ASME Trans. Dyn. Syst. Meas. Control* **113**, 620–626 (1991)
50. R. Isermann, B. Freyermuth, Process fault detection based on process model knowledge. Part II: Case study experiments. *ASME Trans. Dyn. Syst. Meas. Control* **113**, 627–638 (1991)
51. M. Ji, Z. Zhang, G. Biswas, N. Sarkar, Hybrid fault adaptive control of a wheeled mobile robot. *IEEE/ASME Trans. Mechatron.* **8**(2), 226–233 (2003)
52. A. Johansson, M. Bask, T. Norlander, Dynamic threshold generators for robust fault detection in linear systems with parameter uncertainty. *Automatica* **42**, 1095–1106 (2009)
53. S. Jung, T.C. Hsia, Explicit lateral force control of an autonomous mobile robot with slip, in *Proceedings of IEEE/RSJ International Conference on Intelligent Robots and Systems (IROS 2005)*, 2005, pp. 388–393
54. M. Kinnaert, Robust fault detection based on observers for bilinear systems. *Automatica* **35**(11), 1829–1842 (1999)
55. M. Kinnaert, Y. Peng, Residual generator for sensor and actuator fault detection and isolation, a frequency domain approach. *Int. J. Control* **61**(6), 1423–1435 (1995)
56. T. Kohda, K. Inoue, H. Asama, Computer aided failure analysis using system bond graphs, in *International Conference on Bond Graph Modeling and Simulation (ICBGM'01)*, Simulation Series, vol. 33, No. 1, 2001, pp. 71–76. ISBN 1-56555-103-6
57. T. Kohda, H. Katsubi, H. Fujihara, K. Inoue, Identification of system failure causes using bond graph models. *IEEE Trans. Syst. Man Cybern.* **5**, 269–274 (1993)
58. J. Korbicz, J.M. Koscielny, Z. Kowalczyk, W. Cholewa, *Fault Diagnosis: Models, Artificial Intelligence, Applications* (Springer, Berlin, 2004), ISBN 3540407677
59. W. Lee, C. Park, G. Kelly, Fault detection in an air-handling unit using residual and recursive parameter identification methods. *ASHRAE Trans. (Part 1)* **102**(1), 528–539 (1996)
60. S.F. Lin, A.P. Wang, Design of observers with unknown inputs using eigenstructure assignment. *Int. J. Syst. Sci.* **31**(6), 705–711 (2000)
61. D. Linkens, H. Wang, Qualitative bond graph reasoning in control engineering: fault diagnosis, in *International Conference on Bond Graph Modeling and Simulation (ICBGM'95)*, Simulation Series, vol. 27, 1995, pp. 189–194, ISBN 1-56555-037-4
62. K. Medjaher, A.K. Samantaray, B. Ould Bouamama, M. Staroswiecki, Supervision of an industrial steam generator. Part II: Online implementation. *Control Eng. Pract.* **14**(1), 85–96 (2005)
63. R. Merzouki, K. Medjaher, M.A. Djeziri, B. Ould Bouamama, Backlash fault detection in mechatronic system. *Mechatronics* **17**(6), 299–310 (2007)
64. R.E. Moore, *Interval Analysis* (Prentice Hall, New Jersey, 1966)
65. P.J. Mosterman, G. Biswas, Diagnosis of continuous valued systems in transient operating regions. *IEEE Trans. Syst. Man Cybern.* **29**(6), 554–565 (1999)
66. A. Mukherjee, R. Karmakar, *Modelling and Simulation of Engineering Systems Through Bond Graphs* (Alpha Sciences International, Pangbourne, 2000)
67. A. Mukherjee, R. Karmakar, A.K. Samantaray, *Bond Graph in Modeling, Simulation and Fault Identification* (CRC Press, Boca Raton, 2006), ISBN: 978-8188237968, 1420058657
68. B. Ould Bouamama, K. Medjaher, M. Bayart, A.K. Samantaray, B. Conrard, Fault detection and isolation of smart actuators using bond graphs and external models. *Control Eng. Pract.* **13**(2), 159–175 (2005)
69. B. Ould Bouamama, K. Medjaher, A.K. Samantaray, M. Staroswiecki, Supervision of an industrial steam generator. Part I: Bond graph modelling. *Control Eng. Pract.* **14**(1), 71–83 (2005)
70. B. Ould Bouamama, A.K. Samantaray, K. Medjaher, M. Staroswiecki, G. Dauphin-Tanguy, Model builder using functional and bond graph tools for FDI design. *Control Eng. Pract.* **13**(7), 875–891 (2005)
71. B. Ould Bouamama, A. K. Samantaray, M. Staroswiecki, G. Dauphin-Tanguy, Derivation of constraint relations from bond graph models for fault detection and isolation, in *International Conference on Bond Graph Modeling and Simulation (ICBGM'03)*, Simulation Series, vol. 35, No. 2, 2003, pp. 104–109, ISBN 1-56555-257-1

72. H.B. Pacejka, Modelling complex vehicle systems using bond graphs. *J. Frankl. Inst.* **319**(1/2), 67–81 (1985)
73. P.M. Pathak, A.K. Samantaray, R. Merzouki, B. Ould-Bouamama, Reconfiguration of directional handling of an autonomous vehicle, in *IEEE Region 10 Colloquium and 3rd International Conference on Industrial and Information Systems, ICIIIS 2008*, art. no. 4798408, 2008
74. R.J. Patton, J. Chen, A review of parity space approaches to fault diagnosis, in *Proceedings of SAFEPROCESS 91*, vol. 1, 1991, pp. 239–255
75. R.J. Patton, J. Chen, Observer-based fault detection and isolation: robustness and applications. *Control Eng. Pract.* **5**(5), 671–682 (1997)
76. R.J. Patton, P.M. Frank, R.N. Clark, *Fault Diagnosis in Dynamic Systems, Theory and Applications* (Prentice-Hall, Englewood Cliff, 1989)
77. R.J. Patton, P.M. Frank, R.N. Clark, *Issues of Fault Diagnosis for Dynamic Systems* (Springer, London, 2000)
78. S. Ploix, M. Desinde, S. Touaf, Automatic design of detection tests in complex dynamic systems, in *16th IFAC World Congress*, Prague, Czech Republic, 2005
79. V. Puig, J. Quevedo, Passive robust fault detection using fuzzy parity equations. *Math. Comput. Simul.* **60**, 193–207 (2002)
80. P. Ralston, G. DePuy, J.H. Graham, Computer-based monitoring and fault diagnosis: a chemical process case study. *ISA Trans.* **40**(1), 85–98 (2001)
81. F. Rambeaux, F. Hamelin, D. Sauter, Optimal thresholding for robust fault detection of uncertain systems. *Int. J. Robust Nonlinear Control* **10**, 1155–1173 (2000)
82. A.K. Samantaray, S.K. Ghoshal, Sensitivity bond graph approach to multiple fault isolation through parameter estimation. *Proc. IMechE Part-I J. Syst. Control Eng.* **221**(4), 577–587 (2007)
83. A.K. Samantaray, S.K. Ghoshal, Bicausal bond graphs for supervision: from fault detection and isolation to fault accommodation. *J. Frankl. Inst.* **345**(1), 1–28 (2008)
84. A.K. Samantaray, S.K. Ghoshal, S. Chakraborty, Bond graph model based design of supervision algorithm for distributed fault tolerant control systems. *Int. J. Autom. Control* **1**, 28–47 (2007)
85. A.K. Samantaray, S.K. Ghoshal, S. Chakraborty, A. Mukherjee, Improvements to single-fault isolation using estimated parameters. *Simulation* **81**(12), 827–845 (2005)
86. A.K. Samantaray, K. Medjaher, B. Ould Bouamama, M. Staroswiecki, G. Dauphin-Tanguy, Component based modelling of thermo-fluid systems for sensor placement and fault detection. *Simul. Trans. Soc. Model. Simul. Int.* **80**(7–8), 381–398 (2004)
87. A.K. Samantaray, K. Medjaher, B. Ould Bouamama, M. Staroswiecki, G. Dauphin-Tanguy, Diagnostic bond graphs for online fault detection and isolation. *Simul. Model. Pract. Theory* **14**(3), 237–262 (2005)
88. A.K. Samantaray, B. Ould Bouamama, *Model-Based Process Supervision—A Bond Graph Approach* (Springer, London, 2008)
89. A. Sanyal, R. Karmakar, Directional stability of truck-dolly-trailer system. *Veh. Syst. Dyn.* **24**(8), 617–637 (1995)
90. A. Seidenberg, An elimination theory for differential algebra. *Univ. Calif. Publ. Math.* **3**, 31–65 (1956)
91. Z. Shi, F. Gu, B. Lennox, A.D. Ball, The development of an adaptive threshold for model-based fault detection of a nonlinear electro-hydraulic system. *Control Eng. Pract.* **13**, 1357–1367 (2005)
92. Z. Shiller, Y. Gwo, Dynamic motion planning of autonomous vehicles. *IEEE Trans. Robot. Autom.* **7**(2), 241–248 (1991)
93. C. Sié Kam, G. Dauphin-Tanguy, Bond graph models of structured parameter uncertainties. *J. Frankl. Inst.* **342**(4), 379–399 (2005)
94. R. Siegwart, I.R. Nourbakhsh, *Introduction to Autonomous Mobile Robots* (The MIT Press, Cambridge, 2004)

95. S. Simani, C. Fantuzzi, R.J. Patton, *Model-Based Fault Diagnosis in Dynamic Systems Using Identification Techniques* (Springer, London, 2003)
96. R. Slier, P.M. Frank, *Robust Observer-Based Fault Diagnosis in Non Linear Uncertain Systems*. Springer, advances in fault diagnosis for dynamic systems: model based approaches edition, 2000
97. M. Staroswiecki, Quantitative and qualitative models for fault detection and isolation. *Mech. Syst. Signal Process.* **14**(3), 301–325 (2000)
98. M. Staroswiecki, G. Comtet-Varga, Analytical redundancy relations for fault detection and isolation in algebraic dynamic systems. *Automatica* **37**, 687–699 (2001)
99. J. Stephan, M. Bodson, J. Chiasson, Real-time estimation of the parameters and fluxes of induction motors. *IEEE Trans. Ind. Appl.* **30**(3), 746–759 (1994)
100. M. Tagina, J.P. Cassar, G. Dauphin-Tanguy, M. Staroswiecki, Bond graph models for direct generation of formal fault detection systems. *Syst. Anal. Model. Simul.* **23**, 1–17 (1996)
101. M. Tagina, J.Ph. Cassar, G. Dauphin-Tanguy, M. Staroswiecki, Localisation de défaillances par l'approche bond-graph. *J. Européen des Systèmes Automatisés (JESA)* **31**, 1489–1508 (1998)
102. P. Taillibert, Various improvement to diagnosing with temporal bands, in *9th International Workshop on Principles of Diagnosis, DX'98*, Massachussets, 1998
103. P. Taillibert, E. Loiez, Polynomial temporal band sequences for analog diagnosis, in *International Joint Conference On Artificial Intelligence, IJCAI'97*, Nagoya, Japan, Aug 1997
104. C. Ündey, E. Tatara, A. Çınar. Real-time batch process supervision by integrated knowledge-based systems and multivariate statistical methods. *Eng. Appl. Artif. Intell.* **16**(5–6), 555–566 (2003)
105. V. Venkatasubramanian, R. Rengaswamy, K. Yin, S.N. Kavuri, A review of process fault detection and diagnosis. Part I: Quantitative model-based methods. *Comput. Chem. Eng.* **27**, 293–311 (2003)
106. V. Venkatasubramanian, R. Rengaswamy, K. Yin, S.N. Kavuri, A review of process fault detection and diagnosis. Part II: Qualitative models and search strategies. *Comput. Chem. Eng.* **27**, 313–326 (2003)
107. V. Venkatasubramanian, R. Rengaswamy, K. Yin, S.N. Kavuri, A review of process fault detection and diagnosis. Part III: Process history based methods. *Comput. Chem. Eng.* **27**, 327–346 (2003)
108. J.P.M. Vissers, *The Control Design for an Overactuated Vehicle*. Master's Thesis, Technische Universiteit Eindhoven, 2005
109. N. Viswanadham, R. Srichander, Fault detection using unknown-input observers. *Control Theory Adv. Technol.* **3**(2), 91–101 (1987)
110. H. Wang, D. Linkens, Intelligent supervisory control, a qualitative bond graph reasoning approach, in *World Scientific Series in Robotics and Intelligent Systems*, vol. 14 (World Scientific, Singapore, 1996)
111. H.B. Wang, J.L. Wang, J. Lam, Robust fault detection observer design: iterative LMI approaches. *J. Dyn. Syst. Meas. Control* **129**, 77–82 (2007)
112. R. Wang, *Statistical Theory* (Xian Jiaotong University Press, Xian, 2003)
113. R.V. Welch, J.R. Dixon, Guiding conceptual design through behavioral reasoning. *Res. Eng. Des.* **6**, 169–188 (1994)
114. A.S. Willsky, A survey of design methods for failure detection systems. *Automatica* **12**, 601–611 (1976)
115. X.G. Yan, C. Edwards, Nonlinear robust fault recognition and estimation using a sliding mode observe. *Automatica* **43**, 1605–1614 (2007)
116. P. Young, Parameter estimation for continuous time models—a survey. *Automatica* **17**(1), 23–39 (1981)
117. A. Zaidi, N. Zanzouri, M. Tagina, Graphical approaches for modelling and diagnosis of hybrid dynamic systems. *WSEAS Trans. Syst.* **5**(10), 2322–2327 (2006)

Chapter 8

Introduction to Robotic Manipulators

8.1 Introduction

Robot is a good example of a mechatronic system. The word Robot has its root in the Slavic languages and means worker, compulsory work, or drudgery. It was popularized as a word for intelligent machines by the Czechoslovakian playwright Karel Kapek in play Rossum's Universal Robot in the year 1921 [8]. A robot is an integration of mechanical, electrical, and software components that can be reprogrammed to perform a variety of tasks both with and without human intervention. Robot Institute of America (RIA) defines a robot as: "A programmable multi-function manipulator designed to move material, parts, or specialized devices through variable programmed motion for the performance of a variety of tasks" [1]. Robotics is the study of robots design, programming, and control. Robots are gradually entering into our daily life. Days are not far when they will be part of our family. Essentially, a robot contains manipulators, sensors, control systems, power supplies, and software all working together to perform a task. Manipulator provides movement. A robot needs to be able to move around its environment. Whether by joint movement, or rolling on wheels, or walking on legs or propelling by thrusters, a robot needs to be able to move. Sensing is required to sense its surroundings and find its own location. Control system provides intelligence. This is where programming enters into the picture. A robot needs to be able to power itself. A robot might be solar powered, electrically powered, battery powered, etc. At present, the application of robotics is concentrated in the following areas:

1. Assembly line: Robots are used extensively in manufacturing where task is repetitive in nature. The use of industrial robot along with computer aided design (CAD) systems and computer aided manufacturing (CAM) systems characterizes the latest trends in the automation of the manufacturing processes.
2. Nuclear power plant: Robots have been developed to handle nuclear and radioactive chemicals for many different uses including nuclear weapons, power plants, and environmental cleanup. Safety is the main concern in these environments.

3. **Welding:** Robots are extensively used in welding as the job is tedious, risky, and unpleasant.
4. **Space, underwater:** Here, minimum maintenance requirements are emphasized. The control in this environment is difficult due to moveable base.
5. **Health care:** Robots are used to assist the surgeons in carrying out surgery.

8.2 Types of Robots

Robots can be classified based on mobility and manipulation. The aim of mobility is to transport while the aim of manipulation is to perform an action on the environment. The mobile robot examples include search and rescue, remote-controlled, tethered, walking, and running robots (one or more legs). The mobile wheeled robots have the capability to move around the environment; however, they need terrain to be flat. On the other hand, mobile legged robots can move in uneven terrain and their study helps us to understand biological locomotion. The manipulator examples include medical robots (teleoperated), space shuttle arm (teleoperated), painting robots, industrial robots (teleoperated and autonomous).

8.3 Basic Terminology

In robotics, one is concerned about location of the object in three-dimensional space. The objects can be described by two attributes: their position and orientation. In order to describe the position and orientation of a body in space, we always attach a coordinate system or *frame*. To begin with, let us do some preliminaries and look at the following definitions.

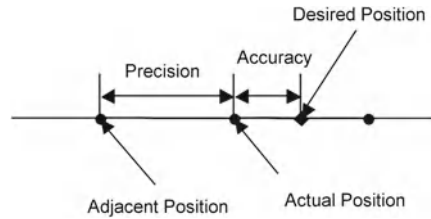
- *Velocity*: The derivative of position with respect to time.
- *Acceleration*: The derivative of velocity with respect to time.
- *Jerk*: The derivative of acceleration with respect to time.
- The *kinematics* refers to relationship between the positions, and the positions derivatives of the links of robot. Kinematics is description of motion without considering forces.
- *Manipulators* consists of rigid links connected by joints which allow relative motion of neighboring links. For rotary or revolute joints, relative displacement between the links are called joint angles and for prismatic joints they are called joint offsets.
- *Forward kinematic*: For a given set of joint angles and offsets, it refers to computation of the position and orientation of the tool frame relative to base frame or represent manipulator position from joint space description to Cartesian space description.

- *Joint space*: Relative coordinates that are referenced to coordinate frames at the robot joints.
- *Cartesian space* or *Task space*: Global or base coordinate frame.
- *Inverse kinematic*: In this one looks for a set of joint angles θ_i and offset d_i that are required to place the end effector at a location and orientation specified by transformation matrix with respect to the base coordinate. Because kinematic equations are nonlinear their solution is not always easy or even possible in closed form. Question of existence of a solution and multiple solutions arise.
- *Jacobian*: It specifies a mapping from velocities in joint space to velocities in Cartesian space. Also, given a desired contact force and moments the calculation of the set of joint torques that are required to generate them also needs Jacobian.
- *Singularity*: Region or point at which the Jacobian is singular.
- *Dynamic equations* of manipulator are needed for the dynamic control of robotic manipulators. The control problem consists of obtaining the governing equation for the robotic dynamics in the form of a dynamic model of the robotic manipulator and specifying the control laws to achieve the desired response. A serial robotic manipulator can be modeled as open loop kinematic and dynamic chain with several rigid bodies or links connected in series by either revolute or prismatic joints. On the contrary, a parallel robotic manipulator has a closed loop kinematic and dynamic chain, more about which will be discussed in Chap. 13. In robotics, statics is concerned with a set of joint forces and torques that achieves a required set of forces and torques for the end effector while keeping the system under static equilibrium. In robot dynamics, we are concerned with calculating joint torques to produce given joint positions, velocities, and accelerations. There are three approaches to arrive at the set of differential equations describing the dynamics of robotic manipulator. These approaches are: (1) Bond graph dynamic modeling, (2) Newton-Euler dynamic modeling, and (3) Lagrange dynamic modeling. The other approaches called recursive approaches are: (1) Newton-Euler recursive formulation and (2) Lagrangian recursive formulation.

The governing equations of manipulator are generally nonlinear coupled second-order differential equations. Each equation contains number of torque or force terms. These terms can be classified into four groups: (i) inertial forces or torques due to the mass or rotary inertia of the links; (ii) reaction forces or torques generated by acceleration at other joints; (iii) centripetal, gyroscopic, and Coriolis type forces and torques between joints; and (iv) gravitational or loading type forces and torques on links. We have seen in earlier chapters that bond graph modeling considers the flow of energy and information from one system port to another system port. Various examples on bond graph modeling of multibody systems have been discussed in Chaps. 5 and 6. Thus, bond graph representation is especially useful for modeling of robotic manipulators.

- *Linear position control*: Most of the manipulators are driven by actuators which supply a force/torque to result in the desired motion. A primary concern of the position control system is to automatically compensate for errors in knowledge of the parameters of the system and to suppress the disturbances, which try to perturb the system from the desired trajectory. To accomplish this, position and velocity

Fig. 8.1 Schematic description of accuracy and precision



sensors are monitored by the control algorithm, which computes the force and torque commands for the actuators. Control algorithm synthesis may be based on linear approximation of the dynamics of a manipulator.

- *Nonlinear position control*: Control systems based on approximate linear models are popular in current industrial robots. Nonlinear dynamics of manipulator if considered during control synthesis gives better performance.
- *Trajectory and force control*: While moving in free space, we come across position control task, whereas force control situation arises when coming in contact with constraint surface. The aim of the force control is to control forces when the manipulator touches parts, tools, or work surfaces. Force control is complementary to position control. Since manipulator is rarely constrained to move in all the directions simultaneously we have hybrid control problem.
- A *robot programming language* serves as interface between the human user and the industrial robot. Robot manipulators differentiate from fixed automation by being flexible which means programmable. An offline programming system is a robot programming environment which has been sufficiently extended by means of computer graphics by which the development of robot programs can take place without access to the robot itself.
- *Workspace*: It is defined as the volume in space that the manipulator can reach.
- In *manipulator design* factors such as size, speed, load capability, number of joints, and their geometric arrangements are considered. These considerations impact upon the manipulator workspace size and, stiffness of manipulator structure. Other issues are location of actuators, transmission system, internal position, and force sensor.
- *Repeatability*: How well a robot can return to the same point.
- *Accuracy*: How well a robot can move to an arbitrary point in space.
- *Precision*: The smallest increment with which a robot can be positioned. Accuracy and precision are schematically explained in Fig. 8.1.

8.4 Manipulator Transformations

As we discussed in introduction, robotic manipulators are used to move parts or tools in space. When we move parts and tools, there should be some way to represent where the parts and tools have reached and in what orientation. We can also talk

about the position and orientation of mechanism. To represent and manipulate the mathematical quantities representing the positions and orientations, we need to define a reference coordinate system.

Once the coordinate system is set, we can locate any point in space by a 3×1 position vector. Let, ${}^A P$ represents a vector or position vector in space, or ordered set of three numbers

$${}^A P = [p_x \ p_y \ p_z]^T.$$

To describe the orientation of a body, we attach a coordinate system to the body and then give description of this coordinate system relative to the reference system. Thus, position of points in a body is described by a vector and orientation of body is described with an attached coordinate system.

8.4.1 Notations

Coordinate systems are represented with brackets such as $\{A\}$, $\{0\}$, etc.

Vectors: Let us look at a vector P described in Frame A . To describe it mathematically, we can use a leading superscript to describe the frame in which the vector is described. Individual elements of a vector can be described by a trailing subscript as shown in Eq. 8.1.

$${}^A P = \begin{bmatrix} p_x \\ p_y \\ p_z \end{bmatrix} \quad (8.1)$$

Matrix: Original frame of reference is shown by leading subscript while new frame of reference is given by leading superscript. For example ${}^A_B T$ represents transformation from frame $\{B\}$ to frame $\{A\}$ through a transformation matrix T .

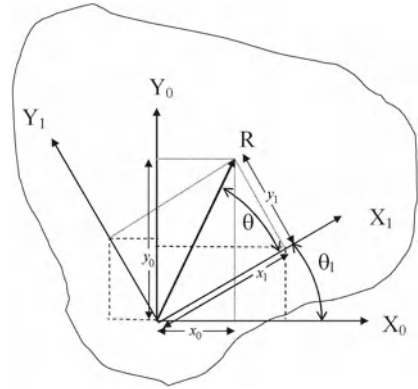
8.4.2 Rotation

Let, there be a vector R as shown in Fig. 8.2 and we need to express R which we know in Frame $\{1\}$ in Frame $\{0\}$. To do this, let us do a simple construction as shown in Fig. 8.2.

From Fig. 8.2, we see that if we express R in frame $\{1\}$ then,

$$\begin{aligned} x_1 &= R \cos \theta \\ y_1 &= R \sin \theta \end{aligned}$$

Fig. 8.2 Representation of a point in two frames



If we express R in frame $\{0\}$ then,

$$\begin{aligned} x_0 &= x_1 \cos \theta_1 - y_1 \sin \theta_1 \\ y_0 &= x_1 \sin \theta_1 + y_1 \cos \theta_1 \end{aligned} \quad (8.2)$$

In matrix form Eq. 8.2 can be written as

$$\begin{bmatrix} x_0 \\ y_0 \end{bmatrix} = \begin{bmatrix} \cos \theta_1 & -\sin \theta_1 \\ \sin \theta_1 & \cos \theta_1 \end{bmatrix} \begin{bmatrix} x_1 \\ y_1 \end{bmatrix} \quad (8.3)$$

or in short,

$$\begin{bmatrix} x_0 \\ y_0 \end{bmatrix} = [T] \begin{bmatrix} x_1 \\ y_1 \end{bmatrix} \quad (8.4)$$

Here, $[T]$ is called transformation matrix. Now if we want to map it from frame $\{0\}$ to frame $\{1\}$, then we can write

$$\begin{bmatrix} x_1 \\ y_1 \end{bmatrix} = [T]^{-1} \begin{bmatrix} x_0 \\ y_0 \end{bmatrix} \quad (8.5)$$

Now, the question is how to find the inverse of $[T]$. If we look at the columns and rows of $[T]$, we see that they have a norm of one. Also if we take the dot product of the columns we find they are orthogonal to each other. So, $[T]$ is an orthonormal matrix. Thus, its transpose is its inverse. Thus, if

$$[T] = \begin{bmatrix} \cos \theta_1 & -\sin \theta_1 \\ \sin \theta_1 & \cos \theta_1 \end{bmatrix}$$

then

$$[T]^{-1} = \begin{bmatrix} \cos \theta_1 & \sin \theta_1 \\ -\sin \theta_1 & \cos \theta_1 \end{bmatrix}$$

This was a simple example of planar case. Now if we assume that there is Z axis out of the plane and perpendicular to X and Y axes, then a rotation around the Z axis will not affect the Z position of the vector R . Thus, the three-dimensional transformation matrix about the Z axis is:

$$[T]_z = \begin{bmatrix} \cos \theta_1 & -\sin \theta_1 & 0 \\ \sin \theta_1 & \cos \theta_1 & 0 \\ 0 & 0 & 1 \end{bmatrix} \tag{8.6}$$

Similarly, for rotations around the X axis we get

$$[T]_x = \begin{bmatrix} 1 & 0 & 0 \\ 0 & \cos \theta_1 & -\sin \theta_1 \\ 0 & \sin \theta_1 & \cos \theta_1 \end{bmatrix} \tag{8.7}$$

For rotations around the Y axis, we get

$$[T]_y = \begin{bmatrix} \cos \theta_1 & 0 & \sin \theta_1 \\ 0 & 1 & 0 \\ -\sin \theta_1 & 0 & \cos \theta_1 \end{bmatrix} \tag{8.8}$$

For multiple transformations about Z axis first by γ and then by ϕ , we simply multiply by more matrices.

$$[T(\gamma + \phi)]_z = \begin{bmatrix} \cos \phi & -\sin \phi & 0 \\ \sin \phi & \cos \phi & 0 \\ 0 & 0 & 1 \end{bmatrix} \begin{bmatrix} \cos \gamma & -\sin \gamma & 0 \\ \sin \gamma & \cos \gamma & 0 \\ 0 & 0 & 1 \end{bmatrix} \tag{8.9}$$

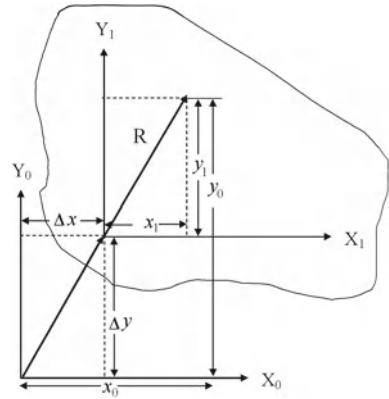
$$= \begin{bmatrix} \cos \phi \cos \gamma - \sin \phi \sin \gamma & -\cos \phi \sin \gamma - \sin \phi \cos \gamma & 0 \\ \sin \phi \cos \gamma + \cos \phi \sin \gamma & -\sin \phi \sin \gamma + \cos \phi \cos \gamma & 0 \\ 0 & 0 & 1 \end{bmatrix} \tag{8.10}$$

Since $\sin(\phi + \gamma) = \sin \phi \cos \gamma + \cos \phi \sin \gamma$ and $\cos(\phi + \gamma) = \cos \phi \cos \gamma - \sin \phi \sin \gamma$, we can write Eq. 8.10 as

$$[T(\gamma + \phi)]_z = \begin{bmatrix} \cos(\phi + \gamma) & -\sin(\phi + \gamma) & 0 \\ \sin(\phi + \gamma) & \cos(\phi + \gamma) & 0 \\ 0 & 0 & 1 \end{bmatrix} \tag{8.11}$$

So, if we have multiple rotations about the same axes we can just add the angles of the matrices. So, now we can rotate a vector to and from an arbitrary angle in space. What If we want to express it in a translated frame, then how can we do that?

Fig. 8.3 Representation of vector in a translated frame



8.4.3 Translating Coordinate Frames

Let, there be a vector R represented in frame $\{1\}$ as shown in Fig. 8.3. Suppose, we have another frame $\{0\}$ which is translated by a distance Δx , Δy from X_1 and Y_1 axis as shown in Fig. 8.3.

From Fig. 8.3, we can see that

$$\begin{aligned} x_0 &= x_1 + \Delta x \\ y_0 &= y_1 + \Delta y \end{aligned} \quad (8.12)$$

or in vector form we can write

$$R_0 = R + \Delta R \quad (8.13)$$

We can write Eq. 8.12 as

$$\begin{bmatrix} x_0 \\ y_0 \\ 1 \end{bmatrix} = \begin{bmatrix} 1 & 0 & \Delta x \\ 0 & 1 & \Delta y \\ 0 & 0 & 1 \end{bmatrix} \begin{bmatrix} x_1 \\ y_1 \\ 1 \end{bmatrix} \quad (8.14)$$

Equation 8.14 is known as homogeneous form of representation of translation. What if we have a rotation and a translation? First, we can rotate the frames and then we can translate.

$$\begin{bmatrix} x_0 \\ y_0 \end{bmatrix} = [T] \begin{bmatrix} x_1 \\ y_1 \end{bmatrix} + \begin{bmatrix} \Delta x \\ \Delta y \end{bmatrix}. \quad (8.15)$$

8.4.4 Homogeneous Transformation Matrices

In homogeneous form of representation, the 3×3 rotation matrix can be written as

$$T_1 = \begin{bmatrix} C_1 & -S_1 & 0 \\ S_1 & C_1 & 0 \\ 0 & 0 & 1 \end{bmatrix} \quad (8.16)$$

where $C_1 = \cos \theta_1$ and $S_1 = \sin \theta_1$. Similarly, in homogeneous form of representation, a 3×1 displacement vector can be written as

$$R_1 = \begin{bmatrix} x_1 \\ y_1 \\ z_1 \end{bmatrix}$$

If we have rotation as well as translation then we can write, the new vector as

$$[R_0] = [T_1] [R_1] + [\Delta R] \quad (8.17)$$

- 4×4 Homogeneous Matrix

If we want to perform transformation in three dimension and say we want to perform a rotation and a translation with one operation, we can create a homogeneous transformation matrix as follows.

$$\begin{bmatrix} x_0 \\ y_0 \\ z_0 \end{bmatrix} = [T_1] \begin{bmatrix} x_1 \\ y_1 \\ z_1 \end{bmatrix} + \begin{bmatrix} \Delta x \\ \Delta y \\ \Delta z \end{bmatrix} \quad (8.18)$$

where

$$T_1 = \begin{bmatrix} C_1 & -S_1 & 0 \\ S_1 & C_1 & 0 \\ 0 & 0 & 1 \end{bmatrix}$$

In homogeneous form of representation, Eq. 8.18 can be written as

$$\begin{bmatrix} x_0 \\ y_0 \\ z_0 \\ 1 \end{bmatrix} = [T_H] \begin{bmatrix} x_1 \\ y_1 \\ z_1 \\ 1 \end{bmatrix} \quad (8.19)$$

where

$$T_H = \begin{bmatrix} C_1 & -S_1 & 0 & \Delta x \\ S_1 & C_1 & 0 & \Delta y \\ 0 & 0 & 1 & \Delta z \\ 0 & 0 & 0 & 1 \end{bmatrix}.$$

So in homogeneous transformation matrices, a pure translation looks like

$$T_T = \begin{bmatrix} 1 & 0 & 0 & x \\ 0 & 1 & 0 & y \\ 0 & 0 & 1 & z \\ 0 & 0 & 0 & 1 \end{bmatrix}$$

and a pure rotation looks like

$$T_R = \begin{bmatrix} C_1 & -S_1 & 0 & 0 \\ S_1 & C_1 & 0 & 0 \\ 0 & 0 & 1 & 0 \\ 0 & 0 & 0 & 1 \end{bmatrix}$$

Homogenous transformations represent three things: (i) describe a frame, (ii) map from one frame to another frame, and (iii) act as an operator to move within a frame. Let us see these representations.

1. Transformations describe frames

Frames can be described by a homogenous transformation matrix

$${}^A_B T = \begin{bmatrix} & & & {}^A P_{BorgX} \\ {}^A_B R & & & {}^A P_{BorgY} \\ & & & {}^A P_{BorgZ} \\ 0 & 0 & 0 & 1 \end{bmatrix}$$

where ${}^A_B R = \begin{bmatrix} C_1 & -S_1 & 0 \\ S_1 & C_1 & 0 \\ 0 & 0 & 1 \end{bmatrix}$. Columns of ${}^A_B R$ are the unit vectors defining the directions of the principal axes of $\{B\}$ in terms of $\{A\}$.

$${}^A_B R = [{}^A \hat{X}_B \quad {}^A \hat{Y}_B \quad {}^A \hat{Z}_B] = \begin{bmatrix} {}^B \hat{X}_A^T \\ {}^B \hat{Y}_A^T \\ {}^B \hat{Z}_A^T \end{bmatrix}$$

Rows of ${}^A_B R$ are the unit vectors defining the directions of the principal axes of $\{A\}$ in terms of $\{B\}$. ${}^A P_{BORG}$ is the location of the origin of $\{B\}$ in terms of $\{A\}$.

2. Mapping between frames

${}^A_B T$ Maps vector from frame $\{B\}$ to frame $\{A\}$. ${}^A_B R$ will rotate a vector to project its components originally described in frame $\{B\}$ in the frame $\{A\}$. ${}^A P_{BORG}$ will translate the vector to adjust its origin from frame $\{B\}$ to its new origin in $\{A\}$.

3. Acts as an operator within a coordinate frame

${}^A_B T$ Operator will rotate and translate a vector. R defines the angle to rotate about whereas P_{BORG} defines the distance to translate.

8.5 D-H Parameters

Denavit-Hartenberg (D-H) parameters are used to describe a robot link. Here, one coordinate system is created for each link. While creating a coordinate system each axis is taken to be orthogonal. Right-hand rule is used in axis direction assignment. Links are assumed to be rigid. Kinematic function of a link is to maintain the fixed relationship between the two neighboring joint axes of the manipulator. This fixed relationship can be described by two parameters namely link length a and link twist α . The links are connected to neighboring links at joints. Two parameters namely link offset d and the joint angle θ are used to describe the connection. Thus, four parameters are used to describe a link and its connection completely. These parameters can be explained with the help of Fig. 8.4. Let us see these parameters one by one.

1. a_{i-1} is called link length. It is measured from Z_{i-1} to Z_i along X_{i-1} . It is measured by the common perpendicular between the two axes Z_{i-1} and Z_i . The common perpendicular is the shortest distance between these two axes in space. The shortest distance does not necessarily lie in the physical link. If axes intersect then it is zero. It is not defined for prismatic joint, and is thus set to zero.
2. α_{i-1} is called link twist angle. It is measured from Z_{i-1} to Z_i about X_{i-1} .
3. d_i is called link offset. It is measured from X_{i-1} to X_i along Z_i . It is joint variable for prismatic joint.
4. θ_i is called joint angle. It is measured as the angle between X_{i-1} and X_i , measured around Z_i from X_{i-1} and X_i .

8.5.1 Assigning Coordinate Frames

1. First, place the Z axes along the joint axes of rotation, or translation. Imagine them of infinite length.
2. Identify the common perpendiculars or point of intersection between each pair of Z axes. Place the X_i axes along the common perpendicular between axes i and $i + 1$. If the axes intersect X_i is assigned normal to the plane containing the intersecting axes.
3. Use the right-hand rule to define the Y axes.

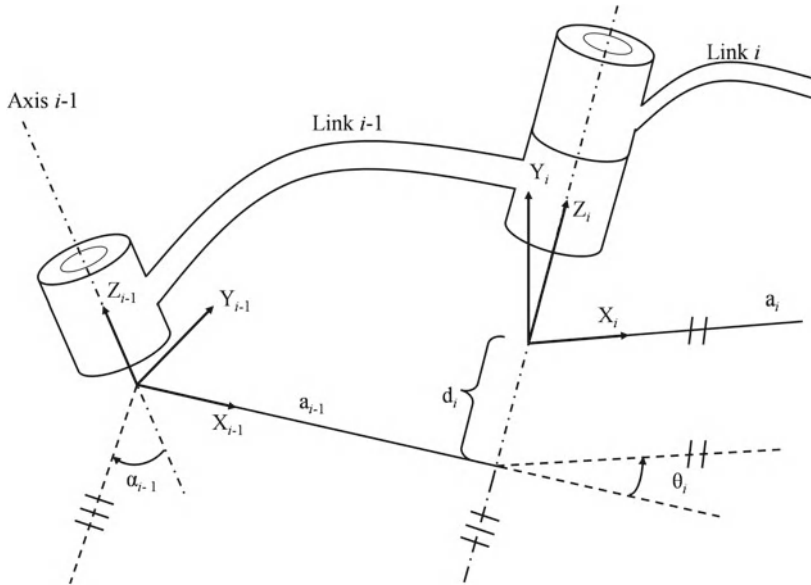


Fig. 8.4 Representation of D-H parameters

4. The base frame $\{0\}$ is fixed and does not move. It is usually picked to be coincident with frame $\{1\}$, thus frame $\{0\}$ and $\{1\}$ overlap when the first joint variable is zero. Choose the origin and direction of frame $\{N\}$ freely, but in general assign it so as to make as many parameters zero as possible.

8.5.2 Special Cases

1. If $a_i = 0$ then the Z axes intersect, so pick X_i to be normal to the plane defined by Z_i and Z_{i+1} . This leads to two possible definitions of X and thus Y .
2. If Z_i and Z_{i+1} are parallel, then the assignment of X_i is arbitrary.

8.5.3 D-H Parameters

We can construct a matrix of D-H parameters for all the links in the robot. This will make defining the transformation from one axes to another much easier. Forward kinematics is used to move from joint coordinates to end-effector coordinates. We will use D-H parameters to define frames. Each link will be assigned a frame. Transformation will be used to move between links. We will start at the bottom and work our way out through the chain of links. A transformation between frame $\{i-1\}$ and $\{i\}$ can be defined as having four steps each containing only one link parameter.

1. Translate along Z_i by d_i .
2. Rotate around Z_i by θ_i .
3. Translate along X_{i-1} , by a_{i-1} .
4. Rotate around X_{i-1} , by α_{i-1} .

We can perform this with two transformations

- (i) First, a translation and rotation with regards to Z_i .
- (ii) Second, a translation and rotation with regards to X_{i-1} .

Thus, the transformations can be given as,

$${}^i{}_{i-1}T = \begin{bmatrix} 1 & 0 & 0 & a_{i-1} \\ 0 & c\alpha_{i-1} & -s\alpha_{i-1} & 0 \\ 0 & s\alpha_{i-1} & c\alpha_{i-1} & 0 \\ 0 & 0 & 0 & 1 \end{bmatrix} \begin{bmatrix} c\theta_i & -s\theta_i & 0 & 0 \\ s\theta_i & c\theta_i & 0 & 0 \\ 0 & 0 & 1 & d_i \\ 0 & 0 & 0 & 1 \end{bmatrix}$$

where $c\theta = \cos \theta$, and $s\theta = \sin \theta$. After matrix multiplication,

$${}^i{}_{i-1}T = \begin{bmatrix} c\theta_i & -s\theta_i & 0 & a_{i-1} \\ s\theta_i & c\theta_i & c\alpha_{i-1} & -s\alpha_{i-1} & -s\alpha_{i-1} & d_i \\ s\theta_i & s\alpha_{i-1} & c\theta_i & s\alpha_{i-1} & c\alpha_{i-1} & c\alpha_{i-1} & d_i \\ 0 & 0 & 0 & 0 & 0 & 1 \end{bmatrix} \quad (8.20)$$

The matrix given by Eq. 8.20 gives D-H based transformation matrix.

Forward kinematics is used to move from joint coordinates to end-effector coordinates. To do this, we can just multiply the individual transformation matrices. For a robot with N joints, we will get N transformations. Then, overall transformation can be given as:

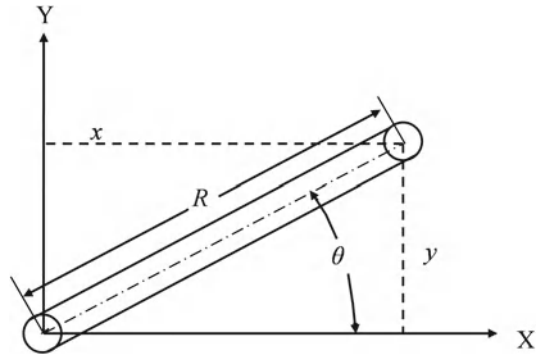
$${}^0T = {}_1^0T_2^1T_3^2T \dots {}_N^{N-1}T$$

If we are interested in a point beyond the last joint such as an end effector or a tool then we define a coordinate system for the tool point of interest and perform a transformation from the last joint to the desired point.

We find it helpful to define other points in the robot work space with coordinate systems relative to the robot base system. Following are some of the standard frames:

- Wrist Frame $\{W\}$: It is same as the last robot frame, i.e., frame $\{N\}$.
- Base Frame $\{B\}$: It is located at the base of the manipulator, it is same as frame $\{0\}$.
- Station Frame $\{S\}$: It is usually used as the base point for robot motions. It is calculated relative to the base frame.
- Tool Frame $\{T\}$: It can be tip of a torch, point between finger of a gripper or the lens of a camera. It is specified relative to the $\{W\}$ frame.
- Goal Frame $\{G\}$: It is location where the robot is desired to move. At the end of motion $\{G\}$ and $\{T\}$ should coincide.

Fig. 8.5 Sketch of one DOF link



8.6 Manipulator Kinematics

Manipulator kinematics can be classified as forward and inverse kinematics. In forward kinematics one is interested in finding the tip position for given joint angles whereas in inverse kinematics we find out joint angles for given tip position.

8.6.1 Forward Kinematics

Example 1: Let us look at a simple link (one DOF) as shown in Fig. 8.5. In forward kinematics, we want to know the end point of link in terms of joint angle. We have length of link R and inclination of link from X axis θ . From geometry, we can determine the position of the end point and then the velocity of the end point.

$$\begin{aligned} x &= R \cos \theta \\ y &= R \sin \theta \end{aligned} \quad (8.21)$$

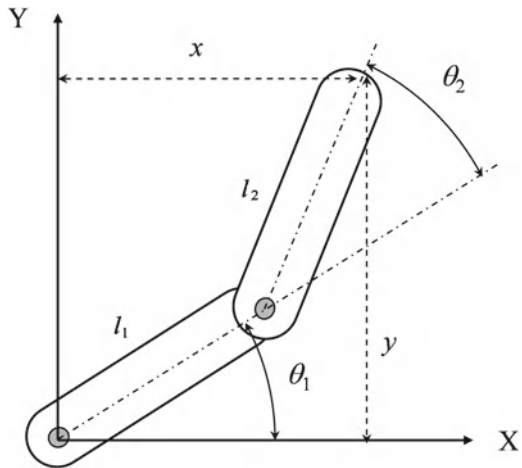
$$\begin{aligned} \dot{x} &= -R \dot{\theta} \sin \theta \\ \dot{y} &= R \dot{\theta} \cos \theta \end{aligned} \quad (8.22)$$

Example 2: Let us look at a two DOF manipulator as shown in Fig. 8.6. In forward kinematics, we want to know the end point of link in terms of joint angles. We have length of links as l_1 and l_2 . Let, the inclination of link 1 from X axis be θ_1 and the inclination of link 2 from link 1 axis be θ_2 . From geometry, we can determine the position of the end point and then the velocity of the end point as

$$\begin{aligned} x &= l_1 \cos \theta_1 + l_2 \cos(\theta_1 + \theta_2) \\ y &= l_1 \sin \theta_1 + l_2 \sin(\theta_1 + \theta_2) \end{aligned} \quad (8.23)$$

or in matrix form we can write the above expression as

Fig. 8.6 Sketch of a two DOF manipulator



$$\begin{bmatrix} x \\ y \end{bmatrix} = \begin{bmatrix} \cos(\theta_1) & \cos(\theta_1 + \theta_2) \\ \sin(\theta_1) & \sin(\theta_1 + \theta_2) \end{bmatrix} \begin{bmatrix} l_1 \\ l_2 \end{bmatrix} \tag{8.24}$$

Also velocities in X and Y direction of tip can be given as

$$\begin{bmatrix} \dot{x} \\ \dot{y} \end{bmatrix} = \begin{bmatrix} -l_1 \sin \theta_1 - l_2 \sin(\theta_1 + \theta_2) & -l_2 \sin(\theta_1 + \theta_2) \\ l_1 \cos \theta_1 + l_2 \cos(\theta_1 + \theta_2) & l_2 \cos(\theta_1 + \theta_2) \end{bmatrix} \begin{bmatrix} \dot{\theta}_1 \\ \dot{\theta}_2 \end{bmatrix} \tag{8.25}$$

Example 3: Now, let us take an example of two DOF cooperative manipulator [10] as shown in Fig. 8.7. In this figure, {A} represents the absolute frame, {B} represents the base frame, {0} frame is located at the base of the robot, and {1} and {2} are the frames located at first and second joint, respectively. The frame {3} locates the tip of the robot. Lengths of the links are assumed along the X axis of respective frames. The direct kinematic model gives the position and orientation of the end effector as a function of the joint variable and other joint-link constant parameters. Let, l_1 be the length of the first link, l_2 be the length of the second link, and r be the distance between the base center of gravity (CG) and the first joint. Let, ϕ represents the rotation of base, and θ_1 and θ_2 be the joint angles as shown in Fig. 8.7. Same parameters are used to describe the left-side robot and right-side robot. Let, a be the distance between the CG of the base of two robots. Let, the inertial frame coincides with the base frame of left robot.

Then, the overall transformation matrix for the end effector of the manipulator is given as

$$T_o = T_2(\theta_2)T_1(\theta_1)T_0(\phi)$$

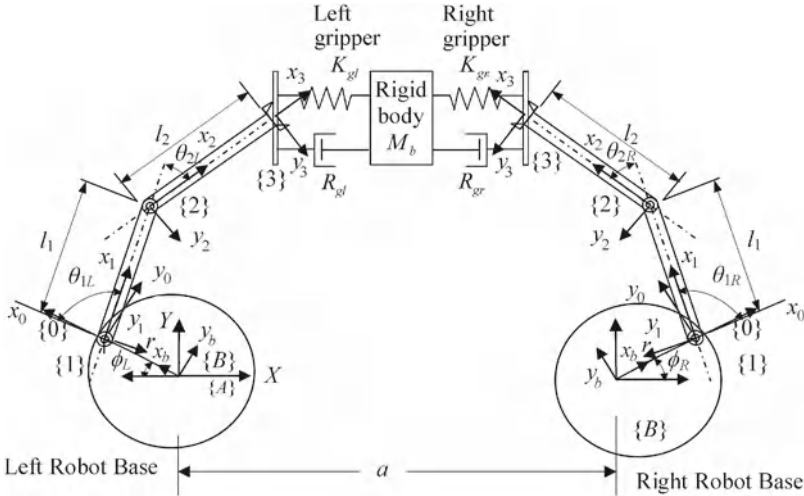


Fig. 8.7 Sketch of a two DOF cooperative manipulator

$$T_o = \begin{bmatrix} c(\phi + \theta_{12}) & -s(\phi + \theta_{12}) & 0 & rc\phi + l_1c(\phi + \theta_1) + l_2c(\phi + \theta_{12}) \\ s(\phi + \theta_{12}) & c(\phi + \theta_{12}) & 0 & rs\phi + l_1s(\phi + \theta_1) + l_2s(\phi + \theta_{12}) \\ 0 & 0 & 1 & 0 \\ 0 & 0 & 0 & 1 \end{bmatrix} \quad (8.26)$$

where $c = \cos$, $s = \sin$ and $\theta_{12} = \theta_1 + \theta_2$. From the expression of overall transformation matrix, the kinematic relations for the tip displacement X_{tip} , Y_{tip} in X and Y directions for the left robot can be given as,

$$X_{tipL} = r \cos \phi_L + l_1 \cos(\phi_L + \theta_{1L}) + l_2 \cos(\phi_L + \theta_{1L} + \theta_{2L}) \quad (8.27)$$

$$Y_{tipL} = r \sin \phi_L + l_1 \sin(\phi_L + \theta_{1L}) + l_2 \sin(\phi_L + \theta_{1L} + \theta_{2L}) \quad (8.28)$$

The tip angular displacement with respect to X axis is given as

$$\theta_{tipL} = \phi_L + \theta_{1L} + \theta_{2L} \quad (8.29)$$

8.6.2 Inverse Kinematics

For a given position and orientation of the end effector with respect to an inertial reference frame, it is required to find a set of joint variables that would bring the end effector in the specified position and orientation. The inverse kinematics transforms the output position into the joint coordinate.

To illustrate the inverse kinematic, let us take the example of cooperative manipulator shown in Fig. 8.7. For a given X_{tipL} and Y_{tipL} , if we take ϕ as constant, then Eqs. 8.27 and 8.28 become

$$X_{tipL} - r \cos \phi_L = l_1 \cos(\phi_L + \theta_{1L}) + l_2 \cos(\phi_L + \theta_{1L} + \theta_{2L}) \quad (8.30)$$

$$Y_{tipL} - r \sin \phi_L = l_1 \sin(\phi_L + \theta_{1L}) + l_2 \sin(\phi_L + \theta_{1L} + \theta_{2L}) \quad (8.31)$$

If we assume $X_{tipL} - r \cos \phi_L = X_L$ and $Y_{tipL} - r \sin \phi_L = Y_L$, then

$$X_L = l_1 \cos(\phi_L + \theta_{1L}) + l_2 \cos(\phi_L + \theta_{1L} + \theta_{2L}) \quad (8.32)$$

$$Y_L = l_1 \sin(\phi_L + \theta_{1L}) + l_2 \sin(\phi_L + \theta_{1L} + \theta_{2L}) \quad (8.33)$$

By squaring and adding Eqs. 8.32 and 8.33, we get.

$$X_L^2 + Y_L^2 = l_1^2 + l_2^2 + 2l_1l_2 \cos \theta_{2L} \quad (8.34)$$

For a known value of X_{tipL} , Y_{tipL} , r and ϕ , let

$$X_L^2 + Y_L^2 = R_L^2, \quad (8.35)$$

Then, from Eq. 8.34 we get,

$$\theta_{2L} = \cos^{-1}[(R_L^2 - l_1^2 - l_2^2)/2l_1l_2] \quad (8.36)$$

From Eq. 8.32, we get

$$X_L = l_1 \cos(\phi_L + \theta_{1L}) + l_2 \cos(\phi_L + \theta_{1L}) \cos \theta_{2L} - l_2 \sin(\phi_L + \theta_{1L}) \sin \theta_{2L}$$

$$X_L = \cos(\phi_L + \theta_{1L})[l_1 + l_2 \cos \theta_{2L}] - l_2 \sin(\phi_L + \theta_{1L}) \sin \theta_{2L}$$

$$X_L = k_{1L} \cos(\phi_L + \theta_{1L}) - k_{2L} \sin(\phi_L + \theta_{1L}) \quad (8.37)$$

where $k_{1L} = l_1 + l_2 \cos(\theta_{2L})$ and $k_{2L} = l_2 \sin(\theta_{2L})$. Similarly from Eq. 8.33 we get,

$$Y_L = k_{1L} \sin(\phi_L + \theta_{1L}) + k_{2L} \cos(\phi_L + \theta_{1L}) \quad (8.38)$$

If $p_L = \sqrt{k_{1L}^2 + k_{2L}^2}$ and $\beta_L = \text{atan2}(k_{2L}, k_{1L})$ where $\text{atan2}(y, x)$ is the signed arctan(y/x) function defined in the domain $(-\pi, \pi)$, then $k_{1L} = p_L \cos \beta_L$ and $k_{2L} = p_L \sin \beta_L$. Equation 8.37 can now be rewritten as

$$X_L = p_L \cos \beta_L \cos(\phi_L + \theta_{1L}) - p_L \sin \beta_L \sin(\phi_L + \theta_{1L}) \quad (8.39)$$

$$X_L/p_L = \cos(\beta_L + \phi_L + \theta_{1L})$$

Similarly from Eq. 8.38, we can write

$$Y_L/p_L = \sin(\beta_L + \phi_L + \theta_{1L}) \quad (8.40)$$

From Eqs. 8.39 and 8.40, we can write $\beta_L + \phi_L + \theta_{1L} = \text{atan2}(Y_L, X_L)$. So

$$\theta_{1L} = \text{atan2}(Y_L, X_L) - \beta_L - \phi_L \quad (8.41)$$

The equation for the right robot can be derived similar to left robot as, $a - X_{tipR} - |r \cos \phi_R| = X_R$ and $Y_{tipR} - r \sin \phi_R = Y_R$. If $X_R^2 + Y_R^2 = R_R^2$ then, we have

$$\theta_{2R} = \cos^{-1}[(R_R^2 - l_1^2 - l_2^2)/2l_1l_2] \quad (8.42)$$

and

$$\theta_{1R} = \text{atan2}(Y_R, X_R) - \beta_R - \phi_R \quad (8.43)$$

where $\beta_R = \text{atan2}(k_{2R}, k_{1R})$, $k_{1R} = l_1 + l_2 \cos(\theta_{2R})$ and $k_{2R} = l_2 \sin(\theta_{2R})$.

8.7 Linear and Rotational Frames in Rigid Bodies

8.7.1 Translational Motion of Rigid Bodies

Let us, attach a reference frame to each body. Now, we can study the motion of each frame relative to the next. This is the same methodology that we have used to study the forward position of the manipulator. Let us look at frame $\{A\}$ and $\{B\}$ as shown in Fig. 8.8. Let us consider a vector Q fixed in frame $\{B\}$, i.e. ${}^B Q$. We want to describe the motion of this vector relative to frame $\{A\}$. Let us assume that $\{A\}$ is fixed and $\{B\}$ is located relative to $\{A\}$ by a position vector ${}^A P_{BORG}$ and a rotation matrix ${}^A_B R$.

Now, three motions can be described: (i) the vector ${}^A P_{BORG}$ can be changing, (ii) the vector ${}^B Q$ can be changing, (iii) the orientation of $\{B\}$ with respect to $\{A\}$ may be changing. Now first let us look at linear motion and thus assume ${}^A_B R$ is not changing. So, we need only to represent both velocity components in terms of $\{A\}$.

$${}^A V_Q = {}^A V_{BORG} + {}^A_B R {}^B V_Q \quad (8.44)$$

Since velocity of Q is just a vector, so we can use standard rotation matrices to transform its value from one frame to another. If we know $Q(t)$ and ${}^A P_{BORG}(t)$, we can differentiate and insert into the Eq. 8.44 to find velocity of Q relative to frame $\{A\}$.

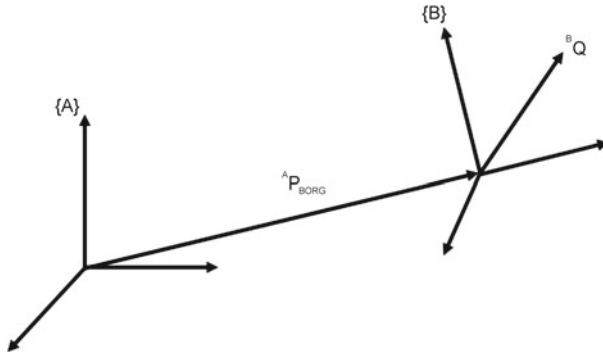
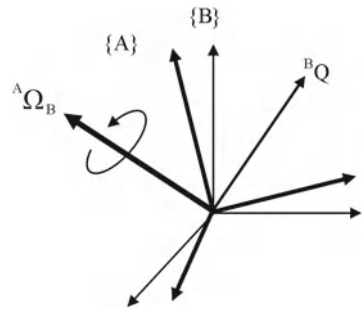


Fig. 8.8 Description of frame {B} translation relative to frame {A}

Fig. 8.9 Velocity of a vector fixed in frame {B} when frame {B} rotates relative to frame {A}



8.7.2 Rotational Motion of Rigid Bodies

Now, Let us assume that Q is constant and fixed in B i.e., ${}^B V_Q = 0$. Although Q has no velocity relative to $\{B\}$, it is clear that it can still have motion relative to $\{A\}$. The motion is due to two components. First, the vector ${}^A P_{BORG}$ is changing. Second, the orientation of $\{B\}$ with respect to $\{A\}$ is changing in time due to velocity ${}^A \Omega_B$. Let us look first at the change due to rotation as shown in Fig. 8.9. Let us look at Q after a small time Δt as shown in Figs. 8.10 and 8.11. The change in Q i.e., ΔQ for a very small motion is just the radius times the change in the angle. Radius is $Q \sin\theta$. Remember Q is not changing in time. So, $\Delta Q = {}^A Q \sin\theta {}^A \Omega_B \Delta t$. Thus, ${}^A V_Q$ is just the cross-product of ${}^A Q$ and ${}^A \Omega_B$, i.e.,

$${}^A V_Q = {}^A \Omega_B \times {}^A Q \tag{8.45}$$

In general if Q changes with time, then

$${}^A V_Q = {}^A \Omega_B \times {}^A Q + {}^A ({}^B V_Q) \tag{8.46}$$

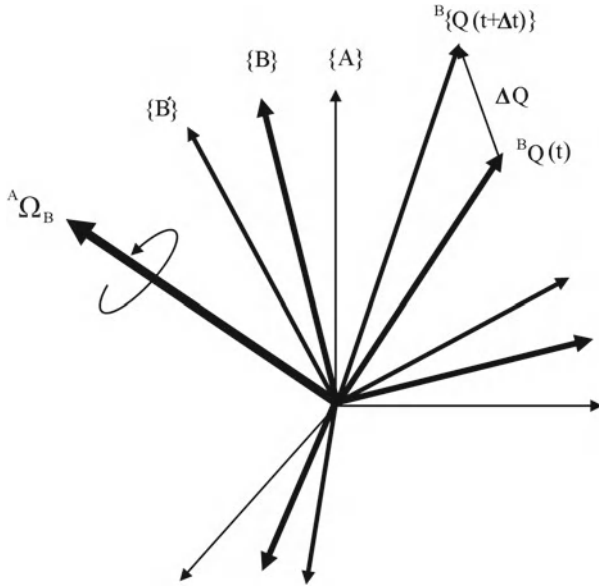
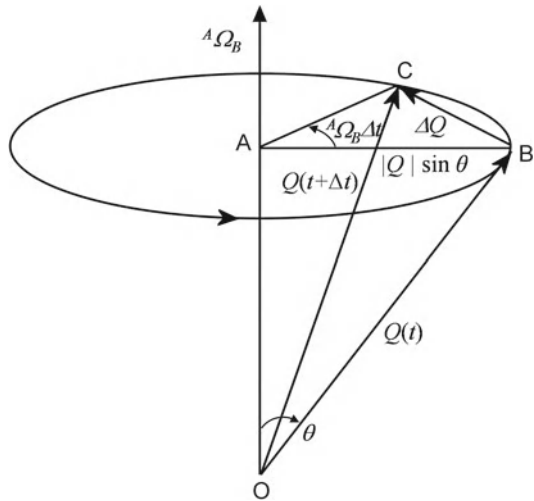


Fig. 8.10 Position of a vector ${}^B Q$ at time $t+\Delta t$ when frame $\{B\}$ rotates relative to frame $\{A\}$

Fig. 8.11 Derivation of velocity of a vector Q fixed in frame $\{B\}$ when frame $\{B\}$ rotates relative to frame $\{A\}$



or we can write it as

$${}^A V_Q = {}^A \Omega_B \times {}^A_B R {}^B Q + {}^A_B R {}^B V_Q \tag{8.47}$$

Thus if simultaneous translational and rotational motion is there then,

$${}^A V_Q = {}^A V_{BORG} + {}^A \Omega_B \times {}^A_B R {}^B Q + {}^A_B R {}^B V_Q \tag{8.48}$$

8.7.3 Velocity Propagation from Link to Link

The velocity of link $i + 1$ is the velocity of link i , plus the velocity component added at joint $i + 1$. Angular velocities can be added if they are represented in the same frame. Remember, we have defined all joint motions to be around or along Z . In mathematical form, this can be written as

$${}^i\omega_{i+1} = {}^i\omega_i + {}^i_{i+1}R \dot{\theta}_{i+1} {}^{i+1}\hat{Z}_{i+1} \quad (8.49)$$

where

$$\dot{\theta}_{i+1} {}^{i+1}\hat{Z}_{i+1} = {}^{i+1}[0 \ 0 \ \dot{\theta}_{i+1}]^T$$

The translational velocity propagation can be given as

$${}^i v_{i+1} = {}^i v_i + {}^i\omega_i \times {}^i P_{i+1} \quad (8.50)$$

If we want the translational and angular velocities in terms of $i + 1$ we simply premultiply by the rotation matrix. Remember that the derivatives are still taken relative to a universal frame. So, v_i is the velocity of the origin of link frame $\{i\}$ and ω_i is the angular velocity of link frame $\{i\}$. They can be expressed in any frame even frame $\{i\}$.

$${}^{i+1}v_{i+1} = {}^{i+1}_i R \left({}^i v_i + {}^i\omega_i \times {}^i P_{i+1} \right) \quad (8.51)$$

$${}^{i+1}\omega_{i+1} = {}^{i+1}_i R \left({}^i\omega_i + {}^i_{i+1}R \dot{\theta}_{i+1} {}^{i+1}\hat{Z}_{i+1} \right) = {}^{i+1}_i R \left({}^i\omega_i + \dot{\theta}_{i+1} {}^{i+1}\hat{Z}_{i+1} \right) \quad (8.52)$$

Similarly in the case of a translational joint we get,

$${}^{i+1}\omega_{i+1} = {}^{i+1}_i R {}^i\omega_i \quad (8.53)$$

We observe that there is no additional angular velocity component since it is a translational joint. We require just a change of reference frame. For translational velocity, the expression can be given by

$${}^{i+1}v_{i+1} = {}^{i+1}_i R \left({}^i v_i + {}^i\omega_i \times {}^i P_{i+1} \right) + \dot{d}_{i+1} {}^{i+1}\hat{Z}_{i+1} \quad (8.54)$$

Here, we need to remember that we have to add contribution due to linear motion of the joint along Z axis.

8.7.4 Jacobian

Let us say we have two functions $x = F(\theta_1, \theta_2)$ and $y = G(\theta_1, \theta_2)$ and we want to find the velocity v_x and v_y . We use the chain rule to take the derivative

$$\dot{x} = \frac{\partial x}{\partial t} = \frac{\partial F(\theta_1, \theta_2)}{\partial t} = \frac{\partial F}{\partial \theta_1} \frac{\partial \theta_1}{\partial t} + \frac{\partial F}{\partial \theta_2} \frac{\partial \theta_2}{\partial t} \quad (8.55)$$

$$\dot{y} = \frac{\partial y}{\partial t} = \frac{\partial G(\theta_1, \theta_2)}{\partial t} = \frac{\partial G}{\partial \theta_1} \frac{\partial \theta_1}{\partial t} + \frac{\partial G}{\partial \theta_2} \frac{\partial \theta_2}{\partial t} \quad (8.56)$$

In a matrix form Eqs. 8.55 and 8.56 can be written as

$$\begin{bmatrix} \dot{x} \\ \dot{y} \end{bmatrix} = \begin{bmatrix} \frac{\partial F}{\partial \theta_1} & \frac{\partial F}{\partial \theta_2} \\ \frac{\partial G}{\partial \theta_1} & \frac{\partial G}{\partial \theta_2} \end{bmatrix} \begin{bmatrix} \dot{\theta}_1 \\ \dot{\theta}_2 \end{bmatrix} = [J] \begin{bmatrix} \dot{\theta}_1 \\ \dot{\theta}_2 \end{bmatrix} \quad (8.57)$$

where J is Jacobian. It is a multidimensional form of the derivative. At any instant, the Jacobian is linear transformation. The Jacobian will vary as a function of time. Most common Jacobian deals with joint velocities. It relates the Cartesian coordinates of the tip of the robot arm to the joint velocities. The number of rows in Jacobian corresponds to the number of DOF while the number of columns corresponds to the number of joints in manipulator. For a general case of say a robot with six joints, Jacobian is a 6×6 matrix, joint velocity vector will be 6×1 , Cartesian velocity vector will be 6×1 , which includes 3×1 translational velocity vector and 3×1 rotational velocity vector. The Jacobian matrix need not be square always.

8.8 Manipulator Dynamics

Manipulator dynamics give the relationship between the robot's position (and its derivatives) and forces or torques. Forward dynamics deals with the calculation of joint position, velocity, and acceleration vector for a given joint torque vector whereas inverse dynamics computes the joint torques required to achieve the specified state of joint position, velocity, and acceleration. Forward dynamics is used in simulating the manipulator while inverse dynamics is used in controlling the manipulator.

Various methods to study the dynamics of manipulators are

1. Lagrangian formulation

This method is energy based. In this method, we calculate potential and kinetic energies of robot. With this method, we can determine forces directly.

2. Newton-Euler formulation

This method is based on force balance. We calculate velocity and acceleration and use it to get forces.

3. Bond graph modeling

This method is based on power conservation as discussed in Chap. 2.

Before we look into these methods, let us discuss some preliminaries.

- Acceleration of a rigid body

Linear acceleration of a vector Q described with respect to frame $\{B\}$ as seen from frame A (see Fig. 8.8) is given by

$${}^A\dot{V}_Q = {}^A\dot{V}_{BORG} + {}^A_B R {}^B\dot{V}_Q + 2 {}^A\Omega_B \times {}^A_B R {}^B V_Q + {}^A\dot{\Omega}_B \times {}^A_B R {}^B Q + {}^A\Omega_B \times ({}^A\Omega_B \times {}^A_B R {}^B Q) \tag{8.58}$$

In Eq. 8.58, \dot{V}_{BORG} is the acceleration of origin of frame $\{B\}$ with respect to frame $\{A\}$, ${}^B V_Q$ is the velocity of Q with respect to frame $\{B\}$, ${}^A_B R$ is rotation matrix, ${}^A\Omega_B$ is angular velocity of frame $\{B\}$ with respect to frame $\{A\}$, ${}^B Q$ is the position vector of Q described with respect to frame $\{B\}$.

Angular acceleration of frame $\{C\}$ with respect to frame $\{A\}$ can be given as

$${}^A\dot{\Omega}_C = {}^A\dot{\Omega}_B + {}^A_B R {}^B\dot{\Omega}_C + {}^A\Omega_B \times {}^A_B R {}^B\Omega_C \tag{8.59}$$

In Eq. 8.59, it is assumed that frame $\{B\}$ is rotating with respect to frame $\{A\}$ by ${}^A\Omega_B$, and frame $\{C\}$ is rotating with respect to frame $\{B\}$ by ${}^B\Omega_C$.

- Moment of Inertia

Inertia is the tendency of a body to remain in a state of rest or uniform motion. A force or moment is required to change this state. Motion could be linear or rotational. Linear inertia is known as mass. The frame in which the inertia is measured is known as the inertial reference frame. For a single degrees-of-freedom system, we can speak of just a mass for linear motion. For rotation, the equivalent term is known as the mass moment of inertia. A body has three mass moments of inertia I_{xx}, I_{yy}, I_{zz} and three mass products of inertia I_{xy}, I_{yz}, I_{zx} . The mass moments and mass products depend on the shape and mass distribution of the body. It is convenient to create a matrix that represents the inertia of a body. It is known as the inertia tensor and it is given as

$$I = \begin{bmatrix} I_{xx} & -I_{yx} & -I_{xz} \\ -I_{xy} & I_{yy} & -I_{zy} \\ -I_{xz} & -I_{yz} & I_{zz} \end{bmatrix} \tag{8.60}$$

We can select a reference frame such that the products of inertia are zero. In such case, the moments of inertia are known as the principal moments and the axes as the principal axes. Inertia around an axis other than centroidal axis can be calculated through the parallel axis theorem. Moments of inertia of simple objects can be combined to compute moments of inertia of complex objects.

8.8.1 Lagrange Formulation

Lagrange formulation is an energy based approach to study dynamics. Kinetic energy is defined as work required to bring a body to rest. For translatory motion, it is defined as

$$K_{Tran} = \frac{1}{2} M V^2, \quad (8.61)$$

where M is the mass of the body and V is the magnitude of its contemporary velocity. Kinetic energy for rotational motion is defined as

$$K_{rot} = \frac{1}{2} I \omega^2 \quad (8.62)$$

where I is the mass moment of inertia of the body about axis of rotation and ω is the angular speed of the body. Potential energy of a body is its capacity to do work in virtue of its position. It is measured by the amount of work done by the force to restore the body from its present position to its standard position (reference position). If the present position of the body is specified by a vector r and its standard position by a vector r_0 , we have

$$U = \int_r^{r_0} f(r) \cdot dr \quad (8.63)$$

where U is the potential energy and $f(r)$ is the force. Total energy is defined as

$$E = K + U \quad (8.64)$$

The Lagrangian is defined by

$$L(q_n, \dot{q}_n) = K - U \quad (8.65)$$

where K is kinetic energy of the whole system, U is potential energy of the whole system, q_n is generalized coordinate, and \dot{q}_n is derivative of generalized coordinate.

The equations of motion based on Lagrange approach is given as

$$\frac{d}{dt} \left(\frac{\partial L}{\partial \dot{q}_n} \right) - \frac{dL}{\partial q_n} = F_n \quad (8.66)$$

where q_n are the generalized coordinates, and F_n are the generalized forces or torques. However, Eq. 8.66 has limitations such as when dissipative forces are present we need to introduce Rayleigh potential function, we cannot handle gyroscopic forces/moments and we cannot handle non-potential forces such as circulatory forces [12].

To develop the dynamic equation of a manipulator, let us find the kinetic energy of a link of manipulator. For i th link, the expression for kinetic energy can be given as

$$k_i = \frac{1}{2} m_i v_{C_i}^T v_{C_i} + \frac{1}{2} {}^i \omega_i^T C_i I_i {}^i \omega_i \tag{8.67}$$

In Eq. 8.67, the first term is the contribution from linear velocity of the link’s center of gravity, and the second term is the contribution from angular velocity of the link. So, the total kinetic energy of the manipulator is sum of the kinetic energy of individual links and is given by

$$k = \sum_{i=1}^n k_i \tag{8.68}$$

Potential energy of link i is given as

$$u_i = -m_i {}^0 g^T {}^0 P_{C_i} + u_{ref_i} \tag{8.69}$$

where ${}^0 g$ is the 3×1 gravity vector, ${}^0 P_{C_i}$ is the vector locating the center of mass of i th link and u_{ref_i} is the constant chosen so that the minimum value of u_i is zero. So, the manipulator total potential energy can be given by

$$u = \sum_{i=1}^n u_i \tag{8.70}$$

In general, the torques of a manipulator are (refer Eq. 8.66)

$$\tau = \frac{d}{dt} \left(\frac{\partial L}{\partial \dot{\Theta}} \right) - \frac{\partial L}{\partial \Theta} = \frac{d}{dt} \left(\frac{\partial K}{\partial \dot{\Theta}} \right) - \frac{\partial K}{\partial \Theta} + \frac{\partial u}{\partial \Theta} \tag{8.71}$$

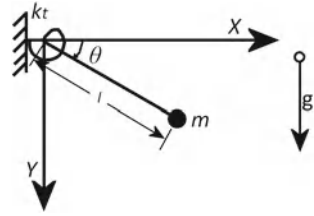
Here, τ is a vector of torques. Manipulator Dynamics equation in joint space can be given as

$$\tau = M(\Theta) \ddot{\Theta} + V(\Theta, \dot{\Theta}) + G(\Theta) \tag{8.72}$$

where M is the mass matrix; V has two elements: (i) Coriolis component as a function of two different velocities, (ii) Centrifugal component as a function of the square of velocity; G contains the gravity terms, and all the terms are also function of position. Example 1: Derive the governing equation for a single jointed manipulator shown in Fig. 8.12 using Euler-Lagrange formulation

$$\text{Kinetic energy } T = \frac{1}{2} m l^2 \dot{\theta}^2 \tag{8.73}$$

Fig. 8.12 Schematic diagram of one DOF robot



Assuming $y = 0$ as datum, potential energy is given as

$$\text{Potential energy } U = \frac{1}{2}k_t\theta^2 - mgl \sin \theta \quad (8.74)$$

Lagrange equation is given by

$$\frac{d}{dt} \left(\frac{\partial L}{\partial \dot{q}} \right) - \frac{\partial L}{\partial q} = \tau \quad (8.75)$$

From $L = T - U$,

$$\frac{d}{dt} \left(\frac{\partial T}{\partial \dot{q}} \right) - \frac{\partial T}{\partial q} + \frac{\partial U}{\partial q} = 0 \quad (8.76)$$

Here $q = \theta$, so

$$\frac{d}{dt} \left(\frac{\partial T}{\partial \dot{\theta}} \right) - \frac{\partial T}{\partial \theta} + \frac{\partial U}{\partial \theta} = 0 \quad (8.77)$$

Now,

$$\frac{\partial T}{\partial \dot{\theta}} = ml^2\dot{\theta}, \quad (8.78)$$

$$\frac{d}{dt} \left(\frac{\partial T}{\partial \dot{\theta}} \right) = ml^2\ddot{\theta} \quad (8.79)$$

$$\frac{\partial T}{\partial \theta} = 0 \quad (8.80)$$

$$\frac{\partial U}{\partial \theta} = k_t\theta - mgl \cos \theta \quad (8.81)$$

Substituting from Eqs. 8.78–8.81 into Eq. 8.77, we obtain

$$ml^2\ddot{\theta} + k_t\theta - mgl \cos \theta = 0 \quad (8.82)$$

8.8.2 Newton-Euler Formulation

The algorithm is composed of two parts. First, calculate the angular velocity and accelerations of the each link. Then calculate the linear velocity and accelerations of the center of mass of each link. Once the accelerations and velocities of the center of mass are calculated we can use the Newton-Euler equations to calculate the forces on the center of mass of each link. Once we have the forces, we can work back from the last link to first link to calculate the joint forces and torques. We can include gravitational loads by giving frame 0 an acceleration of g . This fictitious acceleration causes the same reaction forces and torques at the joints as gravity without additional computational requirements. For the case of six link manipulator with all rotational joints, the equations can be summarized as follows.

Outward iterations for $i = 0$ to 5

$${}^{i+1}\omega_{i+1} = {}^i R^{i+1} \omega_i + \dot{\theta}_{i+1} {}^{i+1} \hat{Z}_{i+1} \quad (8.83)$$

$${}^{i+1}\dot{\omega}_{i+1} = {}^i R^{i+1} \dot{\omega}_i + {}^i R^{i+1} \omega_i \times \dot{\theta}_{i+1} {}^{i+1} \hat{Z}_{i+1} + \ddot{\theta}_{i+1} {}^{i+1} \hat{Z}_{i+1} \quad (8.84)$$

$${}^{i+1}\dot{v}_{i+1} = {}^i R^{i+1} \left({}^i \dot{v}_i + {}^i \dot{\omega}_i \times {}^i P_{i+1} + {}^i \omega_i \times ({}^i \omega_i \times {}^i P_{i+1}) \right) \quad (8.85)$$

$$\begin{aligned} {}^{i+1}\dot{v}_{C_{i+1}} &= {}^{i+1}\dot{v}_{i+1} + {}^{i+1}\dot{\omega}_{i+1} \times {}^{i+1} P_{C_{i+1}} \\ &\quad + {}^{i+1}\omega_{i+1} \times ({}^{i+1}\omega_{i+1} \times {}^{i+1} P_{C_{i+1}}) \end{aligned} \quad (8.86)$$

$${}^{i+1}F_{i+1} = m_{i+1} {}^{i+1}\dot{v}_{C_{i+1}} \quad (8.87)$$

$${}^{i+1}N_{i+1} = C_{i+1} I_{i+1} {}^{i+1}\dot{\omega}_{i+1} + {}^{i+1}\omega_{i+1} \times C_{i+1} I_{i+1} {}^{i+1}\omega_{i+1} \quad (8.88)$$

Inward iterations for $i = 6$ to 1

$${}^i f_i = {}^i R^{i+1} f_{i+1} + {}^i F_i \quad (8.89)$$

$${}^i n_i = {}^i N_i + {}^i R^{i+1} n_{i+1} + {}^i P_{C_i} \times {}^i F_i + {}^i P_{i+1} \times {}^i R^{i+1} f_{i+1} \quad (8.90)$$

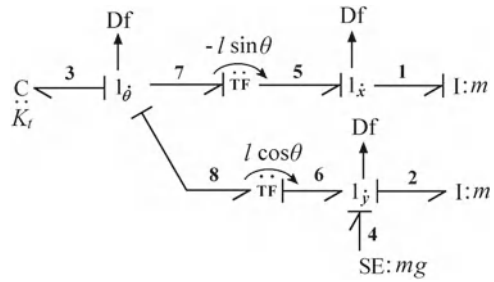
$$\tau_i = {}^i n_i^T {}^i \hat{Z}_i \quad (8.91)$$

If we compare the two formulations i.e., Lagrange and Newton-Euler formulation then we find that computationally Newton-Euler formulation is better whereas Lagrangian formulation gives more information.

8.8.3 Bond Graph Modeling

Bond graph can be used nicely to derive system equations of robots. The concept of bond graph is dealt in Chap. 2. We shall use those concepts to develop the bond graph model here.

Fig. 8.13 Bond graph model one DOF robot



- Example 1: Derive the governing equation for a single jointed manipulator shown in Fig. 8.12 using bond graph modeling.

Figure 8.12 shows the schematic diagram of a one DOF robot. To draw the bond graph of the system, let us do the following kinematic analysis

$$x = l \cos \theta$$

$$y = l \sin \theta$$

So,

$$\dot{x} = -l \sin \theta \dot{\theta} \tag{8.92}$$

$$\dot{y} = l \cos \theta \dot{\theta} \tag{8.93}$$

Using Eqs. 8.92 and 8.93, we can draw the bond graph of single jointed manipulator as shown in Fig. 8.13. From bond graph, we can see that state variables in this problem are P_1, Q_3 . As per the given causal structure to derive the system equation, let us ask two questions:

1. What does elements give to system in term of system variables?

$$C_3 : e_3 = k_t Q_3$$

$$I_1 : f_1 = \frac{P_1}{m}$$

$$I_2 : e_2 = m \dot{f}_2$$

2. What does system give to elements with integral causality?

To $C_3 : f_3$ where

$$f_3 = \dot{Q}_3 = f_7 = \frac{f_5}{-l \sin \theta} = \frac{f_1}{-l \sin \theta} = \frac{P_1}{-ml \sin \theta}$$

$$\dot{Q}_3 = \dot{\theta} = \frac{-P_1}{ml \sin \theta} \tag{8.94}$$

To $I_1 : e_1$ where

$$\begin{aligned}
 e_1 = e_5 &= \frac{e_7}{-l \sin \theta} = \frac{-(e_8 + e_3)}{-l \sin \theta} \\
 &= \frac{-l \cos \theta e_6 - e_3}{-l \sin \theta} = \frac{-l \cos \theta (e_2 - e_4) - e_3}{-l \sin \theta} \\
 &= \frac{-l \cos \theta (m \dot{f}_2 - mg) - k_t Q_3}{-l \sin \theta} \\
 \dot{P}_1 &= -\frac{1}{l \sin \theta} [-k_t Q_3 - (m \dot{f}_2 - mg) l \cos \theta] \quad (8.95)
 \end{aligned}$$

In Eq. 8.95, we have \dot{f}_2 term because I2 element is in differential causality. From these equations, original equation for simple pendulum can be derived as follows: $P_1 = m\dot{x}$, so $\dot{P}_1 = m\ddot{x}$. We have $\dot{x} = (-l \sin \theta) \dot{\theta}$, so $\ddot{x} = (-l \sin \theta) \ddot{\theta} + \dot{\theta}(-l \cos \theta) \dot{\theta}$, or we can write

$$\ddot{x} = (-l \sin \theta) \ddot{\theta} - (l \cos \theta) \dot{\theta}^2. \quad (8.96)$$

Similarly $f_2 = \dot{y} = (l \cos \theta) \dot{\theta}$ so $\dot{f}_2 = (l \cos \theta) \ddot{\theta} + \dot{\theta}(-l \sin \theta) \dot{\theta}$, or we can write

$$\dot{f}_2 = (l \cos \theta) \ddot{\theta} - (l \sin \theta) (\dot{\theta})^2 \quad (8.97)$$

Equation 8.95 can be written as

$$m\ddot{x} = -\frac{1}{l \sin \theta} [-k_t \theta - (m \dot{f}_2 - mg) l \cos \theta]. \quad (8.98)$$

By substituting from Eqs. 8.96 and 8.97 into Eq. 8.98 for \ddot{x} and \dot{f}_2 , we get

$$-(ml \sin \theta) \ddot{\theta} - (ml \cos \theta) \dot{\theta}^2 = -\frac{1}{l \sin \theta} \left[-k_t \theta - ml^2 \cos^2 \theta \ddot{\theta} + ml^2 \cos \theta \sin \theta \dot{\theta}^2 + mgl \cos \theta \right] \quad (8.99)$$

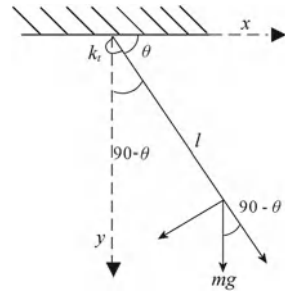
Simplifying the above equation, we get

$$m l^2 \ddot{\theta} = -k_t \theta + mgl \cos \theta \quad (8.100)$$

Now, let us look at Fig. 8.14. If we derive the equation of motion for this, we can do so by equating the restoring torque with the inertial torque.

$$\text{Restoring torque} = mgl \sin(90 - \theta) - k_t \theta$$

Fig. 8.14 Single jointed manipulator with resolved forces



From Newton's second law,

$$ml^2\ddot{\theta} = mgl \sin(90 - \theta) - k_t\theta$$

or

$$ml^2\ddot{\theta} = -k_t\theta + mgl \cos \theta. \quad (8.101)$$

So, we can see that Eq. 8.101 is same as Eq. 8.100. Although this example is very primitive but it explains the procedure for bond graph modeling of manipulators.

Equation 8.101 can also be derived by reduction of the bond graph shown in Fig. 8.13. In the first stage shown in Fig. 8.15 transformer elements with modulus as $-l \sin \theta$ have been added at $1_{\dot{x}}$ junction while transformer elements with modulus as $l \cos \theta$ have been added at $1_{\dot{y}}$ junction. This results in elimination of transformer elements at the left side of $1_{\dot{x}}$ and $1_{\dot{y}}$ junction. Further in the reduction process I and TF element at right side of $1_{\dot{x}}$ and $1_{\dot{y}}$ can be combined resulting in I element with inertia value of $ml^2 \sin^2 \theta$ and $ml^2 \cos^2 \theta$ attached at $1_{\dot{x}}$ and $1_{\dot{y}}$ junctions, respectively. The reduced bond graph is shown in Fig. 8.16. Finally, all $1_{\dot{\theta}}$ junctions can be merged and the resulting bond graph can be shown in Fig. 8.17. If we apply junction law at $1_{\dot{\theta}}$ junction, then we get the system equation which is same as that given by Eq. 8.101.

- Example 2: For an upright single DOF manipulator shown in Fig. 8.18, draw the bond graph model. Assume that the manipulator is driven by a DC motor. For upright manipulator shown in Fig. 8.18, first of all a kinematic analysis is carried out. The tip position can be given as

$$x_T = l \cos \theta \quad (8.102)$$

$$y_T = l \sin \theta \quad (8.103)$$

The tip velocities can be evaluated by differentiating Eqs. 8.102 and 8.103. The tip velocities in X and Y directions can be given as

$$\dot{x}_T = -l \sin \theta \dot{\theta} \quad (8.104)$$

$$\dot{y}_T = l \cos \theta \dot{\theta} \quad (8.105)$$

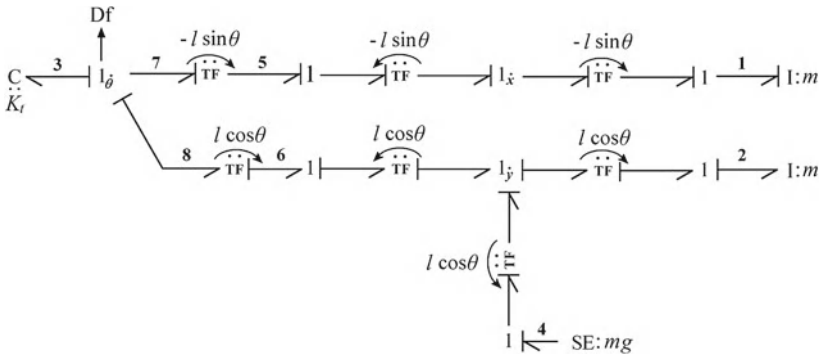


Fig. 8.15 Reduced bond graph model one DOF robot-step1

Fig. 8.16 Reduced bond graph model one DOF robot-step2

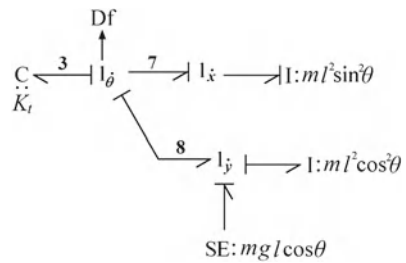
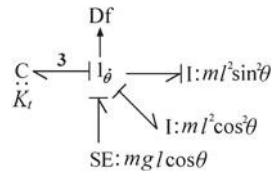


Fig. 8.17 Reduced bond graph model one DOF robot-step3



Likewise velocities of CG can be derived as

$$\dot{x}_{CG} = -l_{CG} \sin \theta \dot{\theta} \tag{8.106}$$

$$\dot{y}_{CG} = l_{CG} \cos \theta \dot{\theta} \tag{8.107}$$

The drawn bond graph of the upright manipulator is shown in Fig. 8.19. In the bond graph, V_{in} is the voltage supplied to motor, I_m is armature inductance, R_m is motor resistance, μ is motor torque constant, R_b is bearing resistance, J is motor rotor inertia, m is mass of link.

- Example 3: For a two jointed manipulator with masses concentrated at tips as shown in Fig. 8.20, derive the dynamic equations using bond graph modeling.

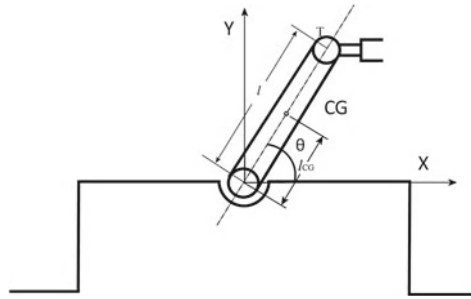


Fig. 8.18 Schematic diagram of one DOF upright manipulator

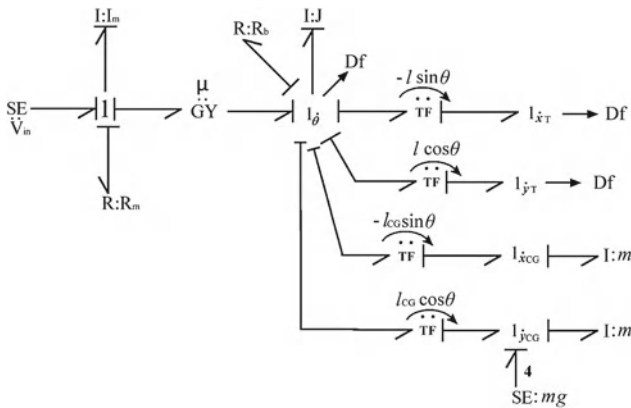


Fig. 8.19 Bond graph model of one DOF upright manipulator

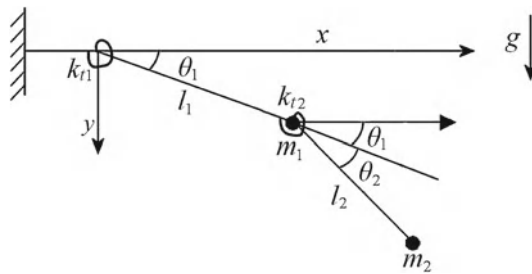


Fig. 8.20 Schematic diagram of a two jointed manipulator

Figure 8.21 shows the bond graph model of robot. To draw the bond graph model transformer moduli can be derived using velocity relations for tip position.

$$\begin{aligned}
 x_{tip} &= l_1 \cos \theta_1 + l_2 \cos(\theta_1 + \theta_2) \\
 y_{tip} &= l_1 \sin \theta_1 + l_2 \sin(\theta_1 + \theta_2)
 \end{aligned}$$

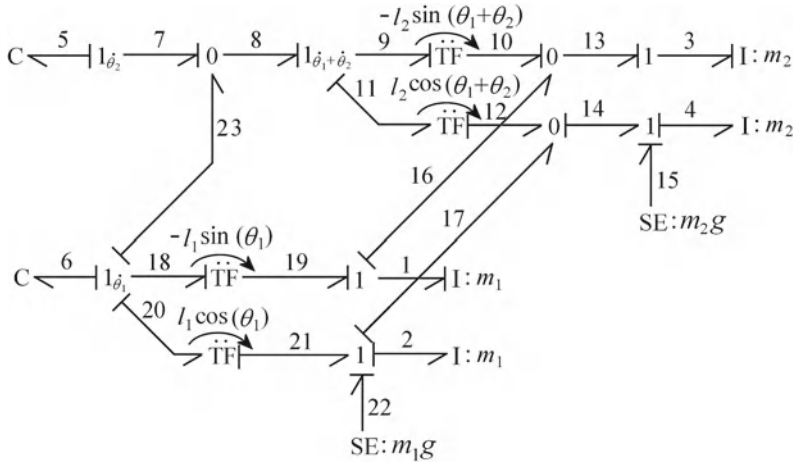


Fig. 8.21 Bond graph model of a two jointed manipulator

$$\dot{x}_{tip} = -l_1 \sin \theta_1 \dot{\theta}_1 - l_2 \sin(\theta_1 + \theta_2)(\dot{\theta}_1 + \dot{\theta}_2) \tag{8.108}$$

$$\dot{y}_{tip} = l_1 \cos \theta_1 \dot{\theta}_1 + l_2 \cos(\theta_1 + \theta_2)(\dot{\theta}_1 + \dot{\theta}_2) \tag{8.109}$$

State variables as seen from bond graph are p_3, p_1, Q_5, Q_6 . Now to derive the system equations, let us again find answers of the two basic questions.

Q1. What do elements give to the system in term of system variables?

$$I_1 : f_1, f_1 = \frac{p_1}{m_1}$$

$$I_3 : f_3, f_3 = \frac{p_3}{m_2}$$

$$C_5 : e_5, e_5 = k_5 Q_5$$

$$C_6 : e_6, e_6 = k_6 Q_6$$

$$I_4 : e_4, e_4 = e_{14} + m_2 g$$

$$e_4 = \frac{e_{11}}{l_2 \cos(\theta_1 + \theta_2)} + m_2 g$$

$$e_4 = \frac{(e_8 - e_9)}{l_2 \cos(\theta_1 + \theta_2)} + m_2 g$$

$$e_4 = \frac{e_7 + \dot{p}_3 l_2 \sin(\theta_1 + \theta_2)}{l_2 \cos(\theta_1 + \theta_2)} + m_2 g$$

$$e_4 = \frac{-e_5}{l_2 \cos(\theta_1 + \theta_2)} + \dot{p}_3 \tan(\theta_1 + \theta_2) + m_2 g$$

$$e_4 = \frac{-k_5 \cdot Q_5}{l_2 \cos(\theta_1 + \theta_2)} + \dot{p}_3 \tan(\theta_1 + \theta_2) + m_2 g \quad (8.110)$$

$$I_2 : e_2, \quad e_2 = e_{21} + e_{22} - e_{17}$$

$$e_2 = \frac{e_{20}}{l_1 \cos \theta_1} + m_1 g - e_{14}$$

$$e_2 = \frac{-(e_{18} + e_{22} + e_6)}{l_1 \cos \theta_1} + m_1 g - (e_4 - m_2 g)$$

$$e_2 = \frac{-[-e_{19} l_1 \sin \theta_1 - k_5 Q_5 + k_6 Q_6]}{l_1 \cos \theta_1} + m_1 g + m_2 g - e_4$$

$$e_2 = \frac{(e_{19} + e_1) l_1 \sin \theta_1}{l_1 \cos \theta_1} + \frac{(k_5 Q_5 - k_6 Q_6)}{l_1 \cos \theta_1} + m_1 g + m_2 g - e_4$$

$$\dot{p}_2 = (\dot{p}_3 + \dot{p}_1) \tan \theta_1 + \frac{k_5(\theta_2 - \theta_1)}{l_1 \cos \theta_1} + m_1 g + m_2 g - e_4 \quad (8.111)$$

Q2. What does the system give to elements with integral causality?

To $C_5 : f_5$,

$$f_5 = f_7 = f_8 - f_{22} = f_9 - f_{18}$$

$$f_5 = -\frac{f_{10}}{l_2 \sin(\theta_1 + \theta_2)} + \frac{p_1}{m_1 l_1 \sin \theta_1}$$

$$f_5 = -\frac{(f_{13} - f_{16})}{l_2 \sin(\theta_1 + \theta_2)} + \frac{p_1}{m_1 l_1 \sin \theta_1}$$

$$f_5 = -\frac{\left(\frac{p_3}{m_2}\right) - \left(\frac{p_1}{m_1}\right)}{l_2 \sin(\theta_1 + \theta_2)} + \frac{p_1}{m_1 l_1 \sin \theta_1}$$

$$\dot{Q}_5 = \frac{1}{l_2 \sin(\theta_1 + \theta_2)} \left(\frac{p_1}{m_1} - \frac{p_3}{m_2} \right) + \frac{p_1}{m_1 l_1 \sin \theta_1} \quad (8.112)$$

To $C_6 : f_6$,

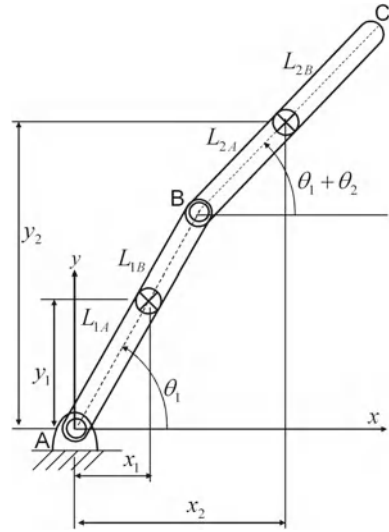
$$\dot{Q}_6 = f_{18} = \frac{-p_1}{m_1 l_1 \sin \theta_1} \quad (8.113)$$

To $I_3 : e_3$, as \dot{p}_3 , find from Eq. 8.110 as

$$\dot{p}_3 = (e_4 - m_2 g) \cot(\theta_1 + \theta_2) + \frac{k_5 Q_5}{l_2 \sin(\theta_1 + \theta_2)} \quad (8.114)$$

To $I_1 : e_1$ as \dot{p}_1 , find from Eq. 8.111 as

Fig. 8.22 Schematic diagram of two link planar robot



$$\dot{p}_1 = (e_2 + e_4 - m_1g - m_2g) \cot \theta_1 - \dot{p}_3 - \frac{k_5 (\theta_2 - \theta_1)}{l_1 \sin \theta_1} \tag{8.115}$$

Equations 8.112–8.115 are the required equations. The bond graph for a two link manipulator may be drawn another way as we shall see in the next example.

- Example 4: Draw the bond graph of a two link planar manipulator shown in Fig. 8.22. To draw the bond graph of planar manipulator let us find out the velocities of points A and B. For body 1, the position of x and y coordinates of point A and B can be given by

$$x_A = x_1 - L_{1A} \cos \theta_1, y_A = y_1 - L_{1A} \sin \theta_1 \tag{8.116}$$

$$x_B = x_1 + L_{1B} \cos \theta_1, y_B = y_1 + L_{1B} \sin \theta_1 \tag{8.117}$$

The velocities in x and y direction of point A and B can be given as

$$\dot{x}_A = \dot{x}_1 + L_{1A} \dot{\theta}_1 \sin \theta_1, \dot{y}_A = \dot{y}_1 - L_{1A} \dot{\theta}_1 \cos \theta_1 \tag{8.118}$$

$$\dot{x}_B = \dot{x}_1 - L_{1B} \dot{\theta}_1 \sin \theta_1, \dot{y}_B = \dot{y}_1 + L_{1B} \dot{\theta}_1 \cos \theta_1 \tag{8.119}$$

For body 2, the velocities in x and y direction of point B and C can be given as

$$\dot{x}_B = \dot{x}_2 + L_{2A} (\dot{\theta}_1 + \dot{\theta}_2) \sin (\theta_1 + \theta_2), \tag{8.120}$$

$$\dot{y}_B = \dot{y}_2 - L_{2A} (\dot{\theta}_1 + \dot{\theta}_2) \cos (\theta_1 + \theta_2) \tag{8.121}$$

$$\dot{x}_C = \dot{x}_2 - L_{2B} (\dot{\theta}_1 + \dot{\theta}_2) \sin (\theta_1 + \theta_2), \tag{8.122}$$

$$\dot{y}_C = \dot{y}_2 + L_{2B} (\dot{\theta}_1 + \dot{\theta}_2) \cos (\theta_1 + \theta_2) \tag{8.123}$$

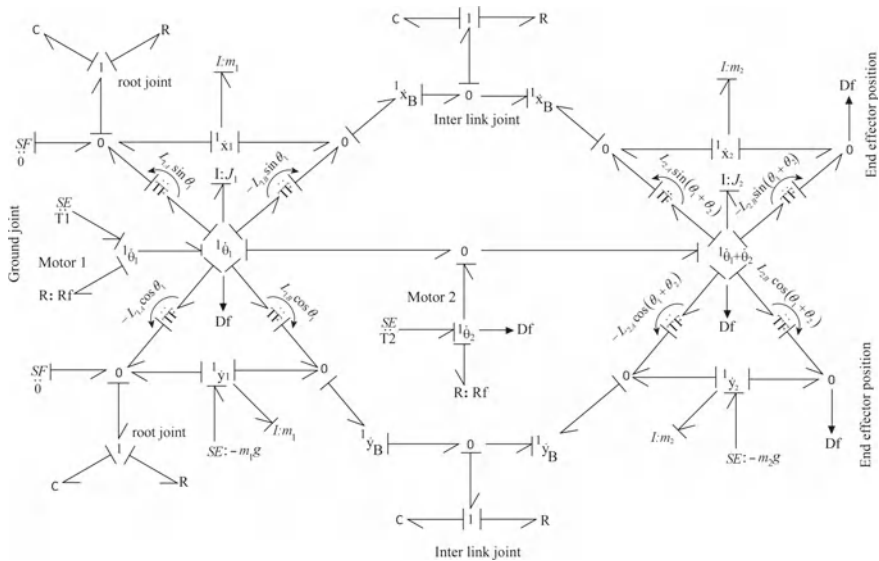


Fig. 8.23 Bond graph model of a two jointed manipulator

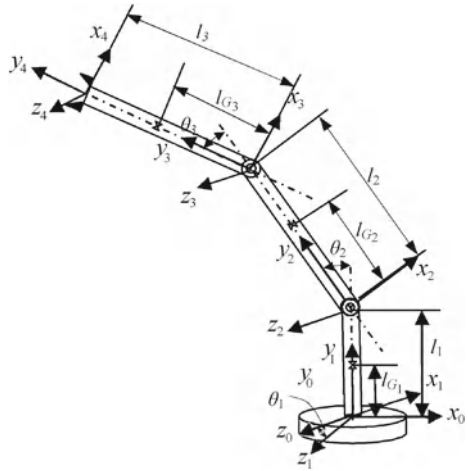
To draw the bond graph model (Fig. 8.23), introduce three velocity junctions for CG motion for each link. Then, create four velocity junctions for two ends. In body 1, end A is fixed (revolute joint) and hence use zero source of flow and pad (pin or joint stiffness and damping). Then, again use joint/pin to connect end B on link 1 to end B on link 2. The torque on the link applied at its root can be applied at its CG because couple moment is a free vector. The reactive torque has to be applied to the base of the link. In the given bond graph, two effort sources supply the joint motor torques T_1 and T_2 . Moreover, the friction at the joints (preventing relative rotation of the links) is modeled by $R:R_f$ elements. This model allows various special cases, e.g., if $T_2 = 0$ and the friction between the two links is high then the robot behaves as a one DOF manipulator. Note that the rotary inertia is the rotary inertia about the CG; not about the root (which anyway is calculated from CG inertia after using parallel axis theorem). More details on modeling of such multibody systems can be consulted in Chap. 5.

- Example 5: Bond graph modeling of three DOF ground robot

Building the model

The schematic diagram of a three DOF manipulator [13] is shown in Fig. 8.24. A coordinate frame is assigned to each link (not as per D-H notations). Links are numbered starting with zero from the base to the last link. The y axis of each frame is along the longitudinal axis of the link. The joint between link i and $i + 1$ is termed as joint $i + 1$ i.e., the frame i is attached rigidly to link i .

Fig. 8.24 Schematic diagram of three DOF ground manipulator



Kinematics of the manipulator

A manipulator is a chain of rigid bodies, each one capable of motion relative to its neighbor. The velocity of link $i + 1$ will be equal to the velocity of link i , plus new velocity component added by joint $i + 1$. Since linear velocity is associated with a point, and angular velocity is associated with a body, the term “velocity of a link” implies the linear velocity of the origin of the link frame, and the rotational velocity of link. It is to be noted that rotational velocities may be added when both angular velocity vectors are written with respect to the same frame. The angular velocity of link $i + 1$ is equal to the angular velocity of link i plus a new component caused by rotational velocity of joint $i + 1$. Thus, the relation for the angular velocity of link $i + 1$ with respect to inertial frame $\{A\}$ and expressed in frame $\{i + 1\}$ coordinate is given by,

$${}^{i+1}({}^A \omega_{i+1}) = {}_i^{i+1} R {}^i({}^A \omega_i) + {}^{i+1}({}^i \omega_{i+1}) \tag{8.124}$$

Similarly, the linear velocity of the origin of frame $\{i + 1\}$ will be equal to sum of the linear velocity of the origin of frame $\{i\}$ plus a new component caused by rotational velocity of link i , i.e.,

$${}^{i+1}({}^A V_{i+1}) = {}_i^{i+1} R [{}^i({}^A V_i) + {}^i({}^A \omega_i) \times {}^i({}^i P_{i+1})] \tag{8.125}$$

The position ${}^i P_{i+1}$ represents the position of the origin of frame $\{i + 1\}$ with respect to frame $\{i\}$ in the i th frame, and the velocity ${}^A V_i$ represents the velocity of the origin of frame $\{i\}$ with respect to inertial frame $\{A\}$, ${}_i^{i+1} R$ represents the orientation of frame $\{i\}$ with respect to frame $\{i + 1\}$. The following rotation matrices will be useful for deriving various velocity relationships.

$${}^0_1R = \begin{bmatrix} c_1 & 0 & s_1 \\ 0 & 1 & 0 \\ -s_1 & 0 & c_1 \end{bmatrix}, \quad {}^1_2R = \begin{bmatrix} c_2 & -s_2 & 0 \\ s_2 & c_2 & 0 \\ 0 & 0 & 1 \end{bmatrix}, \quad {}^2_3R = \begin{bmatrix} c_3 & -s_3 & 0 \\ s_3 & c_3 & 0 \\ 0 & 0 & 1 \end{bmatrix}.$$

Here, $s_i = \sin \theta_i$ and $c_i = \cos \theta_i$. Also, ${}^0({}^0P_1) = [0 \ 0 \ 0]^T$; ${}^1({}^1P_2) = [0 \ l_1 \ 0]^T$; ${}^2({}^2P_3) = [0 \ l_2 \ 0]^T$; ${}^4({}^4P_3) = [0 \ l_3 \ 0]^T$.

Evaluation of angular velocities

In case of ground robot, inertial frame $\{A\}$ is considered as the frame $\{0\}$. So, using Eq. 8.124, angular velocity of links can be derived by substituting for different values of i .

For, $i = 0$,

$$\begin{aligned} {}^1({}^0\omega_1) &= {}^1_0R {}^0({}^0\omega_0) + {}^1({}^0\omega_1) \\ {}^1({}^0\omega_1) &= \dot{\theta}_1 {}^1\hat{Y}_1 \\ {}^1({}^0\omega_1) &= [0 \ \dot{\theta}_1 \ 0]^T \end{aligned} \quad (8.126)$$

For $i = 1$,

$$\begin{aligned} {}^2({}^0\omega_2) &= {}^2_1R {}^1({}^0\omega_1) + {}^2({}^1\omega_2) \\ {}^2({}^0\omega_2) &= {}^2_1R {}^1({}^0\omega_1) + \dot{\theta}_2 {}^2\hat{Z}_2 \end{aligned}$$

Substituting from Eq. 8.126 and noting that ${}^2_1R = {}^1_2R^T$ we get,

$$\begin{aligned} {}^2({}^0\omega_2) &= \begin{bmatrix} c_2 & s_2 & 0 \\ -s_2 & c_2 & 0 \\ 0 & 0 & 1 \end{bmatrix} \begin{Bmatrix} 0 \\ \dot{\theta}_1 \\ 0 \end{Bmatrix} + \begin{Bmatrix} 0 \\ 0 \\ \dot{\theta}_2 \end{Bmatrix} \\ {}^2({}^0\omega_2) &= \begin{Bmatrix} s_2\dot{\theta}_1 \\ c_2\dot{\theta}_1 \\ \dot{\theta}_2 \end{Bmatrix} \end{aligned} \quad (8.127)$$

For $i = 2$,

$$\begin{aligned} {}^3({}^0\omega_3) &= {}^3_2R {}^2({}^0\omega_2) + {}^3({}^2\omega_3) \\ {}^3({}^0\omega_3) &= {}^3_2R {}^2({}^0\omega_2) + \dot{\theta}_3 {}^3\hat{Z}_3 \end{aligned}$$

Substituting from Eq. 8.127 and noting that ${}^3_2R = {}^2_3R^T$, we get,

$${}^3({}^0\omega_3) = \begin{bmatrix} c_3 & s_3 & 0 \\ -s_3 & c_3 & 0 \\ 0 & 0 & 1 \end{bmatrix} \begin{Bmatrix} s_2\dot{\theta}_1 \\ c_2\dot{\theta}_1 \\ \dot{\theta}_2 \end{Bmatrix} + \begin{Bmatrix} 0 \\ 0 \\ \dot{\theta}_3 \end{Bmatrix}$$

$${}^3({}^0\omega_3) = \begin{Bmatrix} s_{23} \dot{\theta}_1 \\ c_{23} \dot{\theta}_1 \\ \dot{\theta}_2 + \dot{\theta}_3 \end{Bmatrix} \quad (8.128)$$

where $s_{23} = \sin(\theta_2 + \theta_3)$; $c_{23} = \cos(\theta_2 + \theta_3)$.

In Eq. 8.125, substituting different values of i , we get,

For $i = 0$,

$${}^1({}^0V_1) = {}^0R[{}^0({}^0V_0) + {}^0({}^0\omega_0) \times {}^0({}^0P_1)] = [0 \ 0 \ 0]^T \quad (8.129)$$

For $i = 1$,

$${}^2({}^0V_2) = {}^2R[{}^1({}^0V_1) + {}^1({}^0\omega_1) \times {}^1({}^1P_2)]$$

Substituting from Eq. 8.126 and noting that ${}^2R = {}^2R^T$ we get,

$$\begin{aligned} {}^2({}^0V_2) &= \begin{bmatrix} c_2 & s_2 & 0 \\ -s_2 & c_2 & 0 \\ 0 & 0 & 1 \end{bmatrix} \left[\begin{Bmatrix} 0 \\ \dot{\theta}_1 \\ 0 \end{Bmatrix} \times \begin{Bmatrix} 0 \\ l_1 \\ 0 \end{Bmatrix} \right] = \begin{bmatrix} c_2 & s_2 & 0 \\ -s_2 & c_2 & 0 \\ 0 & 0 & 1 \end{bmatrix} \begin{bmatrix} 0 & 0 & \dot{\theta}_1 \\ 0 & 0 & 0 \\ -\dot{\theta}_1 & 0 & 0 \end{bmatrix} \begin{Bmatrix} 0 \\ l_1 \\ 0 \end{Bmatrix} \\ {}^2({}^0V_2) &= [0 \ 0 \ 0]^T \end{aligned} \quad (8.130)$$

For $i = 2$,

$${}^3({}^0V_3) = {}^3R[{}^2({}^0V_2) + {}^2({}^0\omega_2) \times {}^2({}^2P_3)]$$

Substituting from Eqs. 8.127 and 8.130 and noting that, ${}^3R = {}^3R^T$, we get,

$${}^3({}^0V_3) = \begin{bmatrix} c_3 & s_3 & 0 \\ -s_3 & c_3 & 0 \\ 0 & 0 & 1 \end{bmatrix} \left[\begin{Bmatrix} s_2\dot{\theta}_1 \\ c_2\dot{\theta}_1 \\ \dot{\theta}_2 \end{Bmatrix} \times \begin{Bmatrix} 0 \\ l_2 \\ 0 \end{Bmatrix} \right]$$

or,

$$\begin{aligned} {}^3({}^0V_3) &= \begin{bmatrix} c_3 & s_3 & 0 \\ -s_3 & c_3 & 0 \\ 0 & 0 & 1 \end{bmatrix} \begin{bmatrix} 0 & -\dot{\theta}_2 & c_2\dot{\theta}_1 \\ \dot{\theta}_2 & 0 & -s_2\dot{\theta}_1 \\ -c_2\dot{\theta}_1 & s_2\dot{\theta}_1 & 0 \end{bmatrix} \begin{Bmatrix} 0 \\ l_2 \\ 0 \end{Bmatrix} \\ {}^3({}^0V_3) &= \begin{Bmatrix} -c_3l_2\dot{\theta}_2 \\ s_3l_2\dot{\theta}_2 \\ s_2l_2\dot{\theta}_1 \end{Bmatrix} \end{aligned} \quad (8.131)$$

For $i = 3$,

$${}^4({}^0V_4) = {}^4R[{}^3({}^0V_3) + {}^3({}^0\omega_3) \times {}^3({}^3P_4)]$$

Substituting from Eqs. 8.128 and 8.131,

$${}^4({}^0V_4) = [I] \left[\begin{array}{c} \left\{ \begin{array}{c} -c_3 l_2 \dot{\theta}_2 \\ s_3 l_2 \dot{\theta}_2 \\ s_2 l_2 \dot{\theta}_1 \end{array} \right\} + \left\{ \begin{array}{c} s_{23} \dot{\theta}_1 \\ c_{23} \dot{\theta}_1 \\ \dot{\theta}_2 + \dot{\theta}_3 \end{array} \right\} \times \left\{ \begin{array}{c} 0 \\ l_3 \\ 0 \end{array} \right\} \end{array} \right]$$

where $[I]$ is the identity matrix.

$$\begin{aligned} {}^4({}^0V_4) &= \left\{ \begin{array}{c} -c_3 l_2 \dot{\theta}_2 \\ s_3 l_2 \dot{\theta}_2 \\ s_2 l_2 \dot{\theta}_1 \end{array} \right\} + \begin{bmatrix} 0 & (\dot{\theta}_2 + \dot{\theta}_3) & -c_{23} \dot{\theta}_1 \\ -(\dot{\theta}_2 + \dot{\theta}_3) & 0 & -s_{23} \dot{\theta}_1 \\ c_{23} \dot{\theta}_1 & s_{23} \dot{\theta}_1 & 0 \end{bmatrix} \begin{Bmatrix} 0 \\ l_3 \\ 0 \end{Bmatrix} \\ {}^4({}^0V_4) &= \left\{ \begin{array}{c} -c_3 l_2 \dot{\theta}_2 - (\dot{\theta}_2 + \dot{\theta}_3) l_3 \\ s_3 l_2 \dot{\theta}_2 \\ s_2 l_2 \dot{\theta}_1 + s_{23} l_3 \dot{\theta}_1 \end{array} \right\} \end{aligned} \quad (8.132)$$

Now,

$${}^0_2R = {}^0_1R {}^1_2R = \begin{bmatrix} c_1 & 0 & s_1 \\ 0 & 1 & 0 \\ -s_1 & 0 & c_1 \end{bmatrix} \begin{bmatrix} c_2 & -s_2 & 0 \\ s_2 & c_2 & 0 \\ 0 & 0 & 1 \end{bmatrix}$$

or,

$${}^0_2R = \begin{bmatrix} c_1 c_2 & -c_1 s_2 & s_1 \\ s_2 & c_2 & 0 \\ -s_1 c_2 & s_1 s_2 & c_1 \end{bmatrix} \quad (8.133)$$

Similarly,

$${}^0_3R = {}^0_2R {}^2_3R = \begin{bmatrix} c_1 c_2 & -c_1 s_2 & s_1 \\ s_2 & c_2 & 0 \\ -s_1 c_2 & s_1 s_2 & c_1 \end{bmatrix} \begin{bmatrix} c_3 & -s_3 & 0 \\ s_3 & c_3 & 0 \\ 0 & 0 & 1 \end{bmatrix}$$

or,

$${}^0_3R = \begin{bmatrix} c_1 c_{23} & -c_1 s_{23} & s_1 \\ s_{23} & c_{23} & 0 \\ -s_1 c_{23} & s_1 s_{23} & c_1 \end{bmatrix} \quad (8.134)$$

and

$${}^0_4R = {}^0_3R {}^3_4R = {}^0_3R [I] = {}^0_3R \quad (8.135)$$

Now,

$${}^0({}^0V_2) = {}^0_2R {}^2({}^0V_2)$$

By Eq. 8.130,

$${}^0({}^0V_2) = [0 \ 0 \ 0]^T \quad (8.136)$$

and

$${}^0({}^0V_3) = {}_3R^3({}^0V_3) = \begin{bmatrix} c_1c_{23} & -c_1s_{23} & s_1 \\ s_{23} & c_{23} & 0 \\ -s_1c_{23} & s_1s_{23} & c_1 \end{bmatrix} \begin{Bmatrix} -c_3l_2\dot{\theta}_2 \\ s_3l_2\dot{\theta}_2 \\ s_2l_2\dot{\theta}_1 \end{Bmatrix}$$

Using Eqs. 8.131 and 8.134,

$${}^0({}^0V_3) = \begin{bmatrix} (s_1s_2\dot{\theta}_1 - c_1c_2\dot{\theta}_2)l_2 \\ -s_2\dot{\theta}_2l_2 \\ (c_1s_2\dot{\theta}_1 + s_1c_2\dot{\theta}_2)l_2 \end{bmatrix} \quad (8.137)$$

Similarly,

$${}^0({}^0V_4) = {}_4R^4({}^0V_4) = {}_3R^4({}^0V_4)$$

Using Eqs. 8.132 and 8.134,

$${}^0({}^0V_4) = \begin{bmatrix} c_1c_{23} & -c_1s_{23} & s_1 \\ s_{23} & c_{23} & 0 \\ -s_1c_{23} & s_1s_{23} & c_1 \end{bmatrix} \begin{Bmatrix} -c_3l_2\dot{\theta}_2 - (\dot{\theta}_2 + \dot{\theta}_3)l_3 \\ s_3l_2\dot{\theta}_2 \\ s_2l_2\dot{\theta}_1 + s_{23}l_3\dot{\theta}_1 \end{Bmatrix}$$

$$\Rightarrow {}^0({}^0V_4) = \begin{bmatrix} (s_1s_2l_2 + s_1s_{23}l_3)\dot{\theta}_1 - (c_1c_2l_2 + c_1c_{23}l_3)\dot{\theta}_2 - c_1c_{23}l_3\dot{\theta}_3 \\ -(s_2l_2 + s_{23}l_3)\dot{\theta}_2 - s_{23}l_3\dot{\theta}_3 \\ (c_1s_2l_2 + c_1s_{23}l_3)\dot{\theta}_1 + (s_1c_2l_2 + s_1c_{23}l_3)\dot{\theta}_2 + s_1c_{23}l_3\dot{\theta}_3 \end{bmatrix} \quad (8.138)$$

The velocities of center of mass of first, second, and third link can be found as follows:

Using Eq. 8.136, ${}^0({}^0V_{G_1}) = [0 \ 0 \ 0]^T$. By substituting $l_2 = l_{G_2}$ in Eq. 8.137

$${}^0({}^0V_{G_2}) = \begin{bmatrix} (s_1s_2\dot{\theta}_1 - c_1c_2\dot{\theta}_2)l_{G_2} \\ -s_2\dot{\theta}_2l_{G_2} \\ (c_1s_2\dot{\theta}_1 + s_1c_2\dot{\theta}_2)l_{G_2} \end{bmatrix} \quad (8.139)$$

By substituting $l_3 = l_{G_3}$ in Eq. 8.138

$${}^0({}^0V_{G_3}) = \begin{bmatrix} (s_1s_2l_2 + s_1s_{23}l_{G_3})\dot{\theta}_1 - (c_1c_2l_2 + c_1c_{23}l_{G_3})\dot{\theta}_2 - c_1c_{23}l_{G_3}\dot{\theta}_3 \\ -(s_2l_2 + s_{23}l_{G_3})\dot{\theta}_2 - s_{23}l_{G_3}\dot{\theta}_3 \\ (c_1s_2l_2 + c_1s_{23}l_{G_3})\dot{\theta}_1 + (s_1c_2l_2 + s_1c_{23}l_{G_3})\dot{\theta}_2 + s_1c_{23}l_{G_3}\dot{\theta}_3 \end{bmatrix} \quad (8.140)$$

Also the initial position of robot tip with respect to base of robot can be given as,

$${}^0({}^0P_4) = {}_3R^3({}^3P_4) + {}_2R^2({}^2P_3) + {}_1R^1({}^1P_2) + {}^0({}^0P_1)$$

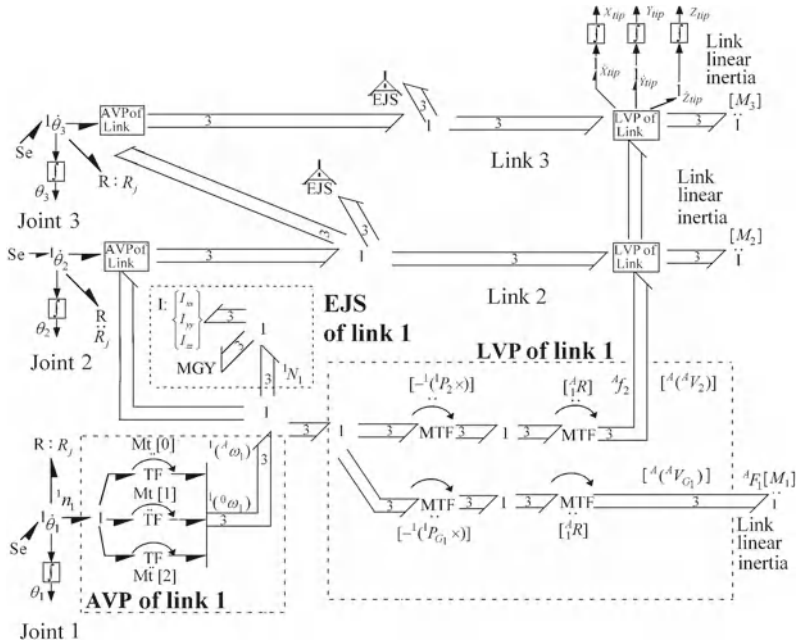


Fig. 8.25 Multi bond graph model of three DOF ground manipulator

$$\begin{aligned}
 {}^0({}^0P_4) &= \begin{bmatrix} c_1c_{23} & -c_1s_{23} & s_1 \\ s_{23} & c_{23} & 0 \\ -s_1c_{23} & s_1s_{23} & c_1 \end{bmatrix} \begin{bmatrix} 0 \\ l_3 \\ 0 \end{bmatrix} + \begin{bmatrix} c_1c_2 & -c_1s_2 & s_1 \\ s_2 & c_2 & 0 \\ -s_1c_2 & s_1s_2 & c_1 \end{bmatrix} \begin{bmatrix} 0 \\ l_2 \\ 0 \end{bmatrix} \\
 &+ \begin{bmatrix} c_1 & 0 & s_1 \\ 0 & 1 & 0 \\ -s_1 & 0 & c_1 \end{bmatrix} \begin{bmatrix} 0 \\ l_1 \\ 0 \end{bmatrix} + \begin{bmatrix} 0 \\ 0 \\ 0 \end{bmatrix} \\
 {}^0({}^0P_4) &= \begin{bmatrix} -c_1s_2l_2 - c_1s_{23}l_3 \\ l_1 + c_2l_2 + c_{23}l_3 \\ s_1s_2l_2 + s_1s_{23}l_3 \end{bmatrix} \tag{8.141}
 \end{aligned}$$

The multi bond graph representation for three DOF ground manipulator is shown in Fig. 8.25 where AVP and LVP represent angular and linear velocity propagations.

8.8.3.1 Bond Graph Modeling of Robots: Advantages

1. Effort equations in single scalar closed form can be used for online computation.
2. Closed form equations are much faster and more efficient than any iterative or recursive form of equation.

3. For a 5 DOF robot, effort equation by Newton-Euler formulation has 702 multiplications and 607 additions whereas with bond graph it has 512 multiplications and 282 additions.
4. Closed form expressions also provide greater insight for control system design.

8.9 Modeling of Flexible-Arm Manipulators

There are three ways of modeling a flexible arm.

1. Euler-Bernoulli beam: In this model, linear inertia of the beam is taken into account.
2. Rayleigh beam: In this model, linear and rotary inertias of the beam are taken into account.
3. Timoshenko beam: In this model, linear inertia, rotary inertia and the effect of shear are considered.

Here flexible link as shown in Fig. 8.26 has been modeled as Euler-Bernoulli beam (Refer to Chap. 5 of this book for details). In Euler-Bernoulli beam model, lumped inertia of the beam is taken into account though rotary inertia and shear deformation are neglected. Since modeling of distributed parameter systems typically begins with finite approximation and hence space reticulation as shown in Fig. 8.27, one can proceed with the governing equations in difference equation form.

Let us assume that an Euler-Bernoulli beam element as shown in Fig. 8.26 has density ρ , cross-sectional area A , and flexural rigidity EI . The governing equations in finite difference form for sufficiently small length, ignoring the influence of second and higher order powers, can be given as

$$V(x + \Delta x) - V(x) = \rho A \Delta x \ddot{y}(x, t) \tag{8.142}$$

$$\psi = \frac{\Delta y(x, t)}{\Delta x} \tag{8.143}$$

$$M(x) = EI \frac{\Delta \psi}{\Delta x} \tag{8.144}$$

Fig. 8.26 Schematic diagram of a beam element

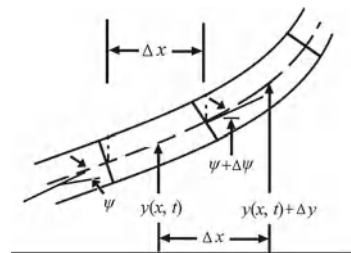
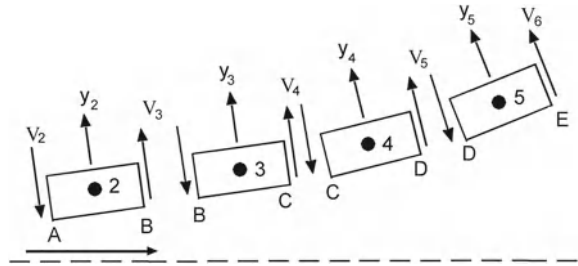


Fig. 8.27 Beam reticulation



$$V(x) = -\frac{\Delta M}{\Delta x} \tag{8.145}$$

where V is shear force, M is bending moment and ψ is the angle made by center line of segment with horizontal (See Fig. 8.26).

The differential equation for transverse vibration is

$$\rho A \ddot{y}(x, t) + EI \frac{\partial^4}{\partial x^4} y(x, t) = 0 \tag{8.146}$$

8.9.1 Beam Models

8.9.2 Euler-Bernoulli Formulation

To create a bond graph model of a flexible link based on Euler-Bernoulli beam formulation, we reticulate a beam as shown in Fig. 8.27. The detailed discussion on the bond graph modeling of flexible link as Euler-Bernoulli beam can be found in [9, 12] and Chap. 5 of this book. The figure also shows the interface shear forces. If we represent the interface shear forces by corresponding 0-junctions, the bond graph model that follows from Eqs. 8.142 and 8.143 is shown in Fig. 8.28. The 1-junctions along the upper line of the ladder structure represent the velocities of the mass centers of the reticules (\dot{y}) to which corresponding inertia elements are attached. The 1-junctions along the lower line represent reticule interface rotation velocities ($\dot{\psi}$). The C elements at 0-junctions along the lower line model the flexural stiffness of the reticules, the values of which can be derived from Eq. 8.144 as $EI/\Delta x$. Transformer moduli shown in bond graph of Fig. 8.28 can be derived using Eq. 8.143 as

$$\dot{\psi} = \frac{\dot{y}_i - \dot{y}_{i-1}}{\left(\frac{\Delta x_{i-1} + \Delta x_i}{2}\right)} \tag{8.147}$$

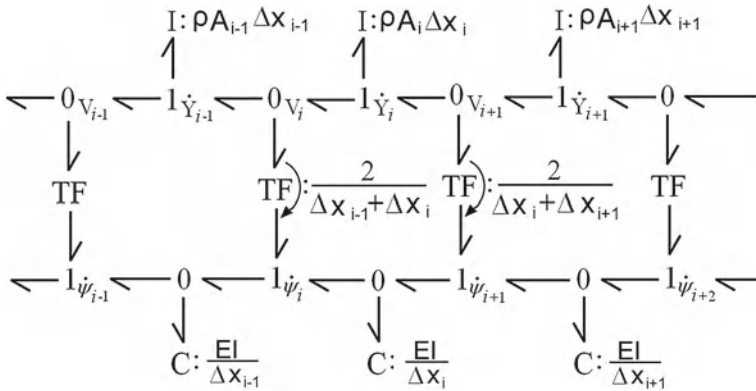


Fig. 8.28 Bond graph of the space reticulated Euler-Bernoulli beam

or,

$$\dot{\psi} = \left(\frac{2}{\Delta x_{i-1} + \Delta x_i} \right) (\dot{y}_i - \dot{y}_{i-1}) \tag{8.148}$$

8.9.2.1 Modeling of One Arm Flexible Terrestrial Robot

In terrestrial robot modeling, it is assumed that the system has single manipulator with revolute joints and is in open kinematic chain configuration. Figure 8.29 shows the schematic sketch of a terrestrial flexible link robot. In this figure $\{X_0, Y_0\}$ represents the absolute frame. The frame $\{X_t, Y_t\}$ locates the tip of the robot. Let, L be the length of the flexible link. The flexible link is divided into four segments of equal length. Let θ be the joint angle as shown in Fig. 8.29. Let the motor be mounted on the joint and has a mass m and it applies a torque τ on the link. The flexible link is uniform with flexural rigidity EI , density ρ , and cross-section area A . The flexible link has been modeled as Euler-Bernoulli beam. Here, motion perpendicular to arm and rotational motion of the arm are considered.

8.9.2.2 Bond Graph Modeling

The kinematic analysis of flexible links is performed in order to draw the bond graph as shown in Fig. 8.30. From the kinematic relations the different transformer moduli used in bond graph are derived. Two type of motion of the links are considered. First motion is the motion perpendicular to the link and second motion is the rotational motion of the links. The bond graph of flexible link shown in Fig. 8.28 can be modified to represent the bond graph model of one arm flexible terrestrial robot. The modified bond graph is shown in Fig. 8.30. In this figure, $\rho AL/4$ represents mass of one segment of flexible link. $4EI/L$ represents stiffness of the flexible link segment.

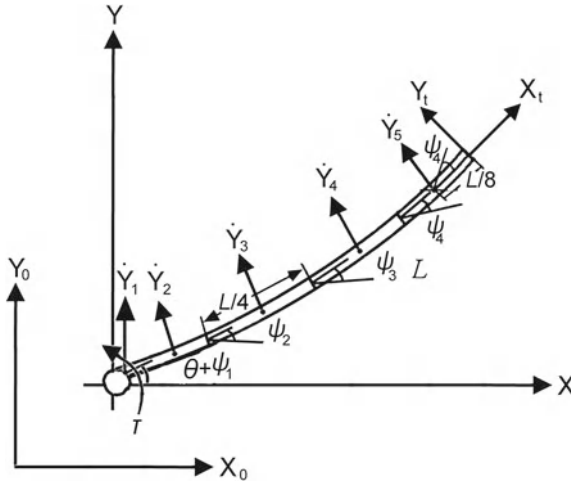


Fig. 8.29 Schematic diagram of one arm flexible terrestrial robot

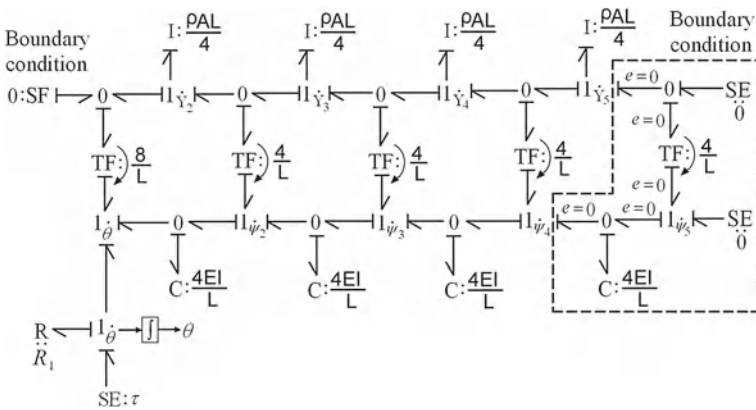


Fig. 8.30 Complete bond graph model of one arm flexible terrestrial robot with boundary condition

Assume that the tip of the robot is free, i.e., there is no external force and moment at the tip. These boundary conditions can be specified in the model as shown in Fig. 8.30. The lower end of the link is attached to motor; so link displacement will be zero there. Moreover, a torque τ is applied by the motor which is shown by an SE element. R_1 represents the bearing resistance. Here, transformer moduli connecting shear force junction to interface rotations will be $4/L$ except for the first one which will be equal $8/L$. Thus, the reduced bond graph can be drawn as shown in Fig. 8.31.

The velocity of the flexible link at junction 5 in X and Y direction with respect to absolute frame can be evaluated as

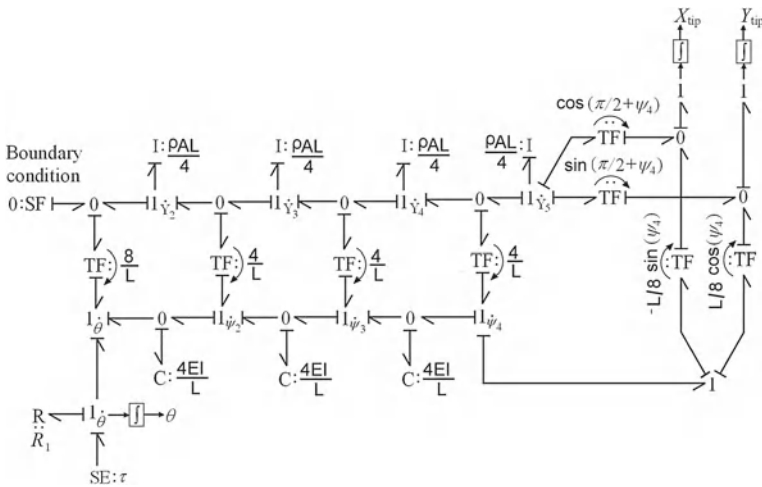


Fig. 8.31 Complete bond graph model of one arm flexible terrestrial robot

$$\dot{X}_{5x} = \dot{Y}_5 \cos\left(\frac{\pi}{2} + \psi_4\right) \tag{8.149}$$

$$\dot{Y}_{5y} = \dot{Y}_5 \sin\left(\frac{\pi}{2} + \psi_4\right) \tag{8.150}$$

Then, the tip velocities in X and Y directions with respect to the absolute frame can be evaluated as

$$\dot{X}_{tip} = \dot{X}_{5x} - \left(\frac{L}{8} \sin \psi_4\right) \dot{\psi}_4 \tag{8.151}$$

$$\dot{Y}_{tip} = \dot{Y}_{5y} + \left(\frac{L}{8} \cos \psi_4\right) \dot{\psi}_4 \tag{8.152}$$

Accordingly, the bond graph model given in Fig. 8.30 can be amended to evaluate the tip velocity as shown in Fig. 8.31.

8.9.2.3 Simulation and Results

The parameters used in simulation of terrestrial one link flexible robot are given in the Table 8.1. For the simulation, the joint is given a constant torque of 1.0Nm. It is also assumed that initial joint angle is 0.0rad. The simulation is performed for 2.0s duration.

Table 8.1 Parameters used for modeling of one arm flexible terrestrial robot

Parameters	Value
Modulus of elasticity	$E = 70 \times 10^9 \text{ N/m}^2$
Link length	$L = 0.5 \text{ m}$
Moment of inertia of cross-section of link	$I = 6.609 \times 10^{-10} \text{ m}^4$
Joint torque	$\tau = 1.0 \text{ Nm}$
Density of aluminum (link material)	$\rho = 2,700 \text{ kg/m}^3$
Cross section area of link	$A = 6.288 \times 10^{-5} \text{ m}^2$
Joint resistance	$R_1 = 0.01 \text{ Nm/(rad/s)}$

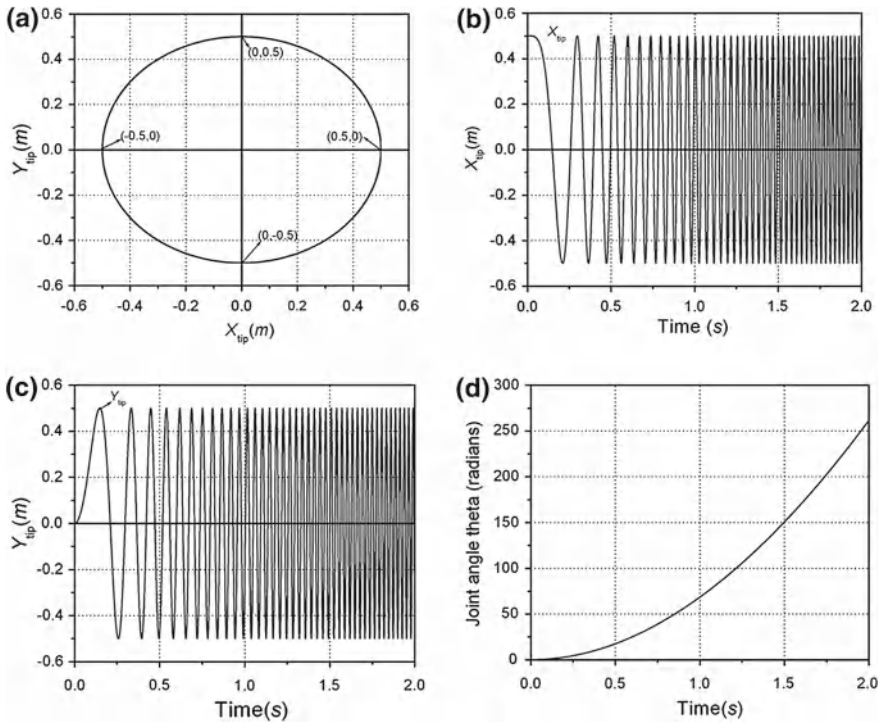


Fig. 8.32 a Tip trajectory of one arm flexible terrestrial robot. b Plot of X_{tip} versus time. c Plot of Y_{tip} versus time. d Plot of joint angle versus time

Figure 8.32a shows the tip trajectory of the robot. It is circular of radius 0.5 m (i.e., the length of the link). Figure 8.32b shows the variation of tip position in X direction with respect to time. Figure 8.32c shows the variation of tip position in Y direction with respect to time. Figure 8.32d shows the variation of joint angle with respect to time.

8.10 Mechatronic Design and Control of a Planar Cooperative Robot

Cooperative robots [10] are useful as compared to single robots as they can handle the objects well. However, coordination is an issue in cooperative robots especially if the task concerns carrying heavy equipment over uncharted terrain. Networked robots could accomplish more than they could individually by coordinating their actions and by sharing sensors. Researchers at NASA have demonstrated that a pair of networked rovers can work together to move large objects, drill holes, and pitch tents in tight coordination. They can also carry out the tasks in an unstructured outdoor environment. The robots' capability for handling and transporting large objects could be used in space exploration, military applications, and in manufacturing industries.

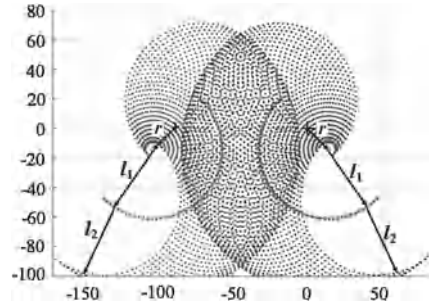
Let us see the design of a cooperative robot system [10] where cooperative action is inbuilt in the design of robot and ensured by error handling.¹ The developed strategy can find application in the cooperative handling of the materials such as the handling of breads in automated bakery plants. One needs to have cooperative control because if the object to be handled is of such a size that it cannot be handled properly by one robot end effector then the other robot end effector must provide cooperative action. Such necessity may arise in docking operations to be carried out by cooperative space robots. This section also presents a complete mechatronic design of a cooperative robot system of two 3-link planar robots to grasp an object at a particular position and transfer it to another position. The cooperative action is achieved by a unique error handling mechanism, which ensures that the object is always in contact with the two grippers. Any alignment disturbances will be corrected by the base motor though it will remain stationary otherwise. The other two motors align the tip carrying the end effector. When both arms are aligned, the end effectors orient themselves and capture the object. In order to minimize disturbances, one motor is moved at one time. After the object is captured, change of position is continuously exchanged between the two arms to make sure that the object is carried to the final position. Here, we will see the design and selection of all mechatronic components such as actuators, sensors, data acquisition system, and controller. A control algorithm is designed based on inverse kinematics of the manipulator discussed in Sect. 8.6.2. The initial and final positions are provided to the controller. The reference trajectory is provided by the controller itself.

8.10.1 Trajectory Plots

The cooperative manipulator under consideration has been already discussed in Fig. 8.7. With the help of forward kinematic equations (discussed in Sect. 8.6.1), work space area covered by the arms of the manipulator is evaluated. Figure 8.33

¹ A part of this section is adapted from these authors' previous work published in [10].

Fig. 8.33 Trajectory plots with $r = 10$ cm, $l_1 = 40$ cm, $l_2 = 30$ cm and distance between the center of the base $a = 90$ cm



shows the workspace for $r = 10$ cm, $l_1 = 40$ cm, $l_2 = 30$ cm and $a = 90$ cm (See Fig. 8.7 for robot geometry). The dimensions of the links were so chosen that there would be no collision among the links. In all the plots, the origin has been marked by a cross.

8.10.2 Manipulator Dynamic Equation

The main concern in designing the system is the calculation of the torques required for the movement of the links. The value of torques would determine the selection of actuators to drive the system. This section presents the calculation of torque at each joint and selection of servo actuators.

- Torque equation for actuator at joint 1:

$$\begin{aligned}
 T_1 = & [(m_1/3 + m_2)l_1^2 + (m_2/3 + m)l_2^2 + (m_2 + 2m)l_1l_2 \cos \theta_2 \\
 & + (m_b + m)l_1^2] \ddot{\theta}_1 + [(m_2/3 + m)l_2^2 + (m_2/2 + m)l_1l_2 \cos \theta_2] \ddot{\theta}_2 \\
 & - [(m_2 + 2m)l_1l_2 \sin \theta_2] \dot{\theta}_1 \dot{\theta}_2 - [(m_2/2 + m)l_1l_2 \sin \theta_2] \dot{\theta}_2^2 \quad (8.153)
 \end{aligned}$$

Here, $\ddot{\theta}_1$ and $\ddot{\theta}_2$ are angular accelerations of motors at first and second joint. Assuming $\ddot{\theta}_1 = \ddot{\theta}_2 = 3 \text{ rad/s}^2$ and for maximum value of T_1 let $\theta_2 = 0^\circ$. So,

$$\begin{aligned}
 T_1 = & [(m_1/3 + m_2)l_1^2 + (m_2/3 + m)l_2^2 + (m_2 + 2m)l_1l_2 \\
 & + (m_b + m)l_1^2] \ddot{\theta}_1 + [(m_2/3 + m)l_2^2 + (m_2/2 + m)l_1l_2] \ddot{\theta}_2 \quad (8.154)
 \end{aligned}$$

For the designed parameters shown in Table 8.2, torque for first joint motor can be calculated as $T_1 = 2.3 \text{ Nm}$.

- Torque equation for actuator at joint 2 can be given as

$$\begin{aligned}
 T_2 = & [(m_2/3 + m)l_2^2 + (m_2/2 + m)l_1l_2 \cos \theta_2] \ddot{\theta}_1 + [(m_2/3 + m)l_2^2] \ddot{\theta}_2 \\
 & + [(m_2/2 + m)l_1l_2 \sin \theta_2] \dot{\theta}_1^2 \quad (8.155)
 \end{aligned}$$

Table 8.2 Designed parameters for mechatronics design of a planar cooperative robot

Parameters	Value
Length of the link 1 and link 2 (l_1 and l_2)	40, 30 cm
Diameter of base ($2r$)	20 cm
Width of both the links	5 cm
Thickness of both the links	2.5 cm
Material of the links	Aluminum
Mass of the first and second link (m_1 and m_2)	400, 300 gm
Thickness of the link’s wall	2 mm
Mass of end-effector (m)	800 gm
Mass of motor at tip of link 2 (m_b)	300 gm
Mass of motor at tip of link 1 (m_d)	300 gm
Mass of base (m_d) (includes the mass of motor at joint frame $\{0\}$)	150 gm

$$T_2 = [(m_2/3 + m) l_2^2 + (m_2/2 + m) l_1 l_2] \ddot{\theta}_1 + [(m_2/3 + m) l_2^2] \ddot{\theta}_2 \quad (8.156)$$

For the designed parameters shown in Table 8.2, torque for second joint motor can be calculated as $T_2 = 0.828 \text{ Nm}$.

- Torque calculation for actuator of base:

The torque required for the base can be derived as

$$T_B = [(T_1/\ddot{\theta}_1) + (m_a r^2) + (m_d r^2/2)] \ddot{\phi} \quad (8.157)$$

Assuming $\ddot{\theta}_1 = \ddot{\phi} = 3 \text{ rad/s}^2$, for the designed parameters shown in Table 8.2, torque for base motor can be calculated as $T_B = 2.31 \text{ Nm}$.

From selection chart of available HiTec servo motors for the calculated torque values, the following motors are selected.

- Motor Selected for Joint 1: Hi-Tech HSR-5995 TG.
- Motor Selected for Joint 2: HiTec HS-322-HD.
- Motor Selected for Robot base: Hi-Tech HSR-5995 TG.
- Motor Selected to orient End-effector: HiTec HS-322-HD.
- Motor Selected for the gripping motion of End-effector: HiTec HS-322-HD.

8.10.3 Controller Design

The controller has been designed in MATLAB and runs on a Pentium IV, 2.8 GHz based PC. It receives and sends data to the controller circuit through the RS-232 serial port. The controller performs the basic task of determining the angular positions of the various links that are required for the end effectors of each robot to reach the required position. Then, it aligns the end effector according to the orientation of the object and

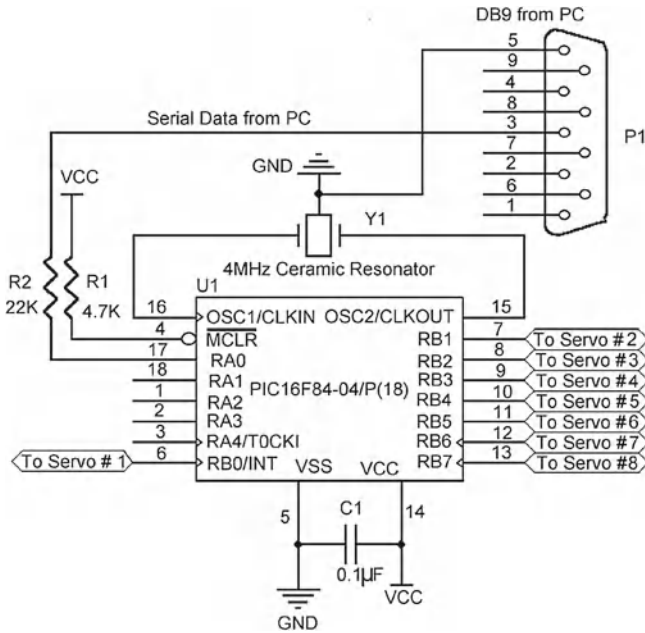


Fig. 8.34 Block diagram of the control flow of system

activates the grippers to hold the object. Next, the controller controls the coordinated movement of the two manipulators so that the object can be cooperatively placed in the desired position. According to the various angular orientations required the controller sends signal in the form of arrays to the particular motor, identified by a number (first element of array), that has to be activated and the angular position (identified by second number) it requires to reach the point. This signal is sent to the motor control circuit, i.e., the PIC16F84A circuit as shown in Fig. 8.34. According to the pulses from the controller, the PIC16F84A circuit generates the appropriate pulse width modulation (PWM) signal for the intended servo motor and sends this signal to the motor to position it. This method is used to control the ten servo motors in the system. In this system, ten servo motors have been controlled to obtain the desired angle between the links.

This information which is transmitted to the PIC using serial communication requires the use of a 22 K Ohm resistor to be connected in series with Pin 3 of the serial port. This information is processed by the PIC which has been preprogrammed to handle this output and generate the appropriate PWM signals to control the angle of rotation of the motors.

8.10.4 Design of Cooperative Robot System

The system consists of two planar cooperative robots. Motion of the links of each robot collectively produce the desired trajectory and place the end effector at the required space coordinate within the common workspace of both robots. The design of each individual item of the system was chosen keeping in mind that they cover all possible points within the workspace of the system smoothly, without creating any hindrance in the motion of each other. While finalizing the design for the various items of the system, it was assumed that in the first phase of motion (reaching the intermediate space coordinate where object has been placed) each robot motion is independent from each other and in the later phase (placing the object at the required space coordinate) the robots have to move in a cooperative manner. Design of the system for planar cooperative robots includes the design of parts such as (i) A flat smooth surface (to reduce friction) (ii) base (iii) Link-1 (iv) Link-2 (v) End effector.

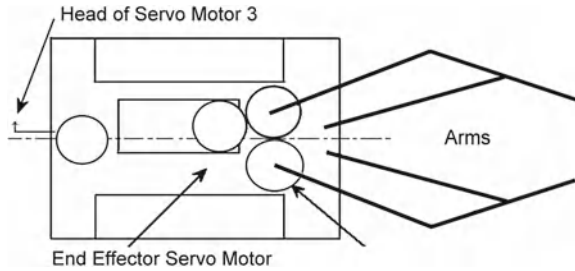
The base is fixed on the head of the base motor. Head of this servo motor is attached to the one end of the Link-1 and to measure the rotation of this servo motor a potentiometer is also fixed on the base to which the rotation is transferred through gears.

Link-1 is the second link of the robot. The relative motion between base and link-1 is generated by the servo motor. This link can be taken as the forearm of the robot. The link is of box section. Link-1 is attached to the base through a revolute joint. The revolute joint is actuated by a servo motor. On the other end of the link, a servo motor is to be fitted which works as an actuator for the Link-2. Hence, joint 2 is also a rotational joint actuated by another servo motor. Link-2 is the third link of the robot. The relative motion between Link-1 and Link-2 is generated by the servo motor. This link can be taken as the front arm of the robot. Link-2 also has a box section. Link-2 is attached to Link-1 through a rotational joint. The rotational joint is actuated by a servo motor (servo motor-2). The servo motor has only 180° rotation; so while designing the link, positioning of the servo motor was the priority so as to cover all possible points in the workspace. On the other end of the link, a servo motor is fitted which is working as an orienting actuator for the end effector. Role of this actuator is to give the end effector the proper alignment before the motor on it can be activated in order to reach the object.

End effector is the last part of the robot. End effector is used to hold and grip the object while in motion, i.e., when it is transferred from one place to another. The design of the end effector is made in such a way that its arms move forward and close simultaneously. This ensures better grip on the object.

End effector was oriented using an actuator fixed on Link-2. The actuation required for the movement of the arms of the end effector is obtained using another servo motor which is fixed on the top of the end effector as shown in Fig. 8.35. This servo motor is fitted upside down. Transfer of motion from the servo motor to the arms of the end effector is done using gears which are fixed as shown in Fig. 8.35. Gear on servo motor is meshed with the gear fixed on one arm, which in turn meshes with the gear fixed on other arm. One side rotation of the servo motor enables the end effector to

Fig. 8.35 Schematic diagram of the designed end effector



grab an object and other side rotation allows releasing. As the servo motor produces high torque so it was able to provide enough force to tightly hold the object. Main body of the end effector contains the head of servo motor, gear fitted on its head and the two other gears for the arms. Figure 8.35 shows the mechanism for end effector. While gripping the object, the end effectors of both robots approach from opposite sides.

8.10.5 Controller Description

The controller for the system has been designed in MATLAB. The basic feature of the controller is the angle calculation between the various links of the robot and trajectory planning of their movements according to the pickup position and drop position. The controller requires the initial and final coordinates as input and accordingly it generates the appropriate pulses to control the motors. Due to dynamic and frictional forces, errors are generated in the positioning of the motors. Therefore, the controller takes input from feedback device (potentiometer) which gives actual angles between the links. Comparing these angles with the required position of the motors, the controller generates the appropriate error correction signal for the motors and repositions them to the required position. This operation is carried out in an iterative manner so that the errors of all the motors in the system is minimized. A proportional controller has been used here, with angular position of the robot joint as feedback and potentiometer as the sensor device. We have used proportional control because we wanted to have simple control scheme in which the control action is proportional to error. Unity gain values (low gain value) have been used to have stable response although steady state error may be slightly more. In this control scheme, cooperative action is achieved by the error handling method. The basic operation of the controller can be divided into the following major parts:

1. Positioning of the end effectors of both the robots to the pickup position.
2. Cooperative, coordinated motion of the two robots to place the object in the required position.

Before these operations are carried out, the controller configures the computer serial ports for RS232 communication. The two serial ports 'COM1' and 'COM2' act as the channels for communication between the computer and interfacing circuits for input and output. In all, there are two PIC16F84A circuits and two PIC16F877 circuits in the system through which input and output operations are carried out.

COM1 communicates with PIC16F84A circuit which acts as interface to drive the servo motors according to the signal from the controller. The speed of serial communication for COM1, i.e., the baud rate, is set as 2,400 bps. Therefore, COM1 is used only for output from the computer to the circuit. No input signal is given to this port.

COM2 communicates with both a PIC16F84A circuit for driving servo motors and a PIC16F877 circuit which acts as interface between the potentiometer and PC. The controller generates appropriate signal to indicate the sensor from which it requires input at that instant. This signal is sent to the PIC16F877 circuit. In reaction to this the interface circuit takes input from the potentiometer and sends it to COM2 as input. So, COM2 acts as a channel for two-way communication, i.e., it does both the functions of transmitting output and also receiving input. While operating the PIC16F877 circuit, the speed of serial communication for COM2, i.e., the baud rate, is set as 9,600 bps.

- (i) Positioning of the end effectors of both the robots to the pick up position
 - (a) *Angular orientation calculation*

The pickup position and drop position of the object in terms of X - Y coordinates are required by the controller as inputs. According to the X - Y coordinates, the controller calculates the required link angular positions to reach the object.

(b) *Pulse signal calculation*

According to the required angles the controller then determines the pulse signal to be given to the appropriate servo motors as input to achieve the required configuration. This pulse signal from the controller is converted into digital pulses having a total of 20 ms cycle. The pulse signals are calculated as follows:

For the high torque HSR-5995 TG servo motors in on duty cycle of 20 ms, the pulses range from 0.9 to 1.9 ms for 0° to 180° orientation, respectively. The equation for pulse signal calculation from angular position is given by:

$$\text{Pulse} = (83/180)\text{Angle} + 110 \quad (8.158)$$

This equation has been determined by linear interpolation from following data: 110 corresponds to 0° ; 193 corresponds to 180° .

For the low torque HS-322 HD servo motors in on duty cycle of 20 ms, the pulses range from 0.5 to 2.5 ms for 0° to 180° orientation, respectively. The equation for pulse calculation from angular position is given by:

$$\text{Pulse} = (170/180)\text{Angle} + 60 \quad (8.159)$$

The above equation has been determined by linear interpolation from following data: 60 corresponds to 0° ; 230 corresponds to 180° .

(c) *Positioning of robots*

The input to PIC16F84A circuit from the controller is in the form of a row array where the first element of the array gives the motor number which is to be activated and the second element gives the pulse to be given to the motor to achieve the desired position, e.g., $A = [2 \ 123]$; $B = [3 \ 200]$ and so on. In all, there are two PIC16F84A execution circuits. One of the circuits controls eight servo motors of the robots and the second PIC16F84A circuit controls the two servo motors required for gripping action of the end-effectors. The signals are given in such a manner that motion of motors takes place in a cyclic manner, i.e., in every cycle each of the motors is moved by a small value. This small value is determined by the difference in pulse for initial position and final position divided into a number of equal intervals. This is done so that the movement of links takes place slowly and the error due to dynamic and frictional forces is minimized. Next, let us see the order in which the motors in the system are moved.

(d) *Cooperative, coordinated motion of the two robots*

This is carried out in a very similar manner to the positioning of the end effectors of both the robots to the pick up position. It follows the same set of steps, i.e.,

- Angular Orientation Calculation: The angular position is calculated by giving the final X-Y coordinates of the spot where the object has to be placed as input.
- Pulse Signal Calculation.
- Positioning of Robots.

On the completion of these steps, as mentioned in the previous section, the grippers open up and drop the object at the final position. This completes the cycle of operation.

(e) *Error handling*

Due to the restricted motion of motors, i.e., 180° , all the positions are not accessible to the robots. So, in the controller, the input positions, i.e., pickup position and drop position, are checked to determine whether they lie within the reach of both the robots. In case both or any one of the positions is outside the range of the robots, an error message is displayed and the program terminates. The flow chart for controller logic is shown in Fig. 8.36.

(f) *PIC controller code*

PIC16F84A has been programmed to control the motion of the servo motors. The code has been made using PIC BASIC Pro software [4]. This programs the PIC to take as input the signal from the serial port in the form of a two-dimensional array such as $[1 \ 135]$, $[2 \ 50]$. The first element indicates the motor number and the second the pulse signal, which is converted into digital pulse by the program and hence used to position the servo motor.

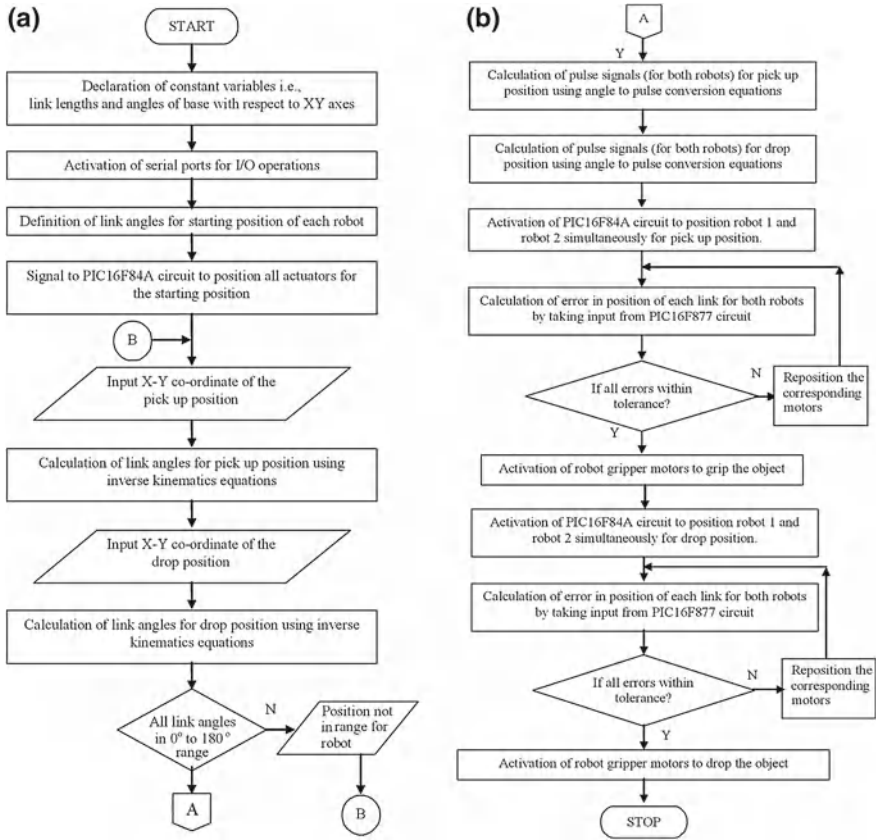


Fig. 8.36 Flow chart for control algorithm

8.10.6 Trajectory Tracking

In order to verify the efficacy of the proposed control scheme for the cooperative manipulation, the initial and final positions of tip were provided to the controller. The controller generated data for the expected/ reference trajectory in the form of angles. The data was modified for conversion of interval between angles into an array and conversion of this array to appropriate pulse signal array, and communicated to the interfacing circuit. The circuit then operated the system. The error in position was continuously transmitted back to the controller.

Two sets of initial and final point values were selected to operate the system. The first set is of (38, 43) and (60, -10) while the other is (30, -60) and (54, 25). To regulate the amount of data, details of only the left arm has been plotted in Fig. 8.37a and b, since the behavior of the right arm is similar. The solid lines

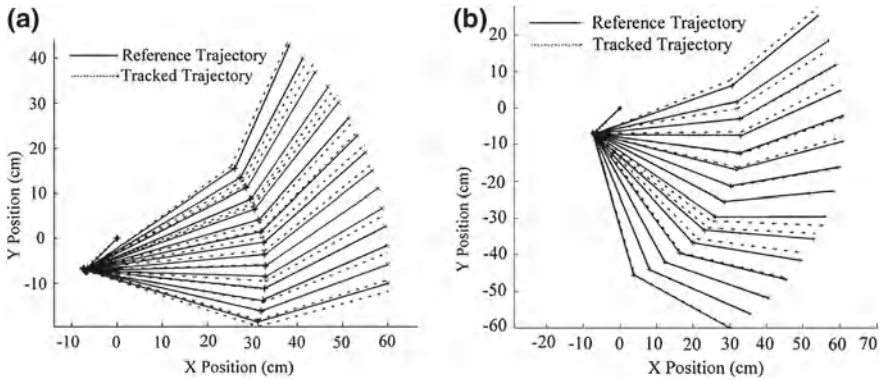


Fig. 8.37 **a** Reference and tracked trajectory plot for initial value (38, 43) and final value (60, -10). **b** Reference and tracked trajectory plot for in initial value (30, -60) and final value (54, 25)

in Fig. 8.37a and b show the reference link positions while dashed lines show the experimentally obtained link positions.

In Fig. 8.37a, the black solid line represents the first link of the system. At all times, this should ideally remain stable, i.e., there should not be any motion of this link as this is the assumption in the analysis. But looking closely at Fig. 8.37b, it can be seen that it is not the case. During the actual working there are always disturbances acting on the first link. This is indicated by the black dotted line which is the actual trajectory of the arm. There are also errors in the next two sets of values, i.e., tips of Link-1 and Link-2. The major source for this error is friction. Since the links rest on the plane, the frictional forces delay the response of the motors driving these links. Since variations in frictional forces cannot be explicitly determined, the errors here are completely random. Another very major source of error is the actuators themselves. In order to move the actuator an integer pulse has to be provided. Due to this restriction, the motor cannot rotate for the full 180° ; rather it has a minimum step of angle increment like 2.20 or 1.70. Figure 8.38a–d shows the different frames of the cooperative robot system during handling of an object.

8.11 Haptic Robots

The term Haptic is derived from the Greek verb “haptesthai” meaning “to touch”. It refers to the science of touch and force feedback in human–computer interaction. According to International Society for Haptics [3], the word haptic refers to the ability to experience the environment through active exploration, typically with our hands, as when palpating an object to assess its shape and material properties. This is commonly called haptic touch.

Vibrating phones, gaming controllers, and force-feedback control knobs in cars, are examples of this technology. Vibrations allow people to be alerted of incoming

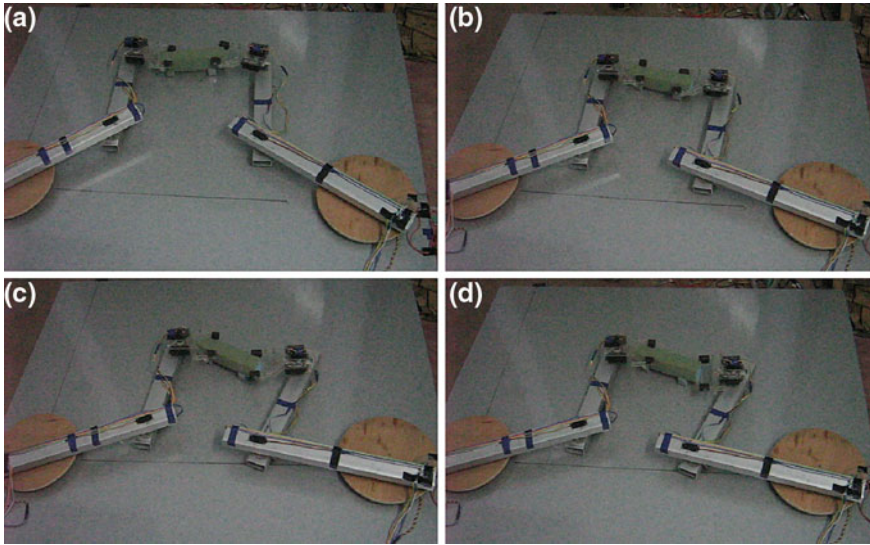


Fig. 8.38 Snapshot of experimental robot **a** initial position **b** intermediate position 1 **c** intermediate position 2 **d** final position

calls without disturbing others. But these are one way information transfer, while in computer haptic the flow of information is two way. It means that computer can give signal of output of desired quantity in appropriate variable and it can also receive and manipulate those signals which it got from user.

The SensAble Technologies PHANTOM[®] [7] product line of haptic devices makes it possible for users to touch and manipulate virtual objects. The PHANTOM Omni model is the most cost-effective haptic device available today.

8.11.1 Working Principle of Haptic Device

Researchers working in the field of haptics are concerned with the development, testing, and refinement of tactile and force-feedback devices and supporting software that permit users to sense (“feel”) and manipulate three-dimensional virtual objects with respect to such features as shape, weight, surface textures, and temperature.

Typically, haptics system includes

- Sensor(s)
- Actuator (motor) control circuitry
- One or more actuators that either vibrate or exert force
- Real-time algorithms (actuator control software) and a haptic effect library
- Application programming interface (API), and often a haptic effect authoring tool.

Fig. 8.39 Picture of PHANTOM Omni

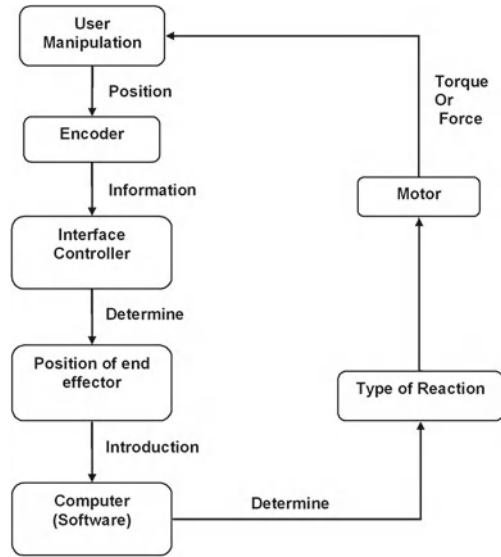


Let us consider one of the devices from SensAble Technologies. The 3 DOF PHANTOM is a small robot arm with three revolute joints, each connected to a computer-controlled electric DC motor. The tip of the device is attached to a stylus that is held by the user. Three degrees of force, in the x , y , and z , directions are achieved through motors that apply torques at each joint in the robotic arm. By sending appropriate voltages to the motors, it is possible to exert up to 1.5 lb of force at the tip of the stylus, in any direction. Figure 8.39 shows the picture of PHANTOM Omni.

The basic principle behind haptic rendering is simple: Every millisecond or so, the computer that controls the PHANTOM reads the joint encoders to determine the precise position of the stylus. It then compares this position to those of the virtual objects the user is trying to touch. If the user is away from all the virtual objects, a zero voltage is sent to the motors and the user is free to move the stylus (as if exploring empty space). However, if the system detects a collision between the stylus and one of the virtual objects, it drives the motors so as to exert on the user's hand (through the stylus) a force along the exterior normal to the surface being penetrated. In practice, the user is prevented from penetrating the virtual object just as if the stylus collided with a real object that transmits a reaction to the user's hand. Different haptic devices—such as Immersion Corporation's CyberGrasp [2] operate under the same principle but with different mechanical actuation systems for force generation. This working principle can be easily described by flowchart shown in Fig. 8.40.

As a user manipulates the end effector, grip or handle on a haptic device, encoder output is transmitted to an interface controller at very high rates. Here, the information is processed to determine the position of the end effector. The position is then sent to the host computer running a supporting software application. If the supporting software determines that a reaction force is required, the host computer sends feedback forces to the device. Actuators (motors within the device) apply these forces based on mathematical models that simulate the desired sensations. For example, when simulating the feel of a rigid wall with a force-feedback joystick, motors within the joystick apply forces that simulate the feel of encountering the wall. As the user

Fig. 8.40 Block diagram showing working of haptic device



moves the joystick to penetrate the wall, the motors apply a force that resists the penetration. The further the user penetrates the wall, the harder the motors push back to force the joystick back to the wall surface. The end result is a sensation that feels like a physical encounter with an obstacle.

8.11.2 Applications of Haptic Devices

Haptic technology has made it possible to investigate in detail how the human sense of touch works by allowing the creation of carefully controlled haptic virtual objects. These objects are used to systematically probe human haptic capabilities, which would otherwise be difficult to achieve. Following are the areas where haptic devices are widely used.

- Teleoperators and simulators:** It is master–slave type operation. Master gives signal to the slave manipulator and gets signal from slave describing its current state. Here, slave enforces position, master presents reaction force. This was widely used in nuclear material handling. Haptic simulators are currently used in medical simulators and flight simulators for pilot training. Haptic technology is also widely used in teleoperation, or telerobotics (See Chap. 12 for more details). In a telerobotic system, a human operator controls the movements of a robot that is located some distance away.
- Computer and video games:** In this application, the virtual environment is created in computer, which looks like real-life atmosphere, and one can manipulate it through haptic input. It also enables the user to feel and manipulate virtual solids,

fluids, tools. Video game makers have been early adopters of passive haptics, which takes advantage of vibrating joysticks, controllers and steering wheels to reinforce on-screen activity (See Chap. 13 for more details). But future video games will enable players to feel and manipulate virtual solids, fluids, tools.

- **Medical:** Remote surgery is another emerging field. Now, doctors are being able to perform surgery without being present at the patient's side, with machine setup and patient preparation performed by local nursing staff. Medical literature reveals that haptic devices have been widely applied in surgery for developing surgical simulators to train surgeons in performing surgeries in virtual environments. Robot-assisted surgery is enhancing the ability of surgeons to perform minimally invasive procedures by scaling down motions and adding additional DOF to instrument tips. Thousands of general, urologic, and cardiac surgical procedures were performed worldwide in the last year with robotic surgical systems. Despite these successes, progress in this field is limited by an unresolved problem: the lack of haptic (force and tactile) feedback to the user.
- **Training:** One can get training in virtual environment using haptic feedback, which will give user complete sense of reaction. People have successfully applied it to training in music drum, tennis, etc., and it can be extended to further areas. Aircraft mechanics can work with complex parts and service procedures, touching everything that they see on the computer screen. And soldiers can prepare for battle in a variety of ways, from learning how to defuse a bomb to operating a helicopter, tank, or fighter jet in virtual combat scenarios. Vehicle and aircraft simulators (See Chap. 13) are used for driver and pilot trainings, respectively.
- **Design in industry:** Integration of haptics into CAD systems such that a designer can freely manipulate the mechanical components of an assembly in an immersive environment.
- **Graphic arts:** Virtual art exhibits, concert rooms, and museums in which the user can login remotely to play the musical instruments, and to touch and feel the haptic attributes of the displays; individual, or cooperative virtual sculpturing across the internet.
- **Education:** Giving students the feel of phenomena at nano, macro, or astronomical scales; "what if" scenarios for non-terrestrial physics; experiencing complex data sets. The latest applications include hand exoskeleton devices that let one feel or touch what you see, thus helping one recognize object shapes, textures, stiffness, or their weight.

8.11.3 Experiments with PHANTOM Omni Haptic Device

Let us take an example of design and development of virtual objects to be used with haptic device [11] PHANTOM Omni.² These virtual objects can be used for motor rehabilitation by incorporating visual and haptic feedback. Developed predominantly

² A part of this section is taken from these authors' previous work published in [11].

for augmentation of motor skill of patient, the objects could be also used for teaching and enhancing writing skill of children.

- Design of virtual objects for training

The system consists of alphabets, numbers, string, maze, and game. Presented system has been designed to give partial guidance to the subject. This system has different exercise for alphabets and numbers which is partially guided. Here, partially guided means object will not react until subject is moving his hand within range of prespecified path. When one tries to move outside of object, system will exert force on stylus and will keep it in range only. Thus, the system is neither fully guided nor fully free. To attain this feature in letters, we created three-dimensional model of letters which consists of walls.

In the present system, Open Graphic Library Utility Toolkit (GLUT) [5] is used for graphical presentation on the computer screen. Haptic Device Application Programming Interface (HDAPI) provides low-level access to the haptic device. It also enables haptics programers to render forces directly, offer control over configuration and the runtime behavior of the drivers. Haptic Library Application Programming Interface (HLAPI) provides high-level haptic rendering and allows significant reuse of existing OpenGL [5] code and greatly simplifies synchronization of the haptics and graphics threads.

- Alphabet and number System

With the help of alphabet and number system virtual objects, one can learn to write alphabets and numbers. The letters has been created in PRO/ENGINEER (Pro/E) [6], solid modeling software. Using this model along with OpenHaptic Toolkit, we created scenario in which one can feel the shape of particular letter and move the cursor along with it. As the subject moves his hand through the shape, the stylus will not exert any reaction force on subject hand. But when stylus tries to run out of the wall of letter, subject will feel reaction force and it cannot move beyond that limit. This ensures that stylus tip remains within certain limit, and thus the subject motion is neither free nor fully constrained. We also aided visual feedback through picture, which helps the subject to remember the used letter and correlate that picture to specific word. It also shows the spelling of that particular object. The flowchart used for creation of a letter is shown in Fig. 8.41a.

First of all, letters or numbers are modeled in Pro/E environment. The created file is in .prt format. This created file is converted in to .3ds format. Then the model is imported into visual C++ environment. The properties of object like mass, stiffness, damping, friction, etc., are set. Picture of the object is added as visual aid. The created alphabet Q is shown in Fig. 8.41b.

For creation of numbers, string, maze, and game, interested readers may refer [11]. The Hyper-bonds concept [14] allows integrated modelling of real and virtual systems in bond graph form. More details on bond graph modelling of such mixed reality systems (including haptic systems and human-machine interfaces) can be consulted in [15, 16].

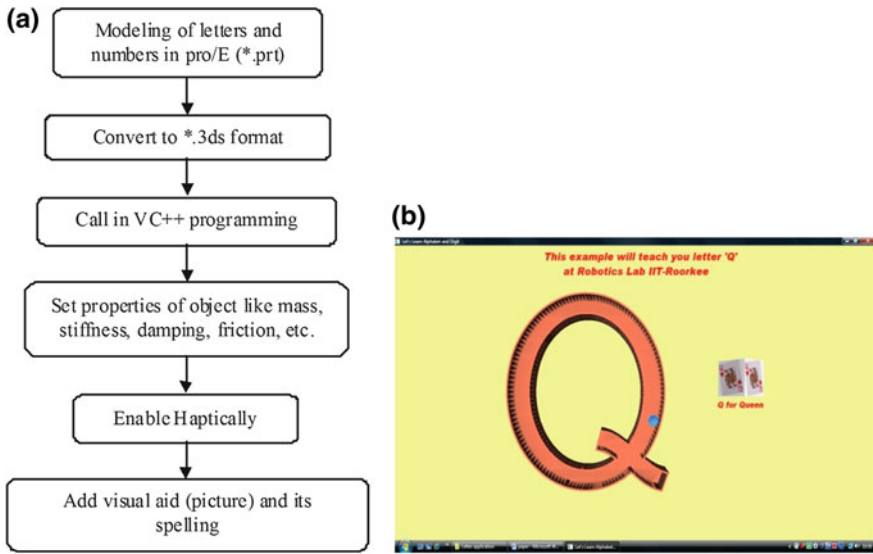


Fig. 8.41 a Flowchart for alphabet and b alphabet exercise

References

1. <http://www.websters-online-dictionary.org>. Accessed 04 July 2012
2. <http://www.immersion.com>. Accessed 04 July 2012
3. <http://www.isfh.org>. Accessed 04 July 2012
4. <http://www.microchip.com>. Accessed 04 July 2012
5. <http://www.opengl.org/documentation/specs/glut/spec3/spec3.html>. Accessed 04 July 2012
6. <http://www.ptc.com>. Accessed 04 July 2012
7. <http://www.sensable.com>, <http://www.sensable.com/haptic-phantom-desktop.htm>. Accessed 12 Oct 2011
8. <http://www.litencyc.com>. Accessed 04 July 2012
9. D.C. Karnopp, D.L. Margolis, R.C. Rosenberg, *System Dynamics: Modeling and Simulation of Mechatronic Systems*, 4th edn. (Wiley, New Jersey, 2006)
10. R. Maheshwari, R. Gupta, R. Jaiwant, H. Patolia, P.M. Pathak, S.C. Jain, Mechatronic design and control of a planar cooperative robot. *Int. J. Adv. Mech. Syst.* **2**(4), 271–280 (2010)
11. J.B. Maniya, P.M. Pathak, B.K. Mishra, Design and development of virtual objects to be used with haptic device for motor rehabilitation. *J. Softw. Eng. Appl.* **3**, 990–997 (2010)
12. A. Mukherjee, R. Karmakar, A.K. Samantaray, *Bond Graph in Modeling, Simulation and Fault Identification* (CRC Press, Boca Raton, 2006)
13. P.M. Pathak, R.P. Kumar, Object oriented bond graph modeling of a robotic manipulator, in *Proceedings of the 10th National Conference on Machines and Mechanisms*, IIT Kharagpur, India, 2001
14. F.W. Bruns, H.H. Erbe, Mixed reality with hyper-bonds-A means for remote labs. *Control Eng. Pract.* **15**(11), 1435–1444 (2007)
15. W. Bruns, Hyper-bonds-distributed collaboration in mixed reality. *Annu. Rev. Control* **29**(1), 117–123 (2005)
16. P.J. Gawthrop, S.A. Neild, A. Gonzalez-Buelga, D.J. Wagg, Causality in real-time dynamic substructure testing. *Mechatronics* **19**(7), 1105–1115 (2009)

Chapter 9

Robust Overwhelming Control and Impedance Control

9.1 Introduction

Based on the insights developed from the bond graph modeling, a robust overwhelming joint controller [1] for a robotic manipulator, which does not require the knowledge of the robot parameters and the payload, can be developed. The overwhelming control strategy has been applied by researchers [3, 4] for robust trajectory control of a two-link planar manipulator. Most robust robot trajectory control strategies assume the plant to be an ideal rigid manipulator. Thus, in the model for the controllers, it suffices to consider only the inertia of the manipulator. Due to the uncertainty in determining parameters of robot, in several cases it is not possible to find out accurately the Coriolis, centrifugal, and gravity terms contribution in the dynamics of robot. Robust trajectory control algorithms are useful here because they are insensitive to variations in the manipulator parameters and retain the desired trajectory [8]. In addition, impedance control is useful in accommodating the robot-environment interaction forces when the robot performs some work with constraints on the applied force or torque at the end effector.

In this chapter, overwhelming and impedance control concepts will be illustrated.

9.2 Concept of Robust Overwhelming Control

The idea behind the design of the robust overwhelming controller may be explained using a simple system as shown in Fig. 9.1a, where the motion of the mass point m (which represents a generalized inertia) is to be controlled by applying a feed-forward force $F(t)$ such that it moves according to a prescribed motion $x_d(t)$ in the direction of x . Let there exist some state and time dependent undetermined variations $\Delta m(x, t)$ of the mass m over its nominal value. The correct evaluation of the feed-forward force becomes impossible as the mass has undetermined fluctuations. Let the mass $m + \Delta m(x, t)$ be attached to a mass M (overwhelmer mass) which is μ_1 ($\mu_1 \gg 1$) times greater than the mass m and the feed-forward effort $F(t)$ now

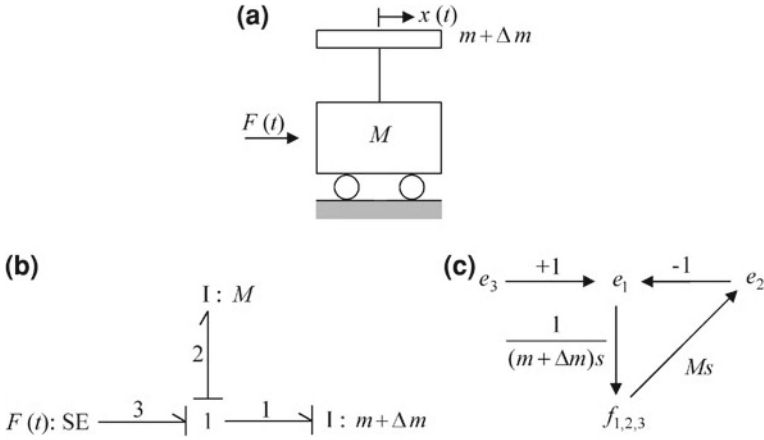


Fig. 9.1 **a** Nominal mass m with Δm variation rigidly attached to a very large mass M . **b** Bond graph model for system shown in **(a)**. **c** Signal flow graph derived from bond graph of **(b)**

calculated on the basis of mass M and the desired trajectory of m , be applied. It is then obvious that the mass M will track the desired path very closely and simultaneously drag the mass $(m + \Delta m)$ along the desired trajectory.

Figure 9.1b shows the bond graph model of the overwhelming controller. Figure 9.1c shows the signal flow graph in terms of effort and flow variables derived from bond graph of Fig. 9.1b. The transfer function between the control effort e_1 on m and applied feed-forward effort e_3 is given by Eq. 9.1 as,

$$e_1(s) = \left[\frac{(m + \Delta m)}{(m + \Delta m + M)} \right] e_3(s) \tag{9.1}$$

where s is the Laplace variable. The effort input to the system calculated from given trajectory and overwhelmer mass is given by,

$$e_3(t) = M\ddot{x}_d \tag{9.2}$$

So

$$e_1 = \left(\frac{m + \Delta m}{m + \Delta m + M} \right) M\ddot{x}_d \tag{9.3}$$

When $M \gg (m + \Delta m)$, $M/(m + \Delta m + M) \cong 1$, therefore, control force to the plant mass is obtained from Eq. 9.3 as,

$$e_1 \cong (m + \Delta m)\ddot{x}_d \tag{9.4}$$

It is evident from Eq. 9.4 that, though feed-forward effort is applied according to mass M , the mass $(m + \Delta m)$ receives its appropriate driving effort. However, the

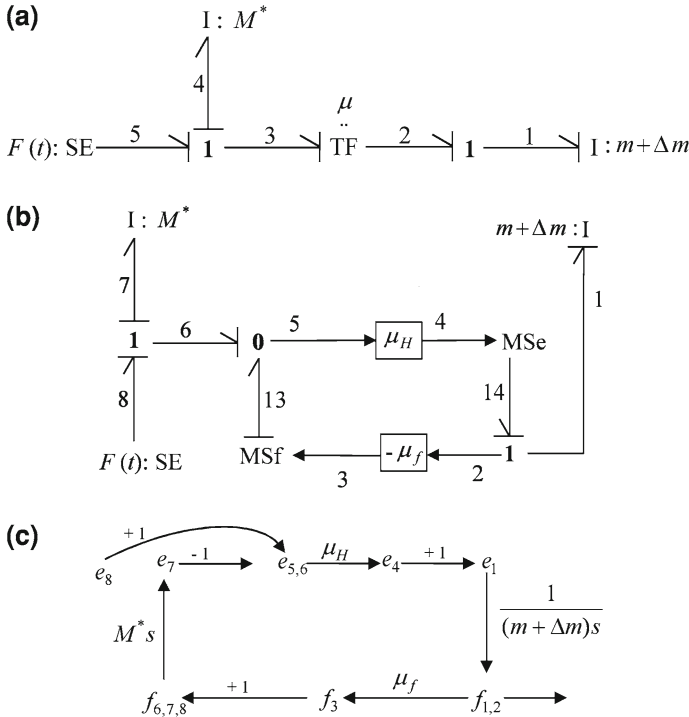


Fig. 9.2 a Modification of Fig. 9.1b. b Split transformer model with asymmetric transformer modulus. c Signal flow graph derived from (b)

above scheme cannot be physically realized except for very tiny systems because of the heavy mass of the overwheeler. To make the system physically realizable, the bond graph of Fig. 9.1b is modified and shown in Fig. 9.2a. In Fig. 9.2a the two inertances are algebraically linked by a transformer with modulus $\mu \gg 1$ such that the modified system of Fig. 9.2a is equivalent to that of Fig. 9.1b. Here M^* can be of the same order as m . The transfer function for bond graph shown in Fig. 9.2a is given as,

$$\frac{f_1(s)}{e_5(s)} = \frac{\frac{\mu}{(m + \Delta m)s}}{1 + \left[\frac{\mu^2 \cdot M^* s}{(m + \Delta m)s} \right]} \tag{9.5}$$

Figure 9.2a shows the physical contraption of the controller. In order to implement the controller, following Ghosh [1], the symmetry in terms of effort and flow of the transformer is broken by first resolving it into two separate transformers, then activating one for effort and the other for flow, and finally making the modulus of the flow activated transformer as unity as shown in Fig. 9.2b. The physical implication of this is that a flow sensor has no power associated with it. The effort-activated transformer is given a high gain, which physically represents an effort-to-effort amplifier.

The actuation power at the output port of this amplifier comes from a tank system sustaining it. The signal flow graph for this system is shown in Fig. 9.2c. From the signal flow graph of Fig. 9.2c the transfer function can be derived as,

$$\frac{f_1(s)}{e_8(s)} = \frac{\frac{\mu_H}{(m+\Delta m)s}}{1 + \left[\frac{\mu_H \cdot \mu_f \cdot M^* s}{(m+\Delta m)s} \right]}. \quad (9.6)$$

Taking $\mu_f = 1$ in above equation and simplifying we get,

$$\frac{f_1(s)}{e_8(s)} = \frac{1}{\left[\left(\frac{m+\Delta m}{\mu_H M^*} \right) + 1 \right] M^* s} \quad (9.7)$$

where $f_1(s)$ and $e_8(s)$ are the Laplace transforms of output flow and input force. In this equation when $\mu_H \gg 1$

$$(m + \Delta m) / \mu_H M^* \cong 0$$

leading to,

$$\frac{f_1(s)}{e_8(s)} = \frac{1}{M^* s} \quad (9.8)$$

Equation 9.8 implies that the dynamics of the system depends on the mass M^* , i.e., dynamics of the plant mass $(m + \Delta m)$ becomes a small perturbation on the controller mass M^* dynamics. This equation can be used to obtain the input force to the controller $e_8(s)$ for a given trajectory $f_1(s)$ through an inverse dynamics solution solely on the basis of controller mass M^* .

9.3 Robust Controller for Terrestrial Manipulators

9.3.1 Case 1: Effort as a Reference Input

To generalize and test the concept discussed in Sect. 9.2, let us consider a second order plant and a second order overwhelming controller with compliance and damping considered as well.¹ The scheme is shown in Fig. 9.3a.

Consider that a single DOF plant is to be driven by a similar single DOF controller through a massless lever (amplifier). The plant parameters m_p (mass), k_p (stiffness), r_p (resistance) may be undetermined functions of time or states whereas the controller parameters M_c (mass), K_c (stiffness), and R_c (resistance) are linear time invariant. A force $e_{ref}(t)$ drives the controller to generate the desired motion. The bond graph

¹ Parts of this and the next section are adapted from these authors' previous work published in [6, 8].

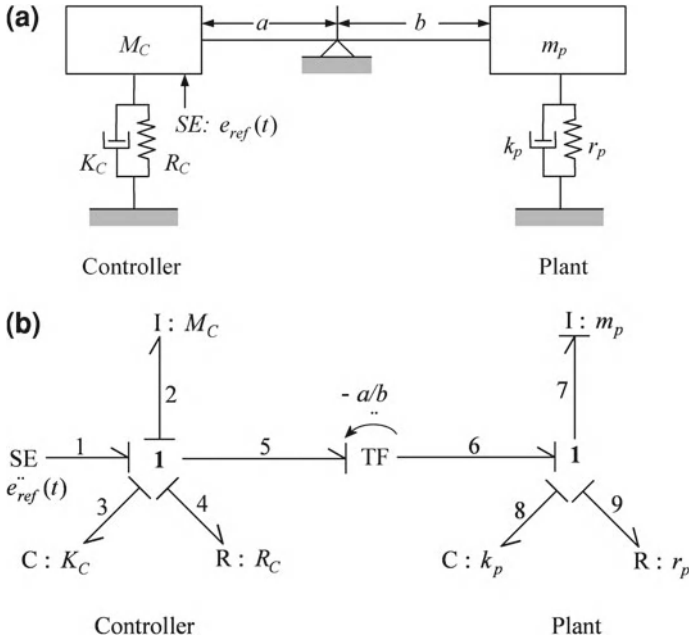


Fig. 9.3 a Schematic diagram of a second order plant and a second order overwhelming controller. b Bond graph of a second order plant and a second order overwhelming controller

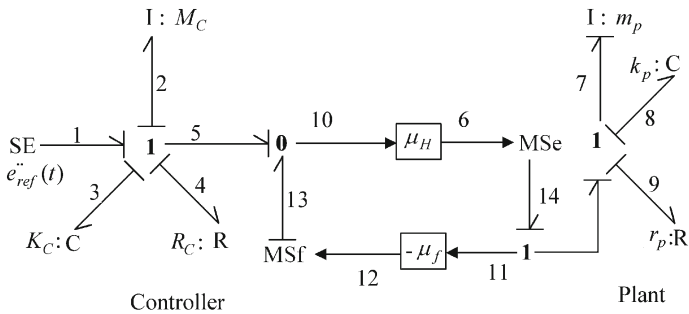


Fig. 9.4 Bond graph of realizable overwhelming controller

model of the system is shown in Fig. 9.3b. Next, the lever of Fig. 9.3b is made non-conservative (as discussed in Sect. 9.2) by using transformers with different gains and activated bonds as shown in Fig. 9.4.

A flow-activated bond transmits only flow information to the system at the port, which is flow causalled. Such a flow-activated bond does not take cognizance of effort information. Likewise, an effort-activated bond transmits only effort information to the system at its ports, which is effort causalled and does not take any cognizance of flow information. The flow activated transformer with modulus as unity is the

Fig. 9.5 Physical equivalent of overwhelming control system

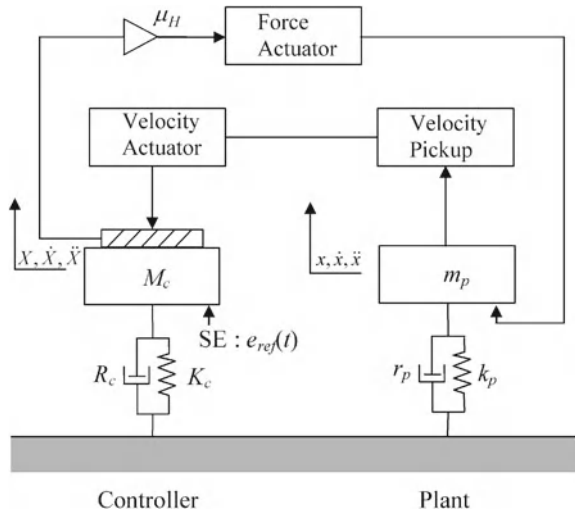
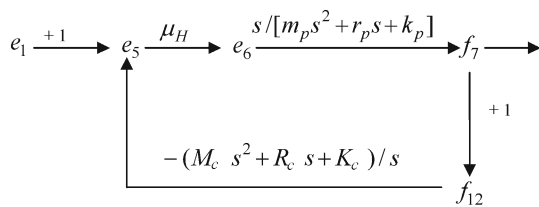


Fig. 9.6 signal flow graph for system shown in Fig. 9.4



feedback path of the flow information with no power associated with it. The effort-activated transformer with high gain is an effort amplifier. The actuation power at the output port of this amplifier comes from a tank system sustaining it. Figure 9.5 shows the actual physical equivalent of the system represented by the modified bond graph.

The transfer functions can be evaluated from the state space equations obtained from the bond graph representation. The transfer function between robot output flow $f_{rob}(s)$ and force input $e_{ref}(s)$ can be derived from the signal flow diagram shown in Fig. 9.6 as,

$$\frac{f_{rob}(s)}{e_{ref}(s)} = \frac{f_7(s)}{e_1(s)} = \frac{\mu_H R(s)}{[1 + \mu_H R(s)C(s)]} \tag{9.9}$$

where s is the Laplace variable. $R(s)$ is the transfer function of the robot between its output flow and driving effort given by,

$$R(s) = f_7(s)/e_6(s) = s/[m_p s^2 + r_p s + k_p] \tag{9.10}$$

and $C(s)$ is the transfer function of the controller between the output effort and command input flow given as,

$$C(s) = e_5(s)/f_5(s) = (M_c s^2 + R_c s + K_c)/s \tag{9.11}$$

When $\mu_H \gg 1$, one obtains from Eqs. 9.9–9.11, the overall transfer function as,

$$\frac{f_{rob}(s)}{e_{ref}(s)} \cong \frac{1}{C(s)} \cong \frac{1}{(M_c s + R_c + K_c/s)} \quad (9.12)$$

Here M_c , R_c , and K_c are the inertia (differential gain), resistance (proportional gain) and stiffness (integral gain) respectively of the overwhelming controller, and μ_H is high feed-forward gain. It is evident from Eq. 9.12 that the plant inertia m_p , compliance k_p , and damping r_p are all overwhelmed by the controller mass M_c , compliance K_c , and damping R_c respectively. This proves that high gain-based overwhelming control concept can also be used for higher order systems involving compliances and dampers. Any desired plant performance parameters may be obtained by suitably selecting the controller parameters. The command $e_{ref}(t)$ is taken of the form,

$$e_{ref}(t) = e_1(t) = M_c \ddot{X}_{ref} + R_c \dot{X}_{ref} + K_c X_{ref},$$

so that, it produces the desired motion $X_{ref}(t)$ of the controller. Therefore $e_{ref}(s) = s^2 M_c X_{ref}(s) + s R_c X_{ref}(s) + K_c X_{ref}(s)$, which gives

$$\frac{X_{ref}(s)}{e_{ref}(s)} = \frac{1}{(M_c s^2 + R_c s + K_c)}. \quad (9.13)$$

Since

$$X_{ref}(s) = f_{ref}(s)/s.$$

Equation 9.13 can be written as,

$$\frac{f_{ref}(s)}{e_{ref}(s)} = \frac{s}{(M_c s^2 + R_c s + K_c)}, \quad (9.14)$$

From Eqs. 9.12 and 9.14 we get,

$$\frac{f_{rob}(s)}{f_{ref}(s)} = 1, \quad (9.15)$$

i.e., the plant follows the command $f_{ref}(s)$. In the next case, we will see that we can give flow as reference input instead of effort as reference input.

9.3.2 Case 2: Flow as a Reference Input

If the bond graph of Fig. 9.4 is modified to the one as shown in Fig. 9.7, to have the reference input as flow input, then the transfer function between $f_{rob}(s)$ and $f_{ref}(s)$

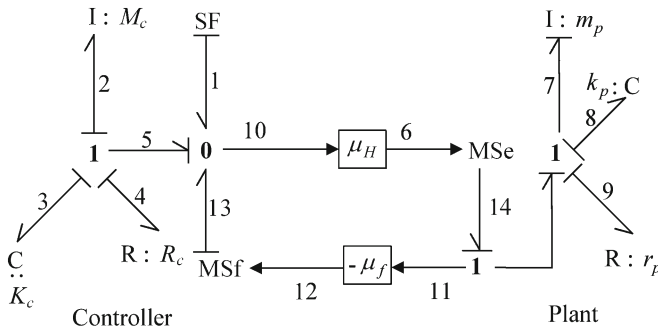


Fig. 9.7 Modified bond graph for realizable overwhelming controller

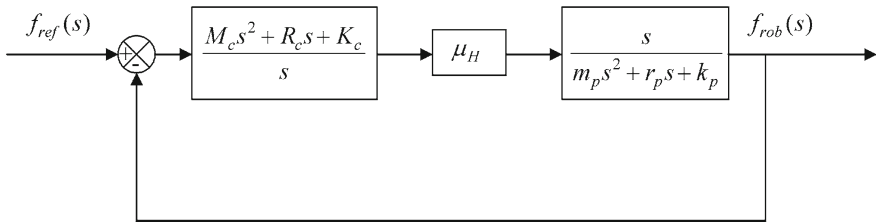


Fig. 9.8 Block diagram of overwhelming controller

is given by,

$$\frac{f_{rob}(s)}{f_{ref}(s)} = \frac{f_7(s)}{f_1(s)} = \frac{\mu_H C(s)R(s)}{1 + \mu_H C(s)R(s)}. \tag{9.16}$$

For $\mu_H \gg 1$,

$$\frac{f_{rob}(s)}{f_{ref}(s)} = 1. \tag{9.17}$$

Again this implies that the plant follows the command. Figure 9.8 shows the control scheme in the form of block diagram. Here the non-causal form of the controller is only artificial and is a consequence of the differential causality in the overwhelmer. The controller is brought to causal form by introducing a soft pad [7].

This scheme has been successfully applied to multidegree of freedom terrestrial manipulators with high degree of nonlinearities and coupled state behavior by Ghosh [1]. He considered a linear time invariant controller coupled to the plant through a set of high feed-forward gains with suitably defined feedbacks. The driving forces for the plant are decided by the linear controller parameters and the plant is dragged along the linear controller trajectory. The high feed-forward gain renders the plant dynamics as a perturbation on the linear controller, and hence the dynamics of the system closely resembles that of the controller. The error in the tracking may be indefinitely reduced by proper choice of parameters in the linear controller and by increasing the feed-forward gains. It is important to note that as long as the feed-forward gains are

sufficiently high, nonlinear or the time varying terms in the plant dynamics can be considered to reduce to first order perturbations on the controller parameters. By this technique the complex and highly nonlinear dynamics of the robotic system can be simply overwhelmed. In this control scheme, each link is taken as a separate system and is driven by a linear controller. Input forces to the controller can be determined by the desired trajectory of the system.

Thus, an overwhelming controller can be designed which takes care of complex and highly nonlinear dynamics of robot and provides robust trajectory control. The controller is fed with the error in trajectory, and controller in turn provides the corrective torques to be applied in the joints of robot. By considering the controller to be in the world coordinate frame, external disturbances and desired input can be directly conveyed to the controller in the world coordinate frame. Conventionally, input forces from the controller to the joints are determined by the desired trajectory of the system and the inverse kinematics of the given robot. Hence, the inverse kinematics transformations can be avoided by considering the controller in the world coordinate frame rather than joint coordinate frame. Under these conditions, the velocities can be transformed from the joint coordinates to the world coordinates using the Jacobian of the forward kinematics relation. In the next section we will consider the behavior of the overwhelming controller on a flexible foundation.

9.4 Robust Overwhelming Controller for Terrestrial Manipulator on a Flexible Foundation

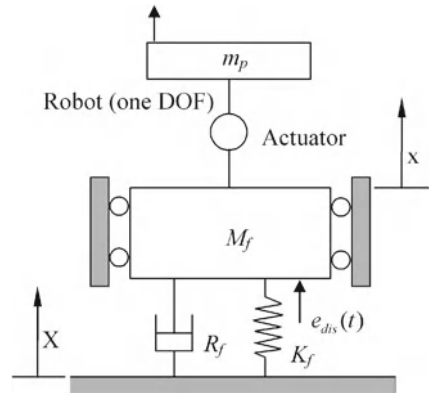
The overwhelming control strategy for terrestrial manipulator was modified by Kumar and Mukherjee [4] for a terrestrial robot with flexible foundation. The principle can be explained by modeling of single DOF robot on a flexible foundation with overwhelming trajectory controller riding on the flexible foundation as shown in Fig. 9.9. To incorporate the foundation disturbance in the world coordinate the foundation velocities in each direction was sensed and feedback to model in controller. The bond graph modeling for Fig. 9.9 is shown in Fig. 9.10a. To incorporate the foundation disturbances in the world coordinate, the foundation velocity is sensed and fed back to the controller. The feedback compensation with gain α acts on the controller through a new MSf element.

The block diagram representation of single DOF robot on flexible foundation with controller and compensation is shown in Fig. 9.10b.

The transfer function for the system between the force input to the robot velocity, derived from the signal flow graph (Fig. 9.10c), can be written as

$$\frac{f_1(s)}{e_4(s)} = \frac{\mu_H R(s)}{[1 + \mu_H R(s)C(s) + (1 - \alpha)\mu_H C(s)F(s)]}, \tag{9.18}$$

Fig. 9.9 Single DOF robot on flexible foundation



where

$$R(s) = 1/(m_p s), \tag{9.19}$$

$$C(s) = (M_c s^2 + R_c s + K_c)/s, \tag{9.20}$$

$$F(s) = s/(M_f s^2 + R_f s + K_f). \tag{9.21}$$

Here $R(s)$, $C(s)$, and $F(s)$ are robot, controller, and foundation transfer functions respectively. In Eq. 9.21, the foundation parameters are M_f (mass), K_f (stiffness) and R_f (damping). For the high feed-forward gains (i.e., $\mu_H \gg 1$) and $\alpha = 1$, on using Eqs. 9.19–9.21 in Eq. 9.18 one obtains,

$$\frac{f_1(s)}{e_4(s)} = \frac{1}{C(s)} = \frac{s}{(M_c s^2 + R_c s + K_c)}. \tag{9.22}$$

The transfer function between the robot end-effector flow $f_{rob}(s)$ and the disturbance force $e_{dis}(s)$ for such a system can be derived as,

$$\frac{f_{rob}(s)}{e_{dis}(s)} = \frac{f_1(s)}{e_5(s)} = \frac{(1 - \alpha)\mu_H R(s)C(s)F(s)}{[1 + \mu_H R(s)C(s) + (1 - \alpha)\mu_H C(s)F(s)]}. \tag{9.23}$$

The transfer functions of Eqs. 9.18 and 9.23 show that if $\alpha = 1$, the foundation has no effect on the trajectory of the robot under the chosen feedback scheme. Thus, the external disturbances can be completely compensated even in the absence of the knowledge of foundation parameters. In the above control scheme, the effort command to the controller has to be calculated based on the given trajectory and the controller parameters as is evident from Eq. 9.22.

By making a slight modification to this scheme as shown in Fig. 9.11, the controller can be made to provide required drag force to the plant which can track the given velocity command effectively. The transfer function for the system between the robot

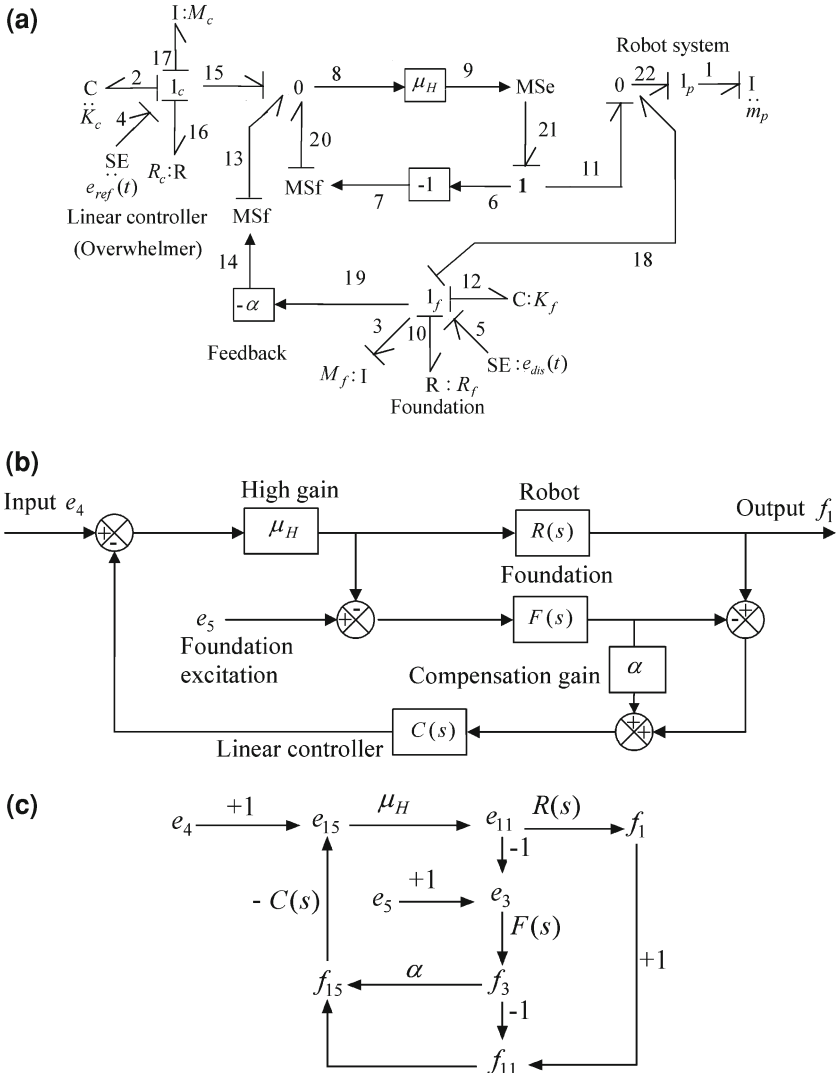


Fig. 9.10 a Bond graph model for Single DOF robot on flexible foundation shown in Fig. 9.9. b Block diagram for bond graph model shown in (a). c Signal flow graph for system shown in (a)

velocity $f_{rob}(s)$ and reference input velocity $f_{ref}(s)$ can be written as,

$$\frac{f_{rob}(s)}{f_{ref}(s)} = \frac{f_1(s)}{f_4(s)} = \frac{\mu_H C(s) R(s)}{1 + \mu_H C(s) R(s) + (1 - \alpha) \mu_H C(s) F(s)}. \tag{9.24}$$

For high feed-forward gain (i.e., $\mu_H \gg 1$) and $\alpha = 1$,

$$\frac{f_{rob}(s)}{f_{ref}(s)} = 1 \tag{9.25}$$

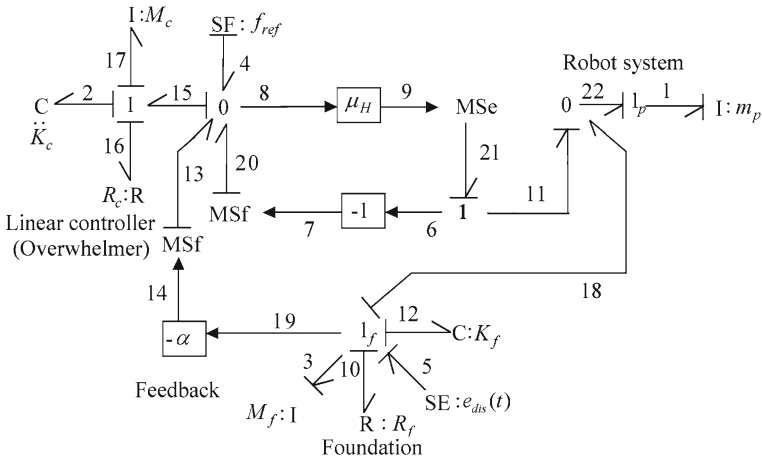


Fig. 9.11 Bond graph model of single DOF robot on flexible foundation, with input as reference velocity

Thus, the transfer function of Eq. 9.25 also shows that if $\alpha = 1$, the foundation has no effect on the trajectory of the robot and robot follows the reference velocity command effectively. Thus, the external disturbances are completely compensated without knowledge of the foundation parameters. A foundation disturbance sensor and a compensating feedback have been introduced to achieve this. The scheme is extendable to multidegree of freedom robotic systems and can be used effectively to track a desired end-effector trajectory. Next section presents the impedance controller for ground robot.

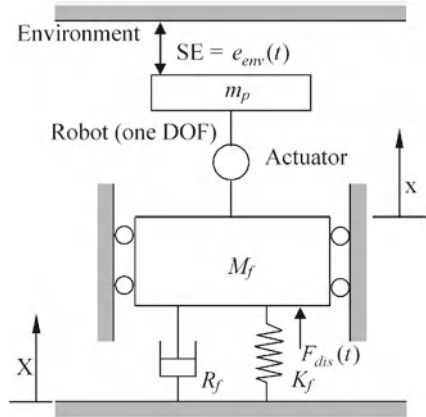
9.5 Impedance Controller for Terrestrial Robots

9.5.1 Considerations for a Position-Force Controller for Ground Robots

The impedance of the system at an interaction port is defined as the ratio between the output effort and the input flow. For applications demanding high trajectory tracking accuracy, the robotic systems are programmed to have high impedance at the end-effector. This leads to poor accommodation of external disturbances during interaction, and hence control of interaction forces is difficult. However, many situations demand a robotic controller to have a balance of both the characteristics, i.e., good trajectory robustness, and accommodation to environment interaction forces or torques. This is achieved by controlling the impedance appropriately instead of controlling the position or the force separately.²

² A part of this section is adapted from these authors’ previous work published in [7, 8].

Fig. 9.12 Single DOF robot on flexible foundation interacting with environment



Another issue in control of robot manipulators is the uncertainty in the dynamic model of the manipulator. These uncertainties include unknown parameters, unknown functions, disturbances, and unmodeled dynamics. Usually, these uncertainties and unmodeled dynamics in the plant are largely due to the presence of unmodeled DOF in the form of compliances like the flexible linkages, drive system backlash, link assembly clearance, etc. Hence, one prefers robust trajectory control strategies that make the system insensitive to variations in the manipulator parameters, and ensure bounded trajectory tracking errors. Moreover, at times, additional DOF are incorporated in the manipulator (like a flexible foundation) for specific purposes. When such additional DOF are introduced/present in the manipulator, suitable modifications in the controller are required for the trajectory tracking robustness. Further, if these additional DOF are suitably designed and incorporated, they can be made to provide a desired accommodation of the external disturbing forces that arise during interaction.

In the following section, a robust impedance controller for ground robots [3] is described.

9.5.2 A Robust Impedance Controller for Terrestrial Robot

Figure 9.12 shows a single DOF robot on flexible foundation, interacting with environment. The foundation compensation is so designed that its impedance can be modulated to limit the forces of interaction [3, 5]. The control paradigm establishes a proper relation between the trajectory controller and the force controller through the manipulation of the robot impedance. The robot stiffness is made very high during trajectory control, and appropriately modulated during force control.

The bond graph for the system is shown in Fig. 9.13a. In this figure f_{ref} is the reference velocity command and $F_{dis}(t)$ is the foundation disturbance force. To incorporate the foundation disturbances in the inertial coordinates, the foundation

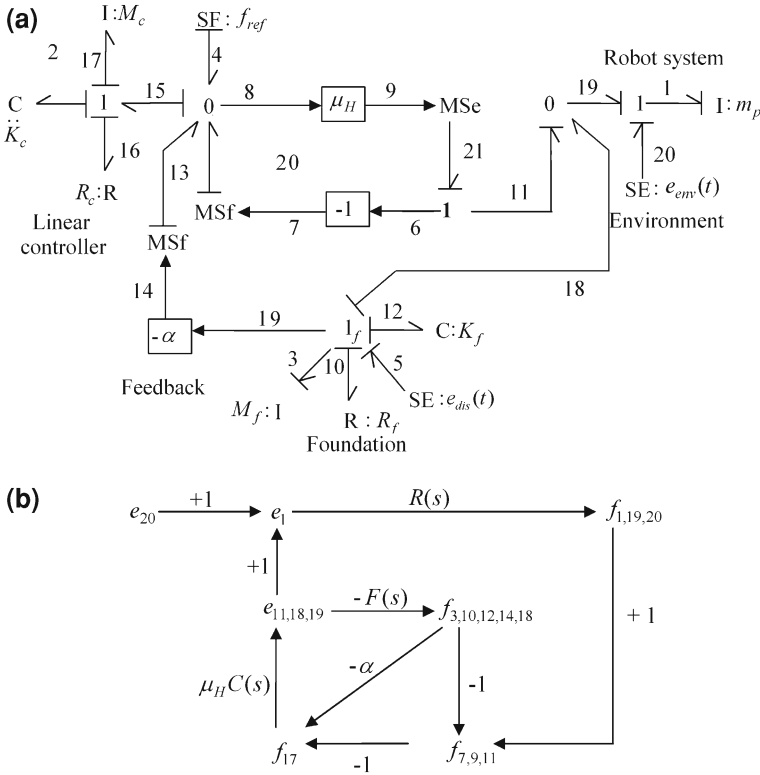


Fig. 9.13 **a** Bond graph of a single DOF robot on flexible foundation interacting with environment, **b** signal flow diagram for bond graph shown in **(a)**

velocity is sensed and fed back to the controller. A gain block with gain α shows the feedback compensation.

The transfer function between the output flow $f_{rob}(s)$ (i.e., the motion of the end-effector) and the input effort $e_{env}(s)$ (by the environment on the robot), represents the admittance $Y_{rob}(s)$ of the robotic system at the interaction port. The impedance $Z_{rob}(s)$ is the inverse of the admittance. Admittance and impedance at the interaction point can be derived from the signal flow diagram of Fig. 9.13b as,

$$\begin{aligned}
 Y_{rob}(s) &= \frac{1}{Z_{rob}(s)} = \frac{f_{rob}(s)}{e_{env}(s)} = \frac{f_1(s)}{e_{20}(s)} \\
 &= \frac{R(s)[1 + \mu_H(1 - \alpha)F(s)C(s)]}{1 + \mu_H C(s)R(s) + \mu_H(1 - \alpha)F(s)C(s)}. \tag{9.26}
 \end{aligned}$$

Here $R(s) = 1/(m_p s)$ is transfer function of the robot, $C(s) = (M_c s^2 + R_c s + K_c)/s$ is transfer function of the controller, and $F(s) = s/(M_f s^2 + R_f s + K_f)$ is transfer function of the foundation.

Equation 9.26 indicates two distinct behaviors of the foundation compensation gain α .

1. When $\alpha = 1$,

$$Y_{rob}(s) = \frac{1}{Z_{rob}(s)} = \frac{f_{rob}(s)}{e_{env}(s)} = \frac{R(s)}{1 + \mu_H C(s)R(s)}, \quad (9.27)$$

i.e., the controller totally rejects the foundation characteristics. If $\mu_H \gg 1$ is also assumed then it will assure trajectory robustness.

2. When $\alpha < 1$, modulation of the impedance to accommodate interaction forces is possible.

The effect of foundation compensation gain α , on the impedance or stiffness of the robot can be observed at the interaction port by studying the response of the system to a constant environmental effort E .

Let $e_{env}(t) = E$. So $e_{env}(s) = E/s$. End-effector displacement $X_{rob}(t)$ is obtained as the integral of its velocity $f_{rob}(t)$, so from Eq. 9.26

$$\begin{aligned} \frac{sX_{rob}(s)}{(E/s)} &= \frac{R(s)[1 + \mu_H(1 - \alpha)F(s)C(s)]}{1 + \mu_H C(s)R(s) + \mu_H(1 - \alpha)F(s)C(s)} \\ \Rightarrow X_{rob}(s) &= \left[\frac{R(s)[1 + \mu_H(1 - \alpha)F(s)C(s)]}{1 + \mu_H C(s)R(s) + \mu_H(1 - \alpha)F(s)C(s)} \right] \frac{E}{s^2}. \end{aligned} \quad (9.28)$$

Substituting the values of $R(s)$, $F(s)$, and $C(s)$,

$$\begin{aligned} \frac{X_{rob}(s)}{E} &= \frac{\frac{1}{m_p s} \left[1 + \mu_H(1 - \alpha) \frac{(M_c s^2 + R_c s + K_c)}{(M_f s^2 + R_f s + K_f)} \right]}{\left[1 + \frac{\mu_H(M_c s^2 + R_c s + K_c)}{m_p s^2} + \frac{\mu_H(1 - \alpha)(M_c s^2 + R_c s + K_c)}{(M_f s^2 + R_f s + K_f)} \right]} \cdot \frac{1}{s^2}, \\ \frac{sX_{rob}(s)}{E} &= \frac{\left[1 + \mu_H(1 - \alpha) \frac{(M_c s^2 + R_c s + K_c)}{(M_f s^2 + R_f s + K_f)} \right]}{\left[m_p s^2 + \mu_H(M_c s^2 + R_c s + K_c) + \frac{\mu_H(1 - \alpha)m_p s^2(M_c s^2 + R_c s + K_c)}{(M_f s^2 + R_f s + K_f)} \right]}. \end{aligned}$$

Using the final value theorem, the steady state response of the function $X_{rob}(s)/E$ can be obtained as,

$$\begin{aligned} \lim_{s \rightarrow 0} \left(\frac{sX_{rob}(s)}{E} \right) &= \frac{1}{K_{rob}} = \frac{[1 + \mu_H(1 - \alpha)(K_c/K_f)]}{\mu_H K_c}, \\ \Rightarrow \lim_{s \rightarrow 0} \left(\frac{sX_{rob}(s)}{E} \right) &= \frac{1}{K_{rob}} = \frac{1}{\mu_H K_c} + \frac{(1 - \alpha)}{K_f}, \end{aligned}$$

or,

$$K_{rob} = \frac{K_c K_f}{\frac{1}{\mu_H} K_f + (1 - \alpha) K_c} \quad (9.29)$$

Here, K_{rob} is termed as driving point stiffness of the robotic system since it is determined at the interaction port. From Eq. 9.29 two important conclusions can be inferred as follows:

- (i) When $\alpha = 1$, (i.e., full foundation compensation)

$$K_{rob} = \mu_H K_c \quad (9.30)$$

Since $\mu_H \gg 1$, K_{rob} will be very high and manipulator will not accommodate any interaction force thus fulfilling the requirement of robust overwhelming trajectory controller.

- (ii) When $\alpha < 1$, and $\mu_H \gg 1$, (i.e., overwhelming control)

$$K_{rob} \cong \frac{K_f}{(1 - \alpha)}. \quad (9.31)$$

i.e., α can be used to change the impedance or stiffness behavior of the robotic system at the interaction port, so as to accommodate forces from the environment. One can similarly carryout the exercise for damping and inertance to see the effects of the compensation gain.

Thus, it is concluded that the impedance of the robotic system at the end-effector is dependent on the compensation gain α to the controller, which is characteristic of the flexible foundation. However, force control using actual foundation is not a good proposition. Therefore, an equivalent controller can be devised with its foundation moved into the controller domain. Next section illustrates the equivalent controller with its foundation moved into the controller domain.

9.6 Concept of Virtual Foundation

In the previous section, robot was assumed to be riding on a physical foundation. Hence, the foundation was termed as existing in physical domain. Impedance controller with foundation moved to controller domain is useful for having an entirely software controlled impedance behavior at the end-effector of the robotic system. This controller is developed through a system based on bond graph approach, where certain transformations are performed among the various junction structures in the multi energy domain preserving the output impedance characteristic of the robotic system. Figure 9.14a shows bond graph at controller manipulator interface junction structure with real foundation i.e., foundation in physical domain.

An alternative bond graph representation of the controller manipulator interface junction structure with foundation moved into controller domain is shown in Fig. 9.14b. Let us assume that the controller delivers an effort e_c and the plant receives velocity information f_p whereas foundation receives a velocity f_f . Then, the other power variables can be determined as shown in Fig. 9.14a, b. The equivalence of two cases can be concluded by observing the power variables at the different bonds.

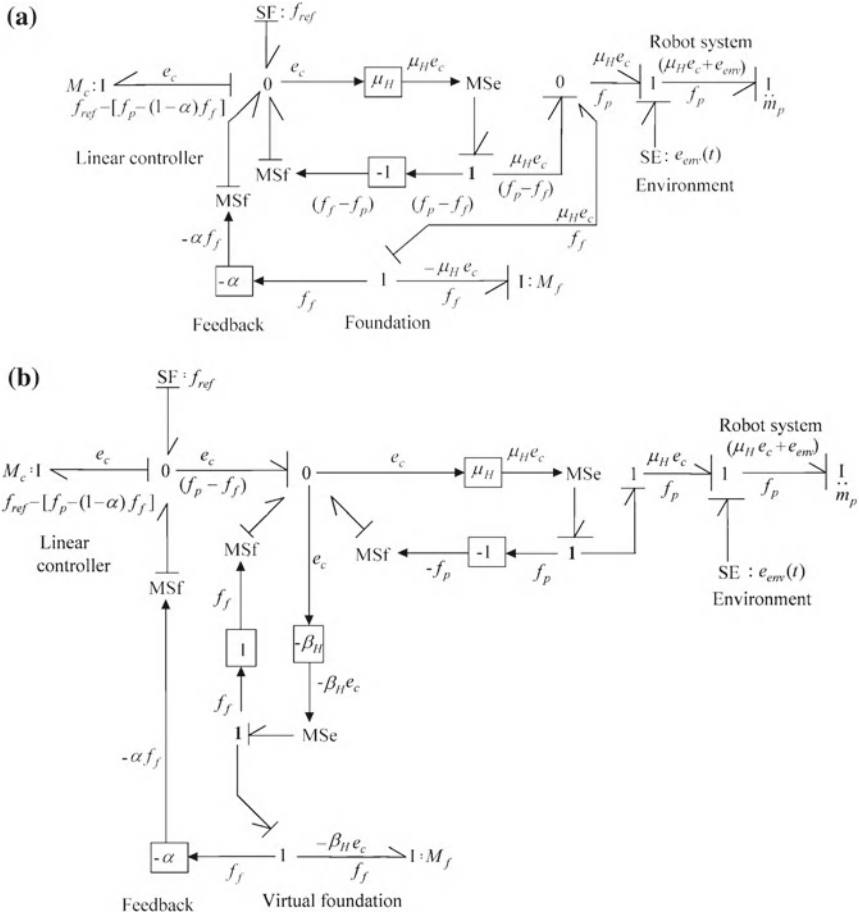


Fig. 9.14 **a** Bond graph representation of controller manipulator interface junction structure with real foundation. **b** Bond graph representation of controller manipulator interface junction structure with real foundation moved into the controller domain

The power variables are same at the plant port, environment port, controller port, and foundation port.

Thus, an alternative junction structure having similar algebraic characteristics as given by bond graph of Fig. 9.13a is shown in Fig. 9.15a, where the additional passive DOF has been transferred to the controller domain.

The admittance of the robotic system at the interaction port can be derived from the signal flow diagram shown in Fig. 9.15b as,

$$Y_{rob}(s) = \frac{1}{Z_{rob}(s)} = \frac{f_{rob}(s)}{e_{env}(s)} = \frac{f_1}{e_{20}} = \frac{R(s)[1 + \beta_H(1 - \alpha)F(s)C(s)]}{1 + \mu_H C(s)R(s) + \beta_H(1 - \alpha)F(s)C(s)} \tag{9.32}$$

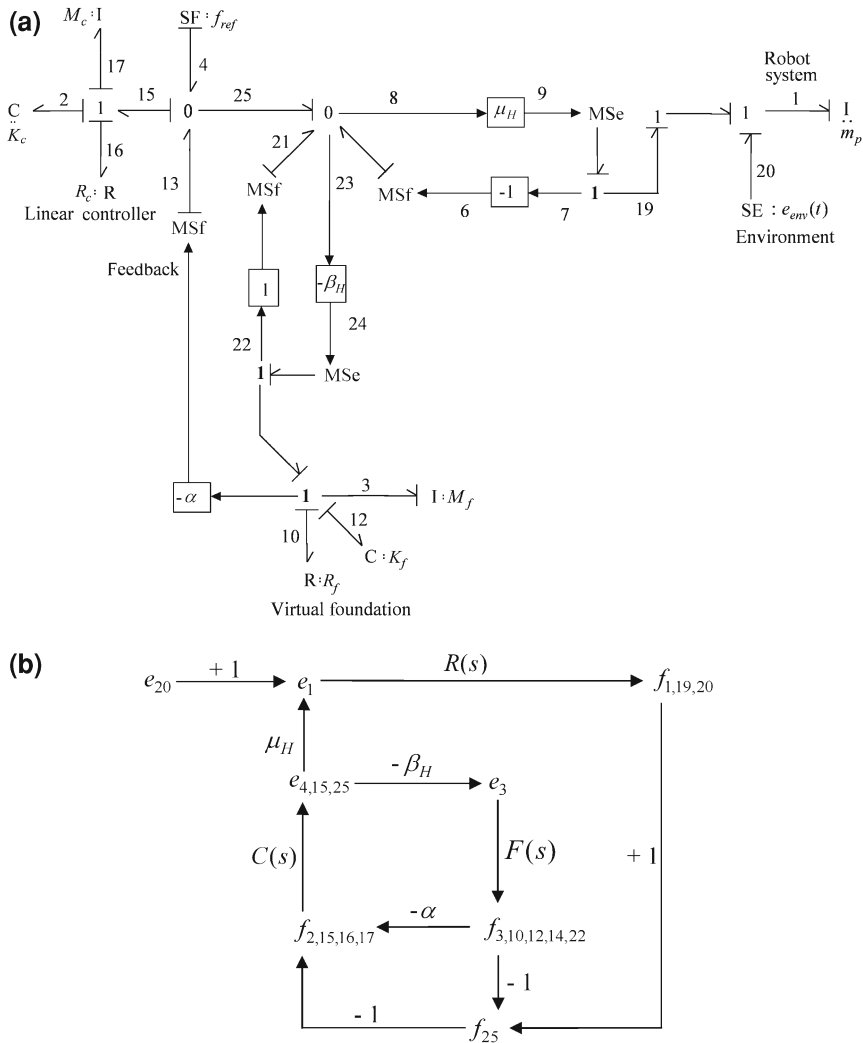


Fig. 9.15 **a** Bond graph of single DOF robot with flexible foundation in controller domain. **b** Signal flow diagram for bond graph shown in (a)

Comparing the admittances given by Eqs. 9.26 and 9.32 we can see that the transformation from the foundation in physical domain to the foundation in controller domain is affected by replacing $\mu_H(1 - \alpha)$ by $\beta_H(1 - \alpha)$. Here, β_H is a high-gain parameter which is equal to the high feed-forward gain. The driving point stiffness $K_{rob}(s)$ of the robotic system at the interface with the environment for a constant environmental effort (E) can also be derived as

$$\frac{1}{K_{rob}(s)} = \frac{1}{\mu_H K_C} + \frac{\beta_H(1-\alpha)}{\mu_H K_f}$$

or,

$$K_{rob}(s) = \frac{K_c K_f}{\frac{K_f}{\mu_H} + K_c \frac{\beta_H}{\mu_H} (1-\alpha)}. \quad (9.33)$$

Note that when, $\alpha < 1$, and $\mu_H, \beta_H \gg 1$

$$K_{rob}(\alpha) \cong \frac{\mu_H K_f}{\beta_H(1-\alpha)} \quad (9.34)$$

and when $\alpha = 1$, and $\mu_H, \beta_H \gg 1$,

$$K_{rob}(\alpha) = \mu_H K_C \quad (9.35)$$

In this case the additional DOF (foundation) is in the controller domain, and hence referred as *virtual foundation*. During accommodation of environmental interaction force, or during trajectory control, the end-effector flow will be compensated by the flow of the virtual foundation residing in the computational domain of the controller. Here, Hogan's [2] basic idea of conceiving a physical paradigm and realizing it in the controller domain is utilized. The virtual foundation is a bond graphic creation of an actual passive foundation. Simple transposition is carried out from physical system concepts. Such controllers can be realized either in active electronic circuits made from operational amplifiers, or from digital control system implementation. However, the virtual foundation in the controller domain need not necessarily be actual physical circuits or devices. It may be in the form of equations residing in the control computer and representing the state of the control system equivalent. It will have the effect of the real system due to the equivalences established in the manner described. Also, the virtual foundation can be oriented in any direction of the ortho-normal coordinate frame in order to provide directional impedance properties.

References

1. A.K. Ghosh, Dynamics and robust control of robotic systems: a bond graph approach. Ph.D. Thesis, Department of Mechanical Engineering, Indian Institute of Technology, Kharagpur, 1990
2. N. Hogan, Impedance control: an approach to manipulation: parts I–III. Trans. ASME J. Dyn. Syst. Measur. Control **107**, 1–24 (1985)
3. C.S. Kumar, Shaping the interaction behavior of manipulators through additional passive degrees of freedom: a new approach to impedance control. Ph.D. Thesis, Department of Mechanical Engineering, Indian Institute of Technology, Kharagpur, 1994
4. C.S. Kumar, A. Mukherjee, Robust control of a robot manipulator on a flexible foundation, in *Fourth International Conference on CAD/CAM, Robotics and Factories of Future*, 1989, (TATA McGraw-Hill, New Delhi, 1989), pp. 727–742

5. C.S. Kumar, A. Mukherjee, M.A. Faruqi, Some finer aspects of impedance modulation on hybrid tracking and force controlled manipulators, in *Proceedings of International Conference on Bond Graph Modeling and Simulation (ICBGM'93)*, 1993
6. P.M. Pathak, A. Mukherjee, A. Dasgupta, Impedance control of space robots using passive degrees of freedom in controller domain. *Trans. ASME J. Dyn. Syst. Measur. Control* **127**, 564–578 (2005)
7. P.M. Pathak, A. Mukherjee, A. Dasgupta, Impedance control of space robot. *Int. J. Model. Simul.* **26**(4), 316–322 (2006)
8. P.M. Pathak, R.P. Kumar, A. Mukherjee, A. Dasgupta, A scheme for robust trajectory control of space robots. *Simul. Model. Pract. Theory* **16**, 1337–1349 (2008)

Chapter 10

Modeling and Control of Space Robots

10.1 Introduction

Dextre, short for the Canadian-built Special Purpose Dexterous Manipulator, is the space robot doing many tasks in the space station. The robot shown in Fig. 10.1 is a multi arm manipulator. Space robots are used for in-orbit construction, in-orbit satellite servicing, and maintenance of large space structures. A brief list of robots with flight experiments is as follows.

- The space satellite's 15 m Canadian-built Remote Manipulator System (RMS) or "Canadarm" first flew on the Space Transportation System (STS-2) of NASA in 1981. It was used routinely for retrieving satellites into the cargo bay and as a mobile platform for astronauts during extravehicular activity (EVA). It has vehicle-to-arm mass ratio of 200:1. In this mission, for the first time remote manipulator system tests were conducted.
- The German Robot Technology Experiment (ROTEX) manipulator was operated inside the space lab and module on STS-55 in 1993. ROTEX [5], robotic arm could capture a free-floating object in space via remote control from earth.
- The Japanese Manipulator Flight Demonstration (MFD) has flown manipulators aboard the shuttle. The MFD manipulator was attached to a support structure in the cargo bay of the shuttle on STS-85 in 1997. It was operated by astronauts from the air flight deck.
- The Engineering Test Satellite (ETS)-VII [14], was launched in 1997. It completed its operation on 30 October 2002. The ETS-VII programme was designed to test key rendezvous, docking, and robotics technologies in space. ETS-VII consists of a target satellite and a chaser satellite. We can find in the literature activities in the area of space robotics in various countries, including Russia [3], Italy [11], Germany [5], Canada [24], and countries in Europe [22]. Woerkom and Misra [25] have discussed dynamic modeling issues and control schemes for space robots, along with a note on various space robots.



Fig. 10.1 The special purpose dexterous manipulator (SPDM), also known as dextre telemanipulator, at work on the international space station (ISS). Canadarm or RMS is also seen in the picture (Source NASA, http://www.nasa.gov/images/content/287299main_dextre_iss017_big_full.jpg)

Space robots are a blend of a vehicle and a robot. They are mechanically more complex than a satellite. Satellites may have only solar arrays or other attachments. The vehicle is equipped with external force actuators such as jet thrusters and internal force actuators such as reaction wheels to maneuver the vehicle locally and also to control the attitude and center of mass (CM). Navigational instruments are required for rendezvous and docking. Solar arrays and batteries are needed for generating and storing power. The internal force actuators use solar energy stored in rechargeable batteries. The amount of energy stored in them is limited so the internal force actuators need to be used judiciously. External force actuators use fuel that is carried by the space robot system from the earth, and hence is limited in quantity and quite expensive to use. Moreover, fuel is used mainly to correct the attitude changes due to gravitational forces and other disturbances, so it is not advisable to use fuel for correcting attitude disturbances caused due to robot motion. Therefore, the use of external force actuators has to be limited to maximize the overall life span of the space robot system.

A free-floating space robotic system is one in which the spacecraft's position and attitude are not actively controlled using external jets/thrusters. It does not interact dynamically with the environment during manipulator activity. For such systems, the linear and angular momenta are conserved. Thus, due to conserved linear and angular momenta, the spacecraft moves freely in response to the dynamical disturbances caused by the manipulator's motion. This disturbance of the base results in deviation of the end-effector from the desired trajectory. Moreover, the angular momentum conservation constraints are non-integrable rendering the system nonholonomic [13]. Typical space applications require precise manipulator control. This is a difficult task

to achieve due to free-floating base of the space robot and dynamic coupling between the manipulator and the base. A large vehicle mass will cause negligible motion of the vehicle when the manipulator moves, but it will be costly to propel such a large payload into orbit. Space robots typically have vehicle to arm ratio closer to 10:1. They cause significant motion of the vehicle when the arm moves to perform its task. The dynamic coupling between the spacecraft and the manipulator has been a subject of intense investigation since the space shuttle RMS went into service in 1982. The reaction torque imparted on the shuttle by RMS operations was not addressed in the original controller design. The resulting motion of shuttle base caused the end effector to miss its target unless the operator visually compensated for errors. This type of problem could be acute during satellite rendezvous in which the error of even a few centimeters could result in a failed capture attempt or even damage to satellite.

The satellite's attitude stabilization is necessary in most cases for electrical power generation from solar panels and to retain the communication link. For this purpose, reaction control system (RCS) using the gas jet thruster is usually used, as the RCS is used for orbit maneuver. But it is always preferred to have other attitude control systems to save the propellant of the space vehicle. Approaches to compensation for the base motion typically fall into two categories [15]. (i) Coordinated control which uses the fixed base arm control strategies but maintains the attitude of the vehicle using thrusters or reaction wheels. This method has the advantage of decoupling the manipulator from the satellite control but at the cost of increased fuel or power consumption. The approach draws primarily from previous work in spacecraft attitude control. (ii) In internal motion control approach, the vehicle drifts but the path of the arm is modified to compensate for the base motion. This method uses less power but requires a more complex strategy for controlling the arm. Pure feedback control (i.e., coordinated control), may be inadequate for overcoming the disturbance forces and torque produced by arm motion. This can be improved by including model-dependent feed forward in the control law, thereby reducing the burden on the feedback control term. This approach however destabilizes a space robot, due to the unmodeled arm cross-coupling terms in the satellite inertial estimate used in generating the feed-forward torque.

Space manipulator tasks can be divided into two different categories. In the first category, the manipulator end-effector is under position or trajectory control. These types of tasks are called motion control tasks. An example of this is when the manipulator grasps an object and moves it to a desired position. The second category of tasks is called force/torque control tasks. These involve a significant force/torque interaction between the space manipulator and its environment. An example of this type of task is when the manipulator performs an operation on an external object, such as disconnecting a cable or turning a knob from a satellite, or assembly which require insertion, push, etc. The typical tasks to be performed by space robots would be deploying or assembling space platforms, space stations, large antennas or solar power stations, and servicing and maintenance of satellites. These manipulators must ensure safe and reliable interaction with objects or environments in their workspace. Robots are subjected to interaction forces whenever they perform tasks involving

motion, which is constrained by the environment. These interaction forces/moments must be accommodated and restricted so as to comply with the environmental constraints. Control of spacecraft and manipulators during capture or manipulation of object has not been given adequate attention by researchers. However, successful performance of a compliant motion is very important for space robots.

There are two main difficulties with the force control of space manipulators. First, a space robot has no fixed point in the inertial space, and moves when a manipulator applies a force or torque on an environment. Second, the physical properties of the environment on which the manipulator applies force are not well known. The first problem can be overcome by using a thruster if force control of the robot is desired, while torque control can be achieved by use of thruster pairs or an attitude controller. The second problem can be overcome by assuring that the force controller is robust against the physical properties of the environment and by providing a passive compliance between the end effector and manipulator. The passive compliance mechanism can absorb an impulse force acting on the end effector and align the end effector along an inclined surface.

Two broad approaches for achieving compliant motion are described in the literature. These approaches are (i) Hybrid position and force control and (ii) Impedance control. The Hybrid position/force control approach [23] is based on the fact that when the robot end-effector is in contact with the environment, the Cartesian space of the end-effector coordinate may be naturally decomposed into a position control subspace and a force control subspace. The position control subspace corresponds to the Cartesian directions in which the end effector is free to move, while the constrained directions correspond to the force control subspace. The hybrid position/force control approach to compliant motion is to track a position/orientation trajectory in the position subspace, and a force/moment trajectory in the force subspace by using separate position and force controllers. On the other hand, the impedance control approach proposes that the control objective should not be tracking of position/force trajectories, but rather should involve the regulation of the mechanical impedance of the robot end-effector which relates velocity and force. Thus the objective of the impedance controller is to maintain a desired dynamic relationship between the end-effector position and end-effector environment contact force. This gives a unified framework for both unconstrained and constrained motion control problems and does not require the control switching as needed in hybrid control [6]. Recent investigations have focused on enhancing the capabilities of robust impedance controllers, and have included efforts to develop adaptive impedance algorithms.

The space environment is very much different from the earth environment. The main differences are the (1) absence of gravity, (2) absence of rigid base, and (3) limited amount of onboard fuel for actuation of the space robot system. The absence of a rigid base imposes momentum constraints on the motion of the system. The limited amount of onboard fuel for actuation of the space robot system puts a limit on the use of thrusters for attitude control or for force and torque control operations.

The dynamic modeling of a space robot involves the modeling of the angular and linear dynamics of the robot arm and the base. Dynamic modeling incorporates modeling of constraints and drives.

This chapter first discusses the space robot as a nonholonomic system. The major difference between the stationary and mobile formulation is presented. Then we shall discuss the mechanics of the space robot. Then the object-oriented bond graph modeling of space robots is presented. The reusable submodels are defined, which are then used to model a single link. A multi bond graph of a space robot is shown with all the created objects. A case study of a three DOF space robot model is presented using these objects, and the simulation results are also presented. Then we present the force and torque control strategy using impedance control.

10.2 Space Robot as a Nonholonomic System

Consider a system specified by n generalized coordinates $q_1, q_2 \dots q_n$. The constraint of the system may be classified in the following ways:

1. Holonomic constraints

Constraints in the form of k independent equations [4], given by Eq. 10.1 as,

$$\phi_j(q_1, q_2, \dots, q_n) = 0, \quad (j = 1, 2, \dots, k), \quad (10.1)$$

are known as a holonomic constraints and a system for which all the constraint equations are holonomic is called a holonomic system.

2. Nonholonomic constraints

Constraints in the form of m constraint equations that are “non-integrable” differential expressions of the form,

$$\sum_{i=1}^n a_{ji} dq_i + a_{jt} dt = 0, \quad (j = 1, 2, \dots, m), \quad (10.2)$$

where the a_{ji}, a_{jt} may be the functions of q 's and time t .

Constraints given by Eq. 10.2 are known as nonholonomic constraints and the system is called nonholonomic even if just one of its constraints is nonholonomic. As a result of the non-integrable nature of the differential equation it is not possible to obtain functions of the form given by Eq. 10.1.

A robotic system in space is considered to be free-floating when it does not use reaction jets and does not interact dynamically with the environment. For such a system, the linear and angular momenta are conserved. From angular momentum conservation we get non-integrable constraint equations in terms of the generalized velocities. Thus a free-floating space robot behaves like a nonholonomic mechanical system.

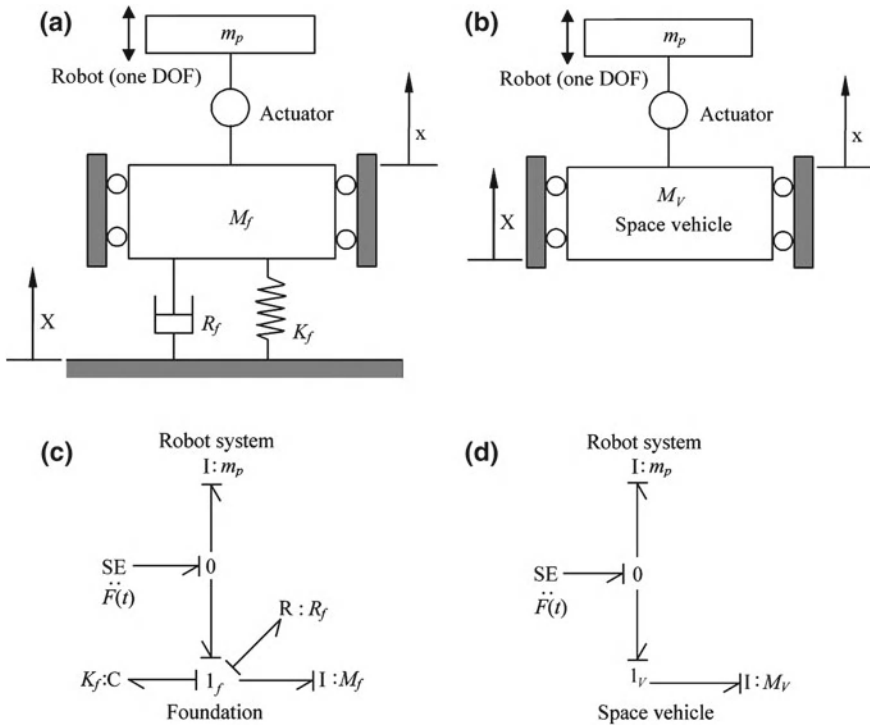


Fig. 10.2 **a** Schematic diagram of single DOF robot on flexible foundation. **b** Schematic diagram of single DOF space robot. **c** Bond graph model of single DOF robot on flexible foundation. **d** Bond graph model of single DOF space robot

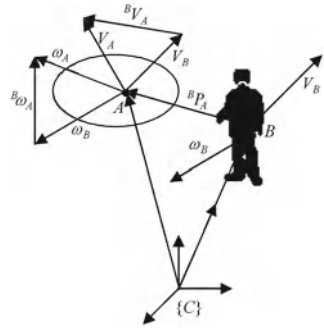
10.3 Stationary Versus Space Robot’s Formulation

The difference between stationary and space robot formulation can be given as

1. The initial conditions for the link 0 velocity and acceleration for each arm will depend on the vehicle state.
2. The vehicle dynamics now depend on the arm interaction forces and moments, f_l and n_l in addition to the external forces and moments acting on the vehicle.

The difference between a ground robot on a flexible foundation and a space robot is illustrated through Fig. 10.2a, b. The corresponding bond graphs are shown in Fig. 10.2c, d. The only difference between a ground robot on flexible foundation and a space robot is that, in case of ground robot on flexible foundation I (inertia i.e., mass), C (compliance), and R (damping) elements are present at foundation velocity junction (1_f), whereas in case of the space robot only I (inertia i.e., mass) element is present at space vehicle velocity junction (1_V).

Fig. 10.3 Description of the position, linear, and angular velocity vectors



10.4 Mechanics of Space Robots

10.4.1 Notation

There are some vectors which depend on the state of the observer, like position vector of a point depends on from where it is being observed, and the observed position may then be expressed in a frame. The same is true for linear and angular velocities. In what follows, it is of considerable advantage if a vector-like position, linear velocity of a point and angular velocity of a body is associated with three qualifying notations, first indicating the point or object of which the position or linear or angular velocities is talked about. The second notation indicates the observer and the third notation indicates the frame in which it is expressed. Thus, in short, it can be written as, Expressed in the frame C (As seen by B Vector(position/linear/angular velocity) Attributed to A)

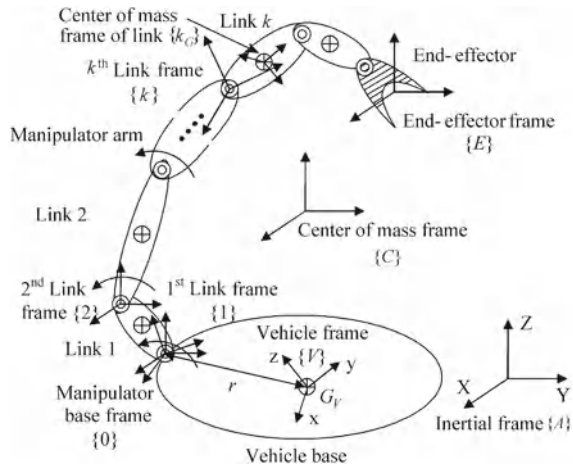
In short, it may be written as ${}^C ({}^B W_A)$, where W is a vector representing position, or linear velocity of a point or angular velocity of a body. Figure 10.3 shows the description of the position, linear, and angular velocity vectors as used in this chapter.

- If the coordinate frame $\{C\}$ is omitted, then the default frame $\{C\}$ is equivalent to frame $\{B\}$ with its origin at the observer B . A concise notation may then be used.

$${}^B W_A \equiv {}^B ({}^B W_A)$$

- Since linear velocity is associated with a point, and angular velocity is associated with a body, the term velocity of link refers to linear velocity of the origin of the link frame, and the rotational velocity of the link.
- For a vector such as force or torque in which there is no reference point, the left-superscript, i.e., $\{B\}$ frame represents the coordinate frame in which the vector is expressed. If no left-superscript is designated, then the coordinate frame is understood to be the inertial reference frame.
- The orientation of a frame $\{A\}$ with respect to frame $\{B\}$ can be represented by a 3×3 rotation matrix ${}^B_A R$ which is the matrix of direction cosines relating the two frames.

Fig. 10.4 Schematic diagram of a space robot



10.4.2 Assumptions

For modeling of space robots, the following assumptions can be made:

1. The spacecraft attitude control system is turned off when the system is operating in free-floating mode and hence the spacecraft can translate and rotate in response to manipulator movement.
2. For simplicity, let the system have a single manipulator with revolute joints and is in an open chain kinematic configuration.
3. Let the joint between links i and $i + 1$ be numbered as $i + 1$. A coordinate frame is attached to each link. The link frames are named by numbers according to the link to which they are attached, i.e., frame $\{i\}$ is attached rigidly to link i . The rotational inertias are defined about frames fixed at the center of mass (CM) of the body (or link). The CM frame is fixed along the principal directions in the vehicle or the link.

The descriptions of the frames are given in Fig. 10.4. To facilitate the derivation of the coupled vehicle and arm dynamics, the dynamics of the vehicle without arm will be derived first.

10.4.3 Space Vehicle Dynamics

10.4.3.1 Linear Dynamics

Let us consider the general case of a rigid spacecraft translating and rotating under the influence of a body fixed actuation device. Let $X, Y,$ and Z represent the inertial

axes, and axes x , y , and z be attached to the CM of the spacecraft base as shown in Fig. 10.4. For a given instant, the body has absolute velocity v . The translational velocity can be resolved into three mutually perpendicular components v_x , v_y , v_z . As per Newton's law, the net force F acting on the body and the linear momentum p can be related as

$$F = \frac{dp}{dt} \quad (10.3)$$

where $p = mv$. If v is expressed with respect to a rotating frame, then net force F is given as

$$F = \left(\frac{\partial p}{\partial t} \right)_{\text{rel}} + \omega \times p \quad (10.4)$$

where $\left(\frac{\partial p}{\partial t} \right)_{\text{rel}}$ is the rate of change of momentum relative to the moving frame. Using the right-hand rule for Eq. 10.4, the component equations can be written as

$$F_x = m\dot{v}_x + m\omega_y v_z - m\omega_z v_y \quad (10.5)$$

$$F_y = m\dot{v}_y + m\omega_z v_x - m\omega_x v_z \quad (10.6)$$

$$F_z = m\dot{v}_z + m\omega_x v_y - m\omega_y v_x \quad (10.7)$$

These nonlinear differential equations are known as Euler's equations. The cross-product terms can be treated as forces in Eqs. 10.5–10.7. The forces can be added at the respective 1-junctions and gyrator-ring structures are formed by using the bond graph which are known as Euler Junction Structures (EJS) (See Chap. 5).

10.4.3.2 Angular Dynamics

Let us assume a vehicle frame $\{V\}$ located at the CM of the vehicle and oriented in the direction of the principal axis of the vehicle. Then, the angular acceleration ${}^V(A\dot{\omega}_V)$ of the vehicle, being acted on by moment ${}^V N_V$, can be found from Euler's equation as,

$${}^V N_V = {}^V(A\dot{h}_V) + {}^V(A\omega_V) \times {}^V(Ah_V) \quad (10.8)$$

For evaluation of angular momentum of vehicle ${}^V(Ah_V)$, it is assumed that inertial frame $\{A\}$ is momentarily coincident with the vehicle frame $\{V\}$, then ${}^V(Ah_V)$ can be evaluated as

$${}^V(Ah_V) = {}^{G_V} I_V {}^V(A\omega_V). \quad (10.9)$$

Hence, ${}^V(A\dot{h}_V) = {}^{G_V} I_V {}^V(A\dot{\omega}_V)$. Here, ${}^{G_V} I_V$ is the vehicle inertia in the vehicle CM frame. Equation 10.8 in the component form can be written as

$$({}^V N_V)_x = ({}^{G_V} I_V)_x {}^V(A\dot{\omega}_V)_x + {}^V(A\omega_V)_x \times ({}^{G_V} I_V)_x {}^V(A\omega_V)_x \quad (10.10)$$

$${}^V N_V)_y = ({}^{G^V} I_V)_y {}^V ({}^A \dot{\omega}_V)_y + {}^V ({}^A \omega_V)_y \times ({}^{G^V} I_V)_y {}^V ({}^A \omega_V)_y \quad (10.11)$$

$${}^V N_V)_z = ({}^{G^V} I_V)_z {}^V ({}^A \dot{\omega}_V)_z + {}^V ({}^A \omega_V)_z \times ({}^{G^V} I_V)_z {}^V ({}^A \omega_V)_z \quad (10.12)$$

Now in a simplified notation let N_x , N_y , and N_z represent the moments acting on the vehicle expressed in vehicle frame; I_x , I_y , and I_z represent the moments of inertia of vehicle expressed in vehicle CM frame; ω_x , ω_y , and ω_z represent the angular velocities of the vehicle as observed from inertial frame and expressed in vehicle frame, in x , y , and z directions. Then Eqs. 10.10–10.12 can be written in a simplified notation as

$$N_x = I_x \dot{\omega}_x + (I_z - I_y) \omega_y \omega_z \quad (10.13)$$

$$N_y = I_y \dot{\omega}_y + (I_x - I_z) \omega_z \omega_x \quad (10.14)$$

$$N_z = I_z \dot{\omega}_z + (I_y - I_x) \omega_x \omega_y \quad (10.15)$$

Equations 10.13–10.15 are used to construct the Euler Junction structure (EJS), in the bond graph model of the angular dynamics of space robot base and arms.

10.4.4 Arm Dynamics

For the arm dynamics, the same methodology as used for the vehicle dynamics was adopted. The only difference is that the velocities are derived by progressing from one link to the next. In bond graph modeling,

- The bond graph is drawn from the base of link to end effector based on the kinematics of the link. The link inertia elements are attached at the CM velocity port of links in the bond graph.
- The joint forces and torques are determined from the force relations starting from the end effector, and moving down up to the base.

The link linear and angular velocities for an l -joint revolute manipulator can be calculated from the kinematic relations starting from the base (i.e., $i = 0$), and moving up to the end effector ($i = l - 1$). The angular velocity relationship is given as

$${}^{i+1}({}^A \omega_{i+1}) = {}_i^{i+1} R {}^i ({}^A \omega_i) + {}^{i+1} ({}^i \omega_{i+1}) \quad (10.16)$$

Here ${}^{i+1}({}^A \omega_{i+1})$ is the angular velocity of $(i + 1)$ link as observed from inertial frame $\{A\}$ and expressed in $(i + 1)$ th frame. ${}^{i+1} ({}^i \omega_{i+1})$ is the angular velocity of the $(i + 1)$ link as observed from i th link and expressed in $(i + 1)$ th frame. ${}_i^{i+1} R$ is rotation matrix for transformation from i th frame to $(i + 1)$ th frame. Equation 10.16, can also be written as

$${}^{i+1}({}^A \omega_{i+1}) = {}_i^{i+1} R {}^i ({}^A \omega_i) + \dot{\theta}_{i+1} {}^{i+1} ({}^{i+1} \hat{U}_{i+1}) \quad (10.17)$$

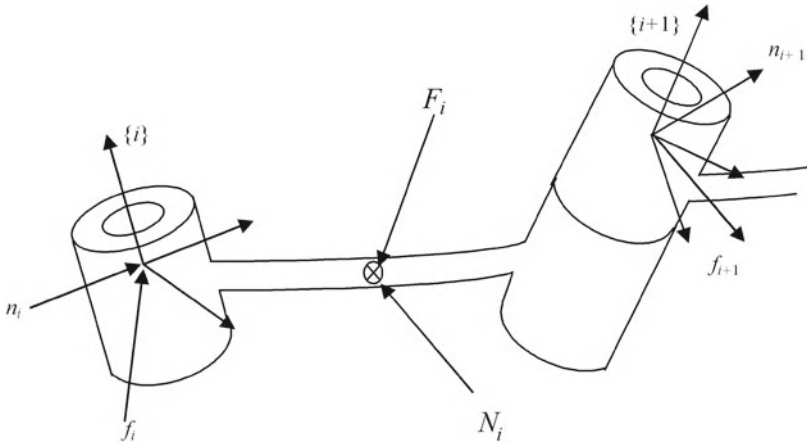


Fig. 10.5 The force balance for a single manipulator link (including inertia forces)

where ${}^{i+1}({}^{i+1}\hat{U}_{i+1})$ is the unit vector and $\dot{\theta}_{i+1}$ is the angular velocity of $(i + 1)$ link as observed from i th link. The expression for the linear velocity of the link is given as

$${}^A({}^A V_{i+1}) = {}^A({}^A V_i) + {}^A R [{}^i({}^A \omega_i) \times {}^i({}^i P_{i+1})] \quad (10.18)$$

Here ${}^A({}^A V_{i+1})$ is velocity of $(i + 1)$ th link as observed from inertial frame $\{A\}$ and expressed in terms of inertial frame $\{A\}$. The velocity of the origin of the CM frame of the i th link can be calculated from Eq. 10.18, by substituting G_i in place of $(i + 1)$ as

$${}^A({}^A V_{G_i}) = {}^A({}^A V_i) + {}^A R [{}^i({}^A \omega_i) \times {}^i({}^i P_{G_i})] \quad (10.19)$$

These equations require the specification of the initial conditions, ${}^0({}^A \omega_0)$ and ${}^A({}^A V_0)$, which will be determined from the vehicle states. The total force and moment acting at the CM for link $(i + 1)$, ${}^A F_{i+1}$, and ${}^{i+1} N_{i+1}$, respectively, will be determined from the link translation and rotational inertias. The total force and moment on link i can be expressed in terms of the interaction forces and moments from link $(i - 1)$ and link $(i + 1)$. This can be done by writing force balance and moment balance equations based on the free-body diagram of a typical link as shown in Fig. 10.5 as

$${}^A f_i = {}^A F_i + {}^A f_{i+1} \quad (10.20)$$

$${}^i n_i = {}^i N_i + {}^i_{i+1} R {}^{i+1} n_{i+1} + {}^i({}^i P_{G_i}) \times {}^i_A R {}^A F_i + {}^i({}^i P_{i+1}) \times {}^i_A R {}^A f_{i+1} \quad (10.21)$$

As we will see, Eqs. 10.20, and 10.21, can be obtained from the bond graph directly. Here ${}^A f_i$ is the force exerted on link i by link $(i - 1)$, expressed in terms of absolute frame, ${}^i n_i$ is the torque exerted on link i by link $(i - 1)$, expressed in terms of $\{i\}$ th

frame, ${}^A F_i$ is the resultant of all the external forces acting on the link, and ${}^i N_i$ are the resultant of all the external moments acting on the link. Using Eqs. 10.20 and 10.21, the force and moment conditions at the end effector can be written as

$${}^A f_{l+1} = {}^A f_e \quad (10.22)$$

$${}^{l+1} n_{l+1} = {}^{l+1} n_e \quad (10.23)$$

where ${}^A f_e$ represents the external forces exerted on the end effector of the manipulator expressed in the absolute frame and ${}^{l+1} n_e$ is the moment exerted on the end effector of the manipulator expressed in $(l + 1)$ th frame. In a bond graph, these conditions are specified by Se elements acting at the tip velocity junctions of the end effector and angular velocity ports of the last link respectively. The joint torques vector τ can be obtained from one of the components of the interaction moments (along the link rotation axis) found from Eq. 10.21 for each link as

$$\tau = \begin{bmatrix} {}^1 n_1^T \hat{U}_1 \\ {}^2 n_2^T \hat{U}_2 \\ \vdots \\ {}^k n_k^T \hat{U}_k \end{bmatrix} \quad (10.24)$$

where ${}^i \hat{U}_i$ is the unit vector indicating the direction of rotation of joint. In a bond graph model the joint torque can be found by the effort on the bond connected to the joint rotation port. The resulting dynamics takes the general form as

$$M(\dot{\Theta})\ddot{\Theta} + C(\Theta, \dot{\Theta}) - J(\Theta)^T F_e = \tau \quad (10.25)$$

where $M(\Theta)$ is the inertia matrix, $C(\Theta, \dot{\Theta})$ is the vector of Coriolis and centripetal torques, $F_e = [f_e^T n_e^T]^T$ is the force and torque applied at the end effector, $J(\Theta)$ is the Jacobian, and τ is the vector of arm joint torques applied by the actuators. Equation 10.25 represents the full dynamical equation of motion for a fixed base manipulator.

10.4.5 Free-Flying Robot Dynamics

Consider the case now, where the base frame for link 1, $\{1\}$ is attached to a moving vehicle body frame $\{0\}$. If the robot has been a ground robot then $\{0\}$ frame would had been the inertial frame. The position of the moving vehicle body frame $\{0\}$ with respect to vehicle frame $\{V\}$ is given by

$${}^V ({}^V P_0) = [r_x \ r_y \ r_z]^T \quad (10.26)$$

Since the base is mobile the initial conditions ${}^0(A\omega_0)$, and ${}^A(AV_0)$, in Eqs. 10.17–10.19 need to be expressed in terms of the base states. The base frame $\{1\}$ and body frame $\{0\}$ are stationary with respect to each other as they are coincident but with different orientations. The initial conditions for the velocity of the base frame $\{0\}$ can be written in terms of the velocity of the vehicle frame $\{V\}$ as follows:

$${}^0(A\omega_0) = {}^0_V R \quad {}^V(A\omega_V) \quad (10.27)$$

$${}^A(AV_0) = {}^A(AV_V) + \frac{A}{V} R [{}^V(A\omega_V) \times {}^V(VP_0)] \quad (10.28)$$

These equations can be obtained from Eqs. 10.17 and 10.18 by substituting $i = V$ and $i + 1 = 0$. The total force and moment, ${}^A F_V$ and ${}^V N_V$ acting on the vehicle body will be decided by the translational and rotational inertia of the vehicle. Once the total forces and moments for the links are found, Eqs. 10.20, and 10.21 can be used to find the total forces and moments exerted on the vehicle by the first link of the arm, $-{}^A f_1$ and $-{}^1 n_1$. To determine the total force and moment on the vehicle for a single arm Eqs. 10.20, and 10.21 could be continued back to the arm base $i = 0$, which essentially becomes the vehicle body. The force balance relationship for the vehicle can be given as

$${}^A f_V = {}^A F_V + {}^A f_1 \quad (10.29)$$

$${}^V n_V = {}^V N_V + \frac{V}{1} R \quad {}^1 n_1 + {}^V(VP_{G_V}) \times \frac{V}{A} R \quad {}^A F_V + {}^V(VP_1) \times \frac{V}{A} R \quad {}^A f_1 \quad (10.30)$$

It is to be noted that the forces and torques on the vehicle body are negative of ${}^A f_1$ and ${}^1 n_1$ respectively. ${}^A f_V$ and ${}^V n_V$ are the resultant of all the external forces and moments on the vehicle. The procedure for modeling can be summarized as follows:

1. The angular and linear velocity relations Eqs. 10.17–10.19 are applied from $i = 0$, to $i = l - 1$, for each arm using the initial conditions for the base link, i.e., Eqs. 10.27 and 10.28 in terms of the vehicle states.
2. Equations 10.20 and 10.21 are applied for each arm from $i = l$ to $i = 1$, to find the link interaction forces and moments using the end conditions given by Eqs. 10.22 and 10.23. However, in bond graph modeling software the force and torque relations are derived by the software itself once the bond graph is made.
3. The total force and moment on the vehicle is found from the drawn bond graph at the port where translational and rotational inertia elements of the vehicle are attached. These are used along with the vehicle interaction forces and torques in Eqs. 10.29 and 10.30 to find the external forces and torques acting on the vehicle. The resulting dynamics of space vehicle with robot takes the form

$$\begin{aligned}
& M ({}^A(A)p_V, {}^V(A)q_V, \theta) \begin{bmatrix} A({}^A\dot{V}_V) \\ V({}^A\dot{\omega}_V) \\ \ddot{\theta} \end{bmatrix} \\
& + C ({}^A(A)p_V, {}^V(A)q_V, \theta, A({}^AV_V), {}^V(A)\omega_V, \dot{\theta}) \\
& - J ({}^A(A)p_V, {}^V(A)q_V, \theta)^T F_e = \begin{bmatrix} A f_V \\ V n_V \\ \tau \end{bmatrix} \quad (10.31)
\end{aligned}$$

Equation 10.31 represents the forward dynamics of the robot which finds the forces and torques to be applied to the robot based upon its motion. This equation is similar to that for a link as in Eq. 10.25, but the coupled dynamics as in Eq. 10.31 depends upon the vehicle states, i.e., vehicle position (${}^A(A)p_V$) and vehicle orientation ${}^V(A)q_V$, in addition to the manipulator states θ . The coupling between the arm and the vehicle occurs through the inertia matrix M and the Coriolis/centripetal force vector C . The forces and torques on the robot now include those acting directly on the vehicle ${}^A f_V$ and ${}^V n_V$, respectively, as well as the arm motor torques τ . The states of the total system can now be written as a combination of the vehicle states and the arm states.

The vehicle and arm states consist of the translational and rotational momentum of the vehicle and the links. The translational momentum is considered with respect to the inertial frame while rotational momentum is with respect to the frame located at the CM of the respective bodies.

10.5 Bond Graph Modeling of Space Robots

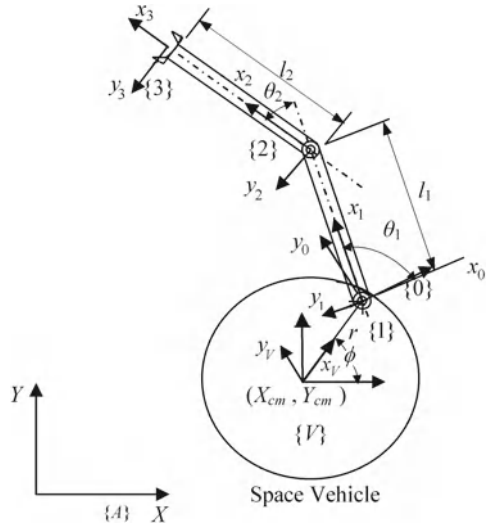
Modeling of a space manipulator includes the modeling for linear and angular dynamics of manipulator and vehicle. To begin with the simplest case, let us take the case of a simple two DOF planar space robot.

10.5.1 Modeling of a Two DOF Planar Space Robot

The modeling of the space robot can be carried out just like a ground robot with a difference that, in case of the space robot, the base is not fixed. In space robot modeling, to make the modeling simpler let us make the following assumptions:

1. The spacecraft attitude control system is turned off when the space robot is operating in a free-floating mode, and hence the spacecraft can translate and rotate in response to the manipulator movement and interaction, if any, with the environment.
2. It is also assumed that the system has a single manipulator with revolute joints and is in open kinematic chain configuration.

Fig. 10.6 Schematic diagram of two DOF planar space robot



The general relations used for linear and angular velocity propagation [2] can be given as

$${}^A({}^A V_{i+1}) = {}^A({}^A V_i) + {}^A_i R [{}^i({}^A \omega_i) \times {}^i({}^i P_{i+1})] \tag{10.32}$$

$${}^{i+1}({}^A \omega_{i+1}) = {}^{i+1}_i R {}^i({}^A \omega_i) + {}^{i+1}_i({}^i \omega_{i+1}) \tag{10.33}$$

Here, the velocities are calculated for the $(i + 1)$ th link. For a two DOF planar space robot the displacement relation can also be derived trigonometrically, and from the time differentiation of these relations, the velocity relations can be found. Figure 10.6 shows the schematic sketch of a two DOF planar space robot. In Fig. 10.6 {A} represents the absolute frame, {V} represents the vehicle frame, {0} frame is located at the base of the robot, {1}, {2} are the frames located at first and second joints respectively. The frame {3} locates the tip of the robot. Let l_1 be the length of the first link, l_2 be the length of second link, and r be the distance between the robot base and CM of the vehicle. Let ϕ represent the rotation of vehicle frame with respect to an absolute frame and θ_1 , and θ_2 be the joint angles as shown in Fig. 10.6. Let X_{CM} and Y_{CM} be the coordinate of the CM of the vehicle with respect to the absolute frame. The kinematic relations for the tip displacement X_{tip} , Y_{tip} in X and Y directions can be written as

$$\begin{bmatrix} X_{tip} \\ Y_{tip} \end{bmatrix} = \begin{bmatrix} X_{CM} \\ Y_{CM} \end{bmatrix} + \begin{bmatrix} r \cos \phi + l_1 \cos(\phi + \theta_1) + l_2 \cos(\phi + \theta_1 + \theta_2) \\ r \sin \phi + l_1 \sin(\phi + \theta_1) + l_2 \sin(\phi + \theta_1 + \theta_2) \end{bmatrix} \tag{10.34}$$

The tip angular displacement with respect to absolute frame X axis is given as

$$\theta_{tip} = \phi + \theta_1 + \theta_2 \tag{10.35}$$

From Eq. 10.34 the velocity of the tip of the robot can be found as

$$\begin{bmatrix} \dot{X}_{tip} \\ \dot{Y}_{tip} \end{bmatrix} = \begin{bmatrix} \dot{X}_{CM} \\ \dot{Y}_{CM} \end{bmatrix} + \begin{bmatrix} -r\dot{\phi} \sin \phi - l_1(\dot{\phi} + \dot{\theta}_1) \sin(\phi + \theta_1) - l_2(\dot{\phi} + \dot{\theta}_1 + \dot{\theta}_2) \\ \sin(\phi + \theta_1 + \theta_2) \\ r\dot{\phi} \cos \phi + l_1(\dot{\phi} + \dot{\theta}_1) \cos(\phi + \theta_1) + l_2(\dot{\phi} + \dot{\theta}_1 + \dot{\theta}_2) \\ \cos(\phi + \theta_1 + \theta_2) \end{bmatrix} \quad (10.36)$$

Using Eq. 10.36 the different transformer moduli for the bond graph modeling of space robot can be derived. Figure 10.7 shows the bond graph model of space robot with different transformer moduli shown.

Further, for a planar case, rearranging the set of Eqs. 10.5–10.7 for $\omega_x = 0$, $\omega_y = 0$ and $v_z = 0$ one obtains

$$F_x = m\dot{v}_x - m\omega_z v_y \quad (10.37)$$

$$F_y = m\dot{v}_y + m\omega_z v_x \quad (10.38)$$

$$F_z = 0 \quad (10.39)$$

Here, $m = M_V$ and $\omega_z = \dot{\phi}$. Hence, a gyrator with modulus $M_V \dot{\phi}$ is used between velocity junctions $1_{\dot{X}_{CM}}$ and $1_{\dot{Y}_{CM}}$, where M_V is the mass of the space robot base and $\dot{\phi}$ is the angular velocity of the space robot base about Z axis.

10.5.2 Object-Oriented Modeling of Space Robots

For a complex system like a space robot, the bond graph model becomes very much involved. To overcome this difficulty, for robotic manipulators the bond graph is fragmented into various submodels like angular velocity propagation submodel, linear velocity propagation submodel, and Euler junction structure submodel, etc. These submodels are created for a single link and can be repeatedly used for the bond graph modeling of the entire system.

10.5.2.1 Kinematics of Rotation (AVP of Link)

The generalized submodel for the principal angular velocity [2] equations can be created using Eq. 10.17, given as

$${}^{i+1}({}^A\omega_{i+1}) = {}_i^{i+1}R {}^i({}^A\omega_i) + \dot{\theta}_{i+1} {}^{i+1}\hat{U}_{i+1} \quad (10.40)$$

The created submodel is shown as part of the main bond graph model of one DOF space robot shown in Fig. 10.8. Joint velocity ($\dot{\theta}_{i+1}$) can be about any one axis of the joint coordinate frame. Based on the axis of joint rotation, one of the transformer moduli connected to joint velocity junction will be unity and the remaining

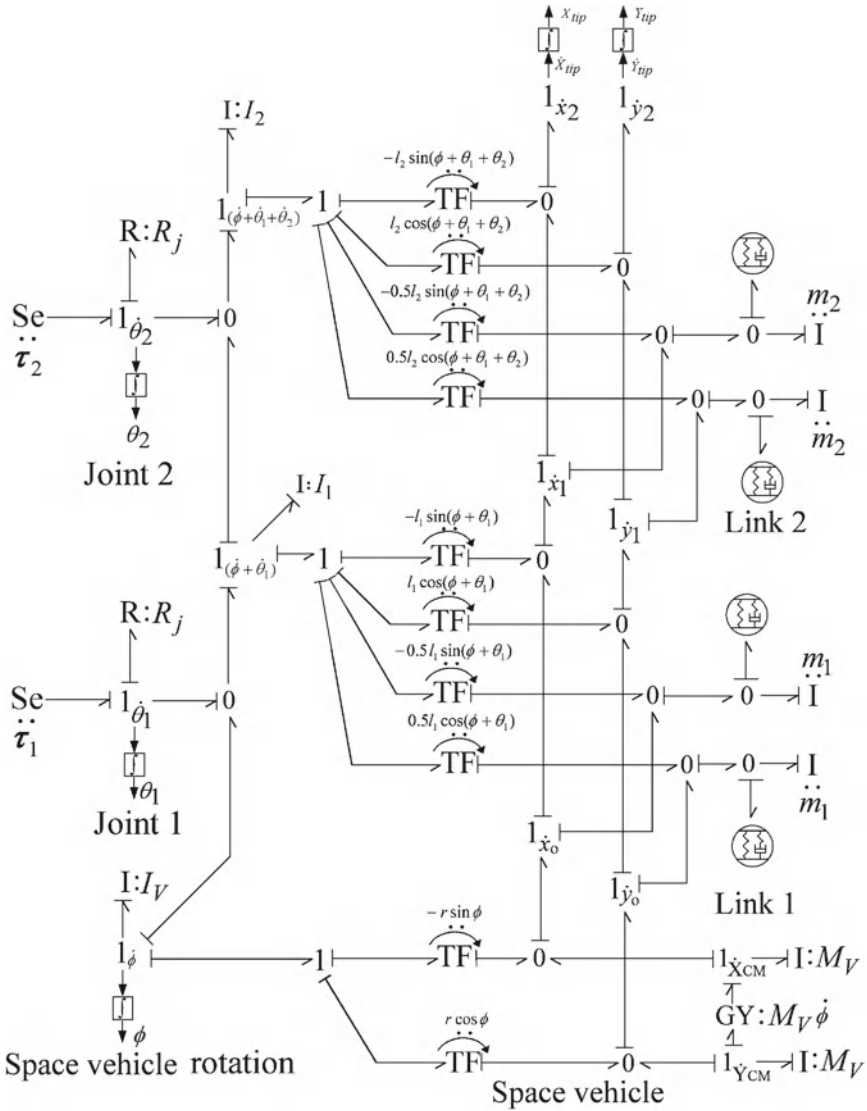


Fig. 10.7 Bond graph modeling of a two DOF planar space robot

will be zero. The matrix multiplication submodel used here is a rotation matrix. This submodel takes the angular velocity of previous link and the joint velocity as inputs. As is evident from the bond graph, the angular velocity of the previous link ${}^i(A)\omega_i$ is multiplied by the rotation matrix ${}^i R$ and the resulting velocity is added to the joint velocity $(\dot{\theta}_{i+1})$ of the current link. The angular velocity of the current link is given at the output of the submodel after calculation.

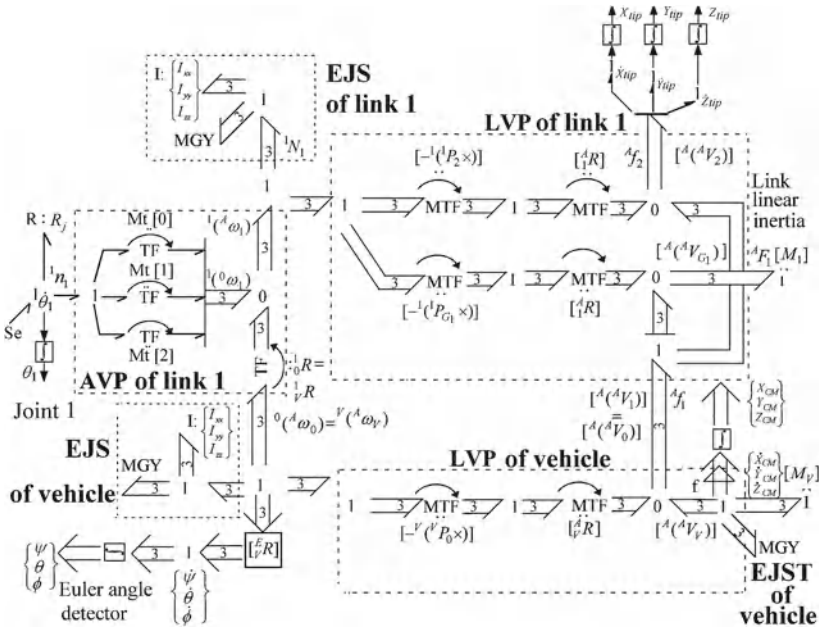


Fig. 10.8 Multi bond graph of the space robot

10.5.2.2 Euler Junction Structure (EJS)

A Euler junction structure is used to represent the rotational dynamics of a rigid body. Hence, it can be used to represent the rotational dynamics of the links of the space robot as well as that of the space vehicle. The Euler equations given by Eqs. 10.13–10.15 are used in the creation of this submodel. These equations are rewritten in this section for easy reference as

$$N_x = I_x \dot{\omega}_x + (I_z - I_y) \omega_y \omega_z, \tag{10.41}$$

$$N_y = I_y \dot{\omega}_y + (I_x - I_z) \omega_z \omega_x, \tag{10.42}$$

$$N_z = I_z \dot{\omega}_z + (I_y - I_x) \omega_x \omega_y. \tag{10.43}$$

The created EJS for the vehicle is shown in Fig. 10.9. Similarly, we can draw the bond graph model for the link.

10.5.2.3 Euler Junction Structure (EJST) for Translational Dynamics

A Euler junction structure (EJST) is used to represent the translational dynamics of base. The Euler equations given by Eqs. 10.5–10.7 are used in the creation of this submodel. These equations are rewritten in this section for easy reference as

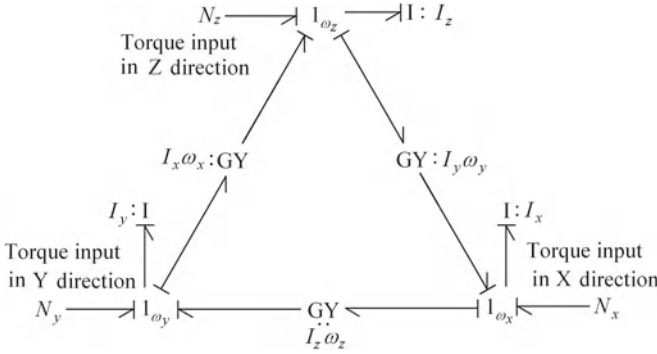


Fig. 10.9 Euler junction structure of space vehicle

$$F_x = m\dot{v}_x + m\omega_y v_z - m\omega_z v_y \tag{10.44}$$

$$F_y = m\dot{v}_y + m\omega_z v_x - m\omega_x v_z \tag{10.45}$$

$$F_z = m\dot{v}_z + m\omega_x v_y - m\omega_y v_x \tag{10.46}$$

10.5.2.4 Kinematics of Translation (LVP of Link)

Equation 10.18, gives the relation for the link translational velocity as

$${}^A({}^A V_{i+1}) = {}^A({}^A V_i) + {}^A R [{}^i({}^A \omega_i) \times {}^i({}^i P_{i+1})] \tag{10.47}$$

Writing in matrix form,

$$[{}^A({}^A V_{i+1})] = [{}^A({}^A V_i)] + [{}^A R] [- {}^i({}^i P_{i+1} \times)] [{}^i({}^A \omega_i)] \tag{10.48}$$

where

$${}^i({}^i P_{i+1}) = \begin{bmatrix} 0 \\ l_i \\ 0 \end{bmatrix}, \text{ and } [{}^i({}^i P_{i+1} \times)] = \begin{bmatrix} 0 & 0 & l_i \\ 0 & 0 & 0 \\ -l_i & 0 & 0 \end{bmatrix}.$$

For position of center of mass ${}^i({}^i P_{G_i}) = [0 \ l_{G_i} \ 0]^T$.

The created submodel is shown as part of the main bond graph model shown in Fig. 10.8. Since CM velocity of links depend on link inertia, in bond graph model I elements are attached at the velocity junction representing the CM velocity of links. Since the starting point of the current link is the same as the tip point of the previous link, the tip velocity of the previous link and the angular velocity of the current link are used to find the tip and CM velocity of the current link.

In Eq. 10.48 ${}^i({}^A \omega_i)$ can be obtained from the angular velocity propagation submodel for the current link. Two matrix multiplication submodels can be created in series for calculation of $[{}^A R]$ and $[- {}^i({}^i P_{i+1} \times)]$. This output is then summed up with

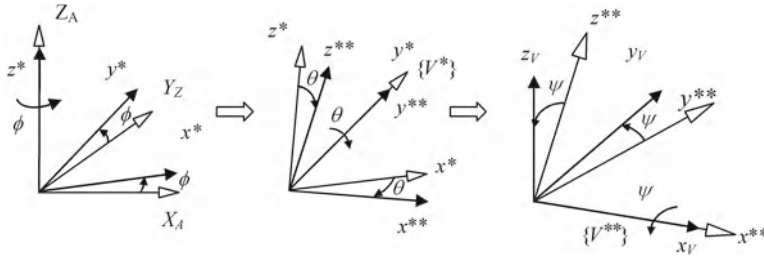


Fig. 10.10 Z-Y-X Euler angles

linear velocity of the previous link tip to get the tip velocity of current link. Linear velocity of *CM* of the current link can be obtained similarly. Using the modified form of Eq. 10.48, i.e., by substituting G_i in place of $(i + 1)$, one obtains

$$[{}^A({}^A V_{G_i})] = [{}^A({}^A V_i)] + [{}^A R][{}^{-i}({}^i P_{G_i} \times)][{}^i({}^A \omega_i)] \tag{10.49}$$

The only difference between Eqs. 10.48 and 10.49 being $[{}^{-i}({}^i P_{G_i} \times)]$ is used in Eq. 10.49 instead of $[{}^{-i}({}^i P_{i+1} \times)]$.

10.5.2.5 Angular Velocity Transformations

1. Euler Angles (Z-Y-X Representation)

The Euler angles are three independent parameters needed to specify the orientation of the space vehicle (See Chap. 5). This gives the relationship between the vehicle fixed reference frame $\{V\}$ and the absolute frame $\{A\}$. In this representation, each rotation is performed about an axis of the moving system $\{V\}$ and each rotation takes place about an axis whose location depends upon the preceding rotations. Because the rotation takes place about the axes, Euler angles are determined by a sequence of three rotations. Figure 10.10 shows the axes of $\{V\}$ after each rotation is applied. Rotation ϕ about z represented by $R_z(\phi)$, causes x to rotate into x^* , and y to rotate into y^* , while z and z^* remain coincident. An additional (*) gets added to each axis with each rotation. With reference to Fig. 10.10 we can use the intermediate frame $\{V^*\}$ and $\{V^{**}\}$ in order to give the description of the orientation of frame $\{V\}$ relative to frame $\{A\}$. Thus,

$${}^A R = {}^A R_{V^*} R_{V^{**}} R_{V^{**}} \tag{10.50}$$

where ${}^A R_{V^*} = R_z(\phi)$, $R_{V^*} = R_{y^*}(\theta)$ and $R_{V^{**}} = R_{x^{**}}(\psi)$.

Equation 10.50 can be written as

$$\begin{aligned} {}^A_V R &= \begin{bmatrix} c\phi & -s\phi & 0 \\ s\phi & c\phi & 0 \\ 0 & 0 & 1 \end{bmatrix} \begin{bmatrix} c\theta & 0 & s\theta \\ 0 & 1 & 0 \\ -s\theta & 0 & c\theta \end{bmatrix} \begin{bmatrix} 1 & 0 & 0 \\ 0 & c\psi & -s\psi \\ 0 & s\psi & c\psi \end{bmatrix} \\ {}^A_V R &= \begin{pmatrix} c\phi c\theta & c\phi s\theta s\psi - s\phi c\psi & c\phi s\theta c\psi + s\phi s\psi \\ s\phi c\theta & s\phi s\theta s\psi + c\phi c\psi & s\phi s\theta c\psi - c\phi s\psi \\ -s\theta & c\theta s\psi & c\theta c\psi \end{pmatrix} \end{aligned} \quad (10.51)$$

Equation 10.51 gives the transformation matrix from the vehicle frame to the absolute frame.

2. Angular Velocity

The Euler angle rates $\dot{\phi}$, $\dot{\theta}$ and $\dot{\psi}$ are not directed along the axes x , y , and z axis of the vehicle frame and consequently do not coincide with the components ω_x , ω_y , and ω_z of the angular velocity in the reference frame fixed to the vehicle. Their directions are those of axes Z_A , y^* and x_V . The angular velocity vector ${}^V\omega = [\omega_x \ \omega_y \ \omega_z]^T$ expressed in vehicle frame is given by

$${}^V \begin{bmatrix} \omega_x \\ \omega_y \\ \omega_z \end{bmatrix} = {}^V_{V^{**}} R \ {}^V_{V^*} R \ {}^V \begin{bmatrix} 0 \\ 0 \\ \dot{\phi} \end{bmatrix} + {}^V_{V^{**}} R \ {}^V \begin{bmatrix} 0 \\ \dot{\theta} \\ 0 \end{bmatrix} + {}^V \begin{bmatrix} \dot{\psi} \\ 0 \\ 0 \end{bmatrix} \quad (10.52)$$

$${}^V \begin{bmatrix} \omega_x \\ \omega_y \\ \omega_z \end{bmatrix} = \begin{bmatrix} 1 & 0 & 0 \\ 0 & c\psi & s\psi \\ 0 & -s\psi & c\psi \end{bmatrix} \begin{bmatrix} c\theta & 0 & -s\theta \\ 0 & 1 & 0 \\ s\theta & 0 & c\theta \end{bmatrix} \begin{bmatrix} 0 \\ 0 \\ \dot{\phi} \end{bmatrix} + \begin{bmatrix} 1 & 0 & 0 \\ 0 & c\psi & s\psi \\ 0 & -s\psi & c\psi \end{bmatrix} \begin{bmatrix} 0 \\ \dot{\theta} \\ 0 \end{bmatrix} + \begin{bmatrix} \dot{\psi} \\ 0 \\ 0 \end{bmatrix} \quad (10.53)$$

On evaluating, the relation turns out to be

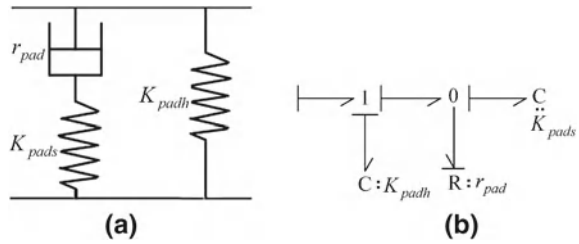
$$\begin{bmatrix} \omega_x \\ \omega_y \\ \omega_z \end{bmatrix} = \begin{bmatrix} 1 & 0 & -s\theta \\ 0 & c\psi & c\theta s\psi \\ 0 & -s\psi & c\theta c\psi \end{bmatrix} \begin{bmatrix} \dot{\psi} \\ \dot{\theta} \\ \dot{\phi} \end{bmatrix} \quad (10.54)$$

Equation 10.54 gives the vehicle angular velocity expressed in the vehicle frame. It is important to note that this matrix is not a rotation matrix, so its norm is not necessarily 1 and therefore $R^{-1} \neq R^T$ in general. The inverted form of Eq. 10.54 is of most useful form and is given by Eq. 10.55.

$$\begin{bmatrix} \dot{\psi} \\ \dot{\theta} \\ \dot{\phi} \end{bmatrix} = \begin{bmatrix} 1 & t\theta s\psi & t\theta c\psi \\ 0 & c\psi & -s\psi \\ 0 & s\psi/c\theta & c\psi/c\theta \end{bmatrix} \begin{bmatrix} \omega_x \\ \omega_y \\ \omega_z \end{bmatrix} \quad (10.55)$$

A matrix multiplication submodel can be created to convert the vehicle angular velocity vector into the Euler angle rates. The input to the submodel is the angular

Fig. 10.11 **a** Schematic diagram of soft pad. **b** Bond graph model of soft pad



velocity vector of the vehicle and the output is the Euler angle rate vector. The three components of the Euler angle rates can be integrated to determine the Euler angles.

10.5.2.6 Modeling Problems: Pads and Coupling Capacitors

In the bond graph representation of robot dynamics, geometric constraints among links result in algebraic relations among the state variables and result in differential causality. The presence of differential causality makes the derivation of equations and their reduction complicated owing to the complexity of junction structure depicting link kinematics. One can avoid the differential causality by imposing artificial compliances at appropriate point in the bond graph. Soft pads are artificial compliances/lumped flexibilities [12] that can be used in bond graph. A soft pad is used to avoid differential causality. In particular, a soft pad is used instead of a pad in order to avoid algebraic loop while deriving equations. Figure 10.11a shows the schematic diagram of a soft pad and Fig. 10.11b shows its bond graph model.

10.5.2.7 Integrated Modeling

Multi Bond Graph of One DOF Space Robot

Figure 10.8 shows the vector bond graph for one link space robot. The aim of showing this figure is to show the internal connectivity of the different submodels. The submodels used are EJS of vehicle, EJS of link 1, AVP of link 1, LVP of link 1. LVP of vehicle is the same as LVP of link. Integrators are used to find CM velocity of vehicle as well as tip velocity of link.

Modeling of Three DOF Space Robot

Now let us make a model of a three DOF space robot using the submodels created in the previous section. Consider a free-floating space manipulator consisting of a serial robot mounted on a satellite base as shown in Fig. 10.12. Joint rotations (θ_i) of manipulator and Euler angles of the base (ϕ, θ, ψ) in 3 – 2 – 1 convention are used as generalized coordinates. Links are numbered starting with zero from the base to

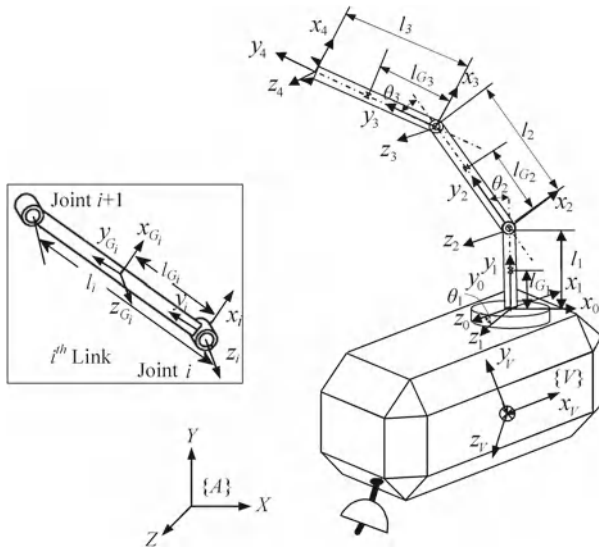


Fig. 10.12 A free-floating space manipulator

the last link. All joints are assumed to be revolute. The vehicle is denoted by frame $\{V\}$ that is located at the CM of the vehicle. An absolute frame $\{A\}$ is considered as shown in the figure. The manipulator base is mounted on the vehicle at a distance of (r_x, r_y, r_z) from the frame $\{V\}$. The joint between link i and $i + 1$ is numbered as $i + 1$. The rotational inertias are defined about the body fixed principal coordinate system. Without loss of generality the following assumptions are made:

1. Links of the manipulator are rigid.
2. The specified task space trajectory is within the reachable workspace of the manipulator. The joints angular velocities are assumed as

$${}^1({}^0\omega_1) = [0 \ \dot{\theta}_1 \ 0]^T, \quad {}^2({}^1\omega_2) = [0 \ 0 \ \dot{\theta}_2]^T, \quad {}^3({}^2\omega_3) = [0 \ 0 \ \dot{\theta}_3]^T.$$

The complete bond graph model of free-floating space vehicle along with the robot is created using the various submodels and is shown in Fig. 10.13. The submodel for the junction structure for angular dynamics, linear dynamics submodel of the link, and Euler junction structure submodel (EJS) are repeatedly used for all the links in the manipulator chain. One Euler junction structure (EJSV) submodel is used to represent the rotational dynamics of the spacecraft. The EJS submodel takes principal angular velocity of the current link as input and returns the torque.

In the bond graph model shown in Fig. 10.13, “AVP of link” represents a submodel for the angular velocity propagation of the link. “AVP of link” submodel takes angular velocity of the previous link and the joint velocity as input and the angular velocity of the current link is given out after calculation. “LVP of link” represents a submodel for linear velocity propagation of the link. “LVP of link” submodel takes angular

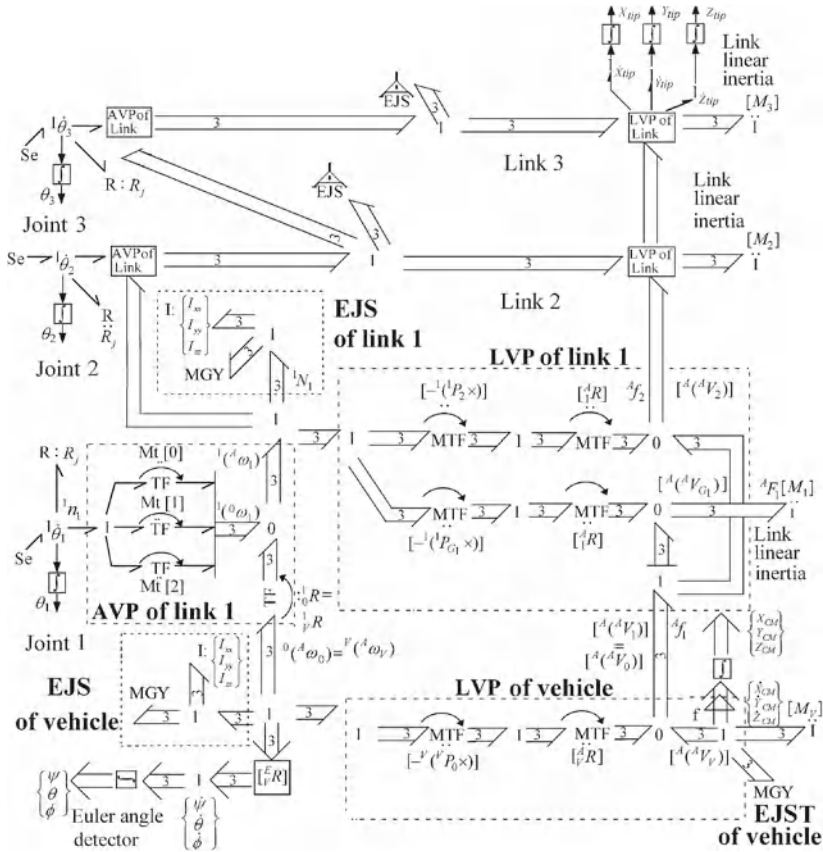


Fig. 10.13 Complete bond graph model of a free-floating space vehicle along with robot

velocity of current link and tip velocity of previous link as input and gives velocity of CM of current link and tip velocity of current link as output. Angular velocity to Euler angle rate submodel is used to convert the angular velocity into Euler angle rates. This submodel takes the angular velocity of the vehicle as input and gives the Euler angle velocity as output. An LVP of link submodel is used to model the linear dynamics of spacecraft. The CM velocity of the spacecraft is obtained from the EJST for translational inertia of the space craft. In order to observe CM velocity of spacecraft, integrators are connected to the ports in the submodel, intended for the tip velocity of previous link. The $1\dot{\theta}_i$ junctions represent the joint relative velocities. The motor inertia is modeled along with link inertia and is represented in EJS of link. The integrators attached to $1\dot{\theta}_i$ junctions measure joint angles.

Higher DOF robots can be modeled similarly by using these submodels and specifying the parameters of the submodel. The parameters which need to be specified are ^{i+1}R , $[-^i P_{i+1} \times]$, $^i R$ and $[-^i P_{G_i} \times]$.

Table 10.1 Details for angular dynamics submodels

Submodel for link	Constraint relation for submodel	For input joint rotation	
		Joint rotation	Specification in Fig. 10.13
1	${}^1(A)\omega_1 = {}^1_0R {}^0(A)\omega_0 + {}^1({}^0\omega_1)$	${}^1({}^0\omega_1) \Rightarrow$	Mt [0] = 0, Mt [1] = 1, Mt [2] = 0
2	${}^2(A)\omega_2 = {}^2_1R {}^1(A)\omega_1 + {}^2({}^1\omega_2)$	${}^2({}^1\omega_2) \Rightarrow$	Mt [0] = 0, Mt [1] = 0, Mt [2] = 1
3	${}^3(A)\omega_3 = {}^3_2R {}^2(A)\omega_2 + {}^3({}^2\omega_3)$	${}^3({}^2\omega_3) \Rightarrow$	Mt [0] = 0, Mt [1] = 0, Mt [2] = 1

Simulation and Results

The following values are assumed for the parameters used in the different submodels of the space robot model:

$${}^V_0R = \begin{bmatrix} 1 & 0 & 0 \\ 0 & 1 & 0 \\ 0 & 0 & 1 \end{bmatrix}, \quad {}^0_1R = \begin{bmatrix} c_1 & 0 & s_1 \\ 0 & 1 & 0 \\ -s_1 & 0 & c_1 \end{bmatrix},$$

$${}^1_2R = \begin{bmatrix} c_2 & -s_2 & 0 \\ s_2 & c_2 & 0 \\ 0 & 0 & 1 \end{bmatrix}, \quad {}^2_3R = \begin{bmatrix} c_3 & -s_3 & 0 \\ s_3 & c_3 & 0 \\ 0 & 0 & 1 \end{bmatrix}.$$

Here $s_i = \sin \theta_i$ and $c_i = \cos \theta_i$.

(i) Angular Dynamics Submodels of Links

The general relation is

$${}^{i+1}(A)\omega_{i+1} = {}^{i+1}_iR {}^i(A)\omega_i + {}^{i+1}({}^i\omega_{i+1}).$$

It is assumed that

$${}^A(A)\omega_0 = {}^A(A)\omega_V$$

The angular velocity ${}^A(A)\omega_V$ will be decided by the rotational inertia of the space vehicle. Table 10.1, specifies the submodel parameters specified for the submodel along with the constraint relations expressed by the submodel. The angular velocity ${}^0(A)\omega_0$ required for evaluating constraint relation for submodel 1 shown in Table 10.1, is given as

$${}^0(A)\omega_0 = {}^0_A R {}^A(A)\omega_0$$

(ii) Linear Dynamics Submodel of Links

The general relation is

$${}^A(A)V_{i+1} = {}^A(A)V_i + {}^A_i R [{}^i(A)\omega_i \times {}^i({}^iP_{i+1})] \tag{10.56}$$

Table 10.2 Parameters used for modeling of space robot

Parameters	Mass (kg)	Ixx (kg m ²)	Iyy (kg m ²)	Izz (kg m ²)	Length (l_i) (m)	Length (l_{Gi}) (m)	θ_i
Link 1	6.13	0.03	0.025	0.03	0.1	0.05	0
Link 2	15.69	0.2153	0.0126	0.2153	0.4	0.2	$\pi/2$
Link 3	11.76	0.0929	0.0094	0.0929	0.3	0.15	$\pi/2$
Vehicle	2000	40.0	40.0	40.0			

or

$$[{}^A({}^A V_{i+1})] = [{}^A({}^A V_i)] + [{}_i^A R] [-{}^i({}^i P_{i+1} \times)] [{}^i({}^A \omega_i)]. \quad (10.57)$$

The velocity of frame {0} is same as frame {1}, hence ${}^A({}^A V_1) = {}^A({}^A V_0)$. The lengths of links are specified as ${}^0 P_1 = [0 \ 0 \ 0]^T$; ${}^1 P_2 = [0 \ l_1 \ 0]^T$; ${}^2 P_3 = [0 \ l_2 \ 0]^T$; ${}^3 P_4 = [0 \ l_3 \ 0]^T$.

(iii) Initial Conditions

The initial tip position of space robot, i.e., frame {4} with respect to robot base, i.e., frame {0} can be given as

$${}^0({}^0 P_4) = \begin{bmatrix} -c_1 s_2 l_2 - c_1 s_{23} l_3 \\ l_1 + c_2 l_2 + c_{23} l_3 \\ s_1 s_2 l_2 + s_1 s_{23} l_3 \end{bmatrix} \quad (10.58)$$

The location of frame {0} with respect to frame {V} is given by

$${}^V({}^V P_0) = [r_x \ r_y \ r_z]^T$$

To begin with, let the tip of space robot be initially at the initial vehicle CM, i.e., at frame {V}. For convenience, let us assume that frame {A} coincides and is located at the CM of vehicle. Then the initial location of the tip with respect to absolute frame is given by

$${}^A({}^A P_4) = {}_V^A R {}^V({}^V P_0) + {}_0^A R {}^0({}^0 P_4) \quad (10.59)$$

The parameters selected for the simulation of a three DOF space robot are given in Table 10.2 [20]. Manipulator base position from spacecraft CM, $r_x = 0.1$ m, $r_z = 0.1$ m, $r_y = 0$ is assumed. It is also assumed that initially $\theta_1 = 0$, $\theta_2 = \theta_3 = \pi/2$.

It is assumed that the first joint has joint resistance of 0.1 Ns/m, while joint 2 and joint 3 resistances are assumed to be 100 Ns/m. For the simulation the first joint is given a constant torque of 10 Nm while torque on second and third joints is zero (the heavy resistance locks those joints). The simulation is carried out for 2.8 s.

If the reaction of space robot on space vehicle had not been there, the tip of the robot would have traced a circular path of radius of 0.4 m (i.e., the length of second link). But for the space robot, as seen from Fig. 10.14a, the tip trajectory fails to trace

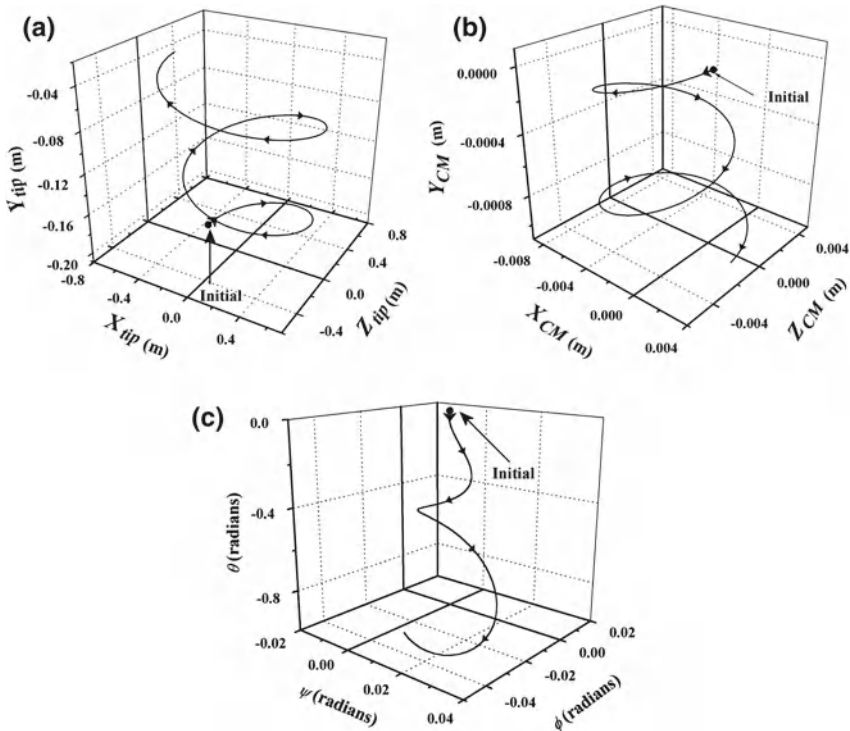


Fig. 10.14 a Tip trajectory of space robot. b Center of mass trajectory of space vehicle. c Euler angle variation of space vehicle

the circular path. The plots of the CM of spacecraft in three dimensions are shown in Fig. 10.14b. The plot shows a continuous drift in the vehicle CM location due to conservation of angular momentum of a free-floating space robot system, i.e., due to nonholonomic nature of the angular momentum conservation constraint.

Figure 10.14c shows a three-dimensional plot of the variations of ψ , ϕ , and θ , in $\psi - \phi - \theta$ space which indicates continuous change of attitude of space vehicle. Figure 10.15a, b and c shows the variation of joint angles θ_1 , θ_2 and θ_3 , respectively, with respect to time. Figure 10.16a–c shows the change of orientation of space vehicle with time given by variation of Euler angles ϕ , θ , and ψ , respectively.

10.6 Trajectory Control of Space Robot

A free-floating space robotic system is one in which the spacecraft’s position and attitude are not actively controlled using external jets or thrusters, and it does not interact dynamically with the environment during manipulator motion. The spacecraft moves freely in response to the dynamical disturbances caused by the manipulator’s motion.

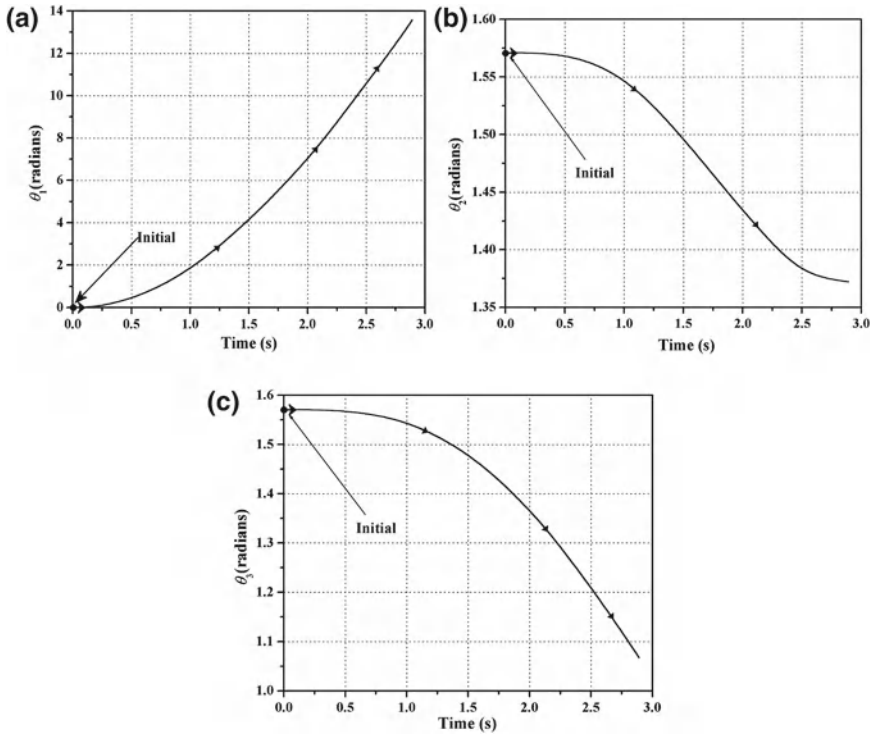


Fig. 10.15 a Plot of first joint angle versus time. b Plot of second joint angle versus time. c Plot of third joint angle versus time

For such systems, the linear and angular momenta are conserved. The disturbance of the base results in deviation of the end effector from the desired trajectory. Thus, it is very difficult to design a control strategy for a space robot end-effector trajectory control. Moreover, the angular momentum conservation constraints are non-integrable rendering the system nonholonomic [13].

Now, let us design the controller for space robot based on the overwhelming controller concept developed in the previous chapter, for the trajectory control of space robots.¹

10.6.1 Robust Overwhelming Controller

Let us take the example of a three DOF space robot to illustrate the control strategy [16] for a free-floating space manipulator consisting of a serial robot mounted on

¹ A part of this section is adapted from these authors' previous work published in [16].

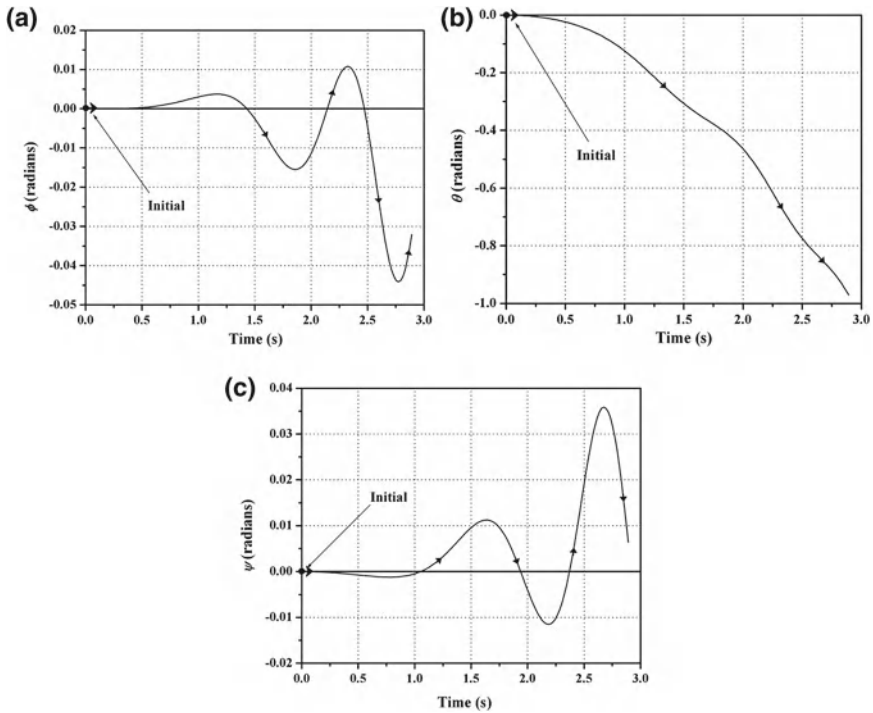


Fig. 10.16 Variation of Euler angles with time. **a** ϕ versus time **b** θ versus time **c** ψ versus time

a satellite base as shown in Fig. 10.12. It is assumed that the specified task space trajectory is within the reachable workspace of the manipulator.

10.6.1.1 Controller Submodel

The bond graph submodel for robust overwhelming controller is shown in Fig. 10.17a which is discussed in the previous chapter. Another form of representation of overwhelming controller is shown in Fig. 10.17b. The tip velocity ports are then connected to three robust overwhelming controller submodels, one for each X, Y, and Z direction.

The angular relative velocities of links are defined as ${}^1\omega_1 = [0 \ \dot{\theta}_1 \ 0]^T$, ${}^2\omega_2 = [0 \ 0 \ \dot{\theta}_2]^T$, ${}^3\omega_3 = [0 \ 0 \ \dot{\theta}_3]^T$.

Here, $\dot{\theta}_1$, $\dot{\theta}_2$ and $\dot{\theta}_3$ are the joint velocities of the first, second, and third joints respectively. Reference flow input for plant is supplied to this submodel from main bond graph shown in Fig. 10.18. This submodel is also provided with robot tip velocity as input from main bond graph and it gives correction efforts as output to (ROC) submodel CTRL. Three robust overwhelming controller (ROC) submodels (one for

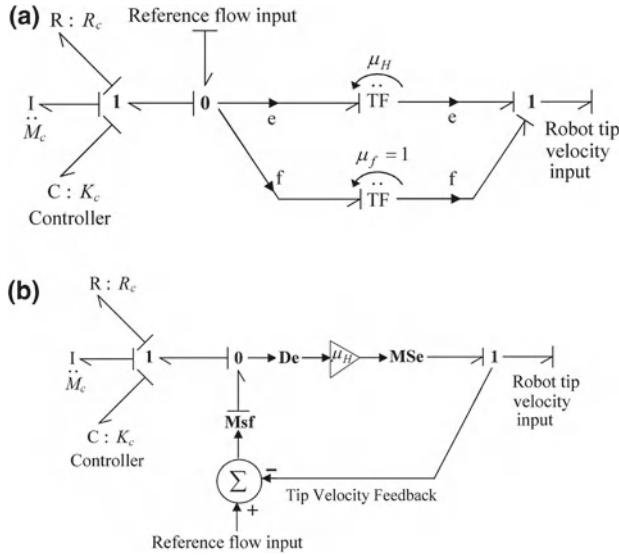


Fig. 10.17 a Robust overwhelming controller submodel. b Another form of representation of robust overwhelming controller submodel

each $X, Y,$ and Z direction) are used to control the space robot as shown in Fig. 10.18. A signal structure (CTRL) can be created using kinematic relations to convert correction efforts from ROC into correction torques to be supplied to different joints.

10.6.1.2 Evaluation of the Jacobian

For creation of this signal structure (CTRL), the tip velocity with respect to robot base frame $\{0\}$ expressed in absolute frame $\{A\}$ can be evaluated as

$${}^A({}^0V_4) = {}^A R {}^0({}^0V_4) \tag{10.60}$$

Here, ${}^k({}^jV_i)$ denotes the velocity of the origin of i th frame as observed from j th frame and expressed in k th frame, ${}^B A R$ represents the orientation of a frame $\{A\}$ with respect to a frame $\{B\}$. The term in Eq. 10.60 can be derived as

$${}^0({}^0V_4) = \begin{bmatrix} (s_1s_2l_2 + s_1s_23l_3) & -(c_1c_2l_2 + c_1c_23l_3) & -c_1c_23l_3 \\ 0 & -(s_2l_2 + s_23l_3) & -s_23l_3 \\ (c_1s_2l_2 + c_1s_23l_3) & (s_1c_2l_2 + s_1c_23l_3) & s_1c_23l_3 \end{bmatrix} \begin{bmatrix} \dot{\theta}_1 \\ \dot{\theta}_2 \\ \dot{\theta}_3 \end{bmatrix} \tag{10.61}$$

where $c_i = \cos \theta_i, s_i = \sin \theta_i, c_{ij} = \cos(\theta_i + \theta_j), s_{ij} = \sin(\theta_i + \theta_j)$.

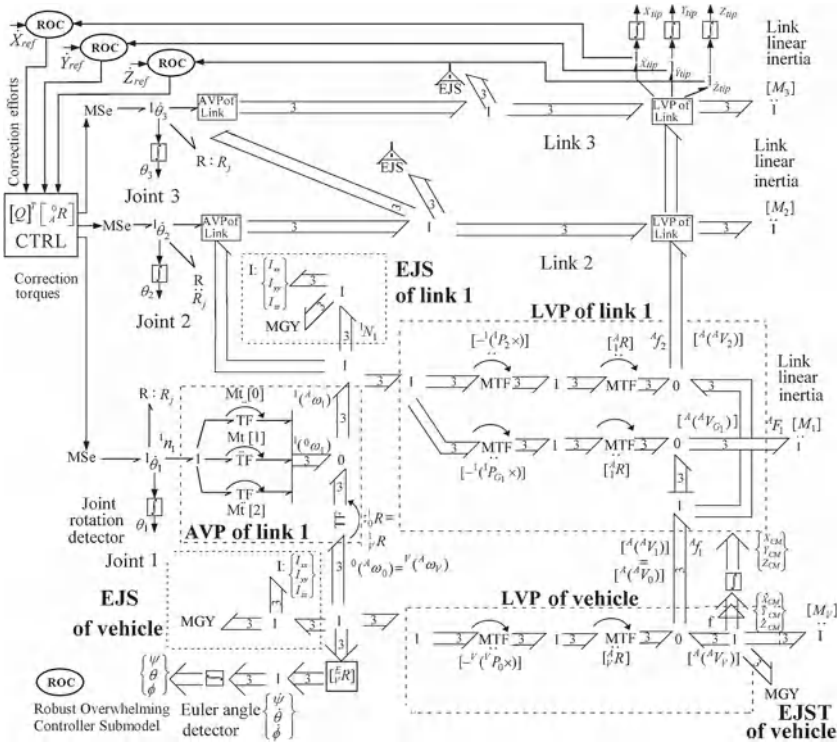


Fig. 10.18 Complete bond graph model of a free-floating space vehicle along with robot and controller

One can write Eq. 10.61 in a compact form as

$${}^0({}^0V_4) = [Q] [\dot{\theta}_1 \ \dot{\theta}_2 \ \dot{\theta}_3]^T$$

where Q represents the transformation matrix in Eq. 10.61. The transformation 0R is computed as

$${}^A_0R = {}^A_VR {}^V_0R$$

where

$${}^A_VR = \begin{pmatrix} c\phi c\theta & c\phi s\theta s\psi & -s\phi c\psi & c\phi s\theta c\psi & +s\phi s\psi \\ s\phi c\theta & s\phi s\theta s\psi & +c\phi c\psi & s\phi s\theta c\psi & -c\phi s\psi \\ -s\theta & c\theta s\psi & & c\theta c\psi & \end{pmatrix} \quad (10.62)$$

and V_0R is identity matrix. Here, $s\psi = \sin \psi$, $c\psi = \cos \psi$, $s\theta = \sin \theta$, $c\theta = \cos \theta$, $s\phi = \sin \phi$, $c\phi = \cos \phi$. Thus Eq. 10.60 can be written as

$${}^A({}^0V_4) = [{}^A_0R] [Q][\dot{\theta}_1 \ \dot{\theta}_2 \ \dot{\theta}_3]^T \quad (10.63)$$

Thus the relationship between joint correction torques and correction efforts from controller can be expressed as

$$[{}^1n_1 \ {}^2n_2 \ {}^3n_3]^T = [Q]^T [{}^0_A R] [F_x \ F_y \ F_z]^T \quad (10.64)$$

where ${}^i n_i$ is the torque exerted on link i by link $(i - 1)$, expressed in terms of frame $\{i\}$. F_x , F_y , and F_z are corrective efforts in X , Y , and Z directions, respectively. The created submodel (*CTRL*) of signal structure for conversion of correction efforts into correction torques is shown in Fig. 10.18.

10.6.2 A Free-Floating Space Manipulator

The complete multi bond graph model of the free-floating space robot with robust overwhelming controller is shown in Fig. 10.18. The tip velocity, which is provided to the ROC submodel (shown in Fig. 10.17), is compared with the reference flow command, and the error in the flow is sent to the controller. The controller returns the correction effort, which is then provided to the robot with a high feed-forward gain. This correction effort is transformed back to joint coordinates as correction joint torques using submodel *CTRL* and applied at the joints. Here, the signal structure *CTRL* from the joint velocities to the tip velocities is created based on the forward kinematics of the manipulator. In Fig. 10.18 integrators are used as sensors of displacement [7]. From the bond graph of Fig. 10.18, it is seen that the joint torque at the first joint is given by

$${}^1n_1 = {}^1N_1 + {}^1_2R \ {}^2n_2 + {}^1({}^1P_{G_1}) \times {}^1_A R \ {}^A F_1 + {}^1({}^1P_2) \times {}^1_A R \ {}^A f_2 \quad (10.65)$$

Here ${}^A f_1$ is the force exerted on link 1 by link 0 (i.e., vehicle), expressed in terms of absolute frame, 1n_1 is the torque exerted on link 1 by link 0 (i.e., vehicle), expressed in terms of frame $\{1\}$, ${}^A F_1$ is the resultant of all the external forces acting on the link, and 1N_1 are the resultant of all the external moments acting on the link. Similarly, from the bond graph the force balance for link 1 can be given as

$${}^A f_1 = {}^A F_1 + {}^A f_2 \quad (10.66)$$

Here, ${}^A f_2$ is the force exerted on link 2 by link 1, expressed in terms of absolute frame. Equations 10.65 and 10.66 are similar to the one which can be obtained by considering force balance and moment balance equations based on the free body diagram of a typical link [2]. Equations similar to Eqs. 10.65 and 10.66 can be written for other links also. In the next section we present a numerical simulation of three DOF space robot with robust trajectory controller.

Table 10.3 Reference velocity command in absolute frame, located at initial position of CM of space vehicle

Reference velocity direction	Velocity expression
X direction (\dot{X}_{ref})	$R \cdot \omega \sin(\omega t)$
Y direction (\dot{Y}_{ref})	$A \sin(2 \omega t)$
Z direction (\dot{Z}_{ref})	$R \omega \cos(\omega t)$

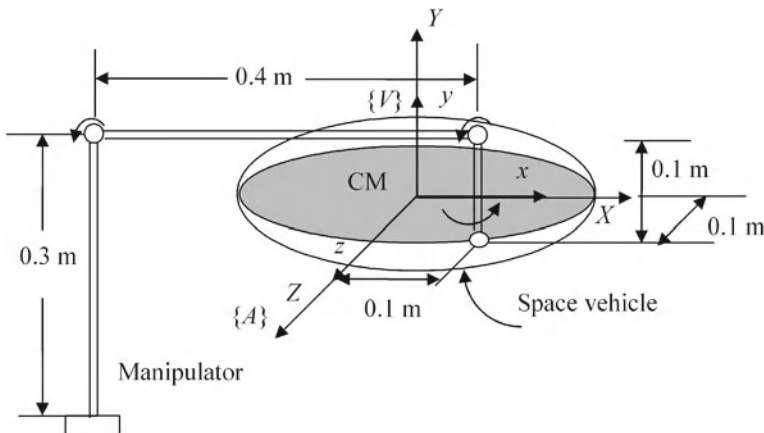


Fig. 10.19 Initial configuration of space robot

10.6.3 Simulation and Validation

The link parameters selected for the simulation of space robot are the same as that shown in Table 10.2, except that the mass of space vehicle is 200kg. All joint resistances are assumed to be 0.1 Ns/m. Overwhelming controller parameters are Mass (M_c) = 1.0; Gain (μ_H) = 10.0. Reference velocity commands are shown in Table 10.3. In Table 10.3, R is the radius of reference circle in $X-Z$ plane and A is the amplitude of velocity in Y direction. It is a circular trajectory in $X-Z$ plane and parabolic trajectory in $X-Y$, and $Y-Z$ plane.

Figure 10.19 shows the initial configuration of the space robot. At the beginning of simulation overwhelmer initial position is initialized to robot tip position. Simulation is carried out for 25 s with R as 0.3 m and A as 0.01 m/s.

Figure 10.20 shows the reference and actual plots of tip trajectories. Figure 10.20a shows a three-dimensional plot of tip movement. Figure 10.20b shows the variation of X tip trajectory along with Z tip trajectory. Figure 10.20c shows the X tip trajectory variation with Y tip variation. Figure 10.20d shows the Y tip trajectory variation with Z tip variation. From these figures it is clear that tip is effectively dragged along the reference trajectory.

Figure 10.21 shows the tip trajectory error plot. The error is taken as the difference between reference and actual tip positions in mm. Figure 10.21a shows the error plot for X tip position versus time. Here, error varies between +0.0054 and -0.0004 mm.

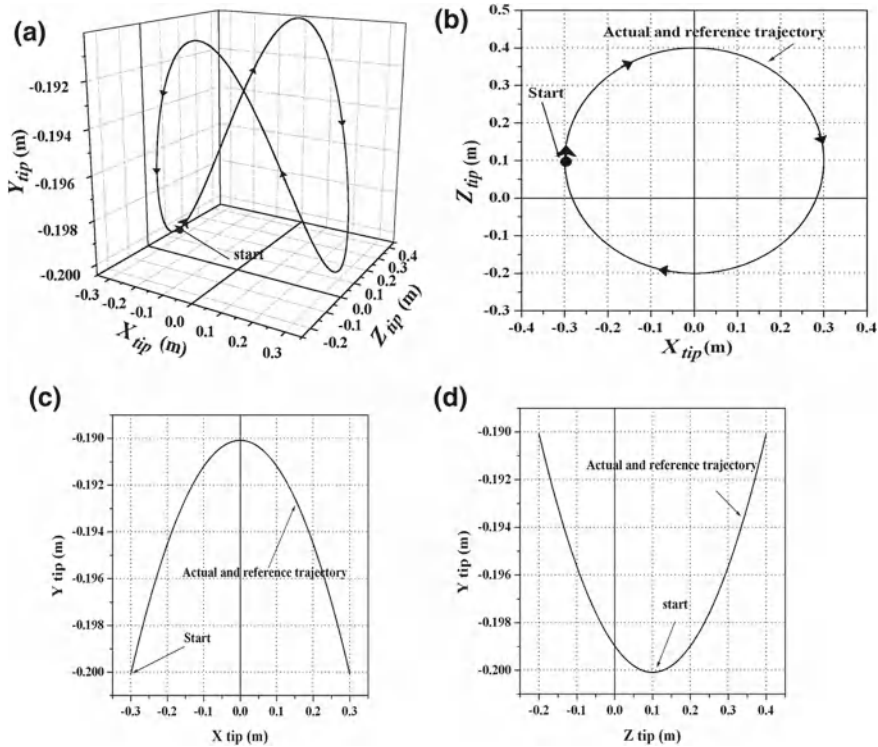


Fig. 10.20 Tip trajectory plots **a** X tip versus Y tip versus Z tip. **b** X tip versus Z tip. **c** X tip versus Y tip. **d** Z tip versus Y tip

Figure 10.21b shows the error plot for Y tip position versus time. In this plot error varies between $+0.0008$ and -0.001 mm. Figure 10.21c shows the error plot for Z tip position versus time. Here, error varies between $+0.008$ and -0.005 mm, except the initial error between $+0.0277$ and -0.007 mm. Initial error is more than the later part of the error because the tip acquires a velocity from the rest position.

The plots of the motion of the CM of spacecraft in three dimensions are shown in Fig. 10.22a. Figure 10.22b shows the variation of X_{CM} versus Z_{CM} . The plot shows a continuous drift in the vehicle CM location in $X-Z$ plane due to conservation of angular momentum of a free-floating space robot, i.e., due to the non-integrability of the angular momentum equation. Figure 10.22c shows the variation of X_{CM} versus Y_{CM} , whereas Fig. 10.22d shows the variation of Z_{CM} versus Y_{CM} .

Figure 10.23 shows the variation of Euler angle with time. Figure 10.23a shows ϕ versus time, Fig. 10.23b shows θ versus time, and Fig. 10.23c shows ψ versus time. Variation in ϕ and ψ is less compared to θ . If the simulation is further continued, the manipulator approaches singularity at θ value of 90° , and the simulation experiment gets terminated. Figure 10.23d shows a three-dimensional plot for ϕ versus ψ versus θ . It clearly shows that even after the tip reaches its initial position, the plot of Euler

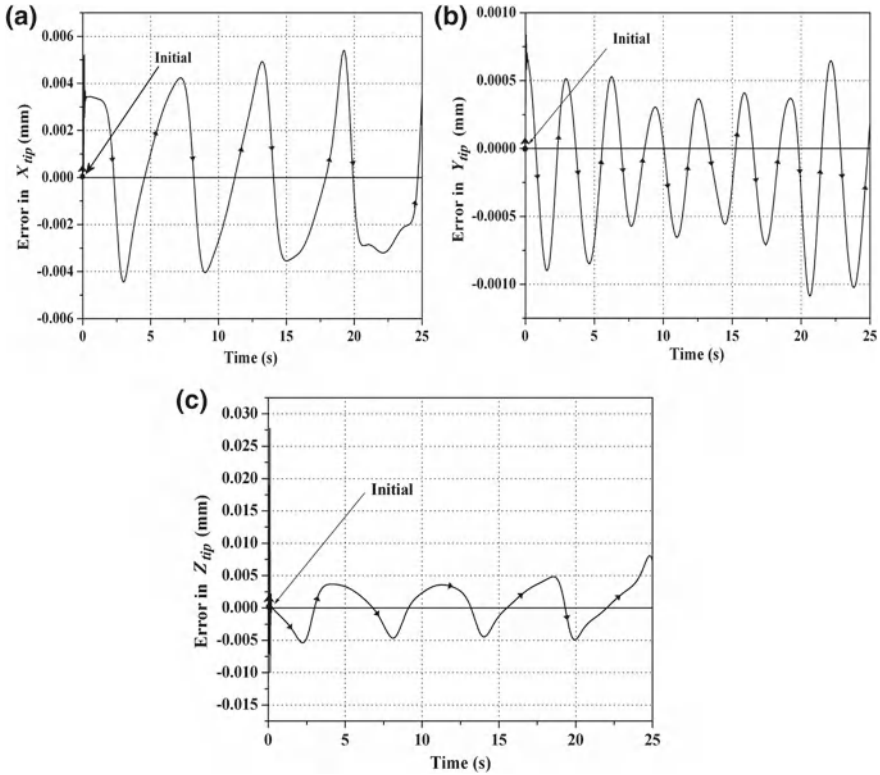


Fig. 10.21 Tip trajectory error plots **a** Error in X tip trajectory versus time. **b** Error in Y tip trajectory versus time. **c** Error in Z tip trajectory versus time

angles does not close. From the simulation of space manipulator model one can get an estimate of drift at the center of mass of spacecraft.

10.7 Impedance Control of Space Robots

10.7.1 Introduction

The control of interaction force between a space robot and its environment is a difficult task as the interaction of the robot tip with the environment causes the base to change its position and orientation. This condition can be avoided by the use of jets/attitude controller. In case of space robots, if conventional force control schemes are used they may lead to instability. Impedance control is an efficient and stable method of providing trajectory and force control in robotic systems. The procedure

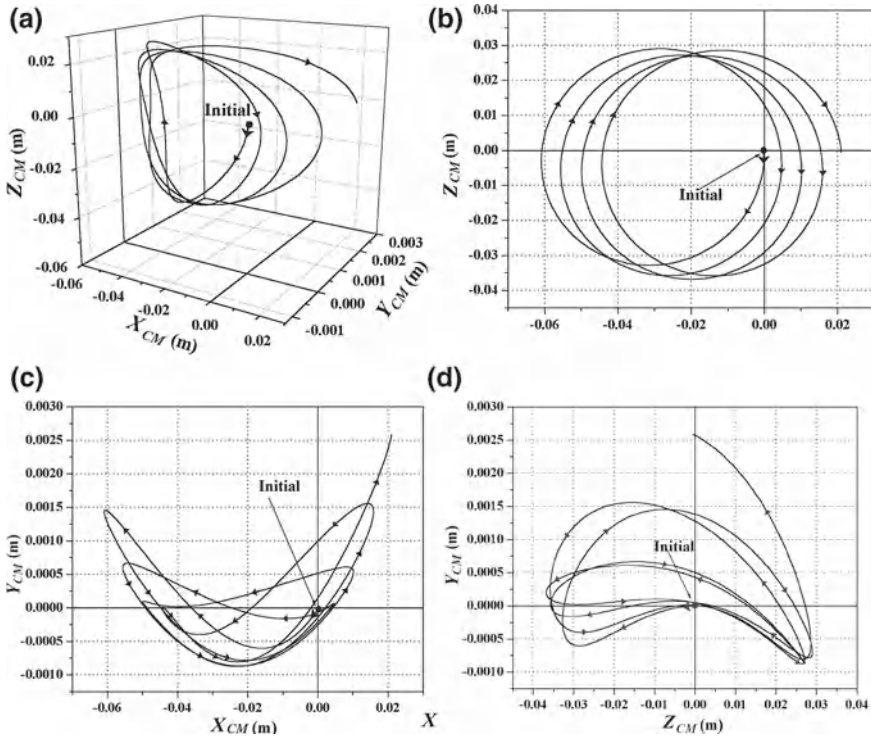


Fig. 10.22 Plots of center of mass of spacecraft **a** X_{CM} versus Y_{CM} versus Z_{CM} . **b** X_{CM} versus Z_{CM} . **c** X_{CM} versus Y_{CM} . **d** Z_{CM} versus Y_{CM}

by which the impedance of the manipulator is changed is a very important aspect in the design of impedance-based control schemes.

Let us discuss a new scheme [18] in which the control of impedance at the interface of the end effector and the space structure is achieved by the introduction of passive degrees of freedom (DOF) in the controller of the robotic system.² The impedance is shown to depend upon a compensation gain for the dynamics of the passive DOF. An explicit relation between the compensation gain and impedance has been derived. First, impedance control of a ground robot on a passive one DOF foundation is discussed. This passive DOF is then taken into the controller domain and is then referred to as virtual foundation. The concepts of bond graph modeling have been used for accomplishing this shifting. The bond graph modeling of the space robot is done by taking the analogy of a ground robot on a flexible foundation. The virtual foundation for the space robot is modeled and is used for the impedance control of the robot. The efficacy of the scheme is demonstrated through simulation and animation of a two DOF space robot.

² A part of this section is adapted from these authors' previous work published in [17, 18].

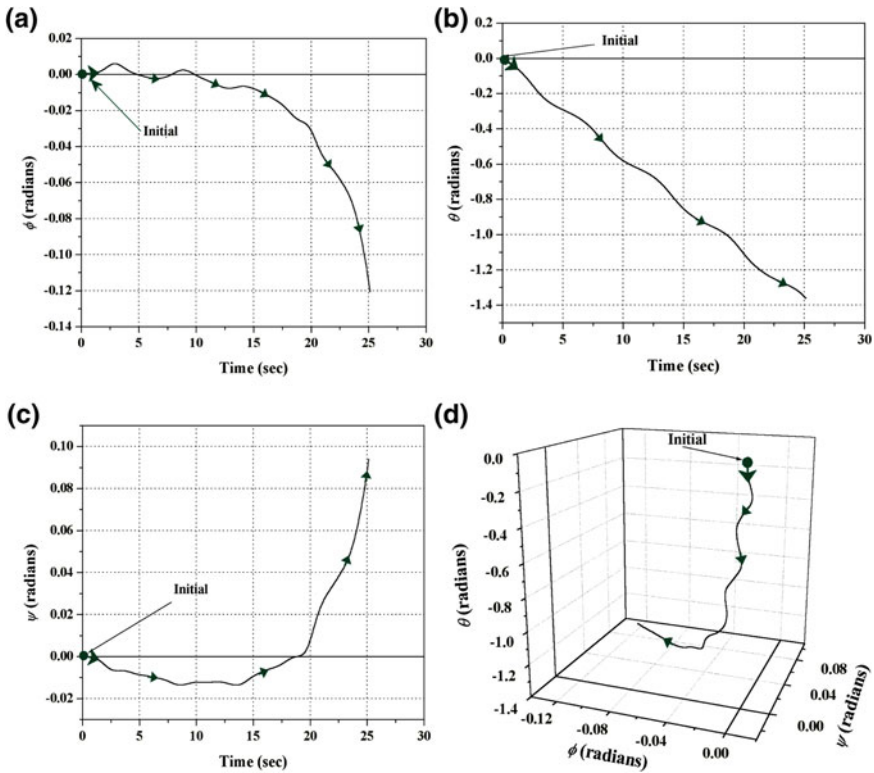


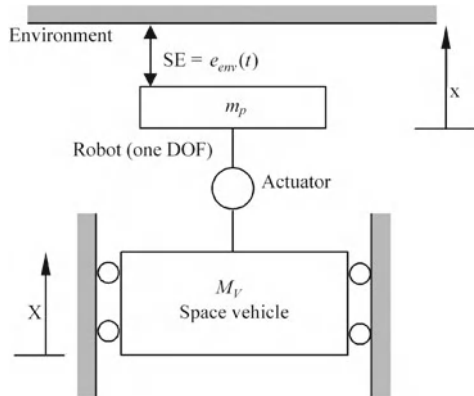
Fig. 10.23 Variation of Euler angles with time. **a** ϕ versus time **b** θ versus time **c** ψ versus time. **d** θ versus ϕ versus ψ

10.7.2 Force Control by Impedance Control

The concept discussed for modeling a ground robot on flexible foundation can be used to model a space robot by replacing the flexible foundation with the base of space robot as discussed at the beginning of this chapter. In general the difference between a space robot (without external jets) and a ground robot on flexible foundation can be listed as

1. In the case of a space robot, translation as well as rotational DOF of the base are present, whereas in a ground robot on a flexible foundation, only translational DOF is present.
2. Nonlinearities are present due to coupled motion of the translation and rotational DOF.
3. Additional constraints of linear and angular momentum conservations are present which lead to problem of nonholonomy in motion planning.

Fig. 10.24 Schematic diagram of one translational DOF space robot with virtual foundation in controller domain



Hence, in modeling and controller design for a space robot, the above factors are required to be taken into consideration.

10.7.3 Modeling of One Translational DOF Impedance Controller

The bond graph modeling of space robot with impedance controller is achieved in following stages:

- STAGE I: Modeling of the Space Robot

The space robot is modeled by considering the translation one DOF ground robot on a flexible foundation. Next, this flexible foundation is replaced by the space vehicle carrying the space robot. To nullify the effect of the motion of space vehicle on the tip velocity of the space robot, the base velocity of space robot is fed back to the controller using a flow-activated bond.

- STAGE II: Modeling of the Impedance Controller

The features of stage I appended to the ground robot with virtual foundation will result in a space robot on a virtual foundation. This virtual foundation is in the controller domain. The compensation gain γ of the virtual foundation in the controller domain can be used to modulate the impedance at the interaction point between the space robot tip and the environment.

The conceived schematic model of the space robot on a virtual foundation is shown in Fig. 10.24. Figure 10.25a shows the corresponding bond graph model. For this model, the admittance at the interaction point is defined as ratio of the robot tip velocity to the environmental effort causing the motion, and can be derived from the signal flow diagram of Fig. 10.25b as

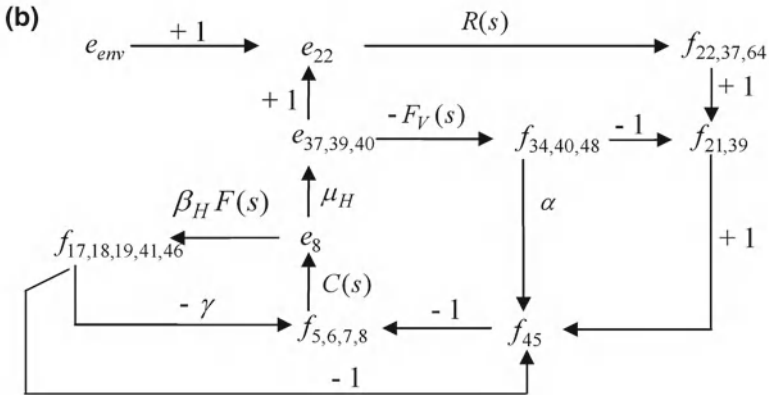
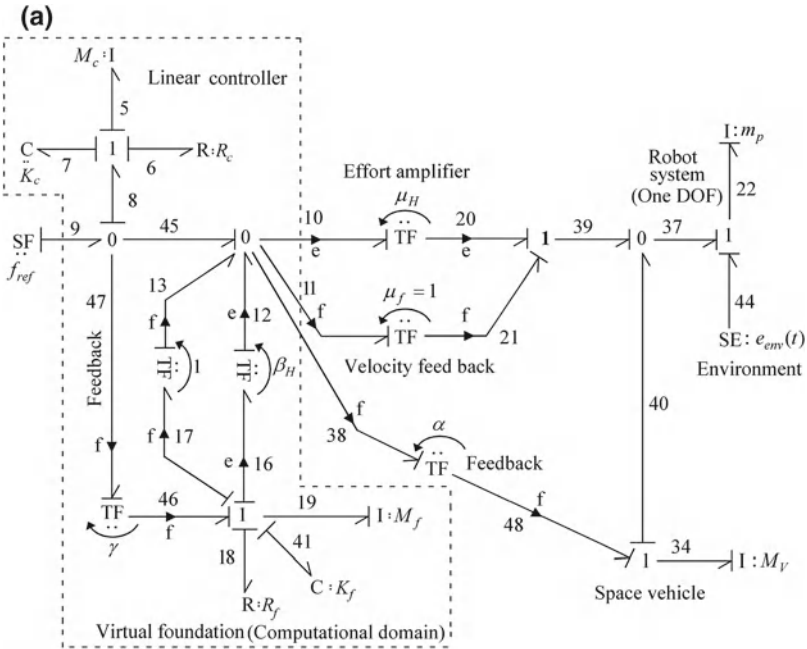


Fig. 10.25 **a** Bond graph model of one translational DOF space robot with virtual foundation in controller domain. **b** Signal flow diagram for bond graph shown in (a)

$$\begin{aligned}
 Y_{rob}(s) &= \frac{1}{Z_{rob}(s)} = \frac{f_{22}}{e_{env}} \\
 &= \frac{R(s)[1 + (1 - \gamma)\beta_H F(s)C(s) + (1 - \alpha)\mu_H C(s)F_V(s)]}{1 + \mu_H C(s)R(s) + (1 - \gamma)\beta_H F(s)C(s) + (1 - \alpha)\mu_H C(s)F_V(s)} \quad (10.67)
 \end{aligned}$$

Here,

- $R(s) = 1/(m_p s)$ is transfer function of the robot,
- $C(s) = (M_c s^2 + R_c s + K_c)/s$ is transfer function of the controller,
- $F(s) = s/(M_f s^2 + R_f s + K_f)$ is transfer function of the virtual foundation,
- $F_V(s) = 1/M_V s$ is transfer function of the space vehicle base,
- α is feedback compensation from space robot base to controller,
- μ_H is high feed-forward gain,
- β_H is high gain (equal to high feed-forward gain),
- γ is feedback compensation from virtual foundation to controller.

At $\alpha = 1$ (i.e., complete velocity feedback compensation from space robot base to controller), Eq. 10.67 reduces to,

$$Y_{rob}(s) = \frac{1}{Z_{rob}(s)} = \frac{R(s)[1 + (1 - \gamma)\beta_H F(s)C(s)]}{1 + \mu_H C(s)R(s) + (1 - \gamma)\beta_H F(s)C(s)} \quad (10.68)$$

From Eq. 10.68 it is implied that,

1. When $\gamma = 1$, the controller totally rejects the foundation characteristic and assures complete trajectory robustness,
2. When $\gamma < 1$, modulation of impedance to accommodate interaction forces is possible.

In the bond graph of Fig. 10.25a, M_V is mass of the space vehicle; M_f , K_f , and R_f are mass, stiffness, and damping, respectively, of the virtual foundation; K_{env} is stiffness of the environmental structure; and f_{ref} is reference velocity. In this bond graph differential causality at the controller inertial element (I_5) exists. This is removed with the help of a pad. Other features of the impedance control such as force error integrator, amnesia remover, velocity correction for amnesia remover, and detailed environment modeling which will be discussed in the following sections are shown in Fig. 10.26. In Fig. 10.26 K_{pad} and R_{pad} are the pad stiffness and resistance, respectively, and e_{44} is a force sensor to measure the interaction force between the robot tip and the environment. Flow activated C elements on bond number 30, 15, and 43 are tip displacement sensor, reference position sensor, and space vehicle displacement sensor, respectively. Assuming that the environment behaves like a linear spring, the SE element is replaced by a C element (C_{31}). SE_{42} source is introduced to nullify the effort developed by the C_{31} element (representing environmental stiffness) due to the unobstructed length covered by the tip.

The impedance establishes the dynamic relationship between end-effector velocity and the corresponding environmental reaction force. Since it is not possible to fulfill both the constraints on the force and trajectory at the same time, impedance can be used as a parameter to control either environmental reaction forces or the velocity of the end effector at the interface. Equation 10.68 suggests that modulation of γ about 1 can be used to change the impedance and make the controller behave in the trajectory control mode when $\gamma = 1$, and in the force control mode when $\gamma < 1$.

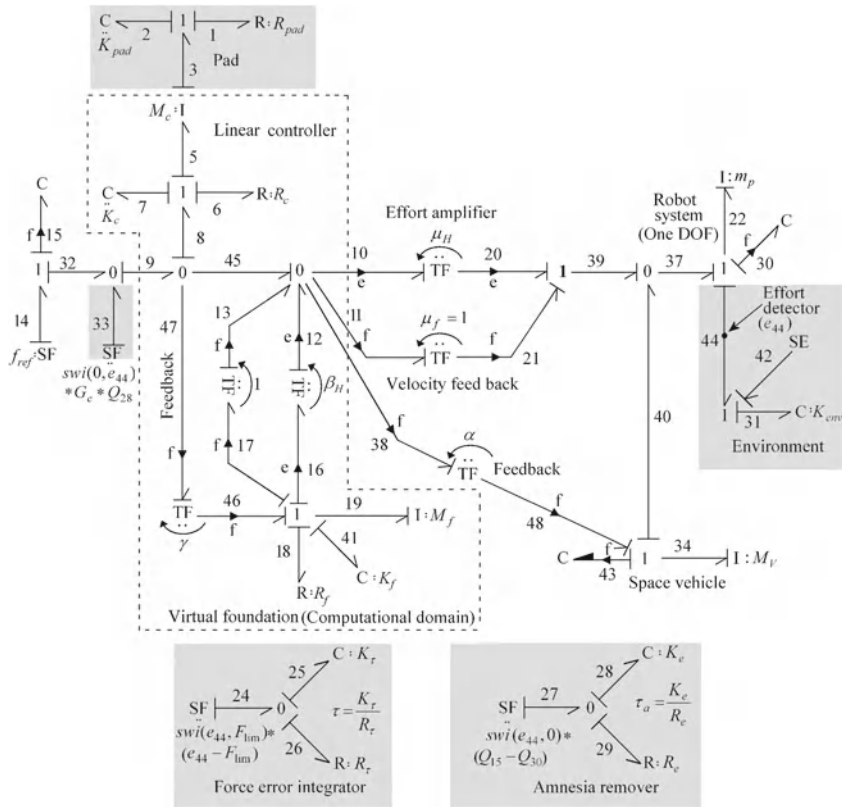


Fig. 10.26 Bond graph model of one translational DOF space robot with virtual foundation in controller domain added with pad, detailed environment, force error integrator, amnesia remover

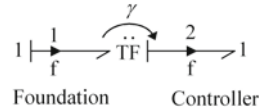
10.7.3.1 Adaptive Gain Modulation

Kumar et al. [9], and Mohan Kumar [10] achieved modulation of virtual foundation compensation gain γ through a heuristic expression involving actual and limiting forces. For the gain modulation of the space robot, the heuristic expression used by them is used here. The heuristic expression for gain modulation is given by Eq. 10.69 as

$$\gamma(F, F_{lim}, t) = 1 - swi(F(t), F_{lim})[K_{ini} + K_{GP}(F(t) - F_{lim}) + K_{GI}Y(t)] \quad (10.69)$$

where $F(t)$ is the actual contact force obtained from force sensor; F_{lim} is the limiting value of the force specified, K_{ini} is a constant (a bias), K_{GP} is a proportional gain term, and K_{GI} is an integral gain term. Equation 10.69 represents a proportional-integral control. The swi defines the switch function in SYMBOLS software. It is defined as

Fig. 10.27 Bond graph of the foundation and controller coupling



$$\begin{aligned} \text{swi}(a, b) &= 1, \text{ for } a \geq b, \\ \text{swi}(a, b) &= 0, \text{ for } a < b, \end{aligned}$$

where a and b are two variables.

Thus from Eq. 10.69 it can be deduced that when

- $F(t) \geq F_{\text{lim}}$, $\text{swi}(F(t), F_{\text{lim}}) = 1$ so that $\gamma \neq 1$, hence, impedance controller works in force control mode.
- $F(t) < F_{\text{lim}}$, $\text{swi}(F(t), F_{\text{lim}}) = 0$ so $\gamma = 1$, hence, impedance controller works in trajectory control mode.

The term $Y(t)$ is given by

$$Y(t) = \text{swi}(F(t), F_{\text{lim}}) e^{-\tau t} \int_{t_i}^t e^{\tau \xi} (F(\xi) - F_{\text{lim}}) d\xi \tag{10.70}$$

Here, τ is a gain relaxation term and t_i is the time when force control is initiated. The expression $Y(t)$ integrates the difference in the interaction force and the force limit to smoothen any sharp change in the variation of impedance. Here, swi function will ensure that force difference $(F(\xi) - F_{\text{lim}})$ is integrated during interaction phase only when the robot tip interacts with the environment.

From the part bond graph shown in Fig. 10.26, the integral expression $Y(t)$ (Eq. 10.70) can be obtained as the state or charge of the error integrating C_{25} element. The input to the part bond graph is given by

$$SF_{24} = \text{swi}(e_{44}, F_{\text{lim}}) (e_{44} - F_{\text{lim}}) \tag{10.71}$$

Then, $Y(t)$ can be written as $Y(t) = Q_{25}$. In Fig. 10.26 the time constant $\tau = (K_\tau / R_\tau)$ can be adjusted for obtaining the desired time taken for the force to recover to the previous value.

10.7.3.2 Effect of Impedance Modulation on Trajectory Control

The coupling between the foundation velocity $f_f(t)$ and the compensation velocity feedback to controller $f_c(t)$ is shown in Fig. 10.27. From the bond graph constitutive law for transformer, the following relation between $f_f(t)$ and $f_c(t)$ can be derived:

$$f_c(t) = \gamma(t) f_f(t) \tag{10.72}$$

Here, γ is the feedback compensation gain of the motion of the virtual foundation, represented by a transformer element of modulus γ . In the differentiated form the above relationship can be written as

$$\dot{y}_c = \gamma(t) \cdot \dot{y}_f(t) \quad (10.73)$$

where y_c is the displacement compensation for trajectory control, and y_f is the passive foundation displacement.

Writing Eq. 10.73 in Pfaffian form

$$\gamma(t)dy_f - dy_c + 0 \cdot dt = 0 \quad (10.74)$$

Considering the coefficients of Eq. 10.74 as a vector V ,

$$\mathbf{V} = [\gamma(t) \ -1 \ 0]^T \quad (10.75)$$

The constraint in Eq. 10.74 is considered holonomic iff,

$$\begin{aligned} V \cdot \nabla \times V &= 0 \\ \therefore \nabla &= i \frac{\partial}{\partial x} + j \frac{\partial}{\partial y} + k \frac{\partial}{\partial t} \end{aligned}$$

Hence

$$\nabla \times \mathbf{V} = \begin{vmatrix} i & j & k \\ \frac{\partial}{\partial x} & \frac{\partial}{\partial y} & \frac{\partial}{\partial t} \\ \gamma(t) & -1 & 0 \end{vmatrix}$$

or

$$\nabla \times V = \frac{\partial \gamma}{\partial t} j \text{ (since } \frac{\partial \gamma(t)}{\partial y} = 0 \text{ as, } \gamma \text{ is not a function of } y \text{).}$$

so

$$\begin{aligned} V \cdot \nabla \times V &= (\gamma(t)i - j + 0k) \cdot (j \frac{\partial \gamma(t)}{\partial t}) \\ \therefore V \cdot \nabla \times V &= -\frac{\partial \gamma(t)}{\partial t} \end{aligned} \quad (10.76)$$

From Eq. 10.76, it can be implied that the transformer coupling the foundation velocity and the feedback compensation term is holonomic iff, $\dot{\gamma}(t) = 0$, or, $\gamma(t) = C$. Here C is a constant. So it can be inferred that during the trajectory control phase

$\gamma = 1$, or, $\dot{\gamma}(t) = 0$, so the constraint is holonomic, whereas during the force control phase,

$$\gamma = \gamma(F(t) - F_{\text{lim}}, t) \quad (10.77)$$

i.e., γ is a function of force difference $(F(t) - F_{\text{lim}})$ and time t .

For the task having cyclic nature, it is desired that when the force control phase is over, the end effector comes back to the reference trajectory. $\gamma = 1$, condition recovers the robustness and high driving point impedance state of the end effector, resulting in accurate end-effector velocity. However, nonholonomicity forces a lag in the manipulator position with respect to the reference trajectory. This loss of position information during the phase when $\gamma < 1$, is called amnesia.

10.7.3.3 Amnesia and Its Recovery Control

Since the velocity and force of the robotic system are strongly interrelated at the environment interaction port through the impedance of the manipulator, accurate trajectory control cannot be achieved simultaneously during interaction. When the end effector does not have interaction with the environment, the value of compensation gain (γ) is one, and the end effector follows the trajectory command. In this condition, a high impedance state exists. During the interaction phase, when the force reaches its bound value, the end-effector motion gets arrested, and yielding of the foundation compensates for the command motion. In this condition the value of compensation gain (γ) is less than one. Due to incomplete compensation and yielding of the foundation, impedance is reduced to a lower value. So, when the interaction phase is over, it leads to a difference between the reference trajectory position and the actual manipulator position. This difference is defined as amnesia [8, 12]. When the interaction phase is over, the compensation gain γ is switched to 1 by the logic in Eq. 10.69 restoring the high impedance state of the system so that the end effector continues to follow the reference trajectory with a lag in the position (i.e., amnesia) of the end effector with respect to reference trajectory. This amnesia needs to be removed. The amnesia is removed as follows:

1. Error recording phase: The controller records the loss in positional information of the trajectory during accommodation of the interaction force. This information is recorded through the time integral of positional error.
2. Error correction phase: The error information above is supplied to the trajectory controller by augmenting it to reference velocity during the non-interaction phase.

Mathematically, the error recording is done by a function like,

$$Y_a(t) = e^{-\tau_e t} \int_{t_s}^t e^{\tau_e \xi} (Y_{ref} - Y_\xi) d\xi \quad (10.78)$$

where Y_{ref} is reference position and $Y_{\hat{i}}$ is the actual position, τ_e is time constant, and t_s is the time when interaction begins. Equation 10.78 can be obtained in similar lines as we obtained $Y(t)$ for the force error integration in Eq. 10.70. The expression $Y_a(t)$ integrates the positional error for gradual removal of amnesia. The augmented trajectory command to reference input velocity is given by

$$SF_c = G_e Y_a(t) \quad (10.79)$$

Here, G_e is gain proportional to residual position error $= (Y_{ref} - Y_{\hat{i}})$. The gain factor G_e and the relaxation terms τ_e control the recovery of amnesia.

Amnesia removal can be represented by part bond graph as shown in Fig. 10.26. The part bond graph consists of a flow source SF_{27} , a C element C_{28} , and R element R_{29} as shown in Fig. 10.26. The C_{28} element in the bond graph is the integrator and the R_{29} element provides the first order relaxation dynamics. The input flow source SF_{27} is computed as the difference of reference and actual position $(Y_{ref} - Y_{\xi})$, during the interaction phase as follows. In the bond graph shown in Fig. 10.26, $Y_{ref} = Q_{15}$ and $Y_{\hat{i}} = Q_{30}$, so,

$$Y_{ref} - Y_{\xi} = Q_{15} - Q_{30}$$

Thus,

$$SF_{27} = \text{swi}(e_{44}, F_{\text{lim}})(Q_{15} - Q_{30}).$$

The $\text{swi}(e_{44}, F_{\text{lim}})$ ensures that the positional error $(Q_{15} - Q_{30})$ is integrated by C_{28} element during interaction phase, i.e., when $e_{44} \geq F_{\text{lim}}$. Now, $Y_a(t)$ will be the same as Q_{28} , where Q_{28} is the state of the C_{28} element. Thus using Eq. 10.79 the velocity correction input to reference velocity is given by

$$SF_c = \text{swi}(F_{\text{lim}}, e_{44})G_e Q_{28} \quad (10.80)$$

In the bond graph of Fig. 10.26 SF_c is represented by SF_{33} . In Eq. 10.80 swi function will ensure that SF_c is supplied when end effector is not in interacting phase, i.e., when $e_{44} < F_{\text{lim}}$.

For jobs that are cyclic in nature the value of force error integrator (Q_{25}) and the amnesia recorder (Q_{28}) are to be made zero by the end of the cycle, so that they are not carried into the next cycle. For force error integrator this is achieved by reducing the value of R_{26} to a very small value (R_{low}) as soon as the interaction phase is over, whereas R_{29} is reduced to a very small value (R_{low}) as soon as the desired accuracy in trajectory is achieved.

Thus impedance controller provides the impedance modulation requirement of force control during any interaction. The robust trajectory controller and the amnesia recovery mechanism meet the trajectory requirements of the task to be performed by the robotic system.

Table 10.4 Parameter values used in simulation of one translational DOF impedance controller

Parameter	Value
Mass of robot	$m_p = 1.0 \text{ kg}$
Pad	$r_{pad} = 2 \text{ N/(m/s)}, k_{pad} = 1,000 \text{ N/m}$
Controller	$M_c = 10.0 \text{ kg}, R_c = 5.0 \text{ N/(m/s)}, K_c = 500.0 \text{ N/m}$
Environment stiffness	$K_{env} = 40000.0 \text{ N/m}$
Interaction force limit	$F_{lim} = 600.0 \text{ N}$
Gain modulation	$K_{ini} = 0.00, K_{GP} = 0.5, K_{GI} = 0.1$
Virtual foundation	$M_f = 1.0 \text{ kg}, R_f = 200.0 \text{ N/(m/s)}, K_f = 10.00 \text{ N/m}$
Mass of space vehicle base	$M_V = 10.0 \text{ kg}$
Location of virtual wall	$y_w = 0.3 \text{ m}$
Force error integration bond graph	$K_\tau = 100 \text{ N/m}, R_\tau = 80 \text{ N/(m/s)}, R_{\tau low} = 0.0001 \text{ Ns/m}$
Feed-forward gains	$\mu_H = 300, \beta_H = 300 \text{ S}$
Amnesia removal bond graph	$K_e = 10 \text{ N/m}, R_e = 6.00 \text{ N/(m/s)}, R_{e low} = 0.0001 \text{ Ns/m}$
Gain used for correcting reference trajectory to remove amnesia	$G_e = 600$

10.7.3.4 Simulation Results

Let us consider that the robot tip follows a half-rectified sine trajectory of amplitude $2A$, i.e.,

$$y = 2A \sin\left(\frac{\pi}{2}t\right) \text{ swi}\left(\sin\left(\frac{\pi}{2}t\right), 0\right) \quad (10.81)$$

Then the reference velocity command for the tip is given by

$$\dot{y} = SF_{14} = 2A \left(\frac{\pi}{2}\right) \cos\left(\frac{\pi}{2}t\right) \text{ swi}\left(\sin\left(\frac{\pi}{2}t\right), 0\right) \quad (10.82)$$

At the start of simulation the tip trajectory is initialized to reference trajectory (i.e., $Q_{15} = Q_{30}$). Let a virtual wall be specified at a distance y_w from the initial tip position. In the bond graph shown in Fig. 10.26, SE_{42} element is used to negate the effort which C_{31} element (representing environment stiffness) gives, due to travel of unobstructed length by the end effector. Thus, $SE_{42} = \text{swi}(Q_{30}, y_w)(K_{en} y_w)$. The parameters used for simulation are shown in Table 10.4.

Figure 10.28a shows the plot for the reference and actual trajectory. From Fig. 10.28a it is observed that the end effector penetrates the environment, located at a distance of 0.3 m from the initial end-effector position, since limit force is not reached. Once limit force is reached the motion of end effector gets arrested. When the reference trajectory command starts receding the actual tip also starts retreating till it reaches the virtual wall position. Thus a small dip is seen in the actual tip trajectory. The tip starts following the reference command, once the reference com-

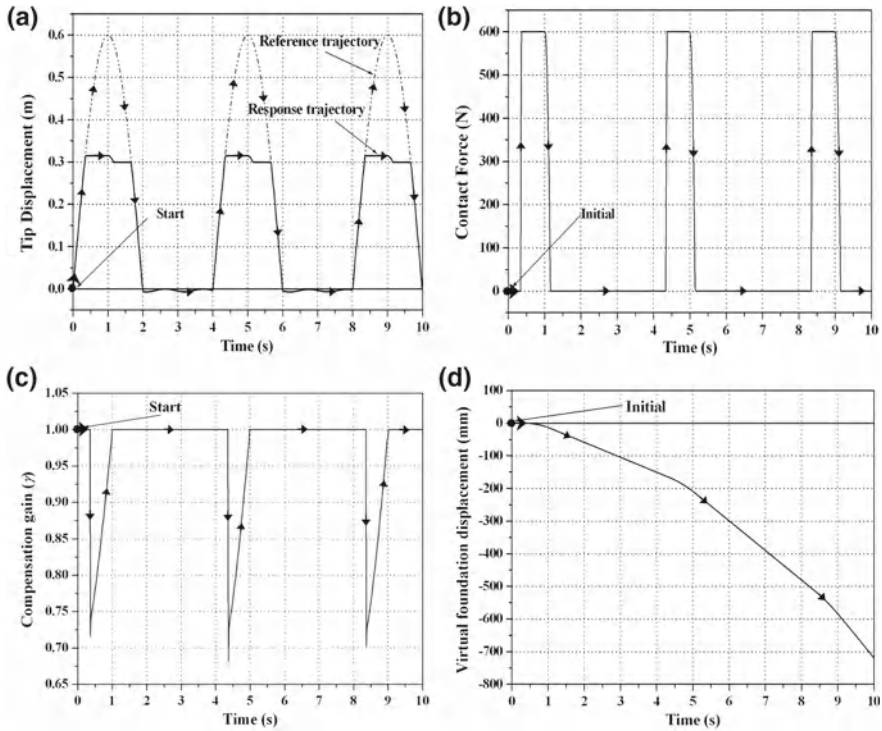
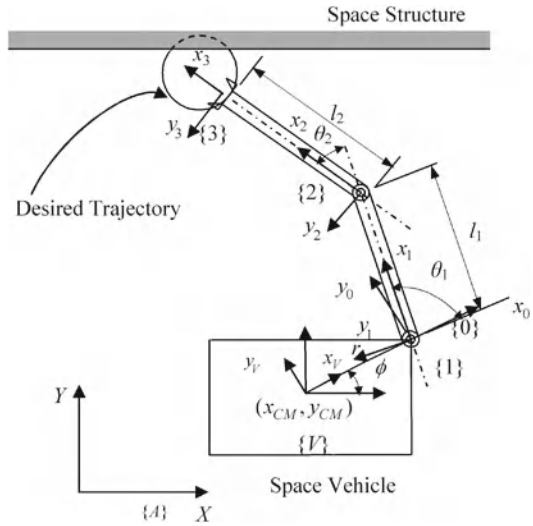


Fig. 10.28 **a** Plot of tip trajectory versus time. **b** Plot of contact force versus time. **c** Plot of compensation gain versus time. **d** Plot of virtual foundation displacement versus time

mand reaches the virtual wall position (i.e., $y_w = 0.3$ m). Figure 10.28b shows the plot of contact force between tip and environment versus time. The force calculated by the multiplication of environment stiffness and the penetration of the tip into the environment differs slightly from the simulated value due to the overwheeler dynamics involved in the simulation results. If the feed-forward gain is made very high then this difference will get minimized. For the first cycle, the reference command starts retreating at 1 s. The moment reference command retreat begins the contact force also starts decreasing, thus we observe the half-width force. Moreover, when the tip disengages from the virtual wall (i.e., $y_w = 0.3$ m) the contact force becomes zero. Figure 10.28c shows the compensation gain (γ) versus time. From Fig. 10.28c it is observed that the compensation gain varies continuously to keep the contact force under limit, whenever the contact force exceeds the force limit. Figure 10.28d shows the displacement of the virtual foundation in the controller domain versus time. Note that the base also moves away a little from its initial position due to the interaction force being transmitted to the base of space robot which is free to translate.

Fig. 10.29 Schematic diagram of two DOF space robot on virtual torsional foundation



10.7.4 Force Control of a Two DOF Planar Space Robot

In the case of multi DOF robots, any constraint in the motion of manipulator will generate forces on the end effector. End-effector motion can be decomposed in a local constraint frame along the normal and tangent to the constraint. In the normal direction, force needs to be controlled, while along the tangent direction robust position control is required. The causality of the interaction between the manipulator and the environment does not allow simultaneous control of motion and force in the same direction. The constrained motion direction and unconstrained motion directions would have different requirements of low and high impedance respectively. This section presents the force control by the impedance control of a two DOF space robot. Now let us consider the two DOF space robot system discussed in Sect. 10.5.1. The interaction of the manipulator with the environment is shown in Fig. 10.29. Figure 10.30 shows the bond graph model of space robot interacting with the environment.

The environment is assumed to be modeled by a spring and damper in parallel, and represented by C_{88} and R_{90} , respectively, in Fig. 10.30. The environment damping in the X direction is represented by the R_{83} element. Flow-activated C elements are used as flow detectors and soft pads are used to remove differential causalities. In Fig. 10.30 some bonds are not numbered to retain clarity in the bond graph.

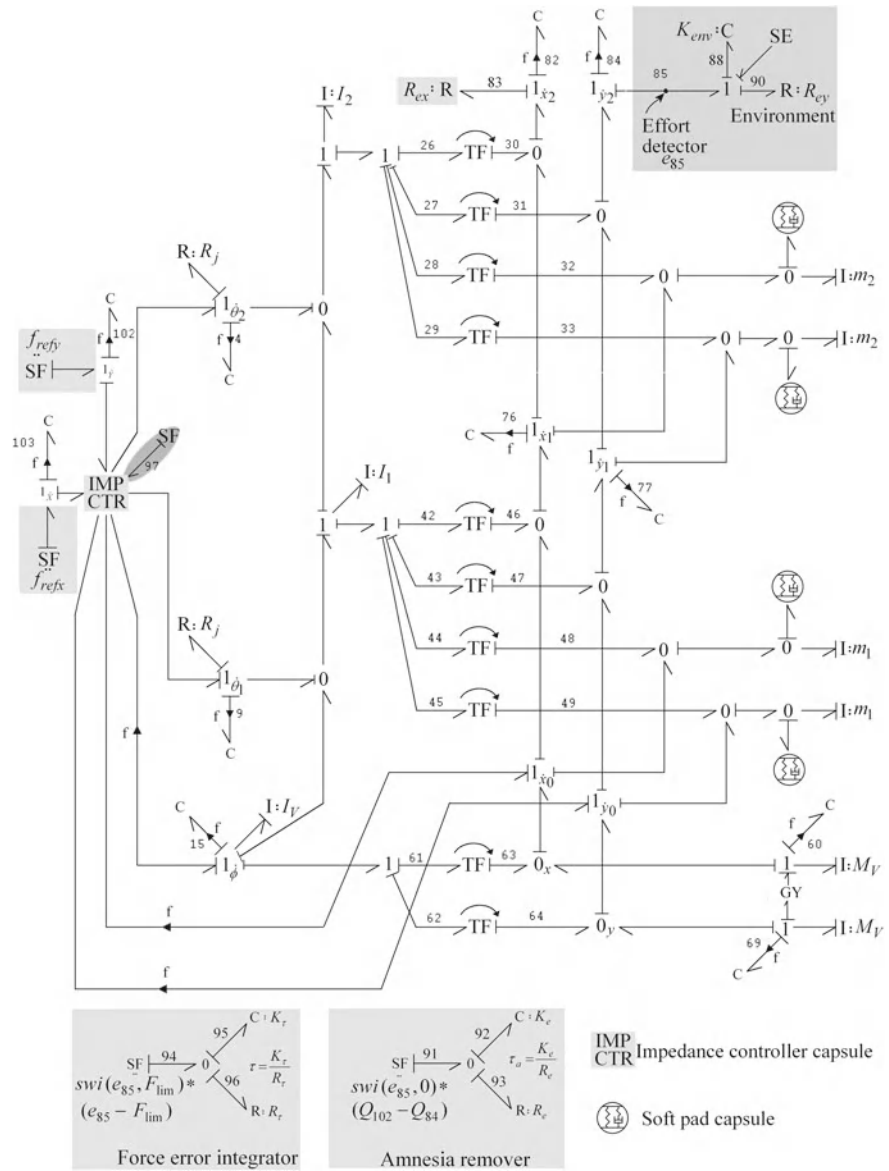


Fig. 10.30 Bond graph model of a two DOF planar space robot

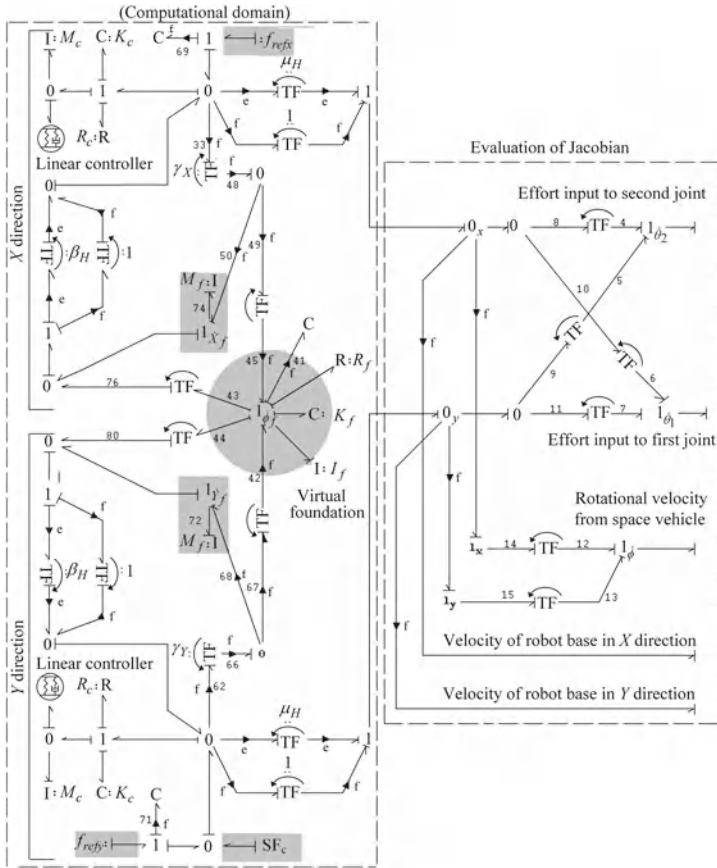


Fig. 10.31 Bond graph model of a two DOF planar space robot controller

10.7.4.1 Controller Design

The bond graph model of a two DOF planar space robot controller is shown in Fig. 10.31. It comprises two main parts. The first part involves the calculation of Jacobian, and the second part is the modeling of the virtual foundation. Both models are represented in the inertial frame. The virtual foundation is modeled similar to that in the one translational DOF space robot, discussed in Sect. 10.7.3.

10.7.4.2 Evaluation of Jacobian

Let us assume that the controller works in the inertial frame and it is provided with reference velocity command in inertial frame. Velocities from joint space are mapped into inertial space using the Jacobian of the forward kinematics. The difference in the

reference and inertial velocity is computed and fed to the controller, which in turn provides the joint torques. The Jacobian of the forward kinematics can be calculated in bond graph as

$$\begin{bmatrix} \text{Tip velocity of} \\ \text{robot with respect} \\ \text{to absolute frame} \end{bmatrix} = \begin{bmatrix} \text{Velocity of robot} \\ \text{base with respect} \\ \text{to absolute frame} \end{bmatrix} + \begin{bmatrix} \text{Velocity of robot tip} \\ \text{with respect to robot} \\ \text{base due to joint motion} \end{bmatrix} + \begin{bmatrix} \text{Linear velocity of robot} \\ \text{tip due to angular} \\ \text{motion of robot base} \end{bmatrix} \quad (10.83)$$

All the above-mentioned velocities are expressed in absolute frame. In equation form, this relation can be written as

$${}^A({}^A V_3) = {}^A({}^A V_0) + {}^A R {}^0({}^0 V_3) + {}^A_V R (-{}^V R {}^0({}^0 P_3) \times {}^V({}^A \omega_V)) \quad (10.84)$$

In the planar case discussed here this relation can be worked out directly from Eq. 10.36 as follows:

$$\begin{aligned} \begin{bmatrix} \dot{X}_{tip} \\ \dot{Y}_{tip} \end{bmatrix} &= \begin{bmatrix} \dot{X}_{CM} \\ \dot{Y}_{CM} \end{bmatrix} \\ &+ \begin{bmatrix} -r\dot{\phi} \sin \phi - l_1(\dot{\phi} + \dot{\theta}_1) \sin(\phi + \theta_1) - l_2(\dot{\phi} + \dot{\theta}_1 + \dot{\theta}_2) \sin(\phi + \theta_1 + \theta_2) \\ r\dot{\phi} \cos \phi + l_1(\dot{\phi} + \dot{\theta}_1) \cos(\phi + \theta_1) + l_2(\dot{\phi} + \dot{\theta}_1 + \dot{\theta}_2) \cos(\phi + \theta_1 + \theta_2) \end{bmatrix} \\ \begin{bmatrix} \dot{X}_{tip} \\ \dot{Y}_{tip} \end{bmatrix} &= \begin{bmatrix} \dot{X}_{CM} - r\dot{\phi} \sin \phi \\ \dot{Y}_{CM} + r\dot{\phi} \cos \phi \end{bmatrix} \\ &+ \begin{bmatrix} -l_1 \sin(\phi + \theta_1) - l_2 \sin(\phi + \theta_1 + \theta_2) & -l_2 \sin(\phi + \theta_1 + \theta_2) \\ l_1 \cos(\phi + \theta_1) + l_2 \cos(\phi + \theta_1 + \theta_2) & l_2 \cos(\phi + \theta_1 + \theta_2) \end{bmatrix} \begin{Bmatrix} \dot{\theta}_1 \\ \dot{\theta}_2 \end{Bmatrix} \\ &+ \begin{bmatrix} -l_1 \sin(\phi + \theta_1) - l_2 \sin(\phi + \theta_1 + \theta_2) \\ l_1 \cos(\phi + \theta_1) + l_2 \cos(\phi + \theta_1 + \theta_2) \end{bmatrix} \{\dot{\phi}\} \end{aligned} \quad (10.85)$$

From Eq. 10.85 the terms for Eq. 10.84 can be easily identified as

$${}^A({}^A V_0) = \begin{bmatrix} \dot{X}_{CM} - r\dot{\phi} \sin \phi \\ \dot{Y}_{CM} + r\dot{\phi} \cos \phi \end{bmatrix} \quad (10.86)$$

$${}^A R {}^0({}^0 V_3) = \begin{bmatrix} -l_1 \sin(\phi + \theta_1) - l_2 \sin(\phi + \theta_1 + \theta_2) & -l_2 \sin(\phi + \theta_1 + \theta_2) \\ l_1 \cos(\phi + \theta_1) + l_2 \cos(\phi + \theta_1 + \theta_2) & l_2 \cos(\phi + \theta_1 + \theta_2) \end{bmatrix} \begin{Bmatrix} \dot{\theta}_1 \\ \dot{\theta}_2 \end{Bmatrix} \quad (10.87)$$

$${}^A_V R (-{}^V R {}^0({}^0 P_3) \times {}^V({}^A \omega_V)) = \begin{bmatrix} -l_1 \sin(\phi + \theta_1) - l_2 \sin(\phi + \theta_1 + \theta_2) \\ l_1 \cos(\phi + \theta_1) + l_2 \cos(\phi + \theta_1 + \theta_2) \end{bmatrix} \{\dot{\phi}\} \quad (10.88)$$

- The first term in Eq. 10.84 (i.e., Eq. 10.86) can be obtained from $1_{\dot{x}_0}$ and $1_{\dot{y}_0}$ junction of the bond graph in Fig. 10.30.
- The second term in Eq. 10.84 is calculated by defining the transformers from $1_{\dot{\theta}_1}$ and $1_{\dot{\theta}_2}$ junctions with modulus obtained in Eq. 10.87 and shown in Fig. 10.31 as

$$TF6-10 = -l_1 \sin(\phi + \theta_1) - l_2 \sin(\phi + \theta_1 + \theta_2) \quad (10.89)$$

$$TF7-11 = l_1 \cos(\phi + \theta_1) + l_2 \cos(\phi + \theta_1 + \theta_2) \quad (10.90)$$

$$TF4-8 = -l_2 \sin(\phi + \theta_1 + \theta_2) \quad (10.91)$$

$$TF5-9 = l_2 \cos(\phi + \theta_1 + \theta_2) \quad (10.92)$$

- The third term in Eq. 10.84, is calculated by defining the transformers from $1_{\dot{\phi}}$ junction with modulus obtained from Eq. 10.88 as

$$TF12-14 = -l_1 \sin(\phi + \theta_1) - l_2 \sin(\phi + \theta_1 + \theta_2) \quad (10.93)$$

$$TF13-15 = l_1 \cos(\phi + \theta_1) + l_2 \cos(\phi + \theta_1 + \theta_2) \quad (10.94)$$

10.7.4.3 Modeling of the Virtual Foundation

In order to modulate the impedance at the robot tip and environment interaction point, a virtual foundation is assumed. The foundation has a rotational compliance K_f , damping R_f , and rotational inertia I_f . Drawing analogy from the space vehicle, the virtual foundation velocity in X and Y direction is also considered. It is determined by translational inertia M_f of virtual foundation. The tip velocity of the robot \dot{X}_{tipf} , and \dot{Y}_{tipf} due to motion of the virtual foundation can be found similar to Eq. 10.36 as

$$\begin{aligned} \dot{X}_{tipf} = \dot{X}_f - [r \sin \phi_f + l_1 \sin(\phi_f + \theta_1) + l_2 \sin(\phi_f + \theta_1 + \theta_2)]\dot{\phi}_f \\ - [l_1 \sin(\phi_f + \theta_1) + l_2 \sin(\phi_f + \theta_1 + \theta_2)]\dot{\theta}_1 \end{aligned} \quad (10.95)$$

$$- [l_2 \sin(\phi_f + \theta_1 + \theta_2)]\dot{\theta}_2 \quad (10.96)$$

$$\begin{aligned} \dot{Y}_{tipf} = \dot{Y}_f + [r \cos \phi_f + l_1 \cos(\phi_f + \theta_1) + l_2 \cos(\phi_f + \theta_1 + \theta_2)]\dot{\phi}_f \\ + [l_1 \cos(\phi_f + \theta_1) + l_2 \cos(\phi_f + \theta_1 + \theta_2)]\dot{\theta}_1 \end{aligned} \quad (10.97)$$

$$+ [l_2 \cos(\phi_f + \theta_1 + \theta_2)]\dot{\theta}_2 \quad (10.98)$$

Here, ϕ_f is the rotation of the virtual foundation. If it is assumed that the controller overwhelms the robot dynamics, then neglecting the coefficients of $\dot{\theta}_1$ and $\dot{\theta}_2$ in Eqs. 10.95 and 10.97 we get

$$\dot{X}_{tipf} = \dot{X}_f - [r \sin \phi_f + l_1 \sin(\phi_f + \theta_1) + l_2 \sin(\phi_f + \theta_1 + \theta_2)]\dot{\phi}_f \quad (10.99)$$

$$\dot{Y}_{tipf} = \dot{Y}_f + [r \cos \phi_f + l_1 \cos(\phi_f + \theta_1) + l_2 \cos(\phi_f + \theta_1 + \theta_2)]\dot{\phi}_f \quad (10.100)$$

Using Eqs. 10.99 and 10.100, the transformer moduli $TF43-76$, and $TF44-80$ (as shown in Fig. 10.31) can be written as

$$TF43-76 = -[r \sin \phi_f + l_1 \sin(\phi_f + \theta_1) + l_2 \sin(\phi_f + \theta_1 + \theta_2)] \quad (10.101)$$

$$TF44-80 = [r \cos \phi_f + l_1 \cos(\phi_f + \theta_1) + l_2 \cos(\phi_f + \theta_1 + \theta_2)]. \quad (10.102)$$

In order to modulate the impedance at the interaction point of the robot tip and the environment, the linear and rotational velocity of the virtual foundation is fed to the controller. To find this velocity in X and Y direction, the following transformer moduli are defined.

$$TF45-49 = TF43-76, \quad (10.103)$$

$$TF42-67 = TF44-80, \quad (10.104)$$

$$TF48-33 = \gamma_X, \quad (10.105)$$

$$TF66-62 = \gamma_Y. \quad (10.106)$$

The bonds having transformer with modulus γ_X and γ_Y represent foundation compensation gain in X and Y directions respectively. These bonds are flow activated as they carry the velocity signal. The other parts of computational domain such as linear controller, and junction structure are the same as defined for translational DOF space robot.

10.7.4.4 Simulation Results

Let us assume that the reference displacement command for the robot tip is a circle of radius R . Then the tip coordinates will be given as

$$X_{ref}(t) = -R \cos(\omega t) + X_0 \quad (10.107)$$

$$Y_{ref}(t) = R \sin(\omega t) + Y_0 \quad (10.108)$$

Here, (X_0, Y_0) is the center of the circular reference circle. The corresponding reference velocity command is given by

$$f_{refx} = R \omega \sin(\omega t) \quad (10.109)$$

$$f_{refy} = R \omega \cos(\omega t) \quad (10.110)$$

Let a space structure be located parallel to the absolute X axis as shown in Fig. 10.29. So, when the tip follows the reference trajectory its motion will be constrained in absolute Y direction. The location of the space structure (Y_w) with respect to inertial frame is specified as

$$Y_w = Y_{tip} + y_{ftip} \quad (10.111)$$

where Y_{tip} is the location of tip initially with respect to absolute frame and y_{ftip} is the location of space structure from the initial tip position. Thus, Y direction will be the direction of force control. In the bond graph model using a swi function a condition is specified that, the environment acts only when tip crosses the space structure, i.e.,

$$K_{en} = \text{swi}(Q_{84}, Y_w) (K_{env})$$

where Q_{84} is the position of the tip in the Y direction. As there is no obstruction to the movement of the tip in X direction $\gamma_X = 1.0$ is considered. The friction in X and Y directions may or may not be present.

The heuristic expression for gain modulation for impedance control in the Y direction is given by

$$\gamma_y(F, F_{lim}, t) = 1 - \text{swi}(F(t), F_{lim})[K_{ini} + K_{GP}(F(t) - F_{lim}) + K_{GI} * Y(t)] \quad (10.112)$$

where $F(t)$ is the actual contact force obtained from force sensor, F_{lim} is the limiting value of the force specified, K_{ini} is constant, K_{GP} is a proportional gain term, K_{GI} is an integral gain term, and $Y(t)$ is given by

$$Y(t) = \text{swi}(F(t), F_{lim})e^{-\tau t} \int_{t_i}^t e^{\tau \xi} (F(\xi) - F_{lim})d\xi \quad (10.113)$$

Here, τ is a gain relaxation term and t_i is the time when force control is initiated. The expression $Y(t)$ integrates the difference in the interaction force and the force limit to smoothen any sharp change in the variation of impedance. The time constant τ can be adjusted for obtaining the desired force recovery time.

From the part bond graph shown in Fig. 10.30, the integral expression $Y(t)$ (Eq. 10.113) can be obtained as the state or charge of the error integrating C_{95} element. The input to the part bond graph is given by

$$SF_{94} = \text{swi}(e_{85}, F_{lim})(e_{85} - F_{lim}) \quad (10.114)$$

Then $Y(t)$ can be identified as the

$$Y(t) = \text{swi}(e_{85}, F_{lim})Q_{95} \quad (10.115)$$

Here, e_{85} is the force of interaction between the robot tip and the environment as measured by the force sensor.

As discussed for one translational DOF space robot, the amnesia is removed in a two-stage process consisting of error recording and error correction phase. Amnesia removal can be represented by part a bond graph as shown in Fig. 10.30. The input flow source SF_{91} is computed as the difference of the position ($Y_{ref} - Y_\xi$). In the bond graph, $Y_{ref} = Q_{102}$, and $Y_\xi = Q_{84}$. Thus SF_{91} is given by

$$SF_{91} = \text{swi}(e_{85}, F_{\text{lim}})(Q_{102} - Q_{84}) \quad (10.116)$$

The C_{92} element in the bond graph is the integrator and the R_{93} element provides the first order relaxation dynamics. The $\text{swi}(e_{85}, F_{\text{lim}})$ ensures that the positional error $(Q_{102} - Q_{84})$ is integrated by C_{92} element for the period only when $e_{85} \geq F_{\text{lim}}$, i.e., during the interaction phase. The velocity correction input is given by

$$SF_{97} = SF_c = \text{swi}(F_{\text{lim}}, e_{85}) G_e Q_{92} \quad (10.117)$$

where $Q_{92} = Y_a(t)$. Here $Y_a(t)$ is defined in the same way as in Eq. 10.78 for one translational DOF space robot. The switch function (swi) will ensure that SF_c will be generated only when $e_{85} < F_{\text{lim}}$, i.e., the end effector is in non-interacting phase. Q_{92} is the state of the C_{92} element, which provides the integrated value of the positional error. Thus the end-effector/environment contact force $F(t)$ becomes

$$F(t) = [0 \ F_y \ 0]^T$$

with F_y given as

$$F_y = \begin{cases} 0, & \text{if } Y \leq Y_w \text{ (No contact)} \\ K_{en}(Y - Y_w), & \text{if } Y > Y_w \text{ (Contact)} \end{cases}$$

The initial robot configuration is specified as $(\theta_1, \theta_2) = (\frac{\pi}{2}, \frac{\pi}{3})$ rad. Let us assume that the frames $\{A\}$ and $\{V\}$ are coincident. The initial tip location with respect to the absolute frame is obtained from Eq.10.34 as

$$[X_{tip0} \ Y_{tip0}]^T = [-0.1598 \ 0.55]^T$$

The center of the circular trajectory can be calculated by substituting $t = 0$ in Eqs. 10.107 and 10.108 as

$$[X_0 \ Y_0]^T = [0.0424 \ 0.55]^T$$

The parameters used for simulation are given in Table 10.5.

Figure 10.32a shows the plot of the reference tip X displacement versus reference tip Y displacement, and actual tip X displacement versus actual tip Y displacement. It is seen from this figure that the end effector closely tracks the reference trajectory in the X and Y directions until contact with environment is made. At contact the robot smoothly ceases to track the Y component of the reference trajectory. It can be seen that the transient forces incurred during the transition from unconstrained to constrained motion are within the set bounds.

Figure 10.32b shows the graph for the plot of reference and actual Y tip displacement versus time. From Fig. 10.32b it is seen that the end effector initially penetrates

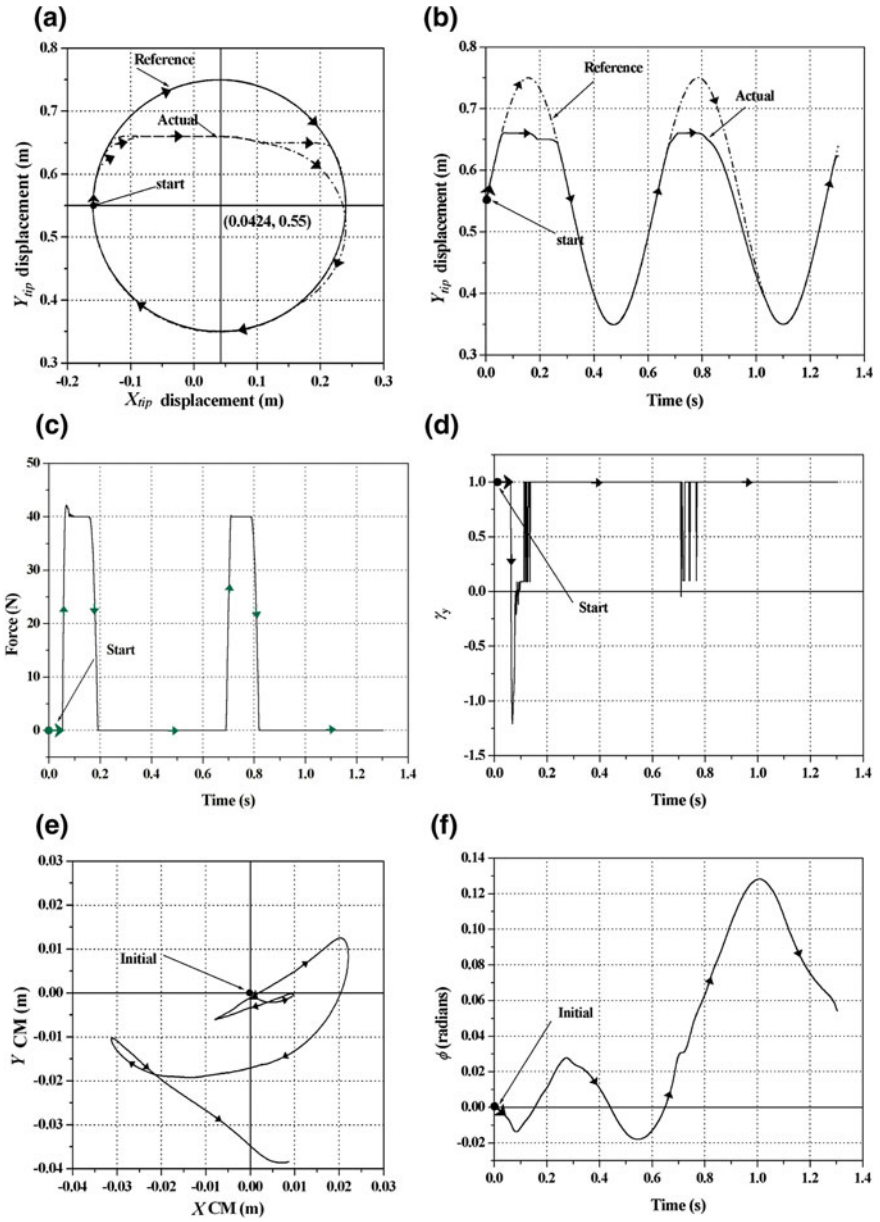


Fig. 10.32 a Plot of reference and actual tip Y displacement versus reference X displacement. b Plot of reference and actual tip Y displacement versus time. c Plot of contact force versus time. d Plot of compensation gain versus time. e Plot of CM of base. f Plot of Base rotation versus time

Table 10.5 Parameters used in space robot modeling

Parameter	Value
Link mass	$m_1 = 15.6828 \text{ kg}; m_2 = 11.7621 \text{ kg}$
Link length	$l_1 = 0.4 \text{ m}; l_2 = 0.3 \text{ m}$
Link Inertia	$I_1 = 0.2153 \text{ kg m}^2; I_2 = 0.0929 \text{ kg m}^2$
Location of robot base from vehicle CM	$r = 0.1 \text{ m}$
Reference circle radius	$R = 0.2 \text{ m}$
Input reference velocity angular velocity	$\omega = 10 \text{ rad/s}$
Controller	$I_c = 1 \text{ kg}; K_c = 1e5 \text{ N/m}; R_c = 1e3 \text{ N/(m/s)}$
Environment stiffness	$K_{env} = 4000.0 \text{ N/m}$
Interaction force limit	$F_{lim} = 40 \text{ N}$
Gain modulation	$K_{ini} = 0.9; K_{GP} = 0.6; K_{GI} = 0.4$
Virtual foundation	$I_f = 40 \text{ kg m}^2; R_f = 1.0e2 \text{ Nm/(rad/s)};$ $K_f = 1.0e3 \text{ Nm/rad}; M_f = 200 \text{ kg}$
Space vehicle base	$M_V = 200.0 \text{ kg}; I_V = 40.0 \text{ kg m}^2$
Location of space structure (virtual barrier) from robot tip	$y_{ftip} = 0.1 \text{ m}$
Force error integration bond graph	$K_\tau = 100 \text{ N/m}; R_\tau = 80 \text{ N/(m/s)};$
Feed-forward gains	$\mu_H = 10; \beta_H = 10$
Amnesia removal part bond graph	$K_e = 100.0 \text{ N/m}; R_e = 60.0 \text{ N/(m/s)}$
Gain used for correcting reference trajectory to remove amnesia	$G_e = 600.0$
Motor inertias	$I_m = 0.001 \text{ kg m}^2$
Joint resistances	$R_j = 0.1 \text{ Nm/(rad/s)}$

the space structure, located at a distance of 0.1 m from initial end-effector position, since limit force is not reached. Once limit force is reached the motion of end effector gets arrested and when the reference trajectory command starts receding the actual tip also starts retreating till it reaches the space structure position. Thus a small dip is seen in the actual tip trajectory as seen in the case of one translational DOF space robot discussed in Sect. 10.7.3.4.

Figure 10.32c shows the plot for force by the environment versus time. In this figure, it is seen that at the point where reference trajectory meets the constraint surface (environment), the robot undergoes an abrupt transition from unconstrained to constrained motion. Also, initially the force developed exceeds the force limit by a small amount, due to the inertia of the system. This is also due to the fact that, in the second cycle the velocity with which the end effector approaches the constraint surface is reduced. This effect is not seen in the second cycle. From Fig. 10.32b, c it is seen that when the reference trajectory in Y direction starts retreating, the contact force also begins to fall. When the tip disengages from the space structure at 0.1 m from initial tip position, the contact force becomes zero.

Figure 10.32d shows the plot for compensation gain in Y direction (γ_Y) versus time. Figure 10.32e shows the plot for CM of base. Figure 10.32f shows the plot for base rotation versus time. From Fig. 10.32e, f it is seen that, due to the motion of

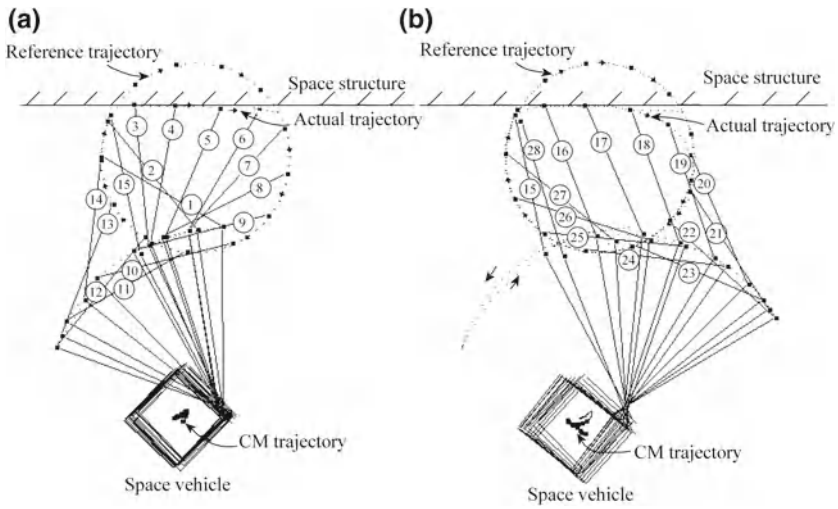
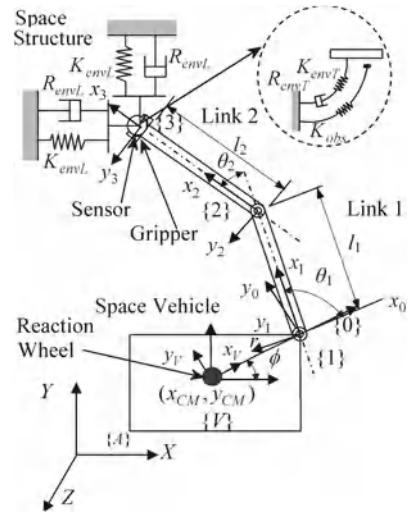


Fig. 10.33 a Animation of space robot for first cycle. b Animation of space robot for second cycle

Fig. 10.34 Schematic diagram of two DOF space robot on virtual torsional foundation



base after some time, the space structure will not remain in the workspace of robot. Figure 10.33a, b shows the animation frames of the space robot. Figure 10.33a shows the animation for the first cycle, whereas Fig. 10.33b shows the animation for the second cycle.

10.7.5 Torque Control of a Two DOF Planar Space Robot

Let us consider a two DOF planar space robot interacting with the environment which may be a space structure as shown in Fig. 10.34. Let the end effector have only torque interaction with the environment, then torque controller is needed to limit the interaction torques between robot tip and environment. The following section first discusses the modeling of two DOF planar space robot followed by controller design.

10.7.5.1 Physical and Bond Graph Model of Space Robot

Let the space robot have single manipulator with revolute joints and in open kinematic chain configuration. In Fig. 10.34 $\{A\}$ represents the absolute frame, $\{V\}$ represents the vehicle frame, $\{0\}$ frame is located at the base of the robot, $\{1\}$, $\{2\}$ are the frames located at first and second joints respectively. The frame $\{3\}$ locates the tip of the robot. Let l_1 be the length of the first link, l_2 be the length of the second link, and r be the distance between the robot base and CM of the vehicle. Let ϕ represent the rotation of vehicle frame with respect to an absolute frame, and θ_1 , and θ_2 be the joint angles. Let X_{CM} and Y_{CM} be the coordinates of the CM of the vehicle with respect to the absolute frame. The kinematic relations for the tip velocity of robot in X and Y directions can be written as

$$\begin{bmatrix} \dot{X}_{tip} \\ \dot{Y}_{tip} \end{bmatrix} = \begin{bmatrix} \dot{X}_{CM} \\ \dot{Y}_{CM} \end{bmatrix} + \begin{bmatrix} -r\dot{\phi} \sin \phi - l_1(\dot{\phi} + \dot{\theta}_1) \sin(\phi + \theta_1) - \\ l_2(\dot{\phi} + \dot{\theta}_1 + \dot{\theta}_2) \sin(\phi + \theta_1 + \theta_2) \\ r\dot{\phi} \cos \phi + l_1(\dot{\phi} + \dot{\theta}_1) \cos(\phi + \theta_1) + \\ l_2(\dot{\phi} + \dot{\theta}_1 + \dot{\theta}_2) \cos(\phi + \theta_1 + \theta_2) \end{bmatrix} \quad (10.118)$$

Using Eq. 10.118 the different transformer moduli for the bond graph modeling of space robot can be derived. To illustrate the efficacy of virtual foundation to control the torque let the torque interaction between space robot tip and environment be assumed as that of drilling a hole on space structure by a drilling device held by the end effector. The tip angular velocity with respect to absolute frame X axis is given as

$$\dot{\theta}_{tip} = \dot{\phi} + \dot{\theta}_1 + \dot{\theta}_2 + \dot{\theta}_m \quad (10.119)$$

where $\dot{\theta}_m$ is the speed of the drilling motor. Equations 10.118 and 10.119 are used to draw the bond graph model of space robot as shown in Fig. 10.35. The resistance offered by the space structure against the drilling tool is modeled by a torsional spring of stiffness K_{envT} and a rotational damper representing the frictional resistance during drilling operation by R_{envT} connected in series as shown in Fig. 10.34. Further, to study the efficacy of the torque controller, it is assumed that an obstruction (i.e., inclusion) is encountered by the drill bit in the process of drilling after a rotation of angle θ_{obs} , from the initial tip orientation. This inclusion is modeled by a spring of stiffness K_{obs} . It is also assumed that the drilling point is fixed in the space structure

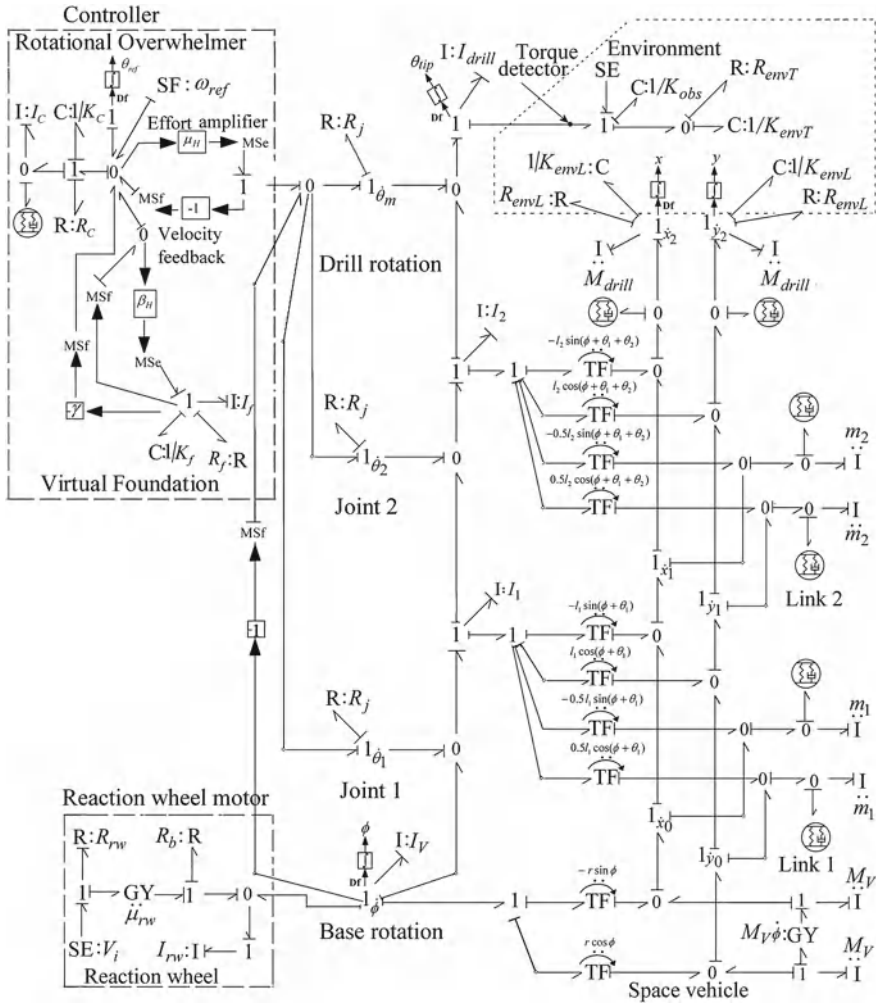


Fig. 10.35 Bond graph modeling of a two DOF planer space robot with controller for torque control

and the end effector does not have translatory motion in XY plane. This constraint for X and Y directions is modeled by a spring of stiffness K_{envL} and a damper of resistance R_{envL} in parallel. The drill is modeled as a link of zero radius but definite mass (M_{drill}) and definite inertia (I_{drill}), i.e., a mass is attached at the tip of the second link. The inertia elements I_1 and I_2 represent the rotational inertia of the motor and link. $1_{\dot{x}_1}$ and $1_{\dot{y}_1}$ junctions represent the first link tip velocities, whereas $1_{\dot{x}_2}$ and $1_{\dot{y}_2}$ junctions represent the second link tip velocities.

10.7.5.2 Controller Design

Equation 10.119 gives the tip velocity of the drill with respect to absolute frame. The information of $\dot{\theta}_{tip}$ is given to the torque controller. It is to be noted that in order to compensate for the base rotation only flow information of base is given to controller. Bond graph model of controller with space robot is shown in Fig. 10.35. The controller consists of a virtual foundation and a rotational overwhelmer along with an effort amplifier and velocity feedback. The virtual foundation has rotational inertia (I_f), torsional compliance (K_f), and rotational damping resistance (R_f), whereas rotational overwhelmer has rotational overwhelming inertia (I_c), a torsional spring of compliance (K_c), and a rotational damper of damping resistance (R_c). The foundation compensation gain (γ) from the virtual foundation to the rotational overwhelmer modulates the impedance at the robot tip and the environment interaction point. Since torque interaction at tip is considered in the modeling of the virtual foundation only rotational inertia of the virtual foundation is considered. The foundation rotation is assumed to be about the Z direction.

Due to interaction of the robot tip with the environment, an interaction torque is generated at the robot tip and the environment interaction port. This torque gets transmitted to the base of the space vehicle, and its attitude gets disturbed. For the space vehicle, the attitude disturbance permitted is of the order of $\pm 0.5^\circ$ [15]. This is required to maintain the communication links and orientation of the solar panels. In order to restore the attitude of space vehicle, a simple reaction wheel is used, as shown in Fig. 10.34. Bond graph representation of the reaction wheel along with the driving motor is shown in Fig. 10.35. In this figure I_{rw} represents the reaction wheel inertia and V_i represents the voltage supplied to reaction wheel motor. A control law is devised for the attitude control of space vehicle. Let us assume that the torque applied by reaction wheel on space vehicle is

$$N = K_p(\phi_d - \phi) + K_v(\dot{\phi}_d - \dot{\phi}) \quad (10.120)$$

where K_p and K_v are the proportional and derivative gains, ϕ_d is the desired orientation of space vehicle, and ϕ is the current orientation of the space vehicle. Then the voltage supplied to the driving motor in order to generate the torque can be written as

$$\begin{aligned} V_i = & -(R_{rw}/\mu_{rw})[K_p(\phi_d - \phi) - K_v\dot{\phi} + K_i \int (\phi_d - \phi)dt] \\ & + (f_{rw} - f_V)(R_{rw}R_b/\mu_{rw} + \mu_{rw}) \end{aligned} \quad (10.121)$$

Here, f_{rw} is the angular velocity of reaction wheel and f_V is the angular velocity of vehicle, R_{rw} is reaction wheel motor resistance, μ_{rw} is torque constant for motor, and R_b is bearing resistance.

10.7.5.3 Simulation and Results

Let the reference angular trajectory of drill be assumed to be a polynomial of third degree given by Eq. 10.122 as

$$\theta(t) = \theta_0 + 3(\theta_f - \theta_0)(t/t_f)^2 - 2(\theta_f - \theta_0)(t/t_f)^3 \quad (10.122)$$

In deriving Eq. 10.122 it is assumed that (i) $\theta(0) = \theta_0$ and $\theta(t_f) = \theta_f$ and (ii) $\dot{\theta}(0) = 0$ and $\dot{\theta}(t_f) = 0$. Hence, the reference angular velocity command for the drill will be given as

$$\dot{\theta}(t) = 6(\theta_f - \theta_0) t (1 - t/t_f)/t_f^2 \quad (10.123)$$

Let a virtual space structure be located parallel to the XY plane. Then the tip angular motion (drill motion) will be constrained against rotation about the absolute Z direction. It is to be mentioned that the axial force, due to axial motion of the drill is not considered as it will not be contributing towards torque in the XY plane. Let the heuristic expression for compensation gain modulation for torque control be given as

$$\gamma(N, N_{\text{lim}}, t) = 1 - \text{swi}(N(t), N_{\text{lim}})[K_{\text{ini}} + K_{GP}(N(t) - N_{\text{lim}}) + K_{GI} Y_N(t)] \quad (10.124)$$

where $N(t)$ is the actual contact torque obtained from torque detector; N_{lim} is the limiting value of the torque specified. Also, in Eq. 10.124, K_{ini} is a constant, K_{GP} is a proportional gain term, and K_{GI} is an integral gain term. Equation 10.124 represents a proportional integral control. The swi defines the switch function. It implies that when, $N(t) \geq N_{\text{lim}}$, $\text{swi}(N(t), N_{\text{lim}}) = 1$, so $\gamma < 1$ hence, impedance controller works in torque control mode and when $N(t) < N_{\text{lim}}$, $\text{swi}(N(t), N_{\text{lim}}) = 0$, so $\gamma = 1$ hence, impedance controller works in trajectory control mode.

The term $Y_N(t)$ is given by

$$Y_N(t) = \text{swi}(N(t), N_{\text{lim}}) e^{-\tau t} \int_{t_i}^t e^{\tau \xi} (N(\xi) - N_{\text{lim}}) d\xi \quad (10.125)$$

where τ is a gain relaxation term and t_i is the time when torque control is initiated. The expression $Y_N(t)$ integrates the difference in the interaction torque and the torque limit to smoothen any sharp change in variation of impedance. Here, swi function will ensure that torque difference $(N(\xi) - N_{\text{lim}})$ is integrated during interaction phase only when robot tip interacts with the environment.

The end-effector/environment contact torque $N(t)$ can be represented as

$$N(t) = [0 \ 0 \ N_Z]^T \quad (10.126)$$

Table 10.6 Parameters used in space robot modeling and torque control

Parameter	Value
Controller	$I_c = 5 \text{ kg}; K_c = 1000 \text{ N/m}; R_c = 100 \text{ N/(m/s)}$
Environment stiffness	$K_{envT} = 1000.0 \text{ Nm/rad}; K_{envL} = 40,000 \text{ N/m}$
Environment resistance	$R_{envT} = 100 \text{ Nm/(rad/s)}; R_{envL} = 0.1 \text{ Ns/m}$
Drilling machine parameters	$M_{drill} = 0.5 \text{ kg}, I_{drill} = 0.001 \text{ kg m}^2$
Location of inclusion from initial drill tip position	$\theta_{obs} = 0.05 \text{ rad}$
Stiffness of inclusion	$K_{obs} = 3,000 \text{ Nm/rad}$
Interaction torque limit	$N_{lim} = 2 \text{ Nm}$
Gain modulation	$K_{ini} = 0.5; K_{GP} = 20; K_{GI} = 20$
Virtual foundation parameters	$I_f = 2; R_f = 0.5; K_f = 0.5$
Space vehicle base	$M_V = 200.0 \text{ kg}; I_V = 40.0 \text{ kg m}^2$
Feed-forward gains	$\mu_H = 10; \beta_H = 10$
Joint resistances	$R_j = 0.1 \text{ Nm/(rad/s)}$
Reference trajectory final position	$\theta_f = 5 \text{ rad}$
Time duration for reference velocity command	$T_f = 6 \text{ s}$
Attitude controller parameters	
Control law gains for reaction wheel motor	$K_p = 400.0, K_v = 100.0, K_i = 35$
Reaction wheel motor resistance	$R_{rw} = 0.2 \text{ Ohm}$
Reaction wheel inertia	$I_{rw} = 0.5 \text{ kg m}^2$
Torque constant of reaction wheel motor	$\mu_{rw} = 0.9 \text{ Nm/A}$
Reaction wheel bearing resistance	$R_b = 0.02 \text{ Nm/(rad/s)}$

where, N_Z is given by

$$N_Z = \begin{cases} 0, & \text{if } \theta \leq \theta_w \text{ (No contact)} \\ K_{envT} \theta - \theta_w, & \text{if } \theta > \theta_w \text{ (Contact)} \end{cases} \quad (10.127)$$

The initial robot configuration is defined by $(\theta_1, \theta_2) = (\pi/2, \pi/3)$ rad. The frame $\{A\}$ and $\{V\}$ are assumed to be coincident. Thus, the initial tip location with respect to the absolute frame will be given as $\theta_{tip} = (5/6)\pi$ rad. The parameters used in simulation are shown in Table 10.6.

For the selected simulation parameters the average power required for first joint, second joint, and drilling motor is approximately 10 W, whereas for reaction wheel motor power required is 0.01 W. Figure 10.36a shows the variation of the tip rotation with time [19]. Figure 10.36b shows the variation of reference angular velocity command with time. Figure 10.36c shows the variation of reaction torque from the environment with time.

From the plot of Fig. 10.36c, it is seen that, torque controller is able to limit the interaction torque to 2 Nm. Due to environment interaction at the tip, the attitude of the space vehicle deviates from the initial orientation. When this deviation becomes

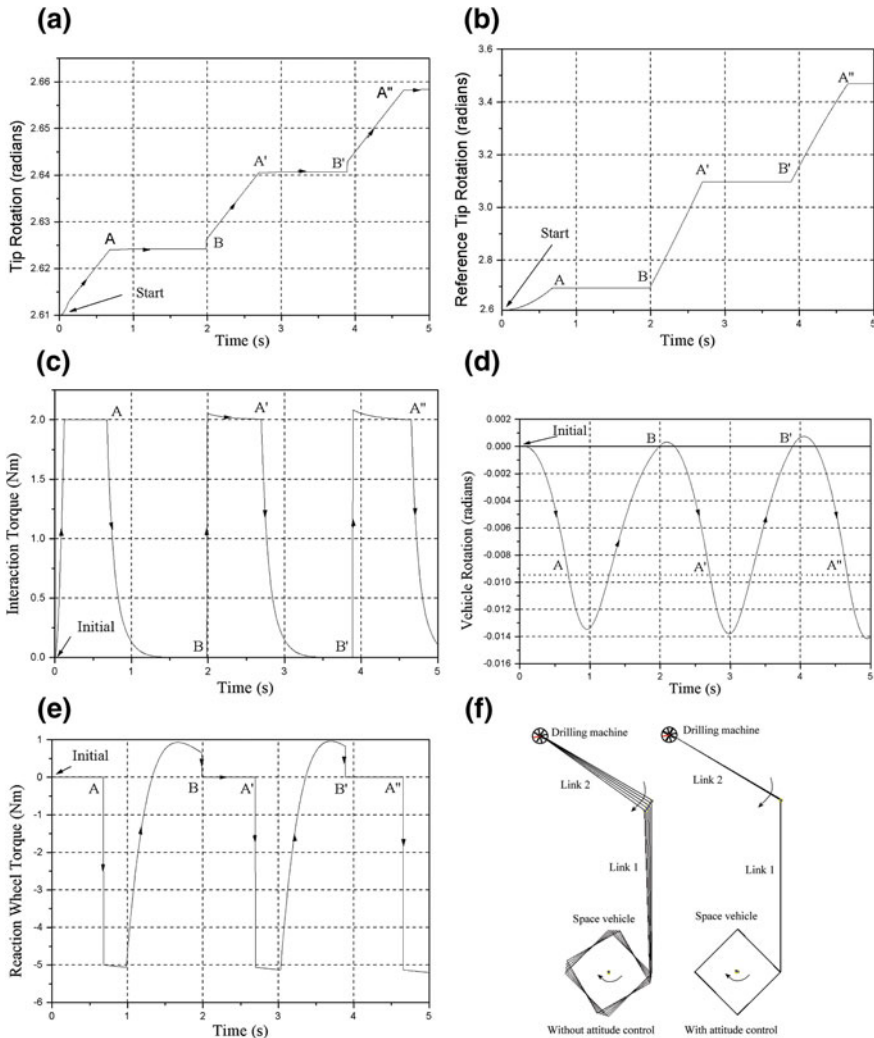


Fig. 10.36 **a** Variation of tip rotation with time. **b** Variation of reference tip rotation with time. **c** Variation of interaction torque with time. **d** Variation of space vehicle rotation with time. **e** Variation of torque supplied by reaction wheel to space vehicle with time. **f** Animation for two DOF space robot for torque control operation without attitude control and with attitude control

more than 0.009 rad (approximately 0.5°) the reference angular velocity command is switched off, and the attitude controller is switched on in order to bring back the vehicle attitude to the initial position, i.e., at $\phi = 0$ rad. Figure 10.36d shows the variation of vehicle rotation with time. From this figure it is seen that the attitude controller brings back the vehicle attitude to the initial position. During this maneuver, the reference command is switched off to avoid complications arising out of simultaneous

working of torque and attitude controller. From Fig. 10.36d it is seen that the vehicle continues to deviate by a small amount even after the reaction wheel is switched on at point A , A' , A'' in plot, or switched off at point B , B' in the plot. This deviation can be reduced if the gains used in reaction wheel control law are increased. But again, these gains cannot be increased by any amount as it will cause the saturation of the reaction wheels. It is seen from Fig. 10.36d that vehicle overshoots the desired orientation by a small angle and the tip starts interacting with the environment as soon as vehicle reaches to $\phi = 0$ orientation. Figure 10.36e shows the variation of reaction wheel torque with time. In simulation it is assumed that the reaction wheel saturates at a torque of 5 Nm. Figure 10.36f shows the animation frames for torque control operation when reaction wheel motor is switched off completely and in the case when reaction wheel motor is switched on and off as per the condition specified in simulation. It is clear from these figures that without attitude control, torque control operation cannot be carried for long durations.

10.8 Conclusions

In this chapter, we have discussed the model-based control of space robots. In particular, we have shown that hybrid force/position control law for the robot can be derived from conceptualization of an added physical system (foundation) and then effectively transferring the dynamics of the added system into an equivalent numerical model in the numerical controller domain. The error or drift accumulated during the interaction period is recovered during the non-interaction period through an amnesia removal compensational loop.

The principles developed in this chapter are applicable to other robots. The underwater robot is of particular interest because in addition to it being a nonholonomic system, it experiences a variety of external forces due to buoyancy, gravity, and fluid drag. Moreover, the acceleration of the fluid around the robot body introduces added mass in the dynamic model. Readers may refer to [1] for a bond graph model and genetic algorithm-based control of a three DOF underwater robot. One can also see [21] for a complete bond graph model and trajectory control of an autonomous underwater vehicle (AUV) manipulator system.

References

1. V. Bende, P.M. Pathak, K.S. Dixit, S.P. Harsha, Energy optimal trajectory planning of an underwater robot using a genetic algorithm. Proc. IMechE. Part I: J. Syst. Control Eng. **226**(8), 1077–1087 (2012)
2. J.J. Craig, *Introduction to Robotics: Mechanics and Control* (Addison-Wesley, Reading, 1986)
3. F. Didot, J. Dettmann, S. Losito, D. Torfs, G. Colombina, Jerico: a demonstration of autonomous robotic servicing on the mir space station. Robot. Auton. Syst. **23**, 29–36 (1998)
4. H. Goldstein, *Classical Mechanics* (Narosa Publishing House, New Delhi, 1998)

5. G. Hirzinger, B. Brunner, J. Dietrich, J. Heindl, in *Proceedings of the IEEE International Conference on Robotics and Automation*, vol. 3, pp. 2604–2611, 1994
6. N. Hogan, Impedance control: an approach to manipulation: parts I–III. *Trans. ASME J. Dyn. Syst. Meas. Control* **107**, 1–24 (1985)
7. D.C. Karnopp, D.L. Margolis, R.C. Rosenberg, *System Dynamics: Modeling and Simulation of Mechatronic Systems* (Wiley, New Jersey, 2006)
8. C.S. Kumar, Shaping the interaction behavior of manipulators through additional passive degrees of freedom: a new approach to impedance control. Ph.D. Thesis, Department of Mechanical Engineering, Indian Institute of Technology, Kharagpur, 1994
9. C.S. Kumar, A. Mukherjee, M.A. Faruqi, Some finer aspects of impedance modulation on hybrid tracking and force controlled manipulators, in *Proceedings of International Conference on Bond Graph Modeling and Simulation (ICBGM'1993)*, 1993
10. S. Mohan Kumar, Accommodation and force control in tracking and manipulation through virtual dissipative degrees of freedom. Ph.D. Thesis, Department of Mechanical Engineering, Indian Institute of Technology, Kharagpur, 1996
11. R. Mugnuolo, S. Di Pippo, P.G. Magnani, E. Re, The spider manipulation system (sms) the Italian approach to space automation. *Robot. Auton. Syst.* **23**, 79–88 (1998)
12. A. Mukherjee, R. Karmakar, A.K. Samantaray, *Bond Graph in Modeling, Simulation and Fault Identification* (CRC Press, Boca Raton, 2006) ISBN: 978-8188237968, 1420058657
13. Y. Nakamura, R. Mukherjee, Non-holonomic path planning of space robots via a bidirectional approach. *IEEE Trans. Robot. Autom.* **7**(4), 500–514 (1991)
14. M. Oda, Experiences and lessons learned from the ETS-vii robot satellite, in *Proceedings of the IEEE International Conference on Robotics and Automation*, San Francisco, CA, pp. 914–919, 2000
15. M. Oda, Y. Ohkami, Coordinated control of spacecraft attitude and space manipulators. *Control Eng. Pract.* **5**(1), 11–21 (1997)
16. P.M. Pathak, R.P. Kumar, A. Mukherjee, A. Dasgupta, A scheme for robust trajectory control of space robots. *Simul. Model. Pract. Theory* **16**, 1337–1349 (2008)
17. P.M. Pathak, A. Mukherjee, A. Dasgupta, Impedance control of space robot. *Int. J. Modell. Simul.* **26**(4), 316–322 (2006)
18. P.M. Pathak, A. Mukherjee, A. Dasgupta, Impedance control of space robots using passive degrees of freedom in controller domain. *Trans. ASME J. Dyn. Syst. Meas. Control* **127**, 564–578 (2005)
19. P.M. Pathak, Strategies for trajectory, attitude, and impedance control of space robots. Ph.D. Thesis, Department of Mechanical Engineering, I.I.T., Kharagpur, 2004
20. P.M. Pathak, A. Mukherjee, A. Dasgupta, Object oriented bond graph modeling of a space robot, in *National Conference on Machines and Mechanisms (NaCoMM)*, IIT Delhi, India, 2003
21. T. Periasamy, T. Asokan, M. Singaperumal, Investigations on the dynamic coupling in AUV-manipulator system and the manipulator trajectory errors using bond graph method. *Int. J. Syst. Sci.* **43**(6), 1104–1122 (2012)
22. P. Putz, Space robotics in Europe: a survey. *Robot. Auton. Syst.* **23**, 3–16 (1998)
23. M. Raibert, J. Craig, Hybrid position/force control of manipulators. *Trans. ASME J. Dyn. Syst. Meas. Contr.* **102**, 126–133 (1981)
24. C. Sallaberger, Canadian space robotics activities. *Acta Astronaut.* **41**(4), 239–246 (1997)
25. P.Th.L.M. Woerkom, A.K. Misra, Robotic manipulators in space: a dynamic and control perspective. *Acta Astronaut.* **38**, 411–421 (1996)

Chapter 11

Intelligent Transportation Systems

11.1 Introduction

Intelligent Transport Systems (*ITS*) associate information and communication technologies (*ICT*) to vehicles and their infrastructures in order to improve the safety, reliability, efficiency, and quality of the transport operation. The new technologies used for collecting the information from vehicle and its surrounding environment allow performing communications between vehicles (Vehicle-to-Vehicle, *V2V*), and between vehicles and static locations (Vehicle-to-Infrastructure, *V2I*). However, ITS are not restricted to road transport; they also include the *ICT* for rail, water, and air transport, including navigation systems.

Modern automotive systems are the pioneer systems where the ITS concept is introduced. Actually, many big projects related to automotive ITS are under development everywhere in the world; some of them concern:

- Use of Short-Range communications, which provide communications between the vehicle and the infrastructure in specific locations.
- Use of Wireless communication systems in the Intelligent Transport Systems and Road Transport and Traffic Telematics to provide a system of systems network connectivity.
- Use of facial recognition technology for changing the radio station in the car through continuous tracking of the driver's eye. This solution eliminates the need to take your hands off the wheel.
- Use of Continuous Air interface for Long and Medium range (*CALM*) to provide continuous communications between a vehicle and the infrastructure using a variety of communication media [6].
- Use of dynamic road information to improve driving safety and efficiency.

The railway industries introduce progressively the concept of ITS for the infrastructure, where the logical traffic signalling will use the Global System for Mobile communications (*GSM*) on high speed railways, as well as for conventional railways when interoperating across national borders.

For aeronautical applications, in order to improve professional services and services for passengers, the ITS is used in air traffic control systems, onboard telecommunication, and Internet. Maritime applications support maritime operations, including navigation, as well as safety purposes. They are present in the land side for port operation, including loading and discharging freight, routing and stocking. The ITS is present also in difficult to access areas such as submarine environment for exploration or tracking of identified target.

Intelligent autonomous vehicles is a class of intelligent transportation systems, which can be operated inside confined and private area or on existing roadway network if they follow accurately in safe condition a manned driven vehicle. Many advantages can be synthesized by using the intelligent autonomous vehicles in our daily life, and can have real impacts for society, from social, economical, and environmental point of views. They can be more reactive than human drivers, in case of dangerous driving situation, where human lives can be saved, and therefore decrease the number of road accidents originally caused by human. Intelligent autonomous vehicles can improve the traffic in term of congestion, when the number of vehicles is dense according to space motion. These vehicles can adapt their velocities and their trajectories according to the traffic status and the environment changes. The auto-control helps significantly in decreasing the emission rate of pollution gases during the vehicles mission. The gas emission depends directly or indirectly on the type of power used in these intelligent vehicles: electric, internal combustion, HCCI,...

Intelligent autonomous vehicles (*IAV*) are the logical transition of the mobile robotics to the scale of urban vehicles. Often, such vehicles have a specific design, with multi-actuated traction and steering systems. This configuration allows the system to be redundant in control, so that different scenarios can be defined to run the vehicle on a segment of the road. Multi-decentralized inputs help finding reconfigurable solutions, when an input fault is detected and isolated. In this case, the vehicle avoids the stop situation, without obstructing the traffic operation.

When talking about autonomous vehicles, it means that they run without a human driver. Due to the complexity of the environment associated to these vehicles, safety becomes increasingly important. For this, we associate a set of sensors, which are embedded on the vehicles effectively, so that collected measurements allow identifying the precise environment surrounding these vehicles in real time. Associating the word *intelligence* for the overall operation of these vehicles, means that programs are implemented to exploit the measured data of various sensors for control, monitoring, and supervision of vehicles, carrying out their tasks.

Knowing that autonomous vehicles cannot replace some scenarios done by vehicles driven manually, which is why they often drive at low speeds, so having the time for calculation, analysis, and reaction. Thus, they help significantly the human operator during the achievement of certain repetitive tasks when traffic conditions are hardened, and human error continues growing.

To improve the efficiency of intelligent and autonomous vehicle, the following information should be determined and available in real time [38]:

Fig. 11.1 Ride vehicle of Robosoft[®] in the Simserhof Fort (Bitché–Moselle–France). Courtesy: RoboSoft [33]



1. Position localization of the vehicle;
2. Kinematic and dynamic states of the vehicle;
3. Evolutive state of the environment surrounding the vehicle;
4. State of the traction and steering controls in presence of obstacles or referred targets;
5. Communication between vehicle-to-vehicle or vehicle-to-infrastructure;
6. Access to the coordinates of the trajectory.

To make a robust supervision of an intelligent autonomous vehicle, the well knowledge of the kinematic and dynamic is important, making possible monitoring and performing the global control in presence of local and external perturbations.

The control of intelligent autonomous vehicle is mainly linked with the environment state. This includes location of environment components surrounding the vehicle, such as: the ground, other vehicles, pedestrians, traffic signals, logical traffic,...

Different sensors are used for sensing the state and mapping the environment surrounding the vehicle, among them: infrared, ultrasound, radar, laser, vision,...

After collecting and associating in real time the data from embedded sensors, a technique of Simultaneous Localization And Mapping (*SLAM*) can be used to generate the accurate maneuvering of the vehicle in presence of obstacles.

In the case where the vehicle is fully autonomous, the main interest is to manage better the traffic congestion, the safety with respect to the environment. The safety is conditioned by the efficient communication between the vehicle and the other vehicles or between the vehicle and the infrastructure. Generally, communication protocol architecture is specified for vehicle-to-infrastructure communications.

Finally, combining the coordinates of the trajectory issued from the *GPS* data and from existing mapping, we can contribute significantly in guiding with high accuracy the intelligent autonomous vehicle.

Some existing full automated vehicles are developed by Robosoft[®] [33], where the *RIDE* systems have been developed to transport people inside confined space during an excursion. This modern transportation system allows to move visitors along a very attractive 1 km long gallery where a show illustrating second world war events is performed (Fig. 11.1).

Fig. 11.2 Gottwald AGV in the ECT Delta terminal, port of Rotterdam (Netherlands), during loading. Courtesy of: Gottwald Port Technology GmbH [7]



Numexia[®] [30] developed an automated container vehicle for freight transportation inside container terminals. The same company developed a new urban passenger transport vehicles, as a standard bus called Automated Passenger Vehicle (APV).

TTS group has innovated the cassette system for container terminals, in which the cassette acts as a floating buffer [45]. This way, various transport vehicles can integrate with manned and automated guided vehicles (AGVs). The TTS AGV can be steered to move in any direction, i.e., it can be conventionally steered, can move diagonally and transversally.

Gottwald Port Technology GmbH [7], based in Düsseldorf (Germany), is one of the pioneers in the development of Automated Guided Vehicles (AGVs) for use in container terminals, including the management and navigation software to control the AGV fleet. This concept is currently in use in the ECT Delta and Euromax (Figs. 11.2 and 11.3) terminals in Rotterdam port and in the CTA terminal in Hamburg port (Fig. 11.4).

Other concepts are developed in the framework of freight and person transportation by different companies all over the world and are well detailed in [38]. Among these concepts, some are supported by specific programmes of European Commission such as *InTraDE* project [9], which is the aim for improving the traffic management by reducing the congestion and space optimization by using the *IAV* system.

There is a strong need to improve the efficiency of existing transport infrastructure of seaport in North West Europe. One of the solutions is to integrate intelligent transportation systems allowing the transportation of goods in the internal traffic of the seaport. A new class of Intelligent and Autonomous Vehicles (IAVs) has been designed in the framework of Intelligent Transportation for Dynamic Environment (*InTraDE*) project funded by European Commission. These vehicles which are technologically superior to the existing Automated Guided Vehicles (AGV) in different technical aspects offer more flexibility and intelligence in maneuver in the area where the logistics operations take place. This includes the ability of pairing/unpairing enabling a pair of 1-TEU (Twenty-foot Equivalent Unit) IAVs join and transport any



Fig. 11.3 Horizontal container transport using AGVs in the ECT Euromax terminal, port of Rotterdam (Netherlands). Courtesy of: Gottwald Port Technology GmbH [7]



Fig. 11.4 Battery-driven AGV in the CTA terminal, port of Hamburg (Germany), operating in a fleet of diesel-electric AGVs. Courtesy of: Gottwald Port Technology GmbH [7]

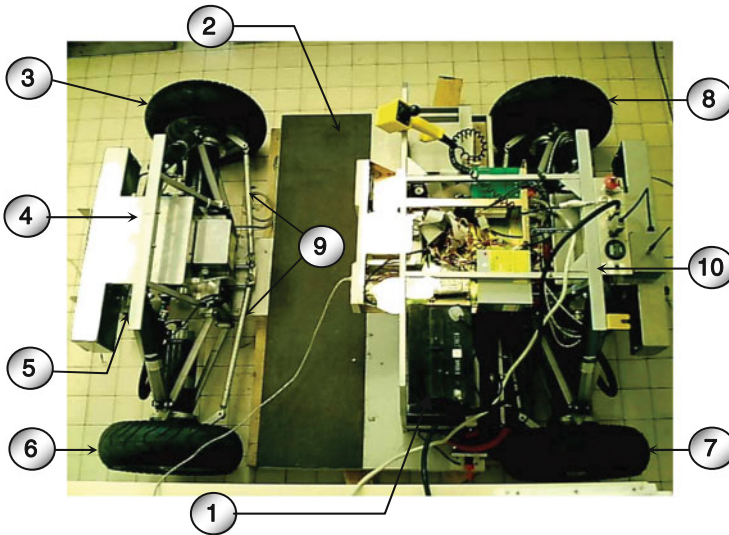


Fig. 11.5 RobuCar's prototype: 1 12 V, 60 Ah sealed seal batteries; 2 honey comb chassis; 3 front right wheel; 4 front control cabinet; 5 front steering electrical jack; 6 front left wheel; 7 rear left wheel; 8 rear right wheel; 9 rear steering electrical jack; 10 rear control cabinet

size between a 1-TEU and a 1-FFE (Forty-foot Equivalent) containers. Such design of intelligent and autonomous vehicles integrates the definition of fault detection and localization algorithms and strategies of control reconfiguration.

11.2 Modeling of a Class of Intelligent Autonomous Vehicles

The following development is done on a specific intelligent autonomous vehicle, commercialized under the name *RobuCar* and designed by the company *Robosoft*[®] [33].

11.2.1 *RobuCar's Electric Vehicle Description*

RobuCar's prototype presented in Fig. 11.5 is an over-actuated electric vehicle, with four actuated wheels and two actuated steering systems. It is a class of Multi Inputs Multi Output (*MIMO*) system with decentralized inputs.

Motor part is defined by a 4 *DC* traction motors, delivering a relatively important mass torque with a decentralized input control. Front and rear steering motions are obtained through 2 *DC* actuators, which allow the vehicle making three drive modes:

1. Single drive mode, where only the front steering is controlled during motion and the rear steering is kept static;
 2. Dual drive mode, where the front and rear steerings are controlled in opposite directions;
 3. Park mode, where the front and rear steerings are controlled in the same direction.
- **Geometry:** the geometry of this wheeled vehicle is characterized by two independent axles.

	Axle1	Axle2
Ride height (mm)	126	126
Reference ride height (mm)	126	126
Reference loaded radius (mm)	200	200
Unsprung mass by wheel (kg)	29	29
Static load-left (daN)	65.2	93.2
1/2 track-left (mm)	560.5	560.5
Wheel base-left (mm)	0	1126.5
Twin wheels	no	no

Free weight (Kg) 310

CG height empty vehicle (mm) 300
 Static vehicle initial roll (°) 0
 Static pitch (°) 0

● **Chassis:**

Sensors: Accelerometer

Name	Relative to	X (mm)	Y (mm)	Z (mm)	Treatment
Accelerometer 0	the body	780	0	220	0
Accelerometer 1	the body	0	0	350	0
Accelerometer 2	the body	800	0	350	0

Other sensors: six optical encoders < 1 mm

	X (mm)	Y (mm)	Z (mm)
GPS	780	0	550
Gyroscope	780	0	220

Position of laser sensors:

	X (mm)	Y (mm)	Z (mm)
Laser	1,610	0	450

● **Car body:** Overall dimensions

	X (mm)	Y (mm)	Z (mm)
Front overhang—axial A	-350	0	0
Front overhang—side B	-350	170	0
Front overhang—side C	-210	310	0
Rear overhang—axial A	1,560	0	0
Rear overhang—axial B	1,560	170	0
Rear overhang—axial C	1,410	310	0

Masses inertia:

Sprung x-axis (kg m ²)	45
Sprung y-axis (kg m ²)	46
Total z-axis (kg m ²)	65

Passengers:

	Mass (kg)	X (mm)	Y (mm)	Z (mm)
Passenger	65	850	0	560

● **Steering:** Symmetrical steering

Steering geometry

	Kind of steering axle	
Axle1	Steering	
Axle2	Steering	
	Geometry Kingpin (°)	Geometry Foot lateral offset (mm)
Axle1	3	10
Axle2	3	10
	Geometry-Center lateral offset (mm)	Geometry-Wheel inertia around kingpin (kg m ²)
Axle1	50	0.63
Axle2	50	0.63

Geometry-Steering wheel diameter (mm)	350
Geometry-Steering wheel angle/horizontal (°)	45

Ball joint assembly positions on wheel housings: Left wheel

	X (mm)	Y (mm)	Z (mm)
Axle1	200	200	0
Axle2	200	200	0

Tie rod assembly positions: Left wheel

	X (mm)	Y (mm)	Z (mm)
Axle1	200	-300	100
Axle2	200	-300	100

Steering system forces

Steering wheel inertia (kg m ²)	0.05
Steering-Steering rack-and-pinion efficiency	90

Power steering

Power steering-Torque amplification coefficient	1
Power steering-Amplification modulation with velocity at 60 km/h (%)	0
Power steering-Amplification modulation with steering (%)	0

● **Electric engine:** Motor 900 W

Name	Motor 900 W
Motor type	Direct current with permanent magnet
Modeling type	Experimental
Rotor mass (kg)	2
Rotor radius of gyration (mm)	50
Power factor	1
Inductance L_j (H)	0.075
Resistance R_{e_j} (Ω)	0.32

Motor-driven group:

Number of gears inertia	1
Gear in use	1

	Driving	Driven	Correction	Efficiency
Ratio1	100	100	1	0.98
Ratio2	100	100	1	0.98
Ratio2	1	12.8	1	0.98

Torque:

Torque constant (experimental description) (A/(N m))	0.5
--	-----

Battery discharge: Nominal characteristic

Nominal characteristic (Ah)	50
Nominal characteristic (V)	12

Engine generator:

Regulation type	1
Specific consumption (g/(kWh))	99.972
Idle consumption per hour (g/(kWh))	19.994

● **Tire:** 130_70 10

Type	125R15
Pressure (bar)	2.2

Dimensions:

Wheel rim diameter (inch)	13
Wheel rim width (mm)	75
Bead width (mm)	85
Tread width (mm)	85

Mass and inertia:

Mass (kg)	3
Gyration radius (mm)	182

Rolling resistance:

Rolling resistance (simplified grip) (N/kN) 12

Simplified radius:

Loaded radius—Reference load (daN)	80
Loaded radius—Free radius (mm)	220
Loaded radius—Deflection (mm)	20
Loaded radius—Minimal radius (mm)	150
Loaded radius—Rolling circumference at reference load (mm)	1,290
Loaded radius—Free radius variation by centrifugation (%)	0.25
Loaded radius—Radial stiffness sensibility (daN/mm/bar)	1

Tire torsion:

Maximum torsion torque (daN m)	1
Maximum torsion angle (°)	5
Reference load (daN)	400

● **Suspension (Front Axle)**

Spring:

Natural frequency (Hz)	2
Bump travel (mm)	100
Rebound travel (mm)	100

Damper:

Bump damping ratio 0.2

Rebound damping ratio 0.4

- **Suspension (Rear Axle)**

Spring:

Natural frequency (Hz) 2

Bump travel (mm) 100

Rebound travel (mm) 100

Damper:

Bump damping ratio 0.2

Rebound damping ratio 0.6

11.2.2 Word Bond Graph of RobuCar's System

The word bond graph of the *RobuCar* system represents the technological level of the model, where the global system is decomposed by the subsystems of Fig. 11.6. Compared to classical block diagram, in this representation, the input and output of each subsystem are defined by power variables represented by a conjugated pair of effort-flow (e, f). The power variables used for the studied system are:

$$\begin{aligned} (\text{Torque, Angular velocity}) &= \{(U_j, \dot{\theta}_{e_j}), (C_j, \dot{\theta}_{e_j}), (N_j \cdot C_j, \dot{\theta}_{s_j})\}, \\ (\text{Force, Linear velocity}) &= \{(F_{x_j}, r_{l_j} \cdot \dot{\theta}_{s_j}), (F_{z_j}, \dot{z}_{j2})\}, \\ (\text{Voltage, Current}) &= \{(U_{0_j}, i_j)\}, \\ (\text{Temperature, Thermal Flow}) &= \{(T_{0_j}, \dot{Q}_{0_j}), (T_j, \dot{Q}_j)\}, \\ (\text{Pressure, Volume Flow}) &= \{(P_j, \dot{V}_j)\}. \end{aligned}$$

These true bond graph variables are associated respectively with electrical, mechanical, thermodynamic, and pneumatic aspects of the physical system.

Some hypothesis are taken in consideration for these part according to the real system characteristics and its environment:

- The contact area between vehicle wheels and the motion surface is assimilated to an ellipsoidal contact area, in order to express the normal effort distribution at the longitudinal and lateral directions;
- The contact efforts are considered dynamic in function of the slip velocity, and considered as an identified input system;
- For the system actuators, only the electrical and mechanical dynamics are considered;
- For dynamic vehicle modeling, longitudinal, lateral, vertical, roll, pitch, and yaw dynamics are considered;

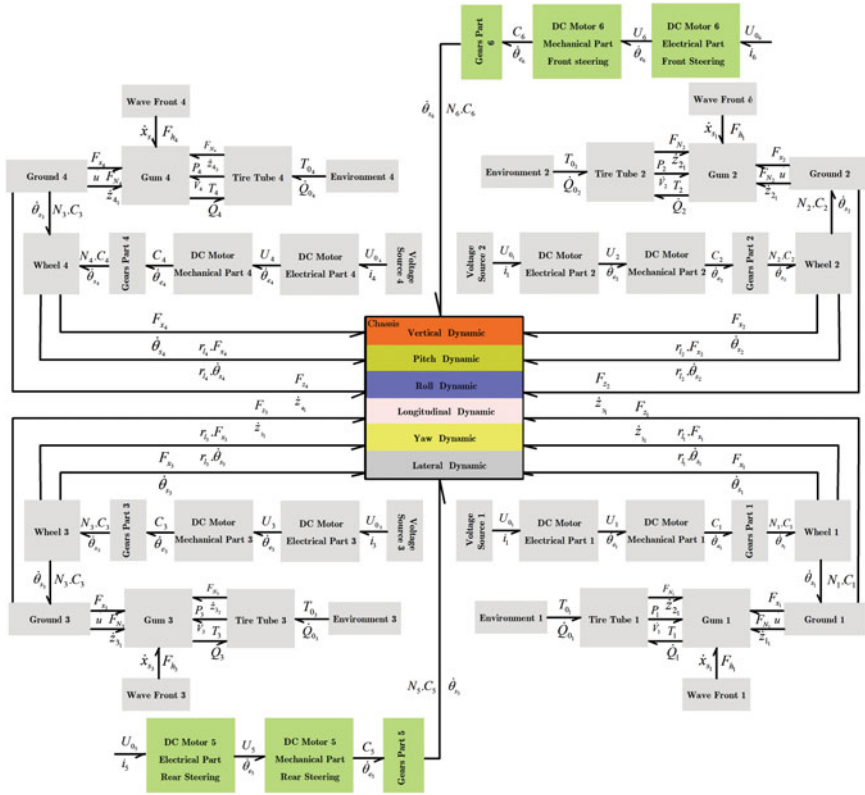


Fig. 11.6 Word bond graph of electric vehicle with a 4×4 decentralized inputs

- he approximate backlash transmitted torque model used in this work is considered only for smooth transmission via a dead zone area.

11.2.3 Kinematic and Geometric Models

Let us consider in Fig. 11.7, the yaw motion configuration of the center of gravity $G(x_G, y_G, \alpha)$ of *RobuCar* in the plan $(X - Y)$. r_1 is the distance from the rear axle to the center of gravity, r_2 is the distance from the front axle to the center of gravity, and d the distance between the two driving wheels (rear and front). \dot{u} , \dot{v} , and $\dot{\alpha}$ are respectively the forward, lateral, and yaw velocities. α_1, α_2 are the measured front and rear steering angles on the real system and r_l is the constant wheel radius.

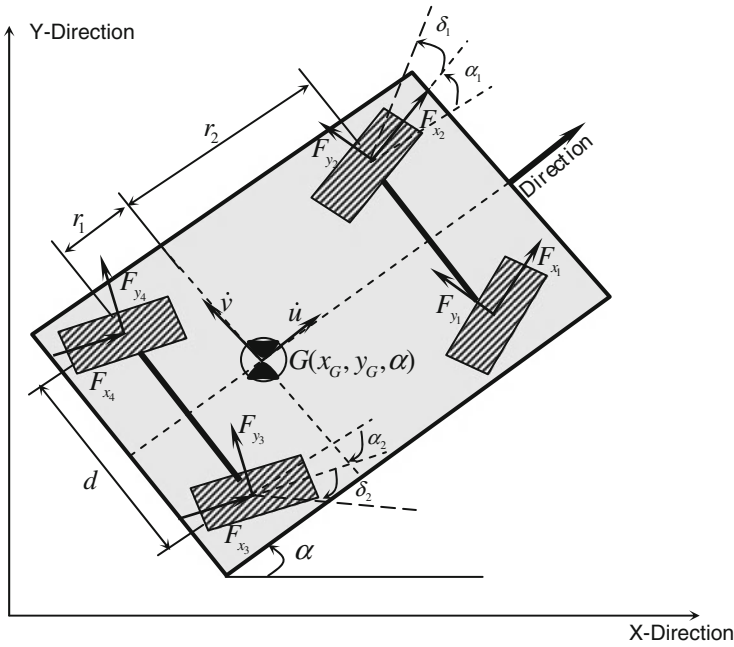


Fig. 11.7 Forces acting on the vehicle

Then full kinematic model for *RobuCar* can be deduced as follows:

- The longitudinal *RobuCar*'s velocity is:

$$\dot{u} = \frac{rl}{4} [(\dot{\theta}_{s1} + \dot{\theta}_{s2}) \cos \alpha_1 + (\dot{\theta}_{s3} + \dot{\theta}_{s4}) \cos \alpha_2] \tag{11.1}$$

- The yaw *RobuCar*'s velocity is:

$$\begin{aligned} \dot{\alpha} = & \frac{rl}{d} [(\dot{\theta}_{s1} - \dot{\theta}_{s2}) \cos \alpha_1 + (\dot{\theta}_{s3} - \dot{\theta}_{s4}) \cos \alpha_2] \\ & + \frac{rl}{r_1 + r_2} [(\dot{\theta}_{s1} + \dot{\theta}_{s2}) \sin \alpha_1 - (\dot{\theta}_{s3} + \dot{\theta}_{s4}) \sin \alpha_2] \end{aligned} \tag{11.2}$$

- The lateral *RobuCar*'s velocity is given in (11.3):

$$\dot{v} = \frac{rl}{4} [(\dot{\theta}_{s1} + \dot{\theta}_{s2}) \sin \alpha_1 - (\dot{\theta}_{s3} + \dot{\theta}_{s4}) \sin \alpha_2] \tag{11.3}$$

Thus, the matrix representation of the Kinematic model can be given as follows:

$$\begin{pmatrix} \dot{u} \\ \dot{v} \\ \dot{\alpha} \end{pmatrix} = f(\alpha_1, \alpha_2) \begin{pmatrix} \dot{\theta}_{s1} \\ \dot{\theta}_{s2} \\ \dot{\theta}_{s3} \\ \dot{\theta}_{s4} \end{pmatrix} \quad (11.4)$$

with:

$$f(\alpha_1, \alpha_2) = \begin{pmatrix} \frac{r_l}{4} \cos \alpha_1 & \frac{r_l}{4} \sin \alpha_1 & \frac{r_l}{d} \cos \alpha_1 + \frac{r_l}{r_1+r_2} \sin \alpha_1 \\ \frac{r_l}{4} \cos \alpha_1 & \frac{r_l}{4} \sin \alpha_1 & -\frac{r_l}{d} \cos \alpha_1 + \frac{r_l}{r_1+r_2} \sin \alpha_1 \\ \frac{r_l}{4} \cos \alpha_2 & -\frac{r_l}{4} \sin \alpha_2 & \frac{r_l}{d} \cos \alpha_2 - \frac{r_l}{r_1+r_2} \sin \alpha_2 \\ \frac{r_l}{4} \cos \alpha_2 & -\frac{r_l}{4} \sin \alpha_2 & -\frac{r_l}{d} \cos \alpha_2 - \frac{r_l}{r_1+r_2} \sin \alpha_2 \end{pmatrix}^T.$$

The heading, velocities, and position of the *RobuCar* in the absolute coordinate (11.5) can be obtained by integration under assumption that the initial conditions are known (11.6):

$$\begin{cases} \dot{x}_G = \dot{u} \cos(\alpha) - \dot{v} \sin(\alpha) \\ \dot{y}_G = \dot{u} \sin(\alpha) + \dot{v} \cos(\alpha) \end{cases} \quad (11.5)$$

where, V_x and V_y are respectively longitudinal and lateral velocities of the center of gravity *CoG* of the vehicle. x_G , y_G , and α , the position of the *CoG* and heading of the vehicle in the world frame.

$$\begin{cases} \alpha = \int_0^t \dot{\alpha} dt \\ x_G = \int_0^t \dot{x}_G dt \\ y_G = \int_0^t \dot{y}_G dt \end{cases} \quad (11.6)$$

11.3 Quarter Vehicle Model

RobuCar's prototype is considered as a concatenation of four symmetrical quarter system of vehicle. In this section, a detailed modeling of quarter *RobuCar* is presented, then, a generalized model of global system will be synthesized in the next sections. Quarter of *RobuCar* of Fig. 11.8 is considered as an electromechanical system composed by:

The quarter system of Fig. 11.8 is the combination of many parts: electrical part of DC motor, mechanical part of DC motor, gears part and wheel part, suspension mechanism, roadway and environment. In the model of Fig. 11.9, only the electro-mechanical system with the wheel are modeled, while the steering and the suspension

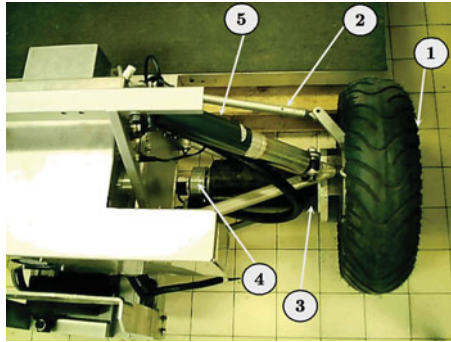


Fig. 11.8 Quarter of intelligent and autonomous vehicle with 1 front left wheel, 2 front steering axis, 3 electromechanical system, 4 optical encoder, 5 suspension system

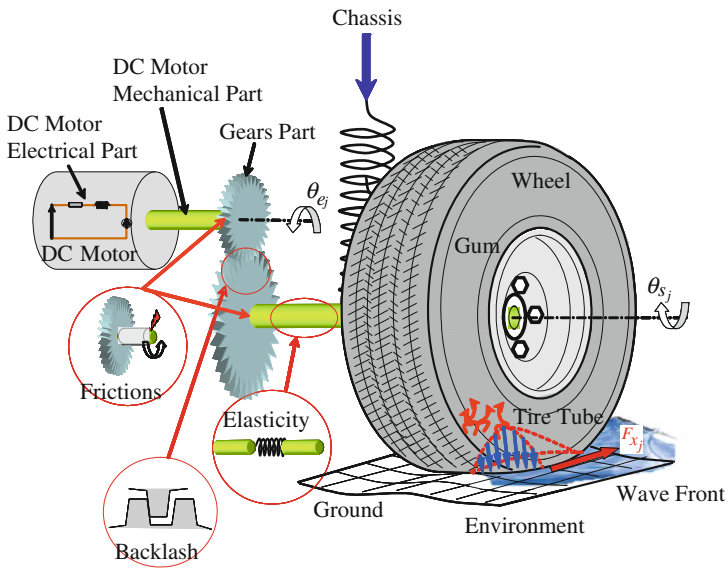
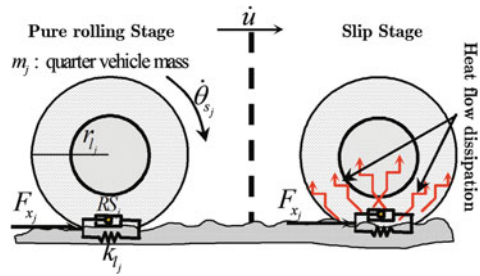


Fig. 11.9 j th electromechanical system of a quarter of RobuCar

systems are modeled in the next section. In this case, the static friction effects are not considered for the DC motor. In the presented modeling, viscous friction, backlash phenomenon, and flexibility of the transmission links are taken into account as a mechanical imperfections for the electromechanical system.

Fig. 11.10 Longitudinal tire gum behavior



11.3.1 Tire Modeling

According to Fig. 11.9, the subsystems: *Gum*, *Wave Front* and *Tire Tube* are modeled separately.

11.3.1.1 3D Elasto-Dynamic Modeling

Longitudinal Behavior

Tire gum is considered as a viscoelastic material, which is deforming with a behavior located between a viscous liquid and an elastic solid.

When the tire is in contact with the ground, we introduce the kinematic terminology of slip velocity \dot{x}_{s_j} related to the j th tire. This latter is the difference between two collinear velocities at the center of tire contact [37]: Longitudinal velocity of the vehicle is \dot{u} and the linear tire velocity $r_{l_j}\dot{\theta}_{s_j}$, with r_{l_j} the tire radius, considered constant and $\dot{\theta}_{s_j}$ the angular velocity of the tire.

$$\dot{x}_{s_j} = \dot{u} - r_{l_j}\dot{\theta}_{s_j} \tag{11.7}$$

Figure 11.10 shows the longitudinal tire gum behavior when the wheel makes an angular and translation motions after contact with the roadway. At the contact level, the generated longitudinal effort F_{x_j} is decomposed into three forces: inertial force due to mass m_j , elastic force from the spring k_{l_j} , and viscous friction force through the resistance RS_j . The resistance element RS_j is used in bond graph theory to model the active resistance which generate the entropy flow from mechanical friction effect. This irreversible transformation from mechanical to thermal power provide the thermal flow \dot{Q}_j to the tire tube.

The corresponding bond graph model which reflects the viscoelastic phenomenon of the tire-road contact is developed in Fig. 11.11. In our case, the known and measurable inputs are respectively the vehicle velocity \dot{u} and the angular wheel velocity $\dot{\theta}_{s_j}$. They are represented by a flow sources ($SF : \dot{u}$) and ($SF : \dot{\theta}_{s_j}$). Then, according to the viscoelastic characteristic of the gum, transmitted mechanical power (in the case

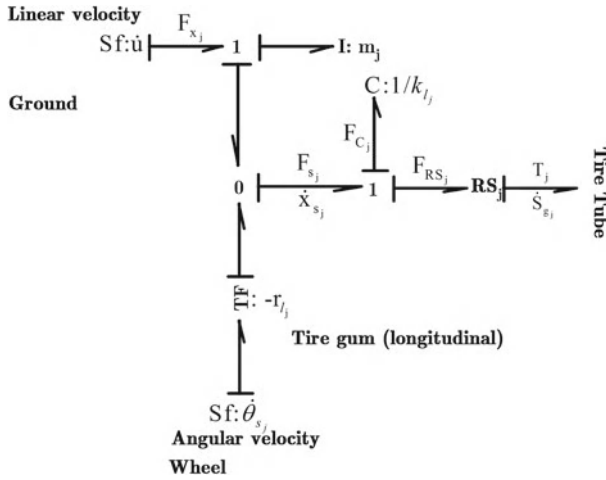


Fig. 11.11 Longitudinal tire gum’ model

where the tire is in contact with the roadway) is decomposed into two parts: The first one is transformed into kinetic through inertia of mass m_j , modeled by I element, and which describe the dynamic of all tire points outside of physical contact. The second part and due to the contact configuration, the slip velocity \dot{x}_{s_j} is transformed into friction (generating a thermal power RS_j element) and into elasticity modeled by a storage element C of value $1/k_{l_j}$.

The longitudinal effort F_{x_j} is estimated using bond graph I element in derivative causality. This causality conflict introduces implicit equation in numerical simulation. This is due of presence of imposed flow source ($SF : \dot{u}$). The slip velocity \dot{x}_{s_j} is calculated by 0 junction and modulated transformer used to transfer angular velocity $\dot{\theta}_s$ to linear format. The deduced equation is given in (11.7).

The mechanical equation of the longitudinal motion of the tire, referring to the contact area could be synthesis from the bond graph scheme and given as follows:

- From junction 1 associated to elements C and RS_j , we obtain the following equation:

$$F_{s_j} = F_{C_j} + F_{RS_j} = k_{l_j}x_{s_j} + RS_j\dot{x}_{s_j} \tag{11.8}$$

- From junction 1 associated to element I , given in derivative causality, and from Eq. (11.8) the following result is obtained:

$$F_{x_j} = m_j\ddot{u} + RS_j\dot{x}_{s_j} + k_{l_j}x_{s_j} \tag{11.9}$$

where x_{s_j} describes the slip displacement, \ddot{u} the longitudinal acceleration of the vehicle, and m_j the j th quarter vehicle mass.

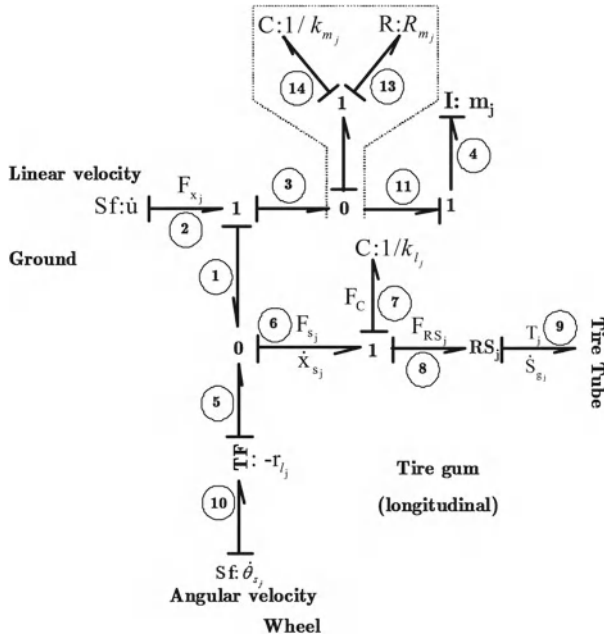


Fig. 11.12 Longitudinal tire gum bond graph with integral causality with new pad

To avoid a derivative causality which introduce implicit equation in numerical simulation, we introduce a pad in between $(SF : \dot{u})$ and $(I : m_j)$ element [11]. This pad describes a rigid stiff spring-damper' combination, with a high value of stiffness and friction coefficient $(R_{m_j} \rightarrow \infty, k_{m_j} = \frac{1}{C} \rightarrow \infty)$. Let us consider that during a dynamic slip motion of the wheel, the points of the tire which do not belong to the contact are not very deformed than those of contact, so it can be the physical meaning of the added pad. The bond graph model of the longitudinal tire gum behavior including the new pad is given in Fig. 11.12.

This last bond graph model is in integral causality. Let us prove that flow f_4 of element $(I : m_j)$ is equal to \dot{u} after adding the new pad.

Consider P_I and e_4 the momentum and force of element $(I : m_j)$:

$$f_4 = \frac{1}{m_j} \int e_4 dt = \frac{P_I}{m_j} \tag{11.10}$$

The displacement q_{14} associated to $C : \frac{1}{k_{m_j}}$ element is calculated from its flow f_{14} as follows:

$$q_{14} = \int f_{14} dt \tag{11.11}$$

Then the state equation of the bond graph model can be deduced as follows:

$$\begin{cases} \dot{P}_I = k_{m_j} q_{14} + R_{m_j} (\dot{u} - f_4) \\ \dot{q}_{14} = \dot{u} - f_4 \end{cases} \quad (11.12)$$

From the second equation of (11.12)

$$\dot{q}_{14} = \frac{\dot{e}_{14}}{k_{m_j}} = \dot{u} - f_4 \quad (11.13)$$

Since $k_{m_j} \gg \dot{e}_{14}$ then

$$\dot{q}_{14} \simeq 0 \quad (11.14)$$

and

$$f_4 \simeq \dot{u} \quad (11.15)$$

According to the affected causality, thermal power generating entropy flow $\dot{S}g_j$ by the active element RS_j , given by Eq. (11.16) and detailed in [26].

$$\dot{S}g_j = \frac{RS_j \dot{x}_{s_j}^2 \alpha_{slip}}{T_j} \quad (11.16)$$

where RS_j is the resistance value and α_{slip} is the slip angle (Fig. 11.13).

Equation (11.16) describes also the transformation of the tire side effort to the heat flow. This is possible by assuming that the action of the tire on the ground surface is changed to thermal energy and it is more detailed [25].

The slip angle α_{slip} is the angle formed by the plane of the wheel and the tangent to the wheel path [23].

A slip angle may be necessary for keeping a vehicle in a straight line. This is what happens when the vehicle is exposed to a cross-wind.

In general case, the tires produce lateral forces depending on lateral slip. This latter is measured with a slip angle, which increases with a saturated tire forces. So, the simplest model for combined slip (i.e., combined braking and cornering) is based on the friction ellipse distribution (Fig. 11.13). It is assumed that F_{y_j} and F_{x_j} (lateral and longitudinal efforts of the j th tire) cannot exceed their maximum values $F_{y_{j \max}}$ and $F_{x_{j \max}}$. The tire force distribution print is assumed to be on the edge of the ellipse [49].

$$\left(\frac{F_{y_j}}{F_{y_{j \max}}} \right)^2 + \left(\frac{F_{x_j}}{F_{x_{j \max}}} \right)^2 = 1 \quad (11.17)$$

where the lateral and longitudinal tire forces F_{y_j} , F_{x_j} in the direction of the wheel ground contact are approximated linear to the slide slip angles α_{slip} . Generally, the

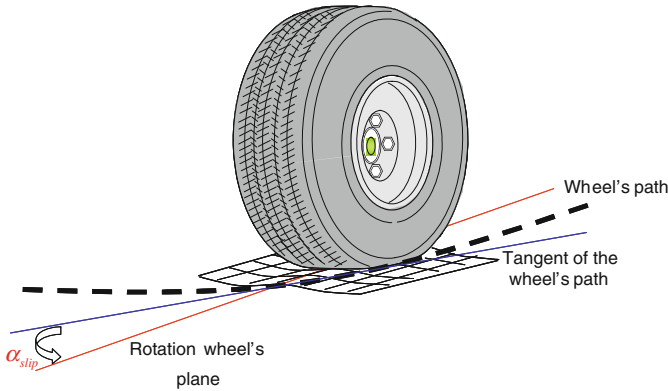
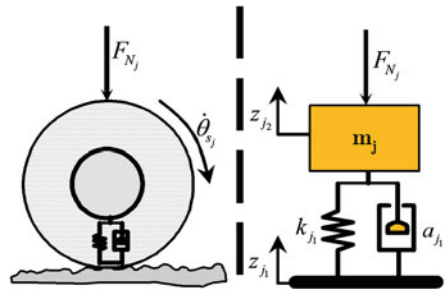


Fig. 11.13 Slip angle

Fig. 11.14 Tire-road normal effort



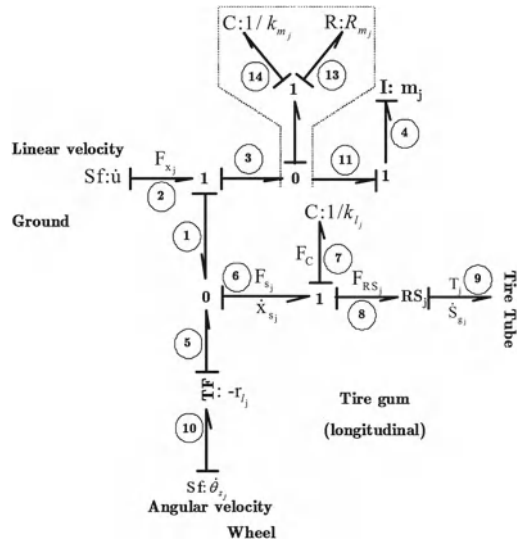
slip angles depend on the steer angle, yaw and lateral velocities [14], and in our case it is considerably measured. In the presented work, only longitudinal effort is estimated and $F_{x_j \max}$ is not identified, so the dimension of the print is used in the next section to calculate the normal force F_{N_j} , using a polar coordinates transformation.

Vertical Behavior

The gum is a viscoelastic material which can be described by (damper, spring, and mass) system of Fig. 11.14. The input variable corresponds to the normal effort F_{N_j} deduced from the pressure variation in the tire tube. The viscous normal friction is represented by a dissipative bond graph element ($R : a_{j1}$) while elasticity is represented by an element C of elasticity k_{j1} which store a potential energy. The quarter vehicle inertia due to its mass m_j is represented by conservative element ($I : m_j$).

In this case, the dynamic element ($I : m_j$) is in integral causality, because the effort F_{N_j} is known. That is why the normal mass velocity \dot{z}_{j2} can be deduced by

Fig. 11.15 Bond graph model of the vertical tire dynamics



integration. ($R : a_{j1}$) is a dissipative R element with any thermal power generation. The bond graph model of the vertical dynamic is given in Fig. 11.15.

The following mechanical equation (11.18) of the j th tire vertical' dynamic is deduced from bond graph of Fig. 11.15

$$m_j \ddot{z}_{j2} + a_{j1} (\dot{z}_{j2} - \dot{z}_{j1}) + k_{j1} (z_{j2} - z_{j1}) = F_{N_j} \quad (11.18)$$

where z_{j2} and \dot{z}_{j2} are the j th vertical gum' displacement and vertical gum' velocity, issued from the load motion and z_{j1} and \dot{z}_{j1} are the j th vertical gum' displacement and vertical gum' velocity, issued from the ground profile.

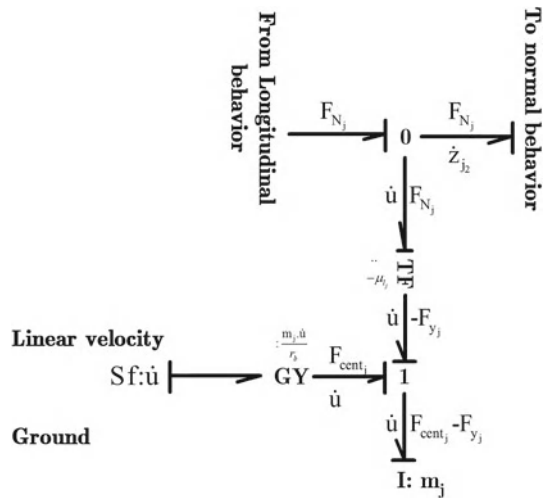
Lateral Behavior

Generally, during the vehicle motion on a circular path of radius r_b , a centrifugal force F_{cent} is generated, which forces the vehicle to go out of its initial curve. Thus, to keep the vehicle on its defined trajectory, the tire-road system generates a lateral force F_y [23], called *centripetal force* or *transversal friction force* and expressed as follows:

$$F_y = \sum_{j=1}^4 F_{y_j} = -F_{cent} = -\frac{m\dot{u}^2}{r_b} \quad (11.19)$$

The bond graph model of the lateral dynamic of quarter of vehicle, including the interaction with the longitudinal and vertical dynamics is described in Fig. 11.16.

Fig. 11.16 Bond graph model of the lateral dynamics



The centripetal force (Fig. 11.17) is a nonlinear function of longitudinal velocity \dot{u} , represented by a modulated gyrator GY by $\frac{m_j \dot{u}}{r_b}$. The lateral force for the j th tire F_{y_j} , depends proportionally of the normal force, F_{N_j} , applied by the quarter of vehicle to the road surface, and of the friction coefficient μ_{l_j} of the j th rubber-road contact.

$$F_{y_j} = \mu_{l_j} F_{N_j}$$

The coefficient μ_{l_j} depends principally on the load pressure and the nature of the rubber and road surface, with the variation of their environment (temperature, wave front, etc.).

11.3.1.2 Hydrodynamic Modeling

Two kinds of interaction forces can generate wave front phenomena: internal interaction forces, which are located between fluid molecules, and external interaction forces, which are present between fluid molecules and molecules of the tire circumference (Fig. 11.18). Each fluid molecule does not run out at the same velocity [23] and follows a velocity profile of Fig. 11.18. Bond graph model of hydrodynamic phenomenon is given in Fig. 11.19.

When each particle located in a cross-section, perpendicular to the overall flow is represented by a velocity vector, the obtained curve from the vectors extremities represents the velocity profile of Fig. 11.18. The movement of the fluid can be regarded as resulting from the slip between the fluid layers. The velocity of each layer is a function of distance h_j of this curve in the fixed plan: $\dot{x}_{f_j} = \dot{x}_{f_j}(h_j)$.

Fig. 11.17 Centrifugal and lateral forces

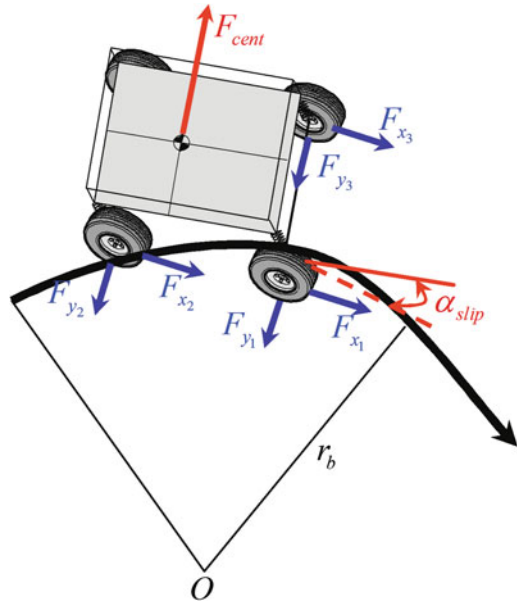
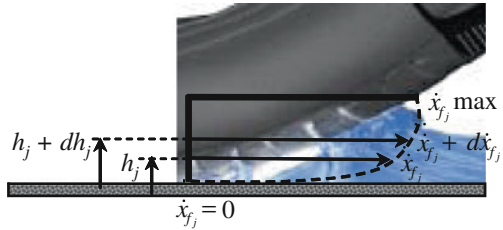


Fig. 11.18 Tire-road hydrodynamic effects



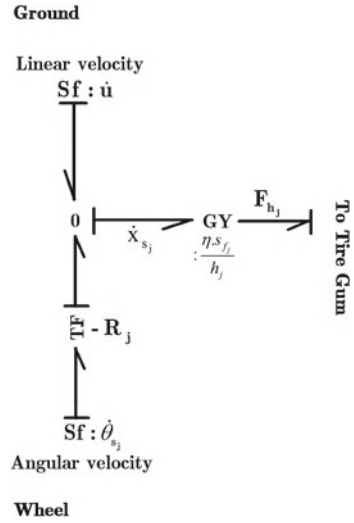
The hydrodynamic pressure generated by a slick tire tread on a bank of water at the slip area (contact area), can be approximated by *Bernoulli's* equation:

$$P_{h_j} = \frac{1}{2} \rho_w \dot{x}_{s_j}^2 \tag{11.20}$$

where ρ_w is the density of the water, in kg/m^3 , \dot{x}_{s_j} is the j th slip velocity of the vehicle located at the contact area of each wheel, in m/s , P_{h_j} being expressed in Pa ($10^5 \text{ Pa} = 1 \text{ bar}$).

Consider two adjacent layers of fluid separated by dh_j . The friction force F_{h_j} exerts on the surface of separation of these two layers to prevent slippage of one layer to another. It is proportional to the difference of layers velocity $d\dot{x}_{f_j}$, their surface s_{f_j} , and inversely proportional to dh_j :

Fig. 11.19 Tire-road hydrodynamic bond graph model



$$F_{h_j} = \eta s_{f_j} \frac{d\dot{x}_{f_j}}{dh_j} \tag{11.21}$$

where η describes the coefficient of dynamic viscosity.

In our case, we take the difference in layers velocity $d\dot{x}_{f_j}$ equal to the velocity slip \dot{x}_{s_j} (i.e. velocity of the first layer is $\dot{x}_{f_j} = 0$ and for the second $\dot{x}_{f_j} = \dot{x}_{s_j}$ in the slip surface for water height level of h_j). So, F_{h_j} can be written as:

$$F_{h_j} = \eta s_{f_j} \frac{\dot{x}_{s_j}}{h_j} \tag{11.22}$$

The transformation from the slip velocity \dot{x}_{s_j} to the hydrodynamic force F_{h_j} can be represented in a bond graph model of Fig. 11.19, by a modulated gyrator element GY with the constant $\frac{\eta s_{f_j}}{h_j}$ as a modulus.

11.3.1.3 Pneumatic Modeling

Tire tube is a synthetic rubber sheet located inside the tire and describes an elastic enclosure containing a perfect gas under pressure. The pneumatic phenomenon inside the tire tube and its associated bond graph model are given respectively in Figs. 11.20 and 11.21. The tire tube exchanges the thermal power with the external environment due to the heat conductivity of tire wall, and stores two types of energies, pneumatic and thermal. The thermal energy' exchange is modeled by the dissipation element R and the storage phenomenon is represented by the two ports C element.

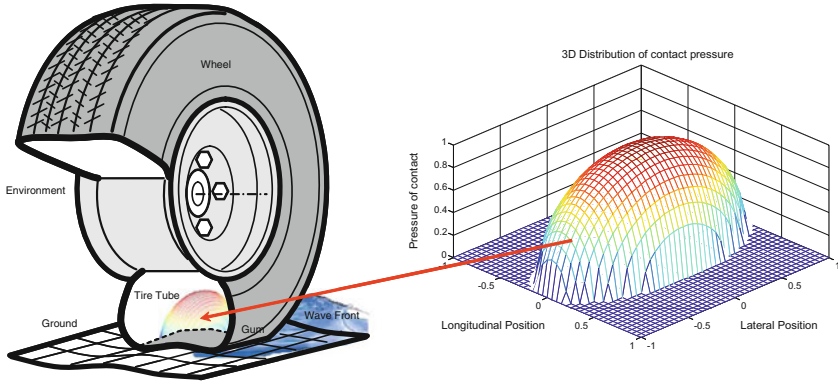


Fig. 11.20 Pneumatic effect inside the tire tube

During the slip stage, the temperature variation acts on the internal pressure inside the tire tube according to the perfect gas equation (11.23)

$$P_j V_j = n \zeta T_j \tag{11.23}$$

where P_j is the gas pressure, V_j the gas volume, T_j the temperature inside the j th tire tube, n the moles number, ζ a gas constant.

Knowing that the j th normal force F_{N_j} of Eq. (11.24), is proportional to the normal pressure distribution $P_j(x, y)$ and the contact surface A_{f_j} between the tire and the ground.

$$F_{N_j} = P(x, y) A_{f_j} \tag{11.24}$$

Let us consider that distribution of pressure during the contact tire-road is represented by an ellipsoidal function of longitudinal and lateral positions [22], as it is shown in Fig. 11.20. From (11.24), F_{N_j} could be expressed as follows:

$$F_{N_j} = A_{f_j} \iint P_j(x, y) = A_{f_j} P_{0_j} \iint \sqrt{1 - \frac{x^2}{a_j^2} - \frac{y^2}{b_j^2}} dx dy \tag{11.25}$$

where P_{0_j} is the maximum pressure magnitude and a_j and b_j are the maximum longitudinal and lateral lengths of the ellipsoidal distributions. Let us use the following variables affectation

$$\begin{cases} X = \frac{x}{a_j} \\ Y = \frac{y}{b_j} \end{cases} \text{ and } \begin{cases} dX = \frac{dx}{a_j} \\ dY = \frac{dy}{b_j} \end{cases} \tag{11.26}$$

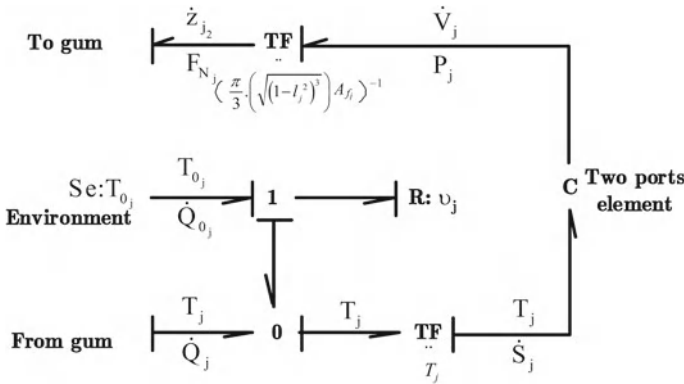


Fig. 11.21 Tire tube bond graph' model

Then, Eq. (11.25) becomes:

$$F_{N_j} = P_{0_j} A_{f_j} \iint \sqrt{1 - X^2 - Y^2} dX dY \tag{11.27}$$

In order to change the double integral defined in *Cartesian* coordinates (X, Y) to the *Polar* coordinates, the following variables transformation is considered:

$$\begin{cases} X = \lambda \cos \varphi \\ Y = \lambda \sin \varphi \end{cases} \tag{11.28}$$

Let us note

$$\sqrt{1 - X^2 - Y^2} = \sqrt{1 - \lambda^2} \tag{11.29}$$

In the XY plane, the coordinate λ for an arbitrary φ varies between 0 and l_j with φ varies between 0 and π .

$$\iint \sqrt{1 - X^2 - Y^2} dX dY = \int_0^\pi d\varphi \int_0^{l_j} \lambda \sqrt{1 - \lambda^2} d\lambda \tag{11.30}$$

After development of Eq. (11.30), the following expression of F_{N_j} is deduced after a double integral in curvilinear coordinates [20]:

$$F_{N_j} = \frac{\pi}{3} P_{0_j} A_{f_j} \left(1 - \sqrt{(1 - l_j^2)^3} \right) \tag{11.31}$$

where l_j describes the contact surface length for the j th tire.

11.3.1.4 Thermodynamic Modeling

The bond graph model of the tire tube is given by Fig. 11.21. Resistance ($R : \nu_j$) represents the heat conductivity of the tire tube. It ensures the heat transfer with the external environment. The model input corresponds to the heat flow \dot{Q}_j originally from the friction of gum, and its output represents the normal effort F_{N_j} , obtained by ellipsoidal distribution of pressure, using the transformer TF . The two ports C element describes the variations of the entropy S_j and the volume V_j inside the tire tube, developed in [27]. The nonlinear state equations of the two ports element C is given in Eq. (11.32):

$$\begin{cases} T_j = T_{0j} \left(\frac{V_j}{V_{0j}} \right)^{-\frac{R_g}{C_v}} e^{\frac{S_j - S_{0j}}{M_m C_v}} \\ P_j = \frac{M_m C_v T_{0j}}{V_{0j}} \left(\frac{V_j}{V_{0j}} \right)^{-\delta} e^{\frac{S_j - S_{0j}}{M_m C_v}} \end{cases} \quad (11.32)$$

where $[S_j, V_j]$ (entropy and volume of the j th tire tube) is the state vector and the output variables are $[T_j, P_j]$ (temperature and pressure the j th tire tube), $\delta = \frac{C_p}{C_v}$, S_j gas entropy, S_{0j} initial entropy of the gas, C_p thermal capacity of the gas in a constant pressure, C_v thermal capacity of the gas in a constant volume, V_{0j} , and T_{0j} represent the initial gas volume and initial temperature of the j th tire tube, R_g is a gas constant and M_m gas molar mass.

The thermal flow entropy \dot{S}_{0j} exchanged between environment and tire tube is given by the following Eq. (11.33):

$$\dot{S}_{0j} = \frac{T_{0j} - T_j}{\nu_j T_j} \quad (11.33)$$

where T_j and T_{0j} are respectively the j th tire tube and environment' temperatures.

In practice, the thermal resistance ν_j is variable of the time and depends on the air flow, according to the wheel velocity. This latter is considered constant in this study case, and justified by:

- the dynamic of this resistance is so complex and difficult to identify online during the experiments;
- the operating mode is the steady state, where ν_j approaches a constant.

The global tire-road bond graph' model can be detailed in Fig. 11.22, where the power exchange between the different subsystems is presented.

For this global model, two principal measurements are needed: linear velocity of the vehicle \dot{u} , and j th angular wheel velocity $\dot{\theta}_{s_j}$. The external temperature can be added as known parameter and the ground profile can be considered as external input. The vertical deformation of the tire gum $z_{j_2} - z_{j_1}$ is estimated through the variation of the normal effort F_{N_j} and the pressure P_j inside the tire tube. This pressure variation is caused by the variation of temperature T_j of the tire tube, and generated from the

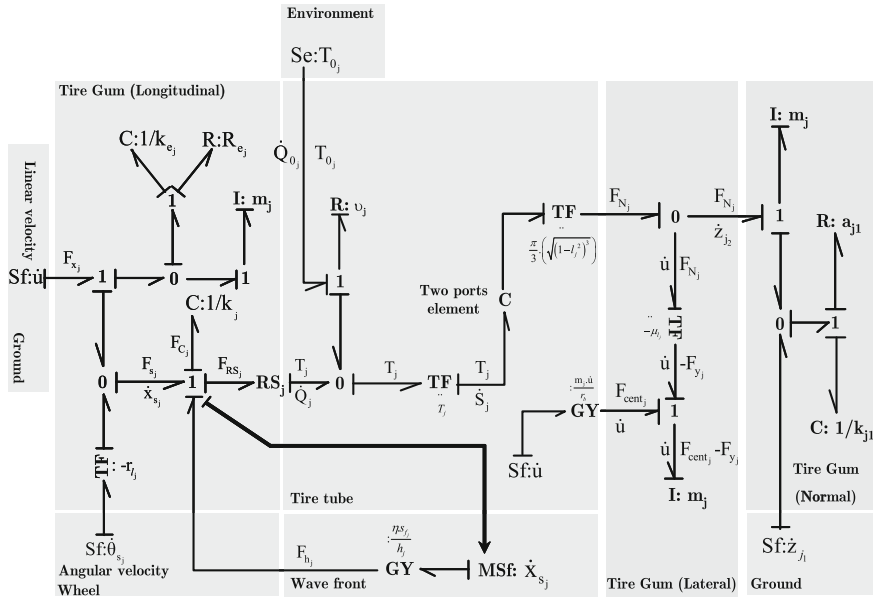


Fig. 11.22 Global tire-road Bond graph’ model

transformation of longitudinal friction force $RS_j \dot{x}_{s_j}$ to the heat flow \dot{Q}_j . In order to represent the ground fluid’ effect on the tire, the wave front subsystem is optionally added in the global model to describe the hydrodynamic effort’ action F_{h_j} .

11.3.1.5 Simulation Results

Because the studied vehicle run at a maximum longitudinal velocity of 18 km/h, the centrifugal force is low and the steering angle is sufficient for setting the vehicle parallel to the desired path. Simulation parameters are given in Table 11.1, and correspond to each j th tire-road system of the vehicle.

The simulations are realized under a specific bond graph software *SYMBOLS 2000* (Fig. 11.23) and *Matlab-Simulink*, using a the property of *S-function* [28]. It is an object-oriented hierarchical modeling, which allows users to create models using bond graph, block-diagram, and equation models. Differential causalities and algebraic loops are solved out using its powerful symbolic solution engine. Nonlinearity and user code can be integrated in single editing *IDE* (Integrated Development Environment). The iconic modeling facility allows system-morphic model layout. It also has many post-processing facilities over the simulated result.

For the simulated scenario, the values of l_j and r_{l_j} are considered well known, deduced when the vehicle is static configuration. RS_j can be identified experimentally

Table 11.1 Simulation parameters for the tire system

Parameter	Value
P_{0j}	2×10^5 (Pa)
l_j	0.1 (m)
r_{l_j}	0.2 (m)
k_{j1}, k_j	6 (N/m), 6 (N/m)
RS_j	12 (N s/m)
a_{j1}	9 (N s/m)
m_j	100 (kg)
V_{0j}	0.03 (m ³)
sf_j	0.1 (m ²)
ν_j	0.23 (W/m K)
A_{f_j}	0.3 (m ²)
k_{e_j}	1,000 (N/m)
R_{e_j}	1,000 (N s/rad)
R_0	8.31 (J mol ⁻¹ K ⁻¹)

as a viscous friction coefficient of the tire, then its final value used for the model is refined during the model validation.

For the longitudinal force, a canonical curve behavior is observed (Fig. 11.24), for driving and braking phases, according to the slip velocity. When the slip velocity increased, longitudinal force rises toward a extremum, reached for a value 0.5 m/s. During this phase we note the effect of the grip between the braking action and the vehicle reaction until the value 2 m/s. This phase corresponds to a fall of the force value generating by the wheel locking and the slip of the vehicle. A quasi-symmetric behavior of the longitudinal force is obtained in the case where the slip velocity is negative.

When the wave front phenomenon is present at the tire-road contact level (Fig. 11.25), we notice that the grip mechanism depends inversely on the water height. Thus, a fall of force value from 0.63 to 0.58 kN when water height varies from 0.3 to 1.5 mm. By increasing the water height on the ground, the grip is decreased, where the force reaches value of 0.52 kN for slip velocity of 2 m/s and 1.5 mm of water height. For the tire side, micro-indenters are flooded, and only the macro ones continue operating.

On a wet ground, viscosity of the water increases when temperature decreases. Thus, the ground becomes more slipping, and the grip potential is decreasing. The maximum force value goes from 0.68 to 0.58 kN when water viscosity varies from 0.5×10^{-3} to 3×10^{-3} kg/ms with the same profile of slip velocity (Fig. 11.26).

The curves of Fig. 11.27 are obtained for initial value of temperature inside the tire tube of 45 °C, and two values of ambient temperature, 15 and 30 °C. The shift between the two curves shows the influence of the ambient temperature on temperature variation inside the tire tube. For the case of 15 °C and for slip velocity profile of Fig. 11.27, a temperature decreasing from 45 to 44.92 °C is noticed when the slip velocity goes to *zero*, then it increases gradually with the slip velocity where the tire

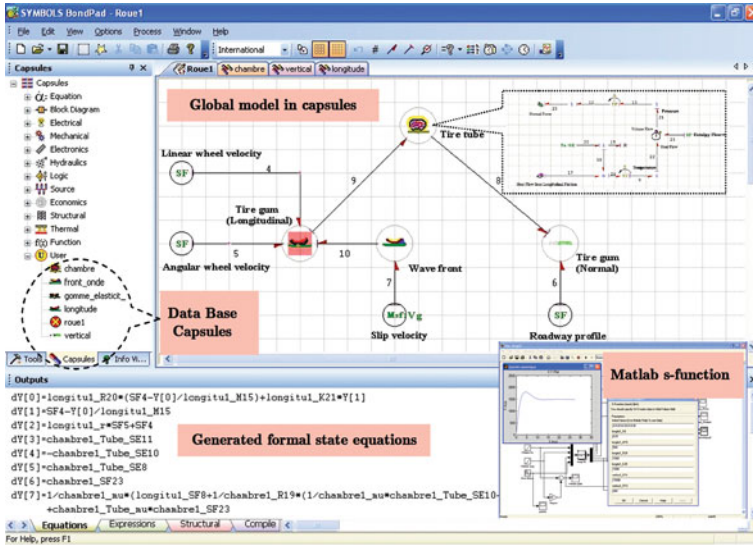


Fig. 11.23 Bond graph simulation

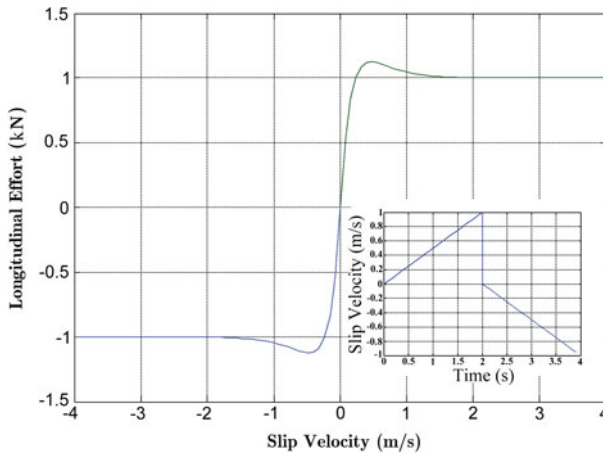


Fig. 11.24 Canonical curve of longitudinal effort

tube releases heat to the external environment because its temperature is higher than outside temperature.

The pressure variation is in relation with the temperature variation, by comparing the curves of Figs. 11.27 and 11.28. When the pressure increases, then the impact effort and temperature are also increasing. We notice that pressure decreases with temperature, which occurs indeed when the slip velocity varies from -1 to 0.2

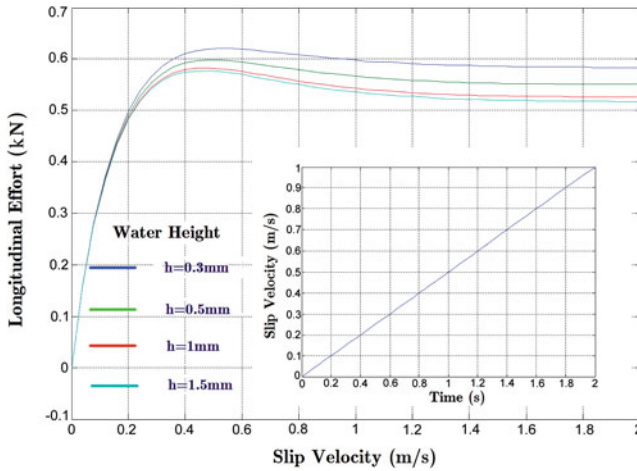


Fig. 11.25 Wave front influence on longitudinal effort

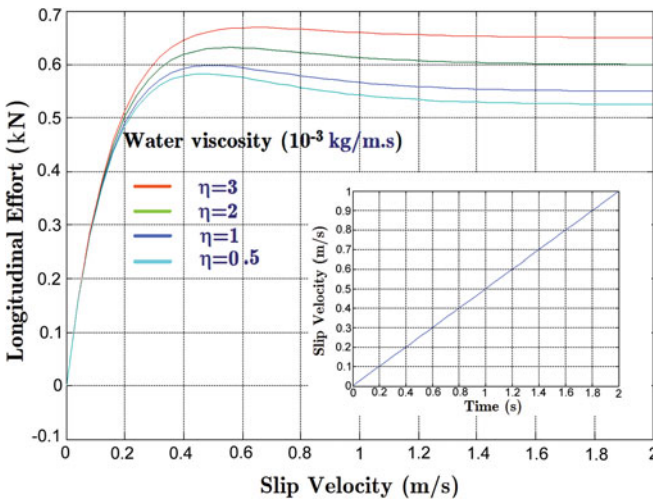


Fig. 11.26 Viscosity influence of wet surfaces

m/s. In this case, pressure varies from 2 to 1.68 bar and temperature goes from 45 to 44.92 °C. Then, a relative increase of pressure is observed when slip and temperature are increasing.

The vertical deformation (Fig. 11.29) of the gum $z_{j2} - z_{j1}$ is estimated according to the variation of the normal effort F_{Nj} and the pressure P_j inside the tire tube.

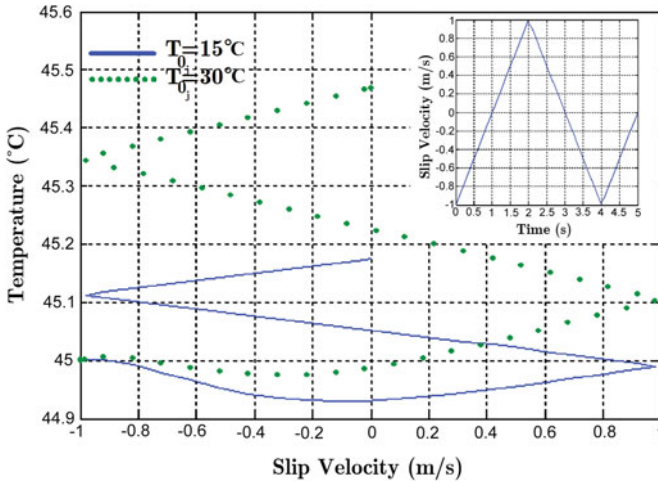


Fig. 11.27 Temperature variation inside the tire tube

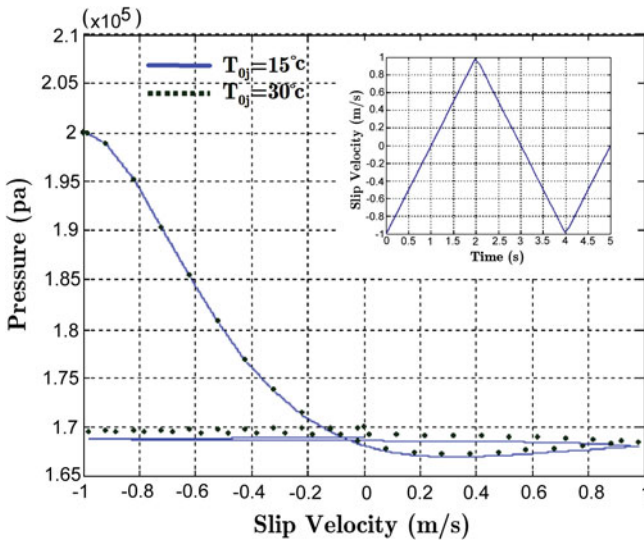


Fig. 11.28 Pressure variation inside the tire tube

11.3.2 Electromechanical Traction System

There are four electromechanical systems for the traction of the vehicle. They are constituted by three principal components (Fig. 11.9): the DC motor part, which is the combination of electrical and mechanical parts, the gears system part and the wheel system part. In this subsection, dynamic bond graph models of all of these

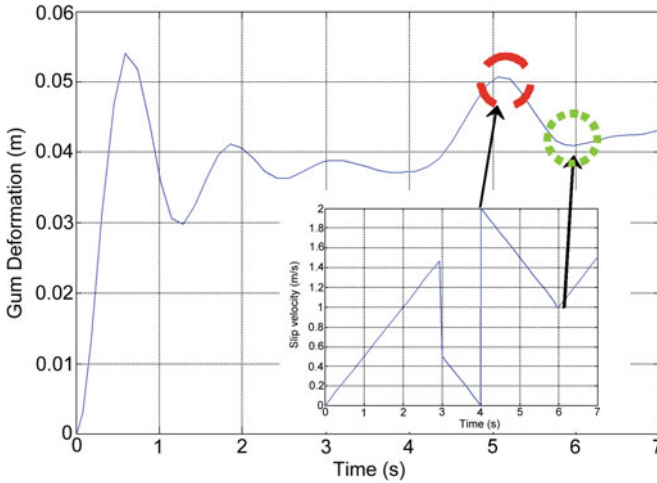
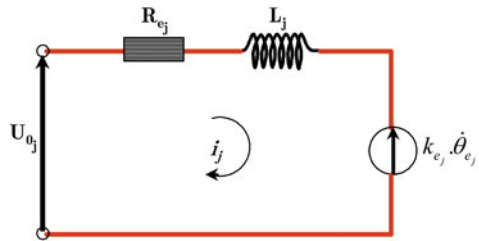


Fig. 11.29 Vertical gum deformation

Fig. 11.30 Electrical RL circuit of the j th DC motor



components are graphically synthesized then expressed by differential equations [22]. The influence of the ground effort is considered in the global dynamic for each j th electromechanical system. Due to the low longitudinal velocity of the vehicle, the lateral effort of the tire-road contact is not considered in the following development.

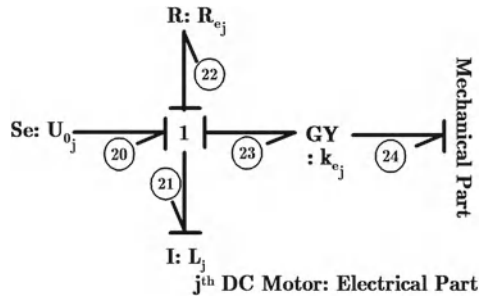
11.3.2.1 Electrical Part of the DC Motor

This part describes the basic RL electrical circuit of the j th DC motor (Fig. 11.30), composed by: input voltage' source U_{0j} , electrical resistance R_{e_j} , inductance L_j , and back electromotive force EMF , which is linear to the angular velocity of the rotor $\dot{\theta}_{e_j}$ and equal to $k_{e_j}\dot{\theta}_{e_j}$ with k_{e_j} the EMF constant. The index $j \in [1, 4]$ corresponds to the j th motor of the whole vehicle.

The corresponding RL circuit bond graph' model is given in integral causality by Fig. 11.31.

Let us note e_{21_j} , P_{21_j} , M_{21_j} , effort, momentum, and algebraic value of element I of the j th motor (Fig. 11.31). The gyrator element GY describes the power transfer

Fig. 11.31 Bond graph model of the electrical part of the j th DC motor



from the electric to mechanic domains by a flow variable f_{24j} of the link 4 and Se_{20j} is the input voltage source, then the following state equation is obtained:

$$e_{21j} = Se_{20j} - R_{ej} \frac{P_{21j}}{M_{21j}} - k_{ej} f_{24j} \tag{11.34}$$

with

$$\begin{cases} f_{20j} = f_{21j} = f_{22j} = f_{23j} = \frac{1}{L_j} \int e_{1j} dt = \frac{P_{21j}}{M_{21j}} = i_j \\ Se_{20j} = U_{0j} \\ f_{24j} = \dot{\theta}_{ej} \end{cases}$$

Thus, the corresponding dynamic equation of circuit of Fig. 11.30 is:

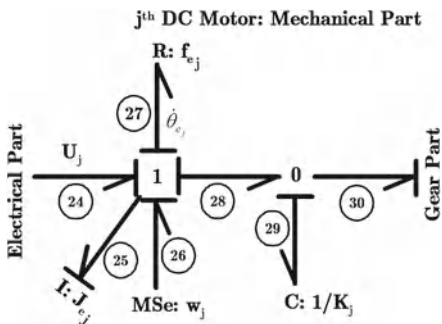
$$L_j \cdot \frac{di_j}{dt} = U_{0j} - R_{ej} \cdot i_j - k_{ej} \cdot \dot{\theta}_{ej} \tag{11.35}$$

11.3.2.2 Mechanical Part of the DC Motor

This model describes the mechanical part of the j th DC motor, characterizing by its rotor inertia J_{ej} , viscous friction parameter f_{ej} , transmission axis rigidity K_j , and a motor torque U_j . In this part, the influence of backlash phenomena expressed by a disturbing torque w_j is represented by a modulated effort source for the bond graph model [21]. This torque is expressed in its simplified nonlinear form, through a continuous function. The corresponding bond graph' model in integral causality is given by Fig. 11.32.

The considered backlash mechanism in this model is represented by a disturbing torque, hampering the smooth functioning of the system, and caused by simultaneous and evaluative reactions of the shock between the two sides of the gears system (Fig. 11.33). This torque is chosen continuous, nonlinear, and differentiable, compared to the size of the gears system and its effect on the global system.

Fig. 11.32 Bond graph model of the mechanical part of the j th DC motor



So, a smooth and nonlinear model of transmitted torque w_j [21], is taken as a modulated effort source ($MSe : w_j$) (Fig. 11.32). This torque is expressed by the following sigmoid function:

$$w_j = A_j K_j \tau_{0j} \frac{1 - e^{-\gamma_j \Delta\theta_j}}{1 + e^{-\gamma_j \Delta\theta_j}} \tag{11.36}$$

where w_j is the disturbing and nonlinear transmitted torque, $\Delta\theta_j = \theta_{e_j} - N_j \theta_{s_j}$ defines the difference between input motor' position θ_{e_j} (i.e. motor axis position) and output motor' position θ_{s_j} (i.e. wheel position), N_j a gearing constant, A_j a graphical parameter which is taken as negative integer to describe the reaction effect of the disturbing torque on the motor torque, K_j the rigidity constant of the transmission system, τ_{0j} is the dead zone amplitude, and $\gamma_j = 1 / (2\tau_{0j})$ the identified slope of the sigmoid function of the j th DC motor [19].

By adding the disturbing torque w_j of (11.36) to the linear transmitted torque C_{0j} , which describes a flexible transmission given by:

$$C_{0j} = K_j \Delta\theta_j \tag{11.37}$$

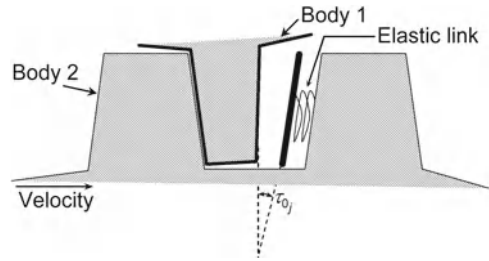
The approximate continuous transmitted torque C_j (Fig. 11.34) is obtained as follows:

$$C_j = K_j \left(\Delta\theta_j - A_j \tau_{0j} \frac{1 - e^{-\gamma_j \Delta\theta_j}}{1 + e^{-\gamma_j \Delta\theta_j}} \right) \tag{11.38}$$

Let's note e_{25_j} , P_{25_j} , M_{25_j} effort, momentum, and algebraic value of element I of Fig. 11.33, f_{24_j} is the flow variable of link 24. f_{29_j} , $1/K_j$ are flow variable and algebraic value of element C , then the following state Eq. (11.39) is obtained:

$$e_{25_j} = -f_{e_j} \frac{P_{25_j}}{M_{25_j}} + e_{24_j} + e_{26_j} - K_j \int f_{29_j} dt \tag{11.39}$$

Fig. 11.33 Backlash mechanism for the j th DC motor



with

$$\begin{cases} f_{24_j} = f_{25_j} = f_{26_j} = f_{27_j} = f_{28_j} = \frac{1}{J_{e_j}} \int e_{25_j} dt = \frac{P_{25_j}}{M_{25_j}} = \dot{\theta}_{e_j}; \\ e_{28_j} = e_{29_j} = K_j \int f_{29_j} dt; \\ f_{29_j} = f_{28_j} - f_{30_j} = \theta_{e_j} - N_j \dot{\theta}_{s_j}; \\ e_{24_j} = U_j = k_{e_j} i_j; \\ e_{26_j} = w_j \end{cases}$$

Thus, the corresponding dynamic equation of mechanical part is given as follows:

$$J_{e_j} \cdot \frac{d\dot{\theta}_{e_j}}{dt} = -f_{e_j} \cdot \dot{\theta}_{e_j} + U_j - w_j - K_j \cdot (\theta_{e_j} - N_j \cdot \theta_{s_j}) \tag{11.40}$$

where U_j is the input motor torque of the j th DC motor, given as function of the current i_j and the torque constant k_{e_j} , supposed equal to the electric constant of the motor.

11.3.2.3 Gear Part

This part concerns the mechanical gear which links between the mechanical and the wheel parts with a gearing constant N_j (Fig. 11.32). Bond graph model of this part is given by Fig. 11.35 and represents a transformer element TF between the j th velocities of the motor axis $\dot{\theta}_{e_j}$ and the wheel $\dot{\theta}_{s_j}$.

According to Fig. 11.35, let's choose f_{30_j} and f_{31_j} as the corresponding flow variables of links 30 and 31:

$$f_{30} = N_j \cdot f_{31} \tag{11.41}$$

which corresponds to the mechanical equation:

$$\dot{\theta}_{e_j} = N_j \cdot \dot{\theta}_{s_j} \tag{11.42}$$

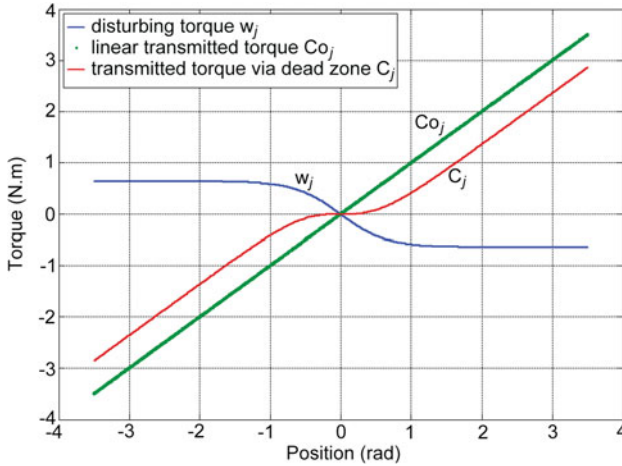


Fig. 11.34 Approximation of transmitted torques via a dead zone

Fig. 11.35 Bond graph model of j th gears part

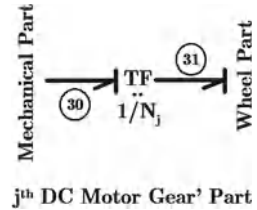
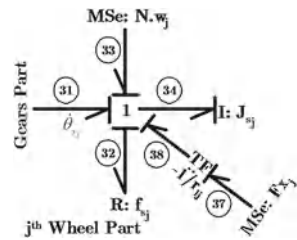


Fig. 11.36 Bond graph model of the j th wheel part



11.3.2.4 Wheel Part

This part represents the wheel part of the j th electromechanical system, characterizing by its inertia J_{sj} , viscous friction parameter f_{sj} , backlash disturbing torque $N_j w_j$, and the longitudinal effort F_{x_j} of Eq. (11.9). The bond graph model of this part in integral causality is given by Fig. 11.36.

Let's note e_{34_j} , P_{34_j} , M_{34_j} effort, momentum, and algebraic value of element I of Fig. 11.27. f_{29} is the flow variable of element C (Fig. 11.36), then the following state Eq. 11.8 is obtained:

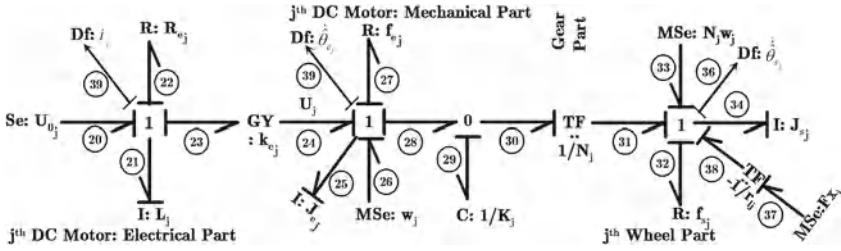


Fig. 11.37 j th global bond graph model of the electromechanical system

$$e_{34_j} = -f_{s_j} \frac{P_{34_j}}{M_{34_j}} + e_{33_j} + e_{31_j} + e_{38_j} \tag{11.43}$$

with

$$f_{31_j} = f_{32_j} = f_{33_j} = f_{34_j} = \frac{1}{J_{e_j}} \int e_{34_j} dt = \frac{P_{34_j}}{M_{34_j}} = \dot{\theta}_{s_j};$$

$$e_{31_j} = N_j e_{29_j} = N_j K_j \int f_{29_j} dt;$$

$$e_{24_j} = k_{e_j} f_{22_j} = k_{e_j} i_j = U_j;$$

$$f_{29_j} = f_{28_j} - f_{30_j} = \dot{\theta}_{e_j} - N_j \dot{\theta}_{s_j};$$

$$e_{33_j} = N_j w_j;$$

$$e_{38_j} = r_{l_j} e_{37_j} = -r_{l_j} F_{x_j}$$

Thus, the corresponding dynamic equation of mechanical part is given as follows:

$$J_{s_j} \frac{d\dot{\theta}_{s_j}}{dt} = -f_{s_j} \dot{\theta}_{s_j} + N_j w_j + N_j K_j (\theta_{e_j} - N_j \theta_{s_j}) - r_{l_j} F_{x_j} \tag{11.44}$$

After a concatenation of the different bond graph models, the global model of the j th electromechanical system is deduced in Fig. 11.37. Knowing that the measured states in the studied case are the angular positions θ_{e_j} , θ_{s_j} of the motor and the wheel and current intensity i_j , while the angular the velocities can be estimated by reconstruction under conditions, using nonlinear observer [21].

Thus, the dynamic nonlinear model of the j th electromechanical system of the electric vehicle is the following:

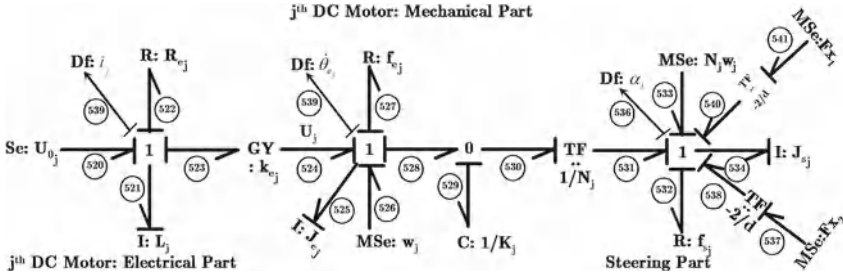


Fig. 11.38 Bond graph model of the steering actuator considering the interaction with the ground

$$\begin{cases} L_j \frac{d}{dt} (i_j) = U_{0j} - R_{e_j} i_j - k_{e_j} \dot{\theta}_{e_j} \\ J_{e_j} \frac{d}{dt} (\dot{\theta}_{e_j}) = -f_{e_j} \dot{\theta}_{e_j} + k_{e_j} i_j - w_j - K_j (\theta_{e_j} - N_j \theta_{s_j}) \\ J_{s_j} \frac{d}{dt} (\dot{\theta}_{s_j}) = -f_{s_j} \dot{\theta}_{s_j} + N_j w_j + N_j K_j (\theta_{e_j} - N_j \theta_{s_j}) - r_{l_j} F_{x_j} \end{cases} \quad (11.45)$$

11.3.2.5 Electromechanical Steering System

The electromechanical steering system of the studied IAV system is composed by a DC motor characterized by its electrical and mechanical domains (Fig. 11.6). Two steering systems exist on this vehicle, one for the front side and the other for the rear side (Fig. 11.5). This double steering configuration gives more mobility to the vehicle. Then the associated bond graph model of the front steering system, according to the word bond graph of Fig. 11.6 is given in Fig. 11.38. The steering part concerns the applied efforts on the wheel and the tire-ground interaction, while $d/2$ represents the vertical distance between the wheel axis and the center of gravity (CoG) (Fig. 11.7). In this case, the lateral efforts of the contact are neglected, because it is supposed acted parallel to the steering axis, where the generated torque is null.

The dynamic nonlinear model of the steering electromechanical system (11.46) is deduced from the bond graph junctions of Fig. 11.38 for the front steering system.

$$\begin{cases} L_j \frac{d}{dt} (i_j) = U_{0j} - R_{e_j} i_j - k_{e_j} \dot{\theta}_{e_j} \\ J_{e_j} \frac{d}{dt} (\dot{\theta}_{e_j}) = -f_{e_j} \dot{\theta}_{e_j} + k_{e_j} i_j - w_j - K_j (\theta_{e_j} - N_j \theta_{s_j}) \\ J_{s_j} \frac{d}{dt} (\dot{\theta}_{s_j}) = -f_{s_j} \dot{\theta}_{s_j} + N_j w_j + N_j K_j (\theta_{e_j} - N_j \theta_{s_j}) - \frac{d}{2} F_{x_1} - \frac{d}{2} F_{x_2} \end{cases} \quad (11.46)$$

Finally, Fig. 11.39 illustrates the quarter of vehicle mechatronics' components with their bond graph' models.

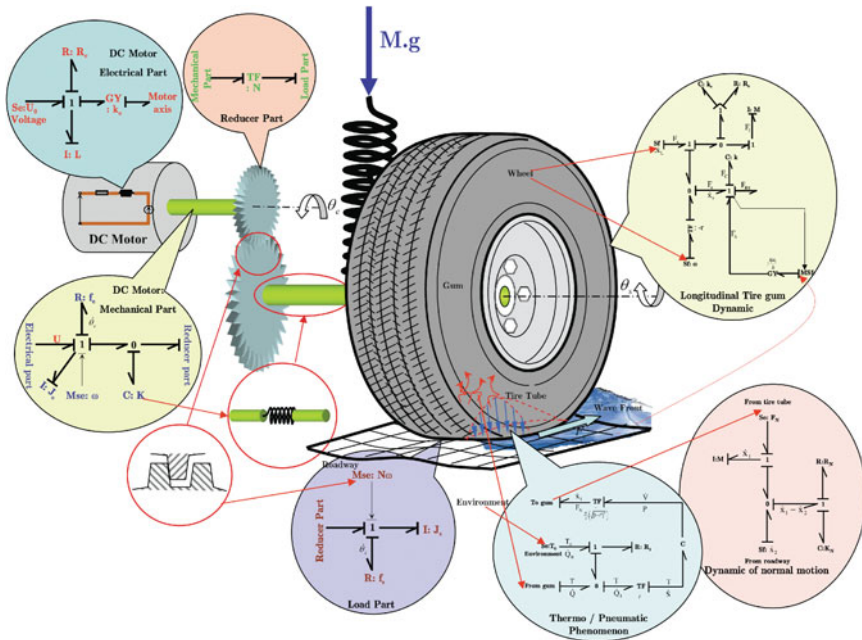


Fig. 11.39 Mechatronics concept of quarter of decentralized vehicle

11.3.2.6 Identification and Validation

In the following, we present a development of a nonlinear observer, allowing to reconstruct unmeasured states and to identify perturbation or the system parameters. It is a second-order sliding mode observer with finite time convergence applied for a *j*th electromechanical system. As consequence of finite time convergence, the sliding mode equivalent control is used to apply identification algorithms in order to characterize the backlash phenomena, where the dead zone amplitude and the disturbing torque are identified asymptotically. In some cases, for a better understanding of the backlash mechanism, the reconstruction of unmeasured states is needed [21]. In our case only the position measurements of the *j*th motor and wheel are available, and the corresponding velocities are synthesized by using this nonlinear observers. For this purpose, the used observers require keeping the finite time convergence even if the system exhibits the backlash phenomenon.

The proposed nonlinear observers, based on the second-order sliding mode super-twisting algorithm [15] are developed. They reconstruct input and output velocities for the *j*th electromechanical system including the backlash phenomena, using position and current measurements. The finite time convergence of these observers allows using properties of equivalent control to identify the backlash as a perturbation, or in a no disturbing frame, using linear regression algorithms to identify the backlash parameters.

Let's consider only the model of the j th electromechanical of system (11.45), after replacing the current i_j by the first derivative of electric charge \dot{q}_j as follows:

$$\begin{cases} L_j \frac{d}{dt} (\dot{q}_j) = U_{0j} - R_{e_j} \dot{q}_j - k_{e_j} \dot{\theta}_{e_j} \\ J_{e_j} \frac{d}{dt} (\dot{\theta}_{e_j}) = -f_{e_j} \dot{\theta}_{e_j} + k_{e_j} \dot{q}_j - w_j - K_j (\theta_{e_j} - N_j \theta_{s_j}) \\ J_{s_j} \frac{d}{dt} (\dot{\theta}_{s_j}) = -f_{s_j} \dot{\theta}_{s_j} + N_j w_j + N_j K_j (\theta_{e_j} - N_j \theta_{s_j}) - r_{l_j} F_{x_j} \end{cases} \quad (11.47)$$

After introducing the variables $x_1 = (q_j \theta_{e_j} \theta_{s_j})^T$, $x_2 = (\dot{q}_j \dot{\theta}_{e_j} \dot{\theta}_{s_j})^T$, the model (11.47) can be rewritten as follows:

$$\begin{cases} \dot{x}_1 = x_2 \\ \dot{x}_2 = \Delta^{-1} [\Phi x_2 + \Psi x_1 + \Gamma U_{0j} + \Omega w_j + F F_{x_j}] \end{cases} \quad (11.48)$$

where

$$\Delta = \begin{pmatrix} L_j & 0 & 0 \\ 0 & J_{e_j} & 0 \\ 0 & 0 & J_{s_j} \end{pmatrix}; \Phi = \begin{pmatrix} -R_{e_j} & -k_{e_j} & 0 \\ k_{e_j} & -f_{e_j} & 0 \\ 0 & 0 & -f_{s_j} \end{pmatrix}; F = \begin{pmatrix} 0 \\ 0 \\ -r_{l_j} \end{pmatrix};$$

$$\Psi = \begin{pmatrix} 0 & 0 & 0 \\ 0 & -K_j & N_j K_j \\ 0 & N_j K_j & -N_j^2 K_j \end{pmatrix}; \Gamma = \begin{pmatrix} 1 \\ 0 \\ 0 \end{pmatrix}; \Omega = \begin{pmatrix} 0 \\ -1 \\ N_j \end{pmatrix}.$$

The proposed observer is formulated as follows:

$$\begin{cases} \dot{\hat{x}}_1 = \hat{x}_2 + \lambda |\tilde{x}_1|^{\frac{1}{2}} \text{sign}(\tilde{x}_1) \\ \dot{\hat{x}}_2 = \Delta^{-1} [\Phi \hat{x}_2 + \Psi \hat{x}_1 + \Gamma U_{0j} + F \bar{F}_{x_j}] + \sigma \text{sign}(\tilde{x}_1) \end{cases} \quad (11.49)$$

where \hat{x}_1 and \hat{x}_2 are the state estimations, $\tilde{x}_1 = x_1 - \hat{x}_1$ is the estimation error, and \bar{F}_{x_j} is the nominal value of the longitudinal effort F_{x_j} . The correction factors based on the super-twisting algorithm developed in [15], where the parameters σ_i and λ_i ($i \in [1; 3]$) of vectors σ and λ are designed so as to fulfill the conditions:

$$\lambda_i > \sqrt{\frac{2}{\sigma_i - f_i^+} \frac{(\sigma_i + f_i^+)(1 + \varepsilon_i)}{(1 - \varepsilon_i)}}$$

where the constants $f_i^+ = 2 \max \dot{x}_{2_i}$, and $0 < \varepsilon_i < 1$, [2].

These observers ensure the finite time convergence of observation states error to zero. In this case, a finite time convergence of the estimated states to the real states values is obtained [21].

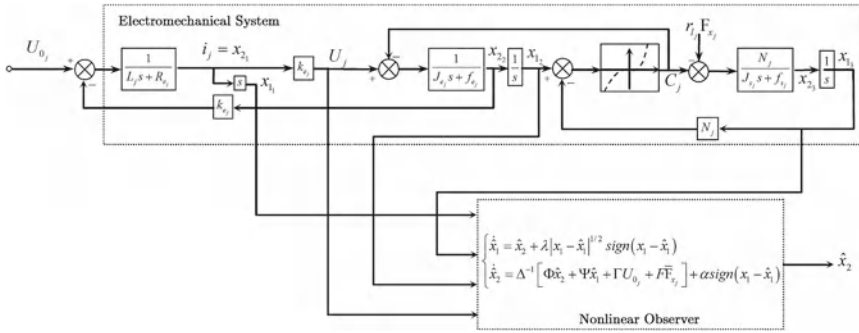


Fig. 11.40 Nonlinear observer structure

Perturbation Identification

As consequence of finite time convergence and the existence of a equivalent control, the sliding motion is guaranteed [46]. This equivalent control allows to directly identify the external perturbations acting on the system (Fig. 11.40).

After applying the super-twisting observer (11.49) on model of (11.48), the equations for the errors become:

$$\begin{cases} \dot{\tilde{x}}_1 = \tilde{x}_2 + \lambda |\tilde{x}_1|^{1/2} \text{sign}(\tilde{x}_1) \\ \dot{\tilde{x}}_2 = \Delta^{-1} [\Phi \tilde{x}_2 + \Psi \tilde{x}_1 + \Omega w_j + F \tilde{F}_{x_j}] + \sigma \text{sign}(\tilde{x}_1) \end{cases} \tag{11.50}$$

with $\tilde{F} = F - \bar{F}$ and $\tilde{x}_2 = x_2 - \hat{x}_2$.

The finite time convergence of x_1 and x_2 ($\tilde{x}_1 \rightarrow 0, \tilde{x}_2 \rightarrow 0, \dot{\tilde{x}}_1 \rightarrow 0, \dot{\tilde{x}}_2 \rightarrow 0$) allows writing:

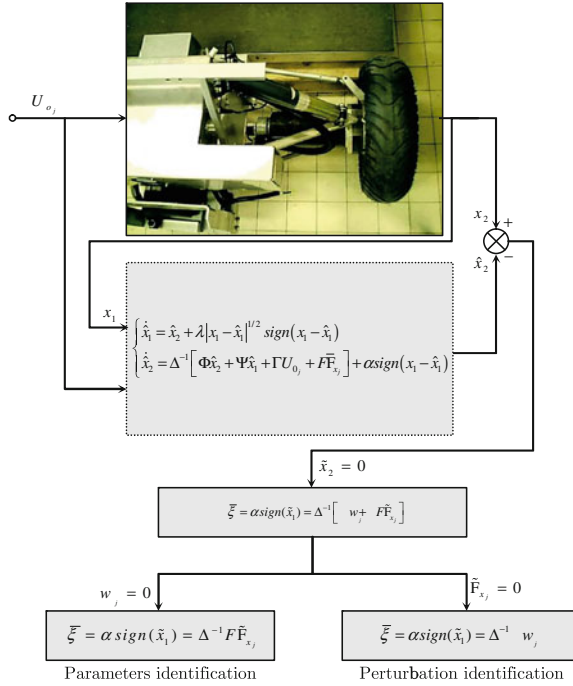
$$\xi = \sigma \text{sign}(\tilde{x}_1) = \Delta^{-1} [\Omega w_j + F \tilde{F}_{x_j}] \tag{11.51}$$

It is assumed that the term ξ changes at a high, theoretically infinite frequency. However, in practice, various imperfections make the state oscillating in some vicinity of the intersection, whereas, the components of ξ are switched at finite high frequency. The high frequency of ξ is filtered out and the motion in the sliding mode is determined by the slow component [46]. It is reasonable to assume that the equivalent control is close to the slow component of the real control. The latter may be derived by filtering out the high frequency component using a low-pass filter. The filter time constant should be sufficiently small to preserve the slow component but enough large to eliminate the high frequency component.

After using $\bar{\xi}$, the filtered version of ξ , expression (11.51) can be formulated as follows:

$$\bar{\xi} = \sigma \text{sign}(\tilde{x}_1) = \Delta^{-1} [\Omega w_j + F \tilde{F}_{x_j}] \tag{11.52}$$

Fig. 11.41 Identification procedure



When the parameters of the tire-road contact and the system Δ are totally known,

$$F_{x_j} = \tilde{F}_{x_j} \tag{11.53}$$

Then, the term $\tilde{F}_{x_j} = 0$ (Fig. 11.41), and $\tilde{\xi}$ gives an estimation of the perturbation w_j ,

$$\tilde{\xi} = \sigma \text{sign}(\tilde{x}_1) = \Delta^{-1} \Omega w_j \tag{11.54}$$

Equation (11.54) describes the disturbing backlash torque for the j th electro-mechanical system.

Parameter Identification

In the case when the transmitted torque C_j through the gear part, modeled in (11.38), without presence of perturbation ($w_j = 0$). Let's consider that only nominal values of the system parameters are known (Fig. 11.41). Then, the use of equivalent control, in combination with identification algorithms, allows identifying the real values of system parameters.

After a finite time duration, the next equality holds for $\bar{\xi}$.

$$\bar{\xi} = \sigma \text{sign}(\tilde{x}_1) = \Delta^{-1} F \tilde{F}_{x_j} \quad (11.55)$$

The equality (11.55) can be described by a model structure for linear regression [40].

$$\bar{\xi}(t) = \Theta \varphi(t) \quad (11.56)$$

where $\bar{\xi}(t)$ is a measurable quantity, $\Theta = \Delta^{-1} F$ is a vector of unknown parameters to be identified, $\varphi(t)$ is a vector of known quantities:

$$\Theta = \begin{pmatrix} 0 \\ 0 \\ -\frac{r_j}{J_{s_j}} \end{pmatrix}; \varphi(t) = \tilde{F}_{x_j} \quad (11.57)$$

It is possible to apply a linear regression algorithm like the least square method to identify dynamic system parameters. Developing least square algorithm, the average expression of time integration with ρ as auxiliary time variable is given by:

$$\frac{1}{t} \int_0^t \bar{\xi}(\rho) \varphi(\rho)^T d\rho = \Delta^{-1} F \frac{1}{t} \int_0^t \varphi(\rho) \varphi(\rho)^T \cdot d\rho \quad (11.58)$$

Therefore, the parameters can be estimated as follows:

$$\hat{\Theta} = \left[\int_0^t \bar{\xi}(\rho) \varphi(\rho)^T d\rho \right] \left[\int_0^t \varphi(\rho) \varphi(\rho)^T d\rho \right]^{-1} \quad (11.59)$$

where $\hat{\Theta}$ is the estimation of $\Theta = \Delta^{-1} F$.

Defining $\Gamma_t = \left[\int_0^t \varphi(\rho) \cdot \varphi(\rho)^T \cdot d\rho \right]^{-1}$ along with the equalities:

$$\begin{cases} \Gamma_t^{-1} \dot{\Gamma}_t = I \\ \Gamma_t^{-1} \dot{\Gamma}_t + \dot{\Gamma}_t^{-1} \Gamma_t = 0 \end{cases} \quad (11.60)$$

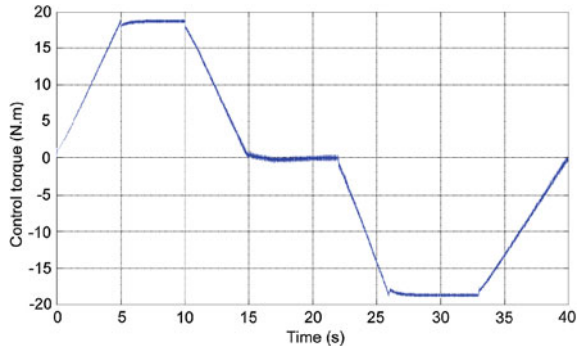
A parameter estimation algorithm can be written. From (11.59), the following equation is obtained:

$$\dot{\hat{\Theta}} = \left[\int_0^t \bar{\xi}(\rho) \varphi(\rho)^T d\rho \right] \dot{\Gamma}_t + \bar{\xi} \varphi^T \Gamma_t \quad (11.61)$$

Using Eq. (11.60), then Eq. (11.61) is written as follows:

$$\dot{\hat{\Theta}} = \hat{\Theta} \Gamma_t^{-1} \dot{\Gamma}_t + \bar{\xi} \varphi^T \Gamma_t \quad (11.62)$$

Fig. 11.42 Input motor torque



Using the equalities of Γ_t given above, the dynamic expression to compute $\hat{\Theta}$ is given by:

$$\dot{\hat{\Theta}} = [-\hat{\Theta}\varphi + \bar{\xi}] \varphi^T \Gamma_t \tag{11.63}$$

After replacing (11.56) in (11.63), we obtain the following:

$$\dot{\hat{\Theta}} = \tilde{\Theta} \varphi \varphi^T \Gamma_t \tag{11.64}$$

where $\tilde{\Theta} = \Theta - \hat{\Theta}$ the estimation error of unknown parameters.

Validation

In order to validate the model, the same input torque (Fig. 11.42) is applied to the simulated and the real system, then a comparison is done between the system and the model outputs. Figure 11.43 shows the estimation of wheel and motor velocities, knowing the calculated maximum dead zone' amplitude is $\tau_{0_j} = 0.01$ rad.

The graphics show the states estimation between 0 and 20 s with a gearing constant $N_j = 13$. Figures 11.44 and 11.45 represent the estimation of the longitudinal efforts and transmitted torque after algorithm convergence ($\sigma_i = 5$; $\lambda_i = 0.045$, $i \in [1; 3]$). We can notice that the amplitude of the dead zone is relatively small, this effect can be neglected at the modeling step, according to the considered scenario.

When the perturbation is neglected ($w_j = 0$), we can use the same method of identification (11.63) to identify j th system parameters. Once the implemented identification algorithm reaches its steady operation, the values of each parameter are taken in one observation window. Some results are given in Figs. 11.46 and 11.47.

For each parameter, a mean and a standard deviation are calculated. The mean corresponds to the nominal value of the parameter.

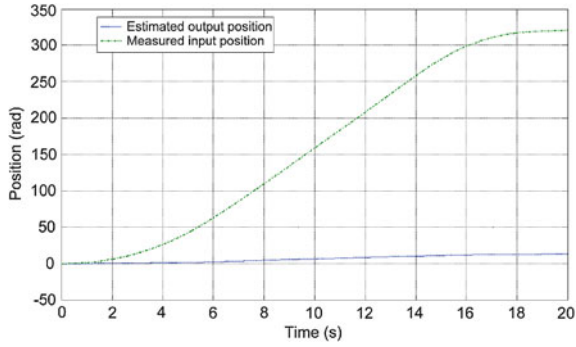


Fig. 11.43 Estimation of wheel and motor velocities

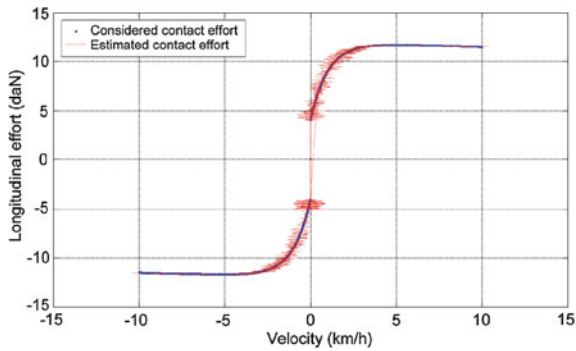


Fig. 11.44 Estimation of the longitudinal effort

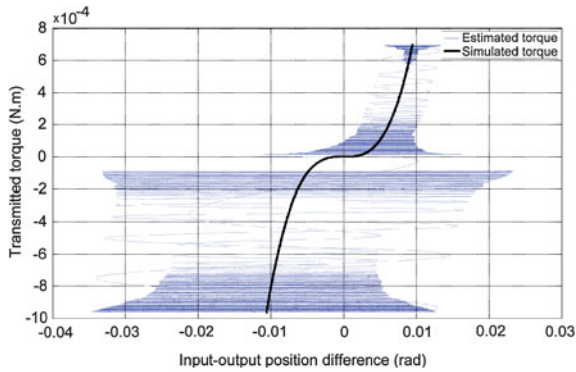


Fig. 11.45 Transmitted torque through the gear system

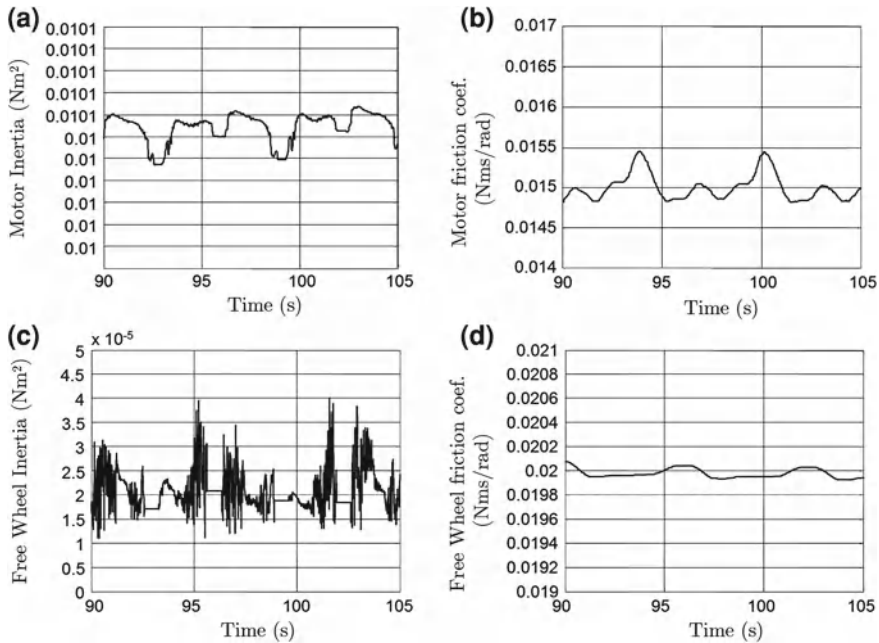


Fig. 11.46 **a** Motor inertia. **b** Viscous friction coefficient of the motor. **c** Free wheel inertia. **d** Viscous friction coefficient of the free wheel

11.4 Dynamic Modeling of the Chassis

The vehicle model used in the following analysis is a six degree of freedom, longitudinal, lateral, vertical, pitch, roll, and yaw motions, with differential and active steering for the rear and forward sides.

11.4.1 Longitudinal Dynamic Modeling

In the studied case, the *RobuCar* system runs with maximum velocity of 18 km/h. Thus, the effect of the centrifugal force is neglected (Fig. 11.48).

The bond graph model of the longitudinal dynamic of *RobuCar*'s vehicle is given in Fig. 11.49. \dot{v} , $\dot{\beta}$, \ddot{u} are the lateral and yaw velocities and longitudinal acceleration of the vehicle. F_{xj} and F_{yj} , $j \in [1; 4]$ are deduced from the tire-road contact efforts' estimation. They are taken as an effort source, modulated respectively with expressions (11.9) and (11.19).

From the bond graph model of the *Longitudinal* dynamic in integral causality, mathematical expression of this dynamic can be deduced as follows:

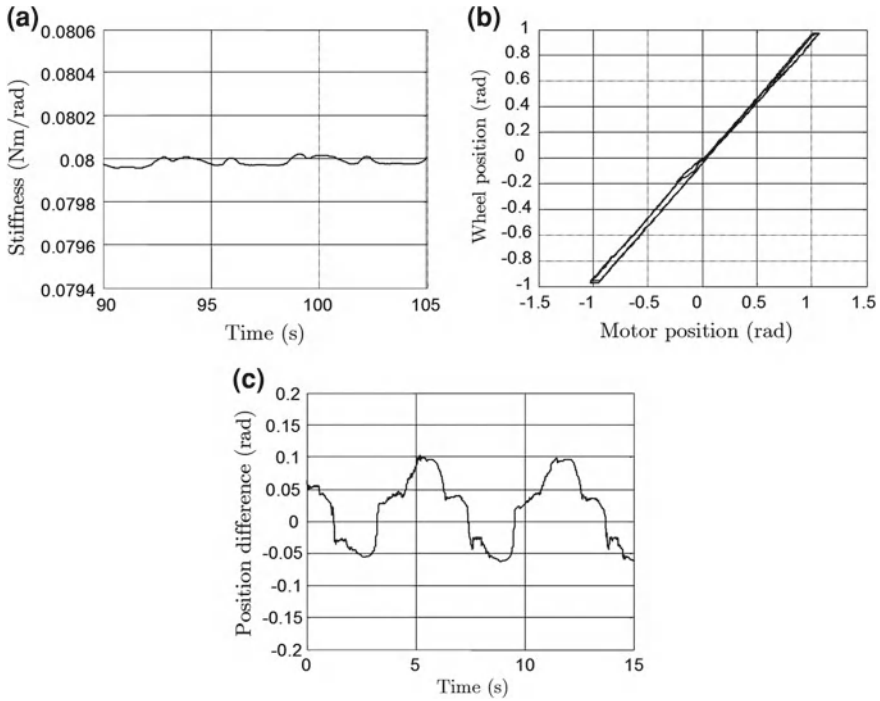


Fig. 11.47 a Axis stiffness. b Input/output hysteresis. c Input/output position difference

$$\begin{aligned}
 m\ddot{u} = & (F_{x1} + F_{x2}) \cos \alpha_1 - (F_{y1} + F_{y2}) \sin \alpha_1 + (F_{x3} + F_{x4}) \cos \alpha_2 \\
 & + (F_{y3} + F_{y4}) \sin \alpha_2 + m\dot{\beta}\dot{v}
 \end{aligned}
 \tag{11.65}$$

11.4.2 Lateral Dynamic Modeling

The same assumption as in the longitudinal motion concerning the effect of the neglected external centrifugal force' effects. Then, the corresponding bond graph model of the lateral dynamic is shown in Fig. 11.50. \dot{v} , \ddot{v} are the lateral velocity and lateral acceleration of the vehicle.

From the bond graph model of the *Lateral* dynamic in integral causality, mathematical expression of this dynamic can be deduced as follows:

$$\begin{aligned}
 m\ddot{v} = & (F_{x1} + F_{x2}) \sin \alpha_1 + (F_{y1} + F_{y2}) \cos \alpha_1 - (F_{x3} + F_{x4}) \sin \alpha_2 \\
 & + (F_{y3} + F_{y4}) \cos \alpha_2 - m\dot{\beta}\dot{u}
 \end{aligned}
 \tag{11.66}$$

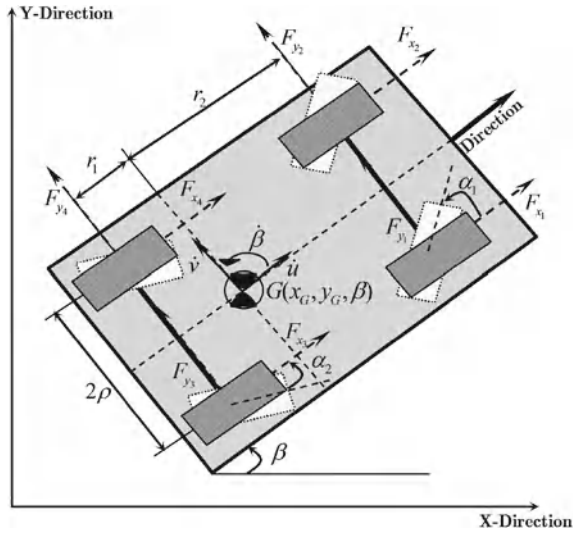


Fig. 11.48 Representation of longitudinal, lateral, and yaw motions

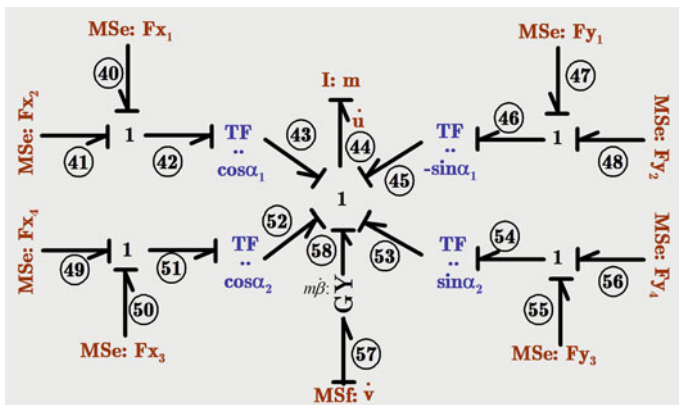


Fig. 11.49 Bond graph model of longitudinal dynamic

11.4.3 Yaw Dynamic Modeling

Definition 11.1 The *Yaw* angle of a vehicle is the angle generated from the rotation around the vertical axis (Fig. 11.48).

The *Yaw* dynamic of the *RobuCar* system is detailed at the bond graph model of Fig. 11.51.

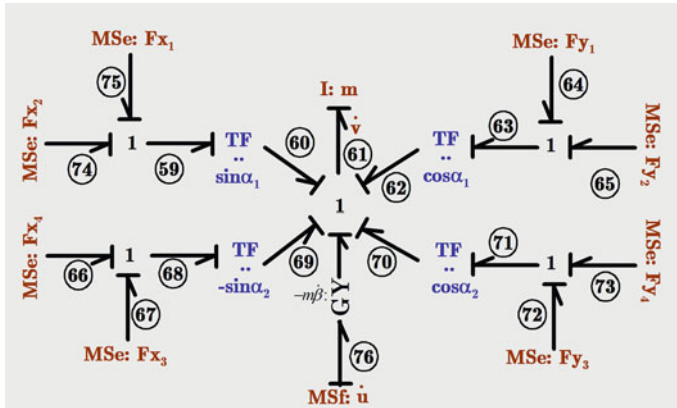


Fig. 11.50 Bond graph model of lateral dynamic

From the bond graph model (Fig. 11.51) of the *Yaw* dynamic in integral causality, mathematical expression of this dynamic can be deduced as it is developed below:

$$\begin{aligned}
 L_G \ddot{\beta} = & r_2 [(F_{x1} + F_{x2}) \sin \alpha_1 + (F_{y1} + F_{y2}) \cos \alpha_1] \\
 & + r_1 [(F_{x3} + F_{x4}) \sin \alpha_2 - (F_{y3} + F_{y4}) \cdot \cos \alpha_2] \\
 & + \frac{d}{2} [(F_{x1} - F_{x2}) \cos \alpha_1 + (F_{x3} - F_{x4}) \cos \alpha_2 \\
 & - (F_{y1} - F_{y2}) \sin \alpha_1 + (F_{y3} - F_{y4}) \sin \alpha_2] \quad (11.67)
 \end{aligned}$$

where L_G is the inertia of the *RobuCar*'s center of gravity calculated according to the vertical axis.

11.4.4 Suspension Dynamics Modeling

Consider the suspended mass m of *RobuCar*'s chassis, as being a rectangular bar of length $r_1 + r_2$ and width 2ρ (with $r_1 + r_2 > 2\rho$), different from d . Figure 11.52 shows schematically the *RobuCar*'s components of roadway impacts excitation (z_{j1} , $j \in [1; 4]$), wheels (mass m_j and their normal displacements z_{j2} , tire viscoelasticity characteristics in normal axis: k_{j1} stiffness and a_{j1} friction coefficient with link stiffness k_{rn} , $i \in [1; 4]$, $n \in [1; 2]$), suspension system (k_{j2} stiffness and a_{j2} viscous friction coefficient, and their normal displacements z_j , $j \in [1; 4]$) and the impact efforts (F_{xj} , F_{yj} and F_{zj} , $j \in [1; 4]$) (Fig. 11.53).

The front side corresponds to AB and the rear one to CD . The center of gravity is located at coordinates (r_2, ρ) relative to corner A , where φ and θ correspond

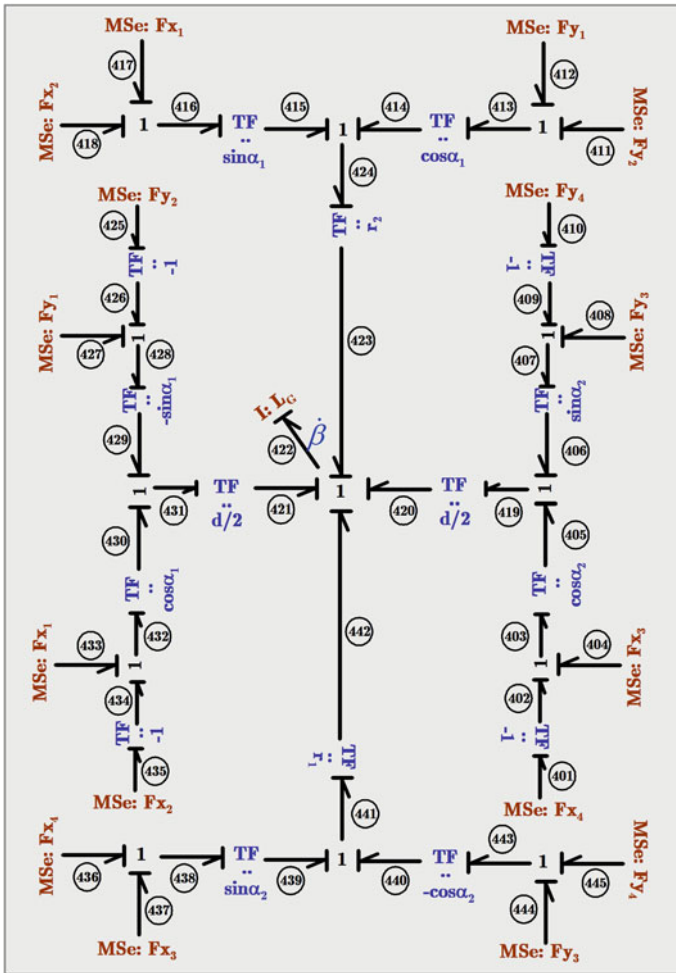


Fig. 11.51 Bond graph model of the Yaw dynamic

respectively to the pitch and roll angles. Clockwise roll ($\theta > 0$) of the bar is defined as ($z_2 > z_1$), and the clockwise pitch ($\varphi > 0$) as ($z_3 > z_1$). The lateral and longitudinal (roll and pitch) moments of inertia are I_G and J_G respectively.

Note that h corresponds to the mass displacement, then according to Fig. 11.54, the following expressions are deduced:

$$\begin{cases} z_1 = h - \rho \sin \theta - r_2 \sin \varphi \\ z_2 = h + \rho \sin \theta - r_2 \sin \varphi \\ z_3 = h - \rho \sin \theta + r_1 \sin \varphi \\ z_4 = h + \rho \sin \theta + r_1 \sin \varphi \end{cases} \quad (11.68)$$

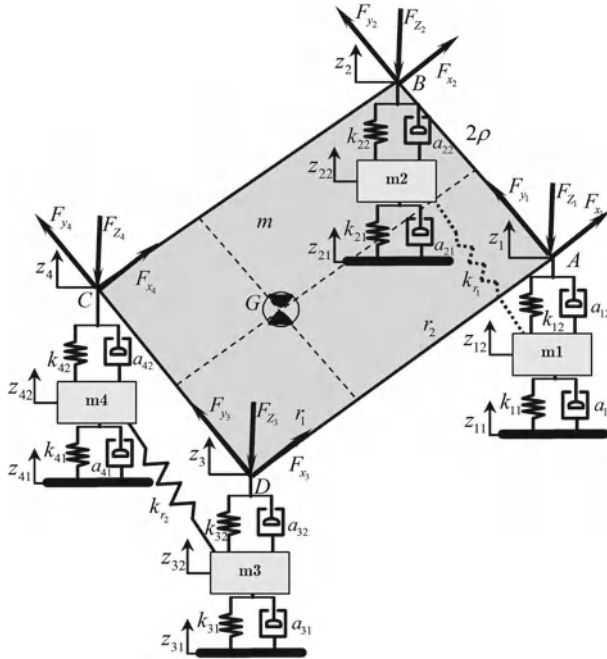
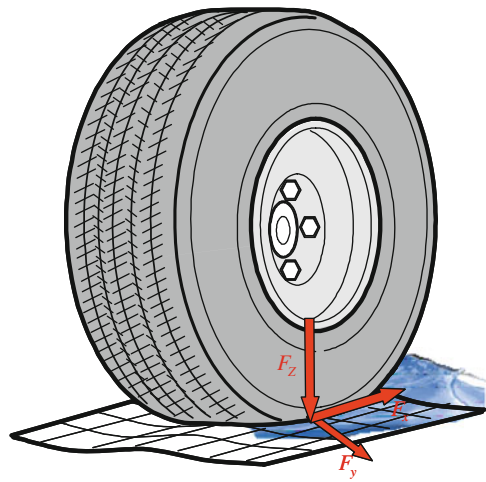


Fig. 11.52 Suspension system of RobuCar

Fig. 11.53 Tire contact forces configuration for RobuCar



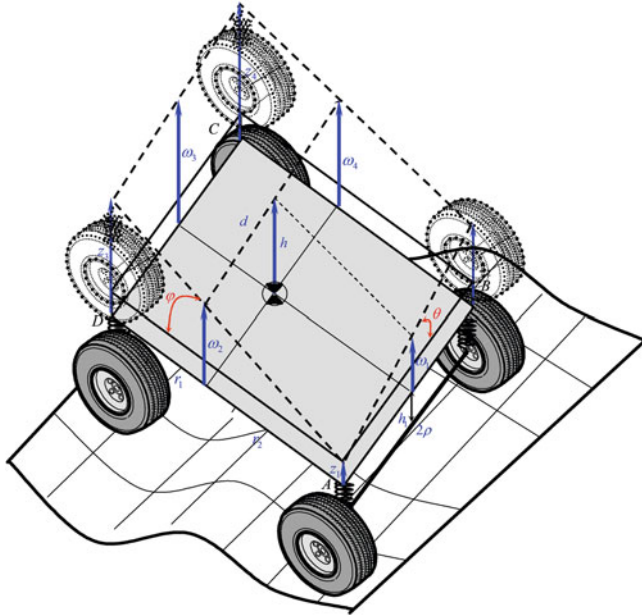


Fig. 11.54 Roll and pitch RobuCar’s chassis movements

Let’s consider that the roll and pitch angular displacement are small, then $\sin \theta \rightarrow \theta$ and $\sin \varphi \rightarrow \varphi$. Expressions (11.68) will become:

$$\begin{cases} z_1 = h - \rho\theta - r_2\varphi \\ z_2 = h + \rho\theta - r_2\varphi \\ z_3 = h - \rho\theta + r_1\varphi \\ z_4 = h + \rho\theta + r_1\varphi \end{cases} \quad (11.69)$$

with

$$\begin{cases} \omega_1 = h - r_2\varphi \\ \omega_2 = h - \rho\theta \\ \omega_3 = h + r_1\varphi \\ \omega_4 = h + \rho\theta \end{cases} \quad (11.70)$$

Measurements of $\omega_i, i \in [1; 4]$ are useful for the location of r_1 and r_2 .

The corresponding bond graph model of the suspension motion related to *RobuCar* system is given by Fig. 11.55.

Thus, the synthesized differential equations from the bond graph model are given as follows:

$$\begin{aligned} m_1 \ddot{z}_{12} &= k_{11}(z_{11} - z_{12}) + k_{12}(h - \rho\theta - r_2\varphi - z_{12}) + a_{11}(\dot{z}_{11} - \dot{z}_{12}) \\ &+ a_{12}(\dot{h} - \rho\dot{\theta} - r_2\dot{\varphi} - \dot{z}_{12}) + k_{r_1}(z_{22} - z_{12}) \end{aligned}$$

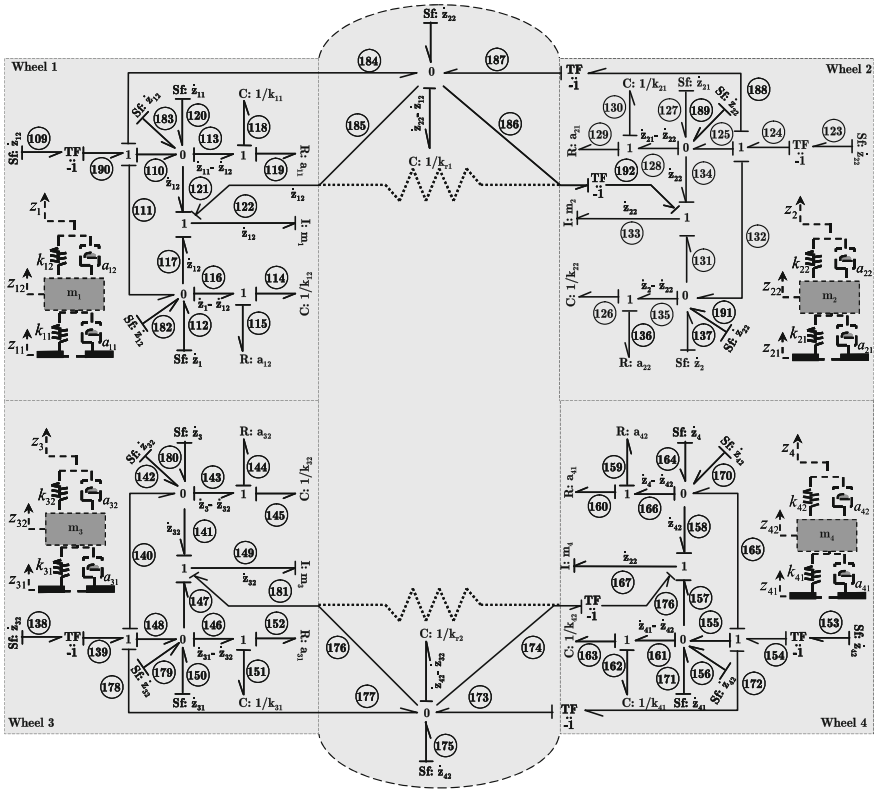


Fig. 11.55 Bond graph model of suspension dynamics

$$\begin{aligned}
 m_2 \ddot{z}_{22} &= k_{21}(z_{21} - z_{22}) + k_{22}(h + \rho\theta - r_2\varphi - z_{22}) + a_{21}(\dot{z}_{21} - \dot{z}_{22}) \\
 &\quad + a_{22} \cdot (\dot{h} + \rho\dot{\theta} - r_2\dot{\varphi} - \dot{z}_{22}) + k_{r_1}(z_{12} - z_{22}) \\
 m_3 \ddot{z}_{32} &= k_{31}(z_{31} - z_{32}) + k_{32}(h - \rho\theta + r_1\varphi - z_{32}) + a_{31}(\dot{z}_{31} - \dot{z}_{32}) \\
 &\quad + a_{32}(\dot{h} - \rho\dot{\theta} + r_1\dot{\varphi} - \dot{z}_{32}) + k_{r_2}(z_{42} - z_{32}) \\
 m_4 \ddot{z}_{42} &= k_{41}(z_{41} - z_{42}) + k_{42}(h + \rho\theta - r_1\varphi - z_{42}) + a_{41}(\dot{z}_{41} - \dot{z}_{42}) \\
 &\quad + a_{42}(\dot{h} + \rho\dot{\theta} + r_1\dot{\varphi} - \dot{z}_{42}) + k_{r_2}(z_{32} - z_{42}) \tag{11.71}
 \end{aligned}$$

Then, it can be represented in appropriate form related to the states by (11.72):

$$\begin{aligned}
 \ddot{z}_{12} &= -\frac{a_{11} + a_{12}}{m_1} \dot{z}_{12} - \frac{k_{11} + k_{12} + k_{r1}}{m_1} z_{12} + \frac{a_{12}}{m_1} \dot{h} + \frac{k_{12}}{m_1} h - \frac{a_{12}\rho}{m_1} \dot{\theta} - \frac{k_{12}\rho}{m_1} \theta \\
 &\quad - \frac{a_{12}r_2}{m_1} \dot{\varphi} - \frac{k_{12}r_2}{m_1} \varphi + \frac{k_{r1}}{m_1} z_{22} + \frac{a_{11}}{m_1} \dot{z}_{11} + \frac{k_{11}}{m_1} z_{11} \\
 \ddot{z}_{22} &= -\frac{a_{21} + a_{22}}{m_2} \dot{z}_{22} - \frac{k_{21} + k_{22} + k_{r1}}{m_2} z_{22} + \frac{a_{22}}{m_2} \dot{h} + \frac{k_{22}}{m_2} h + \frac{a_{22}\rho}{m_2} \dot{\theta} + \frac{k_{22}\rho}{m_2} \theta \\
 &\quad - \frac{a_{22}r_2}{m_2} \dot{\varphi} - \frac{k_{22}r_2}{m_2} \varphi + \frac{k_{r1}}{m_2} z_{12} + \frac{a_{21}}{m_2} \dot{z}_{21} + \frac{k_{21}}{m_2} z_{21} \\
 \ddot{z}_{32} &= -\frac{a_{31} + a_{32}}{m_3} \dot{z}_{32} - \frac{k_{31} + k_{32} + k_{r2}}{m_3} z_{32} + \frac{a_{32}}{m_3} \dot{h} + \frac{k_{32}}{m_3} h - \frac{a_{32}\rho}{m_3} \dot{\theta} - \frac{k_{32}\rho}{m_3} \theta \\
 &\quad + \frac{a_{32}r_1}{m_3} \dot{\varphi} + \frac{k_{32}r_1}{m_3} \varphi + \frac{k_{r2}}{m_3} z_{42} + \frac{a_{31}}{m_3} \dot{z}_{31} + \frac{k_{31}}{m_3} z_{31} \\
 \ddot{z}_{42} &= -\frac{a_{41} + a_{42}}{m_4} \dot{z}_{42} - \frac{k_{41} + k_{42} + k_{r2}}{m_4} z_{42} + \frac{a_{42}}{m_4} \dot{h} + \frac{k_{42}}{m_4} h + \frac{a_{42}\rho}{m_4} \dot{\theta} + \frac{k_{42}\rho}{m_4} \theta \\
 &\quad + \frac{a_{42}r_1}{m_4} \dot{\varphi} + \frac{k_{42}r_1}{m_4} \varphi + \frac{k_{r2}}{m_4} z_{31} + \frac{a_{41}}{m_4} \dot{z}_{41} + \frac{k_{41}}{m_4} z_{41} \tag{11.72}
 \end{aligned}$$

Finally, the dynamic of the *Chassis* is related to the suspension one and it is represented by the following bond graph model of Fig. 11.56.

The corresponding mathematical model is given by the following differential equation:

$$\begin{aligned}
 \ddot{h} &= -\frac{a_{12} + a_{22} + a_{32} + a_{42}}{m} \dot{h} - \frac{k_{12} + k_{22} + k_{32} + k_{42}}{m} h \\
 &\quad + \frac{a_{12} - a_{22} + a_{32} - a_{42}}{m} \rho \dot{\theta} + \frac{k_{12} - k_{22} + k_{32} - k_{42}}{m} \rho \theta \\
 &\quad + \frac{(a_{12} + a_{22})r_2 - (a_{32} + a_{42})r_1}{m} \dot{\varphi} + \frac{F_{z1} + F_{z2} + F_{z3} + F_{z4}}{m} \\
 &\quad + \frac{(k_{12} + k_{22})r_2 - (k_{32} + k_{42})r_1}{m} \varphi + \frac{a_{12}}{m} \dot{z}_{12} + \frac{k_{12}}{m} z_{12} \\
 &\quad + \frac{a_{22}}{m} \dot{z}_{22} + \frac{k_{22}}{m} z_{22} + \frac{a_{32}}{m} \dot{z}_{32} + \frac{k_{32}}{m} z_{32} + \frac{a_{42}}{m} \dot{z}_{42} + \frac{k_{42}}{m} z_{42} \tag{11.73}
 \end{aligned}$$

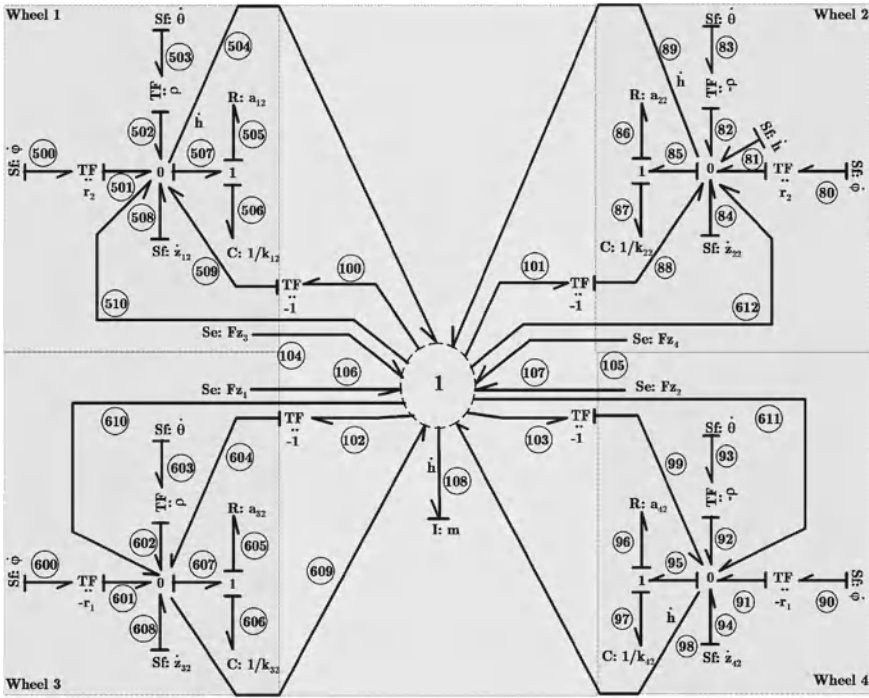


Fig. 11.56 Bond graph model of the Chassis' vertical dynamic

11.4.5 Pitch Dynamics Modeling

Definition 11.2 The *Pitch* angle of a vehicle is the angle generated from the rotation around the lateral axis (Fig. 11.57).

In the studied case, all the system parameters are identified and the states are measured or estimated. *Pitch* and *Roll* velocities $\dot{\varphi}$ and $\dot{\theta}$ are estimated from the inertial central from the real vehicle (Fig. 11.57). F_{x_j} , F_{y_j} , and F_{z_j} ($j \in [1; 4]$) are estimated from the dynamic tire model of Fig. 11.22. The front and rear steering angles α_1 and α_2 are measured directly from the incremental encoders. Then, the bond graph model of the *Pitch* dynamic is given by Fig. 11.58.

From the bond graph model of the *Pitch* dynamic in integral causality, mathematical expression of this dynamic can be deduced as it is developed below:

$$\begin{aligned} \ddot{\varphi} = & \left[\frac{1}{J_G} (a_{12} + a_{22})r_2 - (a_{32} + a_{42})r_1 \right] \dot{h} + \frac{1}{J_G} [(k_{12} + k_{22})r_2 - (k_{32} + k_{42})r_1] h \\ & + \frac{\rho}{J_G} [(a_{22} - a_{12})r_2 + (a_{32} - a_{42})r_1] \dot{\theta} + \frac{\rho}{J_G} [(k_{22} - k_{12})r_2 + (k_{32} - k_{42})r_1] \theta \\ & - \frac{1}{J_G} [(a_{22} + a_{12})r_2^2 + (a_{42} + a_{32})r_1^2] \dot{\varphi} - \frac{1}{J_G} [(k_{22} - k_{12})r_2^2 + (k_{42} + k_{32})r_1^2] \varphi \end{aligned}$$

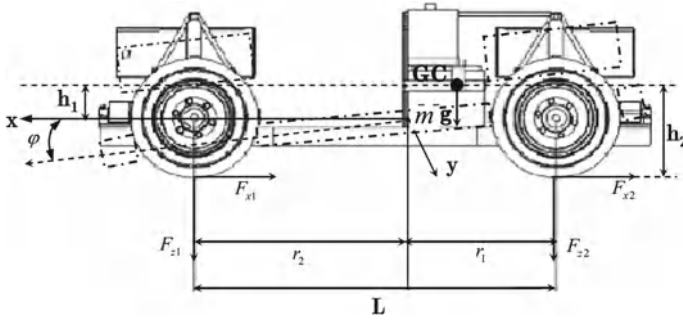


Fig. 11.57 Pitch motion

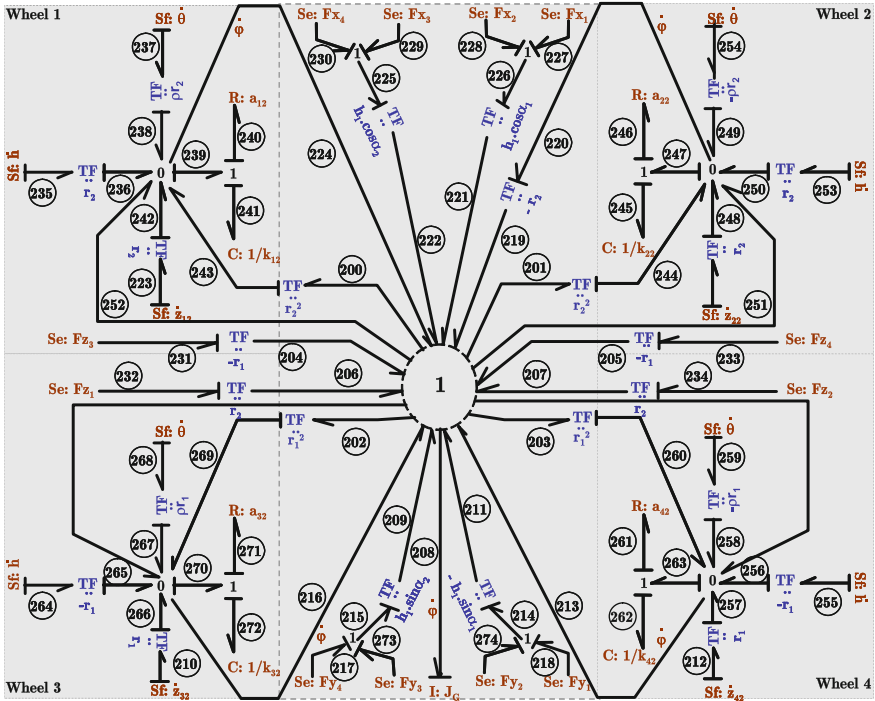


Fig. 11.58 Bond graph model of the pitch dynamics

$$\begin{aligned}
 & -\frac{a_{12}}{J_G} r_2 \dot{z}_{12} - \frac{k_{12}}{J_G} r_2 z_{12} - \frac{a_{22}}{J_G} r_2 \dot{z}_{22} - \frac{k_{22}}{J_G} r_2 z_{22} + \frac{a_{32}}{J_G} r_1 \dot{z}_{32} + \frac{k_{32}}{J_G} r_1 z_{32} + \frac{a_{42}}{J_G} r_1 \dot{z}_{42} \\
 & + \frac{k_{42}}{J_G} r_1 z_{42} + \frac{r_2}{J_G} F_{z1} + \frac{r_2}{J_G} F_{z2} - \frac{r_1}{J_G} F_{z3} - \frac{r_1}{J_G} F_{z4} + \frac{h_1}{J_G} (F_{x1} + F_{x2}) \cos \alpha_1 \\
 & + \frac{h_1}{J_G} (F_{x3} + F_{x4}) \cos \alpha_2 - \frac{h_1}{J_G} (F_{y1} + F_{y2}) \sin \alpha_1 + \frac{h_1}{J_G} (F_{y3} + F_{y4}) \sin \alpha_2 \quad (11.74)
 \end{aligned}$$

By using expressions of (11.68) and (11.69), Eq. (11.74) became:

$$\begin{aligned}
 J_G \ddot{\varphi} = & -k_{12}(z_{12} - h + \rho\theta + r_2\varphi)r_2 - k_{22}(z_{22} - h - \rho\theta + r_2\varphi)r_2 \\
 & + k_{32}(z_{32} - h + \rho\theta - r_1\varphi)r_1 + k_{42}(z_{42} - h - \rho\theta - r_1\varphi)r_1 \\
 & - a_{12}(\dot{z}_{12} - \dot{h} + \rho\dot{\theta} + r_2\dot{\varphi})r_2 - a_{22}(\dot{z}_{22} - \dot{h} - \rho\dot{\theta} + r_2\dot{\varphi})r_2 \\
 & + a_{32}(\dot{z}_{32} - \dot{h} + \rho\dot{\theta} - r_1\dot{\varphi})r_1 + a_{42}(\dot{z}_{42} - \dot{h} - \rho\dot{\theta} - r_1\dot{\varphi})r_1 \\
 & + F_{z_1}r_2 + F_{z_2}r_2 - F_{z_3}r_1 - F_{z_4}r_1 + (F_{x_1} + F_{x_2})h_1 \cos \alpha_1 \\
 & + (F_{x_3} + F_{x_4})h_1 \cos \alpha_2 - (F_{y_1} + F_{y_2})h_1 \sin \alpha_1 \\
 & + (F_{y_3} + F_{y_4})h_1 \sin \alpha_2
 \end{aligned} \tag{11.75}$$

where J_G is the inertia of the *RobuCar*'s center of gravity calculated according to the lateral axis.

11.4.6 Roll Dynamics Modeling

Definition 11.3 The *Roll* angle of a vehicle is the angle generated from the rotation around the longitudinal axis (Fig. 11.57).

The *Roll* dynamic of the *RobuCar* system is detailed at the bond graph model of Fig. 11.59.

From the bond graph model of the *Roll* dynamic in integral causality, mathematical expression of this dynamic can be deduced as it is developed below:

$$\begin{aligned}
 \ddot{\theta} = & \frac{a_{12} - a_{22} + a_{32} - a_{42}}{I_G} \rho \dot{h} + \frac{k_{12} - k_{22} + k_{32} - k_{42}}{I_G} \rho h \\
 & - \frac{a_{12} + a_{22} + a_{32} + a_{42}}{I_G} \rho^2 \dot{\theta} + \frac{\rho}{I_G} F_{z_1} - \frac{\rho}{I_G} F_{z_2} + \frac{\rho}{I_G} F_{z_3} - \frac{\rho}{I_G} F_{z_4} \\
 & - \frac{k_{12} + k_{22} + k_{32} + k_{42}}{I_G} \rho^2 \theta + \frac{(a_{22} - a_{12})r_2 - (a_{42} - a_{32})r_1}{I_G} \rho \dot{\varphi} \\
 & + \frac{(k_{22} - k_{12})r_2 - (k_{42} - k_{32})r_1}{I_G} \rho \varphi - \frac{a_{12}}{I_G} \rho \dot{z}_{12} - \frac{k_{12}}{I_G} \rho z_{12} \\
 & + \frac{a_{22}}{I_G} \rho \dot{z}_{22} + \frac{k_{22}}{I_G} \rho z_{22} - \frac{a_{32}}{I_G} \rho \dot{z}_{32} - \frac{k_{32}}{I_G} \rho z_{32} + \frac{a_{42}}{I_G} \rho \dot{z}_{42} + \frac{k_{42}}{I_G} \rho z_{42} \\
 & + (F_{y_1} + F_{y_2}) \frac{h_1}{I_G} \cos \alpha_1 + (F_{y_3} + F_{y_4}) \frac{h_1}{I_G} \cos \alpha_2 \\
 & + (F_{x_1} + F_{x_2}) \frac{h_1}{I_G} \sin \alpha_1 - (F_{x_3} + F_{x_4}) \frac{h_1}{I_G} \sin \alpha_2
 \end{aligned} \tag{11.76}$$

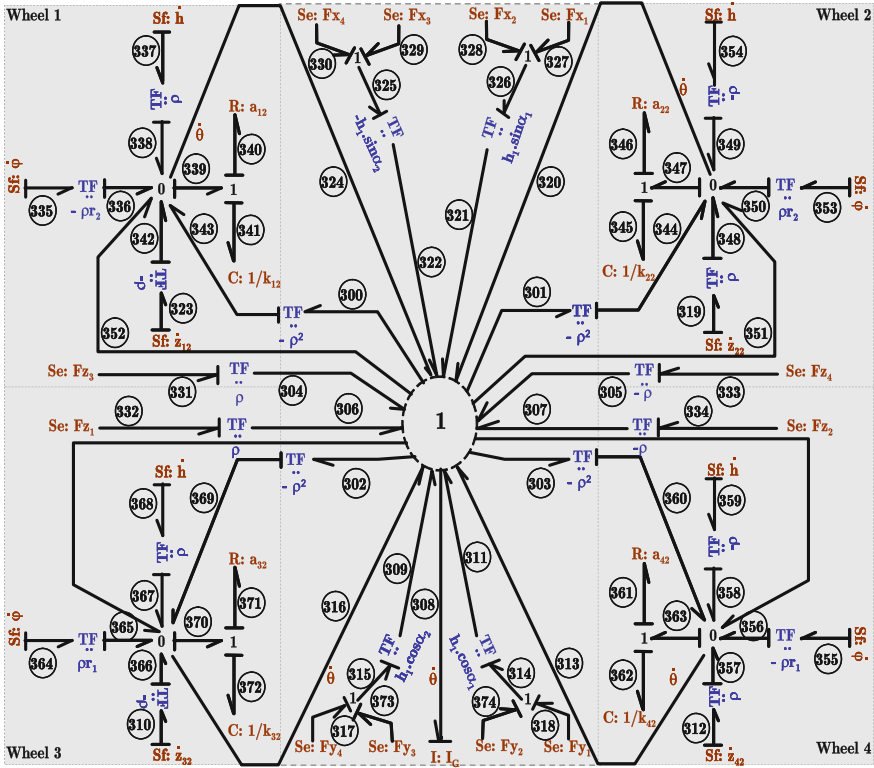


Fig. 11.59 Bond graph model of the roll dynamics

By using expressions of (11.68) and (11.69), Eq. (11.76) became:

$$\begin{aligned}
 I_G \cdot \ddot{\theta} = & -k_{12}(z_{12} - h + \rho\theta + r_2\varphi)\rho + k_{22}(z_{22} - h - \rho\theta + r_2\varphi)\rho \\
 & - k_{32}(z_{32} - h + \rho\theta - r_1\varphi)\rho + k_{42}(z_{42} - h - \rho\theta - r_1\varphi)\rho \\
 & - a_{12}(\dot{z}_{12} - \dot{h} + \rho\dot{\theta} + r_2\dot{\varphi})\rho + a_{22}(\dot{z}_{22} - \dot{h} - \rho\dot{\theta} + r_2\dot{\varphi})\rho \\
 & - a_{32}(\dot{z}_{32} - \dot{h} + \rho\dot{\theta} - r_1\dot{\varphi})\rho + a_{42}(\dot{z}_{42} - \dot{h} - \rho\dot{\theta} - r_1\dot{\varphi})\rho \\
 & + F_{z1}\rho - F_{z2}\rho + F_{z3}\rho - F_{z4}\rho \\
 & + (F_{y1} + F_{y2})h_1 \cos \alpha_1 + (F_{y3} + F_{y4})h_1 \cos \alpha_2 \\
 & + (F_{x1} + F_{x2})h_1 \sin \alpha_1 - (F_{x3} + F_{x4})h_1 \sin \alpha_2
 \end{aligned} \tag{11.77}$$

where I_G is the inertia of the *RobuCar*'s center of gravity calculated according to the longitudinal axis.

11.5 Fault Detection and Isolation

In this section, a model-based Fault Detection & Isolation algorithm (*FDI*) [10, 43] is described, in order to detect the actuators fault on the actuated wheels of *RobuCar*'s vehicle. By using the *FDI* algorithms proposed in [31], a list of *ARR* along with the corresponding *Fault Signature Matrix (FSM)* can be generated. These tools allow to detect and isolate the possible faults present on the physical system.

The *FDI* proposed approach is based on the calculation of the residuals issued from the *Analytical Redundancy Relation (ARR)*, and it makes the difference between the dynamic system in normal and faulty situations. Note that for an observable system, with no unresolved algebraic loops, the number of *ARR* generated is equal to the number of the measured states and are equal to the number of detectors on the bond graph model [31]. In the studied case, the measured states are the two angular velocities of the wheel and the current at the electrical side of each *j*th actuator.

11.5.1 *ARRs* Generation

The main steps to generate the list of *ARR* and *FSM* by using are summarized below:

1. Build the bond graph model in preferred integral causality;
2. Put the bond graph model in preferred derivative causality after dualization of the sensors;
3. Write the constitutive relation for each junction;
4. Eliminate the unknown variables from each constitutive relation by covering the causal paths in the bond graph model;
5. Generate the list of *ARR* and the corresponding *FSM*.

- *ARR_j* Generation

The first *ARR_j* corresponds to those generated from the electrical part of the *j*th of the electromechanical system where its bond graph model in derivative causality is given in Fig. 11.60. This part of the model is presented in preferred derivative causality in order to generate the *ARR*, in order to avoid the case where the initial conditions are not known.

The constitutive relations of the junctions 1_1 , 1_2 , 0_1 , and 1_3 are given by the following equations:

$$\begin{cases} e_{23} = e_{20} + e_{40} - e_{21} - e_{22} \\ e_{28} = e_{24} + e_{39} + e_{26} - e_{25} - e_{27} \\ f_{29} = f_{28} - f_{30} \\ e_{34} = e_{31} + e_{33} + e_{36} + e_{38} - e_{32} \end{cases} \quad (11.78)$$

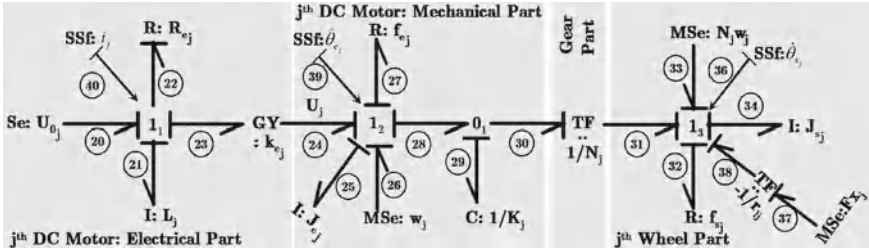


Fig. 11.60 Bond graph model of the j th electromechanical in derivative causality

Three structurally independent ARR_{i_j} ($i \in [1; 3]$) of the j th electromechanical system can be generated from Eq. 11.78 after eliminating the unknown variables. This elimination process is achieved by following the causal paths from unknown to known variables on the bond graph model.

From Eq. 11.78, the unknown variables are given by the following relations:

$$\begin{cases} e_{20} = U_{0j} \\ e_{40} = 0 \\ e_{21} = L_j \frac{d}{dt} (f_{40}) = L_j \frac{d}{dt} (i_j) \\ e_{22} = R_{e_j} f_{40} = R_{e_j} i_j \\ e_{23} = k_{e_j} f_{39} = k_{e_j} \dot{\theta}_{e_j} \end{cases} \quad (11.79)$$

From the junction 1_1 the following equation is deduced:

$$e_{23} = U_{0j} - R_{e_j} i_j - L_j \frac{d}{dt} (i_j) = k_{e_j} \dot{\theta}_{e_j} \quad (11.80)$$

From Eq. 11.80 the following ARR_{1_j} is deduced:

$$ARR_{1_j} : U_{0j} - R_{e_j} i_j - L_j \frac{d}{dt} (i_j) - k_{e_j} \dot{\theta}_{e_j} = 0 \quad (11.81)$$

• ARR_{2_j} Generation

The second ARR_j corresponds to those generated from the mechanical part of the j th electromechanical system where its bond graph model in derivative causality is given in Fig. 11.60. In this model part, the $C : 1/K_j$ element is already in integral causality, because the system is sub-determined with the actual configuration. So, the dualization of the sensor is possible in this case because the initial conditions related to the position between the input and output of the j th mechanical part $\theta_{e_j} - N_j \theta_{s_j}$ is supposed to be known, and then the C element can be presented in integral causality.

From Eq. 11.78, the unknown variables are given by the following relations:

$$\begin{cases} e_{24} = k_{e_j} f_{40} = k_{e_j} i_j \\ e_{39} = 0 \\ e_{26} = w_j \\ e_{25} = J_{e_j} \frac{d}{dt}(f_{39}) = J_{e_j} \frac{d}{dt}(\dot{\theta}_{e_j}) \\ e_{27} = f_{e_j} f_{27} = f_{e_j} \dot{\theta}_{e_j} \\ e_{28} = K_j f_{29} = K_j (\theta_{e_j} - N_j \theta_{s_j}) \end{cases} \quad (11.82)$$

From the junction 1₂ the following equation is deduced:

$$e_{28} = K_j (\theta_{e_j} - N_j \theta_{s_j}) = k_{e_j} i_j - J_{e_j} \frac{d}{dt}(\dot{\theta}_{e_j}) - f_{e_j} \dot{\theta}_{e_j} - w_j \quad (11.83)$$

From Eq. 11.83 the following ARR_{2_j} is deduced:

$$ARR_{2_j} : k_{e_j} i_j - J_{e_j} \frac{d}{dt}(\dot{\theta}_{e_j}) - f_{e_j} \dot{\theta}_{e_j} - w_j - K_j (\theta_{e_j} - N_j \theta_{s_j}) = 0 \quad (11.84)$$

- ARR_{3_j} Generation

The third ARR_j describes the load part corresponding to the model part of the wheel with tire-road contact. Thus, the following unknown variables are identified:

$$\begin{cases} e_{34} = e_{31} + e_{33} + e_{36} + e_{38} - e_{32} \\ e_{31} = N_j e_{30} = N_j e_{28} = N_j K_j (\theta_{e_j} - N_j \theta_{s_j}) \\ e_{33} = N_j w_j \\ e_{36} = 0 \\ e_{38} = -r_{l_j} F_{x_j} \\ e_{32} = f_{s_j} f_{36} = f_{s_j} \dot{\theta}_{s_j} \\ e_{34} = J_{s_j} \frac{d}{dt}(f_{36}) = J_{s_j} \frac{d}{dt}(\dot{\theta}_{s_j}) \end{cases} \quad (11.85)$$

Thus, the deduced ARR_{3_j} is obtained by replacing the unknown variables of the associated Eq. 11.78 by their expressions in 11.85:

$$ARR_{3_j} : N_j K_j (\theta_{e_j} - N_j \theta_{s_j}) + N_j w_j - J_{s_j} \frac{d(\dot{\theta}_{s_j})}{dt} - f_{s_j} \dot{\theta}_{s_j} - r_{l_j} F_{x_j} = 0 \quad (11.86)$$

In addition, the residuals of the FSM are represented instead of ARR , where each residual $p_{n_{i_j}}$ is a numerical evaluation of an ARR_{i_j} . The corresponding residuals $p_{n_{1_j}}$, $p_{n_{2_j}}$, and $p_{n_{3_j}}$ of ARR_{1_j} , ARR_{2_j} , and ARR_{3_j} ($i \in [1; 3]$ and $j \in [1; 6]$) are given by the following relations:

Table 11.2 Fault signature matrix of electromechanical system

Component	Variables	D_b	I_b	p_{n1_j}	p_{n2_j}	p_{n3_j}
Velocity sensors	$\dot{\theta}_{e_j}$	1	0	0	1	0
	$\dot{\theta}_{s_j}$	1	0	0	0	1
Mechanical part	J_{e_j}	1	0	0	1	0
	f_{e_j}	1	0	0	1	0
	J_{s_j}	1	0	0	0	1
	f_{s_j}	1	0	0	0	1
Electrical part	R_{e_j}	1	0	1	0	0
	L_j	1	0	1	0	0
Mechanical backlash	w_j	1	1	0	1	1
Input control	U_{0_j}	1	0	1	0	0
Contact effort	F_{x_j}	1	0	0	0	1

$$\begin{aligned}
 p_{n1_j} &= U_{0_j} - R_{e_j} i_j - L_j \frac{d}{dt} (i_j) - k_{e_j} \dot{\theta}_{e_j} \\
 p_{n2_j} &= k_{e_j} i_j - J_{e_j} \frac{d}{dt} (\dot{\theta}_{e_j}) - f_{e_j} \dot{\theta}_{e_j} - w_j - K_j (\theta_{e_j} - N_j \theta_{s_j}) \\
 p_{n3_j} &= N_j K_j (\theta_{e_j} - N_j \theta_{s_j}) + N_j w_j - J_{s_j} \frac{d(\dot{\theta}_{s_j})}{dt} - f_{s_j} \dot{\theta}_{s_j} - r_{l_j} F_{x_j}
 \end{aligned} \tag{11.87}$$

The corresponding Fault Signature Matrix (*FSM*) of the *j*th electromechanical system is given in Table 11.2.

In this table, the rows represent the components signatures and the columns are respectively the fault detectability D_b , the fault isolability I_b , and the three residuals p_{n1_j} , p_{n2_j} , and p_{n3_j} of each *j*th electromechanical system. A value ‘1’ on respectively D_b and I_b columns means that faults on the corresponding components are detectable and isolable. The presence of value ‘1’ on the residual columns shows the influence of the corresponding component on the residual dynamics. In this application, the *FSM* helps to detect and to distinguish the influences of the nonlinearity from the component fault.

11.5.2 Results of Co-Simulation

The implemented program for co-simulation has been first of all validated on a vehicle dynamic simulator (*CALLAS*[®]) [36] of Fig. 11.61, coupling with *Matlab/Simulink* software.

The considered scenario results in the vehicle making a circular trajectory as shown in Fig. 11.62 for duration of 350 s (obtained by integrating the velocities).

The orientation of the vehicle for this scenario is done by differentiation on the wheel velocities and not on the steering system. Transmitted traction’ torques, in normal situation, are represented by Fig. 11.63. It allows a slow displacement of the vehicle.

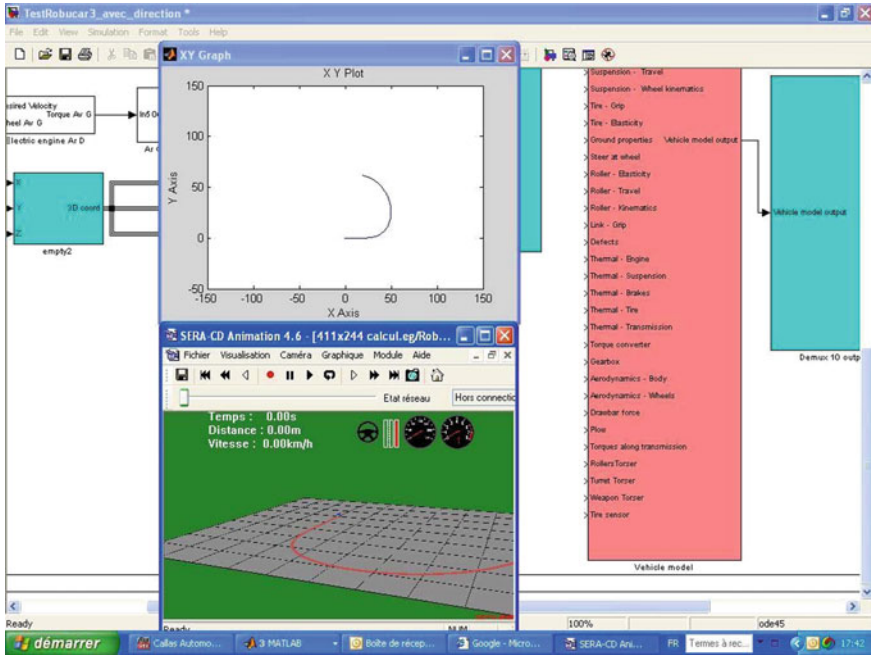
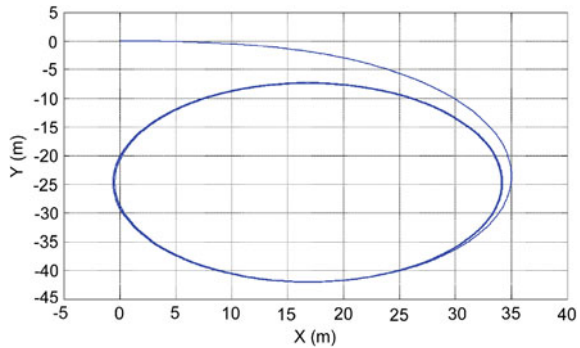


Fig. 11.61 Simulator of vehicle dynamic

Fig. 11.62 X-Y plane trajectory in normal situation



To simulate a fault input scenario, we introduce undesirable control torque of Fig. 11.64 at instant 250 s on the main torque of the mechanical part of the front left actuated wheel.

The new transmitted torques in presence of input fault are presented in Fig. 11.65 where the noticed sensible residual is the second p_{n2_1} of Fig. 11.66 and it corresponds to the description of the designed FSM .

Finally, the new trajectory in presence of input fault on the front left actuated wheel ($j = 1$) is given by Fig. 11.67.

Fig. 11.63 Transmitted control torques in normal situation

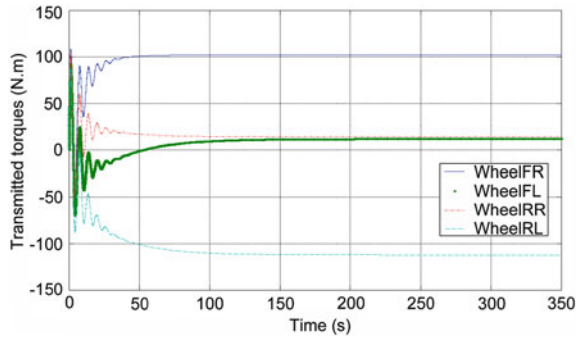


Fig. 11.64 Undesired faulty torque

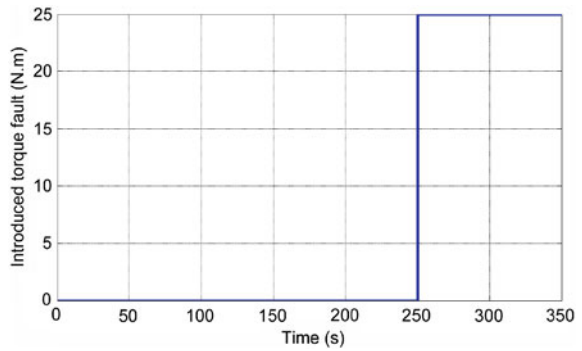
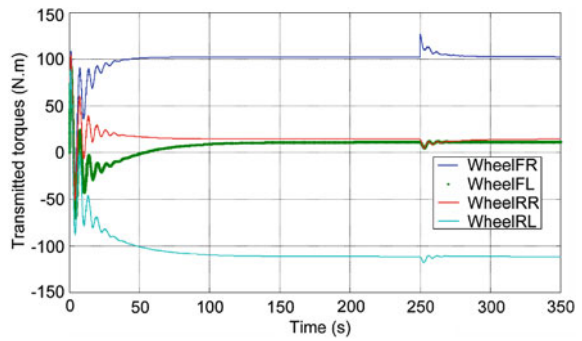


Fig. 11.65 Transmitted torques in presence of input fault



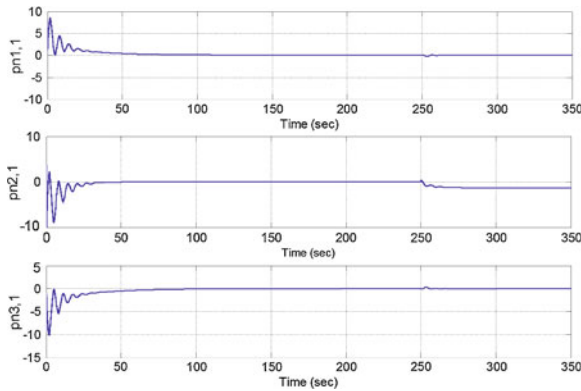
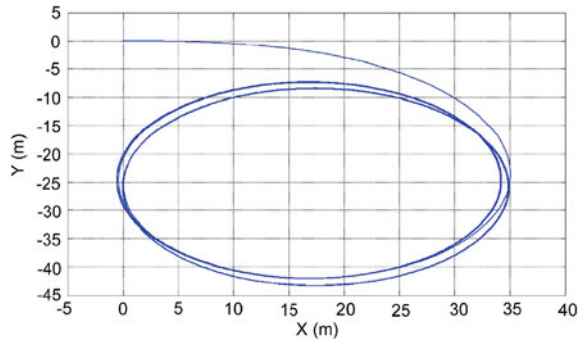


Fig. 11.66 Residuals in faulty situation

Fig. 11.67 Trajectory after input fault on the front left actuated wheel



11.6 Robust Diagnosis

11.6.1 Principle and Definitions

Because of its behavioral, structural, and causal properties, the bond graph tool is used more and more for modeling and fault diagnosis. From Fault Detection and Isolation (*FDI*) and supervision viewpoint, the causal properties of the bond graph tool are used to determine the origin of the faults [31, 34, 35]. The bond graph model can be used to obtain mathematical and graphical representations, allowing the ability to detect and to isolate faults [31].

For modeling purpose, two approaches are proposed for uncertainties modeling using bond graph [39]. The first method consists in describing parameter uncertainties as bond graph elements, and the second uses the Linear Fractional Transformation *LFT* form for the characterization of the parameter uncertainties.

In this section, the bond graph tool as an integrated language for modeling and robust *FDI* is given in *LFT* form [3], in order to generate the Analytical Redundancy

Relations (ARR). The ARR s consist of two perfectly separate parts, a nominal part called p_n which describe the system operating, and an uncertain part called p_u , which is used for sensitivity analysis and evaluation of residuals.

With the same graphical modeling tool, we can perform modeling, robust diagnosis, and sensitivity analysis of residuals, taking into account the parameter uncertainties. Thus, with the association of bond graph and the LFT principle, it is possible to obtain physical behavior of the systems, and improving the monitoring by deducing the adaptive thresholds of the residuals, for robust detection and isolation of imperfections. The different steps of this robust diagnosis are presented as follows:

1. LFT modeling of the nonlinear and uncertain system using the bond graph;
2. Identification of the system parameters, where the parameter uncertainties are calculated using statistical or interval approaches;
3. Generation of ARR for the uncertain system, after decoupling the nominal and the uncertain parts. Residuals correspond to the nominal part of the ARR , while the residual thresholds are calculated from the uncertain parts of the ARR ;
4. Sensitivity analysis of the residual is done by calculating the fault detectability indices, from the uncertain part of the ARR .

Knowing that the introduction of uncertainties does not affect the causality and the structural properties of the bond graph elements in LFT form [3], the monitorability analysis (i.e. ability to generate ARR) is realized using the determinist bond graph model. Monitorability analysis developed in [4] shows that in the case of unknown initial conditions, the system should be proper, observable, and over constrained, sufficient conditions to generate an ARR .

Definition 11.4 *A bond graph model is proper if and only if it does not contain dynamic elements in derivative causality when the model is in preferred integral causality and vice versa [44].*

Definition 11.5 *A bond graph model is structurally observable if and only if the following conditions are satisfied:*

- *On the bond graph model in integral causality, it exists a causal path between all the dynamic elements I and C and detectors De or Df ;*
- *All the dynamic elements I and C admit a derivative causality when the bond graph model is in preferred derivative causality. If some dynamic elements remain in integral causality, the dualization of the detectors De and Df must allow putting them in derivative causality [44].*

Definition 11.6 *When the bond graph model is in derivative causality, the system is considered over constrained, if and only if after dualization the detectors (Effort and flow), De and Df become signal sources SSe and SSf , then the elements I and C can be kept in derivative causality [3].*

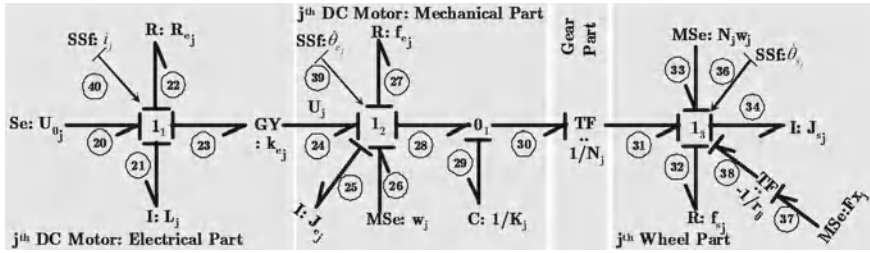


Fig. 11.68 Deterministic bond graph model of the j th quarter of vehicle in derivative causality with inverted detectors

Monitorability analysis shows that the electrical part of the j th DC motor is proper, observable, and over constrained (Fig. 11.68), because there is no conflict of causality in this part of the model. ARR can be generated from the considered junction 1_1 . The mechanical part of the system is proper, observable but under constrained, because the effort in the $C : 1/K_j$ element is unknown, which explains the appearance of a causality conflict at the associated junction 0_1 , for that this element is remained in integral causality. This situation can be avoided when the initial conditions are perfectly known. In this case, the initial condition associated to this element describes the position measurement, which is available through the installed hardware sensors on the system. Finally, wheel part is proper, observable, and over constrained. Due to this properties analysis, three ARR can be generated from the uncertain bond graph model of Fig. 11.68.

11.6.2 LFT Bond Graph Model

In the following development, a model of j th traction system is presented, including structured and unstructured uncertainties [4], using Linear Fractional Transformation form LFT [39]. The principle of this model is to combine between LFT and bond graph to represent the uncertainties. It consists in modeling the uncertain system, by concatenating a nominal part, whose parameters are perfectly known, and an uncertain part, representing various uncertainties. Unstructured uncertainties are considered as modulated sources of unknown effort or flow, assumed present in the system and affect its normal operation. In our studied case, the unstructured uncertainties are assumed present in the mechanical part of the j th DC motor, and on the wheel part, where two modulated sources of efforts w_j and $N_j w_j$ are respectively added to the bond graph model in LFT form. The origin of those uncertainties is the presence of a backlash phenomenon in the gear part, which causes a disturbing torque on the system. The backlash phenomena is generally difficult to model due to its discontinuous nonlinearity, then it is considered as unstructured uncertainty

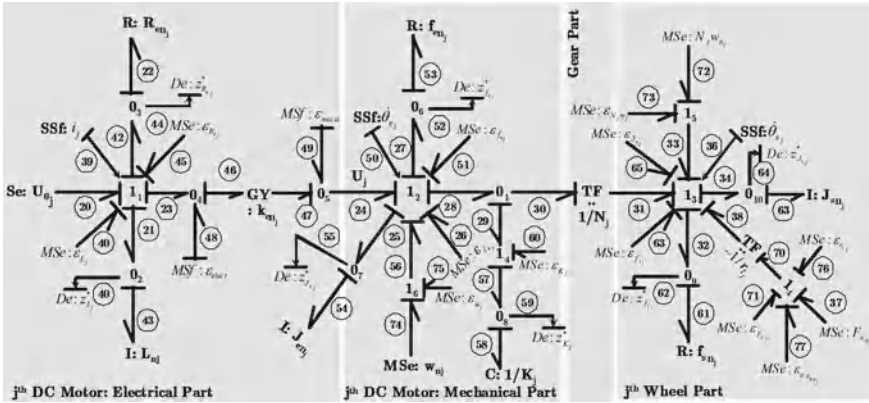


Fig. 11.69 LFT Bond graph model of the system in derivative causality with inverted sensors

and for this purpose, it will be estimated in its continuous nonlinear form, using Eq. (11.54).

For *FDI* analysis, the bond graph model should be given in derivative causality with an inverted detectors (Fig. 11.68) in order to avoid the unknown initial conditions for the step of the *ARR* generation. When a detector is dualized or inverted, it becomes a signal source of effort or flow. This latter is imposed to the considered junction, thus, the detector is no longer optional, and it risks generating conflicts of causality on the bond graph model.

The main advantages of such model for robust diagnosis are summarized in the following points:

- Introduction of uncertainties does not affect the causality and the structural properties of the *BG* elements on the nominal model;
- Representation of structured and unstructured uncertainties;
- Energy added to the system by an uncertainty depends on the energy added by the nominal parameter;
- Uncertain part is perfectly separated from the nominal part.

In this studied case, we consider that the gear ratio parameter N_j is deterministic and its uncertainty is neglected and the disturbing torque w_j is initially identified with a nominal value of the dead zone magnitude τ_{0nj} and its unstructured uncertainty depends principally on the perturbation issued from the variation of this dead zone. Now, the uncertain bond graph model of *j*th electromechanical part including the contact effort is shown in Fig. 11.69, where the source of efforts and flow ϵ describing the uncertainties are modulated by the following expressions:

$$\begin{aligned} \epsilon_{R_{e_j}} &= -\delta_{R_{e_j}} z_{R_{e_j}}^* ; z_{R_{e_j}}^* = R_{e_{j_n}} i_j \\ \epsilon_{L_j} &= -\delta_{L_j} z_{L_j}^* ; z_{L_j}^* = L_{j_n} \frac{di_j}{dt} \end{aligned}$$

$$\begin{aligned}
\varepsilon_{J_{e_j}} &= -\delta_{J_{e_j}} z_{J_{e_j}}^* ; z_{J_{e_j}}^* = J_{e_n_j} \ddot{\theta}_{e_j} \\
\varepsilon_{f_{e_j}} &= -\delta_{f_{e_j}} z_{f_{e_j}}^* ; z_{f_{e_j}}^* = f_{e_n_j} \dot{\theta}_{e_j} \\
\varepsilon_{K_j} &= -\delta_{K_j} z_{K_j}^* ; z_{K_j}^* = K_{n_j} (\theta_{e_j} - N_j \theta_{s_j}) \\
\varepsilon_{J_{s_j}} &= -\delta_{J_{s_j}} z_{J_{s_j}}^* ; z_{J_{s_j}}^* = J_{s_n_j} \ddot{\theta}_{s_j} \\
\varepsilon_{f_{s_j}} &= -\delta_{f_{s_j}} z_{f_{s_j}}^* ; z_{f_{s_j}}^* = f_{s_n_j} \dot{\theta}_{s_j} \\
\varepsilon_{elec} &= -\delta_{k_{e_j}} \dot{\theta}_{e_j} ; \varepsilon_{meca} = \delta_{k_{e_j}} i_j \\
\varepsilon_{r_{l_j}} &= \delta_{r_{l_j}} F_{x_{n_j}} ; \varepsilon_{\varepsilon_{F_{x_j}}} = \delta_{r_{l_j}} \varepsilon_{F_{x_j}} \\
\varepsilon_{N_j w_j} &= N_j \varepsilon_{w_j}
\end{aligned} \tag{11.88}$$

11.6.3 Robust ARR_j Generation

The procedure of ARR generation in presence of structured (parameter uncertainties) and unstructured (perturbations and modeling uncertainties) uncertainties is explained as follows:

1. The bond graph model should be written in preferred derivative causality after dualization of the sensors;
2. From junctions 0 and 1 of an over constrained part, the ARR is deduced by expressing the energetic assessment on the junction;
3. The obtained ARR_j consists of two perfectly separated parts, *j*th nominal part called *p_{n_j}* which describes the deterministic part, and *j*th uncertain part *p_{u_j}* used for the generation of adaptive thresholds during normal operating.

From the bond graph model of Fig. 11.69, a set of ARR_j (11.89) is generated. The first one is generated from the junction 1₁ connected to the dualized sensor *SSf* : *i_j*, the second and the third are respectively generated from the other junctions 1₂ and 1₃ connected to the dualized sensors *SSf* : $\dot{\theta}_{e_j}$ and *SSf* : $\dot{\theta}_{s_j}$. Due to the properties of *LFT* model, each ARR_j is separated in two distinguished parts, given by Eqs. (11.90), (11.91) and (11.92).

$$\left\{ \begin{array}{l}
ARR_{1_j} : U_{0_j} - L_{n_j} \frac{d}{dt} i_j - R_{e_{n_j}} i_j - k_{e_{n_j}} (\dot{\theta}_{e_j} - \varepsilon_{elect}) + \varepsilon_{R_{e_j}} + \varepsilon_{L_j} = 0 \\
ARR_{2_j} : k_{e_{n_j}} (i_j + \varepsilon_{meca}) - J_{e_{n_j}} \ddot{\theta}_{e_j} - f_{e_{n_j}} \dot{\theta}_{e_j} - w_{n_j} - K_{n_j} (\theta_{e_j} - N_j \theta_{s_j}) \\
\quad + \varepsilon_{w_j} + \varepsilon_{J_{e_j}} + \varepsilon_{f_{e_j}} + \varepsilon_{K_j} = 0 \\
ARR_{3_j} : N_j K_{n_j} (\theta_{e_j} - N_j \theta_{s_j}) + N_j w_{n_j} - J_{s_{n_j}} \ddot{\theta}_{s_j} - f_{s_{n_j}} \dot{\theta}_{s_j} + r_{l_j} F_{x_{n_j}} + N_j \varepsilon_{K_j} \\
\quad + N_j \varepsilon_{w_j} + \varepsilon_{J_{s_j}} + \varepsilon_{f_{s_j}} + r_{l_j} \varepsilon_{F_{x_j}} + r_{l_j} \varepsilon_{r_{l_j}} + r_{l_j} \varepsilon_{\varepsilon_{F_{x_j}}} = 0
\end{array} \right. \tag{11.89}$$

$$\begin{cases} p_{n1_j} = U_{0_j} - L_{n_j} \frac{d}{dt} i_j - R_{e_{n_j}} i_j - k_{e_{n_j}} \dot{\theta}_{e_j} \\ p_{u1_j} = \varepsilon_{R_{e_j}} + \varepsilon_{L_j} + k_{e_{n_j}} \varepsilon_{elect} \end{cases} \quad (11.90)$$

$$\begin{cases} p_{n2_j} = k_{e_{n_j}} i_j - J_{e_{n_j}} \ddot{\theta}_{e_j} - f_{e_{n_j}} \dot{\theta}_{e_j} - w_{n_j} - K_{n_j} (\theta_{e_j} - N_j \theta_{s_j}) \\ p_{u2_j} = \varepsilon_{w_j} + \varepsilon_{J_{e_j}} + \varepsilon_{f_{e_j}} + \varepsilon_{K_j} + k_{e_{n_j}} \varepsilon_{meca} \end{cases} \quad (11.91)$$

$$\begin{cases} p_{n3_j} = N_j K_{n_j} (\theta_{e_j} - N_j \theta_{s_j}) + N_j w_{n_j} \\ \quad - J_{s_{n_j}} \ddot{\theta}_{s_j} - f_{s_{n_j}} \dot{\theta}_{s_j} + r_{l_j} F_{x_{n_j}} \\ p_{u3_j} = N_j \varepsilon_{K_j} + N_j \varepsilon_{w_j} + \varepsilon_{J_{s_j}} + \varepsilon_{f_{s_j}} \\ \quad + r_{l_j} \varepsilon_{F_{x_j}} + r_{l_j} \varepsilon_{r_{l_j}} + r_{l_j} \varepsilon_{\varepsilon_{F_{x_j}}} \end{cases} \quad (11.92)$$

By replacing the residual $p_{n_{i_j}}$ and the uncertain part $p_{u_{i_j}}$, $i \in [1; 3]$ of Eqs. (11.90), (11.91), and (11.92) in the ARR_{i_j} of (11.89), we obtain the following equation:

$$p_{n_{i_j}} + p_{u_{i_j}} = 0, i \in [1; 3] \Rightarrow p_{n_{i_j}} = -p_{u_{i_j}} \quad (11.93)$$

Thus, extremum thresholds a_{i_j} is given such that:

$$-a_{i_j} \leq p_{n_{i_j}} \leq a_{i_j} \quad (11.94)$$

with

$$\begin{cases} a_{1_j} = |\varepsilon_{R_{e_j}}| + |\varepsilon_{L_j}| + k_{e_{n_j}} |\varepsilon_{elect}| \\ a_{2_j} = |\varepsilon_{w_j}| + |\varepsilon_{J_{e_j}}| + |\varepsilon_{f_{e_j}}| + |\varepsilon_{K_j}| + k_{e_{n_j}} |\varepsilon_{meca}| \\ a_{3_j} = N_j |\varepsilon_{K_j}| + N_j |\varepsilon_{w_j}| + |\varepsilon_{J_{s_j}}| + |\varepsilon_{f_{s_j}}| \\ \quad + r_{l_j} |\varepsilon_{F_{x_j}}| + r_{l_j} |\varepsilon_{r_{l_j}}| + r_{l_j} |\varepsilon_{\varepsilon_{F_{x_j}}}| \end{cases} \quad (11.95)$$

11.6.4 Results of Co-Simulation

The additive uncertainty on each parameter is considered as the difference between the maximum value of the parameter and its mean value. Thus, the additive uncertainties are related to their multiplicative values according to the following relations:

$$\delta_R = \frac{\Delta R}{R_n}; \delta_{\frac{1}{R}} = \frac{\Delta R}{R_n + \Delta R}; \delta_I = \frac{\Delta I}{I_n}; \delta_C = \frac{\Delta C}{C_n}; \delta_{TF} = \frac{\Delta T}{T_n}; \delta_{GY} = \frac{\Delta G}{G_n}$$

with ΔR , ΔI , and ΔC are respectively the additive uncertainty' values of the bond graph elements R , I , and C . ΔT and ΔG are respectively the additive uncertainty values of the modulus of TF and GY . δ_R , δ_I , δ_C , δ_{TF} , δ_{GY} are the multiplicative

Table 11.3 Co-simulation parameters

Parameters	Nominal value	Uncertainties	Value
L_{n_j}	0.075 (H)	δ_{L_j}	0.05
$R_{e_{n_j}}$	0.32 (Ω)	δ_{R_j}	0.05
$k_{e_{n_j}}$	0.122 (V/rad)	$\delta_{k_{e_j}}$	0.03
$J_{e_{n_j}}$	0.01 (Nms ² /rad)	$\delta_{J_{e_j}}$	0.002
$f_{e_{n_j}}$	0.015 (Nms/rad)	δ_{K_j}	0.0011
K_{n_j}	1 (Nm/rad)	$\delta_{f_{e_j}}$	0.0016
$J_{s_{n_j}}$	8 (Nms ² /rad)	$\delta_{J_{s_j}}$	0.02
$f_{s_{n_j}}$	0.02 (Nms/rad)	$\delta_{f_{s_j}}$	0.0022
$r_{l_{n_j}}$	0.2 (rad)	δ_{r_j}	0.005
$F_{x_{n_j\max}}$	0.125 (kN)	$\delta_{F_{x_j}}$	0.001

uncertainties of the bond graph elements. R_n , I_n , C_n , T_n , and G_n are the nominal values of the bond graph elements. $\delta_{\frac{1}{R}}$ is the multiplicative uncertainty' value on the characteristic functions of R element in conductance causality.

Let's consider the example of the uncertainty on the j th wheel radius, which is identified experimentally. Its nominal value $r_{l_{n_j}}$ is identified initially without presence of external load on the vehicle, and the tire is inflated at the maximum level of pressure (2 bar). The minimum value of the radius $r_{l_{j\min}}$ is identified when the vehicle is full loaded. Then, the additive and multiplicative uncertainties Δr_{l_j} and $\delta_{r_{l_j}}$ are calculated as follows:

$$\begin{cases} \Delta r_{l_j} = r_{l_{jn}} - r_{l_{j\min}} \\ \delta_{r_{l_j}} = \frac{\Delta r_{l_j}}{r_{l_{jn}}} \end{cases} \quad (11.96)$$

The set of parameters and uncertainties of the j th system is given in Table 11.3.

The results presented below are obtained after collecting data acquisition in normal situation, then these data are coupled with a dynamic simulator (*CALLAS*[®]) [36] in order to be co-simulated with the studied traction actuator model. To show the fault accuracy detection and isolation with presence of uncertainties, and the sensitivity to faults, the following scenarios is proposed:

- Residuals generation in normal situation;
- Residuals generation in presence of a fault on the electrical resistance for the j th DC motor for the traction system;
- Residuals generation in presence of a fault on the mechanical part for the j th DC motor for the traction system;
- Residuals generation in presence of the tire puncture fault.

Figure 11.70 shows the residuals and adaptive thresholds in normal situation for the rear left traction system. The residuals are inside the thresholds because there is no fault on the system, then no alarm is generated.

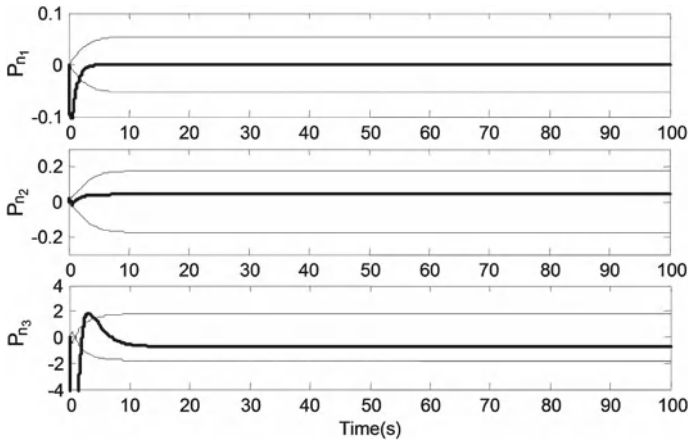


Fig. 11.70 Residuals and adaptive thresholds in absence of fault

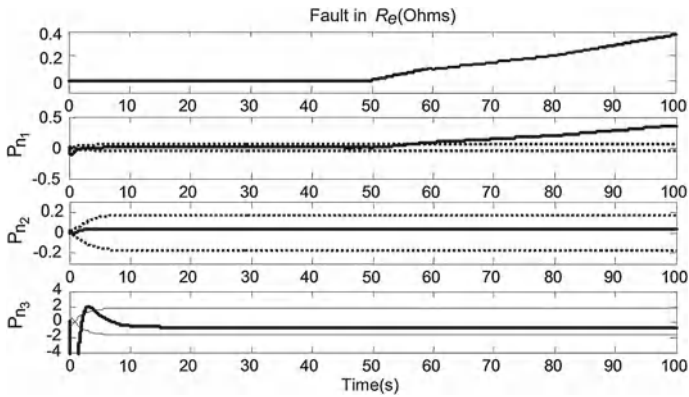


Fig. 11.71 Residuals and adaptive thresholds with a fault in electrical resistance R_e

The profile of the introduced electrical fault is given in Fig. 11.71, which describes the progressive variation of the electrical resistance R_e of the rear left DC motor from its nominal value. The residuals p_n , p_{n_2} and p_{n_3} are shown in Fig. 11.71. The fault appears at time $t = 50$ s and is detected at time $t = 58$ s by the residual p_{n_1} when the fault value reach the value of 0.1Ω . The residuals p_{n_2} and p_{n_3} are not sensitive to this fault and they remain inside the thresholds.

The whole behavior of the vehicle is now changed in presence of the electrical fault, where the new trajectory is given in Fig. 11.72. The appearance of the fault causes a vehicle deviation from the desired trajectory.

The second supposed fault represents an unknown external perturbation on the tire, which can be explained by the tire puncture simulation after a depression. This fault causes a variation of the wheel velocity at time $t = 50$ s (Fig. 11.73). The profile

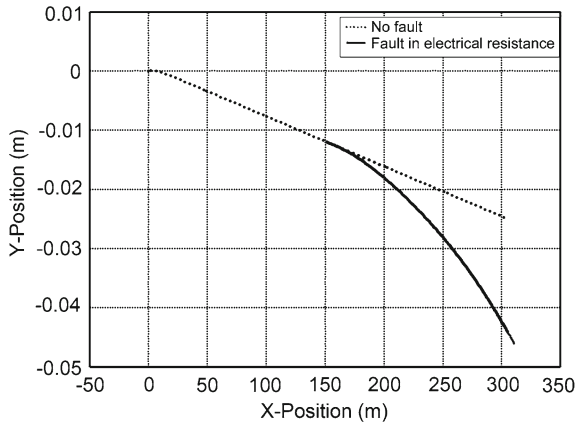


Fig. 11.72 Vehicle trajectory in presence of fault in electrical resistance R_e

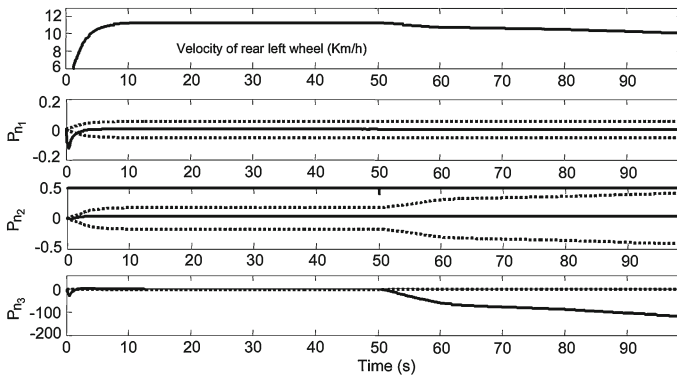


Fig. 11.73 Residuals and adaptive thresholds in presence of external tire puncture

of the residuals p_n , p_{n_2} and p_{n_3} is given in Fig. 11.73. The fault is detected at time $t = 51$ s by the residual p_{n_3} , while residuals p_{n_1} and p_{n_2} are not sensitive to this fault, they remains inside the thresholds. The presence of this fault causes a vehicle deviation from the desired trajectory as shown in Fig. 11.74.

The third fault is introduced at the level of the mechanical part of the rear left *DC* motor, it represents a variation of the viscous friction parameter f_e from its nominal value (Fig. 11.75). The progressive fault is introduced at time $t = 50$ s, and it is detected at time $t = 58$ s by the residual p_{n_1} (Fig. 11.75) after reaching the fault value of 0.08 Nms/rad. Residual p_{n_2} is sensitive to this fault at time $t = 68$ s with a fault value equal to 0.11 Nms/rad. Finally, residual p_{n_3} is less sensitive to this fault, so it remains inside the thresholds. The presence of this fault causes also a vehicle deviation from the desired trajectory as shown in Fig. 11.76.

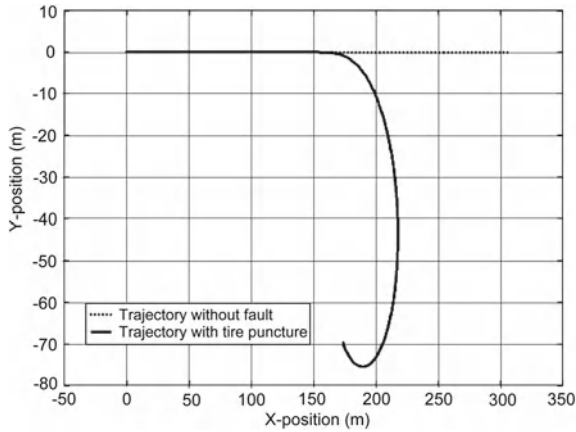


Fig. 11.74 Vehicle trajectory in presence of external tire puncture

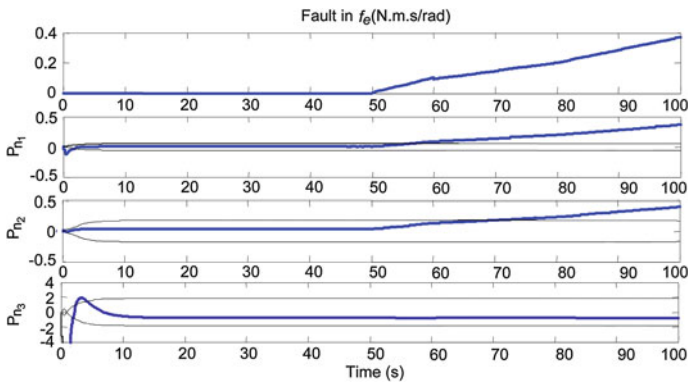


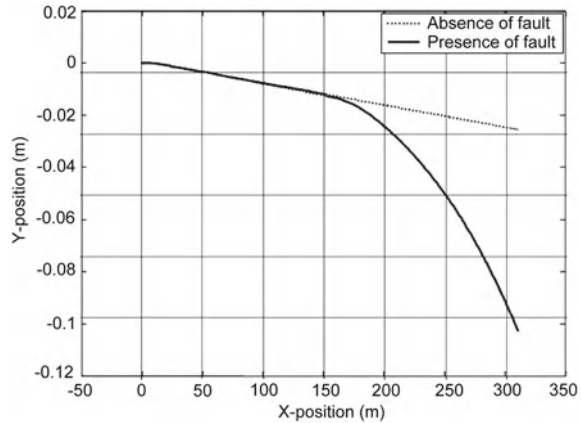
Fig. 11.75 Residuals and adaptive thresholds in presence of a fault in the mechanical part of the rear left DC motor

11.7 Fault Tolerant Control

11.7.1 Objectives and Principle

Fault tolerant control (*FTC*) systems [18], started to be applied at first to safety-critical systems such as, nuclear power plants and in the aircraft field. However, in modern technology systems, improvements regarding reliability, cost efficiency, safety, availability, and quality have lead to the application of fault tolerant control strategies in a more general field of engineering problems, such as, automotive, manufacturing, etc. Often a system is performed to satisfy its purposes, assuming that all the components are in perfect conditions at all the time. Hence, if a fault

Fig. 11.76 Vehicle trajectory in presence of fault in the mechanical part of the rear left DC motor



occurs, unexpected or even catastrophic situations may happen and logically the system does not behave as desired.

The objective of a fault tolerant system is to achieve its mission and maintain the overall stability of the system, even if a system is subject to failures, (e.g., actuators, sensors, or other components of the system), through the application of a closed-loop control strategy.

In [5], the authors classified the *FTC* techniques in two distinct groups, the passive fault tolerant control (*PFTC*) and the active fault tolerant control (*AFTC*) approaches.

The passive approach makes use of robust control techniques, because of its ability to maintain performance in the presence of uncertainties [5]. In this case, the closed-loop control system is fixed and failures are treated as model uncertainties or as unknown disturbances. Hence, this approach can only be applied if it is guaranteed that a fault will act like a bounded uncertainty of the system [32].

PFTC needs taking all possible faults of a system in consideration during the design stage, thus it cannot be guaranteed that unanticipated failures are handled. As an advantage it can be stated that *PFTC* does not require online information regarding the type of faults. The passive *FTC* approaches found in literature are: Reliable Linear Quadratic [8, 16, 24, 47, 51], Reliable H_∞ controller [29, 48, 52], Linear Matrix Inequality [1, 17, 54], and Adaptive compensation [56, 57].

In *AFTC* [18], the control system is reconfigured, such that performance and stability of the overall system can be preserved. Contrarily to the passive approach, the idea here is to use fault information to accommodate a fault. In [32], the author divided this approach in two groups. *Projection-based methods* e.g., control laws are computed a priori and when a faulty situation occurs, a proper controller is selected. *Online automatic controllers redesign methods* e.g., new controller parameters are computed online in response to a fault.

As referred before, *PFTC* only applies robust control technique to deal with faults. On the other hand, the active approach has to follow several steps to make a system fault tolerant. Primarily, a fault needs to be detected and isolated by a fault detection

and diagnosis strategy (*FDD*). After that, the control reconfigurability (*CR*) needs to be verified. Furthermore, a control reconfiguration is performed.

1. **Fault Detection and Diagnosis (FDD):** Fault detection and diagnosis intends to recognize and identify an abnormal occurrence in a system, as quick as possible, so that the failure of the overall system can be avoided. This task is often difficult because the process measurements are usually insufficient and unreliable. For a real implementation of fault diagnosis, the following steps have to be followed.
 - **Fault detection:** determines if a fault has occurred. A special attention to false alarms caused by noise and unmodeled disturbances have to be carefully studied.
 - **Fault isolation:** has to do with the detection of the specific faulty component.
 - **Fault analysis:** identify the type of the fault and its magnitude.
2. **Control Reconfigurability:** The occurrence of a fault may compromise the overall system safety. Control reconfigurability determines the ability of a faulty system remaining stable and achieve its objective after a proper control reconfiguration. Hence, under a faulty situation, there is the need to verify if available redundancy enables a system to be controlled. The goal is to replace or compensate the faulty part of the system by a non-faulty one [18]. There are two types of redundancies: direct and analytical. The first one means that identical hardware or software components are configured in parallel and available for the system. For instance if an actuator fails, it will be replaced by other one with the same characteristics. Analytical redundancy is the major task of *FTC* systems. It has to do with the ability of a system to use the available healthy components to perform or help in the function(s) of the faulty one(s). This is determined by using static or dynamic relations between variables and the components of a system [50]. Thus the interest here is to verify if the input to output mapping of a system does still controllable and observable after a component failure. Some works that verify the level of redundancy suitable for feedback control have been presented in literature [13, 42, 50, 53].
3. **Control methods used for AFTC:** Furthermore, if there is enough redundancy in the system, the active approaches can re-design a new control system, in function of the fault information provided by the *FDD* and the goals of the system. In [55], the authors defined that a control method is suitable for *AFTC* if the following conditions are satisfied.
 - Control reconfiguration must be done automatically, under real-time constraints,
 - The method should always provide a solution even if it is not optimal.

Figure 7 given in [18], presents the existing *AFTC* methods in the literature (Fig. 11.77).

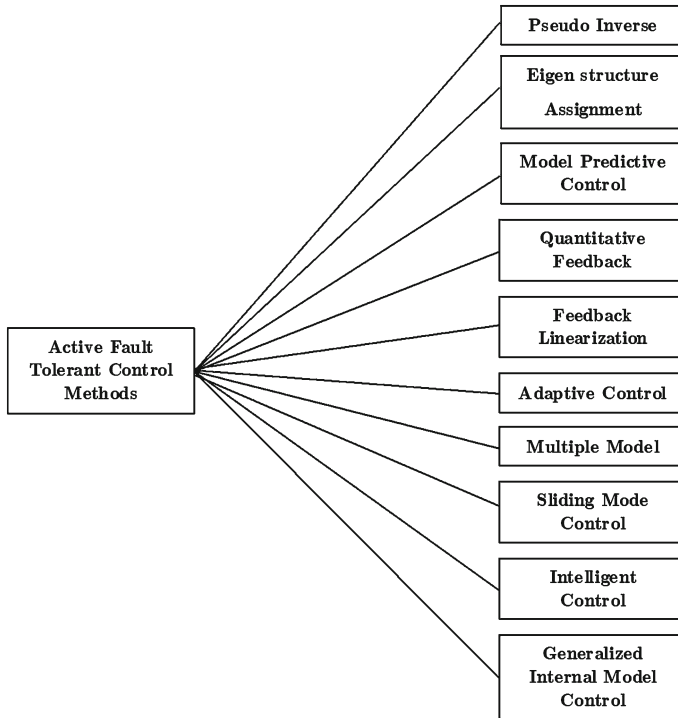


Fig. 11.77 Existing active fault tolerant control methods

11.7.2 Active Reconfiguration and Co-Simulation Results

In the following, we focus on a type of active fault tolerant control applied to *RobuCar* system, by exploiting hardware redundancy of the traction actuators.

Having four controlled inputs (Fig. 11.78), we want to maintain the performance of longitudinal control applied to the vehicle in the presence of an electrical failure on the right front actuator. This induces a decrease in actuator power and thus influences the direction of the vehicle.

The following assumptions have been put forward:

- The vehicle runs on a longitudinal axis with a uniform distribution of contact forces;
- The motion is fixed to a mean longitudinal velocity of 12 km/h;
- The steering control of the vehicle is done by differentiation of linear velocities of the wheels and not on the direct steering system;
- The longitudinal velocity is fixed directly from the trajectory profile, it can be controlled externally, knowing that it is a measured state;
- An auto-reconfiguration is applied in continuous time-domain scenario;

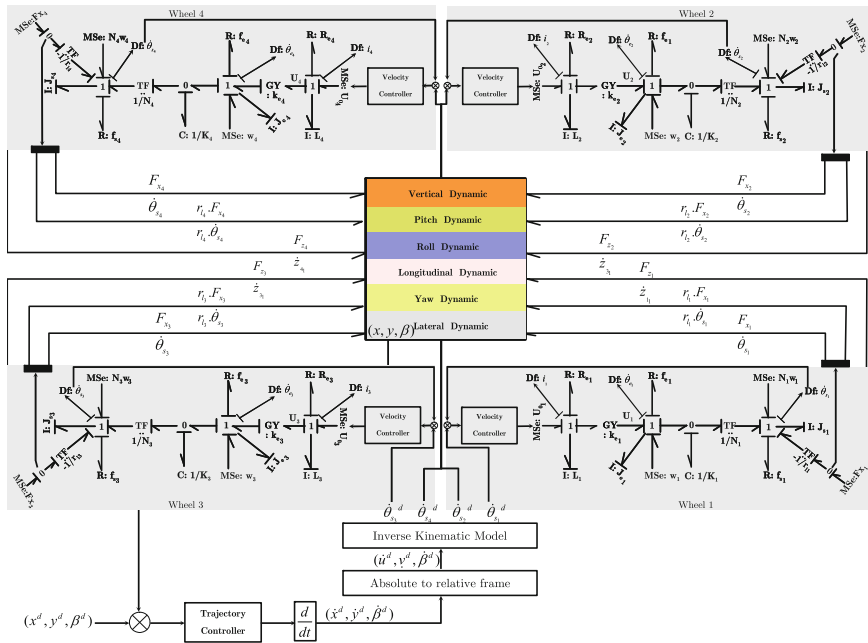


Fig. 11.78 Control strategy of an over-actuated IAV system

- Proportional and Integral (*PI*) controllers are applied for the velocities and trajectory, which have sufficient robustness against the induced fault and easy for implementation in the real system.

Due to sensors on board the vehicle, the following measurements are available: angular velocities of wheels, *GPS* coordinates of the center of gravity and acceleration of: pitch, roll, yaw, longitudinal, lateral, and vertical, through an inertial central system.

Figure 11.78 shows two levels of control: a higher level, for controlling the path of the vehicle in case of drift, and the second level concerns the regulation of angular velocities of the wheels.

The desired trajectory is defined by the profile of the path batch of Fig. 11.79. Where the applied angular velocities are derived by inversion of the direct kinematic model of Eq. (11.4), after the geometric transformation between the absolute and relative frames of Eq. (11.5).

For the **Fault Detection and Diagnosis (FDD)**, until $t = 12$ s, the longitudinal movement is managed by dual controls of wheel velocities and global trajectory. A fault on the right front input (U_{01}) is caused by a disturbance on the electrical part of the actuator (Fig. 11.80), thus causing a decrease in driving power of the corresponding wheel (Fig. 11.81). Residual p_{n11} of Fig. 11.80, shows clearly a divergence and the sensitivity of this residual compared to that fault (Eq. 11.87). Here, the thresh-

Fig. 11.79 X-Y trajectory

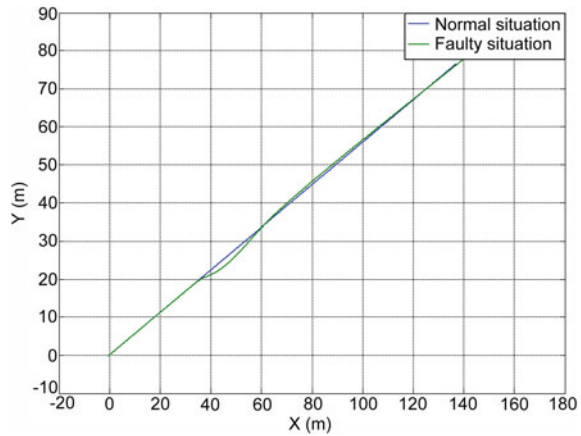
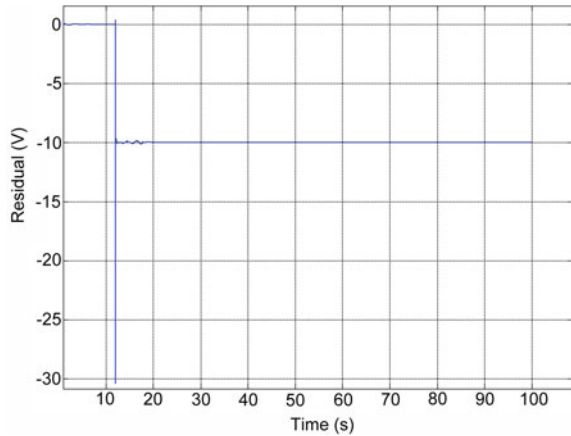


Fig. 11.80 Residual of the electrical part p_{n1_1} for fault on electrical part of the right actuated wheel



olds are adaptive to the residual, calculated by the principle of robust diagnosis of the previous section. The isolation of this fault can be made by a part, namely the electrical part and not directly by component (Table 11.2). The both detection and first reconfiguration times are estimated at 2 s (Fig. 11.82).

Concerning the **Control Reconfigurability**, for the simulated scenario, the dimension of vector control is maintained at 4 in the presence of fault, according to the closed-loop configuration of Fig. 11.78. This means that the system is still controllable and a solution of the control reconfiguration is possible on the operated system. The active control will gradually adapt the wheel velocities, while maintaining the desired path.

The **Control Reconfiguration** scenario is divided into five parts (Fig. 11.82):

1. At the instant of fault detection after loss of actuator power and the drift of the vehicle, decentralized control applied to the front left wheel, adapts its velocity

Fig. 11.81 Control signals during the faulty situation

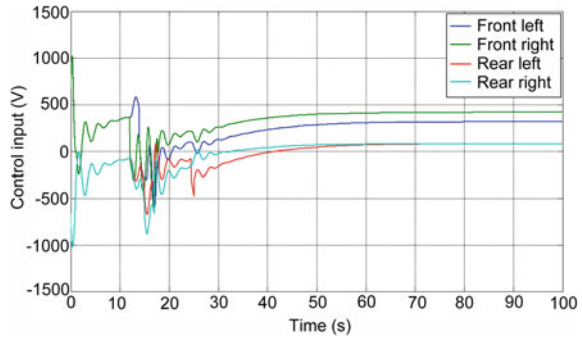
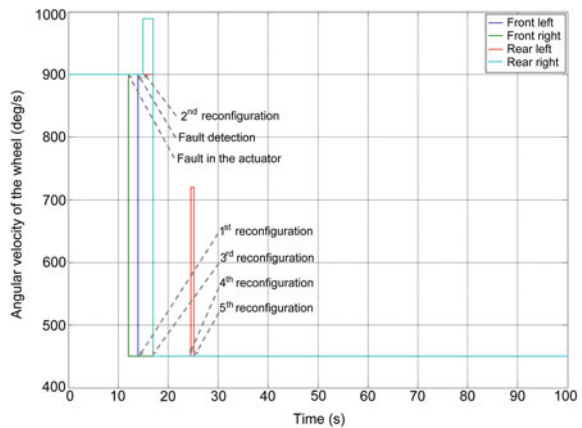


Fig. 11.82 Desired angular velocities of the wheels



to that of the deficient actuator. Figures 11.81 and 11.82 show the transition to this adaptation.

2. At time $t = 15$ s, decentralized control applied to the right rear wheel, increase its velocity up to $900^\circ/\text{s}$ for 2 s, thus re-direct the vehicle to its original course (Fig. 11.83);
3. At time $t = 17$ s, the controls applied to the rear wheels adapt the velocities of the rear wheels than the two front wheels (Fig. 11.81);
4. Finally, a correction on the trajectory is done by increasing the velocity of the left rear wheel for a period of one second at time $t = 24$ s (Figs. 11.83, 11.84, 11.85).

Final trajectory of the vehicle before and during the faulty situation is presented by the continuous curve of (Fig. 11.79). Figures 11.86 and 11.87 show the effect of longitudinal and lateral efforts on the vehicle guidance. When the fault appears and the vehicle starts drifting, the lateral efforts are not neglected (Fig. 11.87), which they converge to zero according the movement scenario when the reconfiguration is completely done.

Fig. 11.83 Measured angular velocities of the wheels

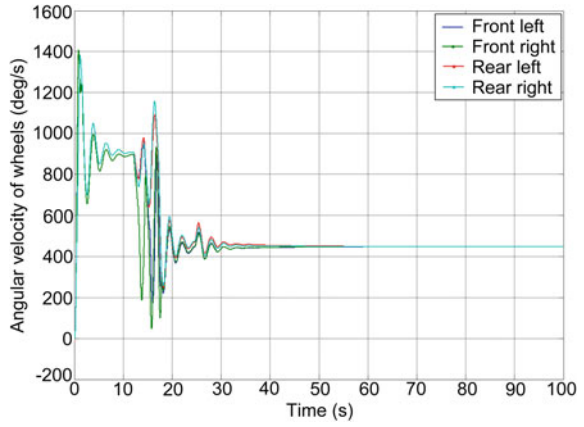


Fig. 11.84 Longitudinal velocity of the vehicle

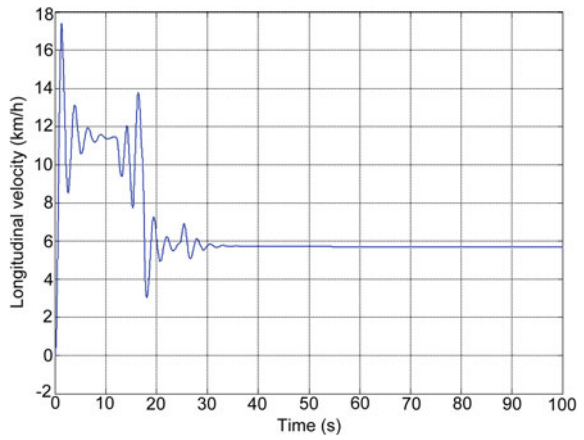


Fig. 11.85 Longitudinal acceleration of the vehicle

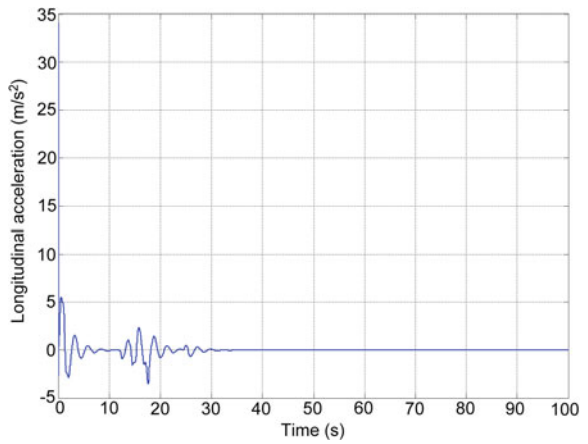


Fig. 11.86 Longitudinal efforts on the tires

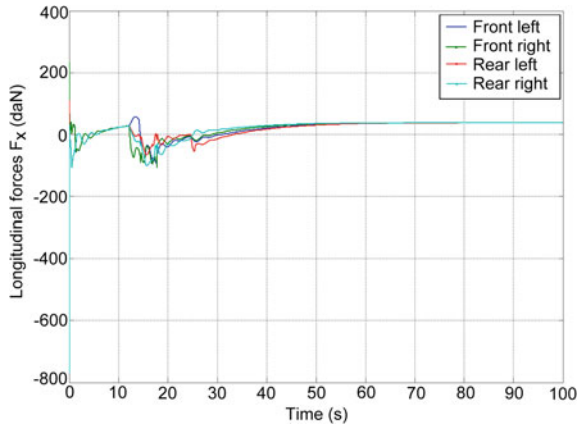


Fig. 11.87 Lateral efforts on the tires

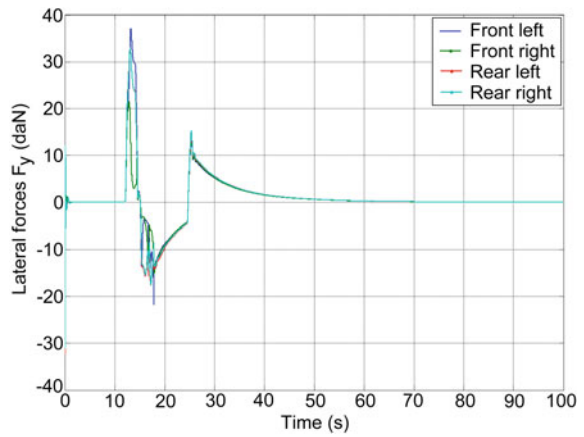


Fig. 11.88 Train of electric vehicles



11.8 Homogeneous Cooperation of Intelligent Autonomous Vehicles

The concept of intelligent autonomous vehicles has expanded with time to train for intelligent vehicles, known by the name of ‘*Platoon*’. This principle is based vehicle convoy of homogeneous vehicles, where a leader vehicle, driven manually or automatically, towing other intelligent vehicles, without physical contact between vehicles. The association of different distance sensors: laser, ultrasonic, or vision, ensures such traffic in convoy under certain conditions related mainly to the low velocity of the leader vehicle. This application may have an interest in the transport of fret and persons in private spaces, such as university campuses, airports, seaports, and bus lines.

The operation of this train is maintained in part by the communication between vehicles and infrastructure. The purpose of this transport configuration is to carry the maximum loads between two distant points across a road. The safety of such system is very important and is mainly defined by the management of inter- distance between vehicles.

In the case where the sensors are faulty or disturbed by the surrounding environment, it is important to find a solution for controlling all vehicles to avoid deadlocks or accident. A possible solution is to replicate the dynamic movement on the follower vehicles in the absence of sensors. This is possible only when this dynamic can be modeled mathematically, where physically it characterizes the *jerky* motion between two follower vehicles.

Thus, the aim of this section is to model the *jerky* motion between vehicles in convoy, not connected by a physical link, but that can communicate between them by exchanging wireless signals.

11.8.1 Modeling of Homogeneous Train of Intelligent Autonomous Vehicles

This subsection describes a deterministic dynamic model of the inter distance of train of vehicles (Fig. 11.88). The considered vehicles are those studied in the previous sections, with decentralized control and double forward and rear steering.

Dynamically, the considered transportation system is composed of a train and autonomous vehicles of Fig. 11.89. The inter distance between vehicles can be described by a virtual interconnection of two mobile bodies ($i, i + 1$) of Fig. 11.14, via a spring-dashpot system with the couple ($k_{i \rightarrow i+1}, f_{i \rightarrow i+1}$) of elasticity and damping coefficient. This virtual interconnection can describe the *Stick-Slip* phenomenon acting between two unconnected follower vehicles. The necessary efforts calculated by the i th vehicle in order to reach the safe inter distance with the $(i + 1)$ th vehicle can be assimilated by a generated effort due to the elongation of the virtual spring.

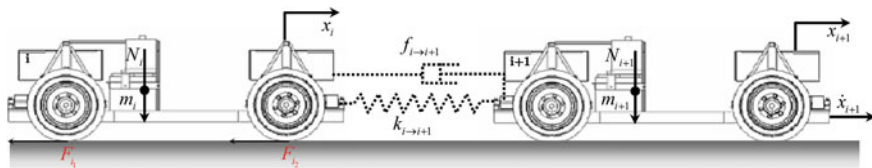
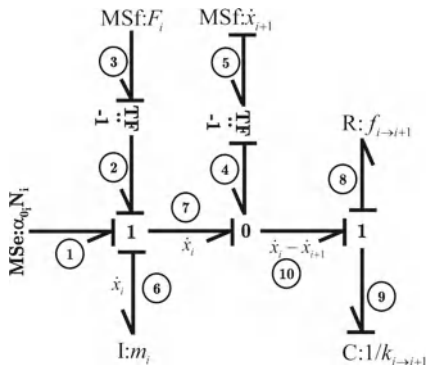


Fig. 11.89 Virtual interconnection of train of vehicles

Fig. 11.90 Bond graph model of the longitudinal dynamic of the i th vehicle



In normal situation, the inter distance is measured using a laser sensor or equivalent (Fig. 11.88).

Initially, when the $(i + 1)$ th vehicle starts moving with constant velocity \dot{x}_{i+1} , then the inter distance is less than the fixed threshold corresponding to the safe inter distance, it means that the virtual spring is relaxed and the i th vehicle is immobile. When the inter distance become bigger than the identified threshold, it means that the virtual spring is stretched with a quantity of x_{i0} by a force of $k_{i \to i+1}x_{i0} + f_{i \to i+1}\dot{x}_{i0}$, necessary to hit the static friction force $\alpha_0 N_i$, the load of mass m_i starts moving and the friction coefficient will be equal to its dynamic value, generally less than the static friction.

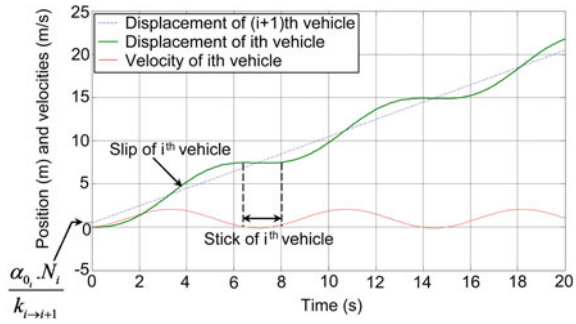
After this short transient dynamic, the *jerk* effect is now starting, where the i th vehicle moves forward before it stops, describing the *Stick-Slip* motion. The physical meaning of this phenomenon is that the static contact friction is greater than its dynamic value.

Let's consider the longitudinal dynamic of the i th vehicle according to the displacement x_i . The normal force N_i generates a global friction force $F_i = \sum_{k=1}^4 F_{ik}$ acting against the longitudinal motion. This force varies nonlinearly with the slip velocity (11.8). The corresponding bond graph model is given by Fig. 11.90.

From the first junction 1, we obtain the following differential equation (11.97) of the i th longitudinal dynamic of the vehicle:

$$m_i \ddot{x}_i + f_{i \to i+1}(\dot{x}_i - \dot{x}_{i+1}) + k_{i \to i+1}(x_i - x_{i+1}t) = \alpha_0 N_i - F_i \quad (11.97)$$

Fig. 11.91 Stick-slip motion representation



where $\alpha_{0_i} N_i$ is the useful effort to overcome the dry friction of coefficient α_{0_i} at the beginning of the motion. The inter distance φ_i between the i th and $(i + 1)$ th (i.e. the virtual spring elongation) is given by (11.98):

$$\varphi_i = \frac{\alpha_{0_i} N_i}{k_{i \rightarrow i+1}} + \dot{x}_{i+1} t - x_i \tag{11.98}$$

Thus, in the case of $\dot{x}_i > 0$, we obtain the differential equation of the spring elongation [41]:

$$m_i \ddot{\varphi}_i + f_{i \rightarrow i+1} \dot{\varphi}_i + k_{j \rightarrow j+1} \varphi_i = F_i \tag{11.99}$$

These two states of the i th vehicle (i.e. position and velocity) can be illustrated by Fig. 11.91 in the case of linear increase of position x_{i+1} . We can notice that x_{i+1} starts from an initial value of $x_{i0} = \frac{\alpha_{0_i} N_i}{k_{i \rightarrow i+1}}$, while the i th vehicle is followed by a succession of a stick and a slip motions.

11.8.2 Modeling of Operation Modes of Intelligent Transportation System

To manage the correct functioning of a system composed of intelligent vehicles, it is advisable to make a supervision system, taking into consideration the different operation modes of ITS. Thus, in what follows, we take an example of a functional model of a convoy of intelligent vehicles, operating in an identified environment.

In this case, intelligent transportation system is composed of intelligent autonomous vehicles, loading and discharging stations, and a road network. This system is made up of three operation modes $\mathcal{M} = \{\mathcal{M}_1, \mathcal{M}_2, \mathcal{M}_3\}$ [12], and it can be represented graphically by a set of nodes and valued arcs of Fig. 11.92:

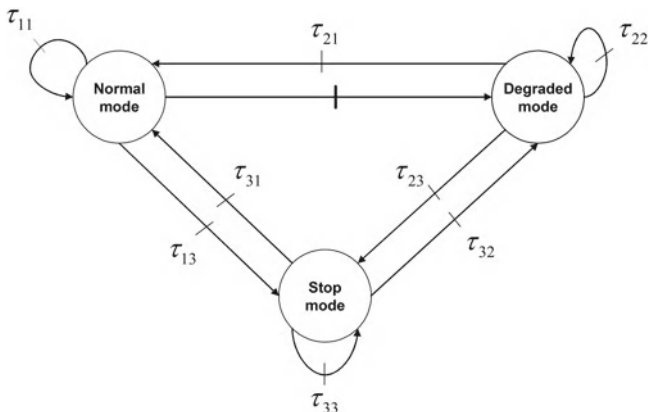


Fig. 11.92 Graphical representation of operation modes

where

- \mathcal{M}_1 : normal mode.
- \mathcal{M}_2 : degraded mode.
- \mathcal{M}_3 : stop mode.

Proposition 11.1 *Let us consider three constraints associated to the ITS: The first constraint E_1 indicates the operation status of the intelligent autonomous vehicles, the second constraint E_2 describes the status of the loading and discharging stations, whereas the third constraint E_3 shows the status of the road network.*

Thus, the value associated to the first constraint is equal to **0** when all the vehicles operate correctly, **2** if all the vehicles are faulty and **1** otherwise. In the same way, the value of the second constraint is supposed **0** if the loading and discharging stations are available, **2** if all the stations are occupied and **1** otherwise. Finally, the value associated to the third constraint is *Boolean*, it is equal to **0** if the road network is accessible and to **1** otherwise. Then $E_1 = \{0, 1, 2\}$, $E_2 = \{0, 1, 2\}$, $E_3 = \{0, 1\}$

Proposition 11.2 *Let us consider $\mathcal{B} = \{\mathcal{B}_1, \dots, \mathcal{B}_Q\}$ the finite set of **18** triplets of constraints $Q = \text{card}(E_1) \times \text{card}(E_2) \times \text{card}(E_3) = 3 \times 3 \times 2 = 18$, where Q is the number of possible constraints combination, such as $\mathcal{B}_q = (C_1, \dots, C_P)$ for $1 \leq q \leq Q$:*

$$\begin{aligned}
 \mathcal{B}_1 &= (0, 0, 0) & \mathcal{B}_7 &= (1, 0, 0) & \mathcal{B}_{13} &= (2, 0, 0) \\
 \mathcal{B}_2 &= (0, 0, 1) & \mathcal{B}_8 &= (1, 0, 1) & \mathcal{B}_{14} &= (2, 0, 1) \\
 \mathcal{B}_3 &= (0, 1, 0) & \mathcal{B}_9 &= (1, 1, 0) & \mathcal{B}_{15} &= (2, 1, 0) \\
 \mathcal{B}_4 &= (0, 1, 1) & \mathcal{B}_{10} &= (1, 1, 1) & \mathcal{B}_{16} &= (2, 1, 1) \\
 \mathcal{B}_5 &= (0, 2, 0) & \mathcal{B}_{11} &= (1, 2, 0) & \mathcal{B}_{17} &= (2, 2, 0) \\
 \mathcal{B}_6 &= (0, 2, 1) & \mathcal{B}_{12} &= (1, 2, 1) & \mathcal{B}_{18} &= (2, 2, 1)
 \end{aligned}$$

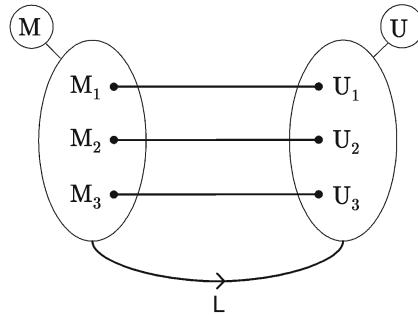


Fig. 11.93 L bijection

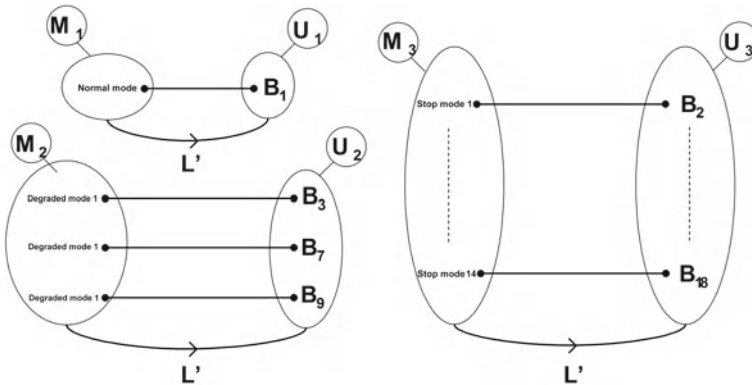


Fig. 11.94 L' bijection

Proposition 11.3 Let us consider the set $\mathcal{U} = \{\mathcal{U}_1, \mathcal{U}_2, \mathcal{U}_3\}$ a partition of \mathcal{B} such as:

$$\mathcal{U}_1 = \{B_1\}$$

$$\mathcal{U}_2 = \{B_3, B_7, B_9\}$$

$$\mathcal{U}_3 = \{B_2, B_4, B_5, B_6, B_8, B_{10}, B_{11}, B_{12}, B_{13}, B_{14}, B_{15}, B_{16}, B_{17}, B_{18}\}$$

We assign to each \mathcal{U}_n a mode $\mathcal{M}_n, n \in [1; 3]$, according to the bijection \mathcal{L} of Fig. 11.93 and for each partition of \mathcal{B} , we assign a sub-mode according to the bijection \mathcal{L}' of Fig. 11.94. These assignments can be represented graphically by Fig. 11.95.

Proposition 11.4 Let us consider that the studied ITS is composed by three IAV, four loading and discharging stations and that the initial operation mode of the overall system is the normal mode \mathcal{M}_1 .

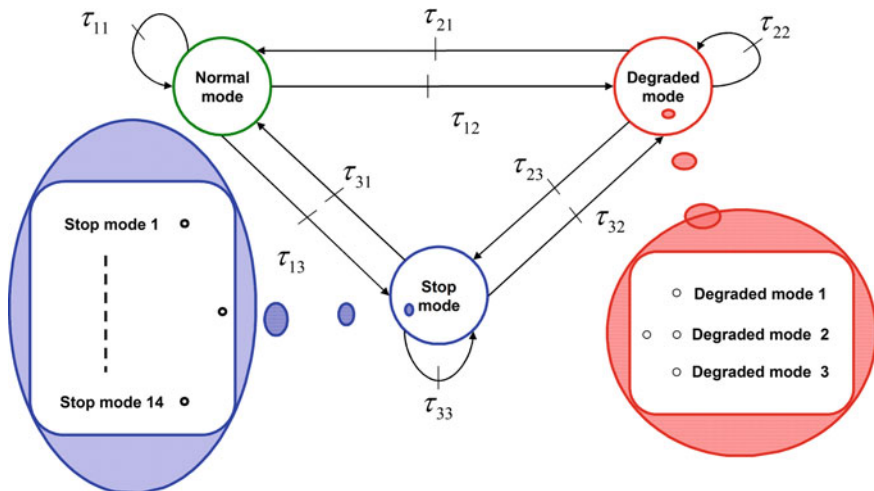


Fig. 11.95 Modes and sub-modes of the ITS

In order to determine the operation mode of the ITS at time t , the following steps are done:

1. Specification of the value of each sub-constraint e_p^k :

$$e_p^k : R^+ \rightarrow \{0, 1\}$$

$$t \rightarrow e_p^k(t)$$

where $p \in \{1, 2, 3\}$ and $k \in \{1, J_1, J_2, J_3\}$ with $J_1 \in \{1, 2, 3\}$ set of three IAV, $J_2 \in \{1, 2, 3, 4\}$ set of four loading and discharging stations and $J_3 \in \{1\}$ set of road network. Each value of these sub-constraints will be determined according to its own rule.

For example the sub-constraint e_1^k is associated to the monitoring status of IAV's inputs, its value is calculated according to the residuals of each actuators, developed previously, where

$$\begin{cases} \text{if } -a_{1_j}^i < p_{n_{1_j}}^i < a_{1_j}^i, \text{ then } e_1^k = 0 \\ \text{else } e_1^k = 1 \end{cases}$$

where $p_{n_{1_j}}^i$ is the j th nominal part of the first residual of the i th vehicle (11.78), and $a_{1_j}^i$ and $-a_{1_j}^i$ are the extremum of the associated thresholds.

2. Determination of value of each constraint C_p according to its J_p sub-constraint:

$$C_p : R^+ \times \{0, 1\} \times \{0, 1\} \times \{0, 1\} \rightarrow E_p$$

$$(t, e_p^1(t), e_p^{J_1}(t), e_p^{J_2}(t), e_p^{J_3}(t)) \rightarrow C_p(t, e_p^1(t), e_p^{J_1}(t), e_p^{J_2}(t), e_p^{J_3}(t))$$

where $p \in \{1, 2, 3\}$ and $E_p \in \{0, 1, 2\}$.

- a. Calculation of the first constraint associated to the IAV, $p = 1$:

$$C_1(t, e_1^1, e_1^2, e_1^3) = \begin{cases} 0 & \text{if } \sup\{e_1^1, e_1^2, e_1^3\} = 0 \\ 1 & \text{if } \inf\{e_1^1, e_1^2, e_1^3\} = 0 \\ & \text{and } \sup\{e_1^1, e_1^2, e_1^3\} = 1 \\ 2 & \text{if } \inf\{e_1^1, e_1^2, e_1^3\} = 1 \end{cases}$$

- b. Calculation of the second constraint associated to the loading and discharging stations, $p = 2$:

$$C_2(t, e_2^1, e_2^2, e_2^3, e_2^4) = \begin{cases} 0 & \text{if } \sup\{e_2^1, e_2^2, e_2^3, e_2^4\} = 0 \\ 1 & \text{if } \inf\{e_2^1, e_2^2, e_2^3, e_2^4\} = 0 \\ & \text{and } \sup\{e_2^1, e_2^2, e_2^3, e_2^4\} = 1 \\ 2 & \text{if } \inf\{e_2^1, e_2^2, e_2^3, e_2^4\} = 1 \end{cases}$$

- c. Calculation of the third constraint associated to the road network, $p = 3$:

$$C_3(t, e_3^1) = \begin{cases} 0 & \text{if } e_3^1 = 0 \\ 1 & \text{if } e_3^1 = 1 \end{cases}$$

3. Find the element of \mathcal{B} which corresponds to the triplet formed from the constraints (C_1, C_2, C_3) found into step 2.
4. Identification of the operation mode and its sub-mode according to the bijections \mathcal{L} and \mathcal{L}' of Figs. 11.93 and 11.94.
5. Evaluation of the graph arcs as follows:

$$\begin{cases} \tau_{\zeta\kappa} = 1 \\ \tau_{\varkappa\rho} = 0 \quad \forall \zeta, \kappa, \varkappa, \rho \in \{1, 2, 3\} \text{ and } (\varkappa, \rho) \neq (\zeta, \kappa) \end{cases}$$

11.8.3 Case Studies

11.8.3.1 Case 1: Normal Mode

In this case, we consider that the ITS is initially in normal operation (Fig. 11.96).

1. Specification of the value of each sub-constraint:
 - a. Vehicles operate correctly: $e_1^1 = e_1^2 = e_1^3 = 0$.
 - b. Loading and discharging stations are available: $e_2^1 = e_2^2 = e_2^3 = e_2^4 = 0$.
 - c. Road network is accessible: $e_3^1 = 0$.
2. Determination of the constraints:

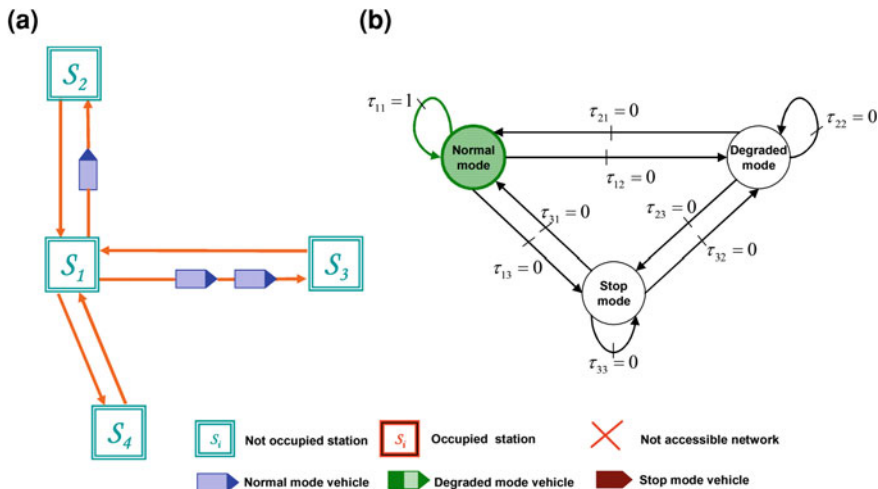


Fig. 11.96 a Simulated normal scenario. b ITS's graphical model of normal operation mode

- a. Calculation of the first constraint: $C_1(t, 0, 0, 0) = 0$.
 - b. Calculation of the second constraint: $C_2(t, 0, 0, 0, 0) = 0$.
 - c. Calculation of the third constraint: $C_3(t, 0) = 0$.
3. The triplet formed from the constraints is $(0, 0, 0)$, it corresponds to the first element of the set \mathcal{A}_1 .
 4. Using the bijection \mathcal{L} , we deduce that the system is in normal mode \mathcal{M}_1 .
 5. Evaluation of the graph arcs:

$$\begin{cases} \tau_{11} = 1 \\ \tau_{\neq\rho} = 0 \forall \neq, \rho \in \{1, 2, 3\} \text{ and } (\neq, \rho) \neq (1, 1) \end{cases}$$

11.8.3.2 Case 2: Degraded Mode

In this case, we consider a faulty scenario for the ITS (Fig. 11.97).

1. Specification of the value of each sub-constraint:
 - a. The third vehicle is in faulty situation: $e_1^1 = e_2^1 = 0$ and $e_3^1 = 1$.
 - b. The second loading and discharging station is occupied: $e_2^2 = e_3^2 = e_4^2 = 0$ and $e_2^2 = 1$.
 - c. The road network is accessible: $e_3^1 = 0$.
2. Determination of the constraints:
 - a. Calculation of the first constraint: $C_1(t, 0, 0, 1) = 1$.

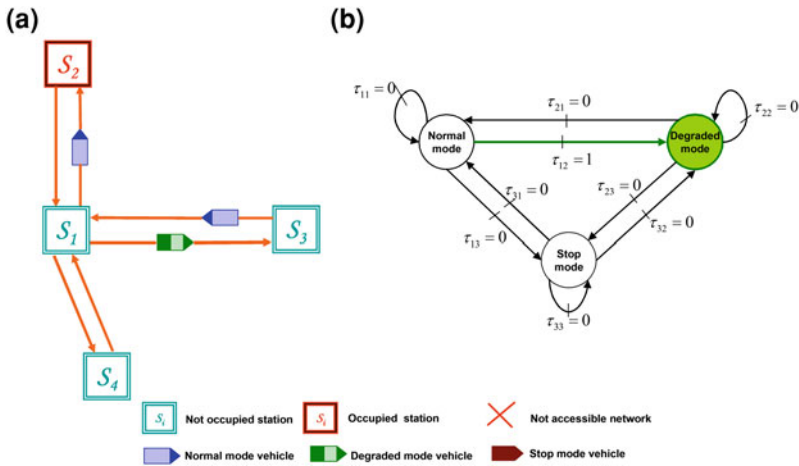


Fig. 11.97 a Simulated faulty scenario. b ITS's graphical model of degraded operation mode

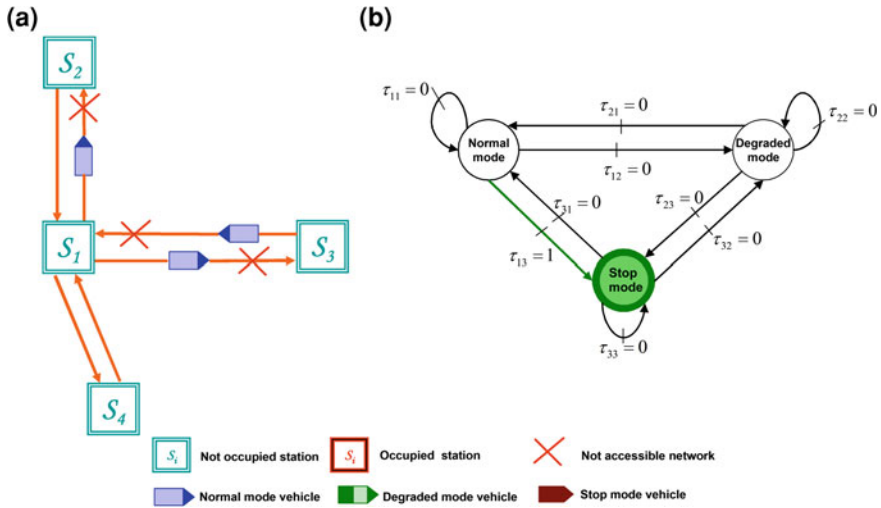


Fig. 11.98 a Simulated blocking scenario. b ITS's graphical model of stop operation mode

- b. Calculation of the second constraint: $C_2(t, 0, 1, 0, 0) = 1$.
- c. Calculation of the third constraint: $C_3(t, 0) = 0$.

3. The triplet formed from the constraints is $(1, 1, 0)$, it corresponds to the third element of the set \mathcal{W}_2 .
4. Using the bijection \mathcal{L} , we deduce that the system is in degraded mode \mathcal{M}_2 . Bijection \mathcal{L}' determines the sub-mode *degraded mode 3*.
5. Evaluation of the graph arcs:

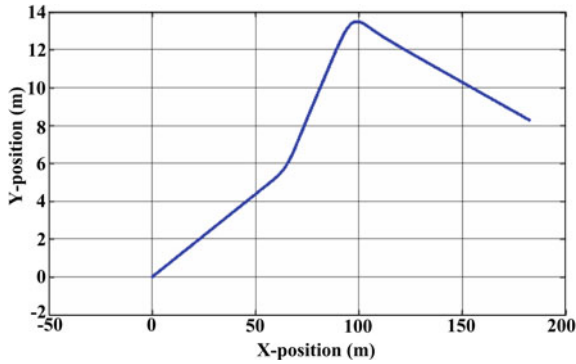


Fig. 11.99 Desired trajectory

$$\begin{cases} \tau_{12} = 1 \\ \tau_{\varkappa\rho} = 0 \quad \forall \varkappa, \rho \in \{1, 2, 3\} \text{ and } (\varkappa, \rho) \neq (1, 2) \end{cases}$$

11.8.3.3 Case 3: Stop Mode

In this case, we consider a major fault which stop the operation of the ITS, starting initially from the normal operation mode (Fig. 11.98).

1. Specification of the value of each sub-constraint:
 - a. Vehicles operate correctly: $e_1^1 = e_1^2 = e_1^3 = 0$.
 - b. Loading and discharging stations are available: $e_2^1 = e_2^2 = e_2^3 = e_2^4 = 0$.
 - c. The road network is not accessible: $e_3^1 = 1$.
2. Determination of constraints:
 - a. Calculation of the first constraint: $C_1(t, 0, 0, 0) = 0$.
 - b. Calculation of the second constraint: $C_2(t, 0, 0, 0, 0) = 0$.
 - c. Calculation of the third constraint: $C_3(t, 1) = 1$.
3. The triplet formed from the constraints is $(0, 0, 1)$, it corresponds to the first element of the set \mathcal{U}_3 .
4. Using the bijection \mathcal{L} , we deduce that the system is in *stop mode* \mathcal{M}_3 . Bijection \mathcal{L}' determines the sub-mode *stop mode 1*.
5. Evaluation of the graph arcs:

$$\begin{cases} \tau_{13} = 1 \\ \tau_{\varkappa\rho} = 0 \quad \forall \varkappa, \rho \in \{1, 2, 3\} \text{ and } (\varkappa, \rho) \neq (1, 3) \end{cases}$$

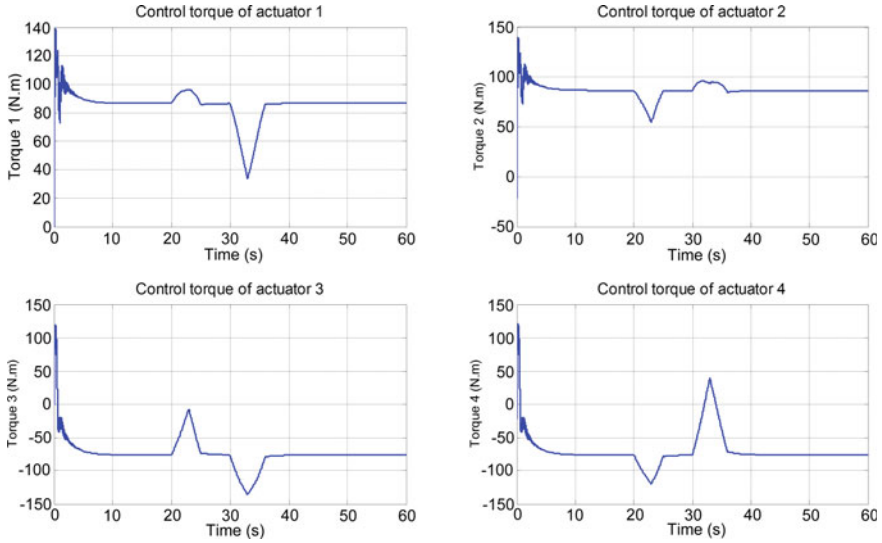


Fig. 11.100 Input torques in normal operation mode

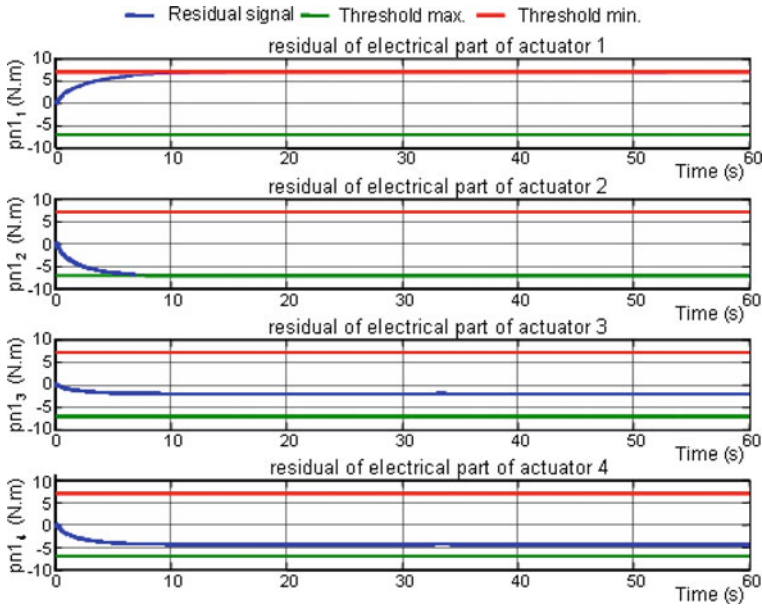


Fig. 11.101 Residuals in normal operation mode of the third vehicle

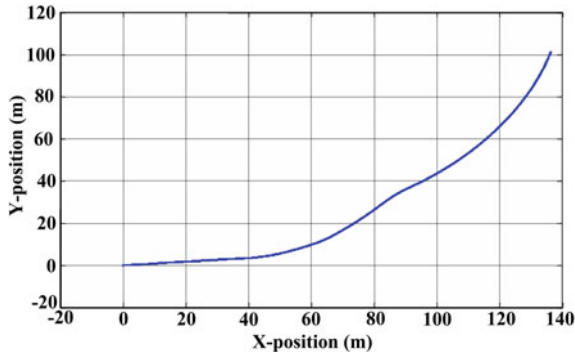


Fig. 11.102 Trajectory realized by the degraded vehicle

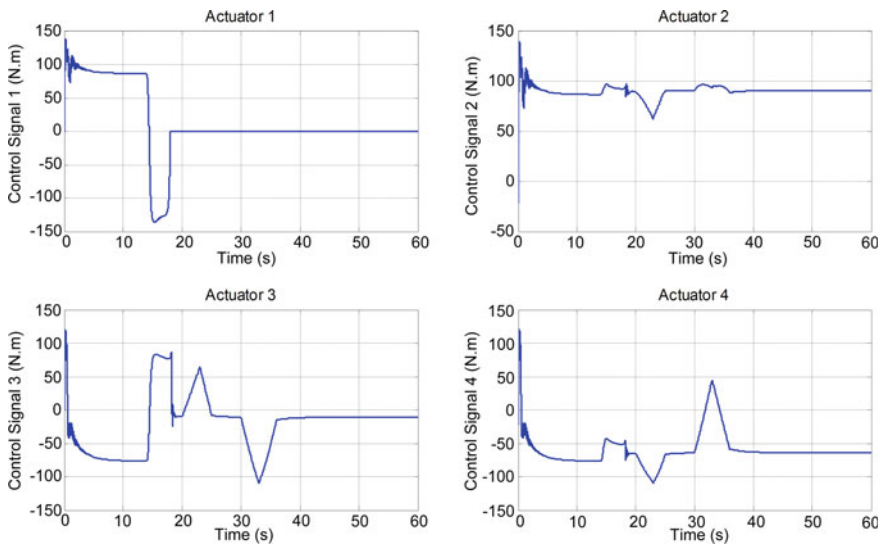


Fig. 11.103 Input torques in degraded operation mode

11.8.4 Results of Co-Simulation

For the following, we consider a control scenario for a train of three *RobuCar*'s system, which allows tracking of the trajectory given by Fig. 11.99 during 60 s.

The positions of mass and velocities of each vehicle are given experimentally from appropriate sensors, and then used for co-simulation with *Callas-Prosper* software [36]. The steering is controlled by using the decentralized traction control of Fig. 11.100. In normal operation mode, the residuals of the electrical part for each traction is given by Fig. 11.101. Electrical fault is simulated, originally from an electrical component of the forward left actuator of the third follower vehicle. This fault

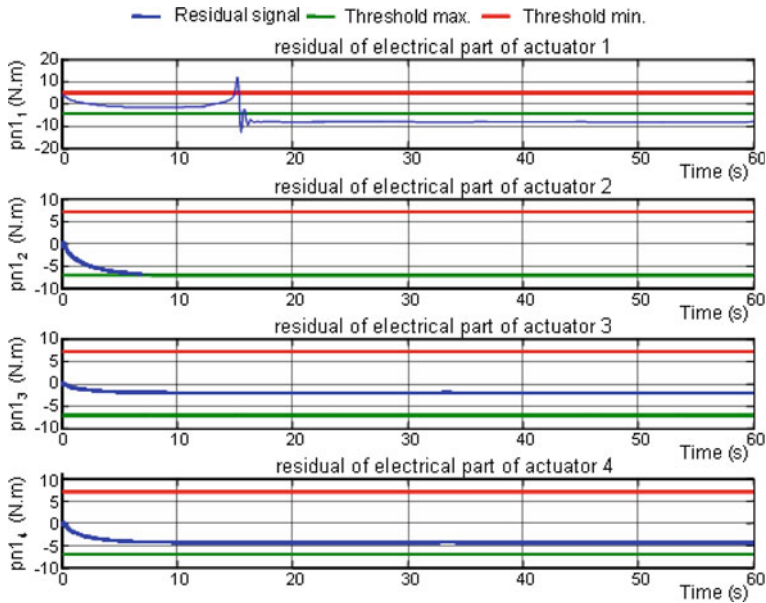


Fig. 11.104 Residuals in degraded operation mode of the third vehicle

is detected at time 14 s as shown in the profile of control torque (Fig. 11.103). This fault does not block the wheel motion and keeps it turning free. The new X - Y trajectory in presence of this fault is given in Fig. 11.102. The profile of the residuals in presence of this fault is shown in Fig. 11.104, where the first residual appears sensitive to this fault.

11.9 Conclusion

Intelligent autonomous vehicle may be a component of an intelligent transport system. This is possible only when it is fully controllable and manageable in situations of normal or faulty operations. Thus, perfect knowledge of the dynamics of the vehicle, including interactions with the ground and the environment is essential for the design of control architecture for safe operation. This helps significantly in the development of a reliable and robust supervision system.

With the association of new technologies and ICT, intelligent vehicles are increasingly autonomous, without completely replacing the classical vehicle piloted manually. Actually, this fully autonomous vehicle is limited in terms of exploitation, especially it is used inside a security area where the presence of human operators is minimized. The progress of the IAV is coming directly from the robotics technologies. It is a real transfer from a robotic scale toward a huge scale, without knowing yet the real impact of the IAV cohabitation with the human.

References

1. J. Chen, R.J. Patton, Z. Chen, An LMI approach to fault-tolerant control of uncertain systems, in *IEEE ISIC/CIRA/ISAS Joint Conference*, 1998
2. J. Davila, F. Fridman, Observation and identification of mechanical systems via second order sliding modes, in *Proceedings of the 8th International Workshop on Variable, Structure*, 2004
3. M.A. Djeziri, R. Merzouki, B. Ould-Bouamama, G. Dauphin-Tanguy, Robust fault diagnosis using bond graph approach. *IEEE/ASME Trans. Mechatron.* **12**(6), 599–611 (2007)
4. M.A. Djeziri, B. Ould-Bouamama, R. Merzouki, G. Dauphin-Tanguy, Bond graph model based for robust fault diagnosis, in *American Control Conference, ACC'2007*, pp. 3017–3022, New York, 2007
5. J.S. Eterno, J.L. Weiss, D.P. Looze, A. Willsky, Design issues for fault tolerant-restructurable aircraft control, in *Proceedings of the 24th Conference on Decision and Control*, pp. 900–905, 1985
6. ETSI, www.etsi.org, The European Telecommunications Standards Institute, 2010
7. Gottwald, www.gottwald.com, Gottwald port terminal website, 2010
8. C.S. Hsieh, Performance gain margins of the two-state LQ reliable control. *Automatica* **38**, 1985–1990 (2002)
9. InTraDE, www.intrade-nwe.eu, website of INTERREG project InTraDE 09–13, 2010
10. R. Isermann, Supervision, fault detection and fault diagnosis methods—an introduction. *Control Eng. Pract.* **5**(5), 639–652 (1997)
11. D.C. Karnopp, An approach to derivative causality in bond graph models of mechanical systems. *J. Frankl. Inst.* **329**, 65–75 (1992)
12. W. Khalil, R. Merzouki, B. Ould-Bouamama, Dynamic modelling of a train of intelligent vehicles inside a confined space, in *12th IFAC Symposium on Control in Transportation*, Redondo Beach, pp. 619–626, 2009
13. A. Khelassi, D. Theilliol, P. Weber, Reconfigurability analysis for reliable fault-tolerant control design, in *7th Workshop on Advanced Control and Diagnosis, ACD'2009*, Zielona Gora, 2009
14. U. Kiencke, L. Nielsen, *Automotive Control Systems: For Engine Driveline and Vehicle* (Springer, Berlin, 2000)
15. A. Levant, Robust exact differentiation via sliding mode technique. *Automatica* **34**, 379–384 (1998)
16. Y.W. Liang, D.C. Liaw, T.C. Lee, Reliable control of nonlinear systems. *IEEE Trans. Autom. Control* **45**, 706–710 (2000)
17. F. Liao, J.L. Wang, G.H. Yang, Reliable robust flight tracking control: an LMI approach. *IEEE Control Syst. Mag.* **10**, 76–89 (2002)
18. J.R. Loureiro, Fault tolerant control based on graphical approach: application to intelligent transportation systems. Scientific report, LAGIS-FRE CNRS 3303, 2010
19. R. Merzouki, J.C. Cadiou, Estimation of backlash phenomenon in the electromechanical actuator. *Control Eng. Pract.* **13**, 973–983 (2005)
20. R. Merzouki, J.C. Cadiou, N.K. MSirdi, Compensation of friction and backlash effects in an electrical actuator. *J. Syst. Control Eng.* **218**, 75–84 (2004)
21. R. Merzouki, J.A. Davila Montoya, L.M. Fridman, J.C. Cadiou, Backlash phenomenon observation and identification in electromechanical system. *Control Eng. Pract.* **15**, 447–457 (2007)
22. R. Merzouki, B. Ould-Bouamama, M.A. Djeziri, M. Bouteldja, Modelling and estimation for tire-road system using bond graph approach. *Mechatronics* **17**, 93–108 (2007)
23. Michelin, Tire encyclopedia, in *Société de Technologie Michelin*, 2001
24. T. Mijsch, A. Gambier, E. Badreddin, Real-time performance comparison of fault-tolerant controllers, in *IEEE Multi-Conference on Systems and Control*, San Antonio, 2008
25. M. Mizuno, Development of tire side force model based on magic formula with the influence of tire surface temperature. *R&D Rev. Toyota CRDL* **38**, 17 (2003)
26. M. Mizuno, T. Takahashi, M. Hada, Magic formula tire model using the measured data of a vehicle running on actual road, in *AVEC'98*, Nagoya, 1998

27. A. Mukherjee, R. Karmakar, *Modelling and Simulation of Engineering Systems Through Bond Graphs* (Alpha Sciences International, Pangbourne, 2000)
28. A. Mukherjee, A.K. Samantaray, System modelling through bond graph objects on SYMBOLS 2000, in *International Conference on Bond Graph Modeling and Simulation (ICBGM'01)*, vol. 33, no. 1, pp. 164–170. Simulation Series, 2001. ISBN 1-56555-103-6
29. H. Niemann, J. Stoustrup, Passive fault tolerant control of a double inverted pendulum—a case study. *Control Eng. Pract.* **13**, 1047–1059 (2005)
30. Numexia, Numexia: www.numexia.com, Official website of Numexia, 2010
31. B. Ould Bouamama, A.K. Samantaray, M. Staroswiecki, G. Dauphin-Tanguy, Derivation of constraint relations from bond graph models for fault detection and isolation, in *International Conference on Bond Graph Modeling and Simulation (ICBGM'03)*, pp. 104–109. Simulation Series, vol. 35, no. 2, 2003. ISBN 1-56555-257-1
32. R.J. Patton, Fault-tolerant control system, in *Proceedings of the 3rd IFAC Symposium on Fault Detection, Supervision and Safety for Technical Processes*, pp. 1033–1055, 1997
33. Robosoft, Robosoft: www.robosoft.fr, Official website of Robosoft, 2010
34. A.K. Samantaray, K. Medjaher, B. Ould Bouamama, M. Staroswiecki, G. Dauphin-Tanguy, Component based modelling of thermo-fluid systems for sensor placement and fault detection. *SIMULATION Trans. Soc. Model. Simul. Int.* **80**(7–8), 381–398 (2004)
35. A.K. Samantaray, K. Medjaher, B. Ould Bouamama, M. Staroswiecki, G. Dauphin-Tanguy, Diagnostic bond graphs for online fault detection and isolation. *Simul. Model. Pract. Theory* **14**(3), 237–262 (2005)
36. Scanner-OKTAL, Scanner driving simulation engine (2012), <http://www.scannersimulation.com/>, Accessed 3 March 2012
37. D.J. Schuring, W. Pelz, M.G. Pottinger, *A Model for Combined Tire Cornering and Braking Forces* (SAE International, Warrendale, 1996), pp. 113–125
38. B. Siciliano, O. Khatib, *Handbook of Robotics* (Springer, New York, 2008). ISBN 978-3-540-23957-4,
39. C. Sié Kam, Les Bond Graphs pour la Modélisation des Systèmes Linéaires Incertains. Ph.D. thesis, Ecole Centrale de Lille and USTL, Lille, 2001
40. T. Soderstrom, P. Stoica, *System Identification* (Prentice Hall International, Hemel Hempstead, 1989)
41. G. Spinnler, Conception des machines. Presses Polytechniques et Universitaires Romandes, 1997
42. M. Staroswiecki, On reconfigurability with respect to actuator failures, in *Proceeding of 15th Triennial World Congress*, Barcelona, 2002
43. M. Staroswiecki, G. Comtet-Varga, Analytical redundancy relations for fault detection and isolation in algebraic dynamic systems. *Automatica* **37**, 687–699 (2001)
44. C. Sueur, G. Dauphin-Tanguy, Structural controllability/observability of linear systems represented by bond graphs. *J. Frankl. Inst.* **326**(6), 869–883 (1989)
45. TTS Group, www.ttsgroup.com/Products/AGV/, AGV for Container Terminals: TTS Group ASA, 2010
46. V. Utkin, J. Guldner, J. Shi, *Sliding Mode Control in Electromechanical Systems* (Taylor & Francis, London, 1999)
47. R.J. Veillette, Reliable linear-quadratic state-feedback control. *Automatica* **31**, 137–143 (1995)
48. R.J. Veillette, J.V. Medanic, W.R. Perkins, Design of reliable control systems. *IEEE Trans. Autom. Control* **37**, 290–304 (1992)
49. J.Y. Wong, *Theory of Ground Vehicle* (Wiley, New York, 2001)
50. N.E. Wu, K. Zhou, G. Salomon, Control reconfigurability of linear time-invariant systems. *Automatica* **36**, 1767–1771 (2000)
51. G.H. Yang, J.L. Wang, Y.C. Soh, Reliable LQG control with sensor failures, in *Proceeding of the 38th Conference on Decision and Control*, Phoenix, 1999
52. G.H. Yang, J. L. Wang, Y.C. Soh, Reliable H-inf controller design for linear systems. *Automatica* **37**, 717–725 (2001)

53. Z. Yang, Reconfigurability analysis for a class of linear hybrid systems, in *Proceedings of 6th IFAC Safeprocess*, Beijing, 2006
54. J.S. Yee, G.H. Yang, J.L. Wang, Reliable output-feedback controller design for discrete-time linear systems: an iterative LMI approach, in *Proceedings of the American Control Conference*, Arlington, 2001
55. Y. Zhang, J. Jiang, Bibliographical review on reconfigurable fault-tolerant control systems. *Ann. Rev. Control* **32**, 229–252 (2008)
56. Q. Zhao, J. Jiang, Reliable control system design against feedback failures with applications to aircraft control, in *Proceedings of the 1996 IEEE International Conference on Control Applications*, Dearborn, 1996
57. Q. Zhao, J. Jiang, Reliable tracking control systems design against actuator failures, in *Proceedings SICE Conference*, Tokushima, 1997

Chapter 12

Telediagnosis of Mechatronic Systems

12.1 Introduction

Telerobotics system is considered as a class of networked control systems (NCS), which is increasingly used nowadays in a wide variety of engineering systems including manufacturing plants, aircraft, automobiles, etc. The standard representation of the NCS is summarized in Fig. 12.1: it is combination of controller, network channel, actuators, system or plant, and sensor components.

In the configuration of Fig. 12.1, the transmission delay effects are considered for whole system dynamics. Thus, the main instantaneous delays are those induced from the sensor to the controller τ_k^{SC} and from the controller to the actuator τ_k^{CA} . Due to many uncertain factors in the real transmission systems, the network-induced delays are generally considered random. Therefore, NCS is generally considered a time-varying system.

Modeling, controlling, and monitoring of NCS are based at first on the analysis of time delayed system, already studied for several years. Networked manufacturing systems, transport systems, teleoperation systems are typical examples of time delayed systems [22]. Characteristics of the delay depend on several parameters such as the transmission protocol, the length of the network, and the characteristics of the NCS equipment. In general, delay occurs during the exchanges of data between different equipment of the NCS. Data sampling and package losses constitute another source of variable delay which need to be included in the whole dynamic model. The simplest model of the networked control system is to consider the delay as constant parameter for all transfers inside the network but it remains far from the real operation of NCS. This can be an adequate model even if the network has varying delays, for instance, if the time scale in the control process is much larger than the delay introduced by the network. One way to achieve a known and constant delay is by introducing the timed buffers after each transfer. By making these buffers longer than the worst case delay time, the transfer time can be viewed as being constant. This method is proposed in [17], but the control delay becomes longer than necessary which can influence on the performance of the system.

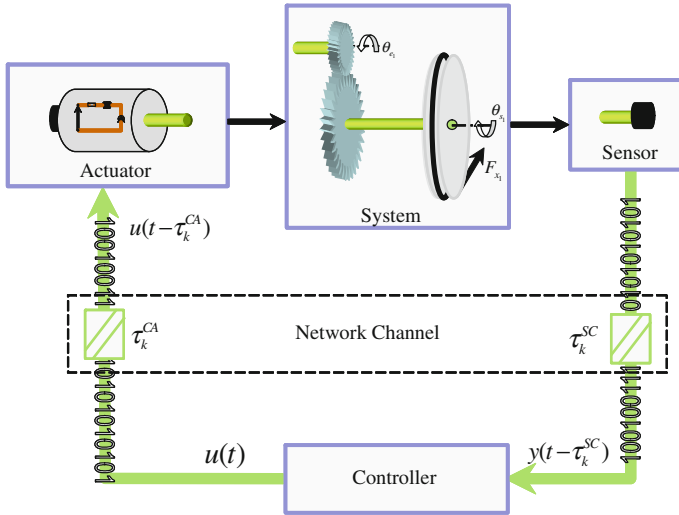


Fig. 12.1 Architecture of a networked control system

Fault diagnosis (FD) and fault-tolerant control (FTC) are very important issues for networked control systems, particularly in safety-critical systems. The fast growth of industrial applications around the NCS has encouraged the development and integration of new tools for their FD and FTC.

12.2 Examples

12.2.1 Online Robot Supervision Using a Mobile Phone

The aim of the application illustrated in Fig. 12.2 can be summarized in the following definition: ‘Simplify communications between the robot and the human operator’.

The proposed NCS architecture can inform any actor of an industrial environment on the status of the manufacturing system. This actor can be a human operator, specialist of maintenance, shop head, quality controller, specialist in reliability, etc. He may have access to information relevant to his job during the time of work. The proposed tool will enable to better manage and plan the tasks regardless of the status of the production system.

To understand the principle, let us take the following example: Imagine, a technician performing maintenance on a robotized production line. One of its missions will be, for example to make a check of the robots after a certain hours of operation. To do so, the operator will have to regularly check the clock of each robot. This can be improved with the proposed tool, which enables the technician to have access to



Fig. 12.2 Teledetection of robot input–output using mobile phone

this information permanently regardless of his position inside the production area; even it allows informing the technician to program the date of maintenance.

The aim of presented tool is collecting relevant information of each robot from a production line and provide this information to the operators by sending only the relevant information according to the desired task.

The application is composed by the following components:

- Main server, on which network links all the equipment of the production chain. It is responsible for collecting and redistributing information;
- Wireless distant servers, connected to the main server via the network, their number would cover the entire surface of the company to allow access to information from different locations;
- Mobile wireless phone provided to each actor to connect to wireless servers.

One demonstration of this concept concerns the teledetection of robot environment through a mobile phone, which can display security alerts. Thus, the server collects information from the robot and sends them to the phone using a Bluetooth technology [4]. If an emergency stop is triggered then the phone displays an alert and begins to vibrate.

In this demonstration, only one robot communication is established, using a Kuka KR6-Arc robot [16], which is controlled by a operating system running under Windows XP Embedded [19]. A cross communication library has been provided to connect an application created in Visual Basic [20] in real-time kernel (Fig. 12.3), which drives the whole robot. This allows access to variables, statements, sensors, and actuators of the robot. An application has been programmed in order to connect the robot to gather some information. This program is connected to the server via TCP (Transmission Control Protocol) and IP (Internet Protocol).

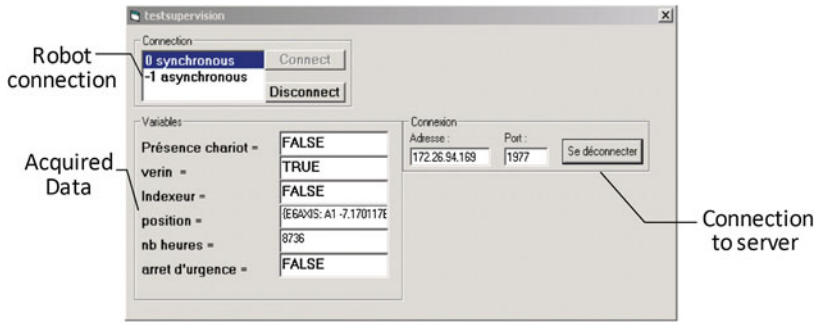


Fig. 12.3 Visual basic human-machine interface

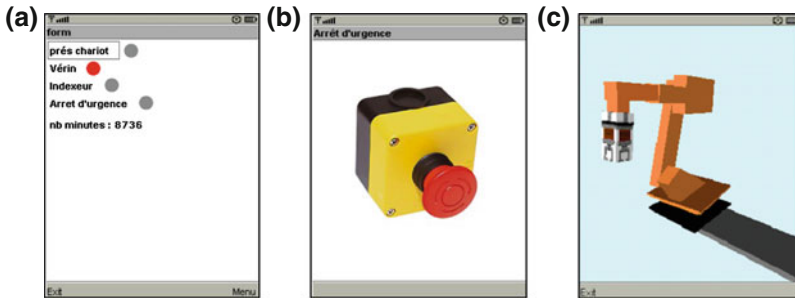


Fig. 12.4 a Acquired data on the phone. b Emergency interface on the phone. c Virtual interface of the robot

The server should be able to receive both types of information, from TCP/IP to connect the robot and from Bluetooth connection to connect the mobile. Wireless Tool Kit of Fig. 12.4a is used to program embedded application on mobile phone in Java [13].

When emergency stop is activated from any part of the production line, an alert is displayed on the phone in order to warn the operator on the mobile. This alert is a warning screen shown in Fig. 12.3, which activates in parallel the phone vibrations (Fig. 12.4b). The use of vibrator was preferred from a bell because it is more likely to alert the operator in a noisy environment rather than a tone that may go unnoticed.

Another demonstration of this concept concerns the robot control via a mobile phone. The server is used as a relay for the phone in order to control the robot to track trajectories, while the robot positions are sent to the server that communicates over the phone. The latter displays in 3D virtual scene the real scenery (Fig. 12.4c). The 3D visualization of the robot movements is interesting for several reasons. It can help to control the operation of the robot or see invisible tasks from distance.

The use of mobile phone allows developing quickly any type of application exchanging data with the robot. This concept is useful because even in the future, it is possible to create a portable and specific device, the phone could be a



Fig. 12.5 Cooperation of robots

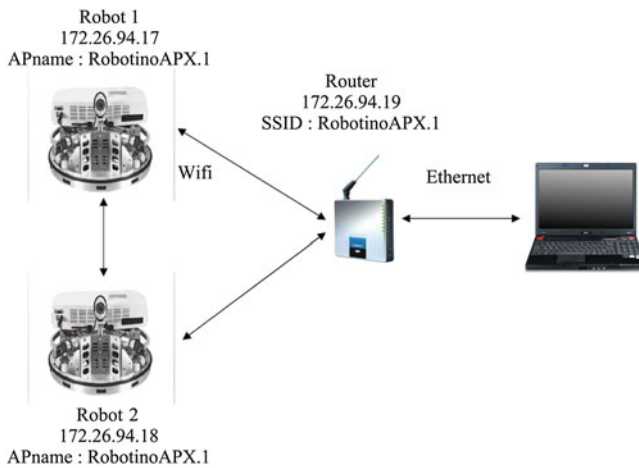


Fig. 12.6 Network configuration

significant basis for experimentation. The choice of Bluetooth is good for this application because the flow of information is not too complex and it has the advantage of being very widespread in mobile telephony.

12.2.2 Cooperation Between Omnidirectional Robots

The objective of this homogeneous cooperation is the common transport of a load by two omnidirectional mobile robots (Robotino[®]) [7] from one point to another (Fig. 12.5), while avoiding different obstacles that may occur in the trajectory.

For that, two robots are connected using a wireless network, using client-server configuration (Fig. 12.6). Each robot exchanges with the other the information of its

surrounding environment using a common dynamic memory. It allows the relative guidance of the robot during the routing and load transport. If an obstacle is detected by one of the involved robot, through their infrared sensors, a Boolean memory variable is modified to inform the other robot about the routing status and obstacle location. Thus, an avoidance scenario is taken to reach the final desired target in a safe way. When obstacles are detected in the both sides of the robots, in this case after exchanging the position of the obstacles by the robots, a structural reconfiguration of the routing is taken, allowing the avoidance of the obstacles while maintaining the transport of the common load.

12.2.3 Intelligent Human–Robot Interaction

The aim of this demonstration is to control the motion of KUKA robot manipulator [16], using a remote console for video games, the Wiimote [21]. The idea is to generate the robot movements online from the operator and avoid the use of pre-programmed trajectories (Fig. 12.7). This remote is equipped with several sensors that allow it to locate in space and recreate the movements applied to it. It communicates with the console through a wireless connection using Bluetooth technology. Wiimote is equipped with accelerometer ADXL330 [1]. It can measure the static acceleration of gravity (inclination measurement) and dynamic acceleration (shock, vibration). Another interesting aspect of this demonstration is the use of a KUKA robot with 6 degrees of freedom, placed on a 7th linear axis.

The problem can be decomposed into three parts:

1. Retrieve information from the Wii controller via a Bluetooth network;
2. Process information from the accelerometer to determine the trajectory and information on the pad buttons to use other actions such as opening or closing the gripper;
3. Send different commands to robot.

To retrieve information from the Wiimote, we manage directly the USB (Universal Serial Port) port [26] in Visual Basic to handle data frames. Regarding data processing, the robot being controlled in position, the implemented solution is an algorithm based on the numerical integration of the measured acceleration, but using adaptive calculation to obtain acceptable results. In terms of sending information to the robot, we can use the serial or Ethernet protocols.

12.3 Fault Diagnosis in Networked Control System

In applications related to networked control systems, we distinguish two aspects:

- Control, where the main issue is related to the delay in the system. A summary of these commands is developed in [22]. Thus, application of unilateral and bilateral teleoperation [11, 15] describes in part the control aspect of NCS.

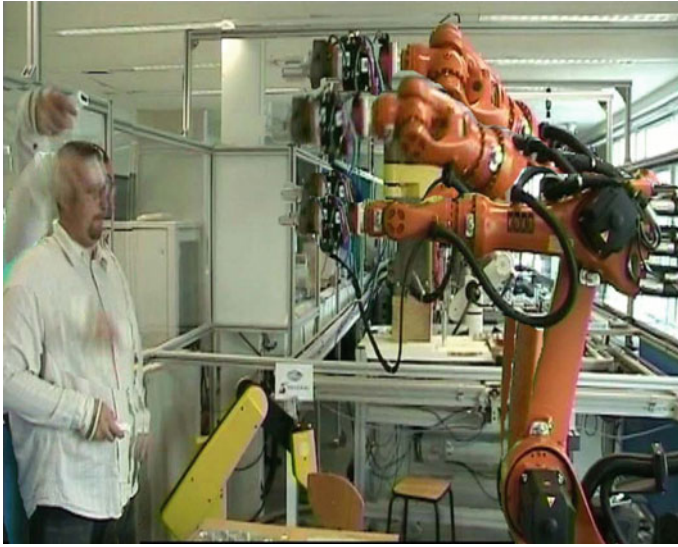


Fig. 12.7 Communication Wii-robot

- Fault diagnosis of NCS, that includes E-maintenance, which is by definition the maintenance of a functional unit from a control center via an industrial network [12]. The example of Tele-alarm is another way to monitor a distant mechatronic system, generating alarms in case of failure detection. Often, these practical solutions do not provide a real image to the supervisor on the origin and location of the fault. The point of having information about the fault allows the operator to switch to another mode when it is possible, to ensure the continuity of the operation. The model-based diagnosis remains an important alternative when the system parameters are well identified. For the case of deterministic model-based fault detection and isolation applied to NCS, discrete state observers are used to detect input faults [27]. Another FD approach of NCS is studied in [28] by using the parity relation approach with the Taylor approximation applied on the input matrix, while in [27, 29] fault diagnosis of NCS uses the parity relation method and Stationary Wavelet Transform (SWT). The two approaches are used to ensure a good performance and robustness toward the induced-delay, and the SWT technique provides both a frequency filter and a fast time response. In [23], the effect of unknown network-induced delays on conventional observer-based residual generator is studied. In order to enhance the robustness of FD, an adaptive evaluation procedure of the residuals is proposed. The threshold margin is estimated using an optimization approach which aims to find the control inputs on the specific time interval such that the performance index is maximized. In [8], NCS model with a random delay and based on the Takagi-Sugeno (T-S) technique is proposed, where the main feature of a the T-S fuzzy model is to express the local dynamics of each fuzzy rule by a simple linear system model. The authors considered an event-driven controller

and a clock-driven actuator. In [31], two fault detection and isolation algorithms for NCS are proposed; the first one is used for the parity space approach and the second is based on a T-S fuzzy observer. Another iterative diagnosis method of NCS based on the Kalman filtering is developed in [30] and in [6], to compensate the induced delay. From an experimental point of view, a Co-design of a NCS and its diagnosis is presented in [2]. The influence of the transmission delay and the packet losses on two different residual generation schemes have been studied for continuous and discrete systems. Comparison is realized through the simulation of a DC motor, where the control and the diagnosis algorithms are implemented under Matlab/Simulink and True Time software. Another Co-simulation approach that is carried out on a system of quadrotor over the network is proposed in [3].

12.4 Hybrid Model-Based Fault Diagnosis in NCS: Application to Telerobotics

In the following section, a fault diagnosis architecture is presented for telerobotics system (Fig. 12.8). It is a hybrid model-based approach, which allows distinguishing the network part from the dynamic system to be controlled. Discrete and stochastic model of the network part is presented, it represents a transmission channel linked to a continuous process. Thus, two fault diagnosis algorithms are used for each considered part, in order to differentiate between network and controlled system faults. The first concerns a stochastic observer-based model for state reconstruction and output estimation of the network system. The dynamic of its associated residual is characterized by a discrete time Markovian's jump. The second fault detection and isolation approach applied for the controlled system is obtained by using the analytical redundancy relations (ARR) technique. By this hybrid model-based diagnosis, it can be possible to separate the induced faults on the network part from the input and output faults of the main controlled system.

12.4.1 Network Part Modeling and Fault Diagnosis Observer

Proposition 12.1 *Let us assume that the network part is represented by a transmission channel, which is a Linear Time Invariant (LTI) system, given by the following discrete form (12.1)*

$$\begin{cases} x_c(k+1) = \bar{A}_c x_c(k) + \bar{B}_c u_c(k - \tau_k^{CA}) + \bar{B}_{f_c} f_c(k) + \bar{B}_{d_c} d_c(k) \\ w(k) = (1 - \gamma) y_c(k) + \gamma y_c(k - \tau_k^{SC}) \end{cases} \quad (12.1)$$

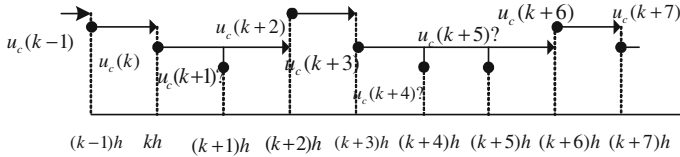


Fig. 12.9 Scheduling sequence of the delay

Markov chain with two states $\{0, 1\}$ [6], with stationary transition probability Π_k given by (12.2).

$$\Pi_k = \begin{pmatrix} p_{00}(k) & p_{01}(k) \\ p_{10}(k) & p_{11}(k) \end{pmatrix} \tag{12.2}$$

where $p_{ij} = P \{ \gamma(k) = j | \gamma(k - 1) = i \}$, $i, j \in \{0, 1\}$ is the conditional probability of jumping from the i th configuration at time $(k - 1)h$ to the j th configuration at time kh , therefore, the $p_{ij}(k)$ satisfies the following relation [30]:

$$\begin{cases} 0 \leq p_{ij}(k) \leq 1 \\ p_{0j}(k) + p_{1j}(k) = 1 \end{cases} \tag{12.3}$$

Proposition 12.2 *Let us consider that sensors and the actuators are clock driven, whereas the controller is event driven, and the data packets reach the controller and the actuators by their initial transmitting sequence if they are not lost [32].*

Proposition 12.3 τ_k^{CA} and τ_k^{SC} are, respectively, the induced delay variables, supposed bounded and identified according to the considered network system.

In NCS, the random variation of induced delay does not make the communication always perfect, due to the problems of packet losses and data congestions. Figure 12.9 gives the scheduling of the delay from the controller to actuator, where some sampling controls are lost ($u_c(k + 1), u_c(k + 4), \dots$) and delay grows up according to the data arrival.

According to the system (12.1) and by considering the identified delays of the network part on the system part to be controlled, the fault diagnosis observer is designed as follows:

$$\begin{cases} \hat{x}_c(k + 1) = \bar{A}_c \hat{x}_c(k) + \bar{B}_c u_c(k - \tau_k^{CA}) + \lambda(w(k) - v(k)) \\ v(k) = (1 - \gamma) \hat{y}_c(k) + \gamma \hat{y}_c(k - \tau_k^{SC}) \end{cases} \tag{12.4}$$

where $v(k)$ is the injection output of the observer (Fig. 12.8). λ is the observer gain vector, calculated using the LMI algorithm (Linear Matrix Inequality) [5] under free fault [6]. The presence of variables τ_k^{CA} and τ_k^{SC} in the observer formulation, implicates that these delay variables are considered known.

By putting the estimation error: $e_c(k) = x_c(k) - \hat{x}_c(k)$, then from (12.1) and (12.4), the state error at time $(k + 1)h$ is given in (12.5):

$$\begin{cases} e_c(k + 1) = x_c(k + 1) - \hat{x}_c(k + 1) \\ = [\bar{A}_c - (1 - \gamma)\lambda\bar{C}_c] e_c(k) - \gamma\lambda\bar{C}_c e_c(k - \tau_k^{SC}) \\ + \bar{B}_{d_c} d_c(k) + [\bar{B}_{f_c} - (1 - \gamma)\lambda\bar{D}_c] f_c(k) - \gamma\lambda\bar{D}_c f_c(k - \tau_k^{SC}) \end{cases} \quad (12.5)$$

A stochastic Lyapunov function (12.6) is considered to demonstrate the observer convergence:

$$V_k(\theta(k), \gamma(k)) = e_c^T(k) P(\gamma(k)) e_c(k) + \sum_{n=k-\tau_k^{SC}}^{k-1} e_c^T(n) Q e_c(n) \quad (12.6)$$

The theorem proved in [6] shows that the free-jump system (12.5) is stochastically stable if there exist $Q > 0$ and $P_i > 0$, $i \in \{0, 1\}$ satisfying the following sufficient condition of the coupled LMI modes:

$$M_s = \begin{pmatrix} \bar{A}_{c_i}^T \tilde{P}_i \bar{A}_{c_i} - \tilde{P}_i + Q & \bar{A}_{c_i}^T \tilde{P}_i \bar{B}_{c_i} \\ \bar{B}_{c_i} \tilde{P}_i \bar{A}_{c_i} & -Q + \bar{B}_{c_i}^T \tilde{P}_i \bar{B}_{c_i} \end{pmatrix} < 0 \quad (12.7)$$

where $\tilde{P}_i = \sum_{j=0}^1 p_{ij} P_j$, $i = \{0, 1\}$.

The residual $r_c(k)$ is synthesized from the difference of the injection output of the system (12.1) and the observer (12.2) as follows:

$$\begin{aligned} r_c(k) = w(k) - v(k) &= (1 - \gamma)\bar{C}_c e_c(k) + \gamma\bar{C}_c e_c(k - \tau_k^{SC}) \\ &+ (1 - \gamma)\bar{D}_c f_c(k) + \gamma\bar{D}_c f_c(k - \tau_k^{SC}) \end{aligned} \quad (12.8)$$

Equation (12.8) shows that the residual of the transmission channel is in function of the induced delay τ_k^{SC} and the output faults $f_c(k)$.

12.4.2 Control System Modeling and Fault Diagnosis

In this part, we consider a controlled system described by the following Eq. (12.9), describing the effects of the non-structured uncertainties or disturbances $d_s(t)$ and the faults $f_s(t)$ on the inputs and the outputs.

$$\begin{cases} \dot{x}_s(t) = A_s x_s(t) + B_s u_s(t) + B_{d_s} d_s(t) + B_{f_s} f_s(t) \\ y_s(t) = C_s x_s(t) + D_{f_s} f_s(t) \end{cases} \quad (12.9)$$

A_s , B_s , B_{d_s} , B_{f_s} , C_s and D_{f_s} are the known matrixes with appropriate dimensions of the system: state, input, uncertainties, faults and output. $x_s(t) \in \mathbb{R}^n$, $u_s(t) \in \mathbb{R}^m$, $y_s(t) \in \mathbb{R}^p$, $d_s(t) \in \mathbb{R}^{n_d}$, $f_s(t) \in \mathbb{R}^{n_f}$.

For monitoring the system of (12.9), a residual generator is synthesized. The latter is based on the parity space principal or more known as Analytical Redundancy Relations (ARR). This quantitative method allows to check the coherence between the mathematical relations of the controlled system and the measurements. The difference between the measured system' dynamic and the calculated system dynamic from the mathematical model is called residual [25]. The analytical redundancy relations are obtained generally by eliminating the unknown state vector $x_s(t)$. For that, it is possible to find a parity matrix W_s , orthogonal to C_s , so that: $W_s C_s = 0$.

From the output equation of the system (12.9), the vector of residual $r_s(t)$, also called Fault Indicator is obtained as follows:

$$r_s(t) = W_s y_s(t) \quad (12.10)$$

This redundancy is called static redundancy, where the generalization defines the dynamic redundancy, based on the dynamic model of the studied system and allows to detect actuator and sensor faults. To illustrate better this generalization, let us re-write the system (12.9) using its discrete form. A residual generator can be built, in order to detect and isolate sensor or actuator faults.

Let us start from the initial state $x_s(k)$, where the final desired state is $x_s(k+q)$, the following succession is obtained:

$$\left\{ \begin{array}{l} x_s(k+1) = \bar{A}_s x_s(k) + \bar{B}_s u_s(k) + \bar{B}_{d_s} d_s(k) + \bar{B}_{f_s} f_s(k) \\ x_s(k+2) = \bar{A}_s x_s(k+1) + \bar{B}_s u_s(k+1) + \bar{B}_{d_s} d_s(k+1) + \bar{B}_{f_s} f_s(k+1) \\ \quad = \bar{A}_s^2 x_s(k) + \bar{A}_s \bar{B}_s u_s(k) + \bar{B}_s u_s(k+1) + \bar{A}_s \bar{B}_{d_s} d_s(k) + \bar{B}_{d_s} d_s(k+1) \\ \quad \quad + \bar{A}_s \bar{B}_{f_s} f_s(k) + \bar{B}_{f_s} f_s(k+1) \\ \vdots \\ x_s(k+q) = \bar{A}_s^q x_s(k) + \sum_{i=1}^q \bar{A}_s^{q-i} \left[\begin{array}{l} \bar{B}_s u_s(k+i-1) + \bar{B}_{d_s} d_s(k+i-1) \\ + \bar{B}_{f_s} f_s(k+i-1) \end{array} \right] \end{array} \right. \quad (12.11)$$

with, $\bar{A}_s = e^{A_s h}$, $\bar{B}_s = \int_0^h e^{A_s s} B_s ds$, $\bar{B}_{d_s} = \int_0^h e^{A_s s} B_{d_s} ds$, $\bar{B}_{f_s} = \int_0^h e^{A_s s} B_{f_s} ds$, $\bar{C}_c = C_c$, $\bar{D}_{f_s} = \int_0^h e^{A_s s} D_{f_s} ds$ are, respectively, the states, inputs, non-structured uncertainties, outputs, and faults matrixes. When an interval of measurements is considered such as $[k, k+q]$, the outputs $y_s(k)$ are deduced as follows:

$$\begin{aligned}
\begin{bmatrix} y_s(k) \\ y_s(k+1) \\ y_s(k+2) \\ \vdots \\ y_s(k+q) \end{bmatrix} &= \begin{bmatrix} \bar{C}_c \\ \bar{C}_c \bar{A}_s \\ \bar{C}_c \bar{A}_s^2 \\ \vdots \\ \bar{C}_c \bar{A}_s^q \end{bmatrix} x_s(k) + \underbrace{\begin{bmatrix} 0 & 0 & \cdots & 0 & 0 \\ \bar{C}_c \bar{B}_s & 0 & \cdots & 0 & 0 \\ \bar{C}_c \bar{A}_s \bar{B}_s & \bar{C}_c \bar{B}_s & \cdots & 0 & 0 \\ \vdots & \vdots & \vdots & \vdots & \vdots \\ \bar{C}_c \bar{A}_s^{q-1} \bar{B}_s & \bar{C}_c \bar{A}_s^{q-2} \bar{B}_s & \cdots & \bar{C}_c \bar{B}_s & 0 \end{bmatrix}}_{B_s(q)} \begin{bmatrix} u_s(k) \\ u_s(k+1) \\ u_s(k+2) \\ \vdots \\ u_s(k+q) \end{bmatrix} \\
&+ \underbrace{\begin{bmatrix} 0 & 0 & \cdots & 0 & 0 \\ \bar{C}_c \bar{B}_{d_s} & 0 & \cdots & 0 & 0 \\ \bar{C}_c \bar{A}_s \bar{B}_{d_s} & \bar{C}_c \bar{B}_{d_s} & \cdots & 0 & 0 \\ \vdots & \vdots & \vdots & \vdots & \vdots \\ \bar{C}_c \bar{A}_s^{q-1} \bar{B}_{d_s} & \bar{C}_c \bar{A}_s^{q-2} \bar{B}_{d_s} & \cdots & \bar{C}_c \bar{B}_{d_s} & 0 \end{bmatrix}}_{B_{d_s}(q)} \begin{bmatrix} d_s(k) \\ d_s(k+1) \\ d_s(k+2) \\ \vdots \\ d_s(k+q) \end{bmatrix} \\
&+ \underbrace{\begin{bmatrix} 0 & 0 & \cdots & 0 & 0 \\ \bar{C}_c \bar{B}_{f_s} & 0 & \cdots & 0 & 0 \\ \bar{C}_c \bar{A}_s \bar{B}_{f_s} & \bar{C}_c \bar{B}_{f_s} & \cdots & 0 & 0 \\ \vdots & \vdots & \vdots & \vdots & \vdots \\ \bar{C}_c \bar{A}_s^{q-1} \bar{B}_{f_s} & \bar{C}_c \bar{A}_s^{q-2} \bar{B}_{f_s} & \cdots & \bar{C}_c \bar{B}_{f_s} & 0 \end{bmatrix}}_{B_{f_s}(q)} \begin{bmatrix} f_s(k) \\ f_s(k+1) \\ f_s(k+2) \\ \vdots \\ f_s(k+q) \end{bmatrix} \\
&+ \underbrace{\begin{bmatrix} \bar{D}_{f_s} & 0 & \cdots & 0 & 0 \\ 0 & \bar{D}_{f_s} & \cdots & 0 & 0 \\ 0 & 0 & \bar{D}_{f_s} & 0 & 0 \\ \vdots & \vdots & \vdots & \ddots & \vdots \\ 0 & 0 & \cdots & 0 & \bar{D}_{f_s} \end{bmatrix}}_{D_{f_s}(q)} \begin{bmatrix} f_s(k) \\ f_s(k+1) \\ f_s(k+2) \\ \vdots \\ f_s(k+q) \end{bmatrix}
\end{aligned} \tag{12.12}$$

Then,

$$\begin{aligned}
Y_s(k, q) &= C_s(q)x_s(k) + B_s(q)U_s(k, q) + B_{d_s}(q)d_s(k, q) \\
&+ (B_{f_s}(q) + D_{f_s}(q))f_s(k, q)
\end{aligned} \tag{12.13}$$

It corresponds to the formulation of static redundancy. After multiplying both sides of the equation by the parity matrix $W_s(q)$, orthogonal to $C_s(q)$, the generalized parity vector or residual vector $r_s(k, q)$ is obtained:

$$r_s(k, q) = W_s(q) [Y_s(k, q) - B_s(q)U_s(k, q)] \tag{12.14}$$

The parity vector is close to zero when all the faults and disturbances are neglected, otherwise it diverges from its normal. Then, the robustness of the FDI depends principally on the design of the fault threshold, in order to avoid the nondetection, delay in detection, and false alarm cases.

12.5 Application to Telerobotic System

Experimental results are done on a telerobotics system composed by a miniature robot of Fig. 12.8 connected to the control/command part via a serial cable channel. The main of this experiment is to show the implementation of the proposed hybrid model-based fault diagnosis approach presented in the previous section on a real system. The studied system is adequate to simulate different faults on the network part and on the robot in presence or absence of the generated transmission delays.

Concerning the closed-loop effect, the considered NCS has only the controlled part which can be configured in closed loop, while the network part is configured in open loop. In this case, the closed loop for controlled system does not affect the performance of the FDI algorithm, because the faults induced from the delay on the communication part are not compensated by the closed-loop regulation. When introducing delay on the network part, the robot is continuous in its motion but diverges from the planned trajectory, because the referred velocities have been affected by this network fault.

12.5.1 Robot System Description

The studied mobile robot Khepera II [14] is a double active wheeled and miniature robot (Fig. 12.10a).

Each wheel is moved by a DC motor coupled with the wheel through a 25:1 reduction gearbox. An incremental encoder, placed on the motor axis, gives 24 pulses per revolution of the motor. This allows a resolution of 600 pulses per revolution of the wheel that corresponds to 12 pulses per millimeter of path of the robot. The motor controller can be used in two control modes (Fig. 12.11): the velocity and the position modes. The active control mode is set according to the kind of command received. If the controller receives a velocity control command, it switches to the velocity mode. If the controller receives a position control command, the control mode is automatically switched to the position mode. Different PID control parameters (K_p , K_i and K_d) can be set for each of the two control modes. This robot is controlled via a serial transmission channel (Fig. 12.3), where the desired position and desired velocity values are introduced outside the robot system. The choice of miniature mobile robot is used to minimize the effect of uncertainty parameter and sensor noises.

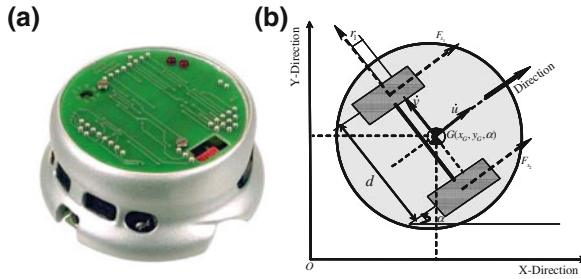


Fig. 12.10 a Khepera II robot. b Robot description schema

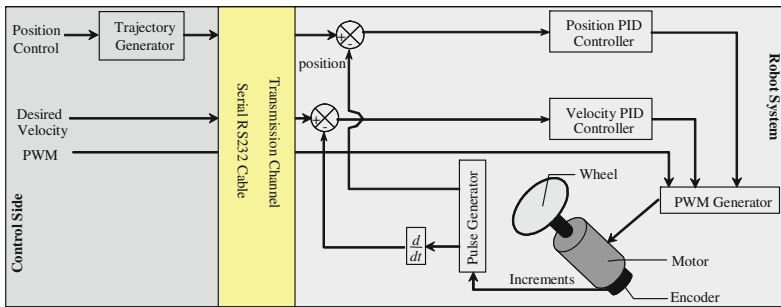


Fig. 12.11 Position and velocity controls schema

Some assumptions are taken in consideration for these parts according to the robot characteristics and its environment:

- The contact area between robot wheels and the motion surface is assimilated to a point contact, due to the rigidity of the wheel tire;
- The contact efforts, between the wheels and the ground, are considered constant. They are taken as known system inputs;
- For the miniature robot actuators, only the electrical and mechanical dynamics are considered;
- For dynamic robot modeling, only longitudinal and yaw dynamics are studied. The lateral dynamic is neglected due to the minor lateral efforts on the robot dynamic motion, issued from a so small width of the contact between the wheel and the ground.

12.5.2 Word Bond Graph

The word bond graph represents the technological level of the model, where the global system is decomposed into four principle subsystems (Fig. 12.12): the cable part, the j th electromechanical part with the j th wheel, the longitudinal and the yaw

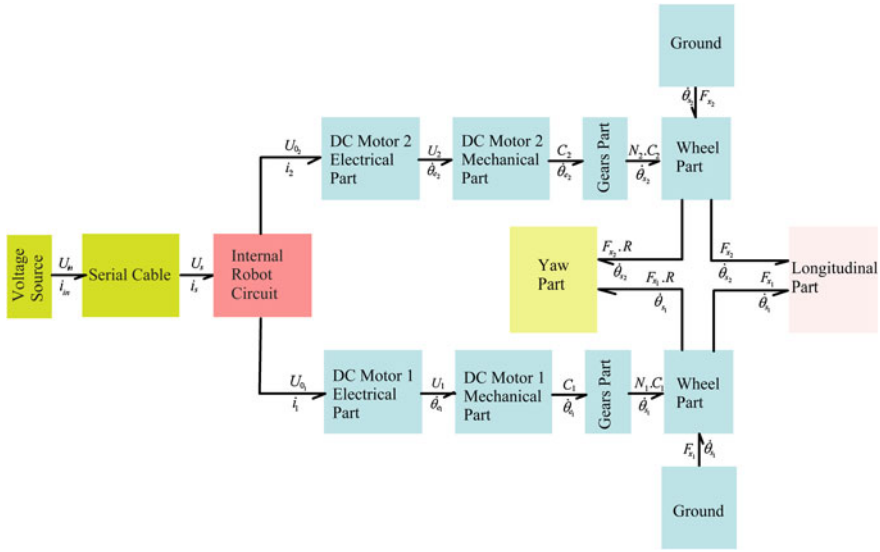


Fig. 12.12 Word bond graph of the miniature mobile robot

parts. Comparing to classical block diagram, the input and output of each subsystems defines a power variables represented by a conjugated pair of effort-flow represented by a half arrow. Power variables used for the studied system are:

$$\begin{aligned}
 (\text{Torque, Angular velocity}) &= \{(U_j, \dot{\theta}_{e_j}), (C_j, \dot{\theta}_{e_j}), (N_j C_j, \dot{\theta}_{s_j}), (R F_{x_j}, \dot{\theta}_{s_j})\}; \\
 (\text{Voltage, Current}) &= \{(U_{in}, i_{in}), (U_s, i_s), (U_{0_j}, i_j)\}.
 \end{aligned}$$

F_{x_j} is the j th traction contact efforts, R is the robot wheel radius, $\dot{\theta}_{s_j}$ is the j th wheel angular velocity, $(U_j, \dot{\theta}_{e_j})$ are the input command applied to the mechanical part and the DC drive velocity. $(C_j, \dot{\theta}_{e_j})$ are the transmitted torque to gears part and the input velocity for the j th electromechanical system. $(N_j C_j, \dot{\theta}_{s_j})$ is the transmitted torque to the j th wheel part and the output angular velocity. (U_{in}, i_{in}) are the input voltage and current of the serial cable, (U_s, i_s) are the output voltage and current of the serial cable, (U_{0_j}, i_j) is the input voltage and current of the j th electromechanical system.

These true and pseudo bond graph variables are associated, respectively, with electrical and mechanical rotation aspects.

The internal robot circuit part of Fig. 12.12 is not modeled in this development, due to the lack of information about this part.

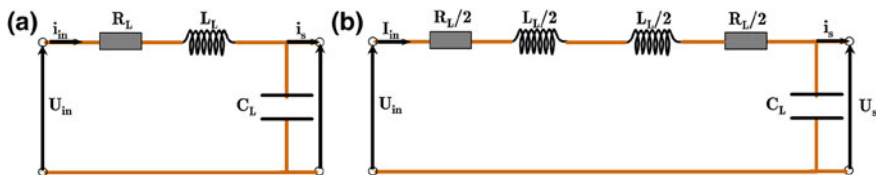


Fig. 12.13 a Standard RLC circuit. b Asymmetric RLC cell

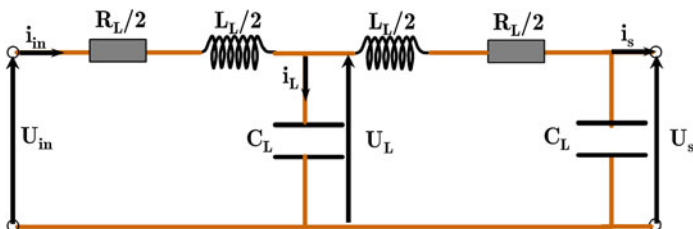


Fig. 12.14 Symmetric RLC cell

12.5.3 Modeling and Fault Diagnosis of Serial Cable

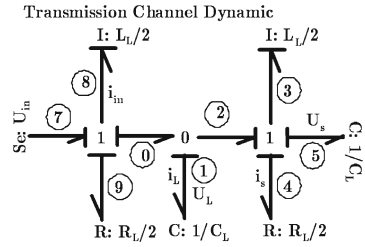
The network part is represented in this system by a transmission channel of a serial cable asynchronous with TTL levels (0–5 V). Several transmission channel models are proposed in the literature according to the applications requirements. Among them, in [24], an approach taking into account the resistive dissipation and based on a concatenation of basic RLC cells is presented. This approach is used for modeling our 2 m length serial cable [9, 10]. It consists on representing the channel as a succession of symmetrical RLC cells, in order to preserve the equality of all the electrical equations for the couple (voltage, current) of each point of the channel, during the transmission time. In Fig. 12.13a, a representation on what could be the RLC cell of the length $l = 2$ m from the channel, and Fig. 12.13b describes an asymmetric RLC cell, where the basic two elements R_L and L_L are divided in order to create other equivalent elements. Figure 12.14 shows the symmetric RLC cell of the channel with the length l .

The studied serial cable is modeled by only one cell on the whole length. The value of its elements can be identified experimentally.

- For the first junction 1, the effort, momentum, and algebraic value of element I of Fig. 12.15 are noted e_{28} , P_{28} , M_{28} , then the following state equation (12.15) is obtained:

$$e_{28} = -\frac{R_L}{2} \frac{P_{28}}{M_{28}} + e_{27} - e_{30} \tag{12.15}$$

Fig. 12.15 Bond graph model in integral causality of one RLC cell of the serial transmission cable



with

$$\begin{cases} f_{30} = f_{29} = f_{27} = f_{28} = \frac{P_{28}}{M_{28}} = i_{in} \\ e_{27} = U_{in} \\ e_{30} = e_{31} = \frac{1}{C_L} \int f_{31} dt = U_L \\ f_{31} = i_L \\ f_{28} = \frac{2}{L_L} \int e_{28} dt \end{cases}$$

Thus, the dynamic equation issued from this junction is the following:

$$\frac{L_L}{2} \frac{d}{dt}(i_{in}) = -\frac{R_L}{2} i_{in} + U_{in} - U_L \tag{12.16}$$

- For the junction 0, the state equation deduced from the bond graph element *C* is given by Eq. (12.17):

$$e_{31} = \frac{1}{C_L} \int f_{31} dt \tag{12.17}$$

with

$$f_{31} = f_{30} - f_{32} = i_{in} - i_s$$

Thus, the dynamic equation issued from this junction is the following:

$$C_L \frac{d}{dt}(U_L) = i_{in} - i_s \tag{12.18}$$

- For the second junction 1, the effort, momentum and algebraic value of element *I* of Fig. 12.15 are noted e_{33} , P_{33} , M_{33} , then the following state equation (12.19) is obtained:

$$e_{33} = -\frac{R_L}{2} \frac{P_{33}}{M_{33}} + e_{32} - e_{35} \tag{12.19}$$

with

$$\begin{cases} f_{32} = f_{33} = f_{34} = f_{35} = \frac{P_{33}}{M_{33}} = i_s \\ e_{35} = \frac{1}{C_L} \int f_{35} dt = U_s \\ e_{32} = e_{30} = \frac{1}{C_L} \int f_{31} dt = U_L \\ f_{33} = \frac{2}{L_L} \int e_{33} dt \end{cases}$$

Thus, the dynamic equation issued from this junction is the following:

$$\frac{L_L}{2} \frac{d}{dt}(i_s) = -\frac{R_L}{2} i_s + U_L - U_s \quad (12.20)$$

Comparing the obtained dynamic equations with those issued from the Kirchoff's law, the following system can be obtained:

$$\begin{cases} \frac{L_L}{2} \frac{d}{dt}(i_{in}) = -\frac{R_L}{2} i_{in} - U_L + U_{in} \\ C_L \frac{d}{dt}(U_L) = i_{in} - i_s \\ \frac{L_L}{2} \frac{d}{dt}(i_s) = U_L - \frac{R_L}{2} i_s - U_s \end{cases} \quad (12.21)$$

where R_L , L_L and C_L are, respectively, the resistance, inductance, and the capacity of the cable of length l and they are estimated experimentally according to the cable characteristics. U_{in} , U_s are, respectively, the known input and output cable voltages.

$$\bar{A}_c = \begin{pmatrix} \frac{-R_L}{L_L} & \frac{-2}{L_L} & 0 \\ \frac{1}{C_L} & 0 & \frac{-1}{C_L} \\ 0 & \frac{2}{L_L} & \frac{-R_L}{L_L} \end{pmatrix}, \quad \bar{B}_c = \begin{pmatrix} \frac{2}{L_L} \\ 0 \\ 0 \end{pmatrix}, \quad \bar{C}_c = (1 \ 0 \ 0),$$

$$\bar{B}_{fc} = \begin{pmatrix} 1 \\ 0 \\ 0 \end{pmatrix}, \quad \bar{B}_{dc} = \begin{pmatrix} 0 \\ 0 \\ 0 \end{pmatrix}, \quad x_c(k) = \begin{pmatrix} i_{in} \\ U_L \\ i_s \end{pmatrix}.$$

where $u_c(k) = U_{in}(k)$, $y_c(k) = i_s(k)$ and $\tau_k^{SC} = \tau_k^{CA} \simeq 2$. The elements of $\Delta \bar{A}_c$ are estimated as the tenth of their nominal values. l corresponds to the channel length, R_L , L_L , and C_L , are respectively, the resistance, inductance, and the capacity of the transmission cable and they are identified experimentally according to its material nature. U_{in} , i_s are, respectively, the measured input voltage and output current of the cable.

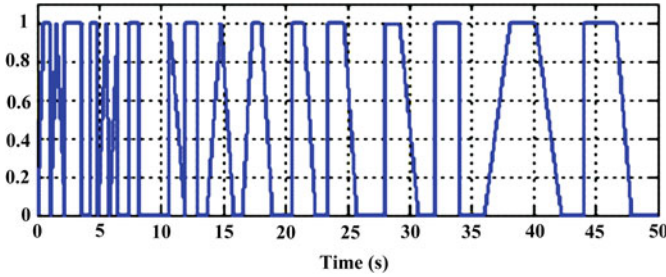


Fig. 12.16 Considered Markov process

Consider that the transition probability matrix is given by $\Pi_k = \begin{pmatrix} 0.6 & 0.3 \\ 0.2 & 0.7 \end{pmatrix}$, and the measurement signal is:

$$w(k) = (1 - \gamma(k))y(k) + \gamma(k)y(k - 2)$$

By using the FD observer of (12.4), we can get the state error and residual equation as follows (12.22):

$$\begin{cases} e_c(k + 1) = [\bar{A}_c - (1 - \gamma)\lambda\bar{C}_c]e_c(k) - \gamma\lambda\bar{C}_c e_c(k - 2) + \bar{B}_d d_c(k) \\ r_c(k) = (1 - \gamma)\bar{C}_c e_c(k) + \gamma\bar{C}_c e_c(k - 2) \end{cases} \quad (12.22)$$

The stochastic variable γ modeled with a Markov chain is taken with the following profile (Fig. 12.16).

12.5.4 Modeling and Fault Diagnosis of the Robot Part

12.5.4.1 Electromechanical System Modeling

There are two electromechanical systems located inside the robot and used for the traction motion. They are constituted by three principal components (Fig. 12.17): the DC motor part, which is the combination of an electrical and a mechanical parts, the gears system part, and the wheel system part. In this subsection, dynamic bond graph models of all of these components are graphically synthesized then expressed by differential equations.

Electrical Part of the DC Motor

This part corresponds to RL electrical circuit of the j th DC motor (Fig. 12.18) composed by: input voltage' source U_{0j} , electrical resistance R_{e_j} , inductance L_j and

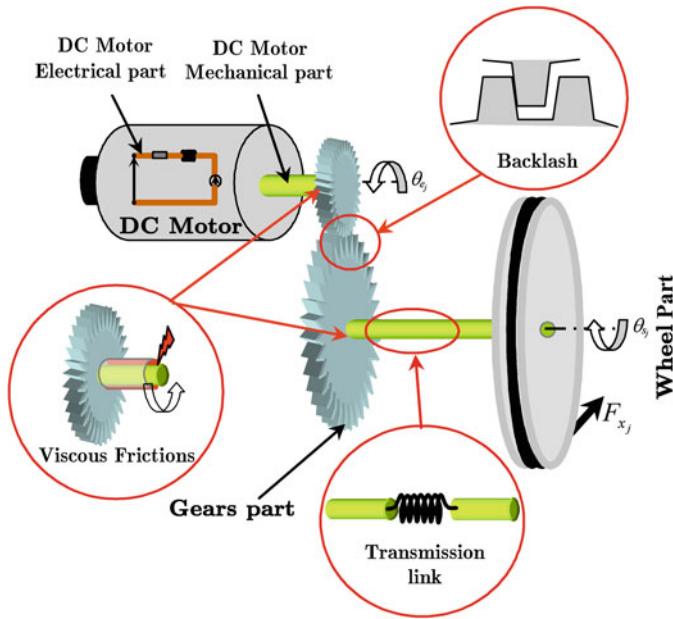
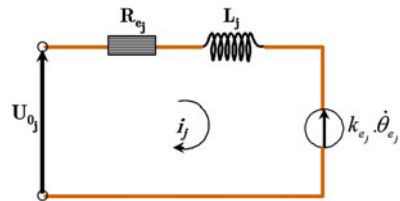


Fig. 12.17 j th electromechanical system of the mobile robot

Fig. 12.18 Electrical RL circuit of the j th DC motor



back electromotive force EMF, which is linear to the angular velocity of the rotor $\dot{\theta}_{e_j}$ and equal to $k_{e_j} \dot{\theta}_{e_j}$ with k_{e_j} the EMF constant. The index $j \in [1, 2]$ corresponds to the j th motor of the robot.

The corresponding RL circuit bond graph model is given in integral causality by Fig. 12.19.

Let us note e_{1_j} , P_{1_j} , M_{1_j} , effort, momentum, and algebraic value of element I of the j th motor (Fig. 12.19). The gyrator element GY describes the power transfer from the electric to mechanic by a flow variable f_{4_j} of the link 4 and Se_{0_j} is the input voltage source, then the following state equation is obtained:

$$e_{1_j} = Se_{0_j} - R_{e_j} \frac{P_{1_j}}{M_{1_j}} - k_{e_j} f_{4_j} \tag{12.23}$$

Fig. 12.19 Bond graph model of the electrical part of the j th DC motor

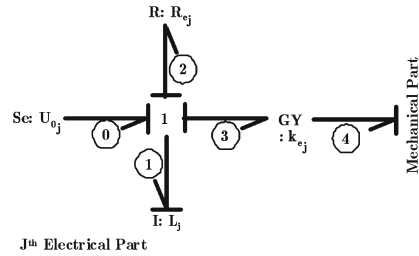
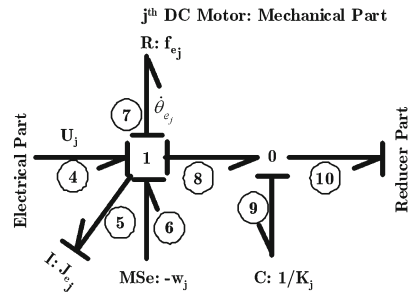


Fig. 12.20 Bond graph model of the mechanical part of the j th DC motor



with

$$\begin{cases} f_{0j} = f_{1j} = f_{2j} = f_{3j} = \frac{1}{L_j} \int e_{1j} dt = \frac{P_{1j}}{M_{1j}} = i_j \\ Se_{0j} = U_{0j} \\ f_{4j} = \dot{\theta}_{e_j} \end{cases}$$

Thus, the corresponding dynamic equation of circuit of Fig. 12.21 is:

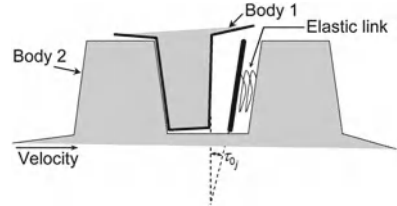
$$L_j \frac{di_j}{dt} = U_{0j} - R_{e_j} i_j - k_{e_j} \dot{\theta}_{e_j} \tag{12.24}$$

Mechanical Part of the DC Motor

This part represents the mechanical part of the j th DC motor, characterizing by its rotor inertia J_{e_j} , viscous friction parameter f_{e_j} , transmission axis rigidity K_j , and a motorized torque U_j . In this part, the influence of backlash phenomenon expressed by a disturbing torque w_j is represented by a modulated effort source for the bond graph model [18]. The corresponding bond graph model in integral causality is given by Fig. 12.20.

The traction system for this miniature mobile robot corresponds to two electro-mechanical actuators, composed by a DC electric motor and a wheel part through a gear transmission of constant 25:1. In the studied case, 1,000 encoder increments of each traction actuator corresponds to 8cm linear displacement, and the initial and maximal dead zone between input and output of the gear system is about 4

Fig. 12.21 Backlash mechanism for the j th DC motor



increments, corresponding to 0.32 cm. It is small and less influent perturbation, but it is important to consider this dead zone at the modeling step for robust diagnosis. Also, the motor axis rigidity differs generally from the load one, it is for that in the proposed model this transmission rigidity is considered.

The backlash mechanism considered in this model is represented by a disturbing torque, hampering the smooth functioning of the system, and caused by simultaneous and evaluative reactions of the shock between the two sides of the gears system (Fig. 12.21). This torque is chosen as it is continuous, nonlinear, and differentiable, compared to the size of the gears system and its effect on the global system.

So, a smooth and continuous model of transmitted torque w_j , which is developed in [18] and illustrated in Fig. 12.20, is taken as a modulated effort source ($MSe : w_j$) (Fig. 12.20). This torque is expressed as follows:

$$w_j = A_j K_j \tau_{0j} \frac{1 - e^{-\gamma_j \Delta\theta_j}}{1 + e^{-\gamma_j \Delta\theta_j}} \tag{12.25}$$

where w_j is the disturbing and nonlinear transmitted torque, $\Delta\theta_j = \theta_{e_j} - N_j \cdot \theta_{s_j}$ defines the difference between input θ_{e_j} and output θ_{s_j} motor positions, N_j a reducer constant, A_j is an integer defining the smooth decreasing of the dead zone region, K_j the rigidity constant of the transmission system, τ_{0j} is the dead zone amplitude and $\gamma_j = 1 / (2\tau_{0j})$ the sigmoid function slope of the j th DC motor.

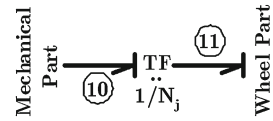
Let us note e_{5_j} , P_{5_j} , M_{5_j} effort, momentum, and algebraic value of element I of Fig. 12.20, f_{4_j} is the flow variable of link 4, $f_{9_j}, 1/K_j$ flow and algebraic value of element C , then the following state equation (12.26) is obtained:

$$e_{5_j} = -f_{e_j} \frac{P_{5_j}}{M_{5_j}} + e_{4_j} + e_{6_j} - K_j \int f_{9_j} dt \tag{12.26}$$

with

$$\begin{cases} f_{4_j} = f_{5_j} = f_{6_j} = f_{7_j} = f_{8_j} = \frac{1}{J_{e_j}} \int e_{5_j} dt = \frac{P_{5_j}}{M_{5_j}} = \dot{\theta}_{e_j} \\ e_{8_j} = e_{9_j} = K_j \int f_{9_j} dt \\ f_{9_j} = f_{8_j} - f_{10_j} = \dot{\theta}_{e_j} - N_j \dot{\theta}_{s_j} \\ e_{4_j} = k_{e_j} i_j \\ e_{6_j} = -w_j \end{cases}$$

Fig. 12.22 Bond graph model of j th gear part



j^{th} DC Gears Part

Thus, the corresponding dynamic equation of mechanical part is given as follows:

$$J_{e_j} \frac{d\dot{\theta}_{e_j}}{dt} = -f_{e_j} \dot{\theta}_{e_j} + k_{e_j} i_j - w_j - K_j (\theta_{e_j} - N_j \theta_{s_j}) \tag{12.27}$$

with U_j the input motor torque of the j th DC motor, given in function of the current i_j and the torque constant k_{e_j} , considered equal to the electrical constant.

Gears Part

This part concerns the mechanical gears which links between the mechanical and the load parts with a reduction constant N_j (Fig. 12.17). Bond graph model of this part is given by Fig. 12.22 and represents a transformer element TF between the j th velocities of the motor axis $\dot{\theta}_{e_j}$ and the wheel $\dot{\theta}_{s_j}$.

According to Fig. 12.22, let us choose f_{10_j} , f_{11_j} , e_{10_j} and e_{11_j} as the corresponding flows and efforts variables of links 10 and 11:

$$\begin{cases} f_{10_j} = N_j f_{11_j} \\ e_{11_j} = N_j e_{10_j} \end{cases} \tag{12.28}$$

which corresponds to the mechanical equation:

$$\begin{cases} f_{10_j} = \dot{\theta}_{e_j} = N_j \dot{\theta}_{s_j} \\ e_{11_j} = N_j C_j \end{cases} \tag{12.29}$$

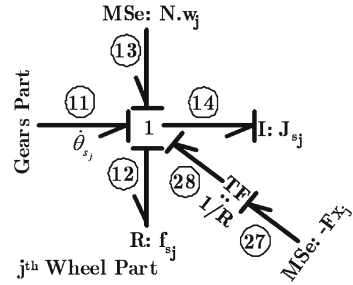
Wheel Part

This part represents the load part of the j th electromechanical system, characterizing by its inertia J_{s_j} , viscous friction parameter f_{s_j} , and backlash disturbing torque $N_j w_j$. The bond graph model of this part in integral causality is given by Fig. 12.26.

Let's note e_{14_j} , P_{14_j} , M_{14_j} effort, momentum and algebraic value of element I of Fig. 12.23. f_{9_j} is the flow and of element C (Fig. 12.20), then the following state equation (12.30) is obtained.

$$e_{14_j} = -f_{s_j} \frac{P_{14_j}}{M_{14_j}} + e_{13_j} + e_{11_j} + e_{28_j} \tag{12.30}$$

Fig. 12.23 j th wheel part bond graph model



with

$$\begin{cases} f_{11_j} = f_{12_j} = f_{13_j} = f_{14_j} = \frac{1}{J_{s_j}} \int e_{14_j} dt = \frac{P_{14_j}}{M_{14_j}} = \dot{\theta}_{s_j}; \\ e_{11_j} = N_j e_{9_j} = N_j K_j \int f_{9_j} dt; \\ f_{9_j} = f_{8_j} - f_{10_j} = \dot{\theta}_{e_j} - N_j \dot{\theta}_{s_j}; \\ e_{13_j} = N_j w_j; \\ e_{28_j} = R e_{27_j} = -R F_{x_j} \end{cases}$$

Thus, the corresponding dynamic equation of mechanical part is given as follows:

$$J_{s_j} \frac{d\dot{\theta}_{s_j}}{dt} = -f_{s_j} \dot{\theta}_{s_j} + N_j w_j + N_j K_j (\theta_{e_j} - N_j \theta_{s_j}) - R F_{x_j} \tag{12.31}$$

where F_{x_j} is the contact efforts which are the origin of the longitudinal and yaw dynamics and R the constant radius of the wheel.

After a concatenation of the different bond graph models, the global model of the j th electromechanical system is deduced in Fig. 12.24. The measured states are shown by detectors element $Df : \dot{\theta}_{e_j}$ and $Df : \dot{\theta}_{s_j}$.

Thus, the dynamic nonlinear model of the j th electromechanical system of the mobile robot with the environment interaction is given by the Eq. (12.32):

$$\begin{cases} L_j \frac{d}{dt} (i_j) = U_{0_j} - R_{e_j} i_j - k_{e_j} \dot{\theta}_{e_j} \\ J_{e_j} \frac{d}{dt} (\dot{\theta}_{e_j}) = -f_{e_j} \dot{\theta}_{e_j} + k_{e_j} i_j - w_j - K_j (\theta_{e_j} - N_j \theta_{s_j}) \\ J_{s_j} \frac{d}{dt} (\dot{\theta}_{s_j}) = -f_{s_j} \dot{\theta}_{s_j} + N_j w_j + N_j K_j (\theta_{e_j} - N_j \theta_{s_j}) - R F_{x_j} \end{cases} \tag{12.32}$$

12.5.4.2 Robot Chassis Modelling

In this subsection, kinematic, geometric, and dynamic models of the chassis of the miniature studied robot are deduced analytically and graphically.

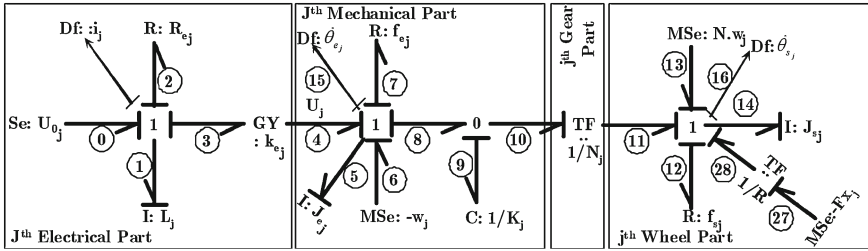


Fig. 12.24 *j*th global bond graph model of the electromechanical system

Kinematic Model

Figure 12.10b shows the robot centre of mass $G(x_G, y_G, \alpha)$, where (x_G, y_G) are the absolute coordinates and α the yaw angle. When the static radius of the robot wheel is R and the measured wheel velocities $\dot{\theta}_{s1}$ and $\dot{\theta}_{s2}$, then the deduced kinematic model of the robot is given as follows:

$$\begin{pmatrix} \dot{u} \\ \dot{v} \\ \dot{\alpha} \end{pmatrix} = \begin{pmatrix} R/2 & R/2 \\ Rr_1/d & -Rr_1/d \\ R/d & -R/d \end{pmatrix} \begin{pmatrix} \dot{\theta}_{s1} \\ \dot{\theta}_{s2} \end{pmatrix} \tag{12.33}$$

with \dot{u} the longitudinal velocity of the centre of mass, \dot{v} the lateral velocity of the centre of mass, $\dot{\alpha}$ the yaw velocity, d the normal distance between the wheels, and r_1 the distance between the wheel axis and the center of the mass.

Geometric Model

This model concerns the deduction of the (x_G, y_G) coordinates at the absolute reference (Fig. 12.10b). Thus, from Eq.(12.33) and after geometrical projection, this following system of equations is obtained.

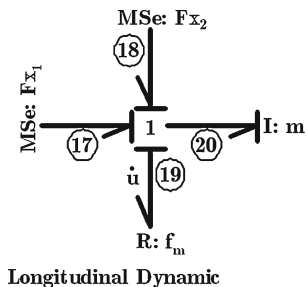
$$\begin{cases} x_G = \int (\dot{u} \cos \alpha - \dot{v} \sin \alpha) dt + x_{G0} \\ y_G = \int (\dot{u} \sin \alpha + \dot{v} \cos \alpha) dt + y_{G0} \end{cases} \tag{12.34}$$

where (x_{G0}, y_{G0}) are the initial positions of the robot.

Dynamic Model of the Robot

This model regroups the longitudinal and yaw dynamics, where the input sources considered in our case are Fx_1 and Fx_2 (Fig. 12.10b). These efforts are supposed known and equal to a necessary effort to tract the system, in our case they are

Fig. 12.25 Longitudinal dynamic of the robot



identified as a Coulomb friction. Then, only the viscous friction is considered as a reaction contact effort, due to the small dimension of the contact area. The following dynamics are synthesized from bond graph representation:

- *Longitudinal dynamic:* From Fig. 12.10b, the following bond graph model (Fig. 12.25) is synthesized:

Let us note e_{20} , P_{20} , M_{20} effort, momentum, and algebraic value of element I of Fig. 12.25, f_{19} is the flow variable of link 19, then the following state equation (12.35) is obtained:

$$e_{20} = -f_m \frac{P_{20}}{M_{20}} + Se_{17} + Se_{18} \tag{12.35}$$

with

$$\begin{cases} f_{17} = f_{18} = f_{19} = f_{20} = \dot{u} \\ Se_{17} = F_{x_1} \\ Se_{18} = F_{x_2} \end{cases}$$

Dynamic longitudinal equation is given in (12.36), where the longitudinal velocity \dot{u} is in function of the measured angular wheel velocities, according to the kinematic model (12.33):

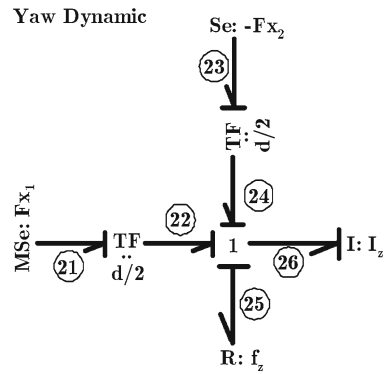
$$F_{x_1} + F_{x_2} - f_m \dot{u} = m \ddot{u} \tag{12.36}$$

- *Yaw dynamic:* From Fig. 12.10b, the following bond graph model (Fig. 12.26) is synthesized:

Let us note e_{26} , P_{26} , M_{26} effort, momentum, and algebraic value of element I of Fig. 12.26, then the following state equation (12.37) is obtained:

$$e_{26} = -f_z \frac{P_{26}}{M_{26}} + e_{22} + e_{24} \tag{12.37}$$

Fig. 12.26 Yaw dynamic bond graph model of the robot in integral causality



with

$$\begin{cases} f_{22} = f_{24} = f_{25} = f_{26} = \frac{P_{26}}{M_{26}} = \dot{\alpha} \\ e_{22} = \frac{d}{2} F_{x1} \\ e_{24} = \frac{d}{2} F_{x2} \end{cases}$$

Dynamic yaw equation is given in (12.38), where the yaw velocity $\dot{\alpha}$ is in function of the measured angular wheel velocities, according to the kinematic model (12.33):

$$(F_{x1} - F_{x2}) \frac{d}{2} - f_z \dot{\alpha} = I_z \ddot{\alpha} \tag{12.38}$$

where F_{x1} and F_{x2} are, respectively, the longitudinal efforts, f_m , f_z are the viscous friction parameters, according to longitudinal and yaw motions. d is the linear distance between the two wheels. As it is mentioned at the introduction of this section, because the longitudinal efforts are supposed known.

Then, according to (12.9), the following vectors are identified:

$$A_s = \begin{pmatrix} \frac{-f_m}{m} & 0 & 0 & 0 & 0 & 0 & 0 & 0 & 0 & 0 & 0 & 0 \\ 0 & \frac{-f_z}{I_z} & 0 & 0 & 0 & 0 & 0 & 0 & 0 & 0 & 0 & 0 \\ 0 & 0 & \frac{-f_{s1}}{J_{s1}} & 0 & 0 & 0 & \frac{-N_1^2 K_1}{J_{s1}} & \frac{N_1 K_1}{J_{s1}} & 0 & 0 & 0 & 0 \\ 0 & 0 & 0 & \frac{-f_{s2}}{J_{s2}} & 0 & 0 & 0 & 0 & \frac{-N_2^2 K_2}{J_{s2}} & \frac{N_2 K_2}{J_{s2}} & 0 & 0 \\ 0 & 0 & 0 & 0 & \frac{-f_{e1}}{J_{e1}} & 0 & \frac{N_1 K_1}{J_{s1}} & \frac{-K_1}{J_{e1}} & 0 & 0 & 0 & 0 \\ 0 & 0 & 0 & 0 & 0 & \frac{-f_{e2}}{J_{e2}} & 0 & 0 & \frac{N_2 K_1}{J_{s2}} & \frac{-K_2}{J_{e2}} & 0 & 0 \\ 0 & 0 & 1 & 0 & 0 & 0 & 0 & 0 & 0 & 0 & 0 & 0 \\ 0 & 0 & 0 & 1 & 0 & 0 & 0 & 0 & 0 & 0 & 0 & 0 \\ 0 & 0 & 0 & 0 & 1 & 0 & 0 & 0 & 0 & 0 & 0 & 0 \\ 0 & 0 & 0 & 0 & 0 & 1 & 0 & 0 & 0 & 0 & 0 & 0 \\ 0 & 0 & 0 & 0 & 0 & 0 & 1 & 0 & 0 & 0 & 0 & 0 \\ 0 & 0 & 0 & 0 & \frac{-k_{e1}}{L_1} & 0 & 0 & 0 & 0 & 0 & \frac{-R_{e1}}{L_1} & 0 \\ 0 & 0 & 0 & 0 & 0 & \frac{-k_{e2}}{L_2} & 0 & 0 & 0 & 0 & 0 & \frac{-R_{e2}}{L_2} \end{pmatrix} ;$$

$$x_s = \begin{pmatrix} \dot{u} \\ \dot{\alpha} \\ \dot{\theta}_{s_1} \\ \dot{\theta}_{s_2} \\ \dot{\theta}_{e_1} \\ \dot{\theta}_{e_2} \\ \theta_{s_1} \\ \theta_{e_1} \\ \theta_{s_2} \\ \theta_{e_2} \\ i_1 \\ i_2 \end{pmatrix}; \quad B_s = \begin{pmatrix} 0 & 0 & \frac{1}{m} & \frac{1}{m} & 0 & 0 \\ 0 & 0 & \frac{d}{2I_z} & \frac{d}{2I_z} & 0 & 0 \\ 0 & 0 & \frac{-R}{J_{s_1}} & 0 & \frac{N_1}{J_{s_1}} & 0 \\ 0 & 0 & 0 & \frac{-R}{J_{s_2}} & 0 & \frac{N_2}{J_{s_2}} \\ 0 & 0 & 0 & 0 & \frac{-1}{J_{s_1}} & 0 \\ 0 & 0 & 0 & 0 & 0 & \frac{-1}{J_{s_2}} \\ 0 & 0 & 0 & 0 & 0 & 0 \\ 0 & 0 & 0 & 0 & 0 & 0 \\ 0 & 0 & 0 & 0 & 0 & 0 \\ 0 & 0 & 0 & 0 & 0 & 0 \\ 0 & 0 & 0 & 0 & 0 & 0 \\ \frac{1}{L_1} & 0 & 0 & 0 & 0 & 0 \\ 0 & \frac{1}{L_2} & 0 & 0 & 0 & 0 \end{pmatrix}; \quad u_s = \begin{pmatrix} U_{01} \\ U_{02} \\ F_{x1} \\ F_{x2} \\ w_1 \\ w_1 \end{pmatrix}$$

$$y_s = \begin{pmatrix} \dot{\theta}_{s_1} \\ \dot{\theta}_{s_2} \\ \dot{\theta}_{e_1} \\ \dot{\theta}_{e_2} \\ i_1 \\ i_2 \end{pmatrix}; \quad C_s = \begin{pmatrix} 0 & 0 & 1 & 0 & 0 & 0 & 0 & 0 & 0 & 0 & 0 & 0 & 0 \\ 0 & 0 & 0 & 1 & 0 & 0 & 0 & 0 & 0 & 0 & 0 & 0 & 0 \\ 0 & 0 & 0 & 0 & 1 & 0 & 0 & 0 & 0 & 0 & 0 & 0 & 0 \\ 0 & 0 & 0 & 0 & 0 & 1 & 0 & 0 & 0 & 0 & 0 & 0 & 0 \\ 0 & 0 & 0 & 0 & 0 & 0 & 0 & 0 & 0 & 0 & 0 & 1 & 0 \\ 0 & 0 & 0 & 0 & 0 & 0 & 0 & 0 & 0 & 0 & 0 & 0 & 1 \end{pmatrix}$$

In Fig. 12.27, a description of overall bond graph model of the miniature mobile robot is presented, including actuators and transmission cable.

From the model of Fig. 12.28, the bond graph of the j th electromechanical system is given in derivative causality, while the detectors are dualized as a sources. The element $C:1/K_j$ is kept in integral causality, because the initial positions of the gear sides are known. Then, three analytical redundancy relations can be generated for each j th system, and the residuals are expressed in (12.39).

$$\begin{cases} r_{1j} = L_j \frac{d}{dt} (i_j) - U_{0j} + R_{e_j} i_j + k_{e_j} \dot{\theta}_{e_j} \\ r_{2j} = J_{e_j} \frac{d}{dt} (\dot{\theta}_{e_j}) + f_{e_j} \dot{\theta}_{e_j} - k_{e_j} i_j + w_j + K_j (\theta_{e_j} - N_j \theta_{s_j}) \\ r_{3j} = J_{s_j} \frac{d}{dt} (\dot{\theta}_{s_j}) + f_{s_j} \dot{\theta}_{s_j} - N_j w_j - N_j K_j (\theta_{e_j} - N_j \theta_{s_j}) + R F_{x_j} \end{cases} \quad (12.39)$$

The FDI algorithm is implemented on the supervisor system, distant from the network and the robot system sides as it is shown in Fig. 12.29.

The serial cable RS232 contains two principal commonly used signals:

- Transmitted Data (TxD), where Data are sent from Data Terminal Equipment (DTE) to Data Circuit-terminating Equipment (DCE).
- Received Data (RxD), where Data sent from DCE to DTE.

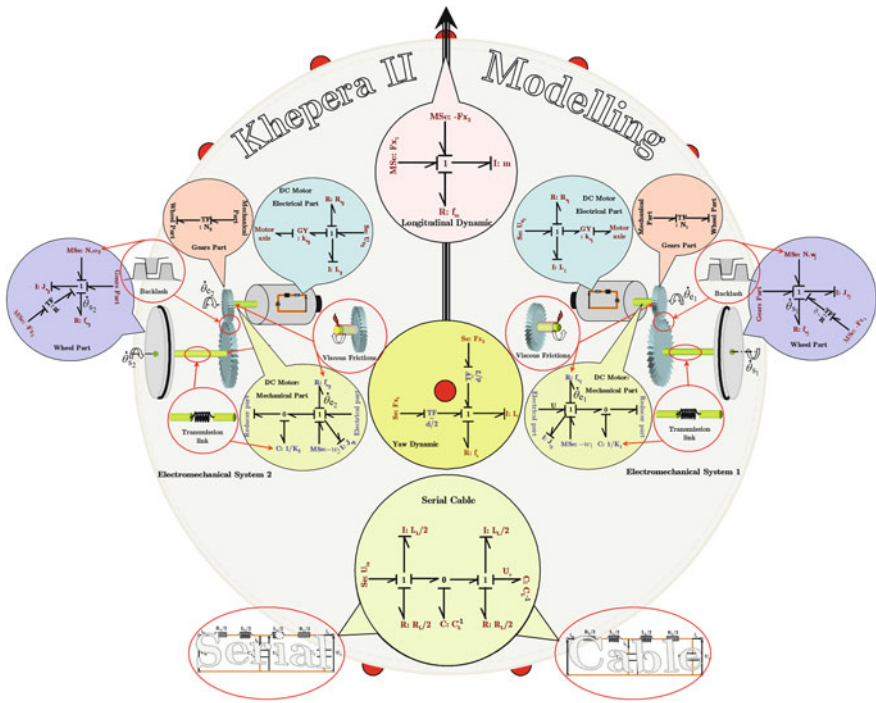


Fig. 12.27 Global bond graph model of the mobile robot system including the transmission serial cable

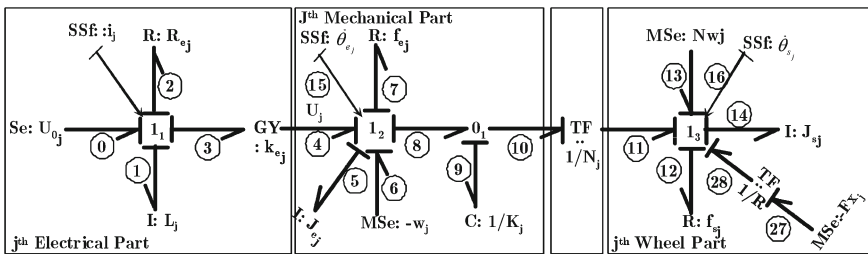


Fig. 12.28 Bond graph model of the *j*th electromechanical system in derivative causality

To generate the cable faulty situation, only the transmitted data (*TxD*) are affected. In this case, the robot continues working using the old velocities' reference. In the studied case, the measured states are the two angular velocities of the traction actuators and the voltage at the end side of the transmission cable.

The identified robot and cable parameters are given in Table 12.1.

Four cases of experiments are presented, they concern the fault free situation, the robot actuators faults, fault on the transmission cable and the generated delay fault. Residuals, control inputs, estimation error, and trajectory of the robot are displayed

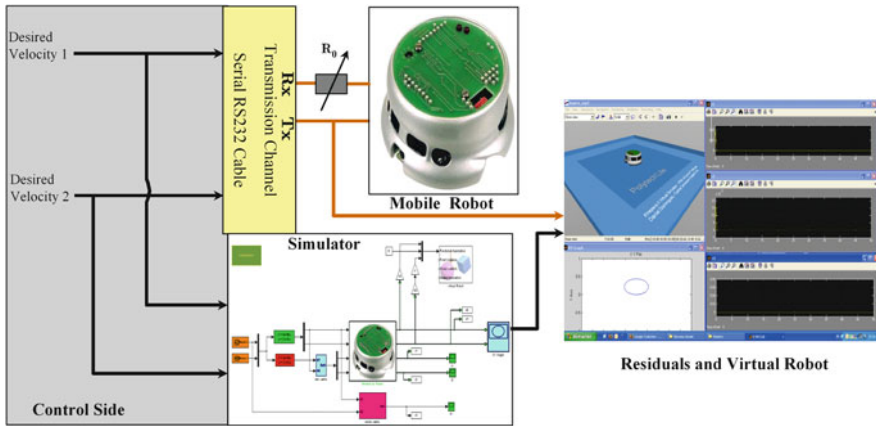


Fig. 12.29 FDI algorithm implementation

Table 12.1 System parameters

Parameters	Values
J_{s1}, J_{s2}	$1 \times 10^{-4} \text{ kg m}^2$
J_{e1}, J_{e2}	$3 \times 10^{-4} \text{ kg m}^2$
f_{s1}, f_{s2}	$3 \times 10^{-4} \text{ Nm s/rad}$
f_{e1}, f_{e2}	$2.5 \times 10^{-3} \text{ Nm s/rad}$
d	$4 \times 10^{-2} \text{ m}$
R_{e1}, R_{e2}	3.2Ω
m	0.25 kg
k_{e1}, k_{e2}	0.24×10^{-2}
C_L	$110 \times 10^{-12} \text{ F}$
f_m	$1 \times 10^{-4} \text{ Nm s/rad}$
f_z	$5 \times 10^{-4} \text{ Nm s/rad}$
I_z	$5.8 \times 10^{-3} \text{ kg m}^2$
r_1	$1 \times 10^{-2} \text{ m}$
R	$5 \times 10^{-3} \text{ m}$
L_1, L_2	$250 \times 10^{-9} \text{ H}$
K_1, K_2	950 Nm/rad
N_1, N_2	25 Nm/A
R_L	$1,000 \Omega$

for each case. In order to avoid the false alarm case, residual threshold are considered for the evaluation step. These thresholds represent the sum of the absolute element values of the uncertainty state matrix $\Delta \hat{A}_c$.

- *Case 1: Fault free operation*

After generating the different residuals, a planned trajectory (Fig. 12.30) is considered. In this case, the time evolution of the system input-output is in normal situation. In Fig. 12.31 a superposed signals of desired and output velocities for each wheels

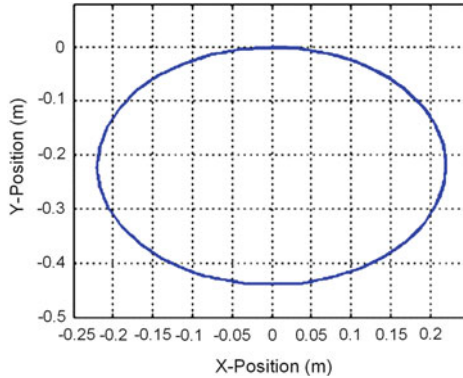


Fig. 12.30 Trajectory of the robot

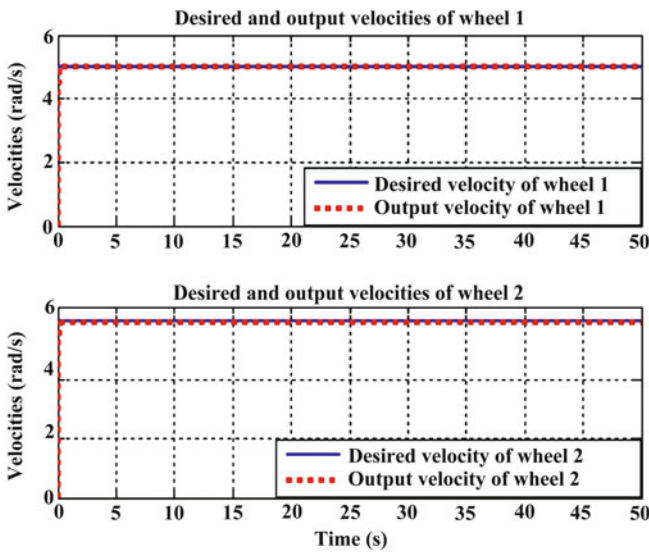


Fig. 12.31 Desired and output velocities of both wheels 1 and 2

are presented. The regulation is made by the robot PID velocity controllers (with $K_P = 3790$, $K_I = 803$, $K_D = 104$ for motor unit increment, where 1unit=8mm/s). Controls and residuals signals are given, respectively, in Figs. 12.32 and 12.33. The convergence of the residuals to zero indicates that the global system is in normal operation.

• Case 2: Actuator fault

After simulating an actuator fault by adding a faulty profile signal to the existing control signal of actuator 1 of Fig. 12.34, then the residuals of Fig. 12.35 and the robot trajectories of Fig. 12.36 show the influence of the introduced fault on the system

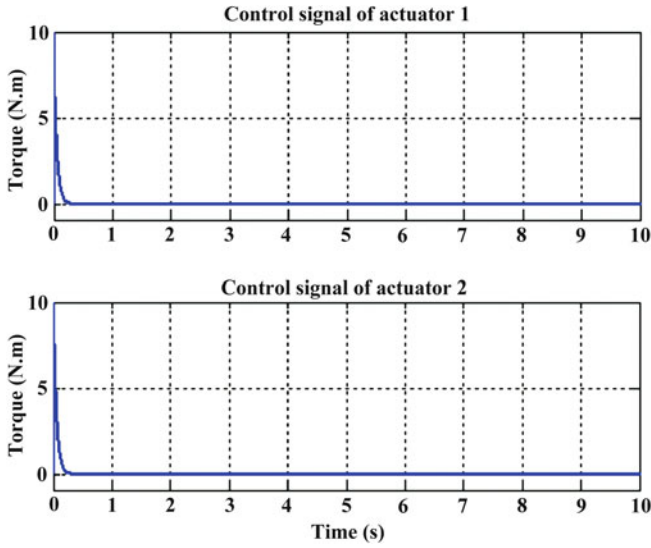


Fig. 12.32 Controls signal of actuators 1 and 2

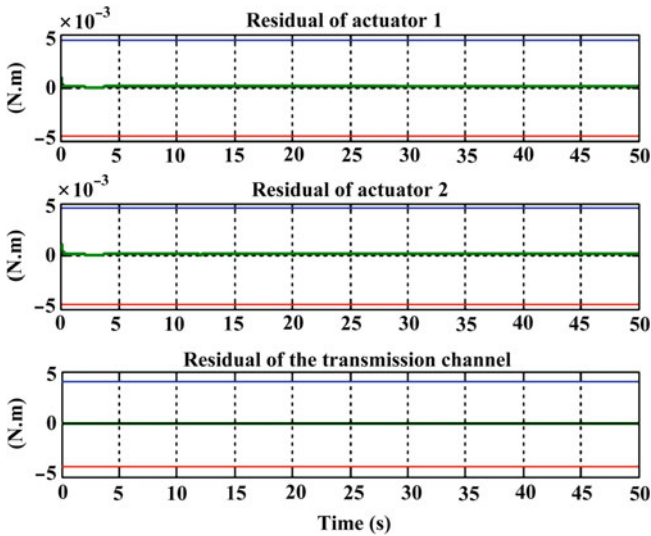


Fig. 12.33 Residuals signal of actuators 1, 2 and transmission cable

performance. In this case this disturbing fault does not effect the transmission cable operation as it is shown by the results.

- *Case 3: Transmission cable fault*

In this case, the resistance R_L is varied manually by putting a resistive potentiometer in serial configuration. This maneuvering allows to simulate a cut in the

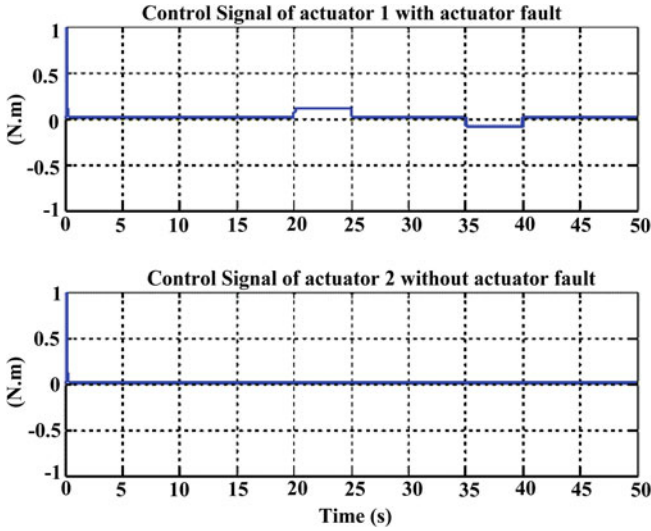


Fig. 12.34 Control signals in presence of fault on actuator 1

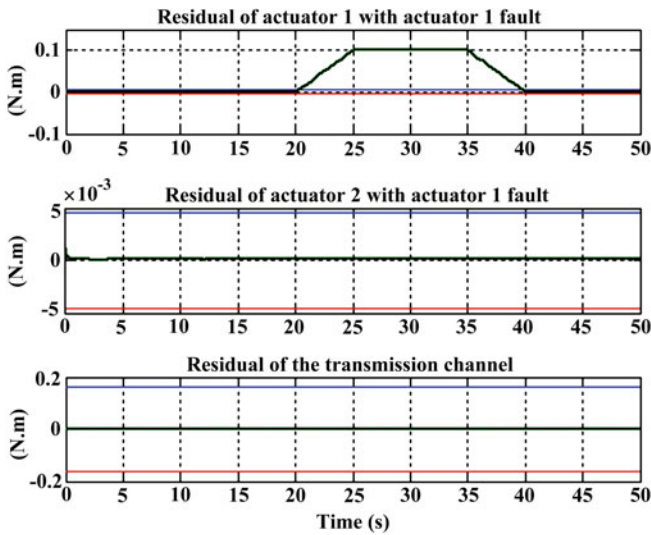


Fig. 12.35 Residuals signal for actuator 1 in presence of fault

transmission channel, we can notice that control signals of Fig. 12.37 are almost insensitive to this fault because the robot residuals are in function of the input control signals coming from the transmission cable. Residual of the cable (Fig. 12.38) is sensible to this cable fault including the estimation error (Fig. 12.32), which has

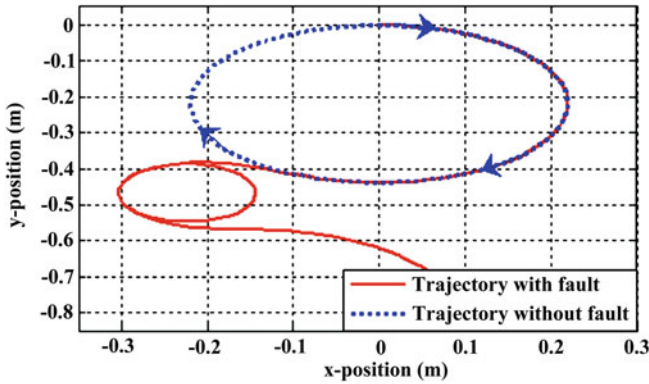


Fig. 12.36 Trajectory in presence of the fault in actuator 1

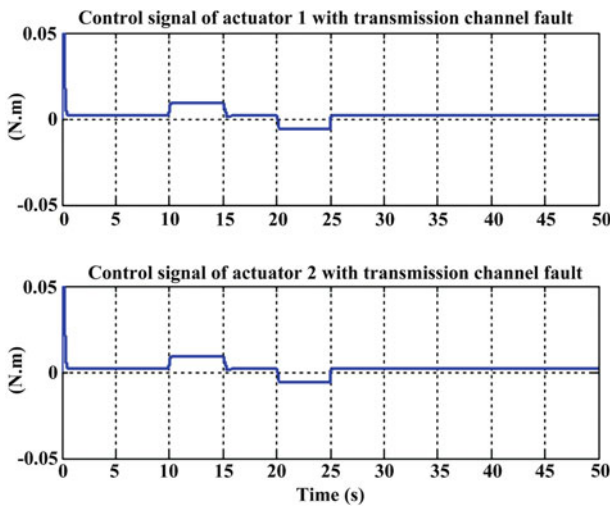


Fig. 12.37 Control signals in presence of cable fault

deviated from zero when the fault has occurred (Fig. 12.39). The deviation on the robot trajectory (Fig. 12.40) shows that the robot continues its trajectory by considering the last data references before the cable fault. Thus, it does not follow the desired trajectory.

- *Case 4: Delay fault*

The generated delay for one input (actuator 1) is taken into account by using the Markov process with the stochastic variable γ (Fig. 12.16). Desired robot trajectory is considered as an hexagon path. Then, the time evolution of the control signal is

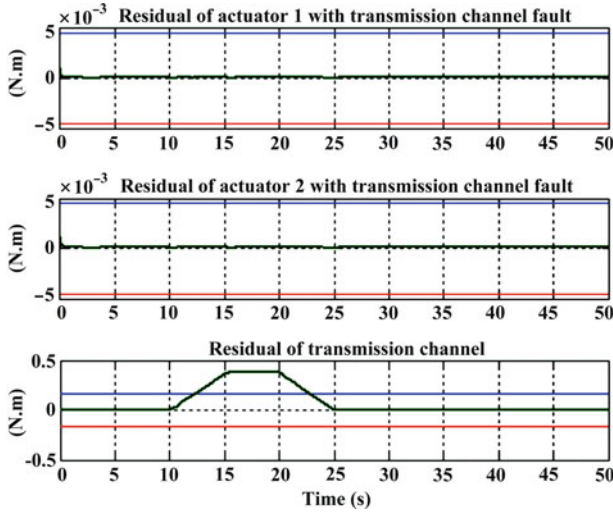


Fig. 12.38 Residuals signal in presence of cable fault

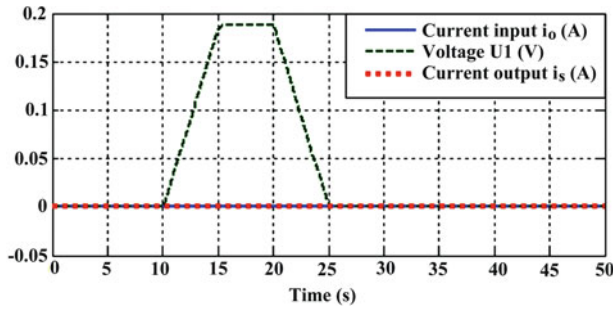


Fig. 12.39 Estimation error in presence of cable fault

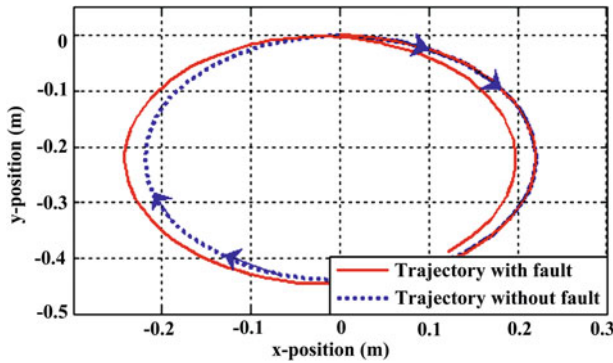


Fig. 12.40 Robot trajectory in presence of cable fault

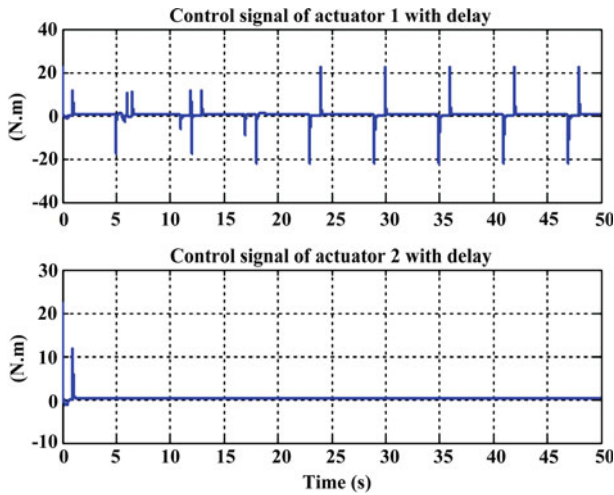


Fig. 12.41 Control signals in presence of delay

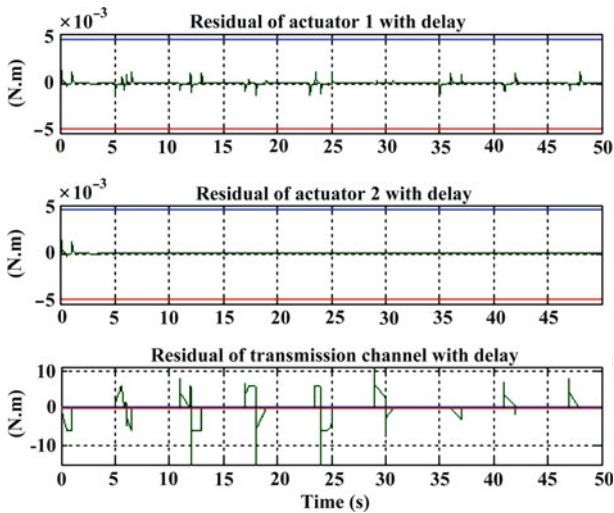


Fig. 12.42 Residuals in presence of delay on control signal of actuator 1

given by Fig. 12.41, where the residual of the cable (Fig. 12.42) is the most sensitive to this generated delay. The estimation error of Fig. 12.43 shows the FD observer convergence and we can notice that the robot diverged completely from its trajectory (Fig. 12.44).

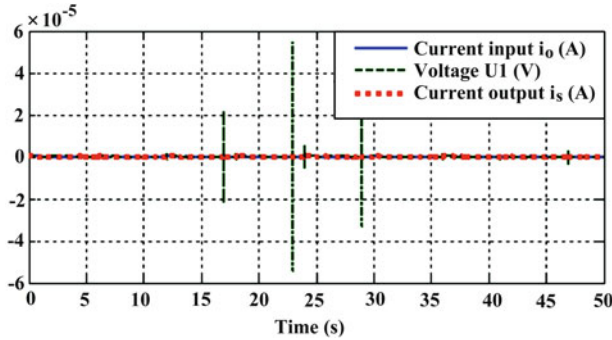


Fig. 12.43 Estimation of error in presence of delay in control signal of actuator 1

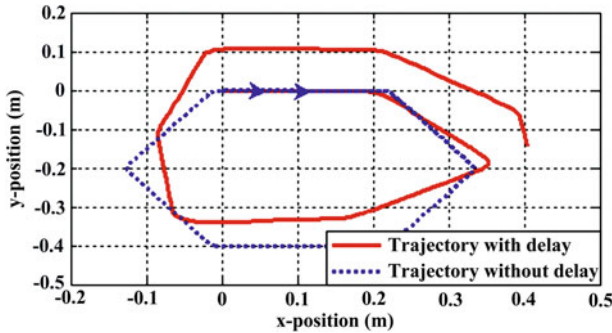


Fig. 12.44 Robot trajectory in presence of delay in control signal of actuator 1

12.6 Conclusion

This chapter describes an approach of hybrid model-based fault diagnosis for a class of NCS, applied on telerobotics system. Today, mechatronic systems are designed with NCS principle in different fields. Of course, the technology evolution during this last decade has allowed the design of safe and reliable mechatronic systems. When these latter are controlled through a network, it is necessary to extend the safety and reliability aspects to the network side. The network part is considered as a full physical system, making the link between the operator and the mechatronic system to be controlled. The network behavior can change according to its nature and associated model. It can be deterministic, uncertain, stochastic, or only a black box. From fault diagnosis point of view, it is an efficient approach to decouple the network part from the system to be controlled, according the operation mode. This can help in differentiating the faults when they appear, i.e., whether the fault originates from the network or other parts of the system.

References

1. Accelerometer ADXL330 (2010), www.analog.com
2. C. Berbra, S. Gentil, S. Leseq, J.-M. Thiriet, Co-design for a safe network controlled DC motor, in *3rd IFAC Workshop on Networked Control Systems Tolerant to Faults*, Nancy, France, 2007
3. C. Berbra, S. Leseq, S. Gentil, J.-M. Thiriet, Co-design of a safe network control quadrotor, in *Proceedings of the 17th IFAC World Congress*, Seoul, Korea, 2008
4. Bluetooth, The official website for the Bluetooth short range wireless connectivity standard (2010), www.bluetooth.com
5. S. Boyd, L. El Ghaoui, E. Feron, V. Balakrishnan, Linear matrix inequalities in system and control theory, in *Society for Industrial and Applied Mathematics (SIAM)*, 1994, ISBN 0-89871-334-X
6. Y. Chen, B. Xiao, Z. Xu, Fault detection filter design for networked control system with communication delays, in *Proceedings of the 6th International Conference on Intelligent Systems Design and Applications (ISDA'06)*, 2006, pp. 867–872
7. Festo Didactic, The official website of Festo Didactic (2010), www.festo-didactic.com
8. H. Fang, H. Zhang, Y. Fang, F. Yang, Quasi T-S fuzzy models and stable controllers for networked control systems, in *Proceedings of the 6th World Congress on Intelligent Control and Automation*, 2006, pp. 220–223
9. K. Fawaz, R. Merzouki, and B. Ould-Bouamama. Fault detection of actuators and channel transmission using virtual simulation, in *17th World Congress of the International Federation of Automatic Control*, Seoul, Korea, 6–11 July 2008, p. 13118
10. K. Fawaz, R. Merzouki, B. Ould-Bouamama, Telediagnosis of transmission channel and actuators faults on a mobile robot, in *17th World Congress The International Federation of Automatic Control*, Seoul, Korea, 6–11 July 2008, pp. 10510–10516
11. P.F. Hokayem, M.W. Spong, Bilateral teleoperation: an historical survey. *Automatica* **42**, 2035–2057 (2006)
12. B. Iung, From remote maintenance to MAS-based e-maintenance of industrial process. *J. Intell. Manuf.* **14**, 59–82 (2004)
13. Java, The website of Java Language Developer (2010), <http://java.sun.com>.
14. K-team (2010), www.k-team.com
15. A. Kheddar, P. Coiffet, *Téléopération et réalité virtuelle*. Systèmes automatisés IC2 (Hermes Edition, Paris, 2002), ISBN: 978-2-7462-0448-5
16. Kuka, The official website of Kuka robotics company (2010), www.kuka-robotics.com
17. R. Luck, A. Ray, An observer-based compensator for distributed delays. *Automatica* **26**, 903–908 (1990)
18. R. Merzouki, J.A. Davila Montoya, L.M. Fridman, J.C. Cadiou, Backlash phenomenon observation and identification in electromechanical system. *Control Eng. Pract.* **15**, 447–457 (2007)
19. Microsoft, The official website of Windows Embedded (2010), www.microsoft.com/windowsembedded
20. Microsoft, The official website of Visual Basic (2010), www.msdn.microsoft.com
21. Nintendo, The official website of the Wiimote (2010), www.nintendo.fr
22. J.P. Richard, Time-delay systems: an overview of some recent advances and open problems. *Automatica* **39**, 1667–1694 (2003)
23. D. Sauter, T. Boukhobza, Robustness against unknown networked induced delays of observer based FDI, in *Proceeding of 6th IFAC Symposium on Fault Detection, Supervision and Safety of Technical Processes*, 2006
24. L. Teppoz *Commande d'un système de conversion de type VSC-HVDC. Stabilité-contrôle des perturbations*. Ph.D. Thesis, INPG, Grenoble, France, 2005
25. R. Toscano. *Commande et diagnostic des systèmes dynamiques*. (Ellipses, Paris, 2005)
26. USB, The official website for the Universal Serial Port (2010), www.usb.org
27. H. Ye, S.X. Ding, Fault detection of networked control systems with network-induced delay, in *Proceedings of 8th International Conference on Control, Automation, Robotics and Vision*, 2004

28. H. Ye, G. Wang, S.X. Ding, A new parity space approach for fault detection based on stationary wavelet transform. *IEEE Trans. Autom. Control* **49**, 281–287 (2004)
29. H. Ye, Y. Wang, Application of parity relation and stationary wavelet transform to fault detection of networked control systems, in *Proceedings of 1st IEEE Conference on Industrial Electronics and Applications*, 2006
30. P. Zhang, S.X. Ding, P.M. Frank, M. Sader, Fault detection of networked control systems with missing measurements, in *Proceedings of the 5th IEEE Asian Control Conference*, 2004, pp. 1258–1263
31. Y. Zheng, H. Fang, H.O. Wang, Takagi-Sugeno fuzzy-model-based fault detection for networked control systems with Markov delays. *IEEE Trans. Syst. Man Cybern. Part B Cybern.* **36**, 924–929 (2006)
32. Y. Zheng, H. Fang, Y. Wang, Kalman filter based FDI of networked control system, in *Proceedings of the 5th World Congress on Intelligent Control and Automation*, Hangzhou, China, 2004, pp. 1330–1333

Chapter 13

Road Vehicle Driving Simulator

The vehicle simulator system integrates vehicle dynamics, sound/visual systems, instructor station, and traffic. A full-fledged human-in-the-loop (HILS) simulator is a complex system developed on a 6-DOF motion-based platform and realistic graphics with additional controls and sensory feedbacks, e.g., realistic feeling of brakes, transmission, steering feedback, gear reduction, etc. Moreover, a Vehicle Stability Control (VSC) system which connects the human driver, controller, and vehicle behavior, is required in emergency situations [6]. The basic human-in-the-loop driving simulator considered in this chapter consists of a three-dimensional vehicle dynamics model, driver interface, Stewart platform, and visual display.¹

13.1 Human–Machine Interface

The vehicle–driver interface of driving simulator, as shown in Fig. 13.1, consists of different subsystems: inversion controller, real-time controller, 3D animator, instructor station (Stewart platform), servosystem with solenoid valve, power supply, AD/DA converter, sensors (pressure transducer and potentiometer), low-pass filter, PI-controller, etc. During real-time simulations, the real-time controller calculates the variables (vehicle behaviour) of the vehicle’s dynamic model with sensed driver-reaction (driver input). Then it provides vehicle’s position (x, y and z-motion), roll, pitch, and yaw angle to the 3D animator which provides visual information to the screen in front of the driver sitting on the Stewart platform. The vehicle’s position (x, y and z-motion), roll, pitch, and yaw angle are also provided to the inverse controller from the real-time controller. The signals from the inversion controller are fed to the solenoid valve of the servo-system after converting to analog signal by the DA converter. In this way, the servo-system along with the solenoid valve controls the motion of the legs of the Stewart platform. The positions and the pressures of the actuators are retrieved by the potentiometers and the pressure transducers,

¹ A part of this chapter is adapted from these authors’ previous works published in [2, 5].

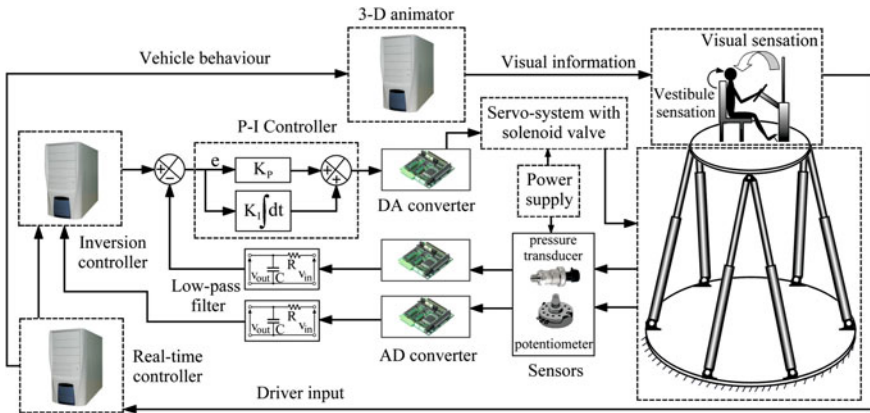


Fig. 13.1 Different subsystems of the driving simulator

respectively. These signals are converted to the digital signals by the DA converter and are filtered with low-pass filters before being fed back to the inversion controller and the P-I controller. This completes the closed-loop control system.

The Stewart platform gives vestibule sensation to the driver. Thus, the platform must reproduce the motions computed from the vehicle model. This must be done in real time so that the driver does not feel the delay in his/her action and the response. Model-based control of a Stewart platform requires a computationally efficient and reasonably accurate inverse model of the system for real-time implementation. Moreover, the design of the platform, its actuators, and the control system requires a detailed model of the system with accurate representation of the dynamic loads so that actuators can be sized appropriately, and the response time of the system and controllers can be optimized. Thus, the system model must account for the leg inertias, electro-hydraulics in the actuator, dynamics of the servo-valve, etc. At the same time, the controller must perform the assigned task (trajectory tracking, and force or impedance control) even when system parameters such as the driver weight are uncertain and measurements are noisy.

13.2 Overwhelming Controller as a System Inversion Tool

Overwhelming control refers to controllers which overwhelm the plant dynamics and force the plant to follow the dynamics as dictated by the controller. An analogy from real life is an adult (controller) taking a baby (plant) for a walk while holding one hand of the baby. Although the plant dynamics may cause small deviations from the desired path, the overall trajectory tracking performance remains satisfactory. This concept has been used in the past to develop controllers for serial robots [8, 11–14] and other applications [9, 18, 19].

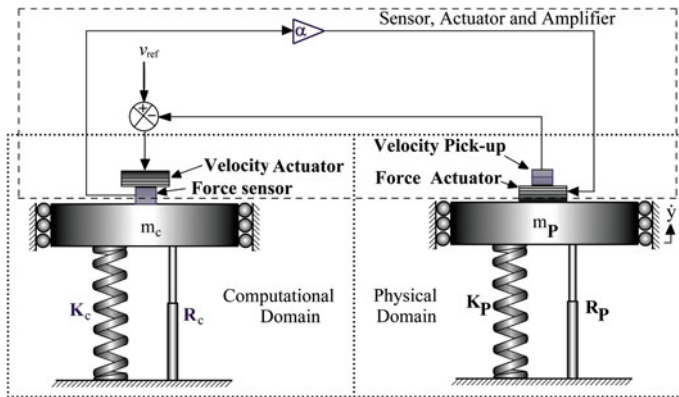


Fig. 13.2 Schema of robust overwhelming control scheme for a spring-mass-damper system

The basic concepts of robust overwhelming control may be explained with the aid of a simple academic example considered here. The schema of a second-order plant and a second-order virtual system in the computational domain is shown in Fig. 13.2. The left part of the figure concerns the controller and right part represents the plant. In Fig. 13.2, m , K and R correspond to mass, stiffness, and damping parameters, respectively, and subscripts P and c refer to the real and controller domains, respectively. This way of using an exact copy of the system in the controller domain to derive control laws is often referred to as physical model-based controller design [17].

In Fig. 13.2, the velocity of the mass point in the real plant is sensed and this sensed velocity signal is compared with a reference velocity (v_{ref}) signal. The error in velocity is applied to the virtual system (left-hand side of Fig. 13.2), which is a model residing in computational domain, i.e., the controller. The application of the error in velocity on the virtual system is shown through a conceptual (not real) actuator in Fig. 13.2. The computational model generates a force as an output. The force command is amplified and applied on the real system through an actual force actuator. Therefore, in Fig. 13.2, there is one real sensor and one real actuator. The measured variable is the velocity of the mass point in the real plant and the actuated variable is the force applied at the same mass point. This applied force is controlled by the controller (left-hand side model) so that the mass point on the real plant moves in a specified way.

Although an exact copy of the real system (i.e., same physical structure) has been used in the controller domain, it is assumed that the real system's parameter values are not perfectly known. Therefore, the parameter values used in the controller domain may be different from the corresponding values in the actual plant.

The causalled bond graph of the integrated real system and the system in the computational domain is shown in Fig. 13.3. The superscript * is used in the model to denote virtual sensors and actuators in the controller domain. The weight corresponding to the plant mass is included in the plant model, whereas it is intentionally

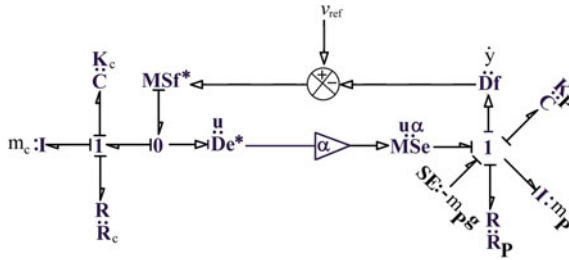


Fig. 13.3 Bond graph model of the system in Fig. 13.2 with the virtual system in the controller showing differential causality

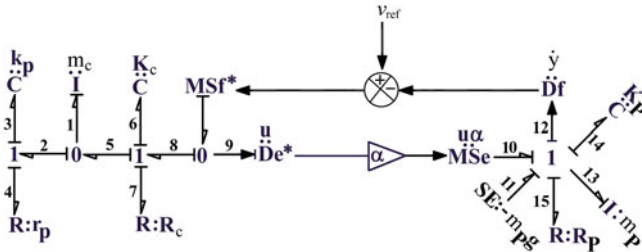


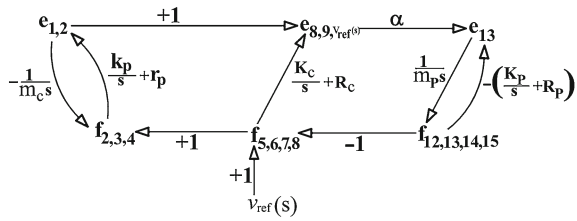
Fig. 13.4 Bond graph model of the system in Fig. 13.2 with the virtual system in the controller assigned integral causality by adding a pad

excluded from the controller side model to check if the controller will be able to overwhelm certain unmodeled external forces or disturbances.

It is noticed that the I-element corresponding to the mass in the controller side is in differential causality. This introduces terms corresponding to differentiation of measurements from the real system. Transferring inertial elements of dependent ports to independent ports cannot be used as a solution here. A coupling capacitor [15] or pad [7, 10–14] is added to the system at an appropriate location to avoid the differential causality, as shown in Fig. 13.4. The pad, in the form of (1-C-R) structure, is appended at the 0-junction where the controller mass is modeled. The pad can also be attached to the 0-junction where virtual actuator (MSf*) element is connected [7, 11–14]. The R-element in the pad is introduced to reduce the solution stiffness that is encountered during simulation. Higher values of C and R-elements reduce the dynamic effects of the pad. Note that the pad stiffness parameter, which has usually a large value, and the damping parameter have to be tuned through trial and error to satisfy two contradictory requirements, i.e., solution accuracy versus the time required for simulation. Further note that in virtual reality simulators, real-time feel is extremely important.

A signal flow graph (SFG) can be constructed from a bond graph model by following the causal paths. The SFG corresponding to the bond graph model of the linear time-invariant (LTI) system in Fig. 13.4 is shown in Fig. 13.5.

Fig. 13.5 Signal flow graph corresponding to the bond graph model in Fig. 13.4



The transfer function of the velocity of the plant mass to the reference velocity can be derived from Fig. 13.5 by straightforward application of Mason’s gain rule

$$G(s) = \frac{f_{13}(s)}{V_{ref}(s)} = \frac{T_2(s)\alpha}{T_1(s) + T_2(s)\alpha} \tag{13.1}$$

where

$$T_1(s) = m_p m_c s^4 + m_p k_p s^2 + m_p r_p s^3 + m_c K_P s^2 + m_c R_P s^3 + k_p K_P + k_p R_P s + r_p K_P s + r_p R_P s^2,$$

$$T_2(s) = m_c K_c s^2 + m_c R_c s^3 + k_p K_c + R_c r_p s^2 + m_c k_p s^2 + m_c r_p s^3 + K_c r_p s + R_c k_p s,$$

and s is the usual complex variable. Thus,

$$\lim_{\alpha \rightarrow \infty} G(s) = \frac{T_2(s)\alpha}{T_2(s)\alpha} = 1 \tag{13.2}$$

This implies that the plant follows the command if the amplifier gain (α) is sufficiently large, which is exactly what implicit system inversion schemes aim at [15]. Further note that the plant parameters (m_p , K_P and R_P), appearing only in the term $T_1(s)$, are all overwhelmed by the controller, i.e., the plant parameters do not appear in the term $T_2(s)$. Therefore, this type of controller can be applied successfully for studying inverse dynamics of the Stewart platform. Note that the causal form of the controller in Eq. 13.1, where the order of the denominator polynomial is one more than the order of the numerator polynomial, degenerates into a non-causal form (Eq. 13.2) as the gain parameter approaches infinity.

However, too high value of gain parameter is not recommended for practical applications. High gain value increases the noise sensitivity and also the time required for simulation [11]. Moreover, large gain values increase the overshoot in the response which may exceed the actuator capacity. In most simulator applications, only the low frequency response is important. Note that pad stiffness and damping values are large. Therefore, when the controller stiffness (K_c) is large, $G(s)$ approaches unity in the

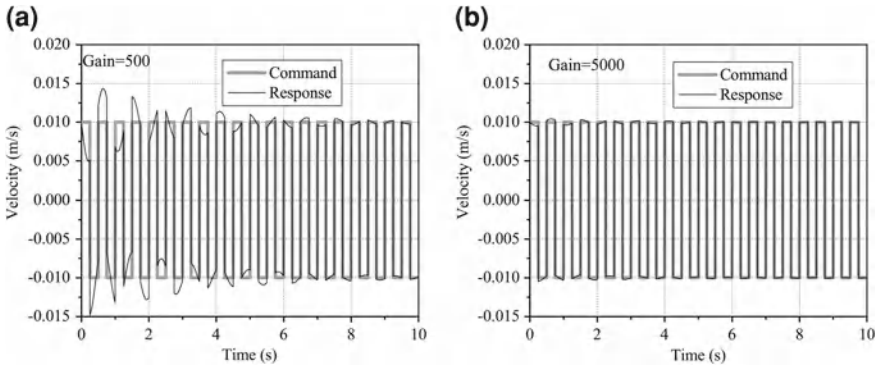


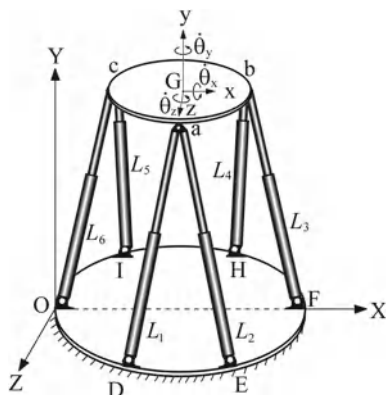
Fig. 13.6 Performance of overwhelming controller for (a) gain value 500 and (b) gain value 5,000

low frequency range even for smaller values of the gain. If K_c is large, a small gain value is needed whereas for small values of K_c , large gain value is required. Therefore, the gain parameter value is designed along with the controller parameter values [17]. A suitable design should aim at such controller parameter values which would filter out the measurement noise within some specific bandwidth (i.e., act as a second order low-pass properizing filter [15]) and as well keep the trajectory tracking performance within acceptable limits. Therefore, there has to be a trade-off between high gain and bandwidth of filtering [11]. This type of design reduces the sensitivity to measurement noise and the numerical stiffness during the simulation of the inverse system [2].

The following parameter values are chosen to evaluate the performance of the overwhelming controller for the example application: $m_p = 1 \text{ kg}$, $K_p = 100 \text{ N/m}$, $R_p = 2 \text{ N s/m}$, $m_c = 1.5 \text{ kg}$, $K_c = 80 \text{ N/m}$, $R_c = 1 \text{ N s/m}$, $k_p = 10,000 \text{ N/m}$, $r_p = 100 \text{ N s/m}$ and $g = 9.81 \text{ m/s}^2$. An arbitrary initial condition (plant mass was displaced by 0.02 m) was applied. The controller parameter values are intentionally given different values than the corresponding plant parameters. The reference velocity command is prescribed as a symmetric square wave of amplitude 0.01 m/s and time period of 0.5 s. Note that a square wave continuously excites transients. At this stage, no constraints are imposed on the actuator dynamics, i.e., on the actuator capacity and slew rate.

The plant response for a low amplifier gain ($\alpha = 500$) is compared with the prescribed velocity in Fig. 13.6a. The same are compared in Fig. 13.6b for a larger amplifier gain ($\alpha = 5,000$) and it is found that the response tracks the command even when the self-weight is not modeled in the controller domain and the controller parameters are grossly different from the plant parameters. This validates the robustness of the controller to unmodeled dynamics and parameter uncertainties.

Fig. 13.7 Schema of the Stewart platform



13.3 Modeling of 3D Stewart Platform

In [3], it is suggested that two models of the manipulator system are required: a lean inverse model for computational efficiency and an accurate forward model for proper representation of dynamic loads. In the following sections, a lean forward model will be developed first from which an inverse model with overwhelming controller will be constructed, and then a full forward model of the platform will be developed.

The schematic representation of the Stewart platform is given in Fig. 13.7, where the movable payload platform is supported by the fixed base through six variable length actuators. This is a six degrees-of-freedom spherical-prismatic-spherical mechanism. The coordinate system {XYZ} of the fixed base is placed at the point O with Y-axis perpendicular to the base plane. The coordinate system {xyz} of the movable platform is located at the center G of the moving platform. All the joints attached to the fixed and movable platform are spherical joints.

The movable platform is considered as a six degrees-of-freedom rigid body. The platform motion is described by three linear displacements along body fixed x, y, and z axes and the rotational motion of the body can be defined by the three Cardan angles. The Newton-Euler equations of the movable platform with attached body fixed axes aligned with the principal axes of inertia are as follows:

$$\sum F_x = m_P \ddot{x}_G + m_P (\dot{z}_G \dot{\theta}_y - \dot{y}_G \dot{\theta}_z) \tag{13.3}$$

$$\sum F_y = m_P \ddot{y}_G + m_P (\dot{x}_G \dot{\theta}_z - \dot{z}_G \dot{\theta}_x) \tag{13.4}$$

$$\sum F_z = m_P \ddot{z}_G + m_P (\dot{y}_G \dot{\theta}_x - \dot{x}_G \dot{\theta}_y) \tag{13.5}$$

$$\sum M_x = J_{Px} \ddot{\theta}_x + \dot{\theta}_z \dot{\theta}_y (J_{Pz} - J_{Py}) \tag{13.6}$$

$$\sum M_y = J_{Py}\ddot{\theta}_y + \dot{\theta}_x \dot{\theta}_z (J_{Px} - J_{Pz}) \tag{13.7}$$

$$\sum M_z = J_{Pz}\ddot{\theta}_z + \dot{\theta}_y \dot{\theta}_x (J_{Py} - J_{Px}) \tag{13.8}$$

The equations for three linear velocities of the point a (Fig. 13.7) in the moving system along three axes are as follows:

$$\dot{x}_a = \dot{x}_G + z_a \dot{\theta}_y - y_a \dot{\theta}_z \tag{13.9}$$

$$\dot{y}_a = \dot{y}_G + x_a \dot{\theta}_z - z_a \dot{\theta}_x \tag{13.10}$$

$$\dot{z}_a = \dot{z}_G + y_a \dot{\theta}_x - x_a \dot{\theta}_y \tag{13.11}$$

Similarly, the equations for three linear velocities of the point b and c in the moving system can be found out. The joint forces acting in the inertial frame and supplied by the actuators at the points A, B, and C connected with the moving platform are transformed through coordinate transformation block (CTF) (See Chap. 5) to get forces in the body fixed direction.

13.3.1 3D Stewart Platform Model Without Leg Inertia

Initially, a lean forward model is developed solely to construct the inverse system representation. The inverse system must be computationally fast because it is the one which will be implemented in a computer for controlling the real platform. Thus, only kinematics consideration is sufficient for model development. The masses of pistons and cylinders of the actuator are neglected. The rate of change of length of the link 1 between the moving point A and the fixed point D can be expressed as

$$\dot{L}_1 = \left(\frac{x_A - x_D}{L_1} \right) \dot{x}_A + \left(\frac{y_A - y_D}{L_1} \right) \dot{y}_A + \left(\frac{z_A - z_D}{L_1} \right) \dot{z}_A \tag{13.12}$$

Similarly, the rate of change of lengths for other links can be found out. The angular velocities of the moving platform in the body fixed frame can be expressed as developed in Chap. 5. The Euler angle rates which are needed for coordinate transformation (CTF) are calculated as follows:

$$\begin{bmatrix} \dot{\theta}_{XE} \\ \dot{\theta}_{YE} \\ \dot{\theta}_{ZE} \end{bmatrix} = \begin{bmatrix} 1 & \tan \theta_{YE} \sin \theta_{XE} & \tan \theta_{YE} \cos \theta_{XE} \\ 0 & \cos \theta_{XE} & -\sin \theta_{XE} \\ 0 & \sin \theta_{XE} / \cos \theta_{YE} & \cos \theta_{XE} / \cos \theta_{YE} \end{bmatrix} \begin{bmatrix} \dot{\theta}_x \\ \dot{\theta}_y \\ \dot{\theta}_z \end{bmatrix} \tag{13.13}$$

where subscripts XE, YE, and ZE are used to indicate Euler angle rates and subscripts x, y, and z indicate body-fixed angular velocities.

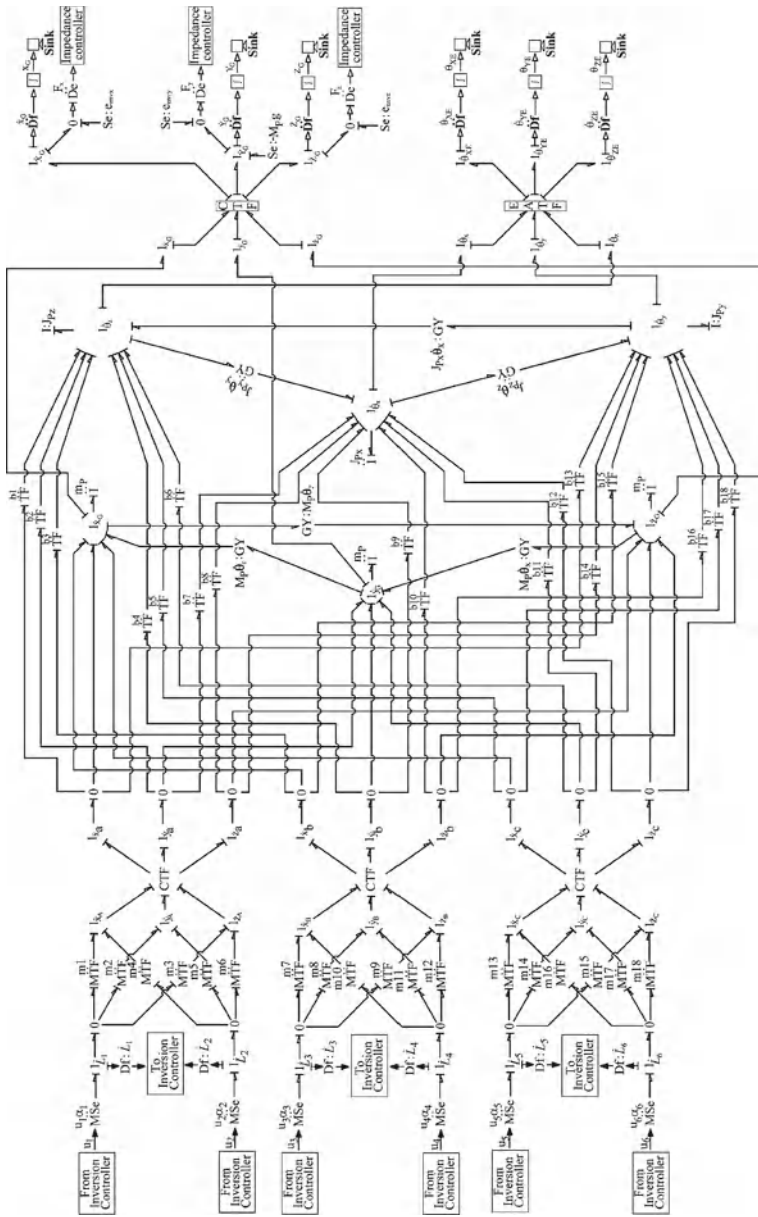


Fig. 13.8 Bond graph model of the 3D Stewart platform without leg inertia

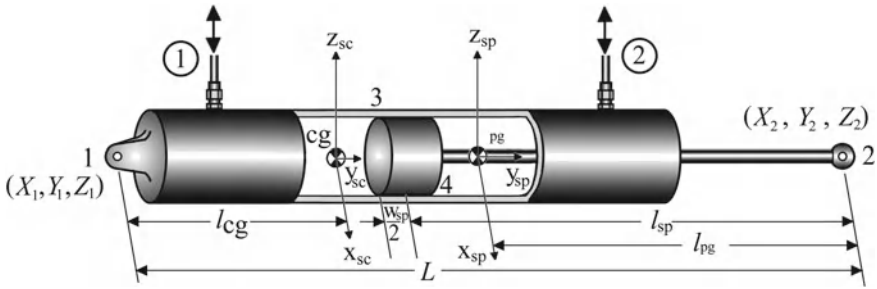


Fig. 13.9 Schema of the hydraulic piston-cylinder prismatic link

The bond graph model of the 3D Stewart platform without considering leg inertia is shown in Fig. 13.8. The movable platform is modeled as a rigid body with six degrees of freedom. The linear and rotary inertias m_p , J_{p_x} , J_{p_y} , and J_{p_z} are coupled by a pair of gyration rings (Euler junction structure), one for translational and the other for rotational velocities, according to Eqs. 13.3–13.8. The weight of the platform in the inertial frame acts on it in non-inertial frame through coordinate transformation (CTF).

The body fixed velocities of the points a, b, and c are found out according to Eqs. 4.39–4.41. The moduli b_1 to b_{18} are calculated from the body fixed distances of the points a, b, and c from the center of gravity G of the platform. The moduli m_1 to m_{18} are calculated from Eq. 4.42 for leg 1 and other similar equations for other legs. In Fig. 4.27, six MSE-elements are modulated by control signals u_1 to u_6 from the inverse model which is discussed later. The gains α_1 to α_6 are associated with the overwhelming control strategy. Six flow sensors (Df-elements) at 1-junctions in the bond graph model measure the rate of deformation of the associated legs.

13.3.2 3D Actuator Model

The hydraulic cylinder is actuated by creating pressure difference across the two sides of the piston. The pressure control is performed by solenoid actuated four-way directional control valve. The schema of the 3D hydraulic actuator is shown in Fig. 13.9. The end 1 of the cylinder is fixed to the base platform and the other end 2 is connected with the moving platform.

The normal body fixed velocities at the contact point 3 on the cylinder along x and z-directions by assuming a thin but long piston are

$$\dot{x}_{3sc} = \dot{x}_{sc} + (L - l_{sp} - l_{cg} - w_{sp}/2) \dot{\theta}_{zsc} \tag{13.14}$$

$$\dot{z}_{3sc} = \dot{z}_{sc} + (L - l_{sp} - l_{cg} - w_{sp}/2) \dot{\theta}_{xsc} \tag{13.15}$$

where $\dot{\theta}$ indicates body-fixed angular velocity about the axis indicated in subscript. At the same time, the body fixed velocities of point 3 on the piston are

$$\dot{x}_{3sp} = \dot{x}_{sp} - (l_{sp} - l_{pg} + w_{sp}/2) \dot{\theta}_{zsp} \quad (13.16)$$

$$\dot{z}_{3sp} = \dot{z}_{sp} - (l_{sp} - l_{pg} + w_{sp}/2) \dot{\theta}_{xsp} \quad (13.17)$$

The normal body fixed velocities at the contact point 4 on the cylinder are

$$\dot{x}_{4sc} = \dot{x}_{sc} + (L - l_{sp} - l_{cg} + w_{sp}/2) \dot{\theta}_{zsc} \quad (13.18)$$

$$\dot{z}_{4sc} = \dot{z}_{sc} + (L - l_{sp} - l_{cg} + w_{sp}/2) \dot{\theta}_{xsc} \quad (13.19)$$

and the same points velocities on the piston along x and z-directions are

$$\dot{x}_{4sp} = \dot{x}_{sp} - (l_{sp} - l_{pg} - w_{sp}/2) \dot{\theta}_{zsp} \quad (13.20)$$

$$\dot{z}_{4sp} = \dot{z}_{sp} - (l_{sp} - l_{pg} - w_{sp}/2) \dot{\theta}_{xsp} \quad (13.21)$$

The rate of change of length of the link between the piston rod end point 2 and the fixed cylinder end point 1 can be expressed as:

$$\dot{L}_i = \left(\frac{X_1 - X_2}{L_i} \right) (\dot{X}_1 - \dot{X}_2) + \left(\frac{Y_1 - Y_2}{L_i} \right) (\dot{Y}_1 - \dot{Y}_2) + \left(\frac{Z_1 - Z_2}{L_i} \right) (\dot{Z}_1 - \dot{Z}_2) \quad (13.22)$$

The bond graph model of the hydraulic actuator is shown in Fig. 13.10. The cylinder and the piston are modelled as rigid bodies with six degrees of freedom each similar to the movable platform. The inertial velocities of the fixed point 1 and the piston rod end point 2 are found out similar to the process of finding the inertial velocities of the points A, B, and C of the movable platform. As one end of the cylinder is fixed, three zero flow sources are inserted into the bond graph model. MTF-elements with moduli μ_x , μ_y , and μ_z are used to calculate the relative velocity between the piston and the cylinder at a 0-junction by Eq. 13.22 and the friction between the piston and the cylinder is modeled by an R-element at that junction. The contact point mechanics at the points 3 and 4 are determined by Eqs. 13.14–13.21. The normal velocity at the contact point on the cylinder is made equal to normal velocity at the contact point on the piston in the inertial frame by providing higher values of contact stiffness and damping parameters. The movement of the piston depends upon the pressure difference between both sides of the piston which are determined in the submodel for four-way directional control valve and are interfaced through ports 6 and 7. The information of the force due to pressure difference, which is necessary for the force controller, is taken out through port 5. In Fig. 13.10, piston side area is A_{sp} and that of the piston rod is A_{sr} . The information of the rate of

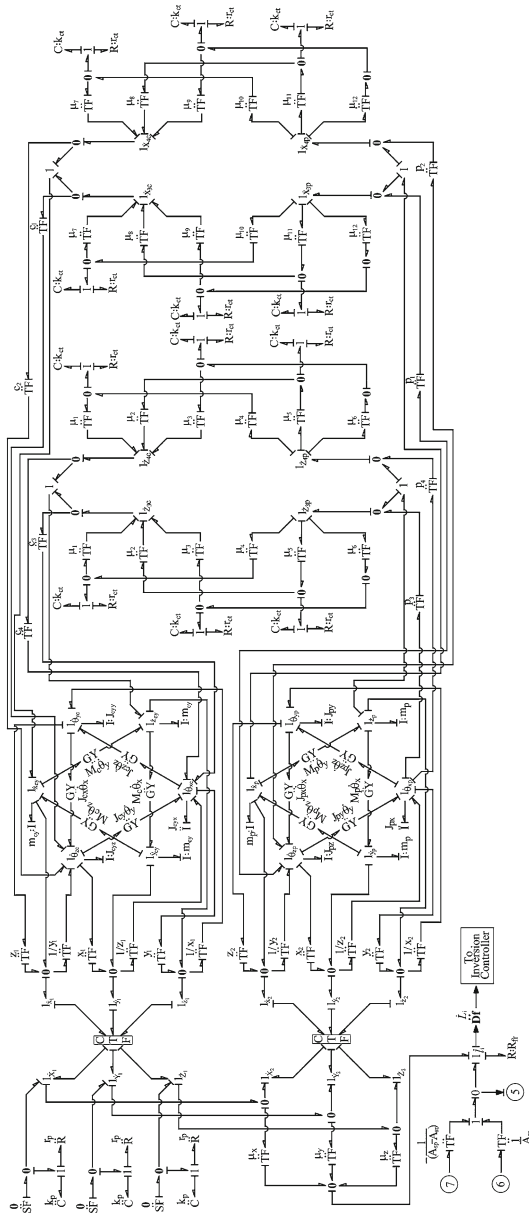


Fig. 13.10 Bond graph model of the hydraulic piston-cylinder 3D prismatic link

deformation (\dot{L}_i) of the real actuator is also taken out for the corresponding part of the simplified inverse model.

13.3.3 3D Stewart Platform Model with Leg Inertia

The bond graph model of the 3D Stewart platform with leg inertia is shown in Fig. 13.11. This model is similar to the bond graph model of the 3D Stewart platform without leg inertia except that space impedance model is replaced by the actual hydraulic actuator model (See Chap. 5).

The actuators 1 and 2 of the 3D Stewart platform are connected with the support point A through frictionless joints. Similarly, the actuators 3 and 4 are connected with support point B and the actuators 5 and 6 are connected with support point C through similar type joints. The C-element with stiffness parameter K_j and R-element with damping parameter R_j , which are in mechanical parallel, are used to model the joints.

13.3.4 Inverse Model of 3D Stewart Platform

The inverse system model in the controller domain, as shown in Fig. 13.12, is a mirror reflection of the simplified model of the Stewart platform given in Fig. 13.8 with some modifications which are required for making it computationally suitable.

The model in Fig. 13.8 is inverted by imposing the rate of change of leg lengths as inputs and forces generated in those legs as outputs. Stiff spring-damper combinations or pads (stiffness k_p and damping r_p) are included in the inverse model to make it computationally suitable.

13.4 Graphics Interface

In the vehicle simulator developed in this book, the graphics interface is programmed in Microsoft Visual C++ environment. Special purpose graphics library GDIplus is used in the programs. GDIplus has inbuilt routines for bitmap rotation, deformation, shading, etc., and is useful for 3D graphics. There are other available commercial software for graphics rendering, for example ScannerStudio [16].

The driver's view area is shown in Fig. 13.13a. It is assumed that aerial view of a large area (the full vehicle track or a city) is available and stored in a bitmap image. Satellite images or other web-based resources like Google earth (www.googleearth.com) or wikimapia (www.wikimapia.com) can be used for this purpose. The driver's view is only a small part of this bitmap image. The vehicle center of gravity and the driver's eye are assumed to be located at the point o (this may be changed suitably if required). The viewing area during driving is the area $\square abcd$ (\square indicates

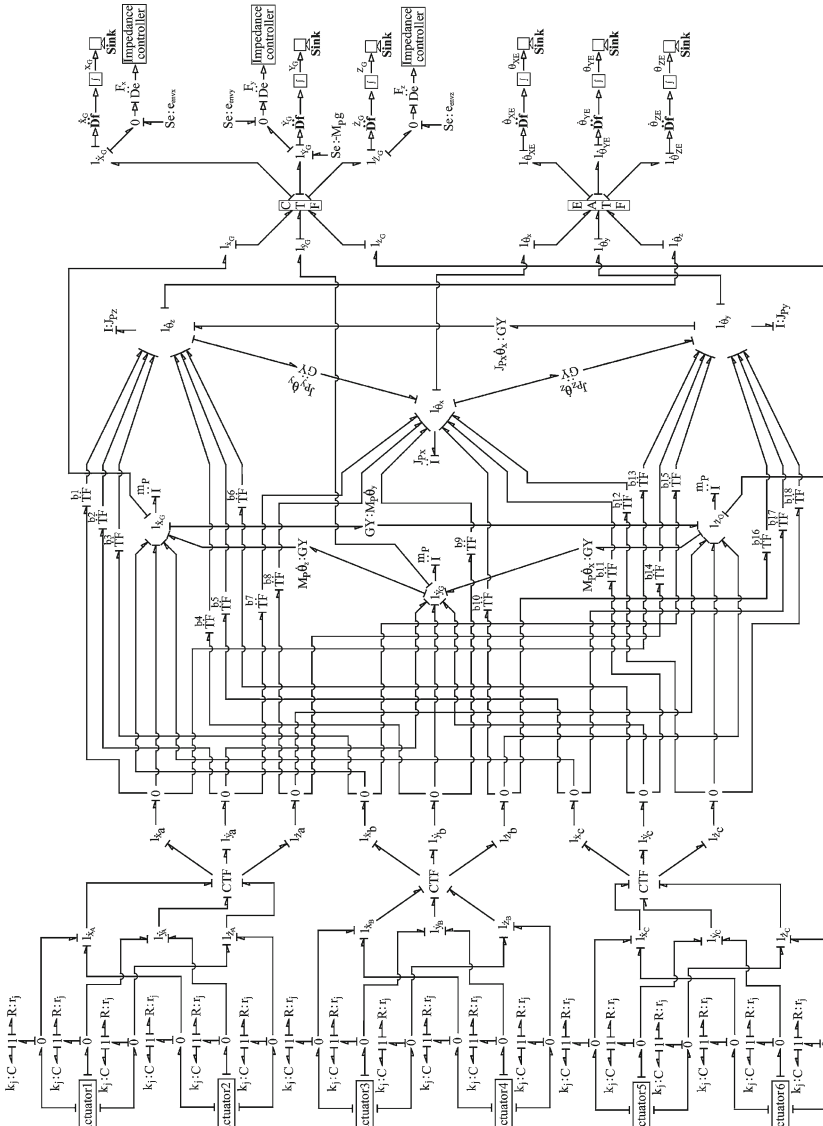


Fig. 13.11 Bond graph model of the 3D Stewart platform with leg inertia

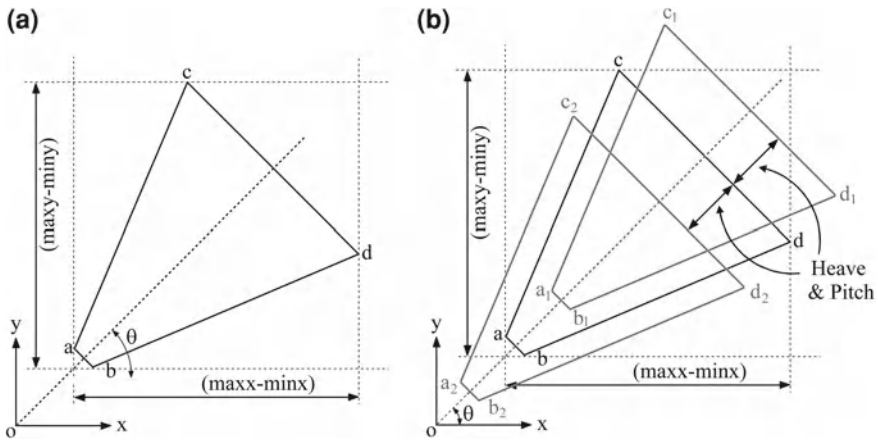


Fig. 13.13 a Driver's front viewing area and b modified front viewing area during heave and pitch

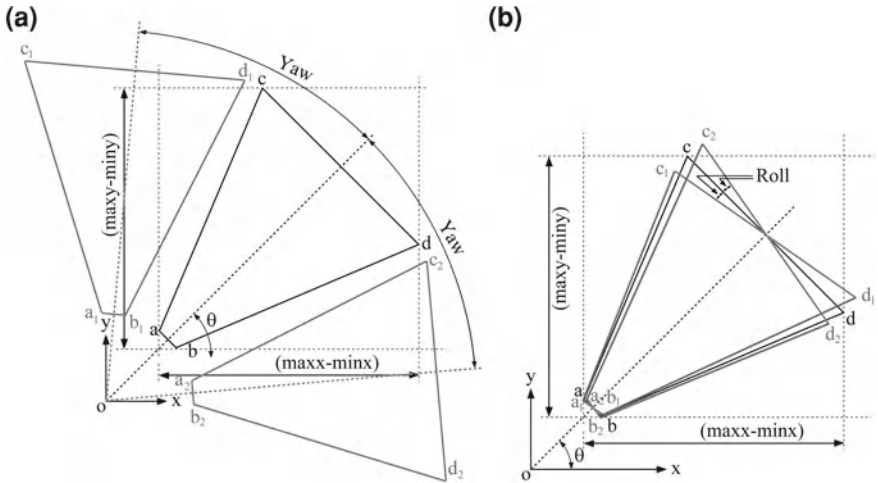


Fig. 13.14 Driver's front viewing area during (a) yaw and (b) roll

a quadrilateral) and the viewing axis is perpendicular to the lines ab and cd . The vision of the area between the origin and line ab is obstructed by the vehicle's dashboard. Line cd indicates horizon. The angle of yaw for the vehicle is θ . The positions of the points a , b , c , and d are found out in terms of the position of the point o and the yaw angle. The distance of the area $\square abcd$ from the origin changes according to the vehicles heave and pitch (see Fig. 13.13b). If the vehicle pitches forward or sinks down then the area $\square abcd$ comes closer to the origin and vice versa. Similarly, the change in the driver's front viewing areas during yaw and roll motions are shown in Fig. 13.14a, b.

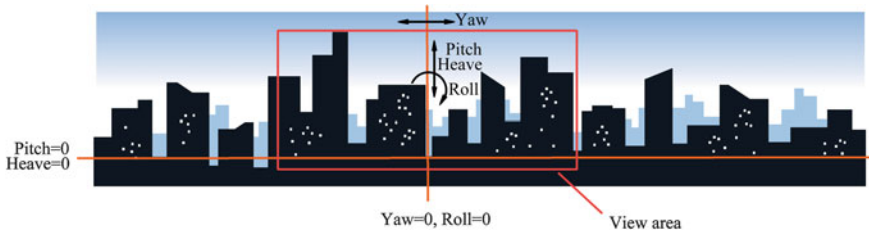


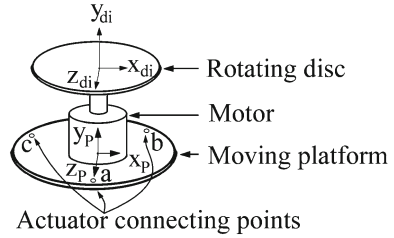
Fig. 13.15 Geometric modeling of skyline as seen by the driver

The minimum and maximum values of x and y among the four points are determined. To copy the original image $\square abcd$ from the global bitmap image of the terrain (e.g., Google earth image), a rectangle with sides $(\max y - \min y)$ and $(\max x - \min x)$ is specified. A new bitmap is created by cloning the specified rectangle. An empty bitmap and a graphics object are created to hold the rotated image. The rotation point is moved to the center of the empty bitmap and the cloned object is rotated about the rotation point through an angle of $(-90^\circ + \theta)$. This rotated image is then drawn on the graphics object.

The brightness of the rotated image which is drawn on the graphics object (an object defined in GDIPlus) can be changed by color matrix and image attributes-object. By reducing brightness of the area in proportion to the distance from the vehicle, fuzziness at the horizon is simulated. The area closest to the vehicle appears brighter. The `StretchBlt` function is applied on strips of the trapezoidal area $\square abcd$ to map it to a rectangular area on the display screen. The height of the rectangular destination area on the screen decreases as its distance from the bottom of the screen (vehicle dashboard) increases. The bitmap stretching produces expanded vision near the vehicle front and condensed vision far away. Coupled with the brightness adjustment scheme, this produces a realistic map of the road and its surroundings. In similar way to rendering of the front-view through the windscreen, the back-view is rendered on the rear-view mirror.

It is assumed that the vehicle track is in an isolated area and there is no vertical structure near its vicinity. Thus, the skyline is far away and the vehicle motion does not change the size of items visible in the skyline. Under this condition, the skyline can be constructed from a static panoramic photograph, i.e., a full 360° map of horizon is stored as a bitmap strip. This image is mapped to the inside surface of a cylinder. A portion of the image from the inside of the cylinder is copied depending upon the value of yaw, roll, pitch and heave, and then the image is flattened as shown in Fig. 13.15. The flattened image is drawn at the top of the screen. When the vehicle pitches forward or heaves down then the skyline moves up and vice versa. Likewise, when the vehicle yaws, the skyline is panned either to left or to right depending upon the yaw angle. The skyline tilts when the vehicle rolls. For more realistic rendering of skyline with static and moving objects, live objects, other vehicles on the track, etc., specialized software like `ScannerStudio` [16] can be used.

Fig. 13.16 Rotating disk for large yaw control



13.5 Stewart Platform for Vehicle Simulator

In a basic vehicle simulator as developed here, the driver physically feels heave, pitch, roll, and yaw motions. The surge and sway effects are difficult to achieve as it requires a movable base, usually on cross rails. However, all these effects are visually conveyed on the simulator screen. The platform designed in previous sections cannot provide full 360° yaw because that would cause the legs to collide. Thus, additional hardware is included as shown in Fig. 13.16 where a motor-driven rotating disk is mounted on the moving platform.

The rotating disk can be used for independent yaw control by a motor. The motor applies a reverse torque on the movable platform, but the platform is not allowed yaw motion, i.e., the yaw command is given as zero in the overwhelming controller of the platform. Thus, there are two control actions: the overwhelming control is used to give small heave, pitch and roll motions, and an independent motor controller (PI angular position control) is used to give large yaw motion.

The driver is mounted on a chair fixed to the rotating disc. The reaction torque from the rotating disc is an un-modelled disturbance on the remaining parts of the Stewart platform and the overwhelming controller overwhelms this disturbance to produce proper trajectory tracking. The commands to the overwhelming controller in the inverse dynamics model of the platform are given in reference inertial frame. The platform's body-fixed velocities are first transformed to inertial frame velocities where overwhelming controllers and reference commands are modelled. Thus, the linear and angular velocities obtained from the vehicle model are transformed to the inertial frame and fed to the Stewart platform's controller. The rotating disk PI-controller receives the vehicle yaw rate information and applies the necessary torque to rotate the disk (with driver, cabin, driver controls and display system).

The forward bond graph model of the Stewart platform with the rotating disk is shown in Fig. 13.17. Note that the inverse model remains the same, i.e., the inverse system does not know the changes made to the actual system. The difference between the two systems is the additional disk which applies some unknown forces and moments on the moving platform. However, the overwhelming controller overwhelms the disturbances, i.e., the forces and moments produced by the additional rotating disk.

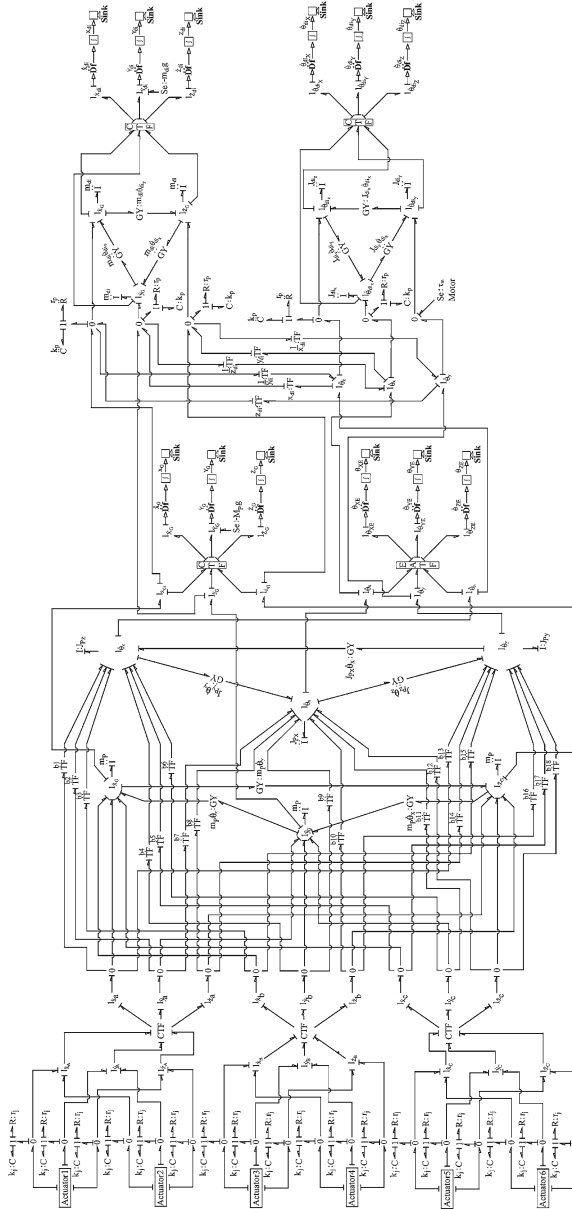


Fig. 13.17 Bond graph model of 3D Stewart platform with rotating disk

The disk is modeled as a separate rigid body with 6-degrees-of-freedom in the top side of the forward bond graph model shown in Fig. 13.17. The motor (shown without the PI-controller) is modeled as a source of effort at a 0-junction so that the relative rotational velocity between the platform and the rotating disk is controlled, and the active (on disk) and reactive (on platform) torques are properly applied. The motor linear inertias are lumped with the platform.

13.6 Results of Test Drive of Driving Simulator

The vehicle behavior is calculated from the vehicle's dynamic model (See [1, 4]) with driver input, i.e., braking, acceleration, steering, etc. The vehicle responses are filtered so that only the low frequency responses are fed to the Stewart platform's controller as reference velocities.

The Stewart platform parameters and configurations are given in Tables 13.1 and 13.2, respectively. The vehicle parameters are taken from [1].

The top view of the test track with initial position of the vehicle on the track is shown in Fig. 13.18. Note that this picture is not visible to the driver. The trapezoid abcd (shown in Fig. 13.13) is then copied from this large image and rendered on the driver display screen. As the driver (in this case, our student Dr. T.K. Bera) accelerates the vehicle and it moves forward (trapezoid abcd also moves forward), the driver sees the right turn. The driver thus mildly decelerates (ABS is the selected vehicle configuration) and applies the steering and after end of the turn, again accelerates after straightening the steering. This way, as the driver completes one loop, brakes are suddenly applied and the vehicle is brought to stop at a position near the starting position. The path of the vehicle centroid and its forward speed at various locations are marked on the top view of the track in Fig. 13.18. Note that the nature of driving varies from person to person depending upon the driver skill and level of training.

Usually, joystick or specialized driving simulator gear (steering, brake, accelerator and clutch pedals with potentiometers for position sensing) are used in driving simulators. In this case, keyboard input is used. The up arrow is used for acceleration, down arrow for brake, and left and right arrows are used for steering. The key-press repeat rate is also used in the program. For example, if down arrow is kept pressed for a fixed duration then it indicates panic braking (See ABS details in [4]). The keyboard interface is similar to any video game, but the real difference is that the vehicle response is calculated in real time from a vehicle dynamics model.

The driver's view (monitor display) while the driver is taking the first right turn is shown in Fig. 13.19. This picture shows the skyline tilt (due to roll) during curve negotiation.

The driver view during braking on a straight path is shown in Fig. 13.20. The visual feedback shows the vehicle is pitching forward (the skyline is moving up), i.e., diving during braking.

The dynamic response of the vehicle model running in the background is shown in Fig. 13.21. The heave and speed of the vehicle are shown in Fig. 13.21a and roll,

Table 13.1 Parameters of 3D Stewart Platform Used in the Simulations

Subsystem	Parameter values		
Platform	$m_P = 100 \text{ kg}$	$J_{Px} = 10 \text{ kg m}^2$	$J_{Py} = 10 \text{ kg m}^2$
	$J_{Pz} = 10 \text{ kg m}^2$	$k_j = 10^7 \text{ N/m}$	$r_j = 10^2 \text{ N s/m}$
	$x_a = 0 \text{ m}$	$y_a = -0.1 \text{ m}$	$z_a = 1 \text{ m}$
	$x_b = 0.866 \text{ m}$	$y_b = -0.1 \text{ m}$	$z_b = -0.5 \text{ m}$
	$x_c = -0.866 \text{ m}$	$y_c = -0.1 \text{ m}$	$z_c = -0.5 \text{ m}$
	Actuator	$w_v = 0.4 \text{ m}$	$l_{cg} = 1.5 \text{ m}$
$l_{pg} = 1.5 \text{ m}$		$k_{ct} = 10^7 \text{ N/m}$	$r_{ct} = 10^2 \text{ N s/m}$
$A_{sp} = 0.01 \text{ m}^2$		$A_{sr} = 0.005 \text{ m}^2$	$R_{fr} = 0.0 \text{ N s/m}$
$m_{sp} = 1 \text{ kg}$		$m_{sc} = 20 \text{ kg}$	$J_{scx} = 5 \text{ kg m}^2$
$J_{scy} = 5 \text{ kg m}^2$		$J_{scz} = 5 \text{ kg m}^2$	$J_{spx} = 0.5 \text{ m}^2$
$J_{spy} = 0.5 \text{ kg m}^2$		$J_{spz} = 0.5 \text{ m}^2$	$x_1 = -1.5 \text{ m}$
$y_1 = 0 \text{ m}$		$z_1 = 0 \text{ m}$	$x_2 = 1.5 \text{ m}$
$y_2 = 0 \text{ m}$		$z_2 = 0 \text{ m}$	
$C_L = 1.8 \times 10^{-11} \text{ m}^5/(\text{Ns})$			
Servo control		$p_S = 10^5 \text{ Pa}$	$\beta = 800 \text{ MPa}$
	$B = 16 \text{ m/A}$	$K_P = 100$	$K_I = 0.00001$
	$\gamma = 1.5 \times 10^{-6} (\text{m}^5/\text{kg})^{1/2}$		
Inverse system	$k_p = 10^7 \text{ N/m}$	$r_p = 10^2 \text{ N s/m}$	$K_c = 10^7 \text{ N/m}$
	$R_c = 10^2 \text{ N s/m}$	$m_c = 10 \text{ kg}$	$J_c = 10 \text{ kg m}^2$
	$m_P^* = 1 \text{ kg}$	$J_{Px}^* = 1 \text{ kg m}^2$	$J_{Py}^* = 1 \text{ kg m}^2$
	$J_{Pz}^* = 1 \text{ kg m}^2$	$\alpha = 50$	$g = 9.81 \text{ m/s}^2$
Rotary disc	$m_{di} = 100 \text{ kg}$	$J_{dix} = 10 \text{ kg m}^2$	$J_{diy} = 10 \text{ kg m}^2$
	$J_{dis} = 20 \text{ kg m}^2$	$x_{di} = 0 \text{ m}$	$y_{di} = 0.1 \text{ m}$
	$z_{di} = 0 \text{ m}$		

Table 13.2 Initial Conditions of Stewart Platform (initial configurations)

$X_A = 2 \text{ m}$	$Y_A = 5 \text{ m}$	$Z_A = 1 \text{ m}$	$X_B = 2.866 \text{ m}$	$Y_B = 5 \text{ m}$
$Z_B = -0.5 \text{ m}$	$X_C = 1.134 \text{ m}$	$Y_C = 5 \text{ m}$	$Z_C = -0.5 \text{ m}$	$X_G = 2 \text{ m}$
$Y_G = 5.1 \text{ m}$	$Z_G = 0 \text{ m}$	$X_D = 1 \text{ m}$	$Y_D = 0 \text{ m}$	$Z_D = 1.732 \text{ m}$
$X_E = 3 \text{ m}$	$Y_E = 0 \text{ m}$	$Z_E = 1.732 \text{ m}$	$X_F = 4 \text{ m}$	$Y_F = 0 \text{ m}$
$Z_F = 0 \text{ m}$	$X_H = 3 \text{ m}$	$Y_H = 0 \text{ m}$	$Z_H = -1.732 \text{ m}$	$X_I = 1 \text{ m}$
$Y_I = 0 \text{ m}$	$Z_I = -1.732 \text{ m}$	$X_O = 0 \text{ m}$	$Y_O = 0 \text{ m}$	$Z_O = 0 \text{ m}$
$L_i = 5.151 \text{ m}$				

pitch, and yaw motions are shown in Fig. 13.21b. These responses can be readily correlated with the motion of the vehicle on the track given in Fig. 13.18.

Apart from the visual feedback, the driver also gets physical feedback from the Stewart platform on which he/she is seated. Although a real Stewart platform has not been used in this work, the response of a simulated Stewart platform is considered. The overwhelming controller in the inverse model of the Stewart platform is fed with the reference velocities (rate of change of the heave, pitch and roll as computed and shown in Fig. 13.21) and the yaw rate is fed to the separately controlled rotary disk.

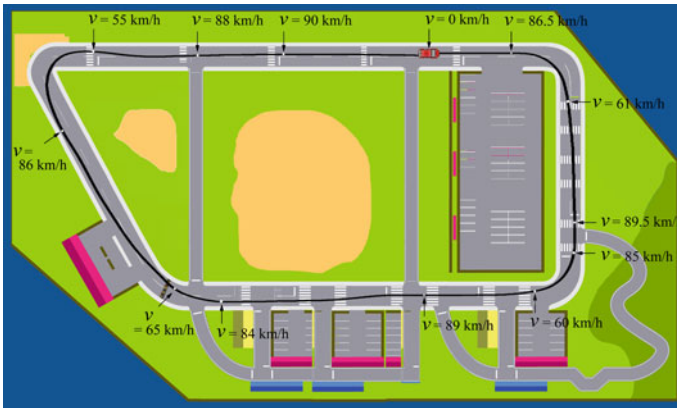


Fig. 13.18 Motion of the vehicle on the track for the driving simulator



Fig. 13.19 Visual perception during yaw motion

Because only low frequency feel is important, the reference velocities are filtered through low-pass filters. The outputs from the inverse model are fed to the forward model of the Stewart platform. In the real case, an actual Stewart platform replaces the forward model of the platform. The response of the Stewart platform is shown in Fig. 13.22. Note that without the actual platform, the driver does not feel these motions.

The discrepancies in the results shown in Fig. 13.22 are due to the low pass filter which introduces a small delay and smoothens the sharp corners in the original response before feeding them as commands to the Stewart platform's controller. However, these discrepancies and delays are too small for the driver to discern them. The low-pass filter is required to improve the computational efficiency. Without the filter, the simulation of the inverse system of the Stewart platform becomes stiff.



Fig. 13.20 Visual perception during braking

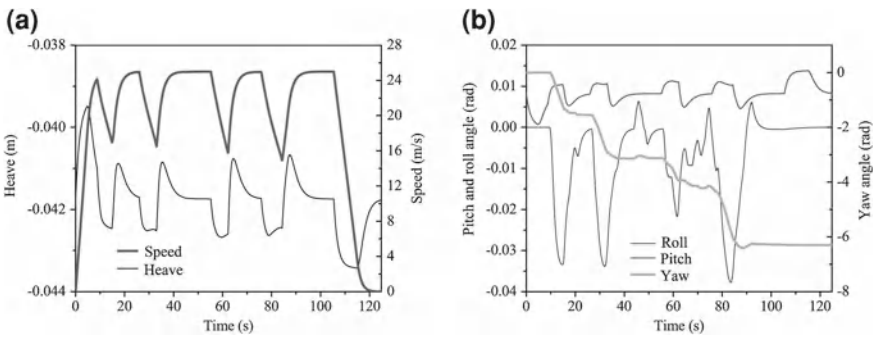


Fig. 13.21 **a** Heave and speed, and **b** roll, pitch, and yaw computed from the vehicle model

Because real-time performance rather than precise trajectory tracking is important in the driving simulator, the errors in platform positioning are not a serious issue in the vehicle simulator. Note that the vehicle dynamics simulation, visual display rendering and Stewart platform control are disjoint applications which should be performed in different computers. The data transfer and synchronisation between these machines is a different issue which is kept outside the purview of this book.

13.7 Conclusions

A basic driving simulator is developed in this chapter. The simulator integrates a complex vehicle-dynamics model, a driver interface and a visual display. The human in the loop simulation system integrates vehicle dynamics, dynamics of Stewart platform, visual display, and control systems. A detailed bond graph model of a vehicle with submodels for its components, especially the braking system, has been

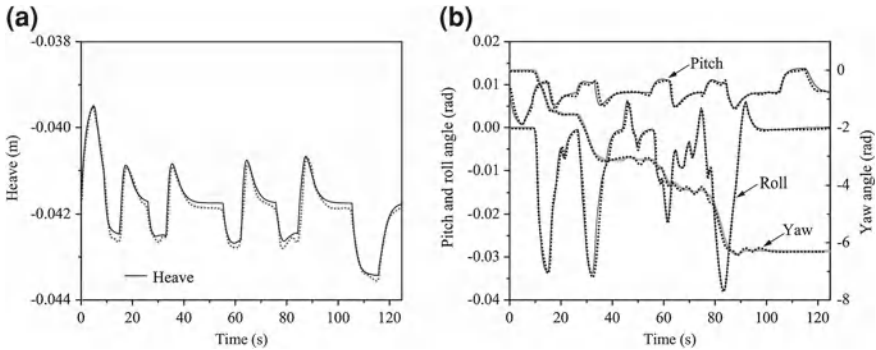


Fig. 13.22 **a** Heave and speed, and **b** roll, pitch, and yaw computed from the vehicle model compared to those of the Stewart platform. The results from the Stewart platform simulation are given in *dotted lines*

developed in [1, 4] in Chap.6. This bond graph model is used in this chapter to compute the vehicle dynamics in response to driver inputs. The full vehicle model includes dynamics of the load transfer on the wheels while the vehicle makes a manoeuvre.

The implementation of a driving simulator requires heavy computational resources. To reduce computational burden, the exact trajectory tracking requirement of the Stewart platform is relaxed. It was possible to run the developed vehicle dynamic model and the graphic rendering together in single IBM Core-2-Duo machine and obtain real-time performance. However, the inverse and forward Stewart platform models could not be simulated in real time in that same machine. Note that it is the forward model of the Stewart platform, which causes the simulation stiffness. The stiffness is essentially due to the dynamics of the hydraulic actuators. In the real driving simulator, the forward model simulation is not required because the real Stewart platform would replace it. Thus, it is assumed that real-time simulations can be achieved when a real Stewart platform is used. Moreover, parallelization of computational load would certainly improve the real-time performance.

Some applications of parallel manipulators require precise trajectory tracking. Moreover, other constraints like limits on the interaction forces are imposed in a variety of critical operations like surgery, space craft docking, etc. These requirements were not considered in this chapter. To satisfy the conflicting requirements of trajectory tracking and force control, the overwhelming control strategy needs amendment so that extra interaction forces can be accommodated [5]. Such control objectives are achieved by using virtual flexible foundations in the controller domain, which has been discussed in the previous chapters dealing with the impedance control of serial manipulators.

References

1. T.K. Bera, K. Bhattacharyya, A.K. Samantaray, Bond graph model based evaluation of a sliding mode controller for combined regenerative and antilock braking system. *Proc. IMechE Part I J. Syst. Control Eng.* **225**(7), 918–934 (2011)
2. T.K. Bera, A.K. Samantaray, Bond graph model-based inversion of parallel manipulator systems. *Int. J. Model. Simul.* **31**(4), 331–342 (2011)
3. T.K. Bera, A.K. Samantaray, R. Karmakar, Robust overwhelming control of a hydraulically driven three-degrees-of- freedom parallel manipulator through a simplified fast inverse model. *J. Syst. Control Eng.* **224**(2), 169–184 (2010)
4. T.K. Bera, K. Bhattacharyya, A.K. Samantaray, Evaluation of antilock braking system with an integrated model of full vehicle system dynamics. *Simul. Model. Pract. Theor.* **19**(10), 2131–2150 (2011)
5. T.K. Bera, R. Merzouki, B. Ould Bouamama, A.K. Samantaray. Force control in a parallel manipulator through virtual foundations. *Proc. IMechE Part I J. Syst. Control Eng.* **226**(8), 1088–1106 (2012)
6. T. Chung, J. Kim, K. Yi, Human-in-the-loop evaluation of a vehicle stability controller using a vehicle simulator. *Int. J. Automot. Technol.* **5**(2), 109–114 (2004)
7. A.K. Ghosh, A. Mukherjee, M.A. Faruqi, Computation of driving efforts for mechanisms and robots using bond graphs. *Trans. ASME J. Dyn. Syst. Meas. Control* **113**(4), 744–748 (1991)
8. N. Hogan, Impedance control: An approach to manipulation: Part I-theory. *J. Dyn. Syst. Meas. Control, Trans AMSE* **107**(1), 1–7 (1985)
9. K. Krishnaswamy, P.Y. Li, Bond graph based approach to passive teleoperation of a hydraulic backhoe. *J. Dyn. Syst. Meas. Control* **128**(1), 176–185 (2006)
10. A Mukherjee, R. Karmakar, and A. K. Samantaray. *Bond Graph in Modeling, Simulation and Fault Identification* (CRC Press), 2006 ISBN: 978-8188237968, 1420058657
11. P.M. Pathak, R.P. Kumar, A. Mukherjee, A. Dasgupta, A scheme for robust trajectory control of space robots. *Simul. Model. Pract. Theory* **16**, 1337–1349 (2008)
12. P.M. Pathak, A. Mukherjee, A. Dasgupta, Impedance control of space robots using passive degrees of freedom in controller domain. *J. Dyn. Syst. Meas. Control Trans ASME* **127**(4), 564–578 (2005)
13. P.M. Pathak, A. Mukherjee, A. Dasgupta, Attitude control of a free-flying space robot using a novel torque generation device. *Simulation* **82**(10), 661–677 (2006)
14. P.M. Pathak, A. Mukherjee, A. Dasgupta, Impedance control of space robot. *Int. J. Model Simul.* **26**(4), 316–322 (2006)
15. A.K. Samantaray, B. Ould Bouamama, *Model-based Process Supervision—A Bond Graph Approach* (Springer, London, 2008)
16. Scanner-OKTAL. Scanner driving simulation engine, (2012) <http://www.scannersimulation.com/>. Accessed 3 March 2012
17. A. Sharon, N. Hogan, D.E. Hardt, Controller design in the physical domain. *J. Franklin Inst.* **328**(5–6), 697–721 (1991)
18. K. Youcef-Toumi, D.A. Gutz, Impact and force control: modeling and experiments. *J. Dyn. Syst. Meas. Control, Trans. AMSE* **116**, 89–98 (1994)
19. Y. Zhu, E.J. Barth, Passivity-based impact and force control of a pneumatic actuator. *J. Dyn. Syst. Meas. Control, Trans ASME* **130**(2), 024501–024507 (2008)

Index

A

Accelerometer, 175
 piezoelectric accelerometer, 177
 seismic accelerometer, 175
Accuracy, 622
AC motor, 138
Activated bond, 39, 165
Activation
 activated bond, 41
 effort activation, 39
 flow activation, 39
Activation energy barrier, 553
Active bond graph elements, 31
Active magnetic bearing, 402
Active suspension, 483
Actuators, 4
Actuator sizing, 276
Adaptive compensation, 844
Adaptive control, 232
Adaptive suspension, 495
Adaptive threshold, 598
Aerodynamic drag, 507
Affinity, 542
 affinity of the reaction, 542
 forward affinity, 542, 543
 reverse affinity, 542, 543
After-burner, 558
Air-fuel ratio, 454
Air gap, 404, 411
Alarm, 583
 generation, 583
 interpretation, 583
Algebraic loop, 245
Alkaline fuel cell (AFC), 538
Amnesia, 746
Analogue to digital (A/D) conversion, 194
Analytical redundancy relation, 581, 582

Andrew's mechanism, 297
Angular dynamics, 711
Angular velocity transformations, 722
Anode, 537, 544
Antilock braking system (ABS), 506
Anti-roll bar, 498
Anti-roll system, 499
Anti-sway bar, 498
Application
 robust FDI, 603
Arm dynamics, 712
ARR, 582
 generation, 596
Artificial intelligence, 7
Artificial muscle, 378
Attitude, 705
Augmented controller and observer, 251
Automated guided vehicle, 772
Automated passenger vehicle, 772
Automatic transmission, 529
Automatic transmission system, 470
Autonomous vehicle, 585
Auxiliary volume, 496

B

Backlash, 121, 124, 458
Beam
 beam column, 328
 boundary conditions, 326, 336
 buckling, 328
 centrifugal stiffening, 337
 damping matrix, 335
 equivalent cross-section, 340
 Euler–Bernoulli beam, 322
 Eulerian convention, 331
 Newtonian convention, 331

- B** (*cont.*)
- Rayleigh beam, 331
 - stiffness matrix, 332
- Bearing**
- attitude angle, 399
 - journal bearing, 397
 - magnetic bearing, 402
 - pressure distribution, 398
 - rolling element bearing, 393
- Behavioral equations, 27
- Behavior model, 267
- Bicausality, 50, 269
- Bicycle vehicle model, 509
- Bimetallic strip, 341
- Bimorph, 361, 363
- Biologically-inspired, 378
- Biologically inspired system, 366
- Bipartite graph, 596
- Bipolar plates, 564
- Bipolar transistor, 205
- as an amplifier, 209
 - buck converter, 212
 - common emitter model, 208
 - Darlington transistor, 212
 - Ebers-Moll equations, 219
 - equivalent circuit, 222
 - h-parameter model, 217
 - laterally diffused NPN BJT, 222
 - linearized model, 217
 - linking current, 222
 - thermal model, 226
- Blending function, 535
- Block diagram, 103, 240
- conversion from bond graph, 59
- Body lean, 497
- Body roll, 497
- Bond**
- activated, 39
 - strong, 44
 - vector bond, 84
- Bond graph**
- bicausal, 50
 - causal, 43
 - definition, 18
 - energy variables, 20
 - invention, 19
 - power variables, 19
 - reduction, 63
 - scalar bond graph, 93
 - simplification, 63
 - software, 101
 - state variables, 56
 - structure, 60
 - uncertain bond graph, 97
 - vector bond graph, 84
 - word bond graph, 15
- Braking torque, 506
- Bulk modulus, 162
- Bumper sensor, 174
- Butler-Volmer equation, 553
- C**
- C-element, 27
- C-field, 155, 480
- for ideal gas, 155
 - four port C-field, 545
- Camber, 497
- Capacity factor, 534
- Cardan angles, 308
- Cathode, 537, 544
- Causal loop, 244
- Causal path, 50, 244
- Causal stroke, 42
- Causality, 42
- assignment, 44
 - conflict, 43
 - derivative, 46, 596
 - derivative causality, 44
 - integral causality, 44, 46
- Causality assignment, 43
- Cell flooding, 565
- Cell temperature, 559, 562
- Center of gravity, 807
- Centrifugal force, 497
- Characteristic polynomial, 240, 259
- Chemical equilibrium, 540, 541
- Chemical potential, 156, 543, 547, 568
- Chemical reaction kinetics, 541
- Choked-flow condition, 157
- Circulatory force, 417
- Clutch, 466
- automatic clutch, 470
 - friction clutch, 466
 - pressure control, 469
 - uniform pressure assumption, 467
 - uniform wear assumption, 468
- Coefficient of absorption, 534
- Coefficient of friction, 505
- Coherence vector, 583
- Collapsible chamber, 449
- Combustion, 454, 558
- efficiency, 455
 - heat of combustion, 455
- Compliance, 28
- Compound planetary gear, 530
- Concentration, 542
- Connecting rod, 447

Constitutive equations, 27
 Constraint space, 276
 Contact patch, 502
 Continuously variable transmission (CVT),
 518, 526
 Controllability, 253
 Controllability matrix, 262
 Control reconfigurability, 845
 Convection of gas mixture, 547
 Coordinate transformation, 310, 522, 916
 Cornering force, 502, 512
 Coulomb friction, 289
 Coupling capacitor, 48
 Coupling element for thermo-fluid (CETF),
 380, 559
 Crank shaft, 462
 Cumulative sum, 580

D

Damper valve, 499
 Data circuit-terminating equipment, 897
 Data terminal equipment, 897
 DC motor
 bond graph model, 102
 brushless motor, 138
 compound wound, 134
 H-bridge control, 137
 maximum power, 136
 permanent magnet, 131
 series wound, 133
 shunt wound, 134
 speed control, 136
 torque speed characteristic, 132, 134
 Decision procedure, 583
 Decision rules, 580
 Decision support system, 580
 Defined element, 83
 Derivative causality, 47
 Detectability Index, 601
 Detector of effort (De), 39
 Detector of flow (Df), 39
 D-H Parameters, 629
 Diagnosis
 uncertain system, 596
 Differential, 459, 502
 bevel gear differential, 461
 epicyclic differential, 459
 Differential causality, 47
 Differentiator circuit, 192
 Diffusion process, 544, 554
 Digital micromirror device, 360
 Diode, 136, 196
 light-emitting diode (LED), 199

 photodiode, 198
 Shockley diode equation, 196
 Directional control valve, 300
 Distributed parameter system, 321
 Double layer capacitor, 374, 569
 Drill motion, 764
 Drive train, 532
 Driver view, 921, 928
 Driving simulator, 909
 Dualized detectors, 596

E

Eddy current, 407, 413
 Efficacy mass, 352
 Electrical transformer, 139, 405
 Electric power assisted steering (EPAS), 502
 Electric vehicle model, 78
 Electro-active polymer, 387
 Electrolyte, 537, 564
 Electromagnet, 404
 Electromagnetic induction, 138
 Electromechanical coupling factor, 346, 352
 Electromotive force, 130, 889
 Electronic control unit (ECU), 437
 Electrostatic actuator, 150
 Encoder, 169
 absolute encoder, 171
 binary code conversion, 172
 gray code, 171
 incremental encoder, 170, 174
 most significant bits (MSB), 172
 resolution, 171
 Energy harvesting system, 370
 Engine, 447, 449
 efficiency map, 455
 engine thermodynamics, 449
 V8 engine, 462
 Enthalpy of reaction, 555
 Entropy change, 540
 Entropy generation, 82, 159, 555
 Equivalent circuit, 407
 Error dynamics, 253
 Euler angle, 308, 313, 317, 722, 916
 Euler equations, 96, 310
 Euler junction structure (EJS), 96, 310, 443, 720

F

False alarm, 580, 583
 Fault accommodation, 578
 Fault detection, 578
 Fault detection and diagnosis, 845
 Fault indicator, 880

F (*cont.*)

Fault isolation, 578
 Fault signature, 592
 Fault signature matrix, 583, 584, 591
 Fault tolerance, 11
 Fault tolerant control (FTC), 592
 FDI
 robust, 596
 Finite element modeling, 321
 Finite zeroes, 267, 271
 First law of thermodynamics, 540
 Flexible body system, 282, 321
 Flexible joint, 290
 Flux density, 139
 Flux leakage, 404, 413
 Flux path, 410
 Flywheel, 447, 463, 532
 Force control, 305, 493, 706
 Force-current factor, 411
 Force-displacement factor, 411
 Forward kinematic, 620
 Forward model, 267, 271, 915, 926
 Free-floating space manipulator, 734
 Free-floating space robot, 704
 Free-flying robot dynamics, 714
 Frequency response, 488
 Friction, 125
 entropy flow rate, 155
 friction law, 125
 stick-slip friction, 126
 Fringing flux, 404, 413
 Fuel cell, 537
 cell temperature management, 566
 hydration level, 565
 reformer, 566
 water content management, 565
 Fuel cell stack, 539, 564
 Fuel utilisation (FU), 556
 Fundamental thermodynamic relation, 545

G

Gas mixture, 545
 Gas short circuit, 565
 Gas spring, 499
 Gearbox, 458
 Gear efficiency, 535
 Gear mesh, 505
 Gear shift, 470, 535
 Generalized displacement, 20
 Generalized likelihood ratio, 580
 Generalized momentum, 20
 Geometrical analysis, 580
 Gibbs-Duhem equation, 159

Gibbs free energy, 551, 555, 568
 Gibbs function, 541
 Gimbal frame, 315
 GY-element
 gyrator modulus, 36
 modulated gyrator, 37
 Gyrator
 definition, 36
 equivalence, 407
 modulation, 37
 ring, 96, 443

H

H-bridge, 136
 Hardware-in-the-loop simulation, 437
 Heat exchanger, 558
 Heat transfer, 158
 Hertzian contact, 288
 Holonomic constraints, 707
 Homogeneous transformation matrices, 627
 Human-in-the-loop simulator, 909
 Human-machine interface, 909
 Hybrid bond graph, 214
 Hybrid electric vehicle (HEV), 525
 Hybrid position/force control, 706
 Hybrid synergy drive (HSD), 528
 Hybrid system, 366
 Hybrid vehicle, 525
 Hydraulic actuator, 300, 490, 918
 Hydraulic cylinder, 302
 Hydraulic damper, 492
 Hydraulic servomotor, 151
 Hydraulic servo-system, 300
 Hysteresis, 407
 Hysteretic damping, 356

I

Ideal gas, 545
 Ideal gas law, 155
 Identification, 578
 I-element, 29
 Impedance, 694
 Impedance control, 695, 706
 Inchworm motor, 366, 369
 Induction, 406
 Induction motor, 141
 squirrel cage motor, 144
 Inertial sliding motion, 348, 364
 Infinite zeroes, 267
 Information and communication
 technologies, 769
 Information bond, 37

Integral power steering, 501
 Integrated circuit (IC), 181
 Integrator circuit, 191
 Intelligent autonomous vehicle, 770
 Intelligent transport systems, 769
 Internal damping, 323, 334
 Internal energy, 155, 540, 545
 Internet protocol, 871
 Inverse kinematic, 621
 Inverse Laplace transform, 251
 Inverse model, 267, 269, 271, 915, 921
 Irreversible process, 540
 Isolability, 583
 Isolatability, 592

J

Jacobian, 621, 640, 752
 Joint clearance, 285, 288
 Junction, 32
 one, 34
 zero, 33

K

Kelvin–Voigt model, 356
 Kinematics of rotation, 718
 Kinematics of translation, 721
 Kinetic energy, 30
 Knowledgebase, 8

L

Lagrange formulation, 642
 Lateral stability, 505
 Law of mass action, 542, 543
 Lenz's law, 130
 LFT
 definition, 97
 Light emitting diode (LED), 170
 Limit switch, 173
 Limiting current, 554
 Linear dynamics, 710
 Linear fractional transformation, 97, 596
 Linear matrix inequality, 844, 878
 Liquid spring, 477
 Load cell, 178
 Load leveling system, 490
 Longitudinal slip ratio, 505
 Lorentz force, 130, 372, 374
 Low-bandwidth system, 490
 Lyapunov function, 516
 Lyapunov stability, 516

M

Maglev system, 402
 Magnetic bearing, 402
 single sided bearing, 410
 two-sided bearing, 411
 Magnetic circuit, 140
 Magnetic field, 130, 373, 403
 Magnetic field intensity, 405
 Magnetic flux, 139, 149
 Magnetic force, 411
 Magnetic permeability, 404, 410
 Magnetohydrodynamic effect, 372
 Magnetomotive force, 139, 148, 405
 Markov process, 903
 Martensite fraction, 376, 380
 Mass transfer, 157
 Material damping, 323
 Mechanical trail, 502
 Mechanism
 belt drive, 128
 cam drive, 116
 Four bar, 115
 gear drive, 120
 slider crank, 112
 Membrane electrode assembly
 (MEA), 549, 560
 Memcapacitor, 391
 Memristive system, 389
 Memristor, 388
 Method of effort map, 69
 Method of flow map, 69
 Method of gradual uncover, 57
 Micro-electro-mechanical systems
 (MEMS), 360
 optical MEMS, 360
 Micro-robotics, 378
 Micromirror, 360
 Microprocessor, 180
 Micropump, 372, 374
 Minimum-phase system, 273
 Misdetection, 580, 583
 Modelling
 levels of modelling, 15
 Modeling uncertainties, 580
 Mole flow rate, 543, 552
 Moment of Inertia, 641
 Monitorability, 583, 591
 Moving average, 580
 MR element, 547
 MR-fluid, 486
 Multi bond graph, 724
 Multibody system, 281, 306
 Multiport
 C-field, 86

M (*cont.*)

- gyrator, 93
- I-field, 88
- IC-field, 91
- R element, 84
- R-field, 92
- transformer, 92
- Multi-scale model, 544

N

- Natural frequency, 495
- Nernst equation, 552, 568
- Nernst voltage, 554, 556
- Networked control system, 869
- Network thermodynamics, 544, 556
- Neural bond graph, 387
- Newton-Euler equations, 310, 318, 442, 915
- Newton-Euler Formulation, 645
- Newton's equations, 307
- Nitinol, 376
- Nodal line, 308
- Non-equilibrium reaction kinetics, 543
- Non-holonomic, 707
- Non-holonomic constraints, 707
- Non-holonomic system, 510, 707
- Non-ideal source, 415
- Non-inertial reference frame, 306
- Non-minimum-phase system, 273
- Non-power-conserving gyrator, 528
- Non-power-conserving transformer, 535
- Nonlinear elements, 79
- Nozzle equation, 548
- Nozzle flow, 85
- Nozzle flow equation, 452
- Null modes, 260, 261
- Nyquist frequency, 274

O

- Object oriented modeling, 718
- Observability, 253
- Observability matrix, 265
- One DOF space robot, 724
- Onsager reciprocity, 544
- Operating mode, 592
- Operational amplifier (op-amp), 181
 - adder circuit, 187
 - comparator, 195
 - differentiator, 192
 - ideal op-amp model, 181
 - integrator, 191
 - inverting configuration, 184
 - non-inverting configuration, 185

- subtraction circuit, 189
 - voltage gain, 185
- Optimal control, 276
- Oversteer, 498
- Over-voltage, 553, 555, 569
 - activation, 553
 - concentration, 554
 - Ohmic, 553
- Overwhelming control, 910
- Overwhelming controller, 683
- Oxygen utilisation (OU), 556

P

- P-V diagram, 465
- Pads, 724
- Pad structure, 49
- Parallel manipulator, 915
- Partial pressure, 545, 554
- Passive elements, 25
- Passive suspension, 476
- Pendulum
 - bob pendulum, 283
 - gyro-pendulum, 308
- Pendulus mass, 500
- Phase transformation, 376
- Phosphoric acid fuel cells (PAFC), 538
- Photo emitter, 174
- Photo resistor, 170, 174
- PI controller, 560, 562
- PID, 900
- Piezo-bar, 177, 352, 356
- Piezoelectric constants, 346
- Piezoelectric effect, 345
- Piezoelectric material constitutive relations, 347
- Piezoelectric sensor, 176
- Pitch plane vehicle model, 73
- Plane impedance, 283
- Planetary gear, 459, 530
- Planetary gear system, 526
- pn junction, 196
- Pneumatic actuator, 153
- Pneumatic suspension, 78
- Point potential method, 65
- Polarisation curve, 557
- Polarization resistance, 374
- Pole placement, 252
- Polymer electrolyte, 564
- Poppet valve, 494
- Positive displacement pump, 151
- Potential energy, 28
- Potentiometer, 168
- Power-assisted steering, 501

Power bonds
 definition, 17, 18
 Power density, 557
 Power direction, 62
 Power modulator, 276
 Power split device (PSD), 526
 Power steering, 501
 Precision, 622
 Preferred derivative causality, 49
 Preferred integral causality, 49
 Pre-heater, 558
 Prismatic actuator, 305
 Prismatic joint, 318
 Proportional gain, 763
 Proton exchange membrane fuel cell (PEM-FC), 538, 564
 Proximity sensor, 174
 Pseudo bond graph, 21, 378, 558
 Pseudo-elasticity, 376
 Pulse width modulation (PWM), 136
 PZT, 345

Q

Quarter car model, 476, 486
 Quaternion, 315

R

Rack and pinion, 502, 505
 slider crank, 122
 Randles equivalent circuit, 374
 Rapson slide, 294
 Rate valve, 496
 Reaction advancement coordinate, 542
 Reaction heat, 568
 Reaction rate, 541
 Received data, 897
 Reconfigurable systems, 6
 Reconfiguration, 495, 592
 Regeneration, 500
 Regenerative braking, 517, 528
 Regenerative suspension, 485
 Relative degree, 266, 267, 271, 273
 R-element, 26
 Reliable linear quadratic, 844
 Reluctance, 140, 405, 413
 Repeatability, 622
 Residual, 580, 582
 evaluation, 580
 generation, 580
 sensitivity, 580
 threshold, 584
 Resistance control, 493

Resonant frequency, 490
 Reversible cell voltage, 556
 Revolute joint, 285, 287
 R-field, 158, 512, 547
 for heat transfer, 158
 transistor model, 209
 Rigid body acceleration, 641
 Rigid body dynamics, 95
 Rigid link, 284
 RobuCar, 585
 Robust overwhelming controller, 730
 Roll pitch and yaw, 309
 Roll stiffness, 497
 Root loci, 267
 Rotation matrix, 310
 Rotation vector, 308
 Rotor
 internal damping, 416
 material damping, 416
 passage through resonance, 424, 425
 rigid rotor, 396
 Sommerfeld effect, 415
 source interaction, 414
 source loading, 418
 unbalance response, 420
 RS element, 82, 159, 452
 RS-field, 362, 547, 554, 570

S

Sample and hold device, 194
 Scalar bond graph, 93
 Second law of thermodynamics, 540
 Self-aligning moment, 441, 502, 512
 Self-leveling, 499
 Self-motor, 462
 Semi-active suspension, 492
 Semi-automatic transmission, 529
 Semiconductor diode, 196
 current-voltage characteristic, 197
 forward bias, 196
 reverse bias, 197
 saturation current, 198
 Sensitivity
 index, 600
 normalized, 600
 Sensitivity analysis, 599
 Sensor, 4, 39
 Sensor element, 38
 Sequential probability ratio, 581
 Seven-body mechanism, 297
 Shannon's sampling theorem
 Shannon frequency, 274
 Shape memory alloy (SMA), 376

S (*cont.*)

SMA wire, 424
 Shift logic map, 536
 Signal bond, 37
 Signal conditioning, 5, 180
 Signal flow graph, 912

- branches and gains, 233
- conversion, 232
- example, 235
- forward path, 237
- loop gain, 237, 249
- Mason's gain rule, 236, 249
- nodes, 233
- receptors, 234

 Simulink, 294
 Simultaneous localization and mapping, 771
 Single fault hypothesis, 591
 Singularity, 621
 Sky-hook damper, 486
 Slalom manoeuvre, 474
 Slider

- planar slider, 291
- three-dimensional slider, 318

 Slider-crank, 447
 Sliding mode control, 514
 Sliding surface, 515
 Sliding velocity, 534
 Slip

- lateral slip ratio, 440
- longitudinal slip ratio, 440
- slip ratio, 469
- Tyre slip, 439

 Slip angle, 498
 Slip control, 506, 514
 Slip-friction curve, 505
 Slow-active system, 490
 Smart actuator, 377
 Software-in-the-loop simulation, 437
 Solenoid, 403
 Solenoid actuator, 147

- clapper solenoid, 149

 Solid oxide fuel cell (SOFC), 538, 539
 Sommerfeld effect, 415
 Source

- effort, 31
- flow, 31
- modulated, 32

 Source-sensor, 269
 Space vehicle dynamics, 710
 Specific enthalpy, 547
 Specific entropy, 545
 Speed ratio, 534, 535
 Spinning top, 315
 Spool valve, 300, 494, 500, 501

Sprung mass, 477, 487, 495
 Stabilizer bar, 498
 State equation, 56
 State space, 55
 State-transition matrix, 275
 Stationary wavelet transform, 875
 Steer-by-wire, 501
 Steering, 446

- Ackermann steering, 446
- slalom manoeuvre, 474
- steering response, 473
- steering wheel, 447
- yaw rate controller, 447

 Steering column, 504
 Steering gear, 501
 Steering linkage, 501, 505
 Steering wheel, 503
 Stepper motor, 145

- claw pole motor, 146
- holding torque, 145
- permanent magnet motor, 146
- step angle, 145
- variable reluctance motor, 145

 Stewart platform, 909, 915
 Stick-slip effect, 348
 Stick-slip friction, 365, 370
 Stoichiometric coefficient, 541
 Strain gauge, 175, 177
 Stress influence coefficient, 382
 Structural analysis, 256, 271
 Structural changes, 578
 Structural controllability, 262, 487
 Structural equations, 32
 Structural independence, 583
 Structural observability, 264
 Structural rank, 259
 Supervisory control, 7
 Suspension system, 444, 474, 498
 Sweet-spot, 506
 switch function, 743
 Switching control, 493
 System inversion, 913

T

Tachogenerator, 175
 Takagi-Sugeno technique, 875
 Test drive, 928
 Tetrahedron of state, 387
 TF-element, 35

- modulated, 35
- transformer modulus, 35
- transformer orientation, 36

 Thermal cracking, 559, 566

- Thermal expansion, 341
 - Thermodynamics, 155
 - Thermofluid transport, 86
 - Three DOF space robot, 724
 - Throttle valve, 453
 - Timer, 227
 - Tip trajectory error, 735
 - Tire sensor, 506
 - Top, 315
 - Torque control, 761
 - Torque converter, 470, 532, 533
 - Torque ratio, 534, 535
 - Torsion bar, 501, 504
 - Trajectory control, 705, 729
 - Transducer, 162
 - active, 163
 - passive, 163
 - Transduction factor, 411
 - Transfer function, 267, 489
 - forward path, 54
 - from bond graph model, 245, 246
 - from signal flow graph, 236
 - from state space model, 238
 - loop gains, 54
 - Mason's gain rule, 54
 - Transformer
 - definition, 34
 - Transformer equivalence, 407
 - Transformer modulus, 35
 - Transistor, 136, 205
 - Transmission control protocol, 871
 - Transmission efficiency, 536
 - Transmitted data, 897
 - Triple phase boundary (TPB), 540, 554
 - True bond graph, 19
 - Turbine, 532
 - Two-force member, 282
 - Tyre
 - Burckhardt formulae, 441
 - composite slip based formulation, 445
 - cornering coefficient, 441
 - friction model, 441
 - longitudinal stiffness, 440
 - Pacejka's magic formula, 441
 - self aligning moment, 441
 - tyre forces, 439
- U**
- Uncertain ARRr
 - generation, 597
 - Uncertain bond graph, 97
 - Uncertain systems, 595
 - Understeer, 498
- U**
- Unicausality, 269
 - Unit circle, 275
 - Universal serial port, 874
 - Unsprung mass, 477, 487, 495
- V**
- Valve timing, 452
 - Vector bond, 84, 93
 - Vector bond graph, 84
 - Vector junction, 93
 - Vehicle
 - model of four wheel vehicle, 438
 - Vehicle simulator, 926
 - Velocity gain, 763
 - Velocity propagation, 639
 - Virtual foundation, 698, 754
 - Virtual reality, 912
 - Voigt notation, 347
- W**
- Wet SMA actuator, 378
 - Wheel
 - model, 444
 - suspension force, 445
 - Wheel acceleration control, 506
 - Wheel locking, 505
 - Wien bridge oscillator, 201
 - Wireless tool kit, 872
 - Word bond graph, 104
 - Workspace, 622
- X**
- XOR gate, 172
- Y**
- Yaw angle, 308, 909
 - Yaw dynamics, 779, 817
 - Yaw motion, 587, 926
 - Yaw rate, 474
 - Yttria stabilized zirconia (YSZ), 539
- Z**
- Zero-dimensional model, 544
 - Zero dynamics, 272
 - Zero-order causal path, 52
 - Zero-order-hold, 275
 - z-Transform, 274
 - Z-Y-X Representation, 722